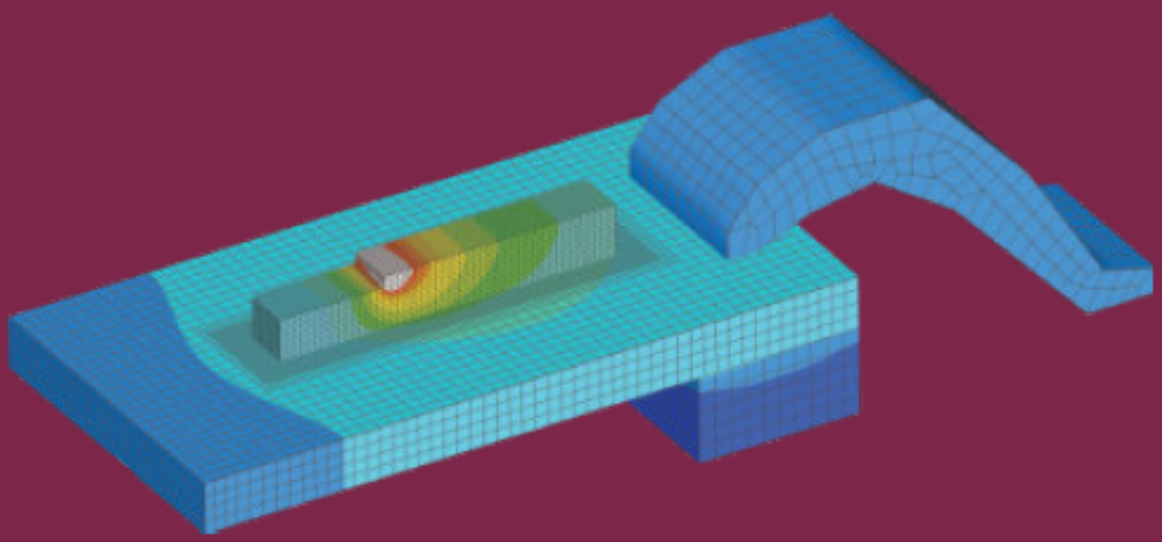
# MATHEMATICAL MODELLING OF WELD PHENOMENA 14

Edited by
C. Sommitsch
N. Enzinger
P. Mayr



# MATHEMATICAL MODELLING OF WELD PHENOMENA 14



The delegates of the 14th International Seminar 'Numerical Analysis of Weldability' held from 21 - 24 September 2025 at Schloss Seggau near Graz, Austria

# MATHEMATICAL MODELLING OF WELD PHENOMENA 14

Selected peer reviewed papers from the
**14th International Seminar**
**Numerical Analysis of Weldability**
September 21 - 24, 2025
Graz - Schloss Seggau - Austria

Edited by

**Christof Sommitsch**
Institute of Materials Science, Joining and Forming
Graz University of Technology

**Norbert Enzinger**
Institute of Materials Science, Joining and Forming
Graz University of Technology

**Peter Mayr**
Materials Engineering of Additive Manufacturing
Technical University of Munich



2026 Verlag der Technischen Universität Graz
Technikerstraße 4, 8010 Graz
verlag@tugraz.at
www.tugraz-verlag.at

ISSN: 2410-0544
ISBN (print) 978-3-99161-089-2
ISBN (e-book) 978-3-99161-090-8
DOI (complete volume) 10.3217/978-3-99161-089-2



This work is licensed under the Creative Commons Attribution 4.0 International (CC BY 4.0) license.
https://creativecommons.org/licenses/by/4.0/deed.en

This CC license does not apply to the cover, third party material (attributed to other sources) and content noted otherwise.

Review Process Coordinator

**Bettina Schreiner-Fößl**

Production Secretary, Typeset, Layout

**Isabella Knollseisen**

Institute of Materials Science, Joining and Forming
Graz University of Technology

Printed & bound
Koralpendruckerei, Deutschlandsberg, Austria
www.koralpendruckerei.at

# Table of Contents

**Introduction** **1**

## I Welding Processes

### a) Arc Welding, Melt Pool & Solidification

**Evaporation and mass transfer in welding** **5**
*P. F. Mendez*

**Numerical sensitivity analysis of material parameters in TIG welding arc modelling** **47**
*M. Le Gal La Salle, S. Cadiou, M. Courtois, M. Carin, A. Brosse*

**Enhancing GMAW simulations through a hybrid Eulerian and Lagrangian method considering an inclined welding torch** **75**
*O. Mokrov, S. Warkentin, L. Westhofen, J. Bender, R. Sharma, U. Reisgen*

**Towards accurate thermal simulations in PBF: A novel calibration strategy for Gauss-Goldak heat-source models** **109**
*M. Hofmann, T. Mayer*

### b) Laser & Electron Beam Welding

**Multi-physics simulation and trajectory optimization in laser welding of copper hairpin windings** **131**
*P. Rana, M. Sreejith, C. Obergfell, M. Kaiser, P. Mayr*

**A statistical investigation of the laser energy absorption and keyhole stability in high-power laser beam welding** **147**
*X. Meng, S. Putra, M. Bachmann, M. Rethmeier*

**Understanding the origin and prediction of laser welding defects in highly reflective metals: A numerical study applied to A2219 alloy** **161**
*B. F. Chetan, M. Courtois, S. Cadiou, M. Carin, V. Nain, F. Machi, A. Alves Ferreira*

**Reconstruction of the time-averaged keyhole geometry in laser beam welding assisted with electromagnetic effect** **179**
*F. Yang, X. Meng, S. N. Putra, M. Bachmann, M. Rethmeier*

**Impact of modeling assumptions on simulated melt pool dynamics compared to high-speed x-ray observations** **195**
*J. Plewinski, F. Hennig, C. Forster, S. Belousov, A. Zakirov, B. Korneev, C. Spurk, M. Hummel, A. Olowinsky, F. Beckmann, J. Moosmann, M. Schmidt, H. Köstler, M. Markl*

**Numerical simulation of laser beam welding with dynamic beam shape sequencing** **225**
*C. Durán, C. Zenz, T. Florian, M. Buttazzoni, A. Otto*

## c) Additive Manufacturing

**Multiphysics simulation of spatial-temporal beam shaping in laser powder bed fusion using openfoam** **249**
*B. Zhou, J. Barode, V. K. Nadimpalli, A. Bauch, D. Herzog, J. H. Hattel, M. Bayat*

**Advanced process modeling and simulation of multi-material directed energy deposition** **267**
*E. Osmanoglu, C. Canaz, N. Hempel, P. Mayr*

**Advanced thermal management strategy for arc-based directed energy deposition assisted by numerical modeling** **281**
*T. Reindl, N. Hempel, P. Mayr*

**Solution approaches for the efficient modelling of the layer build-up in the WAAM manufacturing process using smoothed particle hydrodynamics** **301**
*O. Mokrov, S. Warkentin, L. Westhofen, J. Antonissen, J. Bender, R. Sharma, U. Reisgen*

## d) Special Joining Processes

**Numerical analysis of mechanical behavior during friction stir welding** **315**
*S. Maeda, K. Ikushima, M. Shibahara*

**Numerical analysis of ultrasonic vibration enhanced friction stir welding of TI/AL dissimilar alloys** **337**
*X. Zhang, L. Shi, C. Wu*

**Multiphysics simulation of resistance spot welding** **353**
*I. Ben Bahaffa, M. Courtois, S. Cadiou, E. Geslain, E. Courtois, T. Dupuy, X. Chen*

**Thermohydrodynamic modeling of laser cutting for residual laser energy quantification using a hybrid level set – moving mesh method** **369**
*R. Meillour, M. Courtois, C. Nahed, I. Doyen, M. Carin*

## II Joint Properties

### a) Microstructure and Mechanical Properties

**Modeling and simulation of the anisotropic thermal expansion of TI-6AL-4V processed by PBF-LB/M** **387**
*T. Mayer, P. Capozzi, M. Hofmann, F. Friso, R. Radis*

**Developing a multi-phase welding simulation with damage prediction sourcing on standardized tensile tests and experimental validation by damaging a weldment** **415**
*C. Schröder, T. Loose, M. Brodt*

**Fracture mechanics behavior of HSS steel welded joint heterogeneous structure - experimental and numerical evaluation** **433**
*D. Tomerlin, N. Gubeljak, D. Kozak, W. Li, N. Trišović*

### b) Residual Stresses and Distortion

**Development of residual stress model for welded box sections using probabilistic approach** **455**
*A. Horváth, D. Kollár*

**High-temperature strain gauge measurements in WA-DED: Validation of numerical models** **473**
*H. Drexler, M. Moschinger, N. Enzinger*

**Heat transfer and fluid flow model assisted mechanical analysis for wire arc directed energy deposition to improve residual stress and distortion prediction** **491**
*P. K. Diljith, Aryan, W. Zhang, A. De*

**Prediction of residual stresses of repaired austenitic stainless steel welded joints** **507**
*S. Hilal, S. Hendili, J. Delmas, P. Pereira Alvarez, V. Robin, E. Derniaux, T. Boutin*

**Residual stress simulation of aluminum castings using a temperature-dependent heat transfer coefficient during immersion quenching** **525**
*L. Helml, S. Maier, T. Wlanis, W. Artner, R. Kahlenberg, G. Fuchs, E. Kozeschnik*

### c) Cracking Phenomena and Hydrogen Effects

**Simulation of standardized weldability tests and linkage with fracture and fatigue behavior** **547**
*H. Fu and H. F. Nied*

**Experimental and numerical study on ductility capacity for solidification cracking in laser beam welding** **573**
*N. Habibi, A. Gumenyuk, M. Rethmeier*

## III Methods

### a) Modelling Tools and Computer Programs

**Machine learning-accelerated calibration of complex heat source models for welding and additive manufacturing process simulation** **589**
*Y. Luo, A. Kudva, E. Jang, S. Matan, N. M. Vega Michalak, J. A. Paulson, A. Perrault, B. Alexandrov*

**WA-DED specific topology optimization of a kingpin plate for semi-trailers** **611**
*F. Haunreiter, M. Silmbroth, K. Bharadwaj, H. Drexler, M. Schwendinger, H. Bruhns, A. Bauer*

**Different approaches to visualizing simulations of welding processes** **629**
*L. Kesselburg, S. Warkentin, O. Mokrov, R. Sharma, U. Reisgen*

**A simplified hybrid methodology for determining welding heat source parameters in high-strength steels** **645**
*M. Dadkhah, T. Nitschke-Pagel, K. Dilger*

**A review of welding modelling approaches for nuclear industry** **665**
*A. Brosse, N. Khelif, T. Leveille, S. Gallée*

**Evaluation of FEM-based macro-scale and micro-scale thermal simulation for efficient process adaptation in directed energy deposition additive manufacturing** **681**
*A. M. Pakdel Sefidi, V. Mashetty, M. Ben Ghorbel, R. Ossenbrink, K. Schricker*

**Pipeweld, a software suite for computational welding mechanics for nuclear applications** **711**
*J. Delmas, S. Hendili, S. Hilal, P. Pereira Alvarez, V. Robin*

**An automatic anisotropic meshing algorithm adapted to the multiphysics simulation of a tungsten inert gas welding arc** **727**
*S. Gounand*

**Large-scale numerical analysis of multi-pass welding using automesh and idealized explicit FEM** **741**
*W. Wang, S. Sasaki, S. Maeda, K. Ikushima, M. Shibahara*

**Author Index** **763**

# INTRODUCTION

This volume contains the papers presented at the 14th International Seminar 'Numerical Analysis of Weldability', held from September 21st to 24th, 2025, at Schloss Seggau near Graz, Austria. As always, this location provided an inspiring environment encouraging friendly and intensive discourse between scientists and engineers. The conference stood up to its reputation as one of the most important forums in the science of welding. The meeting was organized by the Institute of Materials Science, Joining and Forming (IMAT) of Graz University of Technology, and the working group 'Mathematical Modelling of Weld Phenomena' of Commission IX of the International Institute of Welding (IIW).

The unique tradition of publishing (all articles refereed, typeset and edited in uniformity; each article is required to be comprehensive in its content) could be maintained also for this edition to serve the welding community as reference literature. The continuity of the previous thirteen volumes, Mathematical Modelling of Weld phenomena 1 – 13, has therefore been preserved thanks to the monumental efforts of the Seggau team of IMAT. Special thanks goes to Bettina Schreiner-Fößl, who was in charge of the entire work of coordinating the peer review as well as Isabella Knollseisen for assisting her in the layout creation and editing procedure in a highly ambitious manner. Volume 14 is again published by Verlag der Technischen Universität Graz and all papers have a DOI and are available open access.

The 2025 seminar was attended by more than 90 delegates coming from 15 countries participating in both, oral sessions and poster presentations in the following sessions:

I. Welding Processes
   a. Arc Welding, Melt Pool & Solidification
   b. Laser & Electron Beam Welding
   c. Additive Manufacturing
   d. Special Joining Processes

II. Joint Properties
   a. Microstructural Modelling in Weld Metal and Heat Affected Zone
   b. Microstructure and Mechanical Properties
   c. Residual Stresses and Distortion
   d. Cracking Phenomena & Hydrogen Effects

III. Methods
   a. Modelling Tools and Computer Programs

The most important observations of this seminar were the fact that modelling approaches in the meantime penetrate many fields of application in welding and recently in additive manufacturing. It helps to solve complex tasks and optimize the welding processes and materials used. By this, it helps to enhance the safety, reliability and economy of welded structures. This was impressively shown by many authors who in addition could verify the calculation results by experimental investigations.

The 2025 IIW Kenneth Easterling Best Paper Award was won by the paper “Modeling and simulation of the anisotropic thermal expansion of Ti-6Al-4V processed by LPBF”, *T. Mayer, P. Capozzi, M. Hofmann, F. Friso, R. Radis* from ZHAW School of Engineering in Switzerland. This paper has been valued by an international committee as the best contribution made over the three years proceeding on the advancement of knowledge or practice in respect of mathematical modelling of weld phenomena.

The next International Seminar ‘Numerical Analysis of Weldability’ will take place from September 24$^{th}$ – 27$^{th}$, 2028 at Schloss Seggau.

Christof Sommitsch, Norbert Enzinger and Peter Mayr
Graz, May 2026

# I Welding Processes

## a) Arc Welding, Melt Pool & Solidification

# EVAPORATION AND MASS TRANSFER IN WELDING

P. F. MENDEZ*

**Canadian Centre for Welding and Joining, University of Alberta, Canada. Email: pmendez@ualberta.ca*

*DOI 10.3217/978-3-99161-089-2-001, license CC BY 4.0*
*https://creativecommons.org/licenses/by/4.0/deed.en*
*This CC license does not apply to third party material and content noted otherwise.*

ABSTRACT

This paper reviews the foundations of evaporation and mass transfer in welding operations, presenting for the first time a treatment with simultaneous barriers to mass transfer in the molten metal, at the evaporating surface, and in the surrounding gases. Evaporation is a crucial aspect of welding operations, as it controls fume emissions, arc properties, droplet temperature, porosity, and onset of explosive metal transfer in GMAW of Al-Mg alloys. When evaporation is large a recoil pressure is significant, leading to keyhole penetration in focused beams. The treatment accounts for multicomponent mass transfer, and explicit expressions for the resistance to mass transfer for each component and each stage are provided. A novel treatment for diffusion in the melt is proposed by using an equivalent mass transfer resistance in the melt which allows for the simultaneous consideration of all mass transfer resistances. The treatment of mass transfer also includes a treatment of recoil pressure. The theory is applied to mass transfer and evaporation in the electrode tip in GMAW, with detailed analysis of three experiments with results supporting the theory. Based on the theoretical foundations a criterion for explosive transfer is proposed, reproducing the type and intensity of explosive transfer observed. The treatment presented is also a foundation for a comprehensive formulation of mass and energy balances in deposition rate.

Keywords: Fumes, Metal vapors, mass balance, Energy balance, Recoil pressure

## INTRODUCTION

Mass transfer and evaporation in welding have been studied often in the past. There are many motivations for this attention. Evaporation is the source of fumes in welding, which are a topic of much relevance to industrial practice [1], especially Mn and $Cr^{6+}$ components that are often viewed as harmful [2]. Manganese in welding fumes is believed to cause an illness (Manganism) with symptoms similar to Parkinson's disease, and $Cr^{6+}$ is considered a carcinogen. In addition to health considerations, fumes caused by metal evaporation cause productivity losses by required cleaning (e.g. before painting).

Not all effects of evaporation are undesirable, for example selective evaporation during local laser melting of Nitinol shape-memory wires results in changes in transition temperature that can be controlled to design tailor-made components.

An understanding of evaporation is needed for a proper treatment of mass and energy balances [3-4]. In addition to the energy associated with evaporation, there is evidence that evaporation plays a significant role in droplet temperature; for example, although steel has a much higher melting temperature than aluminum, their boiling temperatures are comparable, and so are their droplet temperatures in GMAW. Conversely, the addition of Mg (which has a low boiling temperature) in aluminum wires decreases the droplet temperature. Further analysis of these observations requires an understanding of evaporation.

Metal vapors have a large effect on arc behavior and voltage, with the consequent implications in power source control and waveform design. An understanding of evaporation and the metal vapors surrounding the melt is a necessary step to understand the plasma sheaths around the electrode and plate, especially in the anode.

An understanding of mass transfer is needed to treat the observed behavior of explosive transfer observed in solid wires with high amounts of volatile elements, such as 5XXX aluminum wires.

Despite the strong reasons for understanding mass transfer and evaporation in welding, and despite the amount of attention paid to it, mass transfer in the melt, evaporation, and in the gas have not yet been considered together. In [5], only surface evaporation was considered, while in [6] and [7], only the surface evaporation and gas diffusion are considered, and in [8], only diffusion in the melt is considered.

The treatment in this work is based on the physics of mass transfer with emphasis on the engineering concepts of boundary layer and mass transfer resistance. The mathematical treatment is in the form of engineering expressions such as those used in standard textbooks on heat and mass transfer.

The treatment is general, valid for any alloy and inert shielding gas. Oxidizing shielding gases commonly used in steels such as Ar-2%$O_2$ or Ar-10% $CO_2$ are outside the scope of analysis, indeed, even the experiments considered were made with pure Ar. The reason for this limitation is that oxidizing gases react in a way that affects boundary layer thickness, and currently there are no practical expressions for their behavior. The engineering treatment of reactive boundary layers is an exciting area of future work of impact far beyond welding.

The quantitative treatment of boundary layers and mass transfer resistances leverages on the mathematical analogy between fluid flow, heat transfer, and mass transfer, such that advanced expressions for mass transfer can be postulated based on extensive studies of heat transfer, of which the literature is much more abundant.

In all cases, the expressions verified in practice were never accurate than ±20% considering uncertainty in the physics, configurations, and fluid properties. In this work, the sign "=" is used in almost all equations for simplicity instead of "≈", with the understanding that the existing expressions used and the new expressions derived are far from mathematical equalities.

In this work three experiments are considered which are representative of a larger set of experiments performed in the past. The goal of the experiments chosen is to be illustrative, as a proper validation of the foundations presented here will require a few theoretical extensions

listed in the Discussion section, as well of simultaneous measurements that although possible, have never been performed before, such as simultaneous droplet temperature measurements and fume characterization. Similarly, the theory developed has been applied as a case study only to the electrode tip in GMAW, but other applications such as evaporation from the weld pool in GTAW or power beams in conduction mode could readily be considered.

The ultimate goal of this work is on setting a foundation for future modeling and experimental work with a higher level of understanding of the physical mechanisms involved and interplay of process parameters.

## FUNDAMENTALS OF MASS TRANSFER

### THE CONCEPT RESISTANCE TO MASS TRANSFER

The concept of resistance to mass transfer ($\Re$) is an analog of electrical resistance, but it is associated with the steady or quasi-steady mass transfer $\dot{m}$ between two points A and B in the same phase. It is defined in this work as

$$\Re = \frac{c_{\mathrm{A}} - c_{\mathrm{B}}}{\dot{N}} \tag{1}$$

where $c_A$ and $c_B$ correspond to the concentrations of solute in the phase considered in mol $m^{-3}$, and N is the molar flow from point A to point B.

This definition assumes that the chemical potential of the solute in the phase considered is proportional to its concentration. This consideration, it is not directly applicable to the case when points A and B are in different phases such as liquid and gas. When multicomponent mass transfer is considered (e.g. simultaneous mass transfer of Fe and Mn), the component considered is indicated in the subscript, e.g. $\Re_{\mathrm{Fe}}$, $\dot{N}_{\mathrm{Fe}}$ . The definition of $\Re$ stays the same if concentration and flow involve units of mass instead of mol.

When mass transport happens in the gas phase, considering the gases and vapors as ideal gases:

$$c_j = \frac{p_j}{RT} \tag{2}$$

where $c_j$ is the concentration of a vapor component $j$, $p_j$ is its partial pressure, and $T$ its temperature, resulting in

$$\Re_j = \frac{p_{A\,j} - p_{B\,j}}{RT\dot{N}_j} \tag{3}$$

where $p_{A_j}$ and $p_{B_j}$ are the partial pressures of the vapor component $j$ at points A and B, both at the same temperature $T$. The effects of temperature gradients on mass transport in gases are not considered in this work, but future work should incorporate them.

**Resistances in series** One convenient feature of the concept of resistance to mass transfer is that it can tackle with efficiency problems with multiple mass transfer mechanisms. In particular, when the mass transfer mechanisms are sequential, the problem can be modeled as a set of resistance in series.

$$\Re_{\mathrm{tot}_j} = \Re_{1_j} + \Re_{2_j} \tag{4}$$

where $\Re_{\mathrm{tot}_j}$ is the total resistance to mass transfer for component *j*, $\Re_{1_j}$ and $\Re_{2_j}$ are two resistors in series. The applicability of this equation is limited to resistances to mass transfer *in the same phase*. The reason is that the driving force for diffusion is different if a concentration gradient is in one phase (e.g. molten metal) or another (e.g. gas phase).

Under some conditions, it is possible to define an ``equivalent' resistance to mass transfer that takes into account the different phases.

**Dominant resistance** The value of resistances to mass transfer might be different by an order of magnitude or more. When multiple resistances to mass transfer are in series, if a resistance is much smaller than the others, it can be neglected to simplify calculations; if a resistance is much larger than the sum of all others, it can be considered dominant and all other resistances can be neglected. When the largest resistances are of comparable magnitude, they are in an intermediate regime where none is dominant; for example, in the electrode tip in GMAW of Al-Mg alloys, the resistance to mass loss of aluminum is typically dominated by the gas phase, while for Mg, the resistance of evaporation is negligible and the resistances in the melt and in the gas are comparable.

**Resistance per unit area** An important concept associated with mass transfer resistance is that of ``resistance associated with a unit area " $\Re$'':

$$\Re_j'' = \frac{c_{A_j} - c_{B_j}}{J_j} \tag{5}$$

where $J_j$ is the molar flow per unit area (mol $s^{-1}$ $m^{-2}$) of component *j*. This concept is useful when mass transfer happens over an extended area, such as evaporation at the surface of the molten electrode or the molten weld pool.

Typical values of $\Re_j''$ at the electrode tip in GMAW are of the order of $10^3$ s $m^{-1}$ for Mn in molten steel wires, $10^2$ s $m^{-1}$ for Mg in molten aluminum, and $10^{-1}$ s $m^{-1}$ for metal vapors in Ar of the shielding gas. If a resistance per unit area is obtained, a flux can be calculated as

$$J_j = \frac{c_{A_j} - c_{B_j}}{\Re_j''} \tag{6}$$

with its analog for gases:

$$J_j = \frac{p_{A_j} - p_{B_j}}{RT\Re_j''} \tag{7}$$

For an area *A* of constant flux:

$$\Re_j'' = A\Re_j \tag{8}$$

and for an area $A$ over which the flux varies, an average resistance to mass transfer is defined as

$$\overline{\Re''_j} = A\Re_j \tag{9}$$

Note that the magnitude $A$ is multiplied, not divided as would be expected in a quantity associated with a unit area. A mass flux $\dot{m}''$ in kg s$^{-1}$ m$^{-2}$ is related to the molar flux as

$$\dot{m}''_j = M_j J_j \tag{10}$$

where $M_j$ is molar mass of component $j$ in kg mol$^{-1}$. A total mass transfer can be obtained as

$$\dot{m}_j = AM_j\bar{J}_j \tag{11}$$

where $\bar{J}_j$ is the surface average flux over area $A$. The amount of mass evaporated from the tip of a GMAW electrode is of the order of 1% of the electrode mass.

## MECHANISMS OF MASS TRANSFER

Resistances to mass transfer can be associated with different mechanisms. The application of these mechanisms together with the concept of boundary layer result in practical expressions to evaluate mass transfer in welding. These expressions are approximate even under the idealized conditions in which they were developed, with an accuracy not better than 20% [9]. Natural convection is typically negligible for both molten metal [6], shielding gas, and vapors [10] in the active part of welding (around the weld pool and molten consumable). The temperature of a gas evaporating from a free surface at temperature $T_s$ is slightly lower than $T_s$, but they will be assumed to be the same for simplicity.

### *Diffusion*

Diffusion for component $j$ is associated with Fick's law. When diffusivity is constant:

$$\Re_{\text{diff}_j} = \frac{1}{S_j D_j} \tag{12}$$

where $S$ is the "shape factor" associated with a given geometry. Shape factors are tabulated for many ideal geometries [9]. For a sphere of radius $a$ in an infinite medium $S=4\pi a$, and for the case of uniform diffusion across a layer of surface area $A$ and thickness $\eth$ , such as the gas boundary layer on the free surface of molten metal at the electrode or weld pool, $S=A/\eth$ where $\eth$ is the thickness of the layer, resulting in

$$\Re_{\text{diff, layer}_j} = \frac{\eth}{AD_j} \tag{13}$$

and its equivalent associated with a unit area

$$\Re''_{\text{diff, layer}_j} = \frac{\mathfrak{d}}{D_j} \tag{14}$$

When diffusivity varies across the thickness of the layer, an effective value of diffusivity is proposed in Appendix A. Parameters for the calculation of diffusivity of components in molten steel and aluminum are given in Appendix B, and of metal vapors in shielding gases in Appendix C

*Advection*

Advection is the transport of a quantity by the motion of matter. For a given surface of a control volume, advection of a solute across a control surface is

$$J_{\text{adv}_j} = c_j u_j \tag{15}$$

where $c_j$ is the concentration of solute component $j$ and $u$ is the component of velocity perpendicular to the surface of the control volume. the velocity $u$ is a velocity in the molten metal, gas, or vapor.
For vapors exiting the surface during evaporation, if the vapors are treated as an ideal gas and the volume of liquid or solid is neglected:

$$u_j = J_{\text{adv}_j} \frac{RT_s}{p_{s_j}} \tag{16}$$

where $u_j$is the velocity of vapor component $j$ exiting the surface in a direction perpendicular to it, $J_{\text{adv}_j}$ is the molar flow of vapor component $j$, $T_s$ is the temperature of the evaporating surface, and $p_{s_j}$ is the partial pressure of vapor component $j$ just outside the surface. Of course, this equation is valid for subsonic velocities and pressures high enough for an ideal gas behavior.

*Convection*

The combination of diffusion and advection in fluids results in convection. Across an interface in which one side is a fluid, viscous, thermal, and diffusion boundary layers establish on the fluid side (this applies to both sides on a fluid-fluid interphase such as shielding gas over molten metal). Convective mass transport into the fluid happens by diffusion across the diffusion boundary layer, and can be quantified as

$$J_{\text{conv}_j} = \mathfrak{h}_j \left( c_{s_j} - c_{\infty_j} \right) \tag{17}$$

where $c_{s_j}$ and $c_{\infty_j}$ are the concentrations of component $j$ in the fluid near the surface and just outside the boundary layer. The units of $\mathfrak{h}_j$are m s$^{-1}$. Typical values of $\mathfrak{h}_j$ at the electrode tip in GMAW are of the order of $10^{-3}$ m s$^{-1}$ for Mn in molten steel wires, $10^{-2}$ m s$^{-1}$ for Mg in

molten aluminum, and $10^1$ m s$^{-1}$ for metal vapors in Ar of the shielding gas. The mass transfer resistance of convection is obtained by applying the definition of thermal resistance (Equation 5) to Equation 17, resulting in

$$\Re''_{\text{conv}\,j} = \frac{1}{\mathfrak{h}_j} \tag{18}$$

*Evaporation*

Evaporation from a surface is typically described as [11]

$$J_{e\,j} = \beta_j \frac{p_{\text{l,s}\,j} - p_{\text{g,s}\,j}}{\sqrt{2\pi M_j R T_s}} \tag{19}$$

where $p_{\text{l,s}\,j}$ is the vapor pressure of component $j$ in the melt at the free surface, and $p_{\text{g,s}\,j}$ is the pressure of the metal vapor in the gas right at the free surface and $\beta_j$ is the coefficient of evaporation and condensation for component $j$, always below 1, but close to it [11]. Considering the gas as ideal, Equation 2 can be applied to the definition of resistance to mass transfer (Equation 1) resulting in the following mass transfer resistance for evaporation:

$$\Re''_{\text{e}\,j} = \frac{1}{\beta_j}\sqrt{\frac{2\pi M_j}{R T_s}} \tag{20}$$

Although Equation 20 involves both the liquid and gas phases, it is based on the concentrations in the gas phase. If Mn is evaporating from an ER70S steel GMAW electrode (approximately 1 wt% Mn), the concentration used with this mass transfer resistance is not the molar volume of 1 wt% Mn in the molten steel, but instead the much larger molar volume of 1 wt% Mn as a vapor at the temperature of the free surface and corresponding vapor pressure or partial pressure. The resistance associated with evaporation is typically negligible at the electrode tip in GMAW.

**Multicomponent evaporation** In multicomponent evaporation, the partial vapor pressure of component *j* in the melt is proportional to the activity in the alloy [5]

$$p_{\text{l}\,j} = a_j p_{\text{lg}\,j} \tag{21}$$

where $p_{lg\,j}$ is the equilibrium vapor pressure of element $j$ in pure state. In this case, we will approximate the activity $a_j$ using Raoult's law:

$$a_j = X_j \tag{22}$$

where $X_j$ is the molar fraction of $j$ on the evaporating surface.

$$X_j = \frac{c_j M}{\rho} \tag{23}$$

with $\rho$ being the density and $M$ the overall molar mass of the melt

$$M = \left( \sum_j \frac{f_j}{M_j} \right)^{-1} \tag{24}$$

with $f_j$ the mass fraction of component $j$ in the melt. Parameters to calculate vapor pressure are tabulated in Appendix D. Conversion formulae for mass and molar fractions are listed in Appendix E. The overall density and molar mass $M$ are typically very close to those of the main alloy component, such as aluminum or iron.

**Effective diffusion resistance in the melt** Equations 21-23 indicate that composition variations in the melt could be expressed in terms of the vapor pressures associated with each composition.

$$\Delta c_{\mathrm{l}_j} = \frac{\rho}{p_{\mathrm{lg}_j} M} \Delta p_{\mathrm{l}_j} \tag{25}$$

where $\rho$ and $p_{\mathrm{lg}_j}$ are taken at the temperature of the free surface. Replacing the concentration difference in Equation 6, we obtain

$$J_j = \frac{\rho}{M p_{\mathrm{lg}_j} \Re''_{l\,j}} \Delta p_{\mathrm{l}_j} \tag{26}$$

Comparing Equation 26 with Equation 7, we can define an equivalent resistance for diffusion in the melt $\Re''_{\mathrm{l,eq}_j}$ that can be used in the reference frame of metal vapors

$$\Re''_{\mathrm{l,eq}_j} = \frac{p_{\mathrm{lg}_j} M}{\rho R T_s} \Re''_{\mathrm{l}\,j} \tag{27}$$

The conversion factor in Equation 27 is of the order of $10^{-2}$ for Mg in Al and $10^{-4}$ for Mn in steel in the cases considered.

**Recoil pressure** Conservation of momentum indicates that the mass evaporated causes a pressure (``recoil pressure") on the free surface from where it originates. Recoil pressure has been studied in insufficient detail in the past because it requires an understanding of mass flow affected by boundary layers in the liquid and gas phases, as well as evaporation. In [12], the recoil pressure is obtained with electromagnetic arguments alone, while in [13], a recoil pressure is calculated neglecting the heat conducted into the substrate and without accounting for resistance to mass transfer. In [14], the recoil pressure is calculated semi-empirically without accounting for mass transfer mechanisms that dominate the rate of evaporation.

The recoil pressure is in addition to the partial pressure of the vapor. At high surface temperatures, the rate of evaporation is fast and the recoil pressure is significant, for example recoil pressure is the cause of a keyhole in power beam welding. The total recoil pressure is given by the addition of the recoil pressures of each evaporating component

$$p_{\mathrm{rec}_j} = \dot{m}''_j u_j \tag{28}$$

where $\dot{m}''_j$ is the rate of mass of component *j* evaporated (Equation 10) and $u_j$ is the velocity of the vapors exiting the surface (Equation 16), resulting in

$$p_{\mathrm{rec}_j} = {J_j}^2 \frac{M_j R T_s}{p_{\mathrm{g,s}_j}} \tag{29}$$

where $p_{\mathrm{s}_j}$ is the partial pressure of component *j* at the surface, always higher than the recoil pressure, such that

$$p_{\mathrm{g,s}_j} = p_{\mathrm{rec}_j} + p_{\mathrm{diff}_j} \tag{30}$$

with $p_{\mathrm{diff}_j}$ being the partial pressure of component *j* at the surface when considering only diffusion in the gas boundary layer $\Re''_{\mathrm{g}_j}$. Using Equation 7 with a metal vapor pressure of zero away from the boundary layer:

$$p_{\mathrm{diff}_j} = R T_{\mathrm{s}} \Re''_{\mathrm{g}_j} J_j \tag{31}$$

Equations 30 and 31 can be combined to solve for $J_j$, and this flux can be used into Equation 29 resulting in the following equation

$$\frac{p_{\mathrm{rec}_j}}{p_{\mathrm{g,s}_j}} = \left(1 - \frac{p_{\mathrm{rec}_j}}{p_{\mathrm{g,s}_j}}\right)^2 \frac{M_j}{R T_s {\Re''_g}_j^{\,2}} \tag{32}$$

where it can be seen that when the resistance to mass transfer in the gas boundary layer is significant, the recoil pressure is small and can be calculated as

$$p_{\mathrm{rec}_j} = \frac{M_j J_j}{\Re''_{\mathrm{g}_j}} \quad \text{for } p_{\mathrm{rec}_j} \ll p_{\mathrm{g,s}_j} \tag{33}$$

and conversely, if the ratio of mass flow to resistance to mass transfer in the gas boundary layer is large, the recoil pressure dominates the gas pressure on the surface, and $p_{g,s_j} = p_{rec_j}$. In all experiments considered, this was the case, with the recoil pressure being at least 700 times the diffusion pressure. In this case, Equation 29 results in

$$p_{\mathrm{rec}_j} = J_j \sqrt{M_j R T_s} \quad \text{for } p_{\mathrm{rec}_j} \approx p_{\mathrm{g,s}_j} \tag{34}$$

and if the overall dominant resistance to mass transfer is that of evaporation, for example in the evaporation of the main alloy component in vacuum during EBW, incorporating Equation 19, with $p_{s_j}$ results in

$$p_{\mathrm{rec}_j} = \frac{p_{\mathrm{l,s}_j}}{\sqrt{2\pi}/\beta_j + 1} \approx \frac{p_{\mathrm{l,s}_j}}{3.5} \tag{35}$$

This equation gives the maximum possible recoil pressure. The evaporation of pure metals in vacuum was also studied in [15]. Additional mass transfer resistances such as diffusion in the

melt or in the gas will yield lower recoil pressures. For the GMAW cases studied, the recoil pressure was of the order of $10^2$-$10^3$ Pa, much higher than the pressure associated with diffusion (Equation 34), but comparable with the arc pressure at the droplet [16], of a magnitude that could potentially lift the molten droplet.

**Heat loss by evaporation** Evaporating components take away their latent heat as they evaporate. The thermal energy associated with each component is

$$q''_{\mathrm{v}\,j} = \dot{m}''_{\mathrm{v}\,j}\, i_{\mathrm{lg}_j} \tag{36}$$

where $\dot{m}''_{v\,j}$ is the amount of component *j* evaporated (Equation 10) and $i_{lg_j}$ is the enthalpy of evaporation of component *j*. The energy balance due to evaporation has been studied in detail in [17], being of the order of $10^2$ W, or approximately 1% of the whole energy balance for the GMAW experiments performed.

## BOUNDARY LAYERS

Boundary layers are thin regions in a fluid parallel to an interphase, for example in the gas phase surrounding the free surface of molten metal, or in the molten metal just under the free surface. This thin layer contains the significant part of the gradient driving the mass transfer across the interphase.

The concept of boundary layer is valid when it is thin compared to the dimensions of the object being considered. For the case of gases surrounding the molten consumable or the weld pool, the boundary layers need to be much thinner than the characteristic length of the weld pool or molten consumable; for the case of molten metal, the boundary layer needs to be much thinner than the depth of the weld pool or the size of molten consumable.

Three types of boundary layers are relevant in this work: viscous, thermal, and diffusion. There are multiple diffusion boundary layers: one per solute component; for example, in the 5183 aluminum filler metal, there is a diffusion boundary layer for Mg with thickness $ð_{\mathrm{Mg}}$, and another one for Mn with thickness $ð_{\mathrm{Mn}}$, plus additional boundary layers for minor elements.

In this analysis, it is assumed that the solute is relatively dilute in the solvent. This is applicable to steel alloys with approximately 1 wt% of Mn as the volatile component and aluminum alloys which typically contain less than 5 wt% Mg as their volatile component. This hypothesis is not properly fulfilled on occasions in the gas phase when the solute evaporates much more than the solvent. This hypothesis is not appropriate also in multi-princial component alloys. Further work is needed to improve this work under those conditions. An important consequence of considering dilute solutions is that their density can be treated as independent of their composition.

Another consideration in this paper is that of non-reactive boundary layers, i.e., we consider only evaporation in an inert atmosphere such as GMAW of aluminum alloys using pure Ar shielding, and apply the results even in cases of reactive boundary layer such as in GMAW of steel alloys using Ar-$O_2$ or Ar-$CO_2$ shielding. It is known that the reaction reduces the thickness of the boundary layer, resulting in increased evaporation [18-19] and fumes

formation [20] [21]. The association of carbon with oxygen on the surface of the melt can result in decarburization of the melt.

The concept of boundary layer is taken as a good approximation for the case in which the vapor pressure approaches atmospheric pressure. Also, motion at the interphase, such as surface flow velocity of the free surface on a liquid/gas interphase, or velocity caused by the melting or evaporation of the interphase are neglected. These velocities at the interphase are typically negligible when compared to the velocity outside the boundary layer of the fluid in question.

**Diffusion boundary layer** When the diffusivity is constant across the boundary layer (or an effective value is used), the coefficient of mass convection for component *j* relates to the thickness of the diffusion boundary layer as

$$\mathfrak{h}_j = \frac{D_j}{\mathfrak{d}_j} \tag{37}$$

where the thickness of the diffusion boundary layer is defined as

$$\mathfrak{d}_j = \frac{c_{s\,j} - c_{\infty\,j}}{dc_j/dy\,|_s} \tag{38}$$

where $dc_j/dy\,|_s$ is the concentration gradient in the fluid at the interphase. Typical values of diffusion boundary layer thickness at the GMAW electrode tip are 10-100 μm in the melt and 300 μm in the gas phase, both much thinner than the droplet diameter of about 2 mm. The thickness of the diffusion boundary layer is seldom calculated using the definition of Equation 38, so the differential expression seldom needs to be evaluated.

**Viscous boundary layer** The thickness of the related viscous boundary layer is defined in this work as

$$d = \frac{u_\infty}{du/dy|_\mathrm{s}} \tag{39}$$

where $u_\infty$ is the velocity of the fluid just outside the boundary layer and $du/dy|_\mathrm{s}$ is the velocity gradient in the fluid at the interphase. This definition neglects the velocity of the interphase, such as the surface velocity of the molten metal in the weld pool when calculating the boundary layer of gases on the surface of the weld pool.

**Thermal boundary layer** The definition of the thermal boundary layer is

$$\ell = \frac{T_\mathrm{s} - T_\infty}{dT/dy|_\mathrm{s}} \tag{40}$$

where $T_\mathrm{s}$ and $T_\infty$ are the temperature of the fluid at the surface and just outside the boundary layer and $dT/dy|_\mathrm{s}$is the temperature gradient in the fluid at the interphase. The associated convection coefficient for heat transfer is

$$h = \frac{k}{\ell} \tag{41}$$

where *k* is the thermal conductivity of the fluid.

**Tabulation of convection coefficients in boundary layers** The diffusion convection coefficient for each component is tabulated in dimensionless form as the Sherwood number based on a characteristic length *L*.

$$\mathrm{Sh}_j = \frac{\mathfrak{h}_j L}{D_j} = \frac{L}{\mathfrak{d}_j} \tag{42}$$

where the second equality results from application of Equation 37. The thermal convection coefficient is tabulated in dimensionless form as the Nusselt number based on a characteristic length *L*.

$$\mathrm{Nu} = \frac{hL}{k} = \frac{L}{\ell} \tag{43}$$

where the second equality results from application of Equation 41. A mass transfer resistance for the diffusion boundary layer can be obtained from the Sherwood number as

$$\mathfrak{R}_j'' = \frac{L}{D_j \mathrm{Sh}_j} \tag{44}$$

In the laminar case, the average convection coefficients $\overline{h}$, $\overline{\mathfrak{h}}_j$, average Nusselt $\overline{\mathrm{Nu}}$ or average Sherwood $\overline{\mathrm{Sh}}_j$ between *x=0* and *x=L* are $\overline{h}$=*2h*, $\overline{\mathfrak{h}_j}$, $\overline{\mathrm{Nu}}$=2Nu, and $\overline{\mathrm{Sh}}_j$=2Sh$_j$ where *h*, Nu, and Sh$_j$ are local values at *x=L*.

The notation $\overline{\mathfrak{R}_j}$ will indicate a mass transfer resistance calculated with an average Sherwood number ($\overline{Sh_j}$), it is not a mathematical average; however, when integrating mass flux over a surface of area A, because of the parallel nature of mass transfer on each element of surface, it can be stated with mathematical rigor that

$$\mathfrak{R}_j = \frac{AL}{D_j \overline{\mathrm{Sh}}_j} \tag{45}$$

where $\overline{\mathrm{Sh}}_j$ is typically considered that over a flat surface. More accurate calculations are possible for geometries other than a flat surface, but the increase of precision does not justify the increase in complexity in the context of the large uncertainties of the expressions used and the properties of fluids considered.

**Hypotheses of boundary layer theory** Boundary layer theory is based on a number of simplifications that are usually representative of reality. Three key considerations are included here.

The boundary layer is thin compared to the geometry considered: Both $\overline{Sh_j}$ and Nu must be much greater than 1 because the thickness of the boundary layer thickness should be much smaller than the characteristic length. When their value approaches 1, the problem becomes one of static diffusion or conduction heat transfer, not convection.

The flow outside the boundary layer is advection dominated: The Peclet number must be much greater than 1. The Peclet number is a metric of the dominance of advection, and is defined based on the length of the boundary layer *x* as

$$\mathfrak{Pe}_j = \frac{u_\infty x}{D_j} \tag{46}$$

In the experiments considered, the Peclet number was always greater than $10^2$ in the melt and greater than 30 in the gas.

The boundary layer is in quasi-steady state; this implies the hypothesis that the fluid flow is also in quasi-steady state and there was enough time to develop the boundary layer.
A time scale for fluid dynamics can be estimated as

$$t_u = \frac{L}{u} \tag{47}$$

where $L$ is the characteristic length of the flow, and $u$ is the characteristic velocity of the flow. A timescale for the formation of a boundary layer is given by

$$t_{\mathfrak{d}_j} = 0.5\frac{{\mathfrak{d}_j}^2}{D_j} \tag{48}$$

If both $t_u$ and $t_{\mathfrak{d}_j}$ are shorter than the droplet detachment period or waveform times, mass transfer can be approximated as steady-state. For the cases of GMAW studied, $t_u \approx 4$ ms and $t_{\mathfrak{d}_j} \approx 7$ ms, approximately 30% of the droplet detachment time.

*Boundary layer with shear*

When the interphase separates a fluid (molten metal or gas) from a solid (or a static liquid), three types of boundary layers are established: viscous, thermal, and diffusion. The thickness of the viscous boundary layer is relatively independent from the other two and is associated with shear over a solid or liquid surface. The thicknesses of the thermal and diffusion boundary layers depend on the viscous one.

In welding, the motion of gases and molten metal is typically laminar, and this will be the focus of this boundary layer treatment. Some welding processes such as electroslag (ESW) and electrogas (EGW) might involve turbulence. The modeling of the arc in other arc welding processes such as GTAW [10], GMAW, and power beam processes such as laser (LBW) and electron beam (EBW) has traditionally been as laminar flows. There are indications that the weld pool might involve turbulence [22].

Because boundary layers are thin compared to the size of the weld pool or the molten $10^1$able, f$10^3$ quantitative analysis of this section they will be considered as if they were over a flat surface, for which accurate expressions exist [9, 23].

**Viscous boundary layer with shear** Using the definition of Equation 39, the thickness of the viscous boundary layer over a flat plate is

$$d = 3\sqrt{\frac{\nu x}{u_\infty}} \tag{49}$$

where $\nu$ is the kinematic viscosity of the fluid. An effective value of kinematic viscosity is proposed in Appendix A, and temperature-dependent properties for steel and aluminum are in Appendix B. The coordinate *x* is defined along the interphase in the direction of the flow with *x=0* corresponding to the moment the flow starts on the interphase, e.g. the edge of the anode spot on the tip of GMAW electrode of positive polarity, which will be discussed in detail below.

For comparison, the commonly used definition of viscous boundary layer thickness as that where the velocity is 99% of that of the external flow results in a factor of 5 instead of 3 in Equation 49. The concept of viscous boundary layer is valid only when Re $\gg$1. Re is the Reynolds number defined as

$$\mathrm{Re} = \frac{u_\infty x}{\nu} \tag{50}$$

**Thermal boundary layer with shear** The thickness of the thermal boundary in the presence of a viscous boundary layer is

$$\ell \approx \begin{cases} \sqrt{\pi}\sqrt{\dfrac{\nu x}{u_\infty}}\,\mathrm{Pr}^{-1/2} & \text{for } \mathrm{Pr} \ll 1 \\ 3\sqrt{\dfrac{\nu x}{u_\infty}}\,\mathrm{Pr}^{-1/3} & \text{for } \mathrm{Pr} \gtrsim 1 \end{cases} \tag{51}$$

where Pr is the Prandtl number, defined as

$$\mathrm{Pr} = \frac{\nu}{\alpha} \tag{52}$$

with $\alpha$ being the thermal diffusivity. The concept of thermal boundary layer is valid only when Pe $\gg$ 1. Pe is the Peclet number defined as

$$\mathrm{Pe} = \frac{u_\infty x}{\alpha} \tag{53}$$

When using effective values, an effective value for $\alpha$ is proposed in [24]. In molten metals, the value of Pr is typically much less than 1 and in gases is approximately 1, suggesting that the exponent to use in Equation 51 is -1/3. In plasmas Pr is often much less than 1. and the exponent would be -1/2.

A consequence of the value of Pr near or below 1 is that in molten metals and plasmas, the thermal boundary layer is larger than the viscous boundary layer, while for gases the values are comparable. In all cases, the temperature gradient in the viscous boundary layer can be considered approximately linear, making Equation 87 applicable.

Combining equations 41, 51, and 43, a dimensionless expression for thermal convection across a laminar boundary layer with shear is

$$\mathrm{Nu} \approx \begin{cases} \frac{1}{\sqrt{\pi}} \mathrm{Re}^{1/2} \mathrm{Pr}^{1/2} & \text{for } \mathrm{Pr} \ll 1 \\ \frac{1}{3} \mathrm{Re}^{1/2} \mathrm{Pr}^{1/3} & \text{for } \mathrm{Pr} \gtrsim 1 \end{cases} \tag{54}$$

**Diffusion boundary layer with shear** The thickness of the diffusion boundary for each component in the presence of a viscous boundary layer is

$$\mathfrak{d}_j \approx \begin{cases} \sqrt{\pi} \sqrt{\frac{\nu x}{u_\infty}} \mathrm{Sc}_j^{-1/2} & \text{for } \mathrm{Sc}_j \ll 1 \\ 3 \sqrt{\frac{\nu x}{u_\infty}} \mathrm{Sc}_j^{-1/3} & \text{for } \mathrm{Sc}_j \gtrsim 1 \end{cases} \tag{55}$$

where $\mathrm{Sc}_j$ is the Schmidt number, for component $j$ defined as

$$\mathrm{Sc}_j = \frac{\nu}{D_j} \tag{56}$$

In gases, $\mathrm{Sc}_j$ is approximately 1, suggesting that the exponent to use in Equation 55 is -1/3. A consequence of the value of $\mathrm{Sc}_j$ is that in gases the diffusion boundary layer is smaller than the viscous boundary layer. Plasma diffusivity values are not surveyed in this work, but are expected to have a $\mathrm{Sc}_j$ number comparable to gases. Detailed analysis of diffusion in plasmas is in [25 - 27]. In molten metals, the diffusion boundary layer is typically thinner than the thermal boundary layer and in gases it is comparable or thinner. In molten metals, the value of $\mathrm{Sc}_j$ can be larger or smaller than one.

Combining equations 37, 55 and 42, a dimensionless expression for mass convection across a laminar boundary layer with shear is

$$\mathrm{Sh}_j \approx \begin{cases} \frac{1}{\sqrt{\pi}} \mathrm{Re}^{1/2} \mathrm{Sc}_j{}^{1/2} & \text{for } \mathrm{Sc}_j \ll 1 \\ \frac{1}{3} \mathrm{Re}^{1/2} \mathrm{Sc}_j{}^{1/3} & \text{for } \mathrm{Sc}_j \gtrsim 1 \end{cases} \tag{57}$$

*Boundary layer without shear*

At the free surface of the weld pool or at the free surface of the molten consumable, the molten metal is moving, but it is not in contact with a solid that could impose shear forces. In these cases, there is no viscous boundary layer; however, thermal and diffusion boundary layers still exist.

In the absence of shear, there are no steep gradients near the free surface of the molten metal, and this molten metal can be treated as a solid. When the Peclet number (thermal or diffusion) is much larger than 1, conduction and diffusion are essentially 1D processes across

the thickness of the boundary layer, and solutions for a semi-infinite solid such as those in [9] can be applied.

In the absence of shear, the results of equations 51, 55, 54, 57 corresponding to low Pr or low $\mathrm{Sc}_j$ apply to *all* values of Pr or Sc, i.e. the expressions with exponent of 1/2 for Pr or $\mathrm{Sc}_j$ apply to all cases.

### *Mass transfer from a sphere*

The treatment of boundary layers indicates that an analogy between heat and mass transfer is possible by replacing Pr by $\mathrm{Sc}_j$ and Nu by $\mathrm{Sh}_j$ in theoretical or empirical correlations. In addition to the correlations for boundary layer described above, there is a good wealth of empirical correlations for heat transfer for $\mathrm{Pr} \gtrsim 1$ (typical of air, water, and oil) that can be adapted for mass transfer where $\mathrm{Sc}_j \gtrsim 1$ in all relevant cases.

Mass transfer from a sphere of radius $a$ immersed in a fluid of velocity $u_\infty$ can be estimated using the following expression [9]

$$\overline{\mathrm{Sh}_j} = 2 + 0.6\,\mathrm{Re}^{1/2}{\mathrm{Sc}_j}^{1/3} \tag{58}$$

where the Reynolds number is evaluated using the diameter $2a$ as a reference length and the velocity considered is $u_\infty$. The value of 2 corresponds to pure diffusion without advection using the shape factor for a sphere. This equation is an approximation bridging between pure diffusion ($\mathrm{Re} \to 0$) and pure convection ($\mathrm{Re} \gg 1$) using traditional blending [28] with $n$=1. If not using effective values, practical fluid properties are obtained at the "film temperature" intermediate between the surface temperature and the fluid temperature.

## MASS TRANSFER AT THE ELECTRODE TIP IN GMAW

The geometry of the electrode tip varies with time, and this causes the resistances to heat and mass transfer to vary with time. In addition, the local resistances also vary as the geometry and thickness of boundary layers vary across the geometry. The values calculated here are average in space, and for the instant corresponding to each geometry.

### MASS TRANSFER GEOMETRY

The metal transfer configuration has several different configurations [29] [30]. In this work we will consider two representative geometries, illustrated in Figure 1. Future work should be able to capture features such as the molten tail in streaming spray transfer.

In solid wire processes, the droplet diameter is often estimated from droplet detachment frequency, neglecting the mass lost to evaporation:

$$d_{\mathrm{MC}} = \left(\frac{3}{2}\frac{\rho c}{\rho}\frac{U_{\mathrm{C}} d_C^2}{f_{MC}}\right)^{1/3} \tag{59}$$

where $d_{\mathrm{MC}}$ is the droplet diameter, $\rho_{\mathrm{C}}$ is the density of the solid wire, $\rho$ is the density of the melt, $U_{\mathrm{C}}$ is the wire feed speed, $d_{\mathrm{C}}$ is the wire diameter, and $f_{\mathrm{MC}}$ is the frequency of droplet detachment, estimated for the experiments performed using the following empirical expression:

$$f_{\mathrm{MC}} = \begin{cases} CI & \text{for } I \leq I_c \\ AI - B & \text{for } I > I_c \end{cases} \tag{60}$$

where $I_{\mathrm{c}}$, $A$ and $B$ are constants determined empirically, and $C = A - B/I_c$. For ER80S-G, $A$=1.565 $\mathrm{s^{-1}A^{-1}}$, $B$=231.8 $\mathrm{s^{-1}}$, and $I_{\mathrm{c}}$ =180 A. For aluminum wires $A$=2.688 $\mathrm{s^{-1}A^{-1}}$, $B$=319.9 $\mathrm{s^{-1}}$, and $I_{\mathrm{c}}$=128 A. The droplet diameters estimated for the experiments performed are between 0.95 and 2 times the wire diameter.

The area of attachment of the arc to the droplet, in the case of globular and projected spray transfer is approximated as

$$A_{\mathrm{AC,C}} = \pi L_{\mathrm{AC,C}}^2 \tag{61}$$

In the geometry considered, $d_{\mathrm{MC}}$ is the droplet diameter and $L_{\mathrm{AC,C}}$ is the attachment of the arc to the electrode. The size of this attachment is a property of the arc, and there are currently no guidelines on how to predict it. In this work, the size of the arc attachment will be estimated based on the knowledge that the arc attachment at the point of transition from globular to spray transfer is comparable to the wire size. Considering the relationship between wire size and transition current proposed in [31] results in the following approximate estimate for the arc attachment:

$$L_{\mathrm{AC,C}} = CI^2 \tag{62}$$

where $C$=8 $10^{-8}$ m $\mathrm{A^{-2}}$.

## TOTAL MASS EVAPORATED

The total mass evaporated at the electrode tip is composed of the sum of all components of the alloy:

$$\dot{m}_v = \sum_j \dot{m}_{v_j} \tag{63}$$

where $\dot{m}_{v_j}$ is the mass rate of evaporation of each alloying element. The stoichiometry of the metal vapors is different than that of the evaporating melt because of the different vapor pressures of each component. For the examples considered here, steel wires containing 1.7 wt% Mn emit vapors with almost 30 wt% Mn, while aluminum wires with 5% Mg emit vapors with almost 75 wt% Mg.

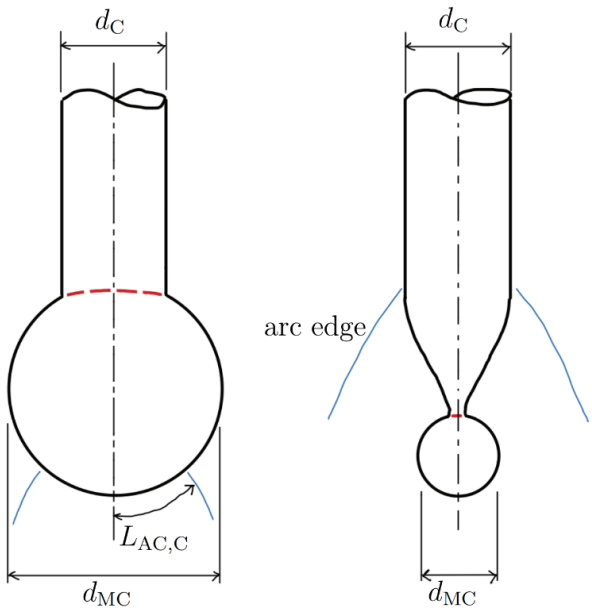



**Fig. 1** Representative configurations for globular transfer (left) and spray transfer (right)

The total mass transport must account for the series resistance to mass transfer in the melt, the interphase, and the gas phase as illustrated in Figure 2. It is convenient to start this analysis with the thermal resistance per unit area defined in Equation 5. These considerations result in the following flux:

$$J_j = \frac{p_j}{RT_s\Re''_{\mathrm{tot}_j}} \tag{64}$$

and the corresponding mass flux:

$$\dot{m}''_j = M_j \frac{p_j}{RT_s\Re''_{\mathrm{tot}_j}} \tag{65}$$

where $p_j$ is the vapor pressure in the melt or partial pressure of vapor in the gas phase and $\Re''_{tot_j}$ total mass transfer resistance.

For the solute, the total resistance is made of the equivalent diffusion resistance in the melt, the mass transfer resistance of evaporation, and the diffusion resistance in the gas phase. Because mass transport happens through both liquid and gas phases, the equivalent diffusion resistance defined in Equation 27 must be used for the melt.

$$\Re''_{\mathrm{tot}_{\mathrm{solute}}} = \Re''_{\mathrm{l,eq}_{\mathrm{solute}}} + \Re''_{\mathrm{e\ solute}} + \Re''_{\mathrm{g\ solute}} \tag{66}$$

For the solvent (eg. Fe or Al), there is no resistance to diffusion in the liquid, instead, as the solute (Mn or Mg) depletes, the solvent concentration increases. The flow of solvent involves only resistances of evaporation and in the gas

$$\mathfrak{R}''_{\mathrm{tot}_{\mathrm{solvent}}} = \mathfrak{R}''_{\mathrm{e}\,\mathrm{solvent}} + \mathfrak{R}''_{\mathrm{g}\,\mathrm{solvent}} \tag{67}$$

and the molar and mass flow is calculated using equations 64 and 65 using the vapor pressure of the melt with higher solvent concentration (depleted of solute at the surface).

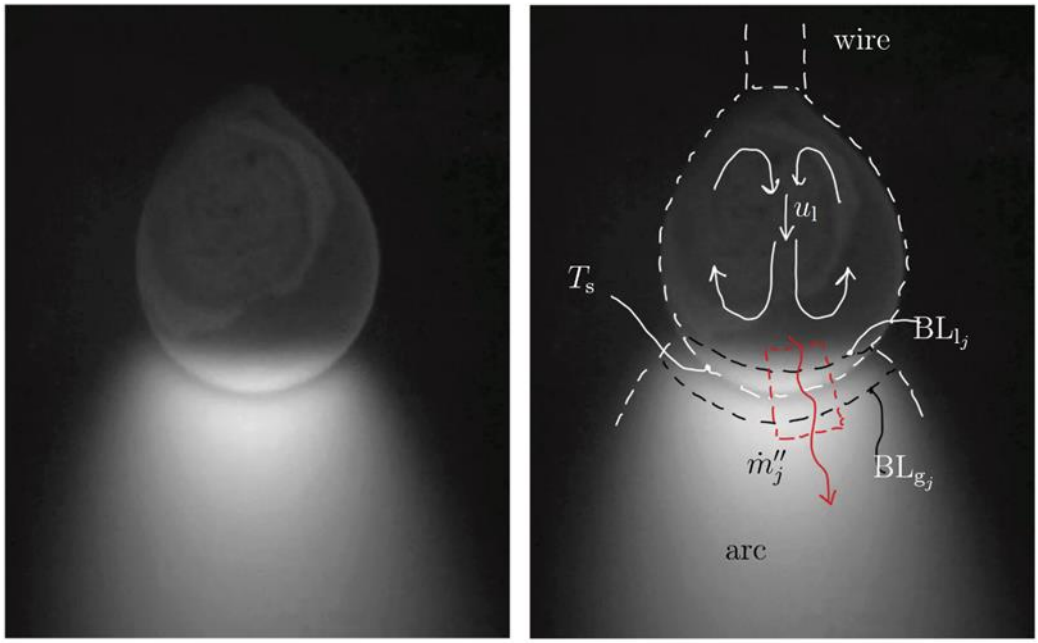



**Fig. 2** Tip of molten electrode illustrating the boundary layer in the melt for component *j* ($BL_{l_j}$), the boundary layer in the gas for component *j* ($BL_{g_j}$), and the control volume for analysis of mass transfer

## RESISTANCE TO MASS TRANSFER IN THE MOLTEN ELECTRODE

The equivalent diffusion resistance per unit area (averaged over the area of diffusion) in the liquid at the electrode tip is calculated based on Equation 27, while the actual resistance is calculated using Equation 18

$$\overline{\mathfrak{R}''_{l}}_{j} = \frac{1}{\overline{\mathfrak{h}_{l_j}}} \tag{68}$$

where the diffusion convection coefficient is calculated from the definition of Sherwood number (Equation 42):

$$\overline{\mathfrak{h}_{l_j}} = \frac{\overline{\mathrm{Sh}_{l_j}} D_{l_j}}{d_{\mathrm{MC}}} \tag{69}$$

with $\overline{\mathrm{Sh}_{l_j}}$ being the average Sherwood number for component $j$ in the molten electrode tip, $D_{l_j}$ the diffusivity of component $j$ in the main metal of the molten electrode, and $d_{\mathrm{MC}}$ is the diameter of the droplet at the tip of the molten consumable, illustrated in Figure 1. Tabulated parameters to calculate diffusivity in the melt are included in Appendix B.

The average Sherwood number involves a diffusion boundary layer just inside the free surface, such that there is no shear, and the treatment of thermal resistance is according to Section 3.3.2. The expression proposed for $\overline{Sh_{l_j}}$ is the following:

$$\overline{\mathrm{Sh}_{l_j}} = 2 + 0.5\mathrm{Re}_{l}^{1/2}\mathrm{Sc}_{l_j}^{1/2} \tag{70}$$

where $\mathrm{Re}_l$ uses $d_{\mathrm{MC}}$ as the characteristic length. This expression is new and was developed for this work, its explanation and its differences with Equation 57 are detailed in this section.

The tip of the molten consumable has a diameter $d_{\mathrm{MC}}$ and two boundary layers: one under the free surface (the object of this analysis), and another boundary layer at the solid/liquid interphase, where the electrode is melting. The thickness of both boundary layers is comparable, and they increase in thickness when the fluid motion inside the electrode tip is slow, as $\mathrm{Re}_l \to 0$. When the thickness of these boundary layers reaches half a diameter of the molten consumable, there is no advection region anymore in the melt, and mass transfer occurs just by diffusion. In that case, the Sherwood number of the boundary layer cannot decrease any more, and can be approximated using Equation 42 where the characteristic length is the diameter of the molten tip ($d_{\mathrm{MC}}$), and the thickness of the diffusion layer is half that diameter. Thus, for very small values of $\mathrm{Re}_l$ the Sherwood number tends to 2.

At higher Reynolds numbers, the boundary layers are thinner and the Sherwood number increases following the behavior of Equation 57 (top, because there is no shear). The characteristic length in this case is a quarter of the perimeter of the molten tip; each boundary layer affects half the tip (near the free surface, and near the solid/liquid interphase, top and bottom of the molten consumable in Figure 1). Also, because of symmetry, each boundary layer is composed of two parts (left and right). Keeping in mind that average values of Sherwood are twice the local value, the coefficient of 0.5 is obtained.

Given the approximate nature of the analysis and of convection expressions in general, it is not worth to apply blending techniques such as those in [28] to better capture intermediate values of Reynolds numbers. The Reynolds number in this case is

$$\mathrm{Re}_l = \frac{u_l d_{MC}}{v_l} \tag{71}$$

where $v_l$ is the kinematic viscosity of the molten metal at the electrode tip, and $u_l$ is the velocity of the free surface. The velocity of the free surface results from the interplay of

multiple physics including electromagnetic and Marangoni forces. Reference [32] proposes that electromagnetic forces are dominant. In spray transfer, the flow of current envelops the molten tip, such that any induced velocity is small and diffusion dominates over advection. In globular transfer and projected spray, an analysis of electromagnetic forces in the melt is similar to that in the arc performed in [16] resulting in the following approximate expression

$$u_l \approx \frac{1}{\sqrt{\pi}}\sqrt{\frac{\mu_0}{\rho_l}}\left(\frac{1}{d_C}-\frac{1}{2L_{\mathrm{AC,C}}}\right)I \tag{72}$$

where $I$ is the welding current, $d_{\mathrm{C}}$ is the diameter of the electrode, $L_{\mathrm{AC,C}}$ is the size of the attachment of the arc indicated in Figure 1, $\mu_0$ is the magnetic permeability of vacuum, and $\rho_{\mathrm{l}}$ is the density of the molten metal. This equation accounts for the fact that if the arc attachment is smaller than the electrode diameter the flow moves upwards, and when the arc attachment is of a size comparable to the electrode diameter the electromagnetic forces are small.

For the case of 1.2 mm steel wires, an arc attachment of 2 mm in diameter, and a molten metal temperature of approximately 2000°C ($\rho_l \approx 6500\,\mathrm{kg\,m^{-3}}$), we obtain $u\,(\mathrm{ms^{-1}})$ =1.5x10$^{-3}$ $I$ (A), which is comparable with the value of 2 x10$^{-3}$ proposed in [32].

A survey of GMAW experiments presented in [17] indicates that the range of $Sh_l$ spans from orders of $10^1$ to $10^3$ in steels and aluminum alloys, indicating that convection dominates over diffusion in the liquid in most cases.

### Resistance to mass transfer at the evaporating surface

The resistance to mass transfer at the evaporating surface can be calculated in a straightforward manner using Equation 20.

$$\mathfrak{R}''_{e\,j} = \sqrt{\frac{2\pi M_j}{RT_s}} \tag{73}$$

### Resistance to mass transfer in the gas surrounding the molten electrode

For the case of diffusion of metal vapors in an inert atmosphere, such as the evaporation of Fe and Mn in Ar, the thermal resistance (averaged over the area of diffusion) in the gas surrounding the electrode tip is calculated based on Equation 18

$$\overline{\mathfrak{R}''_{\mathrm{g}\,j}} = \frac{1}{\overline{\overline{\mathfrak{h}_{\mathrm{g}_j}}}} \tag{74}$$

where the diffusion convection coefficient is calculated from the definition of Sherwood number (Equation 42):

$$\overline{\mathfrak{h}_{g_j}} = \frac{\overline{\mathrm{Sh}_{g_j}} D_{g_j}}{d_{\mathrm{MC}}} \tag{75}$$

with $\overline{\mathrm{Sh}_{g_j}}$ being the average Sherwood number for component $j$ in the gas surrounding the electrode tip and $d_{\mathrm{MC}}$ is the diameter of the droplet at the tip of the molten consumable (Figure 1). The diffusivity $D_{g_j}$ corresponds to component $j$ in the gas surrounding the electrode tip evaluated at a "film temperature" intermediate between the molten surface (of the order of 3000 K for the case of steel and aluminum) and the temperature of the plasma outside the boundary layer near the surface of the electrode (of the order of 7300 K for the case of Ar, resulting in a "film temperature" of approximately 5000 K). Tabulated parameters for the Chapman-Enskog theory to calculate diffusivity in the gas are included in Appendix C.

The average Sherwood number involves a diffusion boundary layer just outside the free surface, such that there is shear of the fast moving gas against the much slower free surface (considered static for this boundary layer). Approximating the electrode tip as a sphere, the Sherwood number of the gas at the tip can be estimated with Equation 58, also used in [33].

$$\overline{\mathrm{Sh}_{g_j}} = 2 + 0.6\mathrm{Re}_{\mathrm{g}}^{1/2}\mathrm{Sc}_{g_j}^{1/3} \tag{76}$$

The Reynolds number in this case is

$$\mathrm{Re}_{\mathrm{g}} = \frac{u_{\mathrm{g}} d_{MC}}{\nu_{\mathrm{g}}} \tag{77}$$

where $u_{\mathrm{g}}$ is the velocity of the gas surrounding the free surface, $\nu_{\mathrm{g}}$ is the kinematic viscosity of the gas surrounding the electrode tip evaluated at a film temperature. The kinematic viscosity and other thermophysical properties for the plasma are provided, for example in [34]. Typical values of $\overline{\mathrm{Sh}_{g_j}}$ are around $10^1$, indicating convection is dominant. Typical values of $\mathrm{Re}_{\mathrm{AC}}$ are of the order of $10^2$. Schmidt numbers in the vapor are around 1.5.

The velocity $u_{\mathrm{g}}$ of gas over the free surface results from the electromagnetic forces present in the arc. In the absence of general correlations, this work will assume that the surface velocity of the gas is the maximum velocity in the arc. This maximum velocity was studied in [16] for the GTAW arc, and will be extended to the GMAW arc, acknowledging the uncertainties in this extrapolation.

$$u_{\mathrm{g}} = \frac{1}{2\pi}\sqrt{\frac{\mu_0}{\rho_{\mathrm{AC}}}}\frac{I}{L_{AC,C}} f_{\mathrm{u_g}} \tag{78}$$

where $\rho_{\mathrm{AC}}$ is the density of the gas in the arc column (at approximately $10^4$ K), and $f_{u_g}$ is a correction factor defined as

$$f_{\mathrm{u_g}} = 0.55\left(\frac{\widehat{\mathrm{Re}}_{\mathrm{AC}}}{4}\right)^{0.073}\left(\frac{2L_{\mathrm{arc}}}{d_C}\right)^{0.0068} \tag{79}$$

with $\widehat{\mathrm{Re}}_{\mathrm{AC}}$ being a nominal Reynolds number calculated using the velocity Eq. 78 without the correction factor $f_{\mathrm{u_g}}$ and the diameter of the molten tip $d_{\mathrm{MC}}$ as a characteristic length. The magnitude $\nu_{\mathrm{AC}}$ is the kinematic viscosity of the plasma at the plasma column temperature (approximately $10^4$ K). The arc length in the experiments made was set at 0.5 in. (12.7 mm), this is a value much longer than typically used in practice but needed to get temperature measurements with the setup used.

### EVAPORATION FLOWS FROM THE ELECTRODE TIP

For the overall flux of component *j*, Equation 7 becomes

$$\bar{J}_j = \frac{p_{\mathrm{l}_j}}{RT_{\mathrm{s}}\overline{\Re''_{\mathrm{tot}_j}}} \tag{80}$$

where $p_{l_j}$ is the vapor pressure at the nominal composition in the bulk of the molten electrode tip, and the vapor pressure of $j$ outside the diffusion boundary layer is 0. In steels and aluminum alloys, the dominant resistance to evaporation of the main component (Fe or Al) is the gas boundary layer (above approximately 95% of total resistance), while for the solute evaporation (Mn or Mg) the resistance of evaporation at the surface is negligible, and the resistance in the melt and in the gas are comparable (typically the resistance in the melt is higher). This is an important finding indicating the importance of boundary layers in mass loses by evaporation, which have been omitted in the welding literature.

### CONCENTRATION PROFILES

Concentrations in the melt and in the gas can be obtained using a standard calculation with mass transfer resistances.

For solute at the surface of the melt:

$$c_{\mathrm{l},s_{\mathrm{solute}}} = c_{\mathrm{l}_{\mathrm{solute}}} - J_{\mathrm{solute}}\Re''_{\mathrm{l}\ \mathrm{solute}} \tag{81}$$

where $J_{\mathrm{solute}}$ is calculated using Equation 26 and equivalent vapor pressures for the melt.

For the solvent, at the free surface of the melt the fraction of solvent is higher because of depletion of solute. Converting the concentration of solute at the surface $c_{l,s_{\mathrm{solute}}}$ to molar fraction ($X_{l,s_{\mathrm{solute}}}$), the molar fraction of solvent is

$$X_{l,s_{\mathrm{solvent}}} = 1 - \sum_j X_{l,s_{\mathrm{solute},j}} \tag{82}$$

In the gas phase it is more convenient to discuss concentration profiles in terms of partial pressure of vapors. The partial pressure of vapors against the free surface can also be

calculated for both solute and solvent using Equation 7, accounting for a zero concentration of metal vapor outside the boundary layer:

$$p_{\mathrm{g,s}_j} = RT_s J_j \mathfrak{R}''_{\mathrm{g}\,j} \tag{83}$$

The overall mass flow of component $j$ is given by Equation 11 using the area of arc attachment $A_{\mathrm{AC,C}}$ (Equation 61), which is an approximation useful for the metal transfer conditions of the experiments performed.

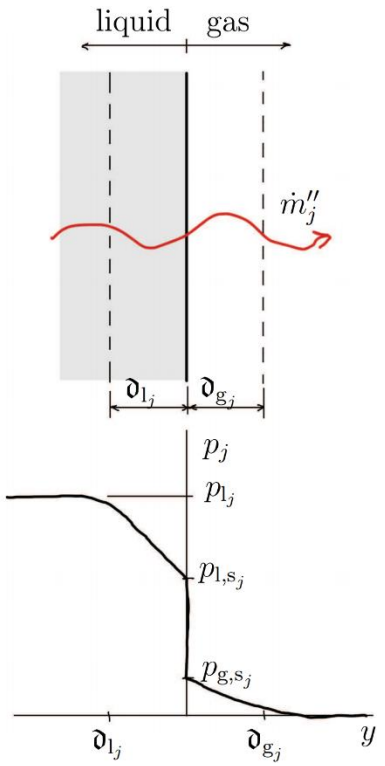



**Fig. 3** Concentration profile for solute component $j$. Gradient in the liquid is due $\mathfrak{R}''_{\mathrm{l}\,j}$, gradient in the gas is due to $\mathfrak{R}''_{\mathrm{g}\,j}$, and the discontinuity at the free surface is due to $\mathfrak{R}''_{\mathrm{e}\,j}$

## EXAMPLE OF APPLICATION

A set of experiments was performed, reported in [17, 35]. Three experiments are selected: E1 for steel consumable ER80S-G (1.7 wt% Mn), E2 for aluminum alloy 5554 (2.7 wt% Mg), and E3 for aluminum 5183 (4.9 wt% Mg). The temperature of the droplet was measured.

## EXPERIMENTS AND PROCESS CONDITIONS

Process conditions and measured temperatures are listed in Table 1, properties of the molten electrode tip are listed in Table 2, and properties of the gas and vapors are listed in Table 3. The properties used for diffusion in the melt indicate that diffusivity of Mg in molten Al is about two orders of magnitude faster than the diffusivity of Mn in molten Fe. This result is surprising, but comparisons with other source for diffusivity in the iron [36] yield similar results. This large difference in diffusivity values also results in large differences in Sc and Sh numbers between steel and aluminum.

**Table 1** Process parameters

| Exp. | Consumable | $f_{solute}$ * wt% | $X_{solute}$ * mol% | $d_C$ mm | $U_C$ cm min$^{-1}$ | $U_C$ m s$^{-1}$ | $I$ A |
|---|---|---|---|---|---|---|---|
| E1 | ER80S-G | 1.74 | 1.77 | 1.20 | 454 | 7.56 $10^{-2}$ | 161 |
| E2 | 5554 | 2.66 | 2.94 | 1.18 | 642 | 1.07 $10^{-1}$ | 141 |
| E3 | 5183 | 4.93 | 5.44 | 1.19 | 612 | 1.02 $10^{-1}$ | 130 |

*solute is Mn and solvent Fe for ER80S-G, solute is Mg and solvent Al for 5554 and 5183

**Table 2** Properties of molten electrode tip

| Exp. | $T_s$ ℃ | $M$* g mol$^{-1}$ | $\rho_C$ † kg m$^{-3}$ | $\rho$ kg m$^{-3}$ | $\nu$ m$^2$s$^{-1}$ | $D_{l_{solute}}$ m$^2$s$^{-1}$ | $Sc_{l_{solute}}$ |
|---|---|---|---|---|---|---|---|
| E1 | 2313 | 55.8 | 7830 | 5424 | 3.03 $10^{-7}$ | 5.37 $10^{-9}$ | 56 |
| E2 | 2210 | 26.9 | 2703 | 1838 | 2.64 $10^{-7}$ | 2.01 $10^{-6}$ | 0.13 |
| E3 | 1730 | 26.8 | 2703 | 2006 | 2.81 $10^{-7}$ | 6.82 $10^{-7}$ | 0.41 |

*molar mass of components in Table3
† solid wire at 20 ℃

The process conditions at the molten electrode tip are listed in Table 4. The molten metal temperature typically exceeds by far the meting temperature, especially for aluminum. The estimated liquid metal velocities are of the order of 0.5 m s$^{-1}$ and the Reynolds number of the order of $10^3$, consistent with the 0.2 m s$^{-1}$ and 500 estimated in [32].

The process conditions in the arc are listed in Table 5. The plasma velocity is surprisingly smaller than the 300 m $s^{-1}$ typical of GTAW. Equation 78 suggests that this is due to the lower plasma temperature (higher gas density) and the larger attachment of the arc to the electrode.

**Table 3** Properties of shielding gas and vapors

| Exp. | Solute § | $M_{\text{solute}}$ g $mol^{-1}$ | $D_{g_{\text{solute}}}$ * $m^2s^{-1}$ | $Sc_{g_{\text{solute}}}$ * |
|---|---|---|---|---|
| E1 | Mn | 54.94 | 1.96 $10^{-3}$ | 0.861 |
| | Fe | 55.85 | 1.98 $10^{-3}$ | 0.853 |
| E2, E3 | Mg | 24.31 | 2.10 $10^{-3}$ | 0.803 |
| | Al | 26.98 | 2.22 $10^{-3}$ | 0.761 |

§ solvent always is Ar
$M_{\text{Ar}}$ =39.95 kg $mol^{-1}$
$v_g$ =1.69 $10^{-3}$ $m^2s^{-1}$∗
$v_{\text{AC}}$ = 5.53 $10^{-3}$ $m^2s^{-1}$ †
$\rho_{\text{AC}}$ = 47.7 $10^{-3}$ $m^2s^{-3}$ †
* at $T_{\text{film}}$ = 5000 K [37]
† at $T_{\text{AC}}$ = 10000 K [37]

**Table 4** Process conditions at the molten electrode tip

| Exp. | $T_s$† | | $d_{\text{MC}}$ | $f_{\text{MC}}$ | $L_{\text{AC,C}}$ | $A_{\text{AC,C}}$ | $u_1$ | $Re_1$ |
|---|---|---|---|---|---|---|---|---|
| | ℃ | K | mm | Hz | mm | $m^2$ | m $s^{-1}$ | |
| E1 | 2313 | 2586 | 1.64 | 44.7 | 2.10 | 1.36 $10^{-5}$ | 0.463 | 2.66 $10^3$ |
| E2 | 2210 | 2483 | 1.73 | 58.0 | 1.58 | 7.86 $10^{-6}$ | 0.622 | 4.21 $10^3$ |
| E3 | 1730 | 2003 | 2.17 | 28.7 | 1.35 | 5.69 $10^{-6}$ | 0.484 | 3.73 $10^3$ |

† from [17]

**Table 5** Process conditions in the arc

| Exp. | $u_g$ m $s^{-1}$ | $f_{u_g}$ | $Re_g$ | $\widehat{Re}_{\text{AC}}$ |
|---|---|---|---|---|
| E1 | 40.0 | 0.631 | 41.2 | 20.0 |
| E2 | 46.4 | 0.639 | 48.9 | 23.4 |
| E3 | 51.3 | 0.652 | 65.8 | 30.8 |

arc length set to $L_{\text{arc}}$ =12.7 mm

## MASS TRANSFER MAGNITUDES

The mass transfer resistances obtained are listed in Table 6. The N/A values for resistance for Fe or Al in the melt is because they are the solvent. In all cases the resistance of evaporation

is negligible. The resistance for mass transfer of solute in the melt is always larger than that in the gas phase, but the resistance in the gas phase cannot be neglected.

Table 7 contains the mass transfer magnitudes associated with each experiment and component. The Sherwood numbers for diffusion in the melt and the gas are large, confirming the relevance of advection over bulk diffusion. The large difference in the values of $\mathfrak{h}_{l_j}$ and $\mathfrak{h}_{g_j}$ is because they are based on different reference systems, one in the liquid phase and another in the gas phase. The thickness of the boundary layers in the melt are different by an order of magnitude between steel and aluminum consumables. This large difference might be due to the very different diffusivities in molten Fe and Al. The boundary layer thickness in the gas phase is consistent around 300 μm.

**Table 6** Mass transfer resistances

| Exp. | Comp. | $\mathfrak{R}''_{l}$ s m$^{-1}$ | $\mathfrak{R}''_{l,eq}$ s m$^{-1}$ | $\mathfrak{R}''_{e}$ s m$^{-1}$ | $\mathfrak{R}''_{g}$ s m$^{-1}$ | $\mathfrak{R}''_{tot}$ s m$^{-1}$ | $\mathfrak{R}''_{l,eq}$ % | $\mathfrak{R}''_{e}$ % | $\mathfrak{R}''_{g}$ % |
|---|---|---|---|---|---|---|---|---|---|
| E1 | Mn | 1.66 10$^{3}$ | 0.241 | 4.01 10$^{-3}$ | 0.157 | 0.401 | 60 | 1.00 | 39 |
| | Fe | N/A | N/A | 4.01 10$^{-3}$ | 0.155 | 0.159 | N/A | 2.53 | 97 |
| E2 | Mg | 6.45 10$^{1}$ | 0.731 | 2.72 10$^{-3}$ | 0.144 | 0.877 | 83 | 0.31 | 16 |
| | Al | N/A | N/A | 2.87 10$^{-3}$ | 0.138 | 0.140 | N/A | 2.04 | 98 |
| E3 | Mg | 1.47 10$^{2}$ | 0.427 | 3.03 10$^{-3}$ | 0.158 | 0.588 | 73 | 0.52 | 27 |
| | Al | N/A | N/A | 3.19 10$^{-3}$ | 0.155 | 0.155 | N/A | 2.06 | 98 |

**Table 7** Mass transfer magnitudes

| Exp. | Comp. | $\mathrm{Sh}_{l_j}$ | $\mathrm{Sh}_{g_j}$ | $\mathfrak{h}_{l_j}$ m s$^{-1}$ | $\mathfrak{h}_{g_v}$ m s$^{-1}$ | $\mathfrak{d}_{l_j}$ μm | $\mathfrak{d}_{g_j}$ μm |
|---|---|---|---|---|---|---|---|
| E1 | Mn | 196 | 5.66 | 6.03 10$^{-4}$ | 6.39 | 8.90 | 307 |
| | Fe | 196 | 5.65 | 6.03 10$^{-4}$ | 6.43 | 8.90 | 308 |
| E2 | Mg | 13.7 | 5.90 | 1.55 10$^{-2}$ | 6.97 | 130 | 302 |
| | Al | 13.7 | 5.83 | 1.55 10$^{-2}$ | 7.27 | 130 | 306 |
| E3 | Mg | 21.6 | 6.52 | 6.80 10$^{-3}$ | 6.34 | 100 | 332 |
| | Al | 21.6 | 6.44 | 6.80 10$^{-3}$ | 6.61 | 100 | 336 |

Table 8 contains the flux, compositions, and partial pressures associated with mass transfer in the experiments. The results show a significant depletion of solute on the surface of the droplet, e.g. only 0.7 wt% Mn in ER80S-G, when it was originally 1.74 wt%; conversely, the solvent is slightly enriched.

The value of $p_{\mathrm{lg}_j}$ corresponds to the vapor pressure of the pure component at the temperature of the melt (listed in Table 4); this pressure is theoretical, and not experienced anywhere in the welding process.

The pressure $p_{\mathrm{l},s_j}$ corresponds to the vapor pressure of the component as part of the alloy at the molten tip of the electrode. This pressure is real, but it will manifest only if gas is nucleated in the molten metal. It can be seen that $p_{\mathrm{l},s_j}$ is quite small for the solvent component (Fe, Al);

this makes sense considering that droplet temperature in GMAW is typically below boiling temperature [17, 35, 38, 39, 40, 41, 42, 43].

For Mn in steel, the vapor pressure in solution is also low; however, for Mn in aluminum alloys, the vapor pressure exceeds one atmosphere. If a Mg vapor bubble nucleates, its high pressure will make it burst causing explosive transfer, as studied in [8]. Figure 4 shows stages of explosive transfer from the experiments in this work. The experiments showed the absence of explosive transfer in the steel wire (E1), the highest intensity of explosive transfer in E2 (Al alloy with lower amount of Mg, but higher temperature), and moderate amount of explosive transfer in E3.

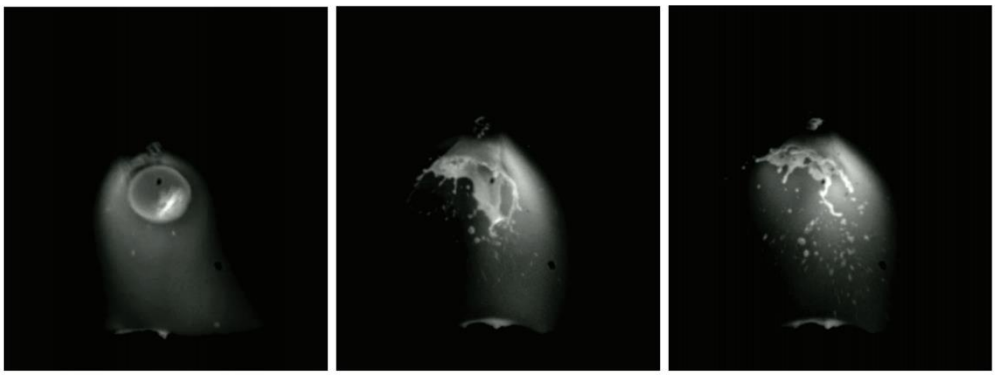


**Fig. 4** Three stages of explosive transfer in 5554 Aluminum alloy

At the free surface, $p_{\mathrm{l},s_j}$ and $p_{\mathrm{g},s_j}$ represent the vapor pressure on the melt and the gas side. In all cases, the vapor pressure in the surface of the melt is below boiling, this is because the resistance to diffusion in the melt depletes the solute (Mn or Mg) from the surface, and with lower solute content, the lower the vapor pressure. The vapor pressure for the solvent is slightly increased as the fraction of solvent is higher at the free surface. at the free surface, the pressure difference between liquid and solid is small, consistently with the small value associated with resistance of evaporation.

**Table 8** Compositions and partial pressures

| Exp. | Comp. | $J_j$ | $X_{l,s_j}$ | $f_{l,s_j}$ | $p_{lg_j}$ | $p_{l_j}$ | $p_{l,s_j}$ | $p_{g,s_j}$ |
|---|---|---|---|---|---|---|---|---|
| | | mol $s^{-1}m^{-2}$ | mol% | wt% | atm | atm | atm | atm |
| E1 | Mn | 0.62 | 0.71 | 0.70 | 3.00 | $5.3\ 10^{-2}$ | $2.12\ 10^{-2}$ | $2.07\ 10^{-2}$ |
| | Fe | 1.76 | 99.3 | 99.3 | $5.99\ 10^{-2}$ | $5.89\ 10^{-2}$ | $5.95\ 10^{-2}$ | $5.80\ 10^{-2}$ |
| E2 | Mg | 26.0 | 0.49 | 0.44 | 158 | 4.64 | $7.74\ 10^{-1}$ | $7.59\ 10^{-1}$ |
| | Al | 8.38 | 99.5 | 99.6 | $2.41\ 10^{-1}$ | $2.35\ 10^{-1}$ | $2.40\ 10^{-1}$ | $2.35\ 10^{-1}$ |
| E3 | Mg | 20.1 | 1.49 | 1.35 | 35.7 | 1.94 | $5.31\ 10^{-1}$ | $5.21\ 10^{-1}$ |
| | Al | 0.25 | 98.5 | 98.7 | $6.57\ 10^{-3}$ | $6.25\ 10^{-3}$ | $6.47\ 10^{-3}$ | $6.34\ 10^{-3}$ |

Table 9 contains the estimated mass flux of Fe, Mn, Al, and Mg in the experiments performed. The amount of Mn lost in the steel alloy is almost 4 wt% of the initial value, resulting in a final composition of 1.67 wt% of Mn, down from the original 1.74 wt% listed in Table 1. The fraction loss of Fe is much lower, but because it is the bulk of the alloy, the small amount of evaporation is significant. The total mass loss to evaporation estimated in the steel experiment is 0.27 wt%. The destination of these metal vapors is in the form of the dust that covers weld shops, but more importantly, in the form of toxic fume that could be breathed if there is insufficient protection in the workspace. Because of the higher evaporation rate, the metallic composition of the fumes is expected to be 26 wt% Mn, much higher than the original alloy stoichiometry. This high value is consistent with reports in the analysis of welding fumes, such as [2]. The exact value is difficult to measure accurately and is the subject of current work.

The amount of Mg lost in the aluminum alloys much higher than in steel, almost 60% loss for E2, which experienced the highest temperature, and almost 20% loss for E3. The material deposited in E2 is estimated to have only 1.1 wt% Mg, instead of the nominal 2.66 wt%. Similarly, for experiment E3 the deposit is estimated as 4.06 wt% Mg instead of 5.44 wt%. These low values of recovery should be confirmed with carefully done experiments. The total mass loss to evaporation estimated in the aluminum experiments is much higher than in steel, approximately 2 wt% for the very hot experiment E2 and almost 1 wt% for the high alloy of Experiment E3. The metallic composition of the fumes is expected to be 74 wt% Mg in E2 and 98 wt% in E3. This very high last value needs to be confirmed. In Al-Mg alloys, in addition to the toxic fumes, the metal vapors condense as undesirable black oxides called “smut” in the weld shops. Cleaning smut is a costly operation.

The recoil pressure associated with the mass loss is mostly associated with the solvent (Fe) in the steel wire, and with the solute (Mg) in the Al-Mg wires. The recoil pressures, of the order of $10^{-3}$ atm to $10^{-2}$ atm seem small; however, they are enough to levitate the droplet.

**Table 9** Mass balances and recoil pressure

| Exp. | Comp. | $\dot{m}_j''$ | $\dot{m}_j$ | $f_{\mathrm{evap}_j}$ | $f_{\mathrm{evap}_{\mathrm{tot}}}$ | $f_{\mathrm{deposit}}$ | $f_{\mathrm{fumes}}$ * | $p_{\mathrm{rec}}$ | $p_{\mathrm{rec,total}}$ |
|---|---|---|---|---|---|---|---|---|---|
| | | kg s$^{-1}$m$^{-2}$ | kg s$^{-1}$ | wt% | wt% | wt% | wt% | Pa | Pa |
| | Mn | 3.42 $10^{-2}$ | 4.63 $10^{-7}$ | 3.98 | | | 26.0 | 21.4 | |
| E1 | | | | | 0.27 | 1.67 | | | 82.3 |
| | Fe | 9.72 $10^{-2}$ | 1.32 $10^{-6}$ | 0.20 | | | 74.0 | 60.9 | |
| | Mg | 6.31 $10^{-1}$ | 4.96 $10^{-6}$ | 58.9 | | | 74.0 | 582 | |
| E2 | | | | | 2.12 | 1.10 | | | 779 |
| | Al | 2.21 $10^{-1}$ | 1.74 $10^{-6}$ | 0.56 | | | 26.0 | 198 | |
| | Mg | 4.89 $10^{-1}$ | 2.78 $10^{-6}$ | 18.4 | | | 98.7 | 404 | |
| E3 | | | | | 0.92 | 4.06 | | | 410 |
| | Al | 6.64 $10^{-3}$ | 3.78 $10^{-8}$ | 0.01 | | | 1.34 | 5.40 | |

*balance of metals only, excluding oxygen

## DISCUSSION

The analysis presented is the first comprehensive treatment of diffusion in the welding process accounting for transport in bo the the melt and the shielding gases. A number of simplifications were needed to arrive to the conclusions, and future work will provide a better treatment of particular aspects. None of the conclusions is expected to change, but quantitative analysis can be made more reliable and general. Some areas for future improvement are the following:

- Better treatment of heat transfer in the melt and arc, especially considering diffusion in thermal gradients. In this work, the molten consumable is treated as isothermal, as well as the gases surrounding the melt, where diffusion on the gas is present. Temperature gradients on the melt surface would be of much influence on what is considered the active area of evaporation.
- Confirm or improve the values of diffusivity in melt. The values obtained for diffusivity in molten steel are approximately two orders of magnitude lower than those in molten aluminum. While this large difference is possible, it should be verified with additional sources and theoretical analysis.
- Generalize treatment to multi-principal component alloys. In this work, an alloying component is dominant, such as Fe or Al, while the other components are small fractions of the total. Commercial alloys such as Inconel 718 and many others lack a single component that can be considered a ``solvent,'' so a more general definition of solvent should be used.

- Account for advection in gas diffusion, especially as the vapor pressure approaches the atmospheric pressure. This work considers only advection associated with the boundary layer (parallel to the surface); however, during evaporation there is another source of advection perpendicular to the surface that eventually becomes dominant at temperatures approaching boiling. There is a conventional treatment that does not account for the high recoil pressure often found in welding. This improved treatment requires special expertise in mass transfer in gases, and perhaps an expansion on what is already known.
- Validate evaporation data against existing and new experiments. The treatment presented here makes predictions of amount of metal vapors and compositions. These magnitude are measurable, but not simply. The amount of fumes is measured with standards such as AWS F1.2 “Laboratory Method for Measuring Fume Generation Rates and Total Fume Emission of Welding and Allied Processes”, which is suitable for relative magnitudes, but not accurate for mass balances. Similarly, measuring the metal balance in fumes involves complexities such as separating spatter particles and other contamination. Both challenges are surmountable, but require a dedicated experimental effort and expertise.
- Improve the treatment of droplet temperature and geometry of metal transfer including streaming spray. There is currently no theory that can predict droplet temperature reliably or the geometry of metal transfer. For the case of GMAW, there is no theory predicting the length of the tail in streaming spray transfer, which is likely to affect the temperature of the molten consumable.
- Extend analysis to weld pool and other geometries. For the weld pool in particular, jet impingement heat transfer correlations exist, which could be extended to mass transfer calculations. There are previous studies of evaporation on the weld pool surface such as [6] that should be compared directly.

## CRITERION FOR EXPLOSIVE TRANSFER

Based on the analysis and observations, a general criterion for explosive transfer can be proposed: Explosive transfer is possible when the vapor pressure of components in the melt reaches the atmospheric pressure. Because the explosion in the droplet requires nucleation of a vapor bubble, it is possible that alloys with impurities that can act as nucleants are more prone to explosive transfer.

Mitigation of explosive transfer can be attempted with lower droplet temperatures, lower alloying content, and higher boiling temperature of the components. Lower droplet temperatures is the most important factor, and can be reached with pulsing. Lower alloying component and higher boiling temperatures might not be possible within alloy specifications. Another possible mitigation strategy is reducing the time in which an element of molten consumable is exposed to high temperatures, for example in streaming transfer in which the melt flows rapidly through a cone, a potential tail, to detach quickly small droplets.

### MITIGATION OF FUME FORMATION

The model presented indicates that a lower droplet temperature is the most important factor also for fume generation. In CV GMAW, the droplet temperature reaches a minimum around the globular to spray transition [17, 35, 38, 39, 42] which is consistent with a minimum in measure fume formation rates [3, 4].

Because droplet temperature increases during the metal transfer process, pulsing can cause droplet detachment before the droplet gets too hot and starts emitting a high rate of fumes.

A lower droplet temperature also implies a lower proportion of volatile elements in the fumes, e.g. lower amount of Mn in fumes of steel welding. Of course, smaller droplets also present lower area of evaporation; however, in streaming spray, the molten tail (not treated in this work) also generates fumes, resulting in a high volume of fumes even when the droplets are small.

In all cases, the boundary layer in the gas plays an important role in the rate of fume generation. Although there is no direct way of controlling this boundary layer without affecting the overall process, a thinner gas boundary layer is likely to result in higher fumes. One of the ways in which the gas boundary layer is undesirably thinned is in the presence of chemical reactions such as oxidation (not treated in this work). It is known that the presence of oxygen in the shielding gases in GMAW results in higher fume formation rate.

## CONCLUSIONS

This paper presents for the first time a comprehensive treatment of mass transfer and evaporation in welding; in particular, the simultaneous barriers to mass transfer in the molten metal, at the evaporating surface, and in the surrounding gases are considered.

Multicomponent mass transfer is considered, and explicit expressions for the resistance to mass transfer for each component and each stage are provided. A novel treatment for diffusion in the melt is proposed by using an equivalent mass transfer resistance in the melt; this treatment is based on the vapor pressure of each component in the melt, and allows for the simultaneous consideration of all mass transfer resistances. The treatment of mass transfer also includes a treatment of recoil pressure.

The particular case of mass transfer and evaporation in the electrode tip in GMAW is considered, and three experiments are analyzed in detail. The results obtained are consistent with observations.

A criterion for explosive transfer is proposed based on the vapor pressure of components in the melt exceeding the pressure surrounding the wire tip (usually atmospheric), reproducing the type and amount of explosions observed.

The treatment of mass transfer presented is enabling for a comprehensive formulation of mass and energy balances and for theoretical treatment of fume generation, which is a topic of large impact in welding practice.

Despite the depth of the treatment, the work presented is more of a foundation than a complete treatment, with concrete suggestions for improvement in the Discussion section.

## ACKNOWLEDGEMENTS

This work builds on the effort and talent of many graduate and undergraduate students over decades. Much gratitude to Nitheesh Kumar for compiling and validating the tabulated molten metal and plasma properties in the appendices and to Nitheesh and Xinrui Liu for translating this very complex document from LaTeX into MS Word.

## References

[1] H. R. CASTNER: 'Gas Metal Arc Welding Fume Generation Using Pulsed Current', *Welding Journal*, pp. 59s-68s, 1995.

[2] N. T. JENKINS: *Chemistry of Airburne Particles from Metallurgical Processing*, Doctor of Philosophy, MIT, 2003.

[3] P. F. MENDEZ, N. T. JENKINS, and T. W. EAGAR: 'Effect of Electrode Droplet Size on Evaporation and Fume Generation in GMAW', in *Gas Metal Arc Welding for the 21st Century*, Orlando, FL, American Welding Society, pp. 325-332, 2000.

[4] N. T. JENKINS, P. F. MENDEZ, and T. W. EAGAR: 'Effect of Arc Welding Electrode Temperature on Vapor and Fume Composition'," in *Trends in Welding Research*, Pine Mountain, GA, 2005.

[5] A. BLOCK-BOLTEN and T. W. EAGAR: 'Metal Vaporization from Weld Pools', *Metallurgical Transactions B*, vol. 15B. pp. 461-469, 1984.

[6] R. T. C. CHOO, J. SZEKELY, and S. A. DAVID: 'On the Calculation of the Free Surface Temperature of Gas-Tungsten-Arc Weld Pools from First Principles: Part II. Modeling the Weld Pool and Comparison with Experiments', *Metallurgical Transactions B*, vol. 23B, pp. 371-384, 1992.

[7] T. DEBROY, S. BASU, and K. MUNDRA: 'Probing Laser-Induced Metal Vaporization by Gas-Dynamics and Liquid Pool Transport Phenomena', *Journal of Applied Physics*, vol. 70, no. 3, pp. 1313-1319, 1991.

[8] U. REISGEN *et al.*: 'Task of volumetrical evaporation and behaviour of droplets in pulsed MIG welding of Al Mg alloys', *Welding in the World*, vol. 57, pp. 507-514, 2013.

[9] T. BERGMAN, A. LAVINNE, F. INCROPERA, and D. DEWITT: *Introduction to Heat Transfer*, Sixth, New Jersey, United States: John Willey and Sons, 2002.

[10] J. MCKELLIGET and J. SZEKELY: 'Heat Transfer and Fluid Flow in the Welding Arc', *Metallurgical Transactions A*, vol. 17A, pp. 1139-1147, 1986.

[11] G. M. POUND: 'Selected Values of Evaporation and Condensation Coefficients for Simple Substances', *J. Phys. Chem. Ref. Data*, vol. 1, no. 1, 1972.

[12] C. PERROTT: 'The role of electrode vaporization in GMA welding', *Welding Technology*, vol. 82, pp. 299-309, 1982.

[13] J. F. LANCASTER: *The Physics of Welding*, 2nd ed. Pergamon Press, 1986.

[14] C. XI and W. HAI-XING: 'A calculation model for the evaporation recoil pressure in laser material processing', *Journal of Physics D: Applied Physics*, vol. 34, no. 17, p. 2637, 2001.

[15] J. SAFARIAN and T. A. ENGH: 'Vacuum evaporation of pure metals', *Metallurgical and Materials Transactions A*, vol. 44, no. 2, pp. 747-753, 2013.

[16] P. F. MENDEZ, M. A. RAMIREZ, G. TRAPAGA, and T. W. EAGER: 'Order-of-magnitude scaling of the cathode region in an axisymmetric transferred electric arc', *Metallurgical and Materials Transactions B-Process Metallurgy and Materials Processing Science*, vol. 32, no. 3. pp. 547-554, 2001.

[17] P. F. MENDEZ, Z. YAN, V. N. SÁNCHEZ, and S. CHEN: 'Physical Mechanisms Governing Deposition Rate in Arc Welding with a Consumable Electrode', in *Mathematical Modelling of*

*Weld Phenomena 13*, C. Sommitsch, N. Enzinger, and P. Mayr, Eds., Graz-Seggau, Austria: Verlag der Technischen Universität Graz, 2022.

[18] E. TURKDOGAN, P. GRIEVESON, and L. DARKEN: 'The formation of iron oxide fume', *JOM*, vol. 14, no. 7. pp. 521-526, 1962.

[19] E. TURKDOGAN, P. GRIEVESON, and L. DARKEN: 'Enhancement of diffusion-limited rates of vaporization of metals', *The Journal of Physical Chemistry*, vol. 67, no. 8. pp. 1647–1654, 1963.

[20] S. E. FERREE: 'New generation of cored wires creates less fume and spatter', *Welding Journal*, vol. 74, no. 12. pp. 45-49, 1995.

[21] K. CARPENTER, B. MONAGHAN, and J. NORRISH: 'Influence of Shielding Gas on Fume Formation Rate For Gas Metal Arc Welding of Plain Carbon Steels', *Trends in Welding Research*. pp. 436-442, 2009.

[22] R. T. C. CHOO and J. SZEKELY: 'The Possible Role of Turbulence in GTA Weld Pool Behavior', *Welding Journal*, pp. 25s-31s, 1994.

[23] H. SCHLICHTING: *Boundary-layer theory*, 7th ed. in McGraw-Hill classic textbook reissue series, New York: McGraw-Hill, 1987.

[24] P. F. MENDEZ: 'Calculation of thermal features in welding and additive manufacturing', in *Modelling of Casting, Welding and Advanced Solidification Processes, MCWASP*, Banff, AB, 2023.

[25] A. B. MURPHY: 'A comparison of treatments of diffusion in thermal plasmas', *Journal of Physics D: Applied Physics*, vol. 29, no. 7, p. 1922, 1996.

[26] A. B. MURPHY: 'Treatments of diffusion in thermal plasmas', *High Temperature Material Processes: An International Quarterly of High-Technology Plasma Processes*, vol. 4, no. 1, 2000.

[27] A. B. MURPHY: 'Calculation and application of combined diffusion coefficients in thermal plasmas', *Scientific Reports*, vol. 4, no. 1, p. 4304, 2014.

[28] P. F. MENDEZ: 'Reduced order models for welding and solidification processes', *15th International Conference on Modelling of Casting, Welding and Advanced Solidification Processes, MCWASP*, vol. 861. p. 012003, 2020.

[29] A. SCOTTI, V. PONOMAREV, and W. LUCAS: 'A scientific application oriented classification for metal transfer modes in GMA welding', *Journal of Materials Processing Technology*, vol. 212, no. 6, pp. 1406-1413, 2012.

[30] J. NORRISH: 'A review of metal transfer classification in arc welding (IIW DOC. XII-1769-03. Bucharest)', *Villepinte, France: International Institute of Welding*, 2003.

[31] J. LOWKE: 'Globular and Spray Transfer in MIG Welding', *Welding in the World*, vol. 55, pp. 19-23, 2011.

[32] J. H. WASZINK and G. J. P. M. VAN DEN HEUVEL: 'Heat Generation and Heat Flow in the Filler Metal in GMA Welding', *Welding Journal*. pp. 269s-282s, 1982.

[33] C. REDDING: 'Fume model for gas metal arc welding', *Welding Journal*, vol. 81, no. 6, pp. 95-S, 2002.

[34] A. B. MURPHY and C. ARUNDELL: 'Transport coefficients of argon, nitrogen, oxygen, argon-nitrogen, and argon-oxygen plasmas', *Plasma Chemistry and Plasma Processing*, vol. 14. pp. 451-490, 1994.

[35] Z. YAN, K. SCOTT, S. CHEN, and P. MENDEZ: 'Deposition Rate in GMAW of ER1100 and ER5183 Aluminum Alloys', *Welding Journal*, vol. 101. pp. 289s-292s, 2022.

[36] B. ZHANG: 'Calculation of self-diffusion coefficients in iron', *AIP Advances*, vol. 4, no. 1, 2014.

[37] A. B. MURPHY and E. TAM: 'Thermodynamic properties and transport coefficients of arc lamp plasmas: argon, krypton and xenon', *Journal of Physics D: Applied Physics*, vol. 47, no. 29, p. 295202, 2014.

[38] E. SODERSTROM, K. M. SCOTT, and P. F. MENDEZ: 'Calorimetric Measurement of Droplet Temperature in GMAW', *Welding Journal*, vol. 90, no. 4. pp. 77s-84s, 2011.
[39] K. M. SCOTT: *Heat Transfer and Calorimetry of Tubular Ni/WC Wires Deposited with GMAW*, MSc, University of Alberta, 2011.
[40] J. CHAPUIS, K. M. SCOTT, S. D. GUEST, E. SODERSTROM, and P. F. MENDEZ: 'Temperature and Size Measurements of Droplet During Free Flight Gas Metal Arc Welding (Mesures de température et de taille de goutte en vol libre lors d'une opération de soudage MIG-MAG)', *Canadian Welding Association Annual Conference*. 2011.
[41] J. CHAPUIS, K. M. SCOTT, S. D. GUEST, E. SODERSTROM, and P. F. MENDEZ: 'Droplet Calorimetry and High Speed Videography of Free Flight Metal Transfer in Gas Metal Arc Welding', *IIW Annual Assembly*. p. Doc.212-1232-12, 2012.
[42] C. MCINTOSH, J. CHAPUIS, and P. F. MENDEZ: 'Effect of Ar-CO2 Gas Blends on Droplet Temperature in GMAW', *Welding Journal*, vol. 95, no. 8. pp. 273s-279s, 2016.
[43] C. MCINTOSH and P. F. MENDEZ: 'Fall Voltages in Advanced Waveform Aluminum GMAW', *Welding Journal*, vol. 96. pp. 354s–366s, 2017.
[44] T. SAITO, Y. KAWAI, K. MARUYA, and M. MAKI: 'Diffusion of some alloying elements in liquid iron', *Sci. Rep. Res. Inst. Tohoku Univ. Ser. A Phys. Chem. Metall*, vol. 11, pp. 401-410, 1959.
[45] Y. DU *et al.*: 'Diffusion coefficients of some solutes in fcc and liquid Al: critical evaluation and correlation', *Materials Science and Engineering: A*, vol. 363, no. 1-2, pp. 140-151, 2003.
[46] M. R. BELLÉ *et al.*: 'Density, Surface Tension, and Viscosity of Liquid Low-Sulfur Manganese–Boron Steel via Maximum Bubble Pressure and Oscillating Crucible Methods', *Steel Research International*, vol. 96, no. 5, p. 2400252, 2025.
[47] A. DINSDALE and P. QUESTED: 'The viscosity of aluminium and its alloys–A review of data and models', *Journal of Materials Science*, vol. 39, no. 24, pp. 7221-7228, 2004.
[48] P. M. SMITH, J. W. ELMER, and G. F. GALLEGOS: 'Measurement of the density of liquid aluminum alloys by an X-ray attenuation technique', *Scripta Materialia*, vol. 40, no. 8, pp. 937-941, 1999.
[49] C. R. REID, J. M. PRAUSNITZ and B. E. POLING: 'The Properties of Gases and Liquids', McGraw-Hill, 1987.
[50] D. R. POIRIER and G. GEIGER: *Transport phenomena in materials processing*, Springer, 2016.
[51] R. C. REID, J. M. PRAUSNITZ and B. E. POLING: *The properties of gases and liquids*. McGraw Hill Book Co.,New York, NY, 1986, [Online] Available: https://www.osti.gov/biblio/6504847.
[52] E. TURKDOGAN: 'Diffusivities of gases and metal vapors at elevated temperatures', in *Steelmaking: The Chipman Conference*, MIT Press Cambridge, Mass., 1965, pp. 77-87.
[53] C. B. ALCOCK, V. ITKIN, and M. HORRIGAN: 'Vapour pressure equations for the metallic elements: 298-2500K', *Canadian Metallurgical Quarterly*, vol. 23, no. 3, pp. 309-313, 1984.
[54] T. TOMOOKA, Y. SHOJI, and T. MATSUI: 'High temperature vapor pressure of Si', *Journal of the Mass Spectrometry Society of Japan*, vol. 47, no. 1, pp. 49-53, 1999.
[55] P. D. DESAI: 'Thermodynamic properties of manganese and molybdenum', *Journal of Physical and Chemical Reference Data*, vol. 16, no. 1, pp. 91-108, 1987.

# APPENDICES

## EFFECTIVE VALUES

### EFFECTIVE DIFFUSIVITY

When diffusion varies across the thickness of the layer the exact calculation can be done using the following effective diffusivity

$$D_{\text{eff}} = \left[\frac{1}{y_{\text{B}} - y_{\text{A}}} \int_{y_{\text{A}}}^{y_{\text{B}}} \frac{dy}{D(y)}\right]^{-1} \tag{84}$$

where $y$ is the direction perpendicular to the layer, and $y_{\text{A}}$ and $y_{\text{B}}$ are the coordinates of each face of the layer.

The dependence of diffusivity on space is typically a dependence of diffusivity with temperature, with temperature depending on space. If the temperature across a layer profile is linear (i.e. the temperature gradient is constant, such as diffusivity within a thermal boundary layer at the surface of molten metal), the effective diffusivity can be expressed as

$$D_{\text{eff}} = \left[\frac{1}{T_{\text{B}} - T_{\text{A}}} \int_{T_{\text{A}}}^{T_{\text{B}}} \frac{dT}{D(T)}\right]^{-1} \tag{85}$$

where $T_{\text{A}}$ and $T_{\text{B}}$ are the temperatures of each face of the layer. Because in molten metals and in gases the diffusion boundary layer is typically comparable or thinner than the thermal boundary layer, the temperature gradient in the diffusion boundary layer can be considered approximately linear, making Equation 85 applicable.

### EFFECTIVE KINEMATIC VISCOSITY

For flow of constant density between parallel plates an exact effective value of effective kinematic viscosity is

$$\nu_{\text{eff}} = \left[\frac{1}{y_{\text{B}} - y_{\text{A}}} \int_{y_{\text{A}}}^{y_{\text{B}}} \frac{dy}{\nu(y)}\right]^{-1} \tag{86}$$

where $y$ is the direction perpendicular to the plates, and $y_{\text{A}}$ and $y_{\text{B}}$ are the coordinates of each face of the plates.

The dependence of kinematic viscosity on space is typically a dependence with temperature, where temperature depends on space. If the temperature profile between the layers is linear (i.e. the temperature gradient is constant, such as kinematic viscosity within a thermal boundary layer of molten metal at the melting front), the effective kinematic viscosity can be expressed as

$$\nu_{\text{eff}} = \left[\frac{1}{T_{\text{B}} - T_{\text{A}}} \int_{T_{\text{A}}}^{T_{\text{B}}} \frac{dT}{\nu(T)}\right]^{-1} \tag{87}$$

where $T_{\text{A}}$ and $T_{\text{B}}$ are the temperatures of each face of the plates. Of course, welding seldom involves parallel plates, but the proposed effective kinematic viscosity can be used as an approximation in other cases too. if the magnitude in question were viscosity, an effective viscosity can be estimated with the same approach.

## TRANSPORT PROPERTIES OF MOLTEN METALS

The temperatures of molten metal during welding can approach boiling, which is above the range in which measurements were made and correlations developed. In the absence of better data, the values of properties at high temperatures are extrapolated assuming the standard correlations still hold.

## DIFFUSIVITY

In molten and solid metal, the diffusivity is captured well with an Arrhenius expression:

$$D(T) = D_0 \exp\left(-\frac{Q}{RT}\right) \tag{88}$$

where $Q$ is the activation energy, $R$ the universal gas constant, and $D_0$ is a kinetic constant, tabulated for molten steel and molten aluminum in Table 10.

**Table 10** Constants for diffusion in molten metals. Calculated values of diffusivity in Fe and Al added for reference

| | Solvent | Solute | $D_0$ $m^2 s^{-1}$ | $Q$ kJ $mol^{-1}$ | Source | $D$ $m^2 s^{-1}$ |
|---|---|---|---|---|---|---|
| | pure Fe | Si | $5.0\ 10^{-8}$ | 42.7 | | $6.80\ 10^{-9}$ |
| | C-saturated Fe | Si | $2.4\ 10^{-8}$ | 34.3 | | $4.84\ 10^{-9}$ |
| | pure Fe | S | $4.8\ 10^{-8}$ | 36.0 | | $8.99\ 10^{-9}$ |
| Fe | C-saturated Fe | S | $2.8\ 10^{-8}$ | 31.4 | [44] | $6.40\ 10^{-9}$ |
| | C-saturated Fe | Mn | $1.9\ 10^{-8}$ | 24.3 | | $6.22\ 10^{-9}$ |
| | 2.5% C-Fe | Fe | $9.9\ 10^{-7}$ | 65.7 | | $4.60\ 10^{-9}$ |
| | | Mg | $9.90\ 10^{-5}$ | 71.6 | | $2.63\ 10^{-6}$ |
| | | Si | $1.34\ 10^{-7}$ | 30.0 | | $2.93\ 10^{-8}$ |
| | | Ti | $4.29\ 10^{-7}$ | 36.3 | | $6.81\ 10^{-8}$ |
| | | Cr | $2.53\ 10^{-7}$ | 32.8 | | $4.80\ 10^{-8}$ |
| | Al | Mn | $1.93\ 10^{-7}$ | 31.0 | [45] | $4.01\ 10^{-8}$ |
| | | Fe | $2.34\ 10^{-7}$ | 35.0 | | $3.97\ 10^{-8}$ |
| | | Ni | $9.54\ 10^{-8}$ | 26.0 | | $2.55\ 10^{-8}$ |
| | | Cu | $1.06\ 10^{-7}$ | 24.0 | | $3.14\ 10^{-8}$ |
| | | Zn | $5.12\ 10^{-8}$ | 22.2 | | $1.66\ 10^{-8}$ |

Reference temperature for diffusivity in Fe is 2300℃, and for Al is 2100℃. Calculated values are extrapolations to temperatures representative of the molten electrode tip in GMAW

## VISCOSITY

Viscosity is often approximated as an Arrhenius expression

$$\eta(T) = \eta_0 \exp\left(\frac{Q}{RT}\right) \tag{89}$$

For steel the values used are $\eta_0 = 7.37\ 10^{-5}$ Pa $s^{-1}$ and $Q = 66.74$ kJ$mol^{-1}$ [46], for aluminum, the values used are $\eta_0 = 2.57\ 10^{-4}$ Pa $s^{-1}$ and $Q = 13.08$ kJ$mol^{-1}$[44]. Temperature-dependent kinematic viscosity values are obtained from the ratio

$$\nu(T) = \frac{\eta(T)}{\rho(T)} \tag{90}$$

## DENSITY

Density is often approximated with a linear expression.

$$\rho(T) = \rho_0 - A(T - T_0) \tag{91}$$

For steel the values used are $\rho_0 = 7057$ kg m$^{-3}$at $T_0 = 1550$ and $A = 2.14$ kg m$^{-3}$K$^{-1}$ [46], for aluminum, the values used are $\rho_0 = 2380$ kg m$^{-3}$at $T_0 = 660$ and $A = 0.35$ kg m$^{-3}$K$^{-1}$ [48]

## DIFFUSIVITY OF GASES

In gases and metal vapors, the standard kinetic theory of gases is not accurate enough to capture diffusivity well [27], but the Chapman-Enskog theory provides useful estimates [49]. Using this theory, the diffusivity of gas *j* in gas *i* is

$$D_{j,j} = \frac{AT^{312}}{p\sigma_{i,j}^2 \Omega_j M_{ij}^{1/2}} \tag{92}$$

where $D_{i,j}$ is in cm s$^{-2}$, A is a universal constant equal to 2.66 $10^{-3}$, p is the gas pressure in bar (usually atmospheric), and $\sigma_{i,j}$ is the effective cross section of atoms in Å.

$$\sigma_{i,j} = \frac{\sigma_i + \sigma_j}{2} \tag{93}$$

with the cross sections tabulated for many components in Table 11. The effective molar weight $M_{i,j}$ in $g\ mol^{-1}$ is calculated as

$$M_{i,j} = 2\left(\frac{1}{M_i} + \frac{1}{M_j}\right)^{-1} \tag{94}$$

and the collision integral $\Omega_j$ has the following general expression [50]:

$$\Omega_j = \frac{1.06036}{T_j^{*0.15610}} + \frac{0.193}{\exp(0.47635\, T_j^*)} + \frac{1.03587}{\exp(1.52996\, T_j^*)} + \frac{1.76474}{\exp(3.89411\, T_j^*)} \tag{95}$$

The value of $T_j^*$ is provided by [19] as

$$T_j^* = \frac{kT}{\varepsilon_{i,j}} \tag{96}$$

$$\varepsilon_{i,\,j} = \sqrt{\varepsilon_i \varepsilon_j} \tag{97}$$

where T is the temperature of the gas, and the Lennard-Jones energies ε are tabulated in Table 11.

## VAPOR PRESSURE OF MOLTEN METALS

The vapor pressure of the component is typically tabulated as [53]:

$$\log p_{\mathrm{lg}_j} = \mathrm{A} + \mathrm{B}T^{-1} + \mathrm{C}\log T + \mathrm{D}T^{-3} \tag{98}$$

where $p_{\mathrm{lg}_j}$ is in atm, and the values of $A$, $B$, $C$, $D$ listed in Table 12.

## COMPOSITION OF MIXTURES

The molar fraction of component $i$ ($X_i$) and mass fraction of component $i$ are related as

$$X_i = \frac{f_i M}{M_i} \tag{99}$$

where $M_i$ is the molar mass of component i, and M is the overall molar mass of the mixture:

$$\mathrm{M} = \left( \sum_i \frac{f_i}{M_i} \right)^{-1} \tag{100}$$

$$\mathrm{M} = \sum_i X_i M_i \tag{101}$$

**Table 11** Chapman-Enskog constants for gas diffusion. Calculated values of diffusion in Ar at 5000K added for reference

| | Element | σ Å | ε $10^{-20}$J | Source | $D_{Ar,j}$@ 5000K $10^{-3}m^2s^{-1}$ |
|---|---|---|---|---|---|
| Shielding gas | He | 2.55 | 0.0141 | [51] | - |
| | $CO_2$ | 3.94 | 0.269 | | - |
| | Ar | 3.54 | 0.129 | | - |
| Metal vapor | Li | 2.98 | 2.52 | [52] | 3.53 |
| | Na | 3.66 | 1.83 | | 1.89 |
| | Mg | 3.18 | 2.18 | | 2.10 |
| | Al | 2.76 | 3.70 | | 2.22 |
| | Si* | 2.86 | 5.62 | | 2.05 |
| | K | 4.54 | 1.64 | | 1.30 |
| | Mn* | 2.58 | 3.71 | | 1.96 |
| | Fe | 2.47 | 4.93 | | 1.98 |
| | Co | 2.43 | 5.00 | | 1.98 |
| | Ni | 2.43 | 4.90 | | 1.99 |
| | Cu | 2.44 | 4.51 | | 1.96 |
| | Zn | 2.51 | 1.87 | | 2.05 |
| | Ga | 2.80 | 3.58 | | 1.75 |
| | Ag | 2.74 | 3.87 | | 1.65 |
| | Cd | 2.97 | 1.65 | | 1.64 |
| | In | 3.16 | 3.75 | | 1.45 |
| | Sn | 3.25 | 4.83 | | 1.37 |
| | Sb | 3.18 | 2.72 | | 1.46 |
| | Pb | 3.29 | 3.16 | | 1.33 |
| | Hg | 2.92 | 1.00 | | 1.63 |
| | Tl | 3.19 | 2.75 | | 1.71 |
| | Bi | 3.37 | 2.78 | | 1.31 |
| | Pu | 3.11 | 5.67 | | 1.32 |

Estimated error of these parameters is $\pm$10% [19].

**Table 12** Constants for vapor pressure of liquid metals

| Element | A | B | C | D |
|---|---|---|---|---|
| Li | 5.055 | -8023 | | |
| Na | 4.704 | -5377 | | |
| Mg ‡ | 4.89 | -6685.1 | | |
| Al | 5.911 | -16211 | | |
| Si § | 5.84 | -20800 | | |
| Ti | 6.358 | -22747 | | |
| Cr | 6.8 | -20733 | 0.4391 | -0.4094 |
| Mn † | 4.94 | -11542 | | |
| Fe | 6.347 | -19574 | | |
| Ni | 6.666 | -20765 | | |
| Cu | 5.849 | -16415 | | |
| Zn | 5.378 | -6286 | | |
| Ag | 5.752 | -13827 | | |
| Pt | 6.386 | -26856 | | |

All values from [53], except ‡ from boiling temperature and enthalpy, § from [54], and † from boiling temperature and enthalpy in [55]. Estimated error of these parameters is ±5% [53].

# NUMERICAL SENSITIVITY ANALYSIS OF MATERIAL PARAMETERS IN TIG WELDING ARC MODELLING

M. LE GAL LA SALLE*,**, S. CADIOU**, M. COURTOIS**, M. CARIN**, A. BROSSE**

**Framatome, 69007, Lyon, France*
***Univ. Bretagne Sud UMR CNRS 6027 IRDL, 56100, Lorient, France*

*DOI 10.3217/978-3-99161-089-2-002, license CC BY 4.0*
*https://creativecommons.org/licenses/by/4.0/deed.en*
*This CC license does not apply to third party material and content noted otherwise.*

## ABSTRACT

The simulation of the TIG/GTAW process with arc-melt pool coupling involves several material properties that are not well known. The main goal of this study is to quantify the numerical sensitivities of these arc material properties on the melt pool behaviour and provide recommendations on influential parameters. The most sensitive properties are thermal conductivity, density, heat capacity and viscosity of argon. For instance, a 10% increase in $C_p$ can result in an increase of more than 23% in the melt pool volume. This sensitivity study includes a detailed presentation of the 2D axisymmetric magneto-thermo-hydrodynamic finite element simulation developed with a dynamic coupling between the arc and melt pool and free surface deformation of the plasma-anode interface.

Keywords: GTAW, TIG, magneto-thermo-hydrodynamic, arc, melt-pool

## INTRODUCTION

Numerical modelling of the TIG process is a relatively recent subject of research. One of the founding models is probably the works of Hsu and Pfender [1] when he produced a magneto-thermo-hydrodynamic model of the arc in a stationary regime and in an axisymmetric configuration. His model is applied to currents between 100 and 300 A and arc heights between 10 and 20 millimetres. This numerical work is associated with experimental temperature measurements by spectrometry, with two objectives. First, to adjust the material parameters associated with electron emission and ion neutralization at the surface of the tungsten electrode. Secondly, to quantify the predictivity of the numerical results. These numerical and experimental results are enriched by the work of McKelliget and Szekely [2].

Hsu noted the sensitivity of the electromagnetic resolution near the cathode. This was the subject of work by Lowke et al. [3], who developed a methodology to simulate the transition between the cathode and the plasma without taking into account ambipolar diffusion and performed a mesh decoupling between thermo-hydrodynamics and electromagnetics. Recently, a model focusing solely on the arc was studied by Velázquez-Sánchez et al. [4] to better understand the mechanisms dominating heat transfer. Maps were thus proposed to locate the dominant heat input and output in the different areas of the arc. In parallel with the work on the arc, the modelling of the melt pool has been the subject of numerous studies involving an approximation of the effect of the arc by electromagnetic, thermal and hydrodynamic source terms. The work of Oreper et al. [5], Szekely et al. [6], Zacharia et al. [7], Choo et al. [8], and Debroy et al. [9] are based on this methodology, providing an improved understanding of the phenomena inside the melt pool.

Subsequently, arc-melt pool coupling was developed in 2D axisymmetric configuration with, for example, the work of Lin et al. [10] integrating a stationary simulation of the arc and the melt pool with surface deformation. This model was used by Kim et al. [11] to study the effect of current pulsation on melt pool behaviour. A reference model is the work of Tanaka et al. [12] for which multiple iterative developments have been carried out, such as the consideration of metal vapours in the arc coming from the melt pool with Murphy et al. [13]. Recently, Brochard [14] resumed the development of this model. He developed the justification and analysis of the multiple assumptions with an experimental comparison focused on the heat absorbed by the anode. Traidia et al. [15] added to the model the deformation of the interface between the plasma and the melt pool which is a very important element to consider at high intensities. The deformation of the surface under the effect of the arc pressure is calculated by an approach that minimizes its mechanical energy by the Helmholtz equation. This model was used to quantify the influence of the shielding gas and the effect of current pulsations. In addition to this work on the 2D axisymmetric model, a methodology was developed to project the results into 3D. This hybrid approach enables the simulation of the melt pool with slow torch advance, which is a major step forward. More recently the 2D axisymmetric model of Nahed et al. [16] integrated an arc-melt pool coupling with a deformable surface. He used a local kinematic and dynamic coupling, which is more physical than the global energy approach. A sensitivity study was conducted with this model to improve the understanding of the electrode sharpening. A fully 3D model of the arc and melt pool with a non-deformable interface was produced. The recent work of Ebrahim et al. [17] and Wu et al. [18] are an example of applications at the industrial process scale. Other more fundamental work studies the modelling of radiative transfers within the arc such as those of Baeva et al. [19], or the effect of metal vapours like Wang et al. [20].

In the nuclear industry, the welding process is used to assemble large steel components. To improve control of the process, numerical simulation of TIG/GTAW (Tungsten Inert Gas/Gas Tungsten Arc Welding), and more specifically of the electric current pulsation cycles, is being developed to develop the understanding of the physical phenomena and their influence on the melt pool, including: welding difficulties (lack of penetration, migration of chemical species, etc.), and effects of process parameters (electric current, torch speed). A magneto-thermo-hydrodynamic model with surface deformation and melt pool-arc coupling in a 2D axisymmetric configuration is developed. This model requires several material parameters for

which limited data is available in the literature, which explains why all previously cited modeling studies relied on the same dataset. These properties are difficult to characterize, especially at high temperatures and based either on thermodynamics analyses or global estimation by inverse methods. Due to the inability to estimate all the variabilities associated with these properties, a sensitivity study is performed to quantify their effects on the melt pool and present an importance analysis. This arc-scale sensitivity study for this specific configuration has not been the subject of any previous work in the literature with a coupling between arc material properties and consequences on the melt pool. These numerical results can be used to justify the necessity of improving the understanding of phenomena that can modify the material properties of the plasma, such as metallic vapor. This study is performed at an arc length of 2 mm, which is closer to the industrial application of the process compared to other works : 5 mm [13], 7 mm [4], 10 mm [1].

The first part of this article provides a comprehensive description of the model, developed with the COMSOL Multiphysics® software, including: a description of the process and the associated physical phenomena, the geometry used in the simulation, the mathematical formulation, the presentation and justification of the associated assumptions, the material properties used, the spatial discretization and the numerical model used. The second part is focused on the numerical analysis, including: a general presentation of the results at the scale of the arc and melt pool, an energy balance of the phenomena involved, and a sensitivity analysis of the material properties.

## MAGNETO-THERMO-HYDRODYNAMIC SIMULATION OF THE TIG PROCESS

### PROCESS PRESENTATION AND PHENOMENA INVOLVED

The TIG/GTAW (Tungsten Inert Gas/Gas Tungsten Arc Welding) process is an arc welding method. An electrical arc is formed between an infusible tungsten cathode and an anode consisting of the metal welded. The interstitial medium is a plasmagenic gas such as argon or helium. The heat generated by the arc leads to a localised fusion of the metal. The main physical phenomena in arc welding are electromagnetism, heat transfer, fluid flow, solid mechanics, and metallurgy. The goal of our work is to improve the understanding of the melt pool that is why we study only the physics that have a significant impact on the melt pool: electromagnetism, heat transfer and fluid flow. The right of the figure 1 summarises all the phenomena in the arc and the melt pool.

### GEOMETRY

The configuration studied is a static fusion spot on a stainless steel (304L) cylinder with no filler metal. The weld is made in the center of its upper face. This part is placed on a device developed to have as much as possible dissipation only in convection and radiation. The device is designed to achieve relative axisymmetry of the electromagnetic field. A tungsten electrode

with 2% of thorium is used. The shielding gas is argon (ARCAL™ PRIME) with 99.995% purity according to the supplier. It is blown through a straight ceramic nozzle. The left of the figure 1 is an illustration of the simulated configuration.

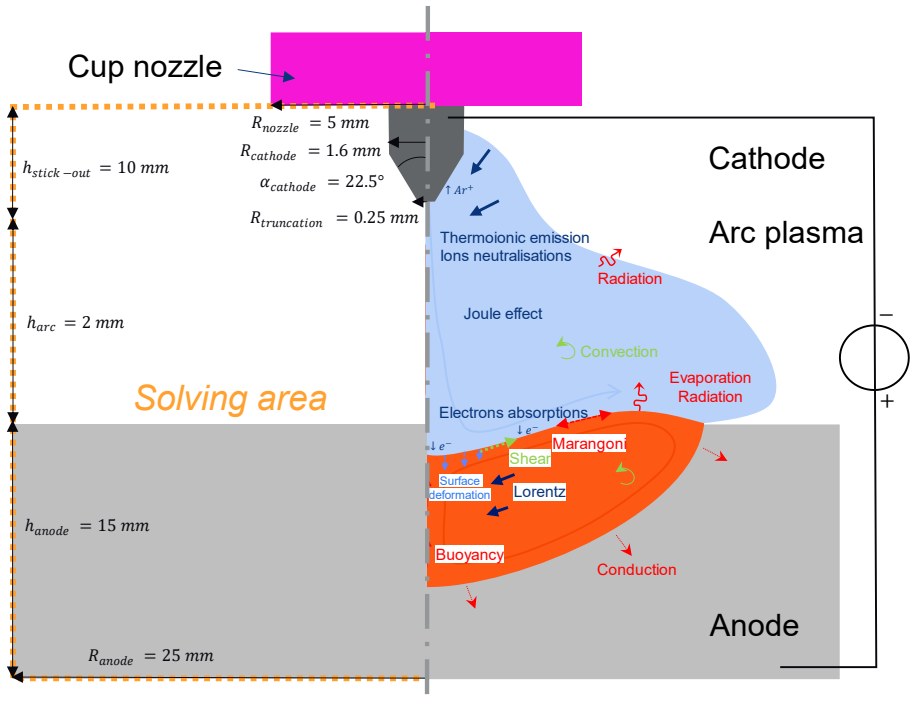



**Fig. 1** Illustration of the phenomena present and the geometry (not at scale) of the TIG process

## MATHEMATICAL FORMULATION

**Nomenclature**

| | | | |
|---|---|---|---|
| $\vec{A}$ | Magnetic vector potential | $\vec{n}$ | Normal vector |
| $A_r$ | Richardson constant | $\nabla_s$ | Surface divergence |
| $B$ | Darcy's law coefficient | $p_1$ | Pressure in plasma |
| $\vec{B}$ | Magnetic flux density | $p_2$ | Pressure in anode |
| $C$ | Darcy's law coefficient | $\phi$ | Axial displacement of the mesh |
| $C_p$ | Heat capacity at constant temperature | $\phi_a$ | Work function at the anode interface |
| $e$ | Elementary charge | $\phi_e$ | Work function associated with thermoionic emission |

| | | | |
|---|---|---|---|
| $\vec{E}$ | Electric field | $\phi_c$ | Work function at the cathode interface |
| $\epsilon$ | Net emissivity | $\psi$ | Axial displacement of the interface anode-plasma |
| $\epsilon_a$ | Anode surface emissivity | $\vec{q}$ | Heat flux vector |
| $\epsilon_c$ | Cathode surface emissivity | $Q_{anode}$ | Total heat flux at anode surface |
| $fl$ | Liquid fraction of metal | $\sigma$ | Electrical conductivity |
| $\vec{g}$ | Acceleration of gravity | $\sigma_B$ | Stefan-Boltzmann constant |
| $\gamma$ | Surface tension coefficient for Marangoni | $\overline{\overline{\sigma_1}}$ | Stress viscous tensor of plasma |
| $\gamma^*$ | Equivalent surface tension coefficient for interface deformation | $\overline{\overline{\sigma_2}}$ | Stress viscous tensor of anode |
| $\gamma_l$ | Equivalent surface tension coefficient for interface deformation | $\rho$ | Density |
| $\gamma_s$ | Equivalent surface tension coefficient at solid state for metal | $\rho_{ref}$ | Reference density for thermal expansion of liquid metal |
| $\vec{H}$ | Magnetic density | $s_{vap}$ | Vaporisation source term |
| $h_{conv}$ | Convection coefficient | $T$ | Temperature |
| $I_0$ | Input intensity | $\vec{t}$ | Tangential vector |
| $\vec{J}$ | Current density vector | $T_{ref}$ | Reference temperature for thermal expansion of liquid metal |

This formulation is inspired and compared with the work of Hsu et al. [1], Tanaka et al. [12], Brochard [14], Traidia et al. [15], Cadiou et al. [21] and Nahed et al. [16] whose arc models are compared to the experimental data of Hsu et al. [1] as shown in the appendix by figures 12 and 13. This simulation involves multiple equations associated with:

- Three physics: electromagnetism, fluid flow in plasma and metal, and heat transfer.
- Plasma-anode interface deformation: Helmholtz's equation for minimising the associated energy and modified Laplace's equation to move the surrounding mesh.

The equations associated with this model are detailed for each physical, but for simplicity, the axisymmetric conditions are not included. These equations apply to the geometric domains and boundaries as shown in figure 2. Figure 3 summaries the couplings between these different equations.

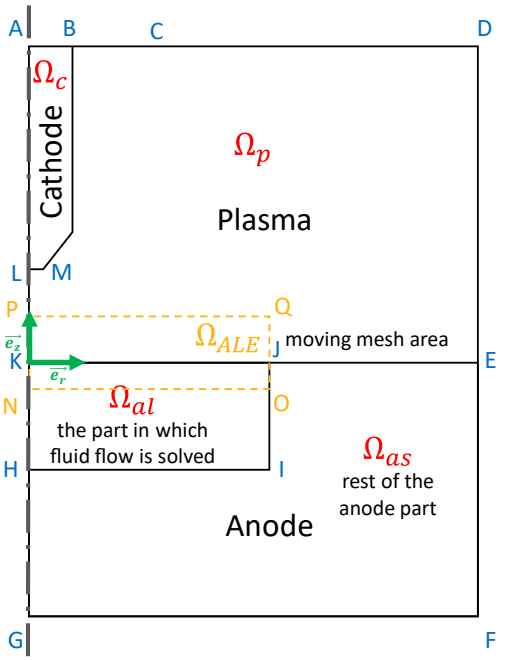



**Fig. 2** Solving domains

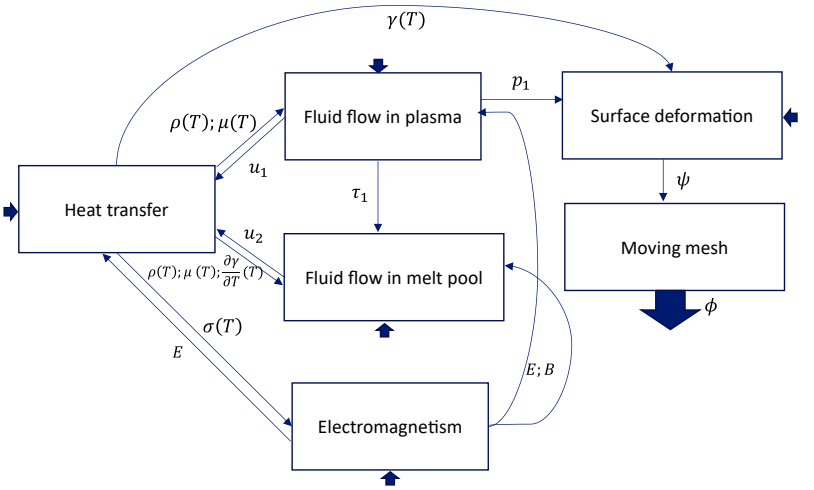



**Fig. 3** Schematic representation of the couplings between equations

*Electromagnetism ($\Omega_c \cup \Omega_p \cup \Omega_{al} \cup \Omega_{as}$)*

The electromagnetic field in cathode, plasma and anode is described by Ampere's law (4), Ohm's law (5) and Faraday's law (6) under static conditions. A Lorentz gauge is introduced by equation (7) to ensure the uniqueness of the solution. At the top of the tungsten electrode ($\partial\Omega\epsilon AB$), the surface integral of the current density is imposed by the equation (8), with $I_0$ as the input intensity. The nullity of the electric potential is defined by equation (9) on the underside of the cylinder ($\partial\Omega\epsilon GF$), where the ground is connected. Electromagnetic isolation conditions are imposed by equations (10) and (11) on the outer boundaries of the domain ($\partial\Omega\epsilon BD \cup DF \cup FG$), with $\vec{n}$ as the normal vector of these boundaries.

$$\vec{B} = \nabla \times \vec{A} \tag{1}$$

$$\vec{B} = \mu_r \mu_0 \vec{H} \tag{2}$$

$$\vec{E} = -\nabla V \tag{3}$$

$$\nabla \times \vec{H} = \vec{J} \tag{4}$$

$$\vec{J} = \sigma \vec{E} \tag{5}$$

$$\nabla . \vec{J} = 0 \tag{6}$$

$$\nabla . \vec{A} = 0 \tag{7}$$

$$\int_{AB} -\vec{J} . \overrightarrow{e_z} dS = I_0 \tag{8}$$

$$V = 0 \tag{9}$$

$$\vec{n} . \vec{J} = 0 \tag{10}$$

$$\vec{n} \times \vec{A} = \vec{0} \tag{11}$$

$j_c$ corresponds to the normal current leaving the cathode at cathode-plasma interface ($\partial\Omega_c \cap \partial\Omega_p$). It includes two distinct phenomena: $j_{em}$, which corresponds to a flow of electrons associated with the thermionic effect (15) using Richardson's law (13) and $j_{ion}$, which corresponds to the neutralisation of ions at the cathode-plasma interface (14). These two current densities later used to consider the associated thermal phenomena.

$$j_c = \vec{J} . \overrightarrow{n_{cathode \rightarrow plasma}} \tag{12}$$

$$j_{em} = A_r T^2 \, exp\left(-\frac{e\phi_e}{k_B T}\right) \tag{13}$$

$$j_{ion} = \begin{cases} j_c - j_{em} \; for \; j_c - j_{em} > 0 \\ 0 \; otherwise \end{cases} \tag{14}$$

$$j_e = j_c - j_{ion} \tag{15}$$

*Heat transfer ($\Omega_c \cup \Omega_p \cup \Omega_{al} \cup \Omega_{as}$)*

The heat equation (16) is solved over the entire domain in its temporal form, including source terms associated with the Joule effect and plasma radiation losses with partial self-absorption (18). The temperature at the top of the tungsten electrode ($\partial\Omega \in AB$) is imposed by equation (19), reflecting the cooling of the torch. At the periphery of the plasma ($\partial\Omega \in BD \cup DE$), a convection loss generated by the fluid outlet is considered, which is why conduction is considered null (20). At the anode boundary ($\partial\Omega \in EF \cup FG$), a loss by convection and radiation is defined by equation (21).

$$\rho C_p \frac{\partial T}{\partial t} + \rho C_p \vec{u}.\nabla T + \nabla.\vec{q} = S \tag{16}$$

$$\vec{q} = -\lambda \times \nabla T \tag{17}$$

$$S = \begin{cases} \vec{J}.\vec{E} - 4\pi\epsilon \; for \; \Omega \in \Omega_p \\ \vec{J}.\vec{E} \; for \; \Omega \in \Omega_{al} \cup \Omega_{as} \cup \Omega_c \end{cases} \tag{18}$$

$$T = T_0 \tag{19}$$

$$\vec{q}.\vec{n} = 0 \tag{20}$$

$$-\vec{n}.\vec{q} = h_{conv} \times (T_0 - T) + \epsilon_a \sigma_B \times (T_0^4 - T^4) \tag{21}$$

At the cathode-plasma interface ($\partial\Omega \in \Omega_\mathrm{p} \cap \Omega_\mathrm{c}$), the flux is defined by equation (22) with the heat input generated by ion neutralisation and heat sink due to thermoionic emission and radiation. At the anode-plasma interface ($\partial\Omega \in (\partial\Omega_\mathrm{p} \cap (\partial\Omega_\mathrm{al} \cup \partial\Omega_\mathrm{as}))$), the flux defined by the equation (23) includes the heat input generated by electron absorption, losses due to radiation and vaporization. The term associated with this last phenomenon is derived from Debroy et al. [22] and is defined by equation (24), using the iron vapour pressure from Kim et al. [23].

$$-\vec{n}.\vec{q} = j_{ion} V_i - j_e \phi_c - \epsilon_c \sigma_B T^4 \tag{22}$$

$$-\vec{n}.\vec{q} = \vec{J}.\vec{n}\phi_a - \epsilon_a \sigma_B T^4 - s_{vap} \tag{23}$$

$$s_{vap} = -10^{\left(2.52+\left(6.121-\frac{18836}{T}\right)-0.5\log_{10}(T)+1\right)} \times L_{vap} \tag{24}$$

*Fluid flow in plasma ($\Omega_p$)*

In the plasma domain ($\Omega_p$), equations (25) and (26) define the conservation of mass and momentum, incorporating the Lorentz force and gravity. The viscous stress tensor for a weakly compressible flow is defined by equation (27). A pressure condition is imposed at point D to ensure the uniqueness of the solution by equation (28). The velocity is considered null at the boundary with anode and cathode ($\partial\Omega \in (\partial\Omega_\mathrm{p} \cap (\partial\Omega_\mathrm{al} \cup \partial\Omega_\mathrm{as} \cup \partial\Omega_\mathrm{c}))$, according to equation (29). An open boundary condition is defined by the nullity of the viscous term at

($\partial\Omega \in (\mathrm{CD} \cup \mathrm{DE})$), as stated in equation (30). The inlet of the shielding gas is governed by the Poiseuille's law, leading to equation (31). The axial displacement of the plasma-anode interface ($\partial\Omega \in (\partial\Omega_\mathrm{p} \cap \partial\Omega_\mathrm{a})$) is equal to $\psi$ involving normal and tangential velocity conditions defined by equations (32) and (33). Note that gravity is taken into account in equation (26) but could be neglected due to its minor contribution.

$$\frac{\partial \rho}{\partial t} + \nabla.(\rho\overrightarrow{u_1}) = 0 \tag{25}$$

$$\rho\left(\frac{\partial \overrightarrow{u_1}}{\partial t} + (\overrightarrow{u_1}.\nabla)\overrightarrow{u_1}\right) = \nabla.\left(-p_1\bar{\bar{I}} + \bar{\bar{\sigma}}\right) + \vec{J} \times \vec{E} + \rho\vec{g} \tag{26}$$

$$\bar{\bar{\sigma}} = \mu\left(\nabla\overrightarrow{u_1} + \nabla\overrightarrow{u_1}^T\right) - \frac{2}{3}\mu(\nabla.\overrightarrow{u_1})\bar{\bar{I}} \tag{27}$$

$$p = 0 \tag{28}$$

$$\overrightarrow{u_1} = \vec{0} \tag{29}$$

$$\bar{\bar{\sigma}}.\vec{n} = \vec{0} \tag{30}$$

$$\overrightarrow{u_1} = -\frac{2Q_v}{\pi} \times \frac{R_{nozzle}^2 - r^2 + \left(R_{nozzle}^2 - R_{cathode}^2\right) \times \log\left(\frac{r}{R_{nozzle}} - \frac{R_{nozzle}}{R_{cathode}}\right)}{R_{nozzle}^4 - R_{cathode}^4 + \frac{\left(R_{nozzle}^2 - R_{cathode}^2\right)^2}{\log\left(\frac{R_{nozzle}}{R_{cathode}}\right)}} \overrightarrow{e_z} \tag{31}$$

$$\overrightarrow{u_1}.\vec{t} = 0 \tag{32}$$

$$\overrightarrow{u_1}.\vec{n} = \frac{\partial \psi}{\partial t} \tag{33}$$

*Fluid flow in melt pool ($\Omega_{al}$)*

Similar to fluid flow in plasma, the following equations introduce mass conservation (34) and momentum conservation (35). The viscous stress tensor (36) is adapted to describe an incompressible fluid. The source term associated with momentum conservation is detailed in equation (37), including the Lorentz force, the Buoyancy force to account for the effect of the density gradient with the incompressible viscous stress tensor, and a Darcy force to model the mushy zone between the liquid and solid phases. A Dirichlet condition is defined by equation (40) on the boundaries of the domain, excluding the anode-plasma interface ($\partial\Omega \in (\partial\Omega_\mathrm{al} \cap \partial\Omega_\mathrm{as})$). Similar to equation (33), the normal velocity at the anode-plasma interface ($\partial\Omega \in \left(\partial\Omega_\mathrm{p} \cap \partial\Omega_\mathrm{al}\right)$) is imposed by equation (41), with $\psi$ representing the axial position of this interface. On this same interface, a tangential force is applied by equation (39), associated with the surface tension gradient, more commonly known as the Marangoni effect.

$$\nabla.(\rho\overrightarrow{u_2}) = 0 \tag{34}$$

$$\rho\left(\frac{\partial \overrightarrow{u_2}}{\partial t} + (\overrightarrow{u_2}.\nabla)\overrightarrow{u_2}\right) = \nabla.\left(-p_2\bar{\bar{I}} + \bar{\bar{\sigma}}\right) + \vec{F} \tag{35}$$

$$\bar{\bar{\sigma}} = \mu\left(\nabla\overrightarrow{u_2} + \nabla\overrightarrow{u_2}^T\right) \tag{36}$$

$$\vec{F} = \vec{J} \times \vec{B} - \rho_{ref}\beta\left(T - T_{ref}\right)\vec{g} - C\frac{(1-fl)^2}{fl^3+B}\overrightarrow{u_2} \tag{27}$$

$$fl = \begin{cases} 0\ for\ t < T_s \\ \frac{T-T_s}{T_l-T_s}\ for\ T_s \leq T \leq T_l \\ 1\ for\ T > T_l \end{cases} \tag{38}$$

$$\bar{\bar{\sigma}}.\vec{t} = \mu\frac{\partial u_{1_T}}{\partial z} + \frac{\partial \gamma}{\partial r} \times \frac{\partial T}{\partial r} \tag{39}$$

$$\overrightarrow{u_2} = \vec{0} \tag{40}$$

$$\overrightarrow{u_2}.\vec{n} = \frac{\partial \psi}{\partial t} \tag{41}$$

*Movement on the plasma-anode interface ($\partial\Omega_{al} \cap \partial\Omega_p$)*

The variable ψ represents the vertical position of the interface. Helmholtz's equation (42) reflects the minimisation of the energies associated with surface tension, plasma surface pressure and gravitational potential energy. The surface tension coefficient is strongly increased when the temperature is lower than the melting temperature in order to avoid movements in the solid phase, as described by equation (43). Conservation of deformed volume is defined equation (44). A Dirichlet condition is imposed at the boundary of the moving interface ($\partial\Omega \in$ J) by equation (45).

$$\nabla_t.\left(\frac{\gamma^*}{\sqrt{1+\frac{\partial\psi^2}{\partial r^2}_T}}\right) = p_1 \tag{42}$$

$$\gamma^* = \gamma_l \times fl + \gamma_s \times (1 - fl) \tag{43}$$

$$\int \psi = 0 \tag{44}$$

$$\psi = 0 \tag{45}$$

*Moving mesh ($\Omega \in \Omega_{ALE}$)*

The axial displacement of the mesh is controlled by a modified form of the Laplace equation (46) to limit distortions in the mesh boundary layer at the plasma-anode interface ($\partial\Omega \in KJ$). A null Dirichlet condition is imposed at ($\partial\Omega \in$ PQ ∪ QO ∪ ON) to ensure continuity with the non-moving mesh by equation (47). At the interface ($\partial\Omega_{\mathrm{al}} \cap \partial\Omega_{\mathrm{p}}$), the axial displacement is equal to the solution of the previously presented Helmholtz equation (48).

$$\frac{\partial}{\partial z}\left(\frac{1}{z}\frac{\partial \phi}{\partial z}\right) = 0 \quad (46)$$

$$\phi = 0 \quad (47)$$

$$\phi = \psi \quad (48)$$

## ANALYSIS OF HYPOTHESES

The main goal of this section is to justify and critically analyse the validity of our model assumptions which are based on Brochard work [14]. First, the problem is axisymmetric due to the geometry of the weld piece and the stationary torch. This assumption enables simplification of numerical resolution. However, it is difficult to reproduce it experimentally. As an example, it has been observed that light scratches on the electrode could disrupt the axisymmetry of the arc. Multiple assumptions associated with the arc are justified by the work of Delalondre et al. [24] :

- local thermodynamic equilibrium (LTE): homogenization of species temperatures, within the arc column except cathodic and anodic interfaces by using LTE-diffusion approximation involving modified electrical conductivity as described by Lowke [25];
- quasi-neutrality;
- magnetostatism;
- elimination of the electrical component of Lorentz force by considering quasi-neutrality hypotheses;
- Thomson's effect neglected; The Thomson effect, as reported in [4] is primarily dominant in the vicinity of the electrodes, particularly the cathode.
- simplified modelling of the anodic interface incorporating only a source term associated with electron absorption and not the anode fall [12], [26];
- plasma transparent and optically thin allowing the use of a net emission coefficient to model radiative losses;
- the impact of plasma radiation on electrode surfaces is not considered because it is assumed negligible for this specific configuration compared to other thermal phenomena.

The solving of fluid flow in the plasma is conditioned by the following assumptions:

- hydrodynamic continuity;
- laminar flow: for simplification the plasma is considered laminar. The justification of this assumption for this specific welding configuration involves a comparison with a turbulent model as conducted by Bauchire [27] or experimental observations in plasma;
- weakly compressible flow ($\mathrm{Ma} = 0.11 < 0.3$): the approximated sound velocity in plasma is calculated by assuming that it is a perfect gas $U_s = \sqrt{\frac{\gamma_g p}{\rho}} \approx \sqrt{\frac{1.4\times 101325}{2E-2}}$

The assumptions associated with the thermo-hydrodynamic of melt pool are:

- Laminar regime: The Reynolds number is 1076. It is calculated with the properties of the liquid metal used in simulation at 2000 K ($\mu = 3E-2\ Pa.s; \rho = 6725\ kg/m^3$), the maximum velocity obtained ($0.6\ m/s$) and the diameter of the melt pool ($8E-3$). This dimensionless number is not representative of the real problem. The viscosity of the fluid is artificially increased by thirty to be laminar for numerical simplification. Experimental observations confirm the surface turbulence of the flow.
- Incompressible flow ($\mathrm{Ma} = 0.0003 \ll 0.3$) : The calculation of this dimensionless number is performed with the same maximum velocity and the velocity of sound in the liquid metal is approximated to be identical than water at ambient temperature.
- The enthalpy of fusion is not taken into account because this phenomenon is negligible in the spot configuration on the behaviour of the flows in the melt pool, as shown by Cadiou [21].

Only the thermal effect of metal evaporation is considered. In the simulation, metallic vapours are considered to have no effect on plasma. This assumption is justified for a relatively short weld duration and low intensity. Numerical and experimental works such as Xiang et al. [28], Lago et al. [29] and Simon et al. [30] study their sensitivities.

## MATERIAL PROPERTIES

Table 1 summaries the material properties associated with the tungsten cathode, the argon plasma and the 304L stainless steel anode. Equations are defined for density (51), heat capacity (54) and thermal conductivity (57). There are obtained from Kim et al. [23] for the liquid phase. The solid phase are experimentally characterised with:

- differential scanning calorimetry (LABSYS evo STA - Setaram);
- diffusivimeter (LFA 475/2/6 – Netzch);
- dilatometer (L75/20C – Linseis).

$$\rho_s = 8.04E3 - 4.62E-1 \times T + 1.69E-5 \times T^2 \quad (49)$$

$$\rho_l = 7.55E3 - 1.12E-1 \times T - 1.51E-4 \times T^2 \quad (50)$$

$$\rho = \rho_s \times (1 - fl) + \rho_l \times fl \quad (51)$$

$$Cp_s = 4.68E2 + 1.39E-1 \times T \quad (52)$$

$$Cp_l = 7.95E+2 \quad (53)$$

$$Cp = Cp_s \times (1 - fl) + Cp_l \times fl \quad (54)$$

$$\lambda_s = 1.31E+1 + 1.19E-2 \times T + 8.75E-7 \times T^2 - 3.72E-10 \times T^3 + 2.11E-14 \times T^4 - 6.49E-19 \times T^5 \quad (55)$$

$$\lambda_l = 1.51E+1 - 1.03E-4 \times T + 1.13E-6 \times T^2 - 2.36E-11 \times T^3 - 2.86E-14 \times T^4 \quad (56)$$

$$\lambda = \lambda_s \times (1 - fl) + \lambda_l \times fl \quad (57)$$

**Table 1** Volume material properties.

| | **Cathode** ($\Omega_c$) | **Plasma** ($\Omega_p$) | **Anode** ($\Omega_{al} \cup \Omega_{as}$) |
|---|---|---|---|
| $\rho$ | $17800\ kg/m^3$ | | *Figure 4 and* (51) |
| $C_p$ | $132\ J/(kg.K)$ | [31] | *Figure 4 and* (54) |
| $\lambda$ | [32] | | *Figure 4 and* (57) |
| $\epsilon$ | ∅ | [29] | ∅ |
| $\mu$ | ∅ | [31] | $\begin{cases} 1E4\ for\ T < T_f \\ 3E-2\ for\ T > T_f \end{cases}$ |
| $\sigma$ | [23] | $\sigma_{tungsten}$ [23] *near cathode*<br>$\sigma_{argon}$ [31]<br>$7.7E5\ S/m$ *near anode* | $7.7E5\ S/m$ |
| $\mu_r$ | 1 | 1 | 1 |

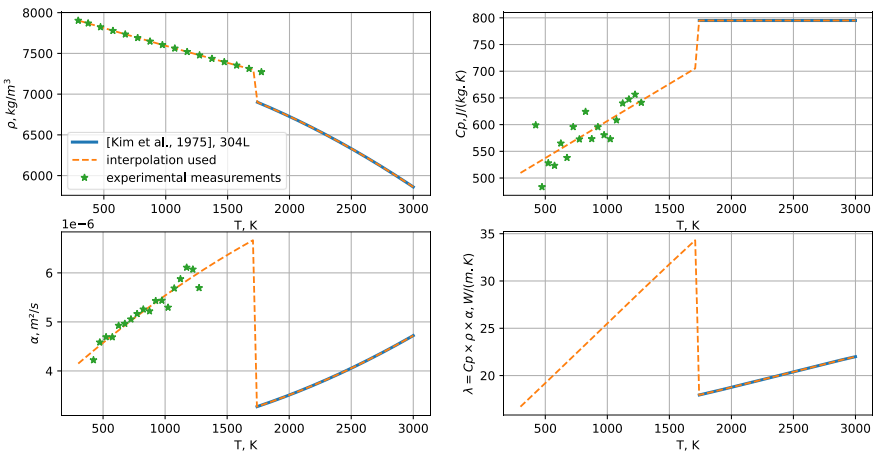



**Fig. 4** Thermophysical properties of 304L

Table 2 presents the constants associated specifically with metal. The surface tension gradient with temperature is a thermo-physical parameter which determines the surface flow in the melt pool (Marangoni effect). This value is extremely sensitive to the activity of the surface-active elements. It can vary strongly for the same stainless grade. The effect of this parameter is not the subject of this article that is why its sensitivity is not studied. For this work, two values are set to study two distinct melt pool configurations and generalise the results of this study:

- $\frac{\partial \gamma}{\partial T} = +2.1E-4\ N/(m.K)$: forming a deep and narrow melt pool;
- $\frac{\partial \gamma}{\partial T} = -2.1E-4\ N/(m.K)$: forming a shallow and large melt pool.

The properties associated with cathode-plasma and anode-plasma interfaces are chosen by Hsu et al. [1]. $\Phi_e$ and $\phi_c$ are determined by inverse method with pyrometric measurement of the electrode surface during welding. The uncertainty associated with this single measurement is not estimated, which justifies the next sensitivity study. $\phi_a$ is based on experimental measurements performed on $Fe-\alpha$. It is observed and demonstrated by Yoshitake [33] that multiple parameters like alloy elements and atomic organisation can strongly influence this value at solid state. The influence of the phase change is not studied. It is therefore also not possible to estimate the variability of this value.

**Table 2** Physical constants.

| Physical constant | Value |
|---|---|
| $T_s$ | $1708\ K$ |
| $T_l$ | $1740\ K$ |
| $C/B$ | $1E9$ |
| $\rho_{ref}$ | $6874\ kg/m^3$ |
| $\beta$ | $1E-4\ K^{-1}$ |
| $T_{ref}$ | $1723\ K$ |
| $\gamma$ | $1.5\ N/m$ |
| $h_{conv}$ | $10\ W/(m^2.K)$ |
| $\epsilon_c$ | 0.4 |
| $\epsilon_a$ | $\begin{cases} 0.7\ if\ T > \frac{T_l+T_s}{2} \\ 0.4\ if\ T < \frac{T_l+T_s}{2} \end{cases}$ |
| $\phi_e$ | $2.63\ V$ |
| $V_i$ | $15.68\ V$ |
| $\phi_c$ | $4.52\ V$ |
| $\phi_a$ | $4.7\ V$ |

## NUMERICAL RESOLUTION

The used mesh consists of tetrahedral elements with linear shape functions for all the physics except Helmholtz equation for which it is quadratic. A boundary layer mesh is chosen for the axis of revolution and electrode interfaces where strong unidirectional gradients are present. The mesh is divided into different areas with different sizes detailed in figure 5. A sensitivity on the mesh size is conducted (see figure 6) to its effect on shear, temperature, pressure, current density at the plasma-anode interface, and velocity, pressure temperature on the axisymmetry axis. The time step and minimum convergence criteria are constants for this study. It is observed that a coarse mesh leads to an underestimation of shear due to an incorrect description of flows at the interface. A satisfactory convergence is observed for a mesh size

equal to 0.15 *mm* without too high calculation time. A finer mesh than 0.07 *mm* results in numerical instability.

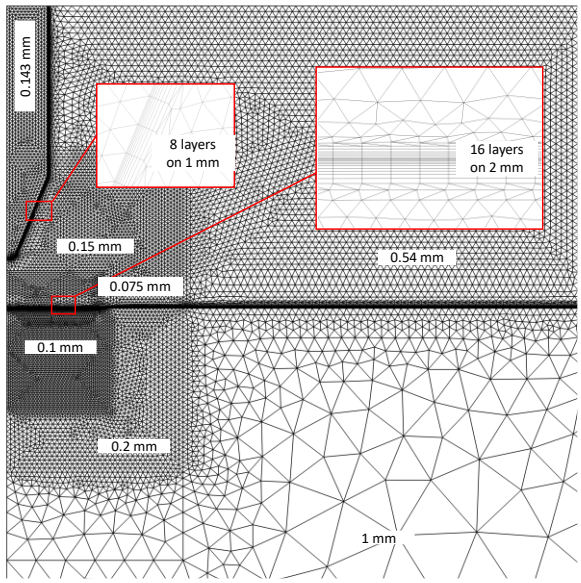



**Fig. 5** Mesh sizes

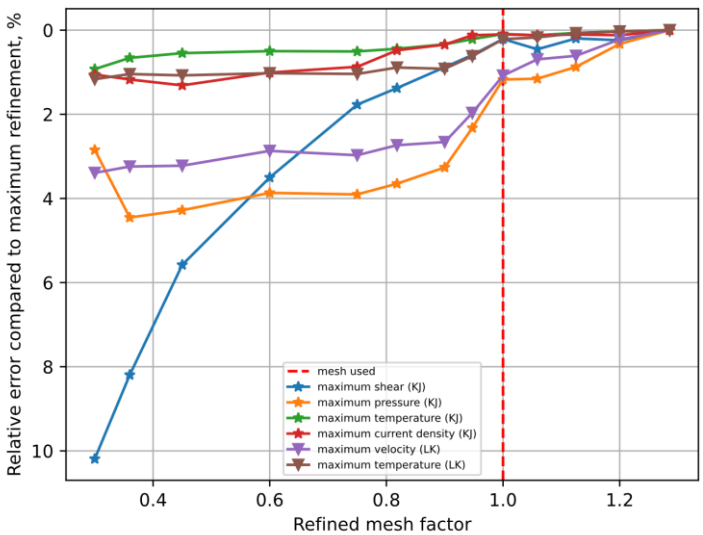



**Fig. 6** Numerical convergence of the mesh

A segregated solver is used with four steps:

- fluid flow, heat transfer in plasma and electromagnetism;
- fluid flow and heat transfer in melt pool;
- moving interface equations;
- moving mesh equation.

The backward differentiation formula (BDF) of second order is used with Anderson acceleration. Simulation of a weld at 150 A with a mesh of 146073 degrees of freedom and 8 cores (Intel® Xeon®W-2295 CPU @3.00Ghz) generates a computation time equals to 7 hours and 36 minutes. The dissociation of the viscous stress tensor of plasma and melt pool leads to a reduction in calculation time by a factor of five. This approach also improves numerical stability. The error criterion used is defined by equation (58) which consists in evaluating iterative stability with $M$ the number of fields, $N_j$ the number of degrees of freedom for the field $j$, $W_j$ the scale and $U_{i,j}$ the solution vector. The calculation is iterated for all variables as long as this relative error is less than $0.1\%$.

$$err = \sqrt{\frac{1}{M}} \sqrt{\sum_{j=1}^{M} \frac{1}{N_j} \sum_{i=1}^{N_j} \left( \frac{\left| U_{i,j_t} - U_{i,j_{t-\Delta t}} \right|}{\max(|U_{i,j_t}|)} \right)^2} \tag{58}$$

## NUMERICAL ANALYSIS

### GENERAL OVERVIEW

Figures 7 and 8 provide a brief overview of the numerical results obtained by this simulation at the melt pool and the arc scale with an intensity equal to $150\ A$ and a weld duration of $10\ s$.

The image on the left of figure 7 shows the temperature field. The tungsten electrode is heated to a temperature of 3600 K. Heating is limited by thermionic emission, which helps to reduce the effect of ion neutralisation. In the plasma, the temperature rises to 16,000 K just below the cathode. In this state, the argon is locally strongly ionized to the first and second degrees. The mechanisms associated with this heating are mainly the Joule effect and, and to a lesser extent, interfacial phenomena. Dissipation occurs through radiation and conduction to the surrounding domains. After stabilisation, the total voltage including the anode and cathode drop is equal to 10.6 V. The anode is partially melted by the heat transmitted by the plasma and the absorption of electrons. The temperature, in this area, reaches a maximum of 2600 K due to thermal pumping associated with vaporization enthalpy. The associated dissipation is mainly through radiation and convection.

The image on the middle of figure 7 shows the velocity fields. In the plasma, the flows are mainly axial, with very strong gradients between the cathode and the anode. The maximum velocity is equal to 160 m/s, due to the action of Lorentz forces and thermal expansion of the fluid. The flows generate an overpressure of 500 Pa at the anode-plasma interface. This causes a deformation of the interface equal to 0.25 mm. This deformation leads to a modification of

the flows in the plasma and the melt pool. In the anode, the liquid zone is in motion mainly due to the action of surface shear and the Marangoni effect at the anode-plasma interface, creating a very large axial gradient. The maximum velocity in this configuration is 0.16 m/s. This value is lower than in the plasma, but the Reynolds number associated is 6.7 times higher due to differences in fluid properties and associated sizes. The flows in the plasma and the melt pool are consequently very different.

The image on the right of figure 7 shows the electric potential field and the electric streamlines in the resolution domain. The potential difference is mainly located in the plasma, with a potential difference of 4.6 V. In addition, interfacial phenomena result in a total difference of 11 V. The streamlines are influenced by the cathode geometry and the deformation of the anode-plasma interface. A strong modification of this interface at high intensity implies a deviation of the electric field at the peripheral of the melt pool, leading to a change in the distribution of Lorentz forces in the melt pool and electron absorption at the surface.

The time-dependent calculation improves the understanding of the phenomena involved in the formation of the melt pool. Figure 8 shows the time evolution of the velocity and temperature fields with the temperature derivative of the surface coefficient equal to $2.1 \, . \, 10^{-4}$ N/(m.K). At 2 s the melt pool has two vortices. The first closest to the axis is centrifugal due to the predominance of the shear compared to the Marangoni effect. Away from the axis, the shear is reduced, allowing the action in the other direction of Marangoni to generate a second centripetal vortex. By increasing the welding time, the width of the melt pool is also increased, contributing to the predominance of the Marangoni effect. This leads to the formation of a single centripetal vortex. This example illustrates the complexity of the kinematics associated with thermo-hydrodynamic movements, justifying the time-dependent calculation.

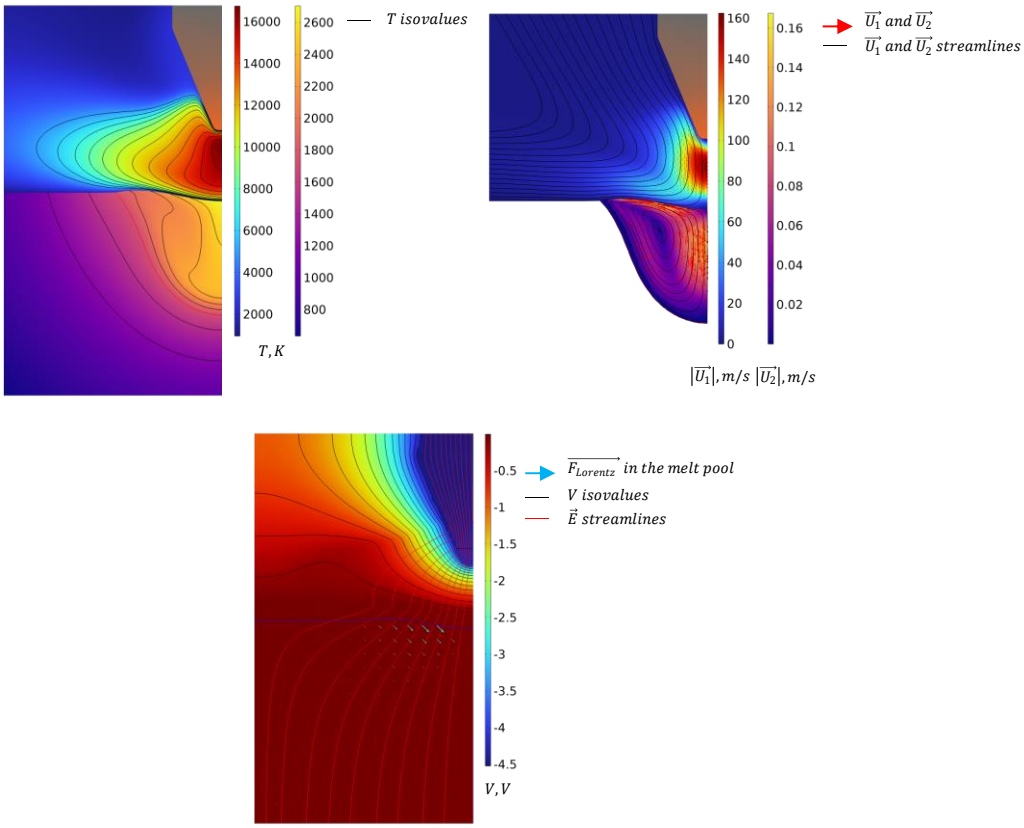



**Fig. 7** Temperature, velocities and electric field

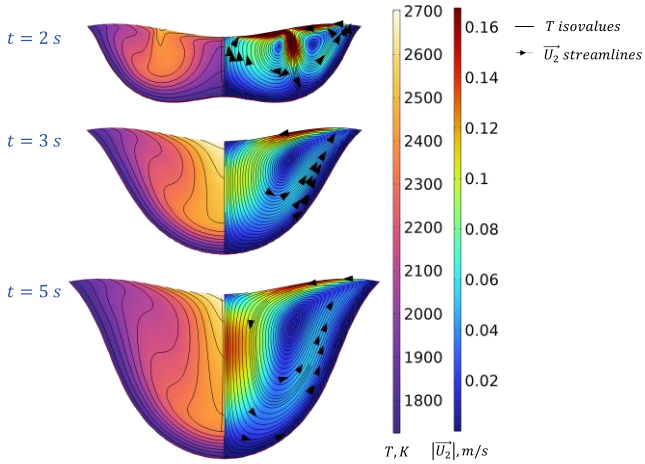



**Fig. 8** Time evolution of temperature and velocity fields into the melt pool

## ENERGY BALANCE

An energy balance is conducted in the cathode, the plasma, and the anode (see figure 9) for a welding duration and an intensity equal to 10 seconds and 150 A. The interest is to quantify the thermal contribution of all the phenomena at the scale of the process. At the end of the welding duration, the cathode has reached thermal equilibrium. The main contribution to heating is the ion neutralization at its surface (89.2%). Most of the dissipation is associated with the electron emission (61.7%) and to a lower but not negligible proportion with conduction at the top (34.9%). In simulation, this dissipation mechanism is simplified by imposing a temperature of $300\,K$ at the stick-out length. Experimentally, the tungsten electrode is cooled by the contact tube $13\,mm$ higher and by forced convection due to the flow of the cold shielding gas in the nozzle. This simplification is justified by the localisation of the thermal gradient at the tip of the cathode. In the plasma, the Joule effect is the phenomenon responsible for the heat input. This heat is redistributed by conduction to 10.8% to the cathode, 76.8% to the anode due to the direction of the fluid flows and 11.4% of the heat is dissipated by radiation with the net emission approach. In the anode, the heat input is 3.6 times higher than the dissipation. The stationary state is reached after approximately $100\,s$ in this configuration. The contribution is firstly associated with plasma conduction (41.4%) and electron absorption (58.3%). The heat generated by this last phenomenon is highly dependent of the work output of the anode ($\phi_a$) but this value is not well known. According to the literature, it depends on multiple factors including the atomistic structure of the argon and stainless steel at the interface [33].This fact greatly justifies the need to realise a sensitivity study of the effect of material parameters. From this multiple information, it is possible to calculate the energy efficiency of the arc by the equation (59) from Nahed et al. [16]. It is

equal to 75.64%, this is consistent with literature values from Nestor et al. [34], Giedt et al. [35], Dupont et al. [36] and Smartt et al. [37]. These values range between 60 and 80% for different arc height and cathode sharpening but at the same intensity.

$$\eta = \frac{s_{cond-anode}+s_{IAP}}{s_{IAP}+s_{ICP}+U\times I} \tag{59}$$

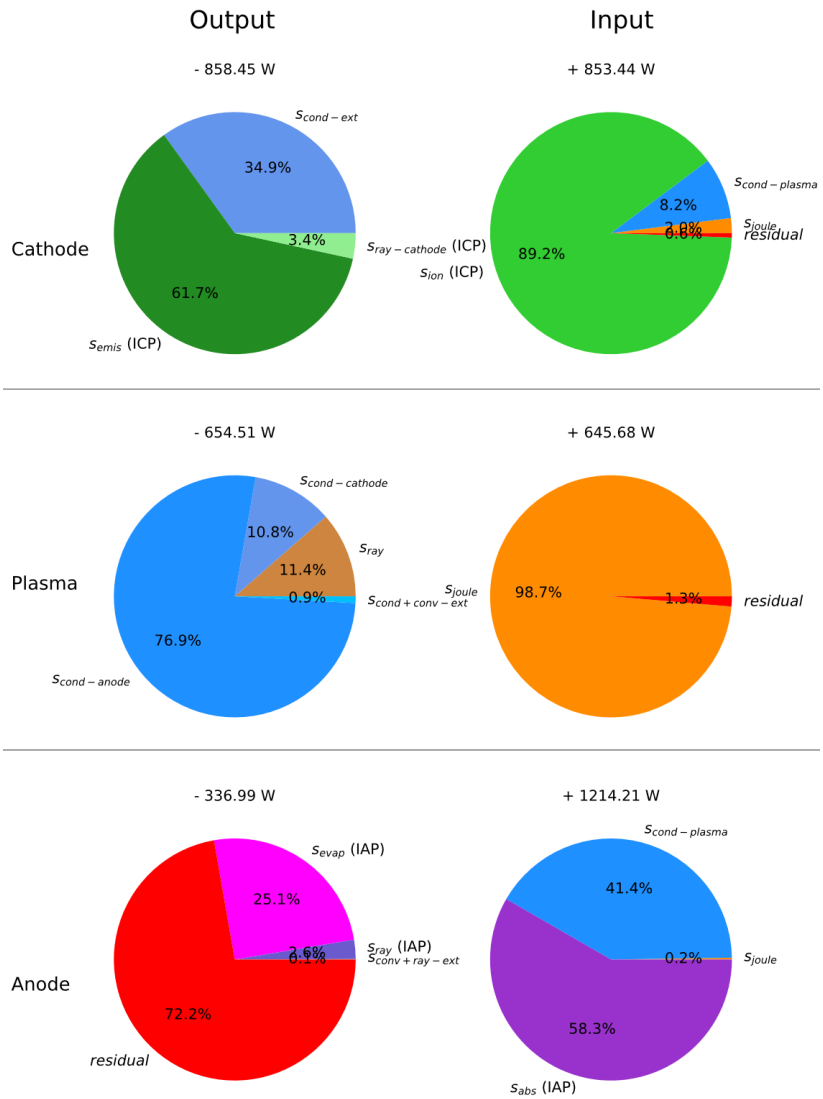



**Fig. 9** Energy balance of the arc model

## EFFECT OF THE ARC ON THE MELT POOL

The influence of the electrical arc over the melt pool is generated by : the heat flux, the shear, the arc pressure and the current density. At $150\,A$, the heat flux and the shear are the predominant phenomena. The objective of this part is to evaluate their influence on the behaviour of the melt pool for a variation of $\pm 10\%$. The evolution of the geometry of the melt pool is studied for two thermocapillary coefficients to generalise this study

Figure 10 illustrates the evolution of the fusion isotherm for a wider, shallower melt pool ($\frac{\partial \gamma}{\partial T} < 0$), and a narrower, deeper melt pool ($\frac{\partial \gamma}{\partial T} > 0$). Table 3 contains the relative differences associated with the dimensions of the melt pool. It is observed that the direction of application of the Marangoni effect has a significant effect on the influence of heat and shear.

The first consequence of increasing the incident heat flux is an approximate 23% increase in the melt pool volume, regardless the sign of $\partial\gamma/\partial T$. However, the shape does not change uniformly. For $\frac{\partial \gamma}{\partial T} > 0$, only the width is affected, whereas for $\frac{\partial \gamma}{\partial T} < 0$, both the width and depth increase.

The action of the shear is more complex due to its interdependence with the Marangoni effect. For $\frac{\partial \gamma}{\partial T} > 0$, the directions of the shear and the Marangoni effect are opposite, and the magnitude of the Marangoni effect is greater than that of the shear. In this case, an increase in the shear leads to a decrease in the total radial stress, which reduces convective movements within the melt pool and, consequently, its volume. Only the depth is affected ; the width is less sensitive to internal convection because it is strongly limited by conduction in the solid part. For $\frac{\partial \gamma}{\partial T} < 0$, the directions of the shear and the Marangoni effect are the same, making the total radial stress less sensitive to variations in the shear. Therefore, the shape of the melt pool is only slightly affected in this configuration.

The main conclusion of this little study is that these two terms can have a significant impact on the morphology of the melt pool. These results fully justify the need to improve the understanding of the influence of the material parameters of the arc model.

**Table 3** Relative differences generated by a 10% change in shear and heat.

| | $\frac{\partial \gamma}{\partial T} = +2.1E-4\ N/(m.K)$ | | $\frac{\partial \gamma}{\partial T} = -2.1E-4\ N/(m.K)$ | |
|---|---|---|---|---|
| **Characteristic** | **Shear** | **Heat** | **Shear** | **Heat** |
| Width | 0.0% | +4.8% | +0.7% | +7.7% |
| Depth | −5.8% | +12.2% | −0.3% | +7.2% |
| Volume | −6.1% | +23.7% | +1.9% | +22.5% |
| $\frac{\text{Width}}{\text{Depth}}$ | +5.9% | −7.5% | +1.0% | +0.5% |

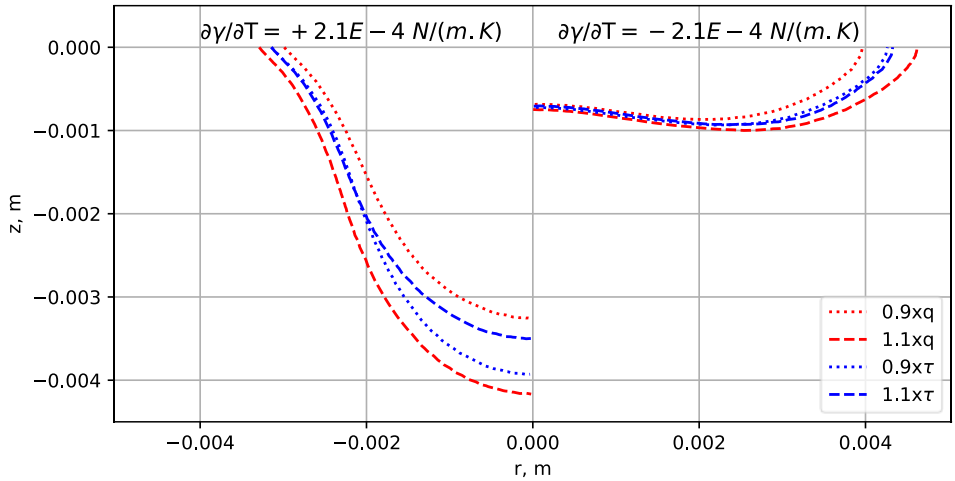



**Fig. 10** Fusion isotherms with shear and heat variations for two Marangoni configurations

## SENSITIVITY OF ARC MATERIAL PROPERTIES

The magneto-thermo-hydrodynamic simulation of the arc involves multiple material parameters. Some of them are very difficult to characterise, for example the thermophysical properties ionised argon ($\lambda, \rho, C_p, \sigma, \epsilon, \mu$). Tanaka et al. [12], Brochard [14], Traidia et al. [15], Cadiou et al. [21] and Nahed et al. [16] have used the same data from Boulos et al. [31]. These values are determined by a thermodynamic model for absolutely pure argon. The applicability of these data is therefore questionable because, experimentally, this is not the case. Metal species from anode fusion and cathode degradation are present in small quantities within the arc participating to modify these properties as shown for example by Zhao et al. [38]. Also, the properties associated with electro-magneto-thermal interfacial phenomena: $\phi_a, \phi_c$ and $\phi_e$ are little known. These three parameters are obtained by inverse method with a complex temperature measurement of the cathode surface through the arc during welding by Hsu et al. [1].

Failing to be able to characterize or known these properties accurately, simulation can be used to identify influential parameters. The properties in table 4 are studied. An individual variation of $\pm 10\%$ is applied to study the effect of the following quantities at the anode-plasma interface: heat flux, shear and pressure. The sensitivity of the material properties on the maxima of the three quantities is synthesised by figure 11. The main conclusion is the significant importance of the thermophysical properties of the shielding gas compared to $\phi_e$, $\phi_a$ and $\phi_c$. The shear is the variable most impacted by the variability of material properties. A little change leads to a modification of flow into the melt pool as demonstrated in the previous part. This study confirms that the material properties of the arc model can have a

significant impact on the incident terms at the anode-plasma interface. The lack of knowledge of these properties can be a limit to the predictivity of the model.

The main limit of this approach is to achieve a simple proportional variation of $\pm 10\%$. The choice of this variation value is questionable. Variations of $40\%$ are for example present in the literature for $\phi_a$, while for $\sigma_W$ is less than $5\%$. It would be relevant to complete this study with a bibliographic review of the totality of material parameters present in the literature to estimate their dispersions. The second weakness is to limit this study to the material properties of the arc. Indeed, the melt pool is also extremely sensitive to the properties of liquid metal in particular the surface tension coefficient responsible for the Marangoni effect.

**Table 4** Arc model material parameters used for sensitivity.

| Location | Symbol | Definition |
|---|---|---|
| Cathode (Tungsten) | $\lambda_W$ | Thermal conductivity |
| | $\rho_W$ | Density |
| Cathode-plasma interface | $h_{ICP}$ | Thickness of the cathodic zone |
| | $V_i$ | Ionisation potential |
| | $\phi_e$ | Effective work function at the cathode interface |
| | $\phi_c$ | Work function at the cathode interface |
| | $\epsilon_c$ | Emissivity of the cathode surface |
| Plasma (Argon) | $\lambda_{Ar}$ | Thermal conductivity |
| | $\rho_{Ar}$ | Density |
| | $C_{p_{Ar}}$ | Heat capacity at constant pressure |
| | $\mu_{Ar}$ | Dynamic viscosity |
| | $\sigma_{Ar}$ | Electrical conductivity |
| | $\epsilon_{Ar}$ | Net emission coefficient |
| Plasma-anode interface | $h_{IAP}$ | Thickness of the anodic zone |
| | $\phi_a$ | Work function at the interface |
| | $\epsilon_a$ | Emissivity of the anode surface |
| Anode (304L) | $\lambda_{304L}$ | Thermal conductivity |
| | $\rho_{304L}$ | Density |
| | $\sigma_{304L}$ | Electrical conductivity |
| | $\epsilon_{radsol}$ | Net emissivity |
| Plasma (Argon) | $\lambda_{Ar}$ | Thermal conductivity |
| | $\rho_{Ar}$ | Density |
| | $C_{p_{Ar}}$ | Heat capacity at constant pressure |
| | $h_{conv}$ | Convective heat transfer coefficient |

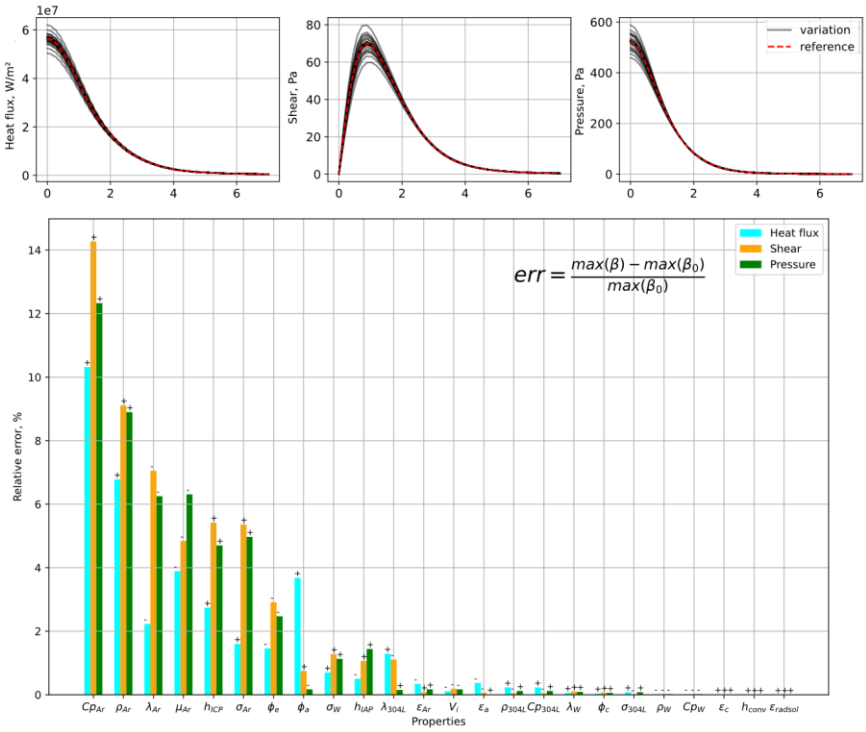



**Fig. 11** Sensitivity of material properties at the anode-plasma interface for an individual variation of 10%

## CONCLUSION

The first part of this article is a presentation as exhaustive as possible of the magneto-thermo-hydrodynamic simulation of the TIG process with arc-melt pool coupling and surface deformation in spot configuration.

This simulation highlights the influence of the arc on the melt pool and to evaluate the sensitivity of material properties on arc behaviour. The most sensitive properties are $\lambda$, $\rho$, $C_p$ and $\mu$ of argon. For instance, a $10\%$ increase in $C_p$ can result in an increase of more than $23\%$ in the melt pool volume. Unfortunately, it is not possible to justify the uncertainties associated with these parameters because they are determined by thermodynamic calculations. The metal vapours can strongly influence these properties. According to mixing law from Wilke et al. [39] the addition of $1\%$ iron results in a $25\%$ decrease in $\mu$. However, this simulation does not include the consideration of metallic vapours, this study clearly illustrates the importance of considering this phenomenon. The work function at the anode-plasma is also little known for liquid metal and proportionally influences the volume of the melt pool. It is therefore very important to improve the knowledge of this value to have a predictive model.

The perspectives associated with this work are to continue these sensitivities at the scale of the melt pool, with a focus on surface tension coefficient which is the predominant phenomenon. Another perspective is to compare the numerical and experimental results in order to evaluate the predictivity of the model with a variation in intensity.

## APPENDIX

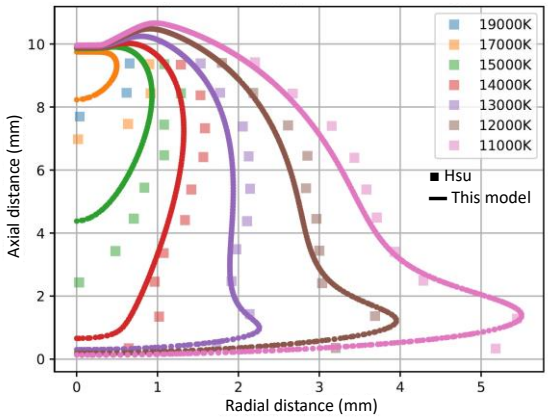



**Fig. 12** Comparison of plasma temperature measured by Hsu et al. [1] for argon, an intensity of 200 A and an arc length of 10 mm

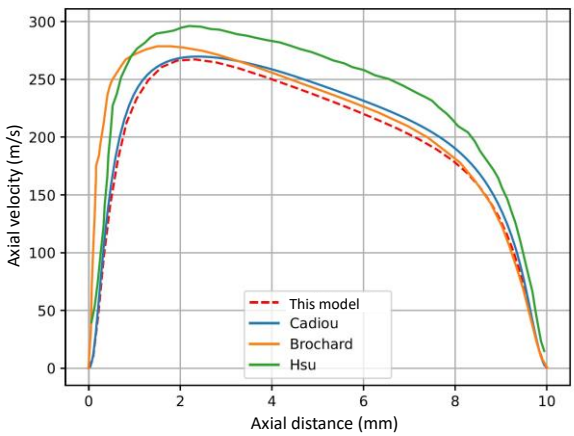



**Fig. 13** Comparison of the axial velocities within the plasma obtained in simulation obtained by Cadiou et al. [21], Brochard et al. [14] and Hsu et al. [1] for argon, an intensity of 200 A and an arc length of 10 mm

## References


[1] K. C. HSU, K. ETEMADI and E. PFENDER: 'Study of the free-burning high-intensity argon arc', *Journal of Applied Physics*, vol. 54, no. 3, pp. 1293-1301, Mar. 1983, doi: 10.1063/1.332195.

[2] J. MCKELLIGET and J. SZEKELY: 'Heat transfer and fluid flow in the welding arc', *Metallurgical Transactions A*, vol. 17, pp. 1139-1148, 1986.

[3] J. J. LOWKE, P. KOVITYA and H. P. SCHMIDT: 'Theory of free-burning arc columns including the influence of the cathode', *J. Phys. D: Appl. Phys.*, vol. 25, no. 11, p. 1600, Nov. 1992, doi: 10.1088/0022-3727/25/11/006.

[4] A. VELÁZQUEZ-SÁNCHEZ, A. DELGADO-ÁLVAREZ, P. F. MÉNDEZ, A. B. MURPHY and M. A. RAMÍREZ-ARGÁEZ: 'Dominant heat transfer mechanisms in the GTAW plasma arc column', *Plasma Chemistry and Plasma Processing*, vol. 41, no. 5, pp. 1497-1515, 2021.

[5] G. OREPER, T. EAGAR and J. SZEKELY: 'Convection in arc weld pools', *Welding Journal*, vol. 62, no. 11, pp. 307-312, 1983.

[6] J. SZEKELY: *Transport phenomena in welds with emphasis on free surface phenomena*, 1989.

[7] T. ZACHARIA, S. DAVID, J. VITEK and T. DEBROY: 'Weld pool development during GTA and laser beam welding of type 304 stainless steel, Part II–experimental correlation', *Welding Journal*, vol. 68, no. 12, pp. 510s-519s, 1989.

[8] R. C. CHOO and J. SZEKELY: 'The effect of gas shear stress on Marangoni flows in arc welding', *Welding Journal*, vol. 70, no. 9, pp. 223-233, 1991.

[9] T. DEBROY and S. DAVID: 'Physical processes in fusion welding', *Reviews of Modern Physics*, vol. 67, no. 1, p. 85, 1995.

[10] M. LIN and T. EAGAR: 'Influence of surface depression and convection on arc weld pool geometry', *Transport Phenomena in Materials Processing*, vol. 10, pp. 63-69, 1983.

[11] W.-H. KIM and S.-J. NA: 'Heat and fluid flow in pulsed current GTA weld pool', *International Journal of Heat and Mass Transfer*, vol. 41, no. 21, pp. 3213-3227, 1998.

[12] M. TANAKA, H. TERASAKI, M. USHIO and J. J. LOWKE: 'A unified numerical modeling of stationary tungsten-inert-gas welding process', *Metall Mater Trans A*, vol. 33, no. 7, pp. 2043-2052, July 2002, doi: 10.1007/s11661-002-0036-2.

[13] A. B. MURPHY, M. TANAKA, K. YAMAMOTO, S. TASHIRO, J. J. LOWKE and K. OSTRIKOV: 'Modelling of arc welding: The importance of including the arc plasma in the computational domain', *Vacuum*, vol. 85, no. 5, pp. 579-584, 2010.

[14] M. BROCHARD: *Modèle couplé cathode-plasma-pièce en vue de la simulation du procédé de soudage à l'arc TIG*, These de doctorat, Aix-Marseille 1, 2009. Accessed: Dec. 09, 2024. [Online]. Available: https://theses.fr/2009AIX11006

[15] A. TRAIDIA and F. ROGER: 'Numerical and experimental study of arc and weld pool behaviour for pulsed current GTA welding', *International Journal of Heat and Mass Transfer*, vol. 54, no. 9, pp. 2163-2179, Apr. 2011, doi: 10.1016/j.ijheatmasstransfer.2010.12.005.

[16] C. NAHED, S. GOUNAND and M. MEDALE: 'A numerical study of the effects of cathode geometry on tungsten inert gas type electric arcs', *International Journal of Heat and Mass Transfer*, vol. 182, p. 121923, Jan. 2022, doi: 10.1016/j.ijheatmasstransfer.2021.121923.

[17] A. EBRAHIMI, C. R. KLEIJN and I. M. RICHARDSON: 'A simulation-based approach to characterise melt-pool oscillations during gas tungsten arc welding', *International Journal of Heat and Mass Transfer*, vol. 164, p. 120535, 2021.

[18] D. WU, J. HUANG, L. KONG, X. HUA and M. WANG: 'Coupled mechanisms of arc, weld pool and weld microstructures in high speed tandem TIG welding', *International Journal of Heat and Mass Transfer*, vol. 154, p. 119641, 2020.

[19] M. BAEVA, Y. CRESSAULT and P. KLOC: 'Comparative Studies on the Radiative Heat Transfer in Arc Plasma and Its Impact in a Model of a Free-Burning Arc', *Plasma*, vol. 7, no. 3, pp. 631-650, 2024, doi: 10.3390/plasma7030033.

[20] X. WANG, S. TASHIRO, M. TANAKA and A. B. MURPHY: 'Numerical Investigation of the Iron and Oxygen Transport in Arc Plasma During an Activated Tungsten Inert Gas Welding Process', *Plasma Chemistry and Plasma Processing*, vol. 44, no. 1, pp. 25-45, 2024.

[21] S. CADIOU, M. COURTOIS, M. CARIN, P. LE MASSON, L. GUILMOIS and P. PAILLARD: 'Development of a two-dimensional axial symmetry model for wire arc additive manufacturing', in *Mathematical Modelling of Weld Phenomena 12. Verlag der Technischen Universität Graz*, 2018. doi: https://doi.org/10.3217/978-3-85125-615-4-56.

[22] T. DEBROY, S. BASU and K. MUNDRA: 'Probing laser induced metal vaporization by gas dynamics and liquid pool transport phenomena', *Journal of Applied Physics*, vol. 70, no. 3, pp. 1313-1319, Aug. 1991, doi: 10.1063/1.350358.

[23] C. S. KIM: 'Thermophysical properties of stainless steels', Argonne National Lab., Ill. (USA), ANL-75-55, Sept. 1975. doi: 10.2172/4152287.

[24] C. DELALONDRE and O. SIMONIN: 'Modelling of high intensity arcs including a non-equilibrium description of the cathode sheath', *J. Phys. Colloques*, vol. 51, no. C5, pp. C5-206, Sept. 1990, doi: 10.1051/jphyscol:1990524.

[25] J. J. LOWKE and M. TANAKA: 'LTE-diffusion approximation' for arc calculations', 2006, doi: 10.1088/0022-3727/39/16/017.

[26] A. TRAIDIA: *Multiphysics modelling and numerical simulation of GTA weld pools*, 2011.

[27] J. M. BAUCHIRE, J. J. GONZALEZ and A. GLEIZES: 'Modeling of a DC Plasma Torch in Laminar and Turbulent Flow', 1997, doi: https://doi.org/10.1023/A:1021847113956.

[28] J. XIANG, F. F. CHEN, H. PARK, K. TANAKA, M. SHIGETA, M. TANAKA and A. B. MURPHY: 'Numerical study of the metal vapour transport in tungsten inert-gas welding in argon for stainless steel', *Applied Mathematical Modelling*, vol. 79, pp. 713-728, Mar. 2020, doi: 10.1016/j.apm.2019.11.001.

[29] F. LAGO, J. J. GONZALEZ, P. FRETON and A. GLEIZES: 'A numerical modelling of an electric arc and its interaction with the anode: Part I. The two-dimensional model', *J. Phys. D: Appl. Phys.*, vol. 37, no. 6, p. 883, Feb. 2004, doi: 10.1088/0022-3727/37/6/013.

[30] M. S. SIMON: *On the mechanism of evaporation-determined arc-cathode coupling in GMA welding*, PhD Thesis, RWTH Aachen University, 2021.

[31] M. I. BOULOS, P. FAUCHAIS and E. PFENDER: *Thermal Plasmas: Fundamentals and Applications*, Springer Science & Business Media, 2013.

[32] C. S. WU, J. CHEN and Y. M. ZHANG: 'Numerical analysis of both front- and back-side deformation of fully-penetrated GTAW weld pool surfaces', *Computational Materials Science*, vol. 39, no. 3, pp. 635-642, May 2007, doi: 10.1016/j.commatsci.2006.08.018.

[33] M. YOSHITAKE: *Work Function and Band Alignment of Electrode Materials: The Art of Interface Potential for Electronic Devices, Solar Cells, and Batteries*. in NIMS Monographs, Tokyo: Springer Japan, 2021. doi: 10.1007/978-4-431-56898-8.

[34] O. H. NESTOR: 'Heat Intensity and Current Density Distributions at the Anode of High Current, Inert Gas Arcs', *Journal of Applied Physics*, vol. 33, no. 5, pp. 1638-1648, May 1962, doi: 10.1063/1.1728803.

[35] W. GIEDT, L. TALLERICO and P. FUERSCHBACH: 'GTA welding efficiency: calorimetric and temperature field measurements', *Weld. J.*, vol. 68, p. 28, 1989.

[36] J. N. DUPONT and A. MARDER: 'Thermal efficiency of arc welding processes', *Welding Journal-Including Welding Research Supplement*, 1995.

[37] H. B. SMARTT, J. A. STEWART and C. J. EINERSON: 'Heat transfer in gas tungsten arc welding', EG and G Idaho, Inc., Idaho Falls (USA), EGG-J-01586; CONF-8510160-19, May 1986. Accessed: Dec. 09, 2024. [Online]. Available: https://www.osti.gov/biblio/5500789

[38] G. Y. ZHAO, M. DASSANAYAKE and K. ETEMADI: 'Numerical Simulation of a Free-Burning Argon Arc with Copper Evaporation from the Anode', *Plasma Chemistry and Plasma Processing*, vol. 10, 1990.

[39] C. R. WILKE: 'A Viscosity Equation for Gas Mixtures', *The Journal of Chemical Physics*, vol. 18, no. 4, pp. 517-519, Apr. 1950, doi: 10.1063/1.1747673.

# ENHANCING GMAW SIMULATIONS THROUGH A HYBRID EULERIAN AND LAGRANGIAN METHOD CONSIDERING AN INCLINED WELDING TORCH

O. MOKROV*, S. WARKENTIN*, L. WESTHOFEN**, J. BENDER**, R. SHARMA*, U. REISGEN*

**RWTH Aachen University, Welding and Joining Institute, 52062 Aachen, Germany*
***RWTH Aachen University, Visual Computing Institute - LuFG Computer Animation, 52056 Aachen, Germany*
*Mokrov: https://orcid.org/0000-0002-9380-6905; Warkentin: https://orcid.org/0009-0004-4514-8962;*
*Westhofen: https://orcid.org/0000-0003-4427-2377; Bender: https://orcid.org/0000-0002-1908-4027;*
*Sharma: https://orcid.org/0000-0002-6976-4530; Reisgen: https://orcid.org/0000-0003-4920-2351*

*DOI 10.3217/978-3-99161-089-2-003, license CC BY 4.0*
*https://creativecommons.org/licenses/by/4.0/deed.en*
*This CC license does not apply to third party material and content noted otherwise.*

## ABSTRACT

The comprehensive simulation of gas metal arc welding (GMAW) remains challenging due to the continuously evolving topologies of both the welding arc region and the weld seam formation zone. GMAW involves phenomena, such as melting, hydrodynamic flows within the weld pool, and crystallization, occurring on timescales significantly distinct from the rapid plasma physics processes in the arc. This plasma exhibits pronounced heterogeneity in voltage gradients, necessitating highly precise modeling of anode and cathode layers. In contrast, traditional simulation methods couple liquid metal and arc behaviour within a single domain, typically employing Volume of Fluid (VOF) or Level Set techniques. These methods often rely on substantial simplifications in the plasma boundary layers, thereby compromising predictive accuracy. To overcome these limitations, this paper presents a hybrid modeling approach coupling a Lagrangian Smoothed Particle Hydrodynamics (SPH) model for weld pool and droplet dynamics with an Eulerian framework tailored for the arc zone. The SPH method effectively captures large-scale phenomena in the weld pool, including heat and mass transfer, droplet detachment, and solidification. On the other hand, the Eulerian model accurately represents the complex electromagnetic and thermal behaviour within the anode and cathode layers of the arc plasma

This study also addresses torch inclination effects on weld pool dynamics, heat flux distribution, and current density on the cathode, providing insights into their influence on weld geometry. Through the synthesis of both, Lagrangian and Eulerian approaches, the proposed method provides a robust tool for addressing the multiscale, multiphysics nature of the GMAW process.

Results from 3D calculations include quasi-stationary Eulerian solutions for the plasma domain and transient SPH simulation of the heat and mass transfer for a drag/push weld.

Although still under active development, this hybrid model shows significant potential for enhancing the predictive capabilities of GMAW simulations, thus offering additional possibilities in process optimization and quality improvement in industrial welding.

Keywords: simulation, modeling, GMAW, Smoothed Particle Hydrodynamics (SPH), FVM, arc plasma, push/pull weld

## INTRODUCTION AND PROBLEM STATEMENT

Gas metal arc welding (GMAW) is a widely used variant of arc welding technologies. In this process, an electric arc forms between a consumable electrode (commonly poled as an anode) and the workpiece (the cathode), creating a plasma - a mixture of ionized gases, Fig. 1**.** The material from both the workpiece and the consumable wire melts, forming a shared weld pool. Upon solidification, this weld pool results in a solid weld seam. The heat required for melting the materials is generated at the sheath layers of both the anode and cathode, mainly through the recombination of ions and free electrons.

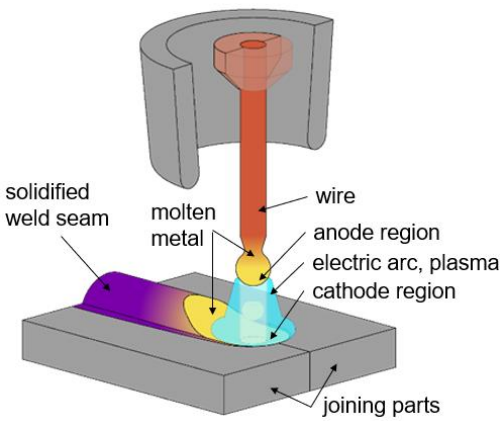



**Fig. 1** Schematic representation of GMAW, illustrating the arc, anode, cathode, and weld pool regions

A key aspect of heat transfer in this process is the interaction of the arc with the anode and cathode surfaces. There is a significant feedback loop between the temperature of the molten pool surface and the physical processes occurring in the anode and cathode layers. Metal evaporation influences both the temperature of the electrodes and the composition of the plasma. Moreover, different coupling configurations alter the electric current paths, thereby affecting electromagnetic forces and heat distribution. Consequently, there is a strong interrelationship between the seam geometry and the arc, influenced by meso-scale processes in the anode and cathode regions.

The inclination of the wire also frequently plays a role, Fig. 2. In real-world welding applications, the topological changes in the process are even more pronounced. For instance,

when welding fillet welds on T-joints or lap joints, variations in plate thickness are common, which adds complexity to the weld pool behavior and seam formation. Moreover, the weld seam is often not straight, as seen in pipe welding, where the seam follows a curved path. These geometric challenges further complicate the mass and heat transfer processes, as they introduce additional variations in the melt pool dynamics and the overall heat distribution. A detailed understanding of these physical phenomena is essential for accurate modeling and remains a challenging research topic in welding simulation.

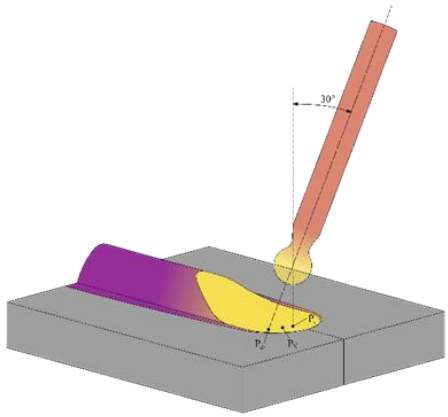



**Fig. 2** Showing an inclined wire over flat plate

The scope of welding process simulation encompasses both academic and scientific questions relating to a fundamental physical understanding of the processes involved in GMAW, as well as the derivation of reference values and standards for the engineering analysis of a welded joint or structure. The decisive factor here is the determination of the temperature field in the component, which allows the mechanical and technological properties of the joint to be characterized. For this purpose, a heat source model of the welding process can be taken into account with varying degrees of abstraction and accuracy.

This study combines two approaches for simulating GMAW. Based on a preliminary analysis of the physical time scales and characteristic spatial dimensions of the corresponding physical processes, optimal numerical methods are proposed for the respective processes. Thus, the fast electromagnetic processes in the plasma are calculated using a quasi-stationary geometry of the wire and molten pool with the mesh-based FEM method, and the slower, transient processes of droplet detachment and weld seam formation are determined using a particle-based SPH solver.

## HISTORICAL DEVELOPMENT AND LITERATURE REVIEW

Welding processes generate complex, time-dependent thermal fields that control the weld pool dynamics and, consequently, the final weld quality. To capture these phenomena, the classification of weld heat source models into five generations proposed by Goldak [1] offers a systematic framework for organizing welding process simulations.
It enables researchers and engineers to balance physical fidelity and computational efficiency according to the goals of the analysis. Each generation adds new physical mechanisms and mathematical complexity to the preceding one. Earlier models remain embedded as special cases in the more advanced generations.

**The first generation** of weld heat source models relies on highly idealized analytical descriptions, such as point, line, or plane heat sources. These models serve primarily to estimate temperature fields analytically, particularly in regions far from the weld pool. The approach simplifies heat input as a delta function and assumes steady-state conditions. While they do not account for actual energy distribution, phase changes, or nonlinear material behavior, they provide energy-conserving solutions with acceptable accuracy for far-field temperature estimates. A classic example is Rosenthal's point source model for shallow welds on thick plates [2,3].

In contrast, **second-generation** models introduce distributed energy input, replacing the delta function with volumetric or surface-based flux or temperature distributions. These models support the simulation of more complex geometries and incorporate temperature-dependent properties, boundary conditions like radiation and convection, and phase transformations. A key development is the double-ellipsoid model by Goldak, which represents power density distribution more realistically. Another important variant involves prescribed temperature distributions. However, second-generation models typically still treat the weld pool geometry as an input parameter and lack internal fluid flow descriptions [4].

**Third-generation** models represent a significant step forward by solving the Stefan problem, allowing for the prediction of the moving liquid-solid interface of the weld pool. These models determine the weld pool shape as part of the solution and incorporate surface forces such as arc pressure and surface tension. By coupling the heat equation with a hydrostatic momentum balance, they approximate the forces acting within a stationary liquid phase. While arc pressure and energy flux are often kept constant, the weld pool surface is computed dynamically, making these models more realistic. Weiss' extensions further included positional effects such as vertical and horizontal welding orientations [5].

Building upon this, **fourth-generation** models introduce full fluid dynamics through the solution of the Navier-Stokes equations. These models account for the complex flow phenomena within the weld pool, such as buoyancy-driven convection, Marangoni forces due to surface tension gradients, and the influence of droplet transfer. They provide a deeper insight into the internal circulation patterns of the weld pool, although they are highly nonlinear and sensitive to turbulent effects. As such, they demand greater computational resources. In practical applications, simplified or semi-empirical velocity fields - such as those developed by Sudnik - are often employed to reduce computational burden while retaining accuracy [6].

**Fifth-generation** models incorporate arc physics by solving the magnetohydrodynamic (MHD) equations alongside the thermal and fluid dynamic equations. These models integrate current density, electromagnetic fields, plasma properties, and their interaction with the weld pool and surrounding gas. The result is a comprehensive but extremely complex simulation framework. Due to the difficulty in ensuring numerical stability and the absence of guaranteed solution uniqueness, these models are primarily used in research settings. Nevertheless, they offer the most complete representation of arc-welding processes, including the interaction of electric arcs and molten metal in high-amperage applications with droplet transfer [7].

**Table 1** Comparison of Weld Heat Source Generations.

| Generation | Geometry Input | Energy Distribution | Pool Prediction | Flow | Arc Physics | Computational Time |
|---|---|---|---|---|---|---|
| 1st | Analytical | Idealized (point/line) | NO | NO | NO | Very Low |
| 2nd | Distributed | Realistic | Optional (input) | No | No | Low |
| 3rd | Dynamic | Realistic | Yes (free surface) | Hydrostatic | Simplified | Moderate |
| 4th | Dynamic | Realistic | Yes | CFD | No | High |
| 5th | Dynamic | Realistic | Yes | Full CFD + MHD | Yes | Very High |

## CONCLUSION AND APPLICATION GUIDANCE

Earlier-generation models, particularly the second generation, are typically sufficient for modelling thermal behavior outside the weld pool. For detailed prediction of weld pool behavior and weld bead formation, third- or fourth-generation models are preferred.

A hierarchical or hybrid modelling strategy is strongly recommended. In this approach, different models are applied to different regions of the domain based on their physical relevance and computational demands. This modular approach simplifies the code, improves numerical robustness, and optimizes computational efficiency.

The classification proposed by Goldak et al. [1] remains a valuable framework for organizing weld heat source models and for understanding their progressive inclusion of physical mechanisms. The fifth generation, based on magnetohydrodynamic (MHD) formulations, represents the most comprehensive approach within this hierarchy, combining heat transfer, fluid flow, and electromagnetic effects. Nevertheless, these models generally treat the arc as an external energy source, neglecting the dynamic feedback between the plasma and the electrode or weld pool surface.

Recent research on

- droplet formation and detachment,
- anode sheath behavior including evaporation effects, and
- arc column models with metal vapor cores, forming a two-zone plasma characteristic of GMAW arcs,

suggests the emergence of a sixth generation of weld heat source models. In these approaches, the coupling between the arc plasma and the electrode surfaces is treated in a self-consistent manner. The models incorporate the mutual influence of plasma composition, metal vapor concentration, and surface temperature on current density and heat flux distributions. Such formulations aim to describe the entire arc–electrode–pool system as an integrated physical entity rather than a sequence of independently parameterized submodels.

Within this context, one concept stands out as particularly relevant for gas metal arc welding (GMAW) - the Evaporation Determined Arc-Cathode Coupling (EDACC) model [8]. While general sixth-generation concepts address plasma-electrode coupling in a broad sense, the EDACC model provides a dedicated formulation for GMAW, where metal evaporation from the molten pool exerts a dominant influence on arc behavior.

In GMAW, the mutual interaction between the plasma and the evaporating metal surface fundamentally determines the arc attachment, current distribution, and heat input. For this reason, the EDACC model can be regarded as a process-specific extension of the classical hierarchy - a tailored approach that captures the unique feedback mechanisms characteristic of this welding process.

## EDACC MODEL

Various mechanisms contributing to cathode emission in GMAW processes have been investigated, including thermionic emission and the role of ionized metal atoms in the plasma. However, existing models often fail to describe these processes adequately. Many modern approaches are based on conditions typical for low-pressure environments or non-consumable tungsten cathodes, where evaporation effects are minimal.

In contrast, in gas metal arc welding, metal vapor and its interaction with the plasma play a dominant role. This interaction leads to lower effective cathode temperatures than expected and has a significant influence on the degree of ionization as well as on the current density distribution near the cathode [9].

To address these limitations, the Evaporation Determined Arc-Cathode Coupling (EDACC) model was developed at ISF in 2019. The model describes in detail the effects of evaporation on the cathode and demonstrates how metal evaporation modifies the local heat flux and flow dynamics. As a new physical concept, EDACC introduces a coupling principle that explicitly accounts for the influence of cold metal vapor on the plasma adjacent to the cathode.

This cooling effect is included as part of the total heat flux balance at the cathode surface:

$$q_{total} = q_{ion} - q_{em} - q_{evap} - q_{rad}, \quad (1)$$

where $q_{ion}$ is the ion heat flux, $q_{em}$ represents the losses due to thermionic emission, $q_{evap}$ the heat flux associated with the evaporation and $q_{rad}$ the radiation losses. Crucial parameter for the arc attachment and the current density distribution is an effective conductivity of the cathode sheath layer:

$$\sigma_{layer}(x) = \frac{j_{total}(x) \cdot t_{sheath}}{U_D}, \tag{2}$$

where the sheath layer $t_{layer}$ and the voltage drop in the layer $U_D$ are constant parameters. The results of the study show that a decrease in the degree of ionization due to the cooling effect of metal vapor can lead to a significant reduction in heat flux on the cathode surface, Fig. 3.

Simulation results obtained using the EDACC model indicate that a decrease in the degree of ionization caused by metal vapor cooling can significantly redistribute the heat flux to the cathode surface (Fig. 3). The cathode surface reaches temperatures slightly below the evaporation temperature, with a maximum heat flux observed at about 2600 K [8]. These findings were confirmed by two-color pyrometry measurements [9], shown in Fig. 4**.**

The results reveal an asymmetric arc attachment to the cathode, with maximum intensity observed along the leading edge of the molten front. This asymmetry strongly affects the heat and current transfer to the weld pool.

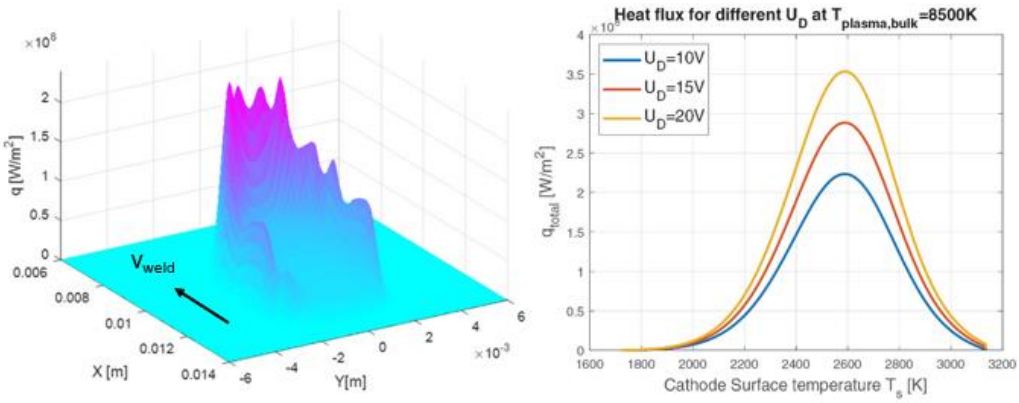



**Fig. 3** Profiles illustrating heat flux distribution using the EDACC model consideration, left: crown-formed distribution pattern, right: maximal heat flux is introduced in regions below the evaporation temperature [8]

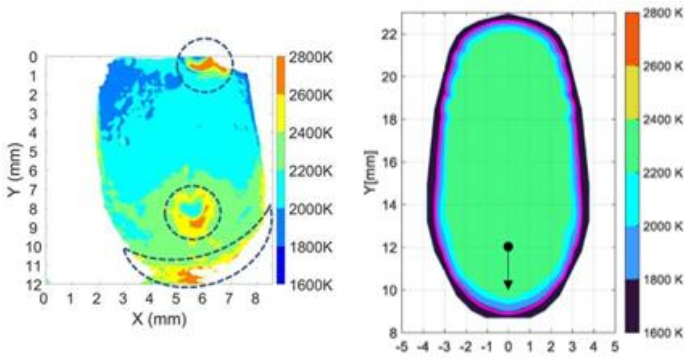



**Fig. 4** Surface temperature of the melt pool, left: Measurement using two-color pyrometry (the wire (top) and its reflection on the surface of the melt pool are circled), right: Calculation result using the EDACC model [9]

In summary, the EDACC model demonstrates that a moderate amount of metal vapor is essential for stable arc attachment in GMAW processes. Excessive local evaporation, however, cools the plasma and alters the current density distribution, leading to a shift of the cathode attachment point toward less evaporated regions. This shift modifies the distributions of heat flux, current density, and Lorentz force, illustrating how evaporation from the cathode surface strongly influences all major sub-processes within GMAW models.

A further implication of this model is that the assumption of axial symmetry in the GMAW arc is a rough simplification. The spatially variable arc attachment predicted by EDACC highlights the inherently three-dimensional and transient nature of the arc–pool interaction.

## THEORETICAL FOUNDATIONS OF EULERIAN GMAW MODELING

The general concept for model development divides the calculation domain in the material dependent areas: wire, arc and workpiece. Normally, wire and workpiece are of the same material. The governing equations of the process include mass (3), momentum (4) and energy conservation (5) in a general, compressible form:

$$\frac{\partial \rho}{\partial t} + \nabla \cdot (\rho \vec{v}) = 0, \tag{3}$$

$$\rho \frac{D\vec{v}}{Dt} = \rho \left( \frac{\partial v}{\partial t} + (\vec{v} \cdot \nabla)\vec{v} \right) = \rho \vec{g} - \nabla p + \nabla \cdot \bar{\bar{\tau}} + \vec{f}_L, \tag{4}$$

$$\frac{\partial \rho\, h}{\partial t} + \nabla \cdot (\rho h \vec{v}) = \nabla \cdot \left( \frac{\lambda}{c_p} \nabla h \right) + S_{Joule} + S_{Net} + S_{Sheets}, \tag{5}$$

where $\rho$ denotes the density [kg m$^{-3}$], $\vec{v}$ the velocity vector [m s$^{-1}$], $p$ the pressure [N m$^{-2}$], $\bar{\bar{\tau}}$ the viscous stress tensor [N m$^{-2}$], $\vec{f}_L$ the external magnetohydrodynamic, volumetric force [N m$^{-3}$], $h$ the specific enthalpy [J kg$^{-1}$], $\lambda$ the thermal conductivity [W K$^{-1}$ m$^{-1}$] and the $S$ terms represent the contribution from volumetric heat sources [W m$^{-3}$]. These volumetric heat

sources as well as the external volumetric force in the momentum equation (4) are introduced by adding electromagnetic considerations which lead to magnetohydrodynamics (MHD) approach. In this approach, the plasma is considered to be a continuous fluid and the problem is covered by the conductive media approximation. The electromagnetic model is coupled to the fluid flow and energy model by the consideration of the current continuity

$$\nabla \cdot \vec{j} = 0 \tag{6}$$

and the Maxwell equations. Here $\vec{j}$ is the electrical current density [A m$^{-2}$]. For a conductive media approximation, the electric current is connected to the electric and magnetic field by the general Ohms law:

$$\vec{j} = \sigma\,(\vec{E} + \vec{v} \times \vec{B}), \tag{7}$$

where $\sigma$ is the electric conductivity [S m$^{-1}$], $\vec{E}$ the electric field [V m$^{-1}$] and $\vec{B}$ the magnet field [T].

For the consideration of the Maxwell equations an auxiliary construction using potentials is introduced. This allows for a more compact and convenient formulation of the field equations, specifically the scalar electric potential $\varphi$ and the vector magnetic potential $\vec{A}$ are widely used. For the electric field $\vec{E}$ an electrical potential $\varphi$ [V]is defined as

$$\vec{E} = -\nabla\varphi. \tag{8}$$

From a simplified formulation of the Ampère's Law

$$\vec{B} = \nabla \times \vec{A} \tag{9}$$

and the vector identity (with the choice of a Coulomb gauge $\nabla \cdot \vec{A} = 0$)

$$\nabla \times (\nabla \times \vec{A}) = \nabla(\nabla \cdot \vec{A}) - \nabla^2 \vec{A} \tag{10}$$

a Poisson-like transport equation for the magnetic vector potential A [V s m$^{-1}$] is derived:

$$\nabla^2 \vec{A} = -\mu_o \vec{j}. \tag{11}$$

The equation (9) directly relates the spatial distribution of the vector potential $\vec{A}$ to the current density $\vec{j}$. The influence of the electromagnetic field on the fluid dynamics is described by the Lorentz force $\vec{f_L}$:

$$\vec{f_L} = \vec{j} \times \vec{B}. \tag{12}$$

And the influence on the heat balance by the Joule heating $S_{Joule}$ is described by:

$$S_{Joule} = \vec{j} \cdot \vec{E}. \tag{13}$$

Plasma radiation is usually considered as a temperature and pressure dependent material property by the kinetic calculation of a net radiation, which is included as volumetric heat loss term $S_{Net}$. The most challenging area in GMAW simulation is the determining of the heat source in the sheath layers, $S_{Sheets}$ [8,10].

### ADAPTIVE AND DEFORMABLE MESH TECHNIQUES

To address dynamic interfaces, adaptive mesh techniques like Arbitrary Lagrangian-Eulerian (ALE) methods and dynamic remeshing have been employed, although these approaches struggle with extensive topological changes such as droplet detachment.

These phenomena are strongly coupled to the geometries of the corresponding surfaces and require special consideration due to their complexity and the effect on both the plasma and the convection in the liquid metal. The approaches range from a simultaneous solution of the whole set of MHD equations and a dynamic resolution of the interface surfaces [11] to an assumption of quasi-stationary geometrical conditions of the molten droplet and weld pool. This assumption is justified because of the much higher reaction rate of the plasma compared to its influence on surface formation [12].

In the calculation procedure, the interface is considered as a static boundary, and the geometry of the droplet or the molten pool is updated with precalculated plasma parameters at the interface. The disadvantage of the first approach, a dynamic resolution of the interface, is a very time consuming simulation and of the second a high number of iterations for different geometric droplet and pool configuration. The decomposition of the process in quasi-stationary states delivers highly accurate values for heat flux and electric current distributions.

Nevertheless, the heat input calculation in these approaches does not consider the full spectrum of physics happening in the sheet layers. Another approach is the focus on the physics of the sheet processes for a detailed description of the phenomena on the microscopic scale. Here a detailed plasma physics calculation including species consideration is taking place. With such models the effects of the sheet processes like particle interaction, ambipolar drift, multiple ionization levels and the consideration of particle number densities are analyzed [8-10,13].

### EULERIAN GRID-BASED METHODS (VOF, LEVEL SET)

The energy input distribution and electrical current distribution on the surface during the simulation of welding processes play a central role in the further evolution of the flow field and the weld shape. An important prerequisite for the numerical coupling of energy is an exact definition of the surface at which the coupling takes place. In Eulerian approaches, a phase boundary can be determined by several methods. The methods differ in the number of domains considered, with each having unique boundary conditions. For cases with two or more domains, the boundary conditions can be defined as external inputs or as interface fluxes. The motion of the boundary on a small scale can be modelled by mesh deformation. If the location of the phase boundary is not known and has to be determined the Volume of Fluid method can be used [14].

This method requires only one computational domain that includes two different fluids. The phase boundary is determined by the concentration of the mass or the distribution of the volume fraction. For this purpose, an additional transport variable is introduced in the calculations, which assigns values between 1 and 0 to the calculation cells according to the content of the medium of interest. Thus, a surface is reconstructed. Traditional Eulerian

methods such as Volume of Fluid (VOF) and Level Set were initially employed for weld simulations. Despite their ability to handle fluid interfaces, these methods face limitations due to the necessity of very fine, static meshes, particularly near regions with steep gradients.

## SMOOTHED PARTICLE HYDRODYNAMICS METHOD FOR WELD POOL SIMULATION

Smoothed Particle Hydrodynamics (SPH), originally developed in astrophysics, has been adapted for welding simulations due to its inherent ability to handle topological changes without mesh adjustments. The SPH method effectively addresses challenges associated with heat and mass transfer, including droplet dynamics, thermal distribution, and solidification phenomena within the weld pool, Fig. 5**.**

In contrast to Eulerian methods that discretize the space and fix the control volumes (or grid) on a coordinate system, SPH is based on the representation of mass distribution connected to dynamically moving integration points. Thus, SPH provides significant advantages in simulating droplet dynamics and free surface flows in molten metal.

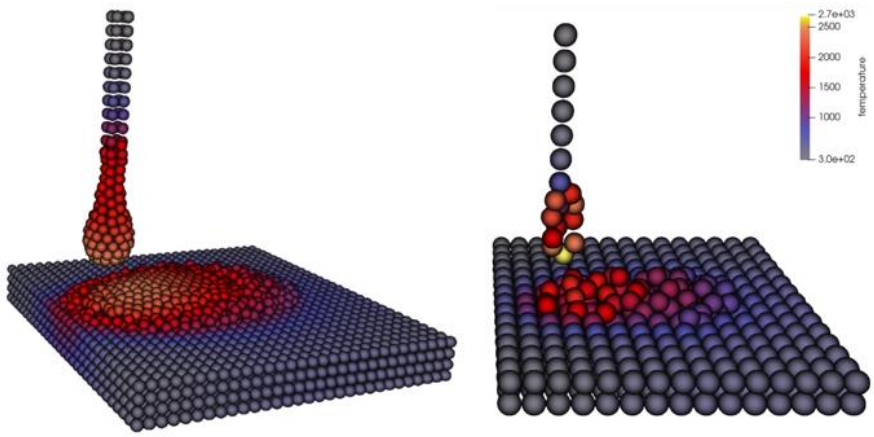



**Fig. 5** Basic capabilities presentation: transient bead on plate weld simulation including heat and mass transfer, droplet detachment and phase change, wire diameter 1 mm. Left: particle radius 0.25 mm, right: particle radius 0.5 mm

### SPH FOUNDATIONS

Smoothed particle hydrodynamics is a mesh-free numeric method that discretizes the continuum into a specific number of Lagrangian particles. This method, originating from astrophysics, has been adopted for fluid flow simulations and further specialized for use in welding simulations [15,16]. The discretization captures the distribution of the mass and the

advection of the mass, dynamically resolving arbitrary topology changes without prior preparation of specific regions of interest. Thus, the computational domain changes its form and boundaries according to the tracked mass distribution. In smoothed particle hydrodynamics the fluid is divided into a number of particles representing the mass included in the predefined geometry. The particles carry values of properties and field variables that are calculated depending on their position and the properties of the surrounding particles. The calculation for values stored in a particle is conducted by an interpolation inside a preset diameter around this particle. The formula for determining a variable $A$ at the location $x_i$ takes the following form according to a Dirac delta approximation:

$$A(x_i) \approx \sum_{j \in N_{x_i}} \frac{m_j}{\rho_j} A(x_j) W(x_i - x_j; h_{smooth}), \tag{14}$$

where $m_j$ is the mass and $\rho_j$ is the density at location $x_j$. $\mathrm{W}(x_i - x_j; h_{smooth})$ represents the kernel function with the smoothing lenght $h_{smooth}$ and $N_{x_i}$ the set of particles within the support radius around $x_i$. The particular advantage of the SPH formalism is that the gradient and divergence operators in the physical equations can be determined by applying them to the kernel:

$$\nabla A(x_i) = \sum_{j \in N_{x_i}} \frac{m_j}{\rho_j} A(x_j) \nabla_i W(x_i - x_j; h_{smooth}). \tag{15}$$

In the following, the short form $\mathrm{W}_{ij}$ for the kernel $\mathrm{W}(x_i - x_j; h_{smooth})$ will be used. For detailed information on the mathematical formulation of the method the reader is referred to the corresponding literature [17].

Numerous investigations have employed the incompressible smoothed particle hydrodynamics method in diverse contexts, encompassing the simulation of tungsten inert gas welding and the computation of weld pool dynamics and weld seam structure in relation to arc forces within the process [18,19]. These studies have consistently demonstrated the efficacy of the smoothed particle hydrodynamics method in accurately capturing heat transfer, non-uniform temperature fields, and weld pool dynamics influenced by numerous factors, including surface tension, Marangoni force, and arc forces [19-21].

A focus on three-dimensional modeling of thermo-mechanical responses in arc welding has emerged in several studies, highlighting the potential of mesh-free smoothed particle hydrodynamics and the coupled smoothed particle hydrodynamics with discrete element method in high-current submerged arc welding for simulating slag and weld pool formation processes [22].

Despite the demonstrated versatility and potential of the smoothed particle hydrodynamics method, existing literature underscores the necessity for ongoing research and refinement to enhance accuracy and expand its applicability. Recommendations for future research encompass the incorporation of more realistic boundary conditions and material properties, the development of increasingly accurate models for heat transfer and phase change, the exploration of alternative numerical techniques for addressing coupled thermomechanical problems, and the validation of smoothed particle hydrodynamics simulations through the utilization of experimental data [22]. Moreover, the consideration of supplementary factors

that affect weld pool dynamics and structure, such as electromagnetic fields or gas flow in welding processes, has been proposed [19]. The smoothed particle hydrodynamics method has gained significant attention in the realm of engineering applications [23] and in particular in welding simulations due to its promising results [24,25].

### PHASE BOUNDARIES AND TOPOLOGY CHANGES

In particle-based smoothed particle hydrodynamics method, the surface can be determined by the so-called color function [26,27]. This function also delivers values between 1 and 0, which characterize the filling of an imaginary volume within the support radius with particles. A value of 1 means that a particle with the corresponding support radius is located in a fully dense region. The closer the particles are to the surface, the lower the values of the color function are. This is because the imaginary volume inside the support radius contains less particles in sum when moving out of the material. Numerically this concept uses the gradient of the color function resulting in the detection of the maximum gradient magnitude for the determination of the surface line. It should be noted that for both methods, Eulerian grid-based and Lagrangian particle-based, comparable concepts are used for the determination of the free surface, but with the advantage of smoothed particle hydrodynamics to use an implicit formulation. The status of the actual research shows that for a meaningful calculation of the weld seam geometry models and approaches need to be developed in order to physically describe the individual system anode, arc and cathode and to record their coupling as an overall system. In the present work the strategy is proposed to use replacement models for the processes in the anode and cathode layer based on the physics of the evaporation determined arc-cathode coupling model. By this means a compensation of the feedback through substitute models for the arc effect, both thermal and electromagnetic, is considered. The findings about the heat input distribution and current density distribution from previous work (evaporation determined arc-cathode coupling) can be integrated in smoothed particle hydrodynamics as an input boundary condition.

## PROPOSED HYBRID COUPLED-DOMAIN APPROACH

To overcome individual limitations, a hybrid approach combining Eulerian grid-based arc modeling and Lagrangian SPH weld pool simulation is proposed. Data coupling strategies enable efficient exchange between domains, facilitating accurate simulations of dynamic interfaces and significant gradient regions. This hybrid model integrates evaporation determined arc-cathode coupling (EDACC) to capture the metal evaporation effects on sheath layers realistically.

The concept involves deriving an equivalent reduced substitute model for small-scale processes such as arc connection, interaction between melt surface temperature (i.e., evaporation) and plasma composition, and current density distribution from stationary FEM MHD calculations. These results will be used to create dynamic boundary conditions for the substitute models of the layer areas for the transient SPH simulation, Fig. 6.

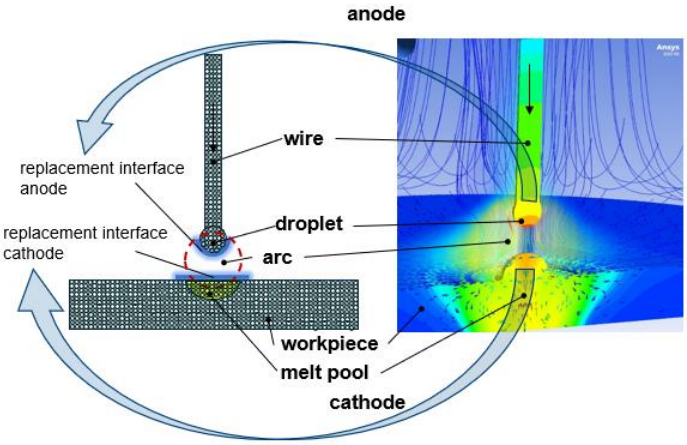



**Fig. 6** Workflow of the proposed hybrid Eulerian-SPH coupling strategy

## FEM 2D AXISYMMETRIC MODEL ACCORDING TO A GMAW CONFIGURATION

Firstly, a validation of the EDACC concept is conducted using a simplified geometry for an axisymmetric case. Fig. 7 shows the computational region containing three domains:

1. Argon
    a. Fluid flow
    b. Heat transfer
    c. Electric and magnetic fields
    d. Material properties: argon plasma with continuous fluid approximation 300 K-30000 K
2. Wire
    a. Heat transfer
        i. Wire feed rate considered by translational velocity for the T-field
    b. Electric and magnetic fields
    c. Material properties: S235
    d. No phase change
    e. Diameter 1 mm
    f. Tip diameter 0.5 mm
    g. Wire tip to workpiece distance 3 mm
3. Workpiece
    a. Heat transfer
    b. Fluid flow
    c. Electric and magnetic fields
    d. Material properties: S235
    e. Phase change: apparent heat capacity method

The 3 domains are thermally decoupled, 3 different variables will be solved for this task: $T$ in argon-plasma domain, $T1$ in wire-domain and $T3$ in workpiece domain. The coupling at the cathode is established by the heat flux components of the equation (1):

$$q_{ion} = \frac{j_i}{e}\left(\frac{k_B T_e}{2} + eU_{Drop} + E_{ion} - A + \frac{H_{vap}}{N_A}\right), \tag{16}$$

$$q_{em} = \frac{j_{em}}{e}(k_B T_s + A), \tag{17}$$

$$q_{evap} = J_{vap} \cdot \frac{H_{vap}}{molar_mass}, \tag{18}$$

$$q_{rad} = \sigma_{const}(T_s - 300\ K)^4, \tag{19}$$

where $T_e$ is the temperature of the argon-plasma domain $T$ and $T_s$ the temperature in the workpiece domain $T1$. A transient calculation is conducted for a current rise from 30 A to 400 A in 0.7 s as shown in Fig. 8**.** The results show a distinct peak in current density on the cathode surface, which occurs at the edge of the melting bath, Fig. 9. The main result of this calculation is a typical temperature and velocity field in the arc and in the molten pool, but a significantly different current density distribution compared to standard models. The 2D investigations serve as an intermediate step for the construction of the 3D model and for the validation of the EDACC concept. This result is in accordance with the findings of the earlier implementations of the EDACC model.

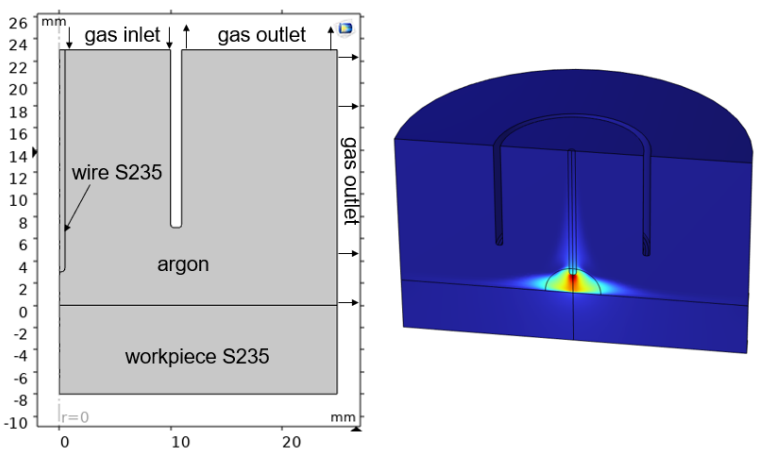



**Fig. 7** 2D axisymmetric computational domain. Left: domain assignment and dimensions, right: 3D representation by a 180° rotation

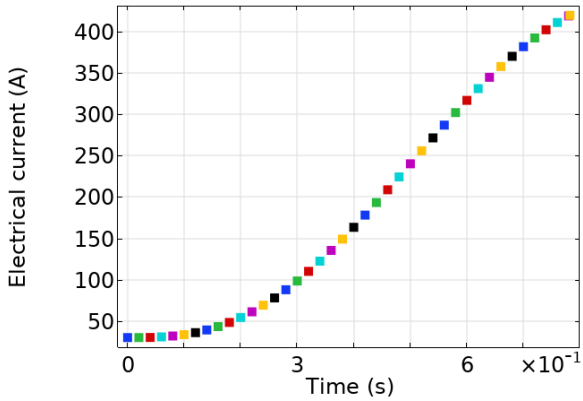



**Fig. 8** Electric current ramp for the 2D axisymmetric calculation

**Table 2** Process parameters

| | | 2D, transient | 3D, stationary |
|---|---|---|---|
| $v_{wire}$ | m min$^{-1}$ | 6 | 6 |
| $v_{weld}$ | cm min$^{-1}$ | - | 50 |
| $v_{shieldingGas}$ | m s$^{-1}$ | 2 | 2 |
| ETWD | mm | 3 | 2 |
| stickout | mm | 5 | 8 |
| current | A | 30-400 | 100, 200, 300, 400 |
| wire Ø | mm | 1 | 1 |
| EDACC parameter | | | |
| $U_{drop}$ | V | 3 | 3 |
| $t_{sheath}$ | mm | 0.1 | 0.1 |

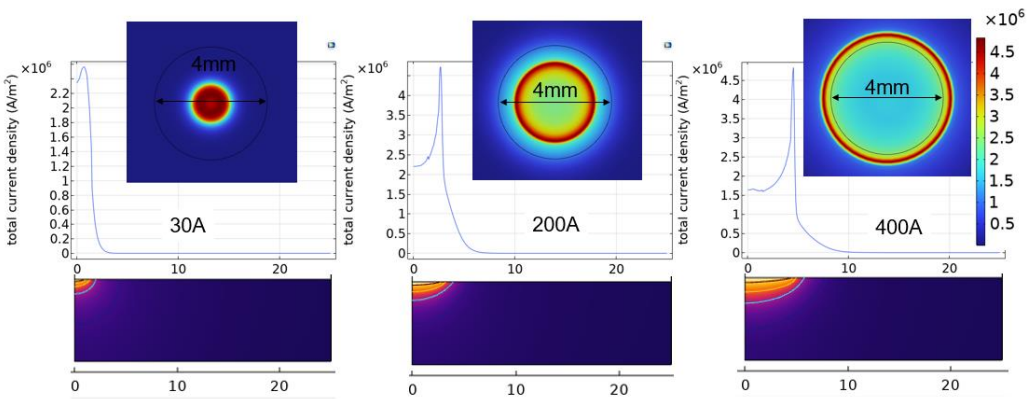



**Fig. 9** Current density distribution on the cathode surface and the corresponding melt pool. Position of the current density peak is close to the melt pool edge.

## FEM 3D GMAW-MODEL WITH TILTED TORCH

The goal of the investigations using a 3D model is the current density distribution with an inclined welding torch, Fig. 10. Here the same settings are used for material and computational domain definitions as for the 2D case, with the additional factor of welding speed being taken into account through a translational movement of the temperature field. Such a configuration allows for the analysis of different wire feed/welding speed and direction configurations on the same mesh, thus reducing the effort for model discretization. A stationary case is assumed for the calculation in order to set selected parameter variations.

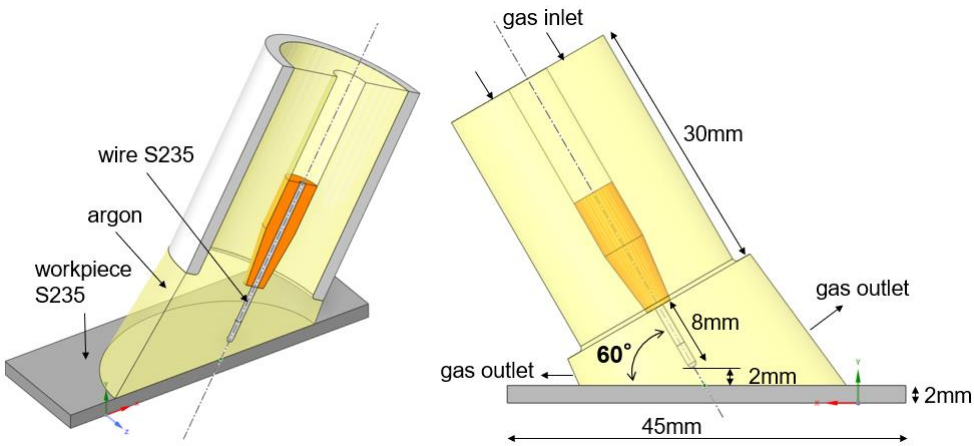



**Fig. 10** 3D GMAW model dimensions

3 cases were calculated: push welding, pull welding and welding with lateral inclination of the torch, Fig. 12. The selection of these configurations serves to vary the heat input on the cathode and to set different melt pool dimensions with the same electrical parameters. It should be noted here that the phase change in the workpiece is not taken into account for the 3D calculations and that the dimensions of the molten pool are analyzed on the basis of the liquidus temperature isotherms on the workpiece surface.

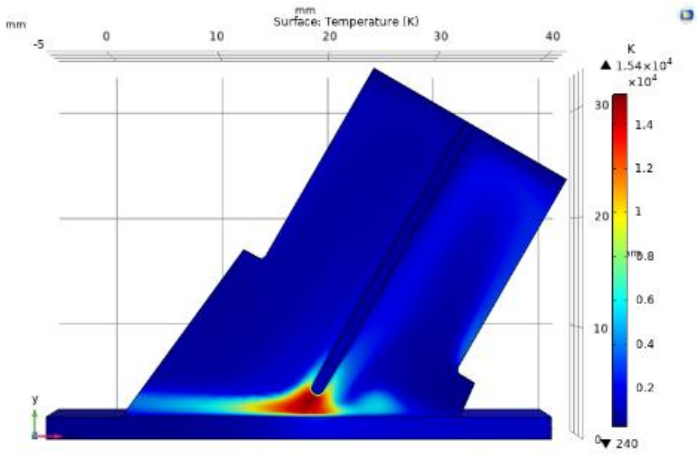



**Fig. 11** Temperature distribution in a cross section view for the 100 A push welding variant

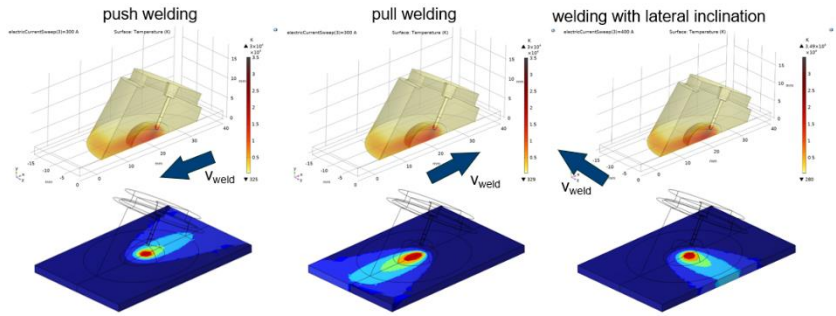



**Fig. 12** Examined variants of the process arrangement

Fig. 13 illustrates the heat flux density on the cathode surface and two key observations can be made:

1. The symmetry of the heat flux density depends on the current level; at low currents, a quasi-Gaussian distribution is calculated, while at high currents, symmetry no longer applies and the distribution pattern becomes crown formed.
2. Most of the heat input occurs at the front of the molten pool, in the welding direction, where the temperature gradients are highest. This distribution is a consequence of the temperature distribution on the surface of the molten bath: the hot liquid area requires only a small amount of heat input to generate metal vapor. This vapor helps to cool the adjacent plasma, thereby reducing the conductivity of the layer. In the front, cold area of the molten bath, more energy can be absorbed (heating of the workpiece in the welding direction and, in addition, a phase change from solid to liquid), so that the conductivity limitation due to fresh metal vapor only sets in later.

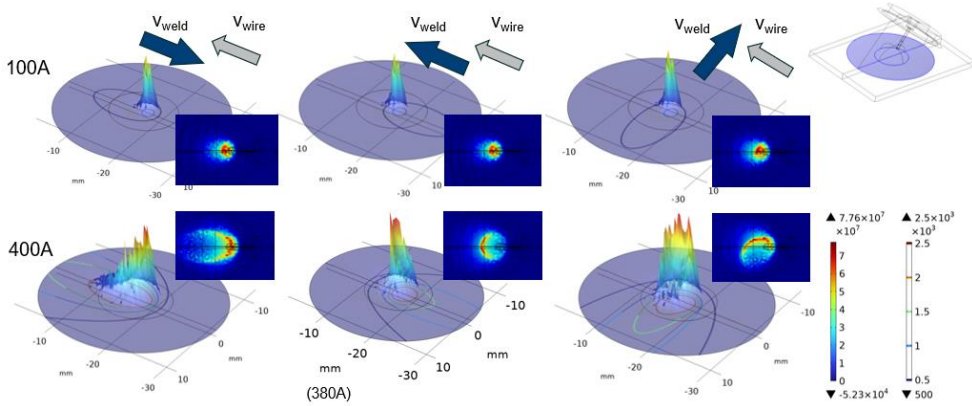



**Fig. 13** Heat flux density on the cathode for 3 process arrangements and 2 electric current values. Focus: axisymmetric Gauss-like heat flux distribution for low current values and asymmetric crown-formed distribution for high current velues.

This characteristic can also be observed in the current density for the three welding configurations examined at 4 current values, with a clear pattern at high current values.

1. Push welding in Fig. 14
2. Pull welding in Fig. 15
3. Lateral welding in Fig. 16

The asymmetry of the electric current density on the cathode is particularly evident in the lateral case, Fig. 16: the burner angle has no influence on the arc connection, and no projection of the wire axis can be extrapolated for the derivation of an arc attachment pattern. Only the temperature distribution on the cathode surface allows clear conclusions to be drawn about the arc connection. A comparison of the configurations examined is shown in Fig. 17 for a current of 300 A. Based on these quasi-stationary results a replacement model for the arc connection is derived. It incorporates a temperature dependent weighting factor for the spatial distribution of the heat input.

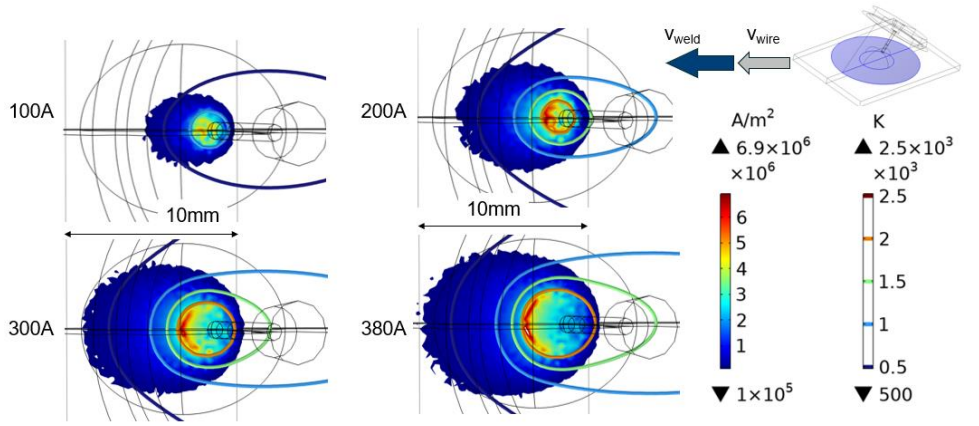



**Fig. 14** Current density on the cathode at push welding configuration for 4 current values

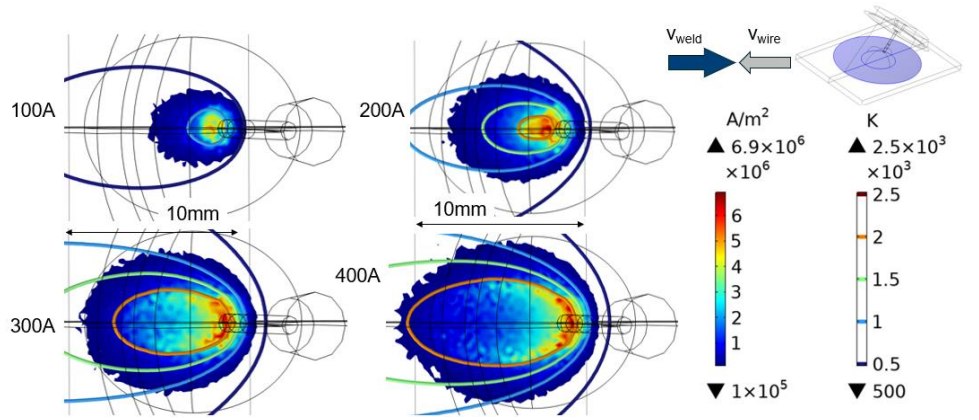



**Fig. 15** Current density on the cathode at pull welding configuration for 4 current values

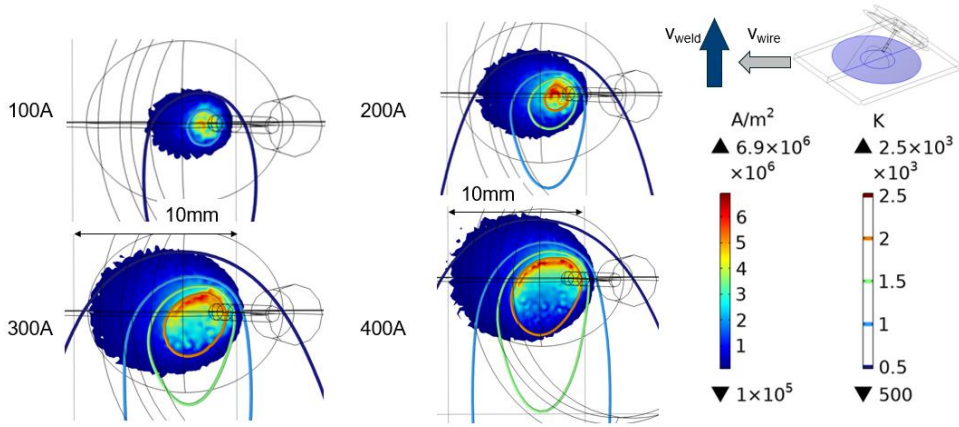



**Fig. 16** Current density on the cathode at lateral welding configuration for 4 current values

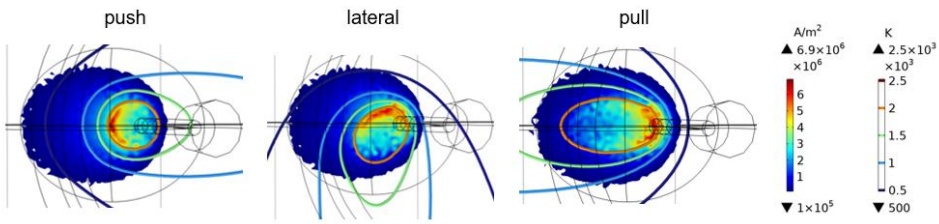



**Fig. 17** Electric current density on the cathode surface for the 3 welding configurations at 300 A. Focus: arc attachment strongly depends on surface temperature distribution

## SURROGATE MODEL FOR THE HEAT INPUT

The temperature dependence of the arc connection is taken into account using a cubic weighting function, equation (20). Table 3 and Fig. 18 show the parameters and the curve of the weighting function, respectively. Most of the heat is introduced in a range of $T_{evap_offset} = 500\ \mathrm{K}$ beneath the evaporation temperature $T_{evaporation}$. The heat input near the evaporation temperature is limited by a steeply falling weighting factor in order to correspond to increased vapor formation and to represent the sharp range of the electric current density presented in Fig. 17. Towards the low temperature, the heat input is limited less strongly and distributed broadly over the surface by a low weighting factor.

**Table 3** Heat distribution weighting function parameters

| | | |
|---|---|---|
| $T_{liquidus}$ | K | 1500 |
| $T_{evaporation}$ | K | 2700 |
| $T_{evaporation_offset}$ | K | 500 |
| $T_{peak}$ | K | $T_{evaporation}$ -$T_{evaporation_offset}$ |
| $w_{max}$ | - | 2 |

$$w_h = \begin{cases} 1, & T < T_{liquidus} \\ 1 + 3x^2 - 2x^3, & T_{liquidus} < T \; and \; T < T_{peak} \\ 2 - 2(3x^2 - 2x^3), & T > T_{peak} \; and \; T < T_{evaporation} \\ 0, & T_{evap} < T \end{cases} \tag{20}$$

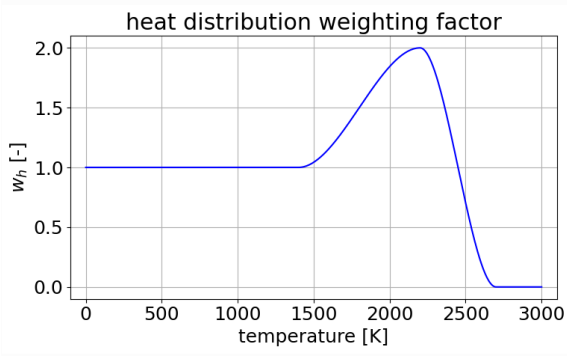



**Fig. 18** Function graph for the weighting of the heat distribution

## SPH-MODEL IMPLEMENTATION AND COMPUTATIONAL SETUP

This model follows the general assumptions outlined above, with restrictions due to the exclusion of temperature dependent density and electromagnetic fields in the actual implementation approach. Moreover, the model is not capable of combining fluids with high density ratios in the same computational domain. To address these constraints, the following assumptions are made:

- Electromagnetism is not directly included in the computation routine; instead, compensation models for electromagnetic effects are introduced.
- No plasma or electrical arc domain is included in the model. Compensation models for the arc effect are introduced on the corresponding surfaces.
- Evaporation (mass loss of molten metal phase) is excluded.
- Buoyant flow resulting from temperature-dependent density is not accounted for.

- Only laminar flow was considered in the melt pool. However, density is assumed constant, and thus hydrodynamics is affected only via droplet momentum.
- Limitation of a temperature maximum for consideration of evaporation loss.
- Constant radiative and convective heat transfer coefficients acting as boundary conditions on the surface.

For the material properties, a material corresponding to structural steel S235 was assumed. The material values were calculated in JMatPro according to S235 structural steel in order to cover a wide temperature range.

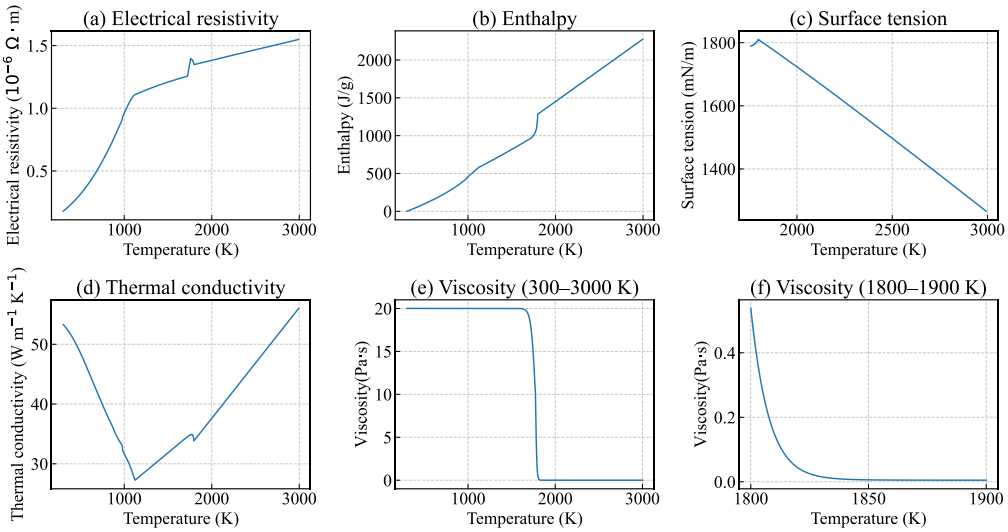



**Fig. 19** Model material based on S235 steel, calculated with JMatPro

The basis for this model and the implementation of the necessary methods was carried out on a model example for tungsten inert gas welding [24]. The computational domain is divided into 3 areas: anode, arc and cathode, Fig. 6. The domains anode and cathode are directly included in the simulation, containing a mass and the according discretization by particles. The arc is not solved within the solution pipeline but is included by substitution models for the arc effects: Lorentz force, as will be described in the following section *Fluid Flow*, and heat input, as in section *Heat Transfer*.

### *Fluid flow*

Based on the Lagrangian formulation for the continuity equation

$$\frac{D\rho}{Dt} = -\rho\nabla \cdot v, \tag{21}$$

the special case for incompressible flow is derived. Firstly, the auxiliary condition that the number of particles is set and remains constant over the simulation progress is given. Secondly, the requirement that the density always corresponds to the density at rest is postulated:

$$\rho(t) = \rho^0, \tag{22}$$

which leads to

$$\frac{D\rho_i}{Dt} = 0. \tag{23}$$

From the incompressibility constraint the divergence-freeness of the velocity field follows as well:

$$\nabla \cdot v = 0. \tag{24}$$

For the case of an incompressible flow, which is assumed in this model, the conservation of the continuity equation is achieved by reducing the velocity divergence to zero by means of balancing the pressure and pressure acceleration. The conservation of momentum for an incompressible fluid is given by the Navier–Stokes equations

$$\rho \frac{Dv}{Dt} = \rho g - \nabla p + \mu \nabla^2 v + S_L + S_{ms}. \tag{25}$$

Here, $v$ is the velocity [m s$^{-1}$], $p$ the pressure [N m$^{-2}$], $\mu$ the dynamic viscosity [Pa s] and the $S$ terms represent external volumetric forces [N m$^{-3}$]. The change of momentum $\rho \frac{Dv}{Dt}$ is the result of acting force density fields on the right hand side, resulting in an acceleration acting on a particle:

$$a_i = \frac{Dv_i}{Dt} = \frac{f_i}{\rho_i}. \tag{26}$$

For the pressure force a symmetric formulation is used:

$$f_{pressure} = \nabla p = \sum_{j \in N_{x_i}} m_j \left(\frac{p_i}{\rho_i^2} + \frac{p_j}{\rho_j^2}\right) \nabla W_{ij}. \tag{28}$$

For an incompressible fluid, the viscous force is defined as $f_{viscosity} = \mu \nabla^2 v$. Since a standard discretization of the Laplacian is problematic because of the sign change of the second derivative of a Gaussian-like kernel the approach by Weiler et al. for a temperature dependent viscosity is chosen. [28] In this approach a combination of a SPH derivative and finite differences is used:

$$f_{viscosity} = \nabla^2 v = d \sum_{j \in N_{x_i}} \frac{m_j}{\rho_j} \frac{(v_i - v_j)(x_i - x_j)}{\|x_i - x_j\|^2 + 0.01h^2} \nabla W_{ij}, \tag{29}$$

where $d$ is a factor representing the number of spatial dimensions and $0.01h^2$ prevents singularities.

$S_L$ represents the Lorentz force with a classical formulation according to equation 10. In the presented model the calculation of the electromagnetic task is not included, but the effect of

the electromagnetic force. Moreover, this effect of the Lorentz force is limited to droplet detachment. No electromagnetic forces act in the molten pool. The force acting on a droplet is based on the geometric conditions of the arc. Firstly, it is assumed that this force acts only in the axial direction of the wire axis. Secondly, it is specified that the droplet is enveloped by the arc. The liquid volume (detection based on the temperature of the particles) is divided into layers with a thickness corresponding to a multiple particle diameter, Fig. 20. In accordance with the conducting wire models of [29,30] where the current lines are determined by the attachment angle of the arc, surrounding the droplet, the force is calculated in dependence of the ratio of the layer diameters to each other:

$$F_L = \frac{\mu_m \, I^2 \, log(r_{down}/r_{up})}{4\pi}. \tag{30}$$

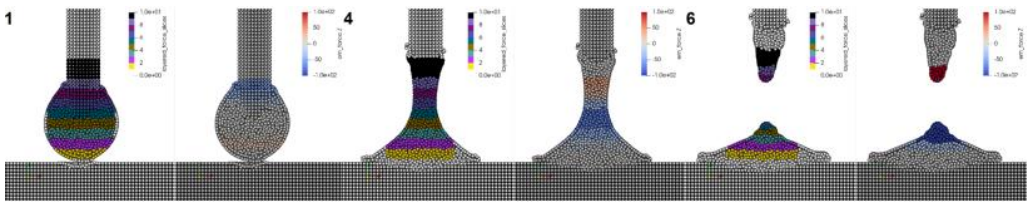



**Fig. 20** Layer force model for the consideration of the Lorentz force in the SPH model. Numbers represent the time evolution in the detachment process.

In the equation (30) $\mu_m$ represents the magnetic constant (also known as the permeability of free space, $4\pi \times 10^{-7} \, N \, m^{-2}$), $I$ the electric current [A] applied on the wire, $r_{down}$ the mean radius of the lower layer [m] and $r_{up}$ the mean radius of the upper layer [m]. It is obvious that $F_L$ from equation 22 is an integral force and it is measured in Newtons. A specific force value for the corresponding layer volume is calculated from the integral force acting on a layer:

$$S_{L,i} = \frac{F_L}{\sum_{j \in layer} m_i}, \tag{31}$$

where $j$ enumerates the number of particles in the layer and $m_i$ a particle's mass [kg]. The model is active inside a sphere around the wire tip with a diameter of $D_{F_L} = 2 \cdot D_{wire}$. Only particles inside this sphere experience an additional acceleration that corresponds to the Lorentz force:

$$a_{i,F_L} = \frac{S_{L,i}}{\rho_i}. \tag{32}$$

$S_{ms}$ is representing a momentum sink. During solidification materials pass through a state that is not fully liquid but also not yet solid. This condition is the so-called mushy zone. The momentum sink, also called the porosity term, is used to account for the significant reduction of momentum during the phase change process from liquid to solid. It adds a negative

acceleration to the particles in dependence of the temperature. The calculation of this term is conducted according to the procedure in the base model [24].

After summing up the individual accelerations of a particle:

$$a_i = a_{i,pressure} + a_{i,viscosity} + a_{i,F_L} + a_{i,ms}, \tag{33}$$

its velocity change

$$a_i = \frac{v_i^{t+1} - v_i^t}{\Delta t} \tag{34}$$

and thus, the position

$$v_i = \frac{x_i^{t+1} - x_i^t}{\Delta t} \tag{35}$$

is updated.

*Heat transfer*

In the process under consideration, the phase changes that occur (e.g. melting, solidification) should also be taken into account. As a result, enthalpy can contain a sudden change. Therefore, the classical heat conduction equation (Fourier equation)

$$\frac{\partial T}{\partial t} = \alpha \nabla^2 T, \tag{36}$$

where $T$ is the temperature [K] and $\alpha$ the thermal diffusivity [$m^2\ s^{-1}$], is extended with the idea that heat conduction can also be expressed by an energy balance. The Lagrangian formulation of the Fourier equation with enthalpy is introduced for this purpose:

$$\rho \frac{Dh}{Dt} = \nabla \cdot (\lambda \nabla T) + q''', \tag{37}$$

where $h$ denotes specific enthalpy [$J\ kg^{-1}$], $\rho$ the material density [$kg\ m^{-3}$], $T$ the temperature [K], $\lambda$ the thermal conductivity [$W\ K^{-1}\ m^{-1}$] and $q'''$ the contribution from volumetric heat sources [$W\ m^{-3}$]. This is particularly relevant when the process is described using an enthalpy approach in order to take into account phase changes or non-linear temperature dependencies of the specific heat. In this formulation, $h$ considers the latent heat of melting, which is included in the temperature-dependent specific heat capacity $c_p(T)$:

$$h(T) = \int_0^T c_p(T) dT. \tag{38}$$

The heat transfer equation (29) will be discretized using smoothed particle hydrodynamics and explicit Euler time integration:

$$\rho_i \frac{h_i^{t+1} - h_i^t}{\Delta t} = \nabla \cdot (\lambda \nabla T)_i^t + q_i^{t'''}. \tag{39}$$

The discretization of the heat conduction term has the form

$$\nabla \cdot (\lambda \nabla T)_i = \sum_{j \in N_{x_i}} \frac{m_j}{\rho_j} \left( \frac{4\lambda_i \lambda_j}{\lambda_i + \lambda_j} \right) (T_i - T_j) \frac{\nabla W_{ij}}{\|x_i - x_j\|^2}. \quad (40)$$

*Heat sources*

The acting heat sources and sinks are summed up in the following equation:

$$q''' = q_J''' + q_A''' + w_h(T) q_C''' + q_{loss}''' \quad (41)$$

Joule heating is considered in the stick-out region (free wire length after the contact nozzle) by

$$q_J''' = \frac{1}{\sigma} j^2, \quad (42)$$

where $q_J'''$ is the produced heat power [W m$^{-3}$], $\sigma$ is the electric conductivity [kg$^{-1}$ m$^{-3}$ s$^3$ A$^2$] and $j$ is the electrical current density [A m$^{-2}$]. For further SPH realization, this local power results in an energy density when multiplied with the time step. This energy is then added to the volume occupied by the discretization particle, raising its temperature. The particles are assigned to the Joule heating model using a cylinder that has a double radius of the wire. For the consideration of the heat produced in the sheath layers the surface of the anode/droplet or cathode is determined using the color function. The areas that represent an arc connection (i.e. layer areas) are then selected. This is done on the basis of a weighting with regard to the wire feed direction and the distance to the reference point in the center of the droplet. The power applied is then divided by the number of particles and divided by their volume. This results in a volumetric heat source. The distribution of the applied power occurs only to the surface particles. The arc effect in the sheath layers that heat the surfaces is based on the energy input by ionization and the material specific work function for electron emission:

$$q_{A,C}''' = j \frac{w_f}{e}, \quad (43)$$

where $q_{A,C}'''$ is the volumetric energy input at the anode or cathode [W m$^{-3}$], $j$ is the electric current density [A m$^{-2}$], $w_f$ is the work function [eV], $e = 1.602176634 \times 10^{-19}\ C$ is the elementary charge. It is assumed that the same material is used for both regions and a uniform current density distribution. The heat losses $q_{loss}'''$ incorporate radiation and natural convection losses:

$$q_{rad} = \varepsilon \sigma_B (T^4 - T_0^4), \quad (44)$$

$$q_{con} = k(T - T_0), \quad (45)$$

with $q_{rad}$ and $q_{con}$ as surface heat losses [W m$^{-2}$], $\varepsilon$ representing the material dependent emissivity factor [-], $\sigma_B$ as the Stefan-Boltzmann constant $5.67 \times 10^{-8}$ W m$^{-2}$ K$^{-4}$, $T_0$ as the ambient temperature [K] and $k$ the heat transfer coefficient [W m$^{-2}$].

For the application of these heat fluxes the determination of the exposed surface area is needed. Here the surface particles are also determined by the color function. The heat flux

leaving a corresponding particle is estimated with a projected cross section of a particle $A = (2r_p)^2$.

## RESULTS

The presented results demonstrate the functionality and predictive capability of the developed hybrid Eulerian-SPH model. The simulations were performed for representative GMAW configurations, focusing on droplet transfer, weld pool evolution, and arc attachment behaviour under different torch orientations and process conditions.

In the hybrid framework, the Eulerian calculations provide quasi-stationary reference data for the arc plasma based on the Evaporation Determined Arc-Cathode Coupling (EDACC) model. These solutions deliver physically consistent distributions of heat flux and current density on the cathode surface, which are subsequently used as surrogate boundary models in the transient SPH simulations. Thus, the plasma-related effects - such as evaporation-driven cooling, conductivity variation, and asymmetric arc attachment - are not recalculated during the SPH computation but are incorporated through precomputed temperature-dependent substitute functions. This separation of domains ensures computational efficiency while maintaining a high degree of physical accuracy.

Fig. 21 shows the transient simulation of droplet transfer and weld pool formation. Although the case represents a relatively simple bead-on-plate configuration, all algorithms of the hybrid model are fully active, including the coupling routines for data exchange between the Eulerian and SPH domains. The influence of torch inclination and motion is dynamically included, with the welding direction intentionally set non-parallel to the plate edge. The sequence illustrates the formation, detachment, and spreading of the droplet on the substrate. The temperature field (in K) highlights localized heating of the droplet, the transient high-temperature zone upon impact, and the subsequent redistribution of thermal energy in the melt pool.

To evaluate the versatility of the SPH formulation, the model was applied to a fillet weld configuration (Fig. 22). The left image presents the raw SPH particle distribution, while the right image shows the reconstructed surface of the deposited material. This example demonstrates the robustness of the SPH method in handling complex joint geometries and multiple contact surfaces. Its mesh-free character allows a natural adaptation to evolving topologies without remeshing, an essential feature for applications such as multi-pass welding or additive manufacturing.

Finally, Fig. 23 illustrates different stages of a vertical weld with varying arc attachment patterns. The deflection of the arc connection corresponds directly to the non-uniform temperature distribution on the cathode surface. These results confirm the sensitivity of current density and heat flux distributions to local surface temperature, validating the EDACC concept and its integration via surrogate models into the hybrid framework. The sequence also demonstrates the model's ability to capture arc attachment asymmetry under realistic process conditions, including changing torch orientation and gravity effects.

Overall, the presented results confirm that the hybrid Eulerian-SPH approach successfully reproduces the essential physical mechanisms of GMAW. The combination of stationary Eulerian pre-calculations with transient SPH melt pool dynamics enables detailed yet computationally efficient modeling of the entire process chain - from arc attachment to droplet impact and solidification - through the consistent use of surrogate boundary conditions derived from physically based arc simulations.

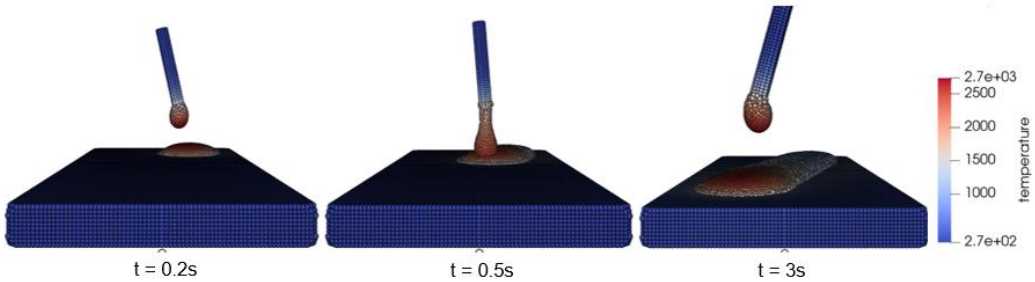



**Fig. 21** SPH-based weld pool and droplet detachment dynamics incorporating thermal and flow effects. Transient simulation of droplet transfer and weld pool formation in GMAW using the hybrid Eulerian–SPH model. Although representing a relatively simple bead-on-plate case, all coupling algorithms of the hybrid model - including EDACC-based boundary conditions - are fully implemented and active. Both torch inclination and torch motion are continuously varied during the simulation, with the welding direction not aligned parallel to the plate edge. The temperature field (K) illustrates droplet detachment, impact, and spreading on the substrate.

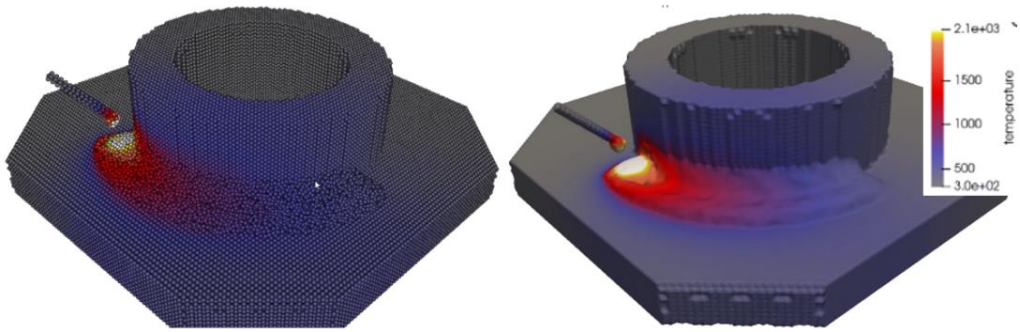



**Fig. 22** Application example of a fillet weld joint modeled with the hybrid Eulerian–SPH approach. Left: raw SPH particle data; right: reconstructed surface of the deposited material. The simulation demonstrates the method's robustness in capturing complex joint geometries and boundary interactions without remeshing.

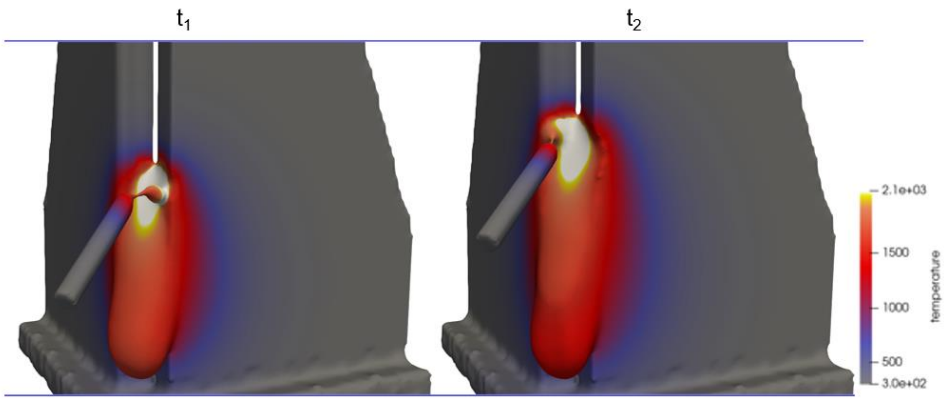



**Fig. 23** Simulation of a vertical weld configuration showing the evolution of arc attachment along the cathode surface. The deflection of the arc attachment correlates with the local surface temperature distribution, confirming the asymmetric energy input predicted by the EDACC model.

## DISCUSSION OF RESULTS

The results of the presented simulations clearly demonstrate the strong coupling between the melt pool surface temperature, the current density distribution, and the local heat flux within the cathode region. This coupling, as described by the Evaporation Determined Arc-Cathode Coupling (EDACC) model, leads to pronounced lateral asymmetry in current density, observed consistently across all investigated torch configurations-push, pull, and lateral inclination. The findings indicate that the commonly applied assumption of axial symmetry in two-dimensional GMAW models deviates significantly more from process reality than previously assumed.

Importantly, this asymmetry is not merely a consequence of torch geometry but an inherent physical property of the cathode sheath governed by the local temperature distribution on the melt surface. Metal vapor generated by evaporation locally cools the plasma, reducing its electrical conductivity and causing the current density peak to shift toward cooler, less evaporated regions. This behavior was clearly observed in both the quasi-stationary three-dimensional calculations and the transient two-dimensional studies.

Despite these limitations, axisymmetric two-dimensional models remain valuable for specific process domains. They can be efficiently applied to describe droplet formation and detachment in the wire region, as well as to compute the anode layer of the arc. However, for the cathode and melt pool regions - especially when the torch is in motion - such models cannot yield an acceptable representation of the heat input, since the observed asymmetry in the cathode area constitutes a native physical feature of the GMAW process.

It should also be noted that the current implementation of the EDACC-based arc model does not yet include the influence of metal vapor entering the arc plasma from the droplet surface. While this omission is not expected to qualitatively alter the main simulation

outcomes, certain quantitative effects-such as slight modifications in arc temperature distribution and local conductivity-may arise once this contribution is incorporated. The inclusion of droplet-derived vapor transport in future models will therefore be an important step toward achieving a fully self-consistent description of plasma–metal interactions in GMAW.

Beyond these aspects, the Smoothed Particle Hydrodynamics (SPH) method proves to be particularly well suited for modeling processes involving strong topological changes. Its mesh-free Lagrangian nature allows physically accurate treatment of complex and evolving geometries without remeshing. Consequently, the same modeling framework can be directly applied to welds with intricate joint configurations or to additive manufacturing processes based on wire or arc deposition, provided that appropriate process control algorithms are implemented. This highlights the natural scalability and general applicability of the proposed hybrid approach.

At the same time, it must be emphasized that welding cases dominated by strong magnetohydrodynamic (MHD) effects - such as high-current arcs or processes with significant electromagnetic feedback - the presented approach is less appropriate in its current form. In such regimes, a fully coupled MHD treatment of both plasma and liquid metal would be required to accurately capture electromagnetic interactions.

These findings provide a consistent physical interpretation of the simulation results and form the basis for developing simplified yet physically grounded boundary conditions for transient weld pool simulations. Building upon these insights, the following conclusions can be drawn.

## CONCLUSION AND OUTLOOK

The presented hybrid simulation concept successfully combines the strengths of Eulerian and Lagrangian formulations for GMAW. According to the heat source classification by Goldak et al., the model merges the SPH-based concepts of the fourth generation with key elements of the sixth generation, represented by the EDACC approach. This combination enables a physically consistent description of plasma–metal interaction and provides a foundation for transient simulations of weld pool dynamics with high physical fidelity.

A particular feature of the model lies in its treatment of evaporation in the cathode region. Here, not the heat loss due to vaporization is dominant, but the resulting change in arc attachment and thus in current density distribution. This effect explains the pronounced asymmetry observed in the cathode area, which cannot be captured by axisymmetric 2D approaches. Consequently, the use of temperature-dependent surrogate functions derived from EDACC allows the asymmetric heat input to be reproduced in simplified transient SPH simulations with acceptable engineering accuracy.

In the broader process context, GMAW covers the complete material transformation cycle - from the solid state through melting and mass transfer to solidification and weld seam formation. During this evolution, thermal expansion and density variations lead to subtle topological changes that influence the joint’s thermomechanical properties. Advances in the SPH method now make it possible to capture these transitions within a unified modeling

environment, using density change as the connecting parameter between different physical stages.

Ultimately, integrating the full range of thermal, fluid, and mechanical phenomena into one consistent hybrid framework will enable a more complete description of the GMAW process, supporting predictive modeling of weld geometry, microstructure, and mechanical performance. A schematic representation of this material transformation cycle is provided in Fig. 24**,** complementing the "Heat Source Evolution" table proposed in the introduction, Table 1**.**

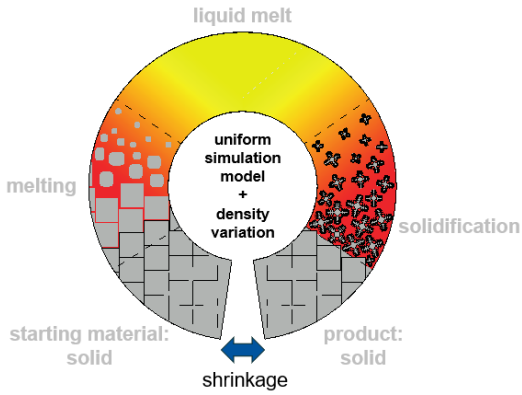



**Fig. 24** Illustration of the complete material transformation cycle in GMAW, showing the interconnected physical stages of the process: heat input and melting, mass transfer and flow within the molten pool, solidification, and the development of thermomechanical properties in the final joint. The SPH method aims to capture this full cycle within a unified framework, consistent with the "Heat Source Evolution" concept presented in the introduction.

## APPENDICES AND ACKNOWLEDGEMENTS

All presented investigations were conducted in the context of the Collaborative Research Centre SFB1120 "Precision Melt Engineering" at RWTH Aachen University and funded by the German Research Foundation (DFG) under the grant number 236616214. For the sponsorship and the support, we wish to express our sincere gratitude. Simulations were performed with computing resources granted by RWTH Aachen University under project rwth0398.

The authors thank Mr. Lukas Kesselburg for his contribution in programming and implementing the models used in our calculations and for the generation of analysis and rendering templates. His supervision and effort on the code maintenance have a great impact on the investigations presented in this work.

## References


[1] J. A. GOLDAK and M. AKHLAGHI: *Computational Welding Mechanics*, Kluwer Academic Publishers, Boston, 2005.

[2] D. ROSENTHAL: 'Mathematical Theory of Heat Distribution During Welding and Cutting', *Welding Journal*, 20, pp. 220-234, 1941.

[3] N. N. RYKALIN: *Berechnung der Wärmevorgänge beim Schweissen*, Verlag Technik, Berlin, 1957.

[4] J. GOLDAK, A. CHAKRAVARTI and M. BIBBY: 'A new finite element model for welding heat sources', *Metallurgical Transactions B*, 15, 2, pp. 299-305, 1984.

[5] D. WEISS, K. H.CHRISTENSEN and J. K. KRISTENSEN: 'Computerized calibration of thermo-mechanical welding models', in: Horst-Hannes Cerjak, H. K. D. H. Bhadeshia, Ernst Kozeschnik (Ed.), *Mathematical Modelling of Weld Phenomena 8*, 1st ed., pp. 469-484, Verlag der Technischen Universität Graz, Graz, 2007.

[6] V. A. SUDNIK, A. V. IVANOV and W. DILTEY: 'Mathematical model of a heat source in gas-shielded consumable electrode arc welding', *Welding International*, 15, 2, pp. 146-152, 2001.

[7] S. CADIOU, M. COURTOIS, M. CARIN, W. BERCKMANS and P. LE MASSON: 'Heat transfer, fluid flow and electromagnetic model of droplets generation and melt pool behaviour for wire arc additive manufacturing', *International Journal of Heat and Mass Transfer*, 148, pp. 119102, 2020.

[8] O. MOKROV, M. SIMON, R. SHARMA and U. REISGEN: 'Arc-cathode attachment in GMA welding', *Journal of Physics D: Applied Physics*, 52, 36, pp. 364003, 2019.

[9] O. MOKROV, M. SIMON, I. SHVARTC, R. SHARMA and U. REISGEN: 'Validation of the EDACC Model for GMAW Process Simulation by Weld Pool Dimension Comparison', in: U. Reisgen et al. (Eds.), *Enhanced Material, Parts Optimization and Process Intensification*, pp. 51-59, Springer International Publishing, Cham, 2021.

[10] I. L. SEMENOV, I. V. KRIVTSUN and U. REISGEN: 'Numerical study of the anode boundary layer in atmospheric pressure arc discharges', *Journal of Physics D: Applied Physics*, 49, 10, pp. 105204, 2016.

[11] S. CADIOU, M. COURTOIS, M. CARIN, W. BERCKMANS and P. LE MASSON: '3D heat transfer, fluid flow and electromagnetic model for cold metal transfer wire arc additive manufacturing (Cmt-Waam)', *Additive Manufacturing*, 36, pp. 101541, 2020.

[12] U. REISGEN, O. MOKROV, A. ZABIROV, I. KRIVTSUN, V. DEMCHENKO, O. LISNYI and I. SEMENOV: 'Task of volumetrical evaporation and behaviour of droplets in pulsed MIG welding of AlMg alloys', *Welding in the World*, 57, 4, pp. 507-514, 2013.

[13] M. BAEVA, R. KOZAKOV, S. GORCHAKOV and D. UHRLANDT: 'Two-temperature chemically non-equilibrium modelling of transferred arcs', *Plasma Sources Science and Technology*, 21, 5, pp. 55027, 2012.

[14] A. PATHAK and M. RAESSI: 'A three-dimensional volume-of-fluid method for reconstructing and advecting three-material interfaces forming contact lines', *Journal of Computational Physics*, 307, pp. 550-573, 2016.

[15] R. A. GINGOLD and J. J. MONAGHAN: 'Smoothed particle hydrodynamics: theory and application to non-spherical stars', *Monthly Notices of the Royal Astronomical Society*, 181, 3, pp. 375-389, 1977.

[16] L. B. LUCY: 'A numerical approach to the testing of the fission hypothesis', *The Astronomical Journal*, 82, pp. 1013, 1977.

[17] D. KOSCHIER, J. BENDER, B. SOLENTHALER and M. TESCHNER: 'Smoothed Particle Hydrodynamics Techniques for the Physics Based Simulation of Fluids and Solids', https://sph-tutorial.physics-simulation.org/ (current as of Jan. 19, 2026).

[18] M. ITO, Y. NISHIO, S. IZAWA, Y. FUKUNISHI and M. SHIGETA: 'Numerical Simulation of Joining Process in a TIG Welding System Using Incompressible SPH Method', *Quarterly Journal of the Japan Welding Society*, 33, 2, pp. 34s-38s, 2015.

[19] M. TRAUTMANN, M. HERTEL and U. FÜSSEL: 'Numerical simulation of weld pool dynamics using a SPH approach', *Welding in the World*, 62, 5, pp. 1013-1020, 2018.

[20] H. KOMEN, M. SHIGETA, M. TANAKA, Y. ABE, T. FUJIMOTO, M. NAKATANI and A. B. MURPHY: 'Numerical Investigation of Heat Transfer During Submerged Arc Welding Phenomena by Coupled DEM-ISPH Simulation', *International Journal of Heat and Mass Transfer*, 171, pp. 121062, 2021.

[21] D. J. PRICE: 'Smoothed particle hydrodynamics and magnetohydrodynamics', *Journal of Computational Physics*, 231, 3, pp. 759-794, 2012.

[22] R. DAS and P. W. CLEARY: 'Novel application of the mesh-free SPH method for modelling thermo-mechanical responses in arc welding', *International Journal of Mechanics and Materials in Design*, 11, 3, pp. 337-355, 2015.

[23] K. BOBZIN, H. HEINEMANN, K. JASUTYN, S. R. JESKE, J. BENDER, S. WARKENTIN, O. MOKROV, R. SHARMA and U. REISGEN: 'Modeling the Droplet Impact on the Substrate with Surface Preparation in Thermal Spraying with SPH', *Journal of Thermal Spray Technology*, 32, 2-3, pp. 599-608, 2023.

[24] S. R. JESKE, M. S. SIMON, O. SEMENOV, J. KRUSKA, O. MOKROV, R. SHARMA, U. REISGEN and J. BENDER: 'Quantitative evaluation of SPH in TIG spot welding', *Computational Particle Mechanics*, 10, 1, pp. 1-18, 2023.

[25] O. MOKROV, S. WARKENTIN, L. WESTHOFEN, S. JESKE, J. BENDER, R. SHARMA and U. REISGEN: 'Simulation of wire metal transfer in the cold metal transfer (CMT) variant of gas metal arc welding using the smoothed particle hydrodynamics (SPH) approach', *Materialwissenschaft und Werkstofftechnik*, 55, 1, pp. 62-71, 2024.

[26] J. P. MORRIS: 'Simulating surface tension with smoothed particle hydrodynamics', *International Journal for Numerical Methods in Fluids*, 33, 3, pp. 333-353, 2000.

[27] M. MÜLLER, D. CHARYPAR and M. GROSS: *Particle-Based Fluid Simulation for Interactive Applications*, (2003).

[28] M. WEILER, D. KOSCHIER, M. BRAND and J. BENDER: 'A Physically Consistent Implicit Viscosity Solver for SPH Fluids', *Computer Graphics Forum*, 37, 2, pp. 145-155, 2018.

[29] J. C. AMSON: 'Lorentz force in the molten tip of an arc electrode', *British Journal of Applied Physics*, 16, 8, pp. 1169-1179, 1965.

[30] L. A. JONES, T. W. EAGAR and J. H. LANG: 'Magnetic forces acting on molten drops in gas metal arc welding', *Journal of Physics D: Applied Physics*, 31, 1, pp. 93-106, 1998.

# TOWARDS ACCURATE THERMAL SIMULATIONS IN PBF: A NOVEL CALIBRATION STRATEGY FOR GAUSS-GOLDAK HEAT-SOURCE MODELS

M. HOFMANN*,**, T. MAYER*

**Institute of Mechanical Systems (IMES), ZHAW Zurich University of Applied Sciences, 8401 Winterthur, Switzerland, michael.hofmann@zhaw.ch*
***Department and Institute of Materials Science (IfW), Technical University of Darmstadt, 64283 Darmstadt, Germany*

*DOI 10.3217/978-3-99161-089-2-004, license CC BY 4.0*
*https://creativecommons.org/licenses/by/4.0/deed.en*
*This CC license does not apply to third party material and content noted otherwise.*

## ABSTRACT

Laser Powder Bed Fusion (PBF-LB) is an advanced additive manufacturing process that fabricates near-net-shape metal components by selectively melting and solidifying powder layers with a laser beam. The intense, localized energy input generates complex thermal cycles that strongly influence microstructural evolution, residual stresses, and mechanical performance. Accurate prediction and control of this thermal history are therefore critical for optimizing part quality and process reliability.

Finite Element (FE) models employing the Gauss-Goldak heat source are widely used to simulate melt pool temperature fields and support residual stress analyses. However, the accuracy of these requires precise calibration of the heat source parameters, particularly the laser absorptivity and volumetric heat flux distribution, which vary with process conditions. This study introduces a novel calibration approach combining melt pool geometry data and in-situ thermographic measurements from the bottom side of a substrate with thermal simulations to inversely identify these parameters. The method enables tailored tuning of the thermal heat input model for specific processing conditions, substantially improving the accuracy of transient temperature predictions. Bayesian optimization was used to effectively identify absorptivity from the far-field temperature, and the shape parameters of the Gauss-Goldak heat source from the melt pool geometry.

The calibrated model demonstrates excellent agreement with experimental data, achieving deviations in simulated melt pool dimensions below 2.8%. Thereby, absorptivity emerges as the key parameter governing the far-field thermal response, underscoring the importance of its precise calibration for accurate part-scale thermal simulations. Furthermore, it is shown that, within the investigated parameter space, the shape parameters of the Goldak model exert negligible influence on the far-field temperature distribution, justifying a two-step approach. Although the calibration was performed using the Gauss-Goldak model, the approach is generalizable and can be extended to alternative heat input formulations. This enhanced modeling fidelity enabled by an accurately calibrated heat-source can facilitate more reliable residual stress and distortion forecasts in PBF manufacturing.

Keywords: powder-bed-fusion; finite element thermal analysis; model calibration; thermographic image; Bayesian optimization; stainless steel 316L, heat input model; absorptivity

## INTRODUCTION

Finite Element (FE) based process simulation are widely employed to investigate the thermo-mechanical behavior of Laser Powder Bed Fusion (PBF-LB). Models exist across various length scales, with macroscale simulations targeting the prediction of temperature, residual stress, and distortion fields at layer-, and part-scale levels.

These simulations typically model the heat input by applying a volumetric heat source along the laser trajectory. A widely used heat input model in this context is the Goldak double-ellipsoid heat source, originally developed for arc-welding applications [1]. Owing to its adjustable shape parameters, the Goldak model can represent both shallow and deep melt pools, making it a flexible and widely adopted choice for PBF-LB simulations.

Most prior studies assume a constant laser absorptivity [2-6], allowing the Goldak model's shape parameters to be tuned to match experimentally observed melt pool geometries under fixed energy input conditions. However, in practice, laser absorptivity - and thus the actual energy input - is highly dependent on process parameters such as laser power, scan speed, and laser diameter [7,8]. While analytical models have been proposed to estimate absorptivity [9,10], only a few studies have directly calibrated absorptivity using temperature measurements from thermocouples [11,12] or top view thermal imaging [13], which enables the determination of the absorptivity in the order of the first decimal. However, thermocouple-based approaches are limited to single-point temperature readings and average temperatures over finite areas, thereby failing to capture spatial gradients. Furthermore, the thermal mass of the thermocouples can influence measurement accuracy, especially in thin-walled components. Top-view thermal imaging, while offering contactless measurement and high spatial resolution, suffers from uncertainty due to emissivity assumptions, which are influenced by material type, wavelength, temperature, and surface condition. Additionally, top-view imaging is often affected by dynamic process emissions such as spatter and vapor, which can obstruct the line of sight and degrade image quality.

This study introduces a novel calibration methodology under real process conditions that leverages in-situ thermal imaging from the bottom side of a thin substrate during single-track PBF experiments - a perspective not previously exploited in the literature. By imaging the process zone from below, this approach eliminates key limitations of top-view thermal imaging, such as occlusion by process emissions and uncertainty in emissivity, while preserving its advantages of high spatial resolution and non-contact measurement. Consequently, the acquired temperature field enables precise calibration of the overall heat input.

## MATERIALS AND METHODS

Accurate simulation of the laser-based powder bed fusion (PBF) process requires a precisely calibrated heat input model. In particular, the model must capture the correct temperature distribution both in the near field as well as in the far field of the weld track. This necessitates an accurate estimation of the overall energy input or more specifically the effective absorptivity. Absorptivity, in the strict physical sense, is defined as the fraction of incident radiation absorbed by the material. In practice, however, the actual energy input into the process is reduced by losses due to vaporization and spatter ejection. In this study, absorptivity is defined as the net energy absorbed by the material, taking into account process related losses.

The calibration strategy for the heat input model follows two sequential steps:

I. The absorptivity is determined using in-situ thermographic measurements of a single laser track recorded from the bottom side of a thin substrate providing information on the actual energy input.
II. With determined absorptivity, the shape parameters of a Goldak double-ellipsoidal heat source model are optimized to reproduce the observed weld geometry of a single-track weld seam.

### EXPERIMENTS

#### *Single Track Experiments*

Single track experiments were conducted on a conventional PBF-LB/M system (Aconity MIDI, Aconity3D, Germany). The machine is equipped with a 500 W single-mode laser (nLight, USA) featuring a Gaussian beam profile, a wavelength of 1070 nm, and a nominal focal spot diameter $d_{laser}$ of 50 µm. By adjusting the laser focus, various spot diameters were realized.

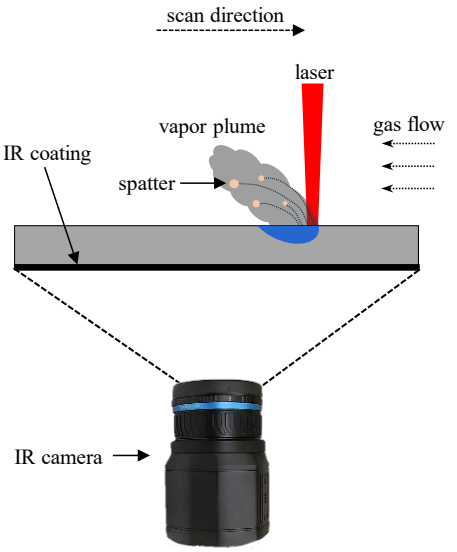



**Fig. 1** Schematic illustration of the experimental setup

In each experiment, a 10 mm long laser track was scanned on a 0.5 mm thin 316L stainless steel substrate using constant laser power $P_{laser}$ and scan speed $v_{scan}$. During the scanning process, the temperature field on the bottom side of the substrate was captured over time using a thermal camera, as illustrated in Fig. 1. This measurement configuration offers several advantages:

- In-situ temperature acquisition under realistic and controlled conditions
- Contactless measurement, avoiding any interference with the process
- Elimination of process emissions such as spatter or vapor on thermal imaging
- Optimal control over the emissivity of the metallic surface by applying a thermographic coating
- High spatial resolution of the recorded temperature field
- Optimal camera placement and viewing angle for thermal imaging

Thermographic measurements were conducted using a FLIR A700 (FLIR Systems, USA) uncooled microbolometer camera operating in the 7.5 µm to 14 µm spectral range with a resolution of 640x480 pixels. A macro lens was used to achieve a spatial resolution of 24 µm/pixel, sufficient to resolve the spatial thermal gradients on the bottom side of the substrate. The total field of view was approximately 15.4 mm × 11.5 mm, and the frame rate 30 Hz.

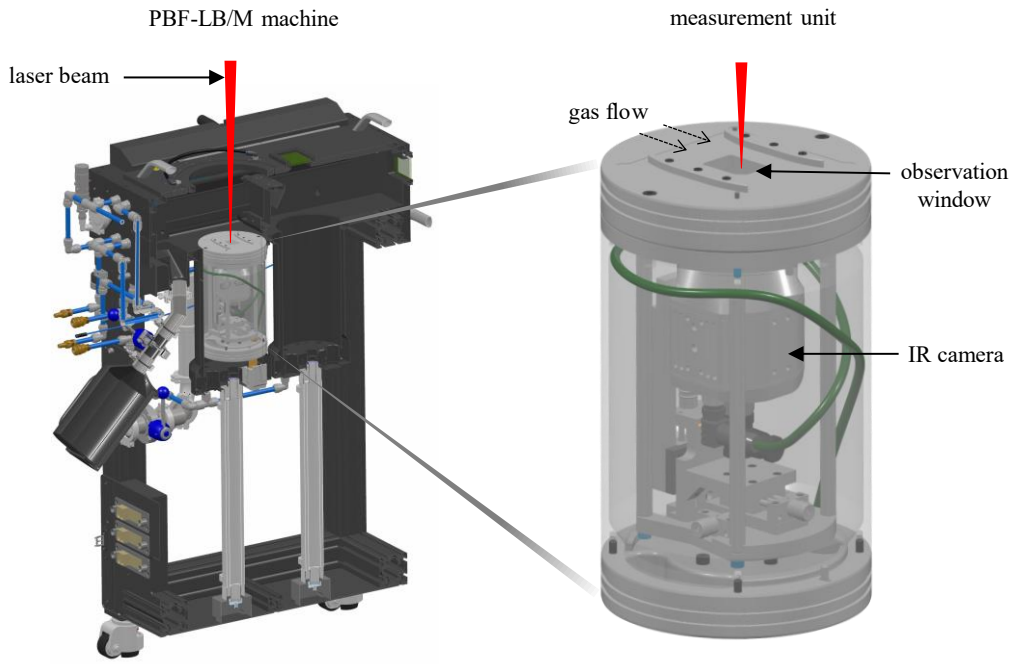



**Fig. 2** Integration of the measurement unit into the PBF-LB/M machine

A custom-made measurement unit was employed to facilitate precise and reproducible camera positioning within the PBF-LB/M system. It includes a rectangular observation window on top, on which the thin substrate plate is mounted, allowing direct optical access from the camera below. The camera is placed in a vertical distance of 18 mm from the substrate bottom side. The substrate is secured using side clamps, which are screwed into the measurement unit and designed to minimize disruption of the process gas flow (see Fig. 2).

Additionally, a time synchronization between the camera and the PBF-LB/M machine was realized allowing for directly correlate the recorded thermal data with the corresponding laser position and time stamps. This is essential for the absorptivity calibration described later. Experiments were performed using three different parameter sets on bare 316L substrate plates, as listed in Table 2.

**Table 1** Process parameters for the single track experiments.

| Acronym | Laser Power [W] | Scan Speed [mm $s^{-1}$] | Laser Diameter [µm] |
|---|---|---|---|
| P150v825d50 | 150 | 825 | 50 |
| P300v700d80 | 300 | 700 | 80 |
| P400v550d110 | 400 | 550 | 110 |

*Emissivity Calibration*

Accurate thermal imaging generally requires a two-step calibration process. The first step involves calibration of the camera sensor response - involving the conversion from voltage to incident radiance. This was performed by the manufacturer using a blackbody radiator. With a known emissivity, the surface temperature can then be calculated using Planck's law. However, emissivity is not a fixed material constant; it depends on several factors, including material type, surface condition, radiation wavelength, and temperature. Therefore, a second calibration step is essential to determine the effective emissivity of the specific measurement setup, as described in the following.

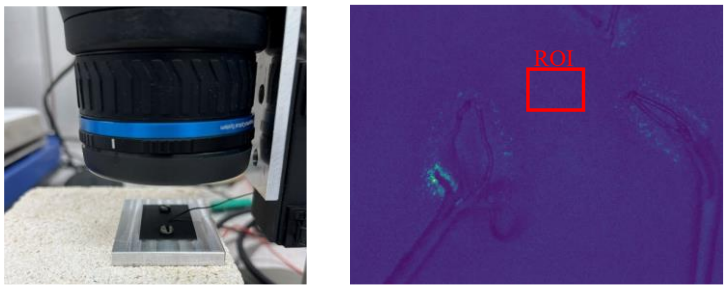



**Fig. 3** Camera setup for emissivity calibration (left) and example radiometric image (right)

The emissivity calibration was carried out using the same thin substrate plate employed in the single track experiments. Type-K thermocouples were welded onto the plate using a micro-TIG welding system. Since the thermal camera observes the substrate from the bottom side, the surface was coated with a thermographic paint (LabIR Paints, Czech Republic). This coating improves the emissivity of the metallic surface, which typically exhibits low emissivity and high reflectivity. It also homogenizes the surface radiative properties, mitigating the influence of scratches or other surface irregularities. As a result, more reliable and accurate temperature measurements are achieved.

To perform the calibration, the coated substrate plate was uniformly heated and then allowed to cool in ambient air. During the cooling phase, both the thermocouple temperature readings and the radiance detected by the thermal camera were recorded. Radiance values were averaged over a region of interest (ROI) near the thermocouples but avoiding the thermocouple welds themselves, as welding can locally alter the surface properties (see Fig. 3).

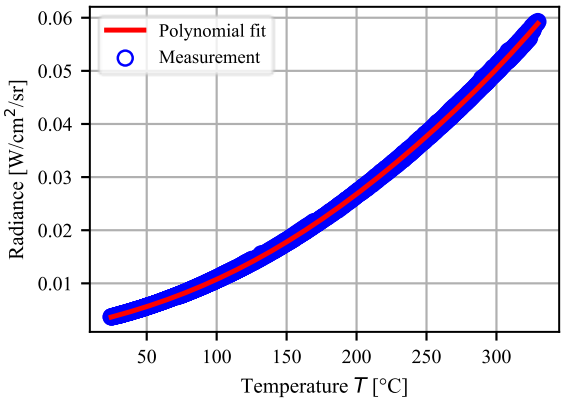



**Fig. 4** Measured radiance as function of thermocouple temperature. A polynomial fit is used to generate a temperature-radiance conversion function

A total of 12 measurements were conducted resulting in a conversion plot, which correlates observed radiance to measured temperature values, as illustrated in Fig. 4. A polynomial fit was applied to the data to interpolate between recorded points. The maximum standard deviation of the fitted temperature for any measured radiance was found to be below 1.25% demonstrating high calibration accuracy. Subsequently, the radiance data recorded during the single track experiments were converted to temperature values on a pixel-wise basis using the fitted polynomial derived from the conversion plot.

## SIMULATION MODEL

This section describes the FE model used for thermal calibration. The model is implemented using the commercial finite element software Abaqus 2022 (Dassault Systèmes, France). The fundamental energy balance is expressed in integral form as:

$$\int_V \rho \dot{U}\, dV + \int_S \mathbf{q_s} \cdot \mathbf{n}\, dS = \int_V q_v\, dV \tag{1}$$

where $V$ and $S$ are the volume and surface area of the model, respectively. $\rho$ is the material density, $\dot{U}$ is the rate of internal energy change, $\mathbf{q_s}$ with the normal vector $\mathbf{n}$ is the surface heat flux leaving the model, and $q_v$ is the volumetric heat input. The specific heat capacity $c_p$ is defined as:

$$c_p(T) = \frac{\partial U}{\partial T} \tag{2}$$

Heat conduction follows Fourier's law, describing the heat flux $\mathbf{q}$ in dependence of materials conductivity $k$ as:

$$\mathbf{q} = -k\nabla T \tag{3}$$

Applying Gauss' theorem leads to the differential form of the energy balance:

$$\rho c_p \dot{T} - \nabla \cdot (k \nabla T) = q_v \tag{4}$$

The volumetric heat input $q_v$ is modeled using the double ellipsoidal Goldak distribution:

$$q_v = \begin{cases} \frac{6\sqrt{3} f_f \eta P_{laser}}{abc_f} \cdot \exp\left(-\frac{3x^2}{c_f^2} - \frac{3y^2}{a^2} - \frac{3z^2}{b^2}\right) & \text{if } x \geq 0 \\ \frac{6\sqrt{3} f_r \eta P_{laser}}{abc_r} \cdot \exp\left(-\frac{3x^2}{c_r^2} - \frac{3y^2}{a^2} - \frac{3z^2}{b^2}\right) & \text{if } x < 0 \end{cases} \tag{5}$$

Here $x$, $y$ and $z$ are spatial coordinates in a moving Cartesian coordinate system centered on the laser beam (Fig. 5). $P_{laser}$ is the laser power, $\eta$ is the absorptivity, and $f_f$ and $f_r$ are the fractions of the absorbed laser power deposited at the front and rear volume of the double ellipsoid, respectively, such that $f_f + f_r = 2$. The values are fixed at $f_f = 0.3$ and $f_r = 1.7$. The shape parameters $a$, $b$, $c_f$, and $c_r$ describe the principal radii of the double ellipsoid. The relationship $a = c_f$ and $c_r = 2c_f$ is assumed [1,13], so only the parameters $a$ and $b$ require calibration. The volumetric heat flux distribution is implemented in the FE model using a Fortran-based DFLUX subroutine.

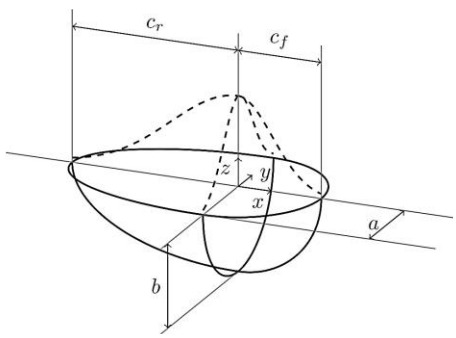



**Fig. 5** Schematic illustration of the double ellipsoidal Gauss-Goldak heat flux distribution

The three-dimensional FE model represents the portion of the substrate plate within the camera's field of view. Accordingly, the model dimensions are 0.5 mm in thickness, 16 mm in length, and 6 mm in width–exploiting the symmetry of the setup. The domain is discretized using 8-node linear hexahedral elements, with a refined mesh size of 10 µm near the laser path (see Fig. 6).

The initial temperature $T_{init}$ is set to the measured temperature of the substrate prior to laser exposure, i.e. approximately 30 °C. The lateral sides of the substrate are held at this temperature throughout the simulation.

Heat convection and radiation are considered on the top surface, while on the bottom surface only radiation is accounted for due to negligible free convection on the downward facing surface.

On the top surface, exposed to laminar process gas flow, a convective heat transfer coefficient of $h_{conv} = 80\ \mathrm{Wm^{-2}K^{-1}}$ is used, following [14]. A surface emissivity of $\epsilon = 0.4$ is applied. The symmetry plane is treated as adiabatic.

The applied boundary conditions are summarized as follows:

$$\begin{gathered} T(x,y,z,t=0) = T_{init} \quad \forall x,y,z \in V \\ T(x,y,z,t) = T_{init} \quad \forall x,y,z \in S_{side} \\ \mathbf{q_{conv}} = -h_{conv}(T - T_{init}) \quad \forall x,y,z \in S_{top} \\ \mathbf{q_{rad}} = \epsilon\sigma(T^4 - T_{init}^4) \quad \forall x,y,z \in S_{top} \cup S_{bottom} \\ \mathbf{q} = \mathbf{q_{conv}} = \mathbf{q_{rad}} = 0 \quad \forall x,y,z \in S_{sym} \end{gathered} \tag{6}$$

Here, $S_{side}$, $S_{top}$, $S_{bottom}$ and $S_{sym}$ denote the side, top bottom and symmetry surfaces, respectively. $\mathbf{q_{conv}}$ and $\mathbf{q_{rad}}$ are the convective and radiative heat fluxes. The Stefan-Boltzmann constant $\sigma$ is set to $5.67 \times 10^{-8}\ \mathrm{Wm^{-2}K^{-4}}$.

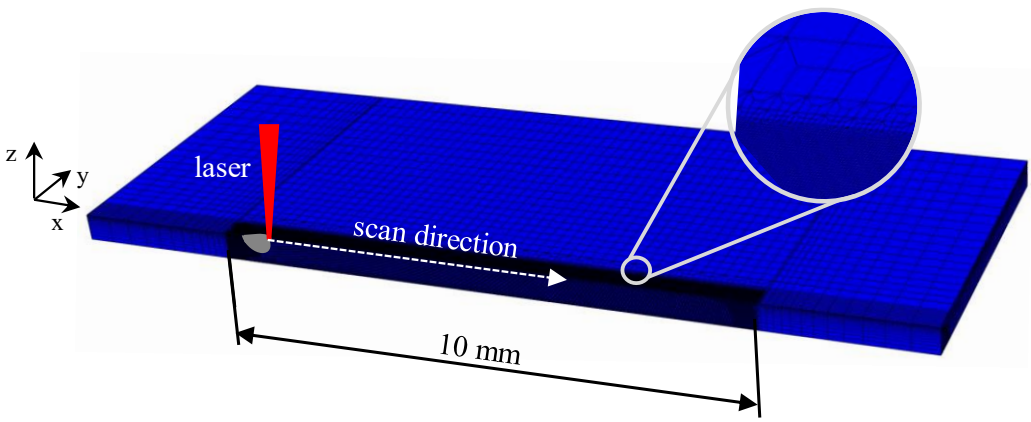



**Fig. 6** Details of FE model for analysis of single track experiments

Since the volumetric heat flux $q_{vol}$ is averaged over each time increment, the time increment size $\Delta t_{inc}$ must be small enough to realistically capture the physical heating duration. During laser irradiation with constant scan speed $v_{scan}$, the physical exposure time corresponds to the time it takes the laser beam to traverse a point, typically estimated as the laser spot diameter $d_{laser}$ divided by $v_{scan}$. For the calibration of the heat source shape parameters, a time increment size of half this exposure time is used:

$$\Delta t_{inc} = \frac{d_{laser}}{2v_{scan}} \tag{7}$$

Temperature-dependent material properties are used for the simulation, see Fig. 7. Experimental measurements were conducted to determine the density, thermal conductivity, and specific heat capacity of 316L stainless steel from room temperature up to the melting point. To extend these properties beyond the melting point, data from Choong [15] is

incorporated. Latent heat of fusion is accounted for by augmenting the specific heat between the solidus and liquidus temperatures (1419 °C and 1453 °C) by 235 kJ $kg^{-1}$. The thermal conductivity is artificially increased to model convective Marangoni flows in the melt pool, which are not captured directly by the simulation [16]. A thermal conductivity of 120W $m^{-1}$ $K^{-1}$ is assumed beyond melting temperature[1] and was implemented using the Fortran-based user subroutine USDFLD.

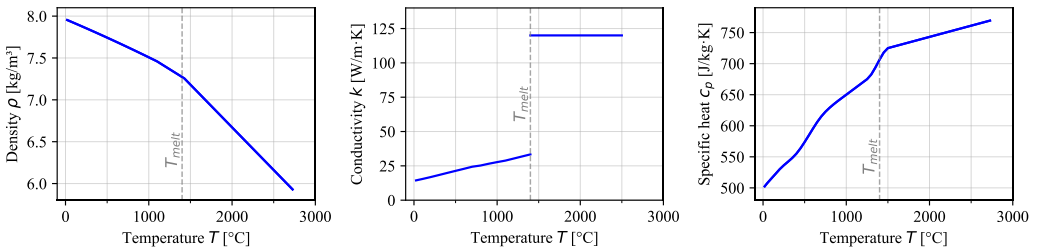



**Fig. 7** Temperature dependent material properties used for the simulation

## CALIBRATION

The calibration strategy of the heat input model is carried out in two sequential steps, as illustrated inFig. 8. In the first step, the absorptivity $\eta$ is calibrated based on the temperature field captured by in-situ thermography. The goal is to adjust the energy input such that the simulated bottom temperature fields closely match the experimental measurements at different points in time. In the second step, the geometric shape parameters $a$ and $b$ of the Goldak heat source model are calibrated. This is done by comparing the simulated melt pool geometry with the experimentally observed melt pool dimensions. By adjusting the width and depth of the Goldak model, a close match to the physical melt pool is achieved.

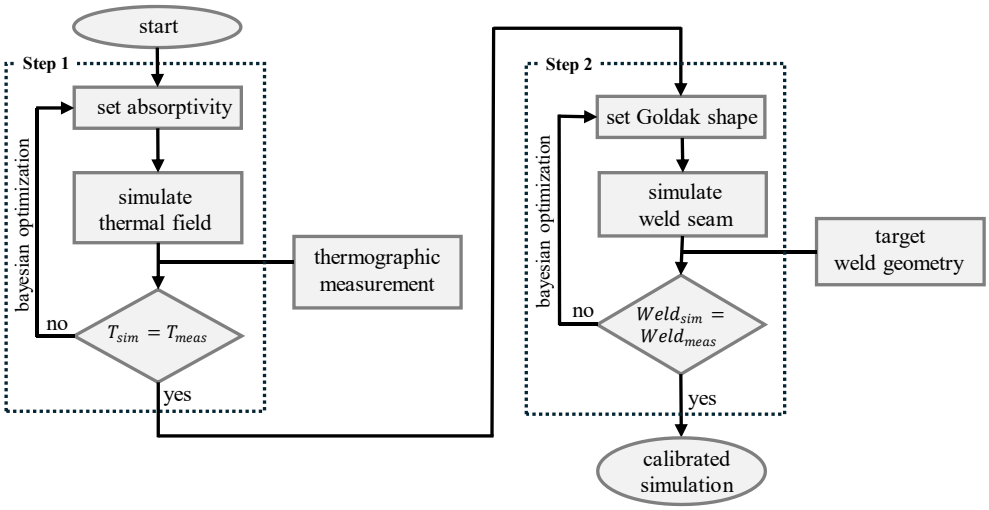



**Fig. 8** Calibration strategy.

*Absorptivity*

To calibrate the absorptivity $\eta$, simulations are performed with fixed Goldak shape parameters ($a = 90$ µm and $b = 150$ µm). The simulated temperature field $T_{sim}$ on the bottom side of the substrate is compared to the measured temperature field $T_{meas}$ captured by the thermographic camera. To enable this comparison, each pixel of the thermal image was mapped both spatially and temporally to the simulation results. An algorithm was developed to determine the laser path in the coordinate system of the camera based on the thermal images. This enables the spatial mapping of the camera pixels to the simulation model's coordinate system.

As a symmetric simulation model is deployed, the measured temperature values are averaged across the left and right sides of the laser path, resulting in a symmetric averaged temperature field suitable for comparison. Rough temporal mapping is initially achieved by synchronizing the thermographic camera with the PBF-LB/M machine. However, due to high laser speeds and steep thermal gradients, this basic synchronization is insufficient. To improve accuracy, an optimized temporal alignment is determined by comparing normalized temperature fields of the simulation and measurements. This involves matching isotherms over multiple time steps to find the best temporal fit. Further details of this process are provided in the Appendix. After completing both spatial and temporal mappings, the temperature fields are compared by evaluating a loss function $\mathcal{L}_{temp}$ at $P = 3$ time points. The loss function is defined as:

$$\mathcal{L}_{temp}(\eta) = \sum_{j=1}^{P} \sum_{i=1}^{N} \frac{\left(T_{ji,meas}(x_i,y_i,t_j) - T_{ji,sim}(x_i,y_i,z=-0.5,t_j)\right)^2}{T_{ji,meas}(x_i,y_i,t_j)^2} \quad (8)$$

where $N$ is the number of pixels used in the comparison.

Bayesian optimization[17] is subsequently employed to minimize the loss function $\mathcal{L}_{temp}$ and identify the optimal absorptivity $\eta_{opt}$. As a probabilistic, model-based optimization method, Bayesian optimization is particularly suited for expensive black-box functions, where each evaluation is time-consuming or costly. It builds a surrogate model using a Gaussian Process that approximates the true objective function and guides the search through the parameter space using an acquisition function. In this context, the objective function is $\mathcal{L}_{temp}$, quantifying the difference between measured and simulated temperature fields. The optimization proceeds iteratively by updating the surrogate model after each evaluation and selecting new candidate points that maximize the acquisition function. This allows efficient exploration of the parameter space while incorporating information from all previous evaluations. A key advantage in this application is that simulation results are reused: the loss function may be re-evaluated against different measurement datasets without rerunning simulations. This enables rapid surrogate model updates and efficient absorptivity optimization at minimal computational cost. The Matèrn 5/2 kernel is used as the covariance function, and expected improvement is employed as an acquisition function.

*Shape Parameters*

In the second step of the heat input model calibration, the previously calibrated absorptivity $\eta$ is fixed, and the shape parameters $a$ and $b$ of the Goldak model are calibrated. This calibration is based on the melt pool width $W$ and depth $d$, derived from a statistical model informed by multiple single track experiments [18]. Although these target values are not directly measured, they are referred to as $W_{meas}$ and $d_{meas}$ for consistency in notation. The simulated melt pool geometry is determined by the iso-surface corresponding to the material's melting temperature, $T_{melt} = 1424$ °C. From the simulation results, the melt pool width $W_{sim}$ and depth $d_{sim}$ are extracted accordingly. To quantify the difference between the simulation and the experimental targets, a loss function $\mathcal{L}_{weld}$ is defined as:

$$\mathcal{L}_{weld}(a,b) = \frac{(W_{meas}-W_{sim})^2}{W_{meas}^2} + \frac{(d_{meas}-d_{sim})^2}{d_{meas}^2} \tag{9}$$

Again, Bayesian optimization [17] is employed to minimize the loss function $\mathcal{L}_{weld}$ and identify the optimal shape parameters $a$ and $b$. The Matèrn 5/2 kernel is used as the covariance function and expected improvement is used as an acquisition function.

## RESULTS AND DISCUSSION

### ABSORPTIVITY

The design space for the absorptivity calibration was defined in the range of 0.3 to 0.8, which corresponds to absorptivity values reported in the literature [7,8,19]. Fig. 9 (left) shows the surrogate model of the loss function $\mathcal{L}_{temp}$ for a representative measurement. The surrogate model is constructed from observation points, which are evaluations of the loss function obtained by comparing the simulated and measured temperature fields.

To identify the optimal absorptivity $\eta_{opt}$ for a given measurement, the surrogate model is minimized using a differential evolution algorithm. To evaluate additional measurements of the same process parameters, existing simulation results are reused. The loss function is re-evaluated using the additional measurement data, and the surrogate model is updated accordingly. This approach enables rapid reevaluation without additional simulation effort. Fig. 9 (right) shows the surrogate models for four measurements performed under identical process conditions.

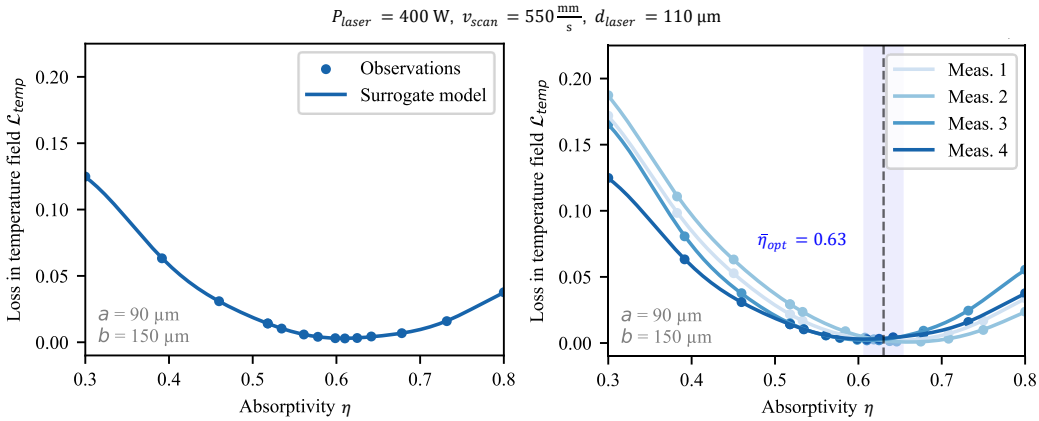



**Fig. 9** Surrogate models of the loss function $\mathcal{L}_{temp}$ for the absorptivity calibration. Single measurement (left) and averaged optimal absorptivity of all measurements (right) for P400v550d110 process parameter set

Fig. 10 presents the surrogate models for two additional process parameter sets, along with their respective mean optimized absorptivity values $\bar{\eta}_{opt}$. These results are also summarized in Table 2, which includes the melt pool width $W_{meas}$, depth $d_{meas}$, and the corresponding aspect ratio $A_{meas} = d_{meas}/W_{meas}$, based on a statistical model from single track experiments. The calibrated absorptivity values fall within the expected range based on other studies [7,8]. The selected process parameters correspond to moderate to high energy densities within the stable processing window. Assuming an upper absorptivity limit of approximately

0.8 in the keyholing regime, the calibrated values appear physically reasonable. As deeper melt pools indicate a transition towards keyholing, higher absorptivity values are anticipated due to multiple reflections trapped inside the deep melt pools [20]. This trend is consistent with the results of this study: parameter sets producing higher aspect ratios also exhibit higher absorptivity values, see Table 2**.**

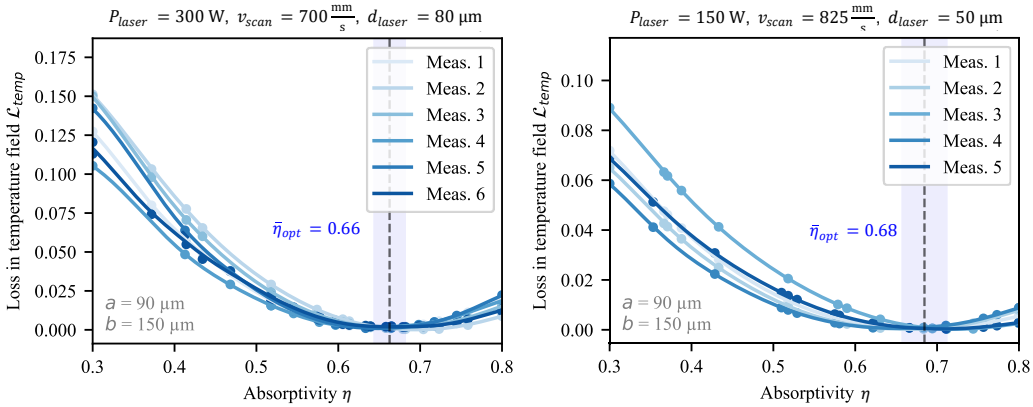



**Fig. 10** Surrogate models of the loss function $\mathcal{L}_{temp}$ for the absorptivity calibration of P300v700d80 (left) and P150v825d50 (right) process parameters

**Table 2** Calibrated absorptivity and weld characteristic for different process parameters.

| Acronym | $\bar{\eta}_{opt}$ | $\sigma_{\bar{\eta}}$ | $W_{meas}$ [µm] | $d_{meas}$ [µm] | $A_{meas}$ |
|---|---|---|---|---|---|
| P150v825d50 | 0.68 | 0.026 | 106 | 69 | 0.65 |
| P300v700d80 | 0.66 | 0.019 | 170 | 109 | 0.64 |
| P400v550d110 | 0.63 | 0.023 | 237 | 135 | 0.57 |

Fig. 11 compares the simulated and measured temperature fields for measurement 3 of the P400v550d110 process parameter set. An optimized absorptivity of 0.62 for the particular measurement was obtained from the calibration and used in the simulation. The comparison demonstrates excellent agreement between the simulated and measured temperature distributions at all three evaluated time steps.

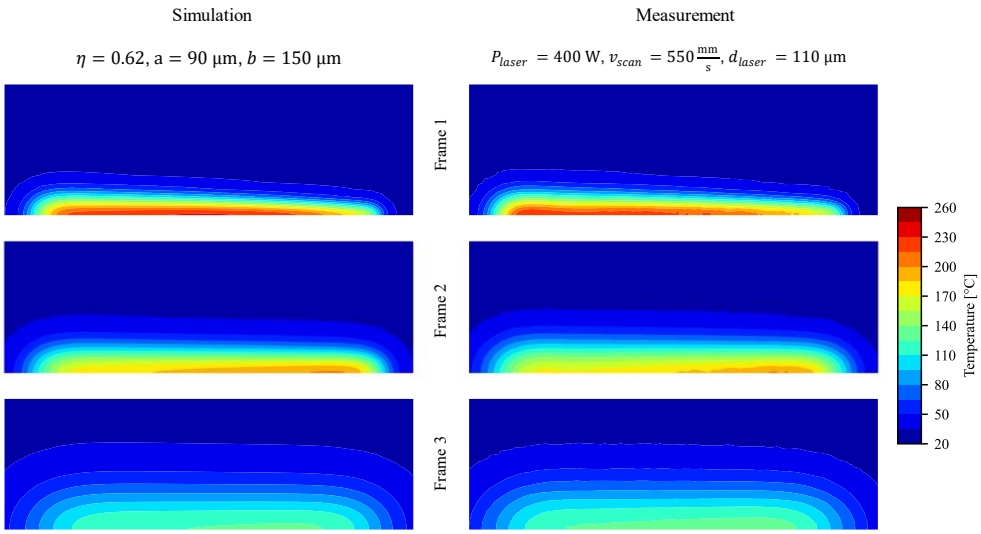



**Fig. 11** Temperature field comparison of simulation and measurement 3 (optimized absorptivity of 0.62)

## SHAPE PARAMETERS

Following the successful calibration of absorptivity, which leads to a good agreement with the measured temperature field in the far field, the shape parameters of the Goldak model are calibrated to better capture the thermal behavior in the near field of the weld. The loss function $\mathcal{L}_{weld}$ is minimized using Bayesian optimization. Fig. 12 illustrates an example of this optimization process. The left plot shows the surrogate model constructed from the evaluations of the loss function at various observation points, while the right plots depict the simulated weld geometry obtained using the optimized shape parameters. Table 3 summarizes the optimized Goldak shape parameters $a_{opt}$ and $b_{opt}$ for the three process-parameter sets. It also compares the simulated weld width $W_{sim}$ and depth $d_{sim}$ to the reference values $W_{meas}$ and $d_{meas}$. The simulation results exhibit excellent agreement with the target geometry, with deviations for all process parameters remaining below 2.8%.

**Table 3** Calibrated shape parameters and weld geometry for different process parameters.

| Acronym | $a_{opt}$ [µm] | $b_{opt}$ [µm] | $W_{sim}$ [µm] | $W_{meas}$ [µm] | Dev. | $d_{sim}$ [µm] | $d_{meas}$ [µm] | Dev. |
|---|---|---|---|---|---|---|---|---|
| P150v825d50 | 77 | 121 | 107 | 106 | 0.7% | 71 | 69 | 2.8% |
| P300v700d80 | 121 | 186 | 171 | 170 | 0.6% | 109 | 109 | 0% |
| P400v550d110 | 148 | 199 | 240 | 238 | 0.8% | 138 | 135 | 2.2% |

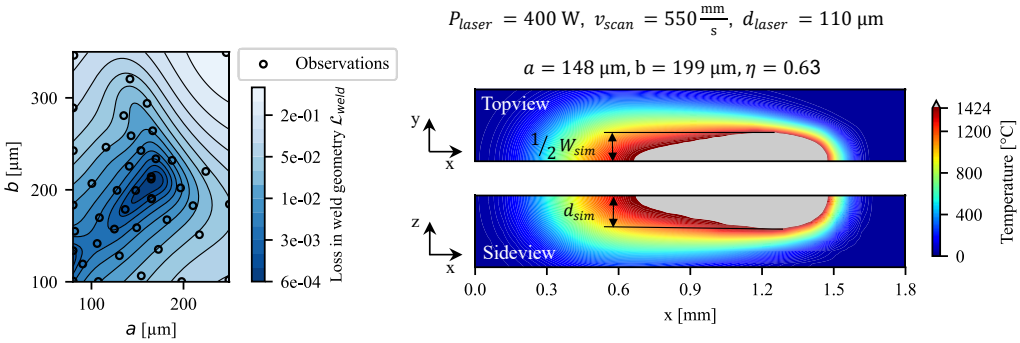



**Fig. 12** Surrogate model of the loss function $\mathcal{L}_{weld}$ (left) and simulated weld geometry for optimized shape parameters a and b (right) for the process parameter set P400v550d110

## VERIFICATION OF THE CALIBRATION STRATEGY

The proposed calibration strategy follows a two-step approach: first, the Goldak shape parameters are held constant to determine the absorptivity; subsequently, the absorptivity is fixed to calibrate the Goldak shape parameters. This sequential approach simplifies the optimization by reducing its dimensionality. However, it is essential to verify the validity of this strategy–specifically, whether fixing the shape parameters in the first step introduces significant variability in the determination of the absorptivity.

The strategy is valid if the shape parameters do not substantially influence the transient temperature distribution in the far field of the weld, i.e., at the bottom surface of the 0.5 mm-thick substrate plate. To verify this assumption, the first step of the calibration is repeated, but this time using the already optimized shape parameters instead of the initially fixed ones. If the recalibrated absorptivity closely matches the original value, it confirms that the two-step strategy yields reliable results. The resulting surrogate models of the loss function $\mathcal{L}_{temp}$ are shown in Fig. 13. The recalibrated averaged absorptivity values show slight deviations of 0.01 well within the standard deviation ranges observed across different measurements. These results confirm that variations in the Goldak shape parameters within the considered range do not significantly affect the far-field temperature response. Thus, the absorptivity is identified as the dominant factor for matching the far-field temperature, and the two-step calibration strategy is valid and suitable for calibrating the heat input model.

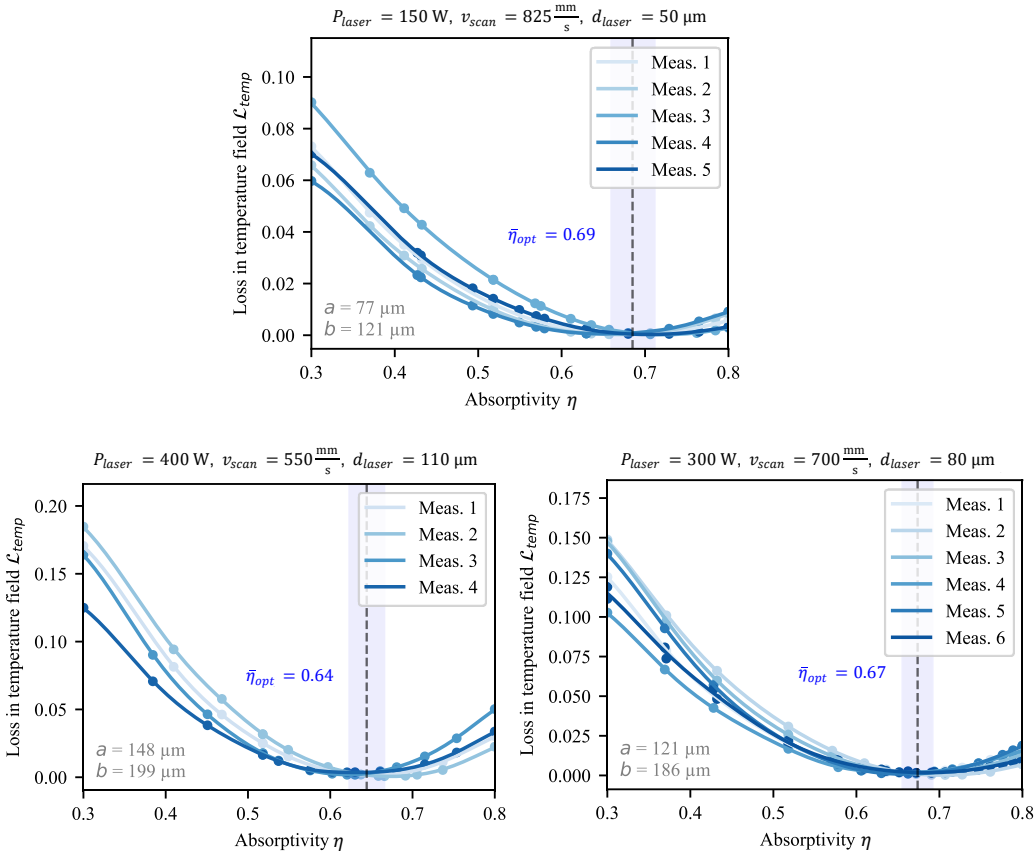



**Fig. 13** Surrogate models of the loss function $\mathcal{L}_{temp}$ performed with optimized shape parameters $a$ and $b$

## CONCLUSIONS

This study introduces an efficient and robust two-step calibration strategy for the heat input model in PBF-LB/M simulations. High-resolution thermographic data, captured in situ from the bottom side of a thin substrate during single-track experiments, enables accurate and realistic calibration under controlled processing conditions. The laser absorptivity is calibrated using far-field temperature measurements, while the melt pool geometry serves to refine the shape parameters of a Goldak double-ellipsoid heat input model.

Bayesian optimization proves highly effective in identifying both absorptivity and shape parameters with minimal computational effort. The calibrated model demonstrates excellent agreement with experimental data, achieving deviations in simulated melt pool dimensions below 2.8%. Furthermore, it is shown that, within the investigated parameter space, the shape

parameters of the Goldak model exert negligible influence on the far-field temperature distribution. This finding validates the two-step calibration strategy, allowing for a simplified yet accurate model tuning.

Absorptivity emerges as the key parameter governing the far-field thermal response, underscoring the importance of its precise calibration for accurate part-scale thermal simulations. The proposed method demonstrates strong potential for reliable determination of absorptivity and robust thermal modeling. Although the calibration was performed using the Goldak model, the approach is generalizable and can be extended to alternative heat input formulations. Future work may apply this strategy to variable powder layer thicknesses and multi-layer builds, leveraging in situ thermal field data to further advance the understanding of heat transfer phenomena in PBF processes.

## References


[1] J. GOLDAK, A. CHAKRAVARTI, M. BIBBY: 'A new finite element model for welding heat sources', *Metall Trans B*, 15 (1984), 299-305, https://doi.org/10.1007/BF02667333.

[2] E. KUNDAKCIOĞLU, I. LAZOGLU, Ö. POYRAZ, E. YASA, N. CIZICIOĞLU: 'Thermal and molten pool model in selective laser melting process of Inconel 625', *Int. J. Adv. Manuf. Technol.*, 95 (2018), 3977-3984, https://doi.org/10.1007/s00170-017-1489-1.

[3] F. AHSAN, L. LADANI: 'Temperature Profile, Bead Geometry, and Elemental Evaporation in Laser Powder Bed Fusion Additive Manufacturing Process', *JOM*, 72 (2020), 429-439, https://doi.org/10.1007/s11837-019-03872-3.

[4] S. BONTHA, N. W. KLINGBEIL, P. A. KOBRYN, H. L. FRASER: 'Effects of process variables and size-scale on solidification microstructure in beam-based fabrication of bulky 3D structures', *Materials Science and Engineering*: *A*, 513-514 (2009), 311-318, https://doi.org/10.1016/j.msea.2009.02.019.

[5] Z.-J. LI, H.-L. DAI, Y. YAO, J.-L. LIU: 'A semi-analytical model for rapid prediction of residual stress and deformation in laser powder bed fusion', *Applied Mathematical Modelling*, 125 (2024), 672-686, https://doi.org/10.1016/j.apm.2023.10.024.

[6] V. HOLLA, J. GRÜNEWALD, P. KOPP, P. M. PRAEGLA, C. MEIER, K. WUDY, S. KOLLMANNSBERGER: 'Validity of Thermal Simulation Models for Different Laser Beam Shapes in Bead-on-Plate Melting', *Integr. Mater. Manuf. Innov.*, (2024), https://doi.org/10.1007/s40192-024-00382-2.

[7] J. YE, S. A. KHAIRALLAH, A. M. RUBENCHIK, M. F. CRUMB, G. GUSS, J. BELAK, M. J. MATTHEWS: 'Energy Coupling Mechanisms and Scaling Behavior Associated with Laser Powder Bed Fusion Additive Manufacturing', *Adv. Eng. Mater.*, 21 (2019), 1900185, https://doi.org/10.1002/adem.201900185.

[8] J. TRAPP, A. M. RUBENCHIK, G. GUSS, M. J. MATTHEWS: 'In situ absorptivity measurements of metallic powders during laser powder-bed fusion additive manufacturing', *Applied Materials Today*, 9 (2017), 341-349, https://doi.org/10.1016/j.apmt.2017.08.006.

[9] T. HEELING, M. CLOOTS, K. WEGENER: 'Melt pool simulation for the evaluation of process parameters in selective laser melting', *Additive Manufacturing*, 14 (2017), 116-125, https://doi.org/10.1016/j.addma.2017.02.003.

[10] A. V. GUSAROV, I. YADROITSEV, PH. BERTRAND, I. SMUROV: 'Model of Radiation and Heat Transfer in Laser-Powder Interaction Zone at Selective Laser Melting', *Journal of Heat Transfer*, 131 (2009), 072101, https://doi.org/10.1115/1.3109245.

[11] M. CHIUMENTI, E. NEIVA, E. SALSI, M. CERVERA, S. BADIA, J. MOYA, Z. CHEN, C. LEE, C. DAVIES: 'Numerical modelling and experimental validation in Selective Laser Melting', *Additive Manufacturing*,18 (2017), 171-185, https://doi.org/10.1016/j.addma.2017.09.002.
[12] P. SCHEEL, R. WROBEL, B. RHEINGANS, T. MAYER, C. LEINENBACH, E. MAZZA, E. HOSSEINI: 'Advancing efficiency and reliability in thermal analysis of laser powder-bed fusion', *International Journal of Mechanical Sciences*, 260 (2023), 108583, https://doi.org/10.1016/j.ijmecsci.2023.108583.
[13] M. KUSANO, H. KITANO, M. WATANABE: 'Novel Calibration Strategy for Validation of Finite Element Thermal Analysis of Selective Laser Melting Process Using Bayesian Optimization', *Materials*,14 (2021), 4948, https://doi.org/10.3390/ma14174948.
[14] J. L. TAN, C. TANG, C. H. WONG: 'A Computational Study on Porosity Evolution in Parts Produced by Selective Laser Melting', *Metall. Mater. Trans. A*, 49 (2018), 3663-3673, https://doi.org/10.1007/s11661-018-4697-x.
[15] K. CHOONG: *Thermophysical Properties of Stainless Stell*, 1975.
[16] H. YIN, T. EMI: 'Marangoni flow at the gas/melt interface of steel', *Metall. Mater. Trans. B*, 34 (2003), 483-493, https://doi.org/10.1007/s11663-003-0015-z.
[17] F. NOGUEIRA: *Bayesian Optimization: Open source constrained global optimization tool for Python*, (2014), https://github.com/bayesian-optimization/BayesianOptimization (accessed January 15, 2025).
[18] M. HOFMANN, T. MAYER, F. FRISO, R. RADIS, C. KONTERMANN, M. FALK, M. OECHSNER: *Statistical modeling of melt pool geometry in PBF of 316L based on a comprehensive single-source dataset*, Unpublished Manuscript (2025).
[19] J. VOLPP: 'Laser beam absorption measurement at molten metal surfaces', *Measurement*, 209 (2023), 112524, https://doi.org/10.1016/j.measurement.2023.112524.
[20] R. FABBRO, K. CHOUF: 'Keyhole modeling during laser welding', *Journal of Applied Physics*, 87 (2000), 4075-4083, https://doi.org/10.1063/1.373033.

# APPENDIX

## TIME SYNCHRONISATION

For the calibration of the absorptivity by comparing simulated and measured temperature fields, it is essential to ensure that the two temperature fields are synchronized in time. A trigger signal based time synchronization between the camera and the PBF-LB/M machine was implemented, enabling the alignment of the recorded images with the corresponding laser positions and time stamps in a rough manner. However, due to high laser scan speeds and steep thermal gradient, this synchronization proved insufficiently accurate. To improve temporal alignment, the data has been post-processed.

The goal is to identify the simulation time that best matches the isothermals observed in the measurement image. This procedure involves the following steps:

I. The measured thermal field is normalized and scaled between 0 and 1. The same normalization is applied to the simulated temperature field at several time points around the pre-synchronized measurement time.

II. The normalized measurement field is compared with the normalized simulation field at these time points.
III. The simulation time point that yields the best match between simulation and measurement is selected.

Fig. 14 illustrates this procedure. The pre-synchronized measurement time is $t = 12$ ms. To refine temporal alignment, the normalized thermal fields from the simulation are analysed at various time points around $t = 12$ ms. The best match is determined by comparing the normalized simulation and the normalized measurement, i.e. Simulation at $t = 8$ ms in Fig. 14. The identified optimal time is then used for a direct comparison of the actual (non-normalized) temperature fields.

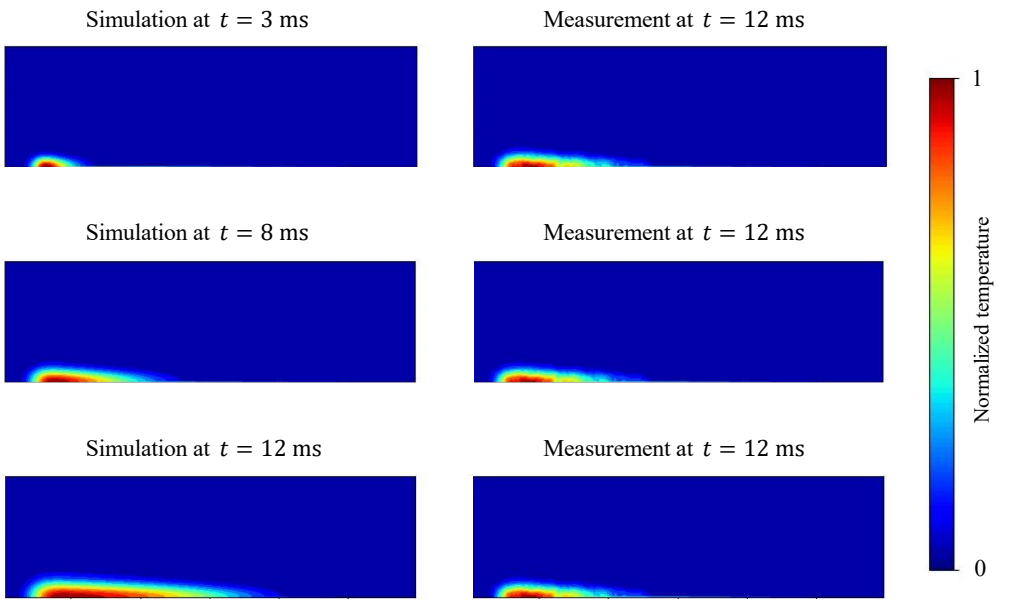



**Fig. 14** Time synchronization algorithm with normalized temperature field

# I Welding Processes

## b) Laser and Electron Beam Welding

# MULTI-PHYSICS SIMULATION AND TRAJECTORY OPTIMIZATION IN LASER WELDING OF COPPER HAIRPIN WINDINGS

P. RANA*, M. SREEJITH**, C. OBERGFELL*,***, M. KAISER*,****, P. MAYR***

**Mercedes Benz AG, Deutschland*
***Mercedes Benz Research and Development, India*
****TU München*
*****TU Braunschweig*
*pulkit.rana@mercedes-benz.com*

*DOI 10.3217/978-3-99161-089-2-005, license CC BY 4.0*
*https://creativecommons.org/licenses/by/4.0/deed.en*
*This CC license does not apply to third party material and content noted otherwise.*

ABSTRACT

The development of a digital process chain for laser welding copper hair pin windings is essential for advancing the manufacturing of components used in electrical vehicles, electronic devices, and energy storage systems. Copper's high thermal conductivity and low infrared light absorption can lead to process instabilities during laser welding, such as melt pool spatter and porosity, resulting in inconsistent weld quality. Understanding the physics involved in laser welding - from keyhole and melt pool formation to the solidification of the melt pool - is crucial. This study employs Cradle CFD for multi-physics analysis to simulate and optimize the laser welding process. This method captures the laser-material interaction, thermal and fluid dynamics, and material solidification. By adjusting welding trajectories, the behaviour of the keyhole and melt pool formation is analyzed. To limit the number of experiments one of the simulation results are validated using experiments. The cut sections are used to validate the melt pool profile, and satisfactory correlation with the experiment results is observed. Additionally, this study investigates thermal and mechanical responses of hairpin windings in laser welded assemblies using FEM-thermo-mechanical and coupled electric-thermal-structural simulations. Six welding locations were analyzed, with cooling simulations revealing heat transfer, thermal stresses, and distortions near constraints. When a 300 A, 20 kHz alternating current was applied, different air cooling strategies showed that forced convection achieved lower and more stable temperatures and deformation than natural convection. The results highlight the need for thicker internal connectors and enhanced support to withstand high temperatures and deformation during operation.

Keywords: Laser welding, Simulation, Keyhole

## INTRODUCTION

The application of hairpin windings in electric vehicles has recently gathered increasing attention due to higher efficiency and power density of hairpin windings [1]. A complex manufacturing process involving laser welding is required to connect the hairpin couples, which can lead to issues such as porosity and spatter. To address these challenges and improve weld quality, extensive experimental and simulation studies have been conducted. Experimental investigations employing different laser sources and welding modes have focused on Cu-Cu hairpin contact welding. Ortolani et al. [2] investigated the geometry of the weld track and weld seam using a high-power blue laser (3 KW). This study demonstrated that a high-power blue diode laser can effectively weld copper hairpin windings using conduction mode, resulting in welds with low porosity and reduced spatter. However, the process is slower than the traditional keyhole welding. J. Ning et al. [3] investigated the effects of laser welding parameters and ultrasonic field parameters on copper hairpin joints. They concluded that laser spot welding under argon protection produces well-formed joints with good repeatability, while the closed scanning path enhances weld bead quality. Additionally, increasing ultrasonic power compresses the molten pool, reducing weld width. Haubold et al. [4] explored laser welding of copper using a novel high-power green disc laser. They used a full-factorial experimental design to identify thresholds between heat conduction and deep penetration welding. Results showed that vapor plume management is critical for stable deep penetration welding, while defocused green beams allow control over weld seam width in heat conduction mode. D'Arcangelo et al. [5] systematically compared the performance of conventional Gaussian beams with novel beam shapes, such as top-hat and annular profiles, across various wavelengths including infrared, green, and ultraviolet. The research assessed key parameters including weld morphology, mechanical strength, electrical resistance, and thermal efficiency. Findings indicated that certain beam shapes and wavelengths offer enhanced energy coupling and reduced thermal gradients, leading to improved weld quality and consistency. The paper provides valuable insights for optimizing laser welding processes in the manufacturing of electric motor components, aiming to enhance performance and reliability. Omlor et al. [6] investigated the influence of laser beam welding (LBW) parameters on the quality of hairpin windings in electric drives. They analyzed the effects of variables such as focus position, feed rate, laser power, oxygen content, and beam shaping on weld seam geometry, spatter formation, and porosity. They found that beam shaping reduced spatter and improved seam stability, while feed rate and focus position significantly impacted penetration depth and seam geometry. Dimatteo et al. [7] investigated the influence of laser power and welding speed on the morphology, mechanical strength, and electrical resistance of continuous-wave laser-welded pure copper hairpins. They found Optimal process parameters at an energy density of 11-12 MJ/cm², which produced welds with low porosity (<1%), high tensile strength, and reduced electrical resistance. Zhang et al. [8] investigated the effects of double-pass welding and extrusion techniques on the mechanical and microstructural properties of fiber laser welded 1.5-mm thick T2 copper

joints. They found that double-pass welding improved joint quality by reducing defects and enhancing mechanical performance compared to single-pass approaches. Yu et al. [9] presented a laser welding method for copper hairpin windings that incorporated visual recognition - utilizing a combination of Hough line detection and K-Means clustering algorithms - to detect and quantify gaps and lateral displacements after clamping. Four specific laser scanning trajectories were designed to match four distinct clamping scenarios. Experimental results demonstrate that by adjusting process parameters, similar weld morphology can be achieved across all scenarios, though the presence of gaps and displacements increases spatter and resistance, while decreasing tensile strength.

To deepen the understanding in various laser welding processes, an extensive comparative analysis of experiments is required, and these experiments require a considerable amount of time and investment. Consequently, digitalization of laser welding process through numerical simulations becomes essential. This approach can reduce experimental costs and duration, thereby reducing time to market. Initially various researchers used FEM-simulations to digitalize the laser welding simulations. Murua et al. [10] introduced a novel multiscale thermomechanical model for Laser Beam Welding (LBW), which automatically adapts the laser heat source to the welding regime, enhancing computational efficiency. Validated through experimental tests, the model accurately predicts welding regimes and vertical deformation, proving effective for LBW modeling. Fleischer et al. [11] focused on the numerical simulation of the hairpin welding process. They introduced a model-based approach using finite element simulations to analyze the influence of heat input during laser welding process. By simplifying the heat transfer problem, the study aimed to optimize welding parameters such as energy input rate and stripping length, reducing material costs and installation space. In the end, they highlighted the importance of early-stage numerical simulations in enhancing production-oriented design and mitigating economic risks in electric mobility.

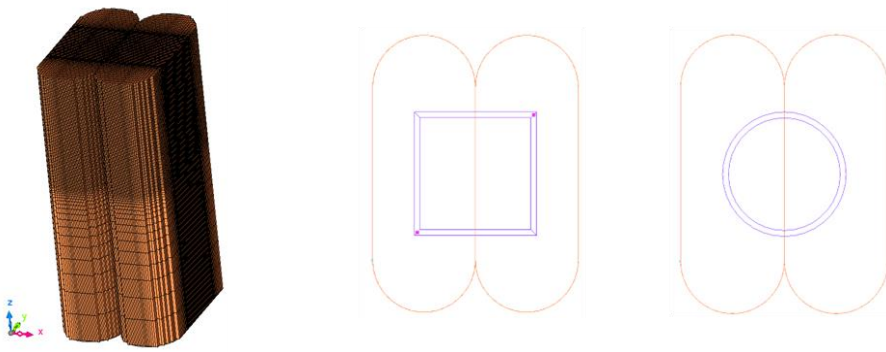
The FEM simulations discussed here are effective for predicting temperature and deformation during the laser welding process. However, to further optimize laser welding process by examining melt pool dynamics, keyhole formation and stability, as well as metal vaporization and the solid-liquid phase transformation, it is essential to implement advanced numerical CFD simulations. Chianese et al. [12-13] used CFD-simulations to explore different laser welding strategies for dissimilar metal with focus on Cu-to-steel interfaces relevant to battery pack manufacturing. They investigated the impact of laser beam shaping, laser beam wobbling and part-to-part gap in laser welding process. For this, a multi-physics CFD simulation model was developed and validated against experimental data. The CFD model provided critical insights into temperature distribution, heat transfer, and melt behavior under varying welding conditions. They highlighted the importance of adapting laser parameters-beam shape, wobble frequency, and power distribution-to stabilize the keyhole, manage thermal gradients, and control mixing in dissimilar material welding. Satyanarayana et al. [14] demonstrated the effectiveness of using CFD simulations combined with the Taguchi method to optimize laser beam welding parameters. The integration of computational welding mechanics, including CFD and finite element models, showed good potential for predicting the thermal, mechanical, and microstructural behavior in welds.

## SIMULATION SETUP

The purpose of this study is to model and analyze the behavior of copper wires during laser welding process and its impact during the product application. This study focuses on developing a digital process chain with the help of multiple simulation software. The simulations were conducted sequentially, starting with a melt pool CFD analysis in Cradle CFD software, followed by a thermomechanical analysis in Simufact Welding software, and concluding with a coupled electric thermal structural Multiphysics analysis in LS DYNA. It must be noted that authors used an in-development feature of scSTREAM (cradle) software, which is not yet officially released. Authors have access to it, due to being part of Cradle software beta testing program. For the other simulations (thermomechanical analysis and coupled electric thermal structural), latest version of software was used.

### MELT POOL CFD ANALYSIS

The CFD analysis focused on a simplified two-wire copper hairpin model to investigate melt pool behavior. The mesh (Fig. 1.a) comprised of 1,116,000 elements with a finer resolution of 34 micrometers within the trajectory boundary and up to 3 millimeters in depth. Copper material properties, including multiple phases, were assigned to the wire. Initial conditions assumed room temperature and a fully solid phase for both the copper wires. Boundary conditions included no-slip boundaries at all fluid interfaces, conduction between solids, log-law heat transfer at fluid-solid boundaries, and adiabatic conditions at the outer boundary. The laser energy source, with a circular cross-section, had a power of 6000W and a speed of 650 mm/s.



(a) (b) (c)

**Fig. 1** (a) The melt pool CFD analysis simulation setup with copper wires meshed at a finer resolution of 34 micrometers within the trajectory boundary and up to 3 millimeters in depth. (b) The square trajectory followed by the laser beam. (c) The circular trajectory followed by the laser beam

The melt pool and keyhole dynamics were simulated using a Multiphysics CFD framework implemented in Cradle CFD. The model solves the conservation equations of mass, momentum, and energy using a one-fluid formulation with free-surface capturing based on the multi-interface advection and reconstruction solver (MARS). Keyhole formation is modelled by incorporating recoil pressure arising from material evaporation at the liquid–gas interface. Multiple laser reflections within the keyhole are considered, enabling realistic prediction of energy concentration and keyhole stability. Fluid flow within the molten pool is driven by surface tension gradients, and Marangoni convection is explicitly included to capture thermocapillary effects influencing melt pool circulation and keyhole instability. In the present implementation, laser absorptivity is assumed constant and is not modelled as a function of temperature or surface condition. While evaporation-driven recoil pressure is considered, explicit porosity formation and stable void retention are not yet predicted.

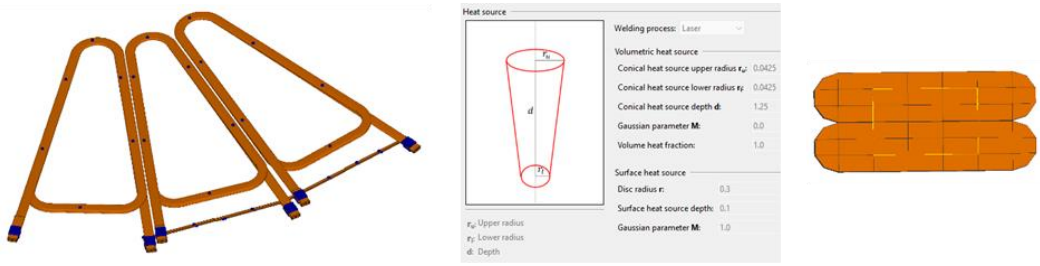
Two cases were set up: one with a square-shaped laser trajectory (Fig. 1.b) and another with a circular-shaped trajectory (Fig. 1.c). The laser beam followed specified trajectories in multiple passes.

## THERMOMECHANICAL ANALYSIS

The second simulation involved a component-level thermomechanical analysis of the complete copper winding assembly, incorporating boundary conditions representing constraints used during the laser welding process (Fig. 2.a). Copper material properties were assigned to the windings, and fixed boundary conditions were applied. The laser energy source, with a circular cross-section, had a power of 6000W and a speed of 650 mm/s.

The transient temperature fields corresponding to the melt pool obtained from the CFD analysis were mapped as a volumetric heat source input (Fig. 2.b) into the thermomechanical welding simulation performed using Simufact Welding. The material behaviour was described using a temperature-dependent elastoplastic constitutive model with isotropic hardening, accounting for thermal expansion and phase-dependent material properties.

The square laser trajectory (Fig. 2.c) was chosen due to its superior weld quality. Welding was performed sequentially at six locations in the assembly.



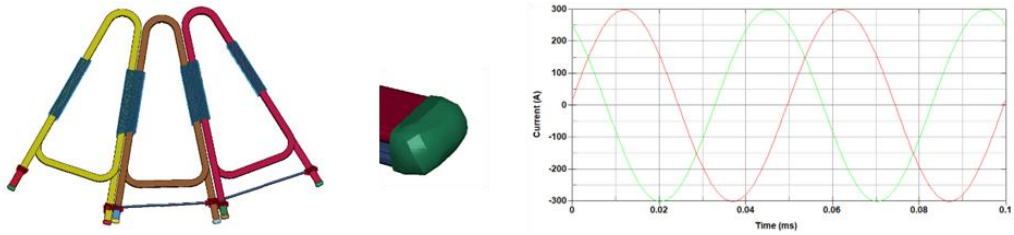

(a) (b) (c)

**Fig. 2** (a) Thermomechanical simulation set up with fixed boundary conditions (blue points). (b) Heat source parameter definition in Simufact welding for one of the passes. (c) Cross section view with the trajectory path (yellow line)

## COUPLED ELECTRIC THERMAL STRUCTURAL ANALYSIS

The third simulation assessed the impact of the laser welding process (presence of weld bead) on the application involving current flow through copper wires. The copper windings assembly, including weld beads and appropriate constraints, was subjected to a high-frequency 3-phase AC current (Fig. 3.a & Fig. 3.b). The loading condition was an alternating current of 300A with a frequency of 20KHz (Fig. 3.c).

Joule heating due to electrical current flow was coupled with structural response, enabling assessment of thermo-mechanical stresses during operational conditions. The coupling was performed in a sequential manner, where thermal fields influenced the mechanical response, consistent with standard industrial practice. This Multiphysics methodology in LS DYNA [15] enabled the computation of current flow through the copper wires, leading to resistive heating, increased temperature, thermal stress, and mechanical distortions. Simulations were conducted with two different convection heat transfer coefficients to evaluate cooling methods (free and forced air cooling) for optimizing thermal management strategies.




(a) (b) (c)

**Fig. 3** (a) Simulation set up for the coupled electric thermal mechanical multi physics analysis with high frequency 3 phase AC. (b) Weld bead model. (c) Input 3-phase current with maximum amplitude 300A and frequency of 20kHz

All the simulations (melt pool CFD analysis, thermomechanical analysis and coupled electric thermal structural analysis) were conducted on HP Z8 Fury G5 Workstation with processor Intel(R) Xeon(R) w5-3435X and 128 GB RAM computer.

## SIMULATION RESULTS

This section presents the results and inferences from the simulations. The findings are discussed in detail, comparing the weld bead quality from different trajectories with respect to melt pool formation. Additionally, the thermomechanical impacts on the copper wires during the laser welding process and the Multiphysics impacts during the current-carrying application are analyzed. The results provide insights into melt pool formation, thermal stresses, and mechanical distortions during the welding process, as well as their impact on performance. The effectiveness of different cooling strategies and the need for optimized connection designs are highlighted.

### MELT POOL CFD ANALYSIS

The CFD analysis compares two cases with different trajectories: a square trajectory with sides of 1.7 millimeters (Fig. 4.a - Fig. 4.g) and a circular trajectory with a diameter of 1.7 millimeters (Fig. 5.a - Fig. 5.g). The laser beam traveled these trajectories six times and melt pool development was captured at the end of each pass.

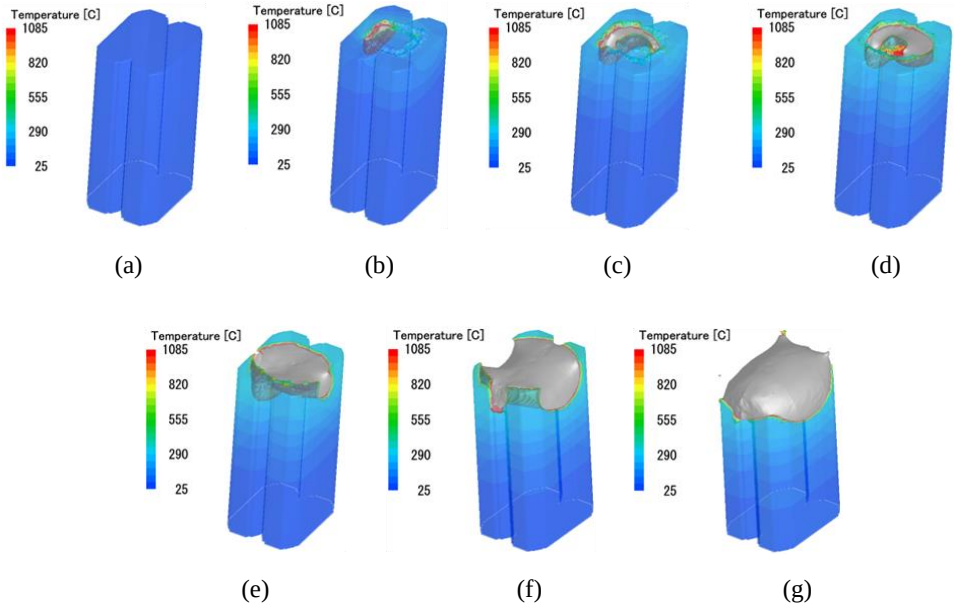



**Fig. 4** Melt pool development with the square trajectory at the end of each pass (a)0s. (b) 0.01s. (c) 0.021s. (d) 0.031(s). (e) 0.042s. (f) 0.052s. (g) 0.063s

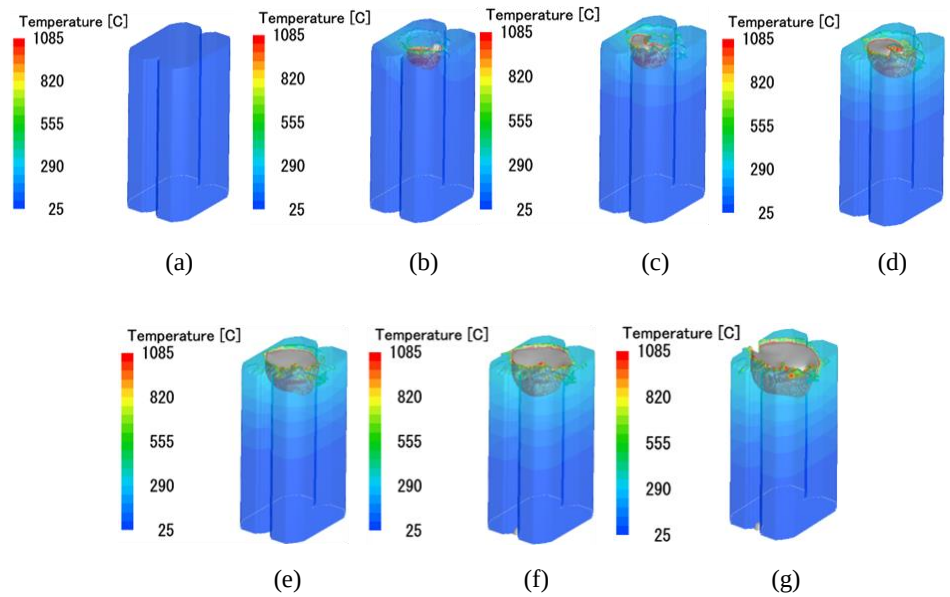



**Fig. 5** Melt pool development with the circular trajectory at the end of each pass (a)0s. (b) 0.008s. (c) 0.016s. (d) 0.025(s). (e) 0.033s. (f) 0.041s. (g) 0.050s

The comparison revealed better melt formation with the square trajectory, resulting in a dome-shaped melt pool. The circular trajectory was shorter, imparting less energy to the copper wires. To eliminate this difference in comparison, the laser beam continued the trajectory for eight passes. The comparison showed that the square trajectory still performed better than the circular trajectory. The square trajectory, being closer to the edges of the copper wire, allowed faster heat transfer to the edges and subsequently faster melting (Fig. 6.a - Fig. 6.c). In contrast, the circular trajectory was more confined to the center region and failed to melt the corner regions, which were important for dome shape formation (Fig. 6.d - Fig. 6.f).

A cut-section view through the center of both copper wires measured maximum melt pool depth at several data points (Fig. 7.a). The plot indicated consistently higher melt pool depth for the square trajectory compared to the circular trajectory (Fig. 7.b).

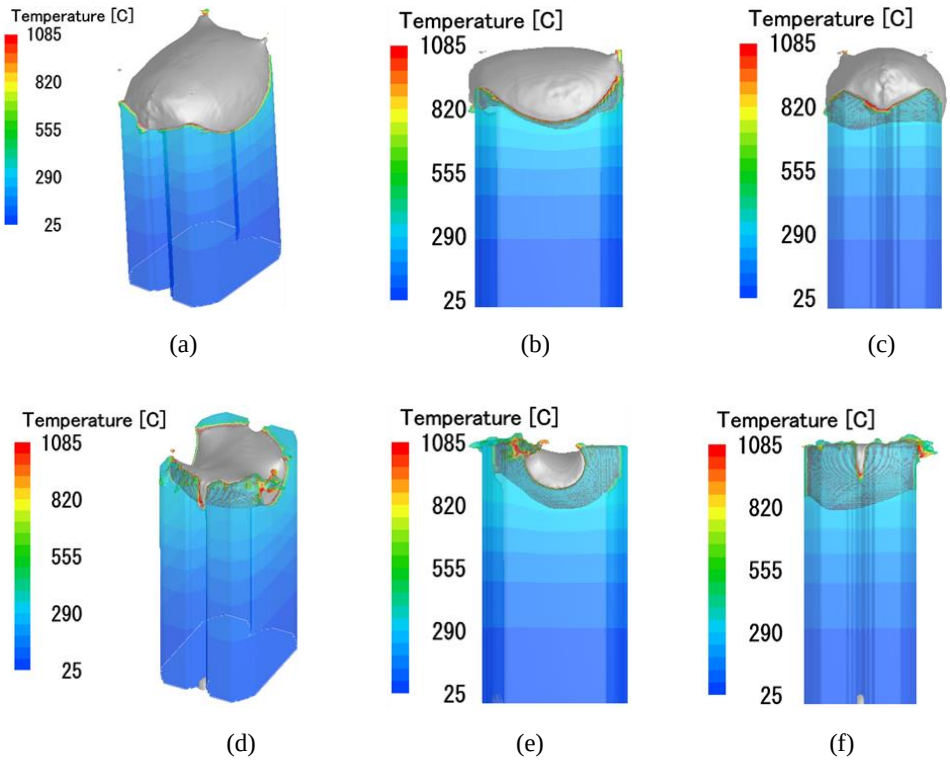
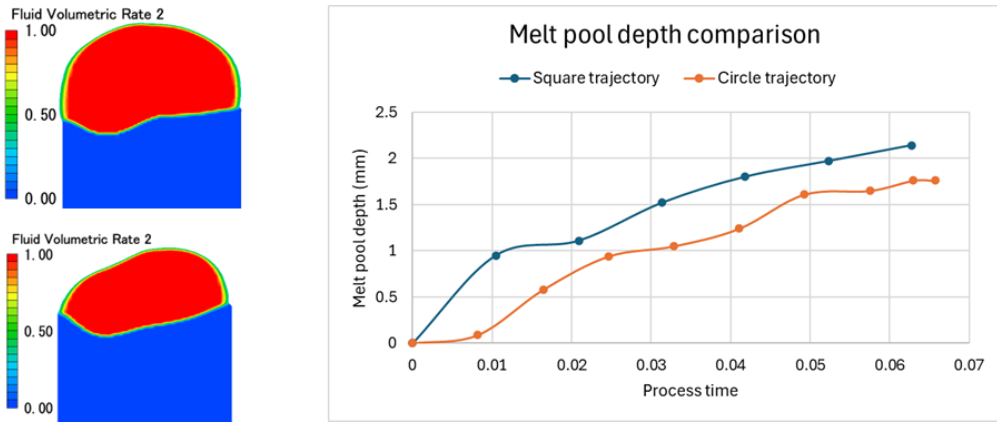


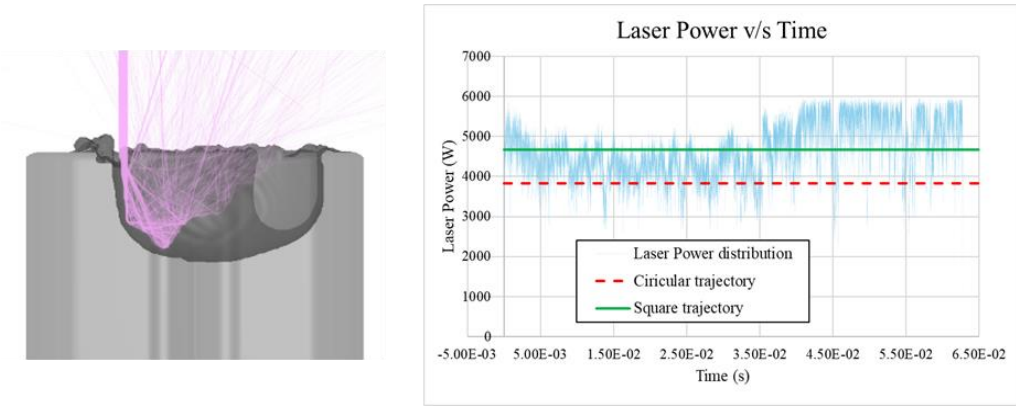

**Fig. 6** The melt pool comparison at the end of 0.063s. Square trajectory completed 6 passes (a) Isometric view. (b) Front view. (c) Side view. Circular trajectory covering the 8$^{th}$ pass (d) Isometric view. (e) Front view. (f) Side view




(a) (b)

**Fig. 7** The melt pool depth measured at different times corresponding to the end of each pass. (a) The top image corresponds to square trajectory and bottom image corresponds to circular trajectory. (b) Melt pool depth comparison between square and circular trajectory

Laser material interaction (Fig. 8.a) was assessed to understand laser energy absorption during the process. The average laser energy absorbed was higher with the square trajectory by approximately 20%, explaining the superior weld quality (Fig. 8.b).

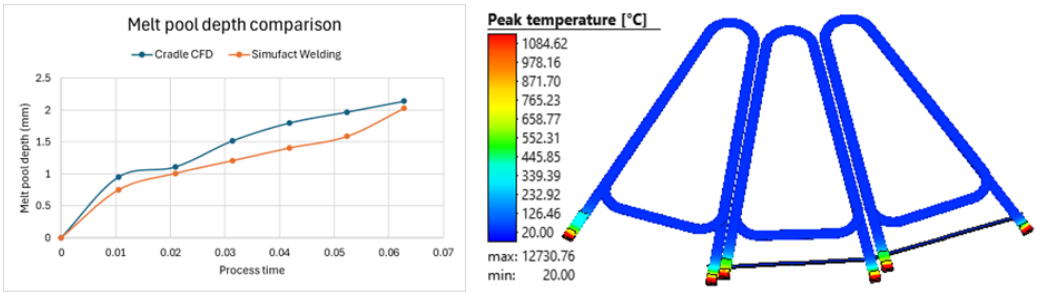



(a) (b)

**Fig. 8** (a) Laser material interaction where laser goes through multiple reflections. (b) Average laser power absorption comparison between square and circular trajectory

## THERMO-MECHANICAL ANALYSIS

The square trajectory was chosen for thermomechanical analysis due to its better weld quality. Maximum melt pool depth at the end of each pass was extracted and scaled to define the heat source volume for each pass in the thermomechanical simulation. The average melt pool depth at each pass closely matched observations from the CFD analysis (Fig. 9.a). The analysis consisted of laser welding processes at 6 locations, 3 connecting the windings to the 3-phase inputs and another 3 for interconnection between the windings.




(a) (b)

**Fig. 9** (a) The melt pool depth comparison between Simufact Welding and Cradle CFD, validating the thermomechanical model. (b) Windings peak temperature (°C) at the end of six welding process (zoomed in image at top right): 3 connecting the 3-phase wires to the windings and 3 providing interconnection between the windings

The second part of the simulation involved cooling hairpin windings at atmospheric conditions, leading to heat transfer by conduction and convection, and formation of thermal stresses and distortions near the fixed boundary conditions. Higher stresses were observed close to the locations where the constraints were provided (Fig. 10.b).

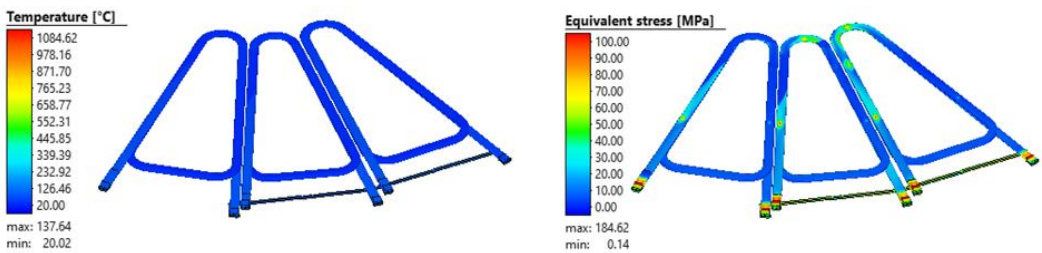



**Fig. 10** (a) The model cooled down to room temperature (°C) with natural atmospheric cooling. (b) Stress formation observed near the constrained locations

## COUPLED ELECTRIC THERMAL STRUCTURAL ANALYSIS

Weld bead models, based on the melt pool shape from the CFD analysis, were used as connections at six locations in the windings' assembly via tied contact option. An electric current of 300A with a frequency of 20kHz was passed through the windings assembly, resulting in alternating current through each winding over time (Fig. 11).

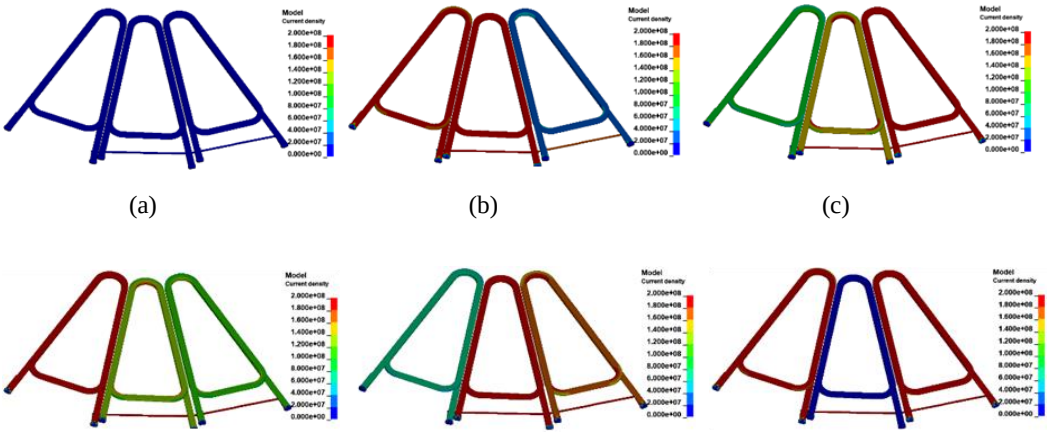
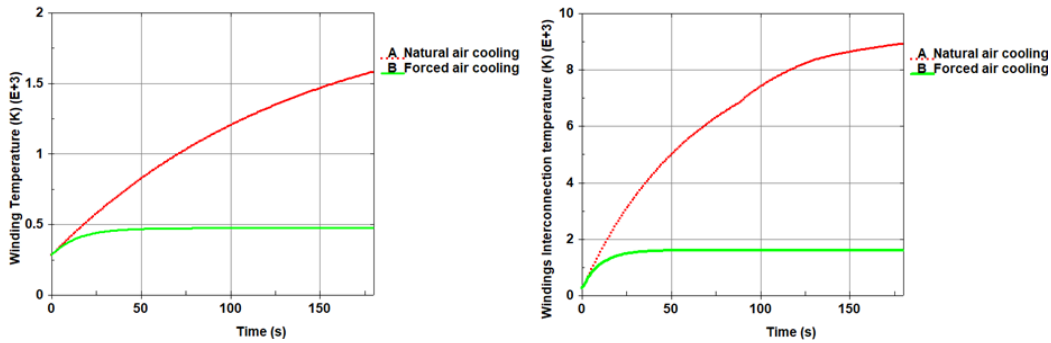



**Fig. 11** The alternating current flow (current density in A/mm²) through the copper wires at different times (a) 0ms. (b) 0.01ms. (c) 0.02ms. (d) 0.03ms. (e) 0.04ms. (f) 0.05ms

The current flow through the windings increased the temperature due to resistive heating of the copper wires, causing thermal stress as the windings were constrained at different locations, restricting thermal expansion. Two simulations with different cooling conditions, natural air cooling (H=10 W/m²K) and forced air cooling (H=100 W/m²K), were performed to optimize thermal management strategies. The current flowed through the windings for three minutes, with forced air cooling reaching thermal equilibrium at 480K in approximately 80 seconds, while natural convection did not reach equilibrium with a temperature of approximately 1500K in 180 seconds. The winding interconnections showed high temperature readings with the forced convection model reaching an equilibrium temperature of 1600K while the natural convection model couldn't attain equilibrium at a temperature of 9000K in 180 seconds.




(a) (b)

**Fig. 12** (a) Windings temperature comparison with natural and forced air cooling. (b) Windings interconnection temperature comparison with natural and forced air cooling

High temperatures and subsequently high deformations were observed in the connector providing internal connections between the three windings in both cases, suggesting design change requirements with thicker internal connections and higher structural support for them during current flow application. Comparatively the forced convection model performed better compared to the natural convection model with a lower level of deformation for the same support conditions.

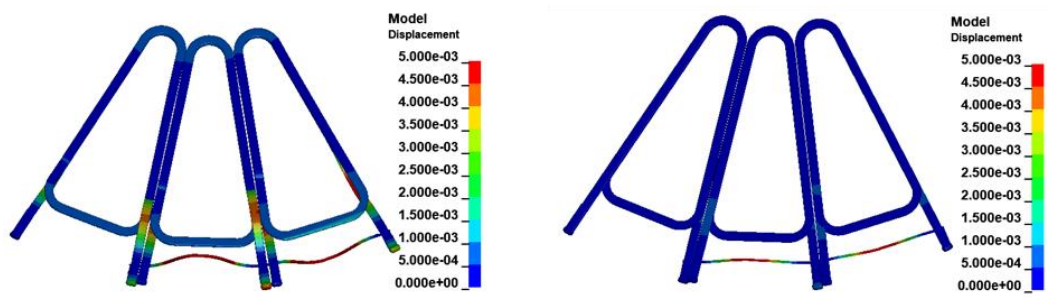



**Fig. 13** The windings internal connections experienced high deformation due to thermal expansion at high temperatures for (a) natural air cooling (b) forced air cooling

## EXPERIMENTAL SETUP AND RESULTS

Copper hairpin specimens with a rectangular cross section measuring 1.5 mm × 4 mm were fabricated from high-purity copper (purity: 99.9%). The experimental setup utilized an infrared laser source with a wavelength of 1060 μm and a beam diameter of 50 μm. Laser processing was conducted at a power of 6000 W and a scanning speed of 650 mm/s. The

laser was programmed to follow a square trajectory, each side measuring 1.7 mm, consistent with the conditions used in corresponding simulation studies.

To ensure experimental reproducibility and reliability, six copper hairpin samples were processed under identical conditions. For each specimen, cross-sectional images were analyzed to assess and document the weld morphology. The results demonstrated high consistency, with analogous structural features observed across all specimens. A representative cross-sectional image is presented to show the experimental findings.

Fig. 1 presents the microstructural characteristics of the welded copper hairpin strips. It can be observed that the maximum melt pool depth on the left side attains 2711µm, exceeding the depth measured on the right side. This asymmetry is due to the initiation of the laser scanning from the left, resulting in prolonged exposure to elevated temperatures and increased localized heat accumulation, thereby producing a deeper melt pool. Additionally, small pores are visible in the cross-sectional micrograph, which are typically attributed to rapid solidification phenomena inherent to laser welding of copper.

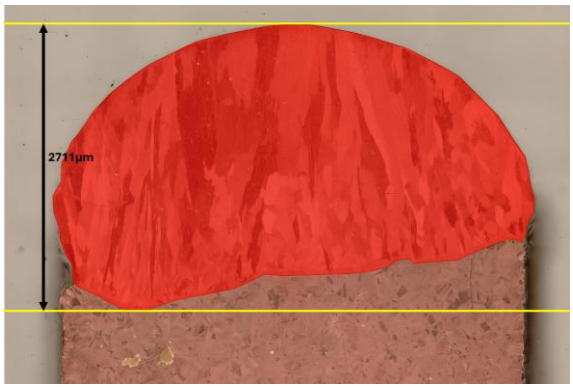



**Fig. 13** Cross-section image of square trajectory

A comparative analysis of Fig. 13 with the simulation results (Fig. 7.a top) reveals a strong correlation between the experimentally measured melt pool geometries and the computational fluid dynamics (CFD) simulation predictions, thereby validating the numerical approach employed in this investigation.

## CONCLUSION

This study examines laser welding in copper hairpin windings using both multiphysics simulations and experimental validation. CFD analyses compared melt pool development for 1.7 mm square and circular laser trajectories across multiple passes. The square trajectory produced superior melt pools - deeper, more uniform, and dome-shaped - due to better thermal distribution and about 20% greater laser energy absorption. Thermomechanical simulations, supported by CFD, showed that the square path reduced thermal stresses and

mechanical distortions. Coupled electric-thermal-structural simulations evaluated current-carrying performance. Forced air cooling (H=100 W/m²K) enabled thermal equilibrium at 480 K in roughly 80 seconds. Natural convection failed to stabilize, with temperatures reaching 1500 K in 180 seconds. High stresses and deformations were observed at internal winding connections, indicating a need for thicker, better-supported connectors. Experimental tests used six high-purity copper hairpin samples and a 6000 W infrared laser following square trajectories. Cross-sectional analysis revealed consistent weld morphology and deeper melt pools on the weld initiation side. These results closely matched CFD predictions. Minor porosity, typical of rapid copper solidification, was also observed. The findings highlight the influence of laser trajectory and cooling strategy on weld quality, thermal management, and mechanical reliability. The validated simulation approach provides a strong foundation for optimizing laser welding.

## ACKNOWLEDGEMENTS

Authors like to express their sincere appreciation to the Cradle support team for their invaluable assistance in the simulation work undertaken for this research. Their technical expertise, prompt guidance, and unwavering support greatly contributed to the successful completion of the study.

## References

[1] A. RIEDEL, M. MASUCH, M. WEIGELT, T. GLÄSEL, A. KÜHL, S. REINSTEIN and J. FRANKE: 'Challenges of the Hairpin Technology for Production Techniques', *21st International Conference on Electrical Machines and Systems (ICEMS)*, Vol. 21, pp. 2471-2476, 2018.

[2] M. ORTOLANI, G. BORZONI, D. NOCCIOLINI, B. PREVITALI and A. G. DEMIR: 'Conduction mode welding of Cu hairpins with a 3-kW blue laser with external features correlated to quality attributes', *The International journal of Advanced Manufacturing Technology,* 137, pp. 1959-1974, 2025.

[3] J. NING and L. ZHANG: 'Non-contact ultrasonic-assisted laser welding of copper hairpins', *journal of Materials Research and Technology,* Vol. 31, pp. 3536-3550, 2024.

[4] M. HAUBOLD, A. GANSER, T. EDER and M. F. ZÄH: 'Laser welding of copper using a high power disc laser at green wavelength', *10th CIRP Conference on Photonic Technologies*, Vol. 74, pp. 446-449, 2018.

[5] S. D'ARCANGELO, L. CAPRIO, D. CHESI, D. NOCCIOLINI, R. CORBINELLI, B. PREVITALI and A. G. DEMIR: 'Comprehensive benchmarking of laser welding technologies including novel beam shapes and wavelengths for e-drive copper hairpins', *Optics & Laser Technology*, Vol. 169, 10964, 2024.

[6] M. OMLOR, N. SEITZ, T. BUTZMANN, T. PETRICH, R. GRÄF, A. HESSE and K. DILGER: 'Quality characteristics and analysis of input parameters on laser beam welding of hairpin windings in electric drives', *The International Journal of Materials Joining*, Vol. 67, pp. 1491-1508, 2023.

[7] V. DIMATTEO, A. ASCARI, P. FAVERZANI, L. POGGIO and A. FORTUNATO: 'The effect of process parameters on the morphology, mechanical strength and electrical resistance of CW laser-welded pure copper hairpins', *Journal of Manufacturing Processes*, Vol. 62, pp. 1491-1508, 2021.

[8] J. NING, L. ZHANG, A. WANG, Q. BAI, J. YANG and J. ZHANG: 'Effects of double-pass welding and extrusion on properties of fiber laser welded 1.5-mm thick T2 copper joints', *Journal of Materials Processing Technology*, Vol. 237, pp. 75-87, 2016.

[9] H. YU, Y. YIN, S. JI, C. ZHANG, T. ZHU and Z. LIU: 'Laser welding method and quality analysis of hairpin windings based on visual recognition of gap and displacement matching process', *Optics & Laser Technology*, Vol. 178, 111224, 2024.

[10] O. MURUA, J. ARRIZUBIETA, A. LAMIKIZ and H. SCHNEIDER: 'Numerical simulation of a laser beam welding process: From a thermomechanical model to the experimental inspection and validation', *Thermal Science and Engineering Progress*, Vol. 55, 102901, 2024.

[11] J. FLEISCHER, L. HAUSMANN and F. WIRTH: 'Production-oriented design of electric traction drives with hairpin winding', *31st CIRP Design Conference*, Vol. 100, pp. 169-174, 2021.

[12] G. CHIANESE, S. JABAR, P. FRANCIOSA, D. CEGLAREK and S. PATALANO: 'A multi-physics CFD study on the part-to-part gap during remote laser welding of copper-to-steel battery tab connectors with beam wobbling', *12th CIRP Conference on Photonic Technologies*, Vol. 111, pp. 484-489, 2022.

[13] G. CHIANESE, Q. HAYAT, S. JABAR, P. FRANCIOSA, D. CEGLAREK and S. PATALANO: 'A multi-physics CFD study to investigate the impact of laser beam shaping on metal mixing and molten pool dynamics during laser welding of copper to steel for battery terminal-to-casing connections', *Journal of Materials Processing Technology*, Vol. 322, 118202, 2023.

[14] G. SATYANARAYANA, K. NARAYANA and B. N. RAO: 'Incorporation of Taguchi approach with CFD simulations on laser welding of spacer grid fuel rod assembly', *Materials Science and Engineering: B*, 137, Vol. 269, 115182, 2021.

[15] M. SREEJITH AND P. RANA: 'Integrated Electrical-Thermal-Structural Analysis in High-Frequency AC Systems Using LS-DYNA', *ANSYS Innovation Conference*, Germany, 2024.

# A STATISTICAL INVESTIGATION OF THE LASER ENERGY ABSORPTION AND KEYHOLE STABILITY IN HIGH-POWER LASER BEAM WELDING

X. MENG*, S. PUTRA*, M. BACHMANN*, M. RETHMEIER**,*,***

**BAM Bundesanstalt für Materialforschung und -prüfung, 12205 Berlin, Germany*
***Technische Universität Berlin, Institute of Machine Tools and Factory Management, 10587 Berlin, Germany*
****Fraunhofer IPK, 10587 Berlin, Germany*

*DOI 10.3217/978-3-99161-089-2-006, license CC BY 4.0*
*https://creativecommons.org/licenses/by/4.0/deed.en*
*This CC license does not apply to third party material and content noted otherwise.*

## ABSTRACT

The behaviour of the weld pool in high-power laser beam welding is significantly influenced by laser absorption and keyhole stability, which determines the final weld qualities. However, their dynamic features and multi-coupled interactions make in-depth analyses difficult. This study addresses the challenges by conducting a thorough statistical evaluation of the effects of welding parameters on laser absorption and keyhole fluctuations, using experimental investigations and a well-validated numerical model. From a statistical aspect, the laser energy distribution and the keyhole collapse, commonly considered highly time-varying, show clear regularities. Three distinct regions of the time-averaged energy distribution are identified. The possibility of the keyhole collapse positions obeys a universal normal distribution. The statistical data show greater potential in revealing some well-known, industry-related but unclearly explained findings, such as the saturation of the weld penetration with increasing heat input and the physical basis of the contributions of different welding parameters in the porosity reduction.

Keywords: Laser beam welding, laser absorption, keyhole stability, multi-physics modelling

## INTRODUCTION

High-power laser beam welding (LBW) has become increasingly attractive in industrial applications due to its high efficiency and precise control [1]. The most important characteristic of LBW is the formation of a narrow and deep keyhole inside the weld pool, generated by intense laser-induced evaporation. Within this keyhole, the laser beam reflects multiple times against dynamic, irregular keyhole surfaces. Although liquid metals exhibit

low direct laser absorptivity [2], the cumulative absorption from repeated reflections enables thermal efficiencies of up to 90% [3]. This absorption mechanism profoundly influences the welding process, driving melting, chemical reactions, and microstructural evolutions. However, these interactions can also lead to common defects such as spatter, hot-cracking, and porosity. Hence, deeper physical insights into laser absorption and keyhole dynamics are critical for optimizing the LBW process.

Monitoring keyhole behaviour during welding is challenging due to the opaque nature of liquid metals and rapidly evolving geometries. Techniques such as Optical Coherence Tomography (OCT) have provided transient one-dimensional measurements of the keyhole depth [4]. Alternatively, the sandwich configuration, using a metal plate and heat-resistant glass, allows a two-dimensional side view of the keyhole, captured through high-speed cameras [5]. However, detailed keyhole features, like fine surface fluctuations, are often obscured in this method due to the image overexposure. The x-ray transmission imaging technique significantly improves visualization, offering clear two-dimensional or even three-dimensional reconstruction of the transient keyhole geometry. High-quality synchrotron x-ray sources achieve micrometer-level spatial and MHz-level temporal resolution, enabling precise observation of fine structural details within keyhole dynamics [6-8].

Direct measurement of laser absorption inside the keyhole remains technically unfeasible. Consequently, indirect strategies, such as reconstructing keyhole shapes using high-speed photography [9] or x-ray radiography [10,11] followed by ray-tracing analysis, have been developed. These approaches estimate energy distribution and overall absorptivity, revealing, for instance, that approximately 40% of the laser energy is absorbed by the front keyhole wall [9].

Recently, multi-physics modelling has become an effective tool for understanding LBW phenomena. By integrating physics-based beam interaction models with interface tracking algorithms, these simulations effectively predict laser absorption and keyhole topology [12-14]. Studies using these models have identified the inclination angle of the keyhole's front wall as a crucial factor influencing absorption and energy distribution [15]. A more inclined front wall, common at higher welding speeds, tends to distribute energy uniformly. Additionally, microscopic protrusions on keyhole walls strongly influence energy absorption, driving keyhole instability and fluctuations [16,17].

However, current experimental and numerical analyses typically examine short and sometimes selective instances of the keyhole dynamics, which lack statistical robustness. Only limited research has been performed from a statistical perspective. For example, in the study of Pang et al., the keyhole depth fluctuations were found to have a normal distribution [18]. Important aspects like average laser absorption during melting or the likelihood of porosity-related keyhole collapse remain unexplored.

Addressing these gaps, this paper presents a comprehensive statistical analysis using multi-physics modelling to investigate laser energy absorption and keyhole stability over an extended duration (more than 100 ms). Statistical evaluations explore how welding parameters (welding speed and focus position) influence keyhole dynamics and energy absorption. This approach reveals novel insights into LBW physics, highlighting the advantages of statistical methods in understanding and optimizing this complex process.

# METHODOLOGY

## EXPERIMENTS

Bead-on-plate welding experiments were performed using 304 stainless steel plates measuring 200 mm length, 60 mm width, and 10 mm thickness. The laser source was a Trumpf disk laser system emitting at a wavelength of 1.03 μm with a focal diameter of 0.42 mm. The laser beam was vertically aligned to the plate surface. Welding parameters investigated included welding speed (1.5 m/min to 3.0 m/min) and focal position (ranging from -6 mm to +3 mm). Before welding, the steel surfaces were mechanically cleaned to remove oxide layers. Cross-sections were prepared from welded samples for further examination, involving grinding, polishing, and etching using a V2A solution. Optical microscopy was utilized to analyse these cross-sections metallographically, capturing the fusion zone profiles and measuring penetration depths to validate experimental results.

## MULTI-PHYSICS MODELLING

Under the following assumptions: (1) the liquid metal behaves as an incompressible Newtonian fluid, (2) fluid flow remains laminar, and (3) buoyancy is modelled using the Boussinesq approximation, where density variations due to temperature are neglected except in buoyancy terms, the governing equations for heat transfer, fluid flow, and free surface deformation during LBW can be expressed as follows:

$$\nabla \cdot \mathbf{v} = 0 \tag{1}$$

$$\rho\left(\frac{\partial \mathbf{v}}{\partial t} + (\mathbf{v}\cdot\nabla)\mathbf{v}\right) = -\nabla p + \mu\nabla^2\mathbf{v} - \mu K\mathbf{v} + \mathbf{S_m} + \mathbf{F} \tag{2}$$

$$\rho\left[\frac{\partial h}{\partial t} + (\mathbf{v}\cdot\nabla)h\right] = \nabla\cdot(k\nabla T) + Q \tag{3}$$

$$\frac{\partial f}{\partial t} + \nabla\cdot(\mathbf{v}f) = 0 \tag{4}$$

Equation (1) represents mass conservation, where **v** is the velocity vector. Equation (2) describes momentum conservation, where $\rho$ denotes material density, $t$ physical time, $p$ pressure, $\mu$ dynamic viscosity, and $K$ the damping coefficient associated with solidification. The vector $\mathbf{S_m}$ includes various source terms such as buoyancy and gravitational forces, while **F** represents volumetric forces derived from surface phenomena [19], including capillary pressure, Marangoni stress, and recoil pressure. Equation (3) expresses energy conservation, with $h$ as enthalpy, $T$ temperature, $k$ thermal conductivity, and $Q$ the heat source term

representing converted surface energy. Equation (4) is the volume-of-fraction (VOF) equation used to track the interface, where *f* is the volume fraction of steel.

The model incorporates key factors affecting melting and keyhole dynamics. Laser heating is simulated using a physics-based beam propagation model, which will be described further in the following part. Additional heat from scattering and absorption is considered through two diffuse heat-source models [20]. Thermal losses from convection, radiation, and evaporation are applied at the interface. Capillary pressure, Marangoni stress, and temperature-dependent recoil pressure [21] are included to simulate the keyhole evolution. The stagnation pressure and shear stress generated by the vapor jet are modelled analytically using the Knudsen layer theory and the free jet theory [20] for accurate simulation of the keyhole dynamics.

Accurate modelling of beam propagation and laser-material interactions is essential for understanding laser absorption and keyhole behaviour. In this study, a ray-tracing algorithm is implemented to track the laser beam, including initial and subsequent reflections on the keyhole surface. Beam focusing or defocusing due to the caustic effect are also considered. Since the VOF method does not explicitly define the interface, reflection accuracy is typically restricted by the cell size [22]. To improve precision, a localized Level-Set (LS) approach reconstructs the keyhole interface mathematically [23], allowing the exact determination of reflection points without significantly increasing computational costs.

Commonly used laser absorption models rely on the incident angle alone, requiring empirical calibration for other physical factors [24,25]. A novel Fresnel reflection model based on the Drude–Lorentz theory [26], calculating the relative electric permittivity of metals, is employed in this study. This new model considers the incident angle, laser wavelength, surface temperature, and electrical conductivity, which eliminates the adjustment/calibration of empirical parameters.

The simulation domain consists of a 10 mm thick metallic phase and a 1 mm thick argon gas phase. The initial mesh includes a uniformly meshed central region (2 mm to 8 mm in the x-direction and -2 mm to 2 mm in the y-direction) with 0.2 mm hexahedral cells, which gradually increase in size to approximately 0.7 mm outside this region. A multi-level mesh adaptation approach is used to refine the mesh progressively from 0.2 mm to 0.1 mm and finally to 0.05 mm within the region of interest (keyhole and weld pool). ANSYS Fluent 23.1 is used to solve the governing equations. The total number of cells increases from an initial 78,000 to around 680,000 as the keyhole and weld pool evolve, as illustrated in Fig. 1. The simulations run on a high-performance computing cluster at Bundesanstalt für Materialforschung und -prüfung, where at least 10 ms of physical simulation time is achieved every 24 hours using 88 cores and 256 GB of memory.

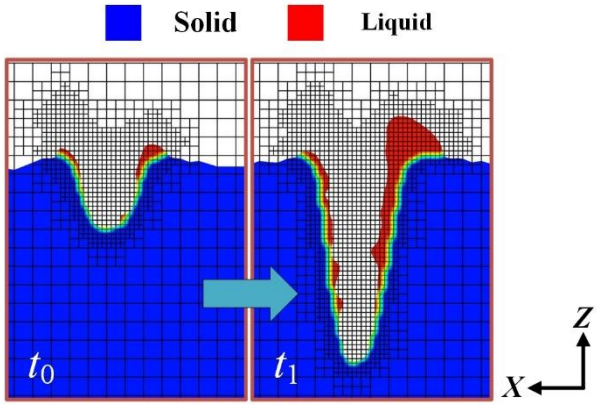



**Fig. 1** The mesh refinement from the multi-level mesh adaptation

## RESULTS AND DISCUSSION

Fig. 2 presents a representative validation of the simulated penetration depths across the studied welding parameter ranges in the current study. The proposed model achieves good accuracy, exhibiting minor deviations of approximately -11% to +5% compared to experimental measurements. In the following section, a detailed parametric investigation will be performed to statistically analyse the effects of welding speed and focal position on laser energy absorption and keyhole stability over an extended period of more than 100 ms.

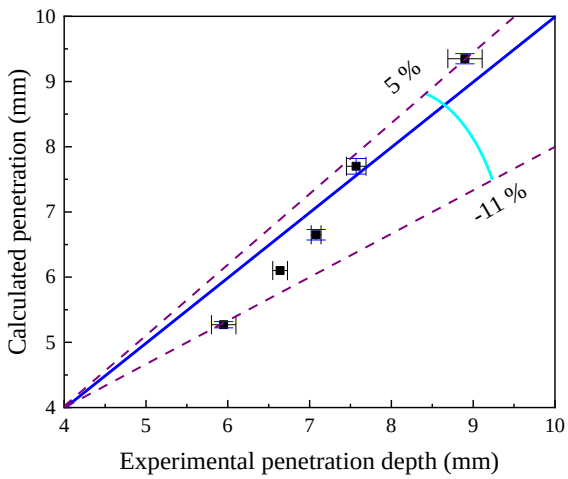



**Fig. 2** Comparison between experimental and simulated penetration depths

## STATISTICAL ANALYSIS OF LASER ABSORPTION

Fig. 3 illustrates the influence of welding speed on the time-averaged laser energy absorption along the longitudinal cross-section. All contours are normalized relative to the maximum power density for the respective welding conditions. A transient keyhole profile (solid black line) is included for spatial reference. At all welding speeds, the front keyhole wall consistently shows higher absorption due to the initial laser incidence. The upper region of the rear wall also absorbs a notable amount of energy. Compared with the transient laser energy density [10,11,16,17], the time-averaged laser energy exhibits a relative regular distribution regime.

To analyse the overall energy distribution along the thickness direction and the welding directions, the time-averaged power density (in W/m²) at each z-level/x-level is integrated to yield a line distribution (in W/m), which is then divided by the welding speed to obtain the averaged linear energy. As shown in Fig. 4(a), three distinct regions are observed along the thickness direction: an upper zone with intensive energy absorption, a middle region exhibiting a relatively uniform distribution, and a lower region where absorbed energy declines sharply. While the welding speed has limited influence on the general distribution shape, an inverse correlation is evident in the upper region, namely higher welding speeds correspond to reduced energy absorption. Fig. 4(b) shows the energy distribution across the front and rear keyhole walls. For clarity, the laser axis is used to separate the front and rear wall regions. Steep gradients in front of the axis indicate concentrated energy absorption on the front keyhole wall, while gentler slopes behind it reflect more gradual absorption on the rear wall. On a time-averaged basis, the absorption ratio on the front wall decreases from 37% to 30.5% as welding speed increases from 1.5 m/min to 3.0 m/min.

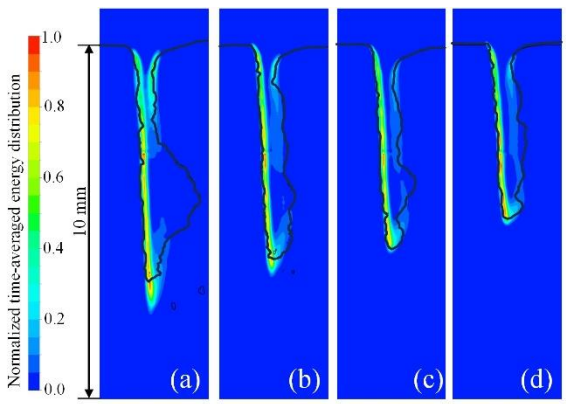



**Fig. 3** The influence of welding speed on time-averaged laser absorption: (a) 1.5 m/min, (b) 2.0 m/min, (c) 2.5 m/min, (d) 3.0 m/min. (laser power: 4 kW, focal position: -3 mm)

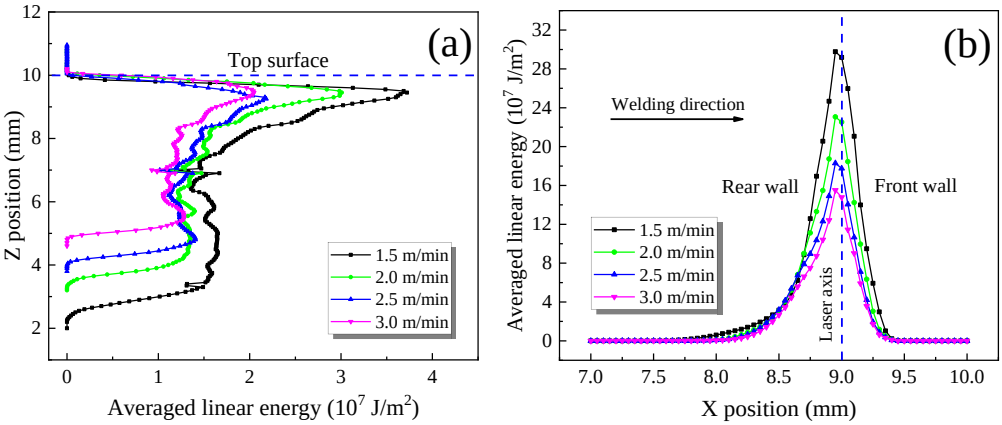



**Fig. 4** Time-averaged linear energy: (a) along the thickness direction, (b) along the welding direction (laser power: 4 kW, focal position: -3 mm)

The focal position has a more pronounced impact on the pattern of laser energy distribution than the welding speed. Even with similar linear energy input, variations in focal position result in different time-averaged energy profiles, leading to different penetration depths, as shown in Fig. 5. Fig. 6 further demonstrates the significant influence of the focal position on the time-averaged energy distribution, particularly in the middle and lower regions of the keyhole. A negative focal position of -3 mm produces the deepest penetration, attributed to a stable absorption zone extending to the keyhole bottom. At focal position of -6 mm, this stable zone becomes less distinct, with a gradual reduction in absorbed energy along the depth. In contrast, with a zero or positive focal position, the absorbed energy increases slightly near the keyhole bottom rather than declining, an unusual distribution potentially associated with the formation of porosity and hot cracking [27]. Additionally, as the focus shifts from positive to negative, the absorption ratio on the front keyhole wall steadily decreases-from 40.5% to 36.8%.

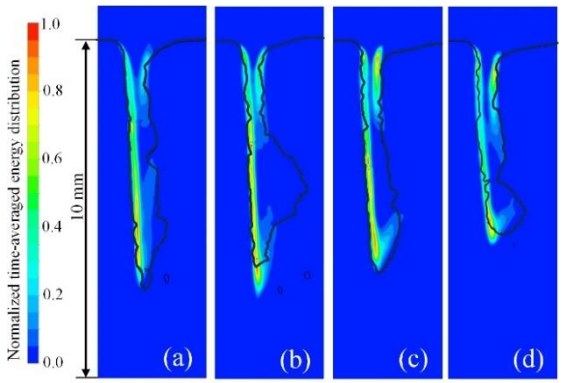



**Fig. 5** The influence of focal position on the time-averaged laser absorption: (a) -6 mm, (b) -3 mm, (c) 0 mm, (d) +3 mm (Laser power: 4 kW, welding speed: 2 m/min)

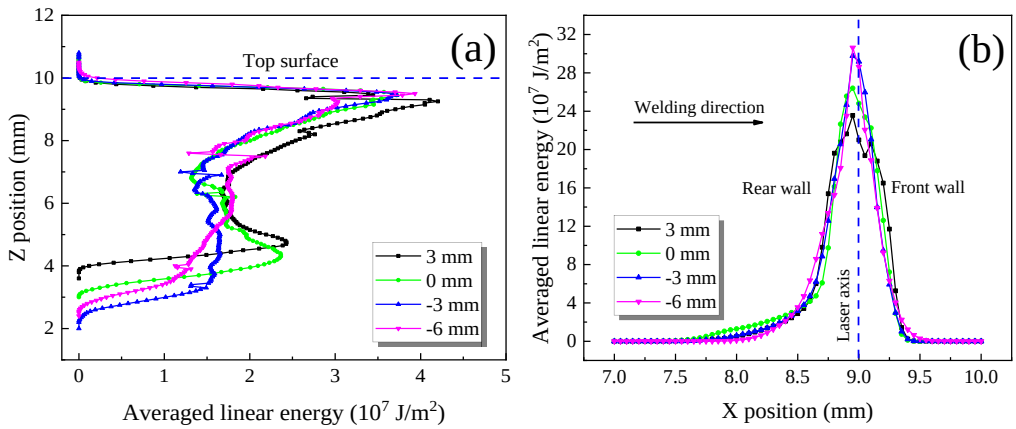



**Fig. 6** Time-averaged total linear energy: (a) along the thickness direction, (b) along the welding direction

## STATISTICAL ANALYSIS OF THE KEYHOLE STABILITY

To comprehensively assess keyhole stability, several indicators are considered in this study: collapse position, fluctuation frequency, and collapse duration. A collapse is defined as the moment when the front and rear keyhole walls come into contact. The location of this contact is a key metric for evaluating stability, while the number of collapses per second is defined as the fluctuation frequency. Each collapse also has a corresponding duration, measured from the initial contact to the moment when the walls separate again.

Fig. 7 presents the possibility of collapse occurrences along the keyhole depth. Most collapses occur near the keyhole tip and follow a normal distribution, aligning well with

previous findings [18,28]. Lower welding speeds, which generate deeper keyholes, are associated with broader collapse ranges. As the welding speed decreases from 3.0 m/min to 1.5 m/min, the collapse range increases from 0.7 mm to 2.0 mm, leading to larger gas bubbles and potentially more serious porosity issue. The collapse frequency remains relatively stable between 7 kHz and 8.4 kHz for welding speeds between 1.5 m/min and 2.5 m/min, but rises sharply to 180 kHz at 3.0 m/min.

Fig. 8 shows a scatter plot of individual collapse durations versus position, with each point representing a single collapse occurrence. The points are color-coded using kernel density estimation (KDE). Higher KDE values (red regions) indicate more frequent collapse behaviour in that area. It is clearly indicated that although keyhole fluctuations occur at high frequencies (from several kilohertz up to hundreds of kilohertz), most collapses are short-existing (under 1 ms) and are rapidly reopened due to a strong recoil pressure. A comparison of Fig. 8(a)-8(d) reveals that increasing welding speed significantly reduces the number of long-duration collapses. Since only collapses with extended durations are likely to form gas bubbles in the weld pool and potentially lead to porosity in the final weld, it can be expected that the reduction of the long-duration collapses will enhance the keyhole stability.

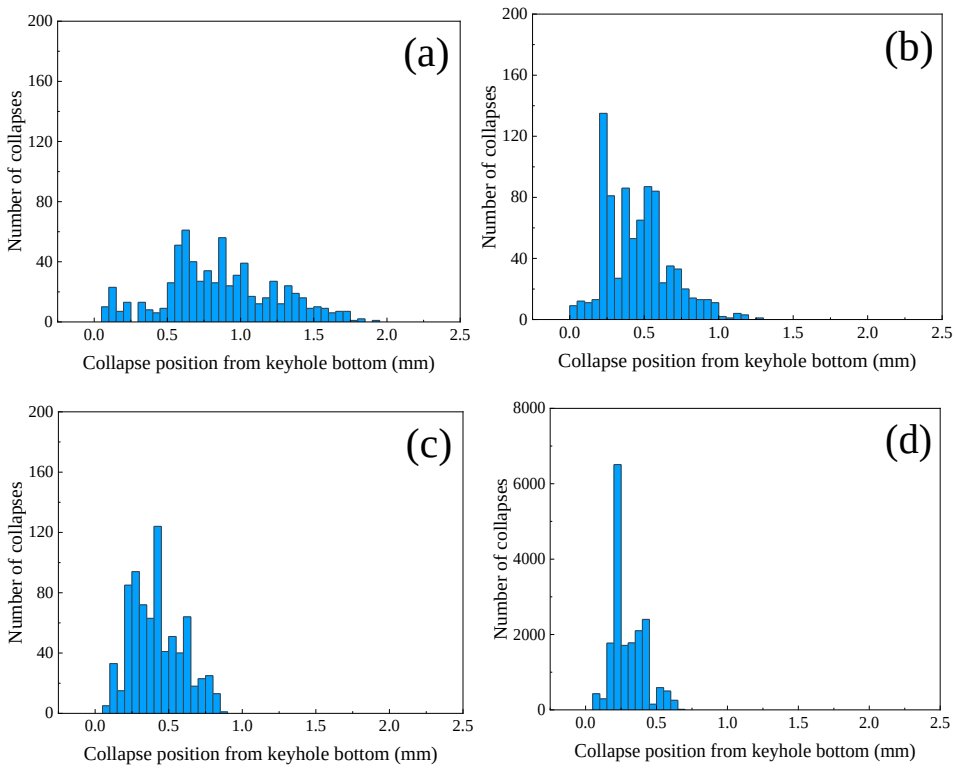



**Fig. 7** The influence of welding speed on collapse number: (a) 1.5 m/min, (b) 2.0 m/min, (c) 2.5 m/min, (d) 3.0 m/min (Laser power: 4 kW Focal position: -3 mm)

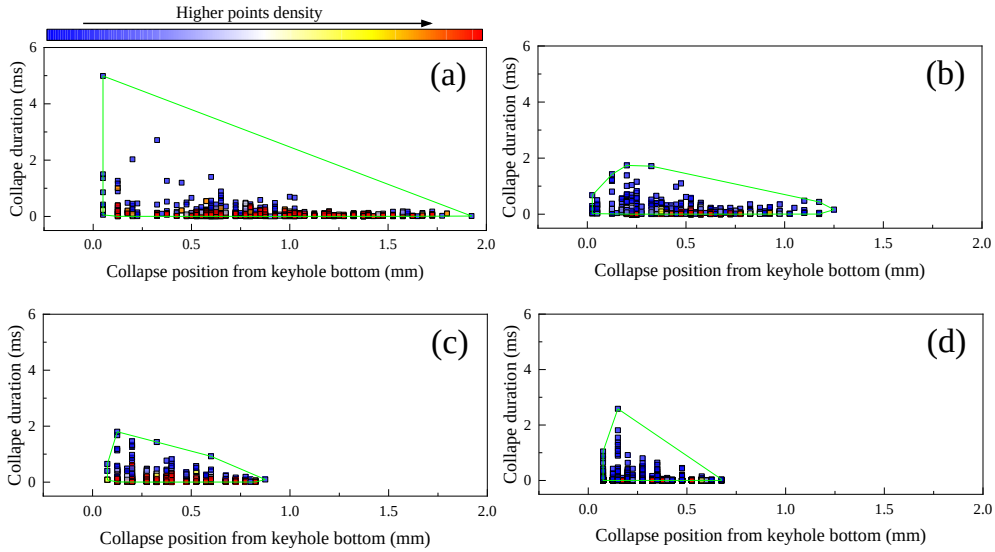



**Fig. 8** Duration of individual collapse at different positions: (a) 1.5 m/min, (b) 2.0 m/min, (c) 2.5 m/min, (d) 3.0 m/min (Laser power: 4 kW Focal position: -3 mm)

Compared to welding speed, the focal position exhibits a complex influence on keyhole stability. A deeply focused beam positioned at -6 mm (relative to the workpiece surface) not only induces collapses at the keyhole bottom, which follows also a normal distribution, but also leads to occasional collapses in the upper keyhole region, as illustrated in Fig. 9(a). These upper-region collapses are typically short in duration and are expected to contribute only marginally to overall keyhole instability, as shown in Fig. 10(a). As the focal position is adjusted upward, these upper-region collapses disappear, and collapses are confined to the keyhole bottom. Fig. 9 and Fig. 10 further demonstrate that the collapse region, closely related to potential bubble size, becomes narrower, and the number of long-duration collapses decreases as the focal plane moves closer to the surface. This behaviour suggests a reduced likelihood of porosity formation at shallower focal positions.

At the same time, the collapse frequency increases from 4.8 kHz to 9.1 kHz as the focus is raised from -6 mm to +3 mm. While this rise in frequency may increase the number of collapses, which potentially contributes to porosity formation, the simultaneous reduction in collapse area and duration may counterbalance this effect. Overall, the impact of focal position on keyhole dynamics is found to be both non-linear and non-monotonic, consistent with observations reported in several experimental studies [29-31].

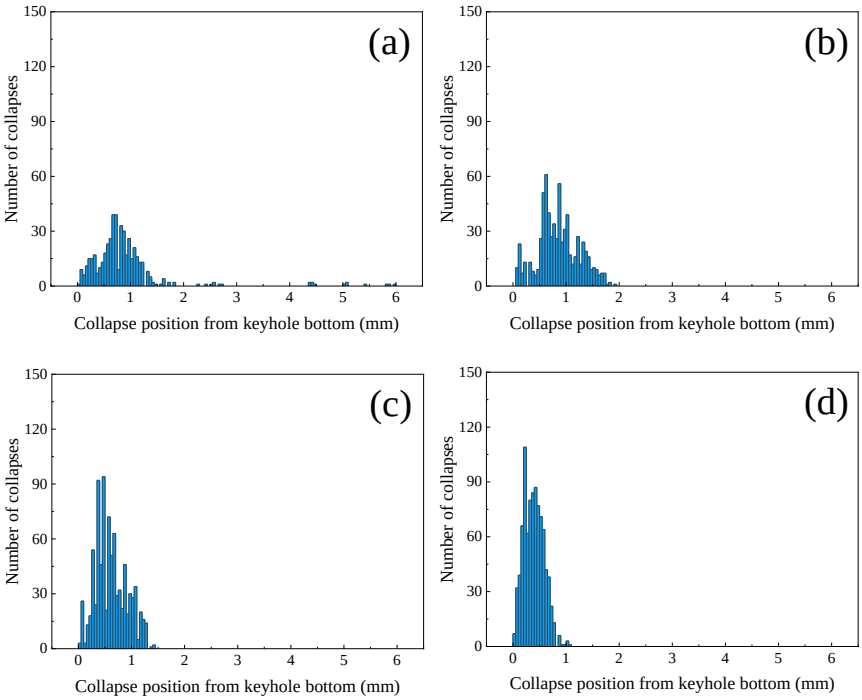



**Fig. 9** The influence of focus position on collapse number: (a) -6 mm, (b) -3 mm, (c) 0 mm, (d) +3 mm (Laser power: 4 kW, welding speed: 2 m/min)

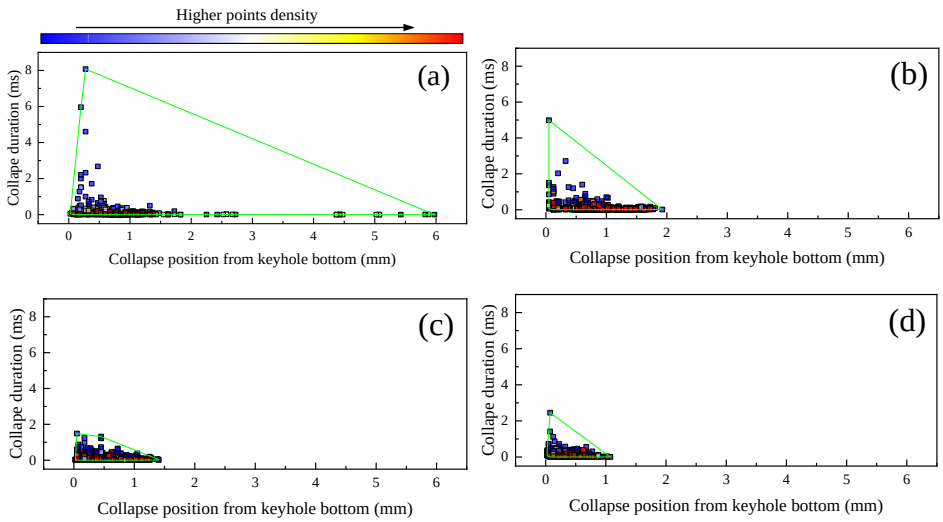



**Fig. 10** Duration of individual collapse at different positions: (a) -6 mm, (b) -3 mm, (c) 0 mm, (d) +3 mm (Laser power: 4 kW, welding speed: 2 m/min)

## CONCLUSION

With the integration of experimental investigation and multi-physics modelling, this paper presents a statistical evaluation of the effects of welding parameters, including welding speed and focus position, on laser energy absorption and keyhole stability in high-power LBW. The main conclusions are summarized as follows:

1. Three distinct regions of laser absorption are identified from a time-averaged perspective: an upper region with higher absorption, a middle region with relatively uniform energy intensity, and a lower region where energy absorption declines sharply. This distribution pattern is only slightly influenced by variations in welding speed whereas focus position exerts a notably stronger impact on the energy distribution.
2. On a time-averaged basis, the front keyhole wall accounts for approximately 30% to 40% of the total absorbed energy due to its intensive and localized interaction with the laser beam.
3. The majority of the keyhole collapses occur in the lower region, and their spatial distribution follows a normal distribution. Increasing welding speed is effective in narrowing the collapse zone and shortening collapse durations. The influence of focus position is found to be non-linear and non-monotonic.

## ACKNOWLEDGMENT

This work is funded by the Deutsche Forschungsgemeinschaft (DFG, German Research Foundation)-Project No. 506270597 and No. 466939224.

## References

[1] M. RETHMEIER, A. GUMENYUK and M. BACHMANN: 'High-power laser beam welding for thick section steels – new perspectives using electromagnetic systems', *Science and Technology of Welding and Joining*, Vol. 27, pp. 43-51, 2022.

[2] E. M. R. SILVA, W. A. MONTEIRO, W. ROSSI and M. S. F. LIMA: 'Absorption of Nd:YAG laser beam by metallic alloys', *Journal of Materials Science Letters*, Vol. 19, pp. 2095-2097, 2000.

[3] Y. KAWAHITO, N. MATSUMOTO, Y. ABE and S. KATAYAMA: 'Relationship of laser absorption to keyhole behavior in high-power fiber laser welding of stainless steel and aluminum alloy', *Journal of Materials Processing Technology*, Vol. 211, pp. 1563-1568, 2011.

[4] C. STADTER, M. SCHMOELLER, L. VON RHEIN and M. F. ZAEH: 'Real-time prediction of quality characteristics in laser beam welding using optical coherence tomography and machine learning', *Journal of Laser Applications*, Vol. 32, p. 022046, 2020.

[5] L. HUANG, P. LIU, S. ZHU, X. HUA and S. DONG: 'Experimental research on formation mechanism of porosity in magnetic-field-assisted laser welding of steel', *Journal of Manufacturing Processes*, Vol. 50, pp. 596-602, 2020.

[6] H. WANG, M. NAKANISHI and Y. KAWAHITO: 'Effects of welding speed on absorption rate in partial and full penetration welding of stainless steel with high-brightness, high-power laser', *Journal of Materials Processing Technology*, Vol. 249, pp. 193-201, 2017.

[7] R. CUNNINGHAM, C. ZHAO, N. PARAB, C. KANTZOS, J. PAUZA, K. FEZZAA and A. D. ROLLETT: 'Keyhole threshold and morphology in laser melting revealed by ultrahigh-speed X-ray imaging', *Science*, Vol. 363, pp. 849-852, 2019.

[8] J. XU, X. WANG, C. YAO, D. ZOU, R. XIONG, R. XIAO and B. ZHANG: 'A dual in-situ monitoring of multiphase dynamics during laser wire fusion process with synchrotron radiation and visible light', *Journal of Manufacturing Processes*, Vol. 131, pp. 2528-2534, 2024.

[9] R. S. MATTI and A. F. H. KAPLAN: 'Post-modelling of images from a laser-induced wavy boiling front', *Applied Surface Science*, Vol. 357, pp. 2277-2284, 2015.

[10] F. FETZER, C. HAGENLOCHER, R. WEBER and T. GRAF: 'Geometry and stability of the capillary during deep-penetration laser welding of AlMgSi at high feed rates', *Optics & Laser Technology*, Vol. 133, p. 106562, 2021.

[11] B. J. SIMONDS, J. TANNER, A. ARTUSIO-GLIMPSE, P. A. WILLIAMS, N. PARAB, C. ZHAO and T. SUN: 'The causal relationship between melt-pool geometry and energy absorption measured in real time during laser-based manufacturing', *Applied Materials Today*, Vol. 23, p. 101049, 2021.

[12] W. E. ALPHONSO, M. BAIER, S. CARMIGNATO, J. H. HATTEL and M. BAYAT: 'On the possibility of doing reduced-order thermo-fluid modelling of laser powder-bed fusion (L-PBF) – assessment of the importance of recoil pressure and surface tension', *Journal of Manufacturing Processes*, Vol. 94, pp. 564-577, 2023.

[13] A. OTTO, H. KOCH, K. H. LEITZ and M. SCHMIDT: 'Numerical simulations – a versatile approach for better understanding dynamics in laser material processing', *Physics Procedia*, Vol. 12, pp. 11-20, 2011.

[14] M. COURTOIS, M. CARIN, P. LE MASSON, S. GAIED and M. BALABANE: 'A new approach to compute multi-reflections of a laser beam in a keyhole for heat-transfer and fluid-flow modelling in laser welding', *Journal of Physics D: Applied Physics*, Vol. 46, p. 505305, 2013.

[15] W. TAN and Y. C. SHIN: 'Analysis of multi-phase interaction and its effects on keyhole dynamics with a multi-physics numerical model', *Journal of Physics D: Applied Physics*, Vol. 47, p. 345501, 2014.

[16] Y. WANG, P. JIANG, J. ZHAO and S. GENG: 'Effects of energy-density attenuation on the stability of keyhole and molten pool during deep-penetration laser welding: a combined numerical and experimental study', *International Journal of Heat and Mass Transfer*, Vol. 176, p. 121410, 2021.

[17] C. ZHAO, Q. GUO, X. LI, N. PARAB, K. FEZZAA, W. TAN and T. SUN: 'Bulk-explosion-induced metal spattering during laser processing', *Physical Review X*, Vol. 9, No. 2, p. 021052, 2019.

[18] S. PANG, W. CHEN and W. WANG: 'A quantitative model of keyhole-instability-induced porosity in laser welding of titanium alloy', *Metallurgical and Materials Transactions A*, Vol. 45, pp. 2808-2818, 2014.

[19] J. U. BRACKBILL, D. B. KOTHE and C. ZEMACH: 'A continuum method for modeling surface tension', *Journal of Computational Physics*, Vol. 100, No. 2, pp. 335-354, 1992.

[20] X. MENG, S. N. PUTRA, M. BACHMANN, F. YANG, A. ARTINOV and M. RETHMEIER: 'A fundamental study of physical mechanisms of wineglass-shaped fusion-zone profile in laser melting', *Journal of Materials Processing Technology*, Vol. 324, p. 118265, 2024.

[21] V. SEMAK and A. MATSUNAWA: 'The role of recoil pressure in energy balance during laser materials processing', *Journal of Physics D: Applied Physics*, Vol. 30, p. 2541, 1997.

[22] J. H. CHO and S. J. NA: 'Implementation of real-time multiple reflection and Fresnel absorption of a laser beam in a keyhole', *Journal of Physics D: Applied Physics*, Vol. 39, p. 5372, 2006.

[23] D. L. SUN and W. Q. TAO: 'A coupled volume-of-fluid and level-set (VOSET) method for computing incompressible two-phase flows', *International Journal of Heat and Mass Transfer*, Vol. 53, pp. 645-655, 2010.

[24] W. I. CHO, S. J. NA, C. THOMY and F. VOLLERTSEN: 'Numerical simulation of molten-pool dynamics in high-power disk-laser welding', *Journal of Materials Processing Technology*, Vol. 212, pp. 262-275, 2012.

[25] S. PANG, L. CHEN, J. ZHOU, Y. YIN and T. CHEN: 'A three-dimensional sharp-interface model for self-consistent keyhole and weld-pool dynamics in deep-penetration laser welding', *Journal of Physics D: Applied Physics*, Vol. 44, p. 025301, 2010.

[26] A. EBRAHIMI, M. SATTARI, S. J. BREMER, M. LUCKABAUER, G. W. R. RÖMER, I. M. RICHARDSON and M. J. HERMANS: 'The influence of laser characteristics on internal-flow behaviour in laser melting of metallic substrates', *Materials & Design*, Vol. 214, p. 110385, 2022.

[27] A. ARTINOV, X. MENG, M. BACHMANN and M. RETHMEIER: 'Study on the transition behavior of the bulging effect during deep-penetration laser beam welding', *International Journal of Heat and Mass Transfer*, Vol. 184, p. 122171, 2022.

[28] S. A. KHAIRALLAH, T. SUN and B. J. SIMONDS: 'Onset of periodic oscillations as a precursor of a transition to pore-generating turbulence in laser melting', *Additive Manufacturing Letters*, Vol. 1, p. 100002, 2021.

[29] N. SETO, S. KATAYAMA and A. MATSUNAWA: 'Porosity-formation mechanism and reduction method in $CO_2$-laser welding of stainless steel', *Welding International*, Vol. 16, pp. 451-460, 2002.

[30] J. S. KIM, T. WATANABE and Y. YOSHIDA: 'Effect of the beam-defocusing characteristics on porosity formation in laser welding', *Journal of Materials Science Letters*, Vol. 14, pp. 1624-1626, 1995.

[31] J. D. TUCKER, T. K. NOLAN, A. J. MARTIN and G. A. YOUNG: 'Effect of travel speed and beam focus on porosity in alloy 690 laser welds', *JOM*, Vol. 64, pp. 1409-1417, 2012.

# UNDERSTANDING THE ORIGIN AND PREDICTION OF LASER WELDING DEFECTS IN HIGHLY REFLECTIVE METALS: A NUMERICAL STUDY APPLIED TO A2219 ALLOY

B. F. CHETAN*,**[1], M. COURTOIS**, S. CADIOU**, M. CARIN**, V. NAIN*, F. MACHI*, A. ALVES FERREIRA*

**IREPA LASER, Parc d'Innovation, 67400 Illkirch, France.*
***Univ. Bretagne Sud, UMR CNRS 6027, IRDL, F-56100 Lorient, France.*
*[1]Corresponding author: fchetan@irepa-laser.com*

*DOI 10.3217/978-3-99161-089-2-007, license CC BY 4.0*
*https://creativecommons.org/licenses/by/4.0/deed.en*
*This CC license does not apply to third party material and content noted otherwise.*

## ABSTRACT

A new approach to modeling and simulating multiple reflections of a laser beam has been developed under COMSOL Multiphysics®. It is based on a special coupling between a modified ray tracing method and Level-set. Initial application results for laser welding on aluminum in static pulse and fusion line cases are compared with theory and experiments.

Keywords: heat transfer; fluid flow; laser welding; multiple reflections; reflective materials; Level-set; keyhole behavior

## INTRODUCTION

Under certain operating conditions, laser welding is subject to undesirable phenomena such as melt instabilities and the formation of defects that affect the integrity of the welded parts. The difficulty of controlling these defects depends on the nature of the materials studied. This study focuses on materials such as aluminum, which are both reflective and good thermal conductors. Indeed, laser welding of aluminum in an industrial context (energy density $\gtrsim 1$ MW/cm$^2$, penetration $\gtrsim 1$ mm) is characterized by fluctuating keyholes and unstable melt

flows. It results in beads potentially affected by defects (notably porosity defects) detrimental to the integrity of the welded parts.

Since the first experimental studies of keyhole dynamics using X-ray imaging by Matsunawa *et al* [1], [2], a link has been established between keyhole fluctuations and non-uniform irradiance distribution. This result was subsequently supported by numerical studies. These include Ke *et al* [3], who discuss keyhole stability and porosity reduction through beam oscillation, and Fetzer *et al* [4], who show that at low welding speeds, the keyhole is subject to strong fluctuations accompanied by significant variations in local irradiance, resulting in trapped gas bubbles and possibly residual porosities.

This shows that the correct representation of energy deposition is a fundamental aspect of the development of an accurate and predictive numerical model of laser welding. There are three approaches in the literature to model energy deposition: analytical, wave and geometrical approaches. The analytical approach, which consists of weighting the laser intensity by an absorptivity coefficient (constant or increasing with keyhole depth, according to Gouffé's formula [5]), does not allow the phenomenon of multiple reflections to be simulated, but only its global effect to be taken into account. The wave-based approach developed by Courtois *et al* [6] involves solving Maxwell's equations. This method was used to develop a 2D multiphysics model of the melt pool under static pulse conditions. The phenomenon of multiple reflections is well represented, and the model can reproduce experimentally observed porosities. However, the method is very demanding in terms of mesh refinement and therefore computation time and has never been used for 3D weld bead models. Finally, the geometrical approach known as Ray tracing, an intermediate solution between the two previous ones (less constraining than electromagnetism and more realistic than an analytical formula), consists of discretizing the beam into a finite number of rays to which the laws of geometrical optics are applied. This option has been used in recent studies on thermohydrodynamic simulation of laser welding: Daligault *et al* [7], Westhofen *et al* [8]. However, the use of Ray tracing is not as straightforward, as its algorithm is not integrated into commercial laser welding simulation software. Researchers are therefore obliged either to develop customized Ray tracing codes or software (e.g. the "in-house code" used in their work by Lind *et al* [9]), or to use the Java or Matlab extensions of commercial software to implement the algorithm for calculating multiple reflections (e.g. the work by Mayi *et al* [10]). In both cases, the digital tool developed becomes the property of the research team and is neither accessible nor exploitable by a third party.

In this study, we have developed a new method to describe laser-matter interaction, considering multiple beam reflections in the keyhole. The method is based on the theory of geometrical optics but differs from conventional Ray tracing in one fundamental respect: all couplings are performed using the same software (COMSOL Multiphysics®), without the need for any additional software (Matlab or Java environment). This ability to couple the thermohydrodynamic problem and the multiple beam reflections in a single computation code means simplicity of implementation, and a saving in calculation time. The physical coherence of the model has been proved. The aim of this paper is to present the first results of this new approach, for a better understanding of the origins of melt instabilities and porosity-type defects in aluminum welding.

## DESCRIPTION OF LASER-MATTER INTERACTION

The new approach developed is based on a modified ray tracing method, in which the velocity of the rays is artificially reduced to ensure compatibility with solvers available in commercial Finite Element Method software. This approach is purely numerical and is intended solely to describe the laser beam trajectory inside the keyhole.

### FUNDAMENTAL EQUATION

The motion of a ray is solved here by Newton's second law with assumption of straight-line propagation:

$$\frac{d}{dt}\left(\frac{d\vec{q}}{dt}\right) = \vec{0} \tag{1}$$

$$\frac{d\vec{q}}{dt} = \vec{V} \tag{2}$$

with $\vec{q}$ the ray's position vector, and $\vec{V}$ its velocity vector.

### MODELING MULTIPLE REFLECTIONS

Ray reflections at the free interface obey the Snell-Descartes laws:

$$\theta_{ref} = -\theta_{inc} \tag{3}$$

$\theta_{inc}$ and $\theta_{ref}$ being respectively the angles of incidence and reflection with respect to the normal $\vec{n}$, (Figure 1). Thus, determining the ray's trajectory after rebound requires knowing the impact point, the surface normal at that point, and the angle of incidence. With fixed-mesh Eulerian Level-set methods, the free interface is diffuse, and it is not possible to impose a bounce boundary condition on the metal surface. The issue is then addressed by developing an appropriate coupling between Ray tracing and Level-set.

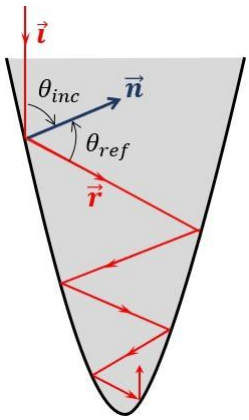



**Fig. 1** Illustration of the phenomenon of multiple reflections in a cavity

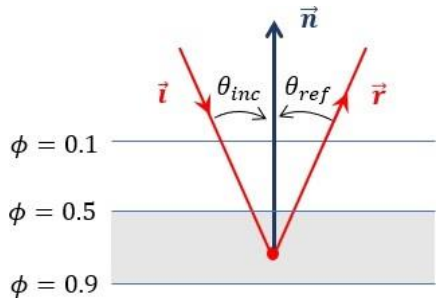



**Fig. 2** Detection and reflection of a ray in the reflective layer (in light gray)

The transport equation for the Level-set variable $\phi$ is written as:

$$\frac{\partial \phi}{\partial t} + \vec{u}.\vec{\nabla}\phi = \gamma_{ls}\vec{\nabla}.\left(\epsilon_{ls}\vec{\nabla}\phi - \phi(1-\phi)\frac{\vec{\nabla}\phi}{|\vec{\nabla}\phi|}\right) \quad (4)$$

$\vec{u}$ is the fluid velocity (gas as liquid metal), $\epsilon_{ls}$ and $\gamma_{ls}$ the numerical parameters of the Level-set method. $\phi$ is 1 in the metal, 0 in the gas and takes on intermediate values in the transition phase. Nevertheless, we define the isosurface $\phi = 0.5$ as the metal/gas interface. The normal at a point on this interface is calculated as:

$$\vec{n} = \frac{\vec{\nabla}\phi}{|\vec{\nabla}\phi|} \quad (5)$$

Ray tracing/Level-set coupling is achieved by defining a "reflective layer", in the metal/gas transition zone, in which the incident ray is detected and redirected (Figure 2). The reflective layer is the zone where $0.5 < \phi < 0.9$. Referring to Figure 1, an incident ray (as opposed to a reflected ray) is analytically defined by $\vec{\imath}.\vec{n} < 0$. In sum, since $\vec{\imath} \parallel \vec{V}$, any ray is reflected whenever:

$$(0.5 < \phi < 0.9) \wedge \left(\vec{V}.\vec{n} < 0\right) \quad (6)$$

and its trajectory remains linear between two consecutive points of impact.

## CONSTRUCTION OF THE THERMAL SOURCE TERM

To translate reflections into energy deposits, an energy property is defined by considering that the power contained in each ray is always proportional to its velocity (Equation 7). Moreover,

since the power drops after each reflection, the rebound velocity must drop in the same proportion: at the i-th reflection,

$$\frac{P_i}{V_i} = \frac{P_0}{V_0}, \quad \forall\, i = 1, \dots, N_{ref} \tag{7}$$

$$P_i = (1 - \alpha_F) P_{i-1} \Longrightarrow V_i = (1 - \alpha_F) V_{i-1} \tag{8}$$

$$(\Delta P)_i = \alpha_F P_{i-1} = \alpha_F \left(\frac{V_{i-1}}{V_0}\right) P_0 \tag{9}$$

with $\alpha_F = \alpha_F(\theta)$ the Fresnel absorptivity. $V_0$ is the initial ray velocity. For a laser beam of power $P_{laser}$ discretized into $N_r$ rays, the initial power of each ray is:

$$P_0 = \frac{P_{laser}}{N_r} \tag{10}$$

The energy deposited in the material is calculated from the power lost by the ray, Equation 9. Finally, it suffices to know, at the i-th bounce of a ray, the incident velocity and angle of incidence to define its contribution to the volume source term, Equation 11:

$$q_i = \left[\alpha_F(\theta_i)\left(\frac{V_{i-1}}{V_0}\right)\cos(\theta_i)\frac{1}{dv}\right] P_0 \tag{11}$$

with $dv$ the volume of the mesh element containing the point of impact, $\theta_i = -\theta_{i-1} = \left|\left(\vec{n}, \vec{V_i}\right)\right|$ the angle of incidence. The bracketed term, homogeneous at $m^{-3}$, is calculated for all rays at each time step, directly creating a dynamic energy map of values between 0 and a maximum.

## Definition of Ray Emission Velocity

Rigorously, the ray emission velocity should be taken to be equal to the speed of light in vacuum, $c$ i.e close to the speed of light in air or metal vapour. Coupling such physics to fluid mechanics, where flows and melt penetration are characterized by velocities of the order of $\mathrm{m/s}$, would induce a numerical time-scale problem. Moreover, detecting high-speed rays through a diffuse interface would require choosing a time step such that they would not cross more than one element between $\mathrm{t}$ and $\mathrm{t} + \Delta\,\mathrm{t}$ (Equation 12). The conventional mesh sizes ($\mathrm{h} \sim 10 - 50\ \mu\mathrm{m}$) would then imply too small time steps.

$$\Delta t \leq \frac{h}{c} \sim 10^{-13}\ s \tag{12}$$

To overcome these obstacles, a sensitivity study was carried out on $V_0$ with the aim of defining an emission velocity that would allow a conceivable time step with an equally acceptable margin of error. The approach used consisted in developing a reference model where $V_0 = c$ with an ALE-type physical interface and then comparison models where $V_0 \ll$

$c$. The ALE not only enables all rays to be detected regardless of $V_0$, but also makes the tests more realistic by simulating interface deformations without solving the momentum equations. Rays are emitted into a cavity created from an initially flat interface, which deforms in three successive phases - penetration, tilting and oscillations (Figure 3)- according to the imposed velocity $\vec{v}_{inter}$:

$$\vec{v}_{inter} = \begin{cases} -v_p exp\left(-\frac{x^2}{{w_0}^2}\right)\vec{y}, & 0 \leq t < 1\ s \\ v_{incl}\vec{x}, & 1 \leq t < 1.5\ s \\ v_{osc} sin(2\,\pi f_{osc}\, t)\vec{y}\,, & 1.5 \leq t \leq 4\ s \end{cases} \tag{13}$$

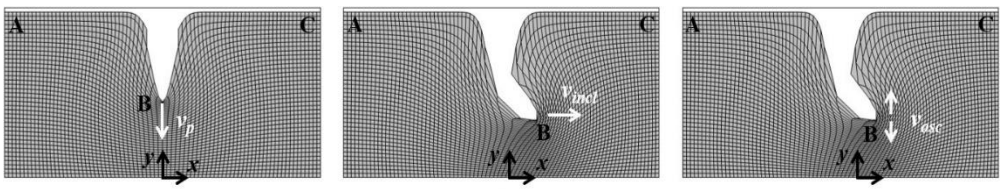



**Fig. 3** Free interface deformations in three phases: a) penetration, b) tilting and c) oscillations. Welding in the $-\vec{x}$ direction is assumed

Penetration velocity $v_p$ and inclination velocity $v_{incl}$ are estimated by analyzing X-ray images (and accompanying videos) from experiments by Wagner *et al* [11], describing the development of the keyhole in laser welding on aluminum. It emerges that these speeds are less than 1 m/s. The amplitude $v_{osc}$ and frequency $f_{osc}$ of the keyhole oscillation are more difficult to estimate.

In this study, we set: $v_p = v_{incl} = 1$ m/s, $v_{osc} = 0.5$ m/s and $f_{osc} = 12500$ Hz. The energy conservation equation is solved considering the properties of aluminum A2219. Mesh size and time step used: h = 50 μm and Δt = 10 μs. The irradiance profiles $I_{V_0}$ on the free boundary during the pulse are compared for $V_0 = 1, 10, ..., c$. The results at 1.5 ms and 4 ms, representative of the overall observation over the entire interaction time, are shown in Figure 4.

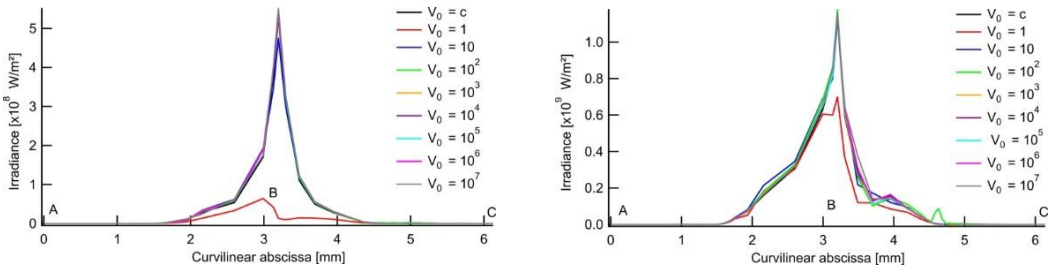



**Fig. 4** Irradiance profiles on the free boundary at a) 1.5 ms and b) 4 ms. Peaks correspond to point B, the bottom of the capillary. Laser parameters used: $P_{laser}$ = 4 kW, $w_0$ = 200 µm

Figure 4 shows that only $V_0 = 1$ m/s yields a markedly different result, i.e. when rays are emitted at a speed of at least 10 m/s, the energy deposition is almost the same as if they were emitted at the speed of light. The study, repeated for emission velocities between 1 m/s and 10 m/s ($V_0$ = 3, 5 and 7 m/s), reveals on the one hand an abrupt deviation of irradiance peaks at point B between $I_{V_0=1}$ and $I_{V_0=3}$ and on the other hand a gradual progress towards the reference profile from $I_{V_0=3}$. This result suggests that the ray emission velocity is acceptable if it exceeds the characteristic velocity of the keyhole dynamics (as a reminder, $v_p$= 1 m/s). However, $V_0$ = 10 m/s will be retained to take account of uncertainties in the case of highly unstable capillaries, where characteristic velocities could be higher than those used in this numerical test.

## LASER WELDING MODELING

### GOVERNING EQUATIONS

The modeling of the thermohydrodynamic problem in laser welding, with free interface tracking by Level-set, is well detailed in the study by Le Mener *et al* [12]. Specific modifications to our model are mentioned here. In summary, three main conservation laws are solved to simulate heat transfer and melt flow: conservation of energy (Equation 14), conservation of momentum (Equation 15) and conservation of mass (Equation 16).

$$\rho c_{p,eq}\left[\frac{\partial T}{\partial t}+\vec{\nabla}\cdot(\vec{u}T)\right]=\vec{\nabla}\cdot\left(k\vec{\nabla}T\right)+q_{\text{laser}}-q_{\text{evap}}\delta(\phi) \tag{14}$$

$$\rho\left(\frac{\partial\vec{u}}{\partial t}+\left(\vec{\nabla}\vec{u}\right).\vec{u}\right)=\vec{\nabla}.\left[-pI+\mu\left(\left(\vec{\nabla}\vec{u}\right)+\left(\vec{\nabla}\vec{u}\right)^{T}\right)\right]+\vec{F}_v+\vec{F}_{inter}.\delta(\phi) \tag{15}$$

$$\vec{\nabla}.\vec{u} = \dot{m}\left(\frac{1}{\rho_v} - \frac{1}{\rho_l}\right)\delta_g(\phi) \tag{16}$$

In Equation 14, $q_{evap}$ represents the energy lost through evaporation. The source term $q_{laser}$ is the sum of the term $q_i$ (Equation 11) over all reflections of all rays. The Fresnel absorption is written as:

$$\alpha_F(\theta) = 1 - \frac{1}{2}\left[\frac{\left(n - (1/\cos\theta)\right)^2 + k^2}{\left(n + (1/\cos\theta)\right)^2 + k^2} + \frac{(n - \cos\theta)^2 + k^2}{(n + \cos\theta)^2 + k^2}\right] \tag{17}$$

In Equation 15, $F_v$ groups together the volume forces (buoyancy, gravity, Darcy condition) and $F_{int}$ the surface forces (surface tension and Marangoni effect). Equation 16 includes a source term to model vaporization, representing the mass addition to the gas phase through a Dirac delta function $\delta_g$, which ensures the incompressibility of the liquid metal:

$$\delta_g = \begin{cases} 2\delta(\phi), \; if \; \phi \leq 0.5 \;\; (gas) \\ 0, \; if \;\; \phi > \; 0.5 \;\; (metal) \end{cases} \tag{18}$$

Finally, the transport equation for the Level-set variable (Equation 19) is modified due to the source term added to the mass conservation equation:

$$\frac{\partial\phi}{\partial t} + \vec{u}\cdot\vec{\nabla}\phi = \dot{m}\left(\frac{1-\phi}{\rho_v} + \frac{\phi}{\rho_l}\right)\delta(\phi) + \gamma_{ls}\vec{\nabla}.\left(\epsilon_{ls}\vec{\nabla}\phi - \phi(1-\phi)\,\frac{\vec{\nabla}\phi}{\left|\vec{\nabla}\phi\right|}\right) \tag{19}$$

## MATERIAL PROPERTIES

The temperature-dependent properties of the A2219 alloy (thermal conductivity, density and heat capacity at constant pressure) are taken from Narender *et al* [13] and Wang *et al* [14]. Given the limited data available at high temperatures, constant values are used above the melting temperature.

Three properties have been calibrated/adjusted for various reasons. The surface tension coefficient ($\sigma_0 \simeq 0.9$ N/m [15]), is reduced to 0.3 N/m for convergence reasons and above all due to the difficulty of properly modeling interface phenomena using the Level-set method. The dynamic viscosity of the liquid metal ($\mu_{liq} \simeq 10^{-3}$ Pa.s [16]) is multiplied by 100 for convergence and numerical stability of the melt pool. As the Fresnel absorption indices are not well known (literature data are often for pure aluminum, [17]), the values n = 1.75 and k = 6.5 (equivalent to an absorptivity of 14% at normal incidence and a maximum of 22% at Brewster incidence) were set to obtain molten pool dimensions close to experiment.

The thermophysical properties of the gas, a mixture of metal vapor and ambient air, are not known. Therefore, those of the air are used. Here too, the dynamic viscosity of air has been overestimated for the same reasons as for the viscosity of the metal liquid.

## GEOMETRIC AND MESH CONSIDERATIONS

As a first step, a calculation in static pulse configuration is carried out using an axi-symmetrical 2D geometry (1× 3 $mm^2$, Figure 5a). A 10 µm quadrangular mesh is used in the area close to the axis of symmetry where the melt is expected to develop and where all physics are considered. An extension of this area, to avoid thermal edge effects, where only heat transfers in the solid are solved, is meshed in coarser triangular elements.

Then, for the weld bead model, a 3D geometry (3× 1× 2 $mm^3$, Figure 5b) is used and meshed using the mesh optimization technique developed by Courtois *et al* [18]. This multiple meshing technique consists of breaking down the complete model into sub-models (components), building as many as there are physics and applying a specific level of refinement to each physics according to the mesh sensitivity of the variables associated with it.

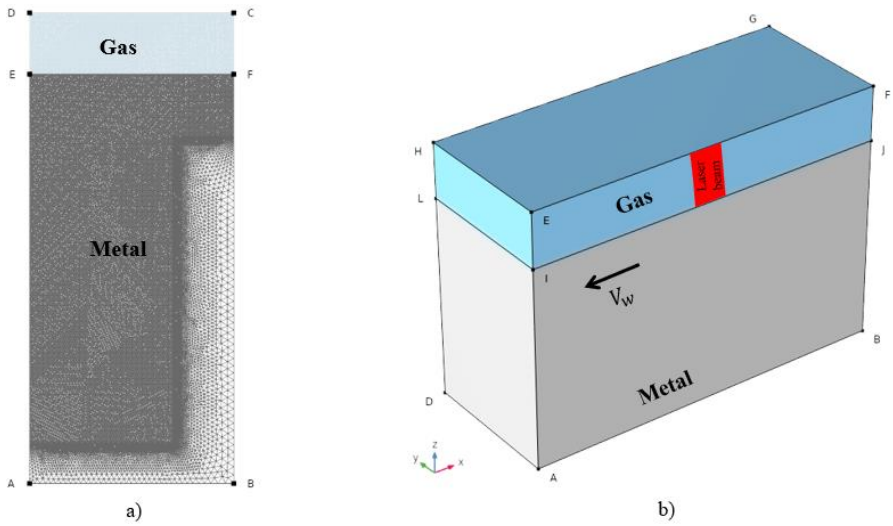



**Fig. 5** Resolution domains. a) 2D axisymmetric geometry with AD the symmetric axis. b) 3D geometry with a plane of symmetry in ABFE. The material passes under the laser source, which is held stationary

## NUMERICAL SOLVER SETTINGS

The PARDISO direct solver is used to solve the equations in a segregated approach. The alpha-generalized time scheme is used with a constant time step of 0.8 µs in 2D axisymmetry and 2.8 µs in 3D. Simulations are run on a computing station with an Intel®Xeon®W-2295 processor, 3.00 GHz, 128 GB RAM, 18 cores. The static pulse simulations presented here run

for up to 20 hours, including the cooling phase, whereas the weld bead model requires up to 6 days for 12 ms of the process.

### VALIDATION EXPERIMENTS

Experiments were carried out with the TRUMPF disk laser, Trudisk 6001, wavelength $\lambda$ = 1030 nm. PRIMES' FocusMonitor FM+ laser beam analyzer was used to determine beam characteristics (energy distribution, quality factor, focal plane radius, Rayleigh length). The temporal profile of laser power was also measured. The laser beam was slightly inclined to avoid reverse reflections in the optical cavity. All tests were carried out without the addition of shielding gas.

Static laser shots were performed on 4 mm-thick A2219 alloy plates at the focal plane ($z = 0$), where the beam radius is $w_0 = 150\ \mu m$. Each configuration was repeated multiple times to assess experimental variability. The weld bead presented here was obtained using a laser power of $P_{laser} = 2$ kW, a welding speed $V_w = 10$ m/min, and a focal position set at 0.

## RESULTS

### STATIC PULSES

The static shot models are compared with experimental results after solidification. The comparison concerns the dimensions (penetration depth and diameter) of the melted zone and checks for the presence of porosity. Figures 6a-c show the experimental melt pool morphology for different laser parameters, while Figures 6d-f present the corresponding numerical results.

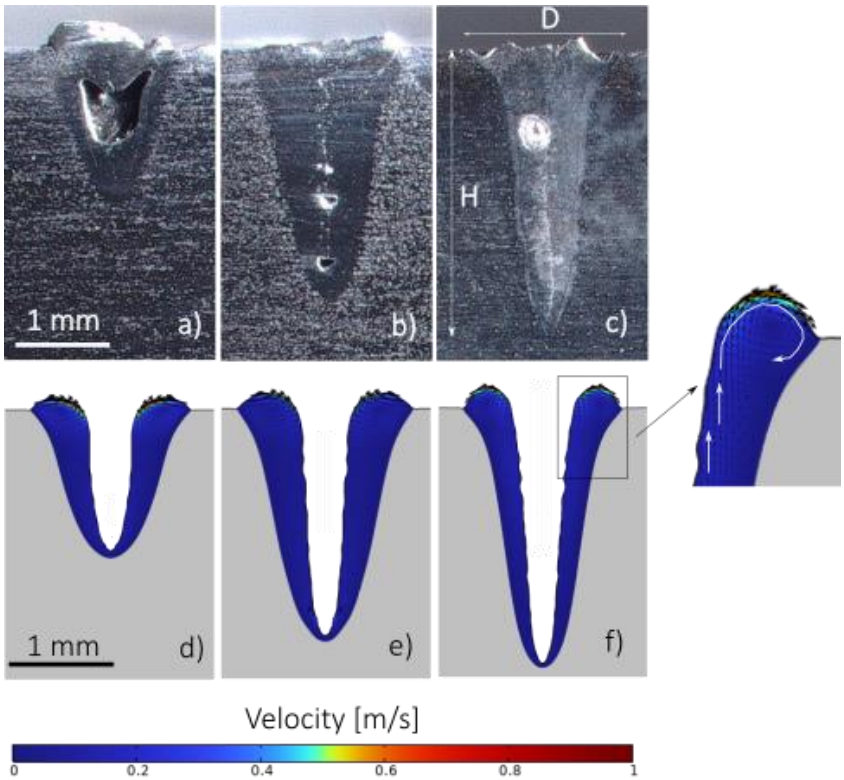



**Fig. 6** Morphology of experimental and numerical melt zones. The experimental results are post-mortem, whereas the numerical results correspond to the melt pool during the laser pulse. H and D represent melt zone depth and diameter respectively. Laser parameters: a) and d) $P_{laser}$ = 2 kW, $t_{pulse}$ = 4 ms, b) and e) $P_{laser}$ = 3 kW, $t_{pulse}$ = 4 ms, c) and f) $P_{laser}$ = 4 kW, $t_{pulse}$ = 2 ms

A notable observation is the presence of residual porosities in the three welds shown (also observed in most other welds not displayed here). This confirms literature reports on the difficulty of determining laser parameter sets that allow porosity -free welds on aluminum. Moreover, the model successfully reproduces the shape of the molten zone.

The calculated flow velocities in the melt pool do not exceed 1 m/s. Although experimental measurements were not carried out, the overestimation of dynamic viscosity in the model should theoretically lead to underestimated numerical velocities. Nonetheless, the flow direction, from inside the keyhole toward the fusion front (Figure 6f), is consistent with the negative sign of the thermocapillary coefficient.

The model predicts the penetration depth and diameter of the molten zone with maximum errors of 38 % and 24 %, respectively, compared to experiments (Figure 7). Repeating the pulses revealed significant variability in some cases, for instance, with $P_{laser}$ = 2 kW and $t_{pulse}$ = 6 ms, where a 62 % difference was noted between two measured depths. These penetration variations, observed under identical power and pulse duration, may result from

local oxidation differences, which affect absorptivity. In addition, cutting techniques may introduce measurement uncertainty when locating the exact center of the laser spot.

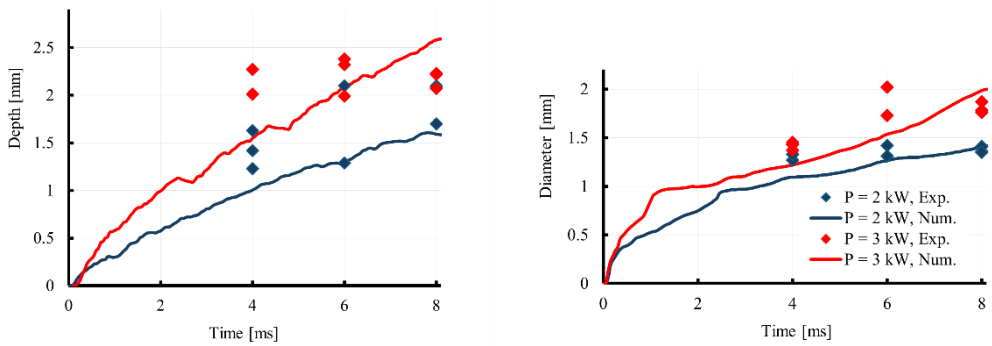



**Fig. 7** Model/experiment comparison of the evolution of dimensions (depth on the left and diameter on the right) of melted zones for $P_{laser}$ = 2 kW and $P_{laser}$ = 3 kW

Since a central objective of this work is to develop a new method for describing laser–material interaction (LMI), it is crucial to discuss the consistency of the energy balance by quantifying the absorbed energy and its impact on keyhole formation and development. Figure 8 illustrates the LMI in different process stages, from an undeformed metallic surface to a deep keyhole.

In the initial stage (before 100 µs), the metal melts but the molten pool surface remains undeformed. The first rays bounce off, nearly retracing their incoming trajectories (Figure 8a). This pure conduction regime lasts barely 0.2 ms, until the vaporization temperature is reached and the surface begins to curve. At this point, rays still reflect after a single bounce but deviate noticeably from their initial paths (Figure 8b). Multiple reflections start to occur around 0.4 ms, when the keyhole aspect ratio (depth/diameter) reaches 0.8. The keyhole then deepens and narrows progressively, trapping many rays at its bottom.

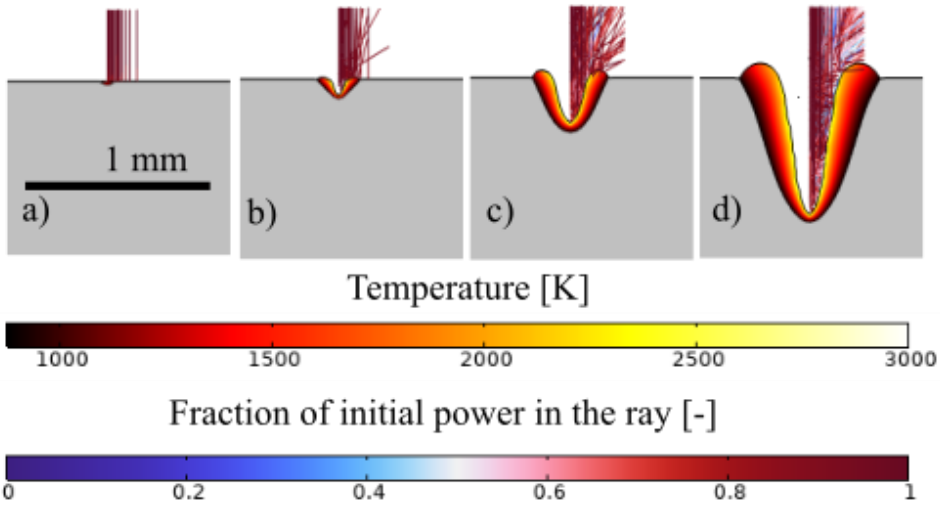



**Fig. 8** Illustration of multiple reflections inside the capillary and temperature field in the melt at a) 0.1 ms, b) 0.2 ms, c) 0.6 ms and d) 2.1 ms for $P_{laser}$ = 2 kW, $w_0$ = 150 µm

The absorptance evolution (absorbed power relative to laser power) over time is plotted in Figure 9, compared with the analytical model of Gouffé [5]. In static pulses, since the keyhole remains relatively regular, knowing its depth and opening diameter at each instant allows plotting the Gouffé profile. The numerical model closely follows both the trend and values of the analytical model, providing further confirmation of the consistency of our method for energy deposition.

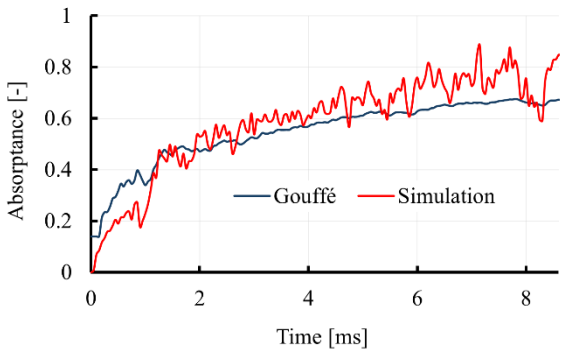



**Fig. 9** Time evolution of calculated absorptance and comparison with Gouffé's analytical prediction. $P_{laser}$ = 2 kW, $w_0$ = 150 µm

FUSION LINE

Given the good results obtained in the static configuration, the model was upgraded to a 3D fusion line model. No major changes were necessary, except for the meshing technique and the relative movement between the laser source and the material. Various views of the melt pool are shown in Figure 10.

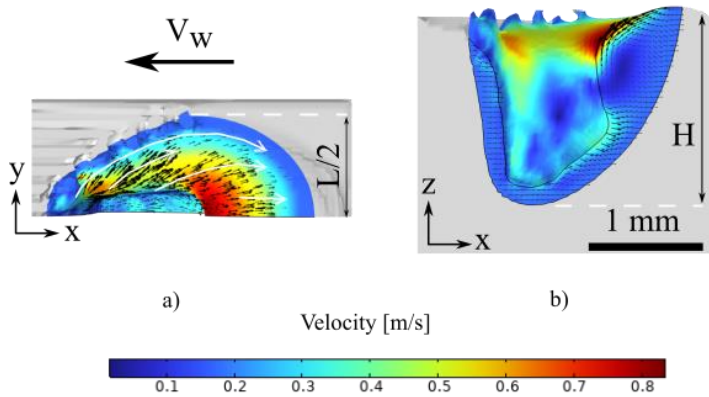



**Fig. 10** Numerical result after 12 ms. a) Top view and velocity field at the surface of the weld pool. Oriented white lines indicate overall flow direction. b) Side view and velocity field in the melt. $P_{laser}$ = 2 kW, $w_0$ = 150 µm, $V_w$ = 10 m/min

The steady state is defined as the final phase of the process, during which the main fields - temperature, velocity, and pressure - show no significant variation. From a macroscopic perspective, the penetration depth reaches a maximum and then oscillates around a mean value. To ensure this regime is attained, numerical results must be analyzed over several tens of milliseconds. However, as this numerical model is still under development, the present simulations are limited to 12 ms and need to be extended to yield fully reliable results. Nonetheless, some indicators suggest that a steady-state regime has at least begun by this point:

- for $V_w$ = 10 m/min, a 2 mm-long weld bead has already formed after 12 ms of laser–material interaction.
- As will be shown later, the keyhole shape at 12 ms exhibits distinct characteristics.

As previously mentioned, simulations will need to be extended to longer process times and repeated for different laser powers and welding speeds before any conclusions can be drawn regarding its robustness. Nevertheless, preliminary analyses of keyhole dynamics are already possible. The dynamics illustrated in Figure 12 over the 12 ms simulation display consistent trends that are worth noting.

Up to 3 ms, the keyhole remains symmetric, the molten zone is roughly balanced on both sides, and the internal surface temperature, except near the solidification front, remains

uniform, much like in static pulse conditions. Starting from 4 ms, the front and rear sides begin to differ as molten metal accumulates at the rear. In addition, temperature fields become increasingly non-uniform (as seen at 10 ms and 11 ms): the front and bottom of the keyhole, directly exposed to the laser, are hotter than the rear and lateral surfaces, which are heated only by reflected laser radiation. By 12 ms, the lower part of the keyhole, whose bulging started at 10 ms, expands further in a direction opposite to the welding movement, while the upper part tends to narrow.

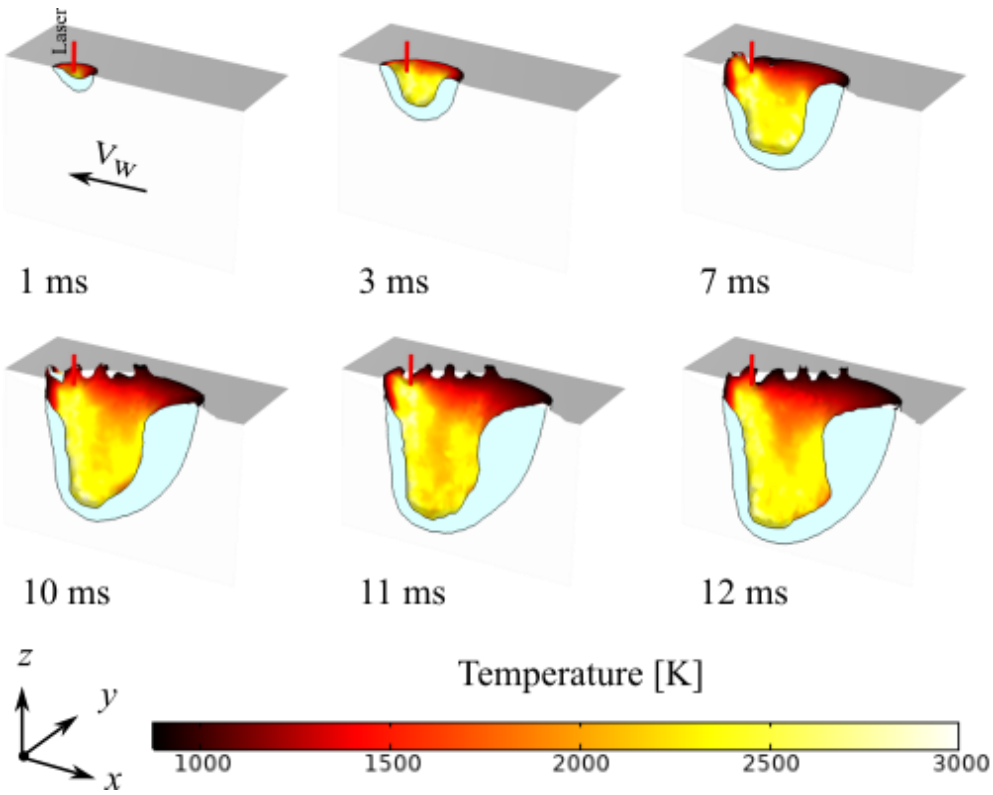



**Fig. 12** Evolution of keyhole geometry and temperature field. The melted volume is shown in light blue. $P_{laser}$ = 2 kW, $w_0$ = 150 µm, $V_w$= 10 m/min

## CONCLUSIONS AND OUTLOOK

The objective of this work was to study keyhole instabilities and related defects during laser welding of aluminum. To better account for multiple laser beam reflections, a new method based on ray tracing was developed and applied to both static pulse and fusion line configurations. The main findings are summarized as follows:

- Our approach offers an innovative way to simplify high-fidelity simulation of melt pool dynamics within commercial software, while reducing computation time.
- In static pulse conditions, the energy deposition predicted by this approach agrees with Gouffé's theory, and the simulated molten zones exhibit morphological features (size, porosity presence) consistent with experimental observations.
- The fusion line model, although still under development, shows initial results that suggest promising potential.

Further calculations will be required to obtain fully conclusive results. Complete model validation will also necessitate additional experimental investigations, including flow visualization, keyhole deformation tracking. Finally, we intend to explore beam shaping strategies to improve process stability and reduce porosity formation.

## References

[1] A. MATSUNAWA, M. MIZUTANI, S. KATAYAMA and N. SETO: 'Porosity formation mechanism and its prevention in laser welding', *Weld. Int.*, vol. 17, no. 6, pp. 431-437, Jun. 2003, doi: 10.1533/wint.2003.3138.

[2] A. MATSUNAWA, J.-D. KIM, N. SETO, M. MIZUTANI and S. KATAYAMA: 'Dynamics of keyhole and molten pool in laser welding', *J. Laser Appl.*, vol. 10, no. 6, pp. 247-254, Dec. 1998, doi: 10.2351/1.521858.

[3] W. KE, X. BU, J. P. OLIVEIRA, W. XU, Z. WANG and Z. ZENG: 'Modeling and numerical study of keyhole-induced porosity formation in laser beam oscillating welding of 5A06 aluminum alloy', *Opt. Laser Technol.*, vol. 133, p. 106540, Jan. 2021, doi: 10.1016/j.optlastec.2020.106540.

[4] F. FETZER, C. HAGENLOCHER, R. WEBER and T. GRAF: 'Geometry and stability of the capillary during deep-penetration laser welding of AlMgSi at high feed rates', *Opt. Laser Technol.*, vol. 133, p. 106562, 2021.

[5] A. GOUFFÉ: 'Corrections d'ouverture des corps noirs artificiels compte tenu des diffusions multiples internes', *Rev. Opt.*, 1945.

[6] M. COURTOIS, M. CARIN, P. L. MASSON, S. GAIED and M. BALABANE: 'A new approach to compute multi-reflections of laser beam in a keyhole for heat transfer and fluid flow modelling in laser welding', *J. Phys. Appl. Phys.*, vol. 46, no. 50, p. 505305, Dec. 2013, doi: 10.1088/0022-3727/46/50/505305.

[7] J. DALIGAULT, M. DAL, C. GORNY, F. COSTE and R. FABBRO: 'Combination of Eulerian and ray-tracing approaches for copper laser welding simulation', *J. Laser Appl.*, vol. 34, no. 4, p. 042042, Nov. 2022, doi: 10.2351/7.0000786.

[8] L. WESTHOFEN ET AL.: 'Ray tracing method with implicit surface detection for smoothed particle hydrodynamics-based laser beam welding simulations', *Mater. Werkst.*, vol. 55, no. 1, pp. 40-52, Jan. 2024, doi: 10.1002/mawe.202300161.

[9] J. LIND, F. FETZER, D. BLAZQUEZ-SANCHEZ, J. WEIDENSDÖRFER, R. WEBER and T. GRAF: 'Geometry and absorptance of the cutting fronts during laser beam cutting', *J. Laser Appl.*, vol. 32, no. 3, p. 032015, Jun. 2020, doi: 10.2351/7.0000024.

[10] Y. A. MAYI, M. DAL, P. PEYRE, M. BELLET and R. FABBRO: 'Physical mechanisms of conduction-to-keyhole transition in laser welding and additive manufacturing processes', *Opt. Laser Technol.*, vol. 158, p. 108811, Feb. 2023, doi: 10.1016/j.optlastec.2022.108811.

[11] J. WAGNER, C. HAGENLOCHER, M. HUMMEL, A. OLOWINSKY, R. WEBER and T. Graf: 'Synchrotron X-ray Analysis of the Influence of the Magnesium Content on the Absorptance during Full-Penetration Laser Welding of Aluminum', vol. 11, no. 5, p. 797, 2021, doi: 10.3390/met11050797.

[12] M. LE MENER, M. COURTOIS, N. DAVIOT, M. CARIN and R. ANDRY: 'Heat transfer and fluid flow modeling of steel-Inconel laser welding in an overlap configuration', *J. Laser Appl.*, vol. 36, no. 4, p. 042006, Nov. 2024, doi: 10.2351/7.0001357.

[13] K. NARENDER, A. S. M. RAO, K. G. K. RAO and N. G. KRISHNA: 'Thermo physical properties of wrought aluminum alloys 6061, 2219 and 2014 by gamma ray attenuation method', *Thermochim. Acta*, vol. 569, pp. 90-96, Oct. 2013, doi: 10.1016/j.tca.2013.07.003.

[14] H. X. WANG, Y. H. WEI and C. L. YANG: 'Numerical simulation of variable polarity vertical-up plasma arc welding process', *Comput. Mater. Sci.*, vol. 38, no. 4, pp. 571-587, Feb. 2007, doi: 10.1016/j.commatsci.2006.03.017.

[15] Y. ZHANG, Z. SHEN and X. NI: 'Modeling and simulation on long pulse laser drilling processing', *Int. J. Heat Mass Transf.*, vol. 73, pp. 429-437, Jun. 2014, doi: 10.1016/j.ijheatmasstransfer.2014.02.037.

[16] A. T. DINSDALE and P. N. QUESTED: 'The viscosity of aluminium and its alloys–A review of data and models', *J. Mater. Sci.*, vol. 39, no. 24, pp. 7221-7228, Dec. 2004, doi: 10.1023/B:JMSC.0000048735.50256.96.

[17] W. M. STEEN and J. MAZUMDER: *Laser Material Processing*, London: Springer London, 2010, doi: 10.1007/978-1-84996-062-5.

[18] M. COURTOIS, M. CARIN, P. L. MASSON, S. CADIOU and S. GAIED: 'A method to reduce calculation time in multiphysic modelling of welding processes. Application to laser and GMAW welding.', 2019.

# RECONSTRUCTION OF THE TIME-AVERAGED KEYHOLE GEOMETRY IN LASER BEAM WELDING ASSISTED WITH ELECTROMAGNETIC EFFECT

F. YANG*,**, X. MENG*, S. N. PUTRA*, M. BACHMANN*, M. RETHMEIER****,*,***

**Bundesanstalt für Materialforschung und -prüfung, 12205 Berlin, Germany*
***Production Technology Group, Technische Universität Ilmenau, 98693 Ilmenau, Germany*
****Fraunhofer – Institut für Produktionsanlagen und Konstruktionstechnik, 10587 Berlin, Germany*
*****Institut für Werkzeugmaschinen und Fabrikbetrieb, Technische Universität Berlin, 10587 Berlin, Germany*

*DOI 10.3217/978-3-99161-089-2-008, license CC BY 4.0*
*https://creativecommons.org/licenses/by/4.0/deed.en*
*This CC license does not apply to third party material and content noted otherwise.*

## ABSTRACT

In laser beam welding (LBW), the time-averaged keyhole shape provides statistical insights into the process compared to its transient geometry, offering a deeper understanding of the overall keyhole behaviour. However, capturing the time-averaged keyhole shape through experimental methods remains challenging. In this paper, a reconstruction algorithm for the time-averaged keyhole is developed and integrated into a three-dimensional transient multi-physical coupled numerical model. The algorithm can accurately capture the key characteristics of the keyhole, including its diameter and centroid. In addition, it can also successfully reproduce the experimentally observed phenomena of keyhole tailing. The overall shape of the keyhole appears smooth, without exhibiting obvious instability features. Furthermore, the time-averaged keyhole shape is compared under different magnetic flux densities when an external oscillating magnetic field is applied. The results indicate that the application of external magnetic fields does not fundamentally alter the overall keyhole shape. With increasing magnetic flux density, the trailing tail becomes progressively less pronounced and a noticeable increase in the curvature of the rear wall is observed. The spatial-average of standard deviation of the keyhole diameter can serve as an effective index for evaluating the keyhole instability. Keyhole stability in LBW of aluminium alloys is improved under the assistance of electromagnetic fields, and this stabilization is positively correlated with increasing magnetic flux density.

Keywords: laser beam welding; keyhole reconstruction; magnetic fields; porosity defects; keyhole stability.

## INTRODUCTION

Deep penetration laser beam welding (LBW) is a high efficiency joining technique characterized by the formation of a keyhole, which is a cavity created by the recoil pressure generated during high power density laser irradiation. This keyhole enables deep penetration with a high aspect ratio, making LBW widely used in industries such as automotive manufacturing, shipbuilding, and aerospace [1-6]. However, the keyhole is inherently unstable due to complex interactions among laser energy absorption, vaporization induced recoil pressure, surface tension, and melt flow [7]. These instabilities manifest as geometric fluctuations in space and time, contributing significantly to the formation of common welding defects such as spatter, porosity, and spiking [8-10]. These defects can severely influence the mechanical performance of welded joints.

The assessment of keyhole instability remains challenging, owing to the inherently transient and nonlinear nature of the process, as well as the opacity of metals. Various approaches, including high-speed imaging [11], optical coherence tomography [12], and in-situ synchrotron X-ray imaging [9,13], have been employed to evaluate keyhole behaviour. However, these methods offer limited insights or require high costs, with restricted accessibility. Metal/glass configurations have been used for visualizing keyhole morphology [14], but the accuracy is limited because of the difference in thermal and optical properties between glass and metal.

Numerical simulations offer a valuable alternative for investigating keyhole dynamics with enhanced temporal and spatial resolution. Previous studies have used simulation-based metrics such as the keyhole depth fluctuation and the keyhole collapse frequency to assess its stability [15,16]. In addition, given that keyhole behaviour is mainly characterized by the changes in keyhole morphology, understanding the evolution of the keyhole shape is essential. Although experimental studies have explored transient and time-averaged keyhole morphologies by stacking thousands of frames [17], numerical simulations provide a lower cost alternative for capturing transient keyhole dynamics. Moreover, the investigations of time-averaged keyhole morphology based on numerical simulations are rare.

Recently, active control of keyhole behaviour has attracted increasing interest. While welding parameter adjustments and ambient pressure variations offer indirect control over keyhole dynamics [15,18], external magnetic fields provide a more direct method. External Lorentz forces can directly act on both the keyhole wall and the weld pool, affecting their behaviour [19].

In this study, we introduce an alternating magnetic field during laser beam welding to actively control the dynamic behaviour of the keyhole and weld pool via Lorentz force interaction. A novel keyhole reconstruction algorithm is developed to evaluate time-averaged keyhole morphologies under different magnetic field conditions. Based on this, a new stability assessment metric is proposed, enabling a systematic and quantitative analysis of keyhole stability. This work provides deeper insights into the mechanisms governing keyhole dynamics and offers a promising approach for improving weld quality in deep penetration laser beam welding.

## EXPERIMENTAL PROCEDURE

LBW experiments were conducted using AlMg3 aluminium alloy plates with dimensions of 300 mm × 100 mm × 10 mm in bead-on-plate welding configuration. The laser source was an IPG YLR-20000 fibre laser, operating at a wavelength of 1070 nm with a focal beam diameter of 520 µm. The focus position was set at the top surface of the workpiece. The laser beam inclination was 10° with a forward angle relative to the vertical axis. A constant laser power of 6 kW and a welding speed of 2 m/min were used for all welding experiments. Argon shielding gas was supplied at a flow rate of 20 l/min to prevent oxidation of the weld pool.

To investigate the influence of electromagnetic forces on keyhole dynamics, oscillating magnetic fields were applied with a pole cross-section of 20 mm × 20 mm and a pole distance of 15 mm. The magnet poles were positioned 2 mm above the top surface of the base metal, as illustrated in Fig. 1. Oscillating magnetic fields were applied at a frequency of 2300 Hz, with root-mean-square (RMS) magnetic flux densities of 100 - 280 mT.

The internal weld quality in terms of porosity was quantified via X-ray inspection. Weld cross-sections were prepared by mechanical sectioning perpendicular to the welding direction and etched to reveal the fusion line. These etched profiles were used to validate the simulation results.

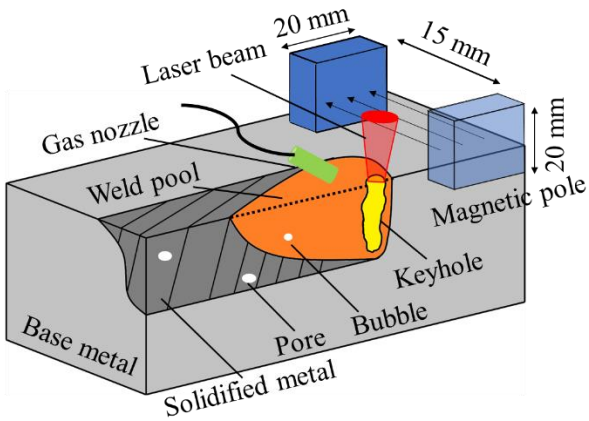



**Fig. 1** Setup of the Laser Beam Welding experiments

## MATHEMATICAL MODELING

To manage the complexity and nonlinearity of the laser beam welding process, several assumptions and simplifications were introduced to improve the solvability and computational efficiency of the mathematical model. The weld pool fluid was modelled as an incompressible, Newtonian, and laminar flow, with buoyancy effects included via the Boussinesq approximation. Seebeck effects, including thermoelectric currents and Joule heating, were

excluded. The magnetic flux density was assumed to remain unchanged along the transverse direction based on cold-condition measurements, with the aluminium alloy treated as having a relative magnetic permeability of one. Additionally, the keyhole gas phase was considered electrically non-conductive with uniform, constant density, and the momentum effect of the shielding gas jet was neglected.

## GOVERNING EQUATIONS

The fluid flow behaviour, heat transfer, and evolution of the free surface in the laser beam welding process are described by solving the continuity, Navier-Stokes, energy conservation, and Volume-of-Fluid (VOF) equations. To account for the influence of electromagnetic fields induced by the applied alternating magnetic field, the magnetic induction equation is also incorporated into the three-dimensional computational fluid dynamics model. All governing equations are formulated within a fixed Cartesian coordinate system, as detailed below.

Mass conservation:

$$\nabla \cdot \vec{v} = 0, \tag{1}$$

Where the $\vec{v}$ is the fluid flow velocity.

Navier-Stokes equation:

$$\rho\left(\frac{\partial \vec{v}}{\partial t} + (\vec{v} \cdot \nabla)\vec{v}\right) = -\nabla p + \mu \nabla^2 \vec{v} + \rho \vec{g} + \vec{S}_m, \tag{2}$$

where $\rho$ is the density, $t$ means the time, $p$ is the hydrodynamic pressure, $\mu$ is the viscosity, $\vec{g}$ is the gravitational acceleration vector, and $\vec{S}_m$ is the additional momentum source term including the fluid flow in the mushy zone, buoyancy forces, surface tension forces, recoil pressure, vapor-induced stagnation and shear forces, and Lorentz forces.

Energy conservation equation:

$$\rho\left[\frac{\partial h}{\partial t} + (\vec{v} \cdot \nabla)h\right] = \nabla \cdot (k \nabla T) + S_q \tag{3}$$

with the enthalpy $h$, the thermal conductivity $k$, and the energy source term $S_q$ accounting for the heat of the laser source, convective and radiative heat transfer, the heat loss of evaporation, heat flux of vapor recondensation, and the heat transfer caused by the vapor induced scattering and absorption effects.

VOF equation:

$$\frac{\partial \phi}{\partial t} + \nabla \cdot (\vec{v}\phi) = 0, \tag{4}$$

where $\phi$ is the liquid phase volume fraction which is used for the free surface tracking.

Magnetic induction equation:

$$\frac{\partial \vec{b}}{\partial t} + (\vec{v} \cdot \nabla)\vec{b} = \frac{1}{\mu_m \sigma_e} \nabla^2 \vec{b} + \left( (\overrightarrow{B_0} + \vec{b}) \cdot \nabla \right) \vec{v} - (\vec{v} \cdot \nabla)\overrightarrow{B_0}, \quad (5)$$

The electromagnetic field within the weld pool was computed using the magnetic induction equation, which is derived from the combination of Ohm's law and Maxwell's equations, as presented in Eq. (5). The resulting secondary magnetic flux density $\vec{b}$ is generated by both the temporal variation of the externally applied magnetic field $\overrightarrow{B_0}$ and the motion of the electrically conductive molten metal. The external magnetic flux density was previously measured under cold conditions [20] and was directly incorporated into the model as an input field.

The induced current density $\vec{j}$ and the corresponding Lorentz force $\overrightarrow{F_L}$ were subsequently calculated according to Eqs. (6) and (7), respectively. The Lorentz force was then introduced as a volumetric source term in the momentum conservation equation to account for electromagnetic effects on the molten metal flow.

$$\vec{j} = \frac{1}{\mu_m} \nabla \times (\overrightarrow{B_0} + \vec{b}), \quad (6)$$

$$\overrightarrow{F_L} = \vec{j} \times (\overrightarrow{B_0} + \vec{b}), \quad (7)$$

where $\mu_m$ is the magnetic permeability.

## PHYSICAL MODELS

The spatial distribution of laser energy on any horizontal plane within the computational domain is represented by a Gaussian profile, as defined by Eq. (8):

$$q_L = \frac{2}{\pi r_z^2} \cdot \exp(-2\frac{x^2+y^2}{r_z^2}) \cdot (I_0 - \Delta I), \quad (8)$$

Where $I_0$ is the laser power, $\Delta I$ refers to the total amount of laser power attenuation induced by metal vapor plume, $r_z$ denotes the laser beam radius at a given axial position and is defined as:

$$r_z = r_f \left[ 1 + \left( \frac{z - z_f}{z_r} \right)^2 \right]^{\frac{1}{2}}, \quad (9)$$

To account for multiple reflections and Fresnel absorption at the keyhole walls, a ray-tracing algorithm was employed [21] with a total of 755 sub-rays discretizing the laser energy density according to the Gaussian distribution in Eq. (8). The accuracy of the ray tracing was influenced by the interface resolution of the VOF method and the local mesh size, which limits the smoothness and continuity of the reconstructed keyhole surface. To mitigate this limitation and improve the resolution of ray interactions with the keyhole boundary, the virtual cell refinement technique [22,23] was incorporated, with a minimum cell size of 0.067 mm.

The Fresnel absorption coefficient $\alpha$ was computed using the following equation:

$$\alpha = 1 - \frac{1}{2}\left(\frac{1+(1-\varepsilon cos\varphi)^2}{1+(1+\varepsilon cos\varphi)^2} + \frac{\varepsilon^2 - 2\varepsilon cos\varphi + 2cos^2\varphi}{\varepsilon^2 + 2\varepsilon cos\varphi + 2cos^2\varphi}\right) \quad (10)$$

Where $\varphi$ is the beam incident angle, $\varepsilon$ is an empirically calibrated parameter based on physical properties of the metal and the laser wavelength.

Time-dependent laser attenuation caused by metal vapor plume oscillations was also incorporated into the heat source model. Metallic nanoparticles in the vapor plume condense and remain suspended, contributing to scattering and absorption of the laser beam. While laser beam refraction and inverse Bremsstrahlung absorption are typically negligible for short-wavelength fibre lasers [24], scattering and absorption effects were modelled using Beer's Law [25,26]. The vapor plume length along the laser path was determined experimentally and fitted via Fast Fourier Transform (FFT) analysis. The energy loss from scattering is then redistributed over the top surface of the weld pool following a Gaussian profile, whereas the absorbed energy is delivered through radiation and convection. The momentum transfer from the vapor plume within the keyhole, including stagnation and shear stress components, was also considered [21]. The recoil pressure arising from vaporization was modelled using the approach presented in [20,27].

## BOUNDARY CONDITIONS AND NUMERICAL SETUP

A structured hexahedral mesh was generated, featuring a uniform fine mesh with a cell size of 0.2 mm in the central region to accurately capture keyhole dynamics and thermal gradients. In the peripheral regions, a progressively mesh coarsening was applied. The boundary conditions for the air phase domain were defined as pressure outlets with adiabatic thermal boundaries and zero electric current density, representing an electrically insulating and thermally isolated environment. For the aluminium phase, the bottom surface was treated as a no-slip wall, with convective heat loss applied and no electric current allowed through the boundary. To reduce computational costs, the simulation domain was modelled as a representative subsection of the full aluminium sheet. Consequently, the lateral surfaces of the aluminium domain were prescribed as no-slip walls for fluid flow. However, for the thermal and electromagnetic analyses, continuity conditions were imposed across these boundaries [28].

All governing equations were numerically solved using the commercial computational fluid dynamics (CFD) software ANSYS Fluent. A second-order upwind discretization scheme was employed for both the momentum and energy conservation equations to ensure numerical accuracy and stability. The coupling between the pressure and velocity fields was handled using the Pressure-Implicit with Splitting of Operators (PISO) algorithm. The aluminium-gas interface was tracked using the Geo-Reconstruct scheme. The thermophysical properties of the AlMg3 aluminium alloy used in the simulation were reported in a previous study [20].

## KEYHOLE RECONSTRUCTION ALGORITHM

In this study, a reconstruction algorithm was developed to reconstruct the time-averaged keyhole geometry and to quantitatively evaluate keyhole stability from a statistical perspective. Given the complexity of the three-dimensional keyhole shape, the concept of an equivalent diameter was introduced to simplify the characterization by reducing the dimensionality of the keyhole geometry.

As shown in Fig. 2, the keyhole domain was firstly discretized along the thickness direction, resulting in a series of horizontal cross-sectional planes. On each plane, the keyhole gas phase region is identified, and its total area is computed. Assuming that the gas-liquid interface on each cross-section can be approximated with a circular shape, the equivalent diameter at a given time step and discrete plane is derived from the gas phase area and then calculate the time-averaged value. To fully reconstruct the keyhole profile, information about the centroid position on each horizontal plane is also required. Assuming that the gas phase density is constant and uniform, the mass centre of the gas phase coincides with its geometric centroid. The calculation equations are shown in Eq. (11) to (14).

$$\sum_j A_{i,j,k} = \frac{\pi {d_{eq}}_{i,k}^{\,2}}{4}, \tag{11}$$

$$\bar{d}_{eq,i} = \frac{1}{t_{k_l} - t_{k_f}} \sum_{k=k_f}^{k_l-1} d_{eq_{i,k}} \cdot (t_{k+1} - t_k), \tag{12}$$

Here, $i$ denotes the the $i$-th discrete layer, $j$ denotes the index of the cell, $k$ denotes the index of discrete time step, $A_{i,j,k}$ is the area of the air phase in the cell with $j$ index on the $i$-th layer at k-th time step, $d_{eq_{i,k}}$ means the equivalent diameter on the $i$-th layer at k-th time step, $\overline{d_{eq_i}}$ denotes the time-averaged equivalent diameter on the $i$-th layer, $t_{k_l}$ is the physical time corresponding to the $k_l$ time step, $t_{k_f}$ is the physical time corresponding to the $k_f$ time step, $k_f$ means the index of the first time step within the specified time span, $k_l$ means the index of the last time step within the specified time span, $t_k$ is the physical time corresponding to the $k$-th time step, $t_{k+1}$ is the physical time corresponding to the $(k+1)$-th time step.

$$\bar{x}_i = \frac{1}{t_{k_l} - t_{k_f}} \sum_{k=k_f}^{k_l-1} \left(\frac{\sum_j x_{i,j,k} \cdot A_{i,j,k}}{\sum_j A_{i,j,k}}\right) \cdot (t_{k+1} - t_k) \tag{13}$$

$$\bar{y}_i = \frac{1}{t_{k_l} - t_{k_f}} \sum_{k=k_f}^{k_l-1} \frac{\sum_j y_{i,j,k} \cdot A_{i,j,k}}{\sum_j A_{i,j,k}} \cdot (t_{k+1} - t_k) \tag{14}$$

Here $\bar{x}_i$ and $\bar{y}_i$ means time-averaged centroid x-coordinate and y-coordinate on the $i$-th layer. $x_{i,j,k}$ and $y_{i,j,k}$ means x and y coordinate value of the cell with j index at the i-th layer and k-th time step. By combining the time-averaged equivalent diameter and centroid position on each cross-sectional plane, a time-averaged 2D keyhole profile is then reconstructed

representing a statistically averaged morphology, providing a more stable and representative description of the keyhole geometry.

Furthermore, the standard deviation of the equivalent diameter over the same time interval provides a quantitative measure of the amplitude of keyhole fluctuations, thereby enabling the assessment of keyhole stability, as shown in Eq. (15).

$$\sigma_i = \sqrt{\frac{\sum_{k=k_f}^{k_l}(d_{eq_{i,k}} - \bar{d}_{eq,i})^2}{k_l - k_f + 1}} \tag{15}$$

Where $\sigma_i$ is the standard deviation of the keyhole diameter on the $i$-th layer over a certain time span.

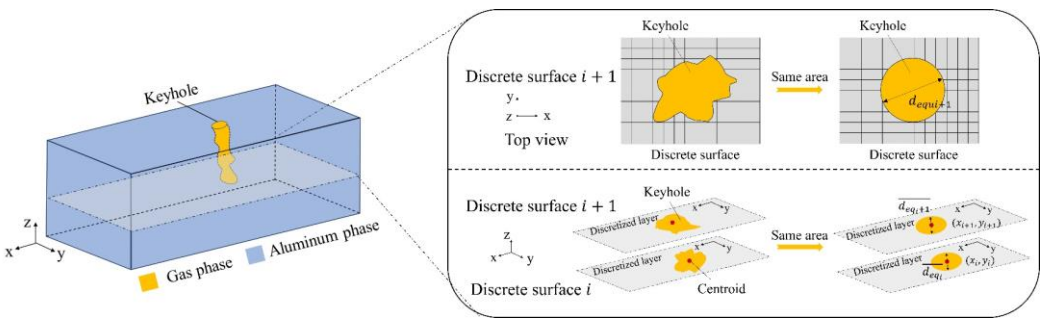



**Fig. 2** Schematic of the keyhole reconstruction principle

## RESULTS & DISCUSSION

### POROSITY RATIO

Fig. 3 illustrates the X-ray inspection results of weld specimens processed with and without the application of magnetic fields. A clear decreasing trend in the porosity ratio is observed with increasing magnetic flux density. Specifically, for the highest applied magnetic flux densities, the porosity ratio decreases to below 1 %.

A noticeable reduction in porosity ratio is observed when a magnetic field is applied as mentioned above, which can be used to infer that keyhole stability is improved. It should be noted that the porosity reduction is not solely controlled by the enhanced keyhole stability. Process porosity during laser beam welding originates from two aspects: (1) the formation of gas bubbles due to a keyhole instability, and (2) the inability of these bubbles to escape the molten pool before being trapped by the advancing solidification front. Oscillating magnetic fields not only influence the keyhole dynamic behaviour but also significantly enhance the

escape of bubbles from the molten pool through an additional electromagnetic expulsive force [20]. To further assess the keyhole stability, this study conducts a statistical analysis based on numerical simulations.

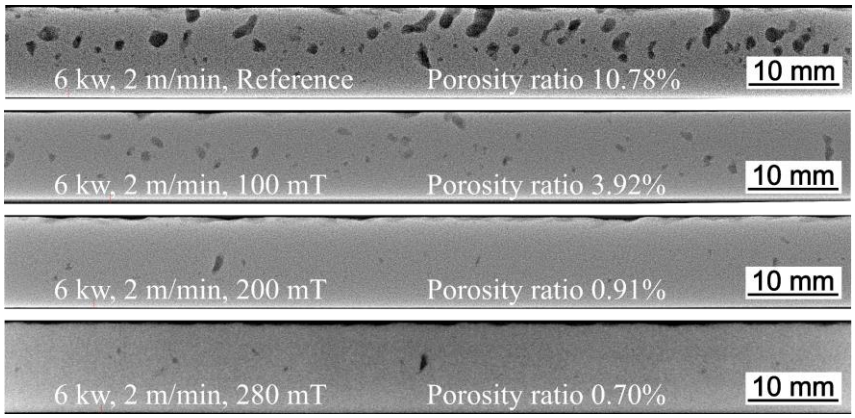



**Fig. 3** X-ray results without and with applied magnetic field

## MODEL VALIDATION

To assess the accuracy of the developed numerical model, the simulated cross-sectional morphology and dimensions of the weld pool were compared with experimental observations under both the reference condition and a result with a magnetic flux density of 200 mT applied, as shown in Fig. 4. In the comparison, the black dashed lines in the computed cross-sections represent the experimentally determined fusion boundaries. The results indicate that the simulated weld pool profiles exhibit good agreement with the experimental data, confirming the model's reasonable predictive capability. However, our current model does not have the capability to simulate the formation of bubbles and porosity retained in the welded joint. A more detailed validation is presented in [20].

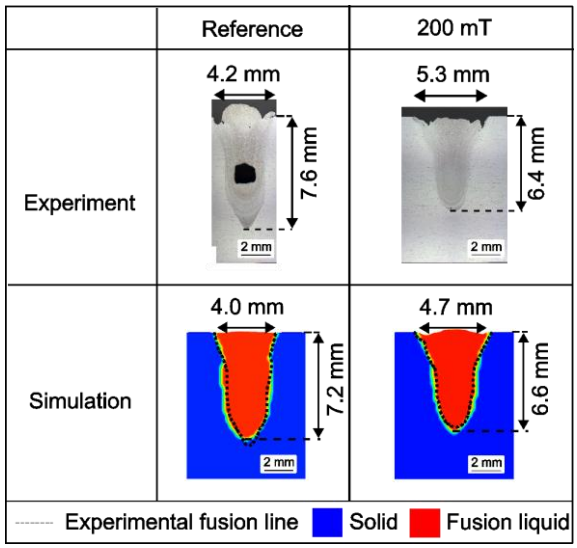



**Fig. 4** Comparison of experimental and calculated cross-sections

## LIMITATIONS OF ONE-DIMENSIONAL METRICS IN EVALUATING KEYHOLE STABILITY

In prior studies, keyhole stability in LBW has commonly been assessed using one-dimensional measurements of the keyhole depth as a quantitative metric, as discussed above [15]. Following this convention, the present study also evaluates keyhole stability based on the temporal evolution of keyhole depth. Fig. 5 illustrates the time-dependent variations in the keyhole depth. The results reveal that the keyhole depth exhibits significant dynamic fluctuations during welding, making it difficult to assess stability based solely on its temporal variation. Thus, the standard deviation of the keyhole depth is also calculated. A noticeable reduction in the standard deviation of the keyhole depth is observed at 100 mT, suggesting that the keyhole depth fluctuations is suppressed by magnetic field effectively. However, at 200 mT and 280 mT, the standard deviation increases to a level comparable to the reference case, indicating a similar degree of keyhole instability. This observation contradicts the visual evidence from the selected keyhole shapes in Fig. 6, which intuitively show a stabilized keyhole after applying the magnetic field.

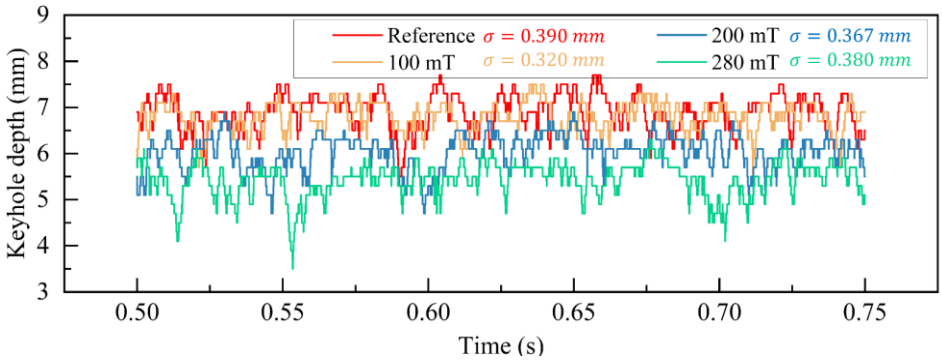



**Fig. 5** Temporal keyhole depth and their time-average and standard deviation values

This contradiction shows the limitation of using keyhole depth and keyhole morphologies as metrics for evaluating keyhole stability. The keyhole depth, by its one-dimensional nature, captures only vertical fluctuations and fails to account for instability phenomena that predominantly manifest in the horizontal directions, such as keyhole collapse or protrusions on the keyhole wall. Although these instabilities can indirectly influence the keyhole depth by altering local energy absorption or keyhole wall dynamics, the measured depth variation is merely a secondary effect, not a direct representation of the underlying instability. Moreover, the keyhole morphologies used for comparison can be deliberately selected, rather than being randomly chosen.

In summary, the two conventional approaches employed in this study, namely the keyhole depth fluctuation and the selected transient keyhole morphology, yield inconsistent conclusions regarding keyhole stability, highlighting the inherent limitations of traditional one-dimensional evaluation methods.

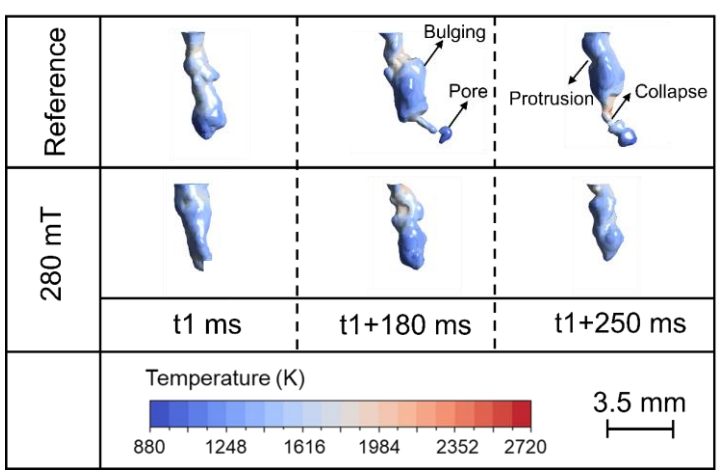



**Fig. 6** Transient keyhole shape in reference and MHD case

## EFFECT OF MAGNETIC FIELD ON KEYHOLE DIAMETER EVOLUTION

Fig. 7(a) presents the temporal evolution of the equivalent keyhole diameter at a location 1 mm above the keyhole bottom across different magnetic flux densities. The diameter exhibits substantial fluctuations within the range of up to 1.4 mm. Localized temporal variations in keyhole diameter alone are insufficient to provide a comprehensive assessment of overall keyhole stability.

To address this limitation, time-averaged keyhole diameters were analysed across different relative depths (except the elongated keyhole region near the top surface) along the keyhole axis under varying magnetic field conditions, as shown in Fig. 7(b). The results clearly reveal that the time-averaged keyhole diameter decreases with increasing magnetic flux density. This behaviour is consistent with findings from our prior work about LBW of steel [29], which indicate that although the applied magnetic field is oscillatory, the resulting time-averaged Lorentz force acts with a downward direction and increases in magnitude with the magnetic flux density. The enhanced downward Lorentz force compresses the molten metal around the keyhole, leading to a narrower keyhole profile. This effect is pronounced in the mid and lower regions of the keyhole.

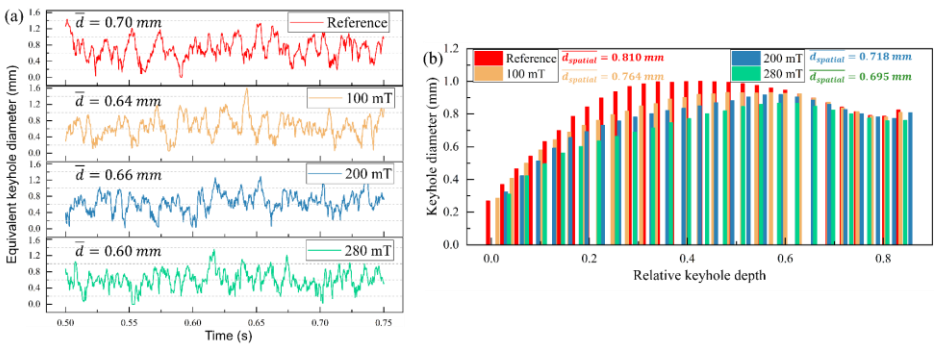



**Fig. 7** (A) Equivalent keyhole diameter 1 mm above keyhole bottom and time-average value, (B) Time-average value of the equivalent keyhole diameter and space-average value

## KEYHOLE STABILITY EVALUATION

The observed diameter changes provide valuable insights into the complex interaction between electromagnetic forces and melt pool dynamics in laser beam welding. However, they cannot fully indicate changes in the keyhole stability. To quantitatively evaluate keyhole stability, the standard deviation of the keyhole diameter is calculated, which can provide direct statistical evidence of the keyhole fluctuation amplitude and a robust indicator of keyhole stability.

Fig. 8 presents the distribution of the standard deviation of the keyhole diameter along the keyhole depth under different magnetic flux densities. The standard deviation of the keyhole

diameter shows an overall decreasing trend with increasing magnetic flux density. To assess keyhole stability from a global perspective, the space-averaged standard deviation across all discrete layers was calculated for each case. As the magnetic flux density increases, this value decreases progressively from 0.263 mm in the reference case reaching 0.217 mm for the applied highest magnetic flux density of 280 mT. Additionally, the variation of the standard deviation along the keyhole depth is significantly reduced with increasing magnetic flux density.

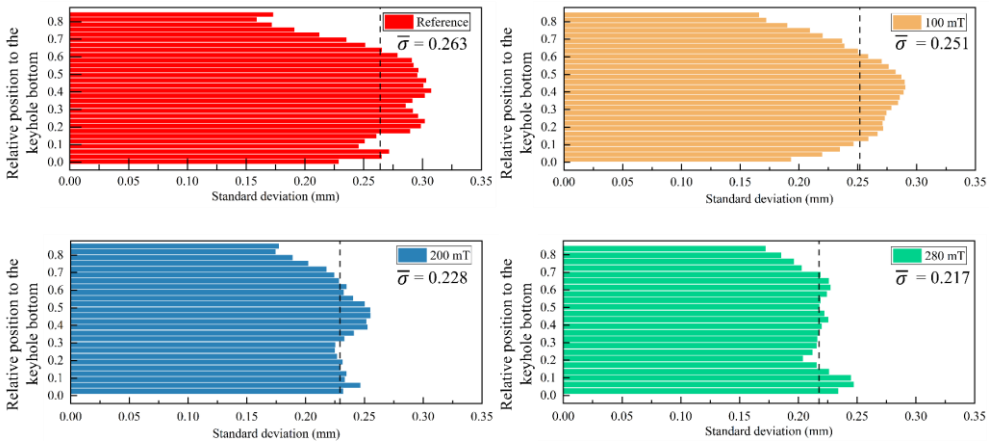



**Fig. 8** Distribution of the standard deviation of the equivalent keyhole diameter along the keyhole axis and its space-average for different magnetic flux densities

These findings confirm that the application of external magnetic fields effectively suppress the keyhole fluctuation, resulting in a more stable keyhole. Importantly, this analysis provides statistical evidence from a multi-dimensional perspective by accounting for both spatial and temporal variations in keyhole behaviour. This method overcomes the limitations of traditional one-dimensional metrics and enhances the ability to understand and control dynamic keyhole phenomena under the influence of magnetic fields. It was thus possible to prove that the magnetic forces can stabilise the keyhole, resulting in less keyhole-induced porosity.

## KEYHOLE RECONSTRUCTION

The reconstructed time-averaged keyhole profiles using the time-averaged equivalent diameter and centroid position at each discrete keyhole layer are presented in Fig. 9. These profiles provide a statistically robust representations of the keyhole geometry. The laser axis remains consistently aligned closer to the front wall of the keyhole. This is primarily because the initial laser incidence is concentrated on the front wall, resulting in significantly higher energy absorption in that region and initiating the melting of cold base metal ahead of the keyhole, which can be evidenced by the calculation results from Meng [18]. The formation of

the keyhole lags behind the moving laser heat source. Thus, the laser axis appears closer to the front keyhole wall, while the centroid of the keyhole is located behind the laser axis. The reconstructed keyhole profiles can capture the characteristic trailing tail at the bottom of the keyhole. The overall shape of the keyhole is smooth and there is no obvious instability characteristics. The application of external magnetic fields does not fundamentally alter the overall keyhole shape. However, with increasing magnetic flux density, the trailing tail becomes progressively less pronounced, indicating a suppressive effect of the magnetohydrodynamic forces on the rear section of the keyhole. Notably, a significant increase in the curvature of the rear keyhole wall is observed when the magnetic flux density exceeds 200 mT, which may be linked to a redistribution of laser energy deposition, particularly at the rear wall.

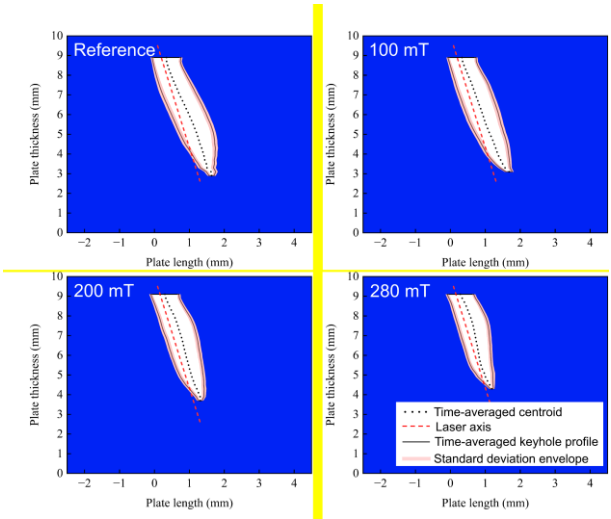



**Fig. 9** Reconstructed keyhole shapes under different magnetic flux densities

## CONCLUSIONS

A novel keyhole reconstruction approach, combined with a statistical assessment method for evaluating the keyhole stability, was developed based on a transient three-dimensional multi-physics LBW model. The main findings are summarized as follows:

- The limitations of conventional methods for evaluating keyhole stability were demonstrated. The transient keyhole geometry or one-dimensional keyhole depth variations are insufficient and may lead to misleading interpretations due to their inability to capture the full spatial and temporal complexity of the process.
- A time-averaged reconstruction of the keyhole profiles revealed a characteristic smooth geometry without pronounced instability features. The application of external

magnetic fields did not fundamentally alter the overall morphology of the time-averaged keyhole.

- The metric of spatial-average of the standard deviation of keyhole diameter certifies that the magnetic field application can stabilize the keyhole effectively. The degree of stabilization positively correlates with an increasing magnetic flux density.

## ACKNOWLEDGEMENTS

This work is funded by the Deutsche Forschungsgemeinschaft (DFG, German Research Foundation)-Project No. 466939224, No. 506270597, and No. 547924277.

## References

[1] H. ZHAO, D. R. WHITE, T. DEBROY: 'Current issues and problems in laser welding of automotive aluminium alloys', *International materials reviews*, 44(6), pp. 238-266, 1999.

[2] A. MATSUNAWA, J. D. KIM, N. SETO, M. MIZUTANI, S. KATAYAMA: 'Dynamics of keyhole and molten pool in laser welding', *Journal of laser applications*, 10(6), pp. 247-254, 1998.

[3] H. ZHAO, D. R. WHITE, T. DEBROY: 'Current issues and problems in laser welding of automotive aluminium alloys', *International materials reviews*, 44(6), pp. 238-266, 1999.

[4] S. KATAYAMA (ED.): *Handbook of laser welding technologies*, 2013.

[5] M. CHATURVEDI (ED.): 'Welding and joining of aerospace materials', *Woodhead publishing*, 2020.

[6] J. R. DEEPAK, R. P. ANIRUDH, S. S. SUNDAR: 'Applications of lasers in industries and laser welding: A review', *Materials Today: Proceedings*, 2023.

[7] A. MATSUNAWA, N. SETO, J. D. KIM, M. MIZUTANI, S. KATAYAMA: 'Dynamics of keyhole and molten pool in high-power CO2 laser welding', *High-Power Lasers in Manufacturing*, 3888, pp. 34-45, 2000.

[8] A. F. H. KAPLAN, J. POWELL: 'Spatter in laser welding', *Journal of laser Applications*, 23(3), 2011.

[9] T. FLORIAN, K. SCHRICKER, C. ZENZ, A. OTTO, L. SCHMIDT, C. DIEGEL, H. FRIEDMANN, M. SEIBOLD, P. HELLWIG, F. FRÖHLICH, F. NAGEL, P. KALLAGE, M. BUTTAZZONI, A. RACK, H. REQUARDT, Y. CHEN, J.P. BERGMANN: 'Combining in situ synchrotron X-ray imaging and multiphysics simulation to reveal pore formation dynamics in laser welding of copper', *International Journal of Machine Tools and Manufacture*, 204, 104224, 2025.

[10] F. FETZER, H. HU, P. BERGER, R. WEBER, P. EBERHARD, T. GRAF: 'Fundamental investigations on the spiking mechanism by means of laser beam welding of ice', *Journal of Laser Applications*, 30(1), 2018.

[11] L. WANG, M. YAO, X. GAO, F. KONG, J. TANG, M. J. KIM: 'Keyhole stability and surface quality during novel adjustable-ring mode laser (ARM) welding of aluminum alloy', *Optics & Laser Technology*, 161, 109202, 2023.

[12] J. ZHAO, J. LI, Y. DING, L. BAI, Y. CHENG: 'Quantitative evaluation of keyhole stability during laser welding using optical coherence tomography', *Welding International*, 38(3), pp. 225-238, 2024.

[13] M. MIYAGI, J. WANG: 'Keyhole dynamics and morphology visualized by in-situ X-ray imaging in laser melting of austenitic stainless steel', *Journal of Materials Processing Technology*, 282, 116673, 2020.

[14] D. ZHANG, M. WANG, C. SHU, Y. ZHANG, D. WU, Y. YE: 'Dynamic keyhole behavior and keyhole instability in high power fiber laser welding of stainless steel', *Optics & Laser Technology*, 114, pp. 1-9, 2019.

[15] L. LI, G. PENG, J. WANG, J. GONG, S. MENG: 'Numerical and experimental study on keyhole and melt flow dynamics during laser welding of aluminium alloys under subatmospheric pressures', *International Journal of Heat and Mass Transfer*, 133, pp. 812-826, 2019.

[16] L. HUANG, X. HUA, D. WU, F. LI: 'Numerical study of keyhole instability and porosity formation mechanism in laser welding of aluminum alloy and steel', *Journal of Materials Processing Technology*, 252, pp. 421-431, 2018.

[17] Y. WANG, P. JIANG, S. GENG, B. XU, J. ZHAO: 'Influence of the wrinkle surface structures on the vapor flow and keyhole stability in 20 kW high power laser welding', *International Journal of Heat and Mass Transfer*, 193, 122958, 2022.

[18] X. MENG, S. N. PUTRA, M. BACHMANN, M RETHMEIER: 'A statistical assessment of the laser energy absorption and keyhole stability in high-power laser welding', *Journal of Manufacturing Processes*, 141, pp. 885-896, 2025.

[19] X. MENG, M. BACHMANN, A. ARTINOV, M. RETHMEIER: 'A study of the magnetohydrodynamic effect on keyhole dynamics and defect mitigation in laser beam welding', *Journal of Materials Processing Technology*, 307, 117636, 2022.

[20] F. YANG, X. MENG, S.N. PUTRA, M. BACHMANN, M. RETHMEIER: 'Numerical studies of process porosity suppression by magnetohydrodynamic technology during the laser beam welding of aluminum alloy', *International Journal of Heat and Mass Transfer*, 253, 127525, 2025.

[21] W. I. CHO, S. J. NA, C. THOMY, F. VOLLERTSEN: 'Numerical simulation of molten pool dynamics in high power disk laser welding', *Journal of Materials Processing Technology*, 212(1), pp. 262-275, 2012.

[22] X. MENG, A. ARTINOV, M. BACHMANN, Ö. ÜSTÜNDAĞ, A. GUMENYUK, M. RETHMEIER: 'The detrimental molten pool narrowing phenomenon in wire feed laser beam welding and its suppression by magnetohydrodynamic technique', *International Journal of Heat and Mass Transfer*, 193, 122913, 2022.

[23] S. W. HAN, J. AHN, S. J. NA: 'A study on ray tracing method for CFD simulations of laser keyhole welding: progressive search method', *Welding in the World*, 60, pp. 247-258, 2016.

[24] S. W. HAN, W. I. CHO, L. J. ZHANG, S. J. NA: 'A study on laser keyhole welding in vacuum by computational fluid dynamics simulations with plume effect models', *Journal of Laser Applications*, 33(1), 012042, 2021.

[25] X. MENG, S. N. PUTRA, M. BACHMANN, F. YANG, A. ARTINOV, M. RETHMEIER: 'A fundamental study of physical mechanisms of wineglass-shaped fusion zone profile in laser melting', *Journal of Materials Processing Technology*, 324, 118265, 2024.

[26] F. YANG, X. MENG, S. N. PUTRA, A. ARTINOV, M. BACHMANN, M. RETHMEIER: 'Numerical analysis of the effect of an oscillating metal vapor plume on the keyhole and molten pool behavior during deep penetration laser beam welding', *Journal of Laser Applications*, 35(4), 042041, 2023.

[27] S. PANG, X. CHEN, J. ZHOU, X. SHAO, C. WANG: '3D transient multiphase model for keyhole, vapor plume, and weld pool dynamics in laser welding including the ambient pressure effect', *Optics and Lasers in Engineering*, 74, pp. 47-58, 2015.

[28] X. MENG, G. QIN, R. ZONG: 'Thermal behavior and fluid flow during humping formation in high-speed full penetration gas tungsten arc welding', *International Journal of Thermal Sciences*, 134, pp. 380-391, 2018.

[29] F. YANG, X. MENG, S. N. PUTRA, M. BACHMANN, M. RETHMEIER: 'Assessment of keyhole stability in laser beam welding with external magnetic field using numerical simulation', *Journal of Laser Applications*, 36(4), 042038, 2024.

# IMPACT OF MODELING ASSUMPTIONS ON SIMULATED MELT POOL DYNAMICS COMPARED TO HIGH-SPEED X-RAY OBSERVATIONS

J. PLEWINSKI*[1], F. HENNIG**[2], C. FORSTER***[3], S. BELOUSOV****[4], A. ZAKIROV****[5], B. KORNEEV****[6], C. SPURK*****[7], M. HUMMEL*****,******[8], A. OLOWINSKY******[9], F. BECKMANN*******[10], J. MOOSMANN*******[11], M. SCHMIDT***[12], H. KÖSTLER**[13], M. MARKL*[14]

*Chair of Materials Science and Engineering for Metals, Friedrich-Alexander-Universität Erlangen-Nürnberg, 91058 Erlangen, Germany, ([1] 0000-0002-4815-7643, jonas.plewinski@fau.de; [14] 0000-0002-3000-7081)
**Chair for System Simulation, Friedrich-Alexander-Universität Erlangen-Nürnberg, 91058 Erlangen, Germany, ([2] 0000-0001-5298-7968; [13] 0000-0002-6992-2690)
***Institute of Photonic Technologies, Friedrich-Alexander-Universität Erlangen-Nürnberg, 91052 Erlangen, Germany, ([3] 0009-0005-9928-8001; [12] 0000-0002-8072-8768)
****Hipercone Ltd., 9434314 Jerusalem, Israel, ([4] 0000-0002-1730-5738; [5] 0000-0001-7346-6635; [6] 0000-0003-1010-6629)
*****Chair for Laser Technology, RWTH Aachen University, 52074 Aachen, Germany ([7] 0000-0002-5190-4187; [8] 0000-0002-9097-9843)
******Fraunhofer Institute for Laser Technology, 52074 Aachen, Germany ([8] 0000-0002-9097-9843; [9] 0000-0002-5231-8251)
*******Institute of Materials Physics, Helmholtz-Zentrum Hereon, 21502 Geesthacht, Germany ([10] 0000-0002-2266-9173; [11] 0000-0002-6761-7182)

*DOI 10.3217/978-3-99161-089-2-009, license CC BY 4.0*
*https://creativecommons.org/licenses/by/4.0/deed.en*
*This CC license does not apply to third party material and content noted otherwise.*

ABSTRACT

Laser beam welding is a widely used advanced manufacturing process for joining metallic components across various industries. The process is prone to various defects, with solidification cracks being among the most common. Understanding the evolution of the solidification front, including temperature gradients, cooling rates and solidification velocity, is crucial to assess the conditions leading to crack formation. Direct experimental measurement of transient solidification conditions is extremely challenging, while numerical simulations of melt pool dynamics provide complementary insights by predicting local solidification conditions.

In this work, we combine high-speed synchrotron X-ray imaging, which captures the evolution and velocity of the solidification front, with state-of-the-art numerical melt pool simulations that are able to provide local solidification conditions. Comparison of experiments and simulations reveals a mismatch in the quasi-stationary welding regime, primarily arising from the neglect of the gas phase in the simulations. Using a reduced model and simulation setup, we demonstrate how changes in modeling assumptions influence melt pool dynamics and shape. Our results highlight that, for deep-penetration laser welding, proper physical modeling of the vapor-filled keyhole is essential for accurate predictions of melt pool and solidification conditions.

Keywords: Laser Beam Welding, Keyhole, Steel, Numerical Simulation, Lattice Boltzmann Method, High Performance Computing, GPU

## INTRODUCTION

Laser beam welding (LBW) is a widely used advanced manufacturing process for joining metallic components across various industries, including automotive, aerospace, and medical devices. Its advantages include high power density, precise heat input control, high welding speed, and minimal heat-affected zones, enabling the joining of challenging materials and complex geometries [1].

Despite its benefits, LBW is susceptible to various defects, with solidification cracks being one common welding error. Solidification cracks are a type of hot crack that forms in the mushy zone during the final stages of solidification, where thermal stresses and strains interact with the fragile, partially solidified microstructure. These cracks evolve when the residual melt in the solidifying material cannot accommodate the tensile stresses induced by thermal contraction and solidification shrinkage. A detailed understanding of the solidification front, including the temperature gradient and solidification velocity, is crucial as these parameters dictate the local solidification conditions and the resulting microstructure, which in turn influence crack susceptibility [2-6].

The solidification conditions are mainly driven by the melt pool dynamics, as they control the heat distribution and mass transport [7]. The keyhole, a vapor-filled cavity formed by the intense laser energy, acts as a primary heat source and its stability and shape significantly influence the melt pool flow and temperature distribution. Changes in keyhole behavior, such as oscillations or collapse, can lead to melt pool instabilities, affecting the solidification front and potentially causing defects like porosity and cracking [8-11].

Experimentally measuring the transient solidification conditions and keyhole dynamics during LBW is extremely challenging due to high temperatures, small spatial scales, and rapid process rates. However, advanced investigations techniques based on synchrotron radiation have provided invaluable insights into these phenomena. Work conducted at facilities like DESY (Deutsches Elektronen-Synchrotron) has utilized high-speed X-ray imaging to track the keyhole shape and melt pool dynamics in situ during LBW. This data allows for the interpretation of process behavior, providing quantitative information on keyhole geometry, melt pool flow patterns, and even estimations of solidification velocities [12-15].

Given the experimental difficulties, numerical simulations of melt pool dynamics offer a suitable and powerful approach to investigate the solidification conditions during LBW in more detail. These simulations can provide crucial information about the solidification

velocity and temperature gradients at the solidification front, which are essential for predicting the resulting microstructure and crack probability. Various numerical approaches have been developed for LBW simulation. Latest models take different combinations of the following phenomena into account: phase changes (evaporation and condensation), compressible gas phase dynamics, beam propagation by means of ray tracing (multiple reflections of the laser beam within the keyhole) and thermo-dynamic properties of the metal vapor [16-24]. However, the optical interaction between the laser beam and the metal vapor itself, particularly absorption and attenuation mechanisms within the metal vapor, is only rarely incorporated in a physically consistent manner [25]. In most existing models, this effect is neglected, although it can significantly influence the redistribution of laser energy inside the keyhole and thereby affect both penetration depth and keyhole geometry [25, 26].

In this work, we combine high-speed synchrotron X-ray imaging with numerical melt pool simulations to investigate melt pool dynamics during LBW under quasi-stationary deep-penetration conditions. In addition to a state-of-the-art simulation approach, we introduce a reduced framework that allows systematic variation of boundary conditions along a predefined vapor capillary. The remainder of this manuscript is structured as follows. First, the experimental setup and synchrotron X-ray measurements are described. Subsequently, the numerical modeling approaches, including both the state-of-the-art simulation and the simplified framework, are introduced. Finally, experimental and numerical results are presented and discussed with respect to melt pool dynamics.

## METHODS

### MATERIAL

All experiments and simulations of this work are conducted with stainless steel 1.4301. The necessary material parameters for the simulations are obtained from the JMatPro[1] software. The calculation was performed through the "Stainless Steel" module, incorporating a measured chemical composition of the material in Table 1. Solidification behavior was specifically analyzed via the "Solidification Module". The simulation was initialized with a starting temperature of 3000 K and concluded at an end temperature of 298 K, employing a temperature step size of 5 K. A fraction of liquid cut-off of 0.01 was applied, and all relevant phases were considered in the calculation. A cooling rate of 10,000 K $s^{-1}$ was specified, and an austenite grain size of 500 μm was assumed for the simulation.

[1] www.sentesoftware.co.uk/

**Table 1** Chemical composition of 1.4301 in wt-%.

| C | Si | Mn | P | S | Cr | N | Ni | Fe |
|---|---|---|---|---|---|---|---|---|
| 0.02 | 0.41 | 1.6 | 0.028 | <0.002 | 19.09 | 0.095 | 8.06 | balance |

The constant material parameters are listed in Table 2. The thermal diffusivity is computed by $\alpha = \lambda/(\rho \cdot c_p)$. The liquid phase fraction is shown in Fig. 1. The liquidus temperature is 1735 K and the solidus temperature is defined at 15 % residual liquid at 1690 K. For all simulations, the liquid phase fraction - as well as respectively the solid phase fraction - is linearly interpolated. The temperature dependent surface tension (see Fig. 1) is approximated by a linear regression above the liquidus temperature

$$\gamma(T) = (-4.102 \cdot 10^{-4}\, K^{-1} \cdot T + 2.51)\ \mathrm{N\,m^{-1}}. \quad (1)$$

**Table 2** Constant material parameters of stainless steel 1.4301 computed with JMatPro.

| Material parameter | | Quantity | Unit |
|---|---|---|---|
| **Density** | $\rho$ | 7026 | $\mathrm{kg\,m^{-3}}$ |
| **Kinematic viscosity** | $\nu$ | 7.158 | $\mathrm{mPa\,s^{-1}}$ |
| **Specific heat capacity** | $c_p$ | 804 | $\mathrm{J\,kg^{-1}\,K^{-1}}$ |
| **Thermal conductivity** | $\lambda$ | 31.531 | $\mathrm{W\,K^{-1}\,m^{-1}}$ |
| **Thermal diffusivity** | $\alpha$ | 5.582 | $\mathrm{mm^2\,s^{-1}}$ |
| **Latent heat** | $L_c$ | 171.401 | $\mathrm{kJ\,kg^{-1}}$ |

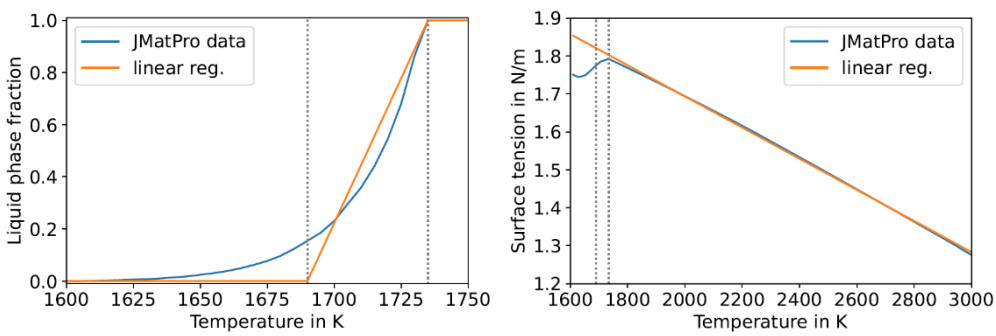



**Fig. 1** Temperature dependent material parameters of stainless steel 1.4301 used in the simulation (orange) compared against the data from JMatPro. The two dashed lines indicate temperature solidus and liquidus used in the simulations.

## EXPERIMENT

In-situ synchrotron X-ray imaging of the LBW process zone was conducted at the P07 (EH4) high-energy beamline at PETRA III, DESY (Hamburg, Germany) [27]. A schematic illustration of the experimental setup is shown in Fig. 2. The X-ray imaging system's core components included the DESY synchrotron (X-ray source), a scintillator, and a high-speed camera. The synchrotron X-ray beam, with a $2 \times 2$ mm$^2$ cross-section, irradiated samples (dimensions: $100 \times 30 \times 2$ mm$^3$) at the process zone. X-ray attenuation within the workpiece is dependent on material density; consequently, the gas-filled keyhole and the liquid melt pool exhibit lower attenuation than the solid material, which leads to different X-ray intensities after the sample. The transmitted and attenuated X-ray beam was converted into visible light by a 1.2 mm thick Cer-doped Gadolinium Aluminum Gallium Garnet (GaGG:Ce) scintillator, positioned approximately 3.5 m after the sample. An i-SPEED 727 high-speed camera (iX Cameras), equipped with a magnification lens, captured the intrinsic luminescence from the scintillator's backside. For these investigations, the beamline operated at a photon energy of 74 keV, and videos were recorded at a resolution of $1600 \times 900$ pixels with a frame rate of 7500 frames s−1. The raw data was further processed to improve the quality according to Forster et al. [15].

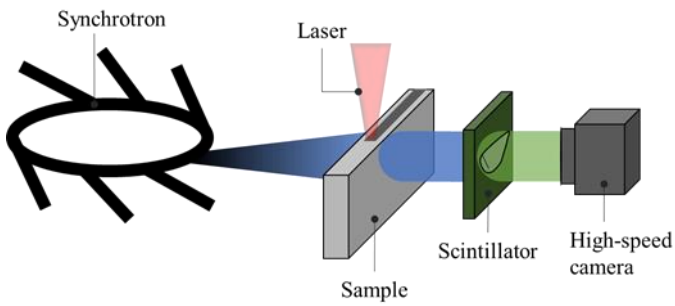



**Fig. 2** Schematic illustration of the experimental setup. Reprinted from [15] under the CC BY-NC-ND 4.0 license

The LBW system featured a Trumpf TruDisk 8001 disc laser with a wavelength of 1030 nm, a 100 μm core diameter fiber optic cable (Newson NV, Dendermonde, Belgium), and a 2D galvanometer scanner system. A collimator lens ($f = 80$ nm) in combination with a f-theta focusing lens ($f = 163$ nm) provided a 1:2 magnification, resulting in a measured laser beam diameter of approximately 214 μm.

The specimens were mounted upright in a clamping device. Welding was carried out on the top edge of the sample. During the experiments, the sample remained stationary while the galvanometer scanner mirrors moved the laser beam at the desired feed rate. The feed rate was varied from 20 mm s−1 to 200 mm s−1, while the laser power ranged from 500 W to 1500 W. A compressed-air cross-jet was employed to protect the welding optics from spatter and metal fumes.

The temperature at the edge of the keyhole was measured using a hyperspectral camera [28]. The measurements showed temperatures between 2700 K and 2900 K during the process. The temperature fluctuations are due to process instabilities.

## SIMULATION WITH KISSAM

The KiSSAM[2] [29] software framework is employed for high-fidelity simulation of the experimental LBW process. KiSSAM provides a detailed and physically comprehensive representation of melt pool dynamics. In previous studies, KiSSAM has been applied to a variety of additive manufacturing problems, including finding optimal parameters of single tracks [30], wetting effects on melt morphology [31], and increased layer thickness strategies in powder bed fusion [32]. In this work, KiSSAM is used as a reference to assess the validity and limitations of the underlying physical effects [29, 33].

KiSSAM explicitly models the gas-liquid interface using a volume-of-fluid (VOF) approach. This enables dynamic evolution of the keyhole shape under the influence of recoil pressure, surface tension, and evaporation-induced mass loss. The hydrodynamics solver is based on a weakly compressible lattice Boltzmann method (LBM) using a D3Q27 stencil. In contrast to macroscopic discretizations of the governing equations, the LBM employs a mesoscopic formulation based on particle distribution functions, which recover the Navier-Stokes equations in the low-Mach-number regime [34]. Hydrodynamics are restricted to the molten region. Heat transfer and phase change are modeled via an enthalpy-based formulation. The laser energy input is computed via ray tracing, accounting for multiple reflections within the keyhole cavity. This physical coupling - alongside modeling of surface tension (including Marangoni effects), strong evaporation and bubbles tracking - allows the simulation of keyhole collapse, bubble formation, and melt pool oscillations. No empirical fitting parameters are introduced; all phenomena are derived from fundamental physics. The only physics that is neglected is the vapor gas dynamics as well as the laser-vapor interactions.

KiSSAM employs dynamic mesh refinement and coarsening around the melt pool to keep correct simulation of the whole sample welded plate while minimizing computational cost in the surrounding solid material. The material domain is split into regions with distinct resolution levels, and the solver operates with high efficiency due to full GPU parallelization and a single-precision numerical implementation.

## SIMULATION WITH WALBERLA

A second numerical model is implemented within the high-performance multiphysics framework WALBERLA [35, 36] combined with the pycodegen[3] family of Python-packages

[2] www.kissam.cloud
[3] pycodegen.pages.i10git.cs.fau.de

for scientific code generation. While KiSSAM aims at a detailed representation of dynamic keyhole formation and melt pool evolution, the WALBERLA-based approach follows a deliberately reduced modeling strategy. Its primary purpose is to investigate the melt pool response under controlled thermal and pressure boundary conditions, thereby enabling a systematic assessment of the influence of keyhole-related assumptions.

The melt pool dynamics are described by the incompressible Navier-Stokes equations and solved using the LBM on a D3Q19 stencil. Phase change between liquid and solid is modeled using the Partially Saturated Method (PSM) [37]. The solid fraction is introduced as a continuous variable defined between solidus and liquidus temperature. In this formulation, the mushy zone is treated as a hydrodynamic damping region: as the solid fraction increases during solidification, melt flow is progressively reduced until motion ceases in the fully solid state. The transition from liquid to solid is therefore represented as a continuous reduction of flow mobility. The model does not account for mechanical stiffness of the solid, volumetric shrinkage, microsegregation, feeding of the mushy zone, or stress evolution during solidification. The influence of the solidifying region on the melt pool is thus limited to hydrodynamic damping and thermal transport.

Thermal transport is modeled using a passive-scalar LBM formulation [38, 39]. The temperature field is tightly coupled to the melt flow and evolves according to convective and diffusive heat transport. Phase change is incorporated using an enthalpy-based approach, in which latent heat effects are accounted for within the energy balance. The local temperature is obtained from the specific enthalpy, considering both sensible heat and latent heat contributions, based on the material properties defined in Section 2.1. This formulation ensures thermodynamic consistency between heat transfer and solidification.

In contrast to KiSSAM, the WALBERLA model does not explicitly resolve evaporation dynamics, recoil pressure formation, or laser energy absorption within the keyhole. Instead, these complex processes are represented implicitly through prescribed boundary conditions at the keyhole surface. Therefore, the keyhole geometry is defined as a fixed spherocylindrical cavity with dimensions comparable to the experimentally observed keyhole. This simplification eliminates the explicit modeling of evaporation-driven interface deformation and gas-phase dynamics.

Laser energy deposition is represented by imposing a constant Dirichlet boundary condition of 2700 K at the keyhole surface, corresponding to the experimentally measured temperature range. In addition, a depth-dependent pressure boundary condition is applied along the keyhole wall to approximate the effect of evaporation-induced recoil pressure. Free-slip conditions are enforced tangentially at the cavity surface, allowing unimpeded melt flow along the interface while preventing normal penetration.

The imposed temperature and pressure distributions are thus implanted rather than computed from first principles. By prescribing these thermodynamic conditions directly at the cavity interface, the model deliberately bypasses detailed laser-matter interaction and evaporation-induced energy losses. The WALBERLA simulations should therefore be interpreted as a controlled numerical study of boundary-condition effects on melt pool flow and geometry rather than as a fully predictive description of the laser-material interaction.

The numerical implementation leverages WALBERLA's block-structured domain decomposition and MPI-based parallelization combined with GPU acceleration. The LBM

kernels are generated automatically using the code-generation frameworks pystencils [40, 41] and lbmpy [42-44], which translate symbolic descriptions of the governing equations into optimized C++/CUDA code at build time. This approach ensures performance portability while enabling rapid modification of physical models and boundary conditions.

A more detailed description of the mathematical formulation, the specific lattice Boltzmann schemes, and the implementation details of the waLBerla simulation and the used models can be found in Appendix.

## MODELING ASSUMPTIONS

It is important to emphasize that both modeling frameworks focus exclusively on the thermo-fluid dynamics of the melt pool. Gas-phase dynamics, thermomechanical coupling, volumetric shrinkage, and stress evolution during solidification are not considered. Consequently, the simulations capture heat and mass transport, but they do not directly predict crack initiation or propagation. While solidification velocity and temperature gradients constitute necessary input parameters for solidification cracking models, the connection to cracking is therefore indirect. Within the research unit FOR5134[4], the computed solidification conditions are provided to complementary subprojects that specifically address the mechanisms and prediction of solidification cracks in an integrated, multi-scale framework.

Both simulation approaches rely on several assumptions, namely, treating the melt as incompressible, representing the transition from liquid to solid as a continuous variation of the local solid fraction between solidus and liquidus temperatures, and neglecting energy absorption and momentum transfer by the vapor phase.

Two complementary simulation strategies are employed. KiSSAM resolves the dynamic evolution of the keyhole, explicitly tracking the gas-liquid interface using a Volume-of-Fluid (VOF) approach. The keyhole geometry evolves under the influence of surface tension and recoil pressure. WALBERLA, in contrast, prescribes a fixed keyhole geometry, suitable for quasi-stationary conditions, allowing a systematic investigation of how boundary conditions influence steady-state melt pool flow.

Laser energy deposition is treated differently in the two models. KiSSAM accounts for multiple reflections within the keyhole using ray tracing, while WALBERLA applies a constant temperature boundary condition at the keyhole surface.

Stainless steel 1.4301 is used as a representative material to study melt pool dynamics during LBW, but it should be noted that phenomena such as evaporation and material properties, including temperature-dependent surface tension and solidification behavior, are highly sensitive to the specific alloy composition and welding conditions.

[4] https://www.for5134.science/en/

## SIMULATION SETUP

Two LBW setups with power levels of 500 W and 1000 W and a feed rate of 100 mm $s^{-1}$ were simulated. The spatial resolution was set to $\Delta x = 5$ µm in all cases. The time step sizes were $\Delta t = 75$ ns for the KiSSAM simulations and $\Delta t = 100$ ns for the WALBERLA simulations. The finest mesh size surrounding the melt pool in the KiSSAM simulations for a fully developed melt pool is $1.1 \times 0.6$ $mm^2$ in $x$ and $y$-direction and 1.4 mm or 2.4 mm for 500 W and 1000 W in $z$-direction, respectively. For WALBERLA, both settings used a domain size of $4 \times 2$ $mm^2$ in $x$ and $y$-direction and 1 mm or 2 mm for 500 W and 1000 W in $z$-direction, respectively. In KiSSAM, the laser moves according to the feed rate and the keyhole develops due to laser absorption and evaporation pressure. In contrast, the keyhole in WALBERLA simulations is geometrically fixed. The keyhole shape is modelled with a spherocylinder [45], consisting of a cylinder and an ending hemisphere with a total depth of 0.66 mm and 1.3 mm for the 500 W and 1000W respectively (diameter similar to the beam diameter). The laser movement is modeled implicitly by shifting the fluid velocity field by the laser's feed rate prior to its use in the thermal update, effectively transitioning to a co-moving reference frame. On the keyhole surface, a constant Dirichlet boundary condition with 2700 K according to the measurements is applied. In addition, a free-slip condition in combination with a pressure gradient is applied to the fluid field permitting unimpeded tangential flow near the keyhole and enabling different pressures inside the keyhole. The additional pressure is linearly increased from zero at the top to 176 kPa at the bottom end of the keyhole shape. The motivation for this choice is the assumption, that on the horizontal walls of the keyhole, the evaporation pressure keeps the keyhole open, and no other major pressures are acting. At the bottom, a significant acceleration occurs, which is well seen during bubble escape. Therefore, a pressure near the evaporation pressure for this material at 2700 K is chosen [46].

The whole domain is initialized at room temperature. KiSSAM uses Dirichlet boundary conditions at the domain boundaries at room temperature accordingly. It further applies no-slip boundary conditions between the melt pool and the solid material as well as pressure boundary conditions incorporating wetting, surface tension, Marangoni and evaporation pressure at the free surface between the melt pool and the atmosphere. WALBERLA applies free-slip boundary conditions for both LBM solvers at the top and bottom domain boundaries, which impose symmetry with respect to the wall-normal direction. On the horizontal boundaries, WALBERLA uses Dirichlet boundary conditions at room temperature. The corresponding fluid boundaries are treated the PSM.

# RESULTS

## EXPERIMENT

Utilizing high-speed synchrotron X-ray imaging, the real-time dynamics of the laser welding process, specifically the formation and evolution of the keyhole and melt pool, were directly observed. As shown in Fig. 3, a series of four representative frames were extracted of a video sequence[5] for a beam power of 1000 W.

The keyhole and melt pool appear brighter in the images compared to the solid material, a result of their lower density and consequently reduced X-ray absorption. At the top of the image, a darker region is visible, representing the resolidified or still molten weld seam surface. For enhanced clarity, the melt pool is delineated with a white dotted line. Due to the phase contrast enhancement inherent in the imaging technique, changes in the refractive index at the keyhole and melt pool boundaries are visualized as a black line. Fig. 3a shows the initial evolution of the keyhole. In Fig. 3b, the keyhole has deepened, and a small melt pool has formed on the side opposite the feed direction. By Fig. 3c, the keyhole has reached its maximum depth, while the melt pool has expanded but is not yet fully developed. Finally, Fig. 3d illustrates the fully developed melt pool with a depth of approximately 1.3 mm, along with the onset of keyhole pore strangulation. These start as bubbles, escaping from the keyhole and being transported within the melt pool flow, exhibiting mean velocities of approximately 0.1 m/s to 1 m/s. Additional measurements indicate that the surface temperature specifically at the keyhole area of the melt pool reaches approximately 2700 K.

[5] https://www.for5134.science/en/teilprojekte/thermo-fluiddynamische-untersuchung/

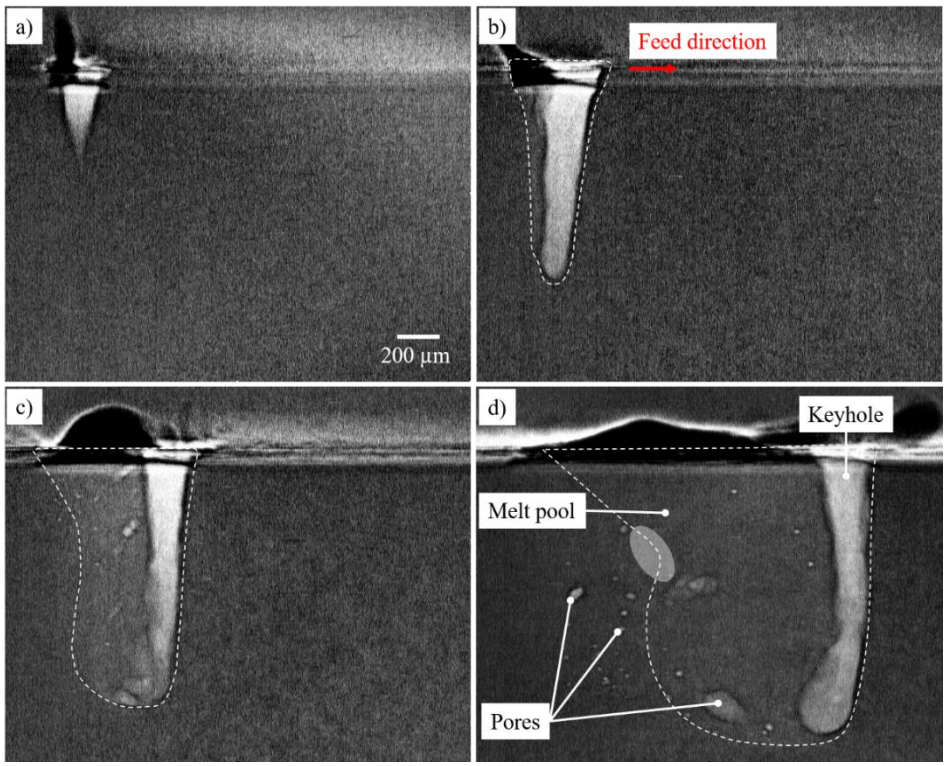



**Fig. 3** X-ray images from laser welding with 1000 W. a) Insertion of the laser into the material, keyhole formation after 0.27 ms; b) Deepening of the keyhole and melt pool formation after 1.2 ms; c) Final keyhole depth after 4.3 ms; d) Fully developed keyhole and melt pool after 11.5 ms. Area of uncertainty regarding the melt pool shape is highlighted in light gray.

## SIMULATION

The results from KiSSAM and WALBERLA are provided for a power of 1000 W. The simulation results are compared via 3D representations of the melt pool and the melt pool velocity in Fig. 4.

In both subfigures, the volume +/- 50 µm in y direction around the center of the simulation domain is shown. The melt pool dynamics are visualized by streamlines of the melt pool with the velocity magnitude represented by color from violet to yellow. The melt pool shape is approximated by the solidus and liquidus isotherms. In the KiSSAM results, the dynamically developed keyhole is determined by a contour surface at a fill level of 50 %. The static, cylindrical keyhole of the WALBERLA simulation is illustrated in red color.

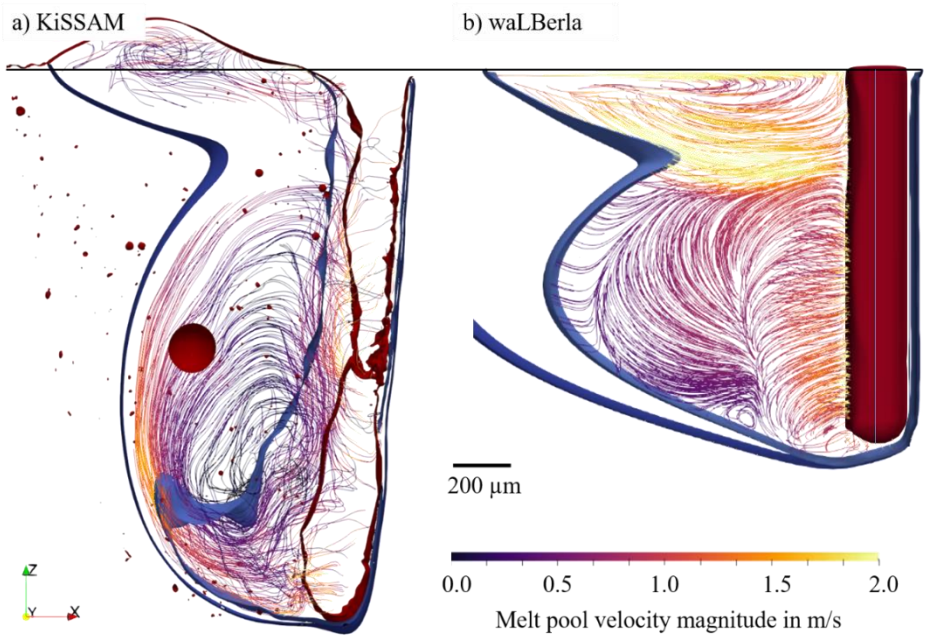



**Fig. 4** Comparison of melt pool shape (represented by the solidus and liquidus isotherms in blue) and velocities via colored streamlines for 1000 W of a) KiSSAM and b) WALBERLA. The keyhole is represented as red isosurface.

*Simulation with KiSSAM*

The simulation results from KiSSAM show a dynamically evolving keyhole and melt pool shape (see Fig. 5 and movie in supplementary material). The liquid melt pool is visualized in blue by the solidus and liquidus isotherms. For comparison, the simulation results are superimposed on the experimental results from Fig. 3.

The laser drills rapidly into the material by pushing the liquid melt out of the keyhole (see Fig. 5a+b). After approximately 1.5 ms the keyhole has a depth of 1.3 mm. The numerical melt pool evolves similar to the experimental observations albeit with a time shift of a few microseconds. The quasi steady state of the keyhole in Fig. 5d is much higher than in the experiment with a depth of appropriately 2 mm, which is discussed in Section 4. The keyhole shape is slightly tilted due to the laser movement. In addition, the keyhole shows an irregular surface. During welding, parts of the melt pool start to drop into the keyhole and in the laser path. Due to a subsequent high laser absorption, this material is directly pushed back into the melt pool. At the bottom of the keyhole, some bubbles escape from the keyhole, similar to the experiment. The melt pool dynamics show a circular vortex in the bottom half of the melt pool and some vertical movement in the upper part. A steady mean temperature over the whole keyhole of approximately 2450 K is established. This mean value is computed by averaging

the temperature of every interface cell at the volume-of-fluid boundary to the keyhole. In contrast, cell-local temperature peaks up to 6900 K are observed at specific points, where the laser is directly hitting the material; however, these peaks are excluded from the reported mean value to provide a more stable representative temperature of the keyhole walls.

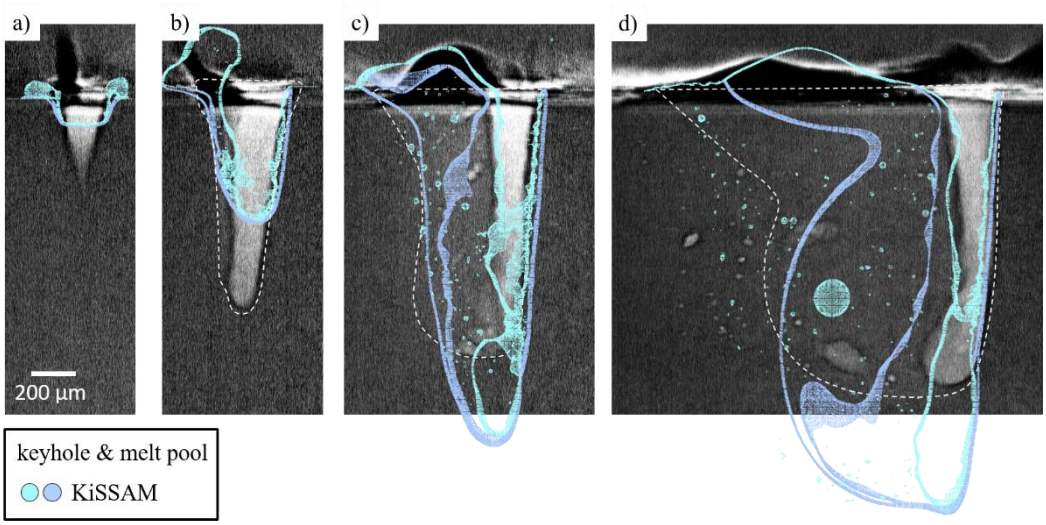



**Fig. 5** X-ray images from Fig. 3 superimposed with KiSSAM simulation results (contour of keyhole in cyan as well as solidus and liquidus isotherms in blue representing the melt pool) at similar times: a) 0.27 ms, b) 1.2 ms, c) 4.3 ms and d) 11.5 ms.

### *Simulation with waLBerla*

Due to the fixed keyhole geometry for the waLBerla simulation, only the steady state is presented in Fig. 5. The final melt pool depth is 1.4 mm, which is only slightly larger than the keyhole itself. Two recirculation zones are obvious. At the top of melt pool there is a fast recirculation zone dominated by the Marangoni effect driven by the surface tension. The second recirculation zone with fast melt pool velocities is observed due to the keyhole forces acting at the bottom of the keyhole. These two eddies lead to a double recirculation zone in the top-middle of the melt pool with low melt pool velocities. Due to the PSM method, the melt pool velocities in the mushy zone between the liquidus and solidus isotherm are almost zero. A remarkable kink is visible in the liquidus isotherm, which is a result of the underlying melt pool dynamics.

## Performance

The computation time for both simulation tools was tracked for two different beam powers of 500 W and 1000 W. A direct performance comparison between the simulation frameworks is not feasible due to fundamental differences in their modeling scope and numerical configurations. Specifically, the two applications differ in physical complexity, LBM stencil choices, numerical precision (single vs. double), and the hardware architectures on which the simulations were executed. These discrepancies preclude a fair and meaningful evaluation of absolute performance metrics such as runtime or throughput.

Despite its high physical and computational complexity, KiSSAM is executed on a single RTX 3090 GPU. The software achieves a total simulation time of the last 7.5 ms (100,000 time steps) for 500 W (approx. 8 million cells) of 1.96 h and for 1000 W (approx. 12 million cells) of 2.99 h, respectively. This outstanding performance is realized by optimized GPU code and mesh refinement surrounding the melt pool. In addition, the advantages of the RTX 3900 are used due to the single-precision execution of the simulation.

In the present state, the grid refinement of waLBerla could not be used here. Therefore, the simulations are executed on 8 NVIDIA A100 GPUs. The software achieves a total simulation time for 30 ms real time (500,000 time steps) for 500 W (approx. 64 million cells) of 1.5 h and for 1000 W (approx. 128 million cells) of 3 h, respectively. The total simulation time is comparable with KiSSAM, although less physical phenomena are tracked. Possible performance improvements are achievable by grid refinement and by replacing double with single precision computations.

# DISCUSSION

## MELT POOL EVOLUTION

The experimentally observed evolution of the melt pool is slightly underestimated by the KiSSAM simulation (see Fig. 5a+b) within the first milliseconds. Here, the melt pool dynamics are mainly driven by the evaporation pressure. KiSSAM underpins, that the covered physics including laser beam ray-tracing, absorption and multi-reflection as well as the hydro- and thermodynamical models are suitable to describe this stage of melting, although there is a small shift in time of a few microseconds until the correct melt pool depth is reached. One reason is the coarse cell size of the finest mesh of 5 µm. With a finer cell size, this effect gets less significant. These results are similar to additive manufacturing examples [30-32], where the melt pool depth is normally smaller than 1 mm. In addition, the initial evolution of the melt pool is of less importance than the quasi-stationary state for welding and additive manufacturing processes.

However, Fig. 5c+d clearly show that the numerical prediction significantly overestimates the melt pool depth once approaching the quasi-stationary state. Consequently, the overall shape of the melt pool does not match the experimental observations. The upper vortex, driven by the Marangoni effect, is considerably smaller than in the experiment and in a low temperature range between solidus and liquidus temperature. In addition, the keyhole walls exhibit stronger instabilities.

In the current KiSSAM simulations, the keyhole walls absorb only minor fractions of laser energy, primarily through multi-reflections. Unless material intrudes into the laser channel, the walls remain comparatively cold. This is consistent with the simulated mean wall temperature of approximately 2450 K, which is significantly lower than the experimentally measured average temperature of about 2700 K. If material enters the beam path, it is rapidly heated and expelled, leading to localized and intermittent heating events. This mechanism results in unsteady melt pool dynamics, reflected by the zig-zag pattern of the temperature isolines (Fig. 5d).

Although KiSSAM has demonstrated high predictive capability for similar processes with different materials under specific parameter sets, the present discrepancies indicate that additional physical mechanisms may be missing. The absence of explicit vapor-phase modeling has two distinct implications. First, the stabilizing vapor pressure inside the keyhole is not resolved. In reality, the metal vapor exerts a distributed pressure along the keyhole walls, counteracting surface tension and hydrostatic forces and thereby contributing to geometric stability. Without this vapor pressure contribution, the simulated keyhole is more susceptible to local wall instabilities and collapse events. Second, laser absorption within the vapor phase is not considered. If a significant fraction of the laser energy is absorbed by the metal vapor before reaching the melt pool bottom, the energy input into the deeper regions of the cavity would be reduced. This would directly influence the melt pool depth and the overall penetration behavior. The overestimation of melt pool depth in the present simulations therefore likely results primarily from the absence of vapor-phase absorption rather than from missing pressure effects alone. Trapp et al. measured the absorptivity of stainless steel SS316L

during keyhole welding and conclude a value of approximately 78 % [47]. In contrast, the energy absorption due to multi-reflection in KiSSAM simulations is almost 100 %. Assuming a significant absorption of the metal vapor inside the keyhole, the melt pool shape and dynamics will change. The consequence is that less laser energy is absorbed at the melt pool bottom, which results in a smaller melt pool depth and in total in less evaporation losses regarding energy and mass.

### QUASI-STATIONARY STATE

A comparative analysis of all simulation results and the experiments for 500 W and 1000 W is presented in Fig. 6. The background displays experimental synchrotron imaging of the cross-section along the laser scanning direction. The keyhole region is highlighted in light gray, enclosed by a dashed contour that delineates the melt pool boundary. Superimposed on these experimental images are the simulation results: the KiSSAM iso-surfaces are depicted as light blue wireframes, while the WALBERLA simulation results are shown in green. This visual overlay enables a direct qualitative comparison of the quasi-stationary state between experimental observations and numerical predictions. The differences in the melt pool evolution between KiSSAM simulation and the experiments are already discussed in Section 4.1. Here, it is obvious that the described mechanism of overestimated evaporation is present for both powers. In contrast, the WALBERLA simulations can reproduce the overall shape and melt pool dynamics of the experiments. Because the keyhole and all boundary conditions do not change over time, a stationary state evolves. The vortices driven by evaporation and the Marangoni effect form the outer shape of the melt pool represented by the liquidus isolines. Both vortices lead to the formation of a kink in this isoline. The evaluation of the melt pool shape from the experiments, especially in this region, is not straight forward. Consequently, the dashed white line has a high uncertainty in this region. Summing up, the defined boundary condition results in a realistic melt pool shape.

It must be noted that the improved accuracy of the simplified waLBerla model does not imply a more complete physical description of the laser-matter interaction. The agreement with experimental melt pool geometries primarily highlights the strong sensitivity of the melt pool shape to the boundary conditions applied on the keyhole walls. By prescribing steady-state temperature and pressure distributions derived from experiments, the model enforces the dominant thermodynamic driving forces in a controlled manner, which enhances numerical robustness within a specific regime. However, this approach does not resolve the dynamic evolution of the keyhole, transient evaporation processes, or vapor-induced energy losses. A fully predictive model must ultimately incorporate these coupled and time-dependent mechanisms.

For a quantitative comparison, the melt pool cross section area and volume are evaluated for both simulation tools (see Table 3). The melt pool volume predicted by KiSSAM is approximately a factor of four smaller than that of the WALBERLA simulation. Similarly, the cross-sectional area of the melt pool in the KiSSAM results is reduced by roughly a factor of two. Moreover, in KiSSAM, the average melt pool temperature is lower, with a substantial fraction of the melt pool residing in the mushy zone, which is not observed in the WALBERLA

simulations. These results support the assumption of overestimated evaporation at the melt pool bottom for the KiSSAM simulation. The highly localized absorption of the laser energy results in extreme surface temperatures within individual computational cells of up to 6900 K and consequently to very high evaporation losses in terms of both energy and mass. In this context, 'local' refers specifically to the temperature of a single cell at the point of laser interaction rather than a region-wide average. As a result, insufficient energy remains within the liquid melt pool. Although the melt pool is deeper, the total volume is too small. It should be emphasized that an explicit modeling of gas-phase flow, recondensation effects, or vapor superheating alone would not fundamentally alter this penetration behavior. While such effects could redistribute energy locally and potentially increase the overall melt pool volume, they would not significantly reduce the penetration depth. A reduction in melt pool depth requires that less laser energy reaches the keyhole bottom. This can only occur if a portion of the laser radiation is absorbed within the metal vapor before interacting with the melted surface. This comparison therefore strengthens the hypothesis that absorption of the laser beam within the vapor phase inside the keyhole plays a decisive role in determining melt pool depth and total evaporation losses.

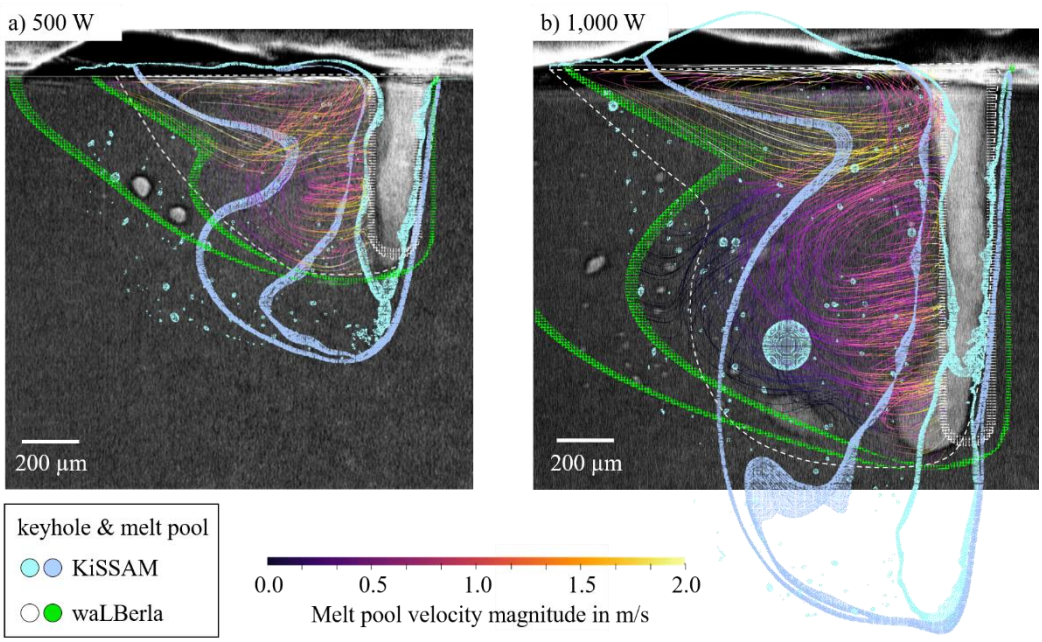



**Fig. 6** Comparison between experiment (keyhole shown in gray), KiSSAM (shades of cyan) and waLBerla (green) simulation results regarding keyhole and melt pool shape (represented by solidus and liquidus isotherms). Additionally fluid velocities inside the pure liquid melt pool are visualized via colored streamlines.

**Table 3** Melt pool evaluations for KiSSAM and waLBerla simulation results.

| Energy Input | 500 W | | 1000 W | |
|---|---|---|---|---|
| Software tool | KiSSAM | waLBerla | KiSSAM | waLBerla |
| Cross section | 0.47 mm² | 0.96 mm² | 0.96 mm² | 2.49 mm² |
| Volume | 0.05 mm³ | 0.20 mm³ | 0.13 mm³ | 0.52 mm³ |

To reflect this change in absorption, the KiSSAM simulations were repeated with the beam power reduced to 80 % after 1.2 ms, once the keyhole has evolved. The results of both simulations are compared to the experimental observations in Fig. 7. As expected, the melt pool reaches now a reasonable depth. However, the unsteadiness of the keyhole walls as well as the underestimated extend of the Marangoni-driven flow region is almost unaffected. This indicates that the simplified treatment of the vapor phase is insufficient to reproduce the experimentally observed stabilization mechanisms. In particular, the absence of an explicit gas-phase model prevents a physically consistent description of vapor pressure and its stabilizing effect on the keyhole, which limits the agreement between simulation and experiment. These topics are addressed in future work.

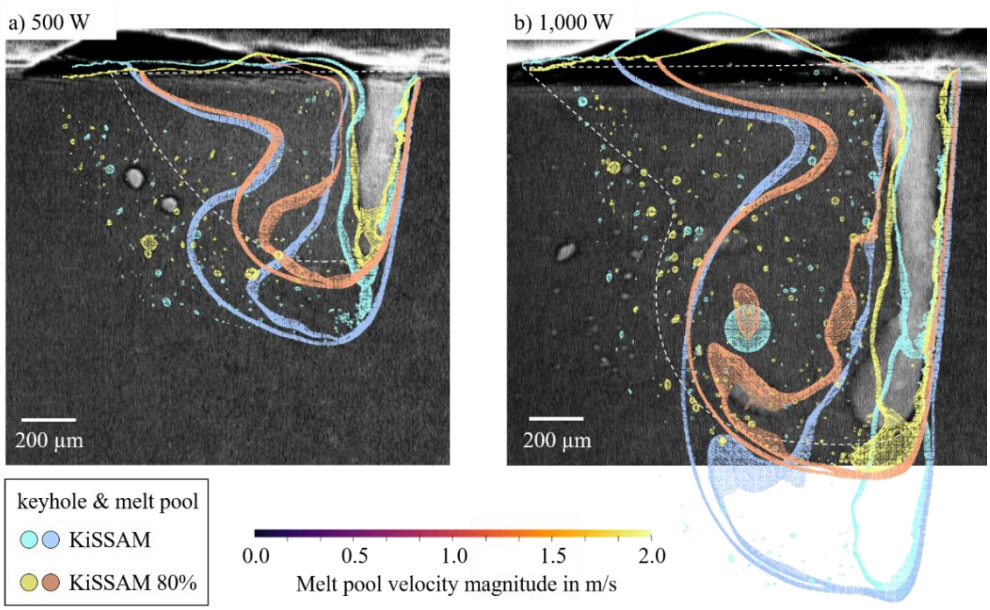



**Fig. 7** The experimental data show the keyhole as a light-gray background region, with the melt-pool geometry indicated by a dashed line. These measurements are compared with the KiSSAM simulations at 80 % beam power, shown in orange and yellow, and at 100 % beam power, shown in blue and cyan, using the solidus, liquidus, and keyhole isotherms for a) 500 W and b) 1000 W.

## CONCLUSION AND OUTLOOK

This work presented experimental and numerical investigations of LBW of stainless steel 1.4301 for two parameter sets in the deep penetration regime. Both simulation frameworks are capable of resolving several microseconds of process time within a few hours on modern GPU architectures. The study focused exclusively on the thermo-fluid dynamics of the melt pool and keyhole. Solidification cracking itself was not modeled directly; instead, solidification velocities and temperature gradients are easy to be extracted to serve as input for complementary mechanical computations.

The comparison between synchrotron experiments and simulations revealed that the transient melt pool evolution is well captured by the state-of-the-art tool KiSSAM. However, significant deviations arise in the quasi-stationary regime. In particular, melt pool depth, keyhole stability, and flow topology cannot be reproduced satisfactorily when the gas phase as well as laser–vapor interaction are neglected.

Using a reduced modeling approach implemented in waLBerla, the experimentally observed melt pool shape could be reproduced by imposing more homogeneous temperature and pressure boundary conditions at the keyhole interface. This comparison leads to two central conclusions.

First, our results confirm previous findings from the literature that the gas phase cannot be neglected in deep-penetration laser welding. For numerical simulations, its presence significantly influences pressure and temperature distributions inside the keyhole, which in turn affect melt pool geometry, flow behavior, and cavity stability.

Second, modeling the gas phase alone is insufficient. Absorption of laser radiation within the metal vapor must be considered to correctly predict the redistribution of energy inside the keyhole. Only a reduction of laser intensity reaching the keyhole bottom can consistently explain the experimentally observed penetration depth. Vapor-phase absorption further influences keyhole stability and characteristic geometric features. The present results therefore indicate that accurate prediction of quasi-stationary keyhole regimes requires a physically consistent coupling of melt flow, vapor pressure effects, and laser-vapor energy interaction.

It should be emphasized that the conclusions drawn here are regime-specific and based on a single alloy investigated under two parameter sets. Since evaporation behavior, surface tension characteristics, and keyhole dynamics are strongly alloy- and process-dependent, broader validation across different materials and welding conditions is required before generalization.

Future work will therefore focus on three directions. First, dedicated experimental investigations will quantify laser absorption and diffraction within the metal vapor inside the keyhole. Second, these experimentally derived absorption models will be integrated into KiSSAM, including explicit vapor-phase modeling and improved ray-tracing approaches. Third, the waLBerla framework will be extended by adaptive grid refinement and single-precision optimization to further enhance computational efficiency while preserving physical fidelity.

## CREDIT AUTHORSHIP CONTRIBUTION STATEMENT

J. Plewinski: Data curation, Formal analysis, Investigation, Methodology, Software, Validation, Visualization, Writing – original draft, Writing – editing; F. Hennig: Software, Writing - original draft; C. Forster: Data curation, Investigation, Validation, Visualization, Writing - original draft; S. Belousov, A. Zakirov, B: Korneev: Investigation, Software, Writing - original draft; C. Spurk, M. Hummel, A. Olowinsky, F. Beckmann, J. Moosmann: Investigation, Resources; M. Schmidt, H. Köstler: Funding acquisition, Project administration, Resources, Supervision, Writing - review and editing; M. Markl: Conceptualization, Funding acquisition, Methodology, Project administration, Software, Supervision, Validation, Visualization, Writing – original draft, Writing - review and editing

## DECLARATION OF GENERATIVE AI AND AI-ASSISTED TECHNOLOGIES IN THE WRITING PROCESS

During the preparation of this work the author(s) used OpenAI's ChatGPT (GPT-5-mini) in order to correct the English grammar. After using this tool/service, the author(s) reviewed and edited the content as needed and take(s) full responsibility for the content of the publication.

## DECLARATION OF COMPETING INTEREST

The authors declare that they have no known competing financial interests or personal relationships that could have appeared to influence the work reported in this paper.

## ACKNOWLEDGEMENTS

This study was funded by the Deutsche Forschungsgemeinschaft e.V. (DFG, German Research Foundation) and carried out within the framework of Research Unit FOR-5134, "Solidification Cracks during Laser Beam Welding: High Performance Computing for High Performance Processing", (Grant No. 434946896). The sponsorship and support are gratefully acknowledged.

The authors gratefully acknowledge the scientific support and HPC resources provided by the Erlangen National High Performance Computing Center (NHR@FAU) of the Friedrich-Alexander-Universität Erlangen-Nürnberg (FAU). The hardware is funded by the German Research Foundation (DFG).

The presented investigations were carried out within the cooperation "Laser Meets Synchrotron" (www.laser-meets-synchrotron.de). The experimental setup and its operation were funded by the Deutsche Forschungsgemeinschaft e.V. (DFG, German Research Foundation) within the framework of the Collaborative Research Centre SFB1120-236616214

“Bauteilpräzision durch Beherrschung von Schmelze und Erstarrung in Produktionsprozessen”. The experiments were carried out in cooperation with Helmholtz-Zentrum Hereon in Hamburg at Beamline P07 of DESY PETRA III as part of proposal BAG-20211050 and we would like to thank F. Beckmann, J. Moosmann and all people involved for their support. Support from the Erlangen Graduate School in Advanced Optical Technologies (SAOT) by the Bavarian State Ministry for Science and Art is also gratefully acknowledged.

Open access funding enabled and organized by Projekt DEAL.

## APPENDIX A: IMPLEMENTATION-DETAILS OF WALBERLA

The second simulation tool is developed on the basis of the high-performance simulation framework WALBERLA combined with the pycodegen family of Python-packages for scientific code generation. WALBERLA [35, 36] is a versatile framework for massively parallel multi-physics simulations. Combining MPI-based distributed memory parallelism with either OpenMP, CUDA, or HIP, it was shown to achieve excellent performance and scalability across a range of applications [48-51].

In this work, two LBM schemes for the hydrodynamics of the melt pool and the overall thermodynamics in the material are combined. In addition, the physical effects of laser absorption, evaporation and Marangoni convection are accounted for by appropriate boundary conditions.

### MELT POOL DYNAMICS

The melt pool dynamics in LBW is essentially described by the incompressible Navier-Stokes equations. In contrast to conventional macroscopic approaches, which discretize these equations directly, the LBM used here uses a mesoscopic description of the melt pool. The LBM is based on the discretization of the Boltzmann equation [34]. The basic equation

$$f_i(\boldsymbol{x} + c_i \Delta t, t + \Delta t) = f_i(\boldsymbol{x}, t) + \Omega_i(\nu, \boldsymbol{x}, t) + F_i(\boldsymbol{x}, t) \tag{2}$$

describes the temporal development of the particle distribution function (PDF) $f_i$ at a grid point $\boldsymbol{x}$ at a time $t$. The discrete velocities $c_i$ of the selected lattice model are defined so that the distance from one point in the grid to the next can be covered within one time step $\Delta t$. $F_i$ represents an external force and $\Omega_i$ describes the collision operator. The collision operator relaxes the distribution functions towards an equilibrium according to the kinematic viscosity $\nu$. The macroscopic quantities density $\rho$ and velocity $\boldsymbol{u}$ can be calculated from the distribution functions $f_i$

$$\rho(\boldsymbol{x}, t) = \sum_i f_i\,(\boldsymbol{x}, t) \qquad\qquad \rho \boldsymbol{u}(\boldsymbol{x}, t) = \sum_i c_i f_i(\boldsymbol{x}, t) \tag{3}$$

A Chapman-Enskog analysis can be used to show that the LBM reproduces the incompressible Navier-Stokes equations in the limiting case of small Mach numbers [34].

Traditionally, the Navier-Stokes equation is applied only in the liquid melt pool. Therefore, a cell type parameter (liquid or solid) is introduced to distinguish whether the melt pool dynamics or a boundary condition is being calculated. The simplest boundary condition is a so-called bounce-back boundary condition, in which the distribution functions flowing into the solid cell are mirrored back to the liquid cell. This procedure corresponds to a no-slip boundary condition, i.e., the melt pool dynamics are entirely suppressed at the melt pool boundary. The bounce-back condition is typically implemented by an if-then-else condition in the innermost loop. This can lead to relatively slow execution speed and a large overhead on current GPU-based computer systems.

In this work, the LBM is extended with the PSM [37], such that the same computation can be performed uniformly without (slow) conditionals throughout the domain. The basic idea is to interpolate the collision operator $\Omega_i$ between the behavior of a liquid and a solid cell through the solid phase fraction of a cell. The modified collision operator is described by

$$\Omega_i(\nu, \boldsymbol{x}, t) = (1 - B)\Omega_i^{\mathrm{f}}(\nu, \boldsymbol{x}, t) + B\Omega_i^{\mathrm{s}}(\boldsymbol{x}, t) \tag{4}$$

with a weighting parameter $B \in [0; 1]$ that represents the solid phase fraction as a linear interpolation between $T_{\mathrm{solidus}}$ and $T_{\mathrm{liquidus}}$. $\Omega_i^{\mathrm{f}}$ describes the cumulant collision operator for the fluid cells [52], and $\Omega_i^{\mathrm{s}}$ the solid collision operator given by

$$\Omega_i^s = \left(f_{\bar{\imath}}(\boldsymbol{x}, t) - f_{\bar{\imath}}^{eq}(\rho, \boldsymbol{u})\right) - \left(f_i(\boldsymbol{x}, t) - f_i^{eq}(\rho, \boldsymbol{u}_s)\right) \tag{5}$$

where $\boldsymbol{u}_s$ describes the velocity of the boundary at the local cell $\boldsymbol{x}$ and $f_i^{\mathrm{eq}}$ the equilibrium value [52]. A positive side effect of the PSM is that no more cell transformations are necessary, since the behavior is controlled by the solid phase fraction.

Free-slip boundaries impose symmetry with respect to the wall-normal direction. This is implemented by negating the PDFs corresponding to velocities normal to the boundary. In addition, no slip boundary conditions are established through the bounce-back method: PDFs streaming into the wall are reflected back into the domain, enforcing zero velocity at the wall. The surface tension force is computed from interfacial tension gradients along the interface that arise due to temperature-dependent variations (Marangoni effect), and is computed via

$$\boldsymbol{F}_{\mathrm{Marangoni}} = \nabla_s \gamma(T), \tag{6}$$

where $\nabla_s$ denotes the surface gradient operator and $\gamma(T)$ is the temperature-dependent surface tension.

## THERMODYNAMICS

The conservation of energy is described by the heat conduction equation. This equation covers the entire energy balance, from heat sources, such as the absorption of the laser, to heat conduction through diffusion and heat sinks, such as evaporation losses. The passive scalar method, a special version of the LBM, is a numerical method to solve this equation [38, 39].

An additional set of distribution functions $h_i$ is defined on the same grid, which is used for melt pool dynamics. These distribution functions are propagated analogously to $f_i$ along discrete grid directions and brought into interaction with each other in a collision step

$$h_i(\boldsymbol{x} + c_i\Delta t, t + \Delta t) = h(\boldsymbol{x}, t) + (1 - \tau_h^{-1}\Delta t)\Phi_i(\boldsymbol{x}, t) \tag{7}$$

with

$$h(\boldsymbol{x}, t) = \frac{\sum_i f_i(\boldsymbol{x},t)h_i(\boldsymbol{x},t)}{\rho(\boldsymbol{x},t)} \quad . \tag{8}$$

Here, $h_i$ represents the distribution function of the specific enthalpy $h$, $\tau_h$ the thermodynamic relaxation parameter and $\Phi_i$ the thermodynamic disequilibrium

$$\Phi_i(\boldsymbol{x}, t) = \frac{c_i - \boldsymbol{u}(\boldsymbol{x},t)}{\rho(\boldsymbol{x},t)c_s^2} \cdot \sum_j c_j f_j(\boldsymbol{x}, t)\Big(h_j(\boldsymbol{x}, t) - h(\boldsymbol{x}, t)\Big). \tag{9}$$

The hydrodynamic quantities $\rho$, $\boldsymbol{u}$ and $f_j$ are taken directly from the LBM, whereby a coupling between melt pool dynamics and thermodynamics takes place. The thermal diffusivity $\alpha$ is related to the thermal relaxation time $\tau_h$ by $\alpha = (\tau_h - 0.5\Delta t)c_s^2$. The specific enthalpy $h$ is converted into the temperature $T$ by

$$T(\boldsymbol{x}, t) = \frac{h(\boldsymbol{x},t)/\rho(\boldsymbol{x},t) - L\big(h(\boldsymbol{x},t)\big)}{c_p} \tag{10}$$

where $c_p$ describes the specific heat capacity, and $L(h)$ the latent heat, which is computed via

$$L\big(h(\boldsymbol{x}, t)\big) = \begin{cases} 0, & h \le h_{\text{solidus}} \\ L_c, & h \ge h_{\text{liquidus}} \\ L_c \frac{h(\boldsymbol{x},t) - h_{\text{solidus}}}{h_{\text{liquidus}} - h_{\text{solidus}}}, & \text{otherwise.} \end{cases} \tag{11}$$

Dirichlet boundary conditions are applied by directly setting all $h_i$ in the respective boundary cells to values corresponding to the enthalpy derived from the target wall temperature. In addition, similar free-slip boundary conditions as for the melt pool dynamics are used.

A decisive advantage of the passive scalar method is its simple implementation and numerical efficiency. It can be based on the existing LBM infrastructure and benefits from its high parallelizability. Due to the regularized approach, the method exhibits improved stability and accuracy. In particular, energy conservation is ensured in contrast to other passive scalar methods, which is crucial for the simulation of thermal processes such as LBW.

## IMPLEMENTATION

The application developed in this work computes in each time step the following steps:

1. Communication of all probability distribution functions (PDFs) $f_i$ and $h_i$ across process boundaries
2. Application of all boundary conditions at the outer boundaries of the simulation domain
3. Execution of thermodynamic LBM (Equation (7))
4. Computation and communication of temperature $T$
5. Application of keyhole pressure and surface tension forces
6. Execution melt pool dynamics LBM (Equation (2))

This approach enables a numerically efficient representation of LBW, capturing key effects such as melt pool convection, solidification, and surface-driven flows.

The implementation utilizes the distributed block-structured domain partitioning and field data structures provided by WALBERLA, as well as its MPI-based data synchronization engine. The described numerical schemes for melt pool dynamics and thermodynamics are implemented on a D3Q19 stencil by the domain-specific languages and code generation capabilities of pystencils [40, 41] and lbmpy [42-44]. The PSM is integrated into to the LBM using an algebraic procedure adapted from [53]. Further supporting operations, such as the computation of boundary conditions, are implemented entirely as symbolic equations. The numerical methods are defined in Python-scripts which are executed during the application build process. At that time, highly optimized target-specific implementations of the numerical kernels are automatically generated from their algebraic descriptions. Hiding the platform and optimization details inside the code generator ensures a significant level of hardware and performance portability. The code generation process is facilitated by a novel toolchain based on the metaprogramming tool pystencils-sfg[6]. Kernels, wrapped into classes adhering to the algorithmic idioms expected by WALBERLA, are thus emitted to C++ source files, which are then compiled alongside the conventionally programmed framweork. This process is illustrated in Fig. 8.

[6] i10git.cs.fau.de/pycodegen/pystencils-sfg

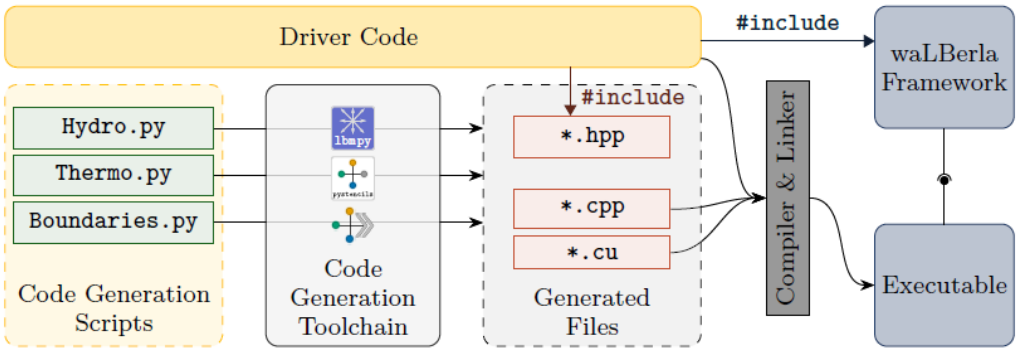



**Fig. 8** Components and build flow of the waLBerla-based application

## DATA AVAILABILITY

Data will be made available on request.

## References

[1] A. KLIMPEL: 'Review and Analysis of Modern Laser Beam Welding Processes', *Materials* 17 (2024) 4657, https://doi.org/10.3390/ma17184657.

[2] W. PUMPHREY: 'A Consideration of the Nature of Brittleness at Temperatures Above the Solidus in Castings and Welds in Aluminium Alloys', *J. of the Inst. Of Metals* 75 (1948), 235-256.

[3] W. R. APBLETT, W. S. PELLINI: 'Factors which influence weld hot cracking', *Welding J. (N.Y.)* Vol: 33 (1954), https://www.osti.gov/biblio/4389407 (accessed August 27, 2025).

[4] J. C. BORLAND: 'Generalized theory of super-solidus cracking in welds', *Br. Weld. J.* 7 (1960), 508-512.

[5] N. PROKHOROV: 'Resistance to hot tearing of cast metals during solidification', *Russian Castings Production* 2.2 (1962), 172-175.

[6] K. ŁYCZKOWSKA, J. ADAMIEC: 'The Phenomena and Criteria Determining the Cracking Susceptibility of Repair Padding Welds of the Inconel 713C Nickel Alloy', *Materials* 15 (2022), 634. https://doi.org/10.3390/ma15020634.

[7] B. FOTOVVATI, S. WAYNE, G. LEWIS, E. ASADI: 'A Review on Melt-Pool Characteristics in Laser Welding of Metals', *Advances in Materials Science and Engineering* 2018 (2018), 1-18, https://doi.org/10.1155/2018/4920718.

[8] K. SCHRICKER, L. SCHMIDT, H. FRIEDMANN, C. DIEGEL, M. SEIBOLD, P. HELLWIG, F. FRÖHLICH, J. P. BERGMANN, F. NAGEL, P. KALLAGE, A. RACK, H. REQUARDT, Y. CHEN: 'Characterization of keyhole dynamics in laser welding of copper by means of high-speed synchrotron X-ray imaging', *Procedia CIRP* 111 (2022), 501-506, https://doi.org/10.1016/j.procir.2022.08.079.

[9] T. KLEIN, M. VICANEK, J. KROOS, I. DECKER, G. SIMON: 'Oscillations of the keyhole in penetration laser beam welding', *J. Phys. D: Appl. Phys.* 27 (1994) 2023, https://doi.org/10.1088/0022-3727/27/10/006.

[10] N. KOURAYTEM, X. LI, R. CUNNINGHAM, C. ZHAO, N. PARAB, T. SUN, A. D. ROLLETT, A. D. SPEAR, W. TAN: 'Effect of Laser-Matter Interaction on Molten Pool Flow and Keyhole Dynamics', *Phys. Rev. Appl.* 11 (2019), 064054, https://doi.org/10.1103/PhysRevApplied.11.064054.

[11] W. KURZ: 'Solidification Microstructure-Processing Maps: Theory and Application', *Advanced Engineering Materials* 3 (2001), 443-452, https://doi.org/10.1002/1527-2648(200107)3:7%3C443::AID-ADEM443%3E3.0.CO;2-W.

[12] F. KAUFMANN, C. FORSTER, M. HUMMEL, A. OLOWINSKY, F. BECKMANN, J. MOOSMANN, S. ROTH, M. SCHMIDT: 'Characterization of Vapor Capillary Geometry in Laser Beam Welding of Copper with 515 nm and 1030 nm Laser Beam Sources by Means of In Situ Synchrotron X-ray Imaging', *Metals* 13 (2023), 135, https://doi.org/10.3390/met13010135.

[13] M. HUMMEL, A. HÄUSLER, S. HOLLATZ, C. HAGENLOCHER, U. HALM, C. SCHÖLER, A. OLOWINSKY, A. GILLNER: 'Temporally and spatially highly resolved reconstruction of vapor capillary geometry during laser beam welding using synchrotron radiation', *Lasers in Manufacturing Conference* 2021, (2021).

[14] C. FORSTER, R. ROTHFELDER, P. KRAKHMALEV, C. SPURK, M. HUMMEL, A. OLOWINSKY, F. BECKMANN, J. MOOSMANN, M. SCHMIDT: 'Unveiling thermo-fluid dynamic phenomena in laser beam welding', *PAMM* 24 (2024), e202400194, https://doi.org/10.1002/pamm.202400194.

[15] C. FORSTER, M. DÖRING, C. SPURK, M. HUMMEL, A. OLOWINSKY, F. BECKMANN, J. MOOSMANN, M. SCHMIDT: 'In-situ observation of end crater crack mechanisms in AA7075 during laser beam welding using synchrotron radiation', *Procedia CIRP* 124 (2024), 464-467, https://doi.org/10.1016/j.procir.2024.08.154.

[16] Y. AI, P. JIANG, X. SHAO, P. LI, C. WANG: 'A three-dimensional numerical simulation model for weld characteristics analysis in fiber laser keyhole welding', *International Journal of Heat and Mass Transfer* 108 (2017), 614-626, https://doi.org/10.1016/j.ijheatmasstransfer.2016.12.034.

[17] Y. AI, P. JIANG, X. SHAO, P. LI, C. WANG, G. MI, S. GENG, Y. LIU, W. LIU: 'The prediction of the whole weld in fiber laser keyhole welding based on numerical simulation', *Applied Thermal Engineering* 113 (2017), 980-993, https://doi.org/10.1016/j.applthermaleng.2016.11.050.

[18] T. YU, J. ZHAO: 'Quantitative simulation of selective laser melting of metals enabled by new high-fidelity multiphase, multiphysics computational tool', *Computer Methods in Applied Mechanics and Engineering* 399 (2022), 115422, https://doi.org/10.1016/j.cma.2022.115422.

[19] M. SCHRETER-FLEISCHHACKER, N. MUCH, P. MUNCH, M. KRONBICHLER, W. A. WALL, C. MEIER: 'A consistent diffuse-interface finite element approach to rapid melt–vapor dynamics with application to metal additive manufacturing', *Computer Methods in Applied Mechanics and Engineering* 442 (2025), 117985, https://doi.org/10.1016/j.cma.2025.117985.

[20] M. COURTOIS, M. CARIN, P. L. MASSON, S. GAIED, M. BALABANE: 'A new approach to compute multi-reflections of laser beam in a keyhole for heat transfer and fluid flow modelling in laser welding', *J. Phys. D: Appl. Phys.* 46 (2013), 505305, https://doi.org/10.1088/0022-3727/46/50/505305.

[21] T. F. FLINT, L. SCOTTI, H. C. BASOALTO, M. C. SMITH: 'A thermal fluid dynamics framework applied to multi-component substrates experiencing fusion and vaporisation state transitions', *Commun. Phys.* 3 (2020), 196, https://doi.org/10.1038/s42005-020-00462-7.

[22] T. F. FLINT, J. D. ROBSON, G. PARIVENDHAN, P. CARDIFF: 'laserbeamFoam: Laser ray-tracing and thermally induced state transition simulation toolkit', *SoftwareX* 21 (2023), 101299, https://doi.org/10.1016/j.softx.2022.101299.

[23] W. TAN, Y. C. SHIN: 'Analysis of multi-phase interaction and its effects on keyhole dynamics with a multi-physics numerical model', *J. Phys. D: Appl. Phys.* 47 (2014), 345501, https://doi.org/10.1088/0022-3727/47/34/345501.

[24] C. ZENZ, M. BUTTAZZONI, T. FLORIAN, K.E. CRESPO ARMIJOS, R. GÓMEZ VÁZQUEZ, G. LIEDL, A. OTTO: 'A compressible multiphase Mass-of-Fluid model for the simulation of laser-based manufacturing processes', *Computers & Fluids* 268 (2024), 106109, https://doi.org/10.1016/j.compfluid.2023.106109.

[25] F. YANG, X. MENG, S.N. PUTRA, A. ARTINOV, M. BACHMANN, M. RETHMEIER: 'Numerical analysis of the effect of an oscillating metal vapor plume on the keyhole and molten pool behavior during deep penetration laser beam welding', *J. Laser Appl.* 35 (2023), 042041, https://doi.org/10.2351/7.0001094.

[26] D. COVIELLO, A. D'ANGOLA, D. SORGENTE: 'Numerical Study on the Influence of the Plasma Properties on the Keyhole Geometry in Laser Beam Welding', *Front. Phys.* 9 (2022), https://doi.org/10.3389/fphy.2021.754672.

[27] N. SCHELL, A. KING, F. BECKMANN, T. FISCHER, M. MÜLLER, A. SCHREYER: 'The High Energy Materials Science Beamline (HEMS) at PETRA III', *Materials Science Forum* 772 (2014), 57-61, https://doi.org/10.4028/www.scientific.net/MSF.772.57.

[28] T. STAUDT, E. ESCHNER, F. TENNER, M. SCHMIDT: 'Deriving spectral information upon the laser welding process employing a hyperspectral imaging technique', *Procedia CIRP* 74 (2018), 636-639, https://doi.org/10.1016/j.procir.2018.08.061.

[29] A. ZAKIROV, S. BELOUSOV, M. BOGDANOVA, B. KORNEEV, I. ISKANDAROVA, A. PEREPELKINA, B. POTAPKIN, 'KiSSAM: efficient simulation of melt pool dynamics during PBF using GPUs', *Prog. Addit. Manuf.* 9 (2024), 1491-1508, https://doi.org/10.1007/s40964-023-00561-1.

[30] D.S. NAKAPKIN, A.V. ZAKIROV, S.A. BELOUSOV, M.V. BOGDANOVA, B.A. KORNEEV, A.E. STEPANOV, A.Y. PEREPELKINA, V.D. LEVCHENKO, A. MESHKOV, 'Finding optimal parameter ranges for laser powder bed fusion with predictive modeling at mesoscale', *2nd International Conference on Simulation for Additive Manufacturing* (2019), 297-308.

[31] B. KORNEEV, A. ZAKIROV, M. BOGDANOVA, S. BELOUSOV, A. PEREPELKINA, I. ISKANDAROVA, B. POTAPKIN, 'A numerical study of powder wetting influence on the morphology of laser powder bed fusion manufactured thin walls', *Additive Manufacturing* 74 (2023), 103705, https://doi.org/10.1016/j.addma.2023.103705.

[32] M. BOGDANOVA, S. CHERNYSHIKHIN, A. ZAKIROV, B. ZOTOV, L. FEDORENKO, S. BELOUSOV, A. PEREPELKINA, B. KORNEEV, M. LYANGE, I. PELEVIN, I. ISKANDAROVA, E. DZIDZIGURI, B. POTAPKIN, A. GROMOV, 'Mesoscale Simulation of Laser Powder Bed Fusion with an Increased Layer Thickness for AlSi10Mg Alloy', *Journal of Manufacturing and Materials Processing* 8 (2024) 7, https://doi.org/10.3390/jmmp8010007.

[33] A. ZAKIROV, S. BELOUSOV, M. BOGDANOVA, B. KORNEEV, A. STEPANOV, A. PEREPELKINA, V. LEVCHENKO, A. MESHKOV, B. POTAPKIN: 'Predictive modeling of laser and electron beam powder bed fusion additive manufacturing of metals at the mesoscale', *Additive Manufacturing* 35 (2020), 101236, https://doi.org/10.1016/j.addma.2020.101236.

[34] T. KRÜGER, H. KUSUMAATMAJA, A. KUZMIN, O. SHARDT, G. SILVA, E.M. VIGGEN: 'The Lattice Boltzmann Method: Principles and Practice', *Springer International Publishing*, Cham, 2017, https://doi.org/10.1007/978-3-319-44649-3.

[35] M. BAUER, S. EIBL, C. GODENSCHWAGER, N. KOHL, M. KURON, C. RETTINGER, F. SCHORNBAUM, C. SCHWARZMEIER, D. THÖNNES, H. KÖSTLER, U. RÜDE: 'waLBerla: A block-structured high-performance framework for multiphysics simulations', *Computers & Mathematics with Applications* 81 (2021) 478-501, https://doi.org/10.1016/j.camwa.2020.01.007.

[36] CHAIR FOR SYSTEM SIMULATION, 'waLBerla (widely applicable Lattice Boltzmann from Erlangen)', (2025), https://doi.org/10.5281/zenodo.16760078.

[37] D. R. NOBLE, J. R. TORCZYNSKI: 'A Lattice-Boltzmann Method for Partially Saturated Computational Cells', *Int. J. Mod. Phys. C* 09 (1998), 1189-1201, https://doi.org/10.1142/S0129183198001084.

[38] R. ZHANG, H. FAN, H. CHEN: 'A lattice Boltzmann approach for solving scalar transport equations', *Phil. Trans. R. Soc. A.* 369 (2011), 2264-2273, https://doi.org/10.1098/rsta.2011.0019.

[39] M. MARKL, A. M. RAUSCH, V. E. KÜNG, C. KÖRNER: 'SAMPLE: A Software Suite to Predict Consolidation and Microstructure for Powder Bed Fusion Additive Manufacturing', *Advanced Engineering Materials* 22 (2020), 1901270, https://doi.org/10.1002/adem.201901270.

[40] M. BAUER, J. HÖTZER, D. ERNST, J. HAMMER, M. SEIZ, H. HIERL, J. HÖNIG, H. KÖSTLER, G. WELLEIN, B. NESTLER, U. RÜDE: 'Code generation for massively parallel phase-field simulations', in: *Proceedings of the International Conference for High Performance Computing*, Networking, Storage and Analysis, ACM, Denver Colorado, 2019, pp. 1-32. https://doi.org/10.1145/3295500.3356186.

[41] CHAIR FOR SYSTEM SIMULATION (Friedrich-Aalexander-Universität Erlangen-Nürnberg), 'pystencils', (2024), https://doi.org/10.5281/zenodo.15276904.

[42] M. BAUER, H. KÖSTLER, U. RÜDE: 'lbmpy: Automatic code generation for efficient parallel lattice Boltzmann methods', *Journal of Computational Science* 49 (2021), 101269, https://doi.org/10.1016/j.jocs.2020.101269.

[43] F. HENNIG, M. HOLZER, U. RÜDE: 'Advanced Automatic Code Generation for Multiple Relaxation-Time Lattice Boltzmann Methods', *SIAM J. Sci. Comput.* 45 (2023), C233-C254, https://doi.org/10.1137/22M1531348.

[44] CHAIR FOR SYSTEM SIMULATION (Friedrich-Alexander-Universität Erlangen-Nürnberg), 'lbmpy', (2024), https://doi.org/10.5281/zenodo.15277053.

[45] J. GÖTZ, K. IGLBERGER, C. FEICHTINGER, S. DONATH, U. RÜDE: 'Coupling multibody dynamics and computational fluid dynamics on 8192 processor cores', *Parallel Computing* 36 (2010), 142-151, https://doi.org/10.1016/j.parco.2010.01.005.

[46] A. KLASSEN, T. SCHAROWSKY, C. KÖRNER: 'Evaporation model for beam based additive manufacturing using free surface lattice Boltzmann methods', *J. Phys. D: Appl. Phys.* 47 (2014), 275303. https://doi.org/10.1088/0022-3727/47/27/275303.

[47] J. TRAPP, A.M. RUBENCHIK, G. GUSS, M.J. MATTHEWS: 'In situ absorptivity measurements of metallic powders during laser powder-bed fusion additive manufacturing', *Applied Materials Today* 9 (2017), 341-349, https://doi.org/10.1016/j.apmt.2017.08.006.

[48] M. HOLZER, M. BAUER, H. KÖSTLER, U. RÜDE: 'Highly efficient lattice Boltzmann multiphase simulations of immiscible fluids at high-density ratios on CPUs and GPUs through code generation', *The International Journal of High Performance Computing Applications* 35 (2021), 413-427, https://doi.org/10.1177/10943420211016525.

[49] M. HOLZER, G. STAFFELBACH, I. ROCCHI, J. BADWAIK, A. HERTEN, R. VAVRIK, O. VYSOCKY, L. RIHA, R. CUIDARD, U. RÜDE: 'Scalable Flow Simulations with the Lattice Boltzmann Method', in: *Proceedings of the 20th ACM International Conference on Computing Frontiers*, Association for Computing Machinery, New York, NY, USA, 2023, pp. 297-303, https://doi.org/10.1145/3587135.3592176.

[50] H. SCHOTTENHAMML, A. ANCIAUX SEDRAKIAN, F. BLONDEL, H. KÖSTLER, U. RÜDE: 'waLBerla-wind: A lattice-Boltzmann-based high-performance flow solver for wind energy applications', *Concurrency and Computation: Practice and Experience* 36 (2024), e8117, https://doi.org/10.1002/cpe.8117.

[51] M. HOLZER: 'Code generation in a lattice Boltzmann framework for exascale computing', 2025, https://open.fau.de/handle/openfau/33506 (accessed January 15, 2025).

[52] M. GEIER, M. SCHÖNHERR, A. PASQUALI, M. KRAFCZYK: 'The cumulant lattice Boltzmann equation in three dimensions: Theory and validation', *Computers & Mathematics with Applications* 70 (2015), 507-547, https://doi.org/10.1016/j.camwa.2015.05.001.

[53] S. KEMMLER, C. RETTINGER, U. RÜDE, P. CUÉLLAR, H. KÖSTLER: 'Efficiency and scalability of fully-resolved fluid-particle simulations on heterogeneous CPU-GPU architectures', (2024), https://doi.org/10.48550/arXiv.2303.11811.

# NUMERICAL SIMULATION OF LASER BEAM WELDING WITH DYNAMIC BEAM SHAPE SEQUENCING

C. DURÁN*,[1], C. ZENZ*, T. FLORIAN*, M. BUTTAZZONI*, A. OTTO*

**TU Wien, Institute of Production Engineering and Photonic Technologies, 1060, Vienna, Austria*
*[1]Corresponding author*

*DOI 10.3217/978-3-99161-089-2-010, license CC BY 4.0*
*https://creativecommons.org/licenses/by/4.0/deed.en*
*This CC license does not apply to third party material and content noted otherwise.*

## ABSTRACT

Dynamic beam shaping enables diverse possibilities to influence the performance of laser-based manufacturing processes, for example by tailoring the spatial intensity distribution of light in real time. One such possibility is shape sequencing, which involves switching between two or more beam shapes during laser-matter interaction, with each shape being active for a specified time frame (shape duration) within the sequence. When properly understood and utilized, shape sequencing could serve as an effective optimization approach in high-power laser materials processing applications such as Laser Beam Welding (LBW).

In this work, a multi-physical simulation model is used as a comprehensive framework to evaluate the impact of shape duration on the dynamics of the LBW process, with the aim of mitigating instabilities that can lead to defects such as pores, spatter, lack of penetration, cracks, etc. The long-term goal is not only to identify optimal welding parameters, but also to understand why certain shaping strategies lead to better or worse process outcomes. As a demonstration, an aluminum-magnesium alloy is chosen as the workpiece material for a deep penetration welding (DPW) scenario. The numerical model is initially validated by comparing simulation results with macrographs of experimentally produced welds and is subsequently used to analyze a welding setup incorporating dynamic beam shape sequencing. The study reveals that shape sequencing can effectively induce vibrations at predefined frequencies on the keyhole surface, manifesting as periodic pulses whose width is determined by the shape durations. This pulsed excitation is subsequently transmitted to the melt pool, influencing its behavior. Certain shape durations favor a more or less effective excitation of the melt pool.

Keywords: dynamic beam shaping, shape sequencing, shape duration, frequency analysis, multi-physical model

## INTRODUCTION

In addition to adjusting process variables such as beam power, feed rate, weld path, or focus position, modulating the properties of the laser beam opens up an even wider range of parameter configurations that may help achieve targeted key performance indicators (KPIs) of the welding process. This approach, referred to as beam shaping, can be implemented by means of various methods and technologies. Schmidt et al. [1] categorize beam shaping into three types: spatial, temporal, and polarizational. Spatial beam shaping involves using shaping devices to produce a specific intensity and/or phase distribution at the workpiece after the beam propagates through free space. Temporal beam shaping refers to the modulation of the wave phase (instantaneous frequency) or amplitude (power) over time. Polarizational beam shaping modifies the polarization state of light using optical elements such as half-wave or quarter-wave plates. A central aspect highlighted in [1] is that, regardless of the beam shaping method or technology, the interaction between a moving laser beam and the material always results in dynamic energy coupling. Therefore, it is crucial that the laser beam interacts with the material within a suitable time frame that can meaningfully influence the welding process or any of its mutually dependent subprocesses.

From a technological perspective, the spatial, temporal, or polarization properties of light can be modulated in an initial step and then remain constant throughout material processing, which is commonly referred to as static beam shaping. However, they can also be modulated "on the fly" and repeatedly during processing, which is referred to here as dynamic beam shaping. This work explores dynamic beam shaping based on Civan's coherent beam combining (CBC) proprietary technology [2], which enables both spatial and temporal modulation of light. For CBC beams, Weber et al. [3] proposed an additional classification by comparing the "relevant time" of the process (or subprocess), referred to therein as the process time constant, with the time(s) determined by the motion of the heat source. In this context, the laser-matter interaction regime is considered quasi-static when the beam moves faster than the response time of a particular physical process, causing the material to experience a temporally and spatially averaged influence of the heat source; dynamic when the beam motion occurs over a time significantly longer than the relevant process timescale; and resonant when the beam motion occurs over a time approximately equal to the characteristic process time.

Building on this, a reasonable follow-up step is to identify the characteristic timescales or frequencies of the subprocesses in LBW and to determine how this information can guide the selection of beam shaping parameters that effectively operate on one or more of these subprocesses to achieve improved welding results. Depending on the technology, beam shaping can involve several independently adjustable parameters, i.e., multiple degrees of freedom, that define the behavior of the laser heat source and, therefore, the process outcome. While this offers great versatility, the complexity of the highly dynamic and interdependent physical interactions during welding makes it difficult to recognize the precise role of each individual shaping parameter in the mechanisms governing weld attributes.

For Civan's CBC technology, experimental studies have been recently conducted to evaluate the impact of different shaping parameters on the welding process. Dittrich et al. [4] performed bead-on-plate (BoP) welding tests on oxide-free copper using 18 beam shapes with

shape frequencies between 0.1 and 300 kHz, at a fixed power and feed rate of 6 kW and 6 m $min^{-1}$, respectively. It was observed that, in the considered process window, simpler shapes such as spots, short lines or small rings, produced better weld quality at different frequencies than larger and more complex shapes. Sawannia et al. [5] investigated the influence of switching frequency (shape duration) when sequencing between a single spot and four spots during welding of AISI 304 stainless steel plates (5 mm thickness), at a welding speed of 6 m $min^{-1}$ and power of 5 kW. They tested switching frequencies of 0.01, 0.1, 1, and 10 kHz (corresponding to shape durations of 100, 10, 1, and 0.1 ms, respectively) and identified a clear process response to shape sequencing for durations larger than 10 ms. Prieto et al. [6] analyzed the influence of beam shape, feed rate, and shape frequency on overlap welding of 0.8-mm-thick AA3003 aluminum alloy sheets using input powers between 2.4 and 3.6 kW. They found that infinity and spiral shape patterns yielded satisfactory results in terms of interface width, penetration, and interface defects when using shape frequencies above 10 kHz at feed rates up to 18 m $min^{-1}$. Olschok et al. [7] carried out BoP tests on 8-mm-thick AH36 steel at a speed of 1.2 m $min^{-1}$. A single-point fixed pattern and three dynamic shapes at frequencies of 0.1 and 100 kHz were tested, all achieving full penetration with powers between 10 and 13 kW. The authors reported that shape frequency strongly influenced the melt pool geometry and resulting weld bead. At 100 kHz, the melt pool became narrower and longer. At 0.1 kHz, the welds produced by the dynamic shapes were similar in geometry and microstructure to the weld produced by the single-point pattern, whereas at 100 kHz, the cross sections showed a markedly different geometry and coarser grains.

Although an impact of dynamic beam shaping on the LBW process can be demonstrated experimentally, as in the examples above, deeper understanding of the specific effects of individual parameters is difficult to obtain through experimentation alone. In this regard, numerical simulation becomes an essential tool for advancing knowledge about the capabilities of different beam shaping strategies with respect to welding process optimization. As an application example, this work investigates one specific shaping parameter from Civan's CBC technology: the switching frequency (or shape duration) during sequencing of two shapes. Numerical simulations using the multiphase Mass-of-Fluid model described in [8] are conducted to gain insights into the effect of this parameter on the welding process. A 5xxx series aluminum-magnesium alloy is selected for the study, focusing on full penetration welds in a BoP configuration with 6 mm thick plates. This alloy series is widely used in aerospace, transportation, and construction owing to their low density, cost-effectiveness, high specific strength, good ductility and toughness, and excellent machinability, weldability, and corrosion resistance [9]. Defects such as pores and cracks are among the main challenges in LBW of such alloys [10].

The first part of this work provides a brief description of the numerical model, with an emphasis on the simulation aspects relevant to this practical application. It includes an overview of the laser heat source and its technology-specific shaping parameters. To ensure the simulation study is conducted within a sufficiently robust numerical framework, the model is validated by comparing simulation results with macrographic cross-section images for two significantly different parameter sets. Using the validated model, sequencing with beam shapes symmetrical about the process mid-plane is simulated with different symmetrical-in-time durations, i.e., identical durations for each shape, to evaluate the effect of this single

parameter on the welding process. The results are presented and discussed in the final part of the document, with the aim of identifying and explaining the main effects of shape duration and the specific shaping strategy on the process outcome, as well as their potential relationship with system dynamics.

## NUMERICAL MODEL AND SIMULATION SETUP

The selected beam shaping strategy was investigated through one-pass BoP welding simulations of 5083 aluminum-magnesium alloy, employing a multi-physical numerical model custom-built within the OpenFOAM® architecture (Open Field Operation and Manipulation) [11], where the systems of coupled partial differential equations are solved via the Finite Volume Method (FVM). Originally introduced over a decade ago [12-13], the model has since been turned into a universal framework capable of simulating various scenarios of laser-based manufacturing both in the domains of micro- and macro-processing [14]. Fig. 1 exemplarily shows one of the deep penetration welding (DPW) processes simulated within this study, highlighting some of the key features captured by the simulation model.

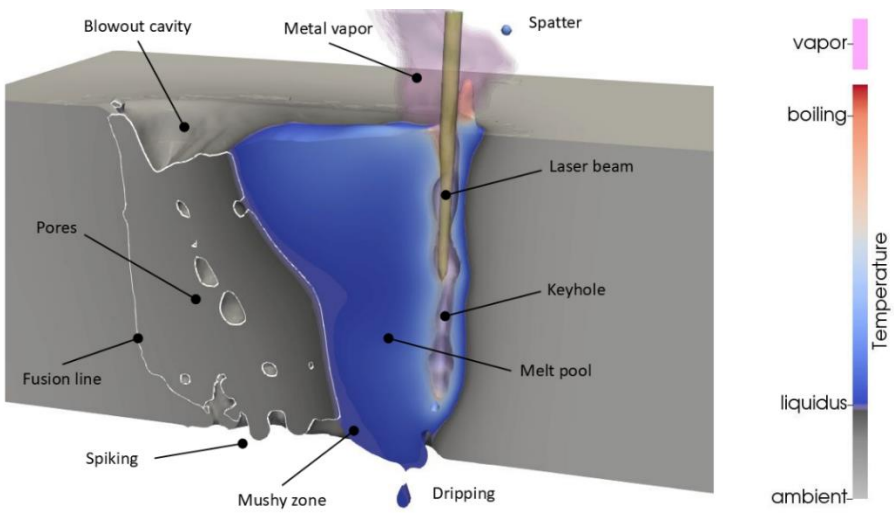



**Fig. 1** Longitudinal clip of the simulated LBW process in a 9 mm-thick 5083 aluminum plate

The model itself was recently described in detail and rigorously validated by Zenz et al. [8]; hence, the reader is referred to [8] for a comprehensive list of underlying assumptions, governing equations, numerical implementation details, and validation results for different materials and process regimes relevant to laser beam welding. Instead of the widely used Volume-of-Fluid (VoF) method, it employs the so-called Mass-of-Fluid (MoF) method, in which the mass and energy of each phase are directly tracked through conservation equations,

yielding an inherently mass- and energy-conservative framework, even across phase-change events and throughout compressible scenarios.

Gaseous phases are included in the modeling domain and, in contrast to virtually all other published models, evaporation and condensation rates are formulated as pressure-dependent, with the local pressure on the gaseous side of the liquid-vapor interface taken into account to yield accurate, dynamic rates of evaporation and condensation. Furthermore, the recoil pressure resulting from newly formed and expanding vapor acting on condensed matter is a direct result of the compressible multiphase formulation including gaseous matter; hence, as opposed to most published approaches, no simplified recoil pressure model is necessary.

Consequently, the MoF-based framework offers strong predictive capabilities for highly dynamic events in laser-material processing, with no need for calibration to a specific scenario (unlike models that neglect pressure-dependent evaporation and condensation), as recently demonstrated by Zenz et al. [15]. On this basis, it is particularly well-suited to reproduce and analyze transient system behavior and the resulting process characteristics under temporally and spatially modulated laser intensity distributions, including the low- and high-frequency response of the system to such modulation. By accounting for local gas-side pressure variations and their dependence on laser irradiation, as well as the topological constraints affecting the transport of newly formed vapor out of the laser irradiation zone, no process-, time- or space-dependent evaporation efficiency is required to capture the resulting non-equilibrium state of evaporation and condensation. Further details and a rigorous comparison of the compressible multiphase MoF model with a simulation model omitting pressure dependence in evaporation and condensation are provided in [15].

While the underlying physics are formulated in a general manner and are universally applicable to many laser-based manufacturing processes, the model requires material properties, process parameters, geometry, and initial and boundary conditions as inputs, just as in real-life applications. The following subsections focus on these parameters.

### General aspects of the simulation setup

For the BoP welding configuration, Fig. 2 shows a schematic of the computational domain, which consists of the 5083-alloy workpiece and upper and lower layers of still air at 1 atm as the surrounding gas. Appendix I lists the temperature-dependent material properties used in the simulations for both the aluminum–magnesium alloy and air. Where no literature data were available for the specific alloy, values for pure aluminum were assumed.

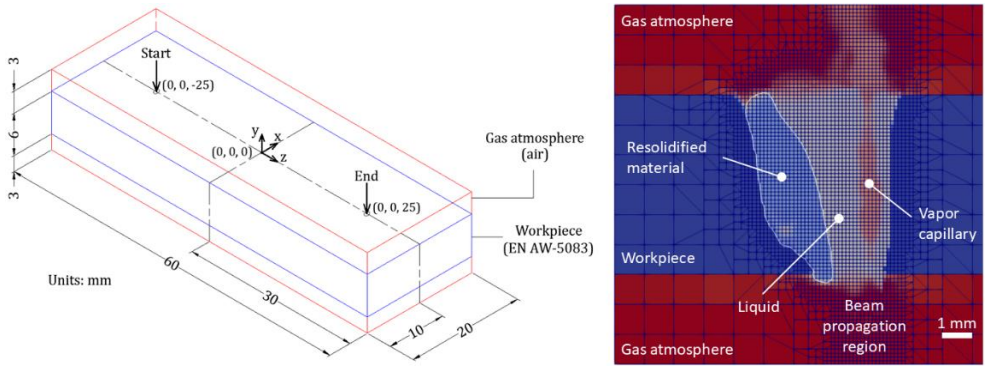



**Fig. 2** Dimensions of the computational domain (left) and mesh (right), with refinement in regions corresponding to beam propagation, liquid, and resolidified material phases

The initial mesh comprises cubic cells of 1 mm side length, distributed uniformly across the computational domain. Dynamic mesh refinement is employed, with a maximum of three refinement levels, resulting in the smallest cell elements having a side length of 125 µm. A portion of the mesh longitudinal section is also included in Fig. 2. The computational time step was adapted according to the Courant–Friedrichs–Lewy (CFL) condition, with a maximum value limited to 0.5 in the present simulations. An upper bound of 3 µs was further imposed on the time step, selected based on the lifetime of a single CBC point of the dynamic shapes employed (see Table 1 in next section). The workpiece boundaries were set to a fixed velocity of (0, 0, 0) and a zero-gradient condition for temperature, while the atmosphere boundaries were assigned a zero-gradient condition for velocity and an inlet/outlet condition for temperature.

In the computational domain, the coordinate system is located at the top of the workpiece. The arrows indicate the start and end positions of the laser's linear path, with the beam oriented perpendicular to the workpiece. The geometry was chosen to be sufficiently large to allow the process to reach a quasi-steady state. An important aspect of the chosen geometry is that no process symmetry is assumed, i.e., the entire weld bead is simulated. This allows, on one hand, modelling the specific shaping strategy analyzed, namely side-by-side shape sequencing, and, on the other hand, capturing asymmetric phenomena, such as the alternating lateral movement of the melt pool, that would be missed if symmetry conditions were assumed.

## HEAT SOURCE AND PROCESS PARAMETERS

Beam shaping is applied using Civan's Dynamic Beam Laser (DBL), which integrates Coherent Beam Combining (CBC) and Optical Phased Array (OPA) technologies. CBC takes a seed laser input, splits it, and amplifies it in parallel across multiple channels before recombining them coherently to produce a single high-power, high-quality beam. OPA controls the phase of each element in a 2D array, allowing the output beam to be shaped and steered arbitrarily without moving parts. Together, CBC maximizes power, while OPA

provides precise control over beam shape and direction [2]. The principle of operation of the DBL, as well as a detailed description of the shaping parameters, can be found in [3]. The beam shapes used in this study are shown in Fig. 3.

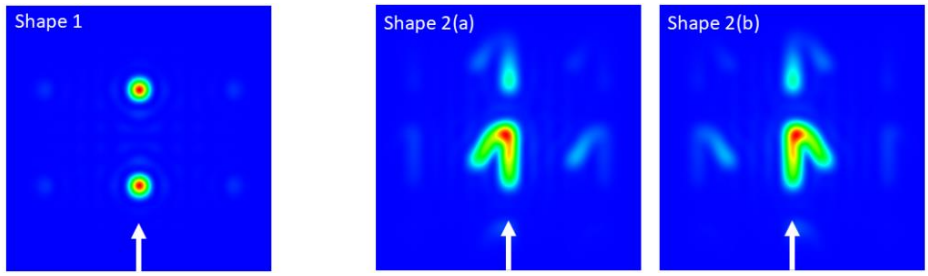



**Fig. 3** Dynamic beam shapes: Shape 1 comprises 2 CBC-points; Shapes 2(a) and 2(b), 22-CBC points each. The white arrow aligns with the weld mid-plane and indicates the feed direction

Each beam shape consists of a sequence of individual CBC points, with only one point active at a time during a shape cycle. Consequently, the patterns observed in Fig. 3 represent the superposition of the focal intensity distributions of all CBC points composing the shape, assuming an infinitely high shape frequency ($f_{SR} \to \infty$). For this study, a main-lobe focal diameter of 85 µm (FWHM) was used, corresponding to a focal length of 1.5 m and a depth of focus of 11.5 mm at a laser wavelength of 1064 nm. At this focal length, the CBC point can cover an area up to 520 µm wide. The main lobe is defined as a single spot at the center of the laser active area. In the numerical model, each CBC point is implemented as a series of two-dimensional arrays describing the intensity distribution at different planes along the propagation direction. Values at out-of-plane positions are linearly interpolated between the two nearest adjacent planes.

Table 1 summarizes the main shaping parameters, following the nomenclature presented in [3], while Table 2 lists the process parameters used for numerical validation (simulations 1a and 1b, based on experiments by Civan) and for examining different switching frequencies when sequencing between Shapes 2(a) and 2(b) (simulations 2a, 2b, and 2c).

**Table 1** Shape parameters

| Shape parameter | Symbol | Shape 1 | Shapes 2(a) and 2(b) |
|---|---|---|---|
| Total number of positions in the shape | $N_{Pos}$ | 2 | 22 |
| Number of set points at the *i*-th position | $N_{C,i}$ | 1 | 1 |
| Total number of points in the shape | $N_{SP} = \sum_{i=1}^{N_{Pos}} N_{C,i}$ | 2 | 22 |
| Shape refresh frequency | $f_{SR}$ | 10 kHz | 15 kHz |
| Point order followed within the shape | - | - | Random |
| Time for drawing the complete shape | $t_{SR} = 1/f_{SR}$ | 100.0 µs | 66.67 µs |
| Lifetime of one single CBC point | $t_{SP} = t_{SR}/N_{SP}$ | 50.0 µs | 3.03 µs |

**Table 2** Process parameter sets

| Parameter | 1a | 1b | 2a, 2b, 2c |
|---|---|---|---|
| Plate thickness | 6 mm | 9 mm | 6 mm |
| Power | 5.5 kW | 9.2 kW | 5.5 KW |
| Feed rate | 35 mm $s^{-1}$ | 60 mm $s^{-1}$ | 35 mm $s^{-1}$ |
| Shape sequencing | No | Yes | Yes |
| Shapes employed | Shape 1 | Shape 2(a)<br>Shape 2(b) | Shape 2(a)<br>Shape 2(b) |
| Shape duration in sequence (switching frequency) † | - | 10 ms (100 Hz) | **2a:** 5 ms (200Hz)<br>**2b:** 10 ms (100 Hz)<br>**2c:** 15 ms (66.67 Hz) |

† The same shape duration applies to Shape 2(a) and Shape 2(b).

## RESULTS AND DISCUSSION

### MODEL VALIDATION

A validation procedure was carried out to ensure that the simulations generated sound numerical results and adequately reflected the process under study, even when performed with widely different parameter sets, namely 1a and 1b. Fig. 4 shows a comparison between the simulation results and experimentally obtained macrographs of the weld cross-sections.

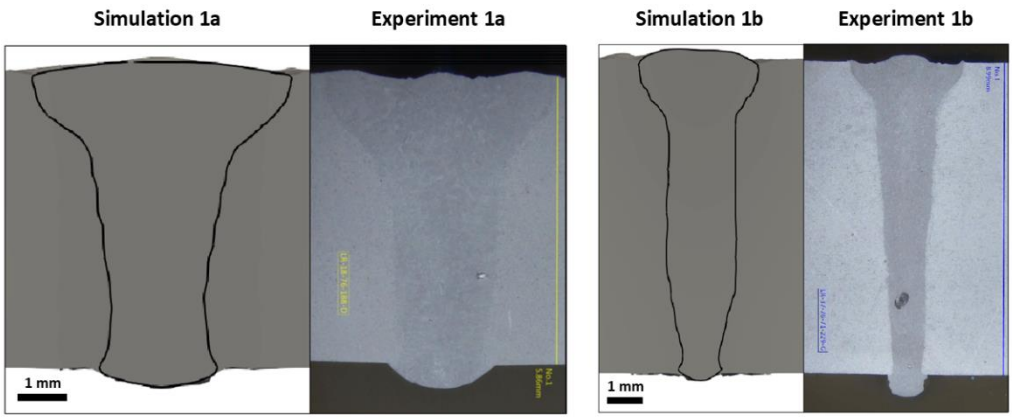



**Fig. 4** Comparison between simulation and experimental results for parameter sets 1a (left) and 1b (right), using cross-sections representative of the process

Despite uncertainties in the material properties, particularly at high temperatures in the liquid state, the simulation results show good agreement with the experimentally obtained

cross-sections. Accuracy can be further improved by increasing the mesh resolution, reviewing the interpolation methods for describing the beam intensity, or performing additional iterations in the identification of thermophysical properties.

For the 9 mm plate, a larger difference is observed between simulation and experiment, mainly in the lower part of the weld bead, where the simulation predicts a wider bead due to more heat reaching the plate's lower section. This discrepancy could be related to a simplified description of the beam intensity distribution along the propagation direction. Although the numerical model is capable of a full three-dimensional description of the caustic, the simulations assumed a constant beam diameter along the plate height, given a depth of focus of 11.5 mm. This simplification appears reasonable for the 6 mm plate, which is the main focus of this study. However, for the 9 mm plate, beam divergence near the lower section can reduce the actual heat input, resulting in a narrower weld.

## WELDING PROCESS EVALUATION

The evaluation of the welding process starts by comparing the influence of the beam shaping parameters on the geometry of the melt pool (~10 mm in length). As shown in Fig. 5, the overall dimensions and shape of the melt pool are very similar across all parameter sets for the 6 mm plate. This is consistent with the fact that the linear heat input (power-to-velocity ratio) is the same for all cases. Furthermore, the lateral asymmetry introduced by the sequencing strategy applied is subtle, since most of the intensity of the half-arrow (see Shapes 2(a) and 2(b) in Fig. 3) is concentrated at the process mid-plane.

Certain features can be identified in the velocity fields included in Fig. 5, which presents exemplary results from Simulation 1a for a plane perpendicular to the laser beam (0.5 mm below the workpiece top surface) and a longitudinal section of the process. In the former, vortices can be observed on each side of the keyhole region, located in the widest part of the melt pool. A high-turbulence region also develops near the necking zone at the rear part of the pool. In the longitudinal view, a clear clockwise recirculation pattern is visible. Despite evolving differently over time, similar flow structures were observed for the parameter sets in which shape sequencing was applied.

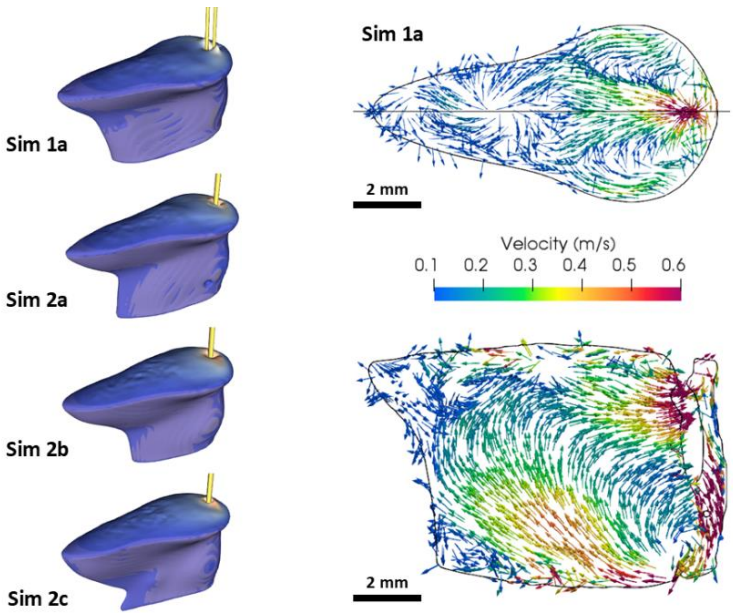



**Fig. 5** Three-dimensional melt pool geometry (left), velocity vectors on a plane perpendicular to the beam (top right), and on the mid-plane (bottom right)

Selected process indicators, including the occurrence of spatter, dripping events, porosity, and keyhole closure events, were examined, and the results are summarized in Fig. 6. For spatter and drips, event monitoring was performed during the simulation with a sampling frequency of at least 333 kHz (corresponding to a computational time step of less than 3 μs), providing very high sensitivity. Only 'macro' droplets with a volume equivalent to that of a sphere with a diameter of minimum 0.15 mm, were considered, as in [16]. Keyhole full closure events were identified based on keyhole aperture measurements at the process mid-plane, 0.5 mm below the workpiece surface. The latter was done in a postprocessing phase, using a sampling frequency of 2 kHz. Porosity was also estimated during postprocessing as the fraction of the bead volume occupied by pores.

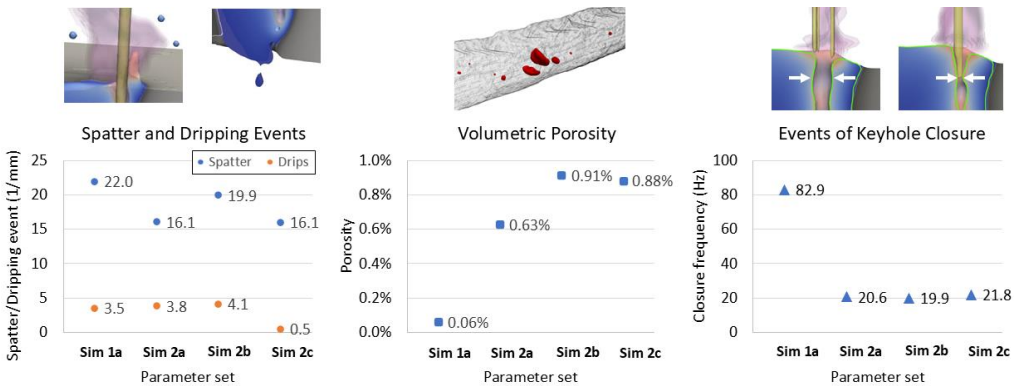



**Fig. 6** Assessment of spatter, dripping, porosity, and keyhole closure

Measurements indicate spatter rates of 16.1-22.0 events per mm of weld (563-770 Hz), while dripping remains lower at 3.5-4.1 events per mm (122-143 Hz), except in Sim 2c, where it was significantly reduced. Among parameter sets 2a to 2c, a shape duration of 10 ms produced the highest spatter rate. Volumetric porosity was lowest for parameter set 1a (2-point shape), at about one-tenth of the porosity obtained for the other parameter sets, where side-by-side sequencing was used. The latter is an important indicator of potential instabilities in the welding process, resulting from the specific shaping strategy and parameters employed. Typical pores for the sequenced shapes at durations of 5, 10, and 15 ms are shown in Fig. 7.

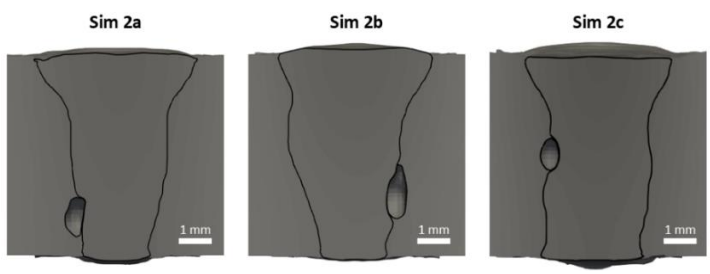



**Fig. 7** Fusion line pores from non-optimal shape durations in side-by-side sequencing

Note the pronounced asymmetry in the bead cross section for the 10 ms shape duration (Sim 2b). This asymmetry appears to promote the formation of a relatively large pore on the opposite side. A comparable, though weaker, effect is observed in the other two cross sections. The pores share similar characteristics, being enlarged and located along the fusion line.

The average keyhole aperture and its standard deviation were estimated as 590 ± 196 µm, 454 ± 155 µm, 418 ± 136 µm, and 449 ± 166 µm for parameter sets 1a, 2a, 2b, and 2c, respectively. These values correspond closely to the maximum displacement of the CBC point for each specific shape pattern, as shown in Fig. 3, where Shape 1 spans a larger distance in the feed direction than Shapes 2(a) or 2(b). Keyhole closure events were observed at a frequency of about 20 Hz for parameter sets 2a to 2c, and about 83 Hz for parameter set 1a.

This relatively large difference can be explained by the behavior of the keyhole along the propagation direction. The leftmost part of Fig. 8 illustrates this, showing a longitudinal clip of the keyhole for both shaping configurations. In the case of the 2-point shape, the measurement routine (due to the way it was implemented) captured not only full keyhole closures but also partial closures, where the path of the rear high-intensity beam is interrupted by molten metal while the leading high-intensity beam continues through the keyhole. The tool for measuring keyhole closure did not account for this specific behavior of the 2-point shape. This situation does not occur with the half-arrow shapes, where only one high-intensity beam is present at a time, accompanied by one or more weaker side maxima depending on the position of the CBC point. When the path of the single high-intensity spot is interrupted, a full closure is very likely to occur.

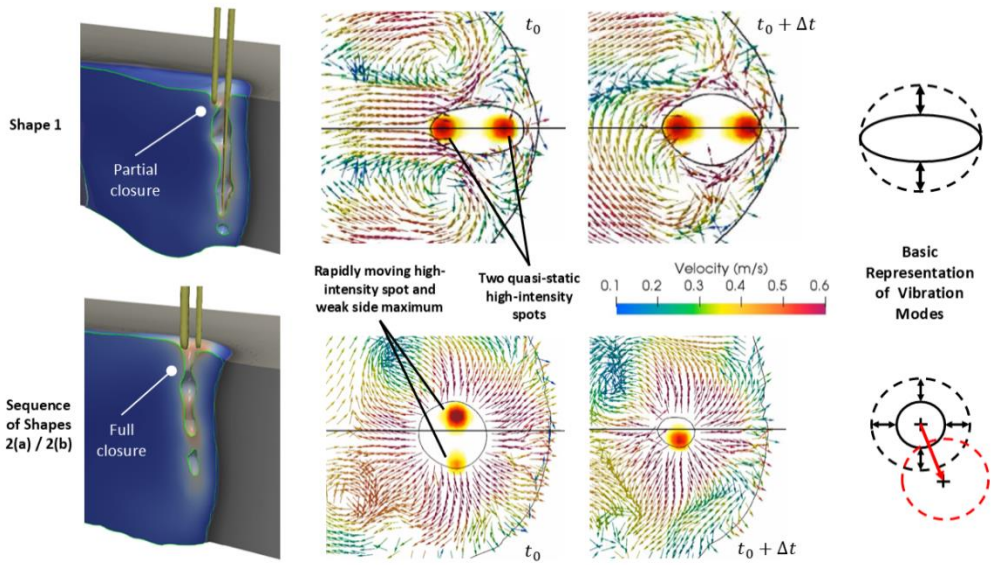



**Fig. 8** Keyhole behavior and vibration modes on a plane perpendicular to beam propagation. The vectors represent the velocity field in the melt pool.

Another interesting observation arises from the behavior of the keyhole in a plane perpendicular to the beam, as shown in the central part of Fig. 8. The keyhole produced by the 2-point shape shows marked differences from that generated by switching between the two half-arrows, in terms of both geometry and vibrational modes, as schematized in the rightmost part of Fig. 8. The modes shown are the most prominent, identified through visual inspection of postprocessed high-resolution simulation videos. The 2-point configuration exhibits a dominant vibration in the transverse direction relative to the feed, where the two high-intensity beams, separated by a constant distance throughout the process, effectively lock the vibration mode in this transverse direction. By contrast, sequencing between two half-arrows results in

a radial vibrational mode, combined with a slight displacement of the keyhole center (exaggerated in Fig. 8), leading to a swaying motion of the keyhole surface.

These findings point to the first important insight: the keyhole exhibits different vibration modes depending on the beam shape and shaping strategy. Therefore, each shaping configuration should be analyzed with respect to its specific vibration modes. In the next subsection, the process dynamics are examined in greater detail.

### INFLUENCE OF SHAPING STRATEGY ON THE WELDING PROCESS

Based on the observed vibrational modes for the shaping configuration with side-by-side sequencing, two sampling points were selected along the process longitudinal plane to monitor the local velocities during welding: $\boldsymbol{v_k}$ at the keyhole wall and $\boldsymbol{v_m}$ at the upper free surface of the melt pool, as shown in Fig. 9. These measurements were used to evaluate how the system responds to different shaping configurations, namely parameter sets 1, 2a, 2b, and 2c. The probe for $\boldsymbol{v_k}$ is at the rear part of the keyhole surface, located 0.5 mm below the workpiece surface, while the probe for $\boldsymbol{v_m}$ is located at the melt free surface, 2 mm behind the moving laser. The velocity measurement was performed at each computational step of the simulation, corresponding to a minimum sampling frequency of 333 kHz.

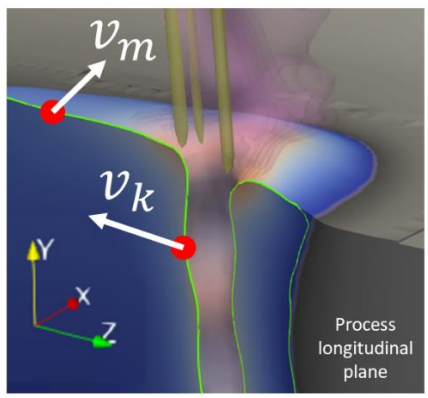



**Fig. 9** Selected probe locations for velocity measurement

After reviewing the different velocity signals obtained at the keyhole, the transverse component with respect to the feed direction, $v_{k,x}$, reveals a particularly interesting behavior, as shown in Fig. 10. When sequencing with two shapes symmetric about the process mid-plane, as in this work, the excitation induced by beam shaping manifests as a pulsed pattern at the keyhole wall, acting in the transverse direction to the feed. The pulse period corresponds to a full sequencing cycle, i.e., the sum of the two shape durations. This is demonstrated in Fig. 10 for all simulations where sequencing was applied. Parameter set 1a, which represents a process-symmetric shape without sequencing, is included for reference.

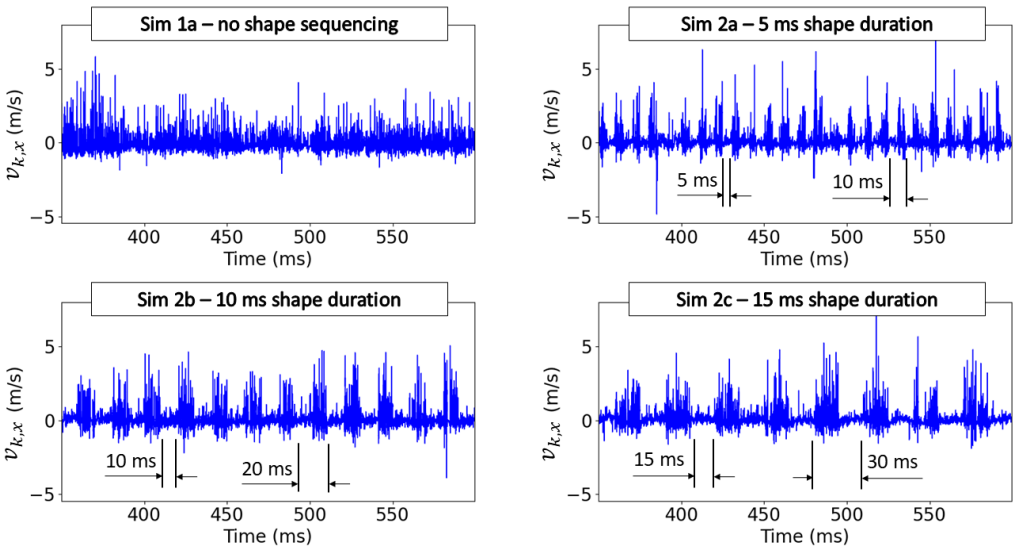



**Fig. 10** Transverse component of the velocity signal at the keyhole, $v_{k,x}$

The nature of the pulses can be understood from the specific beam-shaping strategy applied, exemplified in Fig. 11 with a shape duration of 10 ms.

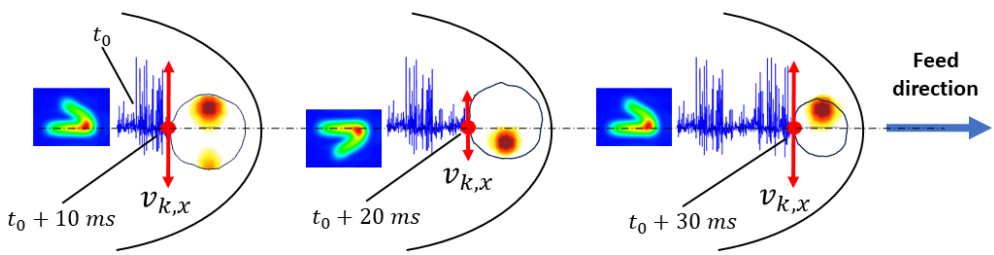



**Fig. 11** Transverse component of the velocity signal at the keyhole, $v_{k,x}$

At time $t = t_0$, the sampling point at the back of the keyhole, initially vibrating at low amplitude, is instantaneously excited by Shape 2(a), inducing a high-amplitude vibration during 10 ms (pulse width). When switching to Shape 2(b), this vibration is effectively cancelled by the opposite excitation, resulting in a relatively calm signal for the next 10 ms. The cycle then repeats. In this case, a complete cycle lasts 20 ms (10 ms + 10 ms), corresponding to a frequency of 50 Hz. For symmetric-in-time sequencing with individual shape durations of 5 and 15 ms, the cycle periods are 10 ms and 30 ms, corresponding to frequencies of 100 Hz and 33.3 Hz, respectively.

The velocity signals from the keyhole wall were further analyzed in the frequency domain using Welch's method [17] to estimate the Power Spectral Density (PSD), which shows the frequencies at which most of the vibration energy is concentrated, making it a useful

complement to the Fast Fourier Transform (FFT) in the identification of dominant frequencies. The results are shown in Fig. 12, where, for each parameter set, both a low-frequency analysis (up to 200 Hz) and a high-frequency analysis (up to 5 kHz) were performed.

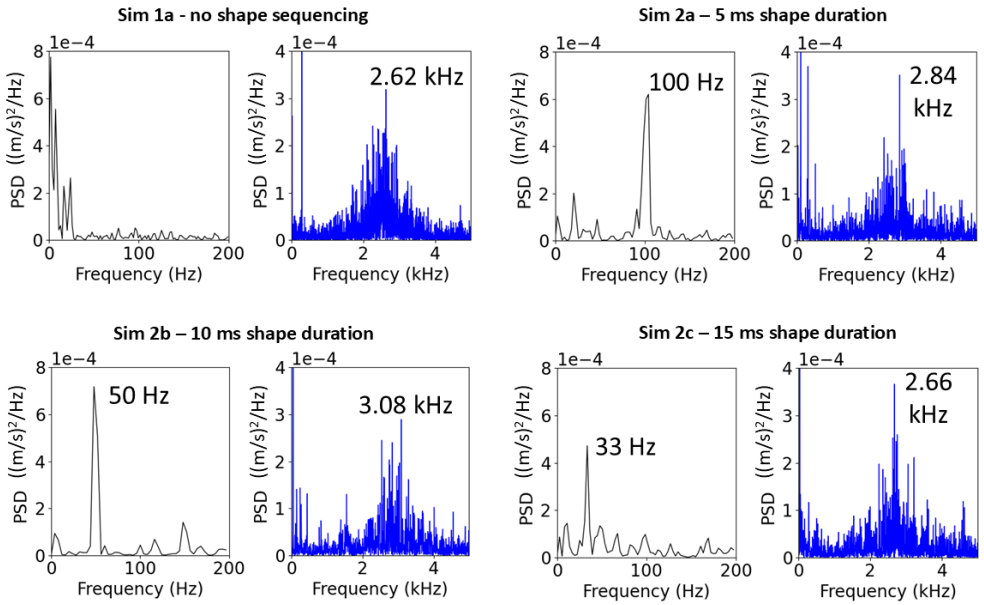



**Fig. 12** PSD analysis for $v_{k,x}$

In the low-frequency domain, the PSD clearly shows that the frequency corresponding to one complete sequencing cycle, i.e., the sum of the shape durations, is directly mirrored at the keyhole surface. This is a remarkable insight, as it demonstrates that the excitation frequency of the keyhole (at least in its upper region) can be directly controlled by adjusting a simple shaping parameter, namely the shape duration. In the high-frequency domain, a very similar frequency appears across all parameter sets, including the one without shape sequencing. This frequency, in the range of 2.5 to 3.5 kHz, is most likely related to local surface modes corresponding to small-scale vibrations of the membrane forming the keyhole wall. Such modes could be excited, e.g., by proper selection of the shape refresh frequency, $f_{SR}$.

The velocity signals at the melt pool free surface and the corresponding frequency analyses are shown in Figs. 13 and 14, respectively. The selected sampling point exhibits a velocity amplitude nearly an order of magnitude lower than that observed at the keyhole. Reduced fluctuations around zero are observed for the sequenced configurations compared to parameter set 1a. In the high-frequency domain (up to 2 kHz), frequencies in the range of 300-500 Hz draw attention. These may correspond to damped oscillations originating from the periodic opening and closing of the keyhole (radial vibration mode) at a higher frequency. A more detailed and precise analysis is required for this specific vibration mode, as well as for the

lateral displacement of the keyhole center, i.e., the swaying or meandering effect illustrated in Fig. 8.

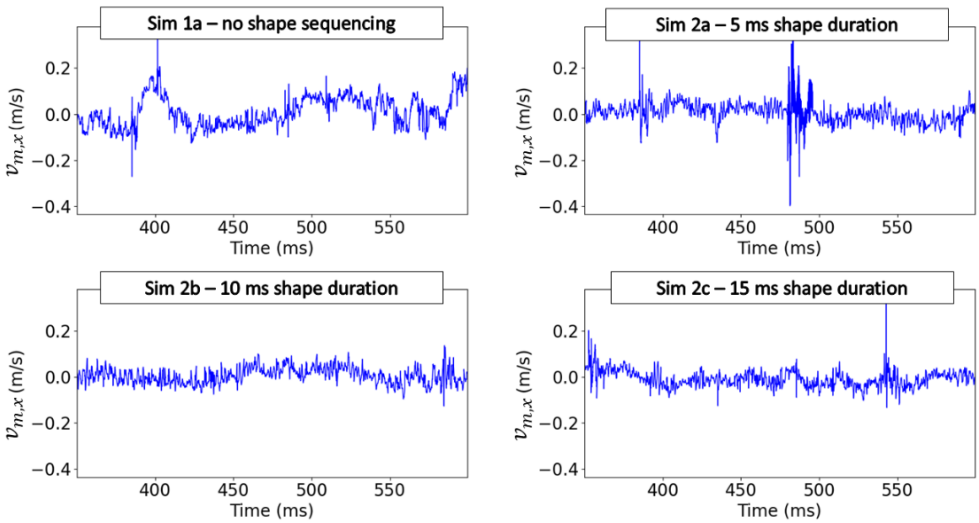



**Fig. 13** Transverse component of the velocity signal at the melt pool upper free surface, $v_{m,x}$

From the measurements at the melt pool, the most notable observation arises in the low-frequency PSD plots in Fig. 14, where the full-cycle sequencing frequencies for symmetric shape durations of 10 and 15 ms (corresponding to 50 and 33.3 Hz, respectively) are clearly identifiable, with the 33 Hz peak being more pronounced than the 50 Hz peak. For parameter set 2a, with a 5 ms shape duration, a peak at 100 Hz is also present, but very weak. The PSD plots for this shape duration show qualitatively similar behavior to that of the reference case without shape sequencing.

The latter suggests two things. First, the mechanical lateral vibrations induced by the laser beam on the keyhole (by means of side-by-side shape sequencing) are successfully transmitted through the melt pool, as observed at a point on its free surface, 2 mm behind the heat source. Second, the excitation produced by certain shape durations is transmitted with higher energy, making these durations more effective in stimulating the vibrating system.

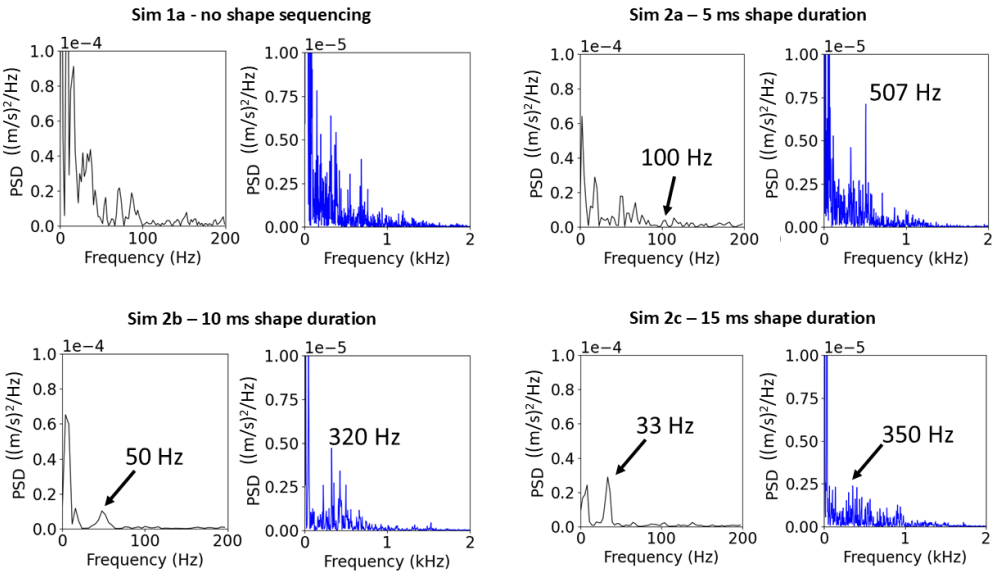



**Fig. 14** PSD analysis for $v_{m,x}$

The beam shapes and shape durations chosen for the applied sequencing strategy clearly influence the process, with some having a stronger effect than others. In this case, since the system could not be properly dynamically balanced, the examined configurations resulted in unsatisfactory welding outcomes, including pores or pronounced asymmetries in the cross section, as shown in the weld characterization presented in the first part of this study. There may exist a specific switching frequency (or multiple frequencies) that yields improved weld quality. The initial idea behind sequencing Shapes 2(a) and 2(b) was to introduce a subtle asymmetry in the process, small enough to preserve overall weld symmetry, yet sufficient to excite the melt pool and influence the temperature gradients that govern, e.g., grain growth during solidification, thereby helping to mitigate defects such as pores or mid-line cracks. However, achieving this effect requires identifying the optimal shape duration(s).

One possible approach is to excite a process subsystem at its resonant frequency. Work in this direction has been carried out, for example, by Otto [18] in $CO_2$-LBW of steel. In his study, the plasma intensity signal emitted during the welding process was measured over time and subsequently analyzed to determine the predominant frequency of the plasma emission. The laser power was then modulated at this frequency (resonant stimulation), which lead to the stabilization of the penetration depth of the weld bead. This temporal beam shaping approach was based on the idea that energy can be supplied very efficiently to an oscillating system by exciting it at its resonant frequency. If an overall system consists of several coupled subsystems, it can be influenced by external periodic excitation so that it performs stable oscillations at the resonant frequency of one of its subsystems. As described in [18], the advantage of this method is that a system with chaotic behavior can be transformed into a system with periodic dynamics without the need for feedback of the system dynamics. Stabilization of the welding process is therefore possible without the use of a closed control

loop. In the case of the specific welding process analyzed in this study, it is still unclear which subsystem and which frequencies are most relevant, and this remains a topic of ongoing research. Determining this is particularly challenging because each system is unique and lacks a standard reference. For example, two systems with different shape durations will vibrate at different eigenfrequencies, even if all other process parameters are identical. The goal is to identify the relevant welding subprocess and its time scale, so that the desired welding outcome can be achieved by stimulating this subprocess at the proper frequency.

## CONCLUSIONS

Although the tested duration times for the selected shape sequencing configuration produced unsatisfactory welds, the key outcome of this work is the demonstration that precise excitation of the keyhole surface can be achieved through dynamic beam shaping by simply adjusting one of the shaping parameters. In this regard, high-fidelity numerical modeling enabled the visualization and analysis of particular aspects of the process that may be beyond the reach of experimental setups. The important insights of this study are summarized below:

1. Different beam shapes and shaping strategies induce different vibration modes in the keyhole, so each configuration should be assessed according to its particular vibration characteristics.
2. Sequencing two shapes that are symmetrical about the process mid-plane, as performed in this work, induces a pulsed excitation transverse to the feed direction on the keyhole surface, with the pulse width determined by the shape durations.
3. The pulsed signal is subsequently transmitted to the melt pool, influencing its behavior. Certain shape durations favor a more or less effective excitation of the melt pool.

This work provides just one example of the many beam shaping configurations that can be analyzed through simulation. Future work will focus on examining other shaping parameters and strategies.

## ACKNOWLEDGEMENTS

All experimental results, beam shape generation tool, and descriptions of the beam shapes used in the numerical implementation were provided by Civan Advanced Technologies ltd. The authors gratefully acknowledge Nina Armon, Rachel Assa, Udi Greenberg, Rami Cohen, Tom Shalev, and Ami Spira for their contributions and valuable discussions.

# APPENDIX I

**Table A1** Material properties of EN AW-5083: **solid state**

| Property | T (K) | Value | Unit | Ref. |
|---|---|---|---|---|
| density $\rho$ | 300 | 2660 | kg $m^{-3}$ | [19] |
| | 773 | 2556 | kg $m^{-3}$ | [19] |
| | 873 | 2510 | kg $m^{-3}$ | [19] |
| bulk modulus $K$ | 300 | $75.2 \cdot 10^9$ | kg $s^{-2}$ $m^{-1}$ | [20] |
| specific heat capacity $c_p$ | 300 | 900 | $m^2$ $s^{-2}$ $K^{-1}$ | [19] |
| | 873 | 1224 | $m^2$ $s^{-2}$ $K^{-1}$ | [19] |
| thermal conductivity $\lambda$ | 300 | 120 | kg m $s^{-3}$ $K^{-1}$ | [19] |
| | 873 | 164 | kg m $s^{-3}$ $K^{-1}$ | [19] |
| surface energy $\sigma$ | 300 | 0.64 | kg $s^{-2}$ | [21] |
| refractive index $n$ | 300 | 0.97 | - | † |
| | 858 | 2.82 | - | † |
| extinction coefficient $\kappa$ | 300 | 10.6 | - | † |
| | 858 | 10.6 | - | † |

† Assumed value based on the absorptivity at ~1 μm wavelength reported in [22].

**Table A2** Material properties of EN AW-5083: **liquid state**

| Property | T (K) | Value | Unit | Ref. |
|---|---|---|---|---|
| density $\rho$ | 950 | 2386 | kg $m^{-3}$ | [23] |
| | 1650 | 2177 | kg $m^{-3}$ | [23] |
| | 2790 | 2040 | kg $m^{-3}$ | [22] |
| bulk modulus $K$ | 933 | $38.0 \cdot 10^9$ | kg $s^{-2}$ $m^{-1}$ | [24] |
| | 2400 | $14.0 \cdot 10^9$ | kg $s^{-2}$ $m^{-1}$ | [24] |
| kinematic viscosity $\nu$ | 864 | $6.10 \cdot 10^{-7}$ | $m^2$ $s^{-1}$ | [25] |
| | 1000 | $4.57 \cdot 10^{-7}$ | $m^2$ $s^{-1}$ | [25] |
| | 1600 | $2.30 \cdot 10^{-7}$ | $m^2$ $s^{-1}$ | [25] |
| | 2793 | $1.41 \cdot 10^{-7}$ | $m^2$ $s^{-1}$ | [25] |
| specific heat capacity $c_p$ | 933 | 1127 | $m^2$ $s^{-2}$ $K^{-1}$ | [23] |
| thermal conductivity $\lambda$ | 933 | 89.3 | kg m $s^{-3}$ $K^{-1}$ | [23] |
| | 1500 | 105.1 | kg m $s^{-3}$ $K^{-1}$ | [23] |
| | 2000 | 112.7 | kg m $s^{-3}$ $K^{-1}$ | [26] |
| | 2600 | 115.1 | kg m $s^{-3}$ $K^{-1}$ | [26] |
| surface energy $\sigma$ | 933 | 0.87 | kg $s^{-2}$ | [26] |
| | 1550 | 0.80 | kg $s^{-2}$ | [26] |
| refractive index $n$ | 933 | 6.65 | - | † |
| | 2793 | 6.65 | - | † |
| extinction coefficient $\kappa$ | 933 | 10.6 | - | † |
| | 2793 | 7.15 | - | † |

† Assumed value based on the absorptivity at ~1 μm wavelength reported in [22].

**Table A3** Material properties of EN AW-5083: **vapor state**

| Property | T (K) | Value | Unit | Ref. |
|---|---|---|---|---|
| density $\rho$ | - | *ideal gas law* | | |
| bulk modulus $K$ | - | $1 \cdot 10^5$ | kg $s^{-2}$ $m^{-1}$ | |
| kinematic viscosity $\nu$ | - | *ideal gas law* | | |
| specific heat capacity $c_p$ | 2800 | 770 | $m^2$ $s^{-2}$ $K^{-1}$ | [27] |
| | 6000 | 845 | $m^2$ $s^{-2}$ $K^{-1}$ | [27] |
| thermal conductivity $\lambda$ | 3000 | 0.15 | kg m $s^{-3}$ $K^{-1}$ | |
| | 5000 | 0.24 | kg m $s^{-3}$ $K^{-1}$ | |
| surface energy $\sigma$ | - | 0 | kg $s^{-2}$ | |
| refractive index $n$ | - | 1 | - | |
| extinction coefficient $\kappa$ | - | 0 | - | |

**Table A4** Material properties of EN AW-5083: **state-independent properties**

| Property | T (K) | Value | Unit | Ref. |
|---|---|---|---|---|
| molar mass $M$ | - | $26.98 \cdot 10^{-3}$ | kg $mol^{-1}$ | [28] |
| solidus $T_{solidus}$ | - | 864 | K | [19] |
| liquidus $T_{liquidus}$ | - | 911 | K | [19] |
| boiling temperature $T_{boiling}$ | - | 2793 | K | [28] |
| latent heat of fusion $L_{fusion}$ | - | $394.3 \cdot 10^3$ | $m^2$ $s^{-2}$ | [29] |
| latent heat of vaporization $L_{vaporization}$ | - | $1.09 \cdot 10^7$ | $m^2$ $s^{-2}$ | [28] |

**Table A5** Material properties of air

| Property | T (K) | Value | Unit | Ref. |
|---|---|---|---|---|
| molar mass $M$ | - | $28.014 \cdot 10^{-3}$ | kg $mol^{-1}$ | |
| density $\rho$ | - | *ideal gas law* | | |
| bulk modulus $K$ | - | $1 \cdot 10^5$ | kg $s^{-2}$ $m^{-1}$ | |
| kinematic viscosity $\nu$ | - | *kinetic theory* | | |
| | | $\nu_0 = 1.593 \cdot 10^{-5}$ | $m^2$ $s^{-1}$ | [27] |
| | | $\rho_0 = 1.1233$ | kg $m^{-3}$ | [27] |
| | | $T_0 = 300$ | K | |
| specific heat capacity $c_p$ | 300 | 1041.3 | $m^2$ $s^{-2}$ $K^{-1}$ | [27] |
| | 1800 | 1270.8 | $m^2$ $s^{-2}$ $K^{-1}$ | [27] |
| thermal conductivity $\lambda$ | 300 | $2.597 \cdot 10^{-2}$ | kg m $s^{-3}$ $K^{-1}$ | [27] |
| | 900 | $6.052 \cdot 10^{-2}$ | kg m $s^{-3}$ $K^{-1}$ | [27] |
| | 1800 | $10.088 \cdot 10^{-2}$ | kg m $s^{-3}$ $K^{-1}$ | [27] |
| surface energy $\sigma$ | - | 0 | kg $s^{-2}$ | |
| refractive index $n$ | - | 1 | - | |
| extinction coefficient $\kappa$ | - | 0 | - | |

## References


[1] M. SCHMIDT, K. CVECEK, J. DUFLOU, F. VOLLERTSEN, C. B. ARNOLD, M. J. MATTHEWS: 'Dynamic beam shaping–Improving laser materials processing via feature synchronous energy coupling', *CIRP Annals*, Vol. 73, No. 2, pp. 533-559, 2024, doi: https://doi.org/10.1016/j.cirp.2024.05.005.

[2] E. SHEKEL, Y. VIDNE, B. URBACH: '16kW single mode CW laser with dynamic beam for material processing', *Proc. SPIE 11260, Fiber Lasers XVII: Technology and Systems*, 1126021, 2020, doi: https://doi.org/10.1117/12.2545900.

[3] R. WEBER, J. WAGNER, A. PETER, C. HAGENLOCHER, A. SPIRA, B. URBACH, E. SHEKEL E, Y. VIDNE: 'Basic Properties of High-Dynamic Beam Shaping with Coherent Combining of High-Power Laser Beams for Materials Processing', *Journal of Manufacturing and Materials Processing*, 9, 85, 2025, doi: https://doi.org/10.3390/jmmp9030085.

[4] D. DITTRICH, S. BÖRNER, J. BARRIOS LARRAÑAGA, T. SAHM, A. JAHN, A. WETZIG: 'Coherent beam combining - Beam characterization of a new 14 kW CBC laser source and first results on copper welding', *Procedia CIRP*, Vol. 124, pp. 724-729, 2024, doi: https://doi.org/10.1016/j.procir.2024.08.211.

[5] M. SAWANNIA, J. WAGNER, P. STRITT, R. RAMSAYER, C. HAGENLOCHER, T. GRAF: 'Response of the melt pool and vapour capillary on dynamic beam shaping in the kHz regime during laser welding', *Procedia CIRP*, Vol. 124, pp. 430-433, 2024, doi: https://doi.org/10.1016/j.procir.2024.08.147.

[6] C. PRIETO, E. VAAMONDE, D. DIEGO-VALLEJO, J. JIMENEZ, B. URBACH, Y. VIDNE, E. SHEKEL: 'Dynamic laser beam shaping for laser aluminium welding in e-mobility applications', *Procedia CIRP*, Vol. 94, pp. 596-600, 2020, doi: https://doi.org/10.1016/j.procir.2020.09.084.

[7] S. OLSCHOK, M. TROISE, U. REISGEN: 'Laser beam welding of high thickness sheet metal with highly dynamic beam shaping', *Procedia CIRP*, Vol. 124, pp. 733-736, 2024, doi: https://doi.org/10.1016/j.procir.2024.08.213.

[8] C. ZENZ, M. BUTTAZZONI, T. FLORIAN, K. E. CRESPO ARMIJOS, R. GÓMEZ VÁZQUEZ, G. LIEDL, A. OTTO: 'A compressible multiphase Mass-of-Fluid model for the simulation of laser-based manufacturing processes', *Computers & Fluids*, Vol. 268, 106109, 2024, doi: https://doi.org/10.1016/j.compfluid.2023.106109.

[9] C.-R. SONG, B.-X. DONG, S.-Y. ZHANG, H.-Y. YANG, L. LIU, J. KANG, ET AL.: 'Recent progress of Al–Mg alloys: Forming and preparation process, microstructure manipulation and application', *Journal of Materials Research and Technology*, Vol. 31, pp. 3255-3286, 2024, doi: https://doi.org/10.1016/j.jmrt.2024.07.051.

[10] J. HAN, Y. SHI, G. ZHANG, V. KORZHYK, W.-Y. LE: 'Minimizing defects and controlling the morphology of laser welded aluminum alloys using power modulation-based laser beam oscillation', *Journal of Manufacturing Processes*, Vol. 83, pp. 49-59, 2022, doi: https://doi.org/10.1016/j.jmapro.2022.08.031.

[11] H. G. WELLER, G. TABOR, H. JASAK, C. FUREBY: 'A tensorial approach to computational continuum mechanics using object-oriented techniques', *Comput. Phys.*, Vol. 12 (6), pp. 620-631, doi: https://doi.org/10.1063/1.168744.

[12] A. OTTO, H. KOCH, R. GÓMEZ VÁZQUEZ: 'Multiphysical Simulation of Laser Material Processing', *Physics Procedia*, Vol. 39, pp. 843-852, https://doi.org/10.1016/j.phpro.2012.10.109.

[13] A. OTTO, H. KOCH, K.-H. LEITZ, M. SCHMIDT: 'Numerical Simulations - A Versatile Approach for Better Understanding Dynamics in Laser Material Processing', *Physics Procedia*, Vol. 12 (A), pp. 11-20, 2011, doi: https://doi.org/10.1016/j.phpro.2011.03.003.

[14] A. OTTO, M. BUTTAZZONI, C. DURÁN, T. FLORIAN, C. ZENZ: *Universal Numerical Simulation Model for Laser Material Processing', preprint, 2026, accepted for publication in 'Scaling of*

*Laser Processing – Making Light Matter*, J. BONSE, A. F. LAGSANI (EDS.), Springer, Cham, Switzerland. Preprint available at: https://doi.org/10.48550/arXiv.2509.22666. The final authenticated version will be available online in the Springer Series in Optical Sciences: https://link.springer.com/book/9783032171320.

[15] C. ZENZ, P. S. COOK, L. VÖRÖS, A. OTTO: 'A critical comparison of one- and two-fluid approaches for the simulation of laser-induced melt pool formation and vaporisation', *Discover Materials*, Vol. 5, 266, 2025, doi: https://doi.org/10.1007/s43939-025-00434-0.

[16] O. BOCKSROCKER, N. SPEKER, M. BERANEK, T. HESSE: 'Reduction of spatters and pores in laser welding of copper hairpins using two superimposed laser beams', *Proc LIM*, pp. 1-8, 2019.

[17] P. WELCH: 'The use of fast Fourier transform for the estimation of power spectra: A method based on time averaging over short, modified periodograms', *IEEE Transactions on Audio and Electroacoustics*, Vol. 15 (2), pp. 70-73, 1967, doi: https://doi.org/10.1109/TAU.1967.1161901.

[18] A. OTTO: 'Transiente Prozesse beim Laserstrahlschweißen', Doctoral dissertation, Friedrich-Alexander-Universität Erlangen-Nürnberg, 1997.

[19] Z. JIANG, X. HUA, L. HUANG ET AL.: 'Effect of multiple thermal cycles on metallurgical and mechanical properties during multi-pass gas metal arc welding of Al 5083 alloy', *Int. J. Adv. Manuf. Technol.*, Vol. 93, pp. 3799-3811, 2017, doi: https://doi.org/10.1007/s00170-017-0771-6.

[20] S. RAJU, K. SIVASUBRAMANIAN, E. MOHANDAS: 'The high temperature bulk modulus of aluminium: an assessment using experimental enthalpy and thermal expansion data', *Solid State Communications*, Vol. 122 (12), pp. 671-676, 2002, doi: https://doi.org/10.1016/S0038-1098(01)00517-8.

[21] P.-F. PARADIS, T. ISHIKAWA: 'Surface Tension and Viscosity Measurements of Liquid and Undercooled Alumina by Containerless Techniques', *Jpn. J. Appl. Phys.*, Vol. 44, 5082, 2005, doi: https://dx.doi.org/10.1143/JJAP.44.5082.

[22] D. MARLA ET AL.: 'Models for predicting temperature dependence of material properties of aluminum', *J. Phys. D: Appl. Phys.*, Vol. 47 (10), 105306, doi: http://dx.doi.org/10.1088/0022-3727/47/10/105306.

[23] M. LEITNER, T. LEITNER, A. SCHMON ET AL.: 'Thermophysical Properties of Liquid Aluminum', *Mater. Trans. A*, Vol. 48, pp. 3036-3045, 2017, doi: https://doi.org/10.1007/s11661-017-4053-6.

[24] R.N. SINGH, S. ARAFIN, A.K. GEORGE: 'Temperature-dependent thermo-elastic properties of s-, p- and d-block liquid metals', *Physica B: Condensed Matter*, Vol. 387 (1-2), pp. 344-351, 2007, doi: https://doi.org/10.1016/j.physb.2006.04.029.

[25] A. T. DINSDALE, P. N. QUESTED: 'The viscosity of aluminium and its alloys--A review of data and models', *J. Mater. Sci.*, Vol. 39, pp. 7221-7228, 2004, doi: https://doi.org/10.1023/B:JMSC.0000048735.50256.96.

[26] A. V. GUSAROV, I. SMUROV: 'Thermal model of nanosecond pulsed laser ablation: Analysis of energy and mass transfer', *J. Appl. Phys*, Vol. 97 (1), 014307, doi: https://doi.org/10.1063/1.1827321.

[27] E. W. LEMMON, I. H. BELL, M. L. HUBER, M. O. MCLINDEN: 'Thermophysical properties of fluid systems', in: Linstrom, P.J. and Mallard, W.G. (eds.) NIST Chemistry WebBook, *NIST Standard Reference Database 69*, National Institute of Standards and Technology, http://dx.doi.org/10.18434/T4D303.

[28] M. TIRYAKIOĞLU, A. E. MAYER: 'On estimating the intrinsic surface tension of liquid aluminum and its temperature coefficient', *J. Mater. Sci.*, Vol. 59, pp. 12781-12792, 2021, doi: https://doi.org/10.1007/s10853-024-09909-6.

[29] A. E. W. JARFORS, P. JANSSON: 'Selecting Cast Alloy Alloying Elements Suitable for a Circular Society', *Sustainability*, Vol. 14, 6584, 2022, doi: https://doi.org/10.3390/su14116584.

# I Welding Processes

## c) Additive Manufacturing

# MULTIPHYSICS SIMULATION OF SPATIAL-TEMPORAL BEAM SHAPING IN LASER POWDER BED FUSION USING OPENFOAM

B. ZHOU*, J. BARODE*, V. K. NADIMPALLI*, A. BAUCH**, D. HERZOG***, J. H. HATTEL*, M. BAYAT*

**Technical University of Denmark, Department of Mechanical Engineering, 2800, Kgs. Lyngby, Denmark, baozh@dtu.dk*
***Fraunhofer Research Institution for Additive Manufacturing Technologies IAPT, 21029, Hamburg, Germany*
****Hamburg University of Technology, Institute for the Industrialization of Smart Materials, 21029, Hamburg, Germany*

*DOI 10.3217/978-3-99161-089-2-011, license CC BY 4.0*
*https://creativecommons.org/licenses/by/4.0/deed.en*
*This CC license does not apply to third party material and content noted otherwise.*

## ABSTRACT

Metal additive manufacturing (MAM) has been applied in various advanced fields due to its flexibility and superiority in producing complex geometries, compared to subtractive manufacturing methods. The powder bed fusion using a laser beam (PBF-LB) process, as a major subbranch of MAM, involves multiple complex physical phenomena, e.g. phase changes, buoyancy, surface tension, evaporation, Marangoni effects, melting, solidification, and microstructural evolution. The interplay between process settings and melt-pool conditions has a significant influence on part quality. Multiphysics simulations that incorporate these phenomena are considered as a robust and reliable tool to study this complex interplay. This study simulates the PBF-LB process for copper and stainless steel 316L (SS 316L) under infrared laser irradiation at the deposition scale, using the open-source code OpenFOAM. The simulation results demonstrate good agreement with benchmark experimental data in terms of the transverse cross-section profiles of the melt regions when applying spatial and temporal beam shaping in PBF-LB. These beam shaping techniques are efficient ways to adjust the melt-pool morphology and eventually to improve the print quality. In this study, continuous Gaussian and ring-shaped laser beam profiles, and pulsed beam shaping techniques are modelled, and their effects on the melt pool are investigated. Moreover, for copper, there has been long controversy in the literature in terms of the correct absorption rate of laser radiation. We hence explore the influence of absorptivity on the melt-region cross-sectional dimension. This work focuses on simulating the melt pool on metal substrates and offers insights into the fundamental impacts of the process settings on melting behavior and absorptivity while using beam shaping.

Keywords: PBF-LB, Metal Additive Manufacturing, Absorptivity, Melt Pool, Beam Shaping

## INTRODUCTION

Metal additive manufacturing (MAM), involving multi-scale and multi-disciplinary phenomena, has emerged in many engineering fields, including the fabrication of aerospace components [1], biomedical instruments [2] and various complex products [3]. Numerical simulations and experimental measurements are two common approaches for studying the thermal, mechanical and fluid dynamic behaviors involved during MAM process. While experiments provide critical benchmarks for validation, simulations enable efficient and cost-effective exploration of parameter spaces.

Among numerical methods, finite volume method (FVM)-based open-source tools such as OpenFOAM [4] have been extensively used for computational fluid dynamics (CFD) simulations [5]. In numerical models of powder bed fusion using a laser beam (PBF-LB), early studies primarily focused on pure conduction modes, later evolving into more comprehensive investigations that incorporated fluid dynamics. In conduction-based models, some researchers addressed purely thermal problems [6-7], while others took into account thermal-mechanical coupling effects [8-9]. Current simulations are usually able to capture a range of physical phenomena, including melting, solidification and evaporation. They are mathematically modelled using mass, momentum, and energy conservation conditions, often with additional surface-tracking methods to account for free-surface deformation [10]. The melt and solid phases are typically identified using threshold temperatures: regions above the liquidus point are considered molten, while those below the solidus temperature are treated as solid. Recent developments such as beamWeldFoam [11] and laserBeamFoam [12-13] within the OpenFOAM framework have enabled simulation of complex phenomena including Marangoni effects, recoil pressure, laser absorptivity calculations using Fresnel equations [14], and multi-laser and multi-material interactions [15].

Copper, due to its high reflectivity and thermal conductivity, encounters unique challenges during the PBF-LB process. Its laser absorption is influenced by multiple factors, including temperature, incident laser intensity, laser wavelength, surface roughness, contamination, and oxidation of the material surface [16]. Accurately predicting copper's absorptivity is both difficult and critical for reliable simulation and process optimization. Reported absorption rates vary widely across the literature. For example, Alphonso et al. [17] reported absorptivity values of 12% for laser radiation in the (near-) infrared spectrum and 40% in the green spectrum. Gargalis et al. [18] recommended around 20% for conduction mode and 53% for keyhole welding [19]. Nordet et al. [20] cited values as low as 4%-5% for laser radiation at a wavelength of around 1070 nm.

Beam shaping is a promising strategy for enhancing the quality of PBF-LB products, encompassing both spatial and temporal modifications. Spatial shaping involves modifying the laser beam profile, with commonly used shapes such as Gaussian [21], ring-shaped [22], tophat [23], and elliptical [24] profiles. They have different influences on melt-pool morphology and defect formation. Gaussian beams, though widely used, tend to concentrate energy at the center, which may cause unwanted spatter and degrade print quality [25]. In contrast, the ring-shaped profile redistributes the beam intensity, thus reducing the spatter [26], affecting surface roughness and porosity [27]. Galbusera et al. [28] showed that the core-to-ring power ratio greatly influences porosity formation, a trend also observed by Hayat et al.

[29] using elliptical and square beam profiles during laser welding of aluminium alloys. Temporal beam shaping involves modulating the laser's on and off state over time. During this process, two key control parameters are the duty cycle which is the ratio of the laser on-time to the cycle time, and the laser switching frequency [30]. From the relevant work presented by Bayat et al. [31], it is observed that these parameters significantly affect track morphology, with distinctive fish-fin surface topologies appearing at low cycle periods. Similar surface features were reported by Zheng et al. [32], who also noted that longer exposure time could produce denser fish-scale patterns. Despite these findings, studies focusing on beam shaping for copper and comparative investigations across different metals remain limited.

In this study, we extend the open-source codes laserBeamFoam [12] which originally included a continuous Gaussian laser beam, to work on temporal and spatial beam shaping, and develop a multiphysics numerical model to simulate the metal PBF-LB process. The numerical model is validated against benchmark data for several cases: continuous Gaussian and ring-shaped lasers on copper, and a pulsed Gaussian laser on stainless steel 316L (SS 316L). Based on the validated framework, we explore the influence of absorptivity on the melt-pool dynamics of copper, presenting absorptivity vs. deviation plots for various laser profiles. The spatial and temporal beam shaping effects on material deposition patterns are investigated as well. The rest of this paper unfolds as follows. The second section describes simulation models, as well as the temporal and spatial beam shaping techniques. The third section presents validation of the simulation by comparison with benchmark results. The fourth section discusses the laser absorptivity of copper and analyzes the influence of beam shaping. The fifth section concludes the paper.

## NUMERICAL MODEL

### GOVERNING EQUATIONS

In numerical simulation of PBF-LB, different assumptions can lead to different forms of the governing equations which generally describe the mass, momentum, and energy conservation conditions of the fluid-thermal field, as well as interface capturing methods. Within the framework of the codes laserBeamFoam [12], the fluid momentum conservation is described by the Navier-Stokes equations

$$\frac{\partial(\rho u_i)}{\partial t} + \frac{\partial(\rho u_i u_j)}{\partial x_j} = -\frac{\partial P}{\partial x_j} + \frac{\partial \tau_{ij}}{\partial x_j} + F_i^b + F_i^s + S_i^D, \tag{1}$$

where the terms in the left-hand side represent transient and convective terms, and those in the right-hand side are the pressure gradient, the viscous term, the buoyancy force $F_i^b$, the surface force $F_i^s$, and the Darcy sink term $S_i^D$. In Eq. (1) $\rho$, $P$, $t$ denote the density, pressure and time, $u_i$, $x_i$ the velocity and space coordinate, and $\tau_{ij}$ the viscous stress tensor. $i, j$ both take values

from 1 to 3. For an incompressible flow which is described by a velocity divergence-free condition

$$\frac{\partial u_i}{\partial x_i} = 0, \tag{2}$$

the viscous stress tensor is $\tau_{ij} = \rho\nu\left(\frac{\partial u_i}{\partial x_j} + \frac{\partial u_j}{\partial x_i}\right)$. Here, $\nu$ is the kinematic viscosity. The surface force $F_i^s$ includes the surface tension, the recoil force due to vaporization, and the Marangoni force, i.e.,

$$F_i^s = \left[\sigma\kappa n_i + P^r n_i + \frac{\partial\sigma}{\partial T}\left(\frac{\partial T}{\partial x_i} - n_i\left(\frac{\partial T}{\partial x_j}n_j\right)\right)\right]|\nabla\alpha|\frac{2\rho}{\rho_1+\rho_2}, \tag{3}$$

where $\sigma$, $\kappa$, $T$, $\alpha$ are the surface tension coefficient, the curvature, the temperature and the volume fraction of dense phase. $\rho_1$, $\rho_2$ are the density of dense material and gas. $n_i$ is the $x_i$-direction component of normal vector. The recoil pressure $P^r$ is computed by

$$P^r = 0.54p_0 e^{\frac{L^v M(T-T^v)}{RT^v T}}, \tag{4}$$

where $T^v$, $M$, $L^v$, $R$ are the temperature at the boiling point, molar mass, latent heat due to vaporization and universal gas constant, respectively. $p_0$ is the vapor pressure. The buoyancy force $F_i^b$ is computed by the Boussinesq approximation

$$F_i^b = -\varepsilon_1\rho g\delta_i\beta(T - T^s), \tag{5}$$

where $g$, $\beta$ and $T^s$ are the gravitational acceleration, the thermal expansion coefficient, and the solidus temperature, respectively. $\varepsilon_1$ is a temperature sensitivity coefficient, which is calculated by

$$\varepsilon_1 = \begin{cases} 0, & T < T^s \\ \frac{T-T^s}{T^l-T^s}, & T^s \le T \le T^l \\ 1, & T > T^l \end{cases}. \tag{6}$$

Here, $T^l$ denotes the liquidus temperature. In Eq. (5) the tuning coefficient $\delta_i = 1$ when the buoyancy $F_i^b$ points in the direction of gravity, otherwise $\delta_i = 0$. The Darcy sink term is computed by

$$S_i^D = -\frac{C_1(1-f_l)^2}{f_l^3 + C_2}u_i, \tag{7}$$

where $C_1$ is a constant multiplier which here takes a large value $10^6$ and $f_l$ is the liquid fraction with the value of 0 in the solid state and 1 in the liquid. To avoid the case where the denominator is zero, a small positive parameter $C_2$ is applied, and here $C_2 = 10^{-12}$. At the solid state, $u_i = 0$ and $f_l = 1$ give $S_i^D = 0$.

To capture the interface between the metal and gas phases, the volume of fluid (VOF) method [33] is applied, which is mathematically described by

$$\frac{\partial \alpha}{\partial t} + \frac{\partial (\alpha u_i)}{\partial x_i} = 0. \tag{8}$$

$\alpha = 1$ represents the pure dense material, $\alpha = 0$ the pure gas, and $0 < \alpha < 1$ the interface.

The energy conservation is formulated by the temperature field

$$\frac{\partial (\rho c^p T)}{\partial t} + \frac{\partial (u_i \rho c^p T)}{\partial x_i} - \frac{\partial}{\partial x_j}\left(k \frac{\partial T}{\partial x_i}\right) = S^H - Q^v - Q^f, \tag{9}$$

where $c^p$ is the specific heat, $k$ the thermal conductivity. $S^H$ is the external heat source. $Q^v$, $Q^f$ are the latent heat due to vaporization and fusion, respectively, which are calculated by

$$Q^v = 0.82|\nabla \alpha| \frac{L^v M p_0}{\sqrt{2\pi MRT}} e^{\frac{L^v M (T - T^v)}{RT^v T}}, \tag{10}$$

and

$$Q^f = L^f \left[\frac{\partial (\rho \varepsilon_1)}{\partial t} + \frac{\partial (\rho u_i \varepsilon_1)}{\partial x_i}\right], \tag{11}$$

where $L^f$ is the latent heat of fusion. The heat source $S^H$ is provided by an external laser, which is the product of laser power $q^{laser}$ and absorptivity $\eta$, i.e. $S^H = \eta q^{laser}$. The formulation of the laser source $q^{laser}$ is presented in Eq. (13).

After each time step is calculated, the relevant physical properties $\Upsilon$ are updated generally by

$$\Upsilon = \alpha \Upsilon_1 + (1 - \alpha)\Upsilon_2, \tag{12}$$

where $\Upsilon_1$ represents the property of dense material phase, with $\Upsilon_2$ the property of the gas phase. Here, the physical properties involved include $\rho$, $T^s$, $T^l$, $\beta$, $\nu$, $l^f$, $c^p$ and $k$.

## SPATIAL AND TEMPORAL BEAM SHAPING

In this work, we apply the lasers with Gaussian and ring-shaped laser beam profiles, as shown in Fig. 1.

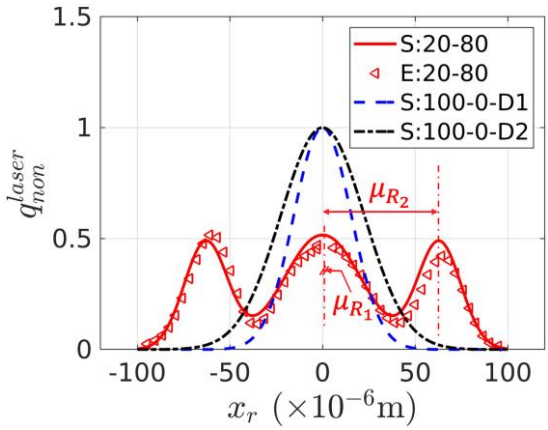



**Fig. 1** One-dimensional Gaussian and ring-shaped beam shapes. $q_{non}^{laser}$ denotes the normalized power intensity, and $x_r$ represents the radial position. $\mu_{R1}$ and $\mu_{R2}$ denote the central position of the core and the ring

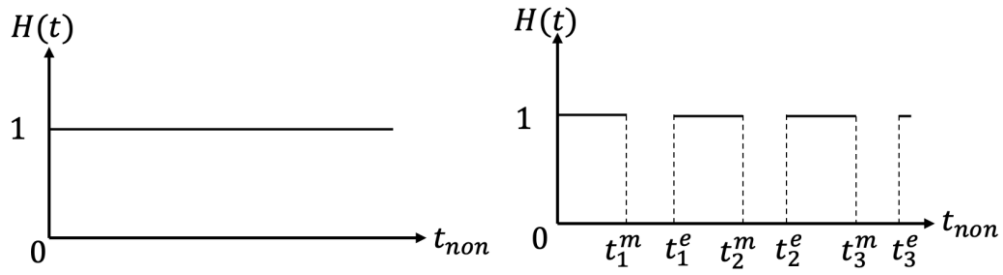
In the legend, S denotes the beam shapes which are applied in our simulations, calculated by Eq. (13) and E denotes the shape used in the referenced experiment [34], and the following number denotes the power ratio of the core to the ring. D1 and D2 denote the diameter of the two Gaussian shapes, respectively. For example, S:100-0-D1 represents the pure Gaussian laser with a diameter of D1 used in the simulations. In the simulation, these shapes are analytically expressed by

$$q^{laser} = H(t)\frac{Q}{\pi(1+a_r)}\left[\frac{1}{\sigma_c^2}e^{-\frac{(d-\mu_{R1})^2}{\sigma_c^2}} + \frac{a_r}{2\sqrt{2}\omega\mu_{R2}\sigma_r}e^{-\frac{(d-\mu_{R2})^2}{\sigma_r^2}}\right], \tag{13}$$

where $\omega$ is an adjustable factor, and $Q$ is the nominal laser power with unit of W. $a_r$ is used to calculate the weight coefficient of the ring power ratio. $\mu_{R1}$ and $\mu_{R2}$ denote the central position of the core and the ring, as shown in Fig. 1. $\sigma_c$ and $\sigma_r$ are the variance of the core and the ring. $\theta$ is the incident angle of the laser beams. $d$ describes the position of the laser, which is defined by

$$d = \sqrt{\left(x - b_g\right)^2 + \left(z - l_g - vt\right)^2} \tag{14}$$

where $b_g$ and $l_g$ are used to define the initial position of the laser in the $x$ and $z$ directions, and $v$ is the laser scanning speed. In Eq. (13), $H(t)$ is a time-dependent function which controls the on and off of the power. For example, in Fig. 2(a), when the laser provides a continuous source of power, $H(t) = 1$ during the whole simulation process.




(a) (b)

**Fig. 2** Schematic of continuous and pulsed laser sources, as shown in subfigures (a) and (b), respectively. $t_{non}$ is the dimensionless time

For a pulsed laser source as shown in Fig. 2(b), when $t_i^e \le t \le t_{i+1}^m$ $H(t) = 1$ otherwise $H(t) = 0$. $t_i^e$ denotes the end time of the $i^{th}$ cycle period. If $t_i^e$ is not the final end time of the simulation, $t_i^e$ also corresponds to the start time of the $(i+1)^{th}$ cycle. For fixed period situations, a period length is computed through $t_{i+1}^e - t_i^e$. $t_{i+1}^m$ is a time step within the $(i+1)^{th}$ cycle, used to adjust the duty cycle which is calculated by $(t_{i+1}^m - t_i^e)/(t_{i+1}^e - t_i^e)$.

## VALIDATION CASES

In this section, several single-track validation cases are presented by comparing the simulated and experimental melt-region cross-sectional dimensions. Fig. 3 briefly describes the simulation model. The computational domain is defined as $x \in [-W_d/2, W_d/2]$, $y \in [0, D_g + D_s]$ and $z \in [0, L_d]$. $L_d$, $W_d$ denote the length and width of the whole computational domain. $D_g$, $D_s$ denote the initial depth of gas and material phases before the simulation starts. In this paper, $L_d = 1000$ μm and $D_g = 200$ μm are applied to all cases, and $W_d$, $D_s$ may vary from case to case. The scanning laser starts at $x = 0, z =$100 μm and ends at $x = 0, z = 900$ μm, with a total scanning distance of 800 μm. The physical properties of copper and SS 316L are provided in Table 1. The universal gas constant is $R = 8.341$ J K$^{-1}$ mol$^{-1}$.

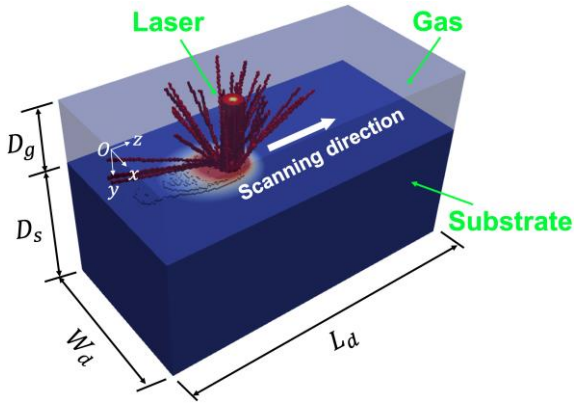



**Fig. 3** Visualization of the numerical model including dense material and gas phases

**Table 1** Physical properties of Copper and SS 316L used in simulations.

| Parameters | Symbol | Copper | SS 316L |
|---|---|---|---|
| Kinematic viscosity ($m^2\ s^{-1}$) | $\nu_1$ | $5.3 \times 10^{-7}$ | $7.64 \times 10^{-7}$ |
| Density ($kg\ m^{-3}$) | $\rho_1$ | 7800 | 7870 |
| Thermal conductivity ($kg\ m\ s^{-3}\ K^{-1}$) | $k_1$ | 200 | $10.829 + 0.0095T$ |
| Specific heat ($J\ kg^{-1}\ K^{-1}$) | $c_1^p$ | 495 | $618.5 + 0.067T$ |
| Solidus temperature (K) | $T_1^s$ | 1335 | 1658 |
| Liquidus temperature (K) | $T_1^l$ | 1337 | 1723 |
| Evaporation temperature (K) | $T^v$ | 3220 | 3090 |
| Latent heat of fusion ($J\ kg^{-1}$) | $L_1^f$ | $2.06 \times 10^5$ | $2.7 \times 10^5$ |
| Latent heat due to vaporization ($J\ kg^{-1}$) | $L^v$ | $4.69 \times 10^6$ | $2.45 \times 10^6$ |
| Thermal expansion coefficient ($K^{-1}$) | $\beta_1$ | $5.85 \times 10^{-5}$ | $5.8 \times 10^{-5}$ |
| Surface tension ($J\ m^{-2}$) | $\sigma$ | 1.304 | 1.6 |
| Temperature derivative of tension ($J\ m^{-2}\ K^{-1}$) | $d\sigma/dT$ | $-2.86 \times 10^{-4}$ | $-8 \times 10^{-4}$ |
| Vapor pressure ($J\ m^{-3}$) | $p_0$ | $1.01 \times 10^5$ | $1.01 \times 10^5$ |
| Molar mass ($kg\ mol^{-1}$) | $M$ | 0.064 | 0.05593 |

An infrared laser with the wavelength of 1070 nm is initially applied to the position defined by Eq. (14) with $b_g = 0$ and $l_g = 100$ μm, moving at a prescribed speed $v$. When presenting the results, for clarity, we represent the width ($W$) and depth ($D$) of the melt region in the manner as shown in Fig. 4.

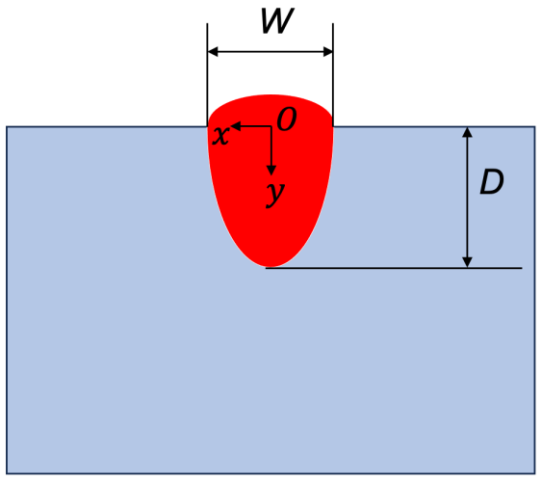



**Fig. 4** Dimension denotation of melt-region width (*W*) and depth (*D*)

## CONTINUOUS GAUSSIAN LASER ON COPPER

The first validation case is a continuous 400 W Gaussian laser applied on a copper plate. A hexahedral cubic mesh with a cell sidelength of 5 μm is used to discretize the numerical model, which is fine enough to achieve high accuracy according to reference [26]. The laser scanning speed is set to $v = 0.5$ m/s. The laser spot radius is 31 μm. The laser shape is computed using Eqs. (13) and (14), and the relevant parameters are presented in Table 2 as G1. The shape is shown as S:100-0-D1 in Fig. 1. A couple of absorption rates of energy are used to conduct the sensitivity analysis of the melt-region dimension with respect to absorptivity, which is discussed in Section ABSOPTIVITY VS. POWER IN COPPER.

**Table 2** Value of required parameters for computing laser beam shapes using Eqs. (13) and (14).

| Label | Power ratio | $a_r$ | $\sigma_c$ (μm) | $\sigma_r$ (μm) | $\mu_{R1}$ (μm) | $\mu_{R2}$ (μm) | $\omega$ |
|---|---|---|---|---|---|---|---|
| G1 | 100-0 | 0 | 21.92 | – | 0 | – | – |
| G2 | 100-0 | 0 | 31.82 | – | 0 | – | – |
| R1 | 20-80 | 0.94 | 29.53 | 16.60 | 0.41 | 62.94 | 0.295 |

Fig. 5(a) compares cross-sections of the simulated and experimental melt regions. Here the local absorption rate is $\eta = 15\%$ in the simulation. Table 3 provides the specific values of the width and depth of the cross section, as Labelled Gaussian. Measured experiment results are referenced from the literature [35], and two sets of reference data are available for each case. Fig. 5(a) only plots one of the two experimental results, and from Table 3 it is seen that the simulated results are within the range of these two sets of values. Note that a particle powder layer with a thickness of 90 μm is added on the substrate surface in the experiment of the paper [35], but considering the computational efficiency we do not include powder in the

simulation. Thus, here we only discuss the penetration dimension without the region above the initial interface.

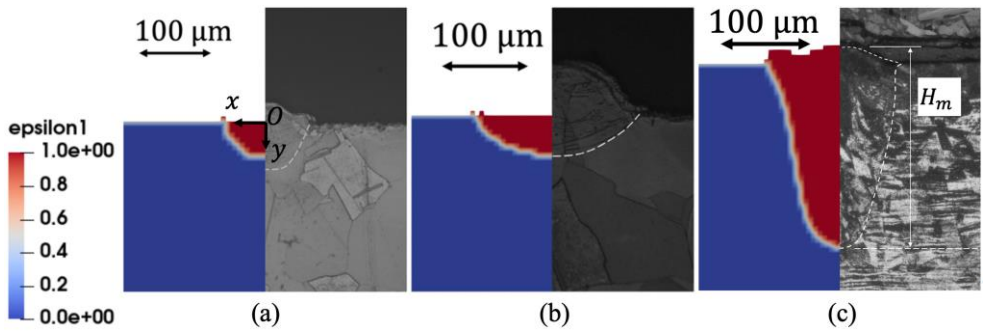



**Fig. 5** Cross sections of the melt regions under (a) continuous Gaussian and (b) continuous ring-shaped laser beams on copper, and (c) a pulsed Gaussian laser beam on SS 316L. The left part is the simulation result, and the right is the experimental result. Subfigure (a): 400 $W$ power, $\eta = 15\%$ absorption rate, 0.5 $m/s$ scanning speed, $90 \times 35$ $\mu m^2$ $(W \times D)$ simulated dimension, and $133 \times 62$ $\mu m^2$ $(W \times D)$ experimental dimension. Subfigure (b): 1300 $W$ power, $\eta = 3.6\%$ absorption rate, 20-80 core-ring power ratio, 0.5 $m/s$ scanning speed, $170 \times 45$ $\mu m^2$ $(W \times D)$ simulated dimension, and $211 \times 45.1$ $\mu m^2$ $(W \times D)$ experimental dimension. Subfigure (c): 260 $W$ power, 6500 $Hz$ frequency, 0.325 $m/s$ scanning speed, and dimensions are given in Table 4; $H_m$ denotes the total height of the melt region.

**Table 3** Width and depth of the melt regions under continuous Gaussian and 20-80 ring-shaped beams on copper. RExp denotes the referenced experimental data measured in the literature [34-35], and 1 and 2 represent the value measured at two positions.

| Label | Width (µm) | | | Depth (µm) | | |
|---|---|---|---|---|---|---|
| | RExp-1 | RExp-2 | Simulation | RExp-1 | RExp-2 | Simulation |
| Gaussian | 133 [35] | 62 [35] | 90 | 62 [35] | 15 [35] | 35 |
| Ring-shaped | 211.0 [34] | 187.6 [34] | 170 | 36.6 [34] | 45.1 [34] | 45 |

## SPATIAL BEAM SHAPING: CONTINUOUS RING-SHAPED LASER ON COPPER

The second case is to validate the application of spatial laser beam shaping on copper. A 1300 W ring-shaped beam, with the scanning speed of 0.5 m/s and the core-ring power ratio of 20-80, is applied in this case. The laser shape is computed using Eqs. (13) and (14), and the relevant parameters are presented in Table 2 as R1. The shape is shown as S:20-80 in Fig. 1.

A couple of absorption rates are used to conduct the sensitivity analysis of melt-region dimension with respect to absorptivity, see Section ABSOPTIVITY VS. POWER IN COPPER. Fig. 5(b) and Table 3 give a comparison of simulated and experimental [34] results. The good agreement of the penetration dimension is reached when the absorption rate is $\eta =$

3.6%. Here we do not model the particle powder layer which is included in the reference experiment [34].

### TEMPORAL BEAM SHAPING: PULSED GAUSSIAN LASER ON STAINLESS STEEL 316L

The third validation case is a temporal beam shaping for SS 316L. Since there are few experimental studies on pulsed PBF-LB on metals in the literature for reference, we conducted a related single-track remelting experiment using our open-architecture PBF-LB machine developed at DTU, Lyngby [36].

#### *Experimental Setup*

Temporal beam shaping is achieved using a 250 W Gaussian infrared laser with a duty cycle of 50%, a cycle length of 153.846 μs corresponding to a switching frequency of 6500 Hz. The spot diameter of the laser is 90 μm, moving at a constant speed of 0.325 m/s. A single track with a length of 20 mm is fabricated on a SS 316L substrate with the dimension of $80 \times 10 \times 1$ mm$^3$ in a nitrogen atmosphere.

To observe the transverse section of the melt region, three samples are extracted from various locations along the scanning direction. These samples are then embedded in a polyfast resin. Grinding was performed using silicon carbide papers ranging from grit 500 to 4000, followed by polishing with diamond suspensions of 3 μm and 1 μm. Final polishing is conducted using a colloidal silica suspension (OP-S). The polished samples are etched with Kalling reagent-2 for 15 seconds. Optical microscopy is performed using a Carl Zeiss Axio Vert A1 microscope to characterize the microstructure. Melt-region dimensions are characterized in terms of width ($W$), height ($H_m$), and depth ($D$), with their definition illustrated in Figs. 4 and 5(c). The result data are presented in Table 4.

**Table 4** Dimension of the melt region under 6500 $Hz$ pulsed Gaussian laser on SS 316L.

| | **Width (μm)** | **Height (μm)** | **Depth (μm)** |
|---|---|---|---|
| Experiment | $133 \pm 11$ | $223 \pm 2$ | $200 \pm 2$ |
| Simulation | 150 | 220 | 200 |

#### *Numerical Implementation*

In the simulation, the laser beam shape is computed using Eqs. (13) and (14), with the parameter corresponding to G2 in Table 2. The shape is shown as S:100-0-D2 in Fig. 1. The pulsed configuration matches that used in the experiment. The resulting melt-region profile is shown in Fig. 5(c), and the corresponding dimension data are provided in Table 4. Since no particle powder is involved in either the experimental or simulated models for this remelting case, the total cross-sectional height, from the bottom to the top, is also compared, in addition

to the penetration dimension. The results demonstrate that the simulation achieves high accuracy.

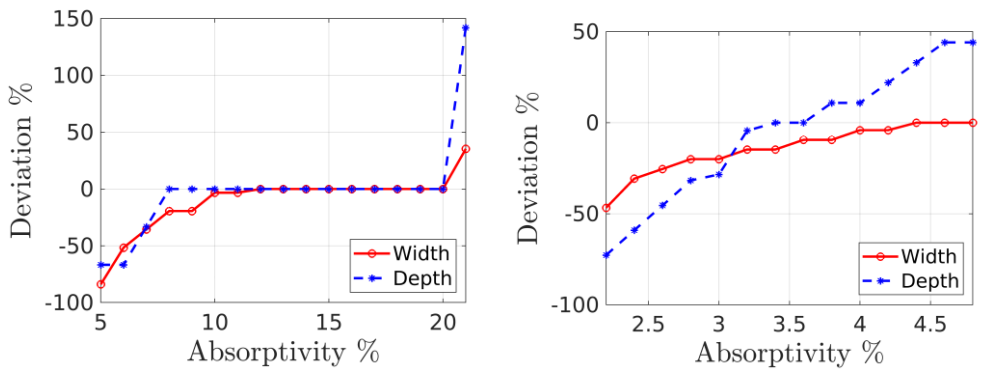
## DISCUSSION

### ABSOPTIVITY VS. POWER IN COPPER

Considering the high thermal conductivity of copper, we apply a series of laser absorption rates ($\eta$) to approach the experimental results in both the Gaussian (absorptivity range of 5% to 21%) and ring-shaped (absorptivity range of 2.2% to 4.8%) validation cases. Figs. 6(a) and 6(b) present the relative deviation of the width and the depth of the transverse melt-region section for both cases. The deviation is calculated by

$$\Delta_r = \frac{\phi - \phi^{ref}}{\phi^{ref}}, \tag{15}$$

where $\phi$ represents the simulated width and depth, and $\phi^{ref}$ corresponds to the referenced experiment results. Since the referenced experiment gives two sets of data for each case as shown in Table 3, if $\phi$ is greater than the larger experimental result, then $\phi^{ref}$ takes the larger value of the two experimental results; if $\phi$ is less than the smaller experimental result, then $\phi^{ref}$ takes the smaller value; if $\phi$ is within the range of the two experimental results, then we set $\Delta_r = 0$. From Figs. 6(a) and 6(b), it is observed that the width and depth both nonlinearly increase with the absorptivity increasing.




(a) (b)

**Fig. 6** Deviation ($\Delta_r$) of cross-section dimension of melt region of copper under continuous (a) Gaussian and (b) 20-80 ring-shaped laser beams for the validation cases

Width varies less with absorptivity than the depth, especially for the ring-shaped cases. This is because that the melt-pool width is greatly limited by the high thermal conductivity of copper and the laser spot size, while the depth is greatly affected by the depression formed by recoil pressure, which is also found in literature [35]. To further explore the influence of power on copper melt-pool dynamics, we extract melt pools at absorptivity of 5%, 15%, 21% under the continuous Gaussian laser irradiation, see Fig. 7. When a small amount of energy is absorbed ($\eta = 5\%$), there is almost no material melted, see Fig. 7(a); when a relatively moderate amount of energy is absorbed, the conduction mode appears, characterized by a round melt pool without noticeable depression, see Fig. 7(b); and when a large amount of energy is absorbed, the keyhole forms, see Fig. 7(c). The keyhole can lead to multiple reflections of the laser rays, significantly increasing the global energy absorption. This is observed in Fig. 6(a) by an increase in melt-region depth, when the local absorption rate $\eta$ slightly increases from 20% to 21%.

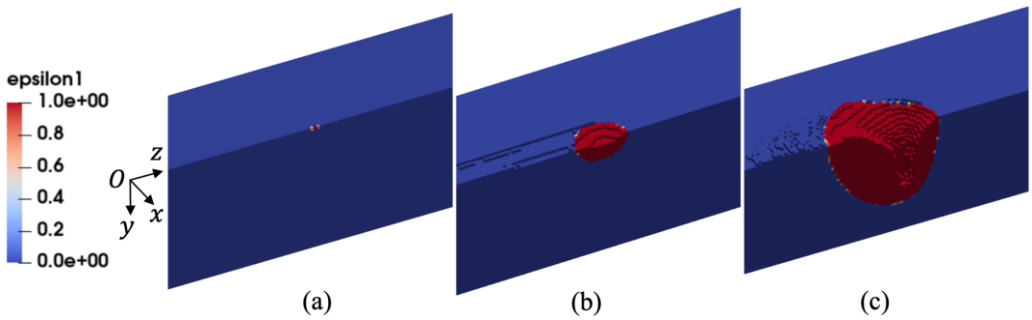



**Fig. 7** Bird-eye view of melt pool of copper under the 400 $W$ continuous Gaussian laser, with the absorptivity of (a) $\eta = 5\%$, (b) $\eta = 15\%$, (c) $\eta = 21\%$

## SPATIAL AND TEMPORAL BEAM SHAPING EFFECTS ON MELT POOL

By comparing the experimental results in Figs. 5(a) and 5(b), it can be seen that the ring-shaped laser beam makes the melt region relatively shallower and wider than that formed by a pure Gaussian laser. This is because the ring-shaped beam distributes a smaller proportion of laser power to the center, decreasing the average intensity in this case. Such spatial beam shaping helps avoid excessive power concentration in the center, reducing vaporization effects, thereby promoting a stable melting which is observed by comparing the material deposition surfaces in Figs. 8(a) and 8(b). The surface deposited under the ring-shaped laser is smoother and flatter.

Fish-scale patterns appear on the deposition surface under pulsed laser irradiation on copper, as shown in Fig. 8(c). These patterns result from multiple discrete melt pools formed during PBF-LB, which partially overlap with one another. Fish-fin patterns are also observed on the SS 316L deposited surface, as shown in Fig. 8(d). Note that in the case of Fig. 8(c), temporal

beam shaping is achieved using a 400 W pulsed Gaussian infrared laser with a duty cycle of 50%, a cycle length of 153.846 μs corresponding to a switching frequency of 6500 Hz. The spot diameter of the laser is 62 μm, the same as in the continuous Gaussian validation case, and it moves at a constant speed of 0.5 m/s. The case in Fig. 8(d) is taken from the above temporal beam shaping validation case.

Comparing Figs. 8(a) and 8(c), the pulsed melt region in Fig. 8(c) is smaller in size even though the same power and beam shape are applied in both cases, and the pulsed laser technique allows for more controlled and refined melting, making it suitable for high-precision applications. A hump is observed during the PBF-LB process of SS 316L but not in copper, as shown in Figs. 8(c) and 8(d). This is attributed to the lower thermal conductivity of SS 316L, which leads to slower heat dissipation. Additionally, stronger Marangoni effects in SS 316L, i.e., the larger magnitude of the temperature derivative of surface tension (as shown in Table 1), promotes localized accumulation of molten material, increasing the likelihood of the hump formation.

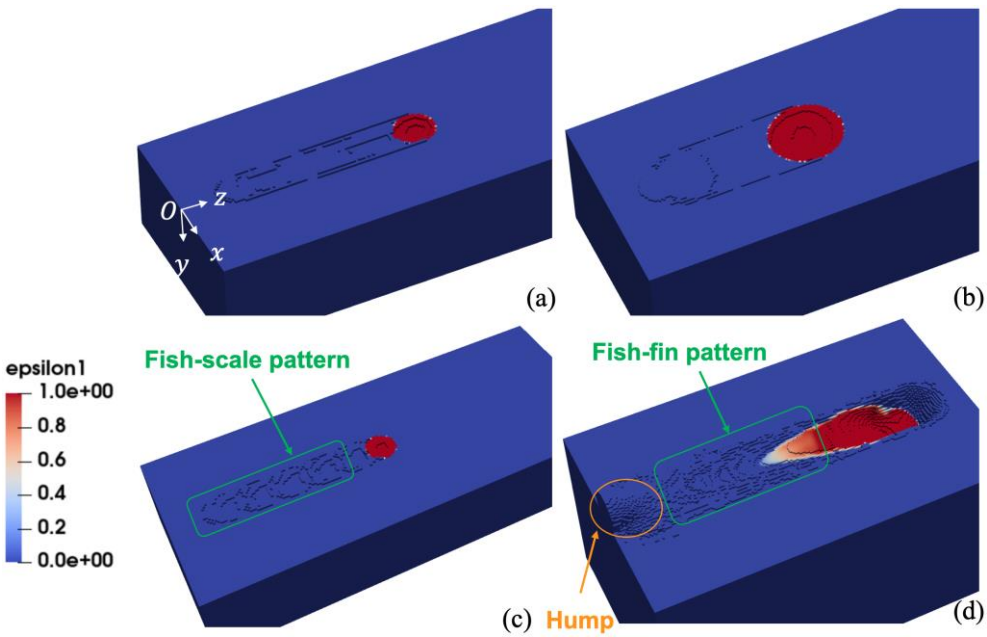



**Fig. 8** Bird-eye view of material deposition surface during PBF-LB. (a) Continuous Gaussian laser on copper. (b) Continuous 20-80 ring-shaped laser on copper. (c) Pulsed Gaussian laser on copper. (d) Pulsed Gaussian laser on SS 316L

## CONCLUSION

This work extends the open-source PBF-LB solver laserBeamFoam to enable simulation of both spatial and temporal beam shaping in metal additive manufacturing. The implementation is validated against experimental results for continuous Gaussian and ring-shaped laser beams on copper, as well as pulsed Gaussian laser beams on stainless steel 316L (SS 316L), with good agreement in melt-region cross-sectional profiles. Based on a sensitivity analysis of copper's laser absorption behavior, the mechanism behind the nonlinear increase in melt-region dimension with rising absorbed energy is investigated. It is shown that the keyhole formation under high-power irradiation may significantly increase the number of laser beam reflections and energy absorption. Compared to the continuous pure Gaussian irradiation, the ring-shaped beam produces more stable and uniform melting, while pulsed laser irradiation tends to generate fish-scale or fish-fin patterns on the deposited surface.

This work currently considers only one situation each for spatial and temporal beam shaping. In future studies, the effects of varying parameters such as core-ring power ratio, duty cycle, and switching frequency on melt-pool dynamics will be explored. The particle powder layer will also be added in the simulation to approximate the real situation.

## ACKNOWLEDGEMENTS

The work is funded by the EU project - GlobalAM (Grant No. 113436) and the Danish-funded project - MicroAM (Grant No. MicroAM-VIL54495). This work has been conducted at Department of Civil and Mechanical Engineering, Section for Manufacturing Engineering. Special thanks are given to Thomas Flint for his support with the laserBeamFoam code.

## References

[1] H. REN, X. TIAN, D. LIU, J. LIU and H. WANG: 'Microstructural evolution and mechanical properties of laser melting deposited Ti–6.5Al–3.5Mo–1.5Zr–0.3Si titanium alloy', *Transactions of Nonferrous Metals Society of China*, vol. 25, no. 6, pp. 1856-1864, Jun. 2015, doi: 10.1016/S1003-6326(15)63792-X.

[2] L. C. ZHANG, D. KLEMM, J. ECKERT, Y. L. HAO and T. B. SERCOMBE: 'Manufacture by selective laser melting and mechanical behavior of a biomedical Ti–24Nb–4Zr–8Sn alloy', *Scr. Mater.*, vol. 65, no. 1, pp. 21-24, Jun. 2011, doi: 10.1016/j.scriptamat.2011.03.024.

[3] J. O. MILEWSKI: 'Additive manufacturing of metals: from fundamental technology to rocket nozzles, medical implants, and custom jewelry', *Springer Series in Materials Science*, vol. 258, 2017, pp. 37-44.

[4] H. JASAK, A. JEMCOV and Z. TUKOVIC: 'OpenFOAM: a C++ library for complex physics simulations', In: *International Workshop on Coupled Methods in Numerical Dynamics*, IUC, Dubrovnik, Croatia, 2007, pp. 1-20.

[5] H. B. BINGHAM, P. S. LARSEN and V. A. BARKER: 'Computational Fluid Dynamics: lecture note for course no. 41317', *Unpublished Note*, Technical University of Denmark, 2018.

[6] D. Q. ZHANG, Q. Z. CAI, J. H. LIU, L. ZHANG and R. D. LI: 'Select laser melting of W–Ni–Fe powders: simulation and experimental study', *The International Journal of Advanced Manufacturing Technology*, vol. 51, no. 5-8, pp. 649-658, Nov. 2010, doi: 10.1007/s00170-010-2641-3.

[7] J. YIN, H. ZHU, L. KE, W. LEI, C. DAI and D. ZUO: 'Simulation of temperature distribution in single metallic powder layer for laser micro-sintering', *Comput. Mater. Sci.*, vol. 53, no. 1, pp. 333-339, Feb. 2012, doi: 10.1016/j.commatsci.2011.09.012.

[8] N. E. HODGE, R. M. FERENCZ and J. M. SOLBERG: 'Implementation of a thermomechanical model for the simulation of selective laser melting', *Comput. Mech.*, vol. 54, no. 1, pp. 33-51, Jul. 2014, doi: 10.1007/s00466-014-1024-2.

[9] L. PARRY, I. A. ASHCROFT and R. D. WILDMAN: 'Understanding the effect of laser scan strategy on residual stress in selective laser melting through thermo-mechanical simulation', *Addit. Manuf.*, vol. 12, pp. 1-15, Oct. 2016, doi: 10.1016/j.addma.2016.05.014.

[10] M. MEGAHED, H.-W. MINDT, N. N'DRI, H. DUAN and O. DESMAISON: 'Metal additive-manufacturing process and residual stress modeling', *Integr. Mater. Manuf. Innov.*, vol. 5, no. 1, pp. 61-93, Dec. 2016, doi: 10.1186/s40192-016-0047-2.

[11] T. F. FLINT, G. PARIVENDHAN, A. IVANKOVIC, M. C. SMITH and P. CARDIFF: 'beamWeldFoam: Numerical simulation of high energy density fusion and vapourisation-inducing processes', *SoftwareX*, vol. 18, p. 101065, Jun. 2022, doi: 10.1016/j.softx.2022.101065.

[12] T. F. FLINT, J. D. ROBSON, G. PARIVENDHAN and P. CARDIFF: 'laserbeamFoam: Laser ray-tracing and thermally induced state transition simulation toolkit', *SoftwareX*, vol. 21, p. 101299, Feb. 2023, doi: 10.1016/j.softx.2022.101299.

[13] T. F. FLINT, J. D. ROBSON, P. ESMATI, N. GRILLI, G. PARIVENDHAN and P. Cardiff: 'Version 2.0 – LaserbeamFoam: Laser ray-tracing and thermally induced state transition simulation toolkit', *SoftwareX*, vol. 25, p. 101612, Feb. 2024, doi: 10.1016/j.softx.2023.101612.

[14] A. I. LVOVSKY: 'Fresnel equations', *Encyclopedia of Optical Engineering*, vol. 27, pp. 1-6, 2013.

[15] T. F. FLINT, L. SCOTTI, H. C. BASOALTO and M. C. SMITH: 'A thermal fluid dynamics framework applied to multi-component substrates experiencing fusion and vaporisation state transitions', *Commun. Phys.*, vol. 3, no. 1, p. 196, Nov. 2020, doi: 10.1038/s42005-020-00462-7.

[16] S. B. BOYDEN and Y. ZHANG: 'Temperature and wavelength-dependent spectral absorptivities of metallic materials in the infrared', *J. Thermophys. Heat Trans.*, vol. 20, no. 1, pp. 9-15, Jan. 2006, doi: 10.2514/1.15518.

[17] W. E. ALPHONSO, M. BAYAT and J. H. HATTEL: 'Comparison between green and infrared laser in Laser Powder Bed Fusion of pure copper through high fidelity numerical modelling at meso-scale', In: *13th International Seminar Numerical Analysis of Weldability*, Graz, Austria, 2023, pp. 21-28.

[18] L. GARGALIS *et al.*: 'Determining processing behaviour of pure Cu in laser powder bed fusion using direct micro-calorimetry', *J. Mater. Process Technol.*, vol. 294, p. 117130, Aug. 2021, doi: 10.1016/j.jmatprotec.2021.117130.

[19] W. E. KING *et al.*: 'Observation of keyhole-mode laser melting in laser powder-bed fusion additive manufacturing', *J. Mater. Process Technol.*, vol. 214, no. 12, pp. 2915-2925, Dec. 2014, doi: 10.1016/j.jmatprotec.2014.06.005.

[20] G. NORDET *et al.*: 'Absorptivity measurements during laser powder bed fusion of pure copper with a 1 kW cw green laser', *Opt. Laser Technol.*, vol. 147, p. 107612, Mar. 2022, doi: 10.1016/j.optlastec.2021.107612.

[21] E. SANTECCHIA *et al.*: 'Microstructural features induced by the Gaussian laser beam shape on 316L stainless steel thin-walled samples fabricated by directed energy deposition', *Progress in Additive Manufacturing*, Mar. 2025, doi: 10.1007/s40964-025-01028-1.

[22] J. GRUNEWALD, J. REIMANN and K. WUDY: 'Influence of ring-shaped beam profiles on spatter characteristics in laser-based powder bed fusion of metals', *J. Laser Appl.*, vol. 35, no. 4, Nov. 2023, doi: 10.2351/7.0001153.

[23] J. D. PEREZ-RUIZ *et al.*: 'Laser beam shaping facilitates tailoring the mechanical properties of IN718 during powder bed fusion', *J. Mater. Process Technol.*, vol. 328, p. 118393, Jul. 2024, doi: 10.1016/j.jmatprotec.2024.118393.

[24] A. EBRAHIMI, M. SATTARI, A. BABU, A. SOOD, G.-W. R. B. E. ROMER and M. J. M. HERMANS: 'Revealing the effects of laser beam shaping on melt pool behaviour in conduction-mode laser melting', *Journal of Materials Research and Technology*, vol. 27, pp. 3955-3967, Nov. 2023, doi: 10.1016/j.jmrt.2023.11.046.

[25] S. A. KHAIRALLAH, A. T. ANDERSON, A. RUBENCHIK and W. E. KING: 'Laser powder-bed fusion additive manufacturing: Physics of complex melt flow and formation mechanisms of pores, spatter, and denudation zones', *Acta Mater.*, vol. 108, pp. 36-45, Apr. 2016, doi: 10.1016/j.actamat.2016.02.014.

[26] M. BAYAT, V. K. NADIMPALLI, D. B. PEDERSEN and J. H. HATTEL: 'A fundamental investigation of thermo-capillarity in laser powder bed fusion of metals and alloys', *Int. J. Heat Mass Transf.*, vol. 166, p. 120766, Feb. 2021, doi: 10.1016/j.ijheatmasstransfer.2020.120766.

[27] M. BAYAT *et al.*: 'Exploring spatial beam shaping in laser powder bed fusion: High-fidelity simulation and in-situ monitoring', *Addit. Manuf.*, vol. 93, p. 104420, Aug. 2024, doi: 10.1016/j.addma.2024.104420.

[28] F. GALBUSERA, L. CAPRIO, B. PREVITALI and A. G. DEMIR: 'The influence of novel beam shapes on melt pool shape and mechanical properties of LPBF produced Al-alloy', *J. Manuf. Process*, vol. 85, pp. 1024-1036, Jan. 2023, doi: 10.1016/j.jmapro.2022.12.007.

[29] Q. HAYAT *et al.*: 'Elucidating the effect of circular and tailing laser beam shapes on keyhole necking and porosity formation during laser beam welding of aluminum 1060 using a multiphysics computational fluid dynamics approach', *J. Laser. App.l*, vol. 35, no. 4, Nov. 2023, doi: 10.2351/7.0001150.

[30] V. K. NADIPALLI, S. A. ANDERSEN, J. S. NIELSEN and D. B. PEDERSEN: 'Considerations for interpreting in-situ photodiode sensor data in pulsed mode laser powder bed fusion', In: *Joint Special Interest Group Meeting between Euspen and ASPE Advancing Precision in Additive Manufacturing*, Nantes, France, 2019, pp. 66-69.

[31] M. BAYAT, V. NADIPALLI and J. Hattel: 'Multiphysics simulation of thermal and fluid dynamics phenomena during the pulsed laser powder bed fusion process of 316-L steel', In: *17th UK Heat Transfer Conference*, Manchester, UK, 2022, pp. 1-6.

[32] M. ZHENG *et al.*: 'Surface morphology evolution during pulsed selective laser melting: Numerical and experimental investigations', *Appl. Surf. Sci.*, vol. 496, p. 143649, Dec. 2019, doi: 10.1016/j.apsusc.2019.143649.

[33] C. W. HIRT and B. D. NICHOLS: 'Volume of fluid (VOF) method for the dynamics of free boundaries', *J. Comput. Phys.*, vol. 39, no. 1, pp. 201-225, Jan. 1981, doi: 10.1016/0021-9991(81)90145-5.

[34] A. BAUCH, P. KOHLWES and I. Kelbassa: 'Laser powder bed fusion of pure copper using ring-shaped beam profiles', *J. Laser. Appl.*, vol. 36, no. 4, Nov. 2024, doi: 10.2351/7.0001562.

[35] A. BAUCH and D. HERZOG: 'Influence of temperature and beam size on weld track shape in laser powder bed fusion of pure copper using near-infrared laser system', *J. Laser. Appl.*, vol. 36, no. 1, pp. 1-9, Feb. 2024, doi: 10.2351/7.0001118.

[36] M. B. KJER, V. K. NADIMPALLI, C. L. BUDDEN and D. B. PEDERSEN: 'Applying systems engineering principles to develop an open source laser based metal powder bed fusion system', *Rapid Prototyp J.*, vol. 30, no. 9, pp. 1911-1928, Oct. 2024, doi: 10.1108/RPJ-12-2023-0422.

# ADVANCED PROCESS MODELING AND SIMULATION OF MULTI-MATERIAL DIRECTED ENERGY DEPOSITION

E. OSMANOGLU*, C. CANAZ**, N. HEMPEL***, P. MAYR****

*Technical University of Munich, Chair of Materials Engineering of Additive Manufacturing, 85748, Garching, Germany, 0000-0003-3868-5407, emre.osmanoglu@tum.de
** Technical University of Munich, Chair of Materials Engineering of Additive Manufacturing, 85748, Garching, Germany, 0009-0001-7704-674X
***Technical University of Munich, Chair of Materials Engineering of Additive Manufacturing, 85748, Garching, Germany, 0000-0001-7316-1065
****Technical University of Munich, Chair of Materials Engineering of Additive Manufacturing, 85748, Garching, Germany, 0000-0003-2530-4644

*DOI 10.3217/978-3-99161-089-2-012, license CC BY 4.0*
*https://creativecommons.org/licenses/by/4.0/deed.en*
*This CC license does not apply to third party material and content noted otherwise.*

## ABSTRACT

As technology advances, materials face increasing demands, especially in the aerospace industry. Metal additive manufacturing (AM), specifically directed energy deposition (DED), addresses these needs by enabling multi-material deposition and in-situ alloying, producing functionally graded materials (FGMs) with tailored properties by combining different materials. Numerical simulations can be used to predict temperature fields and distortions in the DED process, reducing costly trial runs. However, incorporating FGMs in such thermomechanical simulations of DED process requires development of new process models and creation of material models for specific alloy combinations. Using Simufact Welding and extending the capabilities of the software, a DED process is modelled, and material compositions are assigned to layers to construct FGMs virtually in this work. Initial process simulations of CuCrZr-IN718 FGM deposition on a CuCrZr substrate demonstrate successful modelling of the process. These models correlate well with experimental results, predicting temperature fields and distortions effectively. Future work includes further validation and scaling simulations for industrial applications.

Keywords: Directed energy deposition, functionally graded materials, process simulation, multi material additive manufacturing

## INTRODUCTION

In aerospace applications, parts have to perform under extreme conditions. A way to address these challenges is to build multi-material structures that are made of functionally graded

materials (FGM) [1-3]. Various additive manufacturing (AM) methods are used to build FGM structures such as laser directed energy deposition [4-6] and wire arc additive manufacturing [7-8]. In this work, the FGM will be built by combining CuCrZr with IN718, using plasma directed energy deposition or 3D plasma metal deposition (3DPMD).

While there is previous work on multi material metal AM, process digitalization is a relatively underdeveloped area. The goal of process simulation in DED of metals is to predict the temperature field distribution of the printed structure, to calculate the residual stress and resulting distortions as accurately as possible. The simulations also demonstrate the connection between the process parameters, used materials and resulting temperature and stress fields [9-10]. By calibrating the heat source model and the simulation process parameters, it is aimed to provide a representative model that can be used to minimize resulting stress and distortions on the printed body without the costly and time-consuming experimental procedures.

Finite element method (FEM) is a widely used approach for simulating thermomechanical behavior of parts built via DED. It enables the prediction of fields that determine the part's performance, such as temperature distribution, residual stress, and geometric deformation [9-10]. Many finite element (FE) models representing a DED process include the key properties:

- Moving heat source models, such as Goldak or cylindrical types
- Element activation/deactivation technique to model layer-by-layer material deposition
- Adaptive meshing around heat affected zone (HAZ)
- Path-based simulation to mimic heat source movement
- Thermo-mechanical coupling for stress-strain analysis

These well-established numerical methods allow detailed analysis of the DED process. In recent developments, these models are often augmented with machine learning-based surrogate models to improve computational efficiency and gain new insights [11].

In this work, the established simulation methods will be extended to incorporate multi-material deposition process, which is used to manufacture FGMs. For this purpose, new material models will be generated by combining the existing material models using rule of mixtures.

## PROCESS DIGITALIZATION

To simulate large-scale additive manufacturing builds, Ref. [9] created a thermomechanically coupled FE model, concentrating on electron beam deposition of Ti–6Al–4V. To demonstrate the progressive layer-wise addition of material, their model used also a sequential element activation technique and included an elastoplastic material formulation. In this technique, elements representing the deposited material are initially removed, then reintroduced layer by layer in an inactive state. They are activated with their true material properties as the moving energy source approaches. To overcome the computing difficulties of simulating more than 100 layers, authors developed an adaptive meshing approach that greatly reduced the total

degrees of freedom by coarsening the mesh in previously deposited regions while maintaining fine resolution close to the melt pool. A moving volumetric heat source was used to simulate the thermal input, and the temperature distribution, residual stress, and deformation during the printing process were calculated. With prediction errors of less than 29%, validation against experimental distortion measurements were promising. This work offers a computationally effective method for simulating industrial-scale builds, marking a significant leap in the numerical simulation of metal additive manufacturing. Since then, it has been used as a basis for the advancement of adaptive meshing algorithms and element activation techniques in both commercial and research DED simulation systems.

Ref. [12] studied how to simplify the modelling of transient heat source motion in thermomechanical finite element simulations for DED. They used Simufact Welding 2021.1 to model laser DED of an 80-layer stainless steel turbine blade. They suggested the Advanced Thermal Cycle (ATC) method, which groups several thermal increments to simulate the heat input over greater regions. Their results showed that the predicted thermal fields and geometric distortions aligned well with experimental results even when significant simplifications were applied (e.g., 10 to 100 increments grouped together). Grouping 10 increments reduced computation time by up to 90% while keeping the predicted geometry accurate. The study showed that ATC is an effective method for making DED simulations faster, while still maintaining good model quality for industrial use.

As of lately, functionally graded materials (FGMs) have also become a big focus in DED processes. Rather than relying on a single material with uniform properties, the ability to vary the composition and microstructure throughout a printed part has shown great promise in high-performance demanding areas like aerospace. Ref. [13] worked on thermomechanical modelling of two FGM cases manufactured via laser DED with direct deposition of Copper on SS304L, and a functionally graded material (FGM) structure transitioning from SS316L to IN718 to Copper on an SS304L substrate. During the process, temperature data from the substrate was gathered to calibrate and validate the 3D thermomechanical model. Then the resulting distortions and stresses were analysed. Numerical and experimental temperature histories aligned well, with the accuracy increasing as the layers progress. The developed model can predict stress in single material DED parts accurately and help choose better designs and materials.

In this work, the 3DPMD process will be digitalized using Simufact Welding software. In the digitalization process, substrate, clamping solution, and heat source will be transferred to the digital environment and the simulated process will be run according to the process parameters coming from the experiments.

The digitalization that is proposed in this work follows calibration, validation, and simulation steps. In the calibration step, the heat source will be calibrated according to experiment. In the validation step, a new validation experiment is conducted to assess the accuracy of the digital model and determine if the model is overfitted to a specific case. Finally, multi material deposition of a structure made of Cu-Ni FGM by the 3DPMD process is simulated. It will be demonstrated that the proposed method of process digitalization yields accurate time-temperature history with an error less than 10% and generates a model that is not overfitted to a specific case but can be used for different deposition conditions using same equipment.

## EXPERIMENTAL SETUP

The 3DPMD process is conducted using a torch attached to a six-axis industrial robot. The substrates are clamped to the base of the industrial robot. Two different powder feedstocks can be simultaneously supplied to the plasma torch to achieve in-situ alloying.

In the experiments argon is used for plasma gas, shielding gas and transportation gas. The powders of CuCrZr and IN718 have the particle sizes 90% 45-100 μm and 45-106 μm, respectively. The chemical compositions of the powders are given in Table 1.

**Table 1** Chemical compositions of the powders in weight percentages

| Element | Ni | Cu | Cr | Zr | Fe | Si | Ti | Nb | Mo |
|---|---|---|---|---|---|---|---|---|---|
| **IN718** | 53.2 | 0.01 | 18.99 | - | 17.73 | 0.21 | 1.01 | 5.02 | 3.13 |
| **CuCrZr** | - | Bal. | 0.77 | 0.09 | 0.01 | 0.01 | - | - | - |

The substrate plate is heated up to 350 °C using a heating plate. It is then transferred to the robot based and clamped for the deposition process. The welding is started when the plate cools down to 300 °C, which corresponds to interlayer temperature. During the process, this interlayer temperature of 300 °C is controlled using a pyrometer. The pyrometer was calibrated by measuring the surface temperature of the substrate with a thermocouple. In addition to the pyrometer, the temperature of the substrate was recorded with thermocouples. The location and the orientation of the thermocouples at the multi-material experiment are presented in Fig. 1. In the calibration and validation experiments, thermocouples are attached to substrate from bottom. Holes with a depth of 5 mm drilled on the substrate to locate the thermocouples to the surface as close as possible. The location of the thermocouples for the calibration and validation experiments are presented in Fig. 2 and Fig. 3, respectively.



**Fig. 1** Multi material DED deposition of IN718 on a CuCrZr substrate with thermocouples for temperature measurement. Bright point on the top left surface of the deposition is the laser of pyrometer.

The process parameters used for deposition of CuCrZr and IN718 is presented in Table 2. For the transition layers, CuCrZr and IN718 mixed in equal proportions by weight. The deposition is further explained at the corresponding experiment.

**Table 2** Process parameters for the deposition of CuCrZr and IN718

| Process Parameter | Details |
|---|---|
| Welding speed | 2 mm/s |
| Line energy for CuCrZr | 2.75 – 2.60 kJ/mm |
| Line energy for transition zone | 2.45 kJ/mm |
| Line energy for IN718 | 2.20 kJ/mm |
| Powder supply rate | 24.3 g/min |
| Layer height | 2.5 mm |
| Standoff distance | 10 mm |
| Plasma gas flow rate | 1.5 L/min |
| Shielding gas flow rate | 15 L/min |
| Preheating temperature | 300 °C |
| Dwell time between layers | 300 – 60 s |

In the simulations, material models from the materials library of the Simufact Welding are used for CuCrZr and IN718. The material model for the gradient is obtained by mixing the two materials according to the rule of mixtures, which will be discussed in the corresponding chapter.

## SIMULATION MODEL CALIBRATION

In the process calibration step, the digital model of the 3DPMD process is created in Simufact Welding. The main aspect of this step is the calibration of the heat source. The process parameters and the geometries of substrate and deposition are known inputs for the simulation, but the heat source is an unknown. While the dimensions of the heat source dictate the deposition geometry, the efficiency of the heat source scales the heat source power, which affects the time-temperature history.

The first step of the process digitalization is the generation of geometries in the simulation software. In the calibration simulation, only substrate and deposited wall is modelled because the clamping was minimal in the experiments. The simulation model is presented in Fig. 2. This model contains deposition wall, substrate, heat source model, and clamping models.

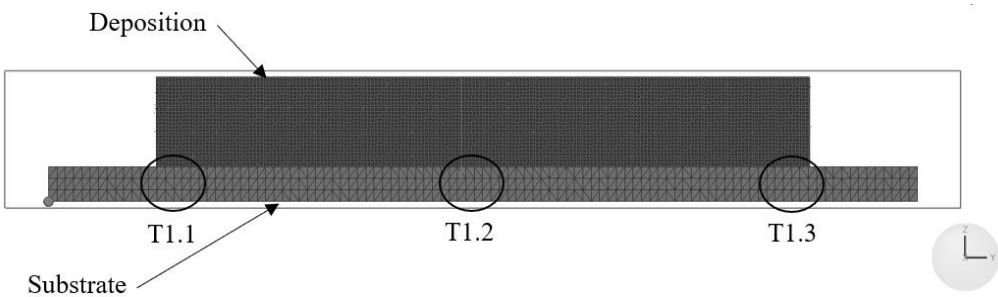



**Fig. 2** Simulation model for the calibration runs. Thermocouples T1.1-3 are attached from the bottom of the substrate, 5 mm deep along the center line of the deposition.

During the experiment, layer dimensions depend on the standoff distance between the torch and the substrate surface. This distance is kept constant at 10 mm but due to the different powder capture efficiencies during the deposition of consecutive layers, the layer height changes ±0.5 mm during the process. For the simulations, a uniform layer height is assumed by dividing the height of the deposited wall to the number of layers, which is 2.5 mm.

In the calibration simulations, heat source size is determined according to the width and the height of the deposited layers. A disk type heat source is generated to encompass the deposition track. The height and radius of the disk are increased by 10% to ensure that the disk can cover the deposition tracks completely and achieve some penetration between the consecutive layers.

For the calibration of the simulation multiple simulation runs were conducted. The goal of the calibration is to match the time-temperature history from the simulations with the measurements from the experiments. In the time-temperature history, peaks correspond to the instances at which the torch is in-line with the thermocouple. Therefore, one must adjust the heat source efficiency to match the peaks. The second aspect of time-temperature history is the cooling behaviour. As the heat source moves away from the thermocouple, the temperature reading starts to drop. This is due to the heat dissipation within the part and heat loss to the environment. Hence, to have an accurate simulation, these factors must be modelled accurately.

First a mesh sensitivity analysis is conducted to eliminate uncertainty associated with mesh size. Then, the efficiency of the heat source is adjusted so that the peaks of the simulated time-temperature history match the measured values. While calibrating the heat source efficiency, the melt pool temperature was also checked to ensure that the temperature surpassed the melting point of the CuCrZr.

The cooling of the deposition did not require an extensive calibration like the heat source as the clamps are omitted in the simulation model. The convection coefficient between the deposition and the environment is calculated to be 19.9 $W/m^2K$ based on the temperature drop rate. The recommended value in the literature for the convection coefficient is 20 $W/m^2K$ [14], which is also the built-in value in the simulation software. Hence, the software recommendation was used in the simulations.

The comparison of the time-temperature measurement with the simulated values for the first layer of the deposition is presented in Fig. 3. The simulated values do not perfectly fit

with measured values because of the dimensional inaccuracy. In the experiments, thermocouples were attached to the substrate from the holes drilled to the bottom of the plate. During the deposition process, the orientation of the substrate was not as accurate as the simulations due to the minimal clamping. Therefore, the deposited wall is not perfectly parallel and coincident to the line formed by the thermocouples. This dimensional inaccuracy means that the reference points in the simulation are different than the actual locations of thermocouples. However, this inaccuracy is within a displacement of 2 mm. Nevertheless, this positioning error causes the peaks in the measurement to shift in time because the expected position of the torch differs from the actual position of the torch.

The simulated peak values and the ramp up to the peak values are in good agreement with the measured values. Yet, the simulated cooling behaviour differs from the measured values, clearly seen when T1.2 and S1.2 are compared in Fig. 2. The cooling is dominated by the heat loss to the environment and to the clamping. As stated previously, convection coefficient is calculated based on the measurement. Therefore, the cause of deviation is from the modelling of the clamping. Because the clamping was minimal and the plate was clamped only from two ends along the deposition axis, clamps were omitted in the simulation. However, the aim of this step was to calibrate the heat source, and the calibration was successful since the peak values for each thermocouple are in good agreement.

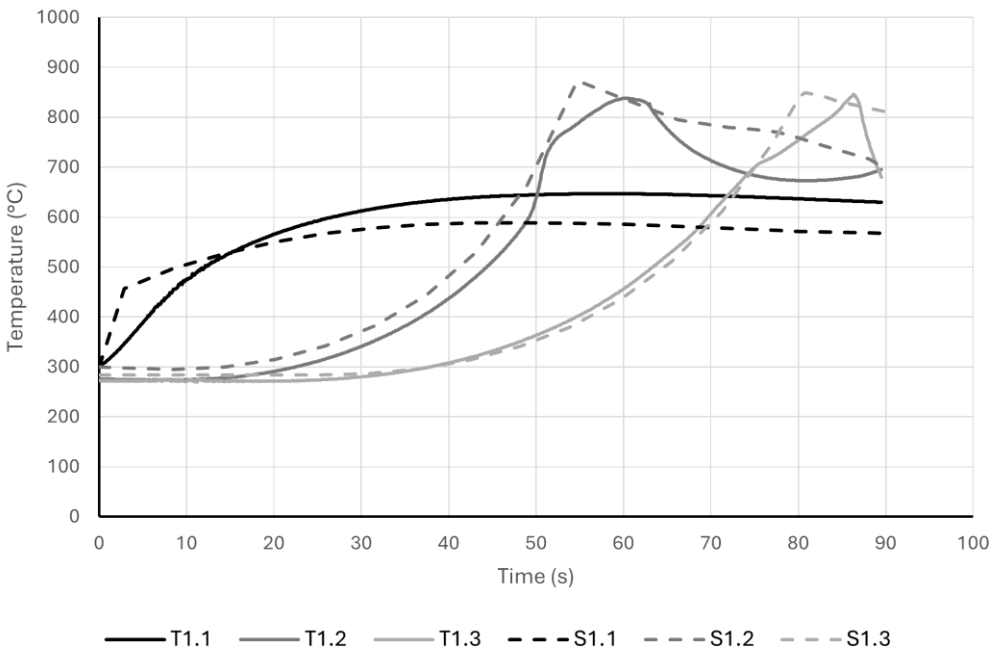



**Fig. 3** Comparison of time-temperature history of the measurement (T) with simulation (S) for the calibration run

## SIMULATION MODEL VALIDATION

In the simulation validation step, a new deposition process is simulated using the same heat source from the calibration step. If the calibration is done accurately, the heat source must be correct for the future processes. The danger of the calibration is to overfit the simulation to a specific case, that is the simulation is calibrated such that it gives correct results only for a given case.

In the validation experiment, the substrate is rotated by 90° along the deposition axis to print on the thin and long edge of the substrate. This orientation is used to imitate the deposited wall and match the deposition track dimensions with the substrate. The deposited wall is about 8 mm wide, and the plate is 10 mm wide. In this experiment, a new vice is used for better clamping and deposition accuracy.

The digitalization of the manufacturing process included modelling of the clamps this time because the area of contact between the clamps and the substrate is considerably larger with respect to the calibration experiment. The simulation model and the location of the thermocouples is presented in Fig. 4.

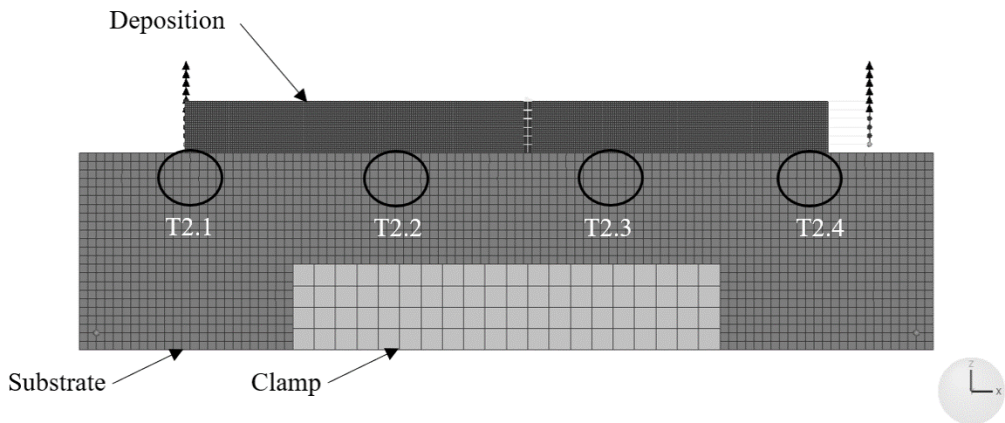



**Fig. 4** Simulation model for the validation runs. Thermocouples T2.1-4 are welded to the substrate from the side surface.

The validation simulations were conducted multiple times for the mesh sensitivity analysis only. The heat source dimensions were not changed since the heat source is calibrated for the given system. The comparison of the time-temperature measurement and simulated values for the first four layers of deposition is presented in Fig. 5.

In the simulations, the cooling behaviour is not accurately predicted because of the simplified clamping model. In the experimental setup, clamping is significantly larger and more complex than the simulated blocks, as shown in Fig. 4. The clamping model used in the simulation is a representative model because the original clamping has a complex geometry with respect to substrate and deposition. To have a reasonable processing time, this simplified model of clamping is utilized in the simulation. Therefore, in the first layer, simulation

predicted overcooling and as the simulation progresses, clamps saturate with heat and cannot absorb as much heat as in the beginning. Hence, from the end of the layer 3, simulations predicted undercooling. Nevertheless, the peak temperatures of the measurements and simulations are in good agreement. There is a temporal shift between the peaks of measurements and simulations. In the experiments, the torch does not turn on instantaneously but requires a time about 5 seconds to ignite. This delay causes a mismatch between the measurements and simulations.

In conclusion, the validation experiment demonstrates that the heat source calibration is done successfully as the measured and simulated temperatures are in good agreement in the validation experiment. This shows that the calibrated heat source is not overfitted to a specific deposition case and the digital model of the manufacturing system is created.

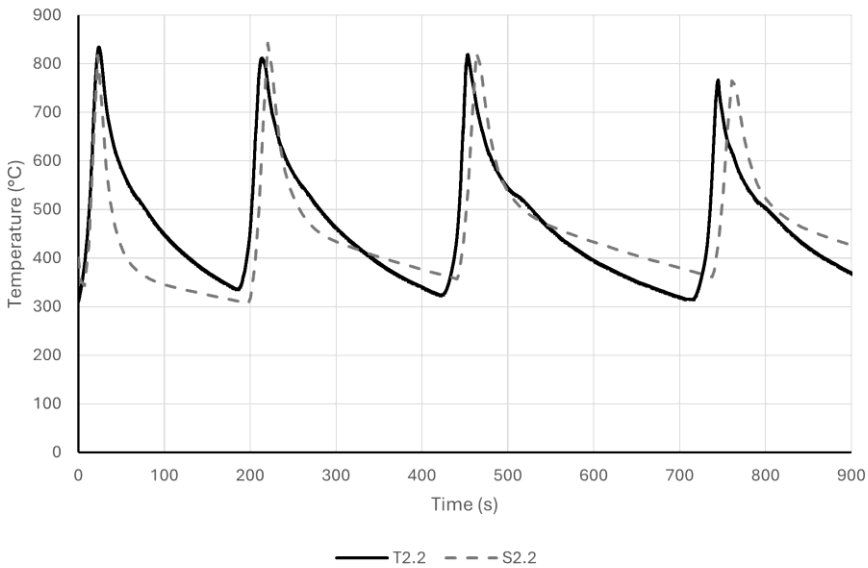



**Fig. 5** Comparison of time-temperature history of the measurement (T) with simulation (S) in the validation run for the first four layers

## MODELLING AND SIMULATION OF A MULTI-MATERIAL PROCESS

To combine the high thermal conductivity of copper with the structural integrity of nickel, multi-material directed energy deposition can be utilized. A structure made of functionally graded material is manufactured with the same experimental setup by combining CuCrZr powder with IN718 powder according to prescribed rates. The transition from CuCrZr to IN718 is done with an intermediate layer which is composed of 50% CuCrZr and 50% IN718 by weight.

The wall built in the experiment is composed of six layers. It begins with two layers of CuCrZr, followed by two layers of 50% Cu 50% Ni alloy, finally ends with two layers of IN718. In this way, an FGM structure is manufactured using 3DPMD. The schematic representation of the deposition process is presented in Fig. 6.




**Fig. 6** Schematic representation of multi material deposition. Each material zone are composed of two layers. The transition zone composed of 50% CuCrZr and 50% IN718 by weight.

In the simulations, a material model is created for the transition layer between copper and nickel alloy by combining the two material models for the alloys in the Simufact Material Database. This new material model is obtained by combining the material properties based on rule of mixtures. Using weight contribution of each constituent, a mixture material model is obtained. This approach assumes that both materials mix perfectly in the melt pool and form a uniform phase. Since copper and nickel has fully solubility in each other, this is a valid assumption.

The simulation model for the manufacturing of the structure with FGM is presented in Fig. 7.

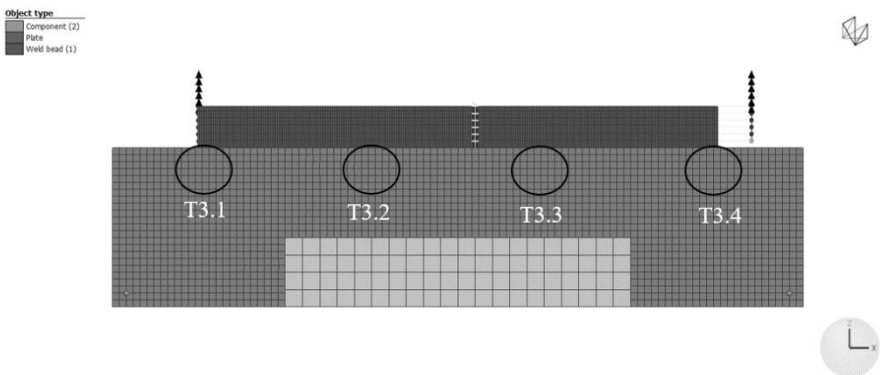



**Fig. 7** Simulation model for the FGM structure. Thermocouples T3.1-4 are welded to the substrate from the side surface.

Normally, Simufact Welding interface does not allow the creation of a mixed material model or assigning more than one material to the deposition. This problem is circumvented by modifying the solver input code generated by the user interface before it is sent to the solver module. Hence, correct material models are assigned to the corresponding layers.

The time-temperature history for the second thermocouple and the simulation results from the same location are presented in Fig. 8. In the simulations, the cooling behaviour is overestimated. This effect diminishes as layers progress because in the initial layers heat loss to the clamping is overestimated. This stems from the simplified model used for the clamping solution. As the clamps heat up, the overcooling effect diminishes. Undercooling is observed at the end of the transition zone. Also, the measurement peaks for the layers five and six are 5 % and 10% smaller than the simulated values, respectively. This indicates a lack of fusion on this level, acting as thermal insulator and manifesting itself as reduced temperature increase in the measurement. However, overall, the simulation results are in good agreement with the measurements.

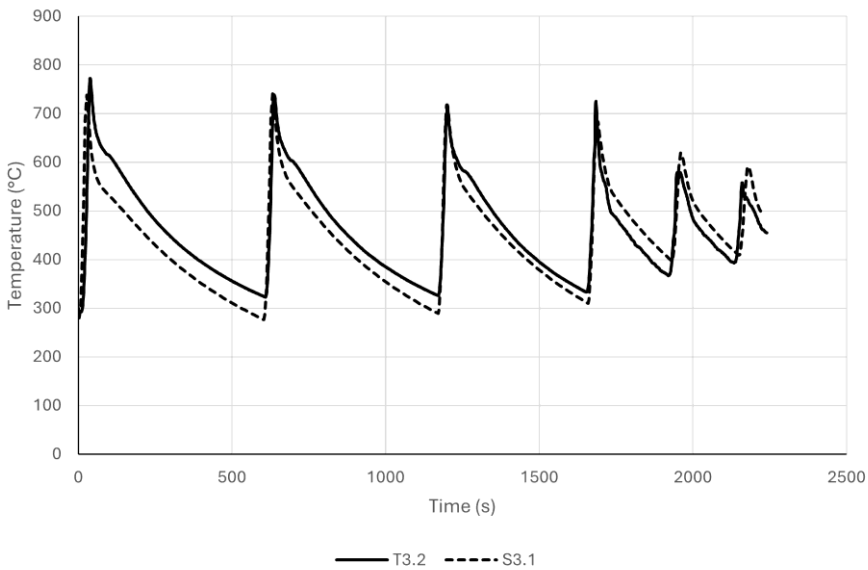



**Fig. 8** Comparison of time-temperature history of the measurement (T) with simulation (S) for the multi-material deposition

## CONCLUSION

This work presents a method for digitizing the multi-material 3DPMD process. Temperature evolution over time is monitored using thermocouples attached to the substrate. Time-temperature data is used to digitize the heat source, modeled as a cylinder with height equal

to the layer height and diameter equal to the layer width × 1.1. Heat source power is based on experimental data, and its efficiency is calibrated to match simulation temperature peaks with measurements.

Using the demonstrated process digitalization method, once a heat source is calibrated, any DED process using the same equipment can be simulated since the digital model of the manufacturing system is obtained. This is demonstrated with the validation test and deposition of FGM.

The digital model generated in this work successfully predicts the time-temperature history of the process within a 10% error margin. The inaccuracies stem from a position error of the substrate during the experiment, and simplified modelling of the clamping solution in the simulation environment.

The capabilities of the Simufact Welding have been extended to simulate multi-material gradient deposition by manipulating the FEM code. The material properties of the gradient layers on which CuCrZr and IN718 are mixed based on the weight can be accurately modelled by combining the material properties of the constituents using the rule of mixtures.

In future work, this digital model can be further expanded by adding mechanical simulation steps to predict distortion and residual stresses. Also, the model can be used to improve process efficiency by finding a better parameter set for shorter interlayer pauses or reduced distortions.

## ACKNOWLEDGEMENTS

This research was funded by the European Union‘s Horizon Europe research and innovation program, grant number 101091860 (DISCO2030).

## References

[1] B. H. RABIN and I. SHIOTA: ‘Functionally Graded Materials’, *MRS Bulletin*, Vol. 20, No. 1, pp. 14-18, 1995.

[2] Z. HU, Z. MA, L. YU, Y. LIU: ‘Functionally graded materials with grain-size gradients and heterogeneous microstructures achieved by additive manufacturing’, *Scripta Materialia*, Vol. 226, 2023.

[3] S. HASANOV, S. ALKUNTE, M. RAJESHIRKE, A. GUPTA, O. HUSEYNOV, I. FIDAN, F. ALIFUI-SEGBAYA, A. RENNIE: ‘Review on Additive Manufacturing of Multi-Material Parts: Progress and Challenges’, *Journal of Manufacturing and Materials Processing*, Vol. 6, No. 1, 2022.

[4] S. YADAV, C.P. PAUL, A. K. RAI, R. SINGH, S. K. DIXIT: ‘Elucidating laser directed energy deposition based additive manufacturing of copper-stainless steel functionally graded material: Processing and material behavior’, *Journal of Manufacturing Processes*, Vol. 92, pp. 107-123, 2023.

[5] M J. SAGONG, E. S. KIM, J. M. PARK, G. M. KARTHIK, B.-J. LEE, J.-W. CHO, C. S. LEE, T. NAKANO, H. S. KIM: ‘Interface characteristics and mechanical behavior of additively manufactured multi-material of stainless steel and Inconel’, *Materials Science and Engineering: A*, Vol. 847, 2022.

[6] S. MAO, D. Z. ZHANG, Z. REN, G. FU, X. MA: ‘Effects of process parameters on interfacial characterization and mechanical properties of 316L/CuCrZr functionally graded material by selective laser melting’, *Journal of Alloys and Compounds*, Vol. 899, 2022.

[7] T. BUNTY and S. SHIVA: 'Microstructure evolution in steel/copper graded deposition prepared using wire arc additive manufacturing', *Materials Letters*, Vol. 380, 2022.
[8] Y. MIAO, C. LI, Y. ZHAO, Y. WU, J. LIU, Z. WANG, B. ZHANG: 'Material properties of gradient copper-nickel alloy fabricated by wire arc additive manufacturing based on bypass-current PAW', *Journal of Manufacturing Processes*, Vol. 83, pp. 637-649, 2022.
[9] E. R. DENLINGER, J. IRWIN, P. MICHALERIS: 'Thermomechanical Modeling of Additive Manufacturing Large Parts', *Journal of Manufacturing Science and Engineering*, Vol. 136, No. 6, 2014.
[10] M. CHIUMENTI, M. CERVERA, A. SALMI, C. AGELET DE SARACIBAR, N. DIALAMI, K. MATSUI: 'Finite element modeling of multi-pass welding and shaped metal deposition processes', *Computer Methods in Applied Mechanics and Engineering*, Vol. 199, No. 37-40, pp. 2343-2359, 2010.
[11] Q. ZHU, Z. LIU, J. YAN: 'Machine learning for metal additive manufacturing: predicting temperature and melt pool fluid dynamics using physics-informed neural networks', *Computational Mechanics*, Vol. 67, No. 2, pp. 619-635, 2021.
[12] M. BIEGLER, B. A. M. ELSNER, I. NEUBAUER, J. LEMKE, M. RETHMEIER: 'Result quality evaluation of Directed Energy Deposition Additive Manufacturing simulations with progressive simplification of transient heat-source motion', *Procedia CIRP*, Vol. 111, pp. 277-281, 2022.
[13] L. LI, X. ZHANG, W. CUI, F. LIOU, W. DENG, W. LI: 'Temperature and residual stress distribution of FGM parts by DED process: modeling and experimental validation', *The International Journal of Advanced Manufacturing Technology*, Vol. 109, No. 1-2, pp. 451-462, 2020.
[14] T. L. BERGMAN, A. LAVINE, F. P. INCROPERA: *Fundamentals of heat and mass transfer*, 2019.

# ADVANCED THERMAL MANAGEMENT STRATEGY FOR ARC-BASED DIRECTED ENERGY DEPOSITION ASSISTED BY NUMERICAL MODELING

T. REINDL*, N. HEMPEL*, P. MAYR*

**Technical University of Munich, TUM School of Engineering and Design, Chair of Materials Engineering of Additive Manufacturing, 85748 Garching, Germany, 0009-0008-4786-8428, 0000-0001-7316-1065, 0000-0003-2530-4644,*
th.reindl@tum.de *(corresponding author)*, nico.hempel@tum.de, peter.mayr@tum.de

*DOI 10.3217/978-3-99161-089-2-013, license CC BY 4.0*
*https://creativecommons.org/licenses/by/4.0/deed.en*
*This CC license does not apply to third party material and content noted otherwise.*

## ABSTRACT

Arc-based Directed Energy Deposition (DED-Arc) offers major industrial potential due to its versatile application possibilities and attractive advantages, such as the flexible, time-efficient near-net-shape manufacturing of large-volume components. However, there are obstacles to overcome, such as the complex thermal history, which limits process stability, component quality, and process efficiency. Therefore, establishing this technology in industry requires solutions capable of monitoring and managing temperature fields. In this context, the focus is increasingly shifting toward real-time-capable, physically based digital solution frameworks. Current efforts primarily emphasize monitoring, simulation, or trial-and-error methods. There is a lack of direct coupling between energy-temperature metrics, standardized analyses and classifications, and effective process optimizations, including adaptive control strategies and design foundations for advanced thermal management.

This work aims to strategically analyze and classify the coupled data from an industrial-grade digital shadow (DS) and numerical modeling. Based on this, targeted optimization measures and process control indicators are identified to enable advanced thermal management. To achieve this, a novel thermal optimization strategy (TOS) was developed to optimize the thermal process of an exemplary tube geometry. Optimizations in path planning, interlayer temperature (ILT) profiles, and temperature change rates were detected and addressed with specific countermeasures. An analysis of the heat balance revealed specific temperature and heat flow gradients providing input for targeted cooling actions. The results highlight the benefits of a coupled monitoring-simulation-control architecture, which eliminates process errors early, enhances thermal stability and control, and optimizes process efficiency.

Keywords: Digital Shadow, Digital Twin, Directed Energy Deposition, Numerical Modeling, Process Optimization, Thermal Management, Thermal Optimization Strategy

## INTRODUCTION

Additive manufacturing (AM) is gaining increasing attention as a valuable technology that complements traditional manufacturing methods. This trend is reinforced by the industry exploring its potential for a wide range of applications and pushing its boundaries. These factors also drive interest in arc-based Directed Energy Deposition (DED-Arc), which offers attractive benefits such as near-net-shape manufacturing of large-volume complex components with high deposition rates [1,2]. This AM process also opens up new possibilities, such as multi-material manufacturing and repair applications [1,3]. Despite the promising technological advantages and possibilities, some challenges must be tackled before DED-Arc becomes further industrially established.

One major issue is the lack of understanding and targeted control of thermal behavior during the process. Poor heat control can cause significant process inefficiencies and deteriorated component properties, ranging from residual stresses and insufficient geometric accuracy to inhomogeneities in the microstructure [2,4-6]. However, thermal profiles and phenomena are difficult to predict, monitor, and control accurately due to the inherent complexity of heat transfer and its effects on the material [5,6]. Addressing this challenge requires a holistic approach that combines multiple research areas. The primary objective is to digitally map and simulate the DED-Arc process and optimize heat transfer in terms of process efficiency and component quality.

Numerical modeling is a key methodology for predicting and analyzing AM processes in depth [7]. As shown in the review by Sampaio et al. [8], DED-Arc simulations can be divided into macro, meso, and micro simulations based on the level of detail. Macro approaches are frequently used for thermal investigations. For example, Farias et al. [9] showed that macro simulations using Simufact Welding software can help predict the resulting interlayer temperatures (ILT) for varying idle times in conjunction with an artificial neural network. Zamiela et al. [10] demonstrated an approach in which the simulation is combined with in situ thermal data to generate a comprehensive thermal history, which is further used for surface deformation detection. Numerical analysis by Hackenhaar et al. [11] using LS-DYNA proved that air jet impingement can significantly influence and control the ILT. Fast simulation methods for thermal management of thin-walled structures [12] or temperature and phase transitions [13] have even used 2D approaches with some simplifications, maintaining high accuracy. This shows that achieving sufficient accuracy quickly and with minimal effort is crucial.

Monitoring is also essential for DED because it can capture the thermal history and numerous other process variables, enabling defect detection and targeted process intervention. Various multi-sensor approaches and frameworks have been developed, providing a digital shadow (DS) [14,15] of the process or even leading to a digital twin (DT) [16-19]. Primarily, process parameters directly related to the energy input (e.g., current, voltage, laser power, robot speed) or the deposition rate (e.g., wire feed rate, powder feed rate) were varied as control variables. This is usually insufficient to fully control the thermal history, because regulating the energy input only works at the deposition spot and is limited to natural cooling rates when the process is paused. Further developments are still needed for an energy- and time-optimized temperature-controlled process.

Together with process prediction and monitoring, the process control strategy and the implementation of thermal management are crucial. Nagallapati et al. [20] distinguished between passive and active management approaches and demonstrated significant influences on mechanical component properties, distortion, and residual stresses. Reis and Da Silva [21] classified thermal management even more precisely into intrinsic, active, passive, and natural types. Intrinsic methods adjust process parameters in response to local heat input (cf. [22,23]), while passive management modifies heat conduction through substrate adjustments, such as water cooling (cf. [24-26]). Active methods, such as near-immersion active cooling (NIAC), significantly reduce component temperatures and process times (cf. [25,27,28]). Other flexible techniques utilize targeted fluid streams to enhance cooling rates and influence the mechanical properties (cf. [26,29]). Natural methods involve process interruptions and surrounding effects. However, much research is generally based on trial and error, without focusing on the precise and targeted use of these techniques, leaving the potential of many thermal management approaches unfulfilled.

This work aims to methodically analyze and classify both measured data and model-based data and predictions to implement targeted thermal process optimization and control within the context of advanced thermal management. For this purpose, a potentially real-time-capable strategy for evaluating and classifying thermal behavior during production must be developed, maximizing component quality and thermal stability while balancing energy and process efficiency through appropriate control measures. Numerical models are created in Simufact Welding and validated using measured data from a DS and metallographic cross-section analyses to achieve these goals. The captured temperature data are strategically processed with MATLAB to derive classified control and optimization data that can be fed directly into the process and the simulation for further iterations. Furthermore, specific design requirements and limitations are derived for required temperature-influencing external elements, like heating or cooling units. The strategy is then critically evaluated regarding industrial applicability and potential real-time capability with extension to a DT.

## METHODOLOGY

The methodological basis of this work comprises five different interrelated key modules, as shown in Fig. 1. A core element is the so-called Thermal Optimization Strategy (TOS), which combines the last three stages of the visualized methodology. Starting from the DED-Arc process, a DS is generated based on time-synchronized measurement data, and an additional validated numerical model is set up. This enables precise process monitoring and process prediction. The numerically and metrologically obtained data further serve as input for thermo-energetic analyses and classifications. Based on component and process requirements, optimization steps are derived and, if necessary, iterated again using numerical modeling. The resulting optimizations are implemented ex situ or, in the case of a real-time process chain, in situ with bidirectional communication as part of a DT framework.

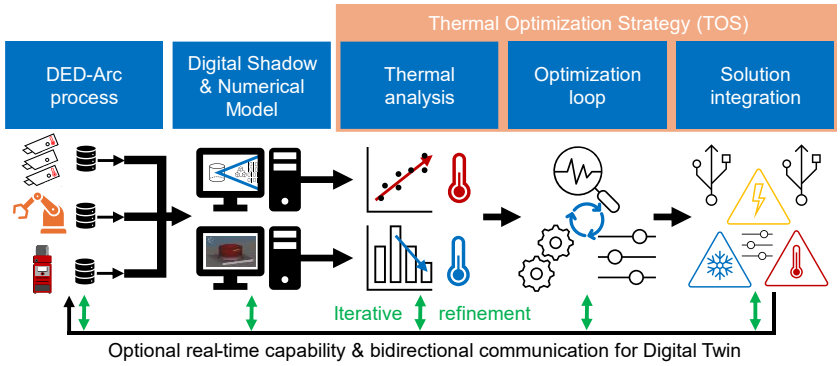



**Fig. 1** Schematic representation of the workflow and methodology

The process sequence involves gas metal arc welding (GMAW) as a wire-based DED-Arc technology, using a Fronius TPS 400i welding power source operated by a six-axis KUKA KR 70 R2100 industrial robot. An advanced version of the framework described in [15] generates the DS. This includes process data from the welding source (gas flow, welding current, voltage, wire feed rate, arc stability), position data from the torch, thermal measurements using thermocouples (type K), pyrometers (Optris CT series, measuring ranges: 50-400 °C or 200-1500 °C), and a thermal imaging camera (Optris Xi400, measuring ranges: 150-900 °C or 200-1500 °C), as well as melt pool, layer geometry, and stick-out monitoring (Cavitar C300 welding camera). The applied framework is illustrated in Fig. 2.

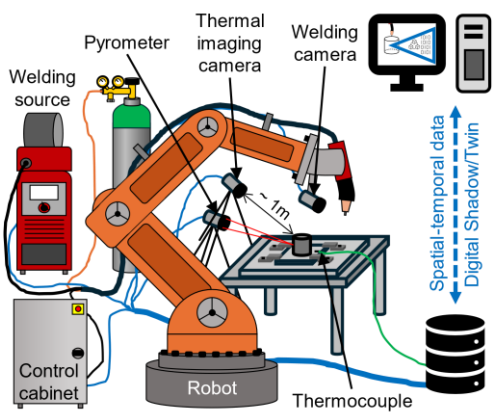



**Fig. 2** Schematic of experimental setup

A supplementary numerical model derived from the high-precision data from the DS provides even more detailed temperature data and potential for prediction. Based on the spatial-temporal geometry and welding source data, a simplified component geometry is created using the double-ellipsoid heat source model, as described by Goldak [30]. The

measured thermal data is used for further model calibration and accuracy improvement. The time efficiency of this approach is enhanced using a macro simulation as classified in [8], which can be performed either thermally or thermo-mechanically. This modeling enables precise measurement and analysis of temperature profiles throughout the process, even in hidden measurement areas. Similar to [9,24,31], the commercial simulation software Simufact Welding is utilized in this work.

The thermal data from the DS and the simulation are implemented in the three-stage TOS. The three stages - thermal analysis, optimization loop, and solution integration - involve four key areas of action. These are divided into energy input, temperature profile, rate of temperature change, and heat control, ranging from path planning to post-weld heat treatment. Fig. 3 provides a comprehensive overview of the TOS scheme.

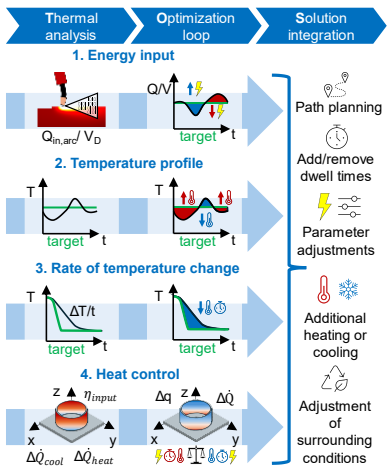



**Fig. 3** Workflow of the TOS procedure

The first area of action, energy input, considers the energy per unit length $E_L$ based on the welding current $I$, welding voltage $U$, and travel speed $v$ at a certain efficiency $\eta$, and classifies it according to the deposited target volume $V_{D,target}$. This volume is calculated in a simplified manner, depending on the wire cross-sectional area and the wire feed speed $v_w$ during a defined time interval $t$. The volumetric energy density $VED$ is then calculated from the energy input by the welding source $Q_{in,arc}$ per $V_D$, and is also considered incrementally and cumulatively. The equations are therefore composed as follows:

$$E_L(t) = \frac{\eta(t) \cdot U(t) \cdot I(t)}{v(t)} \tag{1}$$

$$V_D(t) = \frac{d_w^2 \cdot \pi \cdot v_w(t)}{4} \cdot t \tag{2}$$

$$VED^{[t_0,t_1]} = \frac{Q_{in,arc}}{V_D} = \frac{\int_{t_0}^{t_1} \eta(t) \cdot U(t) \cdot I(t)\, dt}{\int_{t_0}^{t_1} \dot{V}_D(t)\, dt} \tag{3}$$

The MATLAB script analyzes spatial-temporal data based on Eq. (3) to identify correlations between energy peaks and geometric features or process irregularities. The time-interval and location-correlated *VED* values are set in relation to the idealized $VED_{target}$ values as $VED/VED_{target}$. In addition, the ratios $Q_{in,arc}/Q_{in,arc,target}$ and $V_D/V_{D,target}$ are evaluated. Based on the percentage deviations, a classification is made into undercooled/over-deposited, overheated/under-deposited, and tolerated target zones. Afterwards, optimization is carried out, leading to a variation in the welding parameters, motion sequence, or even modified path planning. Using external heating or cooling sources is also an option. It is crucial to consider the relations of the three ratios to correctly interpret and remedy the thermal discrepancies.

The temperature profiles and the rates of temperature change (second and third areas of action) are analyzed at defined measuring points or intervals, with a distinction made between stationary (e.g., seam location) and moving measuring methods (e.g., relative position to the moving torch). Based on a MATLAB script, time-resolved deviations between actual and target temperatures are localized and classified again into tolerated, undercooled, and overheated zones. Predefined material or component-specific intolerable extreme values are identified and flagged accordingly. The combined classification enables the iterative numerical determination of specific optimization approaches, such as targeted process interventions or additional cooling and heating sources, based on the recorded location-time data.

The fourth area of action is heat control, which focuses on the energy balance of the DED-Arc process and final approaches for targeted and potential real-time thermal management. This involves analyzing the energy input via the arc $Q_{in,arc}$, additional heating elements or phenomena $Q_{in,other}$, and losses due to convection $Q_{conv}$, radiation $Q_{rad}$, conduction $Q_{cond}$, and additional cooling elements and phenomena $Q_{out,other}$, all correlated with the process time. The simplified equation for the thermal equilibrium, including the change in internal energy $\Delta U_i$, can be expressed as:

$$Q_{in,arc}(t) + Q_{in,other}(t) = \Delta U_i(t) + Q_{conv}(t) + Q_{rad}(t) + Q_{cond}(t) + Q_{out,other}(t) \quad (4)$$

The equations for the associated internal energy and the heat transfer rates are given in the following, including surface and contact areas ($A_s$ and $A_c$), component volume $V$, Stefan-Boltzmann constant $\sigma$, temperature-dependent density values $\rho$, convective heat transfer coefficient $h$, contact conductivity coefficient $h_c$, specific heat capacity $c_p$, emissivity $\varepsilon$, and location- and time-dependent temperature values (reference $T_{ref}$, surface $T_s$, ambient $T_\infty$, substrate $T_{sub}$, contact $T_c$):

$$\Delta U_i(t) = \int_V \rho\,(T(x,t)) \left[\int_{T_{ref}}^{T(x,t)} c_p(x,\theta)d\theta\right] dV \quad (5)$$

$$\dot{Q}_{conv}(t) = \int_{A_s} h(T(x,t))[T_s(x,t) - T_\infty(x,t)]dA \quad (6)$$

$$\dot{Q}_{rad}(t) = \int_{A_s} \varepsilon(T(x,t))\sigma[T_s^4(x,t) - T_\infty^4(x,t)]F_{s\to\infty}(x,t)dA \quad (7)$$

$$\dot{Q}_{cond}(t) = \int_{A_c} h_c\big(T(x,t)\big)[T_{sub}(x,t) - T_c(x,t)]dA \quad (8)$$

Based on this, MATLAB is used to classify globally and locally at which moment in the process and to what extent predefined threshold values for energy input or loss are exceeded or undercut. Additionally, temperature variations $\Delta T$ and changes in heat flux $\Delta q$ within the component are identified and predicted. Relating the measured energy fractions to the ideal energy fractions further provides a simplified estimate of the efficiency of the energy input $\eta_{input}$, as shown in Eq. (9).

$$\eta_{input} = 1 - \frac{\int_{t_0}^{t}(\dot{Q}_{conv}(\tau)+\dot{Q}_{rad}(\tau)+\dot{Q}_{cond}(\tau)+\dot{Q}_{other}(\tau))d\tau}{\int_{t_0}^{t}(P_{arc,ideal}(\tau)+P_{add,ideal}(\tau))d\tau} \tag{9}$$

Time- and location-specific energy-efficient gradient-controlled heat treatments can also be carried out based on the analysis and classification of the heat balance. $\dot{Q}_{heat}$ and $\dot{Q}_{cool}$ can be estimated as follows:

$$\dot{Q}_{heat}(t) = \frac{1}{\Delta t}\int_V \rho\,(T(x,t))c_p(T(x,t))[T_{target} - T(x,t)]_+ dV \tag{10}$$

$$\dot{Q}_{cool}(t) = \frac{1}{\Delta t}\int_V \rho\,(T(x,t))c_p(T(x,t))[T(x,t) - T_{target}]_+ dV \tag{11}$$

For optimization, it is possible to identify parameters and process conditions that maximize efficiency while monitoring energy losses or accounting for them specifically in thermal process control. Additionally, the targeted energy distribution within the component can be controlled by establishing precise local- or time-graded heating and cooling strategies. This can increase process stability and energy efficiency while minimizing the risk of thermally induced defects. An estimate of the required energy demand for optimizing process time can also be provided.

The final stage in TOS is solution integration. It is essential that the individually derived optimization measures for energy balance and temperature control complement each other harmoniously and do not cancel each other out. While path planning modifications should be made pre-procedurally, parameter variations and adjustments can be made at any time. External cooling and heating solutions can be developed and implemented according to the maximum power levels and gradients that have been investigated. Cooling can be achieved using different fluids and varying flow rates. Heating can be predefined or controlled in situ using different inductors, laser beams, or infrared lights. The additional use of a proportional-integral-derivative (PID) controller can achieve further situational flexibility.

## NUMERICAL MODEL AND VALIDATION

To enhance the precision and predictive capabilities of the DS, initial tests are first conducted to set up and validate a numerical model. For this purpose, a tube geometry ($\emptyset_m$ = 100 mm, h = 77 mm) was deposited via controlled/regulated short-arc with reversing wire on a substrate plate (S235) using the standard G3Si1 filler wire ($\emptyset$ = 1.2 mm). A wire feed speed of 2.5 m/min was used, along with a robot movement speed of approximately 0.6 m/min and a defined layer height of 1.1 mm. An 8% $CO_2$ in Ar shielding gas with a flow rate of ~12 l/min was used. Emissivity coefficients ε in the range of 0.70-0.92 were used for the temperature

measurements for mainly uniformly oxidized surfaces, comparable to the values determined by [32] in the range of 0.70-0.95 for similar conditions and steels.

The numerical model was set up as a transient thermal finite element analysis (FEA) to map the time-dependent thermal process. This included the tube geometry, the substrate, and the base plate. Implementing the clamping tools was neglected due to the punctual clamping mechanism, and was realized as fixed points at identical locations. The multi-phase material models GS1 (deposited material) and S235, included in Simufact Welding (version 2023.4), were used for the simulation, allowing a later extension to a precise thermo-mechanical model. A no-slip condition and a "glued at peak temperature" condition were imposed between the individual simulation components. The contact heat transfer coefficient was defined as 2000 W/m$^2$K, the emission coefficient as 0.8, and the ambient temperature as 20 °C.

The mesh was created using hexahedral elements (Hex8) with a linear interpolation approach, whereby each element has eight nodes and eight integration points. A fine mesh (element size ~1 x 1 x 0.55; 168,000 elements) was applied to the tube to represent the process in detail, and a coarser mesh (element size ~1 x 1 x 1.1; 84,000 elements) was implemented for time-efficient predictions. For precise, high-resolution modeling of the penetration zone and, consequently, the heat transfer area to the substrate, local mesh refinement with a scaling factor of n = 1.2 was performed. The number of adapted elements corresponds to the number of initial elements multiplied by eight to the power of the scaling factor. The Domain Decomposition Method (DDM) and Shared Memory Parallelization (SMP) were employed to reduce the computation time. The simulation was performed using the MUMPS parallel direct solver. A comparison of the high-resolution simulation and the fabricated component is provided in Fig. 4.

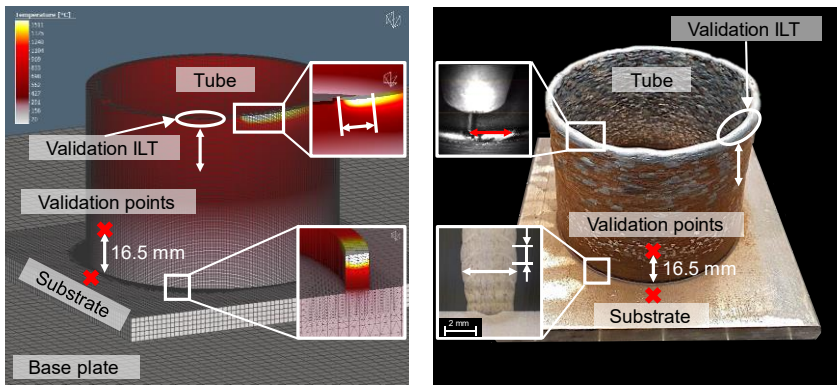



**Fig. 4** Numerical model (fine mesh) and component with highlighted validation methods

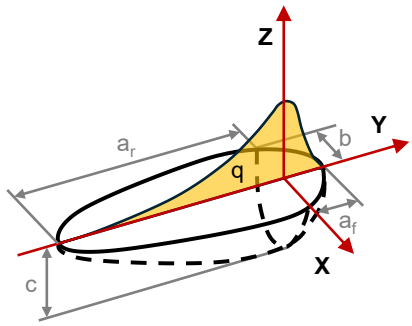
The heat input from the DED-Arc process was modeled in the simulation using the double-ellipsoid model developed by Goldak. Based on the explanations from Goldak et al. [30], the power density distribution in the front quadrant (Eq. (12)) differs from that in the rear quadrant (Eq. (13)). The sum of the front and the rear fraction ($f_f$ and $f_r$) equals two, as shown in Eq. (14). $Q_{in,arc}$ is the product of the efficiency of the heat source $\eta$, the welding current $I$, and

the welding voltage *U*. Fig. 5 shows a visualization of the double-ellipsoid heat source model according to Goldak, along with an overview of the parameters used in the present simulation.

$$q_f(x,y,z) = \frac{6\sqrt{3} f_f Q_{arc}}{a_f b c \pi \sqrt{\pi}} \exp\left(\frac{-3x^2}{b^2}\right)\exp\left(\frac{-3y^2}{a_f^2}\right)\exp\left(\frac{-3z^2}{c^2}\right) \quad (12)$$

$$q_r(x,y,z) = \frac{6\sqrt{3} f_r Q_{arc}}{a_r b c \pi \sqrt{\pi}} \exp\left(\frac{-3x^2}{b^2}\right)\exp\left(\frac{-3y^2}{a_r^2}\right)\exp\left(\frac{-3z^2}{c^2}\right) \quad (13)$$

$$f_f + f_r = 2 \text{ , with } f_f = \frac{2a_f}{a_f + a_r} \text{ and } f_r = \frac{2a_r}{a_f + a_r} \quad (14)$$




| Parameter | Value in mm |
|---|---|
| $a_f$ | 1.8 |
| $a_r$ | 7.2 |
| b | 2.0 |
| c | 3.7 |

**Fig. 5** Double-ellipsoid heat source model according to [30], including the parameter values used in the present simulation

The numerical model was calibrated using the measured temperature fields from the tube deposition test. Selected heat source parameters from Eqs. (12)-(14) and relevant material interaction properties were iteratively adjusted within physically justified limits until the simulated and measured thermal histories aligned. All calibrated values remained constant throughout the simulation. Correlated with the experimental welding parameters, an average $E_L$ of ~1.3 kJ/cm was applied in the simulation. Additionally, the heat source underwent iterative calibration, resulting in a time step width of 0.15 s. Afterwards, the four different approaches visualized in Fig. 4 were used to validate the numerical model. These included fixed-point temperature measurements in Layer 15, ILT, and substrate temperature measurements, investigations of melt pool length, and comparisons of the actual component geometry with the idealized geometry using a cross-section sample.

A comparison of the measured and simulated temperature cycles in the 15th layer is shown in Fig. 6. The minor deviations between the pyrometer and thermal imaging camera measurements demonstrate the reliability of the measurement method. The simulation with a fine mesh revealed temperature deviations of less than 50 °C for the critical extreme values near the heat source, confirming the validity of the numerical model. A coarser mesh resulted in deviations at the peak temperatures, mainly in the range of 50-100 °C. Despite these fluctuations, the heating and cooling curves correspond very well, with only minor differences of a few degrees Celsius. Although the discrepancies limit the applicability for detailed

numerical process replication, the coarser modeling shows excellent potential as a computationally efficient alternative for fast process prediction.

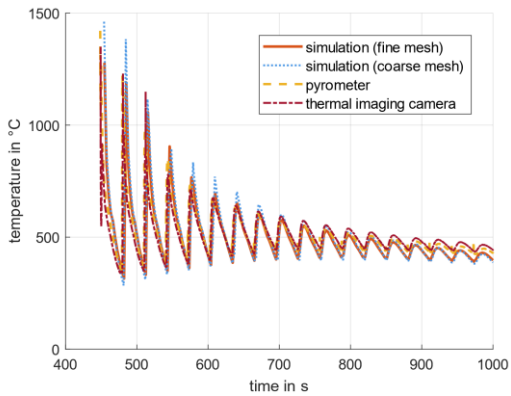



**Fig. 6** Fixed-point measurement validation in Layer 15

The determined substrate temperature profiles and the ILT curves are shown in Fig. 7. The deviations between the measured and simulated substrate plate temperatures were below 50 °C for the detailed model. In contrast, for the coarse model, the differences remained below 70 °C. In general, there were obvious discrepancies between the simulation and the experiment, attributable to the fact that distortion was not considered in the simulation. Consequently, the contact conditions were idealized. The simulated ILT curves showed good agreement with the experiment. As the measurements were taken simultaneously for each layer, comparisons can also be made using the root mean square error (RMSE). The value for the coarse mesh is RMSE = 12.7 °C, while the fine mesh achieved RMSE = 9.7 °C (~25% lower). The validity of the precise simulation is proven once again, as is the ability of the coarse simulation to provide sufficiently accurate predictions.

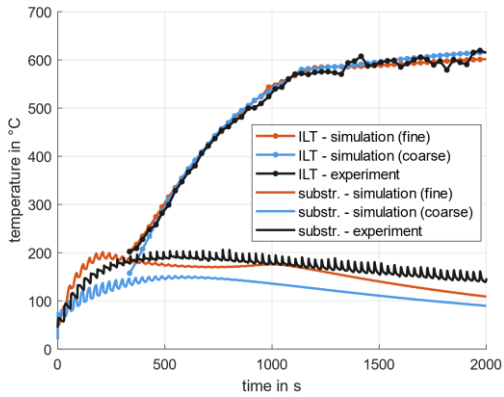



**Fig. 7** Comparison of ILT and substrate temperature measurements

The geometric analysis of the tube geometry of the experiment (cf. Table 1) indicates that suitable geometric simplifications were applied, resulting in deviations of $\leq 5\%$. The experimentally obtained melt pool length varied from 6.5 to 15.8 mm. By comparison, the detailed simulation yielded an RMSE of 0.64 mm, while the coarse simulation resulted in an RMSE of 0.94 mm (~47% higher). Since the simulation does not include dynamic melt pool motions and fluid simulations, both values are within a sufficiently accurate range, ensuring the validity of the numerical models.

**Table 1** Geometrical and melt pool data

| | Experiment | Simulation |
|---|---|---|
| Mean layer width in mm | 3.8 ± 0.2 | 4.0 |
| Mean layer height in mm | 1.1 ± 0.1 | 1.1 |
| Mean total height in mm | 77.5 ± 0.1 | 77.0 |
| Melt pool length in mm | range: 6.5-15.8 | RMSE = 0.64 (fine mesh)<br>RMSE = 0.94 (coarse mesh) |

## RESULTS

The data from the DS and the validated numerical model of the tube geometry are used to further verify and demonstrate the applicability and output of TOS. As targeted thermal management of the DED-Arc process is very versatile and application-specific, the focus was placed on representative standard challenges and applications. For this purpose, the four areas of action of TOS were executed to identify and demonstrate optimization approaches and an advanced control strategy.

The first area, energy input, involved analyzing the torch movements based on the axis movements of the robot in correlation with the welding source parameters. This revealed that movements in the X and Y directions were repeatedly interrupted for 0.3 s at the seam, while the stick-out was readjusted according to the layer height in the Z direction. Fig. 8 shows representative data for the seam transition from the first to the second layer, where the coordinate origin is located at the center of the tube on the substrate surface. The analysis of the ratios of measured values to target values, based on 1-second intervals, yielded $VED = VED_{target}$ for the volumetric energy density, indicating a stable process. The correlating ratios $V_D/V_{D,target}$ and $Q_{in,arc}/Q_{in,arc,target}$ (ratios = 1.3) indicate a material and energy surplus of 30%, which was attributable to the short process delay. This significantly classified irregularity implies a systematic error in the path planning, which led to measurable geometric deviations and temperature peaks. As an optimization for follow-up investigations, the Z movement at the seam was performed as a ramp over several seconds with continuous movement in the X-Y direction. The remaining error is within the tolerance range. Additionally, a total process time saving of ~21 s was achieved.

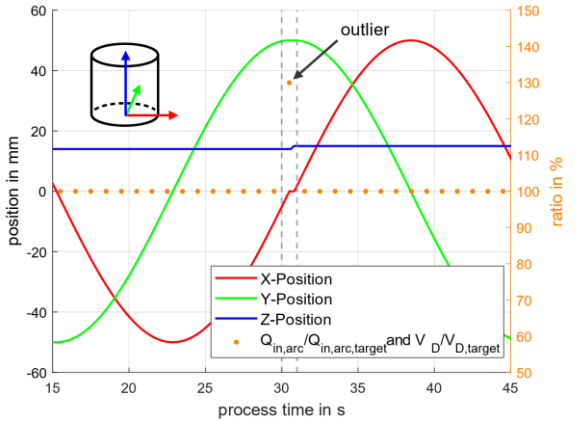



**Fig. 8** Energy input analysis at the tube seam

The second area of action involved analyzing the ILT profile of the manufactured tube. As shown in Fig. 9, the classification into the three zones, overheated, undercooled, and tolerated (200 ± 10 °C; 5% deviation), was conducted concerning the target ILT of 200 °C. The undercooled zone could be easily eliminated by using substrate preheating/heating. The overheated zone is a more complex case, so this study focused on the simplified criterion of ILT ≤ 200 °C, allowing the undercooled zone to remain unchanged. Process interruptions were introduced as an energy-efficient but highly time-consuming optimization strategy, whereby the next layer was only deposited once the criterion ILT ≤ 200 °C was met. As a result, no additional cooling elements were required.

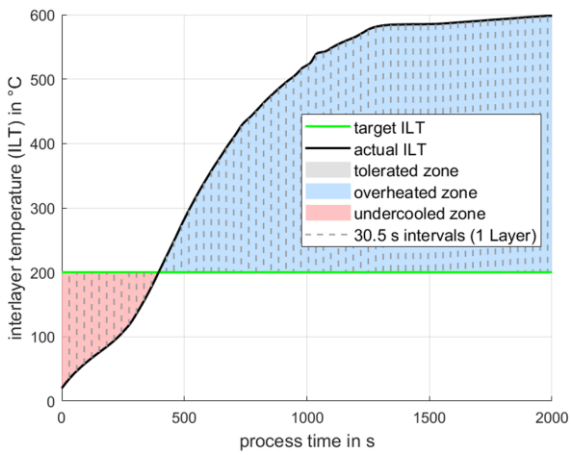



**Fig. 9** Analysis and classification of ILT profiles

The calculated predictions for tube manufacturing with process interruptions to maintain ILT showed an increase in total process time by a factor of 2.8, reaching almost 1 hour and 40 minutes. This timely inefficiency led to the third area of action of TOS, which addressed the rate of temperature change over time. As shown in Fig. 10 for layer 50, the target cooling phase was compared with the predicted cooling phase and classified. Only the overheated zone could be identified, as only increased cooling is required. Overall, the cooling time from deposition to the target temperature of 200 °C should occur within 30.5 s for a non-stop process. In this case, the cooling cycle to 200 °C must be reduced by ~55 s. There are various ways of improvement, ranging from a cooling sequence that is as natural as possible, as in the example, to optimization with the lowest possible cooling capacity required. Based on the classification, the required cooling capacity for each time interval and location can be derived for process design and thermal management planning. In addition, it would be possible to influence the material properties in a targeted manner by controlling the t8/5 cooling rates (from 800 to 500 °C). Nevertheless, these calculations and approaches must be carried out according to individual circumstances and cooling options. However, all data required for strategic thermal management can be obtained from this analysis and classification.

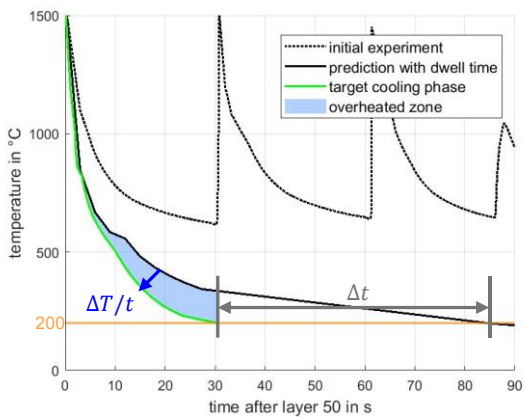



**Fig. 10** Analysis and classification of rates of temperature change

The final area of action involves analyzing the overall thermal condition of the component. Besides recording and classifying heat losses, heat input, and efficiency factors, the primary focus within this study is on the relevant temperature fields and heat flux gradients. Fig. 11 shows a component section classified using heat maps. The temperature distribution is shown on the left, and the heat flux distribution is shown on the right. The simulated dataset, based on real experimental conditions, is visualized at the top, and the predicted solution with implemented dwell phases to comply with the ILT condition (≤ 200 °C) is shown at the bottom. The temperature differences varying across the surface can be determined by comparing the temperature fields at the defined component position. The classification clearly shows the component height at which significant cooling is required to maintain the sample profile with the cooling times. A comparison of the heat flux data shows that maintaining the

ILT reduces the thermal changes and variations, which in turn influence fewer previous layers significantly. In addition, fluctuations in $\Delta q$ in the circumferential direction are also visible.

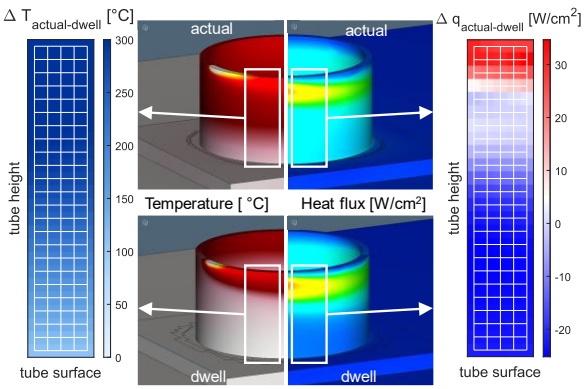



**Fig. 11** Analysis and classification of ΔT and Δq for location-specific heat control

The data processed using TOS shows the cooling and heating actions required for each component area to achieve targeted thermal management. This final optimization step enables the precise implementation of specific process interventions in real-time, such as adjusting the welding source or robot parameters, or interrupting and resuming processes, while maintaining time and energy efficiency. The targeted additional control of external cooling and heating elements is more complex. However, it has been shown that temperature-specific influences can promote and specifically create homogeneous temperature fields. Based on this, design recommendations and requirements for cooling and heating units can be derived, which can then even be controlled via the output values of the DS to achieve an even more advanced thermal process management.

The computation times highlight the overall efficiency and current limitations of the framework. Data acquisition and thermal analysis run within seconds up to near real-time, depending on data volume and complexity. In contrast, numerical model predictions still require several hours, depending on mesh resolution and geometry, with optimization and solution integration times similarly scaling with complexity. These results illustrate both the current capabilities and the remaining potential for further improvement.

## DISCUSSION

The results demonstrated the effectiveness of the data framework, coupled with TOS, in precisely analyzing energy and material inputs, temperature profiles, rates of temperature change, and heat flows for a DED-Arc process. This foundation enables the validation of existing process parameters and serves as a basis for developing thermally optimized control and process management strategies that directly impact component quality and process efficiency. However, for standard industrial implementation and further development, several

issues must be critically examined, ranging from real-time capability and system accuracy to process efficiency.

The study demonstrated that thermal conditions can be recorded and fed back in real-time with practical latency using the advanced framework developed by [15]. However, one major challenge in real-time recording of thermal data in DED-Arc is the varying emission factor, which can vary greatly depending on material, temperature, and surface properties, as the studies [31-33] demonstrate. This can be remedied by applying a corrective overlay to the measurement data or using supporting, fast simulations, as described in [13]. As the review papers [18,19] indicate, it is important to use automated rule-based decision models. TOS provides an initial foundation for this, considering that certain optimization steps can be performed offline before or after the process. According to [18], it is also important to focus only on the real-time control of relevant process parameters to keep computing time and the required computing power of the DT within realistic limits.

Another critical factor in data acquisition, automated analysis, and automated classification for achieving advanced thermal management supported by TOS is the volume of data and the need for efficient processing. This will necessitate robust machine learning (ML) pipelines or the integration of advanced artificial intelligence (AI) for an industrial solution, as suggested by [15]. Furthermore, physics-informed neuronal networks (PINN) can accelerate the prediction of temperature fields compared to FEA and enable precise online parameter identification, as demonstrated by [34,35]. Another work from Mattera and Nele [36] demonstrated real-time ML-based anomaly/defect detection from process signals. Consequently, these studies highlight how real-time and automated TOS implementation for advanced thermal management could be achieved despite high data volumes from DS, simulation, or DT. However, the existing framework needs further development, for example, with targeted ML or PINN approaches to achieve this.

The review by Reis and Da Silva [21] shows that thermal management can be implemented with varying degrees of complexity, flexibility, and efficiency. Their outlook also highlights the need to take a broader, critical view of the additional costs that arise and the balance between the required effort and the process efficiency achieved through the management strategies. In this context, TOS combined with the presented framework is a suitable solution, as the optimization options for targeted thermal management can be precisely defined according to the present possibilities. This can range from offline adjustment of the welding parameters to a DT solution with in situ temperature control by external heat elements. An important aspect is that the final area of action of TOS involves a comprehensive thermal and energy balance of the process, which can also result in additional costs due to energy expenses or downtimes, or cost savings due to quality improvements and reduced process times. This enables component-specific design based on economic preferences and technical feasibility, leading to advanced thermal management.

## SUMMARY & OUTLOOK

The study demonstrated the successful application of the newly developed TOS and the data generation to achieve advanced thermal management on an example tube geometry. To this

end, a data acquisition framework was expanded to include measured thermal and process data as a DS. Additionally, numerical modeling using FEA was established, which was validated for detailed process representation and prediction. By systematically linking these data, all three stages (thermal analysis, optimization loop, and solution integration), including the four areas of action of TOS (energy input, temperature profile, rate of temperature change, and heat control), were carried out for standard challenges and applications in DED-Arc using the exemplary component. The available data, fundamental modules of an advanced thermal management system, were analyzed and strategically classified. Individual optimization potential and options were derived based on thermodynamic basics. Considering economic and financial circumstances, this provided a clear foundation for decision-making in designing an idealized thermal process management system for individual use cases. The key findings can be summarized as follows:

- An industrial-grade DS framework was extended with validated thermal numerical models to enable advanced process monitoring, replication, and prediction.
- An innovative TOS was created that systematically summarizes, analyzes, and classifies all gained data and allows for identifying optimization opportunities that can take thermal requirements, influences on process complexity, and economic factors into account.
- Using the tube sample, a robot path error that previously caused energy and material surpluses was eliminated using fundamental control equations. Moreover, the ILT could be specifically controlled to prevent overheating.
- Further iterative simulations allow for precise time- and location-dependent derivation of necessary cooling or heating actions to optimize the efficiency of the process, depending on component specifications and process capabilities.
- The heat flow analysis demonstrated the significant influence of ILT control and the associated impact on the thermal balance, from which adaptive cooling/heating with maximum energy efficiency can be derived and used for closed-loop control.

The discussion critically examined the TOS and general thermal management for DED-Arc, focusing primarily on real-time capability, data processing, and the balance between industrial applicability and the associated costs with increasing process complexity. The existing framework, in conjunction with the TOS, offers innovative solutions to significant temperature-related process challenges. However, further improvements are required, particularly in the areas of rapid automated data management and process control. Consequently, the following future steps were identified:

- Implement the proposed heat control logic in a real-time feedback system with closed-loop control.
- Use the generated large amounts of thermal and process data for AI-supported optimization loops.
- Further apply TOS to complex, industry-oriented geometries for validation and demonstration of scalability.
- Extend it with thermo-mechanical considerations to realize specific mechanical component properties by using TOS.

- Upgrade to a fully real-time-capable DT framework, where TOS is integrated as an automated decision logic and in situ control foundation.

## ACKNOWLEDGEMENT

This project is supported by the Federal Ministry for Economic Affairs and Climate Action (BMWK) on the basis of a decision by the German Bundestag. Furthermore, the support from the project-involved colleagues from Heidenbluth GmbH and Satron Steuerungstechnik GmbH is gratefully acknowledged.

## References

[1] D. SVETLIZKY, M. DAS, B. ZHENG, A. L. VYATSKIKH, S. BOSE, A. BANDYOPADHYAY, J. M. SCHOENUNG, E.J. LAVERNIA, N. ELIAZ: 'Directed energy deposition (DED) additive manufacturing: Physical characteristics, defects, challenges and applications', *Materials Today*, 49 (2021), 271-295, https://doi.org/10.1016/j.mattod.2021.03.020.

[2] S. C. COSTELLO, C. R. CUNNINGHAM, F. XU, A. SHOKRANI, V. DHOKIA, S. T. NEWMAN: 'The state-of-the-art of wire arc directed energy deposition (WA-DED) as an additive manufacturing process for large metallic component manufacture', *International Journal of Computer Integrated Manufacturing*, 36 (2023), 469-510, https://doi.org/10.1080/0951192X.2022.2162597.

[3] A. HAKAMI, S. A. OJO, D. V. ABERE, F. D. UZUH, R. A. ROBERT: 'Advancements in metal additive manufacturing: opportunities, limitations, impact on properties, and potential solutions: a review', *Prog. Addit. Manuf.*, 10 (2025), 4447-4495, https://doi.org/10.1007/s40964-024-00885-6.

[4] M. CHATURVEDI, E. SCUTELNICU, C.C. RUSU, L.R. MISTODIE, D. MIHAILESCU, A.V. SUBBIAH: 'Wire Arc Additive Manufacturing: Review on Recent Findings and Challenges in Industrial Applications and Materials Characterization', *Metals*, 11 (2021), 939, https://doi.org/10.3390/met11060939.

[5] L. P. RAUT, R. V. TAIWADE: 'Wire Arc Additive Manufacturing: A Comprehensive Review and Research Directions', J. of Materi. Eng. and Perform., 30 (2021), 4768-4791, https://doi.org/10.1007/s11665-021-05871-5.

[6] N. A. ROSLI, M. R. ALKAHARI, M. F. B. ABDOLLAH, S. MAIDIN, F. R. RAMLI, S. G. HERAWAN: 'Review on effect of heat input for wire arc additive manufacturing process', *Journal of Materials Research and Technology*, 11 (2021), 2127-2145, https://doi.org/10.1016/j.jmrt.2021.02.002.

[7] A. LOVE, O. A. VALDEZ PASTRANA, S. BEHSERESHT, Y. H. PARK: 'Advancing Metal Additive Manufacturing: A Review of Numerical Methods in DED, WAAM, and PBF', *Metrology*, 5 (2025), 30, https://doi.org/10.3390/metrology5020030.

[8] R. SAMPAIO, J. PRAGANA, I. BRAGANÇA, C. SILVA, C.V. NIELSEN, P. MARTINS: 'Modelling of wire-arc additive manufacturing – A review', *Advances in Industrial and Manufacturing Engineering*, 6 (2023), 100121, https://doi.org/10.1016/j.aime.2023.100121.

[9] F. W. C. FARIAS, J. DA CRUZ PAYÃO FILHO, V. H. P. MORAES E OLIVEIRA: 'Prediction of the interpass temperature of a wire arc additive manufactured wall: FEM simulations and artificial neural network', *Additive Manufacturing*, 48 (2021), 102387, https://doi.org/10.1016/j.addma.2021.102387.

[10] C. ZAMIELA, R. STOKES, W. TIAN, H. DOUDE, M. W. PRIDDY, L. BIAN: 'Physics-Informed Approximation of Internal Thermal History for Surface Deformation Predictions in Wire Arc Directed Energy Deposition', *Journal of Manufacturing Science and Engineering*, 146 (2024), 081007, https://doi.org/10.1115/1.4065416.

[11] W. HACKENHAAR, J. A. MAZZAFERRO, F. MONTEVECCHI, G. CAMPATELLI: 'An experimental-numerical study of active cooling in wire arc additive manufacturing', *Journal of Manufacturing Processes*, 52 (2020), 58-65, https://doi.org/10.1016/j.jmapro.2020.01.051.

[12] P. QVALE, E. B. NJAASTAD, T. BRÆIN, X. REN: 'A fast simulation method for thermal management in wire arc additive manufacturing repair of a thin-walled structure', *Int. J. Adv. Manuf. Technol.*, 132 (2024), 1573-1583, https://doi.org/10.1007/s00170-024-13427-9.

[13] D. WEISZ-PATRAULT: 'Fast simulation of temperature and phase transitions in directed energy deposition additive manufacturing', *Additive Manufacturing*, 31 (2020), 100990, https://doi.org/10.1016/j.addma.2019.100990.

[14] H. MU, F. HE, L. YUAN, P. COMMINS, D. DING, Z. PAN: 'A digital shadow approach for enhancing process monitoring in wire arc additive manufacturing using sensor fusion', *Journal of Industrial Information Integration*, 40 (2024), 100609, https://doi.org/10.1016/j.jii.2024.100609.

[15] G. SAFRONOV, H. THEISINGER, V. SAHLBACH, C. BRAUN, A. MOLZER, A. THIES, C. SCHUBA, M. SHIRAZI, T. REINDL, A. HÄNEL, P. ENGELHARDT, S. IHLENFELDT, P. MAYR: 'Data Acquisition Framework for spatio-temporal analysis of path-based welding applications', *Procedia CIRP*,130 (2024), 1644-1652, https://doi.org/10.1016/j.procir.2024.10.295.

[16] M. M. MAHDI, M. S. BAJESTANI, S. D. NOH, D. B. KIM: 'Digital twin-based architecture for wire arc additive manufacturing using OPC UA', *Robotics and Computer-Integrated Manufacturing*, 94 (2025), 102944, https://doi.org/10.1016/j.rcim.2024.102944.

[17] V. KARKARIA, A. GOECKNER, R. ZHA, J. CHEN, J. ZHANG, Q. ZHU, J. CAO, R.X. GAO, W. CHEN: 'Towards a digital twin framework in additive manufacturing: Machine learning and bayesian optimization for time series process optimization', *Journal of Manufacturing Systems*, 75 (2024), 322-332, https://doi.org/10.1016/j.jmsy.2024.04.023.

[18] H. MU, F. HE, L. YUAN, P. COMMINS, H. WANG, Z. PAN: 'Toward a smart wire arc additive manufacturing system: A review on current developments and a framework of digital twin', *Journal of Manufacturing Systems*, 67 (2023), 174-189, https://doi.org/10.1016/j.jmsy.2023.01.012.

[19] H. LI, X. SHI, B. WU, D. R. CORRADI, Z. PAN, H. LI: 'Wire arc additive manufacturing: A review on digital twinning and visualization process', *Journal of Manufacturing Processes*, 116 (2024), 293-305, https://doi.org/10.1016/j.jmapro.2024.03.001.

[20] V. NAGALLAPATI, V. K. KHARE, A. SHARMA, S. SIMHAMBHATLA: 'Active and Passive Thermal Management in Wire Arc Additive Manufacturing', *Metals*, 13 (2023), 682, https://doi.org/10.3390/met13040682.

[21] R. P. REIS, L. J. DA SILVA: 'Thermal management approaches for arc additive manufacturing: a comprehensive review over a decade of developments and applications', Int. J. Adv. Manuf. Technol., 136 (2025), 1805-1931, https://doi.org/10.1007/s00170-024-14791-2.

[22] F. CHEN, Y. YANG, H. FENG: 'Regional Control and Optimization of Heat Input during CMT by Wire Arc Additive Manufacturing: Modeling and Microstructure Effects', *Materials* (Basel), 14 (2021), https://doi.org/10.3390/ma14051061.

[23] S. SRIVASTAVA, R. K. GARG, A. SACHDEVA, V. S. SHARMA, S. SINGH: 'An Experimental–Numerical Investigation for Layer-Wise-Heat-Input Management in GMA-Based Additive *Manufacturing*', *J. Inst. Eng. India Ser. C*, 103 (2022), 1059-1070, https://doi.org/10.1007/s40032-022-00868-y.

[24] T. REINDL, N. HEMPEL, P. MAYR: 'Effect of substrate preheating and in situ cooling on dimensional accuracy, microstructure, and hardness of wire-arc directed energy deposition components', *Weld World*, (2025), https://doi.org/10.1007/s40194-025-02104-4.

[25] L. J. DA SILVA, D. M. SOUZA, D. B. DE ARAÚJO, R. P. REIS, A. SCOTTI: 'Concept and validation of an active cooling technique to mitigate heat accumulation in WAAM', *Int. J. Adv. Manuf. Technol.*, 107 (2020), 2513-2523, https://doi.org/10.1007/s00170-020-05201-4.

[26] U. REISGEN, R. SHARMA, S. MANN, L. OSTER: 'Increasing the manufacturing efficiency of WAAM by advanced cooling strategies', *Weld World*, 64 (2020), 1409-1416, https://doi.org/10.1007/s40194-020-00930-2.

[27] F. M. SCOTTI, F. R. TEIXEIRA, L. J. DA SILVA, D. B. DE ARAÚJO, R. P. REIS, A. SCOTTI: 'Thermal management in WAAM through the CMT Advanced process and an active cooling technique', *Journal of Manufacturing Processes*, 57 (2020), 23-35, https://doi.org/10.1016/j.jmapro.2020.06.007.

[28] F. R. TEIXEIRA, F. M. SCOTTI, V. L. JORGE, A. SCOTTI: 'Combined effect of the interlayer temperature with travel speed on features of thin wall WAAM under two cooling approaches', *Int. J. Adv. Manuf. Technol.*, 126 (2023), 273-289, https://doi.org/10.1007/s00170-023-11105-w.

[29] C. MA, C. LI, Y. YAN, Y. LIU, X. WU, D. LI, Y. HAN, H. JIN, F. ZHANG: 'Investigation of the in-situ gas cooling of carbon steel during wire and arc additive manufacturing', *Journal of Manufacturing Processes*, 67 (2021), 461-477, https://doi.org/10.1016/j.jmapro.2021.05.022.

[30] J. GOLDAK, A. CHAKRAVARTI, M. BIBBY: 'A new finite element model for welding heat sources, Metall Trans B', 15 (1984), 299-305, https://doi.org/10.1007/BF02667333.

[31] Y. OSAMA, M. ABDELWAHED, A. ELSABBAGH, M. A. TAHA: 'Experimental and numerical thermal monitoring of SS308L structures processed by wire arc additive manufacturing', *Prog. Addit. Manuf.*, (2025), https://doi.org/10.1007/s40964-025-01084-7.

[32] P. MEHMERT: *Numerische Simulation des Metallschutzgasschweißens von Grobblechen aus un- und niedriglegierten Feinkornbaustahl*, Dissertation, Clausthal, 2003.

[33] J. MÜLLER, J. HENSEL: 'Potential of thermography for the monitoring of DED-Arc processes', *Weld World*, 68 (2024), 505-513, https://doi.org/10.1007/s40194-023-01676-3.

[34] S. HARTMANN, O. MURUA, J. I. ARRIZUBIETA, A. LAMIKIZ, P. MAYR: 'Physics-informed neural network approach to speed up Laser-DED modelling', *Procedia CIRP*, 124 (2024), 352-357, https://doi.org/10.1016/j.procir.2024.08.132.

[35] B. PENG, A. PANESAR: 'Multi-layer thermal simulation using physics-informed neural network', *Additive Manufacturing*, 95 (2024), 104498, https://doi.org/10.1016/j.addma.2024.104498.

[36] G. MATTERA, L. NELE: 'Machine learning approaches for real-time process anomaly detection in wire arc additive manufacturing', *Int. J. Adv. Manuf. Technol.*, 137 (2025), 2863-2888, https://doi.org/10.1007/s00170-025-15327-y.

# SOLUTION APPROACHES FOR THE EFFICIENT MODELLING OF THE LAYER BUILD-UP IN THE WAAM MANUFACTURING PROCESS USING SMOOTHED PARTICLE HYDRODYNAMICS

O. MOKROV*, S. WARKENTIN*, L. WESTHOFEN***,
J. ANTONISSEN **, J. BENDER***, R. SHARMA*, U. REISGEN*

**RWTH Aachen University, Welding and Joining Institute, 52062 Aachen, Germany*
***Guaranteed. B. V., 9060, Zelzate, Belgium*
****RWTH Aachen University, Visual Computing Institute - LuFG Computer Animation, 52056 Aachen, Germany*
*Mokrov: https://orcid.org/0000-0002-9380-6905, oleg.mokrov@isf.rwth-aachen.de*
*Warkentin: https://orcid.org/0009-0004-4514-8962, sergej.warkentin@isf.rwth-aachen.de*
*Antonissen: joachim.antonissen@guaranteed.be*
*Westhofen: https://orcid.org/0000-0003-4427-2377, westhofen@cs.rwth-aachen.de*
*Bender: https://orcid.org/0000-0002-1908-4027, bender@informatik.rwth-aachen.de*
*Sharma: https://orcid.org/0000-0002-6976-4530, rahul.sharma@isf.rwth-aachen.de*
*Reisgen: https://orcid.org/0000-0003-4920-2351, uwe.reisgen@isf.rwth-aachen.de*

*DOI 10.3217/978-3-99161-089-2-014, license CC BY 4.0*
*https://creativecommons.org/licenses/by/4.0/deed.en*
*This CC license does not apply to third party material and content noted otherwise.*

## ABSTRACT

Within Additive Manufacturing (AM) technologies, Wire Arc Additive Manufacturing (WAAM) stands out as a particularly promising process variant. WAAM enables the efficient production of large metal structures and offers significant advantages over traditional processes, especially in the field of repair welding.

A key component for optimizing the WAAM process is simulation, particularly in relation to the concept of a virtual factory. A digital twin could significantly accelerate the wire-and-arc-based AM manufacturing process, especially regarding development, optimization, and certification.

Developing a precise simulation model is crucial to correctly map a weld's geometric shape. In the presented work, Smoothed Particle Hydrodynamics (SPH) is used to develop a model that simulates multiple weld beads building on each other – an area that is not yet fully established due to complex physical interactions and the enormous computing resources required.

The focus of the work is on heat and mass transfer during the WAAM process, aiming to create a model that calculates interactions within a geometry of numerous layer structures while significantly reducing calculation time. The proposed approach fully accounts for mass and heat transfer in the cathode area, while droplet formation and detachment are captured by an equivalent model for more efficient use of computing resources.

The concept for accelerated calculation incorporates a coarse mass discretization and the neglect of a direct resolution of the anode area. Accordingly, the model focuses on the processes in the cathode area concerning the weld to be formed. A side effect of this concept are local deviations in the weld geometry arising from surface tension models in the SPH formalism, affecting global component geometry.

The potential of the model for predicting the temperature field could be demonstrated in the simulative reproduction of an eccentric pin as an industrial reference product. However, there is still no satisfactory agreement between the calculated geometry and the real component. While geometric agreement requires further calibration, the temperature field prediction shows strong consistency with the industrial process. Calculation time still holds potential for improvement.

This work makes a significant contribution to the further development of simulation methods in the field of WAAM and provides valuable information for improving process control and increasing efficiency.

Keywords: WAAM, simulation, SPH, heat and mass transfer, substitute models

## INTRODUCTION

Additive Manufacturing (AM) technologies for metals have gained increasing attention in recent years due to their potential for resource-efficient, flexible, and customized production. Among the various AM methods, laser-based and electron beam-based processes offer high precision but are often limited by low deposition rates, high equipment costs, and a narrow range of processable materials, as powder-based feedstocks are not yet widely established in industrial applications. These methods are particularly suitable for micro-scale investigations, such as the study of microstructural evolution [1], but they remain technologically immature in large-scale manufacturing contexts.

In contrast, arc-based processes – specifically Wire Arc Additive Manufacturing (WAAM) – enable high deposition rates and benefit from low system complexity and cost. WAAM is based on Gas Metal Arc (GMA) welding technology, an arc welding process using a continuously fed consumable wire electrode. The major advantage of GMA welding process lies in its high proportion of welding processes used in industry, which means that a wide variety of certified filler wire materials are commercially available, making WAAM an attractive choice for industrial-scale applications.

Wire-and-arc-based AM has demonstrated notable advantages in terms of targeted material usage, cost-efficiency, and flexibility in design, supporting tailored solutions for both new part production and repair applications. Its potential is evidenced by successful implementations in industrial contexts, such as the repair of high-value components [2], cladding applications including the reinforcement of shell geometries [3], and even the fabrication of hybrid material systems. Nevertheless, recent reviews emphasize the relevance for the analysis of stress development and distortion, with a focus on macroscale simulations in WAAM [4].

Recent contributions from our research partners have advanced the simulation of WAAM processes, focusing on heat transfer modelling using finite element methods [5], as well as the numerical prediction of microstructure and hardness evolution [6]. Moreover, economic aspects such as life cycle assessment [2] and green supply chain management strategies [7] underscore the increasing demand for sustainable solutions in additive manufacturing.

Despite the progress, WAAM still faces several challenges. These include limited contour accuracy, complex thermal behaviour, intricate material responses, and non-trivial path

planning requirements [8]. Given the multitude of interacting process parameters, experimental investigation of every influencing factor is not only time-consuming but often infeasible. While academic studies have explored geometric prediction at the level of individual weld beads or small-layer constructs, these models are rarely suitable for industrial use due to excessive computation time and resource demands.

Physically accurate modelling of the bead geometry remains a major computational challenge, as it requires capturing a wide range of complex phenomena. Numerical methods, although capable, are often pushed to their limits. Simplified approaches – such as the use of equivalent heat sources (e.g., the Goldak model and its extensions using volumetric discretization, [9]) or the activation of predefined mesh elements – are commonly employed to reduce complexity. However, the feedback effect of the existing bead geometry on subsequent layers has only been explicitly modelled in select studies, notably by [10], while in most cases it is either indirectly addressed or merely discussed as a future perspective.

The objective of this study is to transfer a previously developed and experimentally validated SPH-based model [11] for Gas Metal Arc (GMA) welding to the multilayer WAAM process and to demonstrate its applicability using real industrial production data. For the production of the demonstrator component, a highly electrically and mechanically controlled GMA welding process, Cold Metal Transfer® (CMT®), was used. CMT® is a controlled short-circuit GMA welding variant characterized by cyclic wire retraction, enabling reduced heat input and controlled droplet transfer [11]. The capability of the base model to capture the CMT® specific process phases, short-circuit and arc phase, was demonstrated in [11].

All process parameters used in the simulation – including current, voltage, wire feed rate, inter-layer timing, and torch trajectory – were directly extracted from the robot program of an industrial wire-and-arc-based AM production system operated by our project partner Guaranteed.

The overarching goal is the creation of a digital twin of the WAAM process. In this context, computational efficiency is not merely a numerical aspect but a decisive industrial requirement: only if simulation time remains within economically acceptable limits can the model be used for production planning and process preparation.

## INDUSTRIAL FRAMEWORK AND DIGITAL TWIN CONCEPT

The present study was conducted in close collaboration with the industrial partner Guaranteed, a company specializing in large-scale wire-and-arc-based additive manufacturing. The investigated demonstrator component was produced on an industrial robotic WAAM system using certified production parameters.

The simulation model does not rely on artificial test cases or parameter fitting. Instead, the robot program (G-code) used for manufacturing the real component served directly as simulation input. The torch trajectory, average current, average voltage, and wire feed rate were extracted without modification and implemented in the SPH framework.

This approach enables the development of a prototype digital twin of the WAAM process. The objective is not solely the numerical reproduction of bead geometry, but the establishment

of a predictive simulation tool that, after further calibration, can support industrial process design and production preparation.

## METHODS

The methods for the consideration of physical phenomena in a GMA welding process were developed within the frame of SFB 1120 “Precision Melt Engineering”, a Collaborative Research Centre funded by the German Research Foundation (DFG), focusing on the physical understanding and control of melt-based manufacturing processes.

In general, the simulation concept of the GMA welding process pursued in SFB 1120 is based on dividing the domain into three areas: anode, arc and cathode (Fig. 1). This is done by selecting particles based on their geometric positions. Further selection criteria (temperature, surface, orientation, etc.) allow the particles to be assigned to the appropriate models for heat input, replacement model for acceleration due to the Lorentz force or solidification model.

Grid-based numerical methods (Euler methods) are widely used in the simulation of manufacturing pro-cesses [12] [13] [14]. In the event of a significant change in topology in the simulation area, the use of Euler methods results in additional complexity associated with the algorithms for determining the free surface. These methods do not require further development, as they already represent the state of the art. However, it is also known that such simulations are very time-consuming.

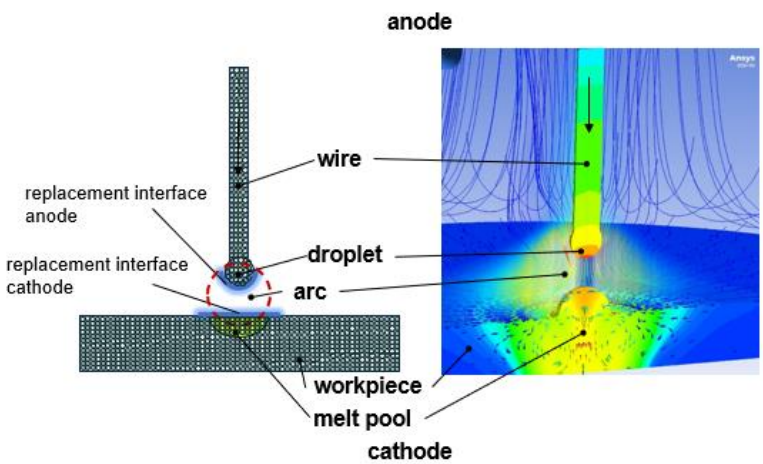



**Fig. 1**: Division of the simulation area into three domains

Mesh-free Lagrangian methods solve these problems using native approaches. The mass is carried by the interpolation points themselves and cannot be lost. The mesh is also replaced by a point neighbourhood, for which efficient data structures exist. This allows topology

changes to be handled implicitly. The Smoothed Particle Hydrodynamics (SPH) method is one such method that has proven itself in physics and has recently also found application in engineering. It impresses with its simplicity, efficient computability and stability. The SPH framework SPlisHSPlasH [15] is being developed at RWTH Aachen University. It already offers modern methods for simulating fluids, elastic bodies, highly viscous materials and coupling with rigid bodies [16–18].

## CONCEPT 1: DROPLET FORMATION AND DETACHMENT CONSIDERATION

The method for WAAM-simulation using SPH was developed based on the work of SFB 1120 and on the platform called SPlisHSPlaSH. This platform includes solvers for general physical phenomena such as heat and mass transport, models for taking surface tension and temperature-dependent viscosity into account, and the definition of kinematic and thermal boundary conditions. Welding process-specific models were integrated that allow the electromagnetic effect and the arc effect to be considered:

- surface heat input through the processes in the anode and cathode layers
- volumetric heat source due to Joule heating
- volumetric acceleration due to the Lorentz force (drop separation)

The compensation models for the physical phenomena are activated in accordance with the CMT® process phases: heat input through the electric arc in the CMT® process arc phase and material transport or droplet detachment through the Lorentz force acceleration model in the short-circuit phase. The replacement model is based on Ampère's force law and relates the disc radii of the conductor through which the current flows. Joule heating is active in both phases. A detailed description of the model was introduced in [11].

On this basis, a dynamic process is mapped with the interaction between the variable wire feed, the heat input from the arc and the melting and detachment of the material. Short-circuit detection and thus the wire movement direction is based on the melt pool or solidification profile. The determined curves for average wire feed and current are set as target values. The phase duration is extrapolated according to the short-circuit detection, using the last value from the average cycle until the phase change.

The result shown in [11] were generated using the following SPH and real process parameters:

**Table 1**: SPH parameters for the CMT® process simulation.

| Particle Ø | mm | 0.2 |
|---|---|---|
| Particle count | - | 300,000 |
| Simulation duration | h | 2 |
| Process duration | s | 4 |
| Number of layers | - | 1 |

## CONCEPT 2: ONE PARTICLE PER DROPLET WITH A SURROGATE MODEL OF THE ANODE AND CATHODE REGION

Extrapolation of the required computing resources shows that a simulation of the WAAM process using the current approach would not be feasible within a reasonable time frame. An acceleration concept was therefore developed in which the anode processes of droplet formation and detachment are not directly mapped, but the heat input and melting are also taken into account. The concept concentrates the computing power on the heat transfer and mass transfer in the workpiece or in the structure formed by the many layers. The approach envisages that the phenomena in the anode are recorded by substitute models until the moment the droplet is free to fly. Fig. 2 demonstrates the area for the activation of pressure and thermal solver. Furthermore, it is assumed that an SPH particle takes on the size of a droplet.

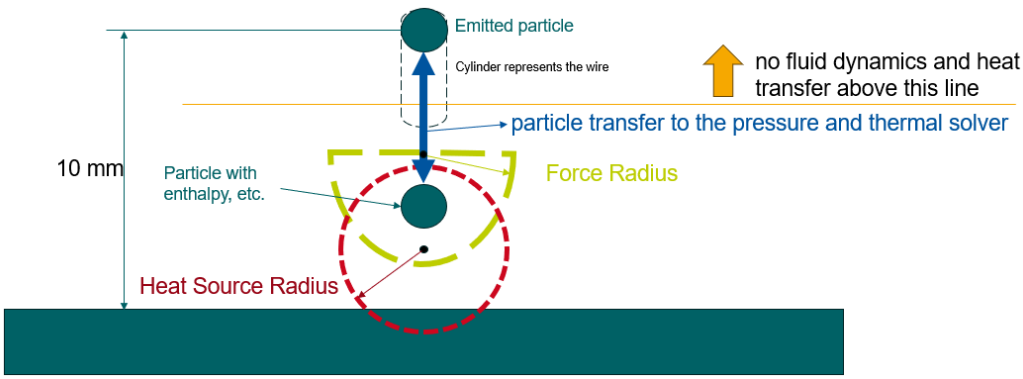



**Fig. 2**: Surrogate models of anode and cathode layers effects

This eliminates the need to represent the anode for the simulation of the WAAM process. This state is clearly visible in the Fig. 2: the droplets or particles are inserted according to the wire feed speed and heated by the heat input model of the arc effect. The speed of the droplets is determined using the Lorentz force acceleration model, whereby, the ratio of the arc radii between the anode and cathode is assumed to be 1:2. According to the developed substitute models, the momentum of the droplet corresponds to the acceleration of a CMT® short-circuit transition.

## RESULTS

With these assumptions a virtual part consisting of 20 layers was simulated, Fig. 3. The simulation parameters are listed in Table 2. This approach shows a significant acceleration resulting in 1 min of process per 1 h of calculation time compared to 2 s of process per 1 h calculation time and an acceleration factor of ≈ 30.

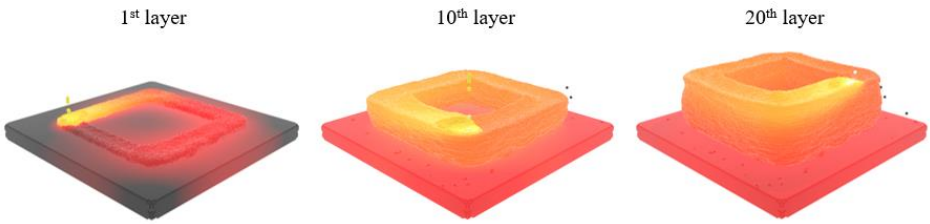



**Fig. 3**: Example for material deposition and layer build-up capability of the "one particle per droplet" concept, 70x70x5 mm substrate, 40x40 mm deposition path

**Table 2**: Simulation parameters for the concept "one particle per droplet", as shown in Fig. 3. The particle count increased during the simulation from 24,000 to 59,000 due to continuous layer deposition. Since the surrogate approach assigns one SPH particle per droplet, the number of particles directly reflects the accumulated deposited material.

| **Particle Ø** | **mm** | **1** |
|---|---|---|
| Number of particles | - | |
| Start of simulation | - | 24,000 |
| End of simulation | - | 59,000 |
| Simulation duration | h | 6 |
| Process duration | s | 450 (7.5 min) |
| Number of layers | - | 20 |

For the development of a digital twin, Guaranteed suggested a component from its own practice and provided the robot program for manufacturing this component, Fig. 4, a. The burner path, consisting of 18 layers, and the welding parameters for the manufacturing process were extracted from the robot program, Fig. 4, b. Fig. 4, c Presents a time step of the manufacturing process using a reconstructed surface. The final geometry of the component as well as the temperature field at a time step in the cooling phase are shown in Fig. 4, d, using particle-based raw data.

The calculation time for the simulated production of the component was 130 hours, while the real manufacturing process required approximately 40 minutes, Table 3. All computations were performed on the CPU 2X Intel Xeon Gold 6326. This comparison is not intended as a limitation but as an evaluation of digital twin feasibility. In industrial process planning, simulation time represents a critical performance indicator. The presented surrogate approach enables, for the first time within our SPH framework, the simulation of an 18-layer industrial

WAAM component using real production parameters. Without the introduced acceleration strategy, such a simulation would not be computationally feasible.

It should be noted here that the total simulation time also includes the cooling process, i.e. approx. 20 minutes of real time. In total, one hour of real process time (WAAM + cool down) was calculated within 130 hours, Table 3. During the transient calculation, the system status was exported every second with the corresponding calculated physical variables. This export frequency results in a memory requirement of 60 GB.

The simulation environment was prepared for the input of external data. The G-code-based robot program used to manufacture the demonstration component serves as the basis. The average values for the heat source were extracted from this program: average current and average voltage. The wire feed was also taken from an average value. The torch movement from the program is specified in the simulation environment in the form of a *.csv file.

Since the torch has equidistant steps for the layers and the power source regulates the arc distance, additional effort is necessary to adopt the emitter height during the simulation.

Also, the speed of the drop must be controlled so that it corresponds to the CMT® process.

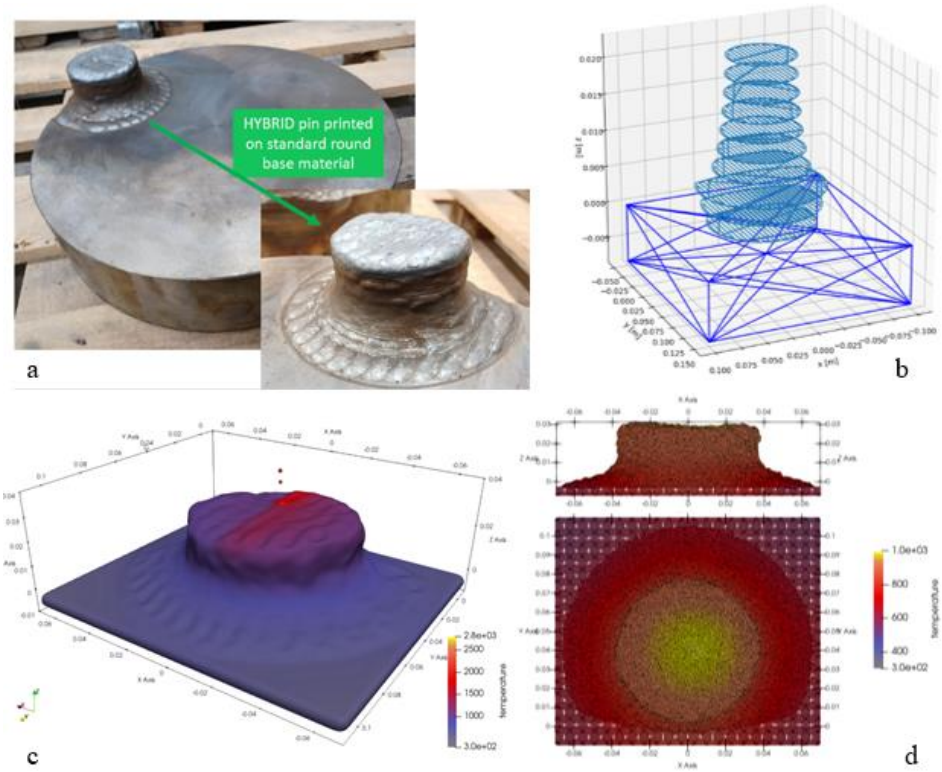



**Fig. 4**: Demonstrator component digital twin results. a: manufactured eccentric pin, b: torch path for the robot program, c: simulation time step for the material deposition process, d: final geometry and time step in the cooling phase of the simulation

**Table 3**: SPH parameters for a WAAM process simulation.

| Particle Ø | mm | 1 |
|---|---|---|
| Number of particles | - | |
| Start of simulation | - | 84,000 |
| End of simulation | - | 330,000 |
| Simulation duration | h | 130 |
| Process duration | s | 2,200 (36.6 min) |
| With cooling time | s | 3,344 (55.7 min) |
| Number of layers | - | 18 |

## DISCUSSION AND OUTLOOK

The developed simulation model demonstrates the successful transfer of a validated SPH-based GMAW welding model to multilayer wire-and-arc-based additive manufacturing. Using unmodified industrial production parameters and the original robot trajectory, an 18-layer demonstrator was simulated. This constitutes a decisive step toward a physics-based digital twin of the WAAM process. By predicting bead geometry across multiple layers, it enables early-stage evaluation and optimization of process parameters, thereby reducing reliance on costly and time-consuming trial-and-error testing. A systematic parameter variation study is beyond the scope of this work, as the primary objective is the transfer of a validated welding model to an industrial WAAM digital twin under fixed production conditions.

The primary achievement of this work lies not only in geometric prediction but in demonstrating computational feasibility under industrial boundary conditions. The surrogate concept (“one particle = one droplet”) represents a necessary abstraction to make multilayer wire-and-arc-based AM simulation practically usable for process preparation and optimization.

The authors see the simulation framework presented here as a module or intermediate step toward a fully comprehensive digital twin, in which the current state does not yet provide a precise geometric match, but nevertheless allows the temperature field, especially inside the component, to be used for analyzing material behavior.

Additional predictive capability will come from incorporating a density-change model that accounts for the metal’s density in the liquid, transition, and solid phases. Including phase-dependent density variations in the simulation can improve the prediction of the solidification process, residual stresses, and final geometry, thereby enhancing the model’s value for process design and qualification.

Despite these advances, computational cost remains a barrier to widespread industrial adoption. Additional performance optimizations are necessary to render the model viable in time-critical production settings.

A particularly promising acceleration strategy is adaptive discretization, which concentrates computational resolution in regions with steep physical gradients. This approach reduces overall computational load while preserving accuracy. Building on this, a natural next step is to adopt a hybrid strategy: apply high-resolution, adaptive discretization in zones that

require strict accuracy, while using the “one particle per droplet” concept in areas where no critical changes in part formation are expected. Such a combined approach enables efficient use of computational resources by matching the level of model fidelity to local process needs.

From a software-architecture standpoint, future deployment will benefit from modularizing the computational backend and decoupling it from the user interface. Such encapsulation facilitates integration into diverse software ecosystems or digital twins without extensive reengineering and permits incremental improvements to the simulation engine without disrupting user-facing components.

Transient simulations generate vast amounts of data, presenting challenges for storage and interactive visualization. A server-centric workflow – storing datasets on high-capacity servers and leveraging server-side rendering for visualization – can mitigate these issues. Visualization can be streamed (e.g., as video) to remote clients, enabling responsive, accessible, and interactive analysis even for large-scale transient simulations.

The main achievements of this work can be summarized as follows:

- Successful transfer of a validated SPH-based GMAW welding model to multilayer WAAM.
- Direct implementation of industrial robot path and production parameters without artificial tuning.
- Simulation of an 18-layer industrial demonstrator component.
- Development of a surrogate modelling strategy enabling digital twin feasibility.
- Identification of remaining geometric deviations and their physical origin within the SPH surface tension formulation.

## APPENDICES AND ACKNOWLEDGEMENTS

All presented investigations were conducted in the context of the Collaborative Research Centre SFB1120 "Precision Melt Engineering” at RWTH Aachen University and funded by the German Research Foundation (DFG). For the sponsorship and the support we wish to express our sincere gratitude.

Simulations were performed with computing resources granted by RWTH Aachen University under project rwth0398.

The authors thank Mr. Lukas Kesselburg for his contribution in programming and implementing the models used in our calculations and for the generation of analysis and rendering templates. His supervision and effort on the code maintenance have a great impact on the investigations presented in this work.

## References

[1] C. LIU, H. GAO, L. LI, J. WANG, C. GUO and F. JIANG: ‘A review on metal additive manufacturing: modeling and application of numerical simulation for heat and mass transfer and microstructure evolution’, *China Foundry*, 18, *4*, pp. 317-334, 2021.

[2] E. PAGONE, J. ANTONISSEN and F. MARTINA: 'Life Cycle Sustainability Assessment of Repair Through Wire and Arc Additive Manufacturing', in: A. Lazou et al. (Eds.), *REWAS 2022: Developing Tomorrow's Technical Cycles (Volume I)*, pp. 387-394, Springer International Publishing, Cham, 2022.

[3] X. F. ZHAO, A. ZAPATA, C. BERNAUER, S. BAEHR and M. F. ZAEH: 'Simulation of Wire Arc Additive Manufacturing in the Reinforcement of a Half-Cylinder Shell Geometry', *Materials (Basel, Switzerland)*, 16, 13, 2023.

[4] R. SAMPAIO, J. PRAGANA, I. BRAGANÇA, C. SILVA, C. V. NIELSEN and P. MARTINS: 'Modelling of wire-arc additive manufacturing – A review', *Advances in Industrial and Manufacturing Engineering*, 6, pp. 100121, 2023.

[5] Y. LING, J. NI, M. ABDEL WAHAB, J. ANTONISSEN and J. VANDE VOORDE: 'A Heat Transfer Finite Element Model for Wire-Arc-Additive-Manufacturing Process', in: M. Abdel Wahab (Ed.), *Proceedings of the 8th International Conference on Fracture, Fatigue and Wear*, pp. 201-215, Springer Singapore, Singapore, 2021.

[6] Y. LING, J. NI, J. ANTONISSEN, H. BEN HAMOUDA, J. VANDE VOORDE and M. ABDEL WAHAB: 'Numerical prediction of microstructure and hardness for low carbon steel wire Arc additive manufacturing components', *Simulation Modelling Practice and Theory*, 122, pp. 102664, 2023.

[7] I. A. FERREIRA, J. P. OLIVEIRA, J. ANTONISSEN and H. CARVALHO: 'Assessing the impact of fusion-based additive manufacturing technologies on green supply chain management performance', *Journal of Manufacturing Technology Management*, 34, 1, pp. 187-211, 2023.

[8] M. S. AMAL, C. T. JUSTUS PANICKER and V. SENTHILKUMAR: 'Simulation of wire arc additive manufacturing to find out the optimal path planning strategy', *Materials Today: Proceedings*, 66, pp. 2405-2410, 2022.

[9] F. MONTEVECCHI, G. VENTURINI, A. SCIPPA and G. CAMPATELLI: 'Finite Element Modelling of Wire-arc-additive-manufacturing Process', *Procedia CIRP*, 55, pp. 109-114, 2016.

[10] Y. OGINO, S. ASAI and Y. HIRATA: 'Numerical simulation of WAAM process by a GMAW weld pool model', *Welding in the World*, 62, 2, pp. 393-401, 2018.

[11] O. MOKROV, S. WARKENTIN, L. WESTHOFEN, S. JESKE, J. BENDER, R. SHARMA and U. REISGEN: 'Simulation of wire metal transfer in the cold metal transfer (CMT) variant of gas metal arc welding using the smoothed particle hydrodynamics (SPH) approach', *Materialwissenschaft und Werkstofftechnik*, 55, 1, pp. 62-71, 2024.

[12] S. CADIOU, M. COURTOIS, M. CARIN, W. BERCKMANS and P. LE MASSON: '3D heat transfer, fluid flow and electromagnetic model for cold metal transfer wire arc additive manufacturing (Cmt-Waam)', *Additive Manufacturing*, 36, pp. 101541, 2020.

[13] U. REISGEN, R. SHARMA, O. MOKROV, S. EMADMOSTOUFI, J. KRUSKA, J. HERMSDORF, M. LAMMERS and T. BOKELMANN: 'Simulation of laser assisted double wire deposition welding with two different approaches with eulerian (FVM) and lagrangian (SPH) methods', in: Christof Sommitsch, Norbert Enzinger, Peter Mayr (Ed.), *Mathematical modelling of weld phenomena 13*, pp. 255-279, Verlag der Technischen Universität Graz, 2023.

[14] A. ZABIROV, O. SEMENOV, V. DEMCHENKO, I. KRIVTSUN, U. REISGEN and O. MOKROV: 'Modelling of the droplet formation process in GMA welding', in: Christof Sommitsch and Norbert Enzinger (Ed.), *Mathematical modelling of weld phenomena 10*, pp. 83-94, Verlag der Technischen Universität Graz, 2013.

[15] J. A. O. BENDER: *SPlisHSPlasH Library*.

[16] S. R. JESKE, J. BENDER, K. BOBZIN, H. HEINEMANN, K. JASUTYN, M. SIMON, O. MOKROV, R. SHARMA and U. REISGEN: 'Application and benchmark of SPH for modeling the impact in thermal spraying', *Computational Particle Mechanics*, 9, 6, pp. 1137-1152, 2022.

[17] S. R. JESKE, M. S. SIMON, O. SEMENOV, J. KRUSKA, O. MOKROV, R. SHARMA, U. REISGEN, and J. BENDER. "Quantitative evaluation of SPH in TIG spot welding," *Computational Particle Mechanics*, 10, *1*, pp. 1–18, 2023.

[18] K. BOBZIN, H. HEINEMANN, K. JASUTYN, S. R. JESKE, J. BENDER, S. WARKENTIN, O. MOKROV, R. SHARMA, and U. REISGEN. "Modeling the Droplet Impact on the Substrate with Surface Preparation in Thermal Spraying with SPH," *Journal of Thermal Spray Technology*, 32, *2-3*, pp. 599–608, 2023.

# I Welding Processes

## d) Special Joining Processes

# NUMERICAL ANALYSIS OF MECHANICAL BEHAVIOR DURING FRICTION STIR WELDING

S. MAEDA*, K. IKUSHIMA*, M. SHIBAHARA*

**Graduate school of engineering, Osaka Metropolitan University, Japan*

*DOI 10.3217/978-3-99161-089-2-015, license CC BY 4.0*
*https://creativecommons.org/licenses/by/4.0/deed.en*
*This CC license does not apply to third party material and content noted otherwise.*

ABSTRACT

A novel numerical analysis method based on a Coupled Eulerian–Lagrangian (CEL) approach with an implicit formulation was developed to simulate the transient thermal and mechanical behavior during Friction Stir Welding (FSW). The proposed method combines an operator-split-based CEL scheme with a dynamic implicit solver optimized for GPU-based parallel computation, enabling stable and accurate simulations with over 1.2 million nodes. This approach permits larger time steps than conventional explicit methods without sacrificing accuracy, achieving a computational cost of about 5.5 hours for each simulated second of welding. The simulation results successfully reproduced key features observed in experiments, including periodic temperature and load fluctuations associated with tool rotation, which are characteristic of onion ring formation. Furthermore, by varying the tool tilt angle, the influence of tool orientation on thermal fields, material flow, and defect generation was quantitatively investigated. A forward tool tilt was found to move the high-temperature region to the front of the tool, leading to the formation of tunnel defects. This provided insight into the defect formation mechanism by revealing that a forward tilt alters material flow and thermal concentration in a way that promotes tunnel defects. These findings demonstrate the effectiveness of the proposed method in capturing complex thermo-mechanical phenomena during FSW and its potential for optimizing welding parameters and improving joint quality.

Keywords: Friction Stir Welding, Coupled Eulerian-Lagrangian method, Thermal elastic-plastic analysis, Implicit formulation

## INTRODUCTION

Friction Stir Welding (FSW) has become a widely adopted joining technique for lightweight metal materials due to its superior mechanical strength and reduced thermal impact. In this process, a rotating and downward-pressured tool travels along the joint line, inducing plastic flow in the material and achieving solid-state bonding. However, the material behavior during FSW is strongly thermo-mechanically coupled, and it remains challenging to accurately capture the thermal, mechanical, and material flow behavior, particularly in the stirred region.

In addition, improper material flow or thermal history during welding can lead to the formation of defects such as tunnel defects and voids. These defects can significantly reduce the structural reliability of the weld, making it essential to predict and prevent such defects in FSW. In addition, concentric patterns, commonly referred to as “onion rings” [1], are sometimes observed on the surface or in cross-sections of the weld, and are considered characteristic features of the process. These structures are believed to indicate the periodic, layered flow of material and have been considered a physical record of the plastic deformation and stirring behavior during welding [2]. However, the detailed mechanism of their formation has not yet been fully clarified.

In recent years, the Coupled Eulerian-Lagrangian (CEL) method [3] has been widely used as an effective approach for analyzing the complex material flow and large deformations that occur during the Friction Stir Welding (FSW) process. The CEL method is capable of accurately handling large material deformations, multi-body contact, and interfacial friction and plastic deformation, making it particularly attractive for reproducing the detailed thermal and mechanical behavior during FSW [4,5]. In particular, ABAQUS/Explicit has been widely used as a finite element analysis software that supports CEL implementation [6], and many previous studies have adopted it [7-13]. Furthermore, in addressing the challenge of high computational cost, some attempts have been made to balance accuracy and efficiency by appropriately applying mass scaling techniques [7,8].

On the other hand, the periodic phenomena specific to FSW require more detailed analysis [8]. To achieve this, it is essential to develop computational environments capable of high-accuracy simulations and to further accelerate the computation. In fact, it has been reported that current simulations involving 200,000 to 300,000 elements require approximately two days to analyze just one second of the process [9,10], indicating that the high computational cost remains a significant challenge for practical applications. If further improvements in simulation accuracy and speed can be achieved, it will become possible to investigate conditions closer to actual processing environments. This is expected to be useful for selecting and optimizing welding parameters, including stirring behavior and periodic phenomena.

In this study, a novel CEL analysis method based on an implicit formulation was developed to accurately and stably capture the transient thermal and mechanical responses during FSW. Compared to conventional explicit methods, the proposed method allows for larger time steps while maintaining computational accuracy, thereby enabling numerically stable simulations. Furthermore, by incorporating GPU-based parallel computation, the method achieves high-speed analysis within practical computation time, even when using a fine mesh resolution. To validate the effectiveness of the proposed method, it was applied to Friction Stir Processing (FSP) of a single plate, and the spatial distributions and time histories of the temperature field, mechanical responses, and stirring behavior were visualized and examined. In addition, the periodic nature inherent in these phenomena was also investigated through the analysis. Additionally, a qualitative comparison with previous experimental results was conducted to evaluate the accuracy and practical applicability of the simulation outcomes. Moreover, simulations with varying tool tilt angles were performed to investigate the influence of tool angle on the temperature field and defect formation, and to explore the mechanisms behind defect generation.

## IMPLICITLY FORMULATED CEL-BASED NUMERICAL ANALYSIS METHOD FOR THE FRICTION STIR WELDING PROCESS

All numerical simulations were performed using an in-house finite element code developed by the authors, in which the Coupled Eulerian-Lagrangian (CEL) framework and the implicit dynamic scheme were implemented based on established numerical methods. In this study, a finite element method (FEM)-based analysis approach grounded in solid mechanics was developed to investigate the mechanical behavior during FSW. The analysis employed the CEL method, which integrates both Lagrangian and Eulerian formulations. Fig. 1 presents the overall analysis flow. As shown in Fig. 1, thermal conduction analysis and thermal elastic-plastic analysis were sequentially performed while accounting for mutual contact between the Eulerian and Lagrangian domains, where meshes are assigned to space and material, respectively. The two analyses were coupled via advection calculations, enabling stable simulation of large deformations occurring near the weld zone during FSW. In the Lagrangian analysis, since the mesh is assigned to the object, it is possible to investigate the effects of geometric changes. However, this approach can suffer from mesh distortion or failure under large deformations, making it unsuitable for severe material flow. In contrast, the Eulerian formulation assigns the mesh to space, and physical variables remain fixed within the spatial domain, allowing stable analysis even when material flow crosses mesh boundaries. In this study, the joining tool, which undergoes relatively small deformation, was modeled using the Lagrangian formulation, while the heavily stirred workpiece material was modeled using the Eulerian formulation.

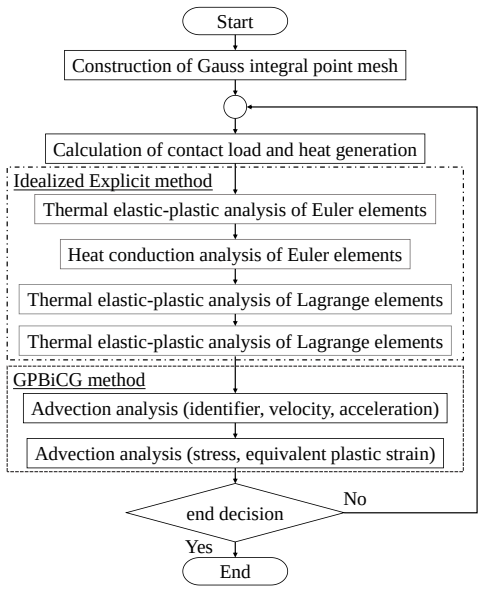



**Fig. 1** Analysis flow of development

## COUPLED EULERIAN–LAGRANGIAN METHOD USING THE OPERATOR SPLIT APPROACH

In this study, a FEM-based analysis approach was developed based on solid mechanics. The friction stir welding (FSW) phenomenon of material deformation is assumed to be governed by the following fundamental equations of solid mechanics.

$$\rho \frac{\partial v_i(X,t)}{\partial t} + \frac{\partial \sigma_{ij}}{\partial x_j} = f_i \tag{1}$$

Here, $\rho$ denotes the density, $\boldsymbol{v}$ the velocity vector, $\boldsymbol{\sigma}$ the stress tensor, $\boldsymbol{x}$ the spatial coordinate, and $\boldsymbol{f}$ the body force. The subscripts $i$ and $j$ indicate the directional components of each variable. During FSW, large localized strains occur; thus, by applying the material derivative to Equation (1), both temporal and spatial variations of the velocity field can be simultaneously considered, leading to the following form:

$$\rho\left(\frac{\partial v_i(x,t)}{\partial t} + v_j \frac{\partial v_i}{\partial x_j}\right) + \frac{\partial \sigma_{ij}}{\partial x_j} = f_i \tag{2}$$

At this stage, the left-hand side of the equation can be divided into a temporal derivative term, an advection term, and a stress gradient term. In this study, the operator-splitting method [14] was applied to Equation (2), whereby Equation (3), expressed in the Lagrangian formulation - where each computational point moves directly - is solved together with Equation (4), expressed in the Eulerian formulation, which computes physical quantities at fixed spatial locations.

$$\rho \frac{\partial v_i(x,t)}{\partial t} + \frac{\partial \sigma_{ij}}{\partial x_j} = f_i \tag{3}$$

$$\frac{\partial v_i(x,t)}{\partial t} + v_j \frac{\partial v_i}{\partial x_j} = 0 \tag{4}$$

For the thermal elastic-plastic calculation in Equation (3), the Newmark-β method [15] was used for discretization, and Idealized Explicit FEM [16-18], which can account for dynamic effects, was adopted as the solver. For the advection calculation in Equation (4), a stabilized FEM based on the SUPG (Streamline Upwind Petrov-Galerkin) method [19,20] was employed, and the Wilson-θ method [21,22] was used for time discretization. The system of equations was solved using the GPBiCG (Generalized Product-type Bi-Conjugate Gradient) method [23,24]. Furthermore, GPU-based parallel computation was applied to both Idealized Explicit FEM and the GPBiCG solver to accelerate the computation [25,26].

Thus, a CEL-based numerical analysis method using a dynamic implicit scheme was developed to simulate the thermal and mechanical behavior during FSW.

## INTERFACE REPRESENTATION USING THE VOLUME OF FLUID (VOF) METHOD

The interface of the workpiece material stirred by the tool was represented using the Volume of Fluid (VOF) method [27], which is commonly employed in Eulerian formulations for free-surface fluid flow. Using a solid interface identifier $\varphi$, the values were defined as follows: $\varphi$ = 0.5 for the solid interface, $\varphi$ = 0.0 for voids, and $\varphi$ = 1.0 for solid material. The evolution of $\varphi$ was calculated using Equation (5).

$$\frac{\partial \varphi}{\partial t} + v_j \frac{\partial \varphi}{\partial x_j} = 0 \quad (0.0 \le \varphi \le 1.0) \tag{5}$$

In addition, defects were evaluated by identifying regions where $\varphi < 0.5$ as defects, while regions with $\varphi \ge 0.5$ were displayed as the base material.

## CONTACT MODEL

The contact and friction between the tool and the workpiece were determined based on the amount of penetration of the Lagrangian tool element into the Eulerian workpiece element, as illustrated in Fig. 2. The volumetric contact force $f_c$ was calculated using the penalty method [28].

$$f_c = \alpha(T)\varphi\psi \tag{6}$$

Here, $f_c$ denotes the magnitude of the contact force. $\alpha(T)$ is the penalty coefficient, and $\psi$ is the solid interface identifier for the joining tool. The value of $\psi$ was assigned as 0.0 at the outermost surface nodes of the tool, 1.0 at the next inner layer, and 2.0 at nodes further inside. Intermediate values between these layers were interpolated using shape functions. The penalty coefficient $\alpha(T)$ was varied based on the temperature-dependent Young's modulus $E(T)$. Using the volumetric contact force $f_c$ calculated from Eq. (6), the body force $F_{ci}$ for each element was computed using the following equation.

$$F_{c_i} = \int_{\Omega_e} f_{c'} n_i \, d\Omega \tag{7}$$

Here, $\Omega_e$ is the element volume, $\Omega$ is the total volume, and $n_i$ is the normal vector.

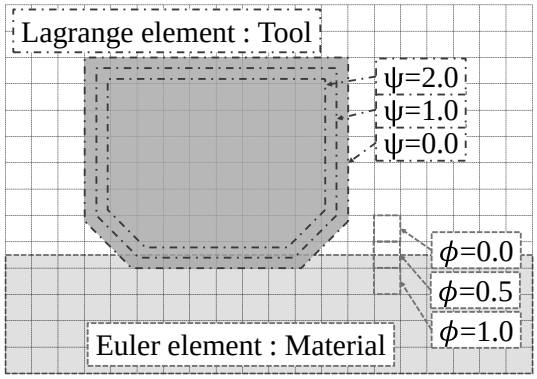



**Fig. 2** Schematic of contact analysis

## PLASTIC AND FRICTIONAL HEAT GENERATION MODELS

In this study, the heat generated during FSW is assumed to originate from two sources: plastic heat generation due to plastic deformation of the material, and frictional heat generation due to contact between the tool and the workpiece. Each is calculated as follows. The amount of plastic heat generation per element, $q_p$, is computed from the work done by plastic deformation in each element using the following equation.

$$q_p = \int \eta_p \bar{\sigma} \Delta \bar{\varepsilon}_p \, dV \tag{8}$$

Here, $\eta_p$, $\bar{\sigma}$, $\Delta\bar{\varepsilon}_p$, and $V$ denote the conversion efficiency of plastic work into heat, equivalent stress, increment of equivalent plastic strain, and unit volume, respectively. In this study, $\eta_p$ was assumed to be 90% [29,30], and the work generated by plastic deformation was converted into heat accordingly.

Additionally, the amount of frictional heat generation $q_f$ at the contact interface was calculated using the frictional force $F_f$.

$$q_f = \int_s \eta_f \boldsymbol{F}_f \boldsymbol{v}_r \, dS \tag{9}$$

$$\boldsymbol{F}_f = \begin{cases} -\mu \left\| \boldsymbol{F}_c \right\| \dfrac{\boldsymbol{v}_r}{\left\| \boldsymbol{v}_r \right\|} & (0 \le \mu \left\| \boldsymbol{F}_c \right\| < f_{r_{\max}}(T)) \\ -f_{r_{\max}}(T) \dfrac{\boldsymbol{v}_r}{\left\| \boldsymbol{v}_r \right\|} & (f_{r_{\max}}(T) \le \mu \left\| \boldsymbol{F}_c \right\|) \end{cases} \tag{10}$$

Here, $\eta_f$ is the thermal efficiency of frictional heat generation, $\boldsymbol{v}_r$ is the relative velocity between the joining tool and the workpiece material. The friction coefficient μ used in the contact model was set to 0.5, and $\eta_f$ was assumed to be 100% [8,9,11-13]. The friction force

is directly formulated as a vector quantity based on the contact force magnitude f_c and the relative velocity, and its magnitude is limited by a temperature-dependent upper bound $f_{r\,max}(T)$, which was determined from the temperature-dependent yield stress $\sigma_Y(T)$.

Heat transfer to the surrounding environment was considered by applying a constant heat transfer coefficient of 0.01 W/m²·°C on the exposed surfaces of the workpiece. The same constant heat transfer coefficient, without temperature dependence, was also applied at the contact interface to account for heat conduction between the tool and the workpiece.

### ELASTIC-PLASTIC MODEL

Although the Johnson–Cook model [31] is frequently used as the material model for FSW processes [8-13], in this study, the von Mises model [32] was employed for both the joining tool and the workpiece materials to calculate the plastic strain and stress during and after the transient joining process. This choice was made because the primary objective of the present study is to investigate the overall thermo-mechanical response, material flow behavior, and defect formation, for which the von Mises model is sufficient under the present processing conditions.

## FSP ANALYSIS OF ALUMINUM ALLOY

Using the analysis method described in the previous chapter, the FSP process for an aluminum alloy AA5083 was simulated. The simulation included tool plunging, dwelling for material stabilization, welding, and tool retraction. The thermal and mechanical states of both the tool and the workpiece material were investigated.

### ANALYSIS MODEL AND CONDITIONS

The geometry and dimensions of the analysis model are shown in Fig. 3. As illustrated in Fig. 3(a), the probe diameter, probe length, and shoulder diameter of the joining tool modeled using Lagrangian elements were set to 5.0 mm, 4.125 mm, and 15.0 mm, respectively. As shown in Fig. 3(b), the base material was modeled using Eulerian elements. The total domain size was set to 200.0 mm in length, 200.0 mm in width, and 14.0 mm in height, while the initial solid region was defined as 200.0 mm in length, 200.0 mm in width, and 4.0 mm in thickness. The minimum mesh size in the stirring zone was set to a cube with a side length of 0.2 mm. The number of nodes and elements in the tool is 5,772 and 5,020, respectively, while the number of nodes and elements in the Eulerian elements used for the space and the plate is 1,219,581 and 1,169,280, respectively. In this study, the x-, y-, and z-directions correspond to the welding, transverse, and normal directions, respectively.

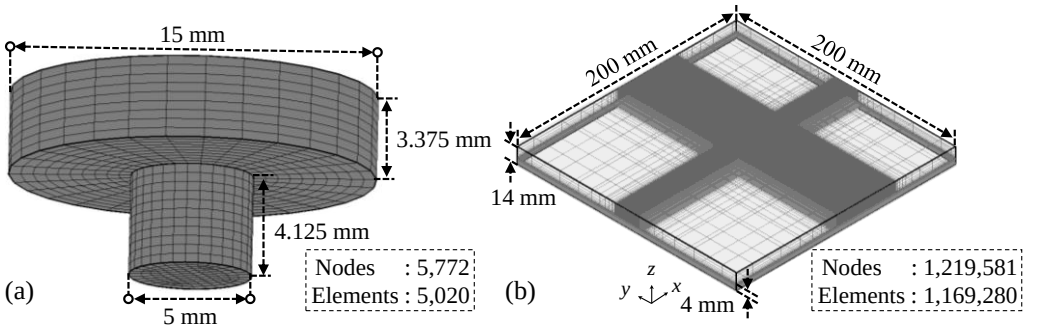



**Fig. 3** Size and shape of FSW model. (a) Tool with Lagrangian elements. (b) Material with Eulerian elements

Aluminum alloy AA5083 was used as the workpiece material, and the tool was made of SDK61. The temperature-dependent material properties of AA5083 [33] and SDK61 [34-36] are shown in Figure 4, while the temperature-independent properties are summarized in Table 1. The material properties for SDK61 were determined by integrating data from multiple sources [34-36].

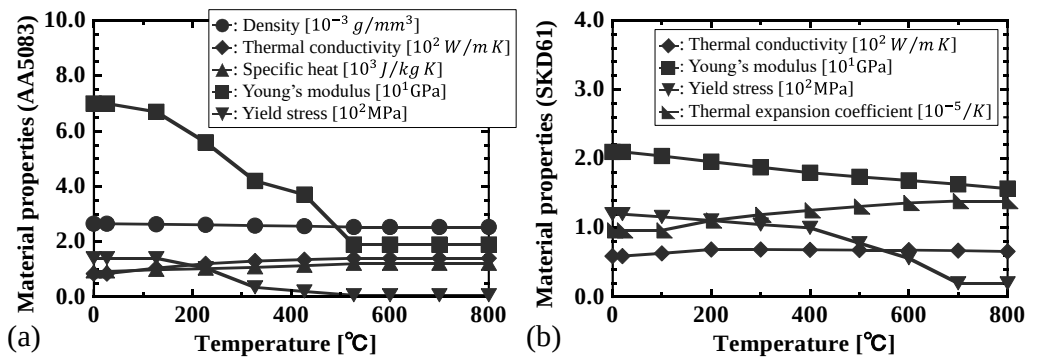



**Fig. 4** Temperature-dependent material properties. (a) AA5083 for material [33]. (b) SDK61 for tool [34-36]

**Table 1** Temperature-independent material properties used in the analysis. Properties marked as "Dependent" are treated as temperature-dependent and shown in Fig. 4.

| Material | AA5083 | SKD61 |
|---|---|---|
| Density [g/mm$^3$] | Dependent (Fig. 4) | $7.98\times10^{-3}$ |
| Specific heat [J/kg K] | Dependent (Fig. 4) | 461.0 |
| Thermal expansion coefficient [1/K] | $2.36\times10^{-5}$ | Dependent (Fig. 4) |
| Poisson's ratio | 0.33 | 0.28 |

Fig. 5 shows the entire process including plunging, dwelling, welding, and retraction. In the present analysis, the FSP process was simulated under displacement-controlled conditions, where the vertical position of the tool was prescribed throughout plunging, dwelling, and welding. As illustrated in the figure, the tool was inserted into the center of the workpiece, held in place for 10 seconds for stabilization, then advanced 40 mm for welding, and finally retracted. The tool's tilt angle was set to 3°, and its rotational speed was fixed at 500 rpm. The plunge depth at the tool center was set to 3.8 mm. The plunge speed, welding speed, and retraction speed were set to 15 mm/min, 250 mm/min, and 150 mm/min, respectively. The total duration of the process was approximately 38.52 seconds, with a time step of 0.002 seconds, resulting in a total of 19,260 computation steps. Displacement control was applied by imposing prescribed displacements on the nodes at the top surface of the tool to achieve tool rotation, translational movement, and holding. In addition, the displacement normal to the surfaces, including the sides and the bottom, was constrained.

Although the dwelling time of 10 seconds is longer than that typically used in practical FSW processes, it was selected to ensure that the thermal and mechanical fields reached a quasi-steady state prior to welding. This was confirmed in the present analysis by the saturation of the peak temperature beneath the tool and by the periodic, rotation-synchronized fluctuations in temperature and tool load without significant temporal drift. The present study focuses on the detailed investigation of transient and periodic thermo-mechanical behavior rather than optimization of computational efficiency; therefore, the time allocation among plunging, dwelling, and welding was not optimized for efficiency.

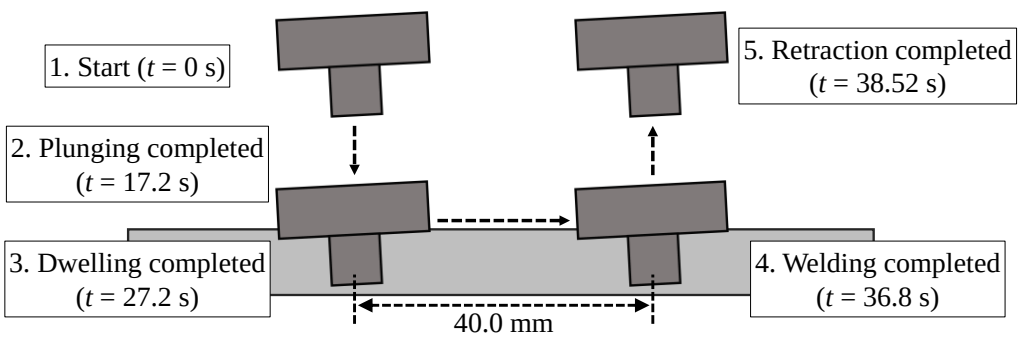



**Fig. 5** Overview of all FSW processes for analysis

## INVESTIGATION OF THERMAL AND FLOW BEHAVIOR OF THE WORKPIECE

Fig. 6 shows the heat generation density distribution on the surface of the base material during the tool plunging process. Figs. 6(a) through (d) correspond to changes in the distance between the center of the tool probe and the base material, illustrating the heat generation behavior at each stage. Fig. 6(a) shows the heat distribution at the moment when the center of the tool first contacts the base material. Due to the 3° tilt of the tool, significant heat generation is observed

on the rear side of the tool when the probe center contacts the surface. In Fig. 6(b), where the plunge depth reaches 1.0 mm, the heat distribution becomes axisymmetric as the tool plunges deeper, with an increase in heat generation particularly near the edge of the probe. In Fig. 6(c), at a plunge depth of 2.0 mm, the base material is pressed upward by the probe, resulting in contact with the shoulder. Additionally, the amount of heat generation near the probe edge decreases, which is likely due to a rise in temperature at the lower part of the probe as plunging progresses, thereby reducing frictional and plastic heat generation. In Fig. 6(d), where the plunge depth reaches 3.0 mm, heat generation on the rear side of the tool becomes dominant again due to the tool's tilt.

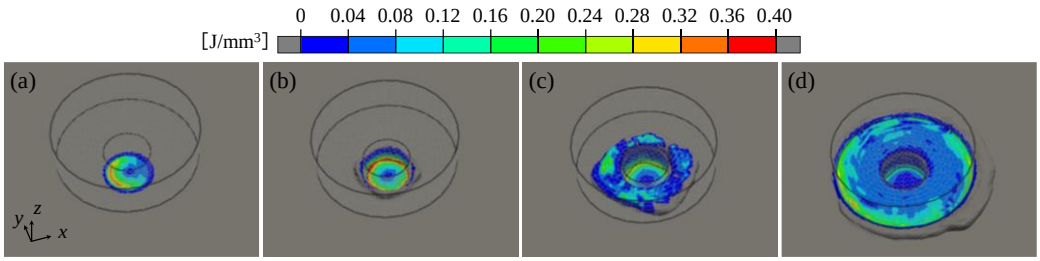



**Fig. 6** Heat density distribution on plate surface according to insertion amount of pin center during tool plunging. (a) 0 mm. (b) 1.0 mm. (c) 2.0 mm. (d) 3.0 mm

Similarly, Fig. 7 shows the heat generation density distribution on the plate surface at the completion of tool plunging, after the dwelling phase, and during welding. From Fig. 7(a), it is evident that at the end of the tool plunging phase, greater heat generation occurs on the rear side of the tool due to its tilt, particularly at the surface where the shoulder contacts the plate. In addition, significant heat generation is observed at the contact point with the shoulder edge, where the peripheral speed is highest. In Fig. 7(b), after the dwelling phase, it can be seen that, similar to the plunging phase, heat generation at the shoulder contact area decreases due to the temperature increase. Furthermore, during the welding phase, as shown in Fig. 7(c), intense heat generation is observed on the front side of the tool - where it contacts the lower-temperature region of the plate - particularly at the outer edge of the shoulder, which has the highest peripheral speed.

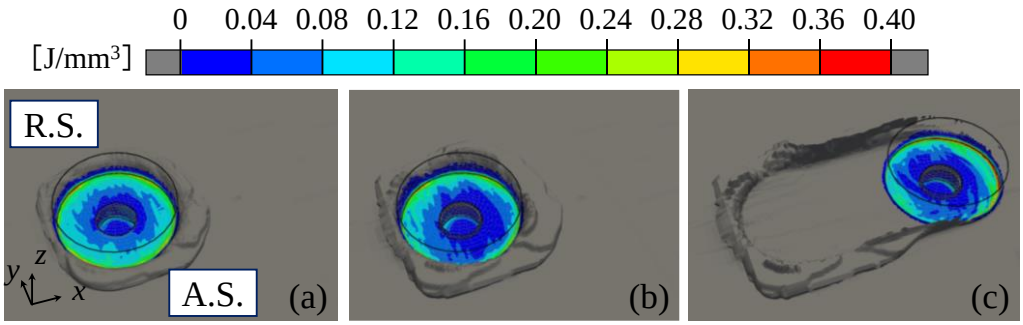



**Fig. 7** Heat density distribution on plate surface at each stage after tool insertion completed. (a) Plunging completed. (b) Dwelling completed. (c) During welding

Fig. 8 shows the temperature distribution on the plate surface at the completion of tool plunging, after the dwelling phase, and during welding. The figure confirms that under the present analysis conditions, a high-temperature region exceeding 540 °C is formed directly beneath the tool throughout all process stages. Comparing Figs. 8(a) and (b), this indicates that the 10-second dwelling phase leads to an overall increase in the base material temperature. Furthermore, a comparison between Figs. 8(b) and (c) indicates that the temperature distribution formed during the dwelling phase is largely maintained as the welding progresses.

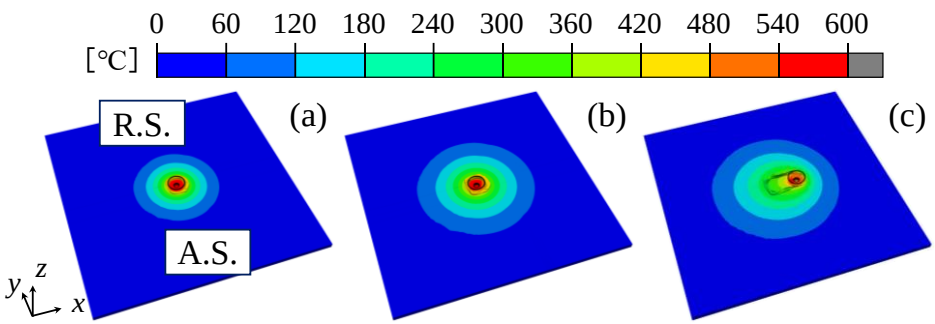



**Fig. 8** Heat density distribution on plate surface at each stage after tool insertion completed. (a) Plunging completed. (b) Dwelling completed. (c) During welding

Fig. 9 shows the temperature distribution on the surface of the base material near the tool during one full rotation of the tool. Fig. 9(a) presents the state at 4.8 seconds after the start of welding, while Figs. 9(b)-(e) show the sequential changes during the subsequent 0.12 seconds, corresponding to one full rotation, divided into quarter-rotation intervals. These results show that due to the tilt of the tool, a high-temperature region is formed on the rear side beneath the tool. Furthermore, a comparison of Figs. 9(a)-(d) reveals that the region exceeding 520 °C moves along the rotation direction of the tool, following its motion. Comparing Figs. 9(a) and

(e), the temperature distributions appear nearly identical, indicating that under the current conditions, the temperature field varies periodically with each full rotation of the tool. This periodic behavior corresponds well with experimental observations that the spacing of onion rings matches the tool's advance per revolution [37]. The observed periodic temperature variation is considered to affect local plastic strain accumulation and material flow behavior, and thus may act as one of the contributing factors to onion-ring formation.

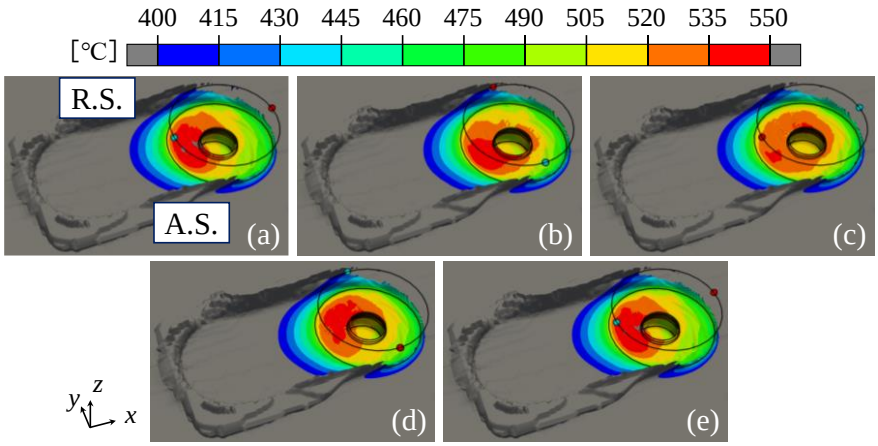



**Fig. 9** Temperature distribution on the plate surface during one rotation of tool. (a) Start of rotation. (b) 1/4 rotation. (c) 1/2 rotation. (d) 3/4 rotation. (e) 1 rotation

Next, in order to examine the material flow during stirring, Fig. 10 shows the temperature distribution and flow velocity distribution on the cross-section at the tool center over a tool rotation (0.12 s) starting from 9.1 seconds after the beginning of welding. In the figure, the contour represents the temperature distribution, while the arrows indicate the direction of material flow within the cross-section at each node. The size of the arrows represent the magnitude of the three-dimensional velocity. As observed on the top surface in Fig. 9, the temperature distribution also changes in the thickness direction following the tool rotation. Similarly, the material flow exhibits periodic behavior synchronized with the tool rotation. In addition, it is evident that high material flow velocities occur near the tool and in regions of high temperature, with the flow velocity on the retreating side (R.S.) being greater than that on the advancing side (A.S.). Furthermore, it can be seen that the flash formed on the R.S. is larger than that on the A.S. This result corresponds to the experimentally observed behavior of flash formation [38], indicating that the numerical analysis successfully reproduces the actual phenomenon. It should be noted that the tool geometry shown in Fig. 10 differs from that in Fig. 3 because plastic deformation of the tool occurs during the plunging process, and the deformed configuration at the corresponding time step is visualized here.

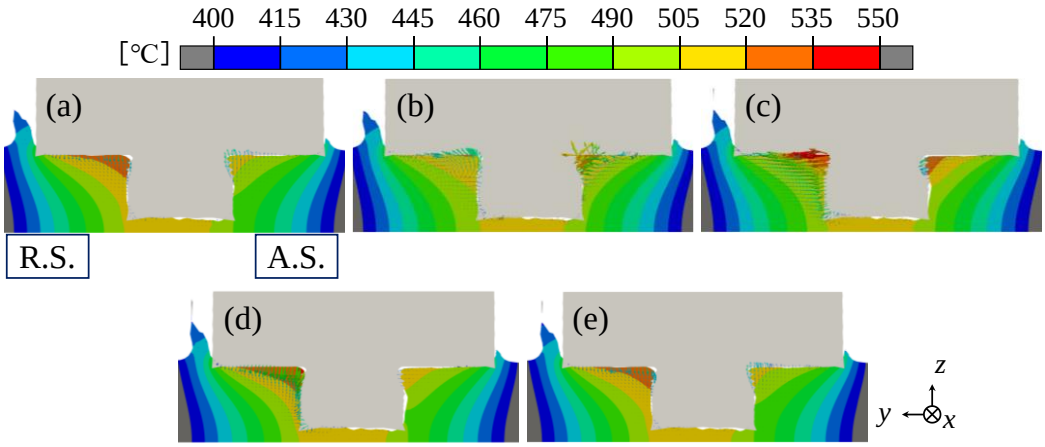



**Fig. 10** Temperature and flow velocity distribution during one rotation of bonding at tool center cross section. (a) Start of rotation. (b) 1/4 rotation. (c) 1/2 rotation. (d) 3/4 rotation. (e) 1 rotation

Fig. 11 shows the flow behavior of nine tracer points placed near the tool at 4.8 seconds after the start of welding. Fig. 11(a) presents the initial state, where the tracers are arranged 3.0 mm in the welding direction from the tool center, at a depth of 0.8 mm from the plate surface, and spaced at 2.0 mm intervals in the width direction. Figs. 11(b)-(e) illustrate the movement trajectories of each tracer over the subsequent 2.5 seconds. The tracer motion was calculated based on the material flow velocity at each time step and the time increment. The figure reveals that the tracers flow along the tool rotation direction and that the flow velocity on the retreating side (R.S.) is greater than that on the advancing side (A.S.). It is also evident that the tracer velocities are lower than the tool's rotational speed and decrease with distance from the probe. Furthermore, some tracers are observed to circulate multiple times around the probe. These results are in good agreement with experimentally observed flow behavior [39,40], indicating that the proposed numerical simulation method can successfully reproduce the actual phenomena.

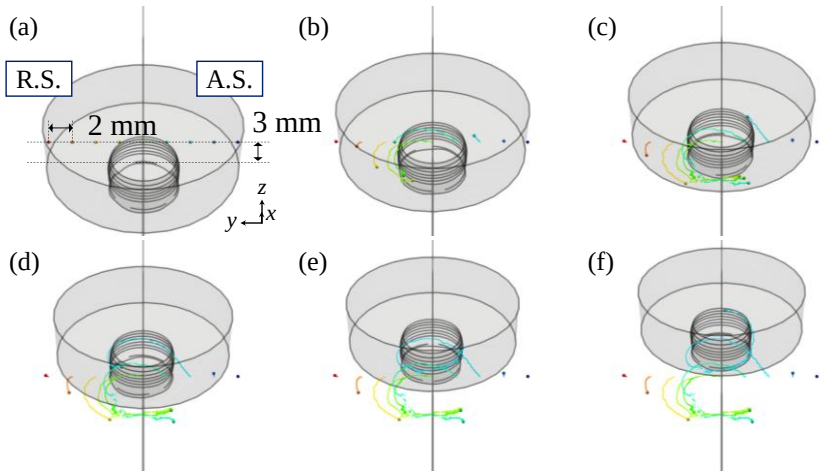



**Fig. 11** Flow behavior near tool during welding. (a) Start of rotation. (b) After 0.5 seconds. (c) After 1.0 seconds. (d) After 1.5 seconds. (e) After 2.0 seconds. (f) After 2.5 seconds

Based on these results, the present analysis method is shown to accurately reproduce real phenomena and demonstrates its effectiveness for analyzing the behavior of the workpiece material.

## INVESTIGATION OF THERMAL AND FLOW BEHAVIOR OF THE WORKPIECE

Fig. 12 shows the temperature distribution on the tool surface at each stage of the process. Figs. 12(a)-(d) correspond to the tool insertion stage, while Figs. 12(e)-(g) depict the results after the completion of insertion. It can be observed that during insertion, the highest temperature occurs at the tip edge of the probe. After insertion is completed, the surface temperature of the tool decreases and remains mostly below 480 °C. These results suggest that under the present conditions, the strength at the probe tip edge significantly decreases during insertion, indicating a high possibility of wear or damage.

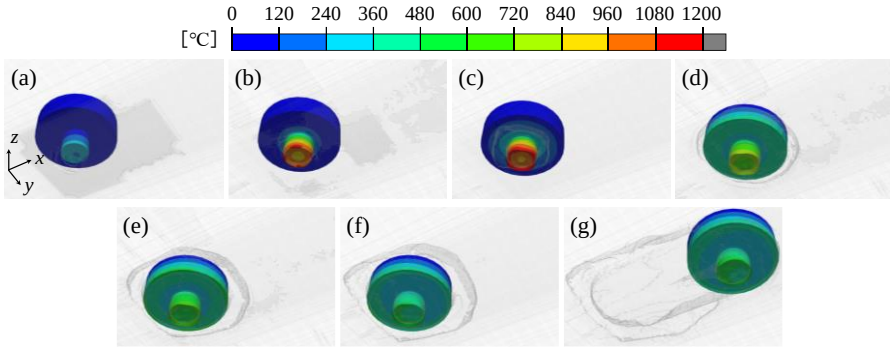



**Fig. 12** Temperature distribution on tool surface at each stage. (a) Pin insertion: 0 mm. (b) Pin insertion: 1 mm. (c) Pin insertion: 2 mm. (d) Pin insertion: 3 mm. (e) Plunging completed. (f) Dwelling completed. (g) During welding

Similarly, Fig. 13 presents the equivalent stress distribution on the tool surface during each stage. The results show that in all stages, a high stress concentration occurs at the boundary between the probe and shoulder. This is particularly evident during the welding stage involving tool movement, where even higher stresses are generated. These findings indicate that under the present conditions, relatively high stress is generated at the probe-shoulder boundary during welding, which may potentially increase the mechanical load on the tool.

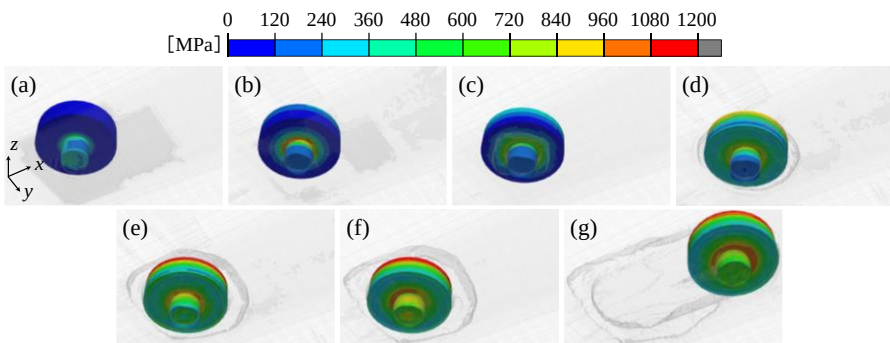



**Fig. 13** Equivalent stress distribution on tool surface at each stage. (a) Pin insertion: 0 mm. (b) Pin insertion: 1 mm. (c) Pin insertion: 2 mm. (d) Pin insertion: 3 mm. (e) Plunging completed. (f) Dwelling completed. (g) During welding

Fig. 14 shows the load history acting on the tool. Fig. 14(a) illustrates the load variation from insertion to retraction, and Fig. 14(b) presents the detailed load behavior over 0.6 seconds during welding. From Fig. 14(a), it is confirmed that the vertical load reaches its maximum during the insertion stage. This trend is consistent with prior studies and experimental observations [41], though dependent on the process conditions. Moreover, the loads in the welding and width directions reach their peaks during the welding stage. Furthermore, after

plunging is completed, significant periodic fluctuations are observed in the load components along the welding and width directions. Fig. 14(b) shows that these oscillations have a period corresponding to one tool rotation, suggesting that the periodicity in the load originates from tool rotation. This result is consistent with experimental observations reporting periodic load fluctuations synchronized with tool rotation [8], and also correlates well with the previously discussed temperature distribution periodicity.

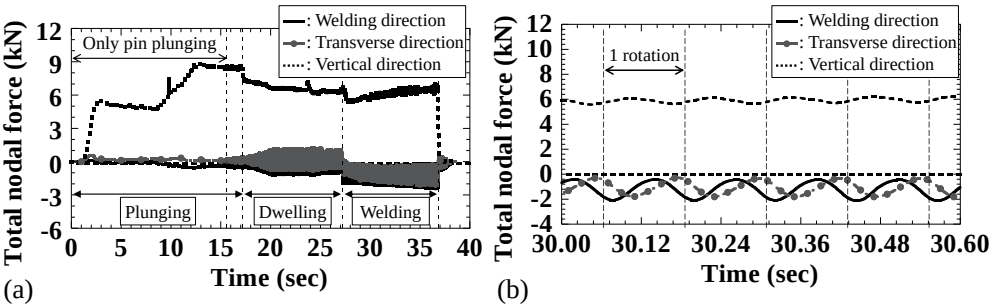



**Fig. 14** Tool load history. (a) Entire process. (b) Details during joining

Based on these results, the proposed numerical analysis method is shown to effectively capture key features of the actual phenomena, suggesting its potential usefulness for analyzing tool behavior.

In this analysis, 5,772 nodes were used for the tool and 1,219,581 nodes for the workpiece to simulate the entire FSP process over 38.52 seconds. The total computation time was approximately 212 hours, yielding a computational efficiency of about 5.5 hours per second of physical time. Compared to previous FSW studies employing explicit dynamic CEL analysis [9,10], this represents a large-scale and highly efficient simulation in terms of both element count and analysis time. Furthermore, the use of an implicit formulation enabled the use of larger time steps while maintaining numerical stability and solution accuracy. These characteristics demonstrate the effectiveness and robustness of the proposed analysis method.

## EFFECT OF TOOL TILT ANGLE ON THERMAL STATE AND DEFECT FORMATION DURING FSP

In this chapter, a series of simulations were conducted by varying the tool tilt angle based on the welding conditions presented in the previous chapter, with the aim of examining its influence on the temperature field and defect formation. Additionally, this analysis aimed to demonstrate that the proposed simulation method is applicable to defect prediction and can contribute to elucidating the mechanisms of defect formation. As shown in Fig. 15, tool tilt angles of 3° (as used in the previous chapter), 0°, and -3° (forward tilt) were investigated. In this figure, the front and rear sides are defined with respect to the welding direction. In this study, the front and rear sides are defined with respect to the welding direction, where the

front side corresponds to the advancing direction of the tool and the rear side (behind) corresponds to the trailing direction.

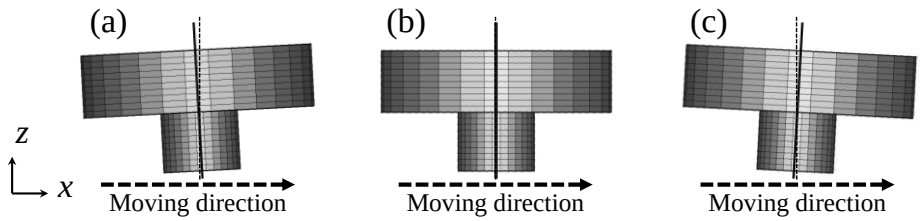



**Fig. 15** Tool tilt angle configurations used in analysis. (a) Tilt angle: 3 °. (b) Tilt angle: 0 °. (c) Tilt angle: -3 °

Fig. 16 presents the temperature distributions on the surface of the workpiece near the tool at 4.8 seconds after the start of welding. When the tool tilt angle is 3°, a high-temperature region is observed behind the tool, consistent with the results shown previously. In contrast, when the tilt angle is changed to 0° and -3°, the high-temperature region shifts toward the front side of the tool. Moreover, under the 0° and -3° tilt conditions, surface defects are observed, with the -3° condition showing particularly elongated defects along the welding direction.

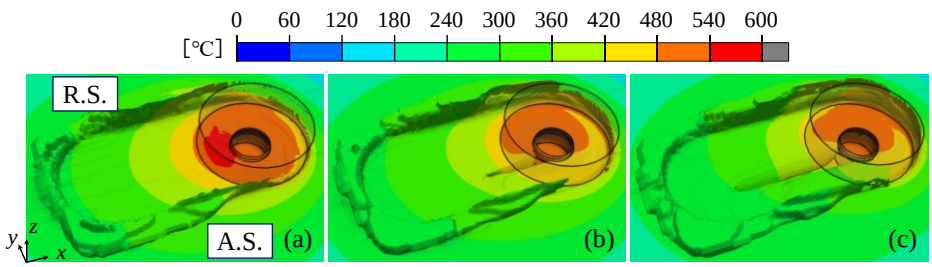



**Fig. 16** Temperature distribution on plate surface during welding at each tool angle. (a) Tilt angle: 3 °. (b) Tilt angle: 0 °. (c) Tilt angle: -3 °.

Fig. 17 illustrates the distribution of defects for each tool tilt condition. The defects shown in the figure are located within 1.0 mm from the surface, and the color represents the position in the thickness direction measured from the bottom surface of the plate. As shown in Fig. 17(a), under the 3° tilt condition, only a small void is observed near the advancing side (A.S.) at the probe tip inside the plate. On the other hand, when the tool tilt angle is changed forward to 0° and -3°, the defect region expands, and tunnel-like defects reaching the surface are clearly visible, as described earlier. This relationship between tool tilt angle and defect formation is consistent with experimental observations [42,43], suggesting that the numerical analysis effectively reproduces the actual physical phenomena.

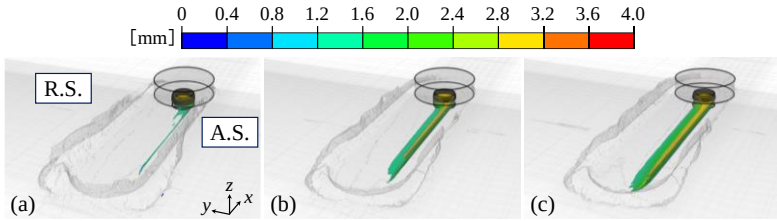



**Fig. 17** Distribution of defects during welding at each tool angle. (a) Tilt angle: 3 °. (b) Tilt angle: 0 °. (c) Tilt angle: -3 °

Fig. 18 shows the material flow behavior under different tool tilt angle conditions over a 0.6-second period starting 4.8 seconds after the beginning of welding. Fig. 18(a) presents the initial positions of the tracers placed around the tool. Excluding the probe region, the tracers were arranged at 2.0 mm intervals in both the welding and width directions, and from 0.4 mm to 1.0 mm in the thickness direction from the top surface of the plate. Figs. 18(b) to (d) show the results for each tool tilt angle condition.

From these figures, it can be observed that with a tilt angle of 3.0°, significant material flow occurs behind the tool. In contrast, as the tilt angle becomes more forward-leaning (0° and -3°), the flow behind the tool decreases while the flow in front increases. This trend corresponds to the distribution of high-temperature regions shown in Fig. 16, suggesting that the forward-leaning tool shifts the high-temperature region forward, suppressing rear-side material flow and contributing to defect enlargement.

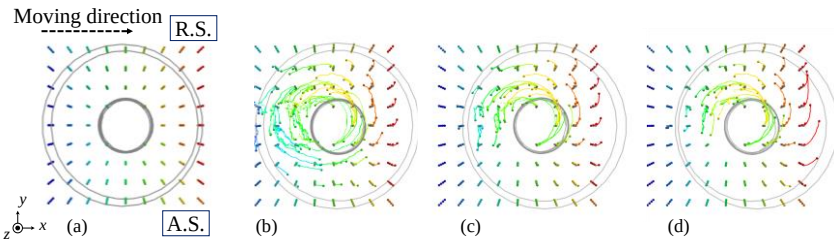



**Fig. 18** Effect of tool tilt angle on material flow behavior near tool. (a) Initial position. (b) Tilt angle: 3 °. (c) Tilt angle: 0 °. (d) Tilt angle: -3 °

These results indicate that adjusting the tool tilt angle enables control over the region where intense stirring occurs, thereby revealing part of the mechanism by which tilt angle influences defect formation.

## CONCLUSION

In this study, a thermal elastic-plastic analysis method was developed by combining a Coupled Eulerian-Lagrangian (CEL) approach based on an implicit formulation with an idealized

explicit FEM solver optimized for GPU parallel computation. This method was applied to FSP (Friction Stir Processing) analysis of aluminum alloy AA5083, yielding the following findings:

1. Temperature distributions and load fluctuations corresponding to one rotation of the tool were confirmed, successfully reproducing behaviors consistent with experimentally observed periodic formation of onion rings and periodic tool loads.
2. Changes in the tool tilt angle significantly altered the location of high-temperature regions and concentrated material flow. In particular, a forward tilt caused tunnel defects to form and expand toward the surface.
3. The occurrence and extent of defects were found to be closely related to the thermal conditions and material flow history around the tool. The influence of tilt angle on the defect formation mechanism was quantitatively clarified.
4. The analysis was successfully performed with over 1.2 million nodes assigned to the tool and base material, achieving a computational efficiency of approximately 5.5 hours per second of physical phenomena. The results demonstrate that the method maintains both numerical stability due to the implicit formulation and a high degree of physical fidelity and computational feasibility.

## References


[1] R. W. FONDA and J. F. BINGERT: 'Texture variations in an aluminum friction stir weld', *Scripta Materialia 57*, pp. 1052-1055, 2007.

[2] M. DHONDT, I. AUBERT, N. SAINTIER and J.-M. OLIVE: 'Mechanical behavior of periodical microstructure induced by friction stir welding on Al–Cu–Li 2050 alloy', *Materials Science and Engineering A 642*, pp. 163-172, 2015.

[3] W. F. NOH: 'CEL: A Time-Dependent, Two-Space-Dimensional, Coupled Eulerian-Lagrangian Code', *Lawrence Radiation Laboratory, University of California*, pp. 1-48, 1964.

[4] M. AKBARI, P. ASADI and T. SADOWSKI: 'A Review on Friction Stir Welding/Processing: Numerical Modeling', *Materials 16*, 5890, 2023.

[5] M. AKBARI, A. ABDOLLAHZADEH and M. ESFANDIAR: 'A Comprehensive Review of Material Flow in FSW/FSP: Experimental Insights and Simulation Perspectives', *Engineering Reports 7*, e70138, 2025.

[6] DASSAULT SYSTÈMES: 'Modeling Extreme Deformation and Fluid Flow with Abaqus', *SIMULIA Training Course Documentation*, 2017.

[7] D. DAS, S. BAG and S. PAL: 'Probing finite element modelling of defects in friction stir welding by tailoring mass scaling factor', *Materials Today Communications 35*, 105646, 2023.

[8] D. AMBROSIO, A. TONGNE, V. WAGNER, G. DESSEIN and O. CAHUC: 'Towards material flow prediction in friction stir welding accounting for mechanisms governing chip formation in orthogonal cutting', *Journal of Manufacturing Processes 85*, pp. 450-465, 2023.

[9] M. HOSSFELD and E. ROOS: 'A new approach to modelling friction stir welding using the CEL method', *International Conference on Advanced Manufacturing Engineering and Technologies*, pp. 1-9, 2013.

[10] M. HOSSFELD: 'Modeling Friction Stir Welding: On Prediction and Numerical Tool Development', *Metals 12*, 1432, 2022.

[11] P. CHAUHAN, R. JAIN, S. K. PAL and S. B. SINGH: 'Modeling of defects in friction stir welding using coupled Eulerian and Lagrangian method', *Journal of Manufacturing Processes 34*, pp. 158-166, 2018.
[12] K. N. SALLOOMI: 'Fully coupled thermomechanical simulation of friction stir welding of aluminum 6061-T6 alloy T-joint', *Journal of Manufacturing Processes 45*, pp. 746-754, 2019.
[13] K.N. SALLOOMI and S. AL-SUMAIDAE: 'Coupled Eulerian–Lagrangian prediction of thermal and residual stress environments in dissimilar friction stir welding of aluminum alloys', *Journal of Advanced Joining Processes 3*, 100052, 2021.
[14] D. J. BENSON: 'Computational Methods in Lagrangian and Eulerian Hydrocodes', *Computer Methods in Applied Mechanics and Engineering 99*, pp. 235-394, 1992.
[15] N. M. NEWMARK: 'A Method of Computation for Structural Dynamics, Journal of the Engineering Mechanics Division', *Proceedings of the American Society of Civil Engineers 85-EM-3*, pp. 67-94, 1959.
[16] M. SHIBAHARA and K. IKUSHIMA: 'Development of analytical method for welding mechanics using idealized explicit FEM', *Transactions of JWRI 39-2*, pp. 384-386, 2010.
[17] M. SHIBAHARA, K. IKUSHIMA, S. ITOH AND K. MASAOKA: 'Computational Method for Transient Welding Deformation and Stress for Large Scale Structure Based on Dynamic Explicit FEM', *Quarterly Journal of the Japan Welding Society 29-1*, pp. 1-9, 2011.
[18] K. IKUSHIMA, M. SHIBAHARA, K. AKITA, H. SUZUKI, S. MOROOKA, S. NISHIKAWA and T. FURUKAWA: 'Numerical analysis of residual stress distribution on peening process', *Weld World 61*, pp. 517-527, 2017.
[19] A.N. BROOKS and T.J.R. HUGHES: 'Streamline Upwind/Petrov-Galerkin Formulations for Convection Dominated Flows with Particular Emphasis on the Incompressible Navier-Stokes Equations', *Computer Methods in Applied Mechanics and Engineering 32*, pp. 199-259, 1982.
[20] T.J.R. HUGHES, G. SCOVAZZI and T.E. TEZDUYAR: 'Stabilized Methods for Compressible Flows', *Journal of Scientific Computing 43*, pp. 343-368, 2010.
[21] E. L. WILSON and R. W. CLOUGH: 'Dynamic Response by Step-By-Step Matrix Analysis', *Proceedings of the Symposium on the Use of Computers in Civil Engineering*, Lisbon, Portugal, 1962.
[22] S. MOHAMMADZADEH, M. GHASSEMIEH and Y. PARK: 'Structure-dependent improved Wilson-θ method with higher order of accuracy and controllable amplitude decay', *Applied Mathematical Modelling 52*, pp. 417-436, 2017.
[23] S.-L. ZHANG: 'GPBi CG: Generalized Product Type Methods Based on Bi CG for Solving Nonsymmetric Linear Systems', *SIAM Journal on Scientific Computing 18-2*, pp. 537-551, 1997.
[24] X.-F. ZHANG, W. DING and T. LI: 'Tensor form of GPBiCG algorithm for solving the generalized Sylvester quaternion tensor equations', *Journal of the Franklin Institute 360*, pp. 5929-5946, 2023.
[25] K. IKUSHIMA and M. SHIBAHARA: 'Prediction of residual stresses in multi-pass welded joint using Idealized Explicit FEM accelerated by a GPU', *Computational Materials Science 93*, pp. 62-67, 2014.
[26] K. IKUSHIMA, S. ITOH and M. SHIBAHARA: 'Development of Idealized Explicit FEM Using GPU Parallelization and Its Application to Large-Scale Analysis of Residual Stress of Multi-Pass Welded Pipe Joint', *Weld World 59*, pp. 589-595, 2015.
[27] C. W. HIRT and B. D. NICHOLS: 'Volume of Fluid (VOF) Method for the Dynamics of Free Boundaries', *Journal of Computational Physics 39*, pp. 201-225, 1981.

[28] O. C. ZIENKIEWICZ, W. L. WOOD, N. W. HINE and R. L. TAYLOR: 'A unified set of single step algorithms. Part 1: General formulation and application', *International Journal for Numerical Methods in Engineering 20-15*, pp. 1529-1552, 1978.

[29] J.J. MASON, A.J. ROSAKIS and G. RAVICHANDRAN: 'On the Strain and Strain Rate Dependence of the Fraction of Plastic Work Converted to Heat: An Experimental Study Using High Speed Infrared Detectors', *Mechanics of Materials 17*, pp. 135-145, 1994.

[30] J. HODOWANY, G. RAVICHANDRAN, A. J. ROSAKIS and P. ROSAKIS: 'Partition of Plastic Work into Heat and Stored Energy in Metals', *Experimental Mechanics 40*, pp. 113-123, 2000.

[31] G. R. JOHNSON and W. H. COOK: 'A Constitutive Model and Data for Metals Subjected to Large Strains, High Strain Rates and High Temperatures', *Proceedings of the 7th International Symposium on Ballistics*, pp. 541-547, 1983.

[32] R. V. MISES: 'Mechanics of solid bodies in the plastically-deformable state', *Nachr. d. Kgl. Ges. Wiss. Göttingen, Math.-phys. Klasse 4*, pp. 582-592, 1913.

[33] M. YU, N. MA, K. NARASAKI, S. TSUTSUMI and H. FUJII: 'Modelling and Measurement of Thick Aluminum FSW Induced Thermal Strain and Residual Stress', *Journal of Light Metal Welding 59-2*, pp. 59-68, 2021.

[34] H. SHI, J.-R. CHO, J.-W. YOON, H.-J. LEE and D.-G. AHN: 'Design of Thermal Stress Control Layers in the Selective Deposition Technology of Hot Axle Forging Dies', *International Journal of Precision Engineering and Manufacturing 18-12*, pp. 1805-1812, 2017.

[35] D.-S. GUK, H.-J. LEE and D.-G. AHN: 'A study on the Effects of Geometrical Parameters of Overlay Coated Layer on the Thermal Stress-strain Distributions of Co-based Super-alloy Deposited Layer on Hot-working Tool Steel', *MATEC Web of Conferences 40*, 01003, 2016.

[36] NIPPON KOSHUHA STEEL CO., LTD.: *KDA1 Series of Thermocouples for Welding*, https://www.koshuha.co.jp/eng/products/kda1.html, accessed 2025-07-28.

[37] M. DHONDT, I. AUBERT, N. SAINTIER and J.M. OLIVE: 'Characterization of intergranular stress corrosion cracking behavior of a FSW Al-Cu-Li 2050 nugget', *Mechanics & Industry 16*, 401, 2015.

[38] T. MARAZANI, S. O. JEJE, M. B. SHONGWE and N. MALATJI: 'Mass flash reduction strategies in friction stir processing of aluminum alloys: A review', *Engineering Reports 6-10*, e12981, 2024.

[39] Y. MORISADA, H. FUJII, Y. KAWAHITO, K. NAKATA and M. TANAKA: 'Three-dimensional visualization of material flow during friction stir welding by two pairs of X-ray transmission systems', *Scripta Materialia 65*, pp. 1085-1088, 2011.

[40] R. KUMAR, V. PANCHOLI and R.P. BHARTI: 'Material flow visualization and determination of strain rate during friction stir welding', *Journal of Materials Processing Technology 255*, pp. 470-476, 2018.

[41] V. SOUNDARARAJAN, S. ZEKOVIC and R. KOVACEVIC: 'Thermo-mechanical model with adaptive boundary conditions for friction stir welding of Al 6061', *International Journal of Machine Tools and Manufacture 45*, pp. 1577-1587, 2005.

[42] L. LONG, G. CHEN, S. ZHANG, T. LIU and Q. SHI: 'Finite-element analysis of the tool tilt angle effect on the formation of friction stir welds', *Journal of Manufacturing Processes 30*, pp. 562-569, 2017.

[43] S. D. MESHRAM and G. M. REDDY: 'Influence of Tool Tilt Angle on Material Flow and Defect Generation in Friction Stir Welding of AA2219', *Defence Science Journal 68*, pp. 512-518, 2018.

# NUMERICAL ANALYSIS OF ULTRASONIC VIBRATION ENHANCED FRICTION STIR WELDING OF TI/AL DISSIMILAR ALLOYS

X. ZHANG, L. SHI*, C. WU

*State Key Laboratory of Advanced Equipment and Technology for Metal Forming, School of Materials Science and Engineering, Shandong University, Jinan, 250061, China*
** Corresponding author, E-mail: lei.shi@sdu.edu.cn*

*DOI 10.3217/978-3-99161-089-2-016, license CC BY 4.0*
*https://creativecommons.org/licenses/by/4.0/deed.en*
*This CC license does not apply to third party material and content noted otherwise.*

## ABSTRACT

Ti/Al hybrid structures offer advantages in lightweight design and cost reduction. However, joining them remains challenging due to the distinct thermophysical properties of the two materials. Conventional friction stir welding (FSW) often results in leads to insufficient material flow capacity when applied to Al/Ti joints. To address this issue, a novel ultrasonic vibration enhanced friction stir welding (UVeFSW) technique was employed to join 2024-T4 aluminum alloy and TC4 titanium alloy. Furthermore, a multi-phase numerical model was developed using computational fluid dynamics (CFD) coupled with the volume of fluid (VOF) method to quantitatively analyze the heat and mass transfer behavior during the Ti/Al dissimilar UVeFSW process. The results reveal that ultrasonic vibration effectively reduces material flow stress and enlarges the plastic flow zone. Overall, the findings demonstrate that UVeFSW is a promising and efficient technique for producing high-quality Ti/Al dissimilar joints, offering a novel approach for advanced lightweight structural applications.

Keywords: Ultrasonic vibration enhanced friction stir welding (UVeFSW); Ti/Al dissimilar welding; Simulation, Temperature, Material flow.

## INTRODUCTION

With the increasing complexity of structural components, the emergence of Ti/Al hybrid structures offers new solutions for the development of multifunctional lightweight systems [1, 2]. However, due to the obvious differences in their thermophysical properties, achieving a high-quality metallurgical bond between titanium and aluminum remains a major challenge [3,4]. As a solid-state joining technique, friction stir welding (FSW) avoids defects such as hot cracks and porosity that are commonly found in fusion welding, making it particularly

suitable for fabricating Ti/Al hybrid structures [5,6]. Ultrasonic vibration enhanced friction stir welding (UVeFSW), as a variant of conventional FSW, utilizes the acoustic-plastic effect of ultrasonic energy to locally soften materials in the weld nugget zone (WNZ) [7]. This process significantly improves material flow behavior, thereby enhancing both joint performance and welding efficiency [8,9].

Nevertheless, the underlying mechanisms of ultrasonic vibration in Ti/Al dissimilar FSW remain insufficiently understood. The FSW process is inherently closed. Therefore, direct observation and visualization of plastic deformation and material flow are extremely difficult [10]. This contrasts with fusion welding, where such phenomena can be more easily observed. Numerical simulation thus provides an effective alternative approach [11,12]. FSW can be numerically simulated using either computational solid mechanics (CSM) [7] or computational fluid dynamics (CFD) based approaches [13]. Within the CFD framework, Eulerian formulations exhibit inherent advantages in handling the severe plastic deformation involved in the FSW process and offer higher computational efficiency [14]. As a result, CFD based methods have been widely adopted for the numerical simulation of both similar and dissimilar FSW processes [14,15]. Accordingly, the establishment of macroscopic numerical models has become a powerful approach for elucidating differences in heat and mass transfer between conventional FSW and UVeFSW processes [16].

This study aims to elucidate the influence mechanisms of ultrasonic vibration on microstructural evolution and mechanical properties in Ti/Al dissimilar FSW through comprehensive numerical simulations. By analyzing the temperature distribution, material flow behavior, and heat generation during the UVeFSW process, this study systematically reveals the enhancement mechanisms of ultrasonic vibration, providing deeper insights into the joining process of Ti/Al hybrid structures.

## EXPERIMENT AND MODELING DETAILS

### EXPERIMENT SETUP

AA2024-T4 Al alloy and TC4 Ti alloy were used as the base materials. The workpiece dimensions were 200 mm in length, 55 mm in width and 4 mm in thickness. Fig. 1 depicts the diagram of Ti/Al FSW and UVeFSW. Ti alloy is placed at the advancing side (AS), while Al alloy is placed at the retreating side (RS). The ultrasonic horn is located at the leading side (LS), with a 20 mm distance from the FSW tool. The angle between the workpiece and the ultrasonic horn is 40°. The ultrasonic horn operates at a frequency of 20 kHz with an amplitude of 40 μm, and the actual power ranges between 250-300 W during UVeFSW. The FSW tool is made of W-Re alloy. It has a flat shoulder with a diameter of 12 mm. The tool pin has a right-handed thread with a pitch of 1.5 mm and a groove with a depth of 0.25 mm. The length of the pin is 3.7 mm, and the pin tip and root diameters are 5 mm and 6 mm, respectively. The tool offset is 2.2 mm, defined as the distance between the tool axis and the Ti/Al interface. The plunge depth of shoulder is 0.2 mm, and the tool tilt angle is 2.5°. The tool rotation speed is 400 rpm, welding speed is 45 mm/min.

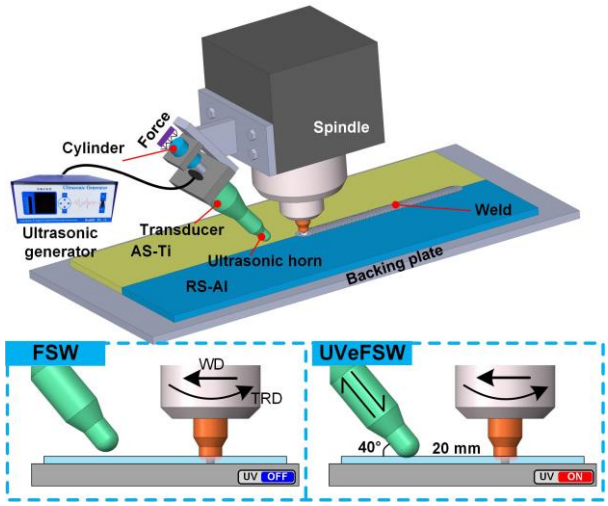



**Fig. 1** Schematic diagram of Ti/Al FSW and UVeFSW

## MODEL ASSUMPTIONS

To understand the difference in heat generation, heat transfer and material flow behavior between FSW and UVeFSW. In this study, Al/Ti FSW and UVeFSW numerical models are developed based on CFD theory. At the same time, the volume of fluid (VOF) method is used to trace the Ti/Al interface.

Fig. 2 shows the details of the CFD macroscopic model. The welding direction is the negative direction of the *x*-axis. The offset used in the model is consistent with the experiment. In the simulation, the Ti and Al workpieces are treated as a single entity, distinguished by phase distribution at the inlet. Heat transfer at the interface is calculated based on their thermophysical properties. Unlike in experiments where a thin air layer exists in front of the tool before welding and affects heat transfer, the simulation assumes direct contact between Ti and Al. Accurately modeling this thin air layer is impractical due to high computational costs and complexity. To balance accuracy and feasibility, we simplify the interface and treat the front region as a single workpiece. Model validation confirms the reliability of this approach. The model origin is located in the center of the bottom of the workpiece. The effect of pin-thread is ignored in the model. Based on Zhai et al., the non-uniform force distribution, slip rate and friction coefficient near the T-W interface were modified to consider the effect of tool tilt angle [19]. Therefore, the shoulder-workpiece interface is divided into complete and incomplete contact areas, as shown in Fig. 3.

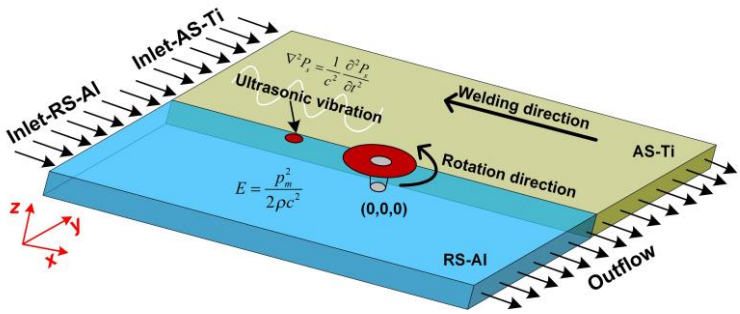



**Fig. 2** Geometric model of Ti/Al dissimilar FSW and UVeFSW simulation

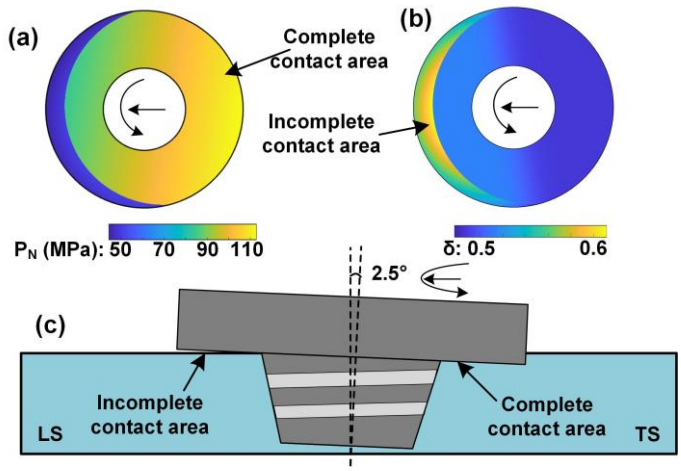



**Fig. 3** Schematic of tilt angle in FSW and (a) rool axial pressure ($P_N$) and (b) slip ratio (δ) distribution at the T-W interface considering (c) tilt angle in the model.

The ultrasonic frequency is 20 kHz, which means the simulation calculation step frequency must exceed 20 kHz to accurately capture the acoustic pressure characteristics during ultrasonic propagation. However, increasing the step frequency inevitably reduces the time step for each calculation, leading to an exponential increase in the computational time for UVeFSW. To address this challenge, a three-step solution method was implemented in this study, reducing the time required to solve the UVeFSW model to 3 to 5 days, which offers a advantage over traditional computational solid mechanics, as shown in Fig. 4.

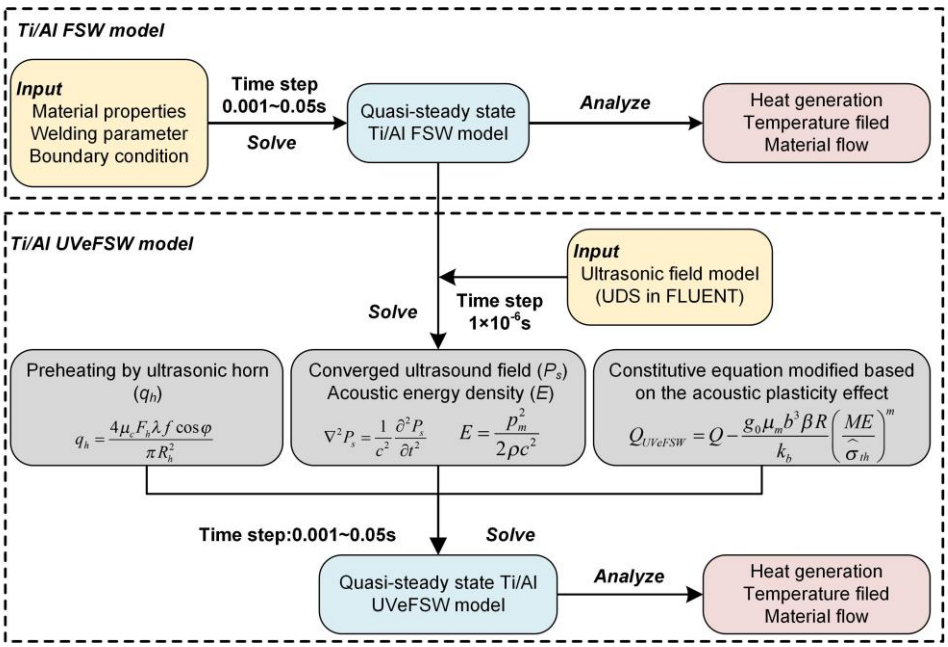



**Fig. 4** Flow chart for solving Ti/Al UVeFSW models

Fig. 5(a) shows the relevant model parameters used in the study. The constitutive equation for the AA2024 alloy was modified based on experimental data from Zhao et al. and the theoretical model established by Shi et al. [18,20]. A similar approach was also used to modify the constitutive model for the TC4 alloy. The revised constitutive model accurately captures the ultrasonic plasticity effects observed in the experiments [18]. Fig. 5(b) shows the trend of $Q_{UVeFSW}$(i.e. plastic deformation activation energy considering acoustic softening) with changes in temperature and ultrasonic energy density. At a constant ultrasonic energy density, a higher temperature results in a higher $Q_{UVeFSW}$. $Q_{UVeFSW}$ is related to the shear modulus of the alloy (equations (13)). As the temperature rises, the shear modulus decreases, leading to an increase in $Q_{UVeFSW}$. Fig. 5(c) and (d) present the thermophysical parameters of AA2024 and TC4 alloys, as well as the methods used for mixing their related parameters. More experimental and modeling details can be found in the article [17].

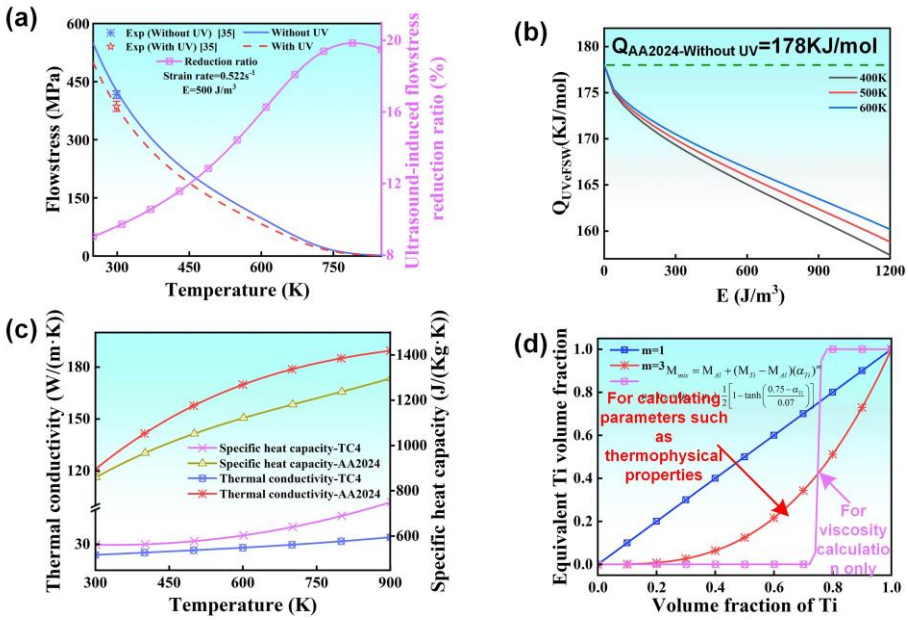



**Fig. 5** Parameters used in the model, (a) The variation of flow stress with temperature and its reduction ratio under the influence of ultrasonic vibration [18]. (b) The curve of activation energy for plastic deformation ($Q_{UVeFSW}$) of AA2024 Al alloy at different temperatures as a function of ultrasonic energy density. (c) Thermal conductivity (TC) and specific heat capacity (Cp) of AA2024 and TC4. (d) The thermo-physical properties of the Ti/Al mixture in the model

## GOVERNING EQUATION

In this model, the plastic material was regarded as a non-Newtonian fluid with high viscosity, thus the conservation equations of mass, momentum and energy are as follows [21],

$$\frac{\partial \rho}{\partial t} + \rho \nabla \cdot \boldsymbol{V} = 0, \tag{1}$$

where $\rho$ is the density, $t$ is the time, $\boldsymbol{V}$ is the fluid velocity vector.

$$\rho \left[ \frac{\partial \boldsymbol{V}}{\partial t} + (\boldsymbol{V} \cdot \nabla)\boldsymbol{V} \right] = -\nabla P + \mu \nabla^2 \boldsymbol{V}, \tag{2}$$

where $P$ is the fluid pressure, $\mu$ is the fluid viscosity.

$$\rho C_P \left( \frac{\partial T}{\partial t} + \boldsymbol{V} \cdot \nabla T \right) = \nabla \cdot (k \nabla T) + S_v, \tag{3}$$

where $C_P$ is the specific heat capacity, $k$ is the thermal conductivity, $T$ is temperature, $S_v$ is the heat generated by the viscous dissipation of the shear layer which is expressed as [22],

$$S_v = \gamma \bar{\dot{\varepsilon}} \sigma_s, \tag{4}$$

where $\gamma$ is a constant that characterizes the degree of mixing between material atoms within the shear layer, which is taken as 0.6. $\bar{\dot{\varepsilon}}$ is strain rate, $\sigma_s$ is the flow stress.

## MATERIAL PROPERTY

The constitutive model used in the model has been modified at high-temperature regions [23],

$$\sigma_s = \frac{1}{\alpha} \ln \left\{ \left( \frac{Z(\bar{\dot{\varepsilon}},T)}{A} \right)^{\frac{1}{n}} + \left[ \left( \frac{Z(\bar{\dot{\varepsilon}},T)}{A} \right)^{\frac{2}{n}} + 1 \right]^{\frac{1}{2}} \right\} \cdot \frac{1}{2} \cdot \left[ 1 - tanh\left( \frac{T-a}{b} \right) \right], \tag{5}$$

where $\alpha$ and $A$ are parameters related to the material, $n$ is the stress index, $a$ and $b$ are correction factors related to the material, $Z$ is the Zener-Holloman parameter, specifically,

$$Z(\bar{\dot{\varepsilon}}, T) = \bar{\dot{\varepsilon}} \exp\left( \frac{Q}{RT} \right), \tag{6}$$

where $Q$ is the activation energy, $R$ is the gas constant, $\bar{\dot{\varepsilon}}$ is strain rate, specifically,

$$\bar{\dot{\varepsilon}} = \sqrt{\frac{2}{3} \dot{\varepsilon}_{ij} \dot{\varepsilon}_{ij}}, \tag{7}$$

where $\dot{\varepsilon}_{ij}$ is the strain rate tensor at a certain moment.

The viscosity of Al alloy and Ti alloy is calculated according to the following formula,

$$\mu_{Al} = \frac{\sigma_{s-Al}}{3\bar{\dot{\varepsilon}}}, \tag{8}$$

$$\mu_{Ti} = \frac{\sigma_{s-Ti}}{3\bar{\dot{\varepsilon}}}, \tag{9}$$

where $\mu_{Al}$, $\mu_{Ti}$, $\sigma_{s-Al}$, $\sigma_{s-Ti}$ are the viscosity and flow stress of Al alloy and Ti alloy, respectively. According to previous research, the viscosity difference between Al alloy and Ti alloy reaches 1 to 2 orders of magnitude [24]. Therefore, for viscosity mixing, the following formula is used for calculation [21],

$$\mu = \mu_{Al} + (\mu_{Ti} - \mu_{Al}) \cdot \frac{1}{2} \left[ 1 - tanh\left( \frac{0.75 - \alpha_{Ti}}{0.07} \right) \right], \tag{10}$$

where $\alpha_{Ti}$ is the volume fraction of Ti. Compared to viscosity, the difference in specific heat capacity and thermal conductivity between Al alloy and Ti alloy is relatively smaller. Due to the presence of titanium particles, the thermal-physical properties of the weld nugget are predominantly governed by the aluminum alloy, and conventional calculations of thermal-physical parameters cannot fully capture the material characteristics. Therefore, in this study, the relevant parameters for aluminum and titanium (including thermal-physical properties, slip rate, viscosity, friction coefficient, and rheological stress) are treated as functionally graded

materials for computation, and the following formula is used to calculate the relevant parameter mixture [21],

$$M_{mix} = M_{Al} + (M_{Ti} - M_{Al})(\alpha_{Ti})^3, \tag{11}$$

where $M_{Al}$ and $M_{Ti}$ are parameters related to Al and Ti alloys, including thermal conductivity, specific heat capacity, slip ratio, flow stress, etc. $M_{mix}$ is the relevant parameter after mixing the two materials in the WNZ.

In the UVeFSW model, the constitutive equation after considering the acoustic plastic effect is proposed by Shi et al. [20],

$$Z(\bar{\dot{\varepsilon}}, T)_{UVeFSW} = \bar{\dot{\varepsilon}} \exp\left(\frac{Q_{UVeFSW}}{RT}\right), \tag{12}$$

where $Z(\bar{\dot{\varepsilon}}, T)_{UVeFSW}$ is the Zener-Holloman parameter considering acoustic softening. $Q_{UVeFSW}$ is the plastic deformation activation energy considering acoustic softening, calculated by the following formula [20],

$$Q_{UVeFSW} = Q - \frac{g_0 \mu_m b^3 \beta R}{k_b} \left(\frac{ME}{\hat{\sigma}_{th}}\right)^m, \tag{13}$$

where $g_0$ is a pre-factor, $\mu_m$ is the shear modulus, $b$ is Burgers vector, $k_b$ is Boltzmann constant, $M$ is the Taylor factor, $E$ is the ultrasonic energy density, $\hat{\sigma}_{th}$ is the thermal component of the mechanical threshold stress, and $m$ is the experimental fitting parameter.

## ULTRASONIC ENERGY FIELD MODEL

In the UVeFSW model, the sound field is expressed as [20],

$$\nabla^2 P_s = \frac{1}{c^2} \frac{\partial^2 P_s}{\partial t^2}, \tag{14}$$

where $P_s$ is the sound pressure, and $c$ is the sound velocity. The sound pressure at a certain distance from the horn-workpiece contact interface between the workpiece and the ultrasonic tool horn within the diffusion range of the sound beam can be expressed as [10],

$$P_d = P_h \exp\left(-\frac{8\pi^2 f^2 \eta'}{3\rho c} r_d\right), \tag{15}$$

where $P_d$ is the sound pressure at a distance of $d$ from the ultrasonic horn. $P_h$ is the sound pressure at the ultrasonic horn. $f$ is the frequency, $\eta'$ is shear viscosity coefficient, $r_d$ is the distance of ultrasonic propagation

The sound energy density $E$ is calculated using the following formula [10],

$$E = \frac{p_m^2}{2\rho c^2}. \tag{16}$$

## RESULTS AND DISCUSSION

### TEMPERATURE DISTRIBUTION

This section shows the temperature distribution obtained from the multi-phase model. In Fig. 6, cross-sectional slices at different positions are displayed, with a spacing of 5 mm between sections. At X = -20 mm, a clear temperature rise is observed in UVeFSW due to the preheating effect of the ultrasonic horn. Fig. 7 verifies the accuracy of the model through experimental temperature measurements during welding. The results show that the ultrasonic preheating effect leads to a more significant temperature increase on the aluminum side compared with the titanium side. This is attributed to the fact that most of the ultrasonic tool is embedded in the retreating side (RS), allowing the generated heat to spread widely through the aluminum.

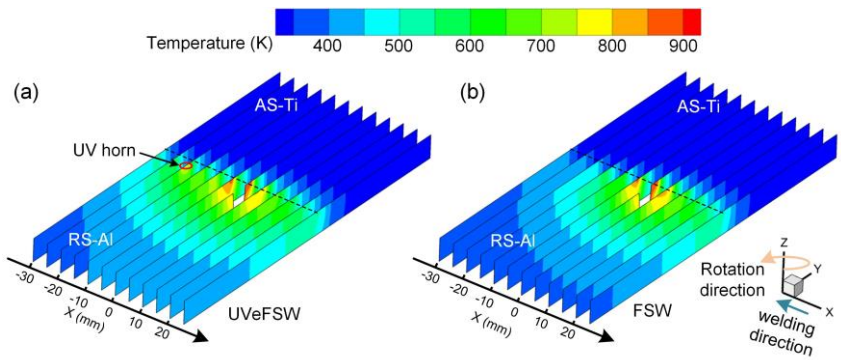



**Fig. 6** Contour map of temperature distribution along different cross-sections in the welding direction. (a) UVeFSW. (b) FSW

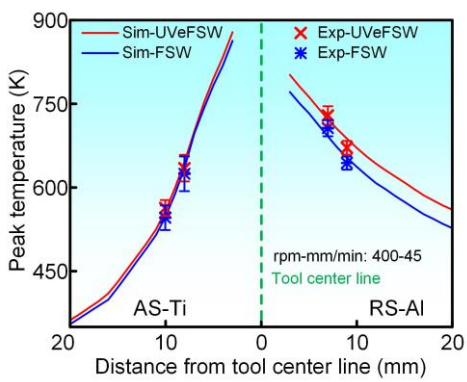



**Fig. 7** Validate the model through thermocouple temperature measurement

Fig. 8 presents the temperature contour maps at the horizontal cross-sections of Z = 3 mm and Z = 1 mm. During FSW, most of the heat is generated by the tool shoulder. Therefore, the high-temperature region at Z = 3 mm is larger than that at Z = 1 mm. A clear temperature difference is observed between the titanium and aluminum alloy sides. The temperature on the titanium side of the WNZ is noticeably higher than that on the aluminum side. This pattern is consistent in both FSW and UVeFSW. The reason is that the poor thermal conductivity of titanium limits heat dissipation from the WNZ, resulting in heat accumulation.

By comparing the temperature contour maps of FSW and UVeFSW, it is found that extensive ultrasonic preheating regions appear in Fig. 8(b) and (d). The temperature in these regions reaches 600-700 K. The size of the high-temperature zone inside the WNZ shows little difference compared with FSW. Moreover, the preheating regions exhibit nearly identical sizes at the top and bottom of the weld, indicating that the ultrasonic preheating effect is nearly uniform through the plate thickness. The preheating effect on the titanium side is weaker than that on the aluminum side, which can also be attributed to the poor thermal conductivity of titanium.

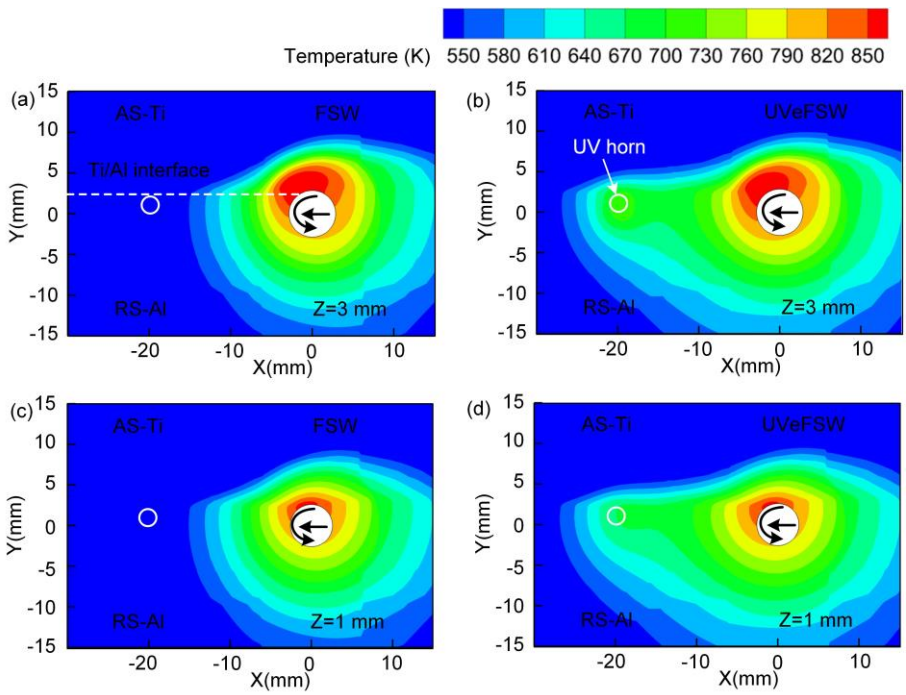



**Fig. 8** Temperature distribution in different horizontal plane, (a) Z = 3 mm of FSW, (b) Z = 3 mm of UVeFSW, (c) Z = 1 mm of FSW, (d) Z = 1 mm of UVeFSW

Fig. 9 presents the welding thermal cycles at different positions on the RS. A pronounced preheating effect caused by the ultrasonic tool head can be observed. As the distance from the

tool center line increases, this preheating effect gradually weakens. On the advancing side (AS) (Fig. 9(d)), a similar ultrasonic preheating effect is observed, showing consistent results with the RS. Comparing those figures, the titanium side shows a much narrower high-temperature diffusion range due to its poor thermal conductivity. In particular, when the distance from the tool center line exceeds 20 mm, the temperature rises in both FSW and UVeFSW becomes almost negligible.

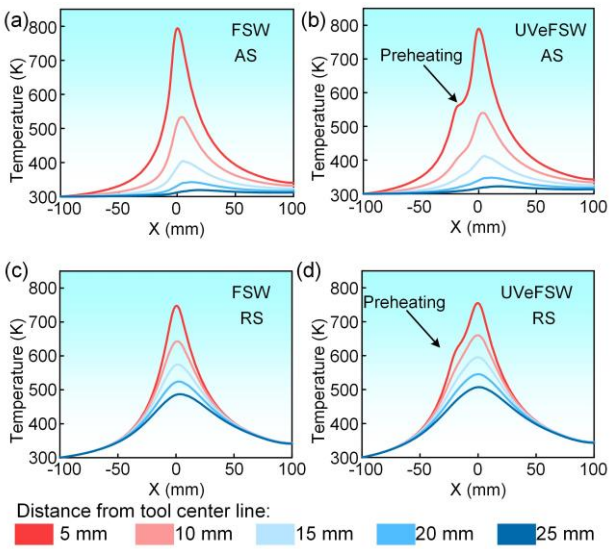



**Fig. 9** Welding thermal cycle at different positions on the (a) AS of FSW, (b) AS of UVeFSW, (c) RS of FSW, (d) AS of UVeFSW

## MATERIAL FLOW

The CFD-based numerical model effectively captures the material flow and mixing patterns during both FSW and UVeFSW processes. Therefore, this section presents a detailed analysis of the CFD simulation results to further explore the underlying mechanisms of ultrasonic assistance in Ti/Al UVeFSW.

Fig. 10 illustrates the material flow velocity distribution at different horizontal planes. During the Ti/Al FSW process, there is a distinct difference in the velocity fields on AS and RS. The aluminum side exhibits obviously higher flow velocity than the titanium side. This difference results from the inherent disparity in material plasticity between titanium and aluminum under FSW temperature conditions. Moreover, in practical welding experiments, the tool is mostly positioned within the aluminum alloy. Consequently, the tool exerts a stronger driving effect on the aluminum alloy, promoting more intense material flow on that side.

At the Z = 3 mm plane, the influence of the tool shoulder leads to a broader material flow zone compared with the Z = 1 mm plane. The additional rotation effect from the shoulder enhances the plastic deformation of materials near the upper surface. On the other hand, the introduction of ultrasonic vibration further softens the material in the WNZ. As a result, the aluminum alloy shows an even wider flow region under UVeFSW compared with conventional FSW, indicating that ultrasonic assistance can effectively promote material plasticization and improve flow uniformity within the weld zone. The material flow velocity profiles at selected locations are extracted and presented in Fig. 10(c) and (f). These comparison curves provide a more intuitive illustration of the enhancing effect of ultrasonic vibration on material flow within the weld nugget zone.

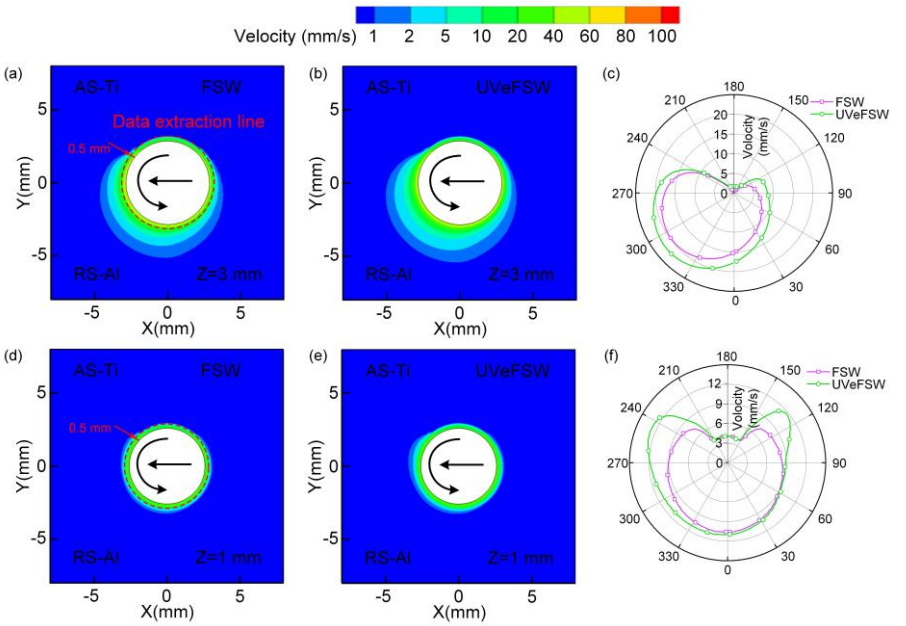



**Fig. 10** Velocity field distribution in different horizontal plane, (a) Z = 3 mm of FSW, (b) Z = 3 mm of UVeFSW, (c) flow velocity comparison in Z = 3 mm horizontal plane, (d) Z = 1 mm of FSW, (e) Z = 1 mm of UVeFSW, (f) flow velocity comparison in Z = 1 mm horizontal plane

During the Ti/Al dissimilar FSW process, two different metals are involved. Therefore, in this study, the VOF method was used to calculate the distribution of the two materials. Fig. 11 shows the phase distribution across different cross-sections along the welding direction. The interface between titanium and aluminum remains clear ahead of X = -5 mm, indicating no material mixing. This observation is consistent with the experimental setup. At X = -5 mm, the influence of the tool shoulder causes partial material flow near the top of the weld. As welding proceeds, fragments of titanium are broken up by the tool and rotate together with it, depositing on the trailing side of the weld. Once the material moves beyond the shoulder

affected zone, the phase distribution remains almost unchanged. The cross-section of the weld clearly shows the Ti/Al interface, which agrees well with experimental observations [17].

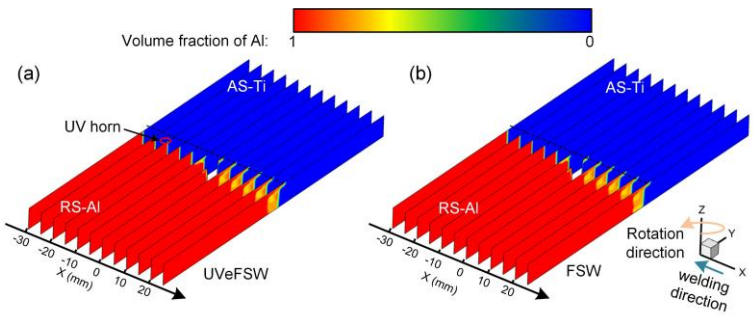



**Fig. 11** Contour map of phase distribution along different cross-sections in the welding direction. (a) UVeFSW. (b) FSW

A comparison between Fig. 11(a) and (b) reveals subtle changes in the cross-sectional structure after the application of ultrasonic vibration. Combined with the phase distributions at different horizontal planes shown in Fig. 12, it can be inferred that the ultrasonic plasticity effect softens the material within the weld nugget zone, enhancing material flow near the tool. Consequently, the aluminum alloy in front of the tool becomes easier to drive, leading to a slightly expanded distribution of titanium fragments within the nugget zone.

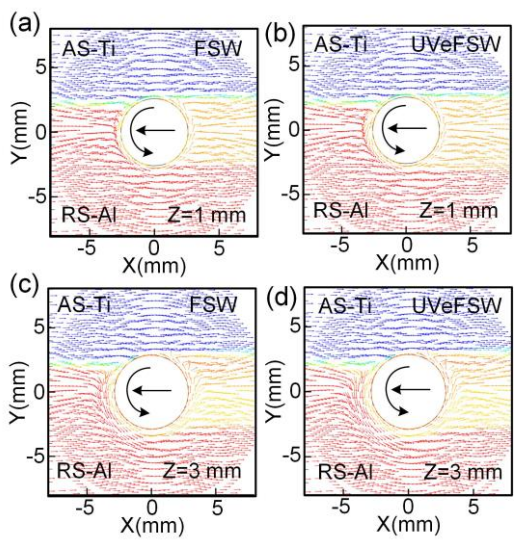



**Fig. 12** Phase distribution map in different horizontal plane. (a) Z = 1 mm of FSW, (b) Z = 1 mm of UVeFSW, (c) Z = 3 mm of FSW, (d) Z = 3 mm of UVeFSW

## CONCLUSION

In this study, a multiphase-coupled numerical simulation based on computational fluid dynamics (CFD) was conducted for Ti/Al dissimilar FSW and UVeFSW processes. The accuracy of the model was validated through simulation results. The main conclusions are as follows:

(1). Ultrasonic vibration introduces a preheating effect in front of the tool, leading to a slight increase in the peak temperature within the heat-affected zone. Both experimental measurements and simulation results capture this preheating phenomenon before welding.
(2). The acoustic plasticity effect induced by ultrasonic vibration improves material flow within the weld nugget zone and expands the flow area. As a result, the phase distribution in the weld cross-section is altered.
(3). UVeFSW addresses a critical challenge in Ti/Al FSW process by achieving an optimal balance between low heat input and adequate material flow. Effectively improved the material flow ability in the weld zone.

## ACKNOWLEDGEMENTS

The authors would like to acknowledge the financial support from the National Natural Science Foundation of China (Grant Nos. 52275349 and 52035005), the Shandong Provincial Science Foundation for Outstanding Young Scholars (Grant No. ZR2024YQ020), the National Key Research and Development Program of China (Grant No. 2022YFB4600902), the Excellent Young Team Project of Central Universities (No. 2023QNTD002) and Key Research and Development Program of Shandong Province (Grant No. 2021ZLGX01).

## References

[1] F. GRASSEL, L. MALASKE, M. HOFFMANN, B. KLUSEMANN: '(Semi-)Solid-state joining of aluminium and titanium alloys – A critical review', *J. Mater. Res. Technol.*, 39 (2025) 3270-3291.
[2] X. LIU, P. ZHANG, W. LI, T. YE, C. XIA, T. ZHANG, J. SHI, J. XIE, Z. NI: 'Microstructure and mechanical properties of TC4 titanium alloy joint fabricated by vortex flow-based friction stir welding', *Chinese Journal of Mechanical Engineering*, 37 (2024) 159
[3] J. W. CHOI, H. H. LIU, H. FUJII: 'Dissimilar friction stir welding of pure Ti and pure Al', *Mater. Sci. Eng. A*, 730 (2018) 168-176.
[4] F.C. Liu, A. H. Feng, X. Pei, Y. Hovanski, R. S. Mishra, Z. Y. Ma, Friction stir based welding, processing, extrusion and additive manufacturing, Prog. Mater. Sci., 146 (2024) 101330.
[5] V. S. GADAKH, V. J. BADHEKA, A. S. MULAY: 'Solid-state joining of aluminum to titanium: A review', *Proc. Inst. Mech. Eng. Pt. L*, 235 (2021) 1757-1799.
[6] S. MENG, H. ZHAO, J. DONG, W. LIU, H. LIU, J. XIAO: 'Effect of process parameters on the mechanical properties of simultaneous double-sided friction stir welding joints', *Chinese Journal of Mechanical Engineering*, 37 (2024) 129.

[7] N. A. MUHAMMAD, P. H. GENG, C. S. WU, N. S. MA: 'Unravelling the ultrasonic effect on residual stress and microstructure in dissimilar ultrasonic-assisted friction stir welding of Al/Mg alloys', *Int. J Mach. Tool. Manu.*, 186 (2023) 104044.
[8] M. YU, H. ZHAO, Z. JIANG, Z. ZHANG, F. XU, L. ZHOU, X. SONG: 'Influence of welding parameters on interface evolution and mechanical properties of FSW Al/Ti lap joints', *J. Mater. Sci. Technol.*, 35 (2019) 1543-1554.
[9] Z. FAN, K. BAI, C. CHEN: 'The application of ultrasound in joining: Principles, processes and properties', *J. Manuf. Process.*, 101 (2023) 269-299.
[10] L. SHI, C. S. WU, G. K. PADHY, S. GAO: 'Numerical simulation of ultrasonic field and its acoustoplastic influence on friction stir welding', *Mater. Des.*, 104 (2016) 102-115.
[11] L. SHI, C. S. WU, X.C. LIU: 'Modeling the effects of ultrasonic vibration on friction stir welding', *J. Mater. Process. Technol.*, 222 (2015) 91-102.
[12] L. SHI, C. S. WU, H. J. LIU: 'The effect of the welding parameters and tool size on the thermal process and tool torque in reverse dual-rotation friction stir welding', *Int. J Mach. Tool. Manu.*, 91 (2015) 1-11.
[13] D. G. ANDRADE, C. LEITÃO, N. DIALAMI, M. CHIUMENTI, D. M. RODRIGUES: 'Modelling torque and temperature in friction stir welding of aluminium alloys', *Int. J. Mech. Sci.*, 182 (2020).
[14] G. Q. CHEN, Q. Y. SHI, Y. FUJIYA: 'Simulation of metal flow during friction stir welding based on the model of interactive force between tool and material[J]', *Journal of Materials Engineering and Performance*, 2014, 23(4): 1321-1328.
[15] P. PANKAJ, A. TIWARI, L. N. DHARA: 'Multiphase CFD simulation and experimental investigation of friction stir welded high strength shipbuilding steel and aluminum alloy[J]', *CIRP Journal of Manufacturing Science and Technology*, 2022, 39: 37-69.
[16] X. NAN, L. ZHOU, T. SUN, M. YU, X. SONG: 'Strengthening mechanism of Al/Ti friction stir butt welded joints via ultrasonic-induced fast diffusion effects', *J. Mater. Process. Technol.*, 338 (2025) 118754.
[17] X. ZHANG, F. ZHAO, L. LI, L. SHI, C. WU, A. KUMAR, S. MIRONOV: 'Ultrasonic vibration enhanced friction stir welding of titanium to aluminum', *Int. J. Mech. Sci.*, 291-292 (2025) 110191.
[18] J. ZHAO, H. SU, C. WU: 'The effect of ultrasonic vibration on stress-strain relations during compression tests of aluminum alloys', *J. Mater. Res. Technol.*, 9 (2020) 14895-14906.
[19] M. ZHAI, C. WU, H. SU: 'Influence of tool tilt angle on heat transfer and material flow in friction stir welding', *J. Manuf. Process.*, 59 (2020) 98-112.
[20] L. SHI, C. S. WU, S. GAO, G. K. PADHY: 'Modified constitutive equation for use in modeling the ultrasonic vibration enhanced friction stir welding process', *Scripta Mater.*, 119 (2016) 21-26.
[21] X. ZHANG, L. SHI, C. WU, C. YANG, S. GAO: 'Multi-phase modelling of heat and mass transfer during Ti/Al dissimilar friction stir welding process', *J. Manuf. Process.*, 94 (2023) 240-254.
[22] G. CHEN, H. LI, G. WANG, Z. GUO, S. ZHANG, Q. DAI, X. WANG, G. ZHANG, Q. SHI: 'Effects of pin thread on the in-process material flow behavior during friction stir welding: A computational fluid dynamics study', *Int. J Mach. Tool. Manu.*, 124 (2018) 12-21.
[23] L. SHI, J. CHEN, C. YANG, G. CHEN, C. WU: 'Thermal-fluid-structure coupling analysis of void defect in friction stir welding', *Int. J. Mech. Sci.*, 241 (2023) 107969.
[24] Y. LI, X. ZHANG, L. SHI, C. WU, S. LI, S. GAO: 'Double side friction stir Z shape butt lap welding of dissimilar titanium aluminum alloys', *Int. J. Mech. Sci.*, 271 (2024) 109135.

# MULTIPHYSICS SIMULATION OF RESISTANCE SPOT WELDING

I. BEN BAHAFFA*, **, M. COURTOIS*, S. CADIOU*, E. GESLAIN*, E. COURTOIS*, T. DUPUY**, X. CHEN**

** Univ. Bretagne Sud, UMR CNRS 6027, IRDL, F-56100 Lorient, France*
*** ArcelorMittal – Global Research and Development Maizières Products, F-57280 Maizières-lès-Metz, France*

*DOI 10.3217/978-3-99161-089-2-017, license CC BY 4.0*
*https://creativecommons.org/licenses/by/4.0/deed.en*
*This CC license does not apply to third party material and content noted otherwise.*

ABSTRACT

Resistance spot welding is widely used in the automotive industry for assembling steel car bodies. However, increasing demands for safety, durability, and weight reduction have led to the development of more advanced steels, which are also more sensitive to welding defects. To better understand issues like material expulsion, this study relies on an innovative multiphysics finite element numerical simulation.

The developed model integrates all the main physical phenomena involved in the process: heat transfer, fluid flow, electromagnetism, and solid mechanics. To manage this complexity, a multi-mesh approach is used, allowing each physics to be solved on a dedicated mesh while maintaining efficient coupling at each time step. The results of this new method will be compared with a more classical Electro-Thermo-Mechanical model, which is the industry standard to highlight the advantages of our approach for studying interfacial expulsion.

Keywords: resistance spot welding, expulsion, numerical simulation, multi-physics coupling, CFD

## INTRODUCTION

The most used welding method in the automotive industry is resistance spot welding (RSW), a joining technique that involves the local melting of materials by Joule heating between two or three sheets. However, new challenges have emerged regarding the weldability of some newly developed steels. In fact, modern ultra-high-strength steels sometimes have a more restricted weldability range due to several unwanted phenomena, including expulsion.

Expulsion is a defect where the molten material between the sheets is violently expelled during welding process. This phenomenon can seriously degrade the mechanical properties of the weld nugget and generates a safety hazard to people and machines around production lines. The molten nugget is usually contained by the electrode pressing on the weld, but as the thermal expansion increases so do the internal pressure of the nugget, which may cause the

expulsion if the containment is insufficient [1]. This reduces the size of the weld and its mechanical strength, making it non-compliant. Expulsion mainly occurs at the sheet interface and typically defines the maximum welding current. The minimum current ensures a sufficient weld diameter, and the range between this minimum and the expulsion limit defines the welding range (NF EN ISO 18278-2, SEP1220-2). Excessive current causes expulsion, although it is not systematic and occurs unpredictably.

Since the 1990s, numerical simulation has improved our understanding of welding phenomena. Electro-thermo-mechanical-metallurgical (ETMM) models can predict the mechanical behavior of the weld nugget, but not expulsion, as they neglect fluid flow and magnetic fields. However, these physics are needed to calculate flow behavior within the molten pool, which modifies heat transfer distribution and equalizes temperature in the nugget ([2];[3]). A magneto-hydrodynamic model [4] shows that convection can reach 0.5 m/s, and the resulting temperature is lower than that predicted by ETMM models. Therefore, an effective simulation of expulsion requires a model that integrates electromagnetism, fluid flow, and solid mechanics.

To our knowledge, such a fully coupled multiphysics model does not yet exist in the literature to provide a better understanding of expulsion onset. However, some studies specifically aim to predict this phenomenon. Browne et al. [5] proposed a criterion based on the ratio between the molten nugget radius ($Rn$) and the compressive contact radius ($R$contact), explaining how increased electrode clamping force delays expulsion. This criterion was reused by Zhang, Shen, & Lai [6]. Senkara et al. [1] and Valaee-Tale [7] describe a “force balance model”, comparing the effective force of the electrodes to the pressure inside the nugget, accounting for liquid compressibility and volume changes. Poor electrode symmetry could also lead to premature expulsion.

In this paper, a new approach of resistance spot welding (RSW) simulation is presented. This method enables the coupling of fluid flow and solid mechanics within the RSW process. A 2D axisymmetric finite element model is proposed, integrating electromagnetic, heat transfer, mechanical, and fluid flow phenomena. The mathematical formulation of the problem is first introduced, followed by a detailed description of the proposed approach. Finally, to demonstrate the potential of this method, a comparison with a classical electro-thermo-mechanical (ETM) model and experimental data is provided.

## MATHEMATICAL FORMULATION FOR RSW MULTIPHYSICS MODELING

Since the resistance spot welding process is multiphysic, modelling it involves several strongly coupled physical phenomena, which makes it a complex simulation.

Many phenomena involved are governed by solid mechanics. During welding, the electrodes indent the sheets, creating variable contact between the different components. This contact evolves with temperature, which is itself influenced by the electric current flowing through the assembly. Moreover, the current density passing through the sheets directly depends on the contact area generated by the indentation. These interactions highlight the strong interdependence between electrical, thermal, and mechanical phenomena, which are often modelled using an electro-thermo-mechanical (ETM) approach.

The novelty of our approach lies in the introduction of additional couplings: fluid flow and magnetism. Indeed, during the formation of the molten nugget, a very high pressure can develop, sufficient to slightly push back the electrodes during the welding process. With this addition, our goal is to better represent convection effects in the molten pool, and thus improve the thermal modelling of the nugget, providing a more accurate description of the phenomena related to its expansion during the process.

## MATHEMATICAL DESCRIPTION

In this study, we used for this simulation the commercial finite element software, COMSOL Multiphysics®. The physical phenomena considered include electromagnetism, heat transfer, solid mechanics, and fluid flow (with moving meshes). All the material properties used in the model are dependent on the temperature and were provided by ArcelorMittal.

### *Electrokinetic equations*

Under the quasi-steady-state approximation, electrical phenomena can be treated as an electrokinetic problem, for which the current conservation equation is written as (1).

$$div\vec{J} = 0 \tag{1}$$

where J is the current density in [A·m$^{-2}$].

The flow of electric current through the material leads to the generation of heat by Joule effect ($Q_J$), which is related to the electric potential ($V$) and the current density, according to Ohm's law (2), and expressed as (3).

$$\vec{J} = -\sigma_{elec}\,\overrightarrow{grad}\,V \tag{2}$$

$$Q_J = \frac{1}{\sigma}J^2 = \sigma_{elec}\left(\overrightarrow{grad}\,V\right)^2 \tag{3}$$

where $Q_J$ is in [W/m$^3$] and $\sigma_{elec}$ is the electrical conductivity in [S·m$^{-1}$].

### *Heat Transfer Equations*

Heat conduction and advection are governed by the heat equation, which is derived from the principle of energy conservation, and is expressed in transient form by equation (4). This equation accounts for the energy balance within an elementary volume of material, considering the heat generated by the Joule effect and the dissipation by conduction and advection (through $v$, the fluid velocity).

$$\rho c_p^* \frac{\partial T}{\partial t} + \rho C_p^* v * \nabla T = \vec{\nabla}\left(\lambda\,\vec{\nabla}\,T\right) + Q_J \tag{4}$$

here, $\rho$ is the density in [kg·m$^{-3}$], $\lambda$ the thermal conductivity in [W·m$^{-1}$·K$^{-1}$], $C_p$ the equivalent specific heat capacity in [J·kg$^{-1}$·K$^{-1}$], and $Q_J$ the volumetric heat source term due to the Joule effect in [W·m$^{-3}$].

In this model, the phase changes of melting and solidification are modelled using the equivalent specific heat capacity method (5).

$$c_p^*(T) = c_p(T) + L_f D_f(T) \tag{5}$$

$$D_f = \frac{1}{\sqrt{\pi(T_{liq}-T_{sol})^2}} exp\left(-\frac{(T-T_f)^2}{(T_{liq}-T_{sol})^2}\right) \tag{6}$$

with $C_p$ the specific heat capacity [J·kg$^{-1}$·K$^{-1}$], $L_f$ the enthalpy of phase change of steel [J·kg$^{-1}$], $D_f$ the fraction of phase transformed (liquidus–solidus) [K$^{-1}$], and $T_{sol}$, $T_{liq}$ respectively the solidus and liquidus temperatures.

### *Mechanical Equations*

The large thermal variations observed in the assembly require the use of mechanical behavior laws adapted to wide temperature ranges. In the context of resistance welding, although the temperatures reached could theoretically induce viscous effects, these remain negligible in our studies due to the small deformations observed (around 5% for thin sheets) [8]. Therefore, an elasto-plastic model with isotropic hardening is sufficient to describe the material behaviour. Moreover, the electrodes are modelled with an elastic law, in accordance with experimental observations reported in the literature [9].

The mechanical problem consists in solving the local mechanical equilibrium equation. In this study, inertial forces are assumed negligible, and the mechanical loads are considered to be static.

$$div(\sigma) + f = 0 \tag{7}$$

where $\sigma$ is the Cauchy stress tensor and $f$ represents the volume force.

Given the size of the system and the deformations involved, the small deformation assumption can be applied. The balance of macroscopic strains $\varepsilon$ can thus be written as:

$$\epsilon = \epsilon^e + \epsilon^{th} + \epsilon^p \tag{8}$$

with $\epsilon^e$ the elastic strain, $\epsilon^{th}$ the thermal strain due to expansion, and $\epsilon^p$ the plastic strain. The elastic part is calculated using Hooke's law, which, for an isotropic material, is expressed as follows:

$$\epsilon^e = \frac{1+\nu}{E}\sigma - \frac{\nu}{E} tr(\sigma) I \tag{9}$$

where $E$ is the Young's modulus, $\nu$ the Poisson's ratio, and $I$ the second-order identity tensor.

A large part of the deformation is generated by thermal expansion resulting from the heating of the assembly. This strain can be quantified using equation (10).

$$\epsilon_i^{th} = \alpha_i * \Delta T \tag{10}$$

with $\epsilon_i{}^{th}$ the strain due to thermal expansion, $\alpha_i$ the thermal expansion coefficient of the phase [K$^{-1}$], and $\Delta T$ the temperature change.

During the transition from the solid to the liquid state, a sudden drop in density ($\rho$) can be observed. This results in a sharp increase in the volumetric expansion coefficient ($\beta_i$), which in turn leads to a significant variation in the thermal expansion coefficient ($\alpha_i$). Equation (11) illustrates how the variation of $\rho$ with respect to temperature influences the expansion coefficient $\alpha_i$:

$$3\alpha_i = -\frac{1}{\rho} * \frac{\Delta\rho}{\Delta T} \tag{11}$$

Consequently, the plasticity criterion $C_{plasticty}$ can be expressed as follows:

$$C_{plasticity} = \sigma_{VM} - R_p - \sigma_y \tag{12}$$

with $\sigma_y$ the yield strength, $R_p$ the isotropic hardening (14), and $\sigma_{VM}$ the von Mises equivalent stress, which can be written as follows:

$$\sigma_{VM} = \sqrt{\frac{3}{2}\sigma' : \sigma'} \quad avec\ \sigma' = \sigma - \frac{1}{3}tr(\sigma)I \tag{13}$$

Within the sheets, a Voce law (14) is used to describe the hardening behavior of the material.

$$R_p = \sigma_{sat}\left(1 - e^{-\beta\epsilon_{pe}}\right) \tag{14}$$

where $\sigma_{sat}$ denotes the saturation value of the isotropic hardening, $\beta$ is a material parameter controlling the rate of hardening, and $\varepsilon_{pe}$ is the equivalent plastic strain.

### *Fluid flow Equations*

The Navier–Stokes equations describe the motion of fluids by accounting for the conservation of momentum (15) and mass (16).

$$\rho\left[\frac{d\vec{v}}{dt} + \vec{v}.\nabla\vec{v}\right] = -\nabla p + \mu\nabla^2\vec{v} + \overrightarrow{f_{HD}} \tag{15}$$

$$\frac{\partial\rho}{\partial \mathrm{t}} + \nabla.(\rho.\vec{v}) = 0 \tag{16}$$

With $\overrightarrow{f_{HD}} = \overrightarrow{F_{flot}} + \overrightarrow{F_{lorentz}}$, the volume force acting on the fluid, which are detailed later. It is assumed that the molten metal behaves as a Newtonian fluid with variable density in a laminar flow regime. To distinguish motion between solid and molten regions, the equivalent viscosity method is used. This method consists in artificially increasing the viscosity in regions where the temperature is below the melting point, thereby preventing fluid movement. Only the liquid zones, where the viscosity remains low, are then able to flow.

Within the molten pool, convective flows can be generated due to the temperature gradient between the edges of the molten zone and its center. These flows can be described by the following equation based on the Boussinesq approximation:

$$\overrightarrow{F_{flot}} = \left[-\rho \cdot \beta \cdot \left(T - T_{fusion}\right) \cdot \vec{g}\right] \tag{17}$$

Due to the high electric current, an electromagnetic force called the Lorentz force is generated. It acts throughout the metal but is strongest where the current density is highest. This electromagnetic force acts on the molten pool and creates movement in the molten zone that is potentially dominant.

$$\overrightarrow{F_{lorentz}} = \vec{j} * \vec{B} \tag{18}$$

$$\overrightarrow{F_{lorentz}} = \begin{cases} -j_z * B_\theta \\ 0 \\ j_r * B_\theta \end{cases} \tag{19}$$

With $\vec{B} = \begin{cases} 0 \\ B_\theta \\ 0 \end{cases}$

## MULTI MESH METHOD

One of the main challenges of our approach lies in managing the fluid-structure interaction. During the resistance spot welding process, a force is applied to an assembly of sheets, then a high electric current passes through the assembly, causing the metal to melt at the interface between the sheets. This creates a significant challenge in handling the fluid-solid interface. Indeed, at the beginning of the process, the material is entirely solid, but as welding progresses, it gradually transforms from solid to liquid, thereby creating a moving fluid-structure interface starting from nothing.

To address this, we used the Multi-Mesh method [10]. This approach allows the use of different meshes to solve the same problem, each specifically adapted to the physics it represents. An interpolation and projection method of variables between meshes at each time step then enables the redefinition of all couplings from one mesh to another.

The classical approach generally consists in using a single mesh, constructed according to the constraints of the most restrictive equation. In contrast, here, the use of distinct meshes for each coherent group of equations allows for optimization of local accuracy. However, this decoupling requires projecting solutions between meshes via interpolation, which can lead to a loss of precision, especially when transferring from a fine mesh to a coarser one. Through a process of validation and convergence study not presented here, the model remains relevant, as demonstrated previously [10].

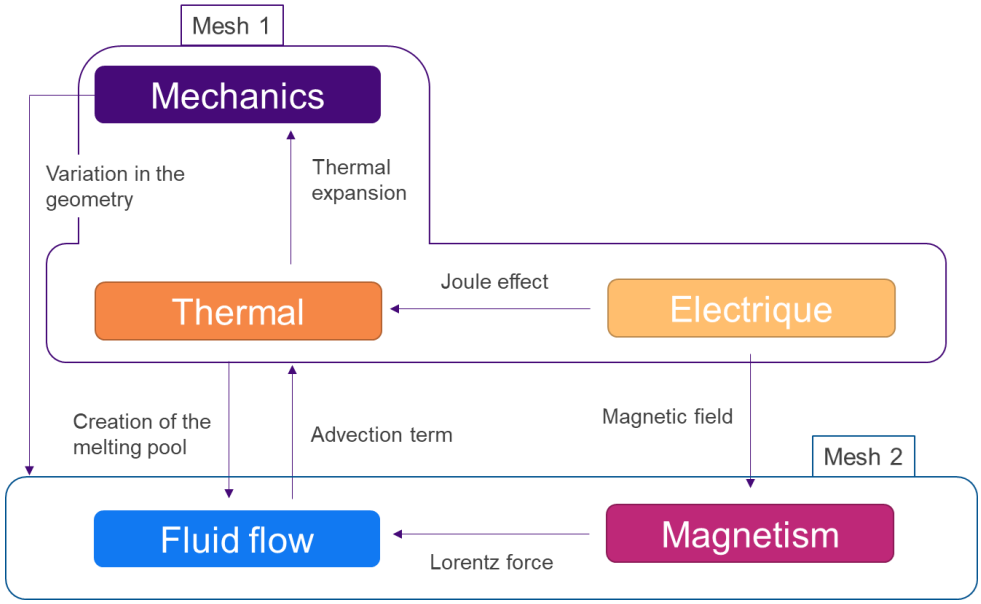



**Fig. 1** Diagram of multiphysics couplings and the resolution meshes for each physics

Fig 1 shows the distribution of the physics according to the meshes. In mesh 1, the problems of solid mechanics, heat transfer, and electrical physics are solved. Then, in a second mesh, the fluid flow and magnetism problems are solved. The solution can be considered a strong coupling, as all physics are solved at each time step. In this version of the model, the fluid-structure coupling is done through geometry changes, by imposing the displacement field obtained from solid mechanics onto mesh 2 (where fluid flow is solved), which is modified using an ALE moving mesh method. Thus, fluid flow is solved in the correct deformed geometry, allowing very precise calculation of the thermal field, a central element of the entire problem. The use of two meshes eliminates the issue of the appearance of the liquid zone and simplifies convergence.

### *Meshes*

Using mesh 1, the following physics are solved: solid mechanics, electrical, and heat transfer.

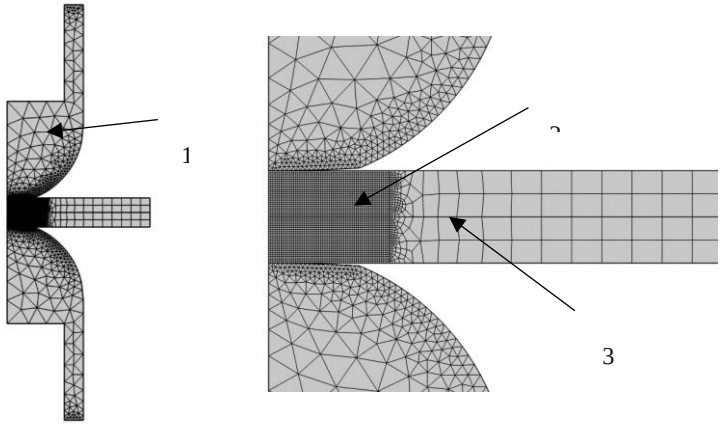



**Fig. 2** Distribution of elements in mesh 1

The geometry is divided into three key regions, each meshed according to its importance using triangular or quadrilateral elements:

1. Electrodes (Free triangles, max size: 2.8 mm)
2. Sheets – contact zones between Electrode/Sheet (E/S) and Sheet/Sheet (S/S), as well as the weld nugget development area (Structured quadrilaterals, max size: 0.07 mm)
3. Sheets – area outside the weld nugget (Free quadrilaterals, max size: 1 mm)

Using mesh 2, the following physics are solved: fluid flow and magnetism (for Lorentz forces).

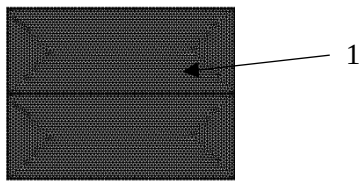



**Fig. 3** Distribution of elements in mesh

1. Fusion zone development area. (Free triangles, maximum size 0.06 mm)

# RESULTS AND DISCUSSION

## WELDING PARAMETERS

The welding parameters are defined by several standards. In our case, we used the SEP-1220-2 standard, which provides welding parameters based on the thickness of the sheet used, the mechanical strength of the steel grade (Rm), and the presence of a coating. Our case describes a symmetrical assembly of DP600 steel sheets with a thickness of 1.5 mm and no coating. Using the material properties of the studied grade, the following welding parameters were chosen (the electrode geometry is described by the ISO 5821 norm):

**Table 1** *:* Welding parameters provided by the SEP-1220-2 standard for the steel grade studied

| Type of electrodes | Welding force | Numbers of pulses | Welding time | Hold time |
|---|---|---|---|---|
| F1-16-20-6 | 4.5 kN | 1 | 340 ms | 250 ms |

## RESULTS AND COMPARISON WITH AN ELECTRO-THERMO-MECHANICAL MODEL

The most commonly used models in the industry are the Electro-Thermo-Mechanical (ETM) numerical models. These models are generally used to predict the size of the molten pool. However, the absence of fluid flow prevents an accurate representation of the temperature field, with calculated temperatures often significantly higher than those observed in reality. To benchmark our model, we compared it to this type of ETM model in order to highlight the possible differences. Thus, two 2D axisymmetric models were solved using the same software, COMSOL Multiphysics 6.2®, and under similar conditions and assumptions. The multiphysics model including fluid flow is referred to as the ETMMHD (Electrical – Thermal – Mechanics – Magnetic – Hydrodynamics).

Fig 4 presents a mirrored view of the 2D axisymmetric model. It illustrates the stress and the displacements along the vertical axis (z axis). One can observe the separation of the sheets caused by indentation, as well as their thermal expansion. A very small displacement is visible at the electrode level, which can be explained by the thermal expansion of the sheet. As the thermal expansion is slightly lifting the electrodes, it’s almost resetting the displacement of the electrodes.

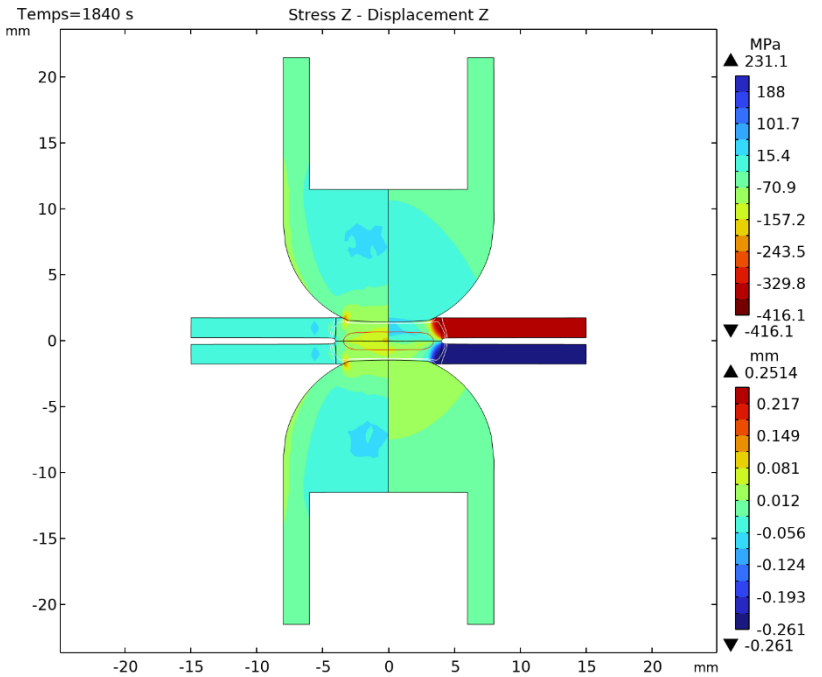



**Fig. 4** Stress (left) and Displacement (right) along the z-axis for the ETMMHD model

Fig 5 shows the temperature field (on the left) and the velocity field within the molten zone (on the right), as computed by the model. In white, the contour represents the heat-affected zones (Ac1: 713 °C, Ac3: 825 °C), while the fusion contour delineating the molten zone is drawn in red. The magenta arrows indicate the flow directions of the molten pool. At first, we can observe the overall velocity field ranges is between 0 and 0.2 m/s, with isolated spikes along the axis of symmetry reaching up to 0.7 m/s. Although prior studies report molten-pool velocities between 0.3 and 0.6 m/s [4], the observed instabilities remain the subject of ongoing investigation. This behaviour is not unexpected, as asymmetric 2D models are inherently susceptible to anomalies along the symmetry axis.

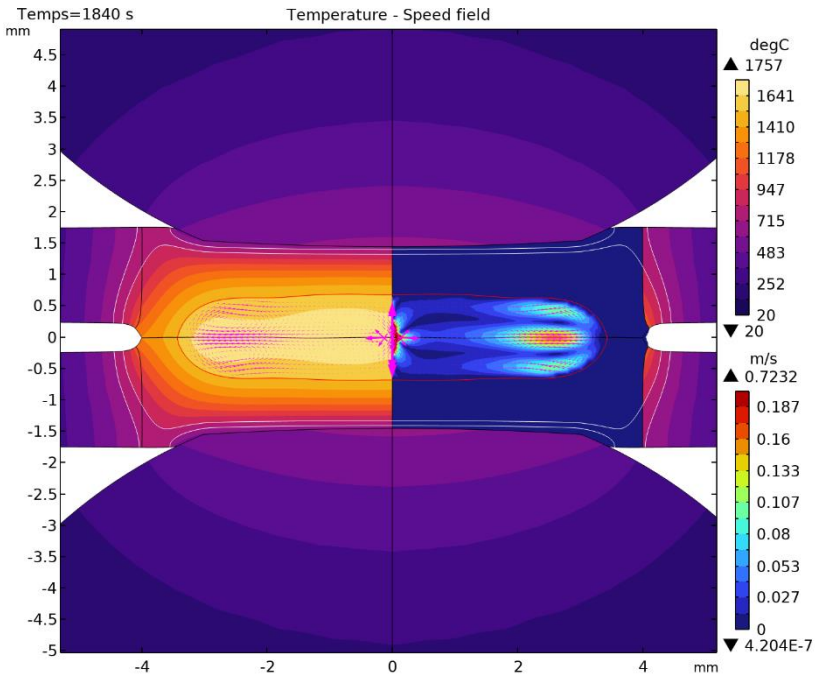



**Fig. 5** Temperature and velocity fields in the molten pool (ETMMHD) at 340 ms (end the welding phase) for the ETMMHD model

In Fig 6, a very different temperature gradient can be observed, along with a different heat-affected zone. As previously mentioned, the integration of fluid flow into the model enables the representation of convection flows within the molten pool, leading to thermal homogenization that is not captured by conventional models (ETM), resulting in an overall inaccurate determination of the temperature field. As suggested in [2], the maximum expected temperature within the molten pool is approximately 1650 °C. However, Fig. 6 shows that the ETM model reaches a peak temperature of 2565 °C, which is significantly higher than that predicted by the ETMMHD approach ($T_{max}$= 1757 °C). This observation is consistent with the findings of [11], who reported notable differences between the thermal fields obtained using traditional electro-thermal and a magneto-hydro-dynamic models. Moreover, a notable difference appears in the shape of the molten zone, although it remains comparable in diameter to that obtained with the Electro-Thermo-Mechanical model alone.

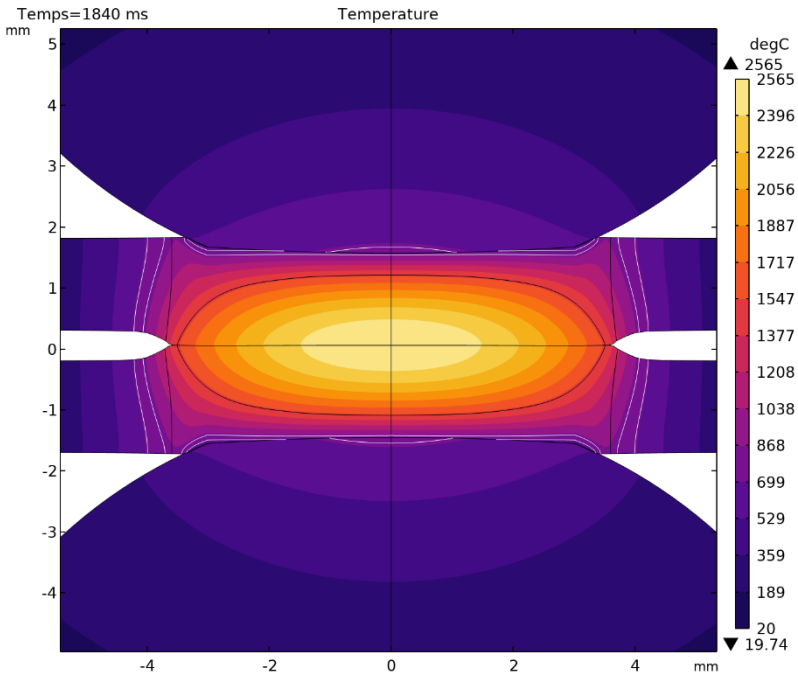



**Fig. 6** Temperature field (Electro-Thermo-Mechanical Model) at 340 ms (end the welding phase)

Fig 7 presents a comparative graph of the molten zones and heat-affected zones (Ac1: 713 °C, Ac3: 825 °C) obtained for the two models. The Electro-Thermo-Mechanical model is shown in orange squares, while the ETMMHD model, integrating fluid flow and electromagnetism, is shown in purple triangles. As seen in Fig 5 and 6, there is a notable difference in the maximum temperature, with the ETMMHD model showing a reduction of approximately 825 °C. The addition of fluid flow allows for better thermal homogenization within the molten nugget. The detailed description of heat transfer within the molten pool influences areas beyond the liquid zone, with repercussions both on solid mechanics (through material properties) and on the understanding of the phenomenon under study, the interfacial expulsion.

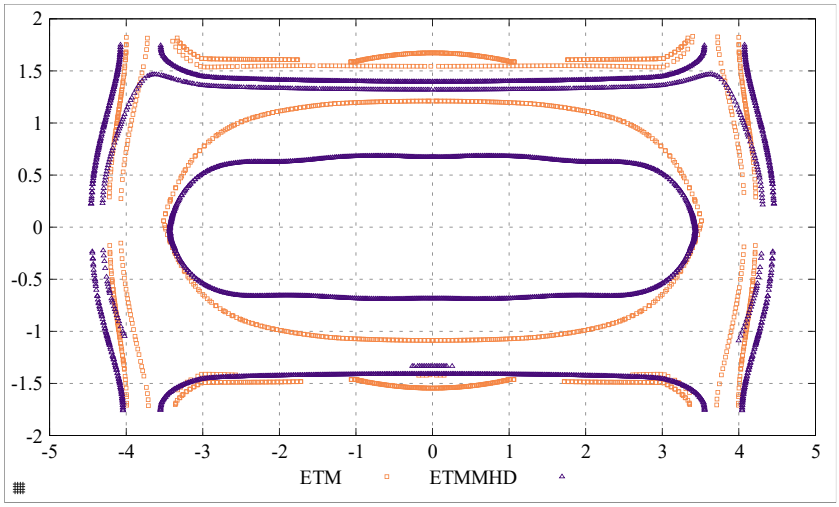



**Fig. 7** Dimensions of the HAZ (Ac1 and Ac3 temperatures) and the MP for the two models (ETM: orange square – ETMMHD: purple triangle)

## COMPARISON WITH EXPERIMENTAL DATA

To validate the numerical model, a comparison with experimental data was performed. The same welding parameters as those used in the simulation were applied, the only variation being the welding time, which ranged experimentally from 40 ms to 340 ms. This allowed us to observe the evolution of the molten pool during the welding process. Each configuration was repeated three times to ensure repeatability, and all dimensions were measured through macrographic cross-sections.

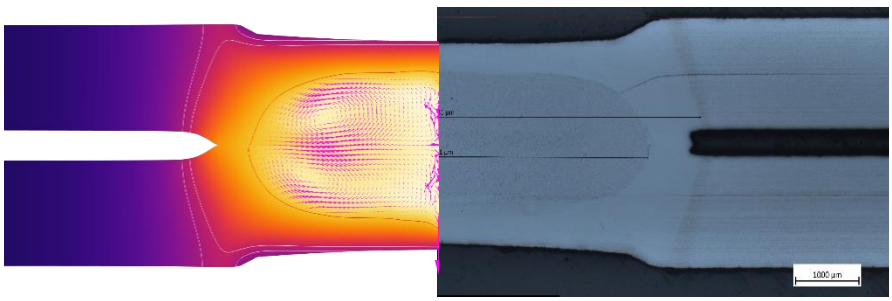



**Fig. 8** Cross section comparison with the simulation

Fig 9 illustrates the evolution of the molten pool diameter during the welding phase. The ETM results are shown in orange (dashed line), the ETMMHD results in purple, and the

experimental data points are represented in red. Initially, both the ETM and ETMMHD models show an earlier onset of molten pool formation compared to the experimental results, with a lead of approximately 20 ms. Despite this time discrepancy, both models follow a similar trend and tend to overestimate the molten pool diameter during the welding phase. However, by the end of the welding phase, the predicted pool sizes from both models closely align with the experimental measurements.

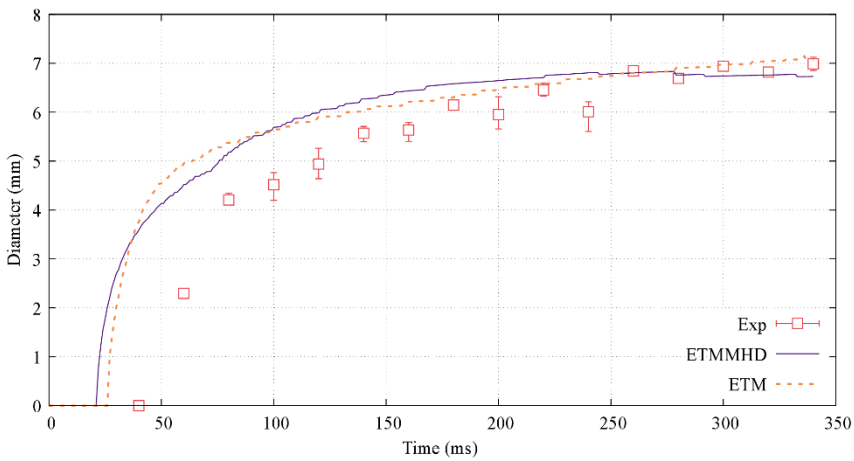



**Fig. 9** Evolution of the molten pool diameter according to the ETM and ETMMHD models, and experimental data

Fig 10 shows the evolution of the molten pool thickness during the welding phase. Like the previous figure, both models predict an earlier appearance of the molten nugget compared to the experimental data. At the beginning of the process, the molten pool initially grows vertically, forming a thick nugget. As the indentation increases, the nugget becomes wider and thinner. The ETM model does not accurately capture this behaviour, as it continuously predicts an increasing nugget thickness. In contrast, the ETMMHD model, which incorporates a more realistic representation of convection within the nugget, shows a decrease in thickness over time like the experiment. Similar to the findings in [4], the results highlight the necessity of including fluid flow to accurately characterize the evolution of the melt-pool thickness. Although the ETMMHD model underestimates the nugget thickness throughout most of the process, it achieves a final molten pool thickness that matches the experimental result.

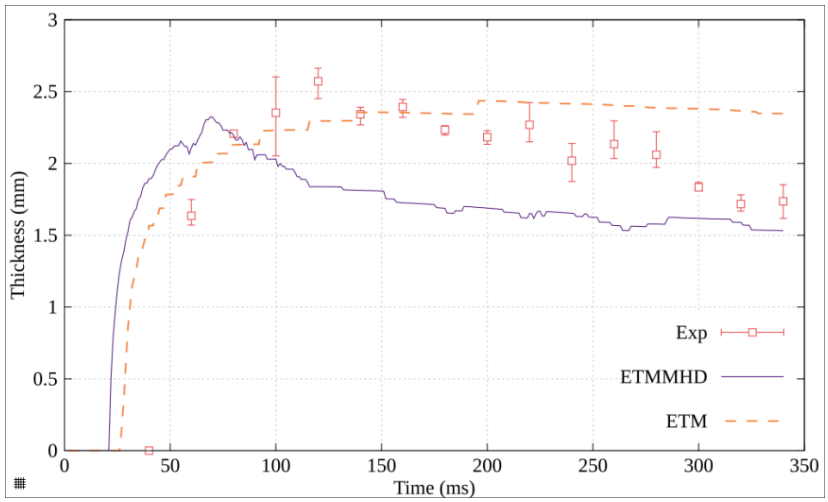



**Fig. 10** Evolution of the molten pool thickness according to the ETM and ETMMHD models, and experimental data

## CONCLUSION

This work presents a new simulation approach for the resistance spot welding (RSW) process, with the future goal of applying it to the study of the interfacial expulsion phenomenon. The developed model has demonstrated the feasibility of a strong, dynamic, and fully coupled interaction between electromagnetic, thermal, solid mechanical, and fluid flow phenomena using moving meshes (Arbitrary Lagrangian-Eulerian Formulation (ALE)). The key principle of using two separate meshes was introduced, allowing the model to overcome several constraints.

The initial results have highlighted the advantages of this approach, particularly through the improved representation of the temperature field, made possible by the explicit inclusion of molten pool flow, itself computed in geometry modified by solid mechanics. Comparison to both classical ETM model and experiments have shown the interest of the approach with satisfactory results. To our knowledge, this bidirectionally coupled approach solved at each time step has not yet been proposed in the literature for this type of process.

Building on this foundation, several improvements remain to be implemented. One priority involves refining contact conditions, particularly the adhesion models that represent the formation of the corona bond, which relates to the joining of material beyond the solid-state bonding temperature. Additionally, accounting for the thermal expansion coefficient of the fluid during the melting phase is another area for improvement, as this coefficient increases sharply during the solid-to-liquid transition.

Finally, an essential phase of a more thorough experimental validation of the model will be conducted, to assess the model's predictive capability and to fine-tune its parameters.

A final step in this project will be the transition to a 3D configuration, which would allow the consideration of directional aspects of expulsion and provide a more realistic representation of process imperfections, especially electrode misalignment.

## References


[1] J. SENKARA, H. ZHANG and S. J. HU: 'Expulsion Prediction in Resistance Spot Welding', *Welding Journal – New-York,* vol. 83, No.4, pp 123-134, 2004.

[2] W. V. ALCINI: 'Experimental Measurement of Liquid Nugget Heat Convection in Spot Welding', *Welding Journal,* vol. 69, No.5, pp 177-180, 1990.

[3] Y. Li, Z. Luo, Y. Bai, et S. S. Ao: 'Investigation of induced magnetic force on liquid nugget during resistance spot welding', *Sci. Technol. Weld. Join.*, vol. 18, No 4, pp. 329-336, 2013.

[4] Y. B. LI, Z. Q. LIN, S. J. HU, ET G. L. CHEN: 'Numerical analysis of magnetic fluid dynamics behaviors during resistance spot welding', *J. Appl. Phys.*, vol. 101, No 5, pp. 101-109, 2007.

[5] D. J. BROWNE, H. W. CHANDLER, J. T. EVANS, P. S. JAMES, ET J. WEN: 'Computer Simulation of Resistance Spot Welding in Aluminum: Part II', *Welding Journal-Including Welding Research Supplement*, vol. 74, No 12, pp 417-422, 1995.

[6] Y. ZHANG, J. SHEN, ET X. LAI: 'Influence of Electrode Force on Weld Expulsion in Resistance Spot Welding of Dual Phase Steel with Initial Gap Using Simulation and Experimental Method', *ISIJ Int.*, vol. 52, No 3, pp 493-498, 2012.

[7] M. VALAEE-TALE, M. SHEIKHI, Y. MAZAHERI, F. MALEK GHAINI, ET G. R. USEFIFAR: 'Criterion for predicting expulsion in resistance spot welding of steel sheets', *J. Mater. Process. Technol.*, Vol. 275, pp. 116329, 2020.

[8] C. SRIKUNWONG: *Modélisation du procédé de soudage par points*, thesis, ENMP, Paris, France, 2005.

[9] R. RAOELISON: *Etude de l'influence des conditions interfaciales sur le développement du noyau lors du soudage par résistance par point*, thesis, Giens, France, 2011.

[10] COURTOIS, MICKAËL, CARIN, MURIEL, LE MASSON, PHILIPPE, ET GAIED, SADOK: 'Complete 3D heat and fluid flow modeling of keyhole laser welding and methods to reduce calculation times', *Math. Model. Weld Phenom.*, No.12, pp 1-11, Verlag der Technischen Universität Graz, 2018.

[11] Y. B. LI, Z. Q. LIN, S. J. HU, ET G. L. CHEN: 'Electromagnetic Phenomena in Resistance Spot Welding and its Effect on the Weld Nugget Formation', *Progress In Electromagnetics Research Symposium Proceedings*, Vol.3, pp 744-748, 2009.

# THERMOHYDRODYNAMIC MODELING OF LASER CUTTING FOR RESIDUAL LASER ENERGY QUANTIFICATION USING A HYBRID LEVEL SET – MOVING MESH METHOD

R. MEILLOUR*'**, M. COURTOIS**, C. NAHED***, I. DOYEN*, M. CARIN**

**CEA, Service de Recherche en Matériaux et procédés Avancés, Université Paris – Saclay, Gif-sur-Yvette 91191, France*
***Université Bretagne Sud, UMR CNRS 6027, IRDL, Lorient 56100, France*
****CEA, Service d'Etudes Mécaniques et Thermiques, Université Paris – Saclay, Gif-sur-Yvette 91191, France*

*DOI 10.3217/978-3-99161-089-2-018, license CC BY 4.0*
*https://creativecommons.org/licenses/by/4.0/deed.en*
*This CC license does not apply to third party material and content noted otherwise.*

## ABSTRACT

Although widely used and investigated in manufacturing, the laser cutting process remains an emerging technology for nuclear dismantling, where the challenges differ significantly. Indeed, while cutting quality is essential in manufacturing processes, it is not a relevant criterion in nuclear dismantling. Nevertheless, the residual laser energy, which is the focus of this study, is of particular relevance to nuclear safety issues for dismantling.

This paper presents a thermohydrodynamic model for simulating the laser cutting process of 5 $mm$ thick 304L stainless steel, accounting for heat transfer and fluid flow in all phases (gas, liquid and solid), and employing the Level Set method to dynamically capture the gas-metal interface. The model is first validated through a comparison of the cutting front angles with experimental observations, demonstrating good agreement with a difference of less than 6%. The simulation results show good agreement with experimental observations regarding the cutting front angle, with a difference of less than 6%. Then, a hybrid Level Set – moving mesh method is proposed to discretize the interface in order to quantify the residual laser energy using the ray tracing approach.

Keywords: Laser cutting, heat and fluid flow, residual laser energy, Level Set, moving mesh, ray tracing.

## INTRODUCTION

Since the first studies in the 1960s [1-2], the laser cutting process has been used across applications in various fields [3-6]. Among the industrial sectors involving the process, the

manufacturing industry is by far the most represented in the literature [7-9]. Indeed, in this sector the cutting quality, which is strongly affected by the formation of striations, remains a major weakness of the process. Most studies have investigated this phenomenon through both experimental [10] and numerical [11] analyses in order to eliminate striations.

In many numerical studies, both analytical and thermohydrodynamic models have been developed to describe physical mechanisms involved in laser cutting to predict the formation of striations as a function of operating parameters [12-13]. The thermohydrodynamic models provide a detailed representation of the process through the key physics such as heat transfer and fluid flow, as well as the gas – metal interface dynamic.

Both Amara *et al.* [14] and Kheloufi *et al.* [15] proposed thermohydrodynamic models for the laser cutting process on iron sheets (thickness $\leq 3\ mm$), relying on the Eulerian Volume Of Fluid (VOF) approach to capture the gas-metal interface and by solving the governing equations using the Finite Volume Method (FVM). Each thermohydrodynamic model [14-15] allows the investigation of the effect of certain operating parameters, such as the cutting velocity, on the kerf geometry and its temperature field, showing a good agreement with experimental work [16]. Amara *et al.* [13] extended their work with a more in-depth study that investigates the effect of laser wavelength on the cut quality, using a mesh adaption based on the temperature gradients to improve accuracy in regions of interest and reduce computational cost. More recently, Nie *et al.* [17] modeled the laser cutting of a $0.15\ mm$ aluminum alloy sheet, using a thermohydrodynamic approach and localized mesh refinement method as well. This study focused on particle ejection, highlighting mechanisms behind particle formation and characterizing their size and velocity post-ejection.

In nuclear application, challenges differ from those in the manufacturing industry. While cutting quality is a major interest in manufacturing, it is not a significant concern when dismantling nuclear facilities [18]. However, the portion of laser energy transmitted through the plate (Fig. 1), commonly referred to as residual laser energy, is largely overlooked in the literature, yet it requires particular attention in the context of nuclear safety issues for dismantling. Indeed, the residual laser energy could compromise the integrity of background structures due to its thermo-mechanical impact. The generation and dispersion of aerosols in the environment also present a challenge [19], however this aspect is not addressed in the present work.

This paper presents a 3D thermohydrodynamic model of laser cutting of a $5\ mm$ thick 304L stainless steel plate, including heat transfer and fluid flow equations for the three phases (gas, liquid and solid), as well as the Level Set method [20] to dynamically capture the gas-metal interface. A comparison with an experimental study [21] enables the first validation of the model by comparing cutting front angle, using the same operating parameters as those applied in the experiments. Then, a hybrid Level Set – moving mesh method coupled with a ray tracing approach is proposed to quantify the residual laser energy. The development of both the laser cutting model and the quantification of residual laser energy are carried out using the finite element software COMSOL Multiphysics®.

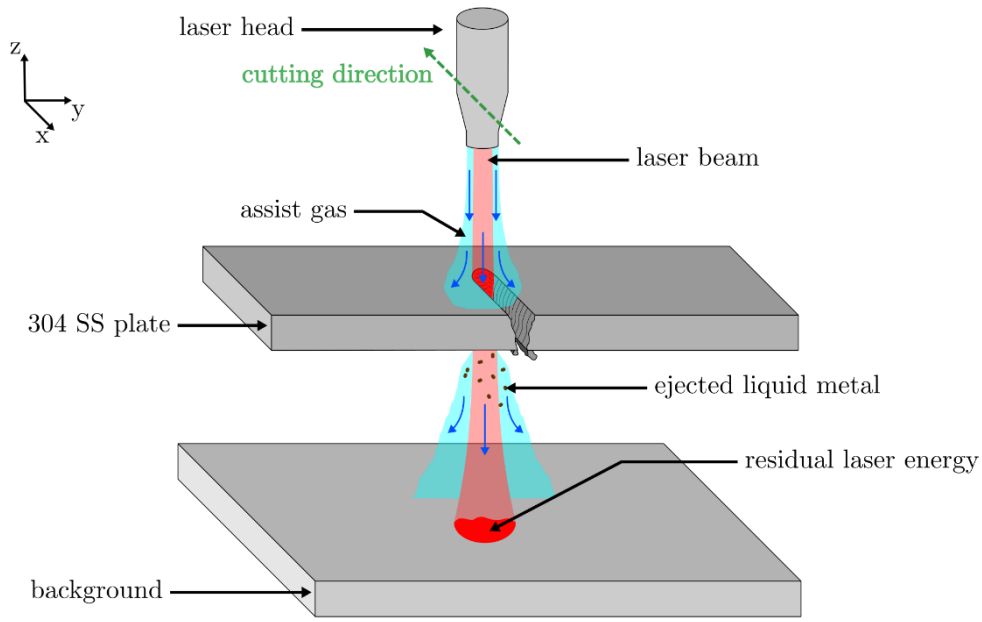



**Fig. 1** Schematic view of the laser cutting process and the associated residual laser energy

## MATHEMATICAL FORMAULATION OF THE LASER CUTTING MODEL

The present laser cutting modeling involves a multiphase and multiphysics approach. On the one hand, it must account for the gas, and metallic liquid and solid phases. On the other hand, it requires solving both heat transfer and fluid flow phenomena. Regarding these physics, the model is based on the following assumptions:

- Although Duan *et al.* [22] have shown that for plate thickness greater than 3 mm, multiple reflections of the laser within the kerf may influence the energy input into the plate, this phenomenon is not taken into account in this preliminary work.
- The process is modeled using an inert gas (nitrogen), and no chemical reactions are included.
- The properties of gas and metal (except for its thermal conductivity) are assumed constant with respect to temperature. A sensitivity analysis (not shown here) was performed on the thermophysical properties, which showed a limited impact on results.
- Given the complex nature of the hydrodynamics of the assist gas, it is not explicitly modeled, but rather represented by a friction force and a dynamic pressure, as proposed by Vicanek *et al.* [23].
- Based on the previous assumption, the flow is treated as laminar and the supersonic convective heat is not modeled.

Fig. 2 illustrates the thermohydrodynamic model used to simulate the laser cutting of a $5\,mm$ thick 304L stainless steel plate. The computational domain has dimensions of $6 \times 3.5 \times 7\ mm^3$. Owing to the symmetric nature of the process, the model includes only half of the cut, thus reducing the computational time. Although, in nuclear dismantling, the reference setup involves a static sample with a teleoperated or controlled laser head installed on a robotic arm, the model assumes a static laser cutting head while the plate moves along the x-axis at a cutting velocity $\overrightarrow{v_d}$. Indeed, this allows the computational domain to be reduced while preserving relevant information about the cutting front, thus lowering computational time.

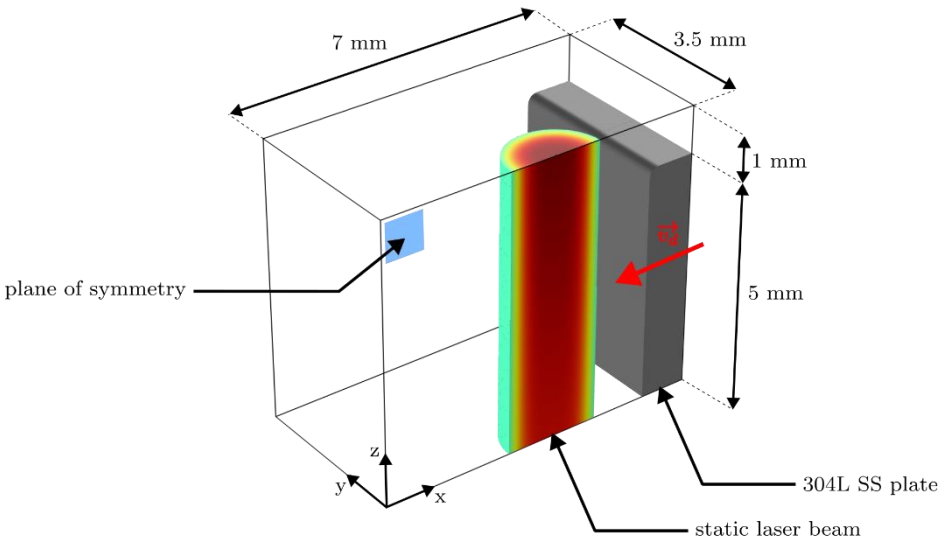



**Fig. 2** Schematic representation of the thermohydrodynamic laser cutting model

## GAS - METAL INTERFACE CAPTURING

The Level Set method, originally introduced by Osher and Sethian [20], is an Eulerian approach based on a fixed mesh and is employed in the model to dynamically capture the gas – metal interface, following the formulation of *Li et al.* [24]. The phase variable $\phi$ (refer to equation 1), which takes the value 0 in the gas phase and 1 in the metal phase (see Fig. 3), is determined by the following equation:

$$\frac{\partial \phi}{\partial t} + \vec{u} \cdot \vec{\nabla}\phi = \gamma_{LS}\, \vec{\nabla} \cdot \left[ \varepsilon_{\mathrm{LS}}\, \vec{\nabla}\phi - \phi\,(1-\phi)\frac{\vec{\nabla}\phi}{|\vec{\nabla}\phi|} \right] \tag{1}$$

Where $\gamma_{LS}\ [m.s^{-1}]$ corresponds to the reinitialization parameter, and $\varepsilon_{\mathrm{LS}}\ [m]$ determines the thickness of the interface separating $\phi = 0$ and $\phi = 1$ phases in the Level Set formulation.

Here, the variable $\phi$ is advected by the velocity vector $\vec{u} = \{u, v, w\}$, as obtained from the Navier-Stokes equations (equations 14 and 15). Equation 2 presents $\delta(\phi)$, which is a smoothed approximation of the Dirac delta distribution. It enables the deposition of the physical phenomena occurring on the interface since no explicit boundary is defined. All properties are defined as a function of the variable $\phi$, according to the formulation given in equation 3.

$$\delta(\phi) = 6\,|\phi(1-\phi)|\,\left|\vec{\nabla}\phi\right| \tag{2}$$

$$\xi = \xi_{gas} + \left(\xi_{metal} - \xi_{gas}\right)\phi \tag{3}$$

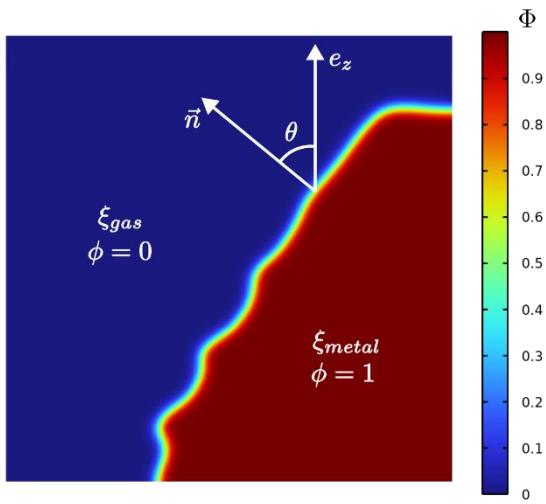



**Fig. 3** Example of a 2D representation of the field $\boldsymbol{\phi}$

## HEAT TRANSFER AND FLUID FLOW DESCRIPTIONS

The mathematical description of heat transfer, based on the previous assumptions, is computed by the thermal energy balance equation for isotropic and homogeneous materials (equation 4). The source terms include laser energy distribution $S_{laser}$ (equation 5), and heat loses by vaporization $S_{vap}$ (equation 10) and radiation $S_{rad}$ (equation 13).

Here, the $S_{laser}$ term accounts for the effect of the incidence angle $\theta$ (see figure 3) on the absorptivity $\alpha_{moy}$ through Fresnel's equations (equation 6 and 7) [25], the beam divergence from the focal plane position $p_{fl}$ (equation 9), located 35 $mm$ above the bottom surface of the plate, and a narrow Gaussian distribution due to the small diverging angle of the laser (6° [18]). $S_{vap}$ is based on a modified Langmuir expression [26] and depends on the evaporated mass flux $\dot{m}$ $[kg.m^{-2}.s^{-1}]$ as a function of temperature $T$ (equation 11). Considered of the second order, latent heat of fusion is omitted in the present model.

$$\rho_\phi \, c_{p_\phi} \left( \frac{\partial T}{\partial t} + \vec{u} \cdot \vec{\nabla} T \right) = \vec{\nabla} \cdot \left( \lambda_\phi \, \vec{\nabla} T \right) + \left( S_{laser} + S_{vap} + S_{rad} \right) \delta(\phi) \tag{4}$$

$$S_{laser} = \alpha_{moy}(\theta) \frac{P_{laser}}{\pi \, w(z)^2} \exp\left[ - \left( \frac{({x_{laser}}^2 + {y_{laser}}^2)}{w(z)^2} \right)^2 \right] \cos\theta \tag{5}$$

$$\alpha_p(\theta) = 1 - \frac{(n^2 + k^2)\cos^2\theta - 2\,n\cos\theta + 1}{(n^2 + k^2)\cos^2\theta + 2\,n\cos\theta + 1} \tag{6}$$

$$\alpha_s(\theta) = 1 - \frac{(n^2 + k^2) - 2\,n\cos\theta + \cos^2\theta}{(n^2 + k^2) - 2\,n\cos\theta + \cos^2\theta} \tag{7}$$

$$\alpha_{moy}(\theta) = \frac{\alpha_p(\theta) + \alpha_s(\theta)}{2} \tag{8}$$

$$w(z) = w_0 \sqrt{1 + \left( \frac{z - p_{fl}}{z_R} \right)^2} \tag{9}$$

$$S_{vap} = -\dot{m} \, L_v \tag{10}$$

$$\dot{m} = (1 - \beta_r) \left( \frac{m}{2\,\pi \, k_B \, T} \right)^{\frac{1}{2}} p_{sat}(T) \tag{11}$$

$$p_{sat}(T) = p_0 \exp\left[ \frac{\Delta H_v}{k_B \, T_{vap}} \left( 1 - \frac{T_{vap}}{T} \right) \right] \tag{12}$$

$$S_{rad} = \varepsilon \, \sigma \, (T_{amb} - T)^4 \tag{13}$$

Where $\rho$ is the density, $c_p$ the heat capacity, $\lambda$ the thermal conductivity, $P_{laser}$ the laser power, $n$ and $k$ respectively the refraction index and the extinction coefficient, $w(z)$ the radius as a function of distance $z$ and $w_o$ the waist of the laser beam, $x_{laser}$ and $y_{laser}$ the coordinates of the laser, $z_R$ the Rayleigh , $\beta_R$ the retrodiffusion coefficient, $m$ the atomic mass, $k_B$ the Boltzmann constant, $p_{sat}$ the saturation pressure of the vapor phase, the ambient pressure $p_0$ and temperature $T_{amb}$, $L_v$ the latent heat of vaporization and $\Delta H_v$ the enthalpy of the phase transition (from liquid to vapor), $T_{vap}$ the vaporization temperature, $\varepsilon$ the emissivity and $\sigma$ the Stephan-Boltzmann constant.

Table 1 summarizes the main parameters related to heat transfer, taken from experiments [21] and the literature [26,27-29]. Physical properties of 304L stainless steel are implemented in the model based on data available in the literature [27,29]. Given the absence of data for refractive index $n$ and extinction coefficient $k$ at the laser wavelength of $1030\ nm$ [21], values corresponding to iron at $1060\ nm$, as reported in [26], are employed.

**Table 1** Summary of the main parameters used in heat transfer computation

| Parameter [unit] | Value | Reference |
|---|---|---|
| $\lambda_{304L}$ $[W.cm^{-1}.K^{-1}]$ solid / liquid | $8.116 \times 10^{-2} + 1.618 \times 10^{-4}\ T$ / $1.229 \times 10^{-3} + 3.248 \times 10^{-5}\ T$ | [27] |
| $\rho_{304L}$ $[kg.m^{-3}]$ | 7000 | [29] |
| $n$ / $k$ | 3.6 / 5 | [28] |
| $P_{laser}$ $[W]$ | 7000 | [21] |
| $w_0$ $[\mu m]$ | 900 | [21] |
| $z_R$ $[mm]$ | 50 | [18] |
| $p_{fl}$ $[mm]$ | 35 | [21] |
| $L_v$ $[J.kg^{-1}]$ | 6.1 $10^6$ | [26] |
| $\beta_r$ | 0.18 | [26] |
| $T_{vap}$ $[K]$ | 3134 | [26] |
| $\varepsilon$ | 0.3 | [29] |

The fluid dynamics is described by the continuity equation (equation 14) and momentum conservation equations (equation 15) for laminar flow, considering both the gas and metal as incompressible and Newtonian fluids. The solid phase is modeled using a Darcy condition [30], which forces the solid velocity to tend toward the cutting velocity $v_{d\,x}$ along the $x$ axis, and applying an augmented viscosity ($\mu_{solid} = 1\ Pa.s$) for temperature below the fusion temperature ($T_{fus} = 1700\ K$ [29]). The source terms $\overrightarrow{S_{fric}}$ and $\overrightarrow{S_{dyn}}$, which correspond to the friction force and dynamic pressure respectively, are introduced to account for the action of the assist gas on the molten metal [15,23]. The friction force is assumed to act as a tangential shear stress applied to the cutting front ($xz$-plane), leading to the neglect of the $y$-axis [15]. The surface tension effect $\overrightarrow{S_{st}}$ is also incorporated into the model, while its tangential force, known as the Marangoni effect, and the resulting temperature dependence of the surface tension coefficient $\gamma$ are neglected.

$$\vec{\nabla} \cdot \vec{u} = 0 \tag{14}$$

$$\rho_\phi \left[\frac{\partial \vec{u}}{\partial t} + \left(\vec{u} \cdot \vec{\nabla}\right) \vec{u}\right] = \vec{\nabla} \cdot \left[-p\, I + \frac{1}{2}\, \mu_\phi \left(\left(\vec{\nabla}\, \vec{u}\right) + \left(\vec{\nabla}\, \vec{u}\right)^T\right)\right] + \rho_\phi\, \vec{g} \tag{15}$$

$$+\overrightarrow{S_{Darcy}} + \left(\overrightarrow{S_{fric}} + \overrightarrow{S_{dyn}} + \overrightarrow{S_{st}}\right) \delta(\phi)$$

$$\overrightarrow{S_{Darcy}} = \begin{cases} K\ (u + v_{d\,x}) \\ K\ v \\ K\ w \end{cases} \tag{16}$$

$$K = -C \left(\frac{(1 - f_l)^2}{{f_l}^3 + b}\right) \tag{17}$$

$$f_l = \begin{cases} 0 \; \forall \, T < T_s \\ \dfrac{T - T_s}{T_l - T_s} \; \forall \, T_s < T < T_l \\ 1 \; \forall \, T > T_l \end{cases} \tag{18}$$

$$\overrightarrow{S_{fric}} = \begin{cases} 2\sqrt{\dfrac{\rho_{gas}\,\mu_{gas}}{d}}\; {v_{AG}}^{\frac{3}{2}} \cos\theta \\ 0 \qquad\qquad\qquad\qquad \forall \, T < T_s \\ 2\sqrt{\dfrac{\rho_{gas}\,\mu_{gas}}{d}}\; {v_{AG}}^{\frac{3}{2}} \sin\theta \end{cases} \tag{19}$$

$$\overrightarrow{S_{dyn}} = \frac{1}{2}\,\rho_{gas}\,{v_{AG}}^2 \cdot e_z \quad \forall \, T < T_s \tag{20}$$

$$\overrightarrow{S_{st}} = \gamma\,\kappa\,\vec{n} \quad \forall \, T < T_s \tag{21}$$

Where $T_s$ and $T_l$ denote the solidus and liquidus temperatures, which are $1673$ and $1727$ $K$, respectively [29], $\mu$ the dynamic viscosity of the phase, $\vec{g}$ the gravitational acceleration vector, $C$ and $b$ the coefficients of the Darcy force, $v_{d\,x}$ the cutting velocity, $f_l$ the liquid fraction, $d$ the plate thickness, $v_{AG}$ the assist gas velocity, $e_z$ the unit vector along the $z$-axis, $\gamma$ the surface tension coefficient, $\kappa$ the curvature and $\vec{n}$ the normal vector of the gas-metal interface.

**Table 2** Summary of the main parameters used in fluid flow computation

| Parameter [unit] | Value | Reference |
|---|---|---|
| $\rho_{304L}$ $[kg.m^{-3}]$ | 7000 | [29] |
| $\mu_{304L}$ $[Pa.s]$ solid / liquid | $1$ / $4\ 10^{-3}$ | [29] |
| $d$ $[mm]$ | 5 | [21] |
| $C$ / $b$ | $10^6$ / $10^{-3}$ | [30] |
| $T_s$ / $T_l$ $[K]$ | 1673 / 1727 | [29] |
| $v_{AG}$ $[m.s^{-1}]$ | 943 | [21] |
| $\gamma$ $[N/m]$ | 0.15 | [31] |

## SPATIAL AND TEMPORAL DISCRETIZATION

To reduce computational cost while maintaining an accurate representation of the cutting front, a multimesh approach is employed. Indeed, although the Level Set method requires a fine spatial discretization for the gas-metal interface and its interfacial phenomena, the fluid flow and, in particular, the heat transfer physics, do not require resolution using the same spatial discretization [30]. The multimesh approach is implemented using an identity mapping nonlocal coupling operator, as proposed by COMSOL Multiphysics®. The Level Set mesh

element size is fixed at $100\ \mu m$, with respective increases of $30\ \%$ and $40\ \%$ for the fluid flow and heat transfer meshes. Note that an excessive increase in the mesh size for either of these physics (fluid flow and heat transfer) may affect the accurate representation of the corresponding physical phenomena. The resolution using this spatial discretization represents $215\ 000$ degrees of freedom (DOF). Regarding the spatial discretization, the time step is set to $20\ \mu s$.

## RESULTS OF THE LASER CUTTING MODEL

The previously described mathematical formulation is used to simulate enables laser cutting process of a $5\ mm$-thick 304L stainless steel plate, with a laser power of $8\ kW$ and an assist gas flow rate of $400\ L.min^{-1}$ [21], corresponding to a velocity of $v_{AG} = 943\ m.s^{-1}$ at the nozzle output.

Fig. 4 presents the half kerf profile and the temperature field within the metallic phase for various cutting velocities. The final time step shown corresponds to a plate displacement of $-5\ mm$ along the $x$-axis. One can observe the influence of the cutting velocity on the kerf geometry, particularly on the cutting front and the sidewall angles. In this study, the focus is on the cutting front angle $\theta$ (Fig. 3), which is particularly relevant in relation to the residual laser energy and the experimental validation of the model [21]. Ideally, when the physical phenomena are accurately captured according to the operating parameters, the cutting front angles should closely match the experimental results.

Fig. 4 shows that higher temperatures, especially at the lower part of the cutting front, are reached at the highest cutting velocity ($24\ m.s^{-1}$). A possible explanation is the longer interaction time between the ejected liquid metal and the laser beam along the cutting front. Furthermore, these simulations also provide information regarding the fluid dynamics, such as the velocity magnitude (Fig. 4).

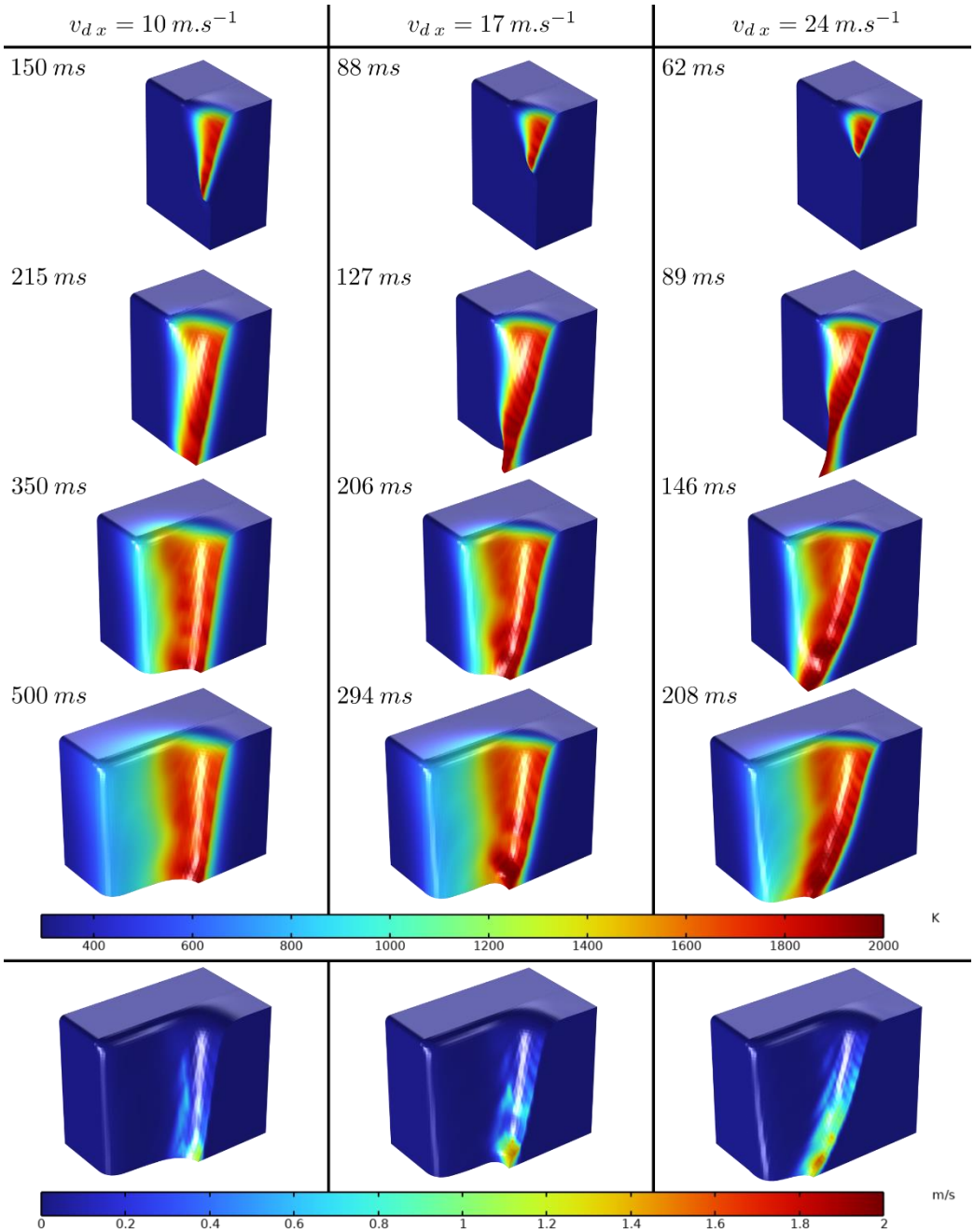



**Fig. 4** Kerf shape and associated temperature and velocity magnitude fields under varying cutting velocities: **10**, **17** and **24** $\boldsymbol{m.s^{-1}}$

Fig. 5 compares the cutting front angles obtained from the experimental study [21] with those predicted by the present simulations. The results indicate a satisfying correlation, with both numerical and experimental data following a similar evolution and exhibiting only minor differences ($< 5°$). Note that the simulated cutting front angles, measured manually post-processing, may be slightly affected by the curvature of the Level Set interface on the top surface of the cutting front.

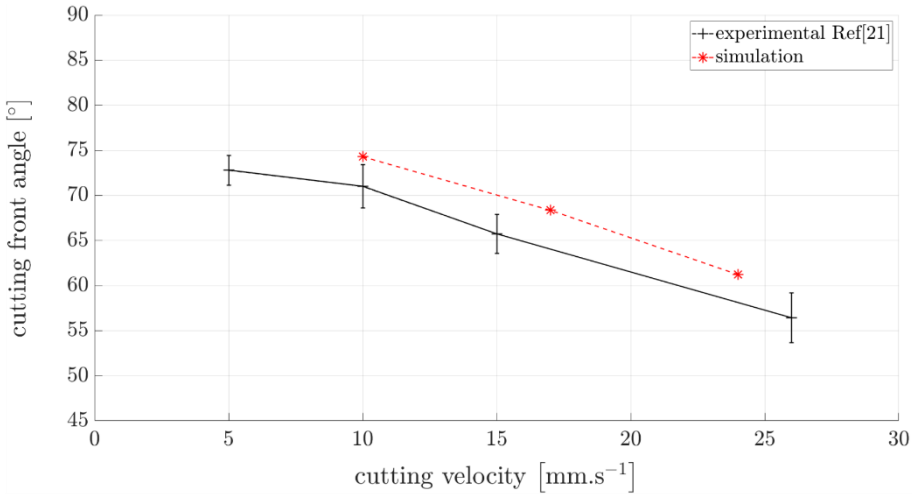



**Fig. 5** Comparison between simulation and experiment of the cutting front angle $\boldsymbol{\theta}$ as a function of the cutting velocity

## RESIDUAL LASER ENERGY QUANTIFICATION

Once the laser cutting process is simulated at the scale of the kerf description, the focus now relates to the quantification of the residual laser energy. Several approaches exist to model laser beam propagation, such as the electromagnetic method [32] and the ray tracing method [33]. For reasons related to feasibility, given the current computing technologies and the geometric scale, the ray tracing approach is employed.

The Level Set method is implicitly described using an Eulerian reference frame, which is incompatible with the explicit trajectory calculations of the ray tracing method. Indeed, the rays must interact with a discrete interface in order to be reflected. The objective is therefore to transform the continuous and diffuse gas-metal interface (from the Level Set method) into a discrete one. To achieve this, a moving mesh method is added to handle the interface transformation through an original dynamic coupling with the Level Set method.

The method consists of moving a mesh along the $x$-axis to track the iso-value $\phi = 0.5$, representing the gas-metal interface in the Level Set method, as governed by equations 22 and 23 during the laser cutting simulation. Here, $\vec{\chi}$ refers to the spatial reference system, and $\overrightarrow{u_{mm}}$

denotes the velocity of the moving mesh. Figure 6 shows the evolution of the moving mesh from time $t_1$ to $t_5$, following the gas-metal interface as defined by the thermohydrodynamic model.

$$\vec{\nabla}^2 \vec{\chi} = \overrightarrow{u_{mm}} \Delta t \tag{22}$$

$$\overrightarrow{u_{mm}} = \frac{0.5 - \phi}{0.5} \hat{x} + 0\hat{y} + 0\hat{z} \tag{23}$$

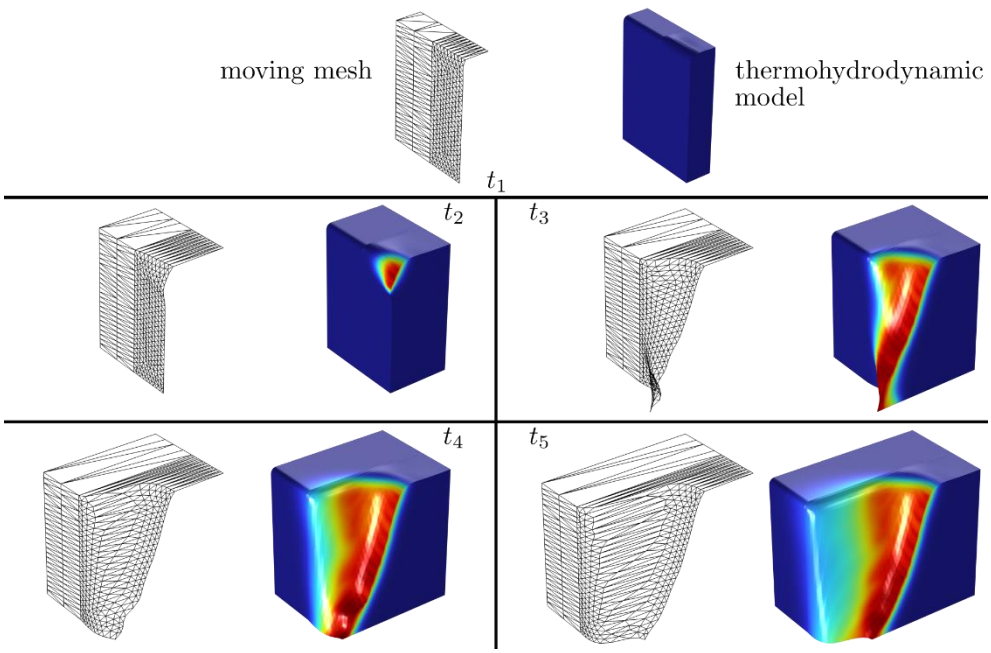



**Fig. 6** Time evolution of the moving mesh method tracking the Level Set interface

After discretizing the cutting front geometry, the ray tracing method can be employed within the same simulation. As shown Fig. 6, elements are stretched, particularly along the side kerf, yet the ray tracing method remains insensitive to this deformation. Fig. 7 shows, for the same previous times (from $t_1$ to $t_5$), the ray propagation reflecting on the cutting front and reaching the background. In accordance with the experimental setup [21], rays are emitted above the laser focal plane (positioned $30\ mm$ above the plate's top surface) and converge toward the focal plane with an angle of 6°, and subsequently diverge following a Gaussian intensity profile.

Before cutting starts, at $t_1$ (figure 7), the background absorbs almost all of the laser beam, corresponding to nearly $4\ kW$ (or half of $P_{laser}$). At $t_2$, the cutting process begins, and the plate progressively masks a portion of the incident laser beam from reaching the background, due to interactions with the material. At $t_5$, when the cutting front geometry tends toward a

quasi-steady state, the residual laser energy approaches therefore a stable distribution. It should be noted that the representation of the residual laser energy on the background is dependent on its spatial discretization.

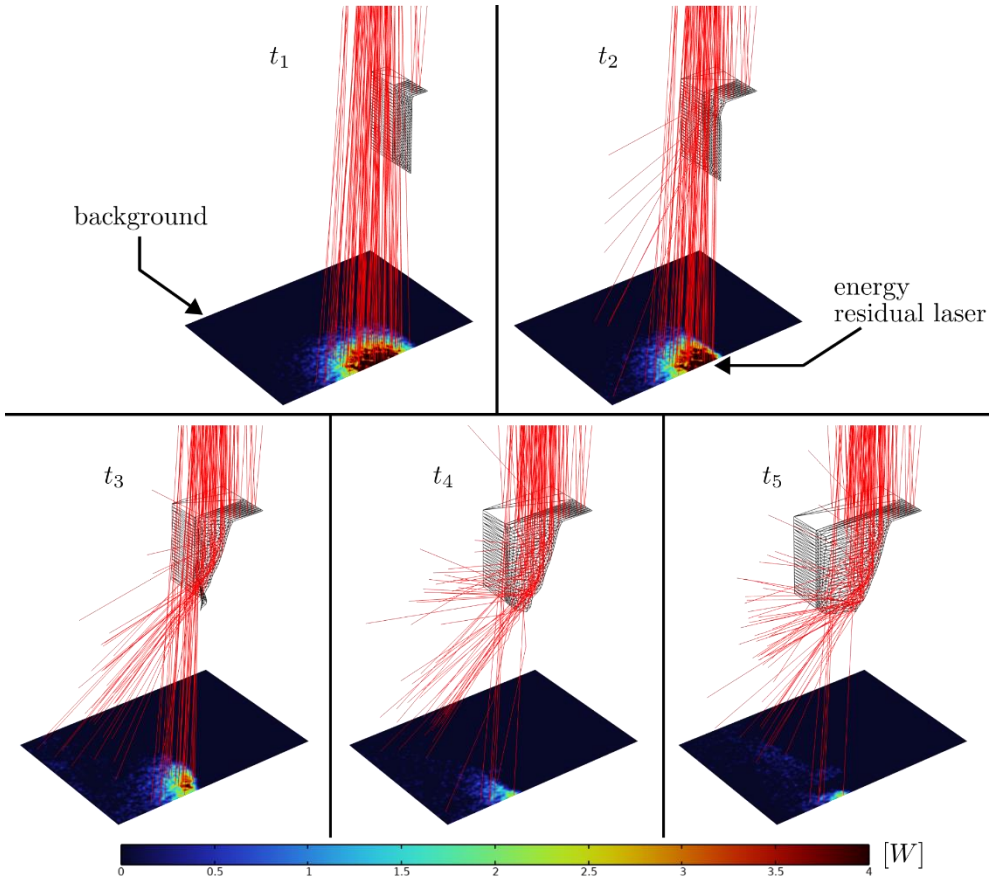



**Fig. 7** Temporal evolution of ray propagation on the moving mesh

Fig. 8 presents the laser beam propagation and the residual laser energy for the three cutting velocities previously simulated using the thermohydrodynamic laser cutting model, after a plate displacement of 5 $mm$, corresponding to a quasi-steady state. The results indicate that as the cutting velocity increases, the residual laser energy decreases. Indeed, as previously discussed, the cutting front angle drops as the cutting velocity increases. Consequently, smaller cutting front angles result in a stronger masking effect on the laser beam reaching the background.

Rays reaching the background are classified into two groups, as also shown in Fig. 8: reflected rays and those that propagate directly to the background. Ray tracing simulations reveal that the dominant portion of the residual laser energy comes from the directly

transmitted rays, since the reflected rays are strongly diffused, and this effect becomes more pronounced with increasing background distance.

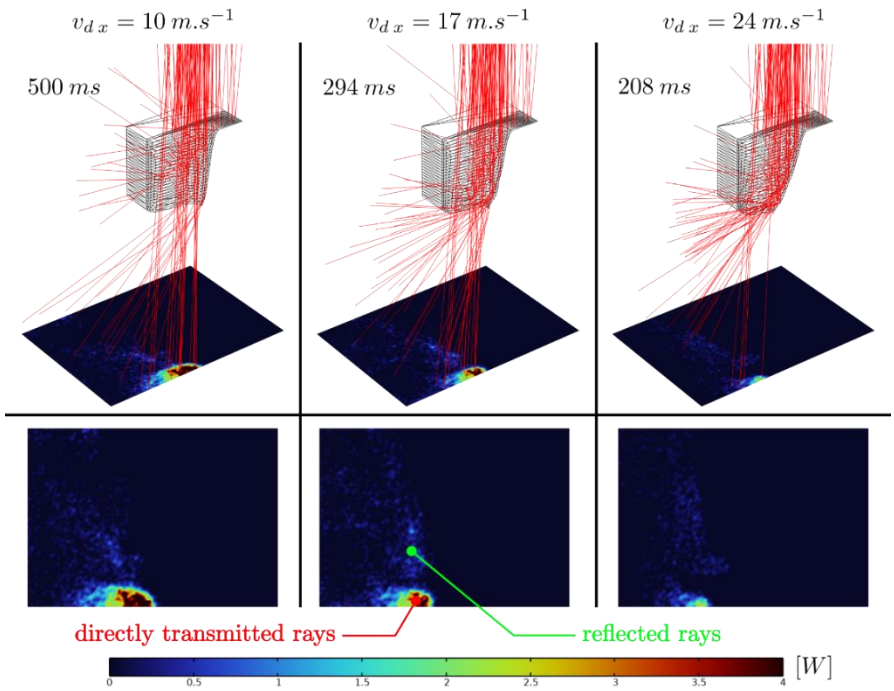



**Fig. 8** Residual laser energy for the three cutting velocities

## CONCLUSION

This paper introduces a thermohydrodynamic model of the laser cutting process applied to the dismantling of nuclear facilities, incorporating heat transfer, fluid flow, and gas-metal interface capturing through the Level Set method. The results demonstrate good agreement with experimental observations by comparing the cutting front angles. It is demonstrated that the model can describe the variation of the cutting front angle with respect to operating parameters, including the cutting velocity examined in this study. A hybrid Level Set – moving mesh method was then introduced to both generate a discrete gas-metal interface and enable the application of ray tracing for residual laser energy quantification. The predicted cutting front geometries is used to quantify the residual laser energy on the background, accounting for both directly transmission and reflection laser. It is shown that the reflected portion is more strongly diffused than the directly transmitted portion, and this effect should become more pronounced as the background distance from the cut plate increases.

Further work will extend the simulations to cutting in air, thereby incorporating the effects of oxidation. Additionally, simulations will be conducted on thicker plates, up to $20\,mm$, where multiple reflections of the laser at the cutting front may become significant. This effect, neglected in the literature on the thinner plates, could be more pronounced in high-thickness materials.

## References


[1] A. B. J. SULIVAN and P. T. HOULDCROFT: 'Gas-jet laser cutting', *British Welding Journal*, Vol. 14, No. 8, pp. 443-445, 1967.

[2] Y. ARATA and I. MIYAMOTO: 'Generation and applications of a CW high power $CO_2$ gas laser', *Technology Reports Osaka University*, Vol. 17, pp. 285-290, 1967.

[3] G. PADMANABHAM and R. BATHE: 'Laser Materials Processing for Industrial Applications', *Proceedings of the National Academy of Sciences, India Section A: Physical Sciences*, Vol. 88, No. 3, pp. 359-374, somewhere, 2018.

[4] N. MUHAMMAD, D. WHITEHEAD, A. BOOR and L. LI: 'Comparison of dry and wet fibre laser profile cutting of thin 316L stainless steel tubes for medicinal device applications', *Journal of Materials Processing Technology*, Vol. 210, No. 15, pp. 2261-2267, 2010.

[5] J. LESCHKE, A. BARROI, B. EMDE, S. KAIERLE and J. HERMSDORF: 'Investigations on underwater laer cutting for decommissioning of marine constructions', *Conference on Maritime Energy (COME)*, Hamburg, Germany, 2017.

[6] K. TAMURA, R. ISHIGAMI and R. YAMAGISHI: 'Laser cutting of thick steel plates and simulated steel components using a 30 kW fiber laser', *Journal of Nuclear Science and Technology*, Vol. 53, No. 6, pp. 916-920, 2016.

[7] Y. ARATA, H. MARUO, I. MIYAMOTO and S. TAKEUCHI 'Dynamic Behavior in Laser Gas Cutting of Mild Steel', *Transactions of JWRI*, Vol. 8, No. 2, pp. 175-179, 1979.

[8] B. S. YILBAS: 'Study of Parameters for $CO_2$ Laser Cutting Process', *Materials and Manufacturing Processes*, Vol. 13, No. 4, pp. 517-536, 1998.

[9] C. WANDERA and V. KUJANPAA: 'Characterization of the melt removal rate in laser cutting of thick-section stainless steel', *Journal of Laser Applications*, Vol. 22, No. 2, pp. 62-70, 2010.

[10] M. SOBIH, P. L. CROUSE and L. LI: 'Elimination of striation in laser cutting of mild steel', *Journal of Physics D: Applied Physics*, Vol. 40, No. 22, pp. 6908-6916, 2007.

[11] D. SCHUÖCKER: 'Theoretical model of reactive gas-assisted laser cutting including dynamic effects', *High Power Lasers and Their Industrial Applications*, Vol. 650, No. 1, pp. 210-219, 1986.

[12] G. V. ERMOLAEV, O. B. KOVALEV, A. M. ORISHICH and V. M. FOMIN: 'Mathematical modelling of striation formation in oxygen laser cutting of mild steel', *Journal of Physics D: Applied Physics*, Vol. 39, No. 19, pp. 4236, 2006.

[13] E. H. AMARA, T. AOUDJIT, K. KHELOUFI, T. TAMSAOUT, S. AGGOUNE, A. AHMANACHE, F. HAMADI and K. BOUGHERARA: 'Simulation by temperature gradient adaption of wavelength effect in metal laser cutting', *Journal of Laser Applications*, Vol. 29, No. 2, pp. 022209, 2017.

[14] E. H. AMARA, K. KHELOUFI, T. TAMSAOUT, R. FABBRO and K. HIRANO: 'Numerical investigations on high-power laser cutting of metals', *Applied Physics A*, Vol. 119, pp. 1245-1260, 2015.

[15] K. KHELOUFI, E. H. AMARA and A. BENZAOUI: 'Numerical Simulation of Transient Three-Dimensional Temperature and Kerf Formation in Laser Fusion Cutting', *Journal of Heat and Mass Transfer*, Vol. 137, No. 11, pp. 112101, 2015.

[16] K. HIRANO and R. FABBRO: 'Experimental investigation of hydrodynamics of melt layer during laser cutting of steel', *Journal of Physics D: Applied Physics*, Vol. 44, No. 10, pp. 105502, 2011.
[17] Y. NIE, K. W. Q. LOW, Z. LIU, L. YANG, Y. WANG, T. LI, H. LI and Y. HE: 'Mechanics insights into particle ejection during laser cutting of metal alloys', *The International Journal of Advanced Manufacturing Technology*, Vol. 137, pp. 1173-1187, 2025.
[18] C. CHAGNOT, G. DE DINECHIN and G. CANNEAU: 'Cutting performances with new industrial continuous wave ND:YAG high power lasers: For dismantling of former nuclear workshops, the performances of recently introduced high power continuous wave ND:YAG lasers are addressed', *Nuclear Engineering and Design*, Vol. 240, No. 10, pp. 2604-2613, 2010.
[19] E. PORCHERON, C. DAZON, T. GELAIN, C. CHAGNOT, I. DOYEN, C. JOURNEAU, E. EXCOFFIER and D. ROULET: 'Fukushima Daiichi debris retrieval: results of aerosol characterization during laser cutting of non-radioactive corium simulants.', *Journal of Nuclear Science and Technology*, Vol. 58, No. 1, pp. 443-445, 2021.
[20] S. OSHER and J. A. SETHIAN: 'Fronts propagating with curvature-dependent speed: Algorithms based on Hamilton-Jacobi formulations', *Journal of Computational Physics*, Vol. 79, No. 1, pp. 12-49, 1988.
[21] R. MEILLOUR, M. COURTOIS, C. NAHED, M. CARIN, F. SIMON and I. DOYEN: 'Primary investigation of oxidation influence on the cutting front profile during high-thickness laser cutting', *Journal of Laser Applications*, Vol. 37, No. 2, pp. 022021, 2025.
[22] J. DUAN, H. C. MAN and T. M. YUE: 'Modelling the laser fusion cutting process: I. Mathematical modelling of the cut kerf geometry for laser fusion cutting of thick metal', *Journal of Physics D: Applied Physics*, Vol. 34, No. 14, pp. 2127-2134, 2001.
[23] M. VICANEK, G. SIMON, H. M. URBASSEK I. DECKER: 'Hydrodynamic instability of melt flow in laser cutting', *Journal of Physics D: Applied Physics*, Vol. 20, No. 1, pp. 140-145, 1987.
[24] C. LI, C. XU, C. GUI and M. D. FOX: 'Level Set evolution without re-initialization: a new variational formulation', *IEEE computer society conference on computer vision and pattern recognition*, Vol. 1, pp. 430-436, 2005.
[25] A. M. PROKHOROV: 'Laser Heating of Metals', *CRC Press*, ISBN 9781351073943, 1990.
[26] K. HIRANO, R. FABBRO and M. MULLER: 'Experimental determination of temperature threshold for melt surface deformation during laser interaction on iron at atmosphere pressure', *Journal of Physics D: Applied Physics*, Vol. 44, No. 43, pp. 435402, 2011.
[27] C. S. KIM: 'Thermophysical properties of stainless steels', *Argonne National Laboratory*, 1975.
[28] F. DAUSINGER and J. SHEN: 'Energy Coupling Efficiency in Laser Surface Treatment', *ISIJ Journal*, Vol. 33, No. 9, pp. 925-933, 1993.
[29] K. C. MILLS: *Recommended values of thermophysical properties for selected commercial alloys*, Woodhead Publishing, 2002.
[30] M. COURTOIS, M. CARIN, P. LE MASSON and S. GAIE: 'Complete 3D heat and fluid flow modeling of keyhole laser welding and methods to reduce calculation times', *Mathematical Modeling of Weld Phenomena*, Vol. 12, 2018.
[31] V. KLAPCZYNSKI, D. LE MAUX, M. COURTOIS, E. BERTRAND and P. PAILLARD: 'Surface tension measurements of liquid pure iron and 304L stainless steel under different gas misxtures', *Journal of Molecular Liquids*, Vol. 350, pp. 118558, 2022.
[32] M. COURTOIS, M. CARIN, P. LE MASSON, S. GAIED and M. BALABANE: 'A new approach to compute multi-reflections of laser beam in a keyhole for heat transfer and fluid flow modelling in laser welding', *Journal of Physics D: Applied Physics*, Vol. 46, No. 50, pp. 505305, 2013.
[33] J. DALIGAULT, M. DAL, C. GORNY, F. COSTE and R. FABBRO: 'Combination of Eulerian and ray-tracing approaches for copper laser welding simulation', *Journal of Laser Applications*, Vol. 34, No. 4, pp. 042042, 2022.

# II Joint Properties

## a) Microstructure and Mechanical Properties

# MODELING AND SIMULATION OF THE ANISOTROPIC THERMAL EXPANSION OF TI-6AL-4V PROCESSED BY PBF-LB/M

T. MAYER*, P. CAPOZZI*, M. HOFMANN*, F. FRISO**, R. RADIS**

*ZHAW Zurich University of Applied Sciences, Institute of Mechanical Systems, 8401, Winterthur, Switzerland
**ZHAW Zurich University of Applied Sciences, Institute of Materials and Process Engineering, 8401, Winterthur, Switzerland

*DOI 10.3217/978-3-99161-089-2-019, license CC BY 4.0*
*https://creativecommons.org/licenses/by/4.0/deed.en*
*This CC license does not apply to third party material and content noted otherwise.*

## ABSTRACT

Additive manufacturing (AM), particularly Laser Powder Bed Fusion of Metals (PBF-LB/M), enables the production of geometrically complex Ti-6Al-4V components with high precision and design flexibility for a wide range of applications in the aerospace, chemical and process engineering, energy, and biomedical sectors. However, rapid solidification in PBF-LB/M produces a non-equilibrium martensitic α′ microstructure with pronounced texture, leading to anisotropic mechanical and thermal behaviour. In particular, the apparent thermal expansion of PBF-LB/M Ti-6Al-4V has been found to be anisotropic due to strains induced during the $\alpha' \rightarrow \beta$ phase transformation (850–1000 °C). These transformation strains lead to pronounced apparent expansion along the build-direction and reduced in-plane apparent expansion. In PBF-LB/M manufactured components, this anisotropy can lead to unexpected residual stresses during the AM process or mechanical integrity issues during post-manufacturing heat-treatments or operation. This study focusses on the modelling of the anisotropic apparent expansion of Ti-6Al-4V and its implementation for Finite Element Analysis (FEA) to enable simulative investigations of the residual stress and distortion evolution in AM components.

A new model is introduced that separates isotropic thermal and transversally isotropic transformation strains. The model accounts for the path and temperature dependent transformation characteristics with varying transformation strains developing during heating ($\alpha' \rightarrow \beta$) and cooling ($\beta \rightarrow \alpha + \beta$). To make this model available to FEA, it was implemented in the FE software Abaqus via an UEXPAN subroutine. The effectiveness of the apparent expansion model and its implementation is demonstrated by comparing simulated and experimentally measured dilatometer curves. In addition, the impact of this anisotropic expansion on the residual stress development is investigated using thermo-mechanical process simulations of 1) a single laser welding track, and 2) the distortion of a cantilever following support structure removal.

The model successfully predicted the apparent expansion in a cylinder printed at a 45° angle. Furthermore, significant differences in vertical stress components and induced plastic strain in a single weld track were found. These are attributed to the additional constraints imposed by the transversally isotropic expansion underpinning the relevance of accounting for the transformation strain. Predictions of distortions in a cantilever following support removal were, however, significantly better when considering isotropic thermal strain only. This could potentially be explained by differences of the PBF-LB/M microstructure in the presence of a support structure. Understanding these mechanisms is crucial for optimizing the mechanical

integrity and dimensional stability of PBF-LB/M-fabricated Ti-6Al-4V components in engineering applications subjected to post-processing heat-treatments or high-temperature applications.

Keywords: PBF-LB/M, Ti-6Al-4V, Thermal expansion, Anisotropy, Phase transformation

## INTRODUCTION

The Laser Powder Bed Fusion process of Metals (PBF-LB/M) induces rapid solidification conditions with cooling rates exceeding $10^6$ K/s [1-4]. In Ti-6Al-4V ,this results in a non-equilibrium martensitic $\alpha'$ microstructure within columnar prior $\beta$ grains that grow epitaxially over multiple layers with their $\langle 001 \rangle_\beta$ direction oriented along the thermal gradient [5-13]. Acicular martensitic $\alpha'$ laths precipitate on the prior $\beta$ grain boundaries obeying the Burgers orientation relationship [14-17] and growing along their invariant directions leading to a crystallographic and morphological texture due to crystallographic variant selection [10], [16]. Thus, the as-printed microstructure deviates significantly from the typically equiaxed bimodal $\alpha + \beta$ grain distribution observed in Ti-6Al-4V components conventionally manufactured by forging [18]. These anisotropic microstructural features [19-23], directly affect the mechanical response of PBF-LB/M-fabricated Ti-6Al-4V [9], [24].

While the anisotropy of the thermal expansion of Ti-alloys caused by the hexagonal close-packed crystal structure and the respective influence of alloy composition has been well studied [25-28], less attention has been paid to the effect of the particular PBF-LB/M microstructure and its impact to post-processing or service conditions. Recent experimental as well as theoretical studies of the present authors [29], have revealed that the apparent thermal expansion of PBF-LB/M-fabricated Ti-6Al-4V exhibits a pronounced build-direction dependence, particularly in the temperature range associated with the $\alpha' \rightarrow \beta$ transformation, i.e. 850 – 1000 °C. Vertically built specimens show a sharp increase in the apparent thermal expansion, whereas horizontally built ones exhibit a dip. These macroscopic effects are not fully captured by phase-specific lattice parameter measurements (e.g., synchrotron X-ray diffraction) [30], [31]. As outlined by [29], the build-direction dependent anisotropic apparent expansion can be explained by the crystallographic and morphological texture of the PBF-LB/M microstructure and the respective anisotropic transformation strains that are superimposed to the effectively isotropic thermal expansion. The anisotropic apparent expansion is expected to have an impact on additively manufactured (AM) components during post-processing heat-treatments or in service conditions at elevated temperatures.

Severe temperature gradients that occur during rapid transient melting and cooling processes together with phase transformations and local plastification during solidification cause either residual stresses or distortions in PBF-LB/M components [32]. To investigate the development of residual stresses and distortion during the PBF-LB/M process dedicated finite element (FE) based thermo-mechanical process simulation (TMPS) approaches have been developed [33-35]. Modern TMPS models are categorized into single-layer [36-44], and multi-layer TMPS models [45-50].

Single-layer models are focused on the laser beam vicinity, while multi-layer approaches are used to investigate temperature, stress, and distortion fields in PBF-LB/M structures. To

study temperatures and stresses along the laser trajectory, single-layer TMPS models typically use a moving Goldak heat source [51] to simplify the complex melt-pool physics [38]. Such models have been used to study the effect of process parameters on microstructure [42-44], distortion [52], and residual stress [35], [41], [46] in PBF-LB/M components.

Modern high-fidelity multi-layer TMPS models follow a multiscale approach to analyse global residual stresses and distortions in AM parts [47-50]. Single-layer microscale models can be used to derive an equivalent heat source representing the melt pool. To account for scanning strategy effects, this is imposed to a hatch block in a mesoscale model [48], [49], [50]. The resulting temperature histories or inherent strains are further applied to a thermo-mechanical [49], [50] or a purely static mechanical [53], [54] macroscopic model, respectively. Element activation is either hatch block wise [48], or layer wise (superlayer approach) [53], [54] with the former approach being the best compromise between accuracy and numerical efficiency [55]. A coupled activation and heat input approach using event series as recently introduced in the commercial FE software Abaqus [49], [50] demonstrated excellent agreement between measured and predicted residual strains in the NIST AM Simulation Benchmark [56].

A simplified weakly-coupled TMPS model implemented in the commercial FE Software Ansys, uses a superlayer approach [57]. Thereby, superlayers, i.e. aggregates of actual powder layers represented by a finite element layer, are instantaneously activated layer-by-layer at close to melting temperature. The resulting temperature field following cooldown is applied in a subsequent mechanical simulation to predict the residual stresses that arise from the constrained thermal contraction. Despite significant simplifications of the complex physical phenomena on a local level, this industrially relevant approach allows to estimate residual stresses and distortions on a part-level at low numerical cost [58]. The accuracy of all outlined simulation approaches is strongly influenced by the underlying constitutive models describing the thermo-physical and thermo-mechanical behaviour of materials. Specifically, the thermal expansion has a significant impact on predicted residual stresses and distortions.

In the present study, a comprehensive model is introduced to describe the apparent build-direction dependent expansion strain in PBF-LB/M manufactured Ti-6Al-4V (Grade 23) in the as-build condition for Finite Element Analyses (FEA). Thereby, the isotropic thermal expansion strain $\varepsilon_{th}$ is modelled independently from the transversally isotropic transformation strain $\varepsilon_{tr}^{h}$ that arises from the $\alpha' \rightarrow \beta$ transformation during heating at > 850 °C. During cooldown, the transformation strain $\varepsilon_{tr}^{c}$ resulting from the $\beta \rightarrow \alpha + \beta$ transformation is modelled as isotropic. In a first step, the model and its implementation as an UEXPAN subroutine for the FE software Abaqus are introduced. To demonstrate the effectiveness and relevance of the apparent expansion model and its implementation, it is applied 1) to predict the expansion in a 45° tilted cylinder, 2) to investigate the residual stresses in a single PBF-LB/M laser weld-track (single-layer TMPS model), and 3) to predict the distortion of a cantilever following stress relief after support structure removal (multi-layer TMPS model).

The availability of a FE simulation model able to account for the anisotropy of the apparent expansion is a prerequisite to investigate the impact of the experimental findings in [29], and to gain more detailed understanding of the underlying mechanisms generating residual stresses and distortion in PBF-LB/M-fabricated Ti-6Al-4V components. This is crucial for optimizing the mechanical integrity and dimensional stability of PBF-LB/M-fabricated Ti-6Al-4V

components in engineering applications subjected to post processing heat treatments or high-temperature applications.

## METHODS

### MATERIAL & EXPERIMENTS

The apparent expansion model established in this study is based on findings presented in [29] on the build-orientation dependent apparent thermal expansion behaviour of Ti-6Al-4V as manufactured by PBF-LB/M.

Vertically and horizontally oriented cylindrical samples were printed on an Additive Industries Metal*FAB1* PBF-LB/M system in single laser mode applying the process parameters summarized in Table 1. The process was conducted under Ar atmosphere using build plate heating at 150 °C. Plasma atomized Ti-6Al-4V (Grade 23) powder was supplied with a chemical composition according to Table 2, an aspect ratio of $D_{min}/D_{max}$ = 0.97, and a characteristic particle size distribution of $D_{10}$ = 21 µm, $D_{50}$ = 35 µm, and $D_{90}$ = 49 µm.

**Table 1** PBF-LB/M process parameters: Ti-6Al-4V (Grade 23).

| Laser Power $P$ [W] | Scan Velocity $v$ [mm/s] | Laser Spot Diameter $d$ [mm] | Layer Thickness $t$ [mm] | Hatch Spacing $h$ [mm] | Hatch Angle $\alpha$ [°] |
|---|---|---|---|---|---|
| 365 | 1025 | 0.10 | 0.06 | 0.05 | 67° (rotating) |

Dilatometry was further conducted on cylindrical ($D$8 mm × $L$120 mm) samples with vertical and horizontal build-orientation in the as-built condition. A NETZSCH DIL402 Expedis® Supreme dilatometer was used to measure the total thermally induced elongation under quasi-static conditions with a heating-rate of 5 K/min in an Ar atmosphere up to 1100 °C. Slow cooling to 450 °C was subsequently applied at a cooling-rate of 5 K/min. During the experiments a controlled measuring force of 0.2 N was maintained and a W standard material was used to correct for the thermal expansion of the measuring system.

**Table 2** Chemical composition [%w]: Ti-6Al-4V (Grade 23, ASTM F3001) powder by AP&C.

| Ti | Al | V | Fe | O | C | N | H | Y | Others (each) | Others (total) |
|---|---|---|---|---|---|---|---|---|---|---|
| bal. | 6.32 | 4.03 | 0.21 | 0.10 | 0.01 | 0.01 | 0.002 | <0.001 | <0.1 | <0.4 |

To verify the effectiveness of the thermal expansion model in the multi-layer thermo-mechanical process simulation, six cantilevers – i.e. three oriented along and three transverse to the Ar gas flow – were manufactured under the same conditions as the dilatometry samples. Subsequently, the support structure of the cantilevers was EDM wire-cut 1 mm above the substrate to release residual stresses according to the cut compliance method (CCM), see Fig. 1. The resulting distortion was measured along three lines (middle, left, right) at the top

of the cantilever using a tactile coordinate measurement machine. Finally, an overall average was calculated for all measurements of the two respective cantilever orientations, i.e. along and transverse to the gas flow.

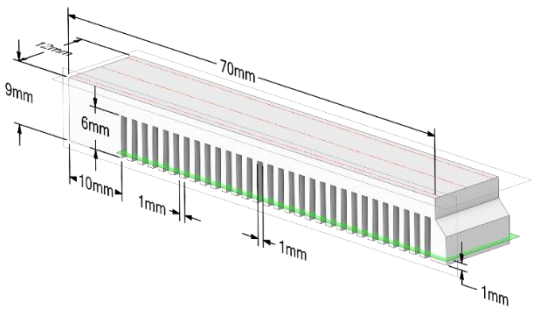



**Fig. 1** Cantilever for validation of multi-layer TMPS according to the cut compliance method. Green: cutting plane. Red: measurement paths for distortions

## MODELLING OF APPARENT EXPANSION

As outlined in [29], the apparent expansion $\varepsilon_{exp}$ observed in the dilatometer experiments of as-printed Ti-6Al-4V varies significantly with the underlying build-orientation, Fig. 2. While the actual thermal expansion strain $\varepsilon_{th}$ is independent of the build-orientation, the transformation strain $\varepsilon_{tr}^{h}$ arising from the $\alpha' \rightarrow \beta$ transformation during heating at approximately 850 °C to 1000 °C varies strongly with the build-orientation, i.e. it is positive for vertically and negative for horizontally built samples. During cooldown from the fully transformed $\beta$ phase to $\alpha + \beta$, the resulting transformation strain $\varepsilon_{tr}^{c}$ can be considered as isotropic.

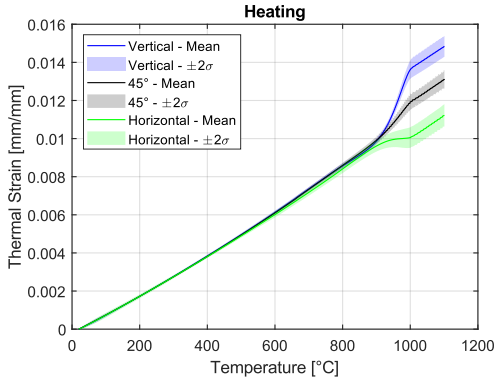



**Fig. 2** Apparent expansion for three build-orientations as determined from dilatometry [29]

Following these experimental observations, a model to describe the total apparent expansion needs to account for

1) path-dependency, i.e. differing behaviour during heating and cooling
2) isotropic thermal expansion
3) transversally isotropic transformation strain during heating, and
4) isotropic transformation strain during cooling.

Consequently, the total apparent expansion strain $\varepsilon_{exp}$ in longitudinal ($L$) and transverse ($T$) direction is additively decomposed into an isotropic thermal expansion strain $\varepsilon_{th}$ and a transversally isotropic transformation strain during heating ($h$) – i.e. $\varepsilon_{tr,L}^{h}$ and $\varepsilon_{tr,T}^{h}$, respectively – and an isotropic transformation strain during cooling ($c$) – i.e. $\varepsilon_{tr}^{c}$ according to Eq. (1).

Heating (d$T$ > 0)
$$\varepsilon_{exp,L}^{h}(T) = \varepsilon_{th}(T) + \varepsilon_{tr,L}^{h}(T) \tag{1a}$$
$$\varepsilon_{exp,T}^{h}(T) = \varepsilon_{th}(T) + \varepsilon_{tr,T}^{h}(T) \tag{1b}$$

Cooling (d$T$ < 0)
$$\varepsilon_{exp,L}^{c}(T) = \varepsilon_{th}(T) + \varepsilon_{tr}^{c}(T) \tag{1c}$$
$$\varepsilon_{exp,T}^{c}(T) = \varepsilon_{th}(T) + \varepsilon_{tr}^{c}(T) \tag{1b}$$

Longitudinal $\varepsilon_{tr,L}^{h}$ and transverse $\varepsilon_{exp,T}^{h}$ transformation strains are determined from dilatometry on vertically and horizontally oriented PBF-LB/M samples, respectively. To discriminate between heating and cooling paths, the temperature increment d$T$ is evaluated, indicating heating if positive and cooling if negative. For constant temperatures, i.e. d$T$ = 0, the increment of the apparent expansion strain is neutral d$\varepsilon_{exp}$ = 0.

The isotropic thermal expansion strain $\varepsilon_{th}$ is modelled using a third-order polynomial

$$\varepsilon_{th}(T) = p_3(T - T_0)^3 + p_2(T - T_0)^2 + p_1(T - T_0) \tag{2}$$

Therein, $T_0$ denotes the reference temperature which is defined as 20 °C throughout this study. $p_1$ to $p_3$ describes the polynomial coefficients.

The transversally isotropic transformation strain $\varepsilon_{tr}$ is modelled using two state functions, i.e. $\phi^h(T)$ and $\phi^c(T) \in [0, 1]$, which reflect the progress of the $\alpha' \rightarrow \beta$ transformation during heating and the $\beta \rightarrow \alpha + \beta$ transformation during cooling, respectively. Inspired by the experimental characteristic of the apparent expansion $\varepsilon_{exp}$, the temperature dependent transformation strain is modelled as the product of a constant transformation strain $\varepsilon_0$ and the respective temperature dependent state function acting as a weighting function.

$$\varepsilon_{tr}^{h}(T) = \varepsilon_0^h \phi^h(T) \tag{3a}$$
$$\varepsilon_{tr}^{c}(T) = \varepsilon_0^c (\phi^c(T) - 1) \tag{3b}$$

Eq. (3) is valid both for $L$ and $T$ components, whereas $\varepsilon_0$ differs for the $L$ and $T$ components during heating assuming transversal isotropy – i.e. $\varepsilon_{0,L}^{h} \neq \varepsilon_{0,T}^{h}$ – while it is assumed isotropic

during cooling – i.e. $\varepsilon_{0,L}^{c} = \varepsilon_{0,T}^{c}$. The different transformation characteristics during heating and cooling are thereby accounted for by separate state functions – i.e. $\phi^{h}(T) \neq \phi^{c}(T)$.

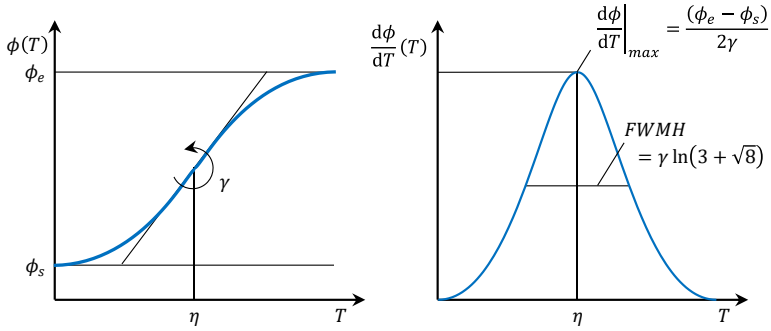



**Fig. 3** Schematic illustrating the state functions ϕ(T) and their temperature derivative

In agreement with the experimental dilatometry [29], a sigmoid function, specifically a generalized $tanh$-function, is adopted for the state functions $\phi(T)$ showing the best agreement between model and experimental data.

$$\phi(T) = \phi_s + \frac{1}{2}(\phi_e - \phi_s)\left(\tanh\left(\frac{T-\eta}{\gamma}\right) + \tanh\left(\frac{\eta}{\gamma}\right)\right) \quad (4)$$

Considering, that the $tanh$-function can be interpreted as a cumulative density function (CDF), i.e. the integral, of a $sech$ probability density function (PDF), the model parameters can be readily interpreted, see Fig. 3:

- $\eta$ corresponds to the temperature at the peak of the PDF or the turning point of the CDF [°C]
- $\gamma$ is associated with the width of the peak of the PDF (FWMH – Full Width at Mean Height) or the maximum slope of the transition from 0 to 1 in the CDF [°C]
- $\phi_s$ corresponds to the value of the state variable at $T \ll \eta$, i.e. the lower asymptote of the CDF [-]
- $\phi_e$ corresponds to the value of the state variable at $T \gg \eta$, i.e. the upper asymptote of the CDF [-]

The temperature characteristic of the transformation strain is fully described by $\phi(T)$ in Eq. (4). Both for heating and cooling, the lower and upper asymptotes of the state functions were defined as $\phi_s$ = 0 and $\phi_e$ = 1, respectively. Due to the different characteristics of the transformation during heating and cooling, the model parameters $\eta$ and $\gamma$ differ - i.e. $\eta^{h}$, $\gamma^{h}$, for $\phi^{h}$ and $\eta^{c}$, $\gamma^{c}$ for $\phi^{c}$. For simplicity, the directional dependence of the transformation strain is fully described by different $\varepsilon_0$ values for *L* and *T*.

To make this model available for FE simulations, an user-subroutine UEXPAN has been developed for the commercial FE software Abaqus. The UEXPAN needs to provide the increment of the apparent expansion strain $\Delta\varepsilon_{exp}$ (i.e. EXPAN) over a time increment and for

all relevant directional components. Thereby, it can be accounted for dependencies of the expansion strain both on temperature and internal state functions. In addition, UEXPAN allows to model orthotropic thermal expansion, when increments of the expansion strain are provided in three orthogonal directions of a material coordinate system, i.e. $\Delta\varepsilon_{exp,11}$, $\Delta\varepsilon_{exp,22}$, and $\Delta\varepsilon_{exp,33}$. By defining two components as equivalent, e.g. $\Delta\varepsilon_{exp,11} = \Delta\varepsilon_{exp,22} = \Delta\varepsilon_{exp,T}$ and different to a third component $\Delta\varepsilon_{exp,33} = \Delta\varepsilon_{exp,L}$, a transversally isotropic expansion can be realized.

In addition to the incremental form of the expansion model defining EXPAN, the user subroutine also allows to define differential strains as temperature derivatives (DEXPANDT).

$$\frac{\mathrm{d}\varepsilon_{exp}}{\mathrm{d}T}(T) = \frac{\mathrm{d}\varepsilon_{th}}{\mathrm{d}T}(T) + \frac{\mathrm{d}\varepsilon_{tr}}{\mathrm{d}T}(T) \tag{5a}$$

$$\frac{\mathrm{d}\varepsilon_{th}}{\mathrm{d}T}(T) = 3p_3(T - T_0)^2 + 2p_2(T - T_0) + p_1 \tag{5b}$$

$$\frac{\mathrm{d}\varepsilon_{tr}}{\mathrm{d}T}(T) = \varepsilon_0 \ \frac{\mathrm{d}\phi}{\mathrm{d}T}(T) = \frac{\varepsilon_0}{2\gamma}\left(\phi_e \ - \phi_s \ \right)\mathrm{sech}^2\left(\frac{T-\eta}{\gamma}\right) \tag{5c}$$

*Model Parameter Identification*

Due to the readily interpretable form of the expansion model, the model parameters can be directly determined from an analysis of dilatometer data. Thereby, dilatometer measurements on vertically built samples are used to determine the parameters for the *L*-components, while data from horizontally built samples yield the parameters for the *T*-components of the expansion model. The following data analysis routine was implemented in MATLAB to determine the nine remaining model parameters.

- **Data Preparation**
  All apparent expansion strain measurements were resampled every 1 °C at equal temperatures. First and second temperature derivatives were calculated and smoothed using local quadratic regression (*loess*) and a 10% span of the data vector.
- **Background Subtraction**
  Based on the first derivative of the apparent expansion strain, $\mathrm{d}\varepsilon_{exp}/\mathrm{d}T$, the peak was identified and removed between 780 °C and 1050 °C (heating) and between 805 °C and 940 °C (cooling), respectively. The remaining data was then fitted with a second order polynomial and shifted to form an overall mean curve, i.e. the background ($\mathrm{d}\varepsilon_{\mathrm{th}}/\mathrm{d}T$). The background is subtracted from the $\mathrm{d}\varepsilon_{exp}/\mathrm{d}T$ curve leaving the first derivative of the transformation strain $\mathrm{d}\varepsilon_{tr}/\mathrm{d}T$.
- **Peak Analysis**
  The peaks of the $\mathrm{d}\varepsilon_{tr}/\mathrm{d}T$ curve ($sech$-PDF) are identified, characterising the turning points in the state functions $\phi(T)$ ($tanh$-CDF). The temperature at the peak defines the model parameter $\eta$, while $\gamma$ is determined from its $FWMH = \gamma\ln\left(3+\sqrt{8}\right)$, and the transformation strain $\varepsilon_0 \ = 2H\gamma$ from the peak height $H$.

- **Parameter Optimisation**
  Following a first analytical identification of the model parameters an overall model fit using the MATLAB optimizer *fmincon* was applied to improve overall accuracy.

Fig. 4 shows a comparison of the respective model predictions using analytically determined model parameters (green line) with measured apparent expansion data (black circles) and the optimized model (red line). In addition, the first derivatives of the thermal and the transformation strains are shown, underpinning the already good agreement of the analytical approach. The optimized model parameters are listed in Table 3 and Table 4.

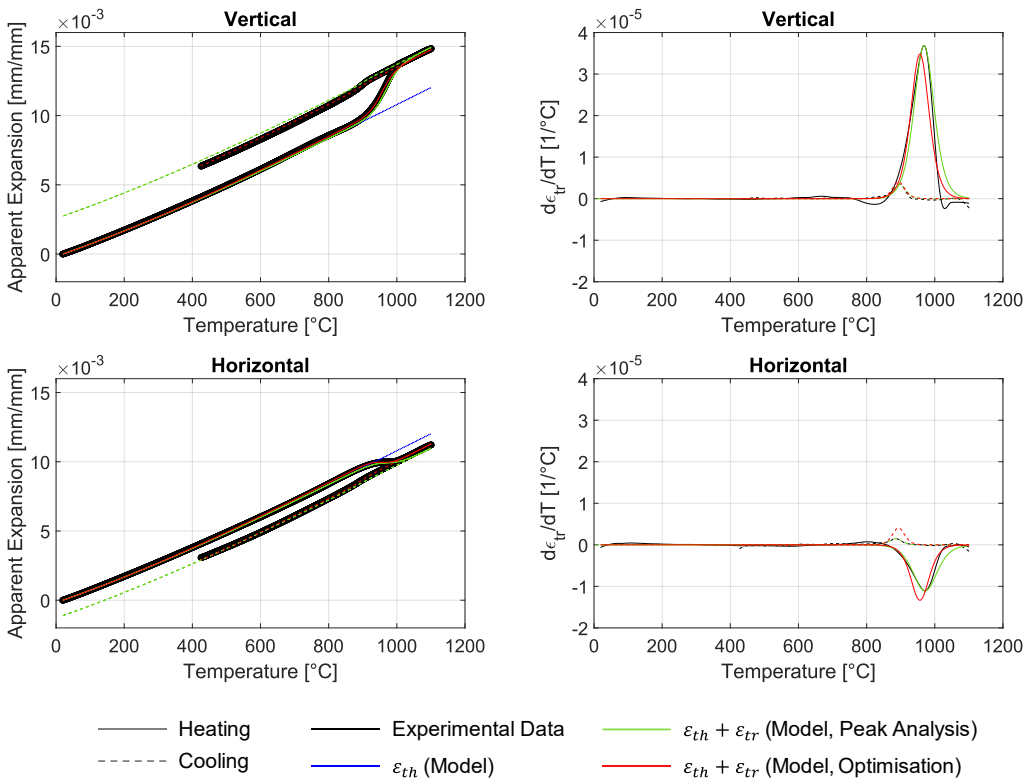



**Fig. 4** Comparison of measured apparent expansion strain (black circles) with model predictions using parameters 1) as analytically determined (green) and 2) as optimised (red). The right column shows the first derivative of the transformation strains $d\varepsilon_{tr}/dT$ after background subtraction.

**Table 3** Optimised model parameters for thermal strain model $\varepsilon_{th}(T)$, cf. Eq. (2).

| $p_3$ | $p_2$ | $p_1$ |
|---|---|---|
| -1.3170e-12 | 3.9358e-09 | 8.6217e-06 |

**Table 4** Optimised model parameters for transformation strain model $\varepsilon_{tr}(T)$, cf. Eq. (3) and (4).

| | $\varepsilon_0^h$ | $\eta_h$ | $\gamma_h$ | $\varepsilon_0^c$ | $\eta_c$ | $\gamma_c$ |
|---|---|---|---|---|---|---|
| *L* | 2.5141e-03 | 956.39 | 36.12 | 3.8683e-04 | 893.50 | 23.7937 |
| *T* | -9.6401e-04 | 956.39 | 36.12 | 3.8683e-04 | 893.50 | 23.7937 |

## SIMULATION MODELS

To demonstrate the effectiveness and relevance of the presented expansion model, three simulations have been implemented, Fig. 5. All simulations were conducted using Abaqus/CAE 2024. The Fortran based UEXPAN user-subroutine was implemented in Microsoft Visual Studio 2022 and compiled using the Intel Fortran Compiler 2019 following the guidelines in [59], [60].

First, the correct implementation of the UEXPAN has been verified by simulating the dilatometer experiment for vertically and horizontally oriented cylinders as used for the model parameter identification. Additionally, the predictive performance of the model is shown for a specimen tilted at 45° with respect to the vertical and horizontal directions used for model calibration.

To further demonstrate the relevance of an anisotropic expansion model accounting for thermal and transformation strains, a weakly-coupled single-layer thermo-mechanical process simulation (TMPS) model of a single PBF-LB/M laser weld track was implemented. Simulated stresses from a model assuming isotropic thermal expansion only are compared to a model assuming the presented expansion model which accounts for transversally isotropic transformation strains.

Finally, a weakly-coupled multi-layer TMPS model was implemented to compare simulated and experimentally determined distortions in a PBF-LB/M printed cantilever after stress relief following support structure removal. It is investigated if the presented expansion model reasonably predicts the residual stresses introduced during the PBF-LB/M process.

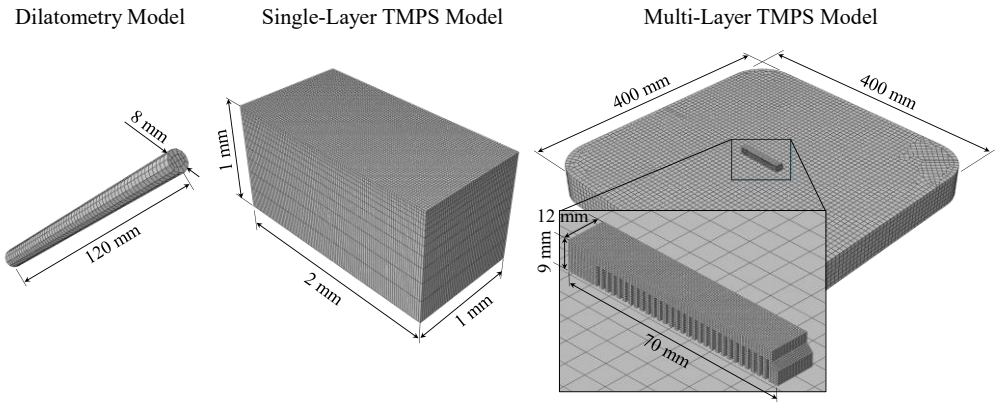



**Fig. 5** Simulation models

*Dilatometry Model*

To simulate the apparent expansion as measured in the dilatometer experiment conducted in [29], a cylinder with 8 mm diameter and 120 mm length was subjected to a thermal heating and cooling cycle (20°C - 1100°C - 20°C) in an implicit static/general procedure.

The 3D cylinder was meshed using 1200 linear hexahedral elements with reduced integration (C3D8R), see Fig. 5 (left).

A local rectangular coordinate system was created to define the material orientation with the 3-direction corresponding to the *L* orientation and the 1- and 2- directions referring to the *T* orientation of the expansion model. By orientating the cylinder either along the 3-direction, the 1- or 2- direction, or along the space diagonal, vertical, horizontal, and 45° tilted build orientations were realized.

The mechanical boundary conditions were defined such that an unconstrained expansion was ensured both in longitudinal and transverse directions. Thereby, the build-up of stresses during the thermal cycle was prevented.

Time incrementation was chosen such that the maximum temperature increment was limited to 5 °C. Like this it was ensured that pronounced change of transformation strains during the $\alpha' \rightarrow \beta$ transformation was appropriately resolved.

*Single-Layer TMPS Model (Weld Track)*

To investigate the relevance of the presented expansion model, a weakly-coupled single-layer TMPS model of a single 1.2 mm PBF-LB/M weld track was set-up using a volumetric Gauss-Goldak heat input model [51] following the approach and using the model parameters outlined by [61], [62] with a trajectory-based event-series implementation provided by Abaqus [50].

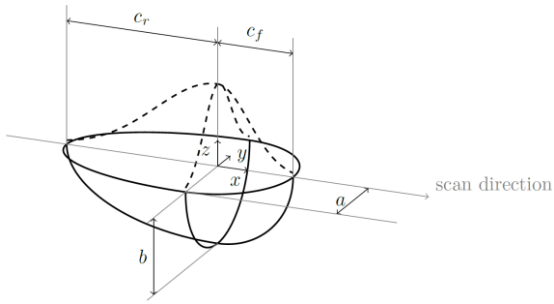



**Fig. 6** Schematic illustrating geometric Gauss-Goldak parameters

For simplicity, only bulk material was considered, and material activation was neglected. This reflects a situation in which an already solidified AM part is exposed to laser irradiation, assuming powder layer properties to be equivalent to bulk properties. The substrate was meshed using 60000 linear (D)C3D8R elements with lateral dimensions of 20 µm × 20 µm and a vertical bias ranging from 20 µm to 200 µm over a depth of 1 mm, see Fig. 5 (middle).

In a first transient heat transfer simulation, the heat input introduced by a scanning laser source (laser power 250 W, laser spot diameter 100 µm) was modelled using a volumetric Gauss-Goldak heat flux which is scanned with a speed of 600 mm/s in 1-direction (*T*). The geometric Gauss-Goldak parameters, see Fig. 6, were defined as $a$ = 50 µm (half width), $b$ = 30 µm (depth), $c_f$ = 50 µm (frontal half axis along laser path), and $c_r$ = 117 µm (rear half axis along laser path) with energy fractions of $f_f$ = 0.6 and $f_r$ = 1.4 [61], [62]. The laser absorptivity was defined as $\eta = 0.55$ and the HTC on top of the plate as 0.02 W/m$^2$K. The resulting instantaneous temperature distribution at the end of the 1.2 mm single PBF-LB/M weld track is illustrated in Fig. 7. As the process parameters and heat-source was adopted from literature and thus not directly calibrated to experimental data, the resulting maximum temperature of > 7300 °C is significantly above melting temperature and thus not considered as realistic. The goal of the present simulation is, however, to provide a relative comparison of residual stresses in the near-field beyond the melt pool as predicted by a model using a simple isotropic thermal expansion coefficient and one that uses the expansion model presented in this study. Thus, the adopted model is judged as sufficient for this purpose.

Following the thermal simulation, the temperature field is imposed to two different mechanical models, i.e. one using a simple thermal expansion coefficient CTE (Fig. 10, right) representing isotropic thermal strain only, and another using the UEXPAN expansion model presented here that accounts for the transversely isotropic transformation strains.

Both, the thermal and the mechanical simulation models used a minimum time increment $\Delta t_{min}$ of $5 \cdot 10^{-7}$ s and a maximum time increment of $\Delta t_{max}$ of $10^{-5}$ s for the simulated time period of $2 \cdot 10^{-3}$ s.

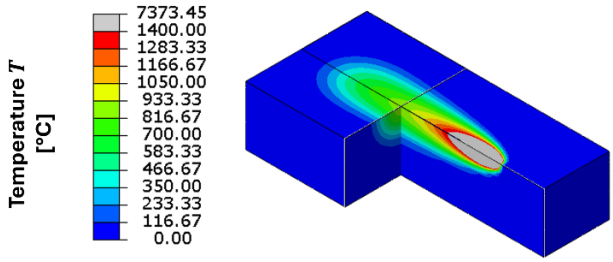



**Fig. 7** Instantaneous temperature distribution in single-track PBF-LB/M weld after 1.2 mm

*Multi-Layer TMPS Model (Cantilever)*

To model the build-up of residual stresses in a cantilever manufactured by PBF-LB/M, a multi-layer TMPS model was implemented in Abaqus using event-series for the layer-wise element activation [50] following the industrially well-established superlayer approach by Ansys [57]. Thereby, a finite element layer, i.e. superlayer (500 µm), represents multiple powder layers (60 µm). Conventionally, these are activated successively at a temperature close to the melting temperature, e.g. 1100 °C, followed by a cooldown phase. Further assuming a reference temperature for the thermal expansion/contraction at the same activation temperature, residual stresses are introduced by constrained shrinkage only. As the build orientation dependent transformation strains occur during heating, a modified approach was additionally adopted within this study:

- Activation of superlayer at room temperature within $4.9 \cdot 10^{-5}$ s (quasi-instantaneous)
- Heating of superlayer to 1100 °C within $4.9 \cdot 10^{-4}$ s (i.e. time to scan superlayer)
- Cooling of superlayer within 91.7 s (i.e. dwell and recoating time for superlayer)

This allows to account for additional residual stresses that arise from the transversally isotropic transformation strains as well as from constrained heating. Following the cooldown of the last layer, the support structure of the cantilever is cut at a height of 1 mm using a model change that deactivates a pre-defined element set. The resulting deflection of the cantilever after stress relief following support removal reflects the extent of the residual stresses introduced in the PBF-LB/M process.

Four model variants are compared within this study: 1) conventional approach + thermal strains, 2) conventional approach + thermal and transformation strains, 3) modified approach + thermal strains, and 4) modified approach + thermal and transformation strains. Thereby, the process parameters defined in Table 1 are assumed for the calculation of superlayer heating- and cooling-times.

The cantilever was meshed using 44255 linear (D)C3D8 elements with dimensions 500 µm × 500 µm × 500 µm, see Fig. 5 (right). It was tied to a 400 mm × 400 mm × 45 mm

substrate plate which was discretized using 25745 (D)C3D8 elements with an approximate size of 7 mm × 7 mm × 7 mm.

Following the thermal simulation, the temperature field is imposed to the mechanical model following a weak-coupling approach. Both, the thermal and the mechanical simulation models used a fixed time increment $\Delta t$ of $4.9 \cdot 10^{-6}$ s in the heating phase allowing to resolve temperature changes in the order of 10 °C per increment, i.e. 1% of the maximum temperature.

### *Material Properties*

Following [62], [63], all simulation models used thermo-physical data by [64] and thermo-mechanical data by [65]. Thermal expansion coefficients (CTE) considering thermal strains only were derived from the dilatometry data in [29] using the model given by Eq. (2) with the optimised parameters listed in Table 3. The simulation models considering the combined thermal and transformation strains used the UEXPAN subroutine with the optimised model parameters listed in Table 4 instead.

Fig. 8 shows the heat capacity, thermal conductivity, and density for bulk Ti-6Al-4V. To model the effect of the phase transformations on the temperature evolution, latent heats were defined as follows [62], [63], [64]:

- solid-solid ($\alpha' \rightarrow \beta$) phase transformation ($T_s$ = 980 °C, $T_e$ = 1010 °C) 4.8·J/g
- solid-liquid phase transformation ($T_s$ = 1604 °C, $T_e$ = 1660 °C) 268·J/g
- liquid-vapor phase transformation ($T_s$ = 3290 °C, $T_e$ = 3390 °C) 983·J/g

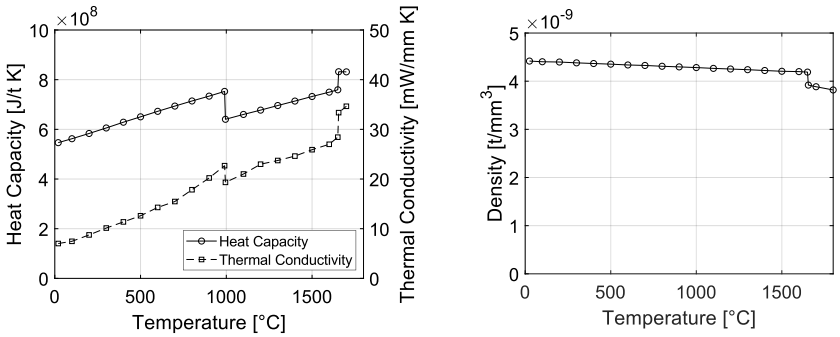



**Fig. 8** Thermo-physical properties used for simulation model as adopted from [64]

Fig. 9 shows the temperature dependent elastic modulus and Poisson ratio as well as the yield stress for bulk Ti-6Al-4V according to [65]. Plasticity was implemented using a multilinear kinematic hardening model to appropriately account for the Bauschinger affect. To ensure numerical stability, low non-zero mechanical properties were defined beyond the melting temperature at 1600 °C.

As required by Abaqus, the UEXPAN subroutine presented in this study provides expansion strain increments which consist of thermal and transformation strain increments.

To demonstrate the impact of the expansion model, the respective simulation results were compared to simulations using isotropic thermal expansion according to Eq. (2) only. As Abaqus requires the definition of temperature dependent mean CTEs in this case, these were derived from the measured thermal strains, see Fig. 10 (left), using the difference quotient according to [66]. Fig. 10 (right) compares the mean CTE of this study with data used by [63].

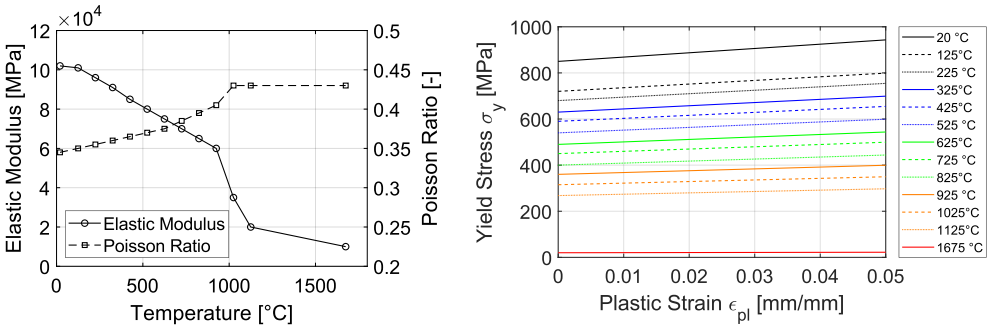



**Fig. 9** Thermo-mechanical properties used for simulation model as adopted from [65]

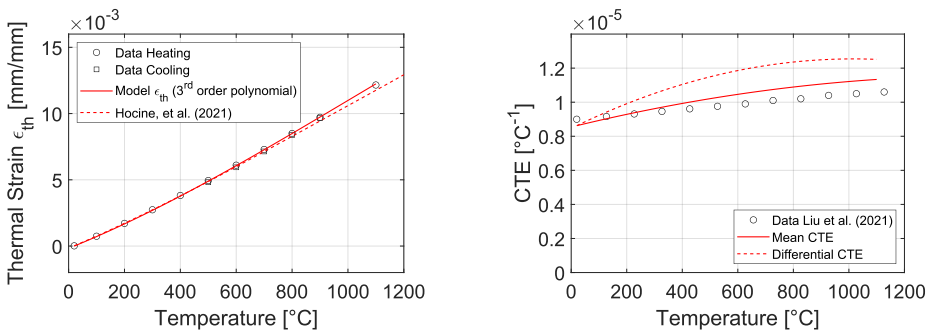



**Fig. 10** Measured and modelled thermal strain (left) and mean CTE (right) used for the simulation models accounting for thermal strain only in this study. Comparison to literature data [62], [63]

## RESULTS AND DISCUSSION

### *Anisotropic Apparent Expansion*

The expansion model described by Eq. (1) to (4) was fitted to experimental apparent expansion data of vertically and horizontally built PBF-LB/M samples [29], yielding the optimised model parameters for the longitudinal (*L*) and transverse (*T*) directions in Table 3 and Table 4. Recalculation of the dilatometry experiments using the expansion model

implemented as UEXPAN demonstrates excellent agreement between simulation and experimental data verifying the correct implementation of the model, see Fig. 11 (left, middle). The expansion model was further applied to predict the apparent expansion in a PBF-LB/M sample printed under a 45° tilt angle which was not used for model calibration. Fig. 11 (right), shows again excellent agreement between the (unseen) experimental data and the model prediction, underpinning the solid predictive performance of the presented expansion model.

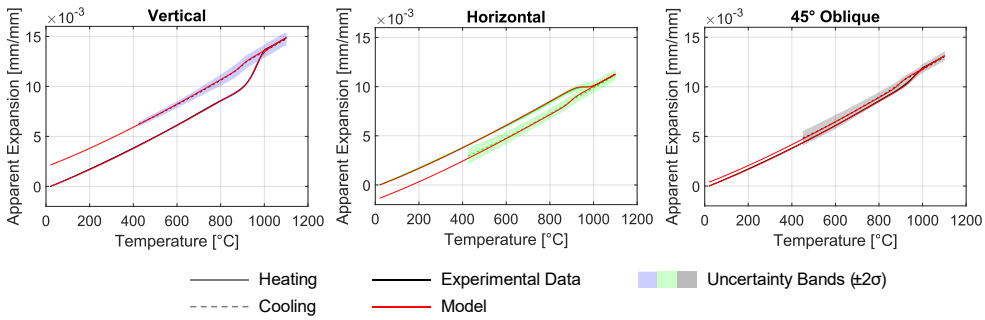



**Fig. 11** Comparison of measured apparent expansion strain with UEXPAN model predictions for vertically, horizontally, and 45° oriented cylindrical dilatometer samples

The findings in [29] show that the apparent difference in the expansion behaviour of vertically and horizontally built samples originates from the morphological and crystallographic texture of Ti-6Al-4V manufactured by PBF-LB/M. Prior $\beta$ grains grow epitaxially with their $\langle 001 \rangle_\beta$ direction along the thermal gradient, i.e. effectively along the build-direction. During cooldown, $\alpha'$ laths precipitate on the prior $\beta$ grain boundaries obeying the Burgers orientation relationship and growing along the invariant directions $\langle 335 \rangle_\beta$ to minimise internal energy. This results in a particular acicular martensitic morphology with $\alpha'$ laths being oriented at a 35 to 55° angle to the prior $\beta$ grain boundaries. During the $\alpha' \rightarrow \beta$ transformation, crystallographic transformation strains occur that macroscopically manifest themselves in positive transformation strains along the major axis of the prior $\beta$ grains, and negative transformation strains along the minor axis.

The investigation by [29] has shown that the transformation strain for the $\alpha' \rightarrow \beta$ transformation (heating) is 0.271% in $L$ (vertical) direction and -0.084% in $T$ (horizontal) direction, while it is -0.037% in $L$ (vertical) direction and -0.013% in $T$ (horizontal) direction for the $\beta \rightarrow \alpha + \beta$ transformation (cooling). This is in excellent agreement with the optimized model parameters $\varepsilon^h_{0,L}$ = 0.251% and $\varepsilon^h_{0,T}$ = -0.096% for heating, and $\varepsilon^c_{0,L} = \varepsilon^c_{0,T}$ = -0.039% for the cooling phase, see Table 4. The minor differences arise from the simplified $tanh$-approach adopted for the state functions $\phi^h$ and $\phi^c$.

Furthermore, the model parameters for the polynomial model to describe the thermal strain appear to differ significantly from the results presented in [29]. Both parameter sets represent the experimental data very well, however, and the differences are merely a consequence of the overall model fit in this study vs. the simple data analysis conducted in [29].

In conclusion, the UEXPAN implementation of the presented expansion model is verified, and its robust predictive performance is shown. Furthermore, the optimized model parameters are in excellent agreement with the experimental observations in [29].

### *Comparison of Residual Stresses in a Single PBF-LB/M Weld Track*

While the expansion model presented in this study well represents the apparent expansion observed in dilatometry experiments, the question arises as to its relevance for practical applications relative to the adoption of a simpler approach accounting for thermal strains only. To study the development of residual stresses during the PBF-LB/M process, both expansion models are compared using a single-layer TMPS simulation of a single PBF-LB/M weld track. Such a simulation model can for instance be used to analyse stresses in the near-field of the melt pool and optimise scan strategies that minimize residual stresses and distortions.

Fig. 12 shows a comparison of the normal stress components and the accumulated plastic strain of a single-layer TMPS model accounting for isotropic thermal strains $\varepsilon_{th}$ only (left column), and one that accounts for both isotropic thermal $\varepsilon_{th}$ and transversally isotropic transformation strains $\varepsilon_{tr}$ (right column). The model considering thermal strains only can be interpreted to reflect the situation in a conventionally manufactured Ti-6Al-4V material volume, while the model accounting for the anisotropic transformation strains represents the situation in a solidified material volume after PBF-LB/M processing. While the stress distributions are qualitatively comparable with relative differences in the in-plane longitudinal and transverse stresses < 4 %, the maximum and minimum vertical stresses are predicted to be approximately 9 % smaller and 9% larger, respectively, by the isotropic $\varepsilon_{th}$ model than by the transversally isotropic $\varepsilon_{th} + \varepsilon_{tr}$ model, see Table 5. The maximum compressive vertical stresses are very localised to the starting point of the weld track and may arise from the enhanced expansion in build-direction and reduced in-plane expansion during the $\alpha' \rightarrow \beta$ transformation given the severe initial temperature gradients. Despite these localized differences, the accumulated plastic strain is approximately 90% larger in the $\varepsilon_{th}$ model than in the $\varepsilon_{th} + \varepsilon_{tr}$ model along the whole weld track.

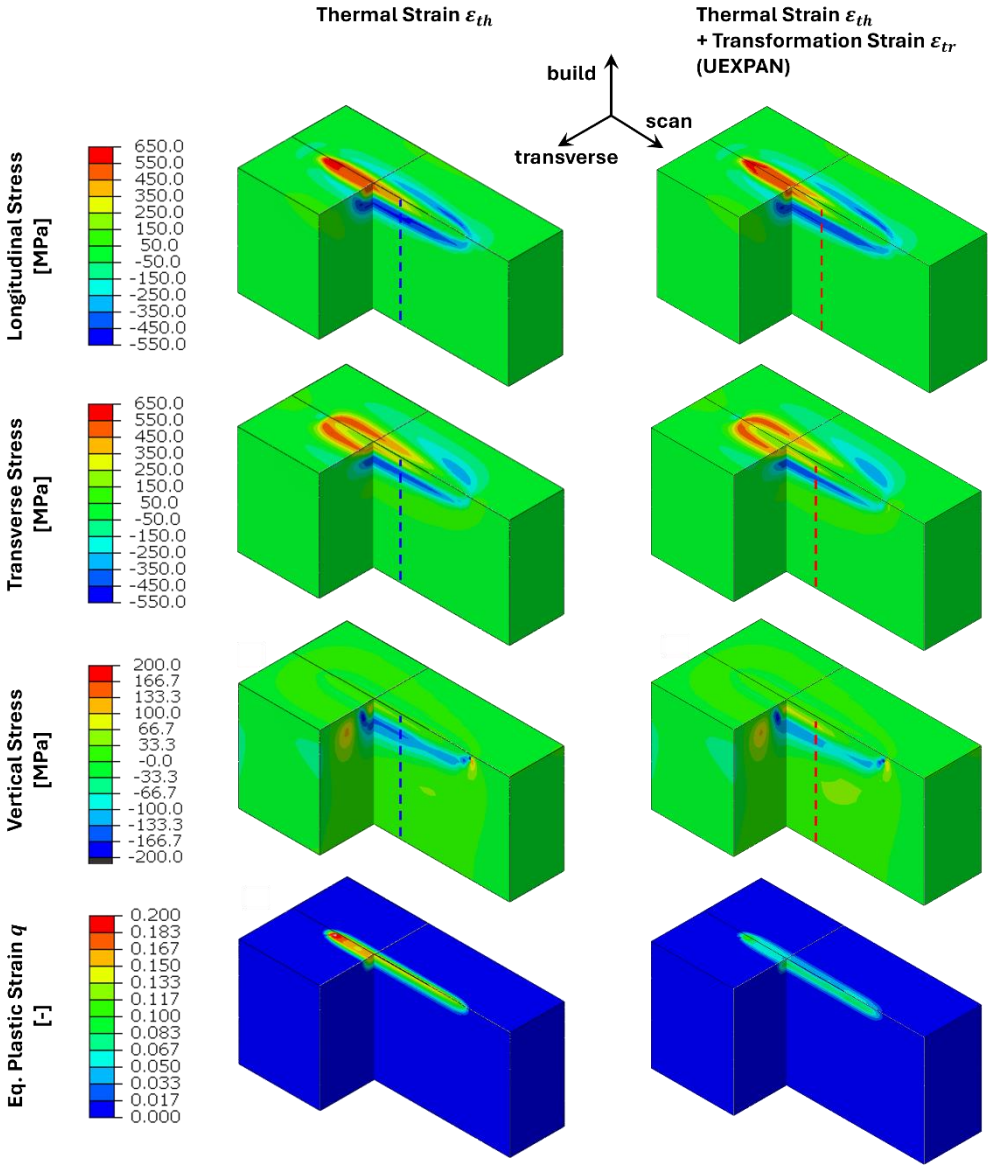



**Fig. 12** Comparison of stress components and accumulated equivalent plastic strain in a single-track PBF-LB/M weld in longitudinal, transverse, and vertical (i.e. build-direction) directions with respect to the scanning direction as predicted by models accounting for thermal strain only (left column) and considering thermal and transformation strains using an UEXPAN subroutine (right column). Paths (blue, red) indicate evaluation region for stresses shown in Fig. 13

**Table 5** Comparison of simulated max/min normal stress components as predicted by models accounting for $\varepsilon_{th}$ and $\varepsilon_{th} + \varepsilon_{tr}$, respectively.

| Stress | $\varepsilon_{th}$ model | $\varepsilon_{th} + \varepsilon_{tr}$ model (UEXPAN) | Relative Difference |
|---|---|---|---|
| *Longitudinal* | 665 MPa | 663 MPa | -0.3 % |
| | -524 MPa | -526 MPa | 0.3 % |
| *Transverse* | 549 MPa | 543 MPa | 1.1 % |
| | -435 MPa | -417 MPa | -4.3 % |
| *Vertical* | 185 MPa | 170 MPa | -8.8 % |
| *(Build-Direction)* | -266 MPa | -292 MPa | 8.6 % |

To better understand these findings, the stress-temperature characteristics have been investigated at three depths - i.e. 75 µm, 115 µm, and 160 µm - along a vertical path in the centre of the weld track, see Fig. 12, that can be considered to be in steady-state. Considering a melting temperature of approximately 1650 °C, these points are located just below the anticipated melt pool. Fig. 13 shows that in-plane (longitudinal, transverse) and vertical normal stress components appear to be well comparable for the locations closest to the melt pool at a depth of 75 µm reaching temperatures > 1500 °C, and furthest away at 160 µm reaching < 500 °C. At the intermediate depth of 115 µm, however, the in-plane stresses predicted by the $\varepsilon_{th}$ model are transitioning from compression to tension during a complete heat-up and cooldown cycle, while the stresses predicted by the $\varepsilon_{th} + \varepsilon_{tr}$ model remain in compression. In contrast, the vertical stresses predicted by the $\varepsilon_{th}$ model first peak in compression before becoming tensile after reaching the peak temperature, while the peak compressive stress predicted by the $\varepsilon_{th} + \varepsilon_{tr}$ model is significantly smaller and the stress at the final temperature becomes neutral.

Initial compressive stresses during heat-up arise from the thermal expansion which is locally constrained by the surrounding material volume at lower temperatures, i.e. further away from the melt pool. As the temperature equilibrates, the hotter surrounding material, i.e. closer to the melt pool, starts pulling on initially colder material up to a point where stresses become tensile. As the transient temperature history has been considered the same for both models, the difference must be due to the transversally isotropic transformation strain considered in the $\varepsilon_{th} + \varepsilon_{tr}$ model. Apparent in-plane expansion strains are reduced with respect to the mere isotropic thermal expansion strains. Thus, the pull exerted by the surrounding material during temperature equilibration in the longitudinal and transverse directions is reduced leading to a reduced tendency of the stresses at a depth of 115 µm to turn tensile. Due to the increased apparent expansion in vertical direction, on the other hand, warmer surrounding material tends to keep the material volumes below under compression as predicted by the $\varepsilon_{th} + \varepsilon_{tr}$ model.

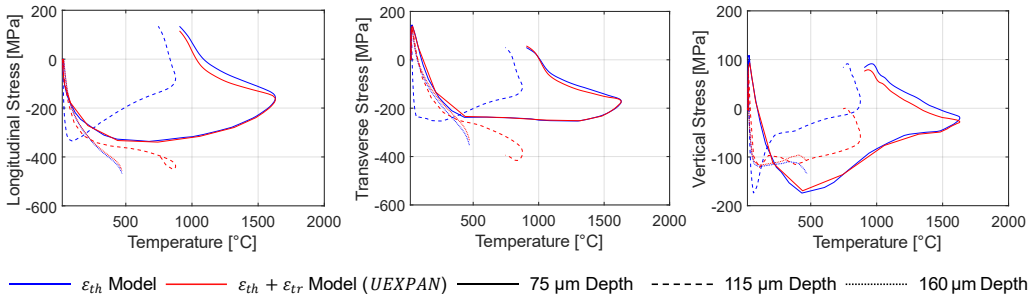



**Fig. 13** Comparison of stress-temperature paths at three depths, i.e. 75 µm, 115 µm, and 160 µm along a vertical path (see Fig. 12) in the centre of a single-track PBF-LB/M weld

While not being experimentally validated, these results clearly show that accounting for the transversal isotropy induced by the transformation strains leads to relevant impacts on predicted stress distributions which need to be considered to better understand the residual stresses induced during the PBF-LB/M process.

### *Comparison of Distortions in Cantilever*

In the following, distortions as measured in a cantilever after support removal (cutting) are compared to model predictions using a multi-layer TMPS approach. Besides comparing two expansion models, i.e. one accounting for thermal strains $\varepsilon_{th}$ only, and a model accounting for both thermal and transformation strains $\varepsilon_{th} + \varepsilon_{tr}$ using the UEXPAN subroutine, two variants of the multi-layer TMPS approach are investigated, i.e. a conventional approach considering cooldown only, and a modified approach considering heat-up and cooldown.

The multi-layer TMPS approach has been widely adopted in industry for a first-level estimation of residual stresses and distortions of critical PBF-LB/M parts due to its numerical efficiency. Conventionally, finite element layers representing several powder layers are instantaneously activated directly at close to melting temperature. Residual stresses are thereby introduced during cooldown through constrained thermal shrinkage. The heating phase is neglected as justified by its much shorter duration and the exceeding of the melting temperature which would erase residual stresses that arise during heat-up. As the complex melt-pool physics and the respective transient thermal history are not accounted for, the activated layer can basically be regarded as a means of introducing thermal loading to the solidified layers below.

Fig. 14 shows that with the conventional approach (dashed lines) and for both expansion models, the predicted maximum vertical distortion is significantly larger with 5.7 mm than the measured values of 2.6 mm. The simpler isotropic $\varepsilon_{th}$ model and the transversally isotropic $\varepsilon_{th} + \varepsilon_{tr}$ model deviate by only 0.01 mm. As the two models merely differ by the isotropic transformation strain of the $\beta \rightarrow \alpha + \beta$ transformation during cooldown, this can be concluded to be negligible.

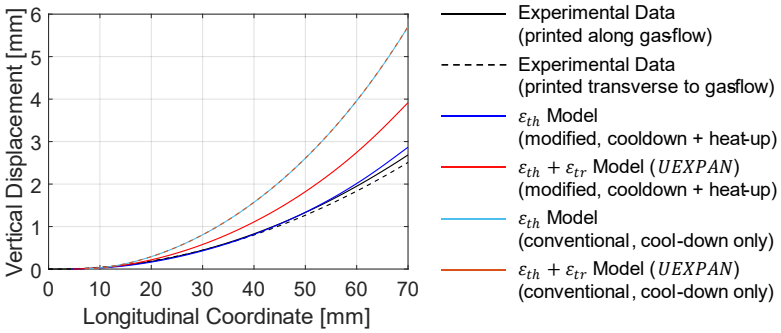



**Fig. 14** Comparison of measured (black) and simulated distortions in a cantilever after support removal. Expansion models considered isotropic thermal strain only (blue, cyan) and thermal and transversally isotropic transformation strains by using the UEXPAN subroutine (red, orange)

To improve the model prediction, a modified multi-layer TMPS approach was implemented which considers activation at room temperature, followed by heating within ca. 0.5 ms, and cooling for ca. 90 s. Fig. 14 shows a significant improvement in both model predictions with the modified multi-layer TMPS approach. While the $\varepsilon_{th} + \varepsilon_{tr}$ model predicts a maximum vertical deflection of 3.9 mm, the $\varepsilon_{th}$ model is unexpectedly more accurate with a deflection of 2.9 mm (+11 %). This result was verified using both finer spatial and temporal discretisations.

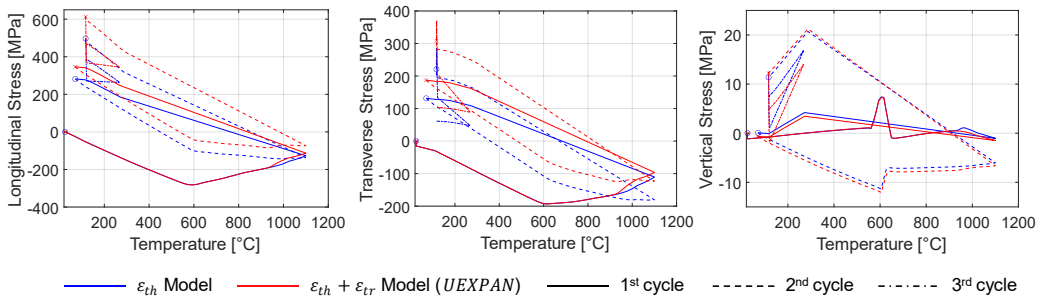



**Fig. 15** Comparison of predicted stress-temperature characteristics at the centre of the cantilever, 2.5 mm below the top surface for initial heating (1st cycle) and two successive re-heating cycles (2nd and 3rd cycle)

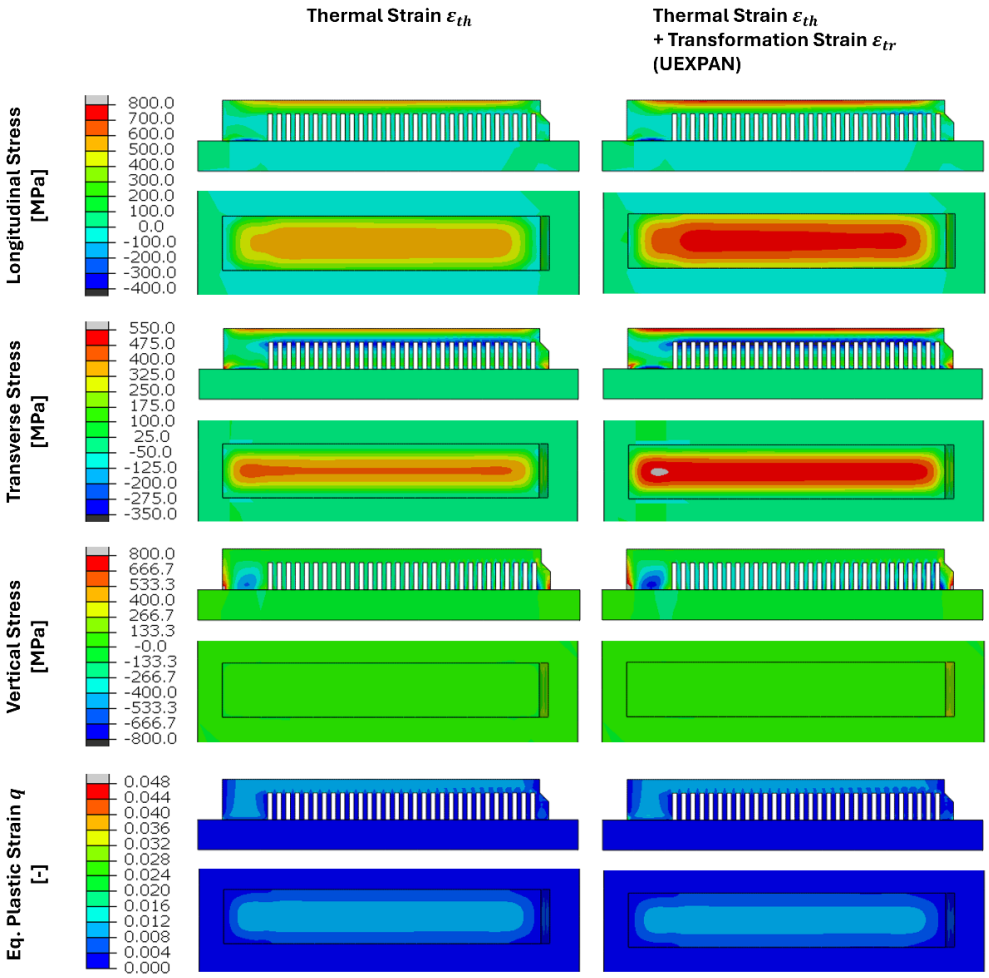



**Fig. 16** Comparison of normal stress distributions in a cantilever prior to cutting for a model considering thermal strain only (left column) and a model considering thermal and transformation strains using a UEXPAN subroutine (right column). The top side-view image refers to a longitudinal cut through the cantilever centre, while the bottom image refers to the top view.

Fig. 15 shows the stress-temperature characteristics at the centre of the cantilever, 2.5 mm below the top surface. The impact of the transversally isotropic transformation is clearly visible in the first and second heating cycle at 900 °C to 1100 °C. In this temperature regime the enhanced apparent expansion in vertical direction leads to a minor reduction of the small vertical stresses, while the reduced in-plane thermal expansion leads to slightly less compressive longitudinal and transverse stresses. This difference in the compressive regime leads to higher tensile stresses after cooldown which is inherited for the following re-heating cycles.

Fig. 16 shows the longitudinal, transverse, and vertical stress distributions in a longitudinal cut through the cantilever centre and a top view prior to support removal. All normal stress components predicted by the $\varepsilon_{th} + \varepsilon_{tr}$ model exceed the predictions of the $\varepsilon_{th}$ model. The distortion after cutting is predominantly determined by the residual longitudinal stress prior to the removal of the supports. These are strongly tensile and significantly larger and more extended in the $\varepsilon_{th} + \varepsilon_{tr}$ model prediction, which explains the larger deflections upon stress relief following support removal. Furthermore, the vertical stresses are significantly smaller than the in-plane stresses which is likely due to the relatively small thickness of the cantilever. It is argued, that with increasing wall thickness, the vertical stresses would increase, leading to a stronger impact of the anisotropic transformation strain.

As the simplified multi-layer TMPS approach using a $\varepsilon_{th}$ model yields excellent agreement with measurements in a cut cantilever, it is hypothesized that the textured PBF-LB/M microstructure developing in the rather thin cantilever may be altered by the underlying support structure significantly enough that the anisotropic apparent expansion behaviour is lost. This could be explained by the reduced heat flux through the support structure leading to higher average temperatures in the cantilever and thus reduced cooling rates and a consequently lower tendency for prior $\beta$ grains to grow epitaxially over multiple layers. This needs to be further investigated in future work. Besides, it needs to be considered that the layer-wise heat input represents an oversimplification for general part geometries. In case of a small cantilever, the time to print a layer is rather short which supports this simplification. In larger parts, however, severe in-plane temperature gradients may arise that would challenge this modelling approach.

## CONCLUSIONS

Following the experimental investigation of an anisotropic apparent expansion in PBF-LB/M-fabricated Ti-6Al-4V [29], an expansion model has been developed assuming isotropic thermal strains and transversally isotropic transformation strains. This model has been implemented in an UEXPAN subroutine in the commercial FE software Abaqus enabling first simulative studies on the impact of anisotropy on the residual stress and distortion evolution during the PBF-LB/M process.

The UEXPAN model was successfully applied to predict the apparent expansion in a cylinder printed at a 45° angle.

The UEXPAN model has predicted significant differences in the vertical stress components and the induced plastic strain in a single PBF-LB/M weld track with respect to model accounting for isotropic thermal expansion. These differences are argued to originate from the varied mechanical constraints imposed by the transversally isotropic expansion.

A modified multi-layer TMPS model is presented that leads to significant improvements in the prediction of distortions in a cantilever following support structure removal. The expansion model accounting for isotropic thermal strains only was shown to yield better results than the UEXPAN model, which accounts for isotropic thermal and transversally isotropic transformation strains. Besides the simplified modelling approach neglecting in-

plane temperature gradients, the actual microstructure of the cantilever may differ from the cylindrical samples used for the dilatometric experiments which form the basis of the expansion model. Such differences could be justified by the support structures which reduce the heat flux away from the process zone in the cantilever leading to a reduced temperature gradient for the formation of a typical PBF-LB/M microstructure. This will be investigated in more detail in future work.

The developed UEXPAN model may further be used to simulate the impact of post-process heat-treatments or transient operating conditions on the residual stress state. In addition, it can be applied to investigate and optimise scan strategies in order to minimize residual stresses and distortion in PBF-LB/M components.

## ACKNOWLEDGEMENTS

Specimens were kindly provided by Sauber Engineering within the scope of the Innosuisse project 50397.1 IP-ENG.

## References

[1] M. H. FARSHIDIANFAR, A. KHAJEPOUR and A. P. GERLICH: 'Effect of real-time cooling rate on microstructure in Laser Additive Manufacturing', *J. Mater. Process. Technol.*, vol. 231, pp. 468-478, May 2016, doi: 10.1016/j.jmatprotec.2016.01.017.

[2] U. SCIPIONI BERTOLI, G. GUSS, S. WU, M. J. MATTHEWS and J. M. SCHOENUNG: 'In-situ characterization of laser-powder interaction and cooling rates through high-speed imaging of powder bed fusion additive manufacturing', *Mater. Des.*, vol. 135, pp. 385-396, Dec. 2017, doi: 10.1016/j.matdes.2017.09.044.

[3] P. A. HOOPER: 'Melt pool temperature and cooling rates in laser powder bed fusion', *Addit. Manuf.*, vol. 22, pp. 548-559, Aug. 2018, doi: 10.1016/j.addma.2018.05.032.

[4] A. PFAFF, S. SCHÄFFER, M. JÄCKLEIN and F. BALLE: 'Measuring the Cooling Behavior of Melt Pools in L-PBF by Pyrometry', *Materials*, vol. 16, no. 10, p. 3647, May 2023, doi: 10.3390/ma16103647.

[5] P. A. KOBRYN and S. L. SEMIATIN: 'Microstructure and texture evolution during solidification processing of Ti–6Al–4V', *J. Mater. Process. Technol.*, vol. 135, no. 2-3, pp. 330-339, Apr. 2003, doi: 10.1016/s0924-0136(02)00865-8.

[6] S. S. AL-BERMANI, M. L. BLACKMORE, W. ZHANG and I. TODD: 'The Origin of Microstructural Diversity, Texture, and Mechanical Properties in Electron Beam Melted Ti-6Al-4V', *Metall. Mater. Trans. A*, vol. 41, no. 13, pp. 3422-3434, Dec. 2010, doi: 10.1007/s11661-010-0397-x.

[7] L. THIJS, F. VERHAEGHE, T. CRAEGHS, J. V. HUMBEECK and J.-P. KRUTH: 'A study of the microstructural evolution during selective laser melting of Ti–6Al–4V', *Acta Mater.*, vol. 58, no. 9, pp. 3303-3312, May 2010, doi: 10.1016/j.actamat.2010.02.004.

[8] B. VRANCKEN, L. THIJS, J.-P. KRUTH and J. VAN HUMBEECK: 'Heat treatment of Ti6Al4V produced by Selective Laser Melting: Microstructure and mechanical properties', *J. Alloys Compd.*, vol. 541, pp. 177-185, Nov. 2012, doi: 10.1016/j.jallcom.2012.07.022.

[9] C. QIU, N. J. E. ADKINS and M. M. ATTALLAH: 'Microstructure and tensile properties of selectively laser-melted and of HIPed laser-melted Ti–6Al–4V', *Mater. Sci. Eng. A*, vol. 578, pp. 230-239, Aug. 2013, doi: 10.1016/j.msea.2013.04.099.

[10] M. SIMONELLI, Y. Y. TSE and C. TUCK: 'On the Texture Formation of Selective Laser Melted Ti-6Al-4V', *Metall. Mater. Trans. A*, vol. 45, no. 6, pp. 2863-2872, Jun. 2014, doi: 10.1007/s11661-014-2218-0.

[11] M. SIMONELLI, Y. Y. TSE and C. TUCK: 'Effect of the build orientation on the mechanical properties and fracture modes of SLM Ti–6Al–4V', *Mater. Sci. Eng. A*, vol. 616, pp. 1-11, Oct. 2014, doi: 10.1016/j.msea.2014.07.086.

[12] A. BASAK and S. DAS: 'Epitaxy and Microstructure Evolution in Metal Additive Manufacturing', *Annu. Rev. Mater. Res.*, vol. 46, no. 1, pp. 125-149, Jul. 2016, doi: 10.1146/annurev-matsci-070115-031728.

[13] J. LI, X. ZHOU, M. BROCHU, N. PROVATAS and Y. F. ZHAO: 'Solidification microstructure simulation of Ti-6Al-4V in metal additive manufacturing: A review', *Addit. Manuf.*, vol. 31, p. 100989, Jan. 2020, doi: 10.1016/j.addma.2019.100989.

[14] W. G. BURGERS: 'On the process of transition of the cubic-body-centered modification into the hexagonal-close-packed modification of zirconium', *Physica*, vol. 1, no. 7-12, pp. 561-586, May 1934, doi: 10.1016/s0031-8914(34)80244-3.

[15] C. CAYRON: 'Importance of the α→β transformation in the variant selection mechanisms of thermomechanically processed titanium alloys', *Scr. Mater.*, vol. 59, no. 5, pp. 570-573, Sep. 2008, doi: 10.1016/j.scriptamat.2008.05.013.

[16] D. BHATTACHARYYA, G. B. VISWANATHAN, R. DENKENBERGER, D. FURRER and H. L. FRASER: 'The role of crystallographic and geometrical relationships between α and β phases in an α/β titanium alloy', *Acta Mater.*, vol. 51, no. 16, pp. 4679-4691, Sep. 2003, doi: 10.1016/s1359-6454(03)00179-4.

[17] M. HUMBERT, L. GERMAIN, N. GEY, P. BOCHER and M. JAHAZI: 'Study of the variant selection in sharp textured regions of bimodal IMI 834 billet', *Mater. Sci. Eng. A*, vol. 430, no. 1-2, pp. 157-164, Aug. 2006, doi: 10.1016/j.msea.2006.05.047.

[18] 'Microstructure control in processing nickel, titanium and other special alloys', in *Microstructure Evolution in Metal Forming Processes*, Elsevier, 2012, pp. 337-383. doi: 10.1533/9780857096340.3.337.

[19] J. YANG, H. YU, J. YIN, M. GAO, Z. WANG and X. ZENG: 'Formation and control of martensite in Ti-6Al-4V alloy produced by selective laser melting', *Mater. Des.*, vol. 108, pp. 308-318, Oct. 2016, doi: 10.1016/j.matdes.2016.06.117.

[20] N. HAGHDADI, R. DEMOTT, P. L. STEPHENSON, X. Z. LIAO, S. P. RINGER and S. PRIMIG: 'Five-parameter characterization of intervariant boundaries in additively manufactured Ti-6Al-4V', *Mater. Des.*, vol. 196, p. 109177, Nov. 2020, doi: 10.1016/j.matdes.2020.109177.

[21] P. L. STEPHENSON, N. HAGHDADI, R. DEMOTT, X. Z. LIAO, S. P. RINGER and S. PRIMIG: 'Effect of scanning strategy on variant selection in additively manufactured Ti-6Al-4V', *Addit. Manuf.*, vol. 36, p. 101581, Dec. 2020, doi: 10.1016/j.addma.2020.101581.

[22] R. DEMOTT, N. HAGHDADI, Z. GANDOMKAR, X. LIAO, S. RINGER and S. PRIMIG: 'Formation and 3D morphology of interconnected α microstructures in additively manufactured Ti-6Al-4V', *Materialia*, vol. 20, p. 101201, Dec. 2021, doi: 10.1016/j.mtla.2021.101201.

[23] R. DeMott, N. Haghdadi, X. Liao, S. P. Ringer and S. Primig: '3D characterization of microstructural evolution and variant selection in additively manufactured Ti-6Al-4 V', *J. Mater. Sci.*, vol. 56, no. 26, pp. 14763-14782, Sep. 2021, doi: 10.1007/s10853-021-06216-2.

[24] B. Meier *et al.*: 'Influences of Surface, Heat Treatment, and Print Orientation on the Anisotropy of the Mechanical Properties and the Impact Strength of Ti 6Al 4V Processed by Laser Powder Bed Fusion', *J. Manuf. Mater. Process.*, vol. 6, no. 4, p. 87, Aug. 2022, doi: 10.3390/jmmp6040087.

[25] R. R. Pawar and V. T. Deshpande: 'The anisotropy of the thermal expansion of α-titanium', *Acta Crystallogr. Sect. A*, vol. 24, no. 2, pp. 316-317, Mar. 1968, doi: 10.1107/s0567739468000525.

[26] D. Gehring, J. A. Monroe and I. Karaman: 'Effects of composition on the mechanical properties and negative thermal expansion in martensitic TiNb alloys', *Scr. Mater.*, vol. 178, pp. 351-355, Mar. 2020, doi: 10.1016/j.scriptamat.2019.11.052.

[27] D. Gehring, Y. Ren, Z. Barghouti and I. Karaman: 'In-situ investigation of anisotropic crystalline and bulk negative thermal expansion in titanium alloys', *Acta Mater.*, vol. 210, p. 116847, May 2021, doi: 10.1016/j.actamat.2021.116847.

[28] J. A. Monroe, D. Gehring, I. Karaman, R. Arroyave, D. W. Brown and B. Clausen: 'Tailored thermal expansion alloys', *Acta Mater.*, vol. 102, pp. 333-341, Jan. 2016, doi: 10.1016/j.actamat.2015.09.012.

[29] T. Mayer, F. Friso, and R. Radis: 'Effect of Build Orientation on Thermal Expansion of LPBF Printed Ti-6Al-4V', *Metall. Mater. Trans. A*, vol. 56, no. 4, pp. 1287-1309, Apr. 2025, doi: 10.1007/s11661-025-07706-7.

[30] J. W. Elmer, T. A. Palmer, S. S. Babu and E. D. Specht: 'In situ observations of lattice expansion and transformation rates of α and β phases in Ti–6Al–4V', *Mater. Sci. Eng. A*, vol. 391, no. 1-2, pp. 104–113, Jan. 2005, doi: 10.1016/j.msea.2004.08.084.

[31] P. P. Dhekne, M. Bönisch, M. Seefeldt and K. Vanmeensel: 'In-situ synchrotron X-ray diffraction investigation of martensite decomposition in Laser Powder Bed Fusion (L-PBF) processed Ti–6Al–4V', *Mater. Sci. Eng. A*, vol. 899, p. 146421, May 2024, doi: 10.1016/j.msea.2024.146421.

[32] P. Mercelis and J. Kruth: 'Residual stresses in selective laser sintering and selective laser melting', *Rapid Prototyp. J.*, vol. 12, no. 5, pp. 254-265, Oct. 2006, doi: 10.1108/13552540610707013.

[33] M. Matsumoto, M. Shiomi, K. Osakada and F. Abe: 'Finite element analysis of single layer forming on metallic powder bed in rapid prototyping by selective laser processing', *Int. J. Mach. Tools Manuf.*, vol. 42, no. 1, pp. 61-67, Jan. 2002, doi: 10.1016/s0890-6955(01)00093-1.

[34] I. A. Roberts, C. J. Wang, R. Esterlein, M. Stanford and D. J. Mynors: 'A three-dimensional finite element analysis of the temperature field during laser melting of metal powders in additive layer manufacturing', *Int. J. Mach. Tools Manuf.*, vol. 49, no. 12-13, pp. 916-923, Oct. 2009, doi: 10.1016/j.ijmachtools.2009.07.004.

[35] M. F. Zaeh and G. Branner: 'Investigations on residual stresses and deformations in selective laser melting', *Prod. Eng.*, vol. 4, no. 1, pp. 35-45, Feb. 2010, doi: 10.1007/s11740-009-0192-y.

[36] N. Contuzzi, S. L. Campanelli and A. D. Ludovico: '3D Finite Element Analysis in the selective laser melting process', *Int. J. Simul. Model.*, vol. 10, no. 3, pp. 113-121, Sep. 2011, doi: 10.2507/ijsimm10(3)1.169.

[37] A. HUSSEIN, L. HAO, C. YAN and R. EVERSON: 'Finite element simulation of the temperature and stress fields in single layers built without-support in selective laser melting', *Mater. Des. 1980-2015*, vol. 52, pp. 638-647, Dec. 2013, doi: 10.1016/j.matdes.2013.05.070.

[38] W. KING, A. T. ANDERSON, R. M. FERENCZ, N. E. HODGE, C. KAMATH and S. A. KHAIRALLAH: 'Overview of modelling and simulation of metal powder bed fusion process at Lawrence Livermore National Laboratory', *Mater. Sci. Technol.*, vol. 31, no. 8, pp. 957–968, Jun. 2015, doi: 10.1179/1743284714y.0000000728.

[39] L. PARRY, I. A. ASHCROFT and R. D. WILDMAN: 'Understanding the effect of laser scan strategy on residual stress in selective laser melting through thermo-mechanical simulation', *Addit. Manuf.*, vol. 12, pp. 1-15, Oct. 2016, doi: 10.1016/j.addma.2016.05.014.

[40] J. WU, L. WANG and X. AN: 'Numerical analysis of residual stress evolution of AlSi10Mg manufactured by selective laser melting', *Optik*, vol. 137, pp. 65-78, May 2017, doi: 10.1016/j.ijleo.2017.02.060.

[41] P. CONTI, F. CIANETTI and P. PILERCI: 'Parametric Finite Elements Model of SLM Additive Manufacturing process', *Procedia Struct. Integr.*, vol. 8, pp. 410-421, 2018, doi: 10.1016/j.prostr.2017.12.041.

[42] Z. DONG, Y. LIU, W. WEN, J. GE and J. LIANG: 'Effect of Hatch Spacing on Melt Pool and As-built Quality During Selective Laser Melting of Stainless Steel: Modeling and Experimental Approaches', *Materials*, vol. 12, no. 1, p. 50, Dec. 2018, doi: 10.3390/ma12010050.

[43] Q. ZHANG, J. XIE, Z. GAO, T. LONDON, D. GRIFFITHS and V. OANCEA: 'A metallurgical phase transformation framework applied to SLM additive manufacturing processes', *Mater. Des.*, vol. 166, p. 107618, Mar. 2019, doi: 10.1016/j.matdes.2019.107618.

[44] Q. ZHANG, J. XIE, T. LONDON, D. GRIFFITHS, I. BHAMJI and V. OANCEA: 'Estimates of the mechanical properties of laser powder bed fusion Ti-6Al-4V parts using finite element models', *Mater. Des.*, vol. 169, p. 107678, May 2019, doi: 10.1016/j.matdes.2019.107678.

[45] N. E. HODGE, R. M. FERENCZ and J. M. SOLBERG: 'Implementation of a thermomechanical model for the simulation of selective laser melting', *Comput. Mech.*, vol. 54, no. 1, pp. 33-51, Jul. 2014, doi: 10.1007/s00466-014-1024-2.

[46] N. E. HODGE, R. M. FERENCZ and R. M. VIGNES: 'Experimental comparison of residual stresses for a thermomechanical model for the simulation of selective laser melting', *Addit. Manuf.*, vol. 12, pp. 159-168, Oct. 2016, doi: 10.1016/j.addma.2016.05.011.

[47] C. LI, J. F. LIU and Y. B. GUO: 'Prediction of Residual Stress and Part Distortion in Selective Laser Melting', *Procedia CIRP*, vol. 45, pp. 171-174, 2016, doi: 10.1016/j.procir.2016.02.058.

[48] C. LI, J. F. LIU, X. Y. FANG and Y. B. GUO: 'Efficient predictive model of part distortion and residual stress in selective laser melting', *Addit. Manuf.*, vol. 17, pp. 157-168, Oct. 2017, doi: 10.1016/j.addma.2017.08.014.

[49] Y. YANG, M. ALLEN, T. LONDON and V. OANCEA: 'Residual Strain Predictions for a Powder Bed Fusion Inconel 625 Single Cantilever Part', *Integrating Mater. Manuf. Innov.*, vol. 8, no. 3, pp. 294-304, Sep. 2019, doi: 10.1007/s40192-019-00144-5.

[50] X. SONG *et al.*: 'Advances in additive manufacturing process simulation: Residual stresses and distortion predictions in complex metallic components', *Mater. Des.*, vol. 193, p. 108779, Aug. 2020, doi: 10.1016/j.matdes.2020.108779.

[51] J. GOLDAK, A. CHAKRAVARTI and M. BIBBY: 'A new finite element model for welding heat sources', *Metall. Trans. B*, vol. 15, no. 2, pp. 299-305, Jun. 1984, doi: 10.1007/BF02667333.

[52] A. J. DUNBAR, E. R. DENLINGER, M. F. GOUGE and P. MICHALERIS: 'Experimental validation of finite element modeling for laser powder bed fusion deformation', *Addit. Manuf.*, vol. 12, pp. 108-120, Oct. 2016, doi: 10.1016/j.addma.2016.08.003.

[53] N. KELLER and V. PLOSHIKHIN: 'New method for fast predictions of residual stress and distortion of AM parts', in *Additive Manufacturing Conference SFF 2014*, 2014, pp. 1229-1237.

[54] X. LIANG, Q. CHEN, L. CHENG, D. HAYDUKE and A. C. TO: 'Modified inherent strain method for efficient prediction of residual deformation in direct metal laser sintered components', *Comput. Mech.*, vol. 64, no. 6, pp. 1719-1733, Dec. 2019, doi: 10.1007/s00466-019-01748-6.

[55] M. CHIUMENTI *et al.*: 'Numerical modelling and experimental validation in Selective Laser Melting', *Addit. Manuf.*, vol. 18, pp. 171-185, Dec. 2017, doi: 10.1016/j.addma.2017.09.002.

[56] L. LEVINE *et al.*: 'Outcomes and Conclusions from the 2018 AM-Bench Measurements, Challenge Problems, Modeling Submissions, and Conference', *Integrating Mater. Manuf. Innov.*, vol. 9, no. 1, pp. 1-15, Mar. 2020, doi: 10.1007/s40192-019-00164-1.

[57] ANSYS: 'Ansys Additive Manufacturing 2024 R2 - LPBF Simulation Guide', ANSYS Inc. Accessed: Jul. 21, 2025, [Online], Available: https://ansyshelp.ansys.com/public/account/secured?returnurl=//////Views/Secured/corp/v242/en/add_ag/add_ag.html

[58] T. MAYER, G. BRÄNDLE, A. SCHÖNENBERGER and R. EBERLEIN: 'Simulation and validation of residual deformations in additive manufacturing of metal parts', *Heliyon*, vol. 6, no. 5, p. e03987, May 2020, doi: 10.1016/j.heliyon.2020.e03987.

[59] R. ENOS: 'Install Abaqus 2024 User-Subroutines: How to Link Abaqus 2024 with Intel oneAPI Fortran Compiler & Visual Studio', Feb. 2024, [Online], Available: DOI: 10.13140/RG.2.2.15382.11843

[60] DASSAULT SYSTEMES: 'SIMULIA Abaqus - User Subroutines - Abaqus/Standard User Subroutines - UEXPAN', [Online], Available: https://docs.software.vt.edu/abaqusv2023/English/?show=SIMACAESUBRefMap/simasub-c-uexpan.htm

[61] E. MIRKOOHI, D. E. SEIVERS, H. GARMESTANI and S. Y. LIANG: 'Heat Source Modeling in Selective Laser Melting', *Materials*, vol. 12, no. 13, p. 2052, Jun. 2019, doi: 10.3390/ma12132052.

[62] S. HOCINE, H. VAN SWYGENHOVEN and S. VAN PETEGEM: 'Verification of selective laser melting heat source models with operando X-ray diffraction data', *Addit. Manuf.*, vol. 37, p. 101747, Jan. 2021, doi: 10.1016/j.addma.2020.101747.

[63] M. LIU *et al.*: 'A characteristic time-based heat input model for simulating selective laser melting', *Addit. Manuf.*, vol. 44, p. 102026, Aug. 2021, doi: 10.1016/j.addma.2021.102026.

[64] 'Ti: Ti-6 Al-4 V (IMI 318)', in *Recommended Values of Thermophysical Properties for Selected Commercial Alloys*, Elsevier, 2002, pp. 211–217. doi: 10.1533/9781845690144.211.

[65] G. WELSCH, R. BOYER and E. W. COLLINGS: Eds., *Materials properties handbook: titanium alloys*. Materials Park, OH: ASM International, 1994.

[66] DASSAULT SYSTEMES: 'SIMULIA Abaqus - Materials - Other Material Properties - Mechanical Properties - Thermal Expansion'. [Online]. Available: https://docs.software.vt.edu/abaqusv2023/English/?show=SIMACAEMATRefMap/simamat-c-thermalexpan.htm.

# DEVELOPING A MULTI-PHASE WELDING SIMULATION WITH DAMAGE PREDICTION SOURCING ON STANDARDIZED TENSILE TESTS AND EXPERIMENTAL VALIDATION BY DAMAGING A WELDMENT

C. SCHRÖDER*, T. LOOSE**, M. BRODT*

*Technologie Institut für Metall und Engineering GmbH, Germany
**Dr. Loose GmbH, Germany

*DOI 10.3217/978-3-99161-089-2-020, license CC BY 4.0*
*https://creativecommons.org/licenses/by/4.0/deed.en*
*This CC license does not apply to third party material and content noted otherwise.*

ABSTRACT

To accurately simulate the strength and potential damage of welded joints in structural steel, a multi-phase welding simulation is required. This is because phase transformations in the heat-affected zone (HAZ) change the local mechanical properties significantly. The main microstructural phases of steel (ferrite/pearlite, bainite, and martensite) exhibit distinct mechanical properties such as tensile strength and fracture elongation. For the prediction of damage in welding seams, these properties play a critical role and must be considered. Welding seams can be simulated with computational welding mechanics (CWM) by calculating stresses, strains, distortions, and microstructural transformations in the HAZ. For the microstructure transformations, the effects on structural properties are considered using multi-phase material models [1], [2]. Such a multi-phase material is developed and implemented in the commercial software LS-DYNA by [3], which is available as keyword ***MAT_GENERALIZED_PHASE_CHANGE (*MAT_254)**. The model was specifically developed for process chain simulations using a consistent material description [4] [5].

The presented work focuses on the numerical simulation of damage evolution in welded joints, under consideration of local phase changes and their underlying properties. The aim was to keep the same material model from welding to loading while considering the effects of local phase transformations for the prediction of damage. To do so, the damage model ***MAT_ADD_GENERALIZED_DAMAGE**, which is a generalized form of ***MAT_ADD_DAMAGE_GISSMO** developed by [6], was adopted. Three optimized sets of parameters of GISSMO, one for each of the three main phases, were identified based on numerical simulations and experimental results using LS-OPT. The approach proposed in [7] reassigns elements to parts characterized by the same mechanical properties after welding. This technique of creating local material clusters was adopted to perform the damage simulation based on the respective present phase of the steel. The three unique sets of parameters were then combined into a multi-phase damage model, which uses a mixing rule to calculate the material properties for arbitrary phase combinations.

For the final damage calculation to verify the correct damage prediction of a welded segment in a three-point bending test, it was realized that the damage model does not work properly in combination with ***MAT_254**. The predicted cracks occurred in an unrealistic manner. Further research must be carried out to determine the exact cause and to fix this problem.

Keywords: GISSMO, MAT_254, multi-phase damage model, welding, Steel C45, phase transformation

## METHODOLOGY FOR MULTI-PHASE WELDING SIMULATION

To capture the influence of microstructural phase transformations on damage evolution in the HAZ of structural steel welds, a systematic workflow was established comprising specimen preparation, experimental characterization, material model calibration, and data-field generation for LS-DYNA's generalized phase-change material (*MAT_GENERALIZED_PHASE_CHANGE*, MAT 254).

Four distinct specimen geometries were manufactured from the same base steel, which was used for the welding task. These geometries were selected to impose varying stress triaxialities during fracture testing. The manufactured specimens were heat treated to create the different phases which are present in the HAZ of the selected base steel.
This results in a suite of specimens representing pure ferrite/pearlite, bainite, and martensite microstructures. Each condition was verified via optical microscopy and image analysis to confirm the expected phases.

The uniaxial stress–strain curves for ferrite/pearlite, bainite, and martensite were each fitted to the piecewise linear plasticity Model (MAT 24). Key parameters (effective plastic strain/yield stress values) were optimized via least-squares matching in LS-OPT. Using the damage model including triaxialities, the GISSMO parameters – triaxial break elongation curve and triaxial material instability curve were calibrated for each phase. The resulting three sets of GISSMO parameters encapsulate the distinct ductile fracture behaviour of each microstructure.

In MAT 254, local phase fractions are provided as state variables at each element. To account for arbitrary mixtures in the HAZ, the single-phase material models must be combined into a continuous material data field. The plastic and fracture responses for the pure phases are tabulated as functions of equivalent plastic strain and stress triaxiality. For any combination of $\varphi_F$, $\varphi_B$, $\varphi_M$ (Ferrite, Bainite, Martensite) the resulting effective plastic strain rate as a function of yield stress is already calculated in MAT 254. For the fracture response, the arbitrary combination of the phases needs to be computed by linear equations into a multi-dimensional material map, which returns the material parameters in relation to the triaxiality. This table is then input to MAT 254 via the phase mixture saved for every element in the history variable keyword, enabling on-the-fly evaluation of the mixed-phase mechanical response during welding simulation.

The second approach uses the generalized GISSMO model: MAT_ADD_GENERALIZED_DAMAGE. This model provides up to three history variable which can be addressed each with own GISSMO parameter. This enables to define the GISSMO parameter separated for ferritic-pearlitic phase, bainitic phase and martensitic phase.

# DEVELOPING MULTI PHASE MATERIAL CARDS

## MATERIAL PHASES AFTER WELDING

To establish the multi-phase welding simulation, the different material properties for the different phases must be tested. Several phases can form during the welding process, such as upper bainite, lower bainite, martensite or tempered martensite. To keep the simulation complexity manageable, the three main phases ferrite-perlite, bainite and martensite are selected. The material chosen was the normalized structural steel C45, as it is prone to harden after welding due to its higher carbon content. The different phases, which can occur in the heat affected zone are shown in the figure below.

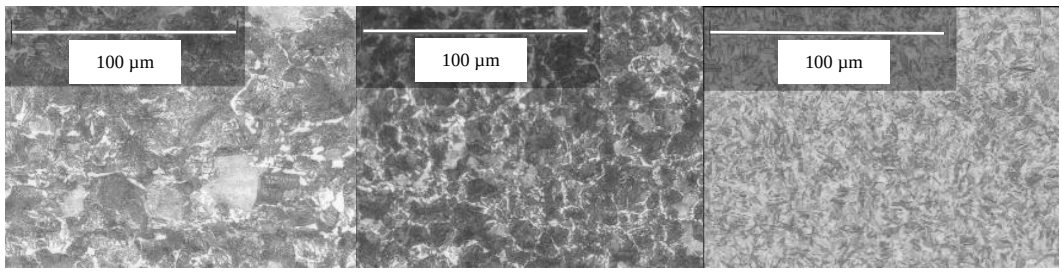



**Fig. 1** Different phases of C45 steel of the tensile test specimens. Left: Ferrite-Pearlite, mid: Bainite, right: Martensite

## PLASTIC MATERIAL PROPERTIES

The material properties are determined through tensile tests. To obtain phase-specific results, the C45 steel was subjected to various heat treatment processes, during which the three phase-pure microstructures martensite, bainite and ferrite/pearlite were produced. The heat treatment process-parameters are explained in table 1.

**Table 1** Heat treatment process-parameters [8]

| Heat treatment | Temperature (Austenite) | Cooling |
|---|---|---|
| Normalisation | 840 °C | Air cooling 20°C |
| Bainitisation | 840 °C | Salt bath 400°C |
| Hardening | 840 °C | Water 20°C |

F. X. C. Andrade developed in [9] special triaxial tensile test specimens, which are also used in this study. The geometry of the tensile test specimens and the mount for the tensile testing machine are shown in Fig. 2. The four geometries were modelled in LS-DYNA and

boundary conditions were applied just as in the experiment i.e. the keyword *BOUNDARY_PRESCRIBED_MOTION was applied to the inner surface half of the upper hole and the keyword *BOUNDARY_SPC was applied to the inner surface half of the bottom hole with full constraints in all directions. The prescribed displacement was selected according to the respective experiment. The simulation time of the implicit simulation was chosen to be 10 s to ensure no dynamics effects are present. To account for large deformations and stretching of the elements during the simulation, element formulation -2 was used, which corresponds to an 8-point hexahedron element whose algorithm is especially suitable for elements with poor aspect ratio. A mesh size of 0.5 mm was used in the critical area around the crack for each simulation. The meshes are shown below for each specimen.

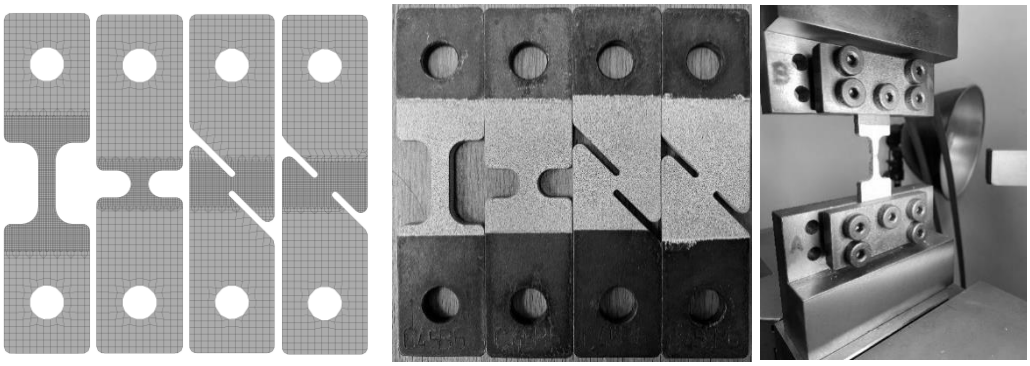


**Fig. 2** Different tensile test specimens for different stress triaxialities. Starting from left to right: short specimen, notched specimen, shear 0° specimen and shear 45° specimen

The plastic material behaviour, which is necessary for the material card in LS-DYNA, was identified based on the experimental median curve of the tensile test with the short specimen (see Fig. 2 on the left). The identification of the parameters was done by least-squares matching in LS-OPT. To do so, the post-critical part of the curves was removed. The tensile tests were carried out for each phase and the results for the normalized experiments are shown in Fig. 3. The nominal cross-section area is 25 mm².

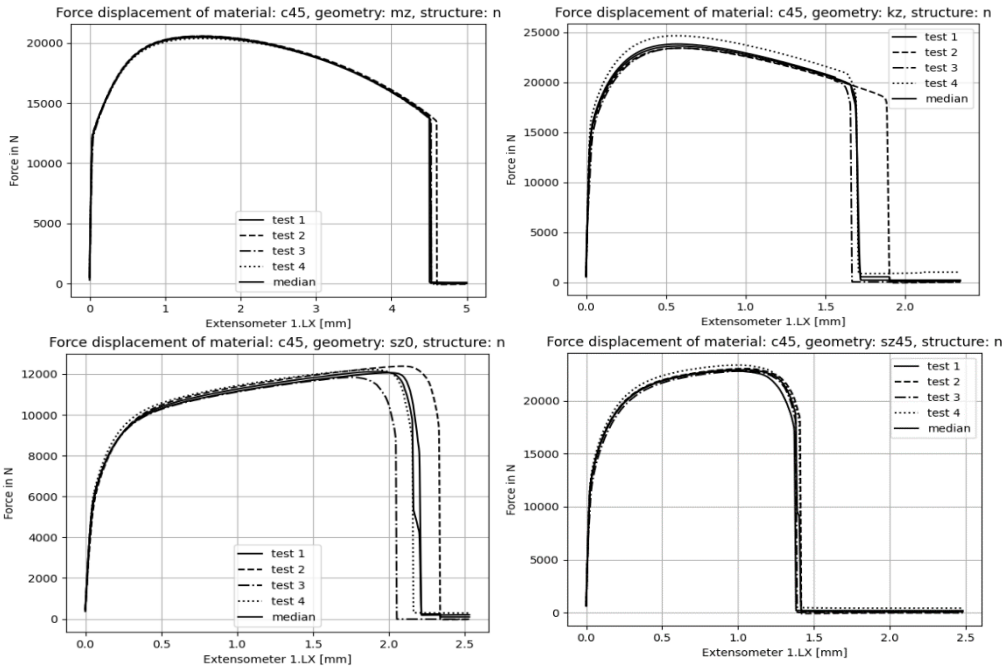



**Fig. 3** Force displacement curves for the normalized specimens: short (MZ), notched (KZ), shear 0° (SZ0) and shear 45° (SZ45). For each specimen, four tests were carried out.

For the martensite specimens, the tests could not be evaluated, because their fracture force was not stable. The reason for this behaviour is the brittleness of quenched martensitic steel. After quenching, the specimens were slightly deformed, so they could not be tested without bending stresses. For the novel multiphase fracture model development, the GISSMO model needs especially the plastic behaviour of the material and Martensite has nearly no plastic elongation anymore, so an approximated value for the tensile strength can be used. To test the hardening rate of the material, the formula

$$HV_{max} = 802 \cdot C + 305\,[C\ in\ \%]$$

can be used to compare the Vickers hardness value with the test specimens [8]. The general behaviour of martensitic steel in relationship to a tempering process of the material is shown in Fig. 4. It becomes clear, that by increasing the tempering temperature, the tensile strength $R_m$ is reduced, and the break elongation A is increased. In the use case of single-layer welding, the tempering process is not present, so the weld seam might have brittle martensitic parts, which can cause cold cracks [10].

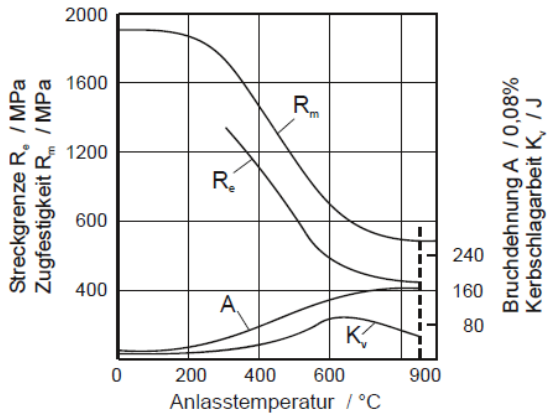



**Fig. 4** The material behaviour of martensite before and after tempering [8]

## GISSMO DAMAGE MODEL MATERIAL PROPERTIES

The GISSMO Model developed by F. Neukamm [6] was primarily conceptualized for sheet metal forming processes. The advantage of this model is that it defines the failure strain curve and the instability curve as a function of triaxiality, which makes implementation into the simulation easy, if tensile tests of different geometries are available. It is parameterized by the two curves mentioned above as well as by its exponents FADEXP and DMGEXP, where the first one controls the post-critical fadeout of the material and the later one controls the type of damage accumulation e.g. linear or non-linear. The parameters of GISSMO were identified by a multi-objective optimization using LS-OPT. The median experimental curve, including post-critical failure, was matched against the resulting curve of the simulation by using the Genetic Algorithm (GA) in combination with the Leapfrog optimizer (LFOP) to speed up the optimization after a global optimum was found by GA. As an error measure, the mean squared error and curve mapping are available within LS-OPT. The authors of [11], showed that the mean squared error is the superior error measure for this optimization problem and, therefore, it was chosen. The identified fracture and critical strain curves are shown below. For the normalized material, the FADEXP and DMGEXP were identified as 2.0 and 1.6 respectively and for the bainitized material they were identified as 2.0 and 2.5 respectively. For the martenized material, the fracture curve was chosen such that the material is allowed to strain up to 0.5 % plastically. This small amount of plastic strain helped with numerical stability and the location of the crack happened reasonable in the middle of the part. Both damage and fade exponent were taken as 1.0.

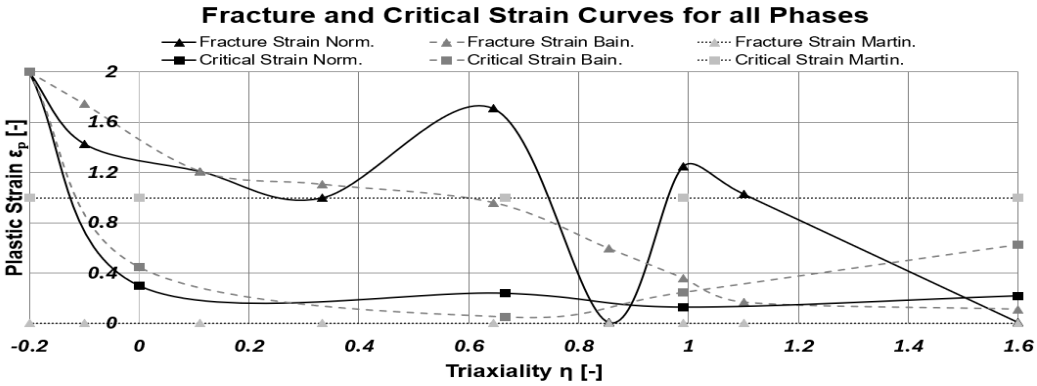



**Fig. 6** Fracture and critical strain curves for all three main phases of steel i.e. ferrite/pearlite, bainite, and martensite

Fig. 7 compares experimental curves with simulations, showing good agreement for MZ, KZ, and SZ0 within the experimental scatter (see Fig. 3).

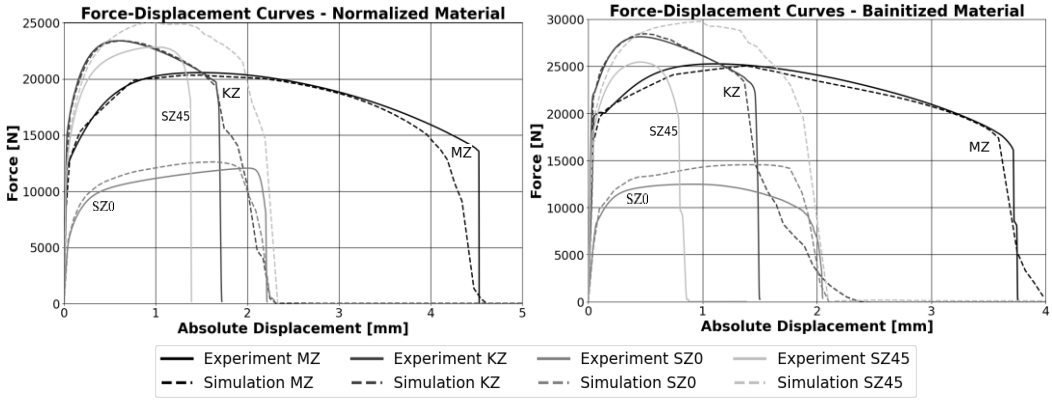



**Fig. 7** Force vs. displacement curves for the GISSMO optimization

However, for the SZ45, both the plastic material behavior and the predicted material failure deviate noticeably from the experimental results. The calculated force exceeds the experimentally measured force, which is a phenomenon reported by the authors of [9] as well. The plastic material model *MAT_024 makes use of the J2-based plasticity model which assumes that yielding of the material happens only due to shear stresses. It neglects the influence of hydrostatic stress states. In reality, however, the material is in a complex combination of stresses and the growth of micro defects, due to hydrostatic stresses, might be a reason for the misprediction of the plastic straining. Further research is required to fully understand the underlying process.

In addition to the misprediction of the plastic straining, the GISSMO damage model predicted the failure to be softer and later than in the experiments. To investigate this, the triaxiality and plastic strain of the deleted elements was plotted. For each specimen, the mean curve of the deleted elements was plotted together with the standard deviation from the mean to also visualize the range of triaxiality. The plot shows that the triaxiality of the SZ45 overlaps with the triaxiality of the MZ and KZ specimens, which means that changing the parameters of either MZ or KZ will influence the curve of the SZ45 as well and thus made the optimization difficult.

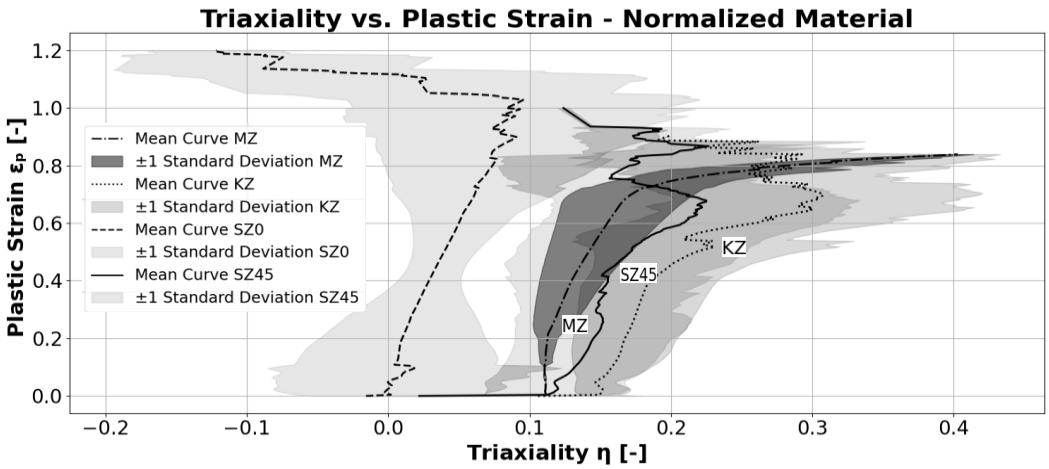



**Fig. 8** Triaxiality vs. plastic strain for the normalized material

A visual comparison of the fracture surfaces from the normalized experimental samples and the simulations is presented below. The fracture surfaces for the MZ and KZ specimens were reproduced well by the simulation. For both cases, a smooth crack can be seen.

For the shear specimens, the experimental fracture surfaces appear macroscopically smooth. In contrast, the simulated fracture shows torn elements, leading to an artificially rough surface. This can be attributed to the relatively large mesh size, which is insufficient to resolve microscale fracture mechanisms. A microscopic examination of the experimental surface would likely reveal features more consistent with those observed in the simulation.

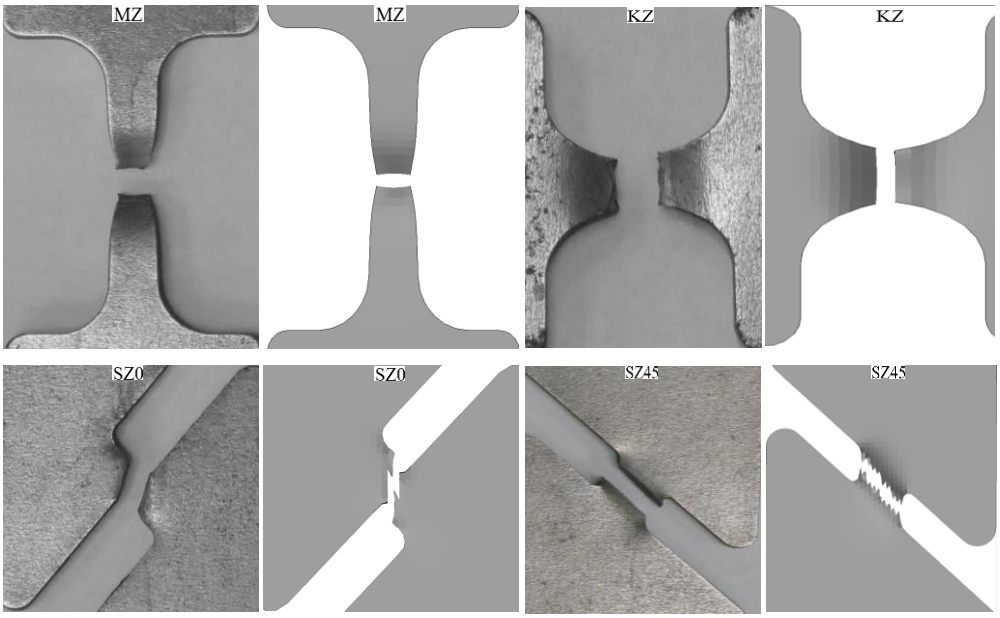



**Fig. 8** Comparison of fracture surfaces of experiments vs. simulation

## INTERPOLATION OF MATERIAL PROPERTIES WITH LINEAR EQUATIONS

To build the multiphase GISSMO damage model, mainly two curves are necessary to define, the material instability curve ECRIT and the failure curve LCSDG. To calculate the two material curves for every phase combination, a linear system of equations is used to find an explicit description for this problem and the described function $\epsilon_\eta$ solves both curves. These equations are working in two curve definitions in LS-Dyna and calculate the material failure properties for every node as a function of stress triaxiality η. To get the solution parameters a-d for every phase composition, the following linear system of equations must be solved, in which $\varphi_F, \varphi_B$ and $\varphi_M$ are the phase rations of ferrite/perlite, bainite and martensite. The first equation

$$\epsilon_\eta \begin{pmatrix} \varphi_F \\ \varphi_B \\ \varphi_M \end{pmatrix} = a * \varphi_F + b * \varphi_B + c * \varphi_M + d$$

describes a straight line in the $\mathbb{R}^4$ and the second equation

$$\varphi_F + \varphi_B + \varphi_M = 1$$

a plane in the $\mathbb{R}^3$ as a boundary condition, because the phases added up cannot be more than 100%. Only three points are necessary to solve this problem with four unknown variables because of the boundary condition, which cuts the solution plane into a solution line. The three

points are already calculated in the GISSMO analysis of the three material simulations with the three different material phases ferrite/perlite, bainite, and martensite. The described solutions

$$\epsilon_\eta \begin{pmatrix} 1 \\ 0 \\ 0 \end{pmatrix} = LCSDG_{\eta,\varphi_F}, \qquad \epsilon_\eta \begin{pmatrix} 0 \\ 1 \\ 0 \end{pmatrix} = LCSDG_{\eta,\varphi_B}, \qquad \epsilon_\eta \begin{pmatrix} 0 \\ 0 \\ 1 \end{pmatrix} = LCSDG_{\eta,\varphi_M}$$

solve the equation $\epsilon_\eta$ for every triaxiality point $\eta$ of the curves ECRIT and LCSDG and the solutions must be entered into the associated material card.

The second approach uses directly the phase proportion ferrite-pearlite, bainite, and martensite. The material instability curve ECRIT and the failure curve LCSDG are defined separately for each phase. The damage index is calculated according to these parameters weighted by the phase proportion.

## MICROSTRUCTURE SIMULATION AND SOURCE DATA

The LS-DYNA Material Model *MAT_GENERALIZED_PHASE_CHANGE (*MAT_254) supports different models to calculate the phase transformation. For this investigation the Koistinen-Marburger Law is applied for the diffusion-free Austenite-Martensite transformation. The decomposition from Austenite to Bainite and Ferrite-Pearlite is calculated with the generalized Johnson-Mehl-Avrami-Kolmogorov model (JMAK). In welding tasks, the cooling is continuous and does not contain any hold times. The transformation is described by Constant-Cooling-Time (CCT) diagrams. The phase proportion at complete cooling is defined by cooling time needed for the temperature-interval between 800 °C and 500 °C. The value for PEQ TAU and N of the JMAK model are kept constant and the Leblond parameter F which describes the transformation velocity depending on the cooling rate is used to adjust the phase transformation. For this work the source data for the phase transformation is taken from WeldWare® [12] [13]. The data based on many physical experiments known as physical welding simulation performed by Seyffarth, Groß and Scharff and published in [14]. WeldWare® provides the data for phase transformation from Austenitisation at 1350 °C down to complete cooling according the cooling time between 850 °C and 500 °C. The chemical composition for the Steel C45 used in this work is given in Table 2.

**Table 2** Chemical Composition C45 in wt. %

| C | Si | Mn | P | S | Cr | Ni | Mo | Cu | Al | Ti | Nb | N |
|---|---|---|---|---|---|---|---|---|---|---|---|---|
| 0,47 | 0,24 | 0,68 | 0,01 | 0,001 | 0,22 | 0,02 | 0,004 | 0,01 | 0,022 | 0,003 | 0,001 | 0,004 |

A simple model of single independent cube is used to check phase transformation. At each cube a thermal cycle with constant cooling rate is applied. Fig. 9 shows the phase – cooling time – transformation diagram with source data from WeldWare® and the result from simulation check.

In addition, the yield stress, tensile stress, elongation at break and hardness for uniaxial tensile test are provided by Weldware® according the cooling time.

*MAT_GENERALIZED_PHASE_CHANGE (*MAT_254) provides eight history variables, which can be defined by user defined functions. This enables the output of the mechanical properties after change of microstructure. Fig. 10 shows the yield stress and tensile stress over cooling time. Fig. 11 shows the elongation at break over cooling time. Both diagrams point out that the source data is hit exactly by the simulation approach.

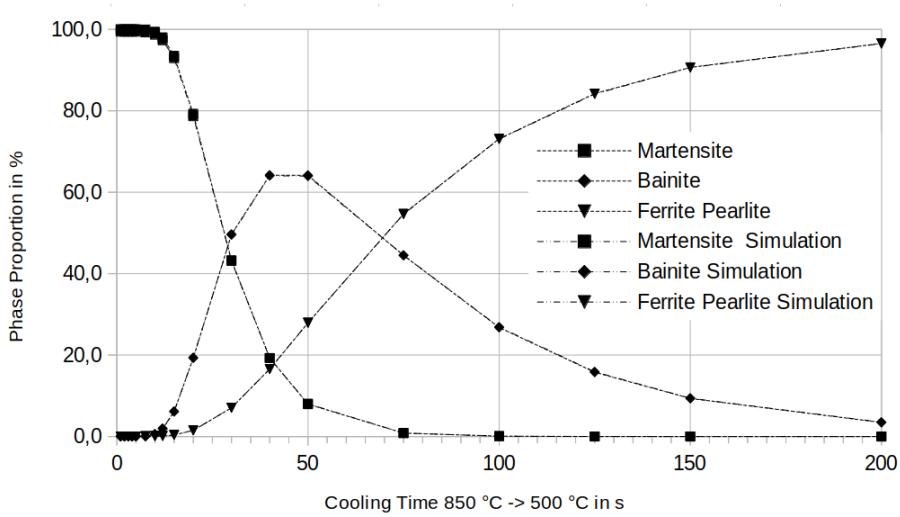



**Fig. 9** Phase Proportion over Cooling Time; Source data vs. simulation

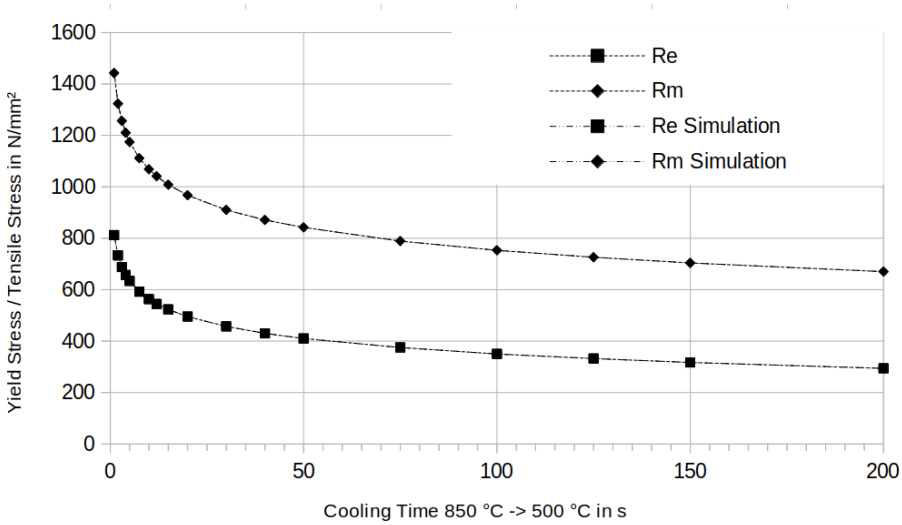



**Fig. 10** Phase Proportion over Cooling Time; Source data vs. simulation

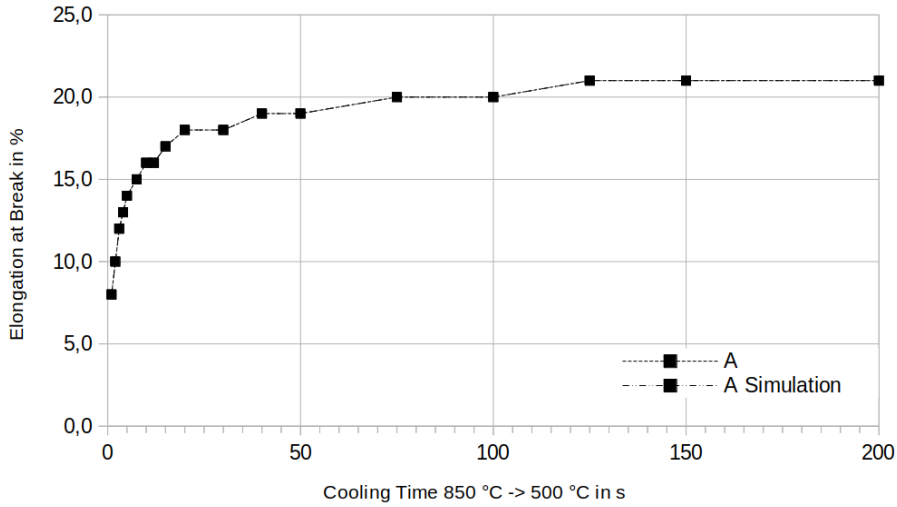



**Fig. 11** Phase Proportion over Cooling Time; Source data vs. simulation

The use of WeldWare® data enables engineering in advance without any physical material testing. In this work, tensile test of the material was performed for base material (normalized), bainitic microstructure and martensitic microstructure. As a result, a difference between tensile tests of the chosen material and WeldWare® data can be seen. The mechanical properties and flow curve data from tensile tests are applied in the material model used for the simulations.

## EXPERIMENTAL VALIDATION OF THE DAMAGE MODEL

In order to validate the predictive capability of the proposed damage model for simulated weld seam strength and fracture behaviour, a series of TIG (Tungsten Inert Gas) welding specimens were produced and mechanically tested with a three-point bending experiment. This chapter details the welding parameters, specimen geometry, testing procedure, and observed results for both top-side and bottom-side bending tests.

### WELDING PROCEDURE

All specimens were produced as blind butt welds in 5 mm thick plates of the selected structural steel. An argon-shielded TIG process was employed with the following nominal parameters:

- Current: 300 A; Voltage: 13 V; Welding Speed: 5 mm/s
- Shielding gas: Argon; flow: 15 L/min
- Joint type: Blind weld (no full penetration)

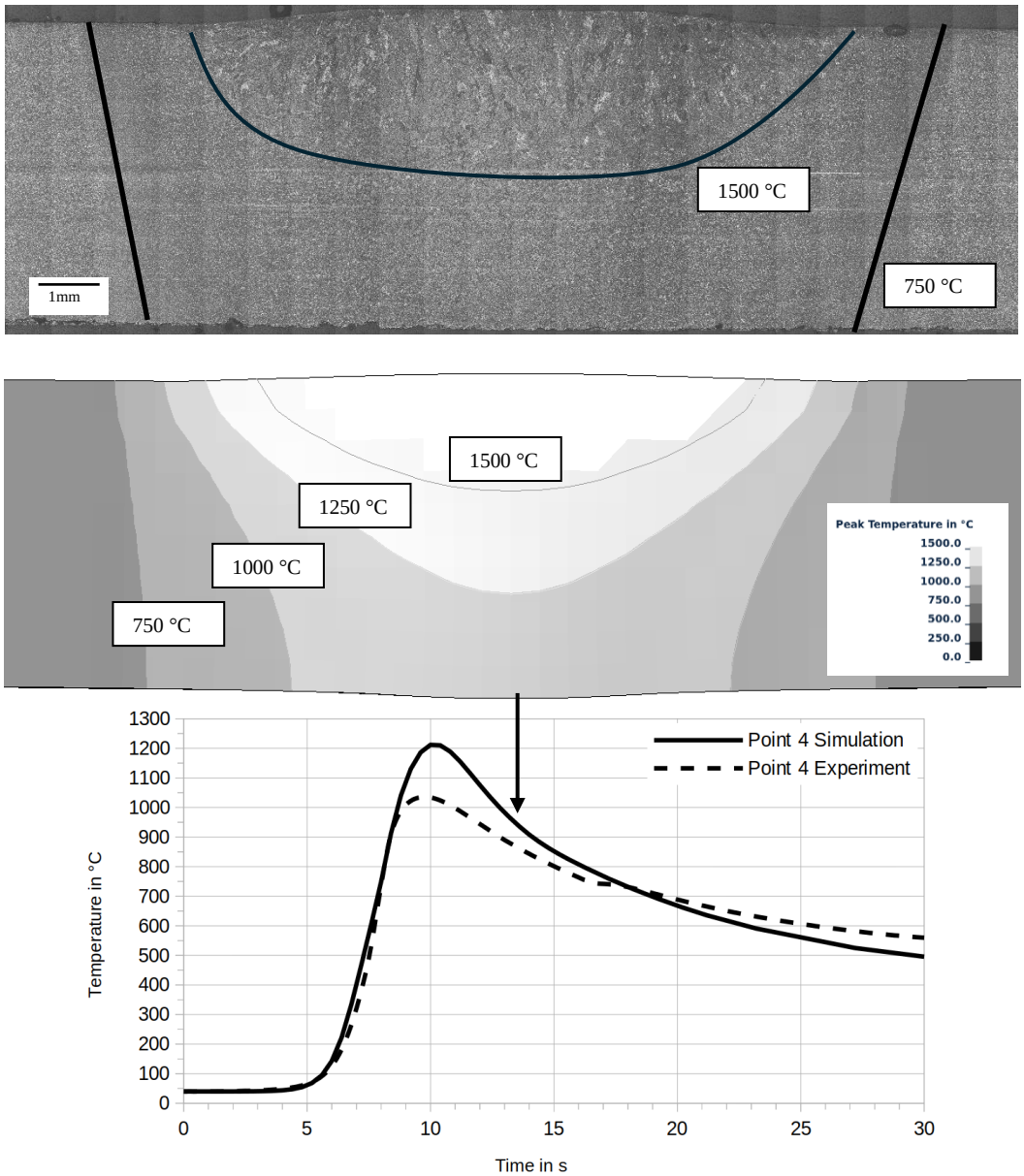



**Fig. 12** Macro section of welding and cross-section with peak-temperature of simulation. The HAZ lines are thick black and the solidification lines are thin black. The temperature progression was measured with TC on the bottom side of the welding seam.

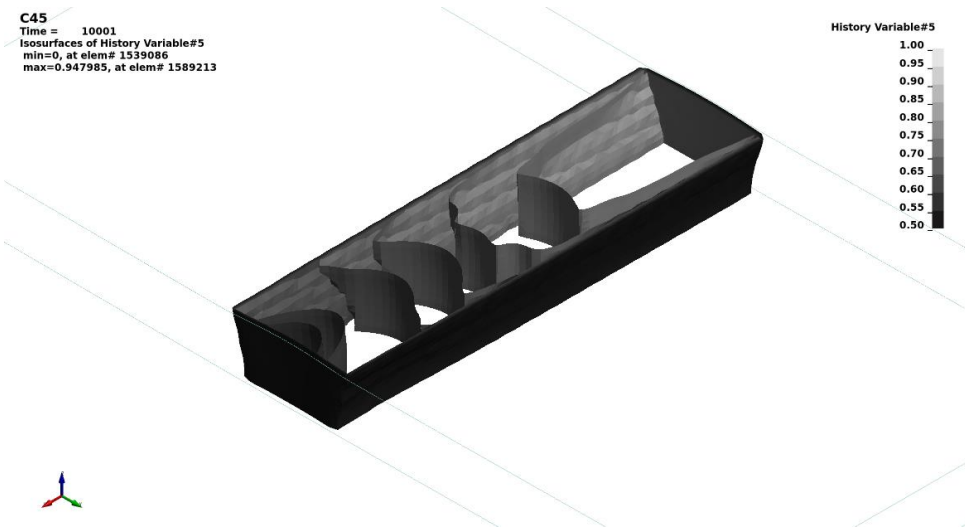



**Fig. 13** Martensite proportion

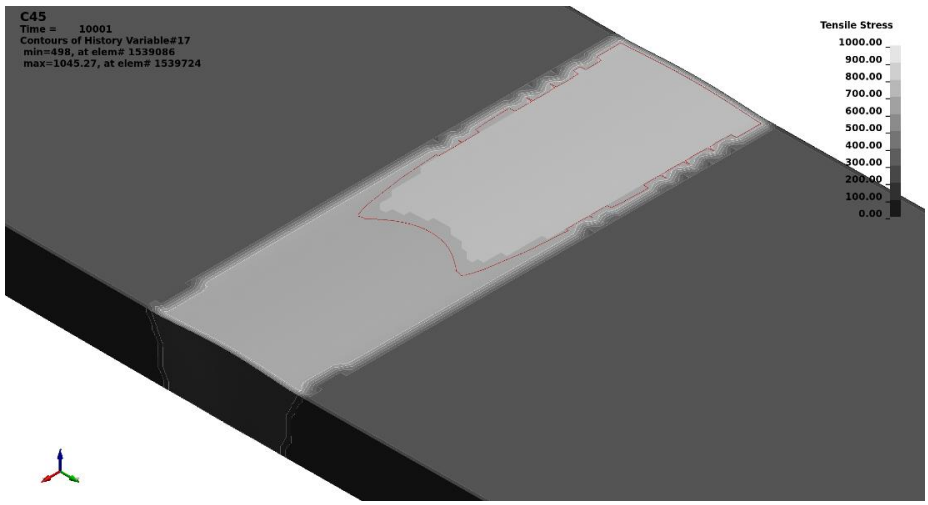



**Fig. 14** Tensile stress after welding according to WeldWare® data

Prior to welding, joint faces were prepared by manual grinding to a clean surface. The root side remained unwelded to simulate a common partial-penetration condition. Each weld pass was executed with no filler material added in the root region to ensure consistent lack of penetration and no material mixing.

After welding, specimens were allowed to cool to ambient temperature under still-air conditions. The resulting macro section of weld experiment, compared with the peak

temperature of the simulation are shown in Fig. 12 and show a good accordance. The temperature over time at bottom side in the centerline measured by thermocouple is also in good accordance with the result of the simulation (Fig. 12).

After welding the plate is cut to the size of specimen for the bending test. The cutting is also considered in the simulation by erasing all elements outside the test specimen.

One result of the simulation is the phase composition of the microstructure. Fig. 13 shows the martensite proportion after welding. The faster cooling at begin of the weld leads to higher martensite composition than at end of the weld.

Fig. 14 displays the tensile stress computed by evaluating the cooling time according to the data provided by WeldWare®.

## THREE-POINT BENDING TEST SETUP

Mechanical validation was performed according to DIN EN ISO 5173 (“Bend Test”) in an universal testing machine. Specimens were machined into rectangular cross-sectional bars (dimensions: 95 mm × 40 mm × 5 mm), with the weld seam running longitudinally at mid-span. Four specimens were tested with the weld crown facing upward (top-side bending) and four with the weld root facing upward (bottom-side bending). During each test, load–deflection curves were recorded continuously.

## FIRST RESULTS

All four top-side specimens exhibited brittle fracture initiating at the weld centerline. The maximum bending load averaged was 19.4 kN. The fracture surfaces exhibit a brittle fracture pattern that continues centrally within the weld seam. The crack-pattern of the top-side specimens are shown in Fig. 15.

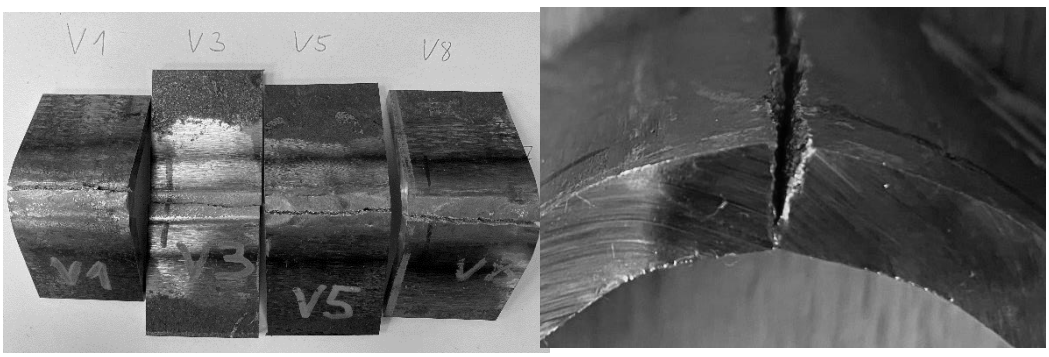



**Fig. 15** Fracture pattern of the top-side specimens with martensitic brittle fracture pattern

In contrast, none of the four bottom-side specimens fractured under the same loading conditions, as shown in Fig. 16.




**Fig. 16** Bottom-side specimens with no fracture after testing. The plastic flow of material around the HAZ is observed.

Instead, the specimens exhibited continuous plastic deformation around the heat-affected zone (HAZ), with material bulging and flowing into the unwelded root gap. Maximum loads reached up to 21.5 kN without any macroscopic crack formation. The described behaviour of the two different tests is shown in the force displacement curves in Fig. 17. The ductile behaviour of the bottom-side of the welding seam confirms that the absence of full penetration allows stress redistribution, preventing critical damage accumulation as described by the model.

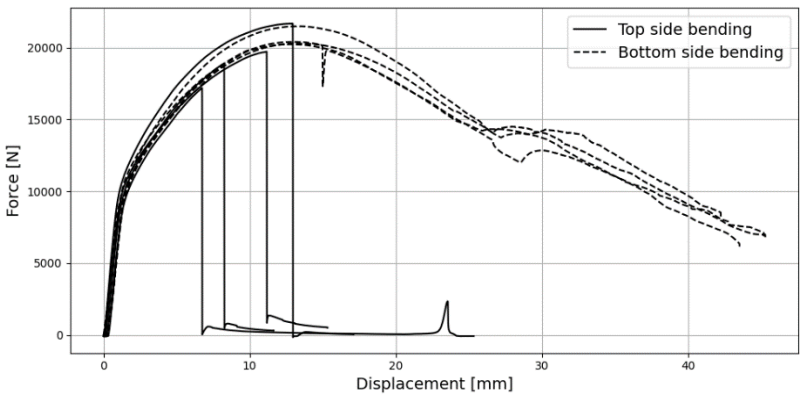



**Fig. 17** Force displacement curves of the bending test. Left: top-side, right: bottom-side

Next step is the simulation of bending test with correct detection of fracture. It will be evaluated which of the both approaches for the damage model fits better the real experiment.

## CONCLUSION

In this study, a methodology for mixing rules for the mechanical properties of different phases in steel was successfully demonstrated. The approach considers both, elastic-plastic

behaviour and damage properties. This was made possible through single-phase, standardized tensile specimens that represent the distinct mechanical characteristics of the steel microstructures.

Based on the proposed linearized mixing rule, the mechanical properties of phase mixtures present in the heat-affected zone of welded joints were subsequently determined. Experimental three-point bending tests provided a basis for validating the developed simulation model.

A final validation has not yet been completed at the time of publication, as errors occur in the applied GISSMO implementation in LS-DYNA in combination with the multiphase material model MAT254. Furthermore, the developed methodology is currently limited to welding processes without filler materials. Additional research is required to incorporate filler metals by accounting for the dynamic melt mixing driven by electromagnetic forces, thereby enabling the consideration of locally evolving alloy compositions and their influence on mechanical properties.

## References


[1] T. LOOSE: *Einfluß des transienten Schweißvorganges auf Verzug, Eigenspannungen und Stabilitäsverhalten axial gedrückter Kreiszylinderschalen aus Stahl*, 2007.

[2] J. HILDEBRAND: *Numerische Schweißsimulation Bestimmung von Temperatur, Gefüge und Eigenspannung an Schweißverbindungen aus Stahl- und Glaswerkstoffen*, 2008.

[3 T. LOOSE and T. KLOEPPEL: *An LS-DYNA material model for the consistent simulation of welding, forming and heat treatment*, 2015.

[4] T. KLÖPPEL, A. ERHART, A. HAUFE and T. LOOSE: 'Recent Developments in LS-DYNA to close the virtual process chain for forming, press hardening and welding', *18th Internationals Esaform Conference on Metal Forming*, 15. - 17. April 2015, Graz, Austria.

[5] T. LOOSE, J. R. J. PREHM and U. DIEKMANN: *Simulation chain of material simulation, heat treatment simulation and welding simulation for industrial application*, 2018.

[6] F. NEUKAMM: *Lokalisierung und Versagen von Blechstrukturen*, 2018.

[7] J. PREHM and T. LOOSE: *Determination of weld joint strength by welding simulation*, 2019.

[8] E. ROOS and K. MAILE: *Werkstoffkunde für Ingenieure*, Springer, 2015.

[9] C. ANDRADE, M. FEUCHT, A. HAUFE and F. NEUKAMM: *An incremental stress state dependent damage model for ductile failure prediction*, CrossMark, 2016.

[10] G. SCHULZE: *Die Metallurgie des Schweißens*, Heidelberg: Springer, 2010.

[11] J. EFFELSBERG and M. FEUCHT: *Identifikation von Materialparametern mit LS-OPT - GISSMO und andere Anwendungen*, 2014.

[12] A. SCHARFF and C. KÖTHE: 'Ermittlung der mechanischen Kennwerte von MAG-Schweißgut mit Hilfe des schweißtechnologischen Beratungssystems WeldWare®', *DVS-Berichte, vol. 156, pp. 102-156, 1993.*

[13] A. SCHARFF: 'WeldWare® - the weldability of steel-based materials', IN *Computer in Welding Education & Engineering, Stockholm*, 1995.

[14] P. SEYFFARTH, B. MEYER and A. SCHARFF: *Großer Atlas Schweiß-ZTU-Schaubilder*, Düsseldorf: DVS-Verlag, 1992.

# FRACTURE MECHANICS BEHAVIOR OF HSS STEEL WELDED JOINT HETEROGENEOUS STRUCTURE - EXPERIMENTAL AND NUMERICAL EVALUATION

D. TOMERLIN*+, N. GUBELJAK**, D. KOZAK*, W. LI***, N. TRIŠOVIĆ****

**Mechanical Engineering Faculty, University of Slavonski Brod, HR-35000 Slavonski Brod, Croatia; 0000-0002-3461-4954*
*dtomerlin@unisb.hr; 0000-0001-6542-0688 dkozak@unisb.hr; +corresponding author*
***Faculty of Mechanical Engineering, University of Maribor, SI-2000 Maribor, Slovenia; 0000-0002-3276-8431*
****School of Mathematics and Statistics, Xidian University, Xi'an, P. R. of China; liweilw@mail.xidian.edu.cn*
*****Faculty of Mechanical Engineering, University of Beograd, 11120 Beograd, Serbia; 0000-0003-1043-5780*

*DOI 10.3217/978-3-99161-089-2-021, license CC BY 4.0*
*https://creativecommons.org/licenses/by/4.0/deed.en*
*This CC license does not apply to third party material and content noted otherwise.*

## ABSTRACT

Due to the physics and chemistry behind the fusion welding process, the welded joints are consequently significantly heterogeneous structures. They can be fundamentally divided into characteristic regions of Base Metal (BM), Weld Metal (WM) and Heat Affected Zone (HAZ). Such heterogeneity of the welded joint material microstructures in relation affects their general mechanical properties, which can vary significantly in relation to individual weld zones. The fracture behavior of welded joints consequently depends on the mechanical properties of the material zone in which the crack is located. The paper considers double-V butt joint (X joint) made of High Strength Steel (HSS), welded with filler metal having slightly overmatching mechanical properties as compared to base metal. The experimental work relies on the initial tensile testing in order to obtain stress-strain material properties, covering all the welded joint material regions of interest. In the continuation, the fracture mechanical testing is done to determine the fracture toughness characteristic parameters, as well as all the characteristic fracture behavior curves. The experimental investigation is carried out on Single Edge Notch Bend (SENB) specimens, located in welded joint zones of interest, namely BM, HAZ, and WM. The prediction of fracture behavior of metallic materials, through the initiation and evolution of damage, can be numerically simulated using the Ductile Damage material model. Such a model in general relies on stress-strain curves obtained from tensile tests of individual material zones within the observed heterogeneous structure. In this paper, using the example of SENB test specimens, the general methodology for modeling and simulating material heterogeneity of welded joints is presented. Finally, experimentally determined fracture mechanics curves and behavior of characteristic welded joint regions are simulated numerically for HSS steel grade. In this way, the possibility of numerically predicting the fracture behavior of heterogeneous structures is demonstrated.

Keywords: heterogeneous welded joint; high strength steel; fracture behavior; Ductile Damage model; numerical analysis

## INTRODUCTION

Welded joints exhibit significant heterogeneity due to the complex thermal cycle involved in the welding process, which leads to the formation of multiple characteristic zones within the joint. During welding, localized melting occurs in specific regions, resulting in distinct microstructural changes and variations in material properties across these zones. The fundamental segmentation of a welded joint typically includes the base material (BM), the weld metal (WM), and the heat-affected zone (HAZ) [1,2]. The width of the HAZ is primarily influenced by the type of welding process employed as well as the specific process parameters, such as heat input, cooling rate, and welding speed. The boundary separating the HAZ from the base material is defined by the fusion line, which marks the transition from fully melted to thermally affected but non-melted material. Each of these zones is characterized by unique microstructures, such as different phases, grain sizes, and hardness levels, that directly affect the joint's overall mechanical properties, including strength, toughness, and ductility. The research on the topic of welded joint heterogeneity, its characteristic zones and related properties has been of significant interest to various researchers such as K.E. Easterling [1], E. F. Nippes [3], W. F. Savage et al. [4], J. C. Lippold [5], M. Lomozik [6] and others.

The heterogeneity of a welded joint is not only characterized by its division into main regions, the BM, HAZ and WM, but also through the strength mismatch within the joint. Welded joint strength mismatch refers to the differences in mechanical properties, especially yield strength, among these regions, focusing on the WM and BM. There are two primary types of mismatch: overmatching (OM), where the weld metal is stronger than the base metal, and undermatching (UM), where the weld metal is weaker. Each type uniquely affects stress distribution, crack initiation, and structural integrity. Weld strength mismatch is typically quantified by the ratio of yield strengths between the WM and BM, as expressed by the equation:

$$M = \frac{\sigma_{\mathrm{YW}}}{\sigma_{\mathrm{YB}}} \tag{1}$$

Where $M$ is the mismatch factor, while $\sigma_{\mathrm{YW}}$ and $\sigma_{\mathrm{YB}}$ represent the yield strength of the WM and the yield strength of the BM, respectively.

The weld strength mismatch behavior is previously investigated by numerous researchers such as M. Koçak et al. [7], J. Spurrier et al. [8], Y. Lei and R. A. Ainsworth [9], Y. J. Kim and K. H. Schwalbe [10-12], G. H. B. Donato et al. [13], U. Zerbst et al. [14], and others. Heterogeneity in steel welded joints and strength mismatch effects, as the topics of research interest, are also being actively researched by the authors of this paper, D. Tomerlin, N. Gubeljak and D. Kozak [15,16].

Welded joint heterogeneity and strength mismatch significantly impact the fracture toughness and fracture behavior of welded steel structures. Variations in microstructure and mechanical properties across different weld zones (BM, WM and HAZ), create stress concentrations that can act as initiation sites for cracks. This microstructural heterogeneity influences crack propagation paths, potentially reducing toughness and increasing susceptibility to brittle fracture. Similarly, strength mismatch, whether OM or UM, affects stress distribution within the joint. OM welds have a WM with higher yield strength,

protecting the lower-toughness weld region from high strains that can lead to fracture during overload. While beneficial overall, OM can create a high triaxial stress state at the crack tip in the HAZ, potentially promoting local crack growth. UM welds have a lower yield strength WM, which offers higher ductility and toughness but can lead to faster fatigue crack growth and more significant deformation in the weld itself. Overall, these factors modulate the fracture toughness, crack initiation, and propagation characteristics of steel welds, highlighting the importance of understanding and controlling heterogeneity and mismatch to ensure structural integrity and safety.

The investigations outlined in this paper build upon a broader research effort by the authors, which focused on the heterogeneity of welded joints made from S690QL1 high-strength structural steel [15,16]. This prior work included developing methods and test specimens for experimental testing of small material zones within the welds [16,17], as well as conducting numerical modeling of heterogeneity within welded joints [16].

Specifically, the stress-strain properties of the heterogeneous welds were examined using Mini Tensile Specimens (MTS), and these findings were complemented by numerical simulations of several welded joint models (WJM) subjected to tensile testing, employing a ductile damage model. These preliminary studies: "*stress-strain properties of HSS steel welded joint heterogeneous structure: experimental and numerical evaluation*" published in "*Mathematical Modelling of Weld Phenomena 13*" [18], serve as the foundation for the current research presented here.

In scope of this paper, the acquisition of stress-strain data for the specific regions of interest: the BM, HAZ and WM, is done initially. Due to the limited size of these material regions, subsize tensile specimens are required. Suitable specimens for testing welded joints include Mini Tensile Specimens (MTS) and small-sized round specimens as specified in ASTM E8. The data obtained from these tensile tests are essential for developing and calibrating ductile damage numerical models.

Next, fracture mechanics testing following the ASTM E1820 standard is carried out to determine the fracture toughness parameters and to develop characteristic fracture behavior curves. These tests use Single Edge Notch Bend (SENB) specimens placed strategically in the weld joint regions of interest, including the BM, HAZ, and WM.

The second part of this paper focused on numerical modeling, initially proposes and establishes the welded joint geometry simplifications for numerical simulations purposes. Using these simplifications, the corresponding models of the SENB fracture test specimens are created specifically to simulate fracture behavior in the BM, HAZ, and WM regions of the welded joint. The fracture behavior, including damage initiation and progression curves, is accurately modeled with ABAQUS simulations utilizing the ductile damage material model. The numerical results are successfully matched with the experimental data, demonstrating the potential of numerical methods to predict the fracture behavior of heterogeneous welded structures.

# MATERIALS AND EXPERIMENTAL METHODS

## MATERIALS AND WELDED JOINT

This paper investigates a butt-welded X joint made from high-strength steel S690QL1, which constitutes the BM [19]. This fine-grained structural steel is produced through the quenching and tempering (QT) process, with a minimum declared yield strength $R_{p0.2} \geq 690$ MPa and a tensile strength $R_m$ ranging from 770 to 840 MPa. The plates used in the welded test coupon are 40 mm thick, in accordance with the EN 10025-6 standard for hot rolled high yield strength structural steels in the QT condition. The fusion welding process, employs a high-strength ferritic filler, Mn3Ni1CrMo (ER110S-G), according to EN ISO 16834-A /AWS A5.28 standards, which constitutes the WM in the welded joint [20]. This filler material has a yield strength $R_{p0.2}$ of approximately 800 MPa and a tensile strength $R_m$ ranging from 840 to 900 MPa.

In this welded joint, the calculated weld strength mismatch factor is $M = 1.16$, indicating the slightly OM weld metal.

The investigated welded test coupon consists of two 40 mm thick steel plates joined in a double V-butt (X-welded) configuration. The groove preparation was performed in accordance with the recommendations specified in EN ISO 9692-1, for joint reference No. 2.5.1, see Fig. 1 (a). Welding was executed using the metal active gas (MAG) 135 process with a 1.2 mm diameter solid filler wire. The shielding gas used was a mixture of 82% Argon and 18% CO2, with a flow rate of 12–16 L/min. The welding was performed in a multi-pass configuration, with a total of 22 passes, as shown in the Fig. 1 (b).

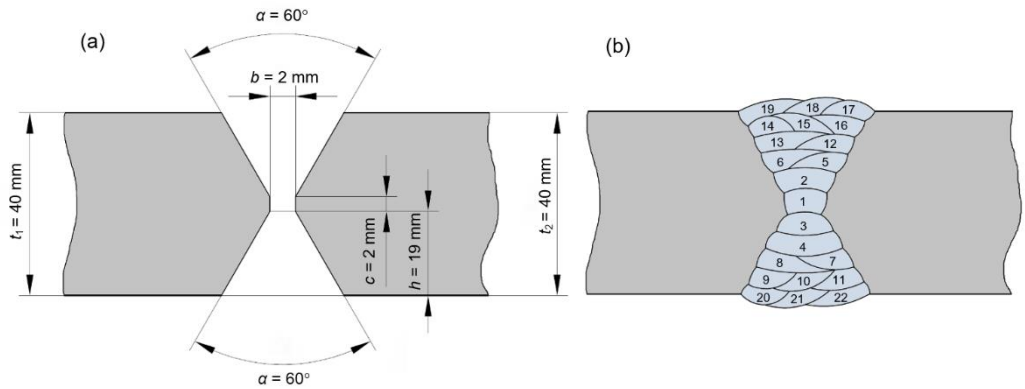



**Fig. 1** X welded joint: (a) joint groove geometry and preparation, and (b) welding passes

To ensure high-quality weld with optimal performance and properties, the process parameters are adjusted to maintain low heat input, below 1 kJ/mm, as indicated in Table 1.

**Table 1** Welding process parameters

| Pass no. | Location | $I$ [A] | $U$ [V] | $v_w$ [cm/min] | $\eta$ | $Q$ [kJ/mm] |
|---|---|---|---|---|---|---|
| 1-3 | root | 195 | 26 | 28.5 | 0.8 | 0.85 |
| 4-22 | fill + cover | 280 | 29 | 45 | 0.8 | 0.87 |

## TENSILE TESTING

To fully characterize the behavior and overall mechanical properties of a welded joint, it is essential to conduct experimental testing on each distinctive region of the heterogeneous weld structure and obtain required data for the following numerical simulations. Standard-sized tensile testing specimens often proposed and used in testing standards and welding codes are unsuitable for such small material volumes, making mechanical testing challenging or even unfeasible. In order to obtain the stress-strain properties of welded joint BM, HAZ and WM regions, the subsize or even miniature sized specimens are required.

As discussed in the introduction of this paper, the authors are investigating testing methods and specimen types suitable for evaluating heterogeneous welds [17], with particular emphasis on those relevant to this specific case:

- ASTM E8 round tensile subsize specimens, shown in Fig. 2 (a): suitable for testing welded joints on a general scale, allowing for the assessment of tensile properties in key segments such as the BM, HAZ, and WM. The specimens have a circular cross-section with a diameter $D$ = 2.5 mm, resulting in a test area of 4.909 mm². However, method is not able to differentiate between specific sub regions within the HAZ, providing only the averaged values for this highly heterogeneos region.
- Mini Tensile Specimens (MTS), shown in Fig. 2 (b): suitable for complete linear characterizing the mechanical behavior of heterogeneous materials. When testing welded joints, this method is particularly valuable for measuring stress–strain properties across the weld's cross-sectional transverse line, with the ability to distinguish between the main segments of the weld, the BM, WM, and individual HAZ sub regions. The specimen has a rectangular cross-section with a width $W$ = 2 mm and thickness $T$ = 0.5 mm, resulting in a test area of 1 mm².

Given the requirement to determine the tensile properties of BM, WM and general HAZ regions, without deeper insights into the HAZ sub regions, the convenient testing method is ASTM E8 round tensile subsize specimens. For the regions of BM and WM the standard sized round tensile specimens can also be used. Test methods for all-weld metal (AWM) are given in EN ISO 15792-1 standard. Generally, the larger the test area covered by the specimen, the more averaged the results will be of the overall properties within the tested region.

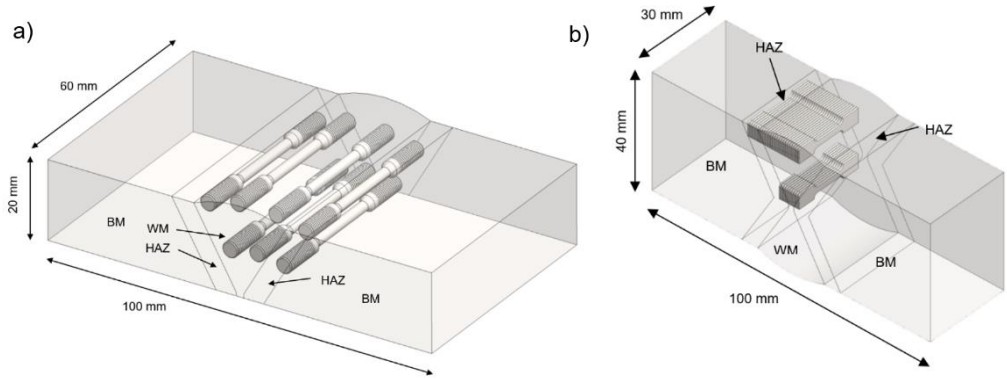



**Fig. 2** Tensile testing methods for heterogeneous welds: (a) ASTM E8 round tensile subsize specimens and (b) Mini Tensile Specimens (MTS)

In case of ASTM E8 testing, 7 round tensile subsize specimens are proposed for welded joint testing, as shown in Fig. 2 (a). WM testing uses three specimens: two in the WM Fill zone and one in the WM Root zone, while 4 specimens are used for HAZ testing. The 3 additional subsize specimens (not illustrated in the figure) are used to test the BM through its 40 mm thickness.

Stress-strain curves are obtained for each tested specimen, while three region representative curves (Fig. 3) are shown and color-coded: BM in yellow, HAZ in blue, and WM in red tones. Results determined for BM the average yield strength $R_{p0.2}$ = 735 MPa, and average tensile strength $R_m$ = 810 MPa, for WM the $R_{p0.2}$ = 780 MPa and $R_m$ = 900 MPa, while for HAZ the $R_{p0.2}$ = 860 MPa and $R_m$ = 940 MPa. Overall strength values trendline is generally moving from BM to WM an finally to HAZ.

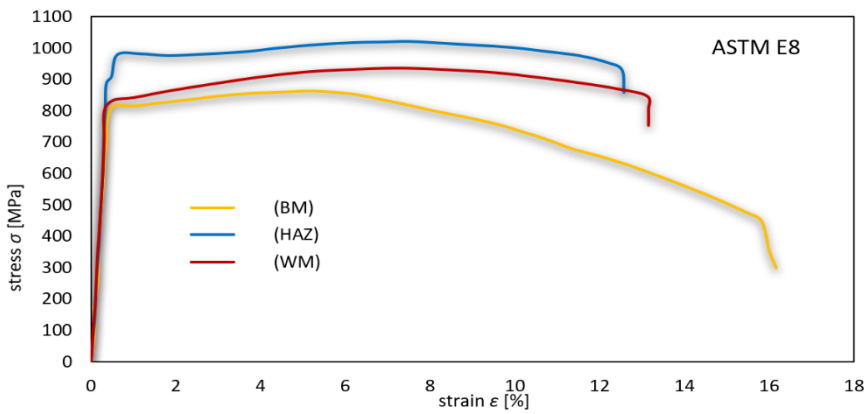



**Fig. 3** ASTM E8 round tensile subsize specimens stress-strain curves

Tensile properties across the transverse line of X weld are determined using two sets of MTS, as shown in Fig. 2 (b). The top set (25 specimens: R1-R24 and R25 at the centerline), characterizes the fill-pass WM (Fill), HAZ, and BM. The central set (10 specimens: C1-C9 and C10 at the centerline), characterizes the root-pass WM (Root), HAZ, and BM. MTS are manufactured using the Electrical Discharge Wire Cutting (EDWC) technology, with the wire diameter 0.25 mm, which also dictates the lateral distance between the test specimens.

After testing, the corresponding $\sigma$–$\varepsilon$ curves are also constructed for each tested MTS specimen, in fill pass Fig. 4 (a) and root pass Fig. 4 (b). Again, the $\sigma$–$\varepsilon$ curves are color coded: BM in yellow, HAZ in blue, and WM in red tones. BM has lowest averaged strength $R_{p0.2} \approx$ 750 MPa and $R_m \approx$ 840 MPa, WM has $R_{p0.2} \approx$ 790 MPa and $R_m \approx$ 860 MPa, while HAZ has highest strength $R_{p0.2} \approx$ 840 MPa and $R_m \approx$ 900 MPa.

In general, for FEA input, either ASTM E8 or MTS results may be used. The averaged experimental stress–strain curves corresponding to the SENB specimen's location within weld regions are applied. The material data used in this study is obtained using MTS testing, and given later in Table 5.

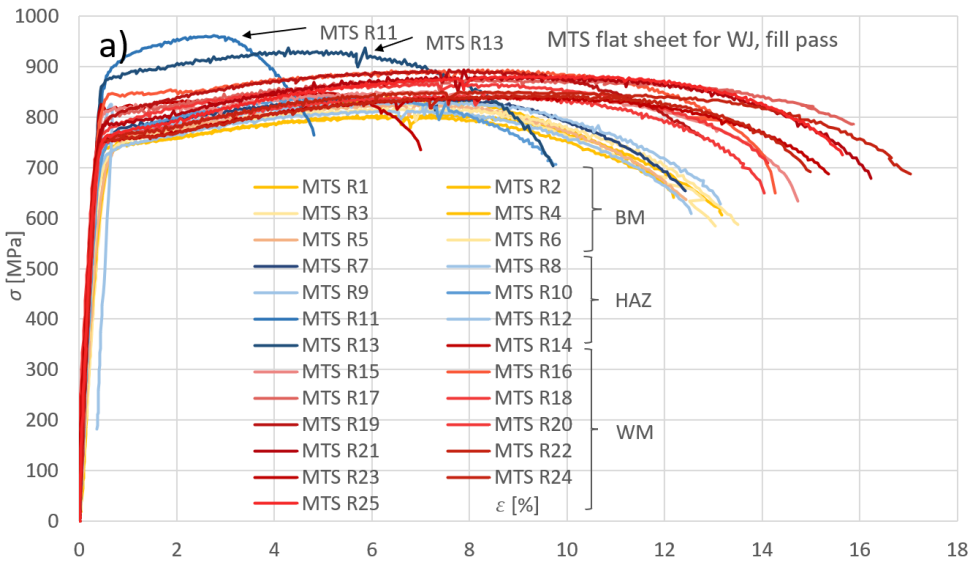



**Fig. 4** MTS flat sheet subsize specimens stress-strain ($\sigma$–$\varepsilon$) curves, a) Fill pass

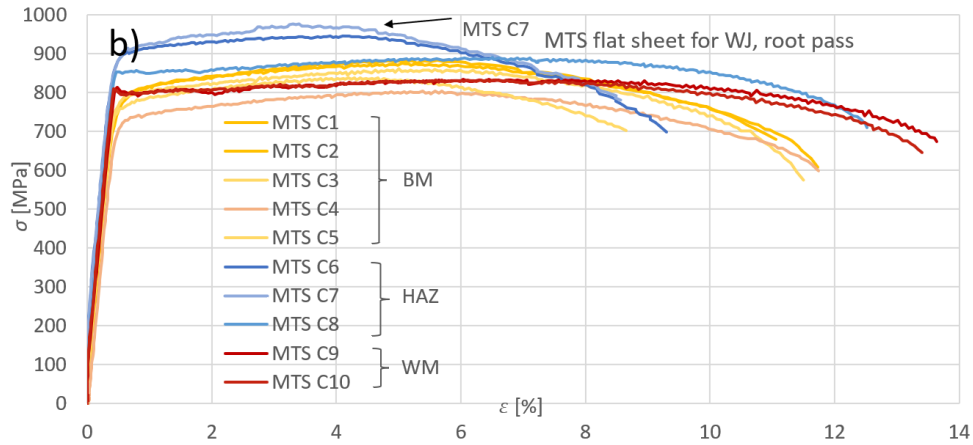



**Fig. 4** MTS flat sheet subsize specimens stress-strain ($\sigma$–$\varepsilon$) curves, b) Root pass

## FRACTURE TESTING

Fracture mechanics testing according to ASTM E1820 standard is performed to evaluate the fracture toughness characteristic parameters, and determine fracture behavior curves (e.g *P*-CMOD curves). Major regions of the X welded joint, the BM, HAZ, and WM are tested. To test these specific areas, the SENB specimens are positioned within the volume of the welded joint. The placement of the specimens and the locations of the notches were selected based on the general guidelines provided in BS 7448: Part 2. This arrangement of SENB specimens within the X weld joint main regions is illustrated in Fig. 5.

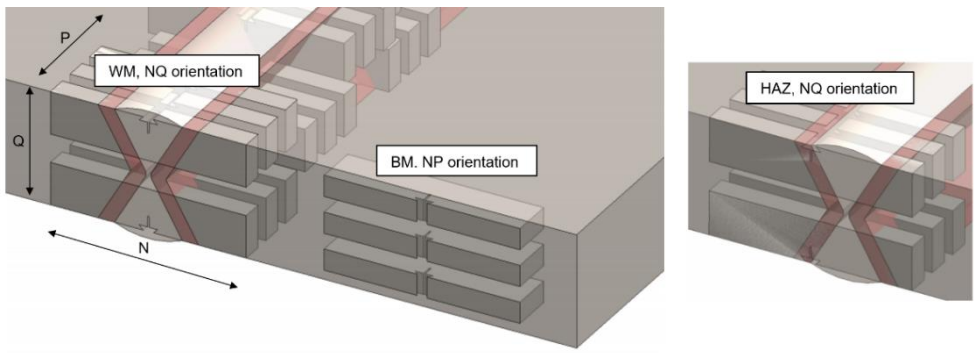



**Fig. 5** Fracture mechanics testing - SENB specimens placement in welded joint BM, HAZ and WM

Based on BS 7448: Part 2, which specifies the crack plane orientation codes for welded fracture toughness specimens, the specimen codes used are: NP (crack opening in the N direction and propagation in P) and NQ (crack opening in the N direction and propagation in Q). Tested SENB specimen configurations are listed in Table 2.

**Table 2** SENB specimens placement, orientation and initial crack location

| SENB Specimen | Welded Joint Zone | Orientation | Crack |
|---|---|---|---|
| 1 | BM | NP | Crack initiation and through BM |
| 2 | WM | NQ | Crack initiation and through columnar WM, weld centre line |
| 3 | HAZ | NQ | Crack initiation in HAZ |

The SENB fracture mechanics testing specimens are chosen and manufactured in relation to ASTM E1820. SENB specimens have dimensions of $W$ = 15 mm, $B$ = 7.5 mm, and a total length of 70 mm. The fatigue crack starter notch geometry, is a narrow notch type, being cut using the electrical discharge wire cutting (EDWC) with a wire diameter of 0.3 mm.

Fracture testing procedure in accordance with the ASTM E1820 standard, implies the initial fatigue precracking, starting from the fatigue crack starter notch. Three-point bending SENB specimens are cyclically loaded using the servo-hydraulic testing machine INSTRON 1255, with a load ratio $R$ = 0.1, and applied $K_{max}/E \leq 1.1\times10^{-4}\text{m}^{1/2}$.

Fracture toughness tests are conducted next (Fig. 6), with crosshead displacement control at rate of 1.5 mm/min, at room temperature of 20°C. The fixture system includes two fixed bottom support rollers with a span distance of $S$ = 58.7 and a top roller at the specimen's center. Top roller applies a downward load $P$ ranging from 9 to 17.5 kN, depending on the individual specimen's resistance. All rollers have a diameter of $R$ = 14 mm.

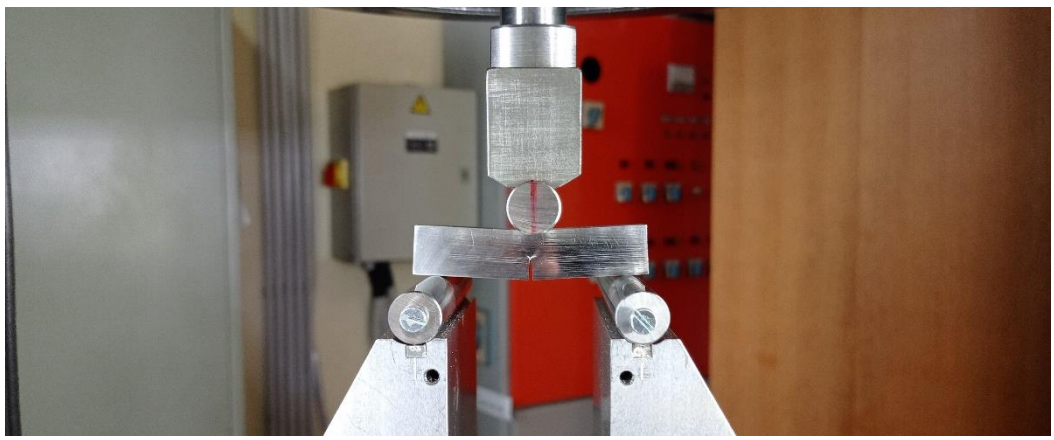


**Fig. 6** Fracture mechanics testing - SENB specimens three-point bending

According to ASTM E1820, the fracture resistance is determined and characterized by $J$–$R$ and CTOD($\delta$)–$R$ curves. The fracture testing characteristic values are determined for three

designated weld zones (BM, WM and HAZ), where $J_{Q(1)}$ is *J*-Integral estimated value, $K_{JIC}$ is Stress Intensity Factor (SIF) evaluated from *J*-Integral and $\delta_{Q(1)}$ is $\delta$ estimated value. Results are shown in Table 3.

**Table 3** SENB specimens fracture toughness testing $J_{Q(1)}$, $K_{JIC}$ and $\delta_{Q(1)}$

| SENB Specimen | Welded Joint Zone | $J_{Q(1)}$ / $J_{IC}$ [kJ/m$^2$] | $K_{JIC}$ [MPa·m$^{1/2}$] | $\delta_{Q(1)}$ / $\delta_{IC}$ [mm] |
|---|---|---|---|---|
| 1 | BM | 278 | 229 | 0.193 |
| 2 | WM | 165 | 181 | 0.120 |
| 3 | HAZ | 536 | 325 | 0.366 |

Observing the results, the HAZ is markedly tougher and more resistant to crack propagation, having highest energy absorption and opening displacement before fracture.

The experimental *P*-CMOD curves obtained from the experimental three-point bending testing SENB specimens, in comparison with numerically obtained curves, are shown later in Fig. 11.

## NUMERICAL MODELLING OF WELDED JOINTS

### SIMPLIFIED WELD MODEL

Given the geometric complexity and irregularity of welded joints, introducing simplifications in numerical modeling of these structures is essential. Some existing fracture behavior assessment procedures allow for the idealization of actual weld geometry, presenting the irregularities of the fusion line, as caused by individual welding passes, using straight lines. S. Hertelé et al. [21] previously proposed a methodology for simplifying and idealizing butt V welds, while P. Štefane et al. [22] extended this to simplified double-sided V welds (X welds). As a further development, the authors introduced a double linear idealization for the fusion lines and the boundary line separating the HAZ from the BM, as shown in Fig. 7.

The simplified model is superimposed on X joint macroscopic image, with extracted dimensions of interest: root zone width $H_r$ = 2 mm, HAZ width $H_{HAZ}$ = 2.5 mm and weld center height $L_W$ = 20 mm, all with rounded values. Simplified model utilizes symmetry along both vertical and horizontal axes of the welded joint, with equal angles $\alpha = \beta = 60°$, resulting in identical upper and lower sides. In this study, the HAZ is treated as a uniform region, without sub-regional division. Welds with detailed HAZ segmentation are outside the scope of this paper, but were investigated by authors [16].

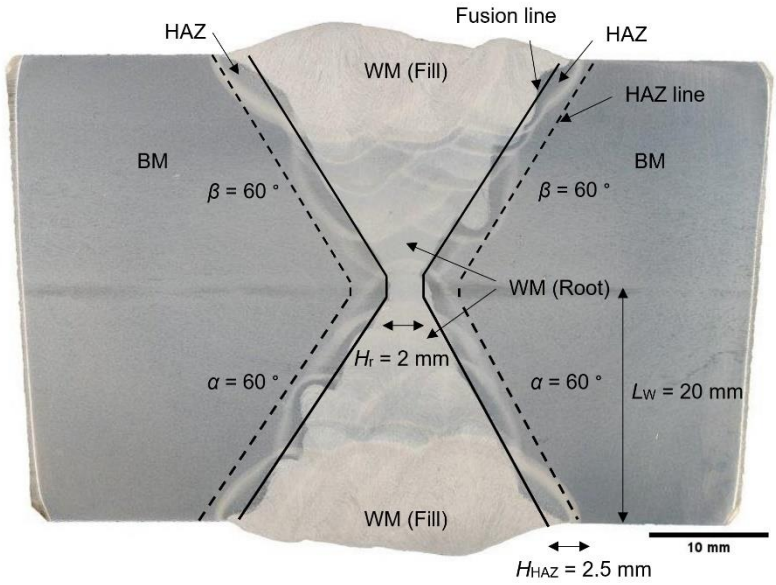



**Fig. 7** X welded joint macrograph with simplified fusion and HAZ lines.

## NUMERICAL MODELS - SENB SPECIMENS

Two-dimensional (2D) numerical model of the SENB test specimen and testing setup is developed, based on the modeling approaches for the specimen, notch, and crack previously used by P. Štefane et al. [22] and L. Starčevič et al. [23]. The authors also employed other modeling techniques for SENB specimens and cracks, as documented by various researchers in the literature [24–26]. All simulations are performed using ABAQUS software [27].

The comprehensive finite element (FE) model of the test setup includes both the SENB specimen and the three-point bending fixture system, as depicted in Fig. 6 (a). The fixture consists of two fixed bottom rollers (U1, U2, UR3 = 0), and one top roller having a prescribed vertical displacement (U2 ≠ 0), variable over time to simulate the applied load $P$. Rollers are modeled as analytical rigid bodies with a diameter of $R$ = 14 mm.

The SENB specimen is modeled as a planar shell and fully discretized using a 4-node bilinear plane strain quadrilateral element CPE4R in an explicit FE analysis. The weld joint region is meshed with a structured or free mesh, with element sizes of 0.1. In regions outside the critical area, the mesh size is increased to 1 mm to optimize computational efficiency, as shown in Fig. 8 (a).

Notch is stage modelled as initial EDWC cut notch with length $a_N$ and width of 3 FE, and fatigue precrack with length $a_0$, width of 1 FE, and blunt end, Fig. 8 (b). The numerically calculated results in ABAQUS, using the ductile damage model, are highly mesh-dependent. The accurate stress–strain fields at the notch tip require a well-refined mesh. In scope of this

investigation the intentionally simplified blunt notch is used, with fairly uniform mesh, giving adequate results and fast computations. In order to get the most accurate results, it is however recommended to use the sharp fatigue precrack tip combined with highly refined mesh at the notch tip itself.

The modelled zones are BM, WM and HAZ, using the MTS testing experimentally obtained tensile properties and corresponding ductile damage parameters, Fig. 8 (c-e).

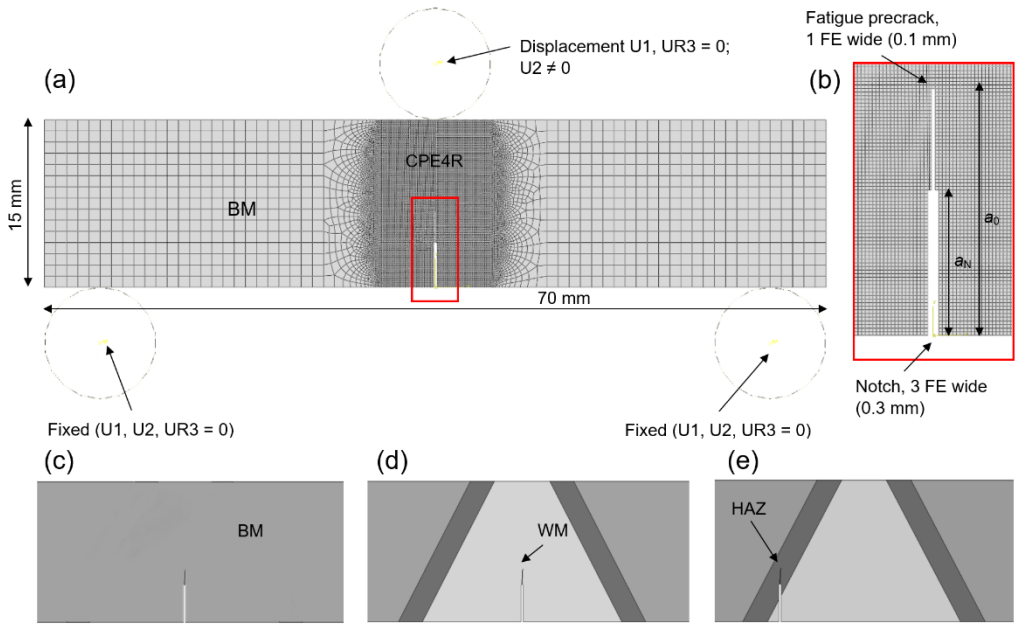



**Fig. 8** Numerical models of SENB specimens: (a) bending test setup, (b) detail of notch and fatigue precrack, (c) BM specimen, (d) WM specimen and (e) HAZ specimen

## DUCTILE DAMAGE MODEL

To model the behavior of elasto-plastic materials with progressive damage up to failure, the ABAQUS software with ductile damage model is employed. This model predicts damage initiation and evolution. The stress-strain curve (Fig. 9) depicts this progression: the initial linear-elastic stage (0a), followed by stable plastic deformation with strain hardening (ab). Point *b* marks the onset of plastic instability with damage parameter $D = 0$. Conversely, in the failure phase (bd), stiffness degradation and damage evolution occur, reaching $D = 1$ at point *d*, where crack initiation indicates failure [27,28].

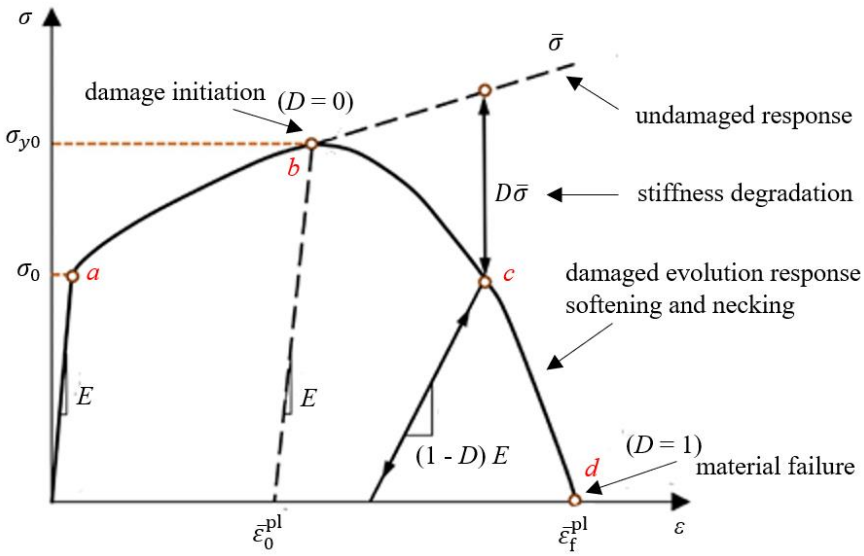



**Fig. 9** Ductile damage model with stress-strain curve showing damage initiation and evolution [28]

The characteristic parameters in ductile damage model are:

- Damage parameter D, changing from 0 (non-damaged) to 1 (material failure).
- $\bar{\varepsilon}_{\mathrm{f}}^{\mathrm{pl}}$ equivalent plastic strain at failure, when the overall damage variable reaches the value $D = 1$
- $\bar{u}_{\mathrm{f}}^{\mathrm{pl}}$ [mm] damage evolution displacement at failure

The ductile damage model has previously been employed in simulations of the tensile behavior of flat sheet specimens, as part of the authors' earlier research published in "*Mathematical Modelling of Weld Phenomena 13*" [18]. Therefore, it will not be restated in this section.

Ductile damage model is readilly being used in numerical simulations for modelling the mismatching behavior of welded joints, as well as behavior of different types of test specimens, as provided in the relevant literature [23,29-32].

The redistribution of the plastic zone in mismatched welds plays a vital role in influencing fracture behavior. Plastic zone location, size, and shape are determined by local material properties, mismatch ratio, and residual stresses. Proper redistribution can either mitigate or exacerbate crack growth tendencies, as proposed by U. Zerbst [14,33,34].

The crack behavior in mismatched welds of high strength steel, using the SENB specimens, is investigated by the authors, and presented in Fig. 10. Material data and ductile damage parameters for the simulations, are provided in Table. 4.

**Table 4** SENB specimens for mismatch welds, material data and ductile damage parameters

| Specimen | Material | $E$ | $R_{p0.2}$ | $R_m$ | $M$ | $\bar{\varepsilon}_f^{pl}$ | $\bar{u}_f^{pl}$ | $\Delta a$ | CMOD |
|---|---|---|---|---|---|---|---|---|---|
| | | [GPa] | [MPa] | [MPa] | | | [mm] | [mm] | [mm] |
| SENB DD1 | BM/WM | 210/210 | 755/780 | 840/890 | 1.03 | 0.075/0.110 | 0.030/0.055 | 4.561 | 1.009 |
| SENB DD2 | BM/WM | 210/210 | 690/780 | 770/890 | 1.13 | 0.090/0.110 | 0.025/0.200 | 1.722 | 1.004 |

In case of slight overmatching with $M$ = 1.03, the crack growth is developing along the WM/BM boundary, as shown in Fig. 10 (a). On the other hand, in case of substantial overmatching with $M$ = 1.13, the crack formed in the weaker BM, has the crack growth arrested on the WM transition front, as shown in Fig. 10 (b).

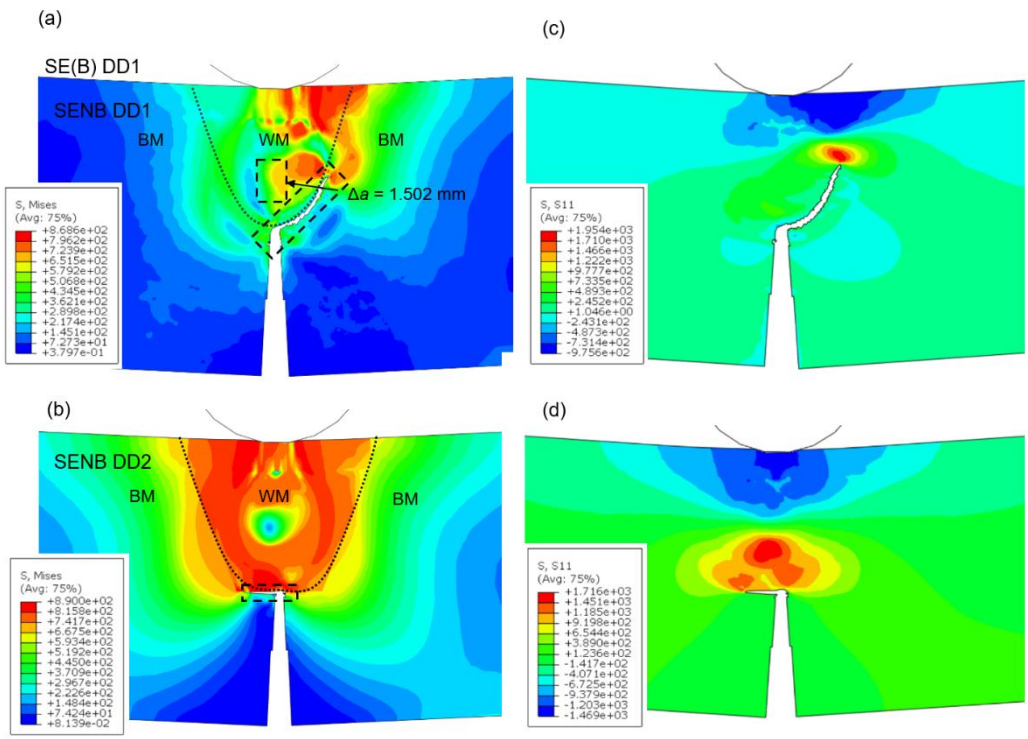



**Fig. 10** SENB specimens for mismatch welds – damage behavior and crack growth: (a) SENB DD1 von Mises, (b) SENB DD2 von Mises, (c) SENB DD1 S11, (d) SENB DD2 S11

The colour stress contours shown in Fig. 10 (a, b) represent Von Mises stress fields, while the normal stress contours S11 are shown in Fig. 10 (c, d). Von Mises stress, being a scalar quantity (i.e. equivalent stress) that doesn't differentiate tension from compression, can misrepresent the stress state when strong compressive regions (under an indenter) coexist with tensile zones (at a crack tip). Tension and compression behavior is adressed using the S11

stress contour plots in Fig. 10 (c, d). The uncracked ligament acts as a plastic hinge, and undergoes gross plastic yielding rather than brittle crack propagation, causing plastic collapse of SENB specimen. This behavior is typical for ductile materials.

It is mandatory to note that numerical analysis of SENB DD1 and SENB DD2 is done just to showcase the specific crack behavior of different types of mismatched welds, having different material regions, related material parameters and ductile damage parameters. The actual experimental testing for those SENB specimens have not been done.

OM welds generally offer advantages under static loading, as the WM higher strength increases its resistance to applied stresses, delaying both crack initiation and growth. This results in enhanced performance and durability, with cracks tending to propagate through the HAZ or BM, as the stronger WM acts as a barrier and diverts crack paths. Conversely, UM welds are more prone to rapid crack initiation and growth, especially under cyclic loading, leading to stress concentrations that challenge the WM structural integrity. Cracks often initiate in the weaker WM and propagate linearly through the weld, increasing the risk of premature failure if not properly controlled [35].

In ductile damage model, the criteria for crack advancement is based on non self-similar crack growth, following the paths of localized plastic deformation. The crack advances in the direction where the elements reach the critical damage $D = 1$, being removed (i.e. deactivated) or have their stiffness set to near zero, forming a new traction-free surface. On the other hand, crack arrest will occur when the energy available for driving crack growth is less than the material's resistance, or when the damage process zone ceases to propagate.

Crack growth path is not typically constrained to move along the bimaterial interface simply because the material properties change abruptly. Instead, it is governed by local driving force vs. local material resistance. As damage accumulates, elements are softened or deleted. The crack follows the path of least resistance, where elements meet damage criteria first, causing them to lose stiffness (damage evolution) and fail, while the stronger material remains intact.

## RESULTS AND DISCUSSION

### FRACTURE BEHAVIOR SIMULATION

The fracture behavior, including damage initiation and progression curves for the BM, WM, and HAZ regions of the X welded joint, is simulated using ABAQUS with the ductile damage material model. The SENB specimens including these characteristic zones are modeled based on the previous numerical simplifications and the selected computational parameters, as previously described and shown in Fig. 8. The material data used for the simulations are obtained from experimental tensile MTS tests of the X weld (Fig. 4), using the averaged stress-strain curves depending on the specific test location inside the chosen material region (e.g. BM, WM, HAZ) and SENB placement location inside the weld. The ductile damage parameters are than calculated and assigned to each specimen accordingly, as summarized in Table 5.

**Table 5** SENB specimens for BM, WM and HAZ, material data and ductile damage parameters

| Specimen | Material | $E$ [GPa] | $R_{p0.2}$ [MPa] | $R_m$ [MPa] | $\bar{\varepsilon}_f^{pl}$ | $\bar{u}_f^{pl}$ [mm] |
|---|---|---|---|---|---|---|
| SENB BM | BM | 210 | 729 | 804 | 0.119 | 0.046 |
| SENB WM | WM | 210 | 741 | 833 | 0.048 | 0.015 |
| SENB HAZ | HAZ | 210 | 745 | 855 | 0.121 | 0.011 |
| | BM | 210 | 735 | 820 | 0.162 | 0.068 |

During the simulation of the welded joint material's fracture behavior, the applied load $P$ is plotted against the Crack Mouth Opening Displacement (CMOD) for the regions BM, WM, and HAZ. The numerical curves and experimental $P$-CMOD curves obtained from the experimental three-point bending testing SENB specimens are plotted in graph in Fig. 11. The results show that the lowest fracture resistance occurs in BM, with a maximum load $P$ = 8.73 kN at CMOD = 0.633 mm. The highest fracture resistance is observed in HAZ, reaching $P$ = 15.54 kN at CMOD = 0.803 mm. The WM region exhibits an intermediate resistance, with an average load of $P$ = 11.85 kN at a CMOD = 0.285 mm, shown in Table 6.

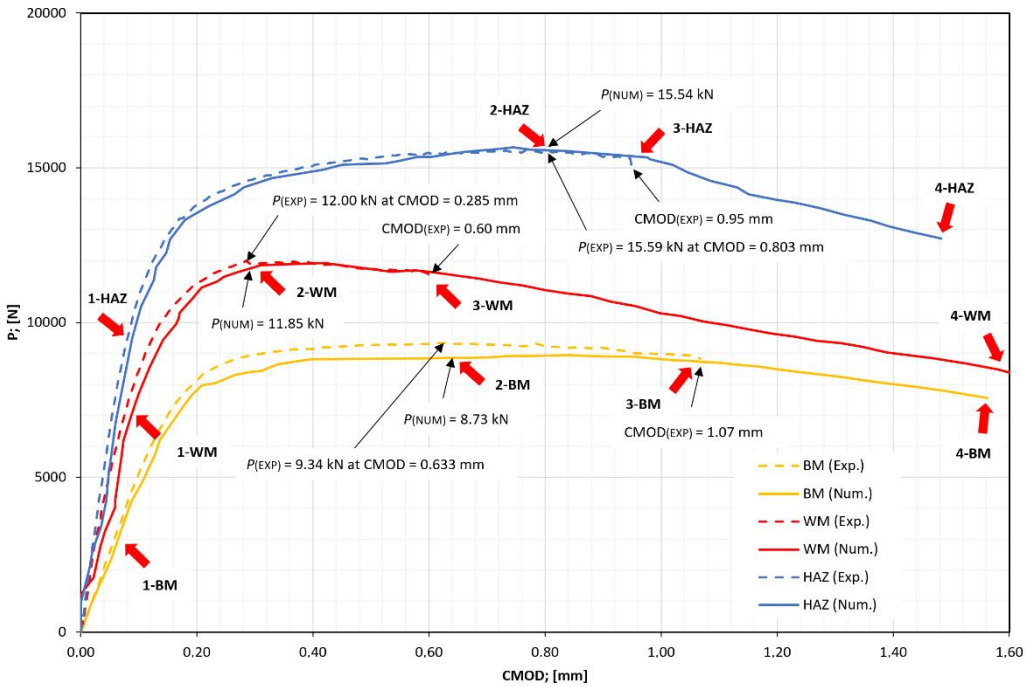



**Fig. 11** SENB specimens for BM, WM and HAZ – $P$-CMOD numerical and experimental curves

**Table 6** SENB specimens for BM, WM and HAZ – *P*-CMOD numerical and experimental values

| Specimen | Material | $P_{max.\ (exp.)}$ [kN] | $P_{max.\ (num.)}$ [kN] | $P_{max.\ (diff.)}$ [%] | $CMOD_{Pmax.}$ [mm] | $CMOD_{max.\ (exp.)}$ [mm] |
|---|---|---|---|---|---|---|
| SENB BM | BM | 9.34 | 8.73 | 6.75 | 0.633 | 1.07 |
| SENB WM | WM | 12.00 | 11.85 | 1.26 | 0.285 | 0.60 |
| SENB HAZ | HAZ/BM | 15.59 | 15.54 | 0.32 | 0.803 | 0.95 |

Numerical curves show good matching with the experimental ones, demonstrating the potential of numerical methods to predict the fracture behavior of heterogeneous welded structures.

The stress state and fracture behavior at specific loading points in the *P*-CMOD curves for each numerically derived representation, including BM, WM, and HAZ samples, is illustrated in Fig. 12, with characteristic points chosen for demonstration.

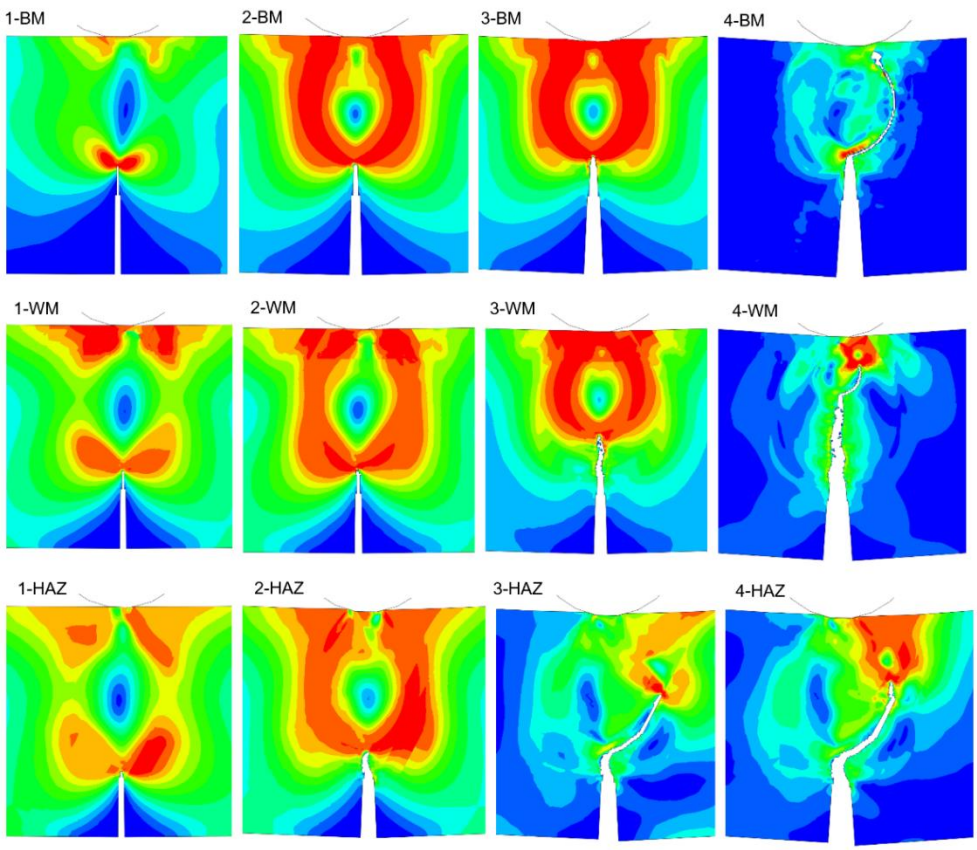



**Fig. 12** *P*-CMOD numerical curves for BM, WM and HAZ – characteristic points

Characteristic to specimen curves, the loading point 1 shows the specific stress field at crack tip, prior to crack initiation. Point 2 correlates with $P_{max.}$ value on curves. Past this point, the crack growth continues at point 3, with final specimen failure at point 4. In case of BM and WM, the crack grows in vertical direction, until the sudden collapse. In case of HAZ it can be observed that crack starts the vertical growth through HAZ region, followed by directional change along the BM/HAZ boundary, until the final failure.

Comparing the numerically obtained physical fracture crack (PFC) size $a_p$ with the actual ones from the experimental testing, it can be observed their good qualitative matching. The actual measured values are: for BM $a_p$ = 7.499 mm, for WM $a_p$ = 5.861 mm and for HAZ $a_p$ = 4.819 mm.

## CONCLUSION

The heterogeneity inherent in welded joints can be effectively incorporated into computational simulations by employing appropriate representative numerical models. These models can encompass three primary weld zones: the base material (BM), the weld material (WM), and the heat-affected zone (HAZ). To make the models manageable and suitable for numerical analysis, certain simplifications of the actual weld geometry are necessary. These simplifications are carefully designed to retain the essential mechanical and geometric characteristics of the weld zones while reducing complexity. For the implementation of the simulations, SENB specimens were modeled, reflecting the real specimen geometry and critical regions of the weld joint. Utilizing the ductile damage material model, combined with tensile properties that were previously obtained through experimental testing of each material zone, enables a detailed simulation of the fracture behavior specific to each zone within the welded joint. These simulations produce fracture resistance curves, represented as *P*–CMOD (i.e. load versus crack mouth opening displacement) curves, which are comparable to experimental results. This approach allows for a comprehensive understanding of how heterogeneity affects fracture behavior, providing valuable insights for the design and assessment of welded structures.

## ACKNOWLEDGMENT

Authors acknowledge the Slovenian Research Agency ARRS for partly funding this investigation in frame of the research program P2-0137 “Numerical and Experimental analysis of Nonlinear Mechanical Systems”.

## References

[1] K. E. EASTERLING: *Introduction to the Physical Metallurgy of Welding,* Second Edition, London, Butterworth-Heinemann, 1992.
[2] S. KOU: *Welding Metallurgy*, Second Edition, John Wiley and Sons, Hoboken, New Jersey, 2003.
[3] E. F. NIPPES: ‘The weld heat-affected zone’, *Weld. J.*, 38 (1), pp. 1-17, 1959.

[4] W. F. SAVAGE, E. F. NIPPES, E. S. SZEKERES: 'A Study of Weld Interface Phenomena in a Low Alloy Steel', *Weld. J.*, 55 (9), pp. 260-268, 1976.
[5] J. C. LIPPOLD: *Welding Metallurgy and Weldability*, John Wiley & Sons, Inc., Hoboken, New Jersey, 2015.
[6] M. LOMOZIK: 'Effect of the welding thermal cycles on the structural changes in the heat affected zone and on its properties in joints welded in low-alloy steels', *Weld. Int.*, 14, pp. 845-850, 2000, doi: 10.1080/09507110009549281.
[7] M. KOÇAK, M. ES-SOUNI, L. CHEN, K.-H. SCHWALBE: 'Microstructure and weld metal matching effects on HAZ toughness', *Proc. of the 8th Int. Conf. OMAE-ASME*, The Hauge, Netherlands, p.p. 623-633, March 19-23 1989.
[8] J. SPURRIER, P. HANCOCK, J. P. CHUBB: 'An assessment of weld mis-matching', *Engineering Fracture Mechanics*, Volume 53, Issue 4, pp. 581-592, 1996, https://doi.org/10.1016/0013-7944(95)00180-8.
[9] Y. LEI, R. A. AINSWORTH: 'Failure assessment diagrams for cracks in welds with mismatched mechanical properties', American Society of Mechanical Engineers (ASME) *pressure vessels and piping conference*, Montreal, Canada, 21-26 Jul 1996, pp. 65-73, 1996.
[10] Y. J. KIM, K. H. SCHWALBE: 'Compendium of yield load solutions for strength mismatched SE(T), SE(B) and C(T) specimens', *Eng. Fract. Mech.* 68, pp. 1137-1151, 2001.
[11] Y. J. KIM, K. H. SCHWALBE: 'Mismatch effect on plastic yield loads in idealized weldments–I: weld centre cracks', *Eng. Fract. Mech.* 68, pp. 163-182, 2001.
[12] Y. J. KIM, K. H. SCHWALBE: 'Mismatch effect on plastic yield loads in idealized weldments–II: heat affected zone cracks', *Eng. Fract. Mech.* 68, pp. 183-199, 2001.
[13] G. H. B. DONATO, R. MAGNABOSCO, C RUGGIERI: 'Effects of weld strength mismatch on J and CTOD estimation procedure for SE(B) specimens', *Int. J. Fract.* 159, pp. 1-20, 2009,
[14] U. ZERBST, R. A. AINSWORTH, H. TH. BEIER, H. PISARSKI, Z. L. ZHANG, K. NIKBIN, T. NITSCHKE-PAGEL, S. MÜNSTERMANN, P. KUCHARCZYK, D. KLINGBEIL: 'Review on fracture and crack propagation in weldments – A fracture mechanics perspective', *Engineering Fracture Mechanics*, 132, pp. 200-276, 2014, 10.1016/j.engfracmech.2014.05.012 .
[15] D. TOMERLIN, N. GUBELJAK, D. KOZAK: 'Gleeble Simulation of HAZ in S690QL Steel: Microstructural and Mechanical Properties', *Key engineering materials*, 966, pp. 115-120, 2023, doi: 10.4028/p-HmvK3N.
[16] D. TOMERLIN, D. KOZAK, L. FERLIČ, N. GUBELJAK: 'Experimental and Numerical Analysis of Fracture Mechanics Behavior of Heterogeneous Zones in S690QL1 Grade High Strength Steel (HSS) Welded Joint', *Materials* 16 (2023) 6929, https://doi.org/10.3390/ma16216929.
[17] D. TOMERLIN, D. KOZAK, N. GUBELJAK, I. PENTEK: 'Tensile testing of S690QL1 HSS welded joint heterogeneous zones using small scale specimens and indentation methods', *Materials Testing* 66(10), pp. 1600-1619, 2024, https://doi.org/10.1515/mt-2024-0136
[18] D. TOMERLIN, D. KOZAK, N. GUBELJAK, M. MAGIĆ KUKULJ: 'Stress-strain properties of HSS steel welded joint heterogeneous structure: experimental and numerical evaluation', *Mathematical Modelling of Weld Phenomena 13*, Verlag der Technischen Universität Graz, 2023, doi:10.3217/978-3-85125-968-1-23
[19] Fine-Grain Structural Steels MAXIL® 690, Ilsenburger Grobblech, 2019.
[20] BÖHLER X 70-IG - Solid wire, low-alloyed, high strength, Böhler Welding by Voestalpine; 2014.
[21] S. HERTELÉ, W. DE WAELE, M. VERSTRAETE, R. DENYS, N. O'DOWD: 'J-integral analysis of heterogeneous mismatched girth welds in clamped single-edge notched tension specimens', *Int. J. Press. Vessel. Pip.* 119, pp. 95-107, 2014.

[22] P. ŠTEFANE, S. HERTELÉ, S. NAIB, W. DE WAELE, N. GUBELJAK: 'Effects of Fixture Configurations and Weld Strength Mismatch on J-Integral Calculation Procedure for SE(B) Specimens', *Materials* 15, 962, 2022.
[23] L. STARČEVIČ, N. GUBELJAK, J. PREDAN: 'The Numerical Modelling Approach with a Random Distribution of Mechanical Properties for a Mismatched Weld', *Materials*, 14, 5896, 2021
[24] S. HERTELÉ, N. O'DOWD, K. VAN MINNEBRUGGEN, M. VERSTRAETE, W. DE WAELE: 'Fracture Mechanics Analysis of Heterogeneous Welds: Validation of a Weld Homogenisation Approach', *Procedia Mater. Sci.* 3, pp. 1322-1329, 2014.
[25] Y. BI, X. YUAN, M. HAO, S. WANG, H. XUE: 'Numerical Investigation of the Influence of Ultimate-Strength Heterogeneity on Crack Propagation and Fracture Toughness in Welded Joints', *Materials*, 15, 3814, 2022
[26] D. N. I. ALVES, J. G. ALMEIDA, M. C. RODRIGUES: 'Experimental and numerical investigation of crack growth behavior in a dissimilar welded joint', *Theor. Appl. Fract. Mech*. 109, 102697, 2020.
[27] ABAQUS: *Abaqus/Explicit User's Manuals*, Version 6.11, Dassault Systèmes Simulia Corp. Providence, RI, USA, 2011.
[28] ABAQUS DUCTILE DAMAGE MODEL: available online: https://abaqus-docs.mit.edu/2017/English/SIMACAEMATRefMap/simamat-c-damageevolductile.htm.
[29] F. YANG, M. VELJKOVIC, Y. LIU: 'Ductile damage model calibration for high-strength structural steels', *Constr. Build. Mater.* 263, 120632, 2020.
[30] W. SONG, X. LIU, F. BERTO, J. XU, H. FANG: 'Numerical simulation of prestrain history effect on ductile crack growth in mismatched welded joints', *Fatigue Fract. Eng. Mater. Struct.* 40, pp. 1472-1483, 2017.
[31] Y. CHO, C. LEE, J.-J. Yee, D.-K. Kim: 'Modeling of Ductile Fracture for SS275 Structural Steel Sheets', *Appl. Sci.*, 11, 5392, 2021, https://doi.org/10.3390/app11125392.
[32] H. XIN, J. A. F. O. CORREIA, M. VELJKOVIC, F. BERTO: 'Fracture parameters calibration and validation for the high strength steel based on the mesoscale failure index', *Theor. Appl. Fract. Mech.* 112, 102929, 2021.
[33] U. ZERBST, M. MADIA, B. SCHORK, J. HENSEL, P. KUCHARCZYK, D-T. NGOULA, D. TCHUINDJANG, J. BERNHARD, C. BECKMANN: *Fatigue and fracture of weldments. The IBESS approach for the determination of the fatigue life and strength of weldments by fracture mechanics analysis*, Springer, Cham, Switzerland, 2019.
[34] U. ZERBST: 'Application of fracture mechanics to welds with crack origin at the weld toe: a review Part 1: Consequences of inhomogeneous microstructure for materials testing and failure assessment', *Weld World* 63, pp.1715-1732, 2019, https://doi.org/10.1007/s40194-019-00801-5.
[35] A. SEDMAK, E. DONCHEVA, B. MEDJO, M. RAKIN, N. MILOSEVIC, D. RADU: 'Crack Size and Undermatching Effects on Fracture Behavior of a Welded Joint', *Materials* 16 (13):4858, 2023, doi: 10.3390/ma16134858. PMID: 37445171; PMCID: PMC10343383.

# II Joint Properties

## b) Residual Stresses and Distortion

# DEVELOPMENT OF RESIDUAL STRESS MODEL FOR WELDED BOX SECTIONS USING PROBABILISTIC APPROACH

A. HORVÁTH *, D. KOLLÁR*

**Budapest University of Technology and Economics, Faculty of Civil Engineering, Department of Structural Engineering, H-1111, Budapest, Hungary, horvath.andras@edu.bme.hu*

*DOI 10.3217/978-3-99161-089-2-022, license CC BY 4.0*
*https://creativecommons.org/licenses/by/4.0/deed.en*
*This CC license does not apply to third party material and content noted otherwise.*

ABSTRACT

Manufacturing processes significantly contribute to the formation of imperfections such as residual stresses and distortions in components. This study focuses on residual stresses induced by welding in box sections made from a combination of normal strength steel (NSS) and high strength steel (HSS) plates. Advanced manufacturing simulations are carried out using a deterministic, uncoupled transient thermomechanical analysis incorporating a double-ellipsoidal heat source model. These simulations evaluate the residual stress distribution in weldments across various steel grades, geometries, and welding parameters (e.g., heat input, welding speed). Furthermore, the study presents a methodology for probabilistic welding simulation. Longitudinal residual stresses are analysed using Monte Carlo simulations with Latin hypercube sampling. The findings support the development of a comprehensive residual stress model that integrates key welding and fabrication characteristics, reflecting the specificities of manufacturing technologies.

Keywords: Welding simulation, Residual stress model, Probabilistic, Box section

## INTRODUCTION

All manufacturing processes, welding in particular, inherently introduce residual stresses and distortions, which significantly affect the structural performance, load-bearing capacity, and durability of the products. As welding became the predominant joining method in the last decades in steel construction industry, understanding its effects is essential. Numerical simulations have become a key tool for understanding the behaviour of structures during fabrication, providing insight into geometric imperfections and residual stresses as well. Since distinct residual stress and distortion magnitudes are generated in different base materials in line with the applied welding process, advanced modelling techniques are required to realistically capture these effects. To fully exploit the potentials in simulations,

validated numerical modelling frameworks are required, supported by limited number of physical experiments. This paper presents an experimental and numerical study on welded box sections made from normal strength steel (NSS) and high strength steel (HSS). A finite element-based, stochastic virtual manufacturing approach is proposed to derive residual stress models that reflect actual fabrication conditions. Probabilistic analysis is particularly important, as it enables a systematic investigation of the sensitivity of the residual stress model to its key parameters. Thereby residual stress model parameters are refined, supporting more reliable and sustainable structural design using advanced numerical tools such as geometrically and materially nonlinear analysis including imperfections.

## MEASUREMENTS

The validation of the numerical simulations discussed in this conference paper is based on previously conducted experimental investigations. The earlier study [1] concentrated on evaluating residual stresses in box sections made from normal strength steel (NSS - S355MC), high strength steel (HSS - S700MC), and their hybrid (NSS + HSS) configurations. A total of nine specimens featuring single-bevel butt welds were tested (see Fig. 1). The wall thicknesses ($t$) ranged from 4 mm to 8 mm, the widths ($B$) of the rectangular cross-sections varied between 200 mm and 220 mm, and the lengths ($L$) were between 700 mm and 800 mm. The geometric parameters and steel grades of the sections are summarised in Table 1, while the mechanical properties of base materials are presented in Table 2. The welding variables for all the analyzed sections presented in this paper are summarized in Table 3.

**Table 1** Measured dimensions and steel grades of all the nine investigated specimens. [1]

| Specimen | Steel grade | | $L$ | $t_1$ | $t_2$ | $B_1$ | $B_2$ | $d_1$ | $d_2$ |
|---|---|---|---|---|---|---|---|---|---|
| | web | flange | [mm] | [mm] | [mm] | [mm] | [mm] | [mm] | [mm] |
| RS4-700A | S700MC | S700MC | 698.8 | 4.17 | 4.11 | 199 | 200 | 280 | 281 |
| RS4-700B | S700MC | S700MC | 699.5 | 4.10 | 4.10 | 200 | 200 | 280 | 281 |
| RS4-H | S700MC | S355MC | 698.5 | 4.11 | 4.16 | 198 | 199 | 279 | 279 |
| RS6-355 | S355MC | S355MC | 799.0 | 6.20 | 6.19 | 219 | 220 | 310 | 310 |
| RS6-700 | S700MC | S700MC | 798.5 | 6.10 | 6.17 | 220 | 219 | 310 | 309 |
| RS6-H | S700MC | S355MC | 798.5 | 6.10 | 6.17 | 220 | 219 | 309 | 309 |
| RS8-700A | S700MC | S700MC | 697.8 | 8.07 | 7.97 | 200 | 199 | 280 | 280 |
| RS8-700B | S700MC | S700MC | 698.5 | 7.98 | 8.00 | 198 | 199 | 280 | 280 |
| RS8-H | S700MC | S355MC | 698.5 | 7.94 | 7.94 | 200 | 199 | 281 | 281 |

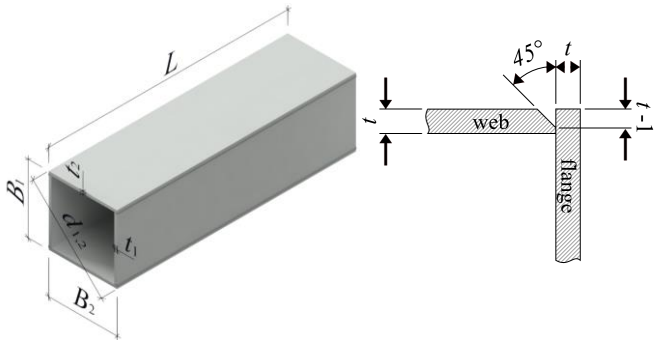
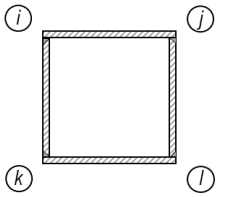



**Fig. 1** Sketch of the investigated welded box sections

**Table 2** Mechanical properties of base materials according to inspection certificates. [1]

| Steel grade | $f_y$ [MPa] | $f_{p0.2}$ [MPa] | $f_u$ [MPa] | $A$ [%] |
|---|---|---|---|---|
| S355MC – t4 | 402 | - | 469 | 37 |
| S355MC – t6 | 446 | - | 570 | 27 |
| S355MC – t8 | 400 | - | 486 | 30 |
| S700MC – t4 | - | 746 | 829 | 22 |
| S700MC – t6 | - | 749 | 833 | 20 |
| S700MC – t8 | - | 738 | 827 | 22 |

**Table 3** Welding variables of the analysed specimens. [1]

| Welding sequence | Specimen | # | - | $I$ [A] | $U$ [V] | $V$ [mm/s] | $q$ [kJ/mm] |
|---|---|---|---|---|---|---|---|
|  | RS4-700A | 1 | *k* | 220 | 19.5 | 7.45 | 0.46 |
| | | 2 | *i* | 205 | 19 | 7.78 | 0.40 |
| | | 3 | *j* | 192.5 | 18.5 | 7.78 | 0.37 |
| | | 4 | *l* | 200 | 18.5 | 8.14 | 0.36 |
| | RS6-H | 1 | *i* | 222.5 | 23.25 | 7.77 | 0.53 |
| | | 2 | *k* | 215 | 22.75 | 7.55 | 0.52 |
| | | 3 | *l* | 225 | 22.75 | 7.69 | 0.53 |
| | | 4 | *j* | 222.5 | 22.75 | 7.41 | 0.55 |
| | RS8-H | 1 | *k* | 215 | 21.75 | 12.96 | 0.29 |
| | | 2 | *i* | 205 | 20.75 | 11.11 | 0.31 |
| | | 3 | *j* | 205 | 20.25 | 11.48 | 0.29 |
| | | 4 | *l* | 205 | 20.25 | 10.61 | 0.31 |
| | | 5 | *k* | 205 | 23.75 | 7.53 | 0.52 |
| | | 6 | *i* | 220 | 24.25 | 7.61 | 0.56 |
| | | 7 | *j* | 220 | 24.75 | 8.05 | 0.54 |
| | | 8 | *l* | 232.5 | 24.25 | 8.14 | 0.55 |

A comprehensive testing program was carried out, incorporating strain gauge measurements, macroscopic inspections, dimensional evaluations, and high-resolution residual stress measurements using the contour method. Among the measurements, the contour method played an important role, which is a destructive residual-stress measurement technique based on Bueckner's superposition principle [2]. It can be regarded as an efficient residual stress measurement technique, since its mean standard deviation (22-34 MPa) in orthotropic steel decks [3] is comparable to the scatter reported for established methods such as neutron and x-ray diffraction (20-40 MPa) [4]. The specimen is cut in two along the centre cross-section using wire electrical discharge machining (WEDM), while being rigidly clamped during cutting. The WEDM releases residual stresses and causes elastic out-of-plane deformation of the new cut surfaces. These deformed surfaces are then measured with a coordinate measuring machine (CMM). The measured deformation fields on the two cut surfaces are averaged, filtered and smoothed using thin-plate smoothing spline. Smoothing is applied according to the methodology recommended by Olson et al. [5], assuming that 68% of the pointwise model errors across the cross-section fall within the mean smoothing-model error. This corresponds to a $\pm 1\sigma$ confidence interval (68%). Smoothed displacement data are mapped onto a linear elastic finite element (FE) model as displacements with opposite sign to compute the full two-dimensional residual stress distribution across the cutting surface. The measurement method allows for accurate quantification of both membrane and through-thickness residual stresses (Fig. 2), from welding and preceding fabrication steps, which serve as crucial input parameters for structural design and numerical modelling.

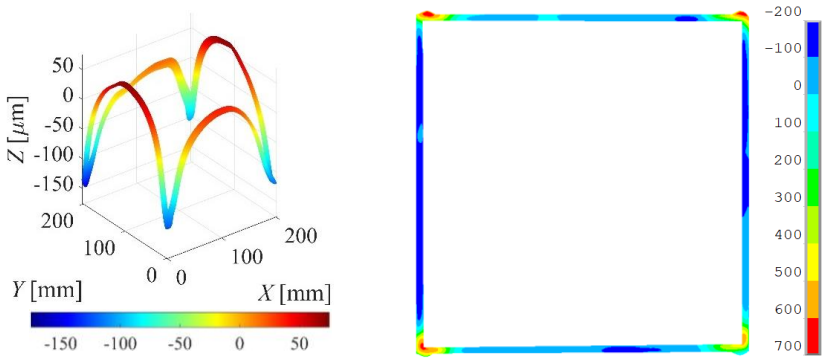
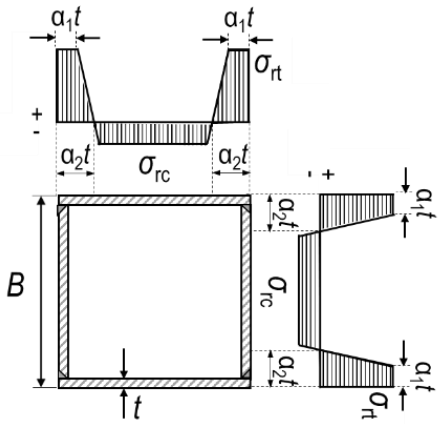



**Fig. 2** Example for measured cut surface [μm], and longitudinal residual stress field [MPa]




$$\alpha_1 = 1.0$$
$$\alpha_2 = -0.3224 \times qA_{w,nom} + 5.6908$$
$$\varepsilon_{rs} = [400 / \max(f_{y.filler}, f_{y,fl}, f_{y.w})]^{1/2}$$
$$\sigma_{rt} = \varepsilon_{rs} \times \max(f_{y.filler}, f_{y,fl}, f_{y.w}) \times n_{w,pass}^{-2/3}$$
$\sigma_{rc}$ based on equlibirium

**Fig. 3** Previously proposed residual stress model for welded box sections

The results confirmed the theory presented in previous publications [6,7] that the magnitude of residual compressive stress decreases with increasing plate thickness. This is related to the reduction of the weld melt zone and confirms the stress-relieving effect of multiple welding passes. The previous study proposed a novel residual stress model (Fig. 3) for NSS, HSS, and hybrid welded box sections, incorporating parameters such as heat input $q$, nominal total cross-sectional area of a single-bevel butt weld seam $A_{w,nom}$, number of weld passes $n_{wpass}$, steel grades of web $f_{y,w}$, flange $f_{y,fl}$ and filler material $f_{y,filler}$. The residual stress model proposed previously in that study is developed exclusively based on the results obtained from the contour method. When compared to existing models, the new formulation demonstrated the highest accuracy in predicting both tensile and compressive residual stress magnitudes, with mean errors of 2.3% and 10.7%, respectively. Its effective application to hybrid box sections represents a notable step forward in the field of design-focused residual stress modelling.

## BACKGROUND OF THE NUMERICAL MODEL

The numerical framework presented in this study is developed in ANSYS, a general-purpose finite element software [8] to simulate the thermomechanical effects of welding in welded box sections. A three-dimensional transient uncoupled thermomechanical analysis is applied. Phase transformations are not considered directly, as there is no explicit phase-transformation simulation in the HAZ (heat-affected zone). However, the thermal material model employs an enthalpy-based formulation (replacing density and specific heat), in which the latent heat associated with the $\alpha \rightarrow \gamma$ phase transformation is accounted for in the enthalpy calculation. In addition, phase-transformation strain and creep strain increments are neglected in the simulations. The finite element (FE) model utilizes eight-node solid elements, SOLID70 for the thermal domain and SOLID185 for the mechanical analysis, with mesh refinement in the vicinity of the weld. A double ellipsoidal heat source model is

implemented to represent the metal active gas welding process. Temperature-dependent thermal and mechanical properties are defined based on EN 1993-1-2 [9], with specific adjustments for high-temperature behaviour. The standard does not distinguish between thermal material properties of normal strength steels with different steel grades (material properties could be used without any modification for structural steel grades up to S700 according to EN 1993-1-12 [9]). Material properties are specified up to 1200 °C in the standard, however, the weld pool temperature significantly exceeds this during welding. Therefore, thermal material properties in general are adjusted, while mechanical properties are set as constant values above the zero-strength temperature ($T_{zs}$ = 1200 °C). As an important remark, the material properties specified in the standard have been successfully applied in previous welding simulations [10]. Latent heat is integrated into an enthalpy-based formulation to manage phase changes. In the mechanical model, a rate-independent elastoplastic material model is used, incorporating isotropic hardening. Thermal boundary conditions include convective and radiative heat losses. A comprehensive description of the numerical framework – including the set of temperature-dependent material properties, all relevant input parameters, boundary conditions, and heat source modelling – is provided in detail in [11]. Although the geometry is symmetric, no symmetry is applied in the initial simulations to fully capture the effects of the welding sequence during model validation. To prevent rigid body motion, only minimal mechanical constraints are introduced. In the subsequent probabilistic analyses, double symmetry is applied to (i) reduce computational time and (ii) investigate extreme residual stress scenarios.

## VALIDATION OF THE NUMERICAL MODEL

Before conducting the probabilistic welding simulations presented in this study, the developed numerical modelling framework is validated against the experimental data described earlier. During the validation process, all relevant data recorded or measured during manufacturing are incorporated into the simulation model. This included the mechanical properties of both base and filler materials based on inspection certificates; measured geometric parameters such as width, height, length, and plate thickness; weld pool characteristics; and welding variables recorded during the process. In addition, the realistic ambient conditions, such as the measured ambient temperature ($T_{amb}$ = 24.2 °C) and fixtures (only rigid body motion is prevented in the model) during manufacturing, were incorporated into the FE model.

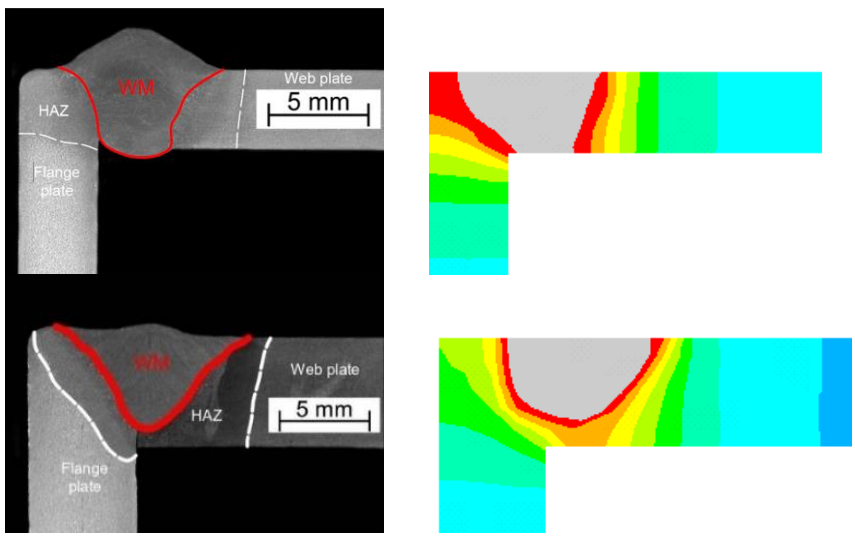
The material properties of the weld region are defined by accounting for the dilution of base and filler materials, as observed in macrographic examinations. The yield and ultimate strengths of the simulated weld elements are determined as a linear combination of the strength properties of the constituent materials. In calculating the mechanical parameters, we assume that - analogously to the weld metal chemical composition reported in [12] - the weld metal mechanical properties can also be estimated as a linear mixture of the characteristics of the filler material and the base material. In the case of hybrid box sections, the weld element properties are determined from a combination of the web, the flange, and the weld materials. To improve the accuracy of the simulation, the effects of plasma cutting

on the flange plates are also included in a simplified form. This effect is considered negligible for the web plates, since part of the heat-affected zone (HAZ) is removed during edge preparation, while the edge is remelted during welding. Before welding, the nodal temperatures at the edges of the flange plates are raised to the liquidus temperature (1525 °C) of the base material, then allowed to cool to ambient temperature prior to the start of welding. The resulting thermal fields are subsequently transferred to the mechanical analysis phase, in the same manner as the welding-induced temperature fields, where the plasma cutting-induced residual stresses are also evaluated.

First, the fusion zones from thermal simulations of box sections with wall thicknesses of 4 mm (RS4-700A from HSS), 6 mm (RS6-H with hybrid configuration), and 8 mm (RS8-H with hybrid configuration) are compared to experimental macrographs of specimens with matching geometries, materials, and welding variables (Fig. 4). This comparison validates the accuracy of the thermal analysis across varying wall thicknesses. The experimental and simulated cross-sectional areas of weld metal (WM) are as follows (without the excess weld metal): 19.4 mm² and 21.7 mm² for $t = 4$ mm, 28.6 mm² and 28.8 mm² for $t = 6$ mm, and 34.0 mm² and 31.0 mm² for $t = 8$ mm, respectively. These results indicate a relatively small average difference of less than 10%. On the other hand, the experimental and simulated effective throat thickness values are 4.0 mm and 4.0 mm (indicating full penetration) for $t = 4$ mm, 5.2 mm and 4.7 mm for $t = 6$ mm, and 6.3 mm and 6.2 mm for $t = 8$ mm, respectively, resulting in an average deviation of approximately 4%. The 8 mm thick specimen features two-pass single-bevel butt welds, while the remaining two specimens are fabricated with single-pass welds.

a)

b)



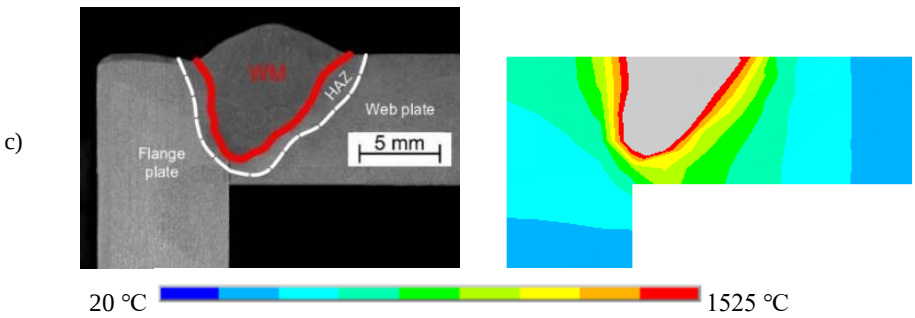
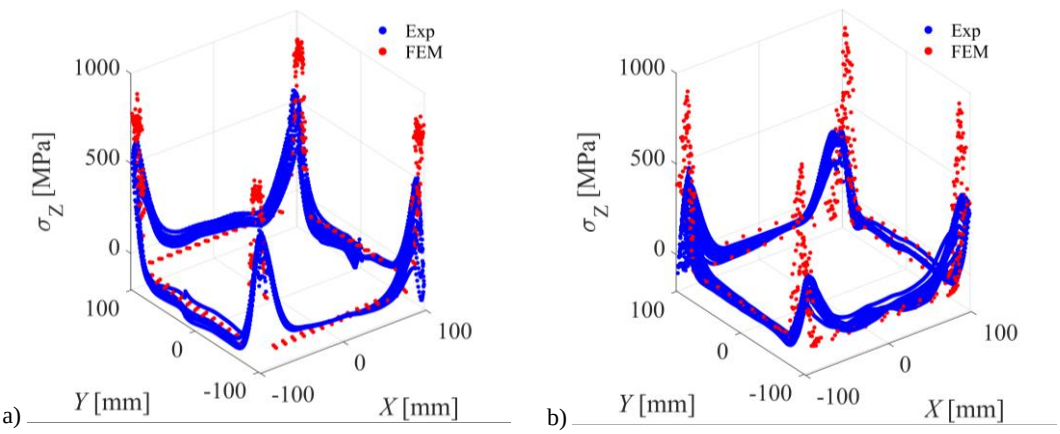
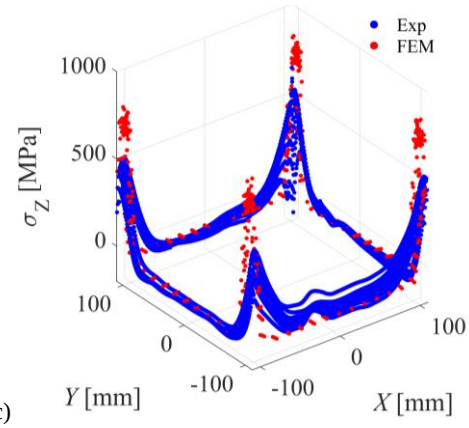



**Fig. 4** Macrographs [1] and FE model-based fusion zones of box sections with wall thickness of a) 4 mm (single-pass weld, RS4-700A), b) 6 mm (single-pass weld, RS6-H), and c) 8 mm (two-pass weld, RS8-H)

Additionally, longitudinal residual stresses obtained via contour method measurements are compared with those predicted by the welding simulation. Contour method provides two-dimensional full-map residual stresses; details of the measurement technique and the evaluation are detailed in [1]. In both cases, midsections of the specimens are analysed. The investigated specimen with thickness of 4 mm is a high strength steel box section (RS4-700A). Constituent plates have proof strength of 753 MPa, while the weld material is considered to have a proof strength of 737 MPa in the model according to the dilution-based approach. The other two box sections are hybrid sections (RS6-H and RS8-H combining NSS plates with yielding plateau and HSS plates with proof strength). Yield strength of the flanges is 446 MPa and 400 MPa, while proof strength is 749 MPa and 738 MPa for the webs in the hybrid specimens with wall thickness of 6 mm and 8 mm, respectively. Material model of the weld metal has a proof strength of 696 MPa and 671 MPa for $t$ = 6 mm and $t$ = 8 mm, respectively.






c)

**Fig. 5** Measured ('Exp') and numerical model-based ('FEM') longitudinal stresses $\sigma_z$ of box sections with wall thickness of a) 4 mm (single-pass weld, RS4-700A), b) 6 mm (single-pass weld, RS6-H), and c) 8 mm (two-pass weld, RS8-H)

Fig. 5 summarize the longitudinal residual stress distributions of the characteristic section in the case of the HSS and hybrid box sections. Simulated compressive stresses are between 63 and 100 MPa in the web plate, while they vary between 74 and 115 MPa based on the experiment for $t$ = 4 mm (RS4-700A from HSS). Moreover, a compressive residual stress range of 66-87 MPa and 64-100 MPa is determined based on simulation and measurement, respectively, for $t$ = 6 mm (RS6-H with hybrid configuration). In addition, the hybrid cross-section with $t$ = 8 mm (RS8-H) results in measured compressive residual stresses of 41-115 MPa and simulated magnitudes of 31-95 MPa (quite significant bending in the constituent plates). These results indicate a good agreement between welding simulation and experimental results. Larger discrepancies only occur in the vicinity of the weld beads, where numerical results locally overestimate the measured tensile residual stresses.

## PROBABILISTIC WELDING SIMUALTION

The welding simulation model presented is also employed in probabilistic finite element analyses to estimate the distribution of residual stresses in HSS box sections, while refining residual stress model parameters on a stochastic basis. For this purpose, the Probabilistic Design System (PDS) module of ANSYS is used to carry out the probabilistic calculations. The selected probabilistic design variables, along with their corresponding distribution types and parameters, are listed in Table 4, following the guidelines of JCSS [13] and the relevant standard [14] for welding-related parameters. In total, five probabilistic parameters are considered, as summarized in Table 4.

**Table 4** Probabilistic variables of welding simulation.

| Probabilistic input variable | | Distribution function | Distribution parameters |
|---|---|---|---|
| Heat source power | $Q = \eta UI$ | Gaussian | $Q_{mean.t4}$ = 2500 W<br>$Q_{mean.t6}$ = 5200 W<br>$Q_{mean.t8.r}$ = 3900 W<br>$Q_{mean.t8.c}$ = 3900 W<br>$\sigma_Q = 0.10 \times Q_{mean}$ |
| Welding speed | $v$ | Gaussian | $v_{mean}$ = 5 mm/s<br>$\sigma_v = 0.10 \times v_{mean}$ |
| Plate thickness | $t$ | Gaussian | $t_{mean}$ = 4 – 6 – 8 mm<br>$\sigma_t = 0.05 \times t_{mean}$ |
| Proof strength | $f_{p0.2}$ | Lognormal | $f_{p0.2,mean}$ = 787.2 MPa<br>$\sigma_{fp0.2} = 0.07 \times f_{p0.2,mean}$ |
| Young's modulus | $E$ | Lognormal | $E_{mean}$ = 200 000 MPa<br>$\sigma_E = 0.03 \times E_{mean}$ |

The heat source power varies depending on the wall thickness of the box sections (indicated as 't4', 't6' and 't8' in the subscript). For the box section with $t$ = 8 mm, which has two weld passes, $r$ refers to the root pass and $c$ to the cover pass. As previously introduced, three distinct geometries are investigated in the probabilistic welding simulation, combining three different plate thicknesses with two plate widths. Specifically, the study included a 200×200 mm box section with nominal wall thickness of 4 mm and 8 mm, as well as a 220×220 mm box section with a nominal plate thickness of 6 mm. Steel grades of the high strength steel constituent plates and the filler material are assumed to be matching. The investigated section is manufactured from S700 steel. Thus, the mean value is calculated from the 5% quantile value by using $f_{p0.2,mean}$ = 700 MPa / 0.8892 = 787.2 MPa. The applied temperature-dependent material models are based on the reduction factors in EN 1993-1-2. However, a temperature-dependent Ramberg-Osgood material model is used for describing the relationship between stresses and strains according to Equation 1 for high strength steels without a yielding plateau. Proof strength is used in the equation instead of yield strength, while $n$ is taken as 14 for high strength steels based on material tests in [15].

$$\varepsilon(\sigma) = \sigma/E + 0.002\,(\sigma/f_{p0.2})^n \tag{1}$$

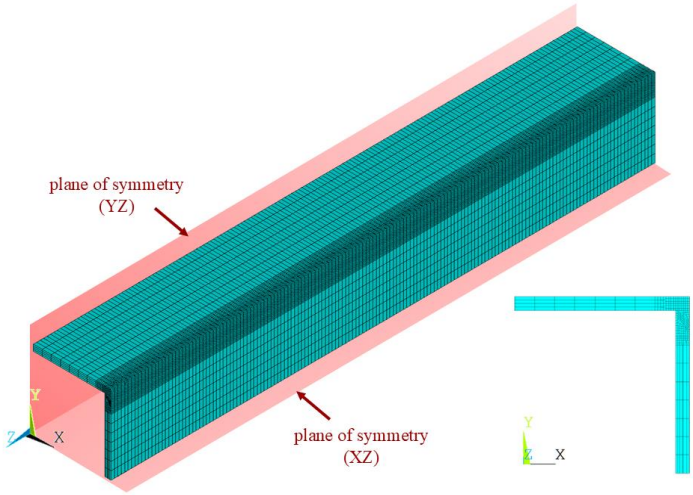



**Fig. 6** Quarter model of the box section used in the probabilistic welding simulation

The probabilistic welding simulation utilizes a quarter cross-section model of the box section (Fig. 6) with a width $B$ of either 200 mm or 220 mm, taking advantage of its double symmetry to minimize computational time. Accordingly, the simulation assumes simultaneous welding, neglecting the effect of welding sequence in order to represent the extreme residual stress scenario.

The probabilistic analysis is conducted using Monte Carlo simulation combined with Latin hypercube sampling, a method that ensures statistically independent samples by avoiding clustering and maintaining awareness of previously generated values. On the other hand, extreme ends of distribution functions are also considered in sampling process. A total of $N$ samples is used in the simulation dividing each random input variable into intervals of equal probability ($p = 1/N$), while random sampling is carried out within each interval. Three output variables are analysed, including $\alpha_1$ and $\alpha_2$ representing the characteristic widths of the tensile zone and $\sigma_{rt}$ as the magnitude of membrane tensile residual stresses as indicated in Fig. 3 previously. On the other hand, the compressive residual stress magnitude $\sigma_{rc}$ is derived from the equilibrium of internal forces and moments in the proposed residual stress model; thus, no regression is carried out in that case. The quantity of simulation loops, i.e., samples, needed for a Monte Carlo simulation to model a quadratic response surface depends on the number of random input variables ($n_{RV}$, which is 5 in this case). The sample size is defined as 27, in accordance with the advanced analysis guide of the software for the given number of probabilistic design variables. The quadratic response surface is described by Equation 2 as follows:

$$Y = c_0 + \sum_{i=1}^{n_{RV}} c_i X_i + \sum_{i=1}^{n_{RV}} \sum_{j=1}^{n_{RV}} c_{ij} X_i X_j \tag{2}$$

where $Y$ is the approximation function, i.e., a quadratic polynomial in this case, for each output variable, $c_0$, $c_i$ and $c_{ij}$ are the coefficients of the constant term, the linear terms and the quadratic terms, respectively, while $X_i$ and $X_j$ are the input variables. To evaluate the coefficients for each output variable, a regression analysis is used such that the sum of squared differences between the true simulation results and the values of the approximation function is minimized.

First, all the longitudinal residual stress data in the midsection are plotted (Fig. 8a) for a total of 3×27 simulations indicating three different nominal wall thicknesses. The key numerical results are summarised in Fig. 7 to describe the specific longitudinal residual stress ranges in the three analysed cross-sections:

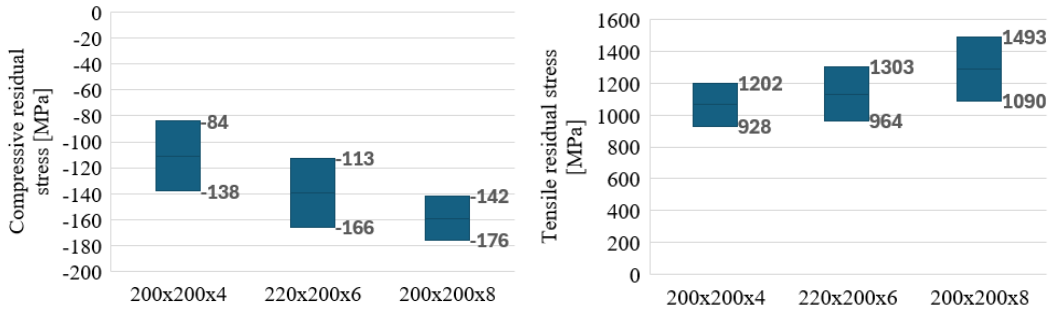



**Fig. 7** a) Maximum compressive residual stresses and b) peak tensile residual stresses of analysed box-sections

Secondly, membrane residual stresses are extracted (Fig. 8b) from the full two-dimensional residual stress fields (Fig. 8a). These curves enable the determination of tensile zone widths ($\alpha_1 t$ and $\alpha_2 t$) and the corresponding magnitude of membrane tensile residual stresses $\sigma_{rt}$. Then, the probabilistic sensitivities of Spearman rank-order correlation coefficients are determined, assuming a nonlinear monotonic increasing correlation between inputs and outputs (Fig. 9). However, it is acknowledged that the certainty of this assumption regarding a monotonically increasing relationship is not guaranteed. It is highlighted that heat source power $Q$ and wall thickness $t$ have a dominant influence on the tensile zone width (i.e., on $\alpha_1$ and $\alpha_2$). Among the considered parameters, the heat source power $Q$, plate thickness $t$, and proof strength $f_{p0.2}$ are found to be statistically significant, whereas the remaining parameters are statistically insignificant at a significance level of 2.5%. Based on the limited number of real experiments, $\alpha_1$ was assumed to be 1.0 indifferently of the manufacturing specialities. Meanwhile, the previously fitted equation for $\alpha_2$, which was calibrated against experimental test results [1], included the heat input and the nominal cross-sectional area of the single-bevel butt weld (which is proportional to $\sim t^2$), with a minus sign indicating a negative correlation. It needs to be underscored, that a wider range of welding speed $v$ would most probably have resulted in a significant input variable for $\alpha_1$ and $\alpha_2$ as heat input is directly calculated based on heat source power and welding speed. Nevertheless, wall thickness $t$ and proof strength $f_{p0.2}$ are statistically significant in the case

of $\sigma_{rt}$. Thus, heat input does not significantly affect the maximum membrane tensile residual stresses. Wall thickness indicates negative correlation, which means that increasing the thickness results in decreased membrane stresses in the weld zone. It is in accordance with theory and practice, since welding may lead to tensile stresses even exceeding the yield strength (or proof strength) locally, while stress gradients and through-thickness stresses could be substantial for larger plate thicknesses. In addition, a positive correlation is observed with proof strength, which is expected. Local material hardening may occur due to the highly nonuniform temperature field and high temperature (i.e., large thermal strains).

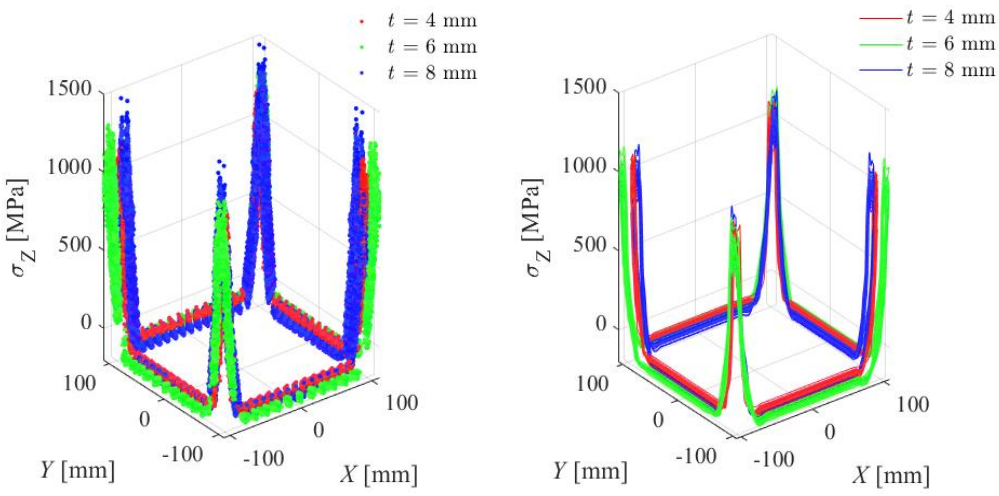



**Fig. 8** a) Longitudinal residual stress fields, and b) membrane longitudinal residual stresses from 3×27 probabilistic simulations ($t$ = 4 mm, 6 mm, and 8 mm). Note: double symmetry is used in plotting

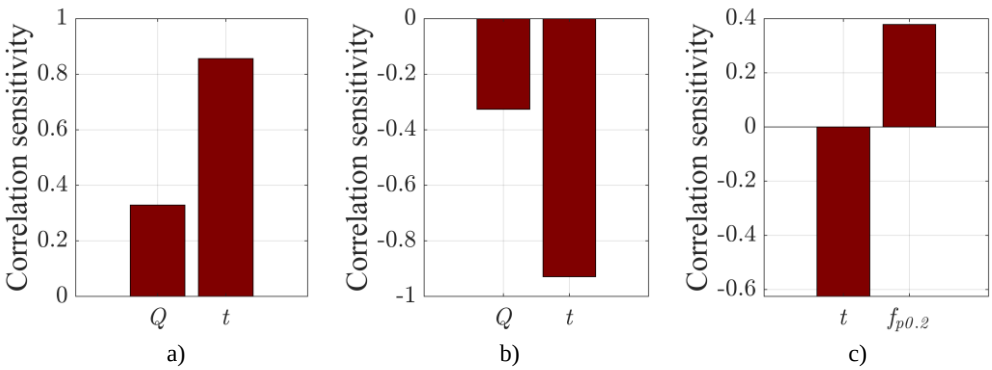
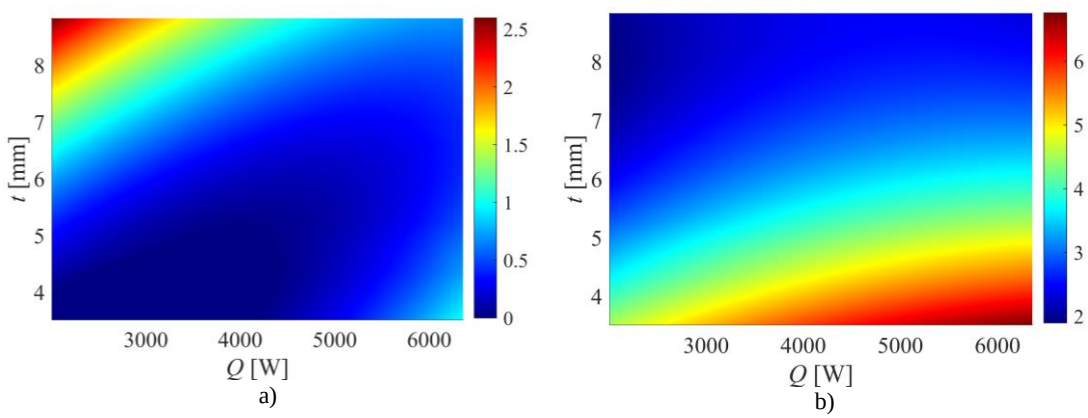


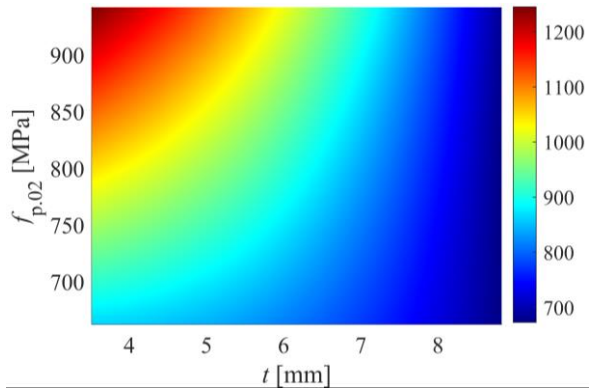

**Fig. 9** Spearman rank-order coefficients for a) $\alpha_1$, b) $\alpha_2$ and c) $\sigma_{rt}$

Finally, the identified coefficients of the significant parameters (Table 5) used in Equation 2, along with the corresponding quadratic response surfaces (Fig. 10), are presented. The output variables include the dimensionless tensile zone width parameters (namely $\alpha_1$ and $\alpha_2$) and the membrane tensile residual stress $\sigma_{rt}$ expressed in [MPa]. The input variables considered in the quadratic polynomial formulations are the welding heat input $Q$ [W], plate thickness $t$ [mm], and proof strength $f_{p0.2}$ [MPa]. By substituting the determined coefficients into Equation 2, the output variables can be predicted within the parameter ranges covered by the probabilistic analysis. For each output variable, two input parameters are identified as significant, resulting in six coefficients per quadratic response surface: one constant, two linear terms, and three quadratic terms (including a cross-term). This modelling approach enables efficient prediction of residual stress characteristics in welded box sections; however, its applicability is currently restricted to the investigated parameter set.

**Table 5** Significant coefficients of the response surfaces. Note: N/A denotes insignificant term.

| | | | Output variable | | |
|---|---|---|---|---|---|
| | | | $\alpha_1$ | $\alpha_2$ | $\sigma_{rt}$ |
| Input variable | $c_0$ | $c_0$ | -8.43552 | 17.34415 | 648.9199 |
| | $c_i$ | $Q$ | 0.001071 | 0.001709 | N/A |
| | | $t$ | -0.12544 | -1.99262 | 34.88991 |
| | | $f_{p0.2}$ | N/A | N/A | 3.054726 |
| | $c_{ij}$ | $Q \times t$ | -0.00013 | -8.01E-05 | 0.030953 |
| | | $t \times f_{p0.2}$ | N/A | N/A | -0.25115 |
| | $c_{ii}$ | $Q^2$ | 9.44E-08 | -5.97E-08 | N/A |
| | | $t^2$ | 0.061392 | 0.124045 | -5.64496 |
| | | $f_{p0.2}^2$ | N/A | N/A | 0.000225 |






c)

**Fig. 10** Response surfaces for a) $\alpha_1$, b) $\alpha_2$ and c) $\sigma_{rt}$ with the statistically significant terms

## CONCLUSIONS

The paper presents a comprehensive numerical simulation method for modelling thermal cutting and welding, while a probabilistic residual stress model is proposed considering manufacturing specialities. The paper reveals the following key findings:

- The thermal model is validated by comparing temperature fields with macrographs; average difference of the cross-sectional area of the weld metal is less than 10%, while an average deviation of approximately 4% is achieved in penetration depth.
- The mechanical model is validated by comparing predicted and measured longitudinal residual stresses in both high strength steel and hybrid (consisting of both NSS and HSS plates) box sections. A difference of less than 20 MPa is revealed in the compressive residual stress magnitudes in a comparison with contour method-based results.
- The methodology for probabilistic welding simulation is presented, serving as a basis for subsequently refining the parameters of residual stress models.
- Parameters of a residual stress model, consisting of trapezoidal shapes, previously proposed by the Authors are refined for welded high strength steel (S700) box sections with single-bevel butt welds. Predictions are limited to wall thickness of 4 to 8 mm with single or two weld passes.

Future research will focus on extending the probabilistic framework to incorporate additional stochastic input parameters (such as a wide range of width and yield strength values, also considering hybrid cross-sections), while using equations with thermophysical background for regression instead of the quadratic response surface used in the conventional Monte Carlo simulation.

## ACKNOWLEDGEMENTS

This research was funded by Hungarian Academy of Sciences, grant number MTA-BME Lendület LP2021-06/2021 “Theory of new generation steel bridges” program. The research reported in this paper and carried out at the Budapest University of Technology and Economics has been supported by the Ministry for Culture and Innovation from source of the National Research, Development and Innovation Fund, grant number ÚNKP-23-3-I-BME-194 (New National Excellence Program). The project supported by the Doctoral Excellence Fellowship Programme (DCEP) is funded by the National Research Development and Innovation Fund of the Ministry of Culture and Innovation and the Budapest University of Technology and Economics, under a grant agreement with the National Research, Development and Innovation Office. The project supported by the University Research Scholarship Programme (EKÖP) is funded by the National Research Development and Innovation Fund of the Ministry of Culture and Innovation and the Budapest University of Technology and Economics, under a grant agreement with the National Research, Development and Innovation Office.

## References

[1] A. HORVÁTH, D. KOLLÁR, B. KÖVESDI: ‘Distortions and residual stresses of NSS, HSS and hybrid box sections with single-bevel butt welds: An experimental study’, *Thin-Walled Structures*, Vol. 208, 112834, doi: 10.1016/j.tws.2024.112834, 2025.

[2] H. BUECKNER: ‘The propagation of cracks and the energy of elastic deformation’, *Transactions of the American Society of Mechanical Engineers*, Vol. 80, pp. 1225-1230, 1958.

[3] D. KOLLÁR, I. VÖLGYI, A. L. JOÓ: ‘Development of residual stress model of orthotropic steel decks using measurements’, *Structures*, Vol. 58, 105601, doi: 10.1016/j.istruc.2023.105601, 2023.

[4] J. D. LORD, A. T. FRY, P. GRANT: ‘A UK residual stress intercomparison exercise – an examination of the XRD and hole drilling techniques’, National Physical Laboratory, *Report CMMT(A) 98*, 2002.

[5] M. D. OLSON, A. T. DEWALD, M. B. PRIME, M. R. HILL: ‘Estimation of uncertainty for contour method residual stress measurements’, *Experimental Mechanics*, Vol. 55, No. 3, pp. 577-585, doi: 10.1007/s11340-014-9971-2, 2015.

[6] L. CHEN, T. WANG, J. PAN, N. MA, R. WANG: ‘Welding Residual Stress Distribution of U-Rib Stiffened Plates of Steel Box Girders and its Influence on Structural Natural Frequencies’, *Frontiers in Materials*, Vol. 9, 876111, doi: 10.3389/fmats.2022.876111, 2022.

[7] C. OLSSON: *Design Handbook for welded steel products*, 6th ed., Techstrat Publishing, Onsala, 2017.

[8] ANSYS INC.: *ANSYS. version 19.5*, Canonsburg, Pennsylvania, USA, 2019.

[9] EUROPEAN COMMITTEE FOR STANDARDIZATION: *EN 1993-1-2:2005 Eurocode 3: Design of steel structures – Part 1-2: General rules – Structural fire design*, Brussels, 2005.

[10] D. KOLLÁR, B. KÖVESDI, J. NÉZŐ: Numerical simulation of welding process – application in buckling analysis, Periodica Polytechnica Civil Engineering, 61 98-109., doi: 10.3311/PPci.9257, 2017.

[11] A. HORVÁTH, D. KOLLÁR: 'Dimensional Analysis and Validity of Uniaxial Residual Stress Distribution for Welded Box Sections', *Journal of Manufacturing and Materials Processing (JMMP)*, Vol. 9, No. 1, 5, doi: 10.3390/jmmp9010005, 2025.
[12] Y. L. SUN, C. J. HAMELIN, T. F. FLINT, A. N. VASILEIOU, J. A. FRANCIS, M. C. SMITH: 'Prediction of Dilution and Its Impact on the Metallurgical and Mechanical Behavior of a Multipass Steel Weldment', *Journal of Pressure Vessel Technology* (JPVT), Vol. 141, No. 6, 061405, doi: 10.1115/1.4044337, 2019.
[13] JOINT COMMITTEE OF STRUCTURAL SAFETY (JCSS): *Probabilistic Model Code*, https://www.jcss-lc.org/jcss-probabilistic-model-code/, 2002.
[14] STANDARDS AUSTRALIA / STANDARDS NEW ZEALAND: *AS/NZS 3992:2015 Australian/New Zealand Standard: Pressure equipment – Welding and brazing qualification*, Sydney, 2015.
[15] B. SOMODI: *Flexural buckling resistance of high strength steel welded and cold-formed square closed section columns*, PhD thesis, Budapest University of Technology and Economics, 2018.

# APPENDIX

## NOMENCLATURE

| Symbol | Description | Unit |
|---|---|---|
| $\alpha_1$ | relative width parameter of residual stress model | [-] |
| $\alpha_2$ | relative width parameter of residual stress model | [-] |
| $A$ | ultimate strain at fracture | [-] |
| $A_{w,nom}$ | nominal total cross-sectional area | [mm²] |
| $B_1$ | full width of box section | [mm] |
| $B_2$ | full height of box section | [mm] |
| $c_0$ | coefficient of the constant term in the quadratic response surface equation | depending on output variable |
| $c_i$ | coefficient of the linear term in the quadratic response surface equation | depending on output variable |
| $c_{ij}$ | coefficient of the quadratic term in the quadratic response surface equation | depending on output variable |
| $d_1$, $d_2$ | diagonal dimensions of a cross section | [mm] |
| $E$ | Young's modulus | [MPa] |
| $E_{mean}$ | mean value of Young's modulus | [MPa] |
| $\varepsilon_{rs}$ | residual stress model factor depending on yield strength | [-] |
| $\eta$ | thermal efficiency | [-] |
| $f_{p0.2}$ | proof strength | [MPa] |
| $f_{p0.2,mean}$ | mean value of proof strength | [MPa] |
| $f_{y,fl}$ | yield strength of flange | [MPa] |
| $f_{y,filler}$ | yield strength of filler material | [MPa] |

| | | |
|---|---|---|
| $f_{y,w}$ | yield strength of web | [MPa] |
| $f_u$ | ultimate strength | [MPa] |
| $I$ | welding current | [A] |
| $L$ | length of box section | [mm] |
| $N$ | number of samples in Monte Carlo simulation | [-] |
| $n_{RV}$ | number of random input variables | [-] |
| $n_{wpass}$ | number of weld passes | [-] |
| $q$ | net heat input | [kJ/mm] |
| $Q$ | heat source power | [W] |
| $Q_{mean.t4}$ | mean value of heat source power for the 4 mm-thick specimens | [W] |
| $Q_{mean.t6}$ | mean value of heat source power for the 6 mm-thick specimens | [W] |
| $Q_{mean.t8.c}$ | mean heat source power for the 8 mm-thick specimens (cover pass) | [W] |
| $Q_{mean.t8.r}$ | mean heat source power for the 8 mm-thick specimens (root pass) | [W] |
| $\sigma_E$ | standard deviation of Young's modulus | [MPa] |
| $\sigma_{fp0.2}$ | standard deviation of proof strength | [MPa] |
| $\sigma_Q$ | standard deviation of heat source power | [W] |
| $\sigma_{rc}$ | magnitude of compressive residual stress | [MPa] |
| $\sigma_{rt}$ | magnitude of tensile residual stress | [MPa] |
| $\sigma_Z$ | longitudinal residual stress | [MPa] |
| $t$ | plate thickness | [mm] |
| $t_1$ | plate thickness of web | [mm] |
| $t_2$ | plate thickness of flange | [mm] |
| $T_{amb}$ | ambient temperature | [°C] |
| $t_{mean}$ | mean value of plate thickness | [mm] |
| $T_{zs}$ | zero-strength temperature | [°C] |
| $U$ | voltage | [V] |
| $v$ | travel speed | [mm/s] |
| $v_{mean}$ | average value of welding speed | [mm/s] |
| $X_i$, $X_j$ | input variables in the quadratic response surface equation | depending on output variable |
| $Y$ | approximation function for quadratic response surface | depending on output variable |

# HIGH-TEMPERATURE STRAIN GAUGE MEASUREMENTS IN WA-DED: VALIDATION OF NUMERICAL MODELS

H. DREXLER*, M. MOSCHINGER**, N. ENZINGER**

** LKR Leichtmetall Kompetenzzentrum Ranshofen GmbH, 5282 Braunau am Inn - Ranshofen, Austria*
*** Institute of Materials Science, Joining and Forming, Graz University of Technology, 8010 Graz, Austria*

*DOI 10.3217/978-3-99161-089-2-023, license CC BY 4.0*
*https://creativecommons.org/licenses/by/4.0/deed.en*
*This CC license does not apply to third party material and content noted otherwise.*

ABSTRACT

In this study, high-temperature strain gauges are used to monitor the in-situ stress during plasma Wire Arc Directed Energy Deposition (WA-DED). A computational temperature compensation is applied to correct the strain signals for thermal effects, enabling accurate stress measurements at high temperatures. The experimental results are compared against a fully coupled thermo-mechanical finite element simulation.

The comparison shows good agreement between measured and simulated stresses, demonstrating that high-temperature strain gauges can reliably capture the stress evolution during WA-DED. This approach goes beyond conventional post-process residual stress measurements by providing time-resolved validation data. The findings underline the potential of in-situ high-temperature strain gauge measurements as a robust tool for validating WA-DED simulations.

Keywords: WA-DED, numerical simulation, strain gauge, in-situ stress measurements

## INTRODUCTION

Wire Arc Directed Energy Deposition (WA-DED) is an additive manufacturing technology that enables the production of large, complex shaped metallic components [1]. The process is characterized by a localized heat input from the arc and the subsequent solidification shrinkage of the deposited material. Both effects lead to the development of residual stresses and distortions, which can significantly influence the mechanical performance and dimensional accuracy of the final component [2]. Understanding and controlling these thermo-mechanical phenomena is therefore crucial to ensure component reliability and to enable the wider industrial adoption of WA-DED.

Numerical simulations have become an important tool for predicting temperature fields, stress evolution, and distortions in WA-DED. Such models allow virtual process optimization,

reducing the need for extensive experimental trial-and-error studies. A key challenge, however, lies in the reliable validation of these simulations. Conventionally, residual stresses are determined by post-manufacturing measurement techniques such as neutron diffraction, X-ray diffraction, hole-drilling, or sectioning methods [3]. These techniques only capture the final residual stress state and thus offer no insight into the transient stress and deformation evolution during deposition. This limitation restricts the validation of numerical models to the final result, leaving uncertainties about the accuracy of the predicted stress history.

For a more comprehensive validation, in-situ measurements during the process are required. Previous approaches have used in-situ digital image correlation (DIC) during the manufacturing process [4], [5]. While DIC enables full-field strain measurements, it requires a complex experimental setup and unhindered visibility of the surface, which limits its applicability in WA-DED. In this context, high-temperature strain gauges offer a promising solution. A prior study has already demonstrated their potential for capturing stress evolution during welding of a single seam [6].

In this study, high-temperature strain gauges are used to measure transient strain fields in a one-sided clamped S355J2 steel substrate during plasma WA-DED. The experimental setup additionally includes a displacement sensor and thermocouples to capture the thermal and mechanical response of the specimen. The measured data are compared with a fully coupled thermo-mechanical finite element simulation performed in Simufact Welding®.

The results demonstrate the feasibility and importance of using high-temperature strain gauges for in-situ validation of WA-DED simulations, contributing to improved predictive modeling in additive manufacturing

## WA-DED EXPERIMENT

A series of three trials was conducted in which a four-layer wall was deposited on a one-sided clamped substrate using the plasma WA-DED process (Fig. 1). The substrates were made of S355J2 structural steel with dimensions of 290 mm × 65 mm × 15m. Prior to welding, all substrates were stress-relief heat treated for two hours at 570 °C to eliminate residual stresses. After heat treatment, the substrates were sandblasted and cleaned. The specimens were clamped between a steel base block and a clamping jaw. The block was machined with a positioning step to ensure reproducible alignment of the substrates. The wire material was ER70S-6 (EMK6, voestalpine Böhler Welding GmbH) with a diameter of 1 mm, selected due to its comparable mechanical properties to the substrate. All deposition experiments were carried out on the SBI M3DP-SL machine at TU Graz. The welding parameters were kept constant across all trials, with a wire feed speed of 50 mm/s, a travel speed of 5 mm/s, a current of 260 A, and a voltage of 25 V. To allow for partial cooling before deposition continued, an interlayer dwell time of 828 s was applied between subsequent layers. The final deposit had dimensions of approximately 250 mm × 8 mm × 6 mm (four single track layers).

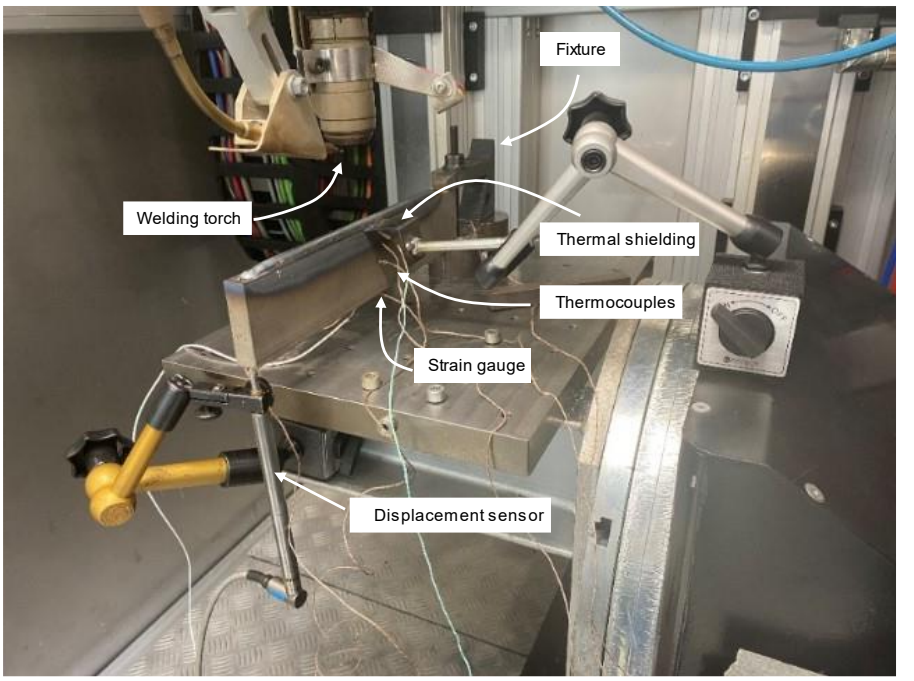



**Fig. 1** Experimental setup

## TEMPERATURE MEASUREMENTS

The thermal history was recorded using spot-welded Type K thermocouples. Five thermocouples were attached directly to the substrate at the positions shown in Fig. 2.

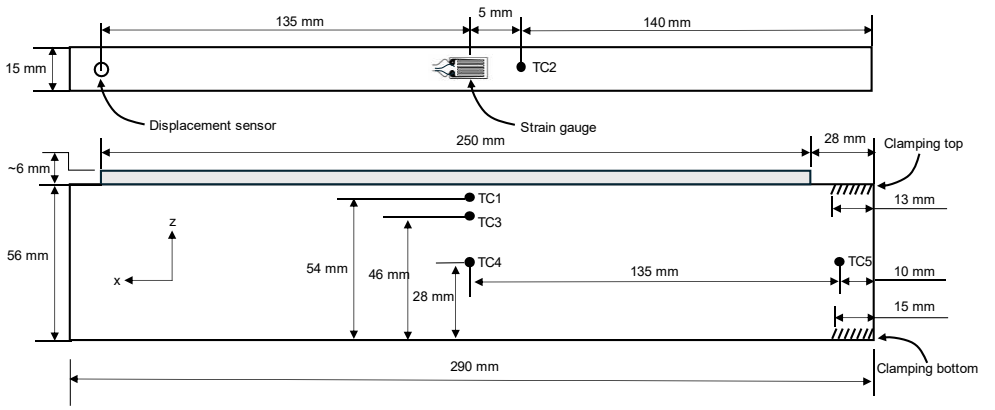



**Fig. 2** Substrate dimensions and location of thermocouples, displacement sensor and strain gauge

To protect the thermocouples from direct exposure to the plasma gas, a small metal shield was installed. In addition, two further thermocouples were mounted on the clamping block and the top clamp to monitor the heat flux into the fixtures. Thermal data acquisition was performed partly using an HBM QuantumX MX440B unit and partly with the integrated data acquisition system of the SBI M3DP-SL machine, both operated at a sampling frequency of 5 Hz.

## DISPLACEMENT MEASUREMENTS

Vertical displacements of the substrate were measured with an HBM WA20 displacement sensor, which was positioned at the bottom of the free end of the substrate (Fig. 2). The sensor signals were recorded with an HBM QuantumX MX440B unit at a sampling frequency of 5 Hz.

## STRESS MEASUREMENTS

Stresses were measured using linear high-temperature foil gauges, combined with computational compensation of the measurement signal, as described later. The gauges were mounted at the center of the bottom surface of the substrate in longitudinal orientation (see Fig. 2 and Fig. 3). Linear gauges were chosen because, at the measurement position, the strain state can be approximated as one-dimensional and thermoelastic in the longitudinal direction. This approximation is justified by the cantilever-like geometry of the substrate, the longitudinal deposition path, and the large distance to the weld bead. All gauges were taken from the same production batch to minimize variability. The main specifications are summarized in Table 1.



**Fig. 3** Mechanical clamping for curing under pressure (left), installed gauge and thermocouple (right)

**Table 1** Main specifications strain gauges

| Parameter | Specification |
|---|---|
| Type | HBM 1-LM11-6/350GE |
| Nominal resistance $R_0$ | 350 Ω ± 0.3 % |
| K-factor $k$ | 2.38 ± 1 % |
| Temperature coefficient of K-factor $\alpha_k$ | -406 ± 10 [$10^{-6}$ $K^{-1}$] |
| Thermal expansion coefficient of the gauge $\alpha_{gauge}$ | α ≈ 10.8 [$10^{-6}$ $K^{-1}$] |
| Combined standard uncertainty $u_c$ | 0.6 · ΔT |
| Polynomial coefficients for intrinsic thermal output $\varepsilon_s(T)$ | $a_0$ = -44.12,<br>$a_1$ = 2.89,<br>$a_2$ = -0.0357,<br>$a_3$ = 5.85×$10^{-5}$,<br>$a_4$ = -5.16×$10^{-9}$ |
| Gauge factor used for polynomial $k_{\text{poly}}$ | 2 |
| Reference temperature $T_{ref}$ | 20 °C |
| Maximum operating temperature | 250 °C (zero-point-related)<br>300 °C (non-zero-point-related, < 5 h) |

Prior to bonding, the substrate surfaces were sanded and cleaned to ensure proper adhesion. The gauges were bonded using a two-component epoxy adhesive (HBM EP310N). The curing procedure was carried out in two stages: first, under pressure with mechanical clamping at 180 °C for two hours, and subsequently a precision curing cycle at 280 °C for two hours without pressure, followed by slow cooling inside the furnace. Pre-trials demonstrated that this precision curing procedure was essential to ensure reliable high-temperature measurements.

Thermocouple TC2 was placed directly next to the gauges to record the local temperature, which was required for the computational temperature compensation. Signal acquisition was performed using an HBM QuantumX MX1615B unit in a 4-wire configuration. The 4-wire configuration compensates for resistance changes in the lead wires that may occur due to thermal influences or differences in cable length. The data was recorded at a sampling frequency of 5 Hz.

## MICROGRAPHS

After the welding experiments, cross-sectional micrographs of the weld beads were prepared to characterize the fusion zone and the heat-affected zone. This microstructural information was subsequently used for calibration of the simulation.

## TEMPERATURE COMPENSATION

Accurate stress measurements at elevated temperatures require compensating for the thermal effects inherent to strain gauges. Without such corrections, the recorded strain signal may no longer represent the true mechanical response but instead include temperature-induced measurement errors. To ensure reliable results in the WA-DED experiments, a computational temperature compensation was applied.

In absence of temperature effects, strain gauges measure strain $\varepsilon$ via the relationship [7]

$$\varepsilon = \frac{\Delta R/R_0}{k} \tag{1}$$

where $\Delta R$ denotes the resistance change, $R_0$ the nominal resistance of the gauge, and $k$ the nominal gauge factor. Assuming purely elastic, uniaxial loading, the corresponding stress $\sigma$ can then be calculated via Hooke's law as

$$\sigma = E * \varepsilon \tag{2}$$

with $E$ being the Young's modulus of the substrate material.

However, during temperature changes, strain gauges measure an apparent strain, even when no mechanical load is present. The apparent strain originates from three main sources:

1. The temperature dependence of the gauge's K-factor
2. Mismatches in the coefficients of thermal expansion (CTE) between the substrate and the gauge, and
3. The intrinsic thermal output of the gauge itself.

To account for the apparent strain at higher temperatures, it is necessary to measure the temperature at the strain gauge location an apply an additional computational correction to the signal [8].

The temperature dependent K-factor $k^*(T)$ is described as

$$k^*(T) = k \cdot \left(1 + \alpha_k (T - T_{\mathrm{Ref}})\right) \tag{3}$$

where $k^*(T)$ is the effective K-factor at temperature $T$, $\alpha_k$ is the temperature coefficient of the gauge factor, and $T_{\mathrm{Ref}}$ is the reference temperature.

Strain resulting from the thermal expansion mismatch is given by

$$\varepsilon_f(T) = \left(\alpha_{\mathrm{substrate}} - \alpha_{\mathrm{gauge}}\right) \cdot \Delta T \tag{4}$$

where $\alpha_{\mathrm{substrate}}$ and $\alpha_{\mathrm{gauge}}$ are the thermal expansion coefficients of the substrate and the strain gauge, respectively.

The intrinsic thermal output of the gauge is usually given by the manufacturer as a polynomial function of temperature:

$$\varepsilon_s(T) = (\mathrm{a}_0 + \mathrm{a}_1\mathrm{T} + \mathrm{a}_2\mathrm{T}^2 + \mathrm{a}_3\mathrm{T}^3 + \ldots) \cdot \frac{k_{\mathrm{poly}}}{k^*(T)} \tag{5}$$

with coefficients $a_n$ provided in the datasheet. Since this polynomial is defined for a fixed reference K-factor $k_{\text{poly}}$, it must be rescaled to the actual temperature-dependent K-factor by multiplying with the ratio $\frac{k_{\text{poly}}}{k^*(t)}$.

Combining these contributions, the corrected strain signal is obtained as

$$\varepsilon_c(T) = \varepsilon \frac{k}{k^*(T)} - \varepsilon_f(T) - \varepsilon_s(T) \tag{6}$$

Finally, in converting compensated strain to stress, the temperature dependence of the Young's modulus $E(T)$ must also be considered:

$$\sigma_C = E(T) \cdot \varepsilon_c(T) \tag{7}$$

## FURNACE EXPERIMENT

To validate the computational temperature compensation and to quantify the influence of thermal effects, a dedicated furnace experiment was conducted prior to the WA-DED deposition trials. In addition, this test was used to determine the coefficient of thermal expansion of the substrate material.

For this purpose, the three substrates equipped with strain gauges and thermocouples were placed inside a chamber furnace (Fig. 4). The specimens were heated to a maximum temperature of 250 °C at a controlled heating rate of 2 °C/min, ensuring a slow and uniform temperature increase. The heating rate was kept low to ensure that thermal equilibrium was maintained throughout the samples, thereby avoiding the generation of additional thermal stresses.

During the entire heating cycle, strain and temperature were recorded simultaneously at the strain gauge location, allowing the characterization of apparent strain in the absence of mechanical loading.



**Fig. 4** Substrates with installed strain gauges in chamber furnace

Fig. 5 shows the mean measured strain $\varepsilon_{mean}$ together with the standard deviation $\sigma_{std}$ of the three gauges without any compensation. For comparison, the combined standard uncertainty $u_c$ specified in the datasheet is also applied to the mean curve and displayed. The experimental standard deviation remains well within the datasheet uncertainty band, confirming the repeatability of the measurements.

Since the selected strain gauge was designed to have a coefficient of thermal expansion closely matching that of the substrate material, the measured strain remains close to zero near room temperature, as expected. However, with increasing temperature, a negative apparent strain develops. This behavior can be attributed to small mismatches in the coefficients of thermal expansion, the temperature dependence of the gauge's K-factor, and the intrinsic thermal output of the strain gauge.

The results highlight that temperature compensation becomes increasingly important at elevated temperatures. At 200 °C, the apparent thermal strain reaches approximately 230 µm/m, which corresponds to about 48.3 MPa when assuming a Young's modulus of 210 GPa. In theory, the datasheet's combined standard uncertainty could add an additional error of roughly ±25 MPa.

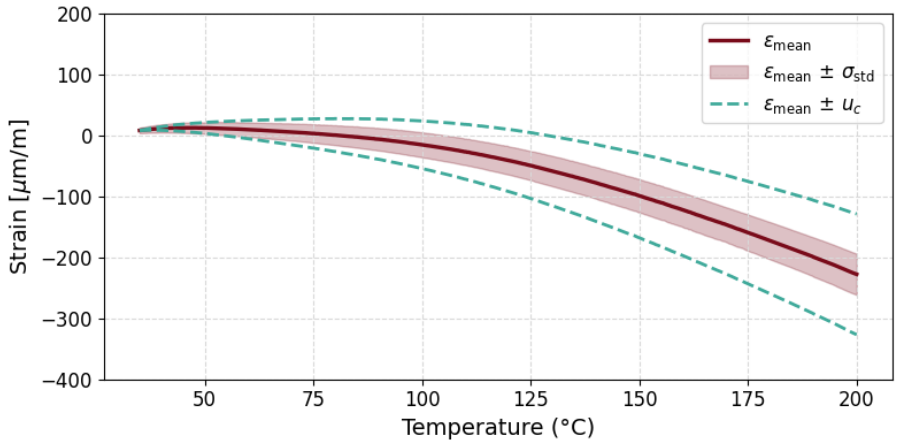



**Fig. 5** Furnace experiment - uncompensated strain

Fig. 6 shows the compensated mean strain $\varepsilon_{c,mean}$ curve according to Eqn. (6) along with the individual correction components. Among these, the polynomial correction $\varepsilon_s$, which compensates for the intrinsic thermal output of the strain gauge, has the largest influence, followed by the correction for the coefficient of thermal expansion $\varepsilon_f$. The temperature dependence of the K-factor, on the other hand, contributes only marginally and could therefore be neglected.

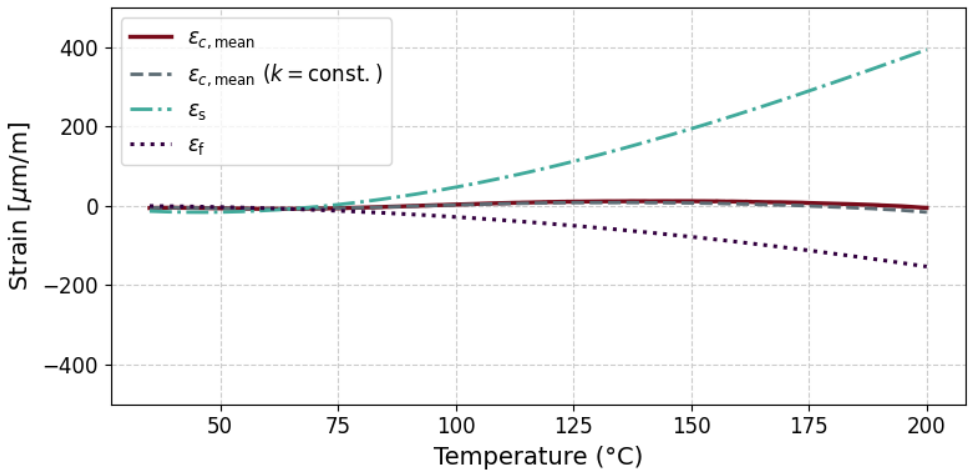



**Fig. 6** Furnace experiment - compensated strain and individual correction contributions

For the temperature compensation, the linear coefficient of thermal expansion of the substrate material $\alpha_{substrate}$ was treated as an unknown parameter. It was fitted such that the

compensated mean strain $\varepsilon_{c,mean}$ is minimized. Fig. 7 compares the fitted linear coefficient of thermal expansion with literature data for a similar material.

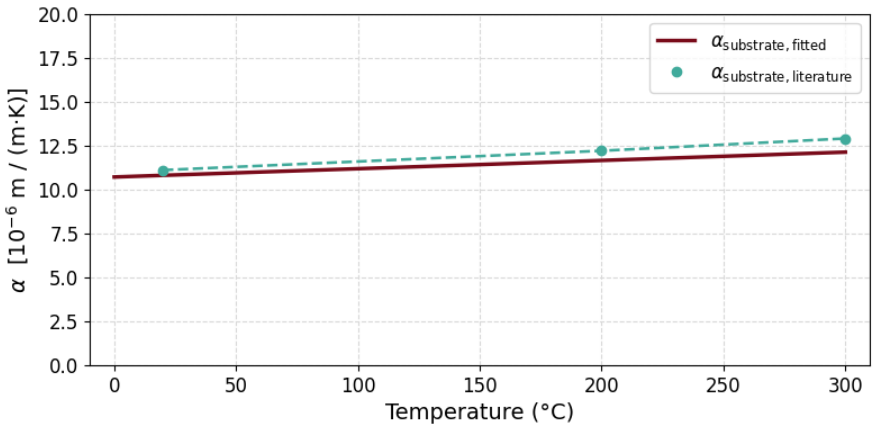



**Fig. 7** Coefficient of thermal expansion of the substrate - fitted from furnace experiment compared to literature data [9]

The results show good agreement. This indicates that the compensation equations were implemented correctly. Possible reasons for the slight underestimation are small differences in the material composition, uncertainties of the strain gauges, or the ambient conditions at the start of the experiment. The strain measurements were zeroed at an environmental temperature of 30 °C, while both the literature values and the datasheet polynomial are referenced to 20 °C.

## NUMERICAL MODEL

A fully coupled thermo-mechanical finite element (FE) analysis of the additive manufacturing process was performed using the commercial software Simufact Welding®.

The finite element model is shown in Fig. 8. In addition to the substrate and deposited welds, the fixture and welding table were also included. To reduce complexity, the weld seams were modeled as rectangular layers with a width of 8 mm and a height of 1.4 mm. The mesh size was set to 2 mm in the substrate and 1 mm in the weld seam. An automatic refinement algorithm was applied to locally refine the mesh in regions with steep thermal gradients. The time step size was adaptive, with a maximum step size limited to 0.5 s.

## BOUNDARY CONDITIONS

No clamping force is considered in this model. Instead, movement of the nodes along the contact area of the fixture is prohibited using single point constraints. Hence, the fixture acts solely as a thermal heat sink. The heat transfer coefficient between bodies in contact was set to 5000 W/m²K.

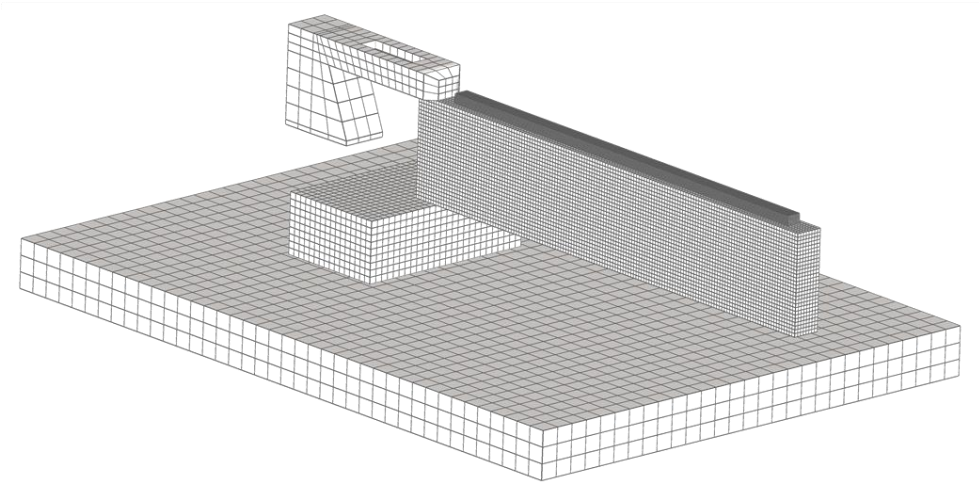


**Fig. 8** Finite element model

Convective and radiative boundary conditions are applied to all outer surfaces. The materials emissivity and the convection coefficient are assumed independent of the temperature and set to 0.7 and 6.5 W/m²K, respectively. The heat transfer coefficients and thermal boundary conditions were calibrated by trial and error, until the temperatures in the simulation are in good agreement with the temperatures measured in the experiments.

## HEAT SOURCE MODELLING

In this study the energy input during the WA-DED process was represented by a moving cylindrical heat source. This model is a simplification of the three-dimensional conical heat source model (TDC) [10]. It defines the volumetric heat generation rate $Q_V$ by a Gaussian distribution as

$$Q_V(r) = Q_0 \cdot \exp\left(-\frac{Mr^2}{r_0^2}\right) \tag{8}$$

where $M$ is the Gaussian parameter, $r_0$ the radius of the cylinder and $r$ the radial coordinate. The maximum heat intensity $Q_0$ is given by

$$Q_0 = \frac{3\eta P e^3}{dr^2\pi(e^3-1)} \tag{9}$$

Here, P denotes the power input, $\eta$ the process efficiency and $d$ the cylinder height. In cases where parts of the heat source extended beyond the calculation mesh, the total heat input was scaled to ensure that the net input energy matched the defined process power.

The heat source path was defined using nodes of the calculation mesh. This approach was necessary because of the large displacements occurring in the cantilever experiment, ensuring that the heat source moved consistently with the deforming mesh.

In the present study the process efficiency was set to $\eta = 0.47$ and was calibrated, similar to the other boundary conditions, by comparing simulated and measured temperature curves. The cylindrical heat source was defined with $r_0 = 9\,mm$, $d = 2\,mm$ and a Gaussian parameter of $M = 1$. Fig 9 compares the experimental cross-sectional micrograph with the simulated maximum temperature distribution, showing that the chosen heat source dimensions reproduce the fusion zone with good agreement.

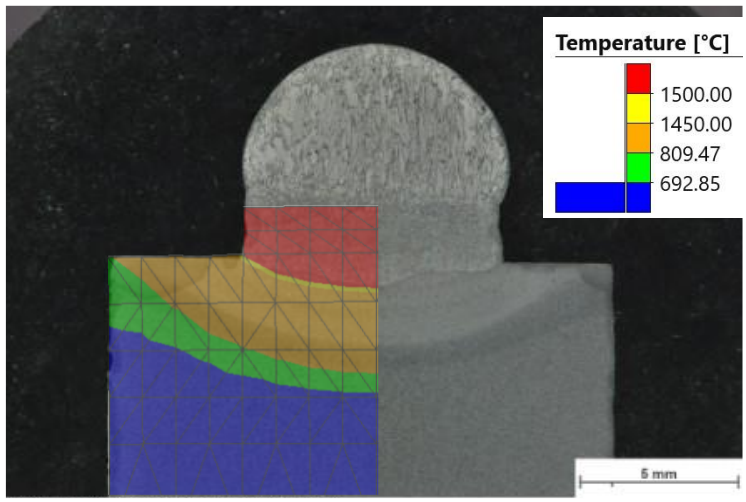



**Fig. 9** Cross-sectional micrograph of the deposited wall compared with the maximum temperature distribution from the simulation.

## MATERIAL MODELLING

The thermo-mechanical behavior was described using a fully coupled thermo-elasto-plastic constitutive model as implemented in Simufact Welding®. Elastic behavior was modeled as linear isotropic elasticity with temperature-dependent Young's modulus and Poisson's ratio. Plastic deformation was governed by a von Mises yield criterion with isotropic hardening, using temperature-dependent flow curves provided by the Simufact material database. Thermal strains were calculated based on the temperature-dependent coefficient of thermal

expansion. Phase transformations were neglected, and therefore no transformation-induced strains or transformation plasticity effects were considered.

The deposition of material was modeled using the quiet element method [11]. In this approach, all deposit elements are included in the mesh from the beginning but are initially set to a "quiet" state, where they do not significantly affect the analysis (e.g., very low thermal conductivity and Young's modulus). As these quiet elements are heated by the moving heat source, their actual thermo-physical properties are activated, thereby mimicking the material deposition process.

State-of-the-art WA-DED simulations often employ the dead element method. In this approach, deposit elements are initially removed from the calculation and are gradually added (e.g., layer by layer) before being activated in the same way as in the quiet element method. This strategy significantly reduces computational effort in the early stages of the simulation. However, it is not well suited for cases involving large deformations, since nodes of new elements are added with their original coordinates. As a consequence, highly distorted or even negative-volume elements may occur.

## RESULTS

This section presents the results of the three WA-DED trials alongside the corresponding FEM simulation. Experimental results are shown as mean values, with the standard deviation reflecting the scatter between the repetitions.

### THERMAL HISTORY

Figure 10 shows exemplary results from two thermocouples (TC1 and TC2) for both experiment and simulation. TC1 is closest to the molten pool, TC2 is located at the strain-gauge position. For the far-field location (TC2), the experimental measurements show only minor scatter between the three trials, indicating good repeatability at the strain-gauge position. In contrast, near the molten pool (TC1) the measurements show significant differences (up to ~150 °C) in peak temperature. Possible reasons are direct interaction with the plasma gas and slight positioning differences. Because of the steep thermal gradients near the pool, even small position offsets can lead to substantial temperature differences. At TC1 location, the simulation predicts a maximum temperature gradient of 95 °C/mm, so an offset of less than 1.6 mm could already cause a deviation of 150 °C. The temperature at strain-gauge location remains within the datasheet's maximum allowable temperature of 250 °C.

Overall, the simulated temperature histories agree well with the mean experimental curves, supporting the adequacy of the thermal calibration and the thermophysical properties used in the model. Measurements from the remaining thermocouples also show similarly good agreement with the simulation.

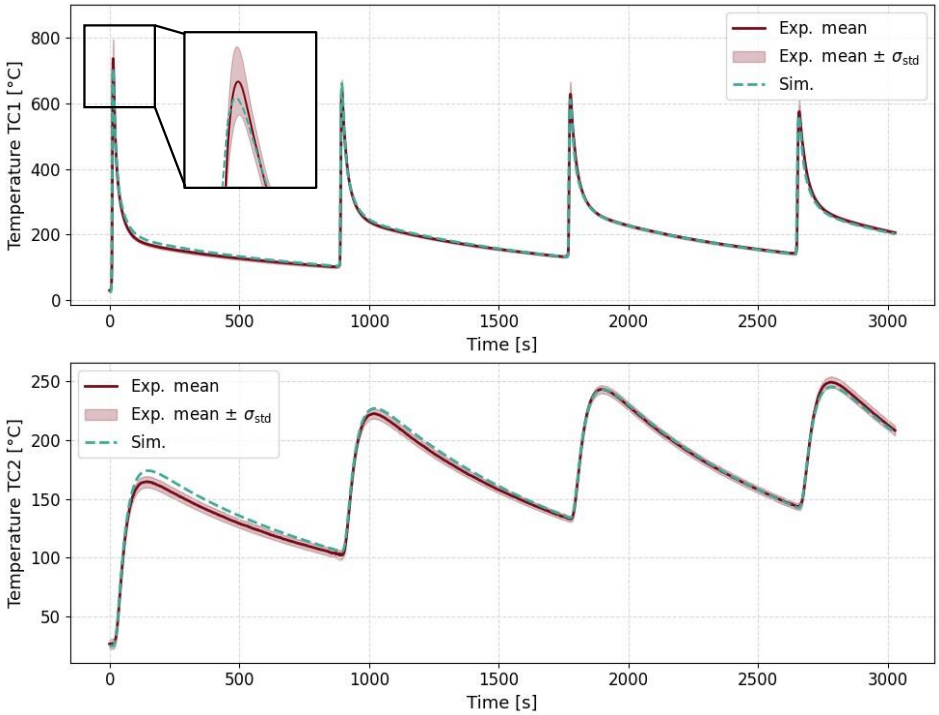



**Fig. 10** Thermal history of thermocouples TC1 and TC2 - experiment vs simulation

## DISPLACEMENT HISTORY

Fig. 11 compares the experimental and simulated vertical displacements at the contact point of the displacement sensor. The small scatter between trials demonstrates the good reproducibility of the setup. At the beginning of the welding process, the substrate bent downward due to the higher thermal expansion of the top surface relative to the bottom. As deposition continued, the substrate gradually bent upward, primarily driven by solidification shrinkage of the deposited weld seam. This downward–upward sequence repeated with each layer, with most of the displacement occurring after the first layer. This behavior is consistent with observations from a previous study [12]. The simulation captured the overall trend but tended to slightly overpredict the downward bends and underpredict the upward bends. Possible reasons include variations in substrate properties, limitations of the material model that neglected phase transformations, an imperfect heat-source representation, and general modeling simplifications."

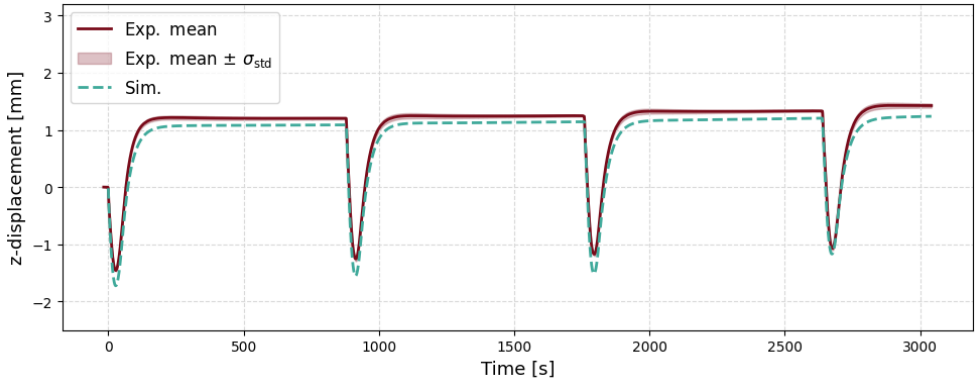



**Fig. 11** Displacement history - experiment vs simulation

*Stress history*

As illustrated in Fig. 12, the stress evolution measured by the strain gauges shows the same qualitative pattern as the displacement history. Scatter between the trials was small, again confirming the reproducibility of the measurements. The largest scatter occurred immediately after each layer was deposited. A possible explanation is that these are the moments of highest temperature, where the deviation of the strain measurement is also most pronounced.

Overall, the simulated stresses align well with the measurements. Similar to the z-displacements, the model tends to slightly overpredict stresses during downward bending, pointing to a modeling rather than measurement error. It should be noted that the stresses measured at the strain-gauge location remain well within the elastic regime of the substrate material throughout the process. Consequently, the thermoelastic assumption used to calculate stress from the measured strain signal at the measurement location is fulfilled.

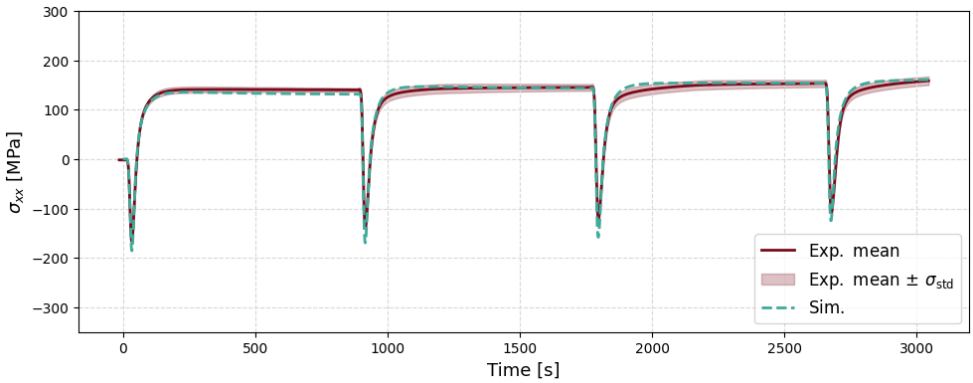



**Fig. 12** Stress history – experiment with compensation vs simulation

Finally, Fig. 13 compares the simulated stresses to the experimental stresses without temperature compensation. While the overall trend is captured and the magnitudes are in the expected range, the curve shape deviates significantly. This clearly demonstrates that temperature compensation is essential for obtaining accurate stress history results.

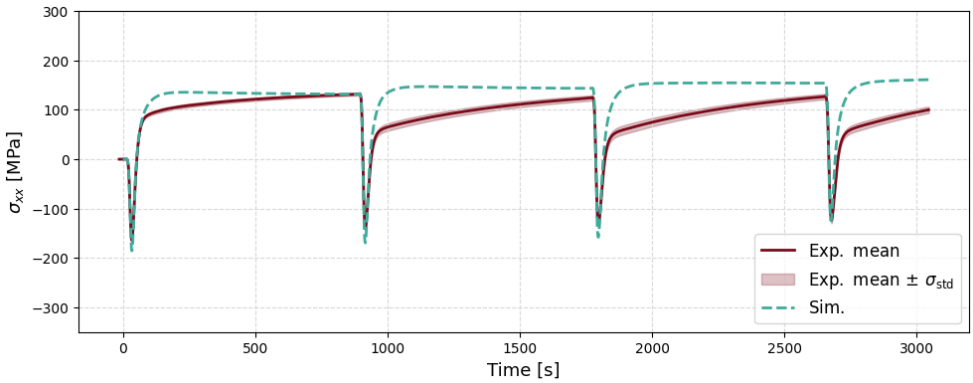



**Fig. 13** Stress history – experiment without compensation vs simulation

## DISCUSSION

The results of this study demonstrate that high-temperature strain gauges can be successfully applied to capture the transient stress evolution during WA-DED. The scatter between repeated trials was very low, indicating high repeatability of both the experimental setup and the measurement procedure.

Comparison of experimental and numerical results showed only minor deviations in both displacement and strain measurements, underscoring the adequacy of the simulation setup and the applied material model.

For reliable stress measurements, accurate temperature compensation is essential. This requires precise knowledge of the temperature at the gauge location as well as of the substrate's thermal expansion coefficient. Another key limitation is the operational temperature range of the strain gauges. Consequently, stress can only be measured at a certain distance from the weld pool, where an optimum must be found between proximity to the weld and exposure to the maximum mechanical loading.

The installation of strain gauges is laborious, requiring careful surface preparation and controlled curing of the adhesive. In this study, a furnace curing cycle was used to ensure accuracy and reproducibility. However, in many cases such a procedure may not be feasible.

Despite these limitations, the method offers several advantages. Strain gauge measurements are non-destructive, relatively compact compared to optical methods, and capable of delivering time-resolved stress data with high precision. However, pre-existing residual stresses in the substrate can influence the results. For this reason, the strain gauge method is

best suited for analyzing relative changes in stress during the process rather than providing absolute residual stress values.

Overall, the present study demonstrates the feasibility of using high-temperature strain gauges for in-situ monitoring and validation of WA-DED simulations, thereby contributing to more reliable predictive modeling in additive manufacturing."

## DECLARATION OF GENERATIVE AI AND AI-ASSISTED TECHNOLOGIES IN THE WRITING PROCESS

During the preparation of this work the authors used ChatGPT to improve the readability and reduce spelling errors. After using this tool, the authors reviewed and edited the content as needed and take full responsibility for the content of the publication.

## APPENDICES AND ACKNOWLEDGEMENTS

The consortium would like to thank the federal ministries of Austria for “Climate Action, Environment, Energy, Mobility, Innovation and Technology” (BMK), the ministry of “Labour and Economy” (BMAW), the Austrian Funding Agency (FFG), as well as the four federal funding agencies Amt der Oberösterreichischen Landesregierung; Steirische Wirtschaftsförderungsgesellschaft m.b.H.; Amt der Niederösterreichischen Landesregierung; Wirtschaftsagentur Wien. Ein Fonds der Stadt Wien for funding project “We3D” (FFG Nr. 886184) in the framework of the 8th COMET call.

## References

[1] M. FLORIAN, M. OLIVER, P. DOMINIC, U. STEPHAN and S.-B. CHRISTIAN: ‘From CAD model to WAM component: implementation of complex geometries using the example of a hydrogen tank’, *IOP Conf. Ser.: Mater. Sci. Eng.*, Bd. 1315, Nr. 1, S. 012002, Okt. 2024, doi: 10.1088/1757-899X/1315/1/012002.

[2] J. HONNIGE, S. WILLIAMS, M. ROY, P. COLEGROVE and S. GANGULY: *Residual Stress Characterization and Control in the Additive Manufacture of Large Scale Metal Structures*, 2016. doi: 10.21741/9781945291173-77.

[3] F. D. GURMESA, H. G. LEMU, Y. W. ADUGNA and M. D. HARSIBO: ‘Residual Stresses in Wire Arc Additive Manufacturing Products and Their Measurement Techniques: A Systematic Review’, *Applied Mechanics*, Bd. 5, Nr. 3, S. 420-449, Sep. 2024, doi: 10.3390/applmech5030025.

[4] M. BIEGLER, B. GRAF and M. RETHMEIER ‘In-situ distortions in LMD additive manufacturing walls can be measured with digital image correlation and predicted using numerical simulations’, *Additive Manufacturing*, Bd. 20, S. 101-110, März 2018, doi: 10.1016/j.addma.2017.12.007.

[5] X. LU ET AL.: ‘In situ measurements and thermo-mechanical simulation of Ti–6Al–4V laser solid forming processes’, *International Journal of Mechanical Sciences*, Bd. 153-154, S. 119-130, Apr. 2019, doi: 10.1016/j.ijmecsci.2019.01.043.

[6] H. E. COULES, L. D. COZZOLINO, P. A. COLEGROVE and S. W. WEN: ‘Measurement and modelling of the transient thermal-mechanical strain field during GMA welding’, Apr. 2011, accessed: 29. Mai 2024, [Online], available under: https://dspace.lib.cranfield.ac.uk/handle/1826/5820.

[7] K. HOFFMANN: *Eine Einführung in die Messung mit Dehnungsmessstreifen*, Hottinger Baldwin Messtechnik GmbH, Damrstadt, Deutschland, 1987.

[8] ‘Temperaturkompensation bei DMS-Viertelbrücken-Anwendungen’, *HBM*, accessed: 28. August 2025, [Online], available under: https://www.hbm.com/de/10083/temperaturkompensation-bei-dms-viertelbruecken-anwendungen/.

[9] *Werkstoff- und Materialeigenschaften 1.0570*, accessed: 28. August 2025, [Online], available under: https://www.hasco.com/de/werkstoffdatenblatt_1.0570.

[10] C. S. WU, H. G. WANG and Y. M. ZHANG: ‘A New Heat Source Model for Keyhole Plasma Arc Welding in FEM Analysis of the Temperature Profile’, 2006.

[11] P. MICHALERIS: ‘Modeling metal deposition in heat transfer analyses of additive manufacturing processes’, *Finite Elements in Analysis and Design*, Bd. 86, S. 51-60, Sep. 2014, doi: 10.1016/j.finel.2014.04.003.

[12] H. DREXLER, F. HAUNREITER, L. RABERGER, L. REITER, A. HÜTTER and N. ENZINGER: ‘Numerical Modeling of Distortions and Residual Stresses During Wire Arc Additive Manufacturing of an ER 5183 Alloy with Weaving Deposition’, BHM *Berg- und Huettenmaenn. Monatsh.*, Bd. 169, Nr. 1, S. 38-47, Jan. 2024, doi: 10.1007/s00501-023-01421-9.

# HEAT TRANSFER AND FLUID FLOW MODEL ASSISTED MECHANICAL ANALYSIS FOR WIRE ARC DIRECTED ENERGY DEPOSITION TO IMPROVE RESIDUAL STRESS AND DISTORTION PREDICTION

P. K. DILJITH*[1], ARYAN**, W. ZHANG**, A. DE*

**Mechanical Engineering Department, Indian Institute of Technology Bombay, 400076, Mumbai, India*
*Orcid Id:0000-0001-9522-7838, 0000-0002-3109-261X*
***Department of Materials Science and Engineering, The Ohio State University, 43221, Ohio, USA*
*Orcid Id:0000-0002-7570-0488, 0000-0003-4543-2563*

*DOI 10.3217/978-3-99161-089-2-024, license CC BY 4.0*
*https://creativecommons.org/licenses/by/4.0/deed.en*
*This CC license does not apply to third party material and content noted otherwise.*

## ABSTRACT

A substantive design of process variables and scanning strategy in wire arc directed energy deposition (DED-Arc) requires an estimation of the thermal distortion and residual stress. Routine sequential heat transfer and thermomechanical stress analyses neglect the convective heat transport in the melt pool that commonly affects the computational accuracy. We propose here to compute the deposit profile and temperature field using a finite volume-based heat transfer and fluid flow model and use the computed temperature field for a subsequent mechanical analysis. The computed melt pool profile, deposition profile and residual stress showed a maximum discrepancy of around 10% against experimentally measured results for single- and multi-track DED-Arc depositions. An assessment of the increased computational demand vis-à-vis enhanced prediction accuracy due to the integration of a heat transfer and fluid flow model over a heat conduction only model is presented. Further efforts to simulate multi-track multi-layer DED-Arc using the proposed approach are underway.

Keywords: Wire arc directed energy deposition, Heat transfer and fluid flow model, Thermomechanical analysis, Residual stress and distortion, Computational accuracy.

## INTRODUCTION

Wire arc directed energy deposition (DED-Arc) is a layer-by-layer additive manufacturing process that uses an electric arc to melt a filler wire, which solidifies to form three-dimensional components [1-2]. DED-Arc has attracted a significant interest due to low cost of filler wire feedstock in comparison to metallic powder [3] and a high deposition rate almost up to 4 kg/h [4]. However, high residual stress [5] and distortion [6] of the deposited part has remained a critical challenge for the DED-Arc built parts. A prior quantitative estimation of the temperature field, and thermomechanical residual stress and distortion is becoming increasingly important in design for DED-Arc process [7]. With the growth of computational capacity and efficiency, high fidelity models are increasingly used to help design DED-Arc process [8].

Sequentially coupled heat conduction and thermomechanical stress analyses are used to simulate the temperature field, and the residual stress and distortion for DED-Arc of small to medium size builds [9-10]. Conventional thermo-mechanical methods based on heat conduction analysis require a pre-defined build profile, which is routinely considered as a simple shape [11-12] or obtained from an experimentally measured deposit [13-14] thereby limiting the model capability. These models also require considering complex heat source configurations such as hemispherical Gaussian [11], double-ellipsoid [15-16], circular surface [17], and conical [18-19]. The pre-defined deposit profile is introduced during the modelling calculations in an artificial manner [20-21]. A physics-based heat transfer model that captures the evolution of melt pool profile and deposit dimensions in a mechanistic manner can minimize errors from assumed geometries and heat sources, ensuring accurate prediction of distortion and residual stress.

To address these limitations, research has focused on incorporating convective flow and integrating thermal-fluid models with mechanical models. Heat transfer and fluid flow models account for convective flows by solving the conservation equations for mass, momentum, and energy. Mukherjee et al. [22] reported a 3D transient heat transfer and fluid flow coupled mechanical analysis for the prediction of residual stress in DED-Arc of simplified geometry. Chen et al. [23] reported a similar coupled thermo-fluid and mechanical analysis for laser powder bed fusion (LPBF) process. Bailey et al. [24] simulated the deposition of three single layers using a coupled fluid flow model and mechanical analysis for the prediction of residual stress. Gao et al. [25] also reported a similar coupled thermo-fluid and mechanical analysis for layer-by-layer deposition. The aforementioned studies reported the challenges of high computational demands and could handle the simulation of either a few tracks or a few layers. Furthermore, despite these advancements, geometric simplifications remain prevalent, and most studies are restricted to simple geometries.

This study presents a high-fidelity modelling approach to compute residual stress and distortion in DED-Arc fabricated components. The framework integrates a thermal-fluid flow model that captures the melting physics of filler wire to generate the temperature distribution and realistic deposition profile, which is then mapped to a mechanical model. The volume of fluid approach in the thermo-fluid analysis eliminates the need to assume an artificial bead profile enabling enhanced predictability and adaptability. In the mechanical model, the elements are activated based on their thermal history using a subroutine that assigns a valid

volume fraction. The computed results are validated against experimentally measured values from independent literature and compared with a conventional heat-conduction-based thermomechanical model. This comprehensive approach will prove essential for a more informed prior assessment of the structural integrity and dimensional consistency of DED-Arc fabricated parts.

## NUMERICAL MODELLING

### HEAT TRANSFER AND FLUID FLOW MODEL

In this work, a finite element volume-based heat transfer and fluid flow model is used to simulate the transient temperature field and material flow for single- and multi-layer DED-Arc process. The solution domain embodies both the substrate and the filler wire. The following assumptions are considered for the modelling calculations. The molten metal flow within the melt pool is assumed to be laminar and incompressible. The effect of shielding gas and the evaporation of alloying elements are neglected [22,26]. The effects of arc pressure [27] and Lorentz forces [28] are omitted, as their influence is negligible at currents below 250 A and for relatively smaller melt pools in DED-Arc in comparison to arc welding.

The arc plasma heat transfer and fluid flow is not directly considered in the simulation. Instead, the current model follows the standard method to represent the effect of arc plasma by applying a surface heat flux in the form of a Gaussian distribution. Such heat flux distribution is described by two parameters: the arc radius and the heat source efficiency. The arc radius is assumed to have a constant value of 1.5 mm based on the literature data for GMAW-based WAAM processes. For the heat source efficiency, the initial values in the range of 0.70 to 0.85 were selected based on the literature data. The value was then adjusted only for the first deposited layer to obtain agreement with experimentally observed bead geometry. For multilayer simulations, the same efficiency value was retained for all subsequent layers, and no further adjustment was applied.

For simplicity, the current model also does not directly consider the filler metal transfer. The addition of filler metal into the melt pool is represented by applying an equivalent mass flux to the melt pool surface.

The following governing equations of conservation of mass, momentum, and energy are solved.

$$\nabla \cdot (\rho\, \vec{v}) = 0 \tag{1}$$

$$\frac{\partial}{\partial t}(\rho\, \vec{v}) + \nabla \cdot (\rho\, \vec{v} \otimes \vec{v}) = \nabla \cdot (\mu \nabla\, \vec{v}) - \nabla P + \rho \vec{g} \tag{2}$$

$$\frac{\partial}{\partial t}(\rho h) + \nabla \cdot (\rho \vec{v} h) = \nabla \cdot (k \nabla T) \tag{3}$$

where $\vec{v}$ and $\vec{g}$ denote the velocity vector and gravitational acceleration vector, respectively, $\rho$ is the density, $\mu$ is the viscosity, $P$ is the pressure, $k$ is the thermal conductivity, and $T$ is the temperature. In Eq. (3), $h$ *is the specific enthalpy that is defined as* $h = \int C(T)dT + (1 - f_s)L$, where $C(T)$, $L$ and $f_s$ are the specific heat, latent heat of melting, and fraction of the solid, respectively.

The deposit profile is modelled using the volume of fluid (VOF) method with each cell of a discretized mesh assigned to a time-dependent fluid fraction function. The function with a value of 1 represents the fluid region (comprising liquid and/or solid metal), 0 represents the non-fluid region, and a value in between 0 and 1 represents the interface containing the free surface, which is governed by partial derivatives in the form of Eq. (4) and solved to track the free surface of the molten pool.

$$\frac{\partial f_l}{\partial t} + \nabla \cdot (\vec{v}\ f_l) = 0 \tag{4}$$

where $f_l$ denotes the fluid volume fraction in a cell, with $f_l$ = 1 representing a cell fully occupied by fluid and $f_l$ = 0 representing a void or gas region, and $\vec{v}$ is the velocity vector. Heat loss due to convection is considered on the deposit and substrate surfaces. Further detailed methodology for the heat transfer and fluid flow analysis is already reported in literature [29] and not repeated here.

## MAPPING OF DEPOSITION PROFILE AND TEMPERATURE DISTRIBUTION

The model integrates the deposition profile and transient temperature field from the heat transfer and fluid flow model into the mechanical simulation. The overall mapping framework is illustrated in Fig. 1. The deposition profile is exported in a tessellated format (stl) from the thermal-fluid simulation. To ensure compatibility with the mechanical model, the stl file is curated to eliminate defects such as non-manifold edges, holes, inverted normal, and self-intersecting faces [30]. The geometry is imported to a commercial finite element method software (ABAQUS ver-2021) environment. A custom plugin is used to reconstruct the deposition geometry from the tessellated data [31].

Following the creation of the deposit geometry in ABAQUS, the domain is partitioned and discretized using three-dimensional tetrahedral elements with displacement degrees of freedom. Tetrahedral meshing is selected to accommodate the complex geometrical features of the deposited material [32], with finer meshes applied in the deposition region to accurately simulate element activation during the build process. Nodal coordinates are extracted, and transient temperature values are mapped from the CFD simulation at predefined time intervals. These temperature values are then applied as predefined boundary conditions in mechanical analysis, enabling coupled thermo-mechanical simulation, as shown in Fig. 1.

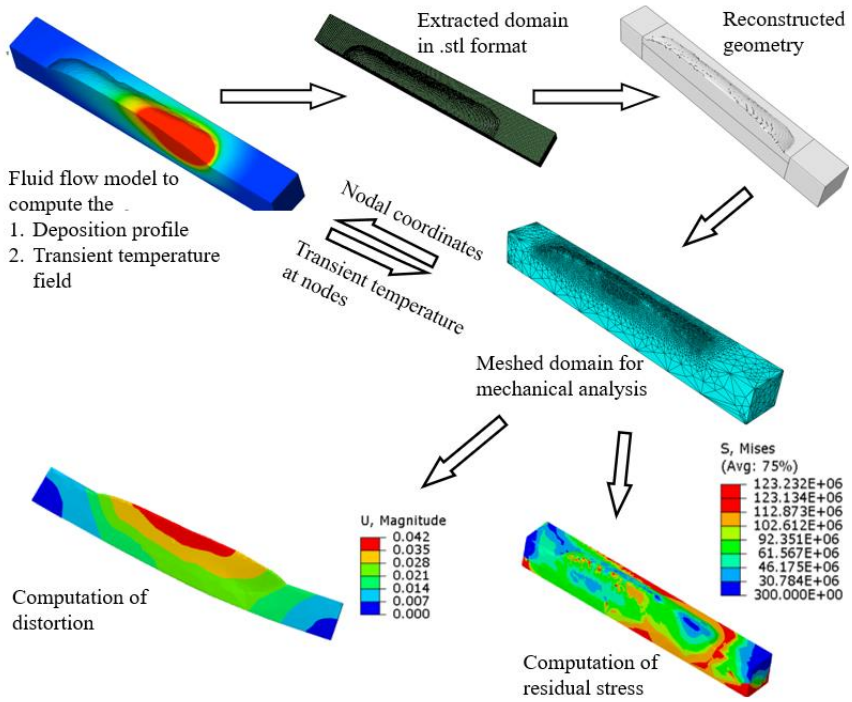



**Fig. 1** Flowchart for the mapping of deposition profile and temperature distribution from CFD model to mechanical model

## MECHANICAL MODEL

From the time varying pre-defined temperature field obtained from the fluid flow model, the displacement field in the mapped solution domain is calculated by solving the force equilibrium equation given by

$$[\mathrm{K}]\{\delta\} - \{f\} = 0 \tag{5}$$

where [K] is the global stiffness matrix, $\{\delta\}$ is the unknown nodal displacement vector at all the nodes of the solution domain and $\{f\}$ embodies the contribution from the thermal strain induced body force from all the elements. Eq. (5) is solved for $\{\delta\}$ considering the structural boundary conditions and for a given temperature gradient between two successive time steps. The nonlinearity due to plasticity is incorporated by defining Von Mises yield criterion and solving for displacement using the Prandtl-Reuss flow rule. The resultant displacement is a sum of elastic, plastic and thermal displacements as shown in Eq. 6. The volumetric strain due to solid-state phase transformation is considered negligible for the selected alloys, AA5356 and austenitic stainless steel, used for the model calculations [33,34].

$$\varepsilon_{total} = \varepsilon_{elastic} + \varepsilon_{plastic} + \varepsilon_{thermal} \quad (6)$$

To model the experimental clamping conditions, all the nodes in the respective positions are restricted in the x, y, and z directions. The boundary condition is given by the Eq. 7.

$$U_x = U_y = U_z = 0 \quad (7)$$

The simulation of material deposition in the mechanical analysis is carried out using an approach that alters the volume fraction of the element. Initially, the elements representing the deposited track are assigned a volume fraction of zero. In the following steps, the elements that obtain an average temperature that equals the melting point of the material is assigned a volume fraction of one using an Abaqus subroutine UEPACTIVATIONVOL.

## MODEL TESTING AND VALIDATION

### APPLICATION OF INTEGRATED MODEL TO SINGLE-TRACK SINGLE-LAYER DEPOSITION MODEL

The present model is demonstrated for a simple single-track, single-layer DED-Arc deposition of AA5356. The process is performed at a printing travel speed of 30 mm/s and an arc power of around 1.6 kW. The chemical composition of the material and their temperature dependent material properties are obtained from the literature [35].

To understand the importance of liquid metal convection over conduction on heat transfer, the Peclet number is estimated which is defined as $Pe = L\,u/\alpha$, where $L$ is the characteristic length (e.g., pool width), $u$ is the representative fluid velocity, and $\alpha$ is the thermal diffusivity. The results calculated by the heat transfer and fluid flow model for the AA5356 melt pool show u = 0.3 m/s and L = 0.006 m, resulting in a Peclet number of ~30. As this value is much larger than 1, the convective heat transport within the melt pool is considered significant for this case.

The transient temperature field computed by the heat transfer and fluid flow model is mapped into the mechanical model. The melt pool profile obtained by the temperature field mapping in the mechanical model is shown at three different locations along the deposition length in Fig. 2 (a-c). The profile simulated by the heat transfer and fluid flow model predicts a layer width of 3.5 mm, a layer height of 2.17 mm, and a penetration depth of 2.66 mm, as illustrated in Fig. 2 (d), confirming that the transient temperature field is transferred to the mechanical model with a satisfactory accuracy. Some distortion in the smoothness of the deposit profile arises from the tetrahedral meshing used to capture the geometry. A comparison between the deposition profile obtained from the fluid flow model and that mapped into the mechanical model is presented in Fig. 2 (e). Minor deviations are observed, which can be attributed to the unavoidable errors due to mapping. Nevertheless, the results show that both the deposition profile and temperature field are transferred from the fluid flow model to the mechanical model with a reasonable fidelity.

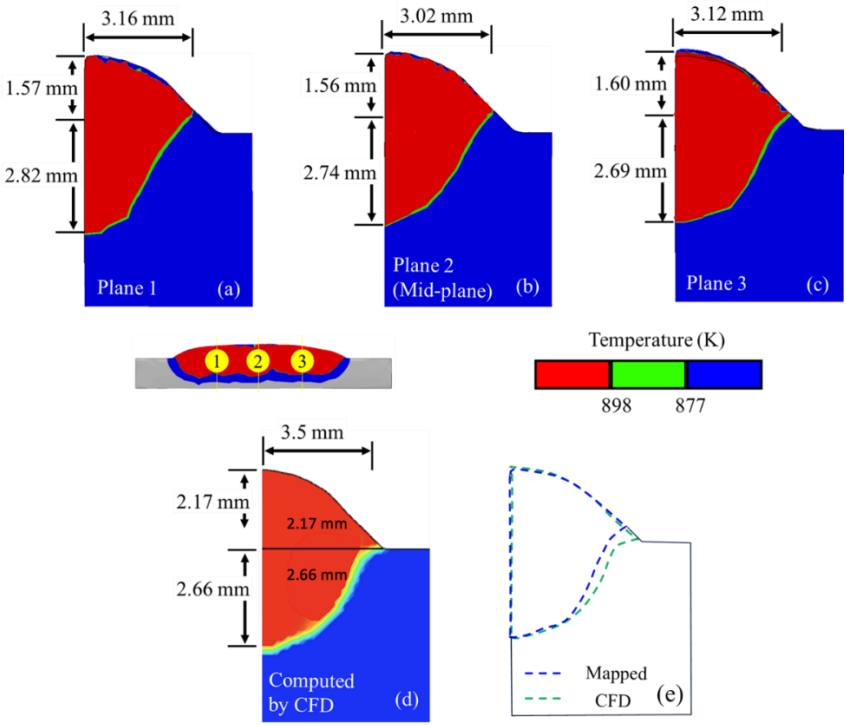



**Fig. 2** Deposit profile in the mechanical model at three planes, (a) plane 1, (b) plane 2 (mid-plane) and (c) plane 3, along the longitudinal direction., (d) Computed deposit shape and melt pool profile using the fluid flow model, and (e) A comparison of the predicted deposit profile using the fluid flow model and that used for the mechanical analysis after mapping.

In contrast to conventional models, where elements are activated using a bounding box or choosing a pre-defined set of elements, synchronized with deposition speed, the present approach employs a subroutine-driven activation method based on the volume fraction technique. Fig. 3 compares the evolving deposition geometry predicted by the fluid flow model with that obtained through the element activation in the mechanical model at different time steps of the simulation. The results demonstrate that the subroutine successfully replicates the advancing deposition profile, with element activation closely matching the fluid flow prediction. Minor discrepancies in the profile topology can be attributed to the relatively coarse mesh and the larger time intervals selected to map the thermal field into the mechanical model. Nevertheless, the isotherms within the deposited region confirm that the temperature distribution is accurately mapped from the fluid flow analysis to the mechanical model.

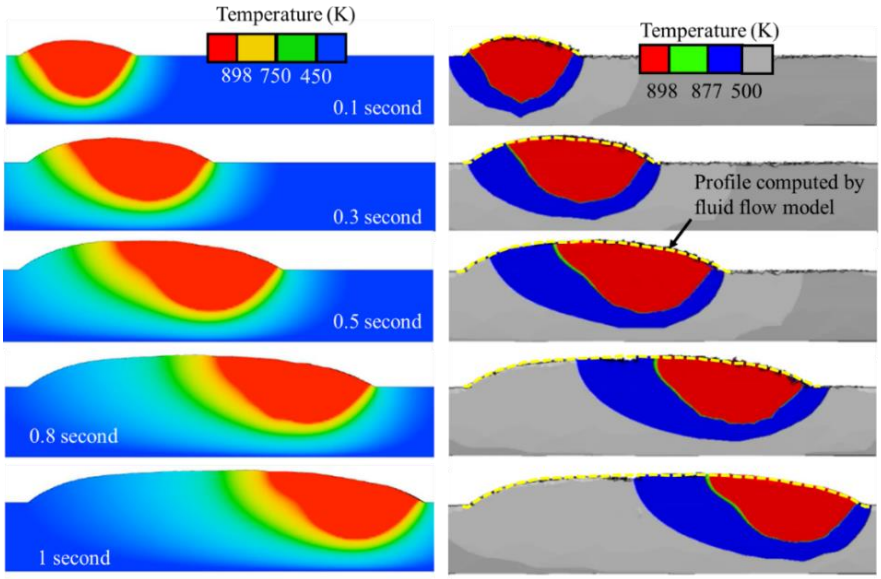



**Fig. 3** The comparison of the deposit profile computed by the fluid flow model and that activated in the mechanical model, using the subroutine, at different time instances in the mechanical analysis. The section presented in the figure is the mid plane in the transverse axis (Y-axis).

Fig. 4 presents the boundary condition (BC) applied and the mechanical results computed by the mechanical model. Taking advantage of the symmetry, the half of the deposited profile computed by the fluid flow model is imported to the mechanical analysis. Fig. 4 (a) presents the symmetrical BC applied along the plane of symmetry [36] and the clamping conditions applied by restricting the displacement of the corresponding nodes along all the directions. After the deposition, the nodes under the clamping BC are released and simple boundary conditions are applied [33]. The longitudinal residual stress along the line 1 is presented in Fig. 4 (b). The model can accurately predict the development of residual stress near the deposition line due to the shrinkage of the molten pool and compensatory stresses away from the deposition centreline [37-38]. The peak magnitude of the tensile and compressive residual stresses, 150 MPa and 75 MPa, are comparable to the stresses reported in the literature [33]. The nature of stress in Fig. 4(b) exhibits a sharp gradient at the centreline (y=0). Theoretically, the slope should be zero due to symmetry. The observed sharpness is attributed to a numerical artifact arising from the tetrahedral mesh at the symmetry boundary.

Fig. 5 (c) illustrates the transverse residual stress predicted by the mechanical model along the line 1, where the magnitude of the transverse stress is significantly lower than the longitudinal residual stress due to the reduced constraint in the transverse direction [39-40]. Near the deposition centreline, the transverse stress exhibits both tensile and compressive values, ranging from 44 MPa tensile to 31 MPa compressive, arising from the contraction and expansion of the metal during solidification, while the regions farther from the centreline approach zero, consistent with observations in the literature [12,40]. Fig. 4 (d) presents the

distortion in the build direction along a line at the bottom of the substrate in the longitudinal direction, where the predicted distortion pattern agrees with previously reported results [12,33]. The relatively low distortion magnitude may be attributed to the short deposition length [12], whereas the asymmetry in the distortion profile could result from the higher thermal gradient near the weld endpoint [41].

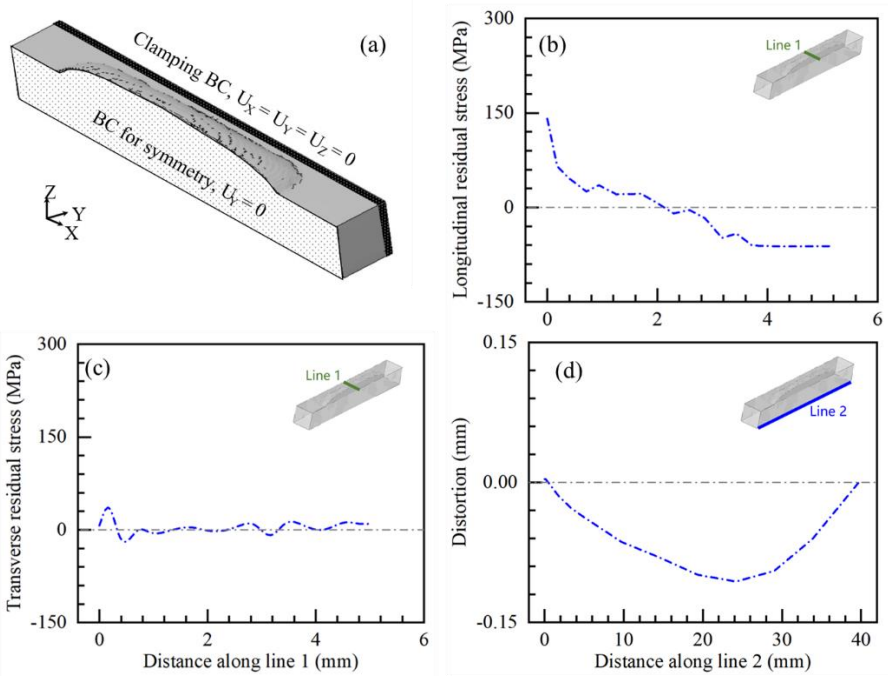



**Fig. 4** (a) Boundary conditions used in mechanical modelling of single track single layer DED-Arc deposition. (b) Longitudinal and (c) transverse residual stress along Line 1 (d) Distortion in the Z direction along the line 2.

## APPLICATION OF INTEGRATED MODEL TO SINGLE-TRACK MULTI-LAYER DEPOSITION

The model is next applied to a single-track, five-layer DED-Arc deposition of SS316L on SS304L and is validated against experimentally measured results reported in the literature [34]. The deposition is carried out at a wire feed rate (WFR) of 3.3 m/min and a printing travel speed (PTS) of 7 mm/s with the first layer being deposited at a slightly higher WFR of 4.2 m/min to ensure proper wetting. A bidirectional deposition strategy with an interlayer dwell time of 35 seconds is employed. Temperature dependent thermophysical properties are employed in the model [42].

The Peclet number for the SS316L melt pool is estimated using the calculation results from the heat transfer and fluid flow model. Given that u = 0.2 m/s and L = 0.006 m, the Peclet number is found to be ~200, indicating that the liquid metal convection plays a critical role in heat transport within the SS316L melt pool. This number is even higher than that for the AA5356 melt pool reported previously which is due to the factor that the stainless steel has much lower thermal diffusivity than the aluminium alloy.

Fig. 5 illustrates the progressive layer-wise melt pool evolution during the single-track five-layer deposition, highlighting the liquidus and solidus isotherms for each layer. In layer 1, as shown in Fig. 5 (a), the melt pool penetrates the substrate, ensuring metallurgical bonding and providing a strong foundation for subsequent layers. The increase in bead width due to higher WFR is also evident in the figure. As additional layers are deposited, the melt pool grows larger and shifts upward, with the overlapping heat-affected zones visible across the adjacent layers. The thermal field demonstrates reheating of underlying material, leading to partial remelting and thermal cycling, as shown in Fig. 5 (b-e). A comparison of computed melt pool profiles with experimentally measured macrograph in Fig. 5 (f) confirms a good agreement in the bead shape and layer buildup. Overall, Fig. 5 shows that the model can fairly predict the melt pool geometry and interlayer fusion for DED-Arc.

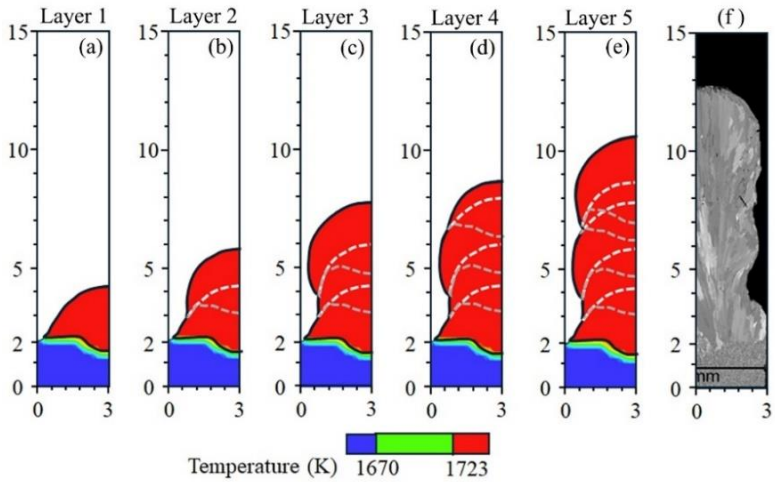



**Fig. 5** Melt pool profile for layers (a-e) one to five in a single-track five-layer deposition and its comparison with (f) experimentally measured macrograph [34]

Fig. 6 presents a comparison of the computed and experimentally measured residual stress [34] for the single-track five-layer DED-Arc deposition. Fig. 6 (a) illustrates the boundary conditions applied in the mechanical model, where symmetry constraints are imposed along the central plane to reduce computational effort. The clamping boundary conditions are applied on the left end of the substrate, and the right end is left free to move as per the experimental conditions [34]. Fig. 6 (b) shows the longitudinal residual stress distribution along the line in the Z-axis at the mid-plane of the deposition length, highlighting differences

between computed and measured values. The computed stress follows a similar trend but slightly overpredicts the tensile stress magnitudes near the top region. Both curves capture the transition from the tensile to the compressive stress across the height. The agreement indicates that the model successfully represents the dominant thermomechanical behaviour despite localized discrepancies.

Fig. 6 (c) presents the normal residual stress along the Z-axis, where both computed and measured results oscillate around zero. The model captures the general fluctuations, though the amplitude shows little local deviations. Fig. 6 (d) shows a comparison between the computed and experimentally measured transverse residual stress distribution across the height. The overall stress magnitudes remain within ±200 MPa, and the computed results reasonably track the experimental fluctuations. Both datasets indicate alternating compressive and tensile zones, reflecting complex thermal contraction effects during solidification. The agreement in stress oscillations validates the robustness of the numerical approach. These results demonstrate that the model can effectively capture three-dimensional stress variations in multi-layer DED-Arc built components.

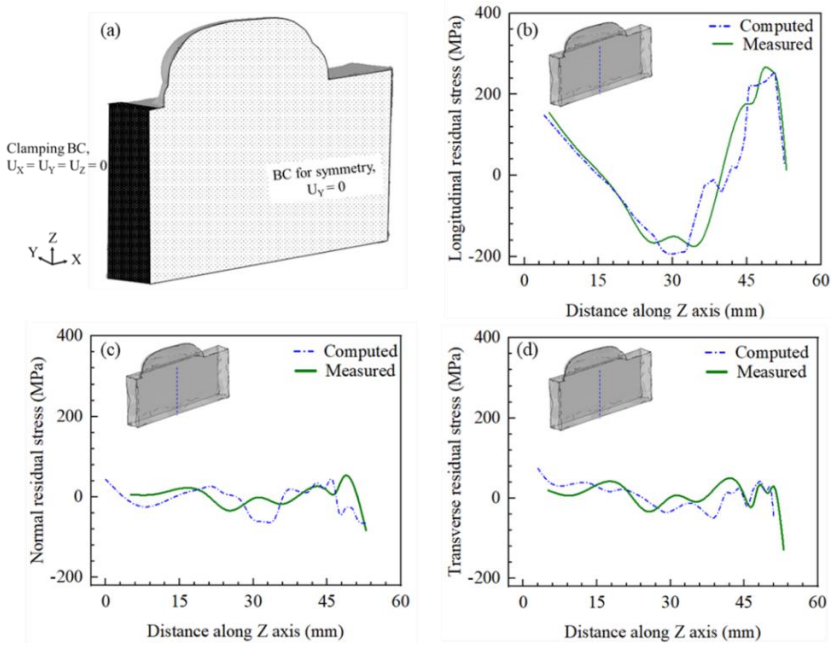



**Fig. 6** (a) Boundary conditions used in mechanical modelling of single-track five-layer deposition. Comparison of computed (b) longitudinal (c) normal and (d) transverse residual stress with that measured by neutron diffraction [34] along the build direction.

## COMPUTATIONAL SUBTILITIES

To compare with the conventional models, newer high-fidelity approaches require a systematic index to evaluate the trade-off between the quality of computed results and the computational subtilities. Models can therefore be differentiated based on their computational requirements and predictive outputs. Important factors influencing this differentiation include accuracy, computational speed, the level of approximations, domain size, the extent of user intervention, and data storage overhead [43-44]. These requirements determine whether a modelling approach is better suited for feasibility studies, process optimization, or detailed validation tasks. Table 1 shows the computational subtilities of a conventional sequentially coupled thermomechanical approach for modelling residual stress and distortion for two single-track multi-layer cases reported in the literature [45]. A single-track twenty-layer deposition of aluminium alloy (case 1) and a single-track four-layer part scale deposition of steel alloy (case 2) is compared with the current approach.

The comparison clearly demonstrates that while conventional thermomechanical approaches provide relatively lower computational costs, they sacrifice accuracy and remain heavily dependent on user intervention. Case 1, with 78.30% accuracy and the longest runtime of 47.72 hours, highlights the inefficiency of simplified assumptions when applied to realistic deposition scenarios. Even though Case 2 improves accuracy to 86.28% and reduces the total runtime to 16.33 hours, it still relies on assumptions about deposition profiles and heat sources. Such reliance not only limits predictive fidelity but also introduces subjective dependencies during model preparation, which can affect repeatability of the computed results. Both cases involve significant manual effort in defining the deposition strategies and heat sources, which undermines their robustness in industrial practice. Additionally, the simplified treatment of process physics restricts their applicability when higher fidelity is essential. Although they demand a modest computational storage, the trade-off comes at the expense of the prediction reliability.

In contrast, the heat transfer and fluid flow integrated thermomechanical model emerges as a relatively more preferable option despite its higher computational demands. With an accuracy of around 90% for the cases considered in the present work, it provides a more reliable representation of the underlying process physics, reducing reliance on assumptions and manual intervention. The mismatch between the computed and measured values falls well within the inherent uncertainty of a reliable model. Such deviations are expected due to the natural dispersion of temperature-dependent thermophysical properties (around 10% as reported in Touloukian's data) [46] along with minor variations in the alloy composition and routine experimental errors. Additional discrepancies also originate from model assumptions and simplified boundary conditions. On the other hand, the experimentally measured residual stress values are also likely to have inherent measurement uncertainty. Considering these unavoidable sources of uncertainty, the agreement achieved by the model can be regarded as fairly satisfactory.

Conversely, the higher predictive accuracy demands higher computation time and storage overhead. The thermal analysis is computationally intensive, but the total simulation time of 34.40 hours is still reasonable given the substantial gain in predictive capability. Furthermore, the model eliminates approximations, ensuring that process-induced stresses and distortions

are captured with greater confidence. While its storage overhead of 184.9 GB is higher, the modern computational resources and software can accommodate such requirements, especially when balanced against the benefits of accuracy and reduced trial-and-error in experiments. The streamlined assumptions, focusing only on material properties and boundary conditions, make the approach more generalizable across different deposition scenarios. Therefore, despite the higher resource consumption, the integrated model offers superior robustness and predictive reliability, making it the most suitable choice for advancing industrial-scale additive manufacturing simulations.

**Table 1** Comparison of the fluid flow integrated mechanical model presented in this paper with conventional thermomechanical models of multi-layer DED-Arc deposits [45].

| **Computational subtility** | **Conventional thermomechanical modelling – Case 1.** | **Conventional thermomechanical modelling – Case 2.** | **Heat transfer and fluid flow integrated thermomechanical model** |
|---|---|---|---|
| Accuracy of prediction | 78.30% | 86.28% | 92.56% |
| Time for thermal analysis | 0.61 hours | 3.55 hours | 30.24 hours |
| Time for mechanical analysis | 46.62 hours | 12.78 hours | 4.16 hours |
| Total time | 47.72 hours | 16.33 hours | 34.40 hours |
| Assumptions | Deposition profile, heat source, material properties, boundary conditions | Deposition profile, heat source, material properties, boundary conditions | Material properties, boundary conditions |
| User intervention | Creating the deposition profile, Designing the heat source, Pre-processing of the solution domain | Creating the deposition profile, Designing the heat source, Pre-processing of the solution domain | Pre-processing of the solution domain, Mapping the deposition profile, Mapping the temperature field. |
| Domain size | 150 × 75 × 28 mm3 | 500 × 60 × 12 mm3 | 5.0 × 0.5 × 2. mm3 |
| Data storage overhead | 15.46 GB | 8.95 GB | 184.9 GB |

## CONCLUSIONS

A heat transfer and fluid flow model integrated thermomechanical analysis is reported here to compute deposition profile, melt pool dimensions, residual stress, and distortions in DED-Arc. The computed results are validated against experimentally measured results, demonstrating its robustness and applicability. The key findings of this work are summarized below:

- The integrated heat transfer and fluid flow–based approach achieves substantially higher accuracy (around 90%) compared to conventional conduction-based models (around 85%), enabling more reliable predictions of stress and distortion.
- By eliminating predefined deposition profiles and heat sources, the framework minimizes pre-processing subjectivity and improves repeatability. Furthermore, the use of UEPACTIVATIONVOL for element activation more faithfully captures the evolving deposition geometry than traditional block-type activation schemes.
- Although some manual input is still required for mapping and preprocessing, these steps can be streamlined in the future, reducing user intervention and improving efficiency.
- The model requires longer simulation time (34.4 h) and higher storage capacity (~185 GB) relative to conventional approaches. However, this is offset by the significant gain in predictive fidelity and the reduced need for experimental trial-and-error, making it increasingly viable with advances in computational power.

Comparing the effectiveness of integrated models requires comparison of not only accuracy but also computational speed, the level of approximations, domain size, the extent of user intervention, and data storage overhead. A unified index will be developed in the future to compare the different modelling approaches.

## References


[1] P. K. CHAURASIA, B. K. BARIK, A. DAS, S. F. GOECKE, A. DE: 'Probing dimensional consistency during multi-track multi-layer gas metal arc directed energy deposition of aluminium alloys', *Weld World* 2024, 68:925-38.

[2] T. MUKHERJEE, J. S. ZUBACK, A. DE, T. DEBROY: 'Printability of alloys for additive manufacturing', *Sci Rep* 2016, 6:19717.

[3] S. W. WILLIAMS, F. MARTINA, A. C. ADDISON, J. DING, G. PARDAL, P. COLEGROVE: 'Wire + Arc Additive Manufacturing', *Mater Sci Technol* 2016, 32:641-7.

[4] H. STINSON, R. WARD, J. QUINN, C. MCGARRIGLE: 'Comparison of Properties and Bead Geometry in MIG and CMT Single Layer Samples for WAAM Applications', *Metals (Basel)* 2021, 11.

[5] Q. WU, T. MUKHERJEE, A. DE, T. DEBROY: 'Residual stresses in wire-arc additive manufacturing – Hierarchy of influential variables', *Addit. Manuf.* 2020, 35.

[6] Q. WU, T. MUKHERJEE, C. LIU, J. LU, T. DEBROY: 'Residual stresses and distortion in the patterned printing of titanium and nickel alloys', *Addit. Manuf.* 2019, 29.

[7] K. KHAN, L. S. MOHAN, A. DE, T. DEBROY: 'Rapid calculation of part scale residual stresses in powder bed additive manufacturing', *Sci. Technol. Weld. Join.*, vol. 28, 2023, p. 145-53.

[8] W. OU, G. L. KNAPP, T. MUKHERJEE, Y. WEI, T. DEBROY: 'An improved heat transfer and fluid flow model of wire-arc additive manufacturing', *Int. J. Heat Mass Transf.* 2021, 167:120835.

[9] M. KÖHLER, L. SUN, J. HENSEL, S. PALLASPURO, J. KÖMI, K. DILGER, Z. ZHANG: 'Comparative study of deposition patterns for DED-Arc additive manufacturing of Al-4046', *Mater. Des.*, 2021, 210:110122.

[10] H. ZHAO, C. GAO, Z. WANG, Q. WANG, C. LIU, Y. ZHAN: 'Residual stress analysis of TC4/Inconel718 functionally graded material produced by laser additive manufacturing based on progressive activation element method', *Int. J. Adv. Manuf. Technol.*, 2023, 129:1443-53.

[11] W. HUANG, Q. WANG, N. MA, H. KITANO: 'Distribution characteristics of residual stresses in typical wall and pipe components built by wire arc additive manufacturing', *J. Manuf. Process.*, 2022, 82:434-47.
[12] J. DING, P. COLEGROVE, J. MEHNEN, S. GANGULY, P. M. S. ALMEIDA, F. WANG, S. WILLIAMS: 'Thermo-mechanical analysis of Wire and Arc Additive Layer Manufacturing process on large multi-layer parts', *Comput. Mater. Sci.*, 2011, 50:3315-22.
[13] A. CHERGUI, N. BERAUD, F. VIGNAT, F. VILLENEUVE: 'Finite Element Modeling and Validation of Metal Deposition in Wire Arc Additive Manufacturing', In: L. Roucoules, M. Paredes, B. Eynard, P. Morer Camo, C. Rizzi, editors, Cham: *Springer International Publishing*, 2021, p. 61-6.
[14] K. P. PRAJADHIAMA, Y. H. MANURUNG, Z. MINGGU, F. H. PENGADAU, M. GRAF, A. HAELSIG, T. E. ADAMS, H. L. CHOO: 'Development of Bead Modelling for Distortion Analysis Induced by Wire Arc Additive Manufacturing using FEM and Experiment', *MATEC Web Conf* 2019, 269:05003.
[15] W. TANG, A. LIU, C. SONG, L. ZHOU: 'Numerical and experimental study of temperature, residual stresses, and microstructural evolution on multi-layer and multi-pass laser cladding of 6061Al alloy', *Mater. Res. Express*, 2024, 11:96512.
[16] K. OYAMA, S. DIPLAS, M. M'HAMDI, A. E. GUNNÆS, A. S. AZAR: 'Heat source management in wire-arc additive manufacturing process for Al-Mg and Al-Si alloys', *Addit. Manuf.*, 2019, 26:180-92.
[17] J. SUN, K. DILGER: 'Influence of preheating on residual stresses in ultra-high strength steel welded components', *J. Mater. Res. Technol.*, 2023, 25:3120-36.
[18] C. HEINZE, C. SCHWENK, M. RETHMEIER: 'Numerical calculation of residual stress development of multi-pass gas metal arc welding', *J. Constr. Steel Res.*, 2012, 72:12-9.
[19] G. AGARWAL, H. GAO, M. AMIRTHALINGAM, M. HERMANS: 'Study of solidification cracking susceptibility during laser welding in an advanced high strength automotive steel', *Metals (Basel)*, 2018, 8:673.
[20] X. F. ZHAO, A. WIMMER, M. F. ZAEH: 'Experimental and simulative investigation of welding sequences on thermally induced distortions in wire arc additive manufacturing', *Rapid Prototyp J.*, 2023, 29:53-63.
[21] D. ZHANG, D. DU, S. XUE, J. QI, Z. PU, Y. LU, Y. TANG, B. CHANG: 'Residual stress and deformation in wire-feed electron beam additive manufactured aluminum components', *Int. J. Adv. Manuf. Technol.*, 2024, 131:1665-76.
[22] T. MUKHERJEE, W. ZHANG, T. DEBROY: 'An improved prediction of residual stresses and distortion in additive manufacturing', *Comput. Mater. Sci.*, 2017, 126:360-72.
[23] F. CHEN, W. YAN: 'High-fidelity modelling of thermal stress for additive manufacturing by linking thermal-fluid and mechanical models', *Mater. Des.* 2020, 196:109185.
[24] N. S. BAILEY, C. KATINAS, Y. C. SHIN: 'Laser direct deposition of AISI H13 tool steel powder with numerical modeling of solid phase transformation, hardness, and residual stresses', *J. Mater. Process Technol.*, 2017, 247:223-33.
[25] M. Z. GAO, B. MONDAL, T. A. PALMER, W. ZHANG, T. DEBROY: 'Integrated modeling of cracking during deep penetration laser welding of nickel alloys', *Sci. Technol. Weld. Join.*, 2023, 28:689-700.
[26] V. MANVATKAR, A. DE, T. DEBROY: 'Heat transfer and material flow during laser assisted multi-layer additive manufacturing', *J. Appl. Phys.*, 2014, 116:124905.
[27] M. L. UN, T. W. EAGAR: *Influence of arc pressure on weld pool geometry*, 1985.
[28] G. EW: 'Heat Transfer and Penetration Mechanisms with GMA and Plasma-GMA Welding', *Weld. J.*, 1981, 60:37-42.
[29] Y. LI, Z. YUN, W. ZHANG, X. LONG, J. ZHU: '3D Modelling of Layer-by-Layer Heat and Mass Transfer in Wire Arc Additive Manufacturing', *Addit. Manuf. Front.*, 2024, 3:200159.

[30] M. SZILVÁSI-NAGY, G. MÁTYÁSI: 'Analysis of STL files', *Math. Comput. Model.*, 2003, 38:945-60.
[31] L. ZHOU, J. LI, G. LIN: 'Implementation of arbitrary polyhedral elements for automatic dynamic analyses of three-dimensional structures', *Sci. Rep.*, 2022, 12:4156.
[32] A. RAMOS, J. A. SIMÕES: 'Tetrahedral versus hexahedral finite elements in numerical modelling of the proximal femur', *Med. Eng. Phys.*, 2006, 28:916-24.
[33] J. SUN, J. HENSEL, M. KÖHLER, K. DILGER: 'Residual stress in wire and arc additively manufactured aluminum components', *J. Manuf. Process.*, 2021, 65:97-111.
[34] S. ROUQUETTE, C. CAMBON, I. BENDAOUD, S. CABEZA, F. SOULIÉ: 'Effect of Layer Addition on Residual Stresses of Wire Arc Additive Manufactured Stainless Steel Specimens', *J. Manuf. Sci. Eng.*, 2024, 146.
[35] SIMUFACT ENGINEERING COMPANY: *Theory and user information*, Germany, 2016.
[36] R. F. V. SAMPAIO, J. P. M. PRAGANA, I. M. F. BRAGANÇA, C. M. A. SILVA, C. V. NIELSEN, P. A. F. MARTINS: 'Modelling of wire-arc additive manufacturing – A review', *Adv. Ind. Manuf. Eng.*, 2023, 6:100121.
[37] H. ZHAO, G. ZHANG, Z. YIN, L. WU: 'Three-dimensional finite element analysis of thermal stress in single-pass multi-layer weld-based rapid prototyping', *J. Mater. Process. Technol.*, 2012, 212:276-85.
[38] Y. LI, W. GAN, W. ZHOU, D. LI: 'Review on residual stress and its effects on manufacturing of aluminium alloy structural panels with typical multi-processes', *Chinese J. Aeronaut.*, 2023, 36:96-124.
[39] J. SUN, T. NITSCHKE-PAGEL, K. DILGER: 'Generation and distribution mechanism of welding-induced residual stresses', *J. Mater. Res. Technol.*, 2023, 27:3936-54.
[40] J. CHEON, S. J. NA: 'Prediction of welding residual stress with real-time phase transformation by CFD thermal analysis', *Int. J. Mech. Sci.*, 2017, 131-132:37-51.
[41] S. BEHSERESHT, Y. H. PARK: 'Warpage Prediction in Wire Arc Additive Manufacturing: A Comparative Study of Isotropic and Johnson–Cook Plasticity Models', *Metals (Basel)*, 2025, 15.
[42] C. S. KIM: *Thermophysical properties of stainless steels*, United States: 1975.
[43] Z. CHEN, L. YUAN, Z. PAN, H. ZHU, N. MA, D. DING, H. LI: 'A comprehensive review and future perspectives of simulation approaches in wire arc additive manufacturing (WAAM)', *Int. J. Extrem. Manuf.*, 2025, 7:22016.
[44] Y. H. KIM, D. R. GUNASEGARAM, P. W. CLEARY, A. B. MURPHY: 'Numerical modelling of wire arc additive manufacturing: methods, status, trends, and opportunities', *J. Phys. D. Appl. Phys.*, 2025, 58:143001.
[45] P. K. DILJITH, P. K. CHAURASIA, B. K. BARIK, A. DE: 'Numerical modelling of gas metal arc directed energy deposition induced residual stress and distortion', *Weld. Int.*, n.d.:1-11.
[46] Y. S. TOULOUKIAN, R. W. POWELL, C. Y. HO, M. C. NICOLAOU: 'Thermophysical Properties of Matter – The TPRC Data Series, Vol. 10: Thermal Diffusivity', *IFI/Plenum*, 1973.

# PREDICTION OF RESIDUAL STRESSES OF REPAIRED AUSTENITIC STAINLESS STEEL WELDED JOINTS

S. HILAL*, S. HENDILI*, J. DELMAS*, P. PEREIRA ALVAREZ*, V. ROBIN**, E. DERNIAUX***, T. BOUTIN*

**Electricité de France R&D, 78400, Chatou, France, sami.hilal@edf.fr*
***Electricité de France Direction Technique, 69007, Lyon, France*
****Electricité de France Direction Technique, 37420, Avoine, France*

*10.3217/978-3-99161-089-2-025, license CC BY 4.0*
*https://creativecommons.org/licenses/by/4.0/deed.en*
*This CC license does not apply to third party material and content noted otherwise.*

## ABSTRACT

The ability to predict residual stresses in welds is important in assessing the integrity of a component subject to degradation mechanisms such as Stress Corrosion Cracking (SCC). In the as-welded condition, multi-pass pipe circumferential butt welds made of austenitic stainless-steel exhibit a typical residual stress profile through the wall of the welded joint. In the case of a non-repaired weld, the shell bending profile places the inner half of the weld joint wall and its vicinity in compression in the axial direction. In contrast, the distribution of residual stresses may be different in the event of a repair, particularly in the case of localised repairs. The impact of repairs on SCC crack propagation was suspected following an inspection of a weld with deep SCC cracks. The particularity of this weld is that it was subjected to two successive repair stages: a complete circumferential repair followed by a localised repair. The specific character of the weld required 3D modelling, since it provides a description of each circumferential zone of the weld and enables verification of the way in which this weld has a particular behaviour (residual stresses, hardness, etc.). This would make it possible to identify potential aggravating factors regarding SCC for this type of weld configuration. This work presents the simulation of this weld, which was carried out in three stages: the initial weld, the first repair, and the localised repair. The expertise carried out following the cutting of the weld made it possible to characterise the strain hardening in the repaired areas and is compared with the simulation results by considering the measurements obtained on a sample taken in the middle of the repair. This comparison is made on hardness profiles in the axial direction of the assembly, at different heights in the thickness. A good correlation is observed between measured and simulated hardness.

Keywords: welding, stress corrosion cracking, pressure water reactor, computational weld mechanics, finite elements, austenitic stainless-steel.

## INTRODUCTION

At the end of 2021, EDF (Electricité de France) began detecting indications on the Safety Injection System (SIS) piping in the French nuclear fleet. Expert assessments revealed the presence of cracks associated with primary water Stress Corrosion Cracking (SCC) phenomenon, located at welds on stainless steel components [1] [2]. Many numerical welding simulations were carried out by EDF to better understand the origin of the phenomenon and the role of welding. Furthermore, these welding simulations were exploited as input data for SCC simulations to assess crack initiation conditions and propagation rates under this damage mechanism [1]. The numerical welding simulation approach is based on finite element modelling of the thermomechanical behaviour of a structure during welding. The methodology follows the French Nuclear Institute (CEA/EDF/FRAMATOME) Good Practice Guide for Numerical Welding Simulation, which is based on the ISO/TS 18166 standard: Numerical Welding Simulation [3]. A 2D axisymmetric modelling assumption is adopted for multi-pass butt welds [1]. The quantities computed in these simulations include welding residual stresses (WRS), local deformations, hardness (via post-processing of calculated strain hardening [4]), the as-welded residual state, and the redistribution of these stresses under service loading. The results are presented as maps showing the influence of the manufacturing process on the local residual state, and through parametric studies to understand the influence of selected parameters (e.g., process parameters, geometry) on stress and deformation trends [1]. In agreement with the literature [5] and operational feedback, simulations of unrepaired welds performed to date show that, in the as-welded state, multi-pass circumferential butt welds on austenitic stainless-steel piping exhibit a typical “S-shaped” residual stress profile across the weld thickness (Fig. 1).

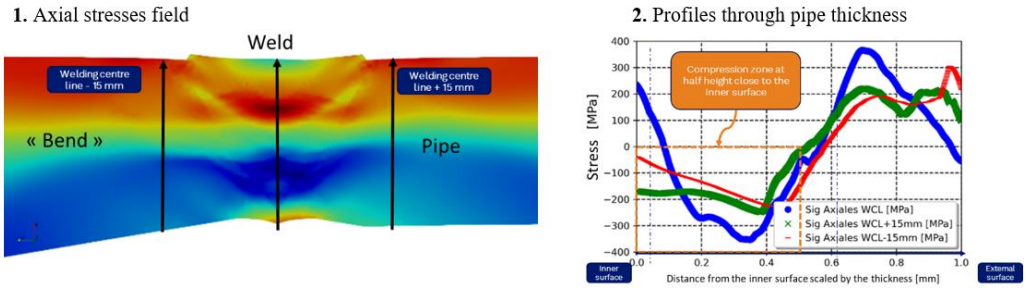



**Fig. 1** Typical axial stress state from simulation performed on a 12’’ schedule 140 (28.58 mm thick) pipe assembly [1]: 1. 2D axial stress field, 2. Profiles through thickness

The welds studied using numerical welding mechanics show a compressive axial stress state over half the thickness from the inner surface, which tends to slow down or even stop potential crack propagation. Near the weld root, the stress state may evolve toward tension at the end of the operation. Differences in stiffness across the weld (e.g., a weld on a pipe elbow), as well as the welding completion sequence, can influence the distribution of tensile stresses

in the root area. Residual stresses result from the development of permanent deformations in the weld zone subjected to successive thermal cycles during welding, as illustrated by numerical modelling [6]. Strain hardening accumulates, altering the local mechanical behaviour and creating a TMAZ in the austenitic stainless steel. This numerical welding simulation approach has been applied to many studies supporting the primary water SCC issue on austenitic stainless-steel SIS. It has also been used to conduct parametric studies to identify the most influential parameters and to ensure the systematic presence of the compressive zone [1].

In 2023, the most severe case of intergranular SCC was reported at the French nuclear power plant located in Penly, specifically within the hot leg of the Safety Injection System. A stress corrosion crack measuring 23 mm in depth was detected in the heat-affected zone (HAZ) of a weld that had undergone a full-depth repair extending over 50° of the pipe's circumference during fabrication. Notably, the crack propagation was confined to the repaired section and did not initiate in the non-repaired areas of the weld. A cross-section analysis centred on the double-repair zone revealed a 23 mm deep crack within the HAZ, along the base metal/filler metal interface. The weld's manufacturing history involved two successive repair operations: an initial *cut-and-weld*, followed by a localised repair on a limited segment of the pipe circumference. Expert assessments enabled the evaluation of hardening levels through hardness mapping performed on multiple samples. The results did not indicate any significant hardening around the repair zone that could explain either the localised initiation of SCC or the extensive crack propagation observed in this weld. Nevertheless, this recent operational experience underscores the potentially adverse impact of weld repairs on SCC susceptibility. Furthermore, according to EDF's SCC propagation model for stainless steels exposed to primary water, crack growth rates are influenced by the combined effects of residual stresses and plastic strain. Therefore, the distribution and magnitude of residual stresses are key factors contributing to SCC propagation.

The objective of the present study is to evaluate the residual condition of the welded assembly, thereby complementing the findings of the expert assessments and identifying aggravating factors associated with SCC in this specific welding configuration. To achieve this, and considering the weld's unique characteristics, an advanced approach mixing two-dimensional axisymmetric and three-dimensional numerical welding simulations is performed to predict the residual stress field and plastic strain distribution throughout the entire welded structure.

## DESCRIPTION OF THE INVESTIGATED WELD JOINT

The assembly studied is a 316L stainless steel "elbow-to-elbow" configuration with a diameter of 10 inches and a thickness of 25.4 mm. The specificity of this assembly is that the weld was subjected to two successive repair operations. Fig. 2 schematically illustrates the various step-by-step stages of assembly.

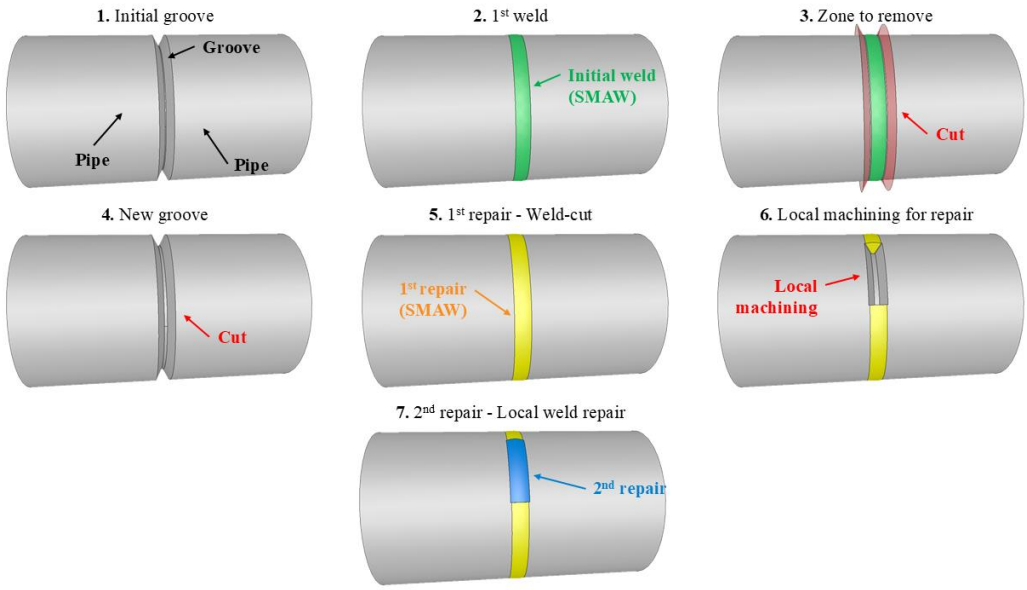



**Fig. 2** Schematic illustration of the different stages of the repaired assembly

The first stage of the process involves the initial weld, referred to as the *workshop weld* (Fig. 2.1 and Fig. 2.2). This weld was performed using the Shielded Metal Arc Welding (SMAW) process, with a "W-joint" groove configuration featuring angles of 45° and 30° on each side. For this manufacturing step, a Welding Procedure Specification (WPS) was available, along with a macrograph of a different weld produced using the same process.

Following the completion of the initial weld, a full circumferential repair known as a *cut-and-weld* was carried out. This operation was performed in two stages. First, the existing weld was removed, to eliminate part of the fusion zone (Fig. 2.3 and Fig. 2.4). Once the excavation was completed, the repair weld was carried out on the full circumference using the SMAW process (Fig. 2.5).

Subsequently, a localised excavation was performed on the internal surface over an angular span of 50°, extending through the full thickness of the joint (Fig. 2.6 and Fig. 2.7), to perform another repair, a localised one. This second repair was also executed using the SMAW process.

It is important to note that the weld was evaluated through macrographic analysis at various circumferential sections. As a result, macrographs are available both within the second repair zone and outside of it. The macrograph corresponding to the area unaffected by the second repair is considered representative of the cut-and-weld configuration (Fig. 3.1).

Based on the interpretation of the WPS and the macrographs analysis, the geometries of the repairs and weld beads were defined. For the *cut-and-weld* configuration, the groove angle identified was approximately 25° (V-joint groove). For the second repair, the macrographic analysis (Fig. 3.2) revealed also a groove angle of 25° (V-joint groove), with a width of 7.5 mm on the inner surface and an external width of 30 mm.

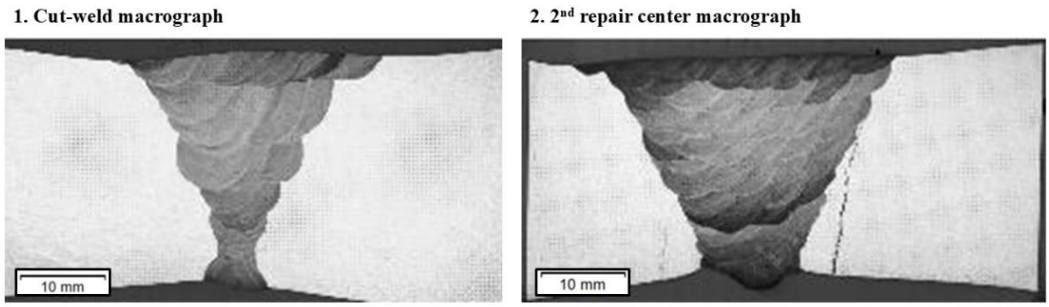



**Fig. 3** Macrograph acquired after characterization of the weld: in the area of the *cut-and-weld* and in the area with local repair

Finally, hardness mappings ($HV_{0.5}$) were performed at various circumferential weld cross-sections, particularly at the centre of the localized repair and on the opposite side (Fig. 4). These measurements will be compared with simulation results to validate the modelling approach.

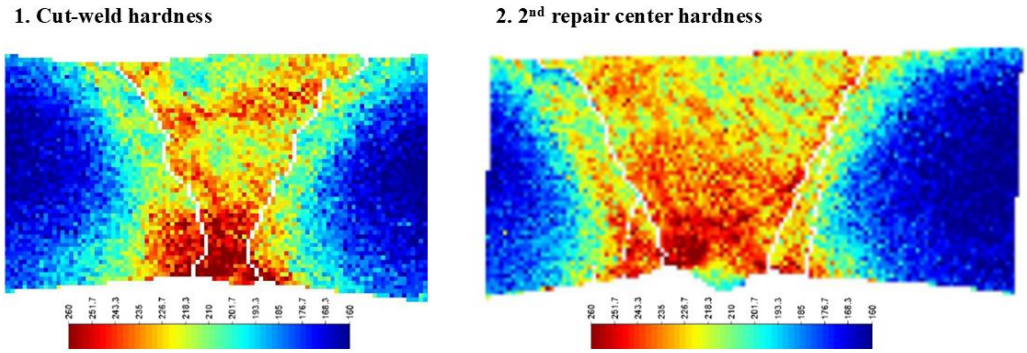



**Fig. 4** Hardness mappings: (1) after the first repair cut-and-weld, (2) after the second local repair

## GENERAL METHODOLOGY AND SIMULATION WORKFLOW

The models considered in this study have been developed using Pipeweld [7], a simulation framework dedicated to computational welding simulation based on code-aster [8], an open-source generalist finite element software of simulation in mechanics and in structural analysis developed by EDF for more than 30 years, integrated within the salome-meca platform [9].

Without externally applied loads, the mechanical impact of welding is primarily driven by thermal gradients within the thermo-mechanically affected zone (TMAZ). Defining the thermal loading is crucial for identifying the stress fields that lead to WRS. These stresses arise from local elastic and inelastic responses, compounded by global internal forces due to

self-bridging effects from colder, more rigid regions. In multi-pass welding, repeated cycles of thermal expansion and contraction are constrained by these stiffer zones, contributing to the development of WRS. As illustrated in Fig. 5, a weak coupling approach, based on the sequential execution of thermal, metallurgical, and mechanical analyses at each welding pass, is sufficient to predict the WRS for the assemblies under consideration.

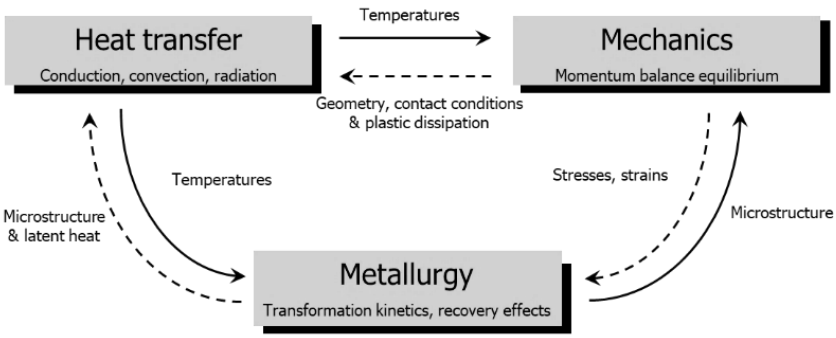



**Fig. 5** Coupling and interaction for WRS assessment: heat transfers, metallurgical phenomena and mechanical consequences

First, the thermal analysis is performed, and its results are subsequently used as input data for the mechanical analysis. The thermal problem is governed by the classical heat conduction equation, where the heat input is modelled as a volumetric density heat flux, with a triangular distribution and uniform along the transverse direction of the weld path. The heat source distribution is mathematically described by the following expressions (with Ω the volume):

$$E = \eta UI = \int_{\Omega} Q(x,y,z).d\Omega = Q_{max} \times S_b \times (\Delta t_1 + \Delta t_2) \times 0.5 \quad (1)$$

$$Q_{max} = \frac{2 \times \eta \times Q}{V_s \times S_b \times (\Delta t_1 + \Delta t_2)} \quad (2)$$

where $E$, $Q$, $\eta$, $V_s$, $S_b$, and $\Delta t_1$ and $\Delta t_2$ represent the net welding energy, the power, the efficiency, the welding speed, the bead cross-section surface and the heat source morphological parameters. Thermal boundary conditions, that include both convective and radiative heat exchanges with the surrounding ambient air.

The evolution of WRS depends on the constitutive laws linking stress and strain, which typically include elastic, thermal, and inelastic parts. Of particular importance is the modelling of plasticity, responsible for permanent deformation and the development of WRS. The mechanical response, driven by the thermal field, is assumed to follow an elasto-plastic behaviour with isotropic hardening. The elastic properties are characterized by Young's modulus, Poisson's ratio, and the coefficient of thermal expansion. Plastic deformation is described using the Von Mises yield criterion combined with a non-linear isotropic hardening law. The hardening behaviour, which depends on both plastic strain and temperature, is derived from stress-strain curves obtained through experimental measurements. The constitutive model employed here incorporates work hardening recovery mechanisms, defined

to describe the behaviour of alloys that do not undergo solid-state phase transformations during welding, such as austenitic stainless steels. The equations for the constitutive behaviour of the material are detailed in the following paragraph.
First, the Von Mises equivalent stress is expressed as follows:

$$f(\sigma_{ij}) = \sigma_{eq} = J_2(s_{ij}). \tag{3}$$

The yield strength of the strain-hardened material is written:

$$\sigma_y(p,\theta) = \sigma_0(\theta) + R(p,\theta), \qquad p = \int_0^t {\dot{\varepsilon}_{eq}}^p . dt \ , \qquad {\dot{\varepsilon}_{eq}}^p = \dot{p} = \sqrt{\frac{2}{3}\dot{\varepsilon}_{ij}^p . \dot{\varepsilon}_{ij}^p} \tag{4}$$

with $p$ the cumulative plastic strain, $R$ the hardening function, $\sigma_0$ the initial yield strength and $\theta$ the temperature.

The recovery of work hardening is modelled by the following equation [10]:

$$\dot{r}(t) = \dot{p}(t) - k(\theta(t))\langle r(t) - r_\infty(\theta(t))\rangle \tag{5}$$

with $r$ the cumulated plastic strain with consideration of the strain hardening recovery, $k$ the coefficient which characterizes the dynamics of recovery according to the temperature and which depends on the considered material, $r_\infty$ the coefficient which characterizes the threshold quantity of plastic deformation which cannot be recovered, and which depends on the temperature and the considered material, and $\langle x \rangle$ which denotes the positive part of $x$.

In the context of SCC, in addition to residual stresses, strain hardening also plays a significant role (initiation and propagation mechanisms) [2]. The strain hardening, often represented by the equivalent plastic strain, is typically computed implicitly during numerical welding simulations and has been shown to correlate directly with hardness measurements. The same relationship that the one established in [4] between strain hardening and hardness is used:

$$HV = HV_{min} + A(1 - e^{-Bp}) \tag{6}$$

The coefficients $HV_{min}$, $A$, $B$ are correlated with microhardness measurements performed on the base metal of welds cut and deposited in the French nuclear fleet.

**Table 1** Correlated coefficient for the relationship between strain hardening and hardness

| $HV_{min}$ | $A$ | $B$ |
|---|---|---|
| 160 | 176,93 | 0,046 |

The proposed approach consists of using 2D for the *initial weld* step and the *cut-and-weld* step because the axisymmetric assumption is considered sufficient for fully circumferential welding operations. Nevertheless, it is essential to consider a fully three-dimensional approach for the third step. A detailed description of each modelling step is provided below. It is important to note that for 2D axisymmetric simulations, the mesh is composed of quadrilateral elements, whereas hexahedral elements are used for the 3D simulations. Thermal simulations, both in 2D and 3D, are performed using linear elements. In contrast, mechanical simulations in 2D and 3D are conducted with quadratic elements and use a reduced integration formulation.

### STEP 1: 2D INITIAL WELD SIMULATION

The first weld is modelled using a 2D axisymmetric finite element approach. The mesh is constructed based on the groove geometry and the number of welding beads, as defined in the welding procedure specification. Process parameters such as heat input and welding speed are also derived from this specification. Due to the 2D axisymmetric assumption, mechanical boundary conditions representing self-restraint are applied to simulate the stiffness of the "cold" regions of the pipe during the heating phase.

### STEP 2: 2D MODELLING OF THE CUT-AND-WELD REPAIR

Fig. 6 illustrates the modelling methodology for the repair weld, commonly referred to as the cut-and-weld process. Given its fully circumferential nature, this stage is also modelled using a 2D axisymmetric approach. The process consists of two main steps. The first involves material removal, for which the deformed mesh from the initial weld simulation is used as the base geometry. The groove geometry after excavation, as well as the subsequent filling, is defined based on macrographic analysis conducted during failure investigations. A mechanical rebalancing is performed to determine the initial stress state of the pipe prior to the deposition of the new weld. The second step involves filling the groove. The number and sequence of welding passes are inferred from macrographic observations. Process parameters are selected using an internal synergy approach, which reconciles macrographic data with the welding procedure qualification record. As in the initial weld simulation, self-restraint boundary conditions are applied due to the axisymmetric modelling assumption.

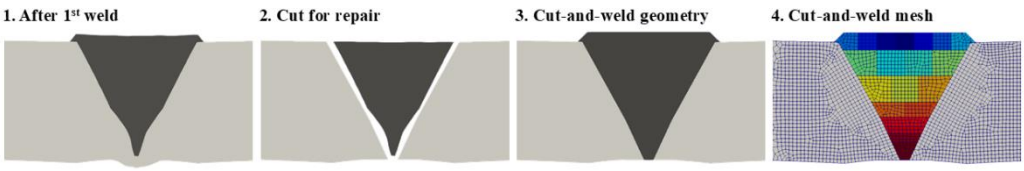



**Fig. 6** Illustration of the required steps for generating the mesh for the cut-and-weld simulation

### STEP 3: 3D MODELLING OF THE LOCALISED SECOND REPAIR

Due to the localised and non-axisymmetric nature of the second repair, this stage is modelled in 3D. To define a compatible initial stress state, the axisymmetric residual stress field from the previous cut-and-weld simulation is mapped onto a three-dimensional structure. This is followed by the modelling of the excavation, which defines the geometry of the assembly after material removal in the repair zone. The excavation profile is modelled with steeper slopes at the ends, and the cross-section and maximum depth are assumed constant along the repair length. The residual stress state after excavation is obtained through a mechanical rebalancing calculation. The sequence of steps used to compute the residual stress field following

excavation of the cut-and-weld repair is illustrated in Fig. 7. Regarding mechanical boundary conditions, three points located at the pipe extremities are constrained to prevent rigid body motion while allowing realistic deformation behaviour.

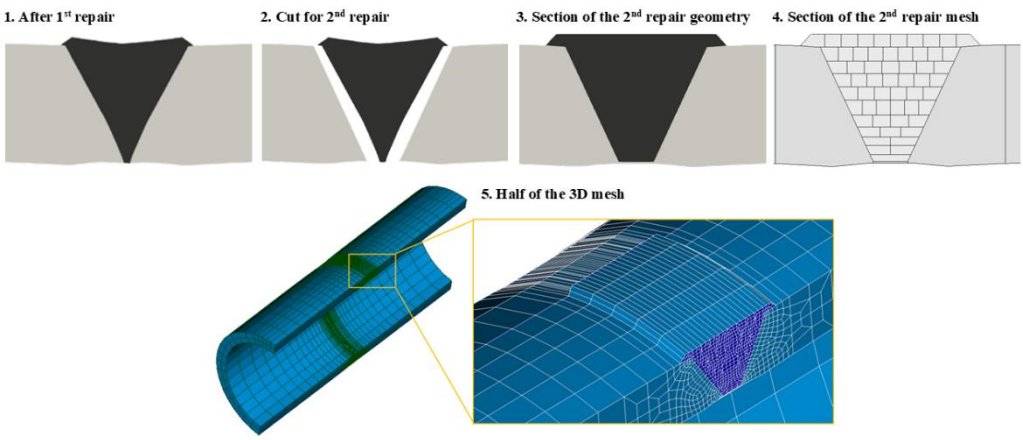



**Fig. 7** Illustration of the required steps for generating the mesh for the local repair simulation

The study was conducted in three main phases (Fig. 8). Initially, a simulation of the welding process was performed. Subsequently, the deformed geometry was extracted to generate a new mesh for the post-weld cut simulation. A two-dimensional simulation of the post-weld cut was then carried out.

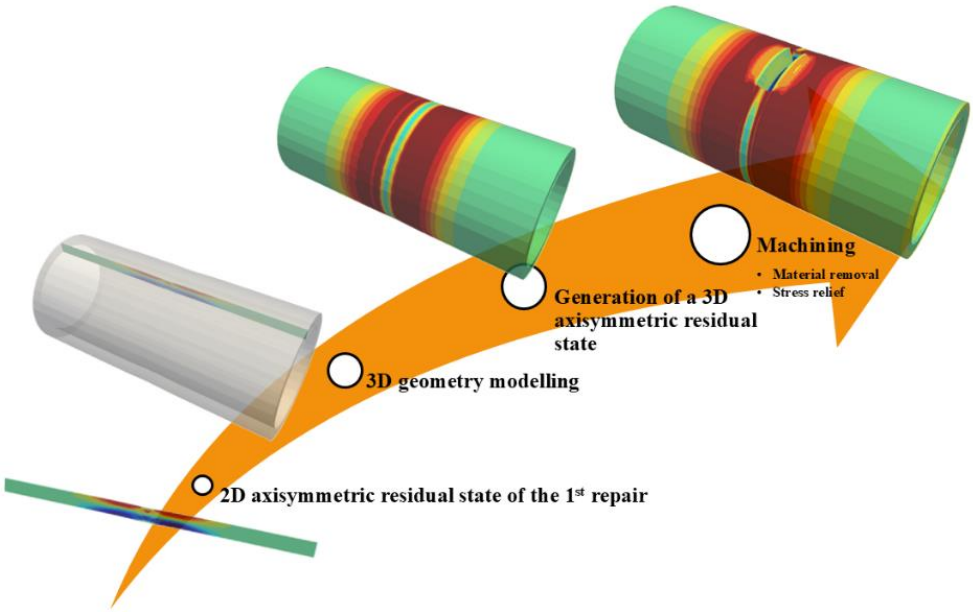



**Fig. 8** Advanced modelling approach: modelling steps of local weld excavation

## RESULTS AND DISCUSSIONS

The computational time for the 2D simulations ranged from approximately 3 to 5 hours, whereas the three-dimensional simulation required around 50 hours on a HPC cluster with 36 CPU.

The results of the study are presented in two stages. First, the initial weld, the post-weld cut, and its mechanical effects are described. This is followed by the presentation and discussion of the results from the second repair phase, which involved a localised repair strategy.

### ANALYSIS OF THE INITIAL WELD AND POST CUT-AND-WELD

Fig. 9 illustrates the axial stress and hardness distributions obtained at each stage of the welding process, up to and including the post-weld cut: the initial weld, the rebalancing phase following excavation, and the first repair weld. At the end of the repair process, the axial stress distribution around the weld joint is characterised by a tensile zone near the inner surface, followed by a compressive region extending to mid-thickness, and then a return to tensile stress near the outer surface.

As shown in Fig. 9, strain hardening increases significantly in the HAZ along the groove edges. Notably, the strain-hardened region in the root bead area is both deeper and more extensive through the thickness compared to that observed during the initial fabrication.

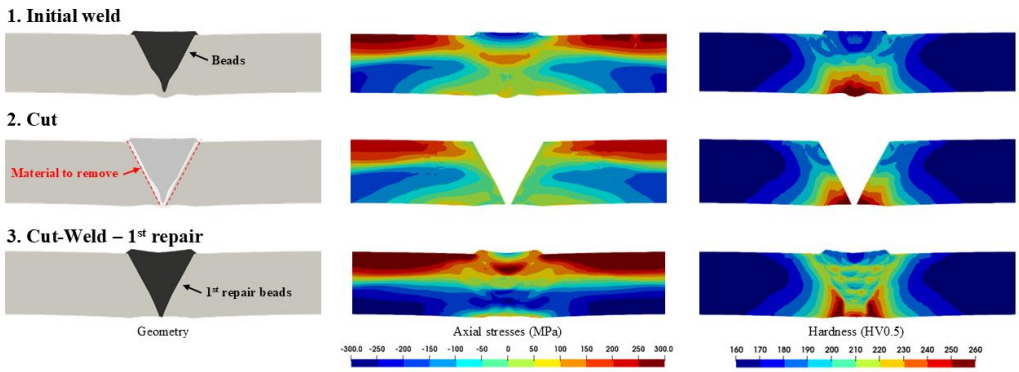



**Fig. 9** Axial residual stress (MPa) and microhardness ($HV_{0.5}$) distributions at three stages: initial weld (prior to excavation), following excavation, and after cut-and-weld

A metallurgical assessment conducted after weld removal enabled the characterisation of strain hardening on samples extracted from the side opposite the repaired zone (Fig. 10). The hardness measurements obtained from these samples are considered unaffected by the repair process. Therefore, they are deemed representative of the residual state prior to repair, corresponding to the post-cut condition of the initial weld.

These experimental results were compared with simulation outputs by evaluating axial hardness profiles at various depths through the thickness (Fig. 11). The origin of the horizontal axis corresponds to the interface between the fusion zone and the base material. A strong correlation was observed between the measured and simulated hardness values, particularly in the vicinity of the fusion zone, with both exhibiting similar magnitudes and trends along the axial direction.

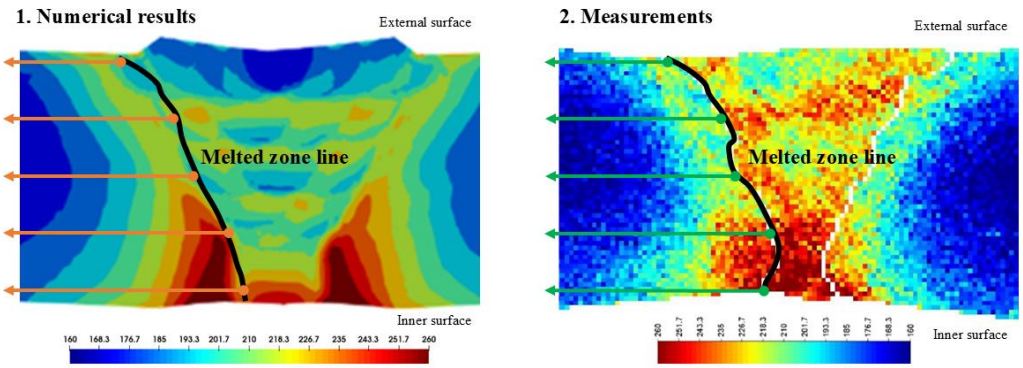



**Fig. 10** Hardness after cut-and-weld: 1. Numerical results, 2. Measurements

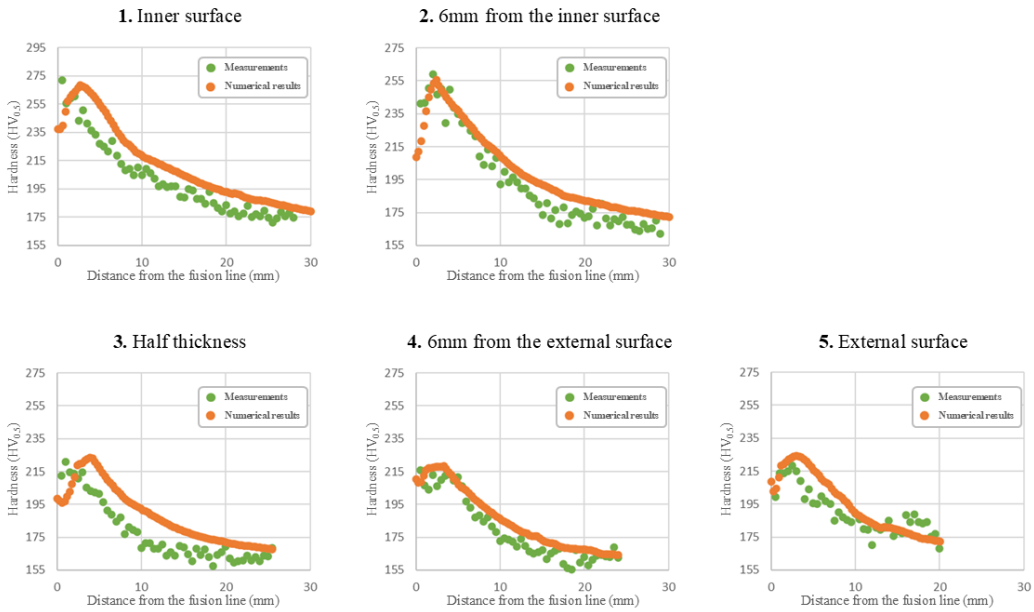



**Fig. 11** Comparison of experimental and numerical results after the cut-and-weld: hardness profiles measured along the longitudinal axis of the assembly at different depths through the pipe thickness

## ANALYSIS OF THE LOCALISED REPAIR

Fig. 12 presents an analysis of axial residual stresses and hardness distributions obtained from a 2D cross-section taken along a median plane of the structure, perpendicular to the axis of

revolution of the assembly. This analysis highlights the localised impact of the repair on the residual state of the assembly, which is confined to a narrow region surrounding the repaired area. Specifically, the residual stress field exhibits a significant reduction in compressive stress through the thickness, while the hardness levels are generally higher in the repaired zone, with a broader and deeper affected region within the pipe thickness. It is also noteworthy that the repair process perturbs the residual state only within a limited area adjacent to the repair. The remainder of the pipe structure remains largely unaffected.

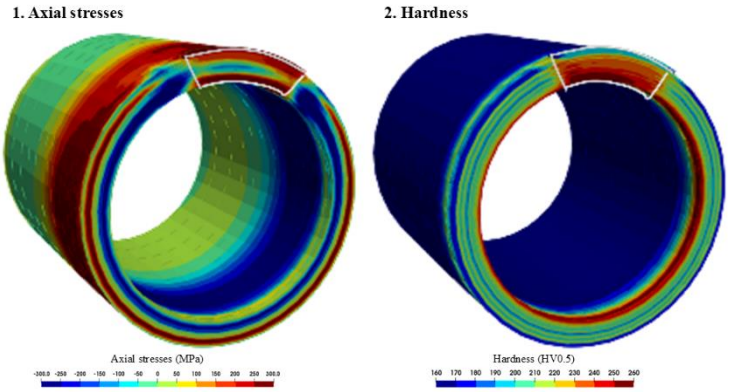



**Fig. 12** Three-dimensional distribution of axial residual stresses (MPa) and hardness ($HV_{0.5}$) represented on a cross-sectional view taken along the mid-plane of the welded joint

To further investigate this behaviour, cross-sections at various azimuthal positions were extracted (Fig. 13). These 2D sections (Fig. 14) reveal atypical residual stress distributions when compared to those observed in unrepaired welds. In particular, relative to prior simulation data for non-repaired welds, the axial stress field in the inner surface exhibits a more pronounced tensile character, with greater depth and extent from the inner wall. Additionally, the compressive zone is weaker and less extensive, and in some cases, nearly absent, especially at the initiation point of the repair.

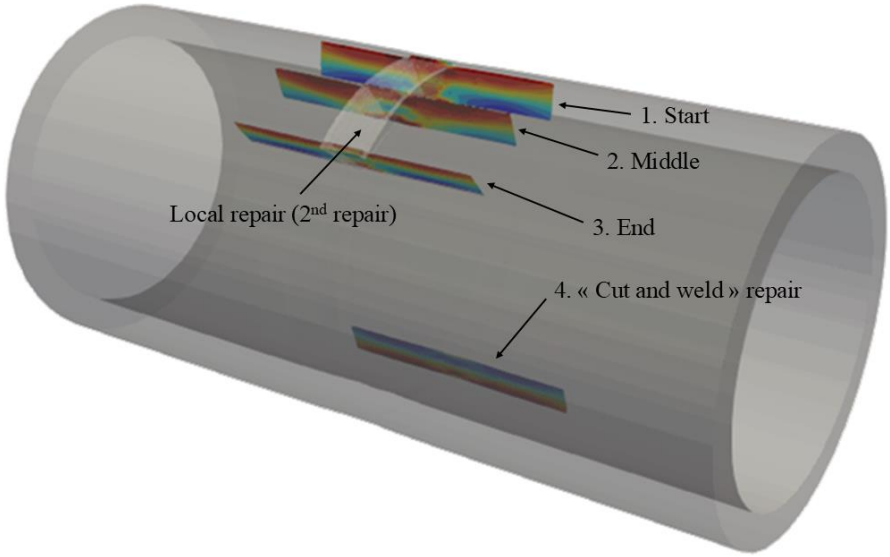



**Fig. 13** Axial stress extraction at selected locations: within the repair zone (positions 1: start, 2: middle, 3: end) and outside the repair (position 4: opposite side of the local repair)

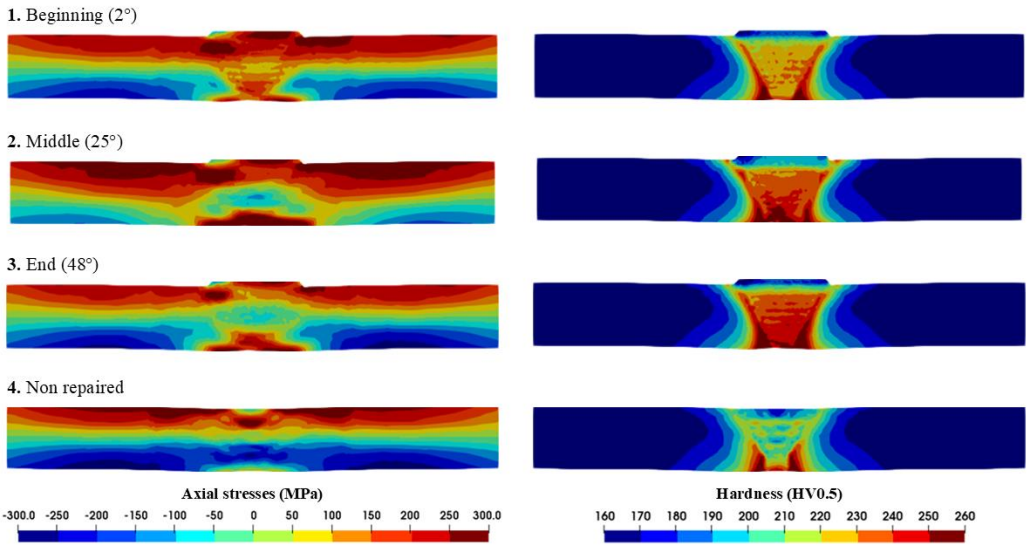



**Fig. 14** Distributions of axial residual stresses (MPa) and hardness ($HV_{0.5}$) extracted at different circumferential locations of the pipe, including the repaired region (start, middle, and end) and a reference position outside the local repair zone

A metallurgical assessment enabled the characterisation of the hardness within the local repair zone (Fig. 15). The results of this assessment were compared with simulation outputs using hardness measurements obtained from a sample extracted at the mid-length of the repair (Fig. 16). This comparison was performed by evaluating axial hardness profiles at various depths through the thickness of the assembly. A strong correlation was observed between the measured and simulated hardness values.

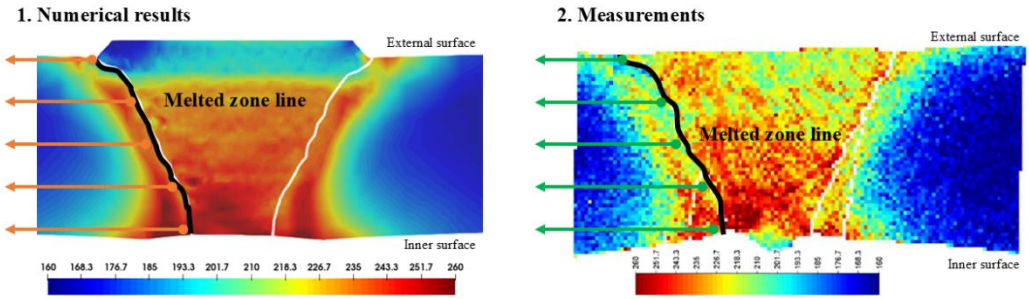



**Fig. 15** Hardness after local repair (middle section): 1. Numerical results, 2. Measurements

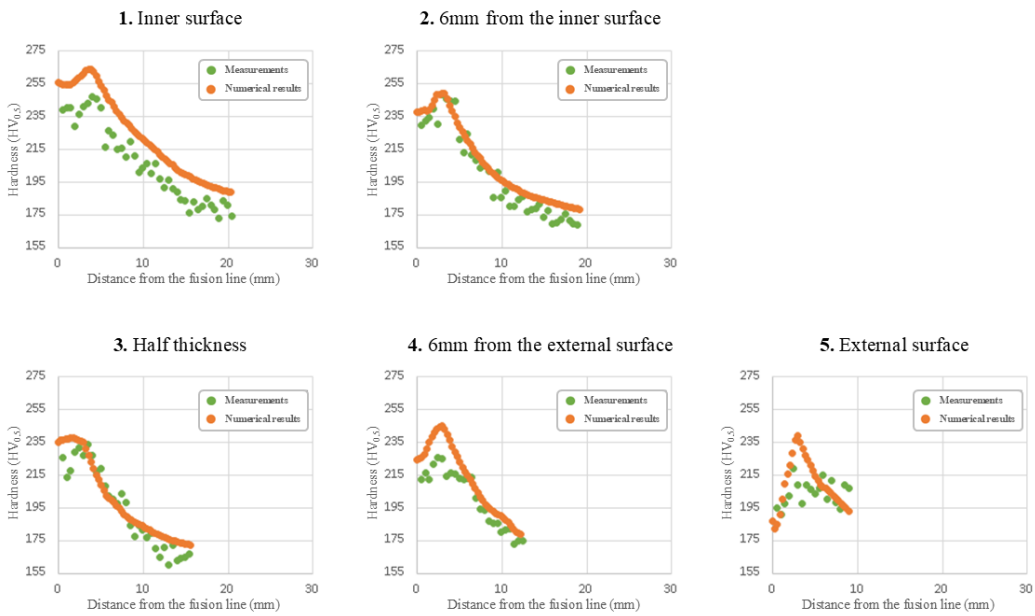



**Fig. 16** Comparison of experimental and numerical results after the local repair: hardness profiles measured along the longitudinal axis of the assembly at different depths through the pipe thickness

## DISCUSSION

The numerical methodology employed in this study, integrating sequential simulations of the initial weld, post-weld cutting, and localised repair, has demonstrated its effectiveness in accurately capturing the mechanical behavior of the assembly. The strong correlation between simulated and experimental data, particularly in hardness profiles, underscores the reliability of the modeling approach.

Firstly, the cut-and-weld operations (fully repaired welds) do not appear to increase the risk of SCC compared to unrepaired welds, based on axial stress levels and hardness measurements. Moreover, a key finding of this study is the highly localized nature of the repair's impact. The residual stress field and strain hardening are significantly modified in the immediate vicinity of the repaired zone, while the rest of the pipe structure remains largely unaffected. This observation is particularly important, as it suggests that localised repairs do not compromise the overall mechanical integrity of the assembly.

Furthermore, the residual stress distributions in the locally repaired zones exhibit atypical characteristics compared to those in unrepaired welds. Notably, tensile stresses near the inner surface are more pronounced and penetrate deeper into the material thickness, while the compressive zone is diminished or even absent in certain regions. These deviations from the typical “S-shaped” stress profiles observed in unrepaired welds may account for the increased susceptibility to SCC.

The comparison between simulated and measured hardness profiles further supports the model’s predictive capability. The consistency observed across different depths and axial positions reinforces the validity of the simulation framework.

## CONCLUSION

This study highlights the effectiveness of a multi-step numerical approach in simulating the mechanical effects of a twice-repaired weld: a fully circumferential cut-and-weld repair followed by a localised weld repair. The main conclusions are as follows:

- The fully repaired weld does not exhibit an increased risk of SCC compared to unrepaired welds, based on axial stress and hardness evaluations.
- The localised repair induces targeted modifications in the residual stress and hardness fields, with minimal influence on the rest of the structure.
- In the localised repair, tensile stresses near the inner surface are more pronounced and extend deeper into the thickness, while the compressive zone is reduced or even absent in certain areas. These deviations may account for the increased susceptibility to SCC.
- The simulation results show strong agreement with experimental measurements, confirming the accuracy and robustness of the numerical model.

Future work will aim to extend the study to various localised repair geometries, with the objective of identifying the most influential repair geometrical features in relation to primary water SCC susceptibility.

## References


[1] V. ROBIN, S. HENDILI, J. DELMAS, S. HILAL, D. IAMPIETRO, M. ABBAS and S. JUTTEAU: 'Modelling of residual stresses in multi-pass pipe circumferential butt welds made of austenitic stainless steel to provide indicators for SCC risk classification', *Proceedings of the ASME 2023 Pressure Vessels and Piping Conference,* PVP2023-107448, 2023.

[2] T. COUVANT, C. VARÉ, J. M. FRUND, S. LECLERCQ, Y. THÉBAULT, N. ETCHEGARAY, J. DELMAS: 'Susceptibility to SCC of cold work austenitic stainless steels in non-polluted primary PWR environment', *Proceedings of FONTEVRAUD 10 conference*, September 19 to 22, Avignon, France, 2022.

[3] CEN ISO/TS 18166:2016, *Numerical welding simulation - Execution and documentation*, 2015.

[4] O. MURÁNSKY ET AL.: 'The influence of constitutive material models on accumulated plastic strain in finite element weld analyses', *International Journal of Solids and Structures,* Vol. 69, pp.518-530, 2015.

[5] P. DONG ET AL.: 'On residual stress prescriptions for fitness for service assessment of pipe girth welds', *International Journal of Pressure Vessels and Piping,* 123-124, pp. 19-29, 2014.

[6] P. DURANTON, J. DEVAUX, V. ROBIN, P. GILLES, J.-M., BERGHEAU: '3D modelling of multipass welding of a 316L stainless steel pipe', *J. Mat. Proc. Tech.*, 153-154, pp. 457-463, 2004.

[7] J. DELMAS, S. HENDILI, P. PEREIRA ALVAREZ, S. HILAL and V. ROBIN: 'Pipeweld, a software suite for computational welding mechanics for nuclear applications', *Proceedings of the 14th International Seminar "Numerical Analysis of Weldability",* 21 - 24 September, Graz - Castle Seggau, Austria, 2025.

[8] ELECTRICITÉ DE FRANCE: 'Finite element code-aster: Analysis of Structures and Thermomechanics for Studies and Research', Open source on www.code-aster.org, 1989-2025.

[9] J. DELMAS, A. ASSIRE: 'Salome-Meca : une plate-forme au service de la simulation mécanique', *Proceedings of the 9ème Colloque National en Calcul des Structures CSMA 2009,* 2009. url: https://hal.archives-ouvertes.fr/hal-1413149.

[10] S. HENDILI, L. LE GRATIET, M. ABBAS: 'Un nouveau modèle simplifié de la restauration d'écrouissage utilisé dans la simulation numérique du soudage', *Proceedings of the 13ème Colloque National en Calcul des Structures CSMA 2017,* 2017.

# RESIDUAL STRESS SIMULATION OF ALUMINUM CASTINGS USING A TEMPERATURE-DEPENDENT HEAT TRANSFER COEFFICIENT DURING IMMERSION QUENCHING

L. HELML*, S. MAIER**, T. WLANIS*, W. ARTNER***, R. KAHLENBERG*, ****, G. FUCHS*****, E. KOZESCHNIK*

**Institute of Materials Science and Technology, TU Wien, 1060 Vienna, Austria, 0009-0007-3897-6745, lukas.helml@tuwien.ac.at*
***Institute of Production Engineering and Photonic Technologies, TU Wien, 1060 Vienna, Austria, 0009-0006-6489-7699*
****XRC – X-ray center of the TU Wien, TU Wien, 1060 Vienna, Austria*
*****Materials Center Leoben Forschung GmbH, 8700 Leoben, Austria*
******Chair of Metal Forging and Casting, TU Munich, 85748 Garching, Germany*

*DOI 10.3217/978-3-99161-089-2-026, license CC BY 4.0*
*https://creativecommons.org/licenses/by/4.0/deed.en*
*This CC license does not apply to third party material and content noted otherwise.*

ABSTRACT

A simulation model is developed to predict residual stresses in aluminum castings during immersion quenching. To describe the cooling conditions, a simplified approach is used, in which the heat transfer coefficient is defined as a function of the surface temperature of the component. Two geometries are used in this study: a simple plate to verify the thermal boundary conditions and a stress lattice to evaluate the residual stress distribution. The heat transfer coefficient, which is experimentally validated using the plate geometry, is implemented in a finite element simulation and then applied to the stress lattice. The mechanical behaviour during quenching is characterized using dilatometer experiments. The simulated stress profile in the stress lattice is verified by X-ray diffraction measurements.

Keywords: aluminum casting, heat treatment, residual stress, immersion quenching

## INTRODUCTION

In modern production technology, the demand for lightweight components and materials is growing [1,2]. These lightweight components are needed in various applications in the automotive and aerospace industries to further reduce energy consumption and carbon emissions. Several strategies can be used to incorporate lightweight engineering. These include the use of lightweight materials such as aluminum, lightweight construction such as topology-optimized or thin-walled components, and the associated manufacturing process, like forming, casting, welding, heat treatment, and machining.

Traditional manufacturing strategies are often insufficient to meet component requirements such as tolerance and strength. Precise knowledge of the initial residual stresses in these components and the ability to model and simulate them are essential to optimize entire process chains. A concept for a holistic view and optimization of the process chain for the production of aluminum cast components is presented in [3]. Often, the heat treatments have the greatest influence on residual stress-related distortions during machining. There are numerous methods for simulating residual stresses during different heat treatments that describe the material behavior and cooling conditions during quenching with varying degrees of complexity [4].

The heat treatment of aluminum alloys is thoroughly investigated [5-9]. The classical route for aluminum cast parts consists of solution annealing followed by quenching and subsequent ageing to create a T6 temper [5]. The same heat treatment can be applied to aluminum welds as a post-weld treatment. During solution annealing, alloying elements like Mg, Si, and Cu are dissolved in the aluminum lattice. Fast quenching to room temperature then creates a supersaturated solid solution. In the subsequent ageing process, the elements in solid solution form metastable precipitates, which increase the strength of the material through precipitation hardening.

Most of the cast-induced residual stresses are relaxed during the solution heat treatment due to the high annealing temperatures. In contrast, the high temperature gradients during subsequent quenching induce high residual stresses [10-13], which can be partially relaxed during the subsequent ageing treatment [14,15]. Robinson et al. [16] give a good overview of the evolution of residual stresses in heat-treatable aluminum alloys during their heat treatment.

For a reliable simulation of residual stresses during water quenching, an accurate description of the cooling conditions is essential. During immersion quenching of aluminum castings, the heat transfer coefficient $\alpha_{\mathrm{imm}}$ passes through three different boiling regimes: film boiling, nucleate boiling, and the convective phase. Initially, when the sample is still at a relatively high temperature, film boiling occurs. During film boiling, the surface of the sample is surrounded by a vapor blanket, resulting in a low $\alpha_{\mathrm{imm}}$. As the part cools and the Leidenfrost temperature is reached, the vapor blanket collapses and the regime transitions to nucleate boiling. The heat transfer coefficient peaks at this stage. When the heat transfer from the sample to the water is no longer sufficient to maintain boiling, the convective stage begins, and $\alpha_{\mathrm{imm}}$ decreases accordingly [5]. Maniruzzaman and Sisson [17] observe the same effects and additionally a regime of partial film boiling, resulting in fluctuating surface temperatures due to unstable vapor formation. Xiao et al. [18] use an aluminum test casting to demonstrate the influence of surface orientation relative to the water surface and conclude that $\alpha_{\mathrm{imm}}$ is lower for surfaces facing the water surface compared to surfaces in other orientations. The influence

of both the quench medium and sample geometry is documented for wrought and cast aluminum alloys, with corresponding temperature-dependent heat transfer coefficients provided [19-21]. Bamberger et al. [22] investigate the heat transfer coefficients for Al, Cu, and Ni during both spray and immersion quenching with different quenching media, including water and water mixed with organic agents.

The cooling conditions during immersion quenching can also be simulated using computational fluid dynamics (CFD). The immersion quenching process of aluminum castings is studied in this context by [23-27]. CFD enables a more detailed description of all boiling regimes. However, the use of CFD involves a significant additional computational effort and is beyond the scope of this work.

The present work presents an efficient and convenient method for the simulation of residual stresses during water quenching of aluminum castings to improve the process chain. The temperature-dependent mechanical properties of the material are determined experimentally and used to model the material behavior. To model the cooling conditions, a surface temperature-dependent heat transfer coefficient is applied to capture the different boiling regimes during water quenching.

## MATERIALS AND EXPERIMENTAL METHODS

### GEOMETRIES

In the present work, we focus on two different geometries. The first geometry is a simple plate, which is primarily utilized to determine the heat transfer coefficient during the immersion quenching process. Three type K thermocouples (TCs) are mounted on the plate geometry. TC1 is cast in the center of the body, TC2 and TC3 are fixed on the surface centers. All three TCs are mounted at the same height. The second geometry is a stress lattice, consisting of a thick bar that is connected to a slim bar by two connection bars. The stress lattice is intentionally designed to induce residual stresses. Fig. 1 shows sketches of both geometries and the positioning of the TCs on the plate. The corresponding dimensions are given in Table 1. Stress lattices are often used for stress analysis in cast iron [28-33]. The geometry of stress lattices can vary, but they are usually symmetrical and consist of a thick bar in the center connected to two slim bars on the outside. In contrast, the stress lattice used in this study is asymmetric, similar to a geometry used by Godlewski et al. [15].

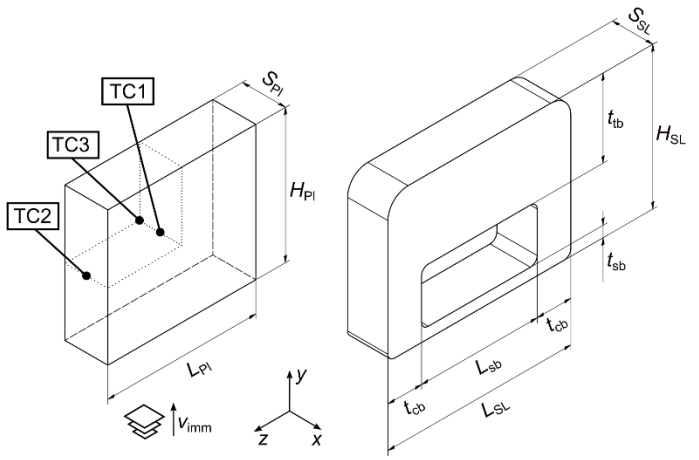



**Fig. 1** Sketches of the two geometries used with their main dimensions. On the left is the plate denoted by the subscript 'Pl' with the location of the TCs indicated. On the right is the stress lattice, denoted by the subscript 'SL'. The stress lattice consists of a thick bar ($t_{tb}$), that is connected to a slim bar ($t_{sb}$) by two connection bars ($t_{cb}$).

**Table 1** Main dimensions of the plate and stress lattice geometry

| **Plate:** | | | **Stress Lattice:** | | |
|---|---|---|---|---|---|
| | $L_{Pl}$ | 100 mm | | $L_{SL}$ | 136 mm |
| | $H_{Pl}$ | 110 mm | | $H_{SL}$ | 106 mm |
| | $S_{Pl}$ | 30 mm | | $S_{SL}$ | 30 mm |
| | | | | $L_{sb}$ | 86 mm |
| | | | | $t_{sb}$ | 8 mm |
| | | | | $t_{tb}$ | 58 mm |
| | | | | $t_{cb}$ | 25 mm |

## MATERIAL

Two different materials are used in this study:

- Plate material: A commercial EN AC-42100 aluminum cast alloy is used for the plate geometry. The plate is produced via gravity casting into a sand mould.
- Stress lattice material: The stress lattice is manufactured from a commercial EN AW-6016 alloy, with an as-cast etching slice provided by AMAG Rolling GmbH. The stress lattice is cut from the slice using a water jet cutter and subsequently milled to its final geometry.

The main chemical composition of both alloys, measured via optical emission spectroscopy (OES), is provided in Table 2.

Due to the high Si content, the cast alloy EN AC-42100 exhibits a microstructure containing eutectic Si. While the eutectic Si influences the mechanical properties of the material, it

remains a challenge to study its isolated effects. To evaluate the matrix behavior independently, we selected a wrought alloy EN AW-6016 in its as-cast state. This alloy has a similar composition to the matrix composition of EN AC-42100 without the eutectic Si. Although the two alloys differ in microstructure and properties [5], they exhibit a comparable precipitation sequence [9], allowing the same traditional heat treatment to be applied. This ensures comparability while eliminating the effects of eutectic Si.

**Table 2** Alloy composition of EN AC-42100 and EN AW-6016 measured by OES in wt.%

| | Si | Mg | Fe | Cu | Mn | Zn | Ti | Al | other |
|---|---|---|---|---|---|---|---|---|---|
| **EN AC-42100** | 7.42 | 0.36 | 0.10 | <0.01 | 0.03 | 0.02 | 0.14 | 91.80 | 0.13 |
| **EN AW-6016** | 1.07 | 0.41 | 0.21 | 0.07 | 0.08 | <0.01 | 0.02 | 98.10 | 0.04 |

## DETERMINATION OF COOLING CURVES

To determine the temperature history of the plate geometry during water quenching, we use the three mounted TCs. As indicated in Fig. 1**,** the water direction relative to the part is in the positive *y*-direction.

The plate is fixed in a stainless-steel basket and brought up to the solution annealing temperature $T_{sol}$ of 540 °C under ambient atmosphere in a resistance-heated chamber furnace. After reaching an equilibrated temperature at $T_{sol}$ for all three TCs, the basket is removed from the furnace and lowered into a water tank by a winch at a constant immersion velocity $v_{imm}$ of 65 $mms^{-1}$. This procedure is repeated five times to improve reliability. The initial water temperature $T_b$ is 15 °C. Measuring the water temperature after the quenching process is difficult because the water temperature is not homogeneous throughout the whole water tank. However, Totten and MacKenzie [5] provide a guideline for industrial applications regarding the minimum tank volume for immersion quenching of aluminum. The maximum acceptable temperature increase of the quenchant is 5.5 °C, and based on this limit, the minimum required tank volume is calculated to be 0.027 $m^3$. For the quench experiments, a tank with a volume of 0.04 $m^3$ is used, and a water temperature increase of 3.5 °C can be expected. The temperature data is recorded at 10 Hz using a multi-channel recorder.

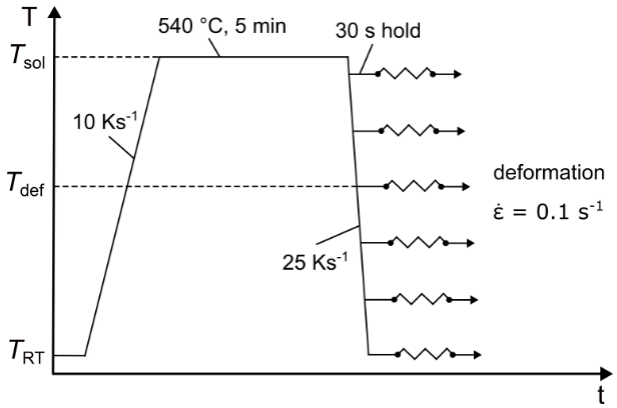



**Fig. 2** Thermomechanical treatment in the dilatometer. The pre-solutionized sample is annealed at $T_{sol}$ for 5 min and quenched to $T_{def}$ at 25 Ks$^{-1}$. After a 30 s isothermal hold, the compression test is carried out isothermally at $T_{def}$.

The mechanical behavior of the EN AW-6016 alloy during quenching is characterized by compression tests using a Baehr DIL 805 D dilatometer. All samples are pre-solution annealed in batches for 2 hours at $T_{sol}$ and water quenched prior to dilatometer testing. A schematic diagram of the thermomechanical treatment in the dilatometer is shown in Fig. 2. To ensure reproducibility and avoid any effects caused by natural ageing, each sample is again heated to $T_{sol}$ at a rate of 10 Ks$^{-1}$ and shortly solution annealed for 5 min. Using He as the quenching medium, the sample is directly quenched to the deformation temperature $T_{def}$ at a cooling rate of 25 Ks$^{-1}$. This is followed by an isothermal step at $T_{def}$ for 30 s to ensure thermal stability during the deformation segment.

The isothermal compression test is performed at a strain rate of 0.1 s$^{-1}$ and deformation temperatures ranging from 500 °C to 100 °C in 100 °C increments, plus one test at room temperature ($T_{RT}$ = 22 °C).

## RESIDUAL STRESS MEASUREMENTS

The stress measurements are carried out on an Empyrean from Panalytical, equipped with an Eulerian cradle. On the primary side, the beam is filtered with a parallel mirror to separate the Cu $K_{\alpha 1,2}$ radiation, a divergent slit of ½°, a 0.04 rad Soller slit, and a 4 mm mask are used. Detection is made with a parallel plate collimator and a scintillation detector.

For the stress evaluation, the $\sin^2(\psi)$ method is used, which relies on measuring lattice strain variations as a function of the tilt angle $\psi$. The peaks are measured from 75° to 82° 2θ, and the tilt angle is varied from 0° to 63.43°. By tilting the sample, the diffraction peak shifts and the surface-near biaxial stress state $\sigma_\Phi$ [34]

$$\sigma_{\Phi} = \frac{E_{[hkl]}}{1+\nu}\frac{1}{d_0}\frac{\partial d(\phi,\psi)}{\partial \sin^2(\psi)} \quad (1)$$

can be calculated from the resulting slope in the $d$-spacing over $\sin^2(\psi)$ plot [35]. For the stress evaluation, we use the (131) Al peak. The Poisson's ratio is 0.33, and the directional Young's Modulus $E_{[hkl]}$ is calculated according to

$$\frac{1}{E_{[hkl]}} = S_{11} - [2(S_{11} - S_{12}) - S_{44}](\alpha^2\beta^2 + \alpha^2\gamma^2 + \beta^2\gamma^2) \quad (2)$$

$S_{11}$, $S_{12}$, and $S_{44}$ are the elastic compliances; values are taken from Rösler et al. [34]. $\alpha$, $\beta$, and $\gamma$ are dependent on the directions [*hkl*]. The resulting directional Young's Modulus in the [131] direction $E_{[131]}$ is 69.61 GPa.

## SIMULATION

### THERMAL SIMULATION AND THE COOLING CONDITIONS FOR WATER QUENCHING

To simulate the immersion process, we use the commercial finite element (FE) software Ansys 2024 R1. The mesh for the plate geometry consists of 22880 SOLID278 elements with a quadratic element order, resulting in 100271 nodes, and the element shape is HEX8. No symmetry condition is applied to the model.

The first law of thermodynamics postulates the conservation of energy, which is the basis for the heat flow used in transient thermal simulations, taking into account all relevant heat transfer mechanisms to simulate the temperature distribution over time in the part. The thermal boundary condition is a specified heat flux acting on the surface of the part, which significantly influences the thermal history during quenching. This is described by the convective heat flux $\dot{q}$,

$$\dot{q} = \alpha_{\mathrm{imm}}(T_{\mathrm{surf}} - T_{\mathrm{b}}) \quad (3)$$

where $\alpha_{\mathrm{imm}}$ is the heat transfer coefficient, $T_{\mathrm{surf}}$ is the surface temperature of the part, and $T_{\mathrm{b}}$ is the temperature of the quenching medium. Radiative heat transfer is neglected in this proposed model, but can be incorporated into the heat transfer modeling approach described in the following section if desired.

#### *Surface temperature-dependent heat transfer coefficient* $\alpha_{\mathrm{imm}}$

To model the heat transfer coefficient $\alpha_{imm}$ during immersion quenching, we follow the approach of Bamberger et al. [22], which proposes that the heat transfer coefficient

$$\alpha_{\mathrm{imm}} = 1.4\sqrt{\lambda\rho C}\exp\left(0.32\frac{T_{\mathrm{surf}}-T_{\mathrm{e}}}{T_{\mathrm{b}}-T_{\mathrm{e}}}\right) + \alpha_{\mathrm{v}} + \alpha_{\mathrm{rad}} \quad (4)$$

depends on the surface temperature of the part $T_{surf}$, and the temperature-dependent thermophysical material properties of the metal. $T_b$ is the initial bulk water temperature, and $T_e$ is the evaporation temperature of the quench medium. The required material parameters are the thermal conductivity $\lambda$, density $\rho$, and specific heat $C$.

This concept is valid only for surface temperatures $T_{surf}$ in the range of 900-250 °C. The heat transfer coefficient for stable film evaporation at high surface temperatures $\alpha_v$ is proposed to have a constant value of 750 $Wm^{-2}K^{-1}$, and the heat transfer coefficient for radiation $\alpha_{rad}$ is neglected. For temperatures out of the validity range of Eq. 4 (from 250°C down to room temperature), the heat transfer coefficient is fitted to match the experimentally determined cooling curves.

### *Implementation of $\alpha_{imm}$ in the FE application*

The heat transfer coefficient proposed by Bamberger et al. [22] is dependent on the surface temperature of the specimen, hence it is important for the implementation to use "thermal solid" elements, which allow the film coefficient to be controlled by the surface temperature of the element. Suitable element types include SOLID70, SOLID87, and SOLID278. Note that these types of elements can be used for thermal analysis exclusively.

The initial condition is a homogeneous body temperature of 540 °C, which marks the end of the solution treatment. The immersion process can be divided into three distinct phases. Fig. 3 shows the x-component of the heat flux $\Phi_{q,x}$ and temperature $T_s$ along a surface path $s$ at certain points in time, representing the three phases during the immersion process. During the first phase, all surfaces are exposed to convection against air, with a constant ambient temperature $T_{amb}$ of 25 °C and a convection coefficient $\alpha_{amb}$ of 35 $Wm^{-2}K^{-1}$ applied. This phase corresponds to the removal of the part from the furnace and lowering it into the water tank. The second phase corresponds to the immersion process and begins when the first surface comes into contact with the water. During this phase, two distinct boundary conditions are present. Surface areas that are above the waterline are still subject to convective heat transfer against air. In contrast, surfaces that are already submerged experience convection against water and, therefore, significantly higher heat transfer rates. The surface temperature-dependent heat transfer coefficient $\alpha_{imm}$ is applied to the surface parts that are already submerged. To capture this behavior in the simulation, surface nodes are reselected based on their position relative to the water level. This reselection process corresponds to the immersion velocity $v_{imm}$ used in the experiments. Phase three begins when the part is fully submerged and all surfaces experience convection against the water. $\alpha_{imm}$ is applied to all surfaces during this phase.

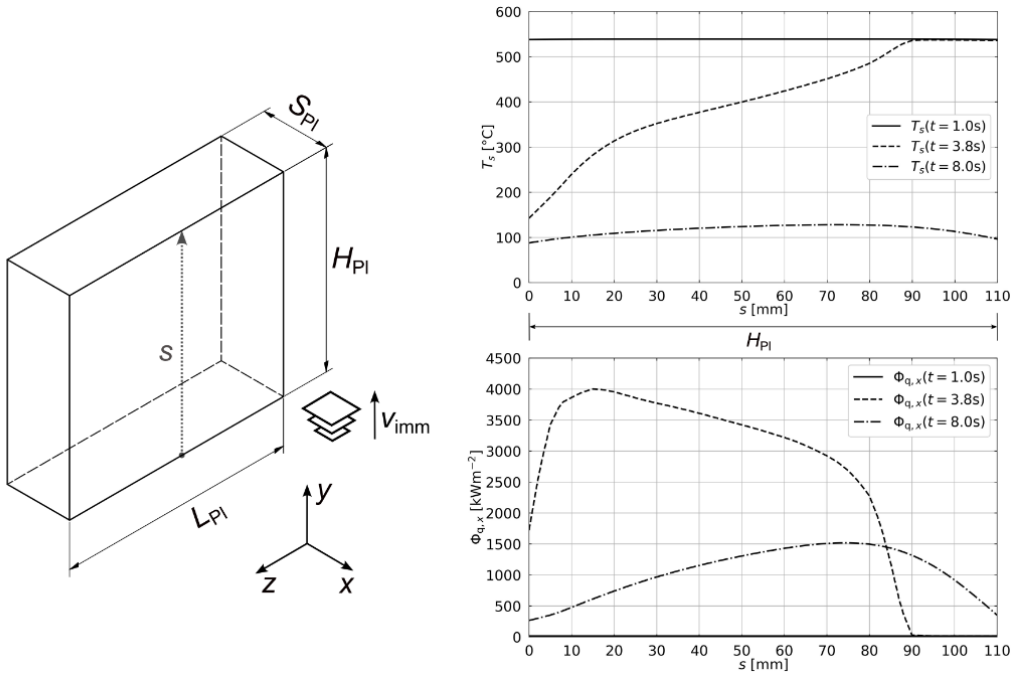



**Fig. 3** The sketch on the left shows the plate geometry during immersion quenching. As indicated, the path *s* is located in the middle of the surface of the plate and is oriented in the positive *y*-direction. The plots on the right show simulation results of the temperature profile $T_s$ and the *x*-component of the heat flux $\Phi_{q,x}$ at different points in time over the path *s*. The points in time are chosen to represent the different stages during immersion quenching. After 1 second, the part has not yet come into contact with the water. At 3.8 seconds, the plate is partially submerged, and after 8 seconds, the plate is completely submerged.

This method is applied to the plate geometry, and the results of the thermal analysis are compared to experimental data to determine $\alpha_{imm}$ accordingly, see Fig. 5. The calibrated cooling conditions are then applied to the geometry of the stress lattice. The stress lattice model consists of 101649 SOLID87 elements with quadratic order, resulting in 144896 nodes. The elements have a TET10 shape. No symmetry conditions are applied to the model.

## THERMOPHYSICAL PROPERTIES

To describe the temperature distribution of the material during the quenching process, a user-defined material is created in Ansys. The values for the thermophysical properties as a function of temperature, see Fig. 4, are taken from the literature. Overfelt et al. [36] provide specific data for the alloy EN AC-42100 on the density $\rho_{mat}$ and the thermal conductivity $\kappa_{tc}$. The isotropic instantaneous coefficient of thermal expansion $\alpha_{te}$ [37] is also specific for the alloy

EN AC-42100. The values for the specific heat at constant pressure $c_p$ [38] refer to pure aluminum.

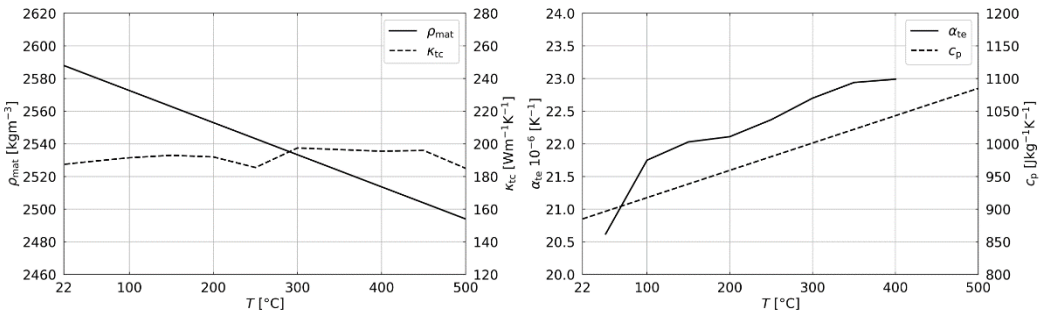



**Fig. 4** Thermophysical properties as a function of temperature. The left diagram shows the density $\rho_{mat}$ [36] and the thermal conductivity $\kappa_{tc}$ [36]. The coefficient of thermal expansion $\alpha_{te}$ [37] and the specific heat at constant pressure $c_p$ [38] are displayed in the right plot.

## MECHANICAL SIMULATION

Since the element types used in the thermal simulation are not suitable for structural analysis, and there is no need for a fully thermal-mechanical coupled simulation, the mechanical simulation is performed separately. This is done by applying a unidirectional coupling of the thermal and mechanical analysis. The results of the thermal analysis are used as an imported load in the mechanical model. The temperature history of the part is then mapped onto a mesh that is suitable for structural analysis.

The mechanical simulation is only carried out for the geometry of the stress lattice. The mesh of the mechanical model consists of 40245 SOLID186 elements with quadratic order, resulting in 177395 nodes. No symmetry conditions are applied. As a mechanical boundary condition, the weak springs option is used with a default spring stiffness in the solver controls to prevent rigid body motion. Due to their low stiffness compared to the model stiffness, it can be assumed that they do not have an effect on the stress state during the quenching simulation.

The mapped temperature history is used in the mechanical model to calculate the thermal strain $\varepsilon_{th}$ according to

$$\varepsilon_{th} = \alpha_{te}(T)(T - T_{ref}) \tag{5}$$

with the thermal expansion coefficient $\alpha_{te}$ and the reference temperature $T_{ref}$. Isotropic elasticity via Hooke's law with a temperature-dependent Young's modulus $E(T)$ and a Poisson's ratio $\nu$ = 0.33 leads to the description of the elastic strain component $\varepsilon_{el}$. The temperature-dependent Young's Modulus $E(T)$

$$E(T) = (69220\ \text{Pa} - 40.1\ \tfrac{\text{Pa}}{^\circ\text{C}}\ T) \cdot 10^6 \tag{6}$$

is calculated using the default values of MatCalc [39].

The 'Multilinear Isotropic Hardening' model is employed to describe the plastic behaviour. This model assumes isotropic material behaviour and that plasticity is independent of the strain rate. In addition, the Von Mises yield criterion with associative flow rule is applied, which can be described as

$$f(\boldsymbol{\sigma}, \sigma_y) = \overline{\sigma}(\boldsymbol{\sigma}) - \sigma_y \leq 0 \tag{7}$$

with the Von Mises equivalent stress $\bar{\sigma}$ and the yield stress $\sigma_y(T, \varepsilon_{pl})$ according to the temperature-dependent flow curves as measured in the compression tests. The experimentally determined flow curves, see Fig. 7, are discretized and given as tabular data for the hardening model.

## RESULTS AND DISCUSSION

### TEMPERATURE PROFILES DURING WATER QUENCHING

The calibrated heat transfer coefficient applied to the plate geometry (dashed line) and the calculated values according to Bamberger et al. [22] (solid line) are shown in Fig. 5. In the temperature range (900–250 °C) valid for Eq. 4, $\alpha_{imm}$ closely follows the calculated values. $\alpha_{imm}$ increases steadily with decreasing surface temperature $T_{surf}$ of the part. After reaching a maximum value of 23000 $Wm^{-2}K^{-1}$ at a temperature of 200 °C, $\alpha_{imm}$ decreases significantly. This abrupt decrease of $\alpha_{imm}$ corresponds to the end of the nucleate boiling phase and the transition to the convective stage of cooling.

Fig. 6 shows the simulation results after applying the calibrated heat transfer coefficient (dashed lines) compared to the experimentally determined mean temperatures (solid lines), surrounded by the minimum and maximum values (shaded areas). During the first phase (about 3 seconds), the temperature drops only slightly. This phase corresponds to pure convection against the air when the part has not yet come into contact with the water. Once the part is immersed in the water, the heat flux increases drastically, resulting in rapid cooling to a temperature of about 200 °C. As the heat transfer coefficient decreases at this temperature due to the transition to the convection phase of cooling, the cooling rate also decreases. The simulated initial cooling rate of TC3 is slightly too fast compared to the experiment, but overall, the simulation allows reproduction of the experimentally determined cooling curves of all three TCs with good accuracy.

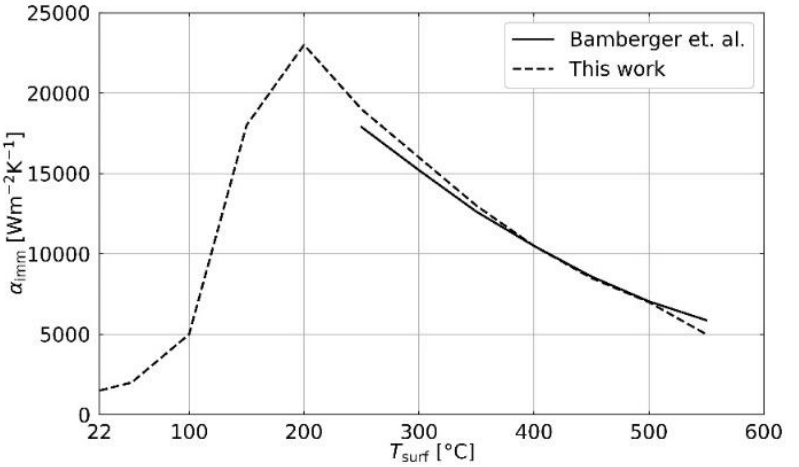



**Fig. 5** The heat transfer coefficient used in the present work (dashed line) as a function of the surface temperature of the sample. The theoretical values proposed by Bamberger et al. [22] (solid line) are valid only for temperatures above 250 °C. In the valid range, the applied heat transfer coefficient closely follows the theoretical values. Below a surface temperature of 250 °C, $\alpha_{imm}$ is adjusted accordingly to reproduce the experimental data.

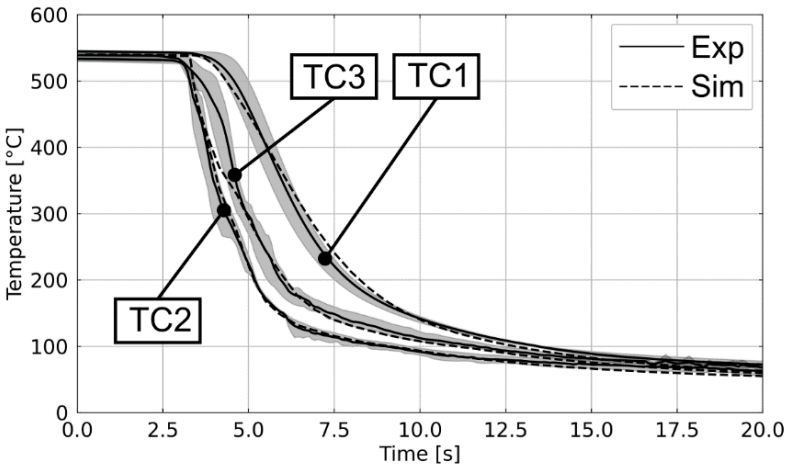



**Fig. 6** Temperature curves for all three TCs of the plate geometry after solution annealing and subsequent water quenching. The experiments are repeated five times. Solid lines mark the mean values, enveloped by the shaded areas, representing the minimum and maximum values. The corresponding results of the FE simulation are indicated by dashed lines.

## MECHANICAL BEHAVIOUR DURING WATER QUENCHING

The flow curves of the EN AW-6016 alloy from the isothermal compression tests and the corresponding initial yield strength $R_{p0.2}$ as a function of the deformation temperature are shown in Fig. 7. At room temperature, $R_{p0.2}$ is approximately 53 MPa and slightly increases between 100 and 300 °C to a plateau value of approximately 60 MPa. Above 300 °C, the initial yield strength decreases significantly.

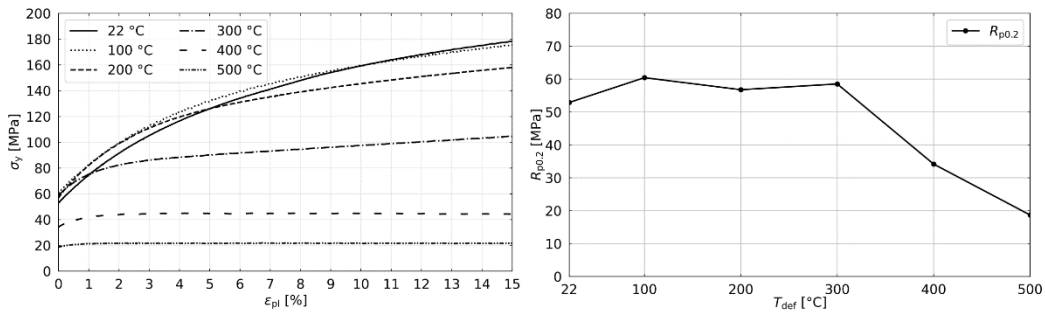



**Fig. 7** The left plot shows the experimental data for the yield stress $\sigma_y$ over true plastic strain $\varepsilon_{pl}$ for different deformation temperatures. All flow curves are recorded at a strain rate of 0.1 $s^{-1}$. On the right, the initial yield strength $R_{p0.2}$ as a function of $T_{def}$ is displayed.

The plateau observed in the $R_{p0.2}$ over $T_{def}$ curve may seem counterintuitive, as the common expressions for the temperature dependency of the yield strength predict a steady decrease with increasing temperature [40]. A possible explanation for this behaviour is the cross-core diffusion effect (CCD) formulated by Curtin et al. [41]. This model describes the contributions of solutes to dynamic strain ageing (DSA) and negative strain rate sensitivity (nSRS), resulting in an increase in the yield strength at elevated temperatures. The underlying mechanism is that solute atoms (e.g., Mg or Si) diffuse to energetically favourable positions within the stress fields around dislocations, thereby hindering dislocation movement. This interaction becomes significant at elevated temperatures, where the diffusivity of the solute atoms is sufficient to enable single-atom jumps through the dislocation core [41]. The effect of CCD on the flow curves is well investigated for Al-Mg alloys [40,42-47]. Since the material in the present work is in a solution-annealed state before quenching, it seems plausible that most Mg and Si atoms are in solid solution and thus contribute to the CCD effect.

In addition to this effect, precipitates can form in the solution-annealed supersaturated condition before and during the compression test, which will also impact the strength of the material. At lower temperatures, this effect will be weak because the time to form the precipitates in larger amounts is insufficient. At medium temperatures, the precipitation strengthening effect under these conditions reaches its maximum effect, until it decreases again at higher temperatures. In the material, both effects will interact with each other and, therefore, lead to a rather complex strengthening behaviour.

The strain rate-dependence is not considered in this analysis, since the flow curves are implemented in tabular form within the multilinear isotropic hardening model. Consequently, the modelled mechanical behaviour is temperature-dependent but not strain rate-dependent. A possible way to take strain rate effects into account in future work is the implementation of the user-defined subroutine 'simple MicroStructure Evolution' (sMSE) [48,49]. sMSE allows for a more detailed material description, including temperature- and strain rate-dependent mechanical properties.

## RESIDUAL STRESS AFTER WATER QUENCHING

The simulation results for the residual stress component in the $\varphi = 45°$ direction are shown in Fig. 8. XRD measurements are taken along the surface path $s_{A\text{-}E}$, and compared with the simulation results. The simulation predicts a symmetrical stress profile along this path, with a relatively constant value of $\sigma_{\varphi=45°}$ at -65 MPa, which decreases toward the edges. The measurements show good qualitative agreement with the simulation between the 0 mm and 28 mm marks; however, they deviate somehow beyond this point. Specifically, an asymmetrical stress profile is observed, with a peak value of -103 ± 10 MPa detected at approximately 40 mm. Overall, the simulation consistently underestimates the absolute stress values when compared to the measured data.

The measured peak value of about -100 MPa would imply a plastic strain of approximately 2.5 %, based on the flow curves obtained from compression tests (see Fig. 7). This level of strain appears unrealistic for the quenching process. In contrast, the simulated strain at the same location is about one order of magnitude lower, resulting in a much lower predicted stress value of about -65 MPa.

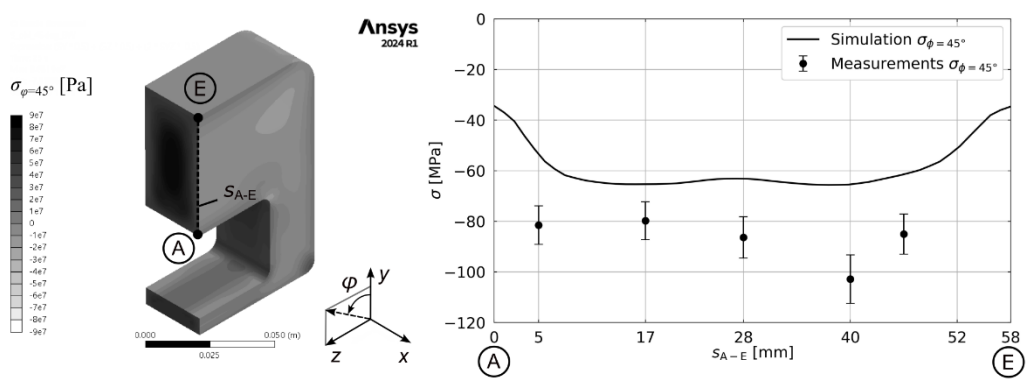



**Fig. 8** The Figure shows a cross-section of the stress lattice model with the surface path $s_{A\text{-}E}$ indicated. The simulation results for $\sigma_{\varphi=45°}$ are compared to XRD measurements.

While the simulation captures the general trend of the residual stress distribution along the path $s_{A\text{-}E}$, notable discrepancies remain compared to the XRD measurements. Several factors

may contribute to these discrepancies. One possible explanation is that the calibration of the heat transfer coefficient $\alpha_{imm}$, based on a simple plate geometry, may not be directly applicable to the more complex stress lattice. To address this issue, further experimental verification is needed. This could be achieved by equipping the stress lattice with thermocouples and comparing simulated cooling curves with data obtained from immersion quenching.

Another potential reason for the discrepancies lies in the limitations of the material description. The hardening model used in the analysis does not account for strain rate-sensitivity, which could affect the accuracy of stress predictions. Furthermore, the thermomechanical treatment applied in the dilatometer for compression tests may not fully represent the material's behaviour under immersion quenching conditions.

## SUMMARY

In the present work, we introduce a simulation approach for predicting residual stresses in aluminum cast parts during immersion quenching. A temperature-dependent heat transfer coefficient $\alpha_{imm}$ is developed and implemented in an FE simulation using ANSYS. $\alpha_{imm}$ is experimentally calibrated using a simple plate geometry and subsequently applied to the more complex stress lattice to simulate the generated residual stresses. The mechanical behavior during quenching is experimentally determined using compression tests, and the resulting stress profiles of the stress lattice are validated by XRD measurements.

The following three key statements can be made:

- The applied model accurately reproduces the experimentally determined cooling curves for the plate geometry. The heat transfer coefficient values closely match those reported by Bamberger et al. [22] within their valid temperature range.
- Compression tests show that the initial yield strength $R_{p0.2}$ of EN AW-6016 exhibits a plateau between 100 °C and 300 °C, which might be explained by the effect of CCD. Additionally, precipitation can occur during isothermal holding, resulting in a complex temperature-dependent behavior.
- The simulation predicts a symmetrical residual stress profile along the examined path. In contrast, the XRD measurements show a slightly asymmetrical profile with a local peak. Overall, the absolute values tend to be underestimated by the simulation. While most areas along the surface path show good qualitative agreement between the simulation and measurements, there are still discrepancies that need to be addressed. To enhance the accuracy of the simulation, further refinement of the cooling conditions and the material description is necessary.

## ACKNOWLEDGEMENTS

The authors gratefully acknowledge the financial support of the Austrian Research Promotion Agency (FFG) and the German Federal Ministry of Economic Affairs and Energy as part of the Cornet/IGF research program in the research project 369 EN 'Integrated Data-based

Process Chain Optimisation in Casting and Machining – IDaP+' of the FQS-Forschungsgemeinschaft Qualität e. V.

Furthermore, the authors thank AMAG Rolling GmbH for the provision of materials and the X-Ray center (XRC) of the TU Wien for the X-Ray diffraction facilities.

## References

[1] CLEARWATER INTERNATIONAL: 'Prognose Zur Materialstruktur in Fahrzeugen Weltweit Im Jahresvergleich 2010 Und 2030', *Statista*, 2016, [Online], Available: https://de.statista.com/statistik/daten/studie/662213/umfrage/prognose-zur-materialstruktur-in-fahrzeugen/. [Accessed: 04-Aug-2025].

[2] CLEARWATER INTERNATIONAL: 'Prognose Zur Menge an Verarbeitetem Aluminium in Fahrzeugkarosserien Weltweit in Den Jahren 2010 Bis 2030', *Statista*, 2016, [Online], Available: https://de.statista.com/statistik/daten/studie/663340/umfrage/prognose-fuer-die-verarbeitete-menge-an-aluminium-in-fahrzeugkarosserien/. [Accessed: 04-Aug-2025].

[3] T. REEBER, M. SICKING, G. FUCHS, S. MAIER, L. HELML, A. KIRNBAUER, H.-C. MÖHRING, D. BIERMANN, W. VOLK, F. BLEICHER and P. H. MAYRHOFER: 'Integrated Data-Based Process Chain in Casting and Machining: A Concept for Holistic Process Improvements', *Production at the Leading Edge of Technology*, W.-G. Drossel, S. Ihlenfeldt, and M. Dix, eds., Springer Nature Switzerland, Cham, pp. 96-103, 2025, https://doi.org/10.1007/978-3-031-86893-1_11.

[4] M. LANDWEHR, F. OEHLER, H. BEHNKEN, H. HOLLING, R. SAMBATHKUMAR, P. GANSER and T. BERGS: 'Influence of Heat Treatment on the Residual Stress-Related Machining Distortion of Ti-6Al-4V Alloy Monolithic Parts', *Procedia CIRP*, 104, pp. 1328-1333, 2021, https://doi.org/10.1016/j.procir.2021.11.223.

[5] G. E. TOTTEN and D. S. MACKENZIE (eds.): *Handbook of Aluminum*, M. Dekker, New York, Basel, 2003.

[6] N. M. SIDDESH KUMAR, DHRUTHI, G. K. PRAMOD, P. SAMRAT and M. SADASHIVA: 'A Critical Review on Heat Treatment of Aluminium Alloys', *Mater. Today Proc.*, 58, pp. 71-79, 2022, https://doi.org/10.1016/j.matpr.2021.12.586.

[7] E. SJÖLANDER and S. SEIFEDDINE: 'The Heat Treatment of Al–Si–Cu–Mg Casting Alloys', *J. Mater. Process. Technol.*, 210(10), pp. 1249-1259, 2010, https://doi.org/10.1016/j.jmatprotec.2010.03.020.

[8] E. SJÖLANDER and S. SEIFEDDINE: 'Artificial Ageing of Al–Si–Cu–Mg Casting Alloys', *Mater. Sci. Eng. A*, 528(24), pp. 7402-7409, 2011, https://doi.org/10.1016/j.msea.2011.06.036.

[9] A. M. A. MOHAMED and F. H. SAMUEL: 'A Review on the Heat Treatment of Al-Si-Cu/Mg Casting Alloys', *Heat Treat. Conv. Nov. Appl.*, p. 55, 2012.

[10] J. S. ROBINSON, S. HOSSAIN, C. E. TRUMAN, A. M. PARADOWSKA, D. J. HUGHES, R. C. WIMPORY and M. E. FOX: 'Residual Stress in 7449 Aluminium Alloy Forgings', *Mater. Sci. Eng. A*, 527(10-11), pp. 2603-2612, 2010, https://doi.org/10.1016/j.msea.2009.12.022.

[11] K. ZHU, B. XIONG, X. LI, Y. ZHANG, Z. LI, Y. LI, K. WEN and L. YAN: 'Finite Element Simulation on Residual Stress during Immersion Quenching and Pre-Stretching of Al7055 Thick Plates', Mater. Res. Express, 9(2), p. 026525, 2022, https://doi.org/10.1088/2053-1591/ac565d.

[12] M. KOÇ, J. CULP and T. ALTAN: 'Prediction of Residual Stresses in Quenched Aluminum Blocks and Their Reduction through Cold Working Processes', *J. Mater. Process. Technol.*, 174(1-3), pp. 342-354, 2006, https://doi.org/10.1016/j.jmatprotec.2006.02.007.

[13] P. JEANMART and J. BOUVAIST: 'Finite Element Calculation and Measurement of Thermal Stresses in Quenched Plates of High- Strength 7075 Aluminium Alloy', *Mater. Sci. Technol.*, 1, p. 765, 1985.

[14] R. WANG, D. RAM, B. STAUDER, R. F. GUTIÉRREZ, E. GARIBOLDI and M. C. POLETTI: 'Stress Relaxation during Artificial Aging of an AlSi7Cu0.5Mg Cast Alloy', *Crystals*, 12(8), p. 1168, 2022, https://doi.org/10.3390/cryst12081168.

[15] L. A. GODLEWSKI, X. SU, T. M. POLLOCK and J. E. ALLISON: 'The Effect of Aging on the Relaxation of Residual Stress in Cast Aluminum', *Metall. Mater. Trans. A*, 44(10), pp. 4809-4818, 2013, https://doi.org/10.1007/s11661-013-1800-1.

[16] J. S. ROBINSON, D. A. TANNER and C. E. TRUMAN: '50th Anniversary Article: The Origin and Management of Residual Stress in Heat-treatable Aluminium Alloys', *Strain*, 50(3), pp. 185-207, 2014. https://doi.org/10.1111/str.12091.

[17] M. MANIRUZZAMAN and R. D. SISSON: 'Heat Transfer Coefficients for Quenching Process Simulation', *J. Phys. IV*, 120, pp. 521-528, 2004, https://doi.org/10.1051/jp4:2004120060.

[18] B. XIAO, Q. WANG, P. JADHAV and K. LI: 'An Experimental Study of Heat Transfer in Aluminum Castings during Water Quenching', *J. Mater. Process. Technol.*, 210(14), pp. 2023-2028, 2010, https://doi.org/10.1016/j.jmatprotec.2010.07.026.

[19] G. S. SARMIENTO, D. M. COSCIA, C. JOUGLARD, G. E. TOTTEN, G. M. WEBSTER, and J. VEGA: 'Residual Stresses, Distortion and Heat Transfer Coefficients of 7075 Aluminum Alloy Probes Quenched in Water and Polyalkylene Glycol Solutions', *ASM Int.*, Materials Park, Ohio, pp. 1118-1124, 2000.

[20] Y. N. LI, Y. A. ZHANG, X. W. LI, Z. H. LI, G. J. WANG, H. W. YAN, L. B. JIN and B. Q. XIONG: 'Effects of Heat Transfer Coefficients on Quenching Residual Stresses in 7055 Aluminum Alloy', Mater. Sci. Forum, 877, pp. 647-654, 2016, https://doi.org/10.4028/www.scientific.net/msf.877.647.

[21] X. YANG, J. ZHU, Z. LAI, Y. LIU, D. HE and Z. NONG: 'Finite Element Analysis of Quenching Temperature Field, Residual Stress and Distortion in A357 Aluminum Alloy Large Complicated Thin-Wall Workpieces', *Trans. Nonferrous Met. Soc. China*, 23(6), pp. 1751-1760, 2013, https://doi.org/10.1016/s1003-6326(13)62657-6.

[22] M. BAMBERGER and B. PRINZ: 'Determination of Heat Transfer Coefficients during Water Cooling of Metals', *Mater. Sci. Technol.*, 2(4), pp. 410-415, 1986, https://doi.org/10.1179/mst.1986.2.4.410.

[23] D. GREIF, R. KOPUN, N. KOSIR and D. ZHANG: 'Numerical Simulation Approach for Immersion Quenching of Aluminum and Steel Components', *Int. J. Automot. Eng.*, 8(2), pp. 45-49, 2017, https://doi.org/10.20485/jsaeijae.8.2_45.

[24] R. KOPUN, L. ŠKERGET, M. HRIBERŠEK, D. ZHANG, B. STAUDER and D. GREIF: 'Numerical Simulation of Immersion Quenching Process for Cast Aluminium Part at Different Pool Temperatures', *Appl. Therm. Eng.*, 65(1-2), pp. 74-84, 2014, https://doi.org/10.1016/j.applthermaleng.2013.12.058.

[25] V. SRINIVASAN, K.-M. MOON, D. GREIF, D. M. WANG and M. KIM: 'Numerical Simulation of Immersion Quench Cooling Process Using an Eulerian Multi-Fluid Approach', *Appl. Therm. Eng.*, 30(5), pp. 499–509, 2010, https://doi.org/10.1016/j.applthermaleng.2009.10.012.

[26] V. SRINIVASAN, K. MOON, D. GREIF, D. WANG and M. KIM: 'Numerical Simulation of Immersion Quench Cooling Process: Part I', *Volume 10: Heat Transfer, Fluid Flows, and Thermal Systems, Parts A, B, and C*, ASMEDC, Boston, Massachusetts, USA, pp. 1941-1954, 2008, https://doi.org/10.1115/imece2008-69280.

[27] V. SRINIVASAN, K.-M. MOON, D. GREIF, D. M. WANG and M. KIM: 'Numerical Simulation of Immersion Quenching Process of an Engine Cylinder Head', *Appl. Math. Model.*, 34(8), pp. 2111-2128, 2010, https://doi.org/10.1016/j.apm.2009.10.023.

[28] U. QUACK, W. STETS and G. WOLF: 'Messung Und Simulation von Eigenspannungen in Gusseisen', *Giesserei*, 97(11), p. 50, 2010.

[29] Y. MOTOYAMA, H. TAKAHASHI, T. OKANE, Y. FUKUDA and M. YOSHIDA: 'Numerical and Experimental Study on Residual Stress in Gray Cast Iron Stress Lattice Shape Casting', *Metall. Mater. Trans. A*, 44(7), pp. 3261-3270, 2013, https://doi.org/10.1007/s11661-013-1683-1.

[30] Y. MOTOYAMA, D. INUKAI, T. OKANE and M. YOSHIDA: 'Verification of the Simulated Residual Stress in the Cross Section of Gray Cast Iron Stress Lattice Shape Casting via Thermal Stress Analysis', *Metall. Mater. Trans. A*, 45(4), pp. 2315-2325, 2014, https://doi.org/10.1007/s11661-013-2126-8.

[31] E. M. JOHNSON, T. R. WATKINS, J. E. SCHMIDLIN and S. A. DUTLER: 'A Benchmark Study on Casting Residual Stress', *Metall. Mater. Trans. A*, 43(5), pp. 1487-1496, 2012, https://doi.org/10.1007/s11661-011-0907-5.

[32] P. HOFER, E. KASCHNITZ and P. SCHUMACHER: 'Distortion and Residual Stress in High-Pressure Die Castings: Simulation and Measurements', *JOM*, 66(9), pp. 1638-1646, 2014, https://doi.org/10.1007/s11837-014-1118-5.

[33] E. GUSTAFSSON, M. HOFWING and N. STRÖMBERG: 'Residual Stresses in a Stress Lattice–Experiments and Finite Element Simulations', *J. Mater. Process. Technol.*, 209(9), pp. 4320-4328, 2009, https://doi.org/10.1016/j.jmatprotec.2008.11.025.

[34] J. RÖSLER, H. HARDERS and M. BÄKER: *Mechanisches Verhalten der Werkstoffe*, Springer Fachmedien Wiesbaden, Wiesbaden, 2019, https://doi.org/10.1007/978-3-658-26802-2.

[35] L. SPIEß, G. TEICHERT, R. SCHWARZER, H. BEHNKEN and C. GENZEL: *Moderne Röntgenbeugung: Röntgendiffraktometrie für Materialwissenschaftler, Physiker und Chemiker*, Springer Fachmedien Wiesbaden, Wiesbaden, 2019, https://doi.org/10.1007/978-3-8348-8232-5.

[36] R. OVERFELT, S. BAKHTIYAROV and R. TAYLOR: 'Thermophysical Properties of A201, A319, and A356 Aluminium Casting Alloys', *High Temp.-High Press.*, 34(4), pp. 401-409, 2002, https://doi.org/10.1068/htjr052.

[37] M. B. GRIEB, H.-J. CHRIST and B. PLEGE: 'Thermomechanical Fatigue of Cast Aluminium Alloys for Cylinder Head Applications–Experimental Characterization and Life Prediction', *Procedia Eng.*, 2(1), pp. 1767-1776, 2010, https://doi.org/10.1016/j.proeng.2010.03.190.

[38] E. H. BUYCO and F. E. DAVIS: 'Specific Heat of Aluminum from Zero to Its Melting Temperature and beyond. Equation for Representation of the Specific Heat of Solids', *J. Chem. Eng. Data*, 15(4), pp. 518-523, 1970, https://doi.org/10.1021/je60047a035.

[39] E. KOZESCHNIK: 'Mean-Field Microstructure Kinetics Modeling', *Encyclopedia of Materials: Metals and Alloys*, Elsevier, pp. 521-526, 2022, https://doi.org/10.1016/B978-0-12-819726-4.00055-7.

[40] J. KREYCA and E. KOZESCHNIK: 'State Parameter-Based Constitutive Modelling of Stress Strain Curves in Al-Mg Solid Solutions', *Int. J. Plast.*, 103, pp. 67-80, 2018, https://doi.org/10.1016/j.ijplas.2018.01.001.

[41] W. A. CURTIN, D. L. OLMSTED and L. G. HECTOR: 'A Predictive Mechanism for Dynamic Strain Ageing in Aluminium–Magnesium Alloys', *Nat. Mater.*, 5(11), pp. 875-880, 2006, https://doi.org/10.1038/nmat1765.

[42] B. VIERNSTEIN, P. SCHUMACHER, B. MILKEREIT and E. KOZESCHNIK: 'State Parameter-Based Simulation of Temperature- and Strain Rate Dependent Flow Curves of Al-Alloys', *Light Met.*, pp. 267-271, 2020, https://doi.org/10.1007/978-3-030-36408-3_38.

[43] P. SCHUMACHER: *Plastisches Verformungsverhalten unterkühlter Aluminiumlegierungen im System Al-Mg-Si*, Dissertation, Universität Rostock, 2018.

[44] F. KABIRIAN, A. S. KHAN and A. PANDEY: 'Negative to Positive Strain Rate Sensitivity in 5xxx Series Aluminum Alloys: Experiment and Constitutive Modeling', *Int. J. Plast.*, 55, pp. 232-246, 2014, https://doi.org/10.1016/j.ijplas.2013.11.001.

[45] R. C. PICU, G. VINCZE, F. OZTURK, J. J. GRACIO, F. BARLAT and A. M. MANIATTY: 'Strain Rate Sensitivity of the Commercial Aluminum Alloy AA5182-O', *Mater. Sci. Eng. A*, 390(1-2), pp. 334-343, 2005, https://doi.org/10.1016/j.msea.2004.08.029.

[46] S. SAMANTA, J. R. SAHOO and S. MISHRA: 'Effect of Dynamic Strain Ageing on Flow Stress and Critical Strain for Jerky Flow in Al-Mg Alloys', *Int. J. Plast.*, 180, p. 104053, 2024, https://doi.org/10.1016/j.ijplas.2024.104053.

[47] S. L. YAN, H. YANG, H. W. LI and X. YAO: 'Variation of Strain Rate Sensitivity of an Aluminum Alloy in a Wide Strain Rate Range: Mechanism Analysis and Modeling', *J. Alloys Compd.*, 688, pp. 776-786, 2016, https://doi.org/10.1016/j.jallcom.2016.07.077.

[48] B. VIERNSTEIN, T. WOJCIK and E. KOZESCHNIK: 'State Parameter-Based Yield Strength Model for Integration in Finite Element User-Material Routines', *Metals*, 12(7), p. 1207, 2022, https://doi.org/10.3390/met12071207.

[49] Y. V. SHAN, B. VIERNSTEIN and E. KOZESCHNIK: 'Microstructure Evolution Subroutine for Finite Element Analysis', Math. Model. Weld Phenom., 13, pp. 407-412, 2023, https://doi.org/10.3217/978-3-85125-968-1-22.

# II Joint Properties

## c) Cracking Phenomena and Hydrogen Effects

# SIMULATION OF STANDARDIZED WELDABILITY TESTS AND LINKAGE WITH FRACTURE AND FATIGUE BEHAVIOR

H. FU* and H. F. NIED*

** Mechanical Engineering and Mechanics, Lehigh University, Bethlehem, PA 18015, USA*
*0000-0002-7668-0431, hfn2@lehigh.edu*

*DOI 10.3217/978-3-99161-089-2-027, license CC BY 4.0*
*https://creativecommons.org/licenses/by/4.0/deed.en*
*This CC license does not apply to third party material and content noted otherwise.*

## ABSTRACT

This study examines the thermo-mechanical strains and stresses experienced by test specimens during weldability qualification tests, with a specific focus on the popular Varestraint and Houldcroft tests. These weldability tests are commonly used to identify critical thresholds for the initiation of hot cracking during the welding process, as well as subsequent crack propagation behavior in the presence of weld-induced residual stresses. The computational analysis in this study is primarily focused on the implementation of finite element models developed using ANSYS and SYSWELD software to simulate the coupled thermo-mechanical behavior during weldability tests. A notable aspect of the Varestraint weldability test is the application of a sudden external load during the welding process, introducing an additional external mechanical strain component in the test specimen. During this loading, the metal in the cooling weld pool is highly susceptible to fracture and is most likely to exhibit "hot cracking" behavior. To accurately determine the localized strains associated with this phenomenon, the finite element models used in this study employ element “birth” and “death” techniques, enabling precise tracking of strain and stress variations over time. This study attempts to accurately quantify the critical threshold strains for hot cracking initiation based on modified Brittleness Temperature Range (BTR) curves. Simulations of room-temperature fatigue crack propagation under the influence of combined welding residual stresses and external mechanical loads are also included. This is enabled by incorporating R-ratio crack growth rate effects in the simulations. Ultimately these simulations provide a more detailed and comprehensive understanding of the failure mechanisms in welded joints. An interesting fatigue crack growth example presented in this study is the numerical simulation of fatigue crack propagation in welded structures subjected to purely compressive external loading (compressive fatigue).

Keywords: Weld Fracture, Fatigue Crack Growth, R-Ratio, Residual Stress, Houldcroft Test, Varestraint Test, Hot Cracking, Brittleness Temperature Range, Compressive Fatigue.

## INTRODUCTION

An important aspect of designing with welds in structural applications includes the anticipation of possible cracking during the welding process and/or subsequent cracking when the welded structure is subjected to external loads [1]. In addition to qualifying the welding metallurgy for specific welding applications, it is also important to accurately quantify the residual stresses that arise during welding and incorporate these stresses in the overall assessment of the likelihood of cracking and possible contribution to fatigue crack growth during service. Thus, it is not sufficient to simply consider the welding process in isolation, but for structural applications the weld design must also include a detailed stress analysis that includes a fracture assessment [1]. Fortunately, modern computational tools, e.g., finite element analysis (FEA), combined with significant improvements in computing power, have greatly improved the quality of large-scale numerical welding analyses for accurate structural stress and fatigue life analysis. Detailed fracture analysis can be linked with welding process simulations and conventional structural stress analysis to facilitate accurate predictions of fatigue crack growth behavior for critical structural applications.

There exist many historical structural failures that are directly attributed to cracking in welds, or cracking that originates in the Heat Affected Zone (HAZ) adjacent to the welds [1-2]. This cracking is usually attributed to metallurgical issues associated with the welding process and small cracks that are introduced into the highly stressed regions in, or adjacent to, the welds. Fig. 1 depicts an interesting example of an unusual structural failure that occurred in a bridge truss on the I-276 Delaware River Turnpike Bridge in New Jersey, USA, on a very cold day in December 2016. Fortunately, no one was injured when the heavy bridge truss suddenly fractured, but the bridge structure between the two supporting piers suddenly dropped approximately 5 cm and shifted loads to adjoining structural components that were not designed to carry this additional weight. In this case, weld filler metal had been used to "fill" improperly positioned bolt holes bored through the beam's flange during the bridge's construction. The fracture that severed the truss, initiated in a narrow zone between the weld filler metal and the boundary of the filled holes.

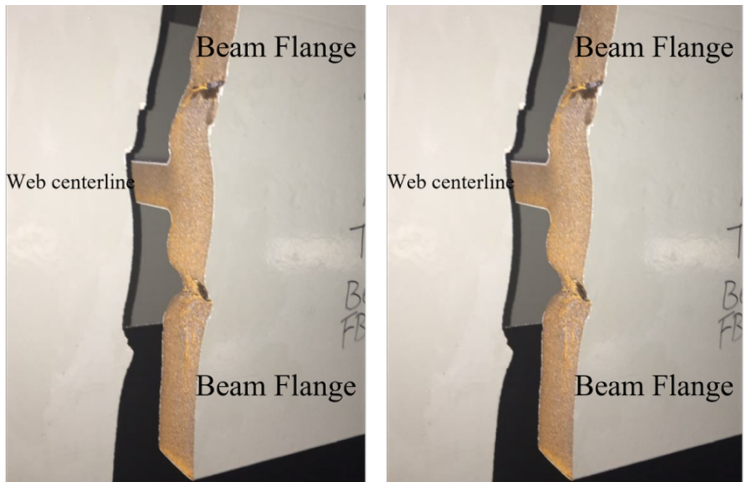



**Fig. 1** Example of Fracture Initiated from the Boundary of Holes Filled with Weld Metal. I-276 Delaware River Turnpike Bridge Truss (2016) [3] [1]

Poor quality welds with slag inclusions introduced crack defects on the circumferential boundaries of the filled holes and because the circa 1950's high-carbon steel used in the bridge construction had a high fracture toughness transition temperature; the result was catastrophic fracture on a cold day.

In most weld related structural failures, crack growth occurs over a long period of time with the primary driving force being an external alternating load. Thus, small flaws that may be introduced during welding, grow in a subcritical manner (fatigue crack growth), until either being detected through Non-Destructive Testing (NDT), or upon reaching a critical length resulting in unstable fracture. Fig. 2 shows cross-section photos from controlled fatigue crack growth experiments conducted at the Fraunhofer-Institut für Werkstoffmechanik (IWM), Freiburg, on welded stiffener test specimens subjected to alternating bending [4]. As demonstrated by the semi-elliptic crack growth shown in Fig. 2, fatigue cracking originates at the toe of the fillet weld and propagates in a plane perpendicular to the maximum tensile bending stress. The rate of crack growth is dominated by the change in the stress intensity factor, $\Delta K$ , along the crack front due to the applied alternating bending. The residual stresses introduced by the fillet weld also play an important, but secondary, role in the fatigue crack growth behavior. Crack initiation usually occurs at the location of the highest combined local principal stress, in this case at the stress concentration located at the toe of the fillet weld. In carbon steel alloys, crack initiation is also closely associated with the formation of brittle Martensite phase in the HAZ.

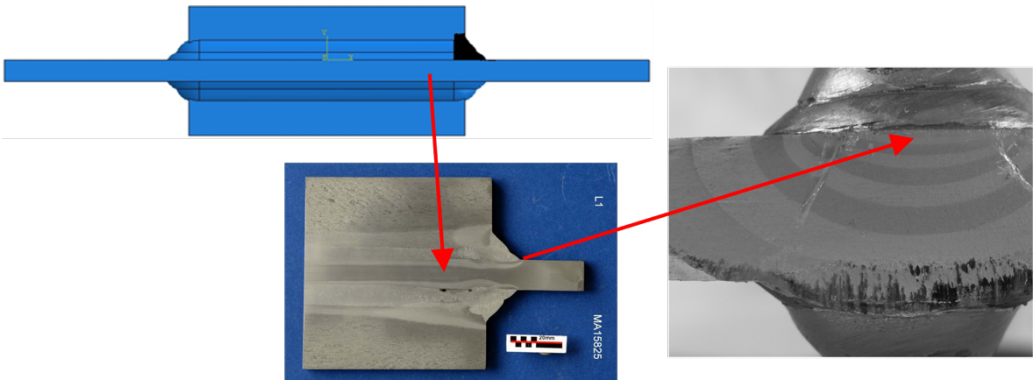



**Fig. 2** Fraunhofer IWM Longitudinal Stiffener Test Specimen with Fatigue Crack Initiation at Weld Toe [4]

Cracking that occurs during the weld solidification process, at temperatures between the liquidus and solidus temperature, is often referred to as "hot cracking" (Fig. 3). The formation of cracks as the weld cools occurs because the strains in the deposited weld metal have exceed some critical strain necessary for the formation of cracks in the central portion of the weld. A variety of qualitative weldability tests have been developed and standardized over the years for assessing a material's susceptibility to solidification cracking. The two tests of particular interest in this study are the Trans-Varestraint test and the Houldcroft "Fishbone" test. These tests are usually conducted in a welding laboratory to help determine appropriate welding process parameters and compatible filler metals needed to avoid hot cracking. Unfortunately, since these standardized tests do not consider detailed information about the stress/strain state in the weld region itself, they can only provide a qualitative sense of the "susceptibility" of crack formation in the weld metal. For example, using the Varestraint test, the imposed external bending strain is usually used to calibrate cracking susceptibility as a function of temperature using a criterion like the Brittleness Temperature Range (BTR) methodology [6]. But the imposed bending strain is not the total strain in the weld metal, which also includes the significant thermomechanical strains that develop in the weld as it cools and solidifies.



**Fig. 3** Example of Hot Cracking in a Fillet Weld [5]

As demonstrated in this paper, detailed welding simulations for these types of susceptibility tests, in conjunction with a critical strain criterion, e.g., the BTR methodology, provides a technique for developing quantitative tests that can provide the necessary data required for accurate prediction of crack initiation in structural welding applications. The BTR method can conveniently be used to define the critical strain values for weld metal cracking at different temperatures during solidification. The upper and lower temperature limits correspond to the weld metal's liquidus and solidus temperatures. As the temperature in the weld metal drops below its melting point and solidification begins, the strain-temperature relationship at specific points in the weld can be tracked. Comparison of the strain during solidification as a function of temperature with the critical strain obtained from an experimentally determined BTR curve, permits a quantitative assessment of the susceptibility of hot cracking for specific welding applications, i.e., if the strain at a given temperature exceeds the measured critical BTR strain, hot cracking will occur at that location in the weld.

Using modern computational techniques, it is feasible to: 1) accurately model the welding process and determine the local residual stress state in the neighborhood of the weld, 2) combine the welding residual stresses with complex external mechanical loading, and 3) accurately simulate 3-D fatigue crack growth based on postulated initial cracks starting from structural welds. As shown in this paper, this generally involves transferring intermediate welding stress results to finite element programs that can include external loading and efficient adaptive remeshing for the simulation of 3-D crack growth.

# NUMERICAL SIMULATION OF VARESTRAINT AND HOULDCROFT TESTS

## DESCRIPTION OF TRANS-VARESTRAINT TESTS

The two standardized weld cracking "susceptibility" tests modelled in this study are the Varestraint test and the Houldcroft "Fishbone" Test. The specific details associated with how these welding tests are conducted are described in many welding textbooks, e.g., [2]. The Varestraint hot cracking susceptibility test (Fig. 4) has two variations. The "regular" Varestraint test depicted in Fig. 4(a) uses a flat plate that is fixtured as a cantilever beam. The plate is suddenly bent to a specified radius of curvature on a bending block with a constant radius of curvature after the welding arc has reached the midpoint in the beam, as shown in Fig. 4(a). This causes an external mechanical bending strain component, acting parallel to the welding direction, that is accurately controlled by the radius of the Varestraint bending block. The key benefit of the Varestraint test is that the applied external strain can be easily controlled by using different radii bending blocks. The combination of the welding residual stresses during cooling and the external bending stress cause the formation of short cracks that are oriented perpendicular to the direction of motion of the weld arc.

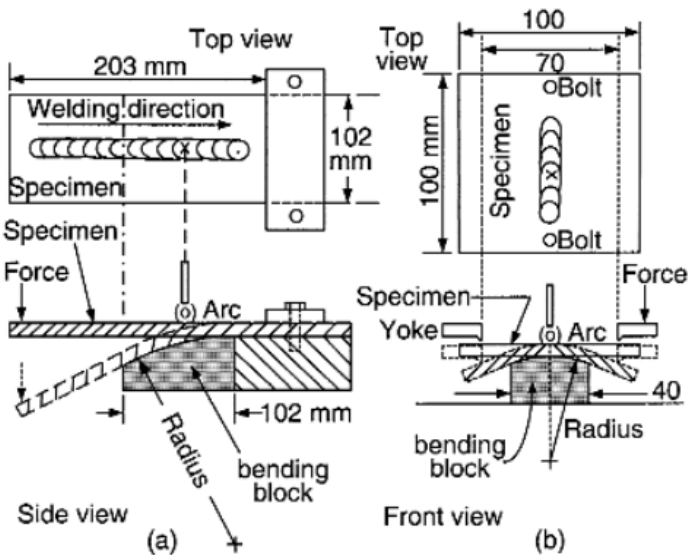
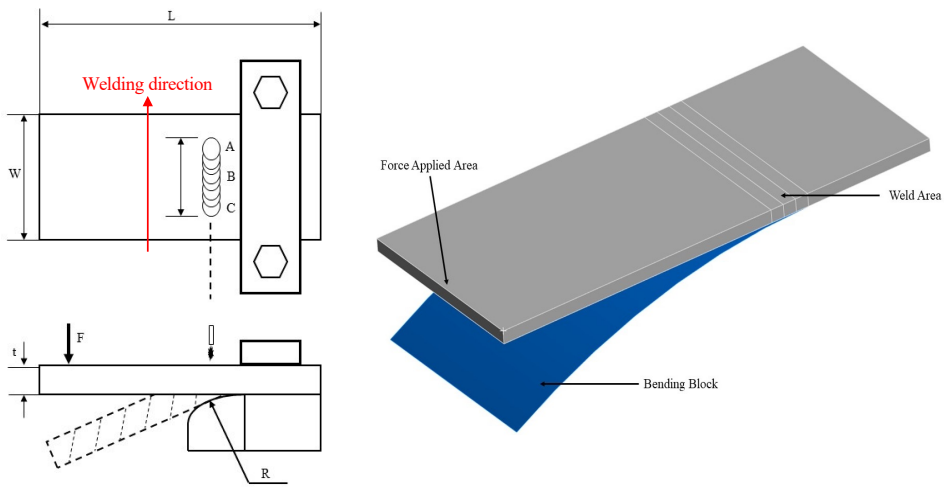



**Fig. 4** (a) Schematic of the Two Different Varestraint Tests: (a) Cantilever Beam Bending, (b) Transverse Bending [2]

The closely related alternative Trans-Varestraint test (Fig. 4(b)), applies an external mechanical bending strain transverse to the welding direction along the entire length of the weld. In the Trans-Varestraint test, cracks will form parallel to the welding direction, replicating the hot cracking seen in fillet welds (Fig. 3) and the cracking that is observed in the Holdcroft test (Fig. 11b). Modelling either type of Varestraint test requires a simultaneous welding and mechanical bending simulation. This is shown schematically in Fig. 5 for a cantilevered Trans-Varestraint test, where a flat plate with an autogenous weld that starts at point C and ends at point A, is bent to a specified radius of curvature on a supporting bending block when the moving weld arc reaches the center of the plate at point B (Fig. 5(a)). This introduces a controlled bending strain perpendicular to the length of the cooling weld. The application of bending deformation during the welding simulation complicates the analysis, since the hot weld metal, which has a very low mechanical stiffness, is also subjected to very large mechanical strains.




(a) (b)

**Fig. 5** (a) Schematic of Cantilevered Transverse Varestraint Test Configuration and (b) FEA Model used for Analysis of Combined Welding Residual Stresses and External Mechanical Bending [7]

The mechanical strains in the portion of the weld at temperatures above the melt liquidus temperature, where the stresses are close to zero, play no role in crack initiation after the weld has cooled and begins to solidify. But the transverse surface displacements between points C and A, which can be quite large, will contribute to the concentrated total strain behind the moving heat source as the weld solidifies. The Trans-Varestraint test was modelled using a combined welding and bending simulation model [7] developed using ANSYS [8] with life/death option elements. This resulted in stable numerical calculations during the entire Varestraint welding simulation.

## NUMERICAL SIMULATION OF TRANS-VARESTRAINT TESTS

Referring to Fig. 5(a), simulations of the Trans-Varestraint hot cracking susceptibility tests were performed on a plate with dimensions, L = 350 mm, W = 150 mm, t = 9 mm. Five different radii were used for the bending block: R = 4500 mm, 2250 mm, 1125 mm, 750 mm, 500 mm. Temperature dependent, rate independent, material properties for austenitic stainless steel (SS316) were used in the simulations. The relevant material properties are the thermal conductivity, specific heat, density, elastic modulus, coefficient of thermal expansion, and uniaxial yield strength. The thermomechanical properties of SS316 relevant for welding simulations with relatively rapid post-weld cooling are well-known and are readily available as a function of temperature, e.g., [9][9]. It should be noted that austenitic stainless-steel alloys do not exhibit the solid-state phase transformation volumetric strains observed in many other alloys, e.g., carbon steel. This simplifies the determination of the local strains for SS316.

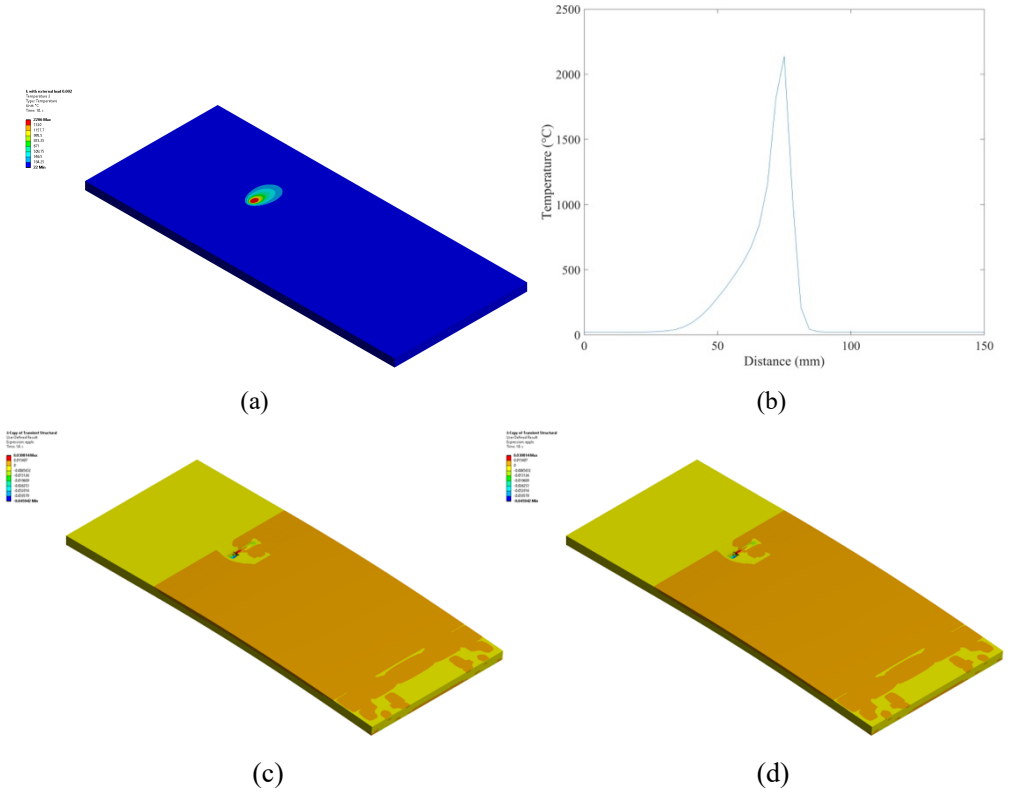



**Fig. 6** Hot Cracking Simulations for Trans-Varestraint Test. (a) Temperature Contours for Moving Weld Arc at Center of Plate, (b) Temperature Distribution on Weld Line, (c) Mechanical Strain Introduced by Bending Deformation (R = 2250 mm), (d) Total Combined Welding and Bending Strains (R=2250 mm, Heat Input 1600 W, v=2.5 mm/s)

However, the solid-state phase transformation volumetric strains can be included in hot-cracking simulations for carbon steels if the relevant experimental data is available [9]-[10]. The ANSYS finite element model for the Trans-Varestraint test, which combines welding simulation with a suddenly applied external bending displacement, [7], is shown in Fig. 6. This mesh contains 16,560 elements with 178,368 nodes. Details concerning sensitivity of local strains to mesh refinement and time increment step size are given in [7]. Figs. 6(a)-(b) depict the temperature distribution during the welding process when the arc has reached the center of the plate based on a double-ellipsoid moving heat source with a heat input of 1600 W and welding velocity of 2.5 mm/s. The peak temperature in the weld attains a maximum temperature of 2206° C, which well exceeds the melting point of SS316 ($T_m$ = 1400° C). Figs. 6(c)-(d) contain contour plots of the tensile strain distribution on the top surface of the Trans-Varestraint specimen perpendicular to the direction of the weld line. Fig. 6(c) depicts the mechanical bending strains acting on the weld line due to the deformation of the test specimen pressed against the radius bending block (R = 2250 mm). These are the strains that would typically be used for calibration of the Varestaint test, even though these strains do not incorporate any deformation behavior related to the welding process itself. The strain $\varepsilon_{xx}$ perpendicular to the weld line in Fig. 6(c), due to plate bending around the R = 2250 mm radius bend block, has a maximum strain of $\varepsilon_{xx} = 1.9 \times 10^{-3}$ (~0.2% strain) in the central portion of the plate between points C and A (Fig. 5(a)). On either side of the plate outside of the $\mathrm{C} \rightarrow \mathrm{A}$ weld zone, the strain slightly decreases to $\varepsilon_{xx} = 1.6 \times 10^{-3}$. Fig. 6(d) shows the much more complex combined thermal and bending strains shortly after the application of the bending deformation during the welding simulation. As shown in Fig. 6(d), the combined strains are not symmetric because of the nonuniform thermal strains associated with the moving heat source.

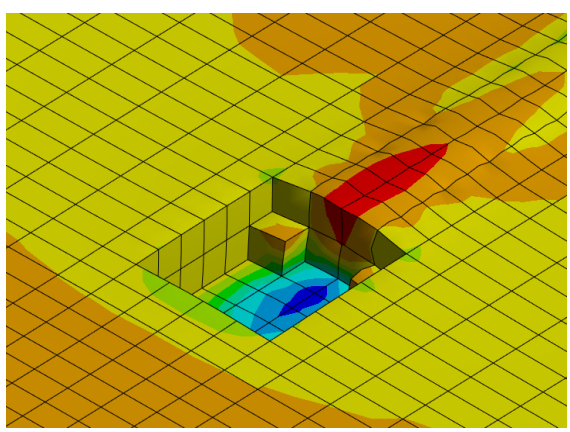


**Fig. 7**. Close-up View of Strain Contours from Fig. 6(d) with Elements Removed (Element Death Option) in the Portion of Melt Pool that Exceeds $T_{\mathrm{m}}$

Fig. 7 shows a close-up view of the finite element mesh details around the moving heat source with the elements in the molten zone (element "death" option) removed for better visualization of the local strains around the double-ellipsoid moving heat source. As can be seen in Fig. 7, large combined total thermomechanical strains occur immediately behind the molten weld pool where weld solidification begins while subjected to the applied bending deformation. This strain concentration effect has been noted by other authors based on finite element simulations of the Trans-Varestraint test using other types of models [11]-[12].

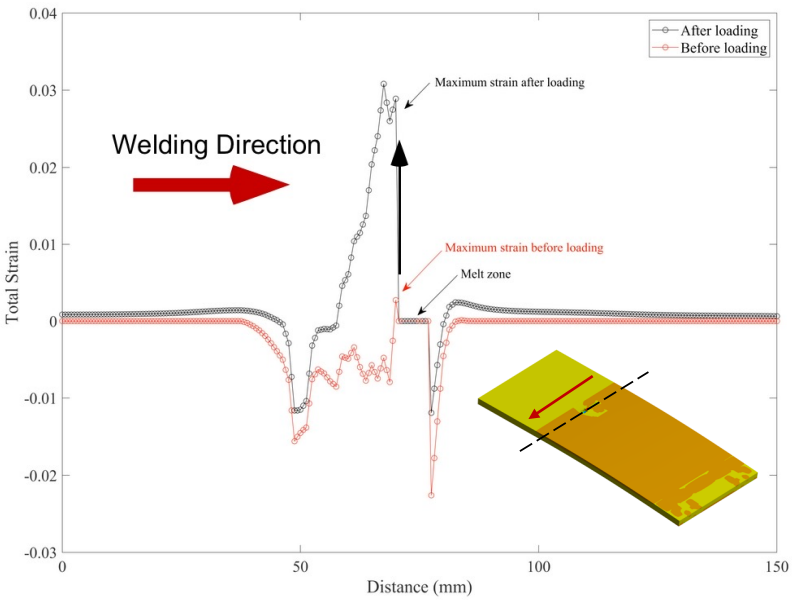



**Fig. 8**. Comparison of Welding and Mechanical Strains in Trans-Varestraint Test, Before and After the Application of the Bending Strain. Distance measured across the width of the plate (see Fig. 5(a))

Fig. 8 contains two plots that compare the total strain component perpendicular to the weld line across the entire width of the plate, just before, and after the application of the mechanical bending deformation. As can be seen in this figure, the thermal strains associated with the moving heat source are mostly compressive ahead of and behind the weld pool prior to the application of the bending displacements. Once the specimen is bent to the specified radius, the strains suddenly become tensile in the zone immediately behind the solidifying melt pool, due to a combination of the local tensile bending strain, the thermal strain associated with the cooling molten metal, and volumetric contraction during solidification. As shown in Fig. 8, the maximum total strain immediately behind the weld pool reaches a value of approximately $\varepsilon_{xx} = 0.03$, which exceeds the combined estimate for the local mechanical strain ( $\varepsilon_{xx} = 0.002$)

and the thermal strain ( $\varepsilon_{xx} = 0.0028$) by approximately a factor of 6x. This indicates that the total strain in the region immediately behind the cooling weld pool is dominated by the coupled thermomechanical strain and the volumetric strain associated with the phase change from the liquid to the solid state. This behavior in the local strains associated with the Varestraint test was also noted in [11]-[12]. As the weld continues to cool and solidify in the region behind the moving heat source, the total strain rapidly decreases, while the tensile residual stresses in the wake of the heat source significantly increases.

Repeating the above Trans-Varestraint simulations, using the same welding parameters, but varying the radii of curvature of the Varestraint bend block permits the construction of an "updated" BTR curve based on the original experimental BTR curve generated in [6], which only considered the specified mechanical bending strain. Fig. 9 provides a comparison between the original BTR curve obtained from [6] with a modified BTR curve generated in this study. Due to the inclusion of the local strains computed from the complete welding model, there is a significant upward shift in the critical strain as a function of temperature in the modified BTR curve. It is believed that the updated BTR curve provides a more accurate representation of the critical strain necessary for hot cracking that can then be used for the prediction of hot cracking using other welding process parameters and geometries – a conclusion also given by other authors [11]-[12]. This will be demonstrated for hot cracking predictions in Houldcroft test specimens.

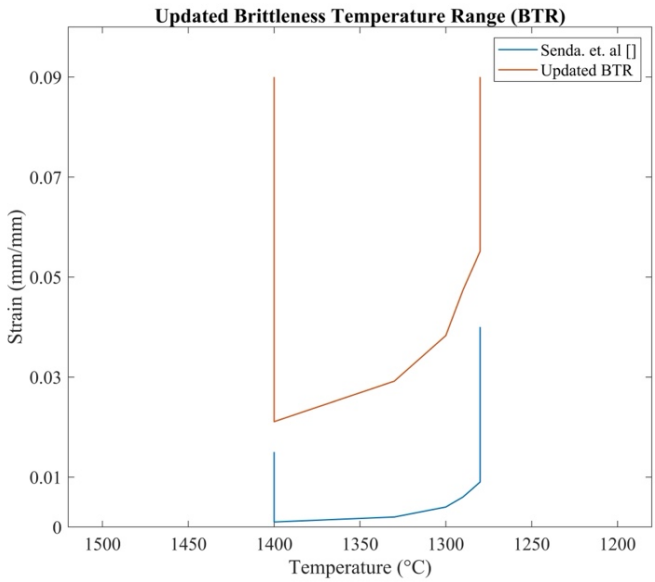



**Fig. 10**. Conventional BTR Curve (lower curve) Based on Mechanically Applied Bending Strains Only [6] and Comparison with Updated BTR Curve (upper curve) that Includes Total Welding Strains and Externally Applied Mechanical Bending

## DESCRIPTION OF HOULDCROFT TESTS

Fig. 11(a) shows the typical geometry of the Houldcroft Test. In the Houldcroft test, vertical slots are cut into a rectangular plate so that there is a variable degree of transverse constraint acting on the weld as it cools. If the constraint is great enough, then cracking will initiate in the region with the greatest constraint (between the smallest slots) and crack arrest will occur when the transverse constraint is insufficient to cause further crack growth (between longer slots).

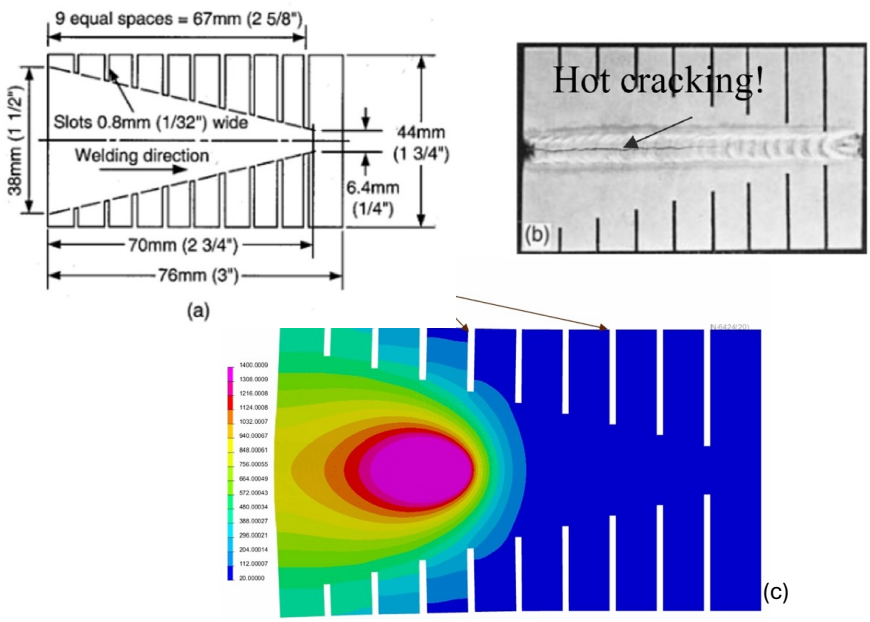



**Fig. 11**. (a) Schematic of Houldcroft "Fishbone" Test [2]. (b) Hot Cracking during Test [2]. (c) Welding Simulation of Houldcroft Test [7] using SYSWELD [9].

An example of hot cracking that can occur during a typical Houldcroft test is shown in Fig. 11(b). The numerical simulation of the Houldcroft test begins with the 3-D transient heat transfer simulation of the moving weld arc as shown in Fig. 11(c). In this study, the Houldcroft simulations were conducted using the FEA weld simulation software SYSWELD [9], [9]. Once the heat transfer calculation is completed, a full thermomechanical stress analysis provides the strains and residual stresses that are responsible for the initiation and propagation of horizontal cracks in the weld.

## NUMERICAL SIMULATION OF HOULDCROFT TESTS

Welding simulations of the Houldcroft susceptibility test were performed using the same material properties, austenitic stainless steel (SS316), that were used for simulating the Trans-Varestraint test. Fig. 12(a) depicts the Houldcroft plate geometry and Fig. 12(b) the

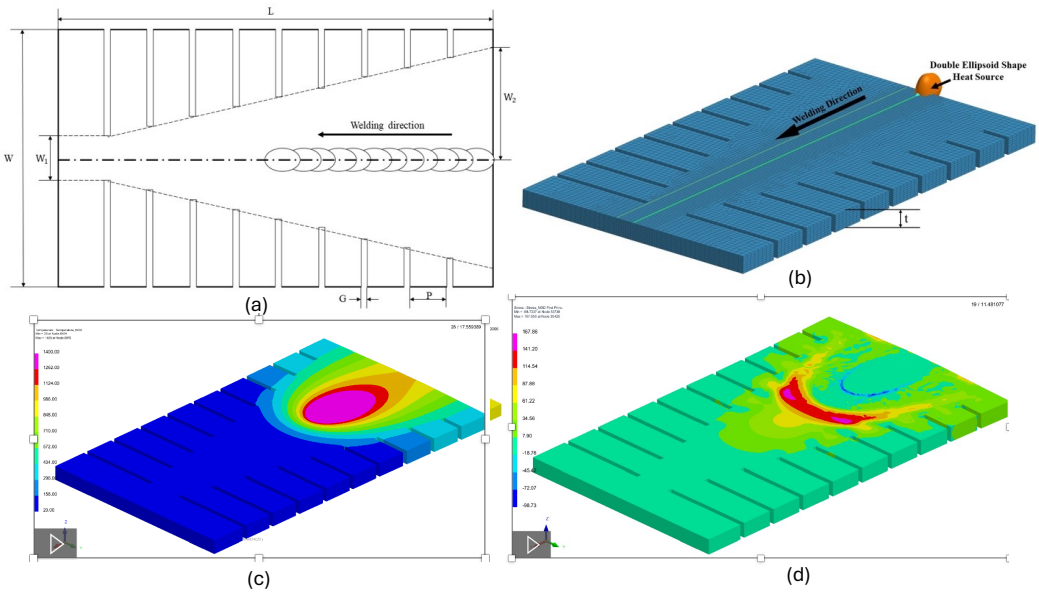



**Fig. 12.** FEA Simulation of the Holdcroft Test. (a) Geometry, (b) SYSWELD Mesh, (c) Temperature Contours, (d) First Principal Stress Contours

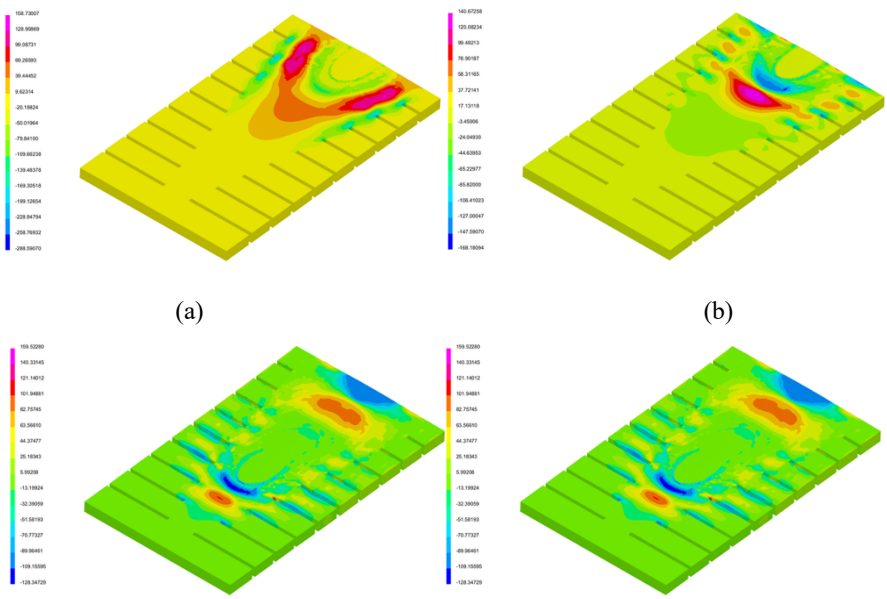
**Table 1**. Houldcroft Plate Dimensions (referring to Fig. 12)

| | **W** | **$W_1$** | **$W_2$** | **L** | **G** | **P** | **t** |
|---|---|---|---|---|---|---|---|
| **(mm)** | 44.6 | 7.72 | 38.78 | 76 | 1 | 6.5 | 3 |

**Table 2**. Constant Power Welding Heat Source for Houldcroft Test Simulations

| | **Constant Heat Input (1650 W)** | |
|---|---|---|
| | Heat input per unit length (J/mm) | Welding speed (mm/s) |
| **Case1** | 1850 | 0.893 |
| **Case2** | 1232 | 1.340 |
| **Case3** | 924 | 1.787 |

3=D finite element mesh. The plate geometric dimensions are given in Table 1. Three welding simulations with welding velocities and heat input per unit length (J/mm) used in the double ellipsoid heat source model, resulting in a constant heat input (W) are given in Table 2. In the 3-D SYSWELD model shown in Fig. 12 there are 65,196 elements and 75,178 nodes. Convective and radiative heat transfer boundary conditions were specified to simulate cooling in air. Fig. 12(c) shows the temperature contours for the moving heat source during an autogenous welding simulation, and Fig. 12(d) shows a typical principal stress contour.



(a) (b)

(c) (d)

**Fig. 13.** Welding Stresses in Holdcroft Test Configuration – Case 1. (a) Longitudinal Stress at t=5s, (b) Transverse Stress at t= 5s, (c) Longitudinal Stress at t=24s, (d) Transverse Stress at t=24s

Fig. 13 shows the contours for the longitudinal and transverse stress components during the Holdcroft welding simulation at two different times as the weld arc moves along the surface

of the plate. The strains at any specific point on the plate surface can be plotted as a function of time and temperature. For the three constant power input cases (1650 W) given in Table 2, the transverse strains as a function of time at a selected point 3.13 mm from the edge of the plate are shown in Fig. 14. By plotting the temperature vs strain on the modified BTR curve previously generated using the Trans-Varestraint simulation, it is possible to make hot cracking predictions in the Holdcroft test configuration. It is interesting to note that only Case 2, with a welding velocity of 1.340 mm/s, clearly falls into the hot cracking range as predicted by the BTR curve, i.e., for the constant heat input welding arc models, welding at a lower or higher velocities does not seem to be as likely to exhibit hot cracking behavior as the intermediate Case 2 velocity.

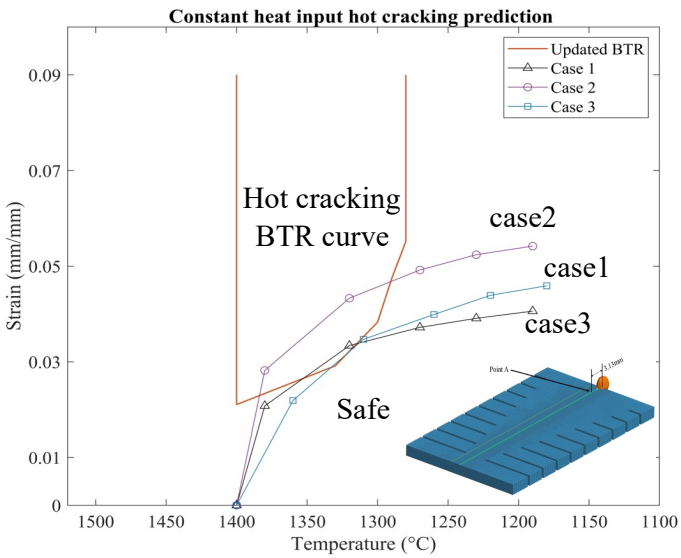
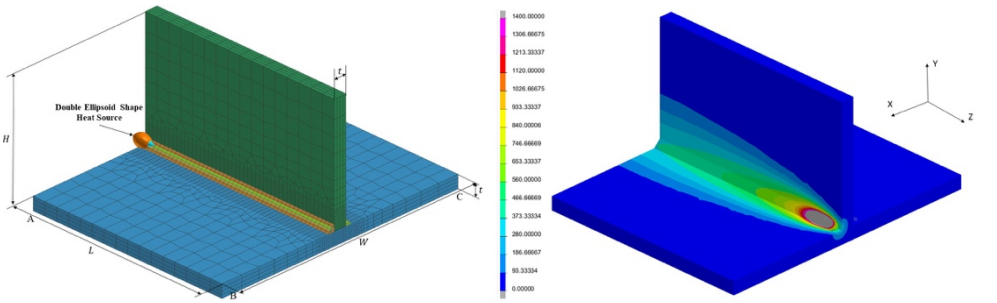



**Fig. 14**. Hot Cracking Susceptibility Predictions for Three Houldcroft Tests based on Modified BTR Curve and Constant Heat Input Weld Arc. Strains at Point A (x = 3.13 mm) as a Function of Temperature

## COMBINED WELDING AND FRACTURE SIMULATIONS

Once it is postulated that cracking may occur during welding, e.g., as predicted by the weld susceptibility tests described above, or if a fracture assessment is to be made based on crack initiation in locations of high stress concentrations, as depicted in Figs. 1 and 2, a 3-D fatigue crack propagation simulation can be performed. Fatigue crack propagation analysis can be used to provide a reasonable remaining life estimate based on experimentally measured fatigue crack growth rate data. The propagation of three-dimensional cracks should be performed considering both the external alternating loads as well as the welding residual stresses. In this

study, an example residual stress distribution is obtained for the SS316 fillet welded T-joint shown in Fig. 15(a), with the dimensions given in Table 3. The T-joint welding model was simulated in SYSWELD [9] to obtain the temperatures (Fig. 15(b)) and the welding residual stress distributions (Fig. 16) used as input for the fatigue crack growth simulation. For the fillet welded T-joint model shown in Fig. 15, there are 14,650 elements with 17,476 nodes. In the welding model, the heat input per unit length is specified to be 550 J/mm with the welding velocity given as 3 mm/s.

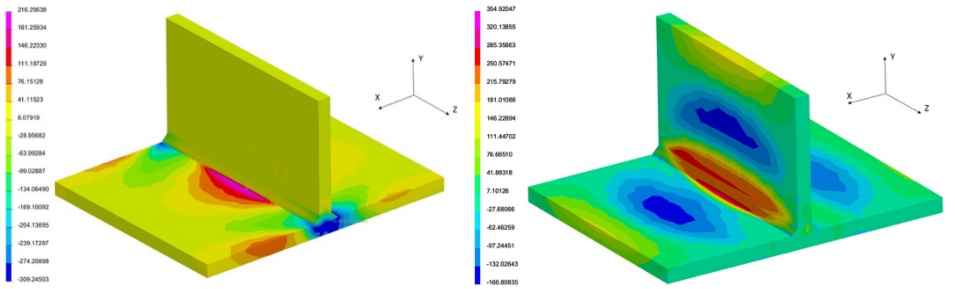



(a) (b)

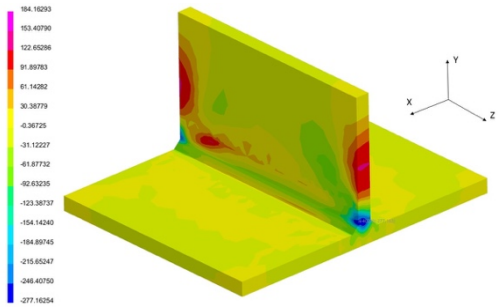
**Fig. 1**. (a) SYSWELD Finite Element Model with Dimensions and Boundary Conditions for Welded T-Joint. (b) Temperature Distribution Towards the End of the First Weld Pass

**Table 3**. Fillet Welded T-Joint Dimensions

| | **H** | **L** | **W** | **t** |
|---|---|---|---|---|
| **(mm)** | 60 | 96 | 120 | 6 |




(a) (b)




(c)

**Fig. 16**. Welding Residual Stresses for T-Joint with Fillet Welds. (a) Stress Component in x-direction Transverse to Weld, (b) Longitudinal Stresses, (c) Stresses in vertical direction

The stress contour plots shown in Fig. 16 contain the residual stresses in the three orthogonal directions after the welded T-joint has cooled down to room temperature.

To prepare the crack growth simulation model, two locations at the toe of the 1st fillet weld were chosen to simulate crack growth from small (2 mm radius) semicircular surface cracks subjected to both the welding residual stresses and an external alternating load. These locations are shown in Fig. 17(a), with one surface crack, Crack1, located at the highest stressed region in the central portion of the plate and another surface crack, Crack2, located at a relatively low stressed region at the fillet weld toe where there is a gradient in the transverse residual stress that will result in nonsymmetric crack growth.

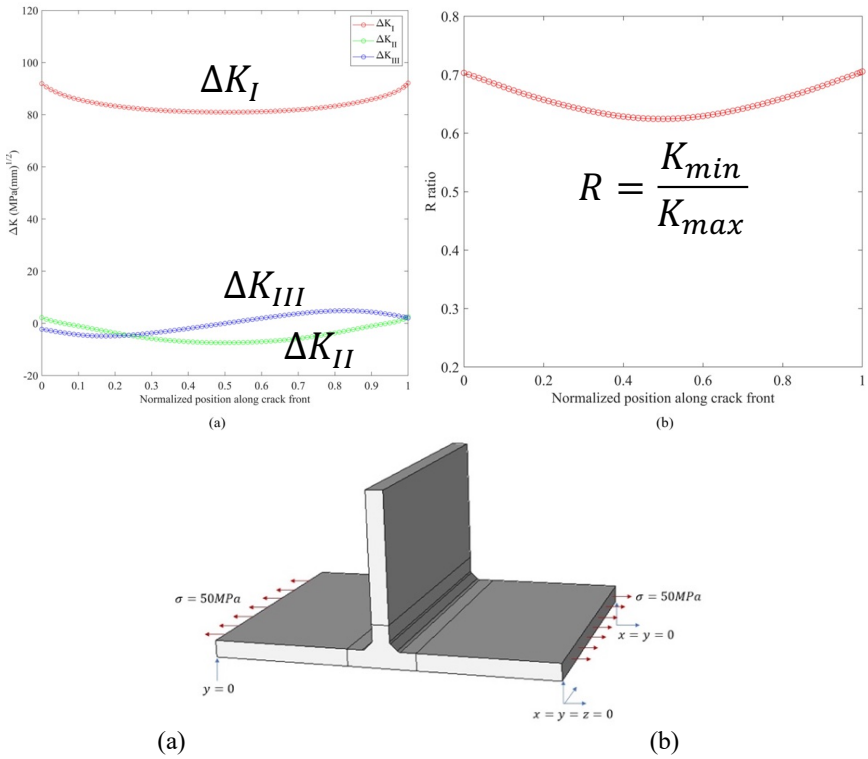



**Fig. 17.** (a) Selected Location for Placement of 2 mm Radius Semicircular Surface Cracks at Fillet Weld Toe. (b) Alternating External Loads, (0, +50 MPa, 0) for Fatigue Crack Growth

For simulation of 3-D crack growth, the residual stresses from the SYSWELD welding model shown in Fig. 16 are mapped to a different, more refined, finite element mesh generated using the automatic meshing program SimModeler [13]. Details concerning mapping of the SYSWELD generated residual stresses to a refined ANSYS mesh containing the embedded crack geometry, suitable for fracture analysis using SimModeler, are given in [7]. These mapped stresses can then be used as "initial" stresses in an ANSYS fracture calculation with the additional external loading boundary conditions shown in Fig. 17(b). The SimModeler meshing software permits the insertion of a surface crack geometry at specific locations in the original uncracked geometry and also automatically generates a highly refined "tunnel" mesh around the crack tip suitable for use in an ANSYS FEA model for the calculation of the stress intensity factors along the crack front. As the crack propagates in fatigue, the geometry changes and the finite element mesh is adaptively remeshed using the SimModeler meshing software. An alternating external (0, +50 MPa, 0) load as shown in Fig. 17(b), applied horizontally to the T-joint flange, provided the external fatigue loading for the simulation of fatigue crack growth in the presence of the existing welding residual stresses.

Incremental simulation of the directional crack growth in this study is based on the maximum circumferential stress criteria [14] where the crack front is advanced in a direction

perpendicular to the maximum local circumferential stress at the crack tip. The local maximum circumferential stress can be determined from the asymptotic crack tip stresses and is expressed in terms of the mixed-mode stress intensity factors $K_I$ and $K_{II}$ at any position along the crack front. Assuming that the critical principal stress for crack advance under mixed-mode conditions is identical to the critical stress necessary for crack growth under mode I conditions, the angle for crack advance $\theta_P$ can be determined from [14],

$$\left(\tan\frac{\theta_p}{2}\right)_{1,2} = \frac{1}{4}\frac{K_I}{K_{II}} \mp \frac{1}{4}\sqrt{\left(\frac{K_I}{K_{II}}\right)^2 + 8} \quad . \tag{1}$$

In (1), for $K_{II} > 0$, the negative sign is taken on the square root term and when $K_{II} < 0$ the sign is positive.

To properly simulate fatigue crack growth (FCG) under the influence of welding residual stresses, a fatigue crack growth rate law that incorporates the effect of the static residual stresses should include the R-ratio in the crack growth rate behavior. For this study, the Walker equation [15] given by

$$\frac{da}{dN} = C\left(\frac{\Delta K_{eq}}{(1-R)^{1-m}}\right)^n , \tag{2}$$

where $a$ is he crack length and $N$ is the number of alternating load cycles, provides a simple crack growth rate relationship with the R-ratio given by

$$R = \frac{K_{\min}}{K_{\max}} \quad . \tag{3}$$

In (2), the equivalent stress intensity factor $K_{eq}$ is defined as

$$K_{eq} = \sqrt{\left(K_I\cos^3\frac{\theta_p}{2} - 3K_{II}\cos^2\frac{\theta_p}{2}\sin\frac{\theta_p}{2}\right)^2 + \frac{K_{III}^2}{(1-\nu)}} \quad , \tag{4}$$

$$\Delta K_{eq} = K_{eq}^{\max} - K_{eq}^{\min} \quad , \tag{5}$$

$$K_{\min} = K_{RS} - K_L \, , \qquad K_{\max} = K_{RS} + K_L \quad . \tag{6}$$

In the above equations, $K_{\min}$ is the minimum stress intensity factor, $K_{\max}$ the maximum stress intensity factor, $K_{RS}$ the stress intensity factor due to the residual stresses, $K_L$ is the stress intensity factor caused by cyclic external loads, and ν is Poisson's ratio. For SS316 the

empirical constants used in the Walker equation (2) were adopted from [15] and are given by $n = 3.159$, $m = 0.32922$, and $C = 1.67154 \times 10^{-13}$ (mm/cycle)·((MPa·√mm)/(1-R)$^{0.67078}$)$^{-3.159}$.

Fig. 18 shows example fatigue crack growth simulation results for Crack1 subjected to the welding residual stresses located in the center of the plate flange, at the edge of the fillet weld toe, as shown in Fig. 17(a), with the alternating external loading shown in Fig. 17(b). In this case, the crack growth simulation continues until the crack grows to a depth of 4.75 mm after N = 20,657 cycles. Fig. 18(b) also contains a side view showing the plane of the crack and Fig. 18(c) shows the initial change in the stress intensity factors along the 3-D semicircular crack front at the beginning of the fatigue crack growth. As can be seen, the crack is dominated by the Δ change in the mode I stress intensity factor, which causes the crack to grow in a smooth planar manner.

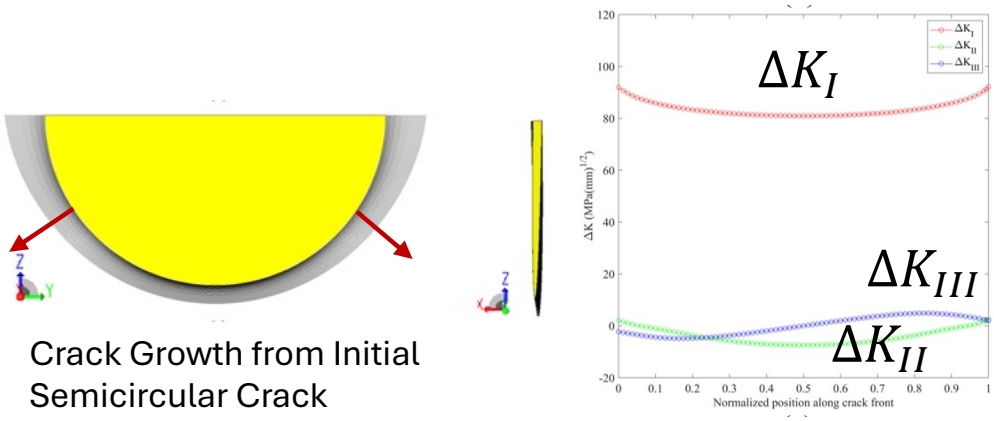
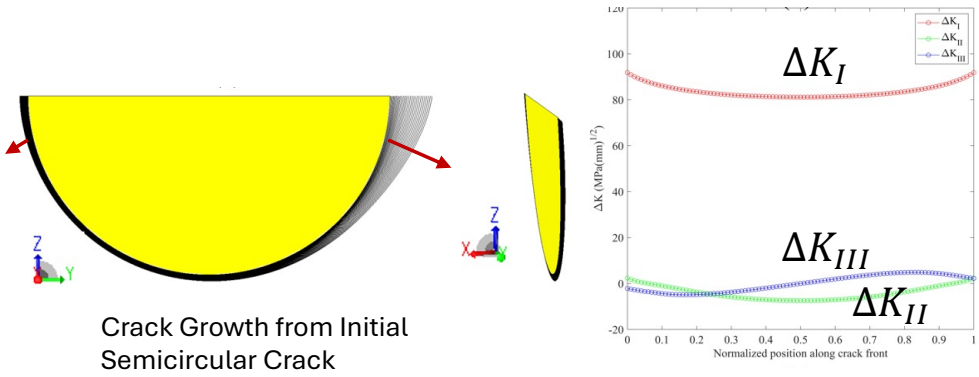



**Fig. 18**. (a) Close-up View of Fatigue Crack1 Simulation Results for Crack Located at Weld Toe using Walker equation, (b) Side View of Crack Growth Plane, (c) Initial Changes in the Stress Intensity Factors Along Semicircular Crack Front due to Alternating External Loading




(a) (b) (c)

**Fig. 19**. a) Fatigue Crack2 Simulation Results for Crack Located at Weld Toe using Walker equation showing Uneven Crack Growth, (b) Side View of Crack Growth Plane, (c) Initial Changes in the Stress Intensity Factors Along Semicircular Crack Front due to Alternating External Loading

Fig. 19 shows the crack growth behavior for the initially semicircular surface crack, Crack2, inserted into the location where there is a much smaller residual stress, but there is a strong stress gradient in the welding residual stresses in the plane of the crack. Since the Walker equation takes into account the influence of the stress ratio *R*, the crack will grow in an uneven manner as depicted in Fig. 19(a), with the more rapid crack growth occurring on the side of the crack subjected to the higher tensile residual stress (see Fig. 17(a)). To attain the crack shape shown in Fig. 19(a), required a much larger number of load cycles, N = 272,968, than for the crack located in the high residual stress region shown in Fig. 18. The nonsymmetry in the crack growth behavior is due to the variation in the R-ratio along the crack front and can be entirely attributed to the welding residual stresses. In this figure, the maximum R-ratio occurs at the right end of the crack front in Fig. 19(a), resulting in faster fatigue crack growth at this end of the crack front. The side view of the crack front shown Fig 19(b) shows that the propagating crack still remains planar. Fig. 19(c) contains the change in the stress intensity factors along the initial semicircular crack front at the beginning of the fatigue simulation. As expected, the change in the stress intensity factors are essentially identical to the stress intensity factors for the crack located in the region with the higher welding residual stresses. This is because the alternating external load, which is identical for both cracks, provides the dominant crack driving force. Though the welding residual stresses play a secondary role in the fatigue crack propagation rates through the R-ratio, it is still the welding residual stresses, in combination with local stress concentration effects, that determines the location of where cracking will initiate.

An interesting and somewhat unusual fatigue crack growth problem can occur in welded structures subjected to only compressive external loading [16]. An example simulation of this phenomenon is demonstrated using the external loading shown in Fig. 20.

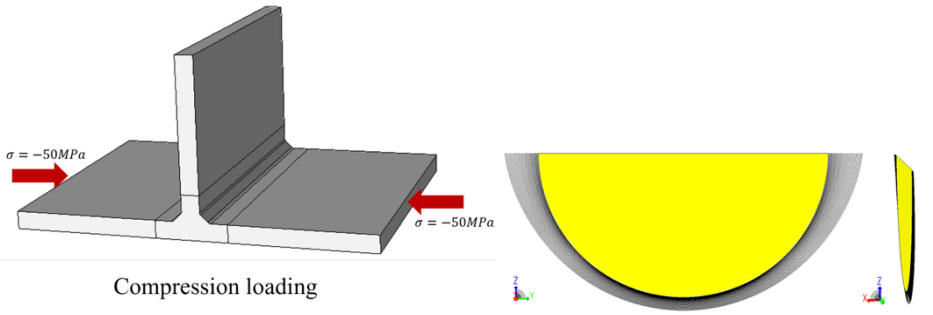



**Fig. 20**. Fatigue Crack Growth for Initial (2 mm radius) Semicircular Surface Crack (Crack1) at Weld Toe Subjected to Alternating Compressive Loads

In this example, the flanges of the T-Joint are loaded in uniform cyclic compression (-50 MPa, 0, -50 MPa). In the absence of any residual stresses, preexisting cracks would not be expected to grow in fatigue. However, in the region of the fillet weld with the tensile residual stresses shown in Fig. 17(a), cracks, e.g., Crack1, will experience a positive ΔK on each load cycle when the -50 MPa load is released. Thus, incremental crack growth will occur every time the flange plate is unloaded. The resulting crack growth behavior is depicted in Fig. 20, where the fatigue crack growth was simulated using the Walker crack growth rate law (2). For the semicircular crack to attain the shape shown in Fig. 20 required N = 47, 041 cycles, more than double the number of cycles needed to obtain approximately the same crack growth (Fig. 18(a)) when the T-Joint is subjected to positive alternating load cycles of the same magnitude.

Fig. 21 contains plots of the positive changes in the stress intensity factors for the compressive alternating loading shown in Fig. 20. The positive ΔK due to unloading is essentially identical to the positive ΔK that occurs for the tensile alternating external loading shown in Fig. 18.

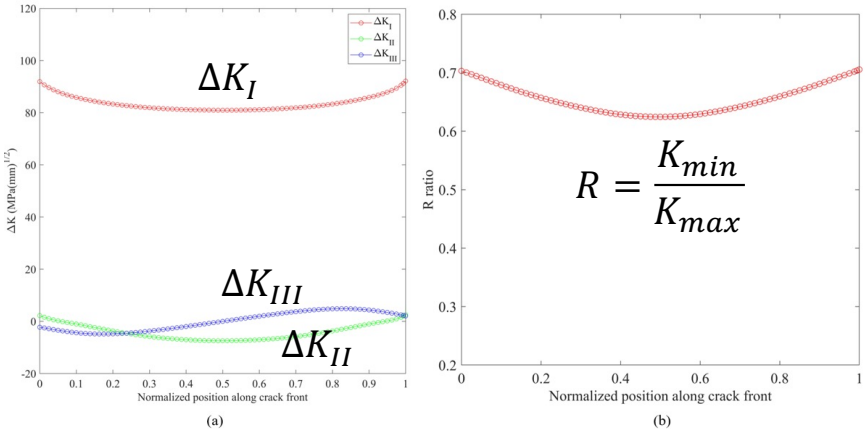



**Fig. 21**. (a) Initial Changes in Stress Intensity Factors Along Crack Front due to Alternating Compressive Loading and Welding Residual Stresses, (b) R-Ratio Along Crack Front

## CONCLUSIONS

Two different types of cracking phenomena were investigated in this paper. The first type of cracking behavior is related to the hot cracking susceptibility tests that are routinely conducted when qualifying new welding processes and determining the weldability of new metallurgical alloys. The detailed numerical simulations presented in this paper demonstrate the feasibility of accurately determining the highly localized strain concentrations that occur at the trailing edge of the cooling weld pool in the Trans-Varistraint test and use welding simulations to update existing BTR curves for improved hot cracking predictions in structural welding applications. Application of this methodology allows one to use the qualitative Trans-Varistraint test results in a quantitative manner for making hot cracking predictions in welding applications with entirely different conditions than the Trans-Varistraint test. An example of this is given for predictions of hot cracking in the Houldcroft test configuration.

The second type of cracking behavior examined in this paper is associated with the modelling of fatigue crack growth behavior in welded structural components. The methodology for incorporating the static welding residual stresses is demonstrated by first obtaining the welding residual stresses using a dedicated FEA welding simulation software package (SYSWELD). Then “mapping” the resulting residual stresses to a finite element program more suitable for detailed crack growth analysis (ANSYS). This is facilitated by using specialized meshing software (SimModeler) that generates adaptive meshes for growing fatigue cracks in the presence of welding residual stresses. The welding residual stresses contribute primarily to fatigue crack growth through the R-ratio effect. Inclusion of R-Ratio effects is of importance in the assessment of fatigue fracture behavior for welded structures. It is demonstrated in this paper that fatigue crack growth, which incorporates the contribution of the welding residual stresses, can be efficiently performed for critical structural

applications. This is demonstrated by the interesting example of compressive fatigue, where crack growth is possible due to the application of cyclic compressive loading only because of the presence of internal welding residual stresses.

## ACKNOWLEDGEMENTS

The authors gratefully acknowledge the academic licenses and software provided by ANSYS, ESI (SYSWELD) and Simmetrix, Inc. (SimModeler) used to develop the simulation models in this study. The authors would like to specifically express their appreciation for the technical assistance provided by Mr. R. Silva (ESI, Inc.) and Dr. A. Loghin (Simmetrix, Inc.).

## REFERENCES

[1] K. MASUBUCHI: *Analysis of Welded Structures*, Pergamon Press, 1980.
[2] S. KOU: *Welding Metallurgy*, 2nd ed., Wiley-Interscience, 2002.
[3] J. DUPONT, H. NIED, R. SAUSE: 'Material Testing and Fracture Analysis of a Truss Cord Member from the NJTA/PTC Delaware River Bridge (Phase 2), Final Report', *ATLSS* No. 17-08, 2017.
[4] H. NIED, D. SIEGELE: 'Study of the Influence of Material and Welding Modeling on the Residual Stresses in Longitudinal Stiffeners', *66th Annual Assembly and International* 19 *Conference, Commission XIII Fatigue of Welded Components and Structures*, Doc. XIII-2479-13, International Institute of Welding, Essen, Germany, Sept. 11-15, 2013.
[5] P. NANAVATI: 'Cracking in the Weld Joint Between X2CrNi12 and CS Joints using E3098L Filler?', *Welding Metallurgy Articles*, https://weldingknowledge.co.in/2021/02/17/cracking-in-the-weld-joint-between-x2crni12-and-cs-joints-using-e309l-filler/, 2021.
[6] T. SENDA, F. MATSUDA, G. TAKANO, K. WATANABE, T. KOBAYASHI, T. MATSUZAKA: 'Fundamental Investigations on Solidification Crack Susceptibility for Weld Metals with Trans-Varestraint Test', *Transactions of the Japan Welding Society,* 2, 2, 45-66, 1971.
[7] H. FU: 'Simulation of 3-D Crack Growth in Welded Structures based on Residual Stresses Obtained from Detailed Welding Process Models'*, Ph.D. Dissertation*, Lehigh University, 2025.
[8] ANSYS, Version 12.0 Ansys Inc. Canonsburg, PA, USA, 2009.
[9] SYSWELD 2021.0 – Documentation Package, ESI North America, Farmington Hills, MI, 2021.
[10] A. ALRUMAYH, H. NIED: 'Simulation of Residual Stresses During the Wire Arc Additive Manufacturing (WAAM) Process', *Mathematical Modelling of Weld Phenomena 13*, Verlag der Technischen Universität Graz, pp. 283-303, 2023.
[11] Y. WEI, Z. DONG, R. LIU, Z. DONG: 'Modeling the Trans-Varestraint Test with Finite Element Method', Comp. Mat. Sci., 35, 84-91, 2006.
[12] S. MAEDA, W. WANG, M. HABATA, K. IKUSHIMA, M. SHIBAHARA: 'Mechanical Study of Trans-Varestraint Test by Using Numerical Analysis of Cracking Based on Idealized Explicit FEM ', Quarterly J. of the Japan Welding Society, 41, 2, 21s-25s, 2023.
[13] SIMMETRIX INC, SimModeler Crack 11.0, Installation, User Guide Release Notes, 10 Executive Park Drive, Clifton Park, NY 12065 USA.
[14] F. ERDOGAN, G. C. SIH: 'On the Crack Extension in Plates Under Plane Loading and Transverse Shear', J. Basic Eng., 85(4), 519-525, 1963.
[15] R. J. SANFORD: Principles of Fracture Mechanics, Prentice Hall, 2003.

[16] D. MALSCHAERT, M. VELJKOVIC, J. MALJAARS: 'Numerical Simulations of Residual Stress Formation and Ist Effect on Fatigue Crack Propagation in a Fillet Welded T-Joint', *Eng. Frac. Mech.*, 306, 2024.

# EXPERIMENTAL AND NUMERICAL STUDY ON DUCTILITY CAPACITY FOR SOLIDIFICATION CRACKING IN LASER BEAM WELDING

N. HABIBI*, A. GUMENYUK*, M. RETHMEIER**,*,***

**Bundesanstalt für Materialforschung und -prüfung (BAM), 12205 Berlin, Germany*
***Technische Universität Berlin, 10587 Berlin, Germany*
****Fraunhofer Institute for Production Systems and Design Technology IPK, 10587 Berlin, Germany*

*DOI 10.3217/978-3-99161-089-2-028, license CC BY 4.0*
*https://creativecommons.org/licenses/by/4.0/deed.en*
*This CC license does not apply to third party material and content noted otherwise.*

## ABSTRACT

Solidification cracking remains a critical challenge in laser beam welding, influenced by thermal, metallurgical, and mechanical factors. This study investigates the local conditions that contribute to this phenomenon in stainless steel 304 by measuring the temperature and strain evolution in the critical region. A custom measurement system was developed to estimate local temperature, strains, and strain rates, during controlled tensile weldability (CTW) experimental tests. This method enables a direct assessment of crack onset by applying a defined strain and strain rate during welding. To complement experimental findings, a parallel numerical study was conducted using a three-dimensional finite element (FE) model in ANSYS to trace the strain and stress development. The model incorporated sub-modeling of the critical area using predefined boundary conditions. This approach allows for the optimization of mesh size and time step to minimize numerical artifacts. Numerical results showed good agreement with experimental, in terms of level and distribution of temperature and strain, confirming the model's reliability. An iterative simulation approach was used to determine the critical strain conditions leading to crack initiation. These results were constantly compared with the experimentally observed data. This integrated method sheds light on the evolution of ductility and local straining conditions, enabling a more precise assessment of solidification cracking susceptibility. Corresponding author: andrey.gumenyuk@bam.de.

Keywords: Solidification Cracking, Laser Beam Welding, Finite Element Method

## INTRODUCTION

Laser beam welding (LBW) is increasingly used in advanced manufacturing due to its precision, flexibility, and contactless operation, which enable it to be applied in aerospace, automotive, medical, and energy industries, where high weld quality is required. However, its

effectiveness is often limited by solidification cracking, which can significantly reduce weld integrity and component safety [1].

Solidification cracking occurs in the mushy zone, the liquid-solid region between the advancing molten pool and the fully solidified weld metal. This region is bounded by the liquidus and solidus isotherms. In LBW, columnar dendritic grains typically dominate this zone unless grain refinement measures are applied [2]. As the weld cools and solidifies, the mushy zone undergoes thermal and solidification shrinkage. Because this contraction is restrained by the surrounding cooler base material, tensile stresses develop, which may separate the dendritic grains and initiate cracking [3]. Furthermore, the ductility of the material decreases significantly within this temperature range, and when the strain imposed on the mushy zone exceeds the available ductility, solidification cracking is likely to occur [4,5]. Several approaches have been developed to evaluate cracking susceptibility in LBW. Prokhorov [6] proposed the use of high-temperature ductility curves, from which the brittleness temperature range (BTR) can be derived. The BTR has been widely used to assess cracking susceptibility because larger BTR values indicate a higher risk of cracking [7].

Rappaz et al. [8] developed a microscopic model for hot tearing based on mass balance between thermal shrinkage and liquid feeding in the mushy zone, introducing RDG criteria based on critical strain rate at the end of solidification. Vernède and Dantzig [9] further elaborated on the mechanical behaviour of alloys during solidification using a mesoscale granular approach. Bellet et al. [10] proposed finite element approaches for thermomechanical simulation of hot tearing during arc welding of stainless steel, accounting for constitutive behaviour in the semi-solid state.

Experimental approaches determining the hot cracking behaviour of welded materials are based commonly on application of external loading of welding specimen combined with measurement of local strain close to the mushy zone or near to the solidification front.

In this regard, Shinozaki et al. [11] employed the U-type hot cracking test with in-situ observation during welding, which was improved in the further study [12] by higher quality imaging. Although this technique provided novel information about solidification cracking, it cannot capture the local strain history, which is essential for defining independent failure strains. To address these issues, promising works with optical measurement was conducted using optical flow technique [13,14]. However, this method only focuses on strains at the surface which is typically not the crack initiation site.

To overcome these challenges, the present work simulates solidification cracking through a controlled hot cracking experiment to provide deeper insight into this phenomenon. It is worth noting that significant contributions to thermomechanical modelling of hot tearing and solidification cracking have previously been made at the microscale. The present work operates at a larger, component-level scale, using a macroscopic FE model to predict crack onset conditions from experimentally applied boundary conditions, and is thus complementary to these microscale approaches.

## EXPERIMENTAL PROCEDURE

The solidification cracking was studied on an austenitic stainless steel sheet of AISI 304 (1.4301) with a thickness of 1 mm through controlled tensile weldability (CTW) test, figure 1. This test developed at the Bundesanstalt für Materialforschung und -prüfung (BAM) in Berlin, is a hot-cracking assessment method. It uses a horizontal tensile testing setup with a 500 kN load capacity, capable of applying a planar tensile strain perpendicular to the welding direction at a controlled rate during welding. The test's principle involves adjusting the local strain rate near the mushy zone by systematically changing the overall applied strain rate (i.e., the cross-head speed). By observing whether cracks form or not, the test determines the critical global strain and strain rate that lead to cracking [15]. In this regard, the test performed in three stages: first, welding stabilization for 35 mm welding with no applied strain; second, the application of external loading at the defined global strain rate until the global strain was reached; and third, the global strain level was held at a constant value until the welding process was ended, when the total weld length is 100 mm. Afterwards, the possibility of hot cracking is investigated at the weld seam through X-ray radiography. As shown in figure 2, in this work, the CTW tests were performed at global strain rates of 0.02, 0.04, 0.06, and 0.08 s-1 at global strains of 0.02, 0.025, 0.03, and 0.035. Since this test forces the solidification cracking form at the centerline of the mushy zone, the track of cracking at the surface becomes easily possible. To measure the local distribution of temperature and strain, the set-up was equipped with a two-color pyrometer, a thermal SWIR [16] double-band camera, and a high-resolution sCMOS camera (the last one is not considered in this paper, detailed information is available in Ref. [17]). Figure 1. The welding parameters were selected to ensure fully penetration of the weld, i.e. a laser power of 1 kW and a constant welding speed of 1 $m.min^{-1}$, under the shielding gas of argon supplied through the lateral nozzle at the flow rate of 20 $min^{-1}$. For this study, the failure condition with strain of 0.025 and strain rate 0.06 $s^{-1}$ was selected for the elaborate study through FE simulations.

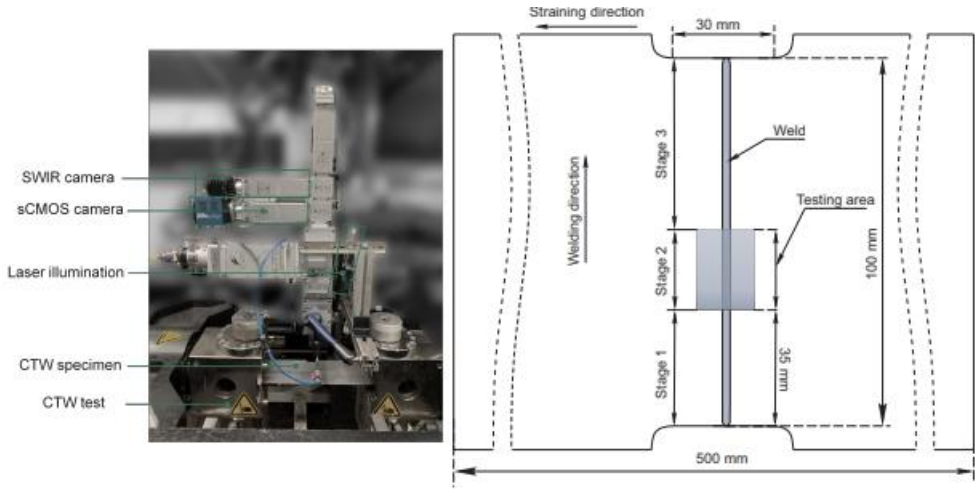



**Fig. 1** (Left) The instrumented CTW-test set-up. (Right) The CTW specimen [14]

| | |
|---|---|
| + | No crack |
| – | Crack |
| | N. A. |

| $\dot{\varepsilon}$ (s$^{-1}$) \ $\varepsilon_{max}$ | 0.02 | 0.025 | 0.03 | 0.035 |
|---|---|---|---|---|
| **0.02** | + | + | – | – |
| **0.04** | + | + | – | –– |
| **0.06** | + | – | –– | –– |
| **0.08** | + | – | –– | –– |

**Fig. 2** The weldability limits of AISI 304 through CTW tests

## NUMERICAL PROCEDURE

Since cracking initiates in the center of thickness, the failure conditions cannot be defined precisely by the experimental set-up. Therefore, a three-dimensional FE model was developed using ANSYS Parametric Design Language (APDL). A full CTW specimen was designed with the adaptive meshing pattern to reduce the computation time. Thus, the fine elements of 0.185 mm × 0.185 mm × 0.2 mm were defined in the critical region, illustrated as the global-model in Fig. 3. The thermal and mechanical properties of the material were defined for a wide range of temperatures from 0 to 1500 °C, which were taken from the material library of Sysweld software [18], Fig. 4. Although the whole procedure modelled similar to the experiments, the laser beam was initially located not at the edge but 5 mm inside of the specimen, to escape the need for application transient thermal model at the process start and to eliminate any convergence problem.

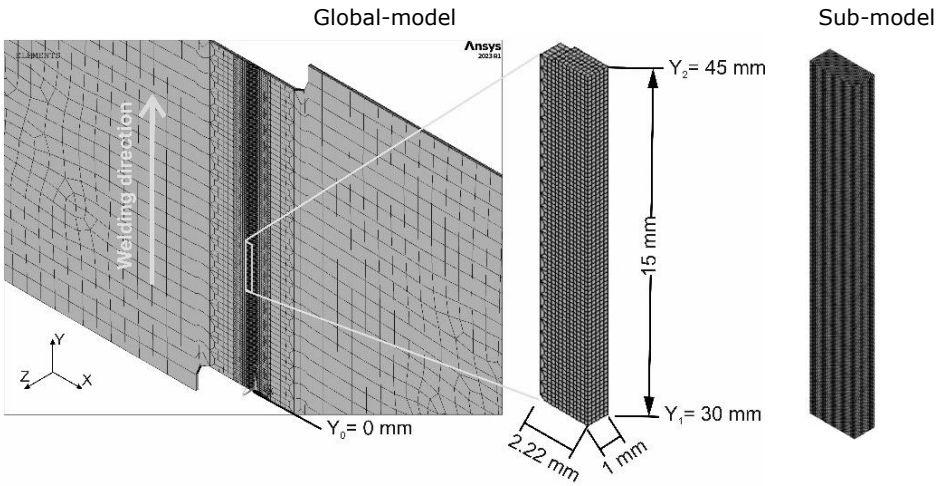



**Fig. 3** The simulation model; (Left) Global-model; (Right) Sub-model

First, the thermal analysis was performed to determine the temperature history. Then, the temperature results were applied incrementally to the mechanical model to calculate stresses and strains. A step size of 0.01 s was defined for both simulations. For thermal model, an equivalent heat source with Dirichlet boundary condition was defined as the melt pool which had the homogeneous temperature of 1460 °C (liquidus temperature). Only the conductive mode was considered for heat transfer, and convection and radiation modes were neglected. The element type was defined as SOLID70 (3-D 8-Node Thermal Solid) [19].

As the chronological order of solidification in the weld seam has a significant influence on the nature and distribution of stresses within the BTR, the melt pool geometry was derived from CFD simulations from Ref. [20] and used as the equivalent heat source in the FEM model. In this regard, first the melt pool's height (z=1 mm) was divided into n planes (here n=20). At each plane, the geometry of the melt pool was approximated by two Lamé curves [21] one for approximation of the front shape (Eqn. 1) and one for the rear shape (Eqn. 2). The center was considered as the laser beam, which travelled along the weld line with the welding speed equal to the experimental tests.

$$\left|\frac{x}{a_f(z)}\right|^2 + \left|\frac{y}{b(z)}\right|^2 = 1 \tag{1}$$

$$\left|\frac{x}{a_r(z)}\right|^2 + \left|\frac{y}{b(z)}\right|^2 = 1 \tag{2}$$

where $a_f(z)$ and $a_r(z)$ are the semi-axes in x-direction for the front and rear parts and $b(z)$ is the semi-axis in y-direction. They were modeled as polynomials in the normalized depth $\xi = z/n$, as follows, in Eqn. 3 to 5:

$$a_f(z) = \sum_{i=0}^{7} c_{f,i}\xi^i \tag{3}$$

$$a_r(z) = \sum_{i=0}^{7} c_{r,i}\xi^i \quad (4)$$

$$b(z) = \sum_{i=0}^{7} c_{b,i}\xi^i \quad (5)$$

where $c_{f,i}$, $c_{r,i}$, and $c_{b,i}$ are the polynomial coefficients, which listed in Table 1 and the melt pool geometry is plotted in Figure 5.

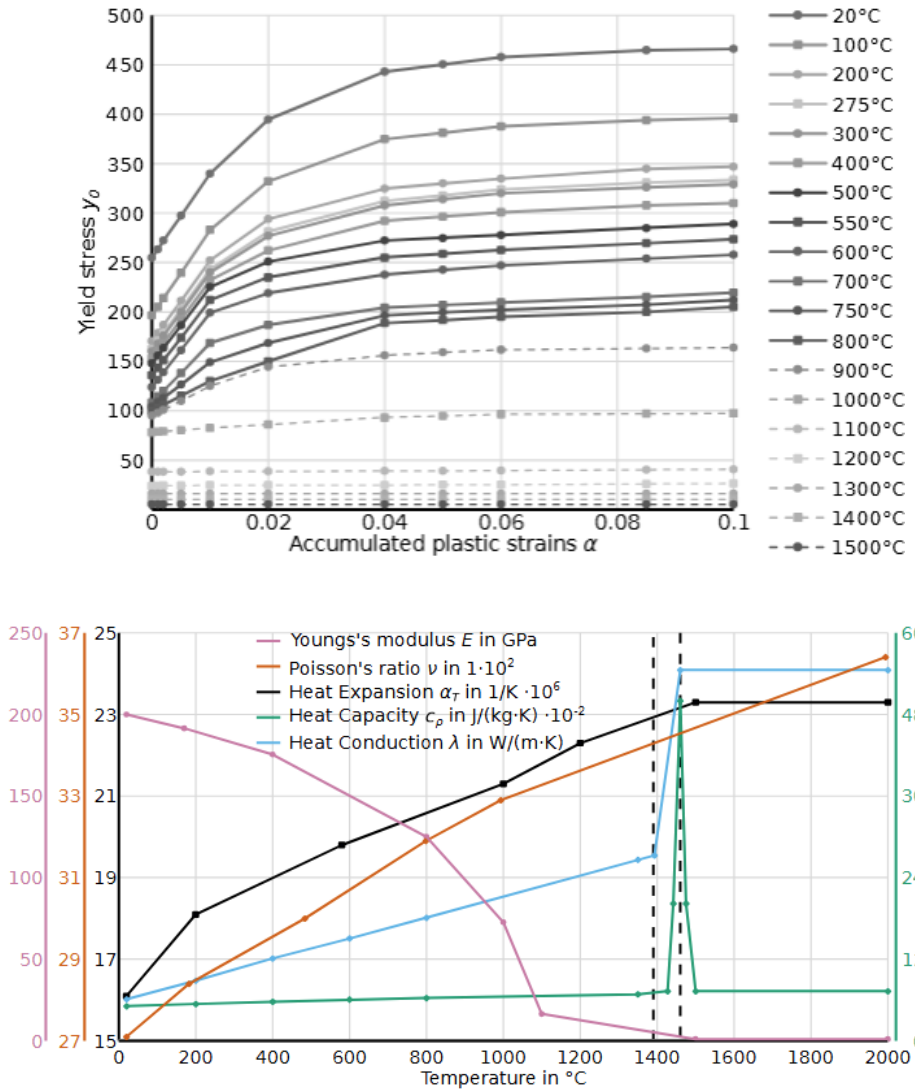



**Fig. 4** The material temperature-dependent properties for the studied material taken from Sysweld software library [14,15]

**Table 1.** The polynomial coefficients for Lamé curves to create the melt pool geometry.

| i | $c_{f,i}$ | $c_{r,i}$ | $c_{b,i}$ |
|---|---|---|---|
| **0** | -3.6749 | 2.4598 | 1.1506 |
| **1** | 5.7263 | -7.2852 | -4.7981 |
| **2** | 1.4621 | 8.0229 | 6.5953 |
| **3** | -6.4566 | -3.9590 | -3.8726 |
| **4** | 3.5316 | 0.7444 | 0.9514 |
| **5** | -0.4531 | -0.0835 | 0.2223 |
| **6** | -0.0356 | 0.1167 | -0.0676 |

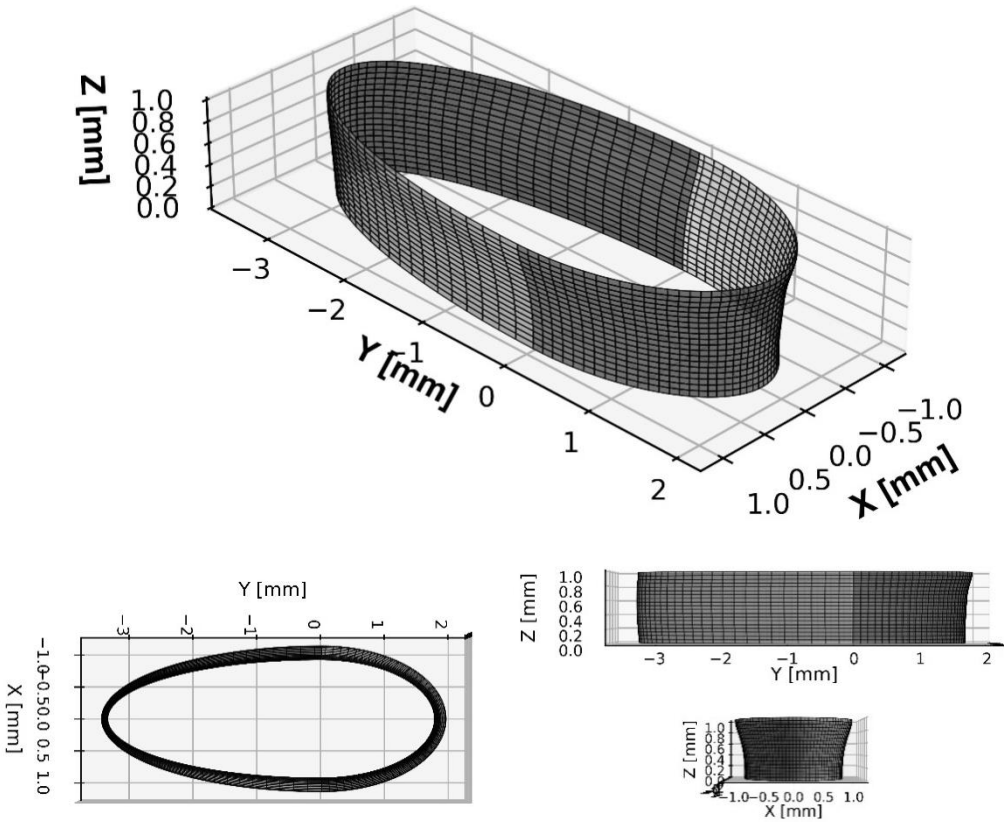



**Fig. 5** The geometry of the melt pool

For the mechanical model, the CTW specimen was pulled from both sides to apply the strain of 0.025 and strain rate 0.06 $s^{-1}$. The element type was converted to SOLID186 (3-D 20-Node Structural Solid). The constitutive law employed in the mechanical analysis is a thermo-elasto-plastic formulation. The material is assumed to behave elastically according to Hooke's

law, with temperature-dependent Young's modulus and Poisson's ratio. Plastic deformation is described using an isotropic hardening model with a von Mises yield criterion, where the yield stress is also a function of temperature. The total strain increment is decomposed into elastic, plastic, and thermal components. This formulation is appropriate for capturing the thermomechanical response of the material during the welding process, including the significant softening that occurs as the material approaches the solidus temperature.

Subsequently, a small section was cut out in order to use the sub-modelling technique with a finer element size of 0.05 mm × 0.05 mm × 0.05 mm. This yielded a total of 264,000 elements in a regular mesh, as shown in Fig. 3. One of the cut edges of the sub-model represents the symmetry plane of the specimen, where the correspondent boundary conditions were applied. Like the global-model, first the thermal simulation was performed with the thermal boundary conditions and then the temperature distribution was transferred to the mechanical simulations to simulate the effects of the mechanical boundary conditions. The thermal and mechanical boundary conditions for the cut edges (except of the symmetry plane) were taken from the global-model, as temperature and displacement increments.

Solidification crack was also considered in the sub-model, based on technological strength theory by Prokhorov [6]. Therefore, the mechanical boundary condition of the nodes located at the symmetry plane were released, and they were able to move freely as long as the total strain of the nodes were within brittle temperature range (BTR) and exceeded the critical strain value. The BTR and critical strain were iteratively selected to predict the closest size and location of the crack in comparison to the experimental results. Note that the employed cracking criterion was the critical total strain at the loading direction (x-direction).

## RESULTS AND DISCUSSION

Fig. 6 shows the good agreement between the temperature distribution from the CFD simulation and the experimental results, as well as the results obtained by the FEM model. The X-ray radiography, Fig. 7, revealed while no crack initiated in the specimen for testing condition of $\varepsilon_{CTW} = 0.02$ and $\dot{\varepsilon}_{CTW} = 0.06\ s^{-1}$, a 2.4-mm crack exists for the testing condition of $\varepsilon_{CTW} = 0.025$ and $\dot{\varepsilon}_{CTW} = 0.06\ s^{-1}$.

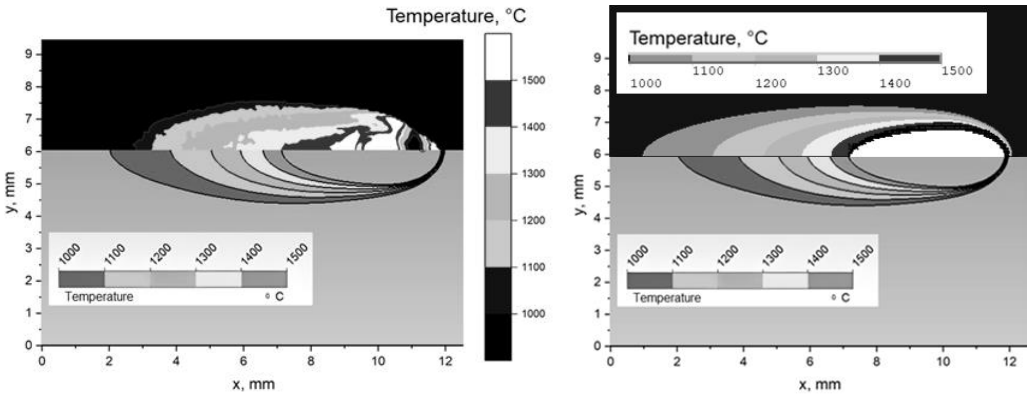



**Fig. 6** The comparison of temperature distribution of the CFD simulation with (left) the experiment, and (right) the FEM simulation

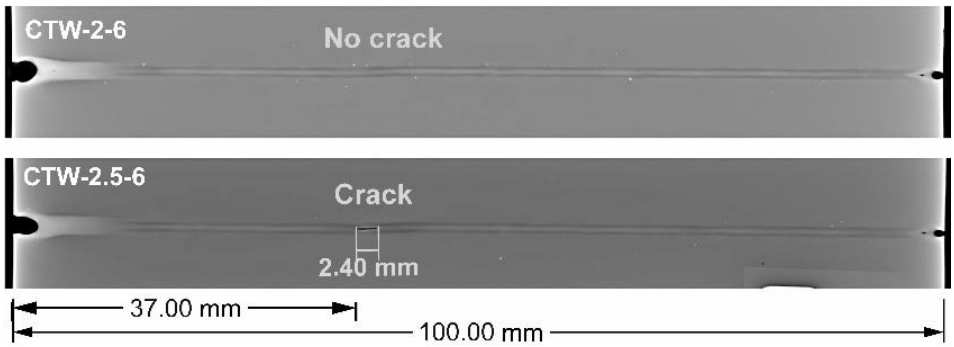
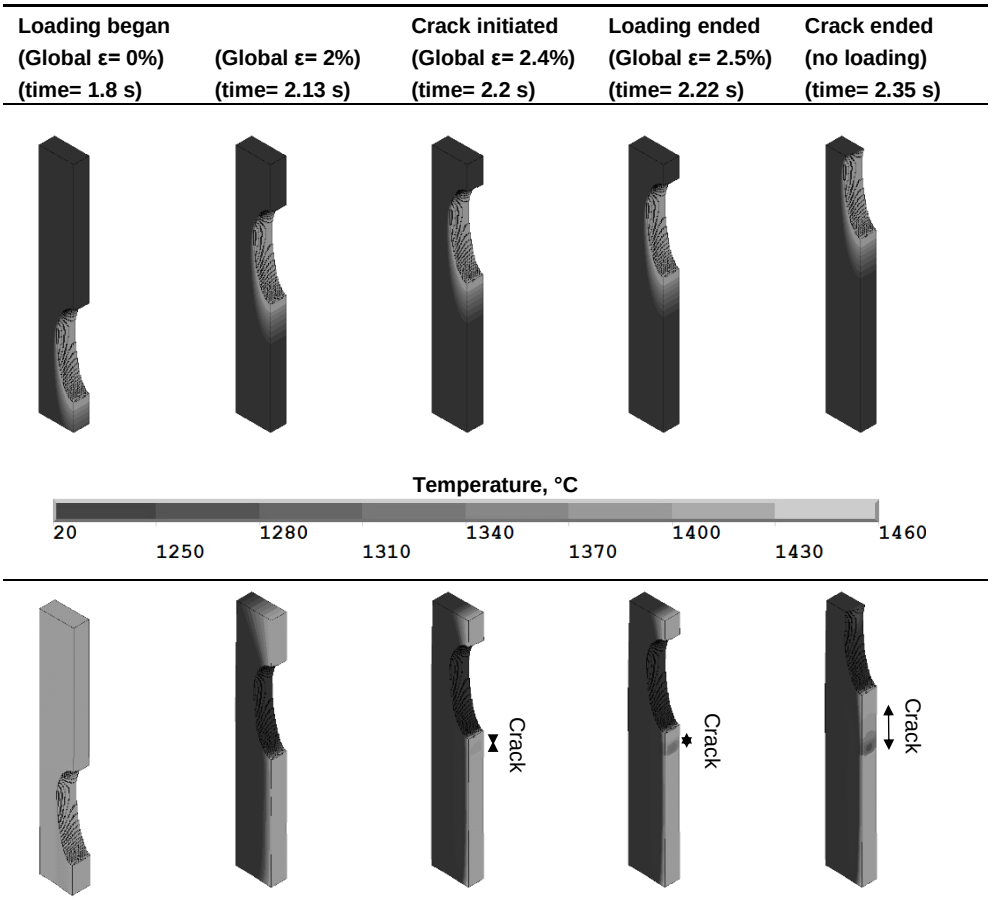



**Fig. 7** Crack investigation by X-ray radiography for two CTW tests; (top) $\varepsilon_{CTW} = 0.02$ and $\dot{\varepsilon}_{CTW} = 0.06\ s^{-1}$ and (bottom) $\varepsilon_{CTW} = 0.025$ and $\dot{\varepsilon}_{CTW} = 0.06\ s^{-1}$

According to the iterative attempts, the brittle temperature range from 1360 to 1430 °C and the critical strain was chosen as 0.13 in the FE simulations led to cracking at the almost similar location and size in comparison to the experiments. Figure 8 illustrates the evolution of the crack. The distributions of temperature, displacement in the x-direction (i.e. the loading direction) and total strain in the x-direction were plotted at the begin of the external loading (t = 1.8 s), the initiation of the crack (t = 2.2 s), the end of the external loading (t = 2.22 s) and the end of the crack growth (t = 2.36 s). The results imply that cracking initiated at $\varepsilon_{CTW} = 0.024$ at the stage 2 of the test and continued even after the external loading is stopped, which corresponds to the stage 3 of the test. To better understand the reason, thermal, mechanical and total strains at x-direction are illustrated in Fig. 9 at the crack initiation, the end of loading, the frame after the end of loading, the end of crack growth, and the next frame of the end of cracking. It is noted that, in a thermomechanical problem, mechanical strain also arises from thermal gradients and structural constraint; the term “mechanical strain” used throughout this

work refers specifically to the strain component driven by the externally applied loading, to distinguish it from the thermally-induced strain component. Here, the focus was only strains at x-direction, although it might not be written each time. To improve the illustration, the specimen is selected at the YZ plane from Y = 37 mm to 41 mm, and the crack elements are deleted from the display. The size and location of the crack can also be seen there. The results show that after the external loading was stopped, the mechanical strain remained constant, as expected. Only the BTR was moving with the laser beam which is associated with the local growth of the thermal strain up to 0.03. Whenever a node was in the BTR and the stored mechanical strain plus the thermal strain, i.e. the total strain, reached 0.13, the critical condition was satisfied, and the mechanical boundary condition was released at that node to form the cracking. While if the stored mechanical strain for a node was small and its sum with the thermal strain did not reach the threshold, the cracking did not occur. Note that, during the external loading, the mechanical strain was higher when the temperature is higher. Therefore, when the loading was stopped, the stored mechanical strain was significantly lower for the elements in front of the laser beam than the ones located behind it.



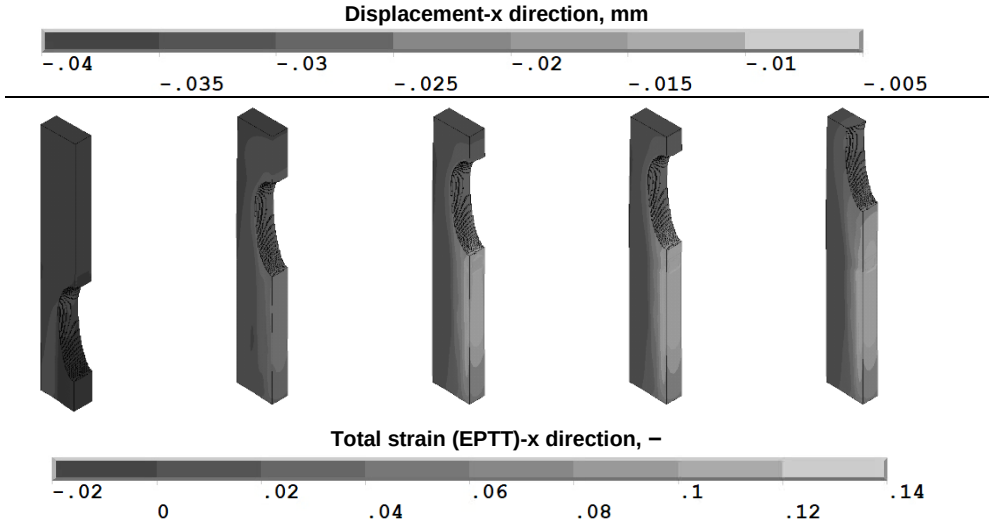
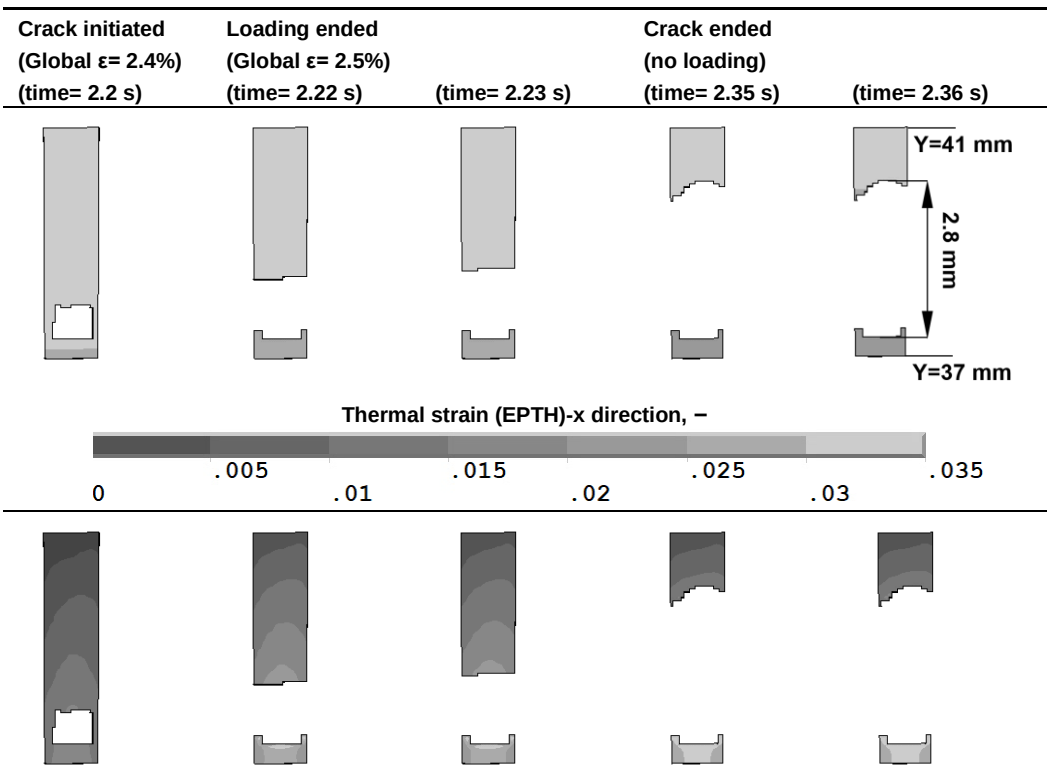



**Fig. 8** Distribution of temperature, displacement, and total strain along x-direction (loading direction). The elements for the weld pool were removed from the display.



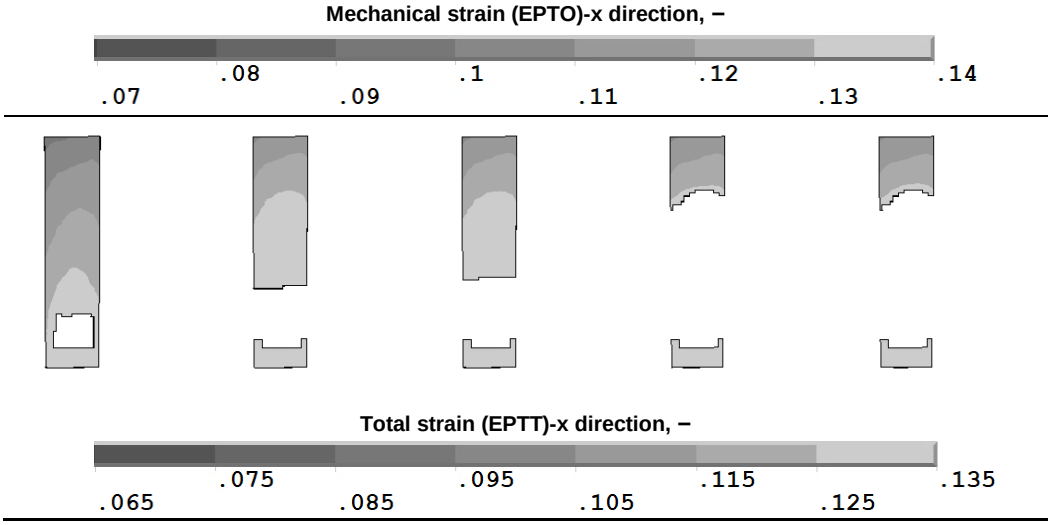



**Fig. 9** Thermal, mechanical, and total strain evolution at x-direction. It is shown at YZ-plane from y=37 to 41 mm.

## CONCLUSION

The sensitivity of AISI 304 to the solidification cracking was evaluated through CTW test. The systematic experimental approach provided valuable information regarding the crack and no crack conditions for the applied external loading. The FEM simulation was used for the elaborate study, which revealed for this material the sum of the mechanical and thermal strains at the loading direction was responsible for cracking i.e. the total strain in the cracking criterion. When this variable reached its threshold at the critical temperature condition (BTR) cracking happened. By stopping the external loading, some mechanical strain stored at the material, which could lead to the further crack growth, if its value plus the thermal strain component still satisfied the critical cracking condition.

## ACKNOWLEDGEMENTS

This research is funded by the Deutsche Forschungsgemeinschaft (DFG, German Research Foundation) - Project ID 434946896, within the research unit FOR 5134: ‘Solidification Cracks during Laser Beam Welding: High Performance Computing for High Performance Processing’.

## References


[1] J. C. LIPPOLOLD: *Welding metallurgy and weldability*, First ed., M. John Wiley & Sons Inc, pp. 85-94, 2015.

[2] T. KOSEIKI, H. INOUE, ET AL.: *Nippon Steel Technology Report*, No. 65, April 1995.

[3] M. C. FLEMINGS: *Solidification Processing*, McGraw-Hill, New York, pp. 251-255, 1974.

[4] S. A. DAVID, C. L. WHITE and V. P. KUJANPAA: 'Formation of Hot Cracks in Austenitic Stainless Steel Welds - Solidification Cracking', *Weld Research Supplement*, No. 65, pp. 203-212, 1986.

[5] K. KADOI, A. FUJINAGA, M. YAMAMOTO and K. SHINOZAKI: 'The effect of welding conditions on solidification cracking susceptibility of type 310S stainless steel during laser welding using an in-situ observation technique', *Weld World*, Vol. 57, pp. 383-390, 2013.

[6] N. N. PROKHOROV: 'Resistance to hot tearing of cast metals during solidification', *Russian Castings Production*, Vol. 2, No. 2, pp. 172-175, 1962.

[7] G. J. DAVIES and J. G. GARLAND: 'Solidification Structures and Properties of Fusion Welds', *International Materials Reviews*, Vol. 20, pp. 83-108, 1975.

[8] M. RAPPAZ, J.-M. DREZET and M. GREMAUD: 'A new hot-tearing criterion', *Metallurgical and Materials Transactions A*, Vol. 30, No. 2, pp. 449-455, 1999.

[9] S. VERNÉDE, J. DANTZIG and M. RAPPAZ: 'A mesoscale granular model for mechanical behaviour of alloys during solidification', *Acta Materialia*, Vol. 57, pp. 1554-1569, 2009.

[10] M. BELLET, G. QIU and J. CARPREAU: 'Comparison of two hot tearing criteria in numerical modelling of arc welding of stainless steel AISI 321', *Journal of Materials Processing Technology*, Vol. 230, pp. 141-152, 2016.

[11] P. WEN, K. SHINOZAKI, M. YAMAMOTO, Y. SENDA, T. TAMURA and N. NEMOTO: 'In-situ Observation of Solidification Cracking of Laser Dissimilar Welded Joints', *Quarterly Journal of JWS*, Vol. 27, No. 2, pp. 134-138, 2009.

[12] S. YANG, T. ITO, K. SHINOZAKI and M. YAMAMOTO: 'The effect of welding and strain conditions on the susceptibility to solidification cracking of a fully austenitic stainless steel', in *77th IIW Annual Assembly and International Conference*, Rhodes, Greece, July 7-12, 2024.

[13] W. HUO, N. BAKIR, A. GUMENYUK, M. RETHMEIER and K. WOLTER: 'Strain prediction using deep learning during solidification crack initiation and growth in laser beam welding of thin metal sheets', *Applied Sciences*, Vol. 13, No. 5, p. 2930, 2023.

[14] W. HUO, N. BAKIR, A. GUMENYUK, M. RETHMEIER and K. WOLTER: 'Detection of solidification crack formation in laser beam welding videos of sheet metal using neural networks', *Neural Computing and Applications*, Vol. 35, No. 34, pp. 24315-24332, 2023.

[15] N. BAKIR, A. GUMENYUK and M. RETHMEIER: 'Determination of critical local straining conditions for solidification cracking at laser beam welding by experimental and numerical methods', *PAMM*, Vol. 24, No. 2, p. e202400020, 2024.

[16] A. GUMENYUK, N. BAKIR and M. RETHMEIER: 'Two-colour thermography for measurement of temperature distribution in laser beam welding', *Procedia CIRP*, Vol. 124, pp. 468-471, 2024.

[17] T. BEVILACQUA, A. GUMENYUK, N. HABIBI, P. HARTWIG, A. KLAWONN, M. LANSER, M. RETHMEIER, L. SCHEUNEMANN and J. SCHRÖDER: 'Large-scale thermo-mechanical simulation of laser beam welding using high-performance computing: a qualitative reproduction of experimental results', *arXiv preprint*, arXiv:2503.09345, 2025.

[18] ESI GROUP: *Sysweld Material Database*, Software, Paris, France, 2009.

[19] ANSYS, INC.: *Ansys Mechanical APDL reference manual (2023 R2)*, Software, Canonsburg, Pennsylvania, US, 2023.

[20] P. HARTWIG, N. BAKIR, L. SCHEUNEMANN, A. GUMENYUK, J. SCHRÖDER and M. RETHMEIER: 'A physically motivated heat source model for laser beam welding', *Metals*, Vol. 14, No. 4, p. 430, 2024.

[21] A. ARTINOV, V. KARKHIN, N. BAKIR, X. MENG, M. BACHMANN, A. GUMENYUK and M. RETHMEIER: 'Lamé curve approximation for the assessment of the 3D temperature distribution in keyhole mode welding processes', *Journal of Laser Applications*, Vol. 32, No. 2, 2020.

# III Methods

## a) Modelling Tools and Computer Programs

# MACHINE LEARNING-ACCELERATED CALIBRATION OF COMPLEX HEAT SOURCE MODELS FOR WELDING AND ADDITIVE MANUFACTURING PROCESS SIMULATION

Y. LUO*, A. KUDVA*, E. JANG**, S. MATAN*, N. M. VEGA MICHALAK*, J. A. PAULSON*, A. PERRAULT*, B. ALEXANDROV*

**The Ohio State University, Columbus, OH, USA*
***Electric Power Research Institute, Charlotte, NC, USA*

*DOI 10.3217/978-3-99161-089-2-029, license CC BY 4.0*
*https://creativecommons.org/licenses/by/4.0/deed.en*
*This CC license does not apply to third party material and content noted otherwise.*

## ABSTRACT

The heat source (HS) models dictate the spatial distribution of applied heat during welding and additive manufacturing processes, making it a critical factor for accurate simulation. However, the problem of calibrating the HS model, i.e., selecting parameters for it that match experimental conditions, has often been overlooked, with parameter selection relying on empirical heuristics and human trial-and-error. This lack of systematic calibration can lead to poor simulation performance and thus limits the expressiveness of HS models that can be used. We present a machine learning framework for efficiently calibrating HS parameters, thereby facilitating use of HS models with greater expressiveness and practical applicability than the conventional double-ellipsoidal Gaussian model. The effectiveness of the proposed methodology is validated through case studies involving spray transfer gas metal arc welding (GMAW) and pulsed GMAW additive manufacturing. Experimental validation, including comparisons of thermal histories and heat-affected zone properties, confirms strong alignment between simulation and real-world observations. This work provides a systematic framework for improving welding simulation accuracy by addressing the long-standing limitations of empirical HS models and facilitating the adoption of more expressive and precise modeling approaches. Ultimately, we conclude that (1) machine-learning optimization-based calibration of HS parameters significantly enhances simulation accuracy compared to using HS models that are calibrated using standard methods; (2) using our framework, expressive HS models that can represent complex energy distribution better align with experimental data compared to the standard double-ellipsoid Gaussian model.

Keywords: heat source modeling and calibration, finite element analysis, machine learning, Bayesian optimization

## INTRODUCTION

Heat source (HS) models are a group of spatial density functions that describe the heat input distribution in the workpiece during welding and additive manufacturing (WAM) processes. They are widely used in simulation of high-temperature material joining processes in replacement of thermal and mechanical kinetic simulations which involve the complex interaction of heat transfer, phase transformation phenomena, non-linear material thermal properties and the fluid dynamics [1-6]. With the application of HS, the simulation of WAM processes can be simplified as a heat transfer problem, where the heat input is modeled as a moving HS that dissipates energy into the workpiece. Advances in high-performance computing have enabled large-scale simulations of WAM processes and optimization methods such as the Computational Design of Experiments (CDoE) [7,8]. Applying data-driven methods of simulation and optimization to complex multi-pass WAM processes involving complex structure poses two challenges to existing HS models: 1) complex structures may require highly customized HS distributions [9] that are difficult to manually calibrate; 2) long-horizon simulations that involve multiple weld passes and long welding duration may require multiple HS models, each of which is applied at a different stage of the process such that reacts to changes in heat distribution and mediates the simulation errors aggregated from simulations of previous weld passes. Compromising such errors is beyond the consideration of empirical calibration, and the human-constrained models are not expressive enough (capable to represent diverse thermal energy distributions) to represent the complex heat transfer and phase transformation phenomena.

Conventional methods that combine expressiveness-limited HS models with trial-and-error calibration following empirical heuristics have become a substantial bottleneck to the application of computational optimization methods to large scale simulations. After reviewing existing approaches to perform WAM processes simulations, we find that parameterized HS models are typically calibrated against experimental data, where the parameters are adjusted to minimize the difference between the simulation and the experimental results. The HS model parameters must be optimized to agree with experimental data because the heat input to the workpiece is not typically measurable experimentally. In practice, the double-ellipsoidal Gaussian (DEG) model [10] is the most frequently used HS model in WAM simulations. The DEG model typically outperforms simple heat sources (e.g., point heat sources [11], surface round heat source [12]), but the agreement it achieves is often imperfect (even when the parameters are set carefully, as we show in our experiments). However, despite this imperfection, higher dimensional HS models are not widely used. We speculate that this is primarily because of a combination of factors, including the perception that higher dimensional HS models require too much experimental data and computation to calibrate with standard approaches and the reduced human interpretability - it is more difficult to intuitively know how to set parameters, which is a barrier for standard approaches.

We hypothesize that the lack of successful high dimensional HS models has slowed down the application of computational methods in the WAM community, especially in complex and long-horizon tasks. In this paper, we propose a machine learning framework for efficiently calibrating HS parameters such that enable a new generation of HS models that are more expressive and practical. We validate the effectiveness of the proposed framework through case

studies involving spray transfer gas metal arc welding (GMAWs) and pulsed gas metal arc (GMAWp) additive manufacturing. The observed validation shows that the proposed calibrated heat source models reduced peak temperature prediction error and the predicted thermal histories well aligned with experiments for the GMAW and GMAW-p AM processes. Thus, we conclude that expressive HS models and efficient calibration methods can improve simulation accuracy.

## RELATED WORK

In this section, we review related work in the analytical and numerical solution of welding dynamics (Section 0) to provide a background for welding process analysis and application of HS models. Additionally, we review parameter optimization methods for HS models (Section 0).

### Analytical and Numerical Solution of Heat Transfer Analysis

Analytical and numerical approaches are two methods to perform heat transfer analysis. The analytical method requires mathematical modeling of the entire environment (i.e., material properties, boundary conditions, heat distribution, etc.) to derive the temperature field function by time and location, while numerical solution uses a discrete representation of the environment and state transition function (e.g., partial differentiate equation) to approach an error-bounded solution iteratively. In practice, the analytical method can only be applied in studies of simple structures, constant material properties, plain boundary conditions [9] and simple HS models [11,12]. Therefore, analytical solution is of limited use for the complex welding environments and processes [9,12-16].

Numerical methods can resolve environments involving complex structures, non-linear material properties, varying boundary conditions and non-plain processes. Transient simulation of welding processes became feasible with finite element model simulation, where de Freitas Teixeira et al. [17] points out that accurate modeling of the heat distribution is critical for resolving thermal dynamics in welding process. Ur Rehman et al. [18] adopts a Gaussian distribution model to compromise FEA-based analysis for WAM process. Eager and Tsai [19] quantifies the application of Gaussian HS models by implementing a simple distribution parameter with which aiming to fit the shape of heat distribution against the weld pool dimensions. Goldak et al. [10,20] adjusts the Gaussian-based HS model to account for the regional contraction and expansion effects of heat distribution caused by moving HSs, introducing the double-ellipsoidal Gaussian (DEG) model. Its extensions later become prevalent in subsequent studies [21-26]. However, the DEG model is prone to over-simplifying the heat distribution especially for a weld pool with deep penetration [10], and in the central region of the weld pool where the simulation results are sensitive to the HS model [16,27]. For such cases, Wahab et al. [16] uses a composite HS model to represent both the surface arc energy and the droplet energy in gas metal arc welding, however the selected spherical heat source model is

not able to represent finger-like penetrations that are common to see in high heat input GMAW processes.

### Parameter Optimization for Heat Source Models

Goldak et al. proposed the DEG model along with an empirical parameterization method that is based on the weld pool dimensions [10,20]. Based on the DEG model, following studies have been conducted to characterize the HS model parameters [17,28,29] by evaluating how the simulated heat-affected zone (HAZ) or the thermal history align with the experimental results. Other studies model the fluid flow in the weld pool [1,4,11,30] and show this modeling leads to better determination of HS parameters. Optimization-based approaches have also been explored. SysWeld™ provides a Heat Source Fitting module that optimizes the HS model parameters by allowing users to iteratively adjust the parameters, thus approaches the experimental morphology of the weld pool [31,32]. Luo [7] developed a brute-force grid search method to calibrate heat source parameters for gas tungsten arc welding (GTAW) process simulation, which formally defines the calibration problem as a parameter optimization problem, but has low computational efficiency. Although there have been studies in parameterization of HS models, to our best knowledge, there is no discussion in developing HS models for matching weld pools resulting from different fluid patterns, nor in the application of machine learning methods to calibrate HS model parameters.

## PRELIMINARIES

In this section, we review the double-ellipsoidal Gaussian HS model and cylinder-semi-sphere HS model, then provide background on the optimization methods that are related to this work.

### Heat source models

**Double Ellipsoidal Gaussian Model (DEG)** [10] is the most widely used HS model in WAM practice. The DEG model uses two ellipsoids to model the heat distribution for the pre- and post-weld region respectively. We rewrite the HS model to depend on the parameters $(\sigma_x, \sigma_y, \sigma_z, \alpha_x^+, \dots, \alpha_z^-, k)$, with $\sigma_{h\in\{x,y,z\}} > 0$ as the boundary at the corresponding axis. Let $Q$ (J/mm) be the heat input rate, and $q(0)$ be the maximum flux at the center of DEG model, defined by:

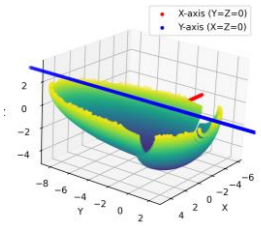
$$q(0) = \frac{2k^{1.5}Q}{\sigma_x\sigma_y\sigma_z\pi^{1.5}}$$

As the $+y$ is the welding direction, $\sigma_x$, $\sigma_y$ and $\sigma_z$ represent the width, length and depth of the heat source respectively. $\alpha_y^+$ and $\alpha_y^-$ are the correction factors at the $+y$ and $-y$ octants that model the pre-weld contraction ($\alpha_y^+ < 1$) and post-weld extension ($\alpha_y^- > 1$) effects.

Similarly, $\alpha_x^+, \alpha_x^-, \alpha_z^+, \alpha_z^-$ allow adjusting boundaries at the HS width and depth, even though they are mostly kept 1 to ensure symmetric width and depth in practice. While the aforementioned parameters control the geometric representation of the DEG model, $k$ controls the spreading of the energy distribution – DEG models with large $k$ have more energy near HS center and vise verse.

$$\forall h \in \{x, y, z\}, \alpha_h = \begin{cases} \alpha_h^+, h \geq 0 \\ \alpha_h^- \text{ otherwise} \end{cases} \quad (1)$$

With the help of the indicator function (Equation (1)), the flux distribution of DEG model is defined as Equation (2).




$$q_{DEG}(x, y, z) = q(0) \exp\left(\sum_{h \in \{x,y,z\}} -\frac{k\alpha_h^2 h^2}{\sigma_h^2}\right) \quad (2)$$

**Fig. 1** Boundary of the DEG model

Fig. 1 shows the surface boundary of DEG model at which the energy intensity $q_{DEG} = fq(0)$. Goldak et al. [10] defined the default value of the parameters as $f = 0.05$, while $\sigma_x, \sigma_z, \sigma_y$ are directly taken from the weld pool width, depth, and length. We used the DEG model parameterized by this method as the baseline HS model and refer to it as empirical DEG model for the rest of paper.

**Cylinder-Semi-Sphere (CSP) model** uses a cylinder with a semi-sphere attached, to model the heat distribution with deep penetration. This model is implemented in SysWeld™ for users to use. It is parameterized by $(r_t, r_b, h_t, h_b, k)$, where $r_t, r_b$ are the top and bottom radiuses of the cylinder, and $h_t, h_b$ are the top and bottom height of the cylinder. A semi-sphere is attached to the bottom of the cylinder with radius $r_b$. The cylinder-semi-Sphere model is defined as Equation (3).

$$R(x, y, z) = \begin{cases} r_t * \dfrac{z - h_b}{h_t - h_b} + r_b * \dfrac{h_t - z}{h_t - h_b}, h_b \leq z \leq h_t \\ r_b, h_b - r_b \leq z < h_b \\ 0, \quad \text{otherwise} \end{cases}$$

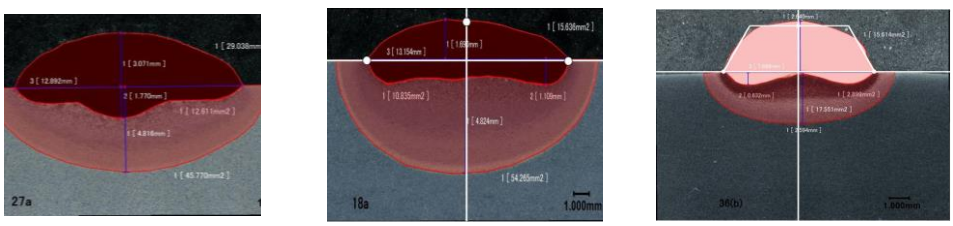
$$r(x, y, z) = \begin{cases} \left|\left|(0,0,z), (x,y,z)\right|\right|^2, h_b \leq z \leq h_t \\ \left|\left|(0,0,h_b), (x,y,z)\right|\right|^2, h_b - r_b \leq z < h_b \\ \infty, \quad \text{otherwise} \end{cases} \quad (3)$$

$$q_{CSP}(x, y, z) = q(0) \exp\left(-k \frac{r(x, y, z)}{R(x, y, z)}\right)$$

Where for each point $(x, y, z)$ in the space, $R(x, y, z)$ represents the distance from its closest point $p$ on the HS axis to where the ray line $(p, (x, y, z))$ falls on the boundary; and $r(x, y, z)$ are the distance from $(x, y, z)$ to the $p$. Like the DEG model, $k$ controls the spreading of the HS energy for the CSP model.

## FLUID FLOW AND HEAT DISTRIBUTION

In arc welding, the distribution of the temperature field is affected by the convective fluid flow, the electromagnetic field, and the surface tension [3-6,16]. Such complex interaction has resulted in different fluid flow patterns in the weld pool. Mills et al. and Li et al. [3, 33] identify three major different weld pool flow patterns caused by the material surface-tension-temperature gradient ($\frac{d\gamma}{dT}$) in liquid phase. Inward flow is observed when $\frac{d\gamma}{dT} > 0$, where the surface flow gets pulled inward, such that the center flow flushes the substrate, causing penetration that is significantly deeper than usual weld pool (Fig. 2a). When under negative $\frac{d\gamma}{dT}$, the surface flow is pushed outward thus spreads to the side of the weld pool, causing the weld pool to have a flat bottom as shown in Fig. 2b. In the case of non-monotonicity of $\frac{d\gamma}{dT}$, the liquid in between the side and center reaches a peak surface-tension, pulling flow from both weld pool center and sides, indicated by Fig. 2c.




(a) $\frac{d\gamma}{dT} > 0$ (b) $\frac{d\gamma}{dT} < 0$ (c) Non-monotonic $\gamma$

**Fig. 2** Cross-sections of typical weld pools in GTAW

To take these fluid flow patterns into account, HS models that can model more complex distribution (i.e., more expressive) than DEG and CSP models are needed. Previous HS models [10-12,20] are designed in ideal conditions where phenomena beyond the torch and arc energy distribution, such as fluid flow patterns, are not considered.

## PARAMETER OPTIMIZATION METHODS

Parameter optimization aims at searching for optimal parameters against an objective function. For scenarios with expensive evaluations and black-box settings, Bayesian optimization is one popular method. Recently, first-order gradient descent methods have drawn significant attention due to their successes in deep neural network optimization.

### *Bayesian Optimization*

Bayesian optimization (BO) is a sample-efficient method for optimizing costly, black-box functions. BO uses a probabilistic surrogate model, typically a Gaussian process ($GP$) [34], to model the unknown objective function and guide sampling through an acquisition function.

Let the HS model be represented as a function $f(h)$, where $h \in \mathcal{H} \subset R^d$ denotes a vector of model parameters in the HS parameter space $\mathcal{H}$. The goal is to solve the calibration problem:

$$h^* = argmin_{h\in\mathcal{H}}\, \mathcal{L}(f(h), y_{exp})$$

where $\mathcal{L}$ is a loss function (e.g., mean squared error) comparing model predictions $f(h)$ to experimental measurements $y_{exp}$. Since direct evaluation of $f(h)$ involves computationally intensive simulations, BO constructs a surrogate $\bar{f}(h) \sim GP(\mu(h),\ k(h,h'))$, where $\mu$ and $k$ denote the predictive mean and covariance.

An acquisition function $\Psi(h;\ D)$, defined based on the GP posterior over $\mathcal{H}$, is then maximized to select the next evaluation point:

$$h_{t+1} = argmax_{h\in\mathcal{H}}\Psi(h; D_t)$$

where $D_t = \{(h_i, L_i)\}_{i=1}^{t}$ is the set of evaluated points and observed losses up to iteration $t$. After each new evaluation, the surrogate model is updated, and the process is repeated until a stopping criterion is met.

### *Gradient-based Optimization*

The most important application of gradient-based optimization is in training deep neural networks (DNN) that potentially approximate arbitrary distributions [35, 36]. In training neural networks, the parameters ($\theta$) of neural networks are optimized for minimal prediction loss with a set of sample and gold values $(X, Y)$, where $X = [x_0, \dots, x_{|X|}], Y = [y_0, \dots, y_{|X|}]$:

$$\theta = argmin_{\theta\in\mathcal{R}^d}\left|\left|DNN_\theta(X), Y\right|\right|^2$$

Let $\mathcal{L}(X) = \left|\left|DNN_\theta(X), Y\right|\right|^2$, assuming that the true mapping $f^\star: X^\star \to Y^\star$ is a smooth function, then the gradient $\frac{\partial\mathcal{L}(X)}{\partial\theta}$ is applied to minimize the prediction loss ($\mathcal{L}$):

$$\theta = \theta - lr * \frac{\partial \mathcal{L}(X)}{\partial \theta}$$

where *lr* is the learning rate.

## HEAT SOURCE CALIBRATION

We propose to **precisely** match the post-weld fusion boundary line (FBL) in HS calibration to account for the complex multifactor phenomena in the weld pool - instead of modeling the complex interactions, a surrogate is adopted by matching their combined effect to the HAZ that can be observed from the post-weld cross-sections. This is accomplished by adopting a more expressive HS models (Section 0) that can represent the complex heat distribution in the weld pool combined with machine learning-based optimization methods to calibrate the HS model parameters for matching the post-weld FBL (Section 0 and 0).

### NEW HEAT SOURCE MODELS

In this section, two new HS models are proposed to address the limitation of the existing DEG model. The first model, called Double-ellipsoidal Gaussian and Cylinder-semi-Sphere (DEGC) model (Fig. 3a), is composed of a DEG model and a CSP model, alike to the approach as Champagne and Pham [37]. The DEGC model is designed to represent the phenomena observed in Fig. 2a. The second model, Dual Double-ellipsoidal Gaussian (DDEG) HS model (Fig. 3b), combines two identical DEG models, but with different energy intensities, such that it represents the complex flow phenomena observed in Fig. 2c, where negative $\frac{d\gamma}{dT}$ cases as Fig. 2b can be represented by the DEG model.

**Double-Ellipsoidal Gaussian and Cylinder-semi-Sphere Model (DEGC)** The weld pool with deep penetration is hard to model with DEG model, as it neglects the heat flow in the $z$ direction [10]. To address the challenge of modeling deep penetration, the DEGC model couples a DEG model on top of a CSP model. Based on Equation (2) and (3), we can define the DEGC model as Equation (4), and the HS boundary is shown in Fig. 3a.

$$q_{DEGC}(x,y,z) = h_r q_{CSP}(x,y,z) + (1-h_r) q_{DEG}(x,y,z) \tag{4}$$




**(a) DEGC** **(b) DDEG**

**Fig. 3** HS boundaries of the DDEG and DEGC heat source model

Where $h_r$ adjust the energy split to the CSP and DEG HSs. Note that both the DEG and CSP are special cases of DEGC, corresponding to $h_r = 0$ and $h_r = 1$, respectively.

**Dual Double-Ellipsoidal Gaussian Model** (DDEG) is modified from the DEG model by composing two identical DEG models, where the energy intensity levels of the two models are adjusted by the indicator $r_x$ ($r_x^+ + r_x^- = 2$) and the distance between the two models $d$. The HS model is defined as Equation (5), whose HS boundary is shown in Fig. 3b.

$$q_{DDEG}(x,y,z) = r_x q(0) \exp\left(-\frac{k\alpha_x^2(|x|-d)^2}{\sigma_x} - \frac{k\alpha_y^2 y^2}{\sigma_y^2} - \frac{k\alpha_z^2 z^2}{\sigma_z^2}\right) \quad (5)$$

The DDEG model is designed to capture the complex flow phenomena as shown in Fig. 2c: the liquid flow creates a "$W$" shape fusion line in the weld pool, which when simulating the heat distribution with DEG model, would need modeling two heat centers. Note that the DEG model is a special case of DDEG model (i.e., when $r_x = 1, d = 0$).

## HEAT SOURCE CALIBRATION

The HS models introduced in Section 0 come with the cost of increasing the number of parameters that must be fit. To address the challenge of calibrating the HS model parameters in the context of the experimental weld HAZ properties, we introduce a heat source calibration framework that can optimize HS model parameters more efficiently.

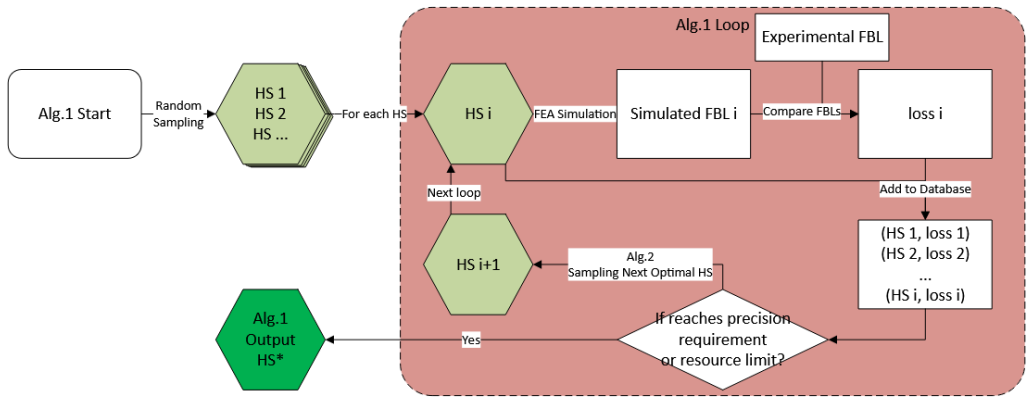



**Fig. 4** Heat Source Calibration Framework

**Alg. 1** Heat Source Calibration (HSC)

**Input:**

$FEA$: Finite Element Model
$\mathcal{H}$: Heat Source Parameter Space
$\tau_\omega$: The HAZ properties of goal experimental weld
$\varphi_\omega$: The Welding parameters of goal experimental weld
$loss(\tau_\delta, \tau_\omega)$: The heat source evaluation function.
$\bar{\mathcal{S}}$: Upper limit of the calibration cases

1: $fl_\omega \sim \tau_\omega$ # Extract fusion line from HAZ of $\tau_\omega$
2: $\mathcal{S} = \emptyset$ # Initialized the set of explored HSs
3: $while\ |\mathcal{S}| < \bar{\mathcal{S}}\ do$
4: $h \sim \mathcal{H}/\mathcal{S}$ # Sample a HS parameter $h$ with **Alg. 2**
5: $\tau_\delta^h = FEA(h, \varphi_\omega)$ # Run weld simulation with $h$ and $\varphi_\omega$
6: $l_h = loss(\tau_\delta^h, \tau_\omega)$ # Calculate the loss value for $h$
7: $\mathcal{S} = \mathcal{S} \cup \{(h, l_h)\}$ # Add h and its loss value $l_h$ to $\mathcal{S}$
8: $end\ while$ # Reach calibration limit
9: return $h_\omega = argmin_{(h,l_h)\in\mathcal{S}} l_h$

Rather than intuitively selecting the parameters according to the experimental weld followed by the trial-and-error method, we introduce a machine learning framework to calibrate the HS model parameters**.** Alg. 1 and Fig. 4 shows the HS calibration procedure which aims to optimize the HS model by repeatedly sampling the potentially better HS model, calculating its loss in simulation, and, when the simulation budget is reached, returning the HS model parameters with lowest loss. Formally, the calibration goal is to match the FBL ($\tau_\omega$) that have been extracted from the experimental weld piece by setting the parameters of the HS model ($h_\omega$) to minimize the simulation error ($\Delta$) when it is used in a simulation along with the welding parameters $\varphi_\omega$ from the experimental weld:

$$h_\omega = argmin_{h\in\mathcal{H}} \Delta(\tau_h^\varphi, \tau_\omega^\varphi)$$

In this paper, we use fusion boundary line (FBL) as the calibration target, because FBL can be observed for many dissimilar metal welding processes using simple image processing methods. For other processes where FBL is indistinguishable, hardness value could be used as calibration criteria if there comes accurate predictive method that relates thermal history to hardness value [38,39]. Contrasting to the Heat Source Fitting module in SysWeld™ that relies on manual interactive adjustment of HS parameters, the principle of the HSC framework is adopting data-driven approach to benefits from all parameters been explored. The data-driven method ensures that all explored HS parameters contribute to profile the HS parameter space, with which, intelligent sampling method can approach global optimal HS efficiently and with confidence. The sampling method omitted Line 4 is introduced in Alg. 2**.**

## MACHINE LEARNING-ACCELERATED CALIBRATION

The sampling of the new HS model parameters ($h$) (Line 4) in the parameter space $\mathcal{H}$ is a crucial step in the HS calibration process. For efficient calibration, the sampling strategy should balance exploration and exploitation in the parameter space, where exploration refers

to searching for new regions in the parameter space that may yield better results, and exploitation refers to refining the search around known good regions.

To achieve this balance, we propose a two-stage hybrid optimization strategy (Alg. 2) for the heat source calibration. Given the set of explored heat source and loss pairs $\mathcal{S}$, we first fit the surrogate model $Q_\theta(h)$ to predict the loss value associated with each heat source parameter $h$ **(**Line 1-3). $Q_\theta(h)$ is a deep neural network (DNN) that takes the heat source model parameters $h$ as input and outputs the loss value. $\theta$ is the parameters of the DNN to be trained on the data $s$. Then in the first sampling stage (Line 4), we use Bayesian optimization (BO) combined with upper confidence bound acquisition function [40] to explore the parameter space and identify potentially optimal regions (near $h$ in Line 5). In the second stage (Line 5-7), we apply a gradient-based optimization method to locally fine-tune the parameter values from the best-found candidate. This hybrid approach enables reliable and sample-efficient calibration based on experimental fusion zone data.

**Alg. 2** Hybrid Learning-Accelerated Calibration (HLAC)

**Input:**

$\mathcal{S} = \{(h, l_h), \dots\}$
$Q_\theta(h) = f: \mathcal{H} \to R$
$l$ : Learning Rate
$K$: Learning Steps
$k$: Sampling Steps

1: $for\ i = 1 \to K\ do$
2: $\quad \theta = \theta - E_{h\in\mathcal{S}}\left[l\frac{\partial[MSE(Q_\theta(h),l_h)}{\partial\theta}\right]$ # Update the surrogate model
3: $end\ for$
4: $f(h) \sim\ GP(\mu_{(h,l)\in\mathcal{S}}(h), k_{(h,l),(h',l')\in\mathcal{S}}(h,h'))$ # Learn Gaussian process function $f(h)$
5: $h = argmax_{h\in\mathcal{H}}\ \Psi(h;\mathcal{S})$
6: $for\ i = 1 \to k\ do$
7: $\quad h' = h' - l\ \frac{\partial[Q_\theta(h')]}{\partial h'}$
8: $end\ for$
9: return $h'$ # Return the new HS parameter

## EVALUATION

The proposed DEGC and DDEG HS models (Section 0) and the machine learning-accelerated calibration method (Section 0) are demonstrated and evaluated in this section. The evaluation is conducted by physical experiments and FEA simulations of spray arc gas metal arc welding (GMAWs) and pulsed arc gas metal welding (GMAWp) wire-arc direct energy deposition (WA-DED) processes. For each process, we run HS calibration (Alg. 1) with the proposed HS models in Section 0 and the HLAC method (Alg. 2).

### EXPERIMENTAL SETUP AND MODELING SETUPS

GMAWs bead on plate weld HHI, MHI, and LHI welds is used in HS calibration for FEA modeling of multi-pass groove welds in Fe-10Ni steel [41]. The GMAWP WA-DED process

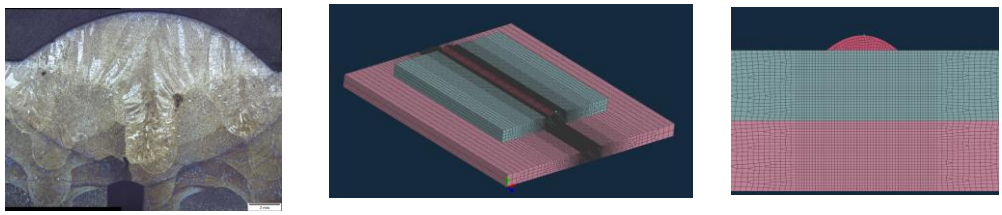
is developed for a single bead per layer additive build of a high strength steel (HSS) [42]. Table 1 **s**hows the welding parameters used with the three processes.

**Table 1** Experimental Setup for the GMAWs and GMAWp processes

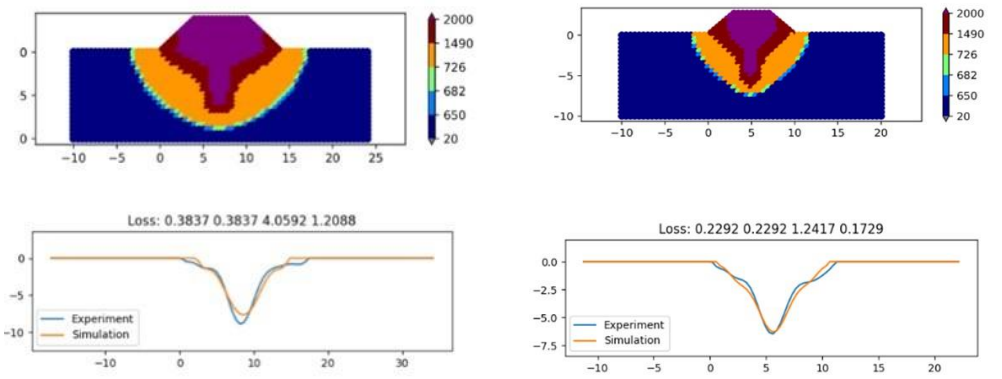
| | GMAWs | | | GMAWp – WA-DED |
|---|---|---|---|---|
| | **LHI** | **MHI** | **HHI** | |
| Base Material | | Fe-10Ni | | A36 steel |
| Filler Material | | Fe-10Ni | | HSS |
| Voltage $V$ | | 27 | | 17.3 |
| Current $A$ | | 300 | | 174 |
| Heat Input $J/mm$ | 993 | 1574 | 2204 | 819 |
| Travel Speed $mm/s$ | 7.9 | 5.04 | 3.8 | 4.23-5.93 |
| Wire Feed Rate $mm/s$ | | 139 | | 245 |
| Wire Diameter $mm$ | | 1.14 | | 1.14 |

The thermal histories experienced in the heat affected zones (HAZ) of these welds and builds are recorded using 0.2 mm diameter Type C thermocouples and a fast-sampling data acquisition system. The thermocouples are installed in ceramic insulators and capacitor-discharge welded to the tips of 1.8 mm diameter holes, located within 1 to 4 mm distance from the anticipated fusion boundaries, as shown in Fig. 5a. The welds and the WA-DED build are cross sectioned, prepared for characterization using standard metallography techniques, and the FBLs extracted using the image processing software ImageJ™.

FEA models of the two processes are developed in SysWeld™ using fusion zone and HAZ mesh size of 0.5 mm. The FEA models are run with process parameters and material properties of the respective base and weld filler metals listed in Table 1. Cross sections of a GMAWs bead on plate weld, and a GMAWp WA-DED build, their respective FEA models used in the HS calibration and evaluation procedures, and extracted FBLs are respectively shown in Fig. 5 and Fig. 6**.**

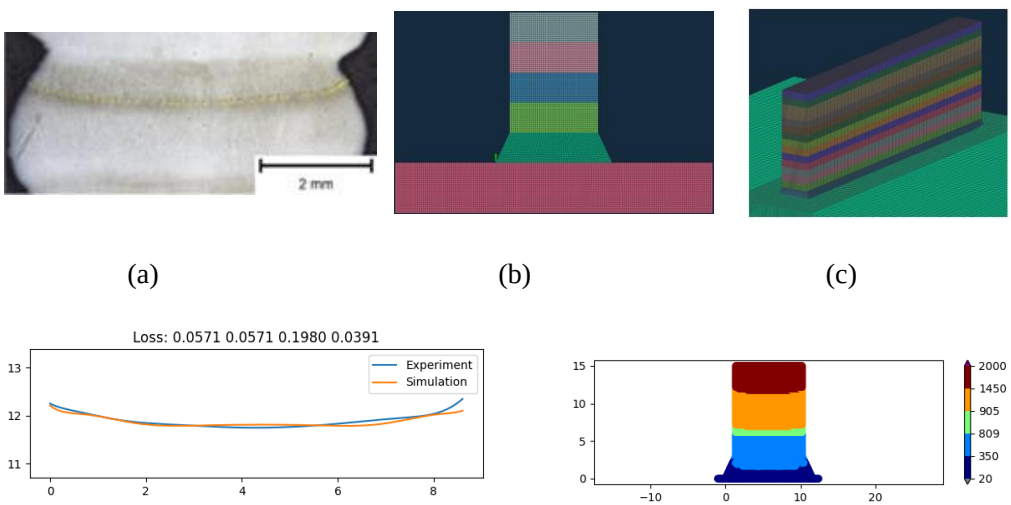


(a) (b)




(c) (d)

**Fig. 5** GMAWs bead on plate weld: a) HHI bead cross section with thermocouple hole location, b) FEA model: weld bead deposited over Fe-10Ni overlay on low alloy steel substrate; experimentally extracted and DEGC HS calibrated FBLs: c) HHI, d) LHI




(a) (b) (c)

(d)

**Fig. 6** GMAWp WA-DED build: a) build cross section with highlighted FBL, b) FEA model, c) experimentally extracted and DDEG HS calibrated FB

## HEAT SOURCE CALIBRATION

For the calibration criteria, we use the FBLs extracted from the experimental welds as the target FBLs. The loss function is defined as the mean square error (MSE) between the simulation and the experimental FBLs as Equation (6).

$$loss_{fl}(\tau_h^{\varphi}, \tau_{\omega}^{\varphi}) = \int_{x_0}^{x_1} \left\| fl_h^{\varphi(x)} - fl_{\omega}^{\varphi}(x) \right\|^2 dx \tag{6}$$

where $fl_h^{\varphi}(x)$ is the FBL of the simulation with HS model $h$, and $fl_{\omega}^{\varphi}(x)$ is the FBL of the experimental weld, both with welding parameters $\gamma$ (Table 1). The parameters of the calibrated GMAWS and GMAWP WA-DED heat sources are listed in Table 2.

**Table 2** Calibrated HS models and parameters

| **Heat Source** | **GMAWs** [41] | | | **GMAWp – AM** [42] |
|---|---|---|---|---|
| | **LHI** | **MHI** | **HHI** | |
| Name | | DEGC | | DDEG |
| $\sigma_x, \sigma_y, \sigma_z\ (mm)$ | 10,6,1 | 16,8,3 | 6,3,0.5 | 11.67,6.17,0.16 |
| $k$ | | 1 | | 0.53 |
| $\alpha_y^+, \alpha_y^-$ | | 1 | | 1 |
| $\alpha_x, \alpha_z$ | | 1 | | 1 |
| $d\ (mm)$ | | 0 | | 1.21 |
| $r_t, r_b\ (mm)$ | 2,3 | 3,4 | 2,3 | - |
| $h_t, h_b\ (mm)$ | 1.5, -1.5 | 2.5, -2.5 | 1.5, -1.5 | - |
| $h_{r(mm)}$ | 0.27 | 0.27 | 0.36 | - |

Images of FEA predicted FLBs using the respective DDEG and DEGC heat source models are shown in Fig. 5c, Fig. 5d and Fig. 6d . There is a very good correlation between the FEA predicted and experimentally extracted FBLs. This demonstrates the capability of the developed DDEG and DEGC heat source models and of the calibration procedure to accurately simulate the fusion boundary regions generated by GMAWs and GMAWp WA-DED processes.

## VALIDATION

The validation of the calibrated HS model compares the simulation and the experimental thermal histories and HAZ properties. Particularly, we run extensive simulation of the experimental welds, then compare the simulation thermal history with the experimental thermal history and compare the predicted with the experimental HAZ properties (hardness and microstructure). We additionally run simulation of the GMAPp WA-DED processes with DEG model, parameterized according to the empirical method in Goldak et al. [10].

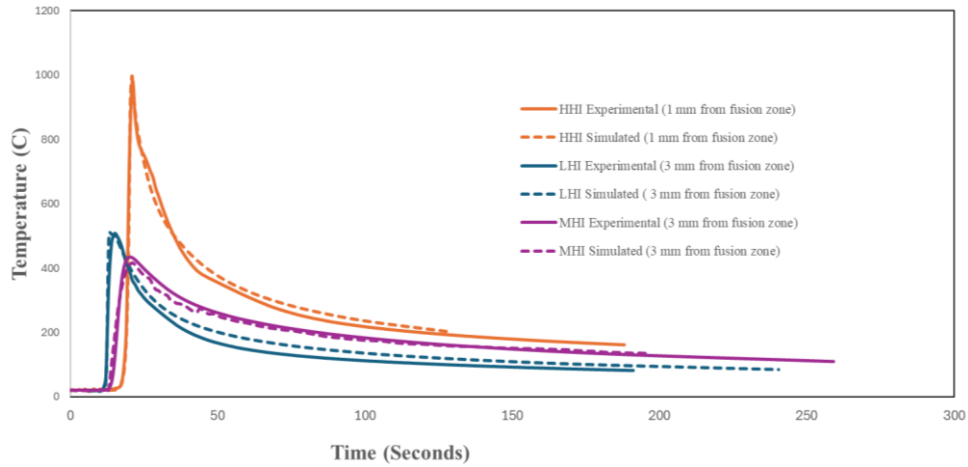
As demonstrated in Fig. 7, Table 3 and Table 4, the predicted thermal histories using calibrated DEGC and DDEG heat sources closely match the measured ones in terms of peak temperatures, heating and cooling rates.

The average error of the predicted peak temperature for the calibrated DDEG heat source model is between 0.3% and 3.4% while that for the calibrated DEGC model is between 0.8% and 4.1%. The small errors in predicting the thermal cycles parameters demonstrate the accuracy of the developed DDEG and DEGC heat source models and the HS calibration procedure.

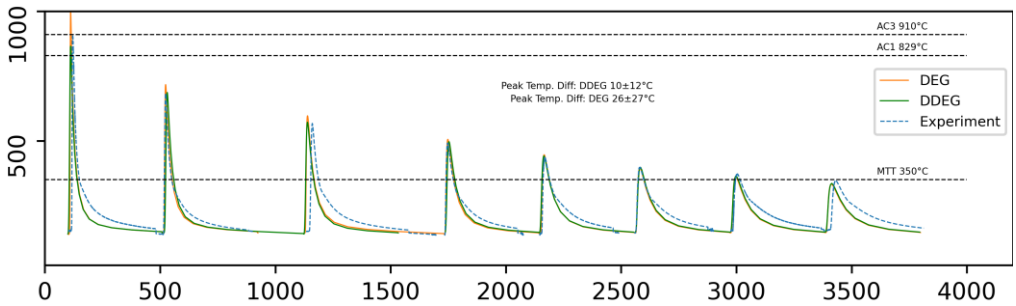
The temperature range of multiple reheat tempering in steels is located between the AC3 temperature and a minimum tempering temperature (MTT) [43], Fig. 7b. Accurate prediction of multiple reheat thermal histories in that temperature range is of importance for efficient process optimization in temper bead welding and additive manufacturing. As shown in Fig. 7b and Table 3, the DDEG heat source demonstrated better accuracy in predicting peak temperatures and cooling times in that temperature range compared to the classical DEG heat source model.

**Table 3** Peak temperature and cooling rate comparison for GMAW-p process simulated with calibrated DDEG HS

| | **Peak Temperature [C]** | | | | | |
|---|---|---|---|---|---|---|
| **Heat Source** | **DDEG** | | | **DEG** | | |
| **Thermal Cycle #** | **Predicted** | **Measured** | **Error (%)** | **Predicted** | **Measured** | **Error (%)** |
| 1 | 681 | 686 | 0.7 | 725 | 686 | 5.4 |
| 2 | 572 | 565 | 1.2 | 592 | 565 | 4.6 |
| 3 | 496 | 491 | 1.0 | 506 | 491 | 3.0 |
| 4 | 441 | 435 | 1.4 | 435 | 435 | 0 |
| 5 | 397 | 398 | 0.3 | 393 | 398 | 1.3 |
| 6 | 363 | 372 | 3.4 | 357 | 372 | 4.0 |
| | **Cooling Time $\Delta t_p/MTT$ $(s)$** | | | | | |
| **Heat Source** | **DDEG** | | | **DEG** | | |
| **Thermal Cycle #** | **Predicted** | **Measured** | **Error (%)** | **Predicted** | **Measured** | **Error (%)** |
| 1 | 13.22 | 13.60 | 2.8 | 14.17 | 13.70 | 3.3 |
| 2 | 8.86 | 8.57 | 3.4 | 9.39 | 8.57 | 8.7 |
| 3 | 6.33 | 6.11 | 3.6 | 6.37 | 6.11 | 4.1 |
| 4 | 4 | 3.93 | 1.8 | 4.25 | 3.93 | 7.5 |
| 5 | 2.77 | 2.47 | 12.1 | 2.90 | 2.47 | 14.8 |




(a) GMAW with DEGC model




(b) GMAWp-AM

**Fig. 7** Thermal history validation for GMAW and GMAW-AM processes

**Table 4** Peak temperature and cooling time comparison for GMAWs process simulated with calibrated DEGC HS

| Heat Input | Peak Temperature [C] | | | $\Delta t_p/MTT\ (s)$ | | |
|---|---|---|---|---|---|---|
| $kJ/mm$ | Predicted | Measured | Error (%) | Predicted | Measured | Error (%) |
| LHI 25 | 511 | 507 | 0.8 | 17 | 20 | 15 |
| MHI 40 | 433 | 416 | 4.1 | 7.5 | 8.5 | 11.7 |
| HHI 55 | 998 | 979 | 1.9 | 32.2 | 34 | 6 |

The developed DDEG and DEGC heat source models and the heat source calibration method are extensively used for microstructure and property predictions, and process optimization in welding and additive manufacturing. Examples of such applications for predicting

hardness distribution in multi-pass GMAWs build in Fe-10Ni steel [41]and in a single pas per layer GMAWp WA-DED build in HSS [42] are shown in Fig. 8 and Fig. 9, respectively.

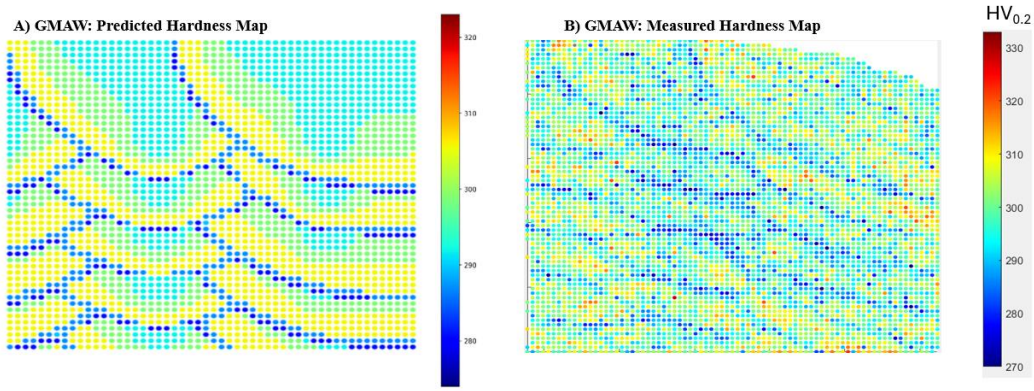
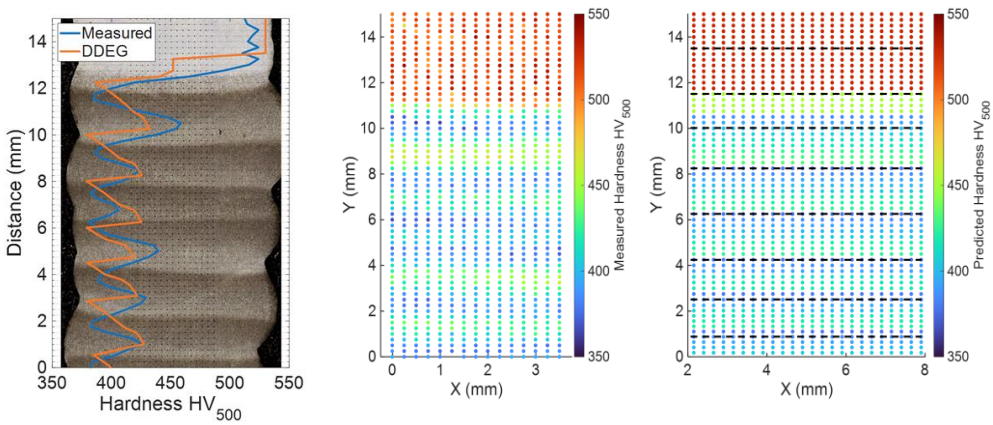



**Fig. 8** Example application of calibrated DEGC heat source in FEA hardness prediction in a GMAWs muti-pass build in Fe-10Ni steel: a) predicted hardness map, b) experimentally generated hardness map

The predicted hardness map in Fig. 8a was developed by FEA modeling of a GMAWs processes using the MHI processes parameters in Table 1, the DGEC heat source in Table 2, and experimentally developed thermal history - hardness relationships [41]. The hardness map in Fig. 8b was generated using LECO LM 100AT hardness mapper with 200g load and 350 $\mu m$ step.




(a) (b) (c)

**Fig. 9** Comparison of the experimental hardness value and predicted by calibrated DDEG model in a GMAWp WA-DED build of HSS

The hardness map in Fig. 9a was generated using LECO LM 100AT hardness mapper with 500g load and 250 $\mu m$ step. The predicted hardness map in Fig. 9b was developed by FEA modeling of a GMAWp WA-DED processes using the respective processes parameters in Table 1, the calibrated DDGE heat source in Table 2, and a modified Grange-Baughman parameter (GBP) representing the tempering response in the tested HHS steel [42]. The GBP was previously modified to account for the effect of multiple reheat weld thermal histories on hardness reduction in weld metals and HAZs of low alloy steels [39,44,43,45,7,46,47].

The close correlation of predicted and experimentally measured hardness distribution shown in Fig. 8 and Fig. 9 demonstrates the benefit of using more expressive heat source models in FEA modeling of WAM processes. The performed validation study demonstrates that by calibrating the proposed DDEG and DEGC heat source models to precisely match the experimental fusion boundary lines, thermal histories and HAZ properties can be accurately predicted in FEA simulations. Comparison made between simulation using calibrated DDEG model and empirical DEG model provides evidence for effective improvement in simulation accuracy using our method. Comparison made between simulation using calibrated DDEG model and empirical DEG model, as shown in Fig. 7b, provides evidence for effective improvement in simulation accuracy using our method.

## CONCLUSION

In this paper, we extended the existing double-ellipsoidal Gaussian (DEG) heat source model to more expressive DDEG and DEGC models that more accurately represent the heat transfer in the molten pool of GMAW and WA-DED processes. We also introduced a novel machine learning-accelerated framework for efficient heat source calibration. The calibrated DDEG and DEGC heat source models were validated and demonstrated by comparing FEA predicted and experimentally measured thermal histories and the hardness distributions in heat affected zones of welded and additively manufactured components.

## References

[1] D. R. ATTHEY: 'A mathematical model for fluid flow in a weld pool at high currents', *Journal of Fluid Mechanics*, Vol. *98*, pp. 787-801, 1980.

[2] A. MAHRLE, J. SCHMIDT and D. WEISS: 'Simulation of temperature fields in arc and beam welding', *Heat and Mass Transfer*, Vol. *36*, pp. 117-126, 2000.

[3] K. C. MILLS, B. J. KEENE, R. F. BROOKS and A. SHIRALI: 'Marangoni effects in welding', *Philosophical Transactions of the Royal Society of London. Series A: Mathematical, Physical and Engineering Sciences*, Vol. *356*, pp. 911-925, 1998.

[4] G. M. OREPER and J. SZEKELY: 'Heat- and fluid-flow phenomena in weld pools', *Journal of Fluid Mechanics*, Vol. *147*, pp. 53, 1984.

[5] T. ZACHARIA, J. M. VITEK, J. A. GOLDAK, T. A. DEBROY, M. RAPPAZ and H. K. D. H. BHADESHIA: 'Modeling of fundamental phenomena in welds', *Modelling and Simulation in Materials Science and Engineering*, Vol. *3*, pp. 265-288, 1995.

[6] T. ZACHARIA, A. H. ERASLAN, D. K. AIDUN and S. A. DAVID: 'Three-dimensional transient model for arc welding process', *Metallurgical transactions. A, Physical metallurgy and materials science*, Vol. *20*, pp. 645-659, 1989.
[7] Y. LUO: *Process Optimization Framework for Temper Bead Welding Procedures*, Master Thesis, The Ohio State University, 2023.
[8] Y. LUO, E. JANG and B. ALEXANDROV: 'Computational Design of Experiment for Temper Bead Welding Design Optimization applied in Overlaying Nickel-based 625 Alloy on Grade 22 Steel', *In Submission*, 2025.
[9] R. I. KARLSSON and B. L. JOSEFSON: 'Three-Dimensional Finite Element Analysis of Temperatures and Stresses in a Single-Pass Butt-Welded Pipe', *Journal of Pressure Vessel Technology-transactions of The Asme*, Vol. *112*, pp. 76-84, 1990.
[10] J. GOLDAK, A. CHAKRAVARTI and M. BIBBY: 'A New Finite Element Model for Welding Heat Sources', *Metallurgical Transactions B*, Vol. *15*, pp. 299-305, 1984.
[11] D. ROSENTHAL: 'Mathematical Theory of Heat Distribution during Welding and Cutting', *Welding Journal*, Vol. *20*, pp. 220-234, 1941.
[12] E. FRIEDMAN: 'Thermomechanical Analysis of the Welding Process Using the Finite Element Method', *Journal of Pressure Vessel Technology-transactions of The Asme*, Vol. *97*, pp. 206-213, 1975.
[13] L.-E. LINDGREN: 'Finite Element Modeling and Simulation of Welding Part 1: Increased Complexity', *Journal of Thermal Stresses*, Vol. *24*, pp. 141-192, 2001.
[14] L.-E. LINDGREN: 'Finite Element Modeling and Simulation of Welding. Part 2: Improved Material Modeling', *Journal of Thermal Stresses*, Vol. *24*, pp. 195-231, 2001.
[15] L.-E. LINDGREN: 'Numerical modelling of welding', *Computer Methods in Applied Mechanics and Engineering*, Vol. *195*, pp. 6710-6736, 2006.
[16] M. A. WAHAB, M. J. PAINTER and M. H. DAVIES: 'The prediction of the temperature distribution and weld pool geometry in the gas metal arc welding process', *Journal of Materials Processing Technology*, Vol. *77*, pp. 233-239, 1998.
[17] P. R. DE FREITAS TEIXEIRA, D. B. DE ARAÚJO and L. A. B. DA CUNDA: 'Study of the gaussian distribution heat source model applied to numerical thermal simulations of TIG welding processes', *Science and Engineering Journal*, Vol. *23*, pp. 115-122, 2014.
[18] A. UR REHMAN, F. PITIR and M. SALAMCI: 'Full-Field Mapping and Flow Quantification of Melt Pool Dynamics in Laser Powder Bed Fusion of SS316L', *Materials*, Vol. *14*, pp. 6264, 2021.
[19] T. W. EAGAR and N. S. TSAI: 'Temperature fields produced by traveling distributed heat sources', Vol. *62*, pp. 346-355, 1983.
[20] J. GOLDAK, M. BIBBY, J. MOORE, R. HOUSE and B. PATEL: 'Computer modeling of heat flow in welds', *Metallurgical Transactions B*, Vol. *17*, pp. 587-600, 1986.
[21] A. ANCA, A. CARDONA, J. RISSO and V. D. FACHINOTTI: 'Finite element modeling of welding processes', *Applied Mathematical Modelling*, Vol. *35*, pp. 688-707, 2011.
[22] S. BARUAH and I. V. SINGH: 'A framework based on nonlinear FE simulations and artificial neural networks for estimating the thermal profile in arc welding', *Finite Elements in Analysis and Design*, Vol. *226*, pp. 104024, 2023.
[23] D. DENG and H. MURAKAWA: 'Numerical simulation of temperature field and residual stress in multi-pass welds in stainless steel pipe and comparison with experimental measurements', *Computational Materials Science*, Vol. *37*, pp. 269-277, 2006.
[24] D. GERY, H. LONG and P. G. MAROPOULOS: 'Effects of welding speed, energy input and heat source distribution on temperature variations in butt joint welding', *Journal of Materials Processing Technology*, Vol. *167*, pp. 393-401, 2005.

[25] J. GOLDAK, M. J. BIBBY, D. DOWNEY and M. GU: 'Heat and Fluid Flow in Welds', *Advanced Joining Technologies*, Springer Netherlands, pp. 69-82, https://doi.org/10.1007/978-94-009-0433-0_6, 1990.
[26] N. T. NGUYEN and J. H. CHUJUTALLI: 'Simulating Convective-Radiative Heat Sinks Effect by means of FEA-based Gaussian Heat Sources and Its Approximate Analytical Solutions for Semi-Infinite Body', https://doi.org/10.21203/rs.3.rs-458143/v1, 2021.
[27] A. K. UNNI and M. VASUDEVAN: 'Determination of heat source model for simulating full penetration laser welding of 316 LN stainless steel by computational fluid dynamics', *Materials Today: Proceedings*, Vol. *45*, pp. 4465-4471, 2021.
[28] J. H. CHUJUTALLI, M. I. LOURENÇO and S. F. ESTEFEN: 'Experimental-based methodology for the double ellipsoidal heat source parameters in welding simulations', *Marine Systems & Ocean Technology*, Vol. *15*, pp. 110-123, 2020.
[29] B. JOSHI, M.-R. AMINI, I. PARTALAS, F. IUTZELER and Y. MAXIMOV: 'Aggressive sampling for multi-class to binary reduction with applications to text classification', *Advances in neural information processing systems*, 2017.
[30] J. A. RAMOS-GREZ and M. SEN: 'Analytical, quasi-stationary Wilson-Rosenthal solution for moving heat sources', *International Journal of Thermal Sciences*, Vol. *140*, pp. 455-465, 2019.
[31] S. K. BATE, R. CHARLES and A. WARREN: 'Finite element analysis of a single bead-on-plate specimen using SYSWELD', *International Journal of Pressure Vessels and Piping*, Vol. *86*, pp. 73-78, 2009.
[32] Y. WANG, L. WANG, X. DI, Y. SHI, X. BAO and X. GAO: 'Simulation and analysis of temperature field for in-service multi-pass welding of a sleeve fillet weld', *Computational Materials Science*, Vol. *68*, pp. 198-205, 2013.
[33] C. LI, Y. SHI, Y. GU, D. FAN and M. ZHU: 'Effects of different activating fluxes on the surface tension of molten metal in gas tungsten arc welding', *Journal of Manufacturing Processes*, Vol. *32*, pp. 395-402, 2018.
[34] M. SEEGER: 'Gaussian Process For Machine Learning', *International Journal of Neural Systems*, Vol. *14*, pp. 69-106, 2004.
[35] D. P. KINGMA and J. BA: *Adam: A Method for Stochastic Optimization*, 2017.
[36] A. KRIZHEVSKY, I. SUTSKEVER and G. E. HINTON: 'ImageNet classification with deep convolutional neural networks', *Advances in neural information processing systems*, Vol. 25, Curran Associates, Inc., 2012.
[37] O. CHAMPAGNE and X.-T. PHAM: 'Numerical simulation of moving heat source in arc welding using the Element-free Galerkin method with experimental validation and numerical study', *International Journal of Heat and Mass Transfer*, Vol. *154*, pp. 119633, 2020.
[38] M. T. FORQUER: *Simplified Computational Modeling Approach for Analysis and Optimization of Temperbead Welding Procedures*, Master Thesis, The Ohio State University, 2018.
[39] J. STEWART: *Temper Bead Welding for Dissimilar Metal Welds and Overlays*, Ph.D. Thesis, The Ohio State University, 2019.
[40] F. NOGUEIRA: *Bayesian Optimization: Open source constrained global optimization tool for Python*, https://github.com/bayesian-optimization/BayesianOptimization, 2014.
[41] S. MATAN and B. ALEXANDROV: 'Computational Framework for Microstructure and Hardness Prediction in Fe-10Ni Welds', *In Submission to Welding Journal*, 2025.
[42] N. M. VEGA MICHALAK, B. ALEXANDROV, L. MCNEIL, D. HARWIG and P. FLATER: 'Understanding and Predicting the In-situ Tempering Effect during Wire-Arc Directed Energy Deposition of a High Strength Steel', *In Submission*, 2025.

[43] J. STEWART, B. ALEXANDROV and B. T. ALEXANDROV: 'Quantification of the hardness response in the heat-affected zone of low alloy steels subjected to temper bead welding', *Journal of Manufacturing Processes*, Vol. *66*, pp. 325-340, 2021.

[44] E. JANG, J. STEWART, Y. LUO, S. QU, ET AL.: 'Tempering Efficiency Evaluation for Dissimilar Weld Overlays', *Volume 1: Codes and Standards*, American Society of Mechanical Engineers, 2020.

[45] E. JANG, Y. LUO, B. ALEXANDROV, S. L. MCCRACKEN, J. TATMAN and D. BARBORAK: 'Quantification of the Tempering Response for Temper Bead Welding of SA-508 Low Alloy Steel', *Volume 1: Codes and Standards*, American Society of Mechanical Engineers, 2022.

[46] E. JANG, B. ALEXANDROV, S. MCCRACKEN and D. BARBORAK: 'Tempering Procedure Effects on the Impact Toughness in Simulated Heat Affected Zone of Grade 22 Steel', *Journal of Pressure Vessel Technology*, Vol. *146*, pp. 041501, 2024.

[47] E. JANG: *Tempering Kinetics and Carbide Precipitation in Low Alloy Steel Heat Affected Zones in Temper Bead Welding*, Ph.D. Thesis, The Ohio State University, 2025.

# WA-DED SPECIFIC TOPOLOGY OPTIMIZATION OF A KINGPIN PLATE FOR SEMI-TRAILERS

F. HAUNREITER*, M. SILMBROTH*, K. BHARADWAJ*, H. DREXLER*, M. SCHWENDINGER**, H. BRUHNS**, A. BAUER**

**LKR Light Metals Technologies GmbH, AIT Austrian Institute of Technology, 5282 Ranshofen, Austria*
***Wilhelm Schwarzmüller GmbH, 4785 Freinberg, Austria*

*DOI 10.3217/978-3-99161-089-2-030, license CC BY 4.0*
*https://creativecommons.org/licenses/by/4.0/deed.en*
*This CC license does not apply to third party material and content noted otherwise.*

## ABSTRACT

Additive manufacturing (AM) offers significant design freedom compared to conventional manufacturing methods. This enables the production of complex, topology-optimized metal components. While powder bed processes are well-established for small to medium-sized parts, large-scale applications benefit from directed energy deposition (DED) techniques such as wire-arc directed energy deposition (wa-DED). Despite its potential, limited research addresses topology optimization specifically tailored to the constraints of wa-DED. This study presents a workflow for wa-DED-compatible topology optimization, using a semi-trailer kingpin plate as a demonstrator geometry. All simulations were conducted using Altair OptiStruct. Multiple optimization scenarios were evaluated to compare the impact of different optimization approaches and manufacturing constraints. The most suitable design achieved a 59 % weight reduction compared to the initial design using minimized mass fraction with stress, deformation and draw type constraints. A nonlinear finite element (FE) analysis confirmed the structural integrity of the optimized geometry under relevant load cases. To validate manufacturability, a quarter section of the design was successfully fabricated using wa-DED.

Keywords: wa-DED, topology optimization, FE reanalysis, Altair Optistruct

## INTRODUCTION

With a share of 49 %, road transport accounts for the largest portion of total freight transport in the European Union (EU) [1]. It is also a major contributor to EU's greenhouse gas emissions. Road freight alone is responsible for 689.8 million tons of $CO_2$ equivalent, approximately 76.7 % of all transport-related emissions [2]. Reducing vehicle weight is a proven strategy for improving fuel efficiency and lowering emissions. For example, a 27-ton truck can save 0.05 l/100 km for every 100 kg of weight reduction [3]. Assuming a diesel price of 1.54 € per Liter [4], a trailer weight of 6000 kg [5] and an annual travelling distance of

100000 km, a 25 % reduction in trailer weight can lead to annual fuel cost savings of approximately 1155 €. Besides environmental impact, weight reduction also offers logistical benefits. Regulations limit the total allowable trailer weight. For example, a three-axle trailer forming part of a vehicle combination is restricted to 24 tons [6]. Thus, reduced trailer weight also leads to increased load capacity, thereby improving overall efficiency. However, achieving significant weight reduction without compromising performance is a complex design task.

Numerical methods, such as topology optimization, can assist in this process. Topology optimization is used to determine the optimal material distribution within a given design space by minimizing an objective function F while satisfying predefined constraints [7]. Several case studies have demonstrated the effectiveness of such methods in reducing the weight of truck trailer components with reported savings ranging from 14 % to 29 % [8–10]. The weight reduction of 29 % was achieved through the combined application of topology and thickness optimization [8].

Combining topology optimization with additive manufacturing (AM) enables the full potential of both technologies [11]. In particular, the increased design freedom offered by AM allows for significant additional weight reductions. The selection of an appropriate AM process depends on several factors such as the component size and its material. Wire arc directed energy deposition (wa-DED) is an AM process well suited for producing large metallic components such as those used in truck trailers. Wa-DED uses an electric arc in combination with wire feedstock [12]. This enables the near-net-shape fabrication of metallic components through robot-controlled process movement. For steel, deposition rates can reach up to 10 kg/h [13]. Compared to laser powder bed fusion, wa-DED offers lower investment and operating costs [14]. Although there is extensive research on topology optimization for powder bed processes [15-17] studies specifically focusing on wa-DED remain limited. However, few existing case studies show promising results. In the case of an aeronautical fastening component, the combination of wa-DED and topology optimization enabled a 31 % weight reduction [18]. Additional research has explored the use of wa-DED in the construction sector producing optimized structural nodes, truss structures and T-joints [19-21].

This work investigates the weight reduction potential achievable by combining topology optimization with wa-DED. A kingpin plate for semi-trailers, sometimes also referred as a skid plate, is used as a demonstrator geometry. Fig. 1 shows the S355 steel kingpin plate used in this study. Its primary function is to provide a secure connection between the tractor and the trailer. The flat surface of the kingpin plate transfers vertical loads from the trailer to the tractor, while the kingpin itself locks into the fifth wheel coupling, allowing only rotational movement during turns. The kingpin is mounted to a separate base plate, designated as the retention plate. This retention plate is welded onto the kingpin plate, and the kingpin is attached to it using bolts.

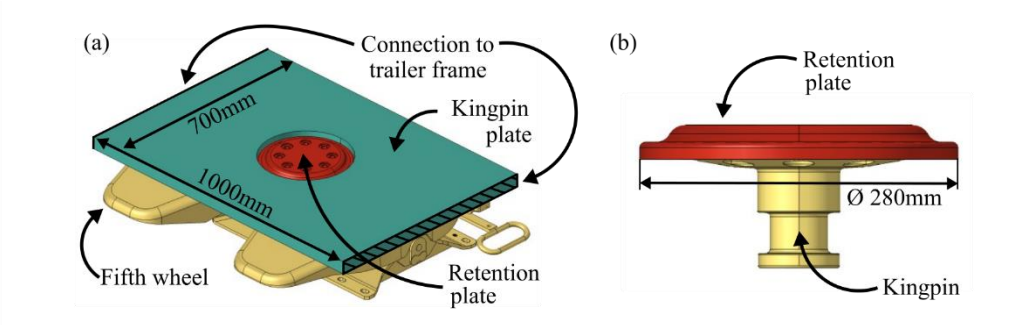



**Fig. 1** Fifth wheel coupling (a) assembly of all components (b) assembly of kingpin and retention plate

## DESIGN AND BOUNDARY CONDITIONS USED FOR TOPOLOGY OPTIMIZATION

Topology optimization involves numerous iterative solution cycles to achieve an optimal material distribution. To improve computational efficiency, the design space was restricted to a 40 mm thick steel plate with dimensions of 1000 mm × 700 mm. Excluding surrounding components not only reduced computational effort but also enabled the use of global stress constraints. The simplified model is shown in Fig. 2. As a predefined design requirement, the wa-DED structure was embedded between two 6 mm thick steel plates. This configuration creates a closed structure that helps prevent dirt and debris accumulation. In the finite element (FE) model, the plates were represented using first order 2D quadrilateral shell elements with four nodes (CQUAD4), each with an element size of 5 mm. The 28 mm thick optimization region was modelled using first order 3D hexahedral solid elements with eight nodes (HEX8). As for the shells, the element size was set to 5 mm. Shell and solid elements were connected via shared nodes to ensure continuity and avoid contact definitions. To maintain a closed geometry, outer elements were excluded from the design space.

Four load cases were considered. Braking and cornering (in two directions) with loads of 120 kN, and acceleration with loads of 60 kN. The forces were applied using an RBE3 element. Additionally, a distributed surface load of 120 kN was applied to the fifth-wheel contact area to represent trailer weight and payload. As shown in Fig. 2, the steel plate's connection to the trailer was modelled using fixed nodes (locked x, y, and z directions) in the weld seam area. During optimization, linear-elastic material properties were assumed for S355 steel, using a Young's modulus of 210000 N/mm² and a Poisson's ratio of 0.3.

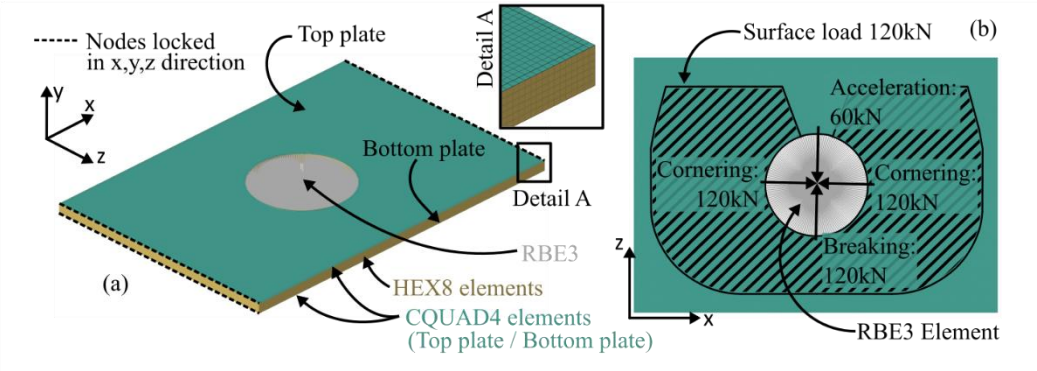



**Fig. 2** FE model for topology optimization (a) isometric view (b) bottom view

## TOPOLOGY OPTIMIZATION

All simulations in this study were performed using Altair OptiStruct. Topology optimization was carried out using the Solid Isotropic Material with Penalization (SIMP) method [22]. In SIMP, element density is treated as the design variable, and a nonlinear relationship between density and stiffness is applied to drive the solution toward discrete, manufacturable designs.

### TOPOLOGY OPTIMIZATION PROBLEM SETUP

Several optimization problem formulations were considered for the kingpin plate [22]. A common approach is to minimize the compliance with constrained volume or mass fraction. Compliance is the inverse of a structure's stiffness [23]. Thus, minimizing the compliance promotes stiffness maximization. Volume fraction describes the ratio between the proposed volume and the original [24]. For example, a volume fraction of 25 % means that only 25 % of the material remain after topology optimization. When working with OptiStruct mass fraction is similar to volume fraction, with the key difference being that mass fraction also considers the non-design mass, while volume fraction only accounts for the design volume [25]. Mass or volume fraction can be used not only as a constraint in optimization but also as an objective function to be minimized, with additional constraints applied to displacements and stresses. Altair OptiStruct supports two types of stress constraints [22]. The first considers global von Mises stress across the entire model, including non-design regions. This method converges quickly, applies stress filtering, and disregards local stress concentrations. The second allows more detailed, component- and subcase-specific definitions of stress types, but often results in slower convergence. Specifications provided by the fifth wheel manufacturer limited the maximum deflection of the bottom plate to ±2 mm. For safety reasons, the maximum stress should not exceed 150 MPa thus ensuring a safety factor greater than two. Based on these criteria, an optimization problem was formulated to minimize mass while

constraining displacements and stress. Additional studies were conducted using increased load values in place of explicit stress constraints. Furthermore, the objective function was modified to minimize compliance, while maintaining constraints on volume and displacement. The resulting designs were compared to identify the most suitable variant for wa-DED manufacturing.

## MANUFACTURING CONSTRAINTS

Altair OptiStruct offers a range of manufacturing constraints to guide the generation of feasible, production-ready designs [26]. Since there are currently no wa-DED specific constraints available, existing ones tailored for other manufacturing processes must be applied instead. Extrusion and draw direction constraints were identified as the most suitable options for achieving a wa-DED manufacturable kingpin plate design.

Fig. 3 shows optimization results using different manufacturing constraints. All simulations were conducted using compliance minimization with a constrained mass fraction of 20 %. To better illustrate the effects of the constraints, the top and bottom shell elements were excluded from the design. Without manufacturing constraints, the resulting geometry is highly complex and not suitable for production via wa-DED. The extrusion constraint enforces a uniform cross-sectional profile along a specified direction, while the draw direction constraint also requires a direction but allows for decreasing cross-sectional areas. Originally developed for casting, the draw constraint also includes a Stamp option, which limits the result to a 2D shell-like geometry. This option was not used, as the kingpin plate must maintain flat surfaces on both the top and bottom to ensure proper assembly.

Additional manufacturing constraints can be applied to control the minimum and maximum member sizes within the design space. This is particularly important for wa-DED, where excessive material accumulation may lead to localized heat buildup and thermal distortion. Such effects are especially critical when using thin substrate plates, such as the 6 mm steel plates employed in this study. However, in OptiStruct, the maximum member size must be at least six times the average mesh size. To achieve a desired layer width between 6 and 9 mm, a mesh size of approximately 1.5 mm would be required. Using a mesh size of 1.5 mm would result in excessively long simulation times and reduced computational efficiency. Therefore, no member size constraints were imposed on the design.

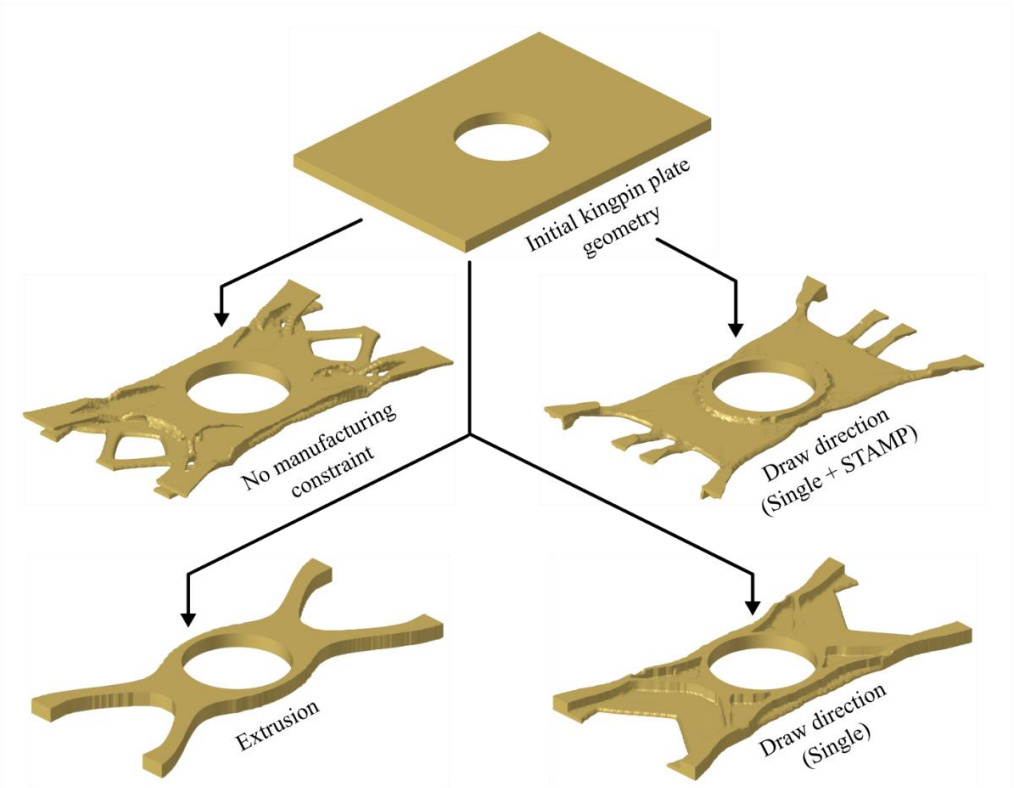



**Fig. 3** Optimization of the initial king plate geometry using different manufacturing constraints

Except for the unconstrained case, all configurations shown in Fig. 3 are considered manufacturable using wa-DED. Based on these findings, subsequent optimization studies used the draw direction constraint (without the Stamp option), as it more closely reflects wa-DED capabilities. Unlike extrusion, wa-DED does not require a constant cross-section throughout the building height, making the draw direction constraint a better fit for the process.

## FE REANALYSIS

During topology optimization, only the solid and shell elements representing the kingpin plate were considered. To assess the structural behaviour under more realistic boundary conditions, a FE reanalysis was performed on the optimized design. The corresponding FE model is shown in Fig. 4. Compared to the simplified model used in Fig. 2, the updated model includes additional components such as the fifth wheel, the retention plate, and the kingpin, as well as their interactions. Surface loads were applied in the regions where the kingpin plate is later connected to the trailer frame. As in the optimization phase, four load cases were simulated,

covering acceleration, cornering, and braking scenarios. The total applied forces in each case matched those used in the optimization setup (see Fig. 2). Fig. 4 (a) schematically illustrates the force directions for the braking load case.

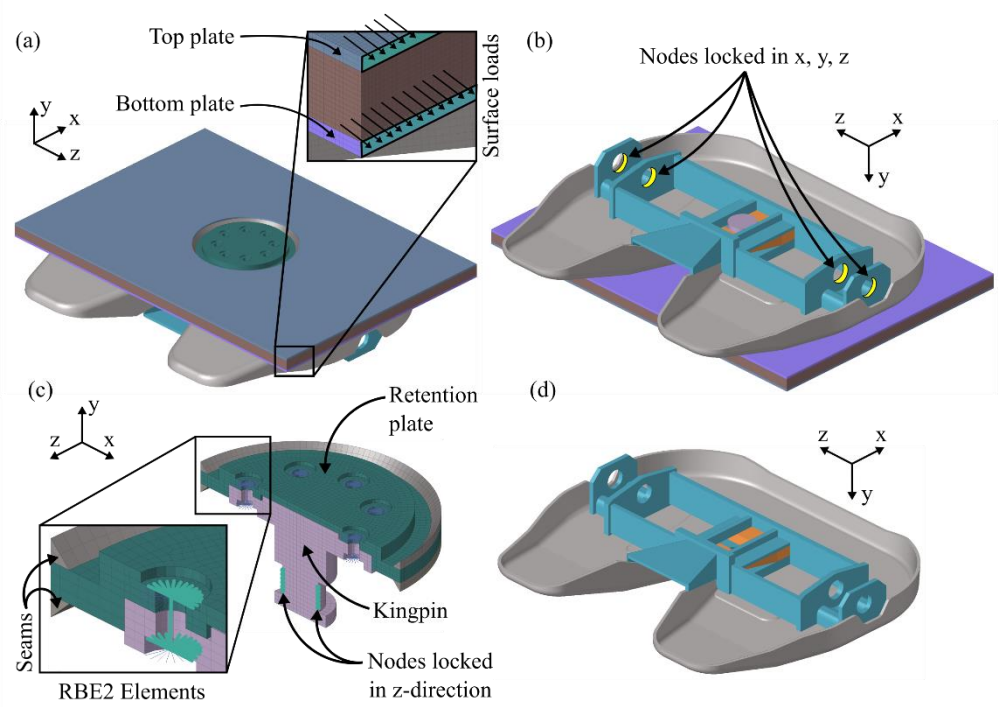



**Fig. 4** Model for FE reanalysis (a) surface load orientation (braking load case) (b) locked fifth wheel nodes (c) constrained kingpin nodes and RBE2 elements for retention plate connection (braking load case) (d) fifth wheel components connected using freezing contact

To fully constrain the system, the nodes at the bolt holes, where the fifth wheel attaches to the tractor, were fixed in the x, y, and z directions (Fig. 4 (b)). Contact interactions between the fifth wheel, kingpin plate, and kingpin were defined assuming a friction coefficient of 0.1 for the lubricated steel on steel contact. To prevent undesired rotation of the kingpin plate, selected nodes on the kingpin were constrained in either the x or z direction, depending on the load case (Fig. 4 (c)). The wa-DED structure and the top and bottom steel plates were meshed using 2 mm elements, while 4 mm elements were used for the fifth wheel and the kingpin. RBE2 elements were employed to connect the kingpin to the retention plate. All fifth-wheel components shown in Fig. 4 (d) were connected using freezing contact, thereby enforcing zero relative motion between the contact faces. The weld seams between the kingpin plate and the retention plate were modelled with a throat thickness (a-dimension) of 7 mm and connected via freezing contact.

## RESULTS

Fig. 5 illustrates the final design of the kingpin plate, which was developed using a single draw-type manufacturing constraint combined with defined limits for stress and deformation. Compared to the initial design using a 40 mm thick steel plate with a weight of 200 kg the mass was reduced by 59 %.

During fabrication, the wa-DED structure is deposited directly onto the substrate plate. In the regions along the four outer edges and the inner circular recess, the layer width is increased by 3 mm to allow for subsequent machining. These areas, indicated by hatching in Fig. 5, are subjected to subtractive post-processing to meet dimensional and surface quality requirements. In addition to the outer contours, the top surface is also machined to ensure a flat and uniform bonding area for the attachment of the top plate.

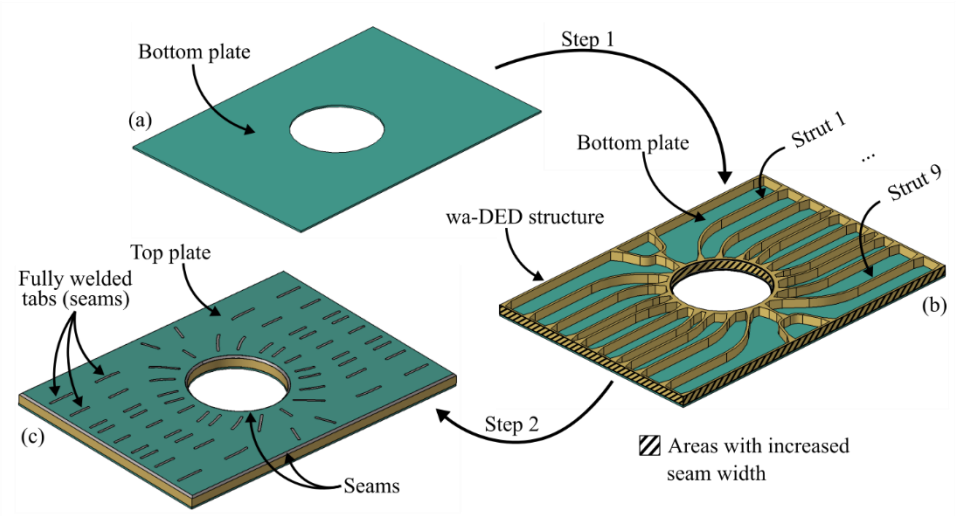



**Fig. 5** Manufacturing steps for the wa-DED optimized kingpin plate (a) bottom plate (b) wa-DED structure on bottom plate with highlighted machining surfaces (c) final design including top plate

Following the machining process, the top plate is positioned and joined to the wa-DED structure. This is accomplished by fully welding the pre-cut tabs in the top plate to the underlying additively manufactured features. Additional fillet welds are applied around the kingpin hole and along the side interfaces to ensure adequate structural performance and reliable load transfer.

A comparative evaluation of three different topology optimization problem setups guided the selection of the final kingpin plate geometry. Fig. 6 presents the results for each setup. All optimization runs incorporated a single draw-type manufacturing constraint to ensure compatibility with wa-DED fabrication requirements. Variants 1 and 2 were formulated to minimize mass fraction while imposing a maximum allowable deformation of ±2 mm.

In Variant 1, an initial optimization was conducted with only the deformation constraint. The resulting geometry served as a non-design space for the subsequent refinement step, referred to as Variant 1 (b). In this step, a global stress constraint was introduced to limit the maximum stress to 150 MPa and avoid critical stress concentrations. While the optimized geometry met the strength and deformation requirements, issues emerged during the subsequent finite element reanalysis (FEA). In the topology optimization phase, all nodes at the interface between the wa-DED structure and the top plate were treated as fully connected. However, in the reanalysis, only nodes located in the actual weld regions, specifically at the fully welded tabs shown in Fig. 5, were modelled as shared. During topology optimization, it was not possible to consider shared nodes only in the actual weld regions, since their definition is based on the geometry resulting from the optimization process. To mitigate the stress concentrations observed in the reanalysis, the number of wa-DED struts was increased. It was found that a configuration with at least seven struts effectively reduced stress in the welded connection zones to acceptable levels. This was achieved by iteratively reducing the maximum allowable stress constraint, with a limit of 120 MPa yielding the desired structural layout.

Variant 2 retained the ±2 mm deformation constraint but followed a different approach to reduce stress concentrations. Instead of applying an explicit stress constraint, the applied loads were scaled by a factor of 1.65 during optimization to indirectly encourage the formation of a seven-strut configuration similar to Variant 1 (b). The scaling factor was determined through iterative refinement.

In Variant 3, the objective function was changed to compliance minimization, with constraints on volume and displacement. With a total of 32 iterations and a CPU time of 35 minutes, the computational costs are low compared to Variants 1 and 2. Although this setup yields a structurally valid solution quickly, it leads to significant material accumulation, making the design unsuitable for wa-DED manufacturing. Consequently, Variant 3 was excluded from further consideration.

Variants 1 and 2 were translated into manufacturable CAD models using Autodesk Inventor. The entire structure was designed such that the wa-DED layers have a width of 7 mm. Exceptions include the inner connection to the kingpin plate, where a 12 mm layer width was applied, and the strut interfaces, where the width was increased to 23 mm to enlarge the bonding surface and reduce stress concentrations.

The final CAD representations of Variants 1 (b) and 2 are shown in Fig. 7. For the final design based on Variant 1 (b), the small struts adjacent to struts 3 and 5 were treated as separate members, resulting in a total of nine struts. Although this configuration weighs 82 kg (1 kg more than Variant 2) it was selected as the final design. The decision was based on its reduced number of intersections. While wa-DED is capable of manufacturing complex three-dimensional geometries, intersections in particular are associated with an increased risk of defects, making a design with fewer such features preferable. In Variant 1 (b), intersections occur only at the four outer edges and at the inner circular recess, whereas Variant 2 additionally exhibits intersections between the individual struts.

The computation time for Variant 2, 1 hour and 42 minutes, is shorter than that of Variant 1 (a and b), which requires 2 hours and 19 minutes. However, this difference was not considered in the decision-making process, as the focus of the study is on the manufacturability of the structure.

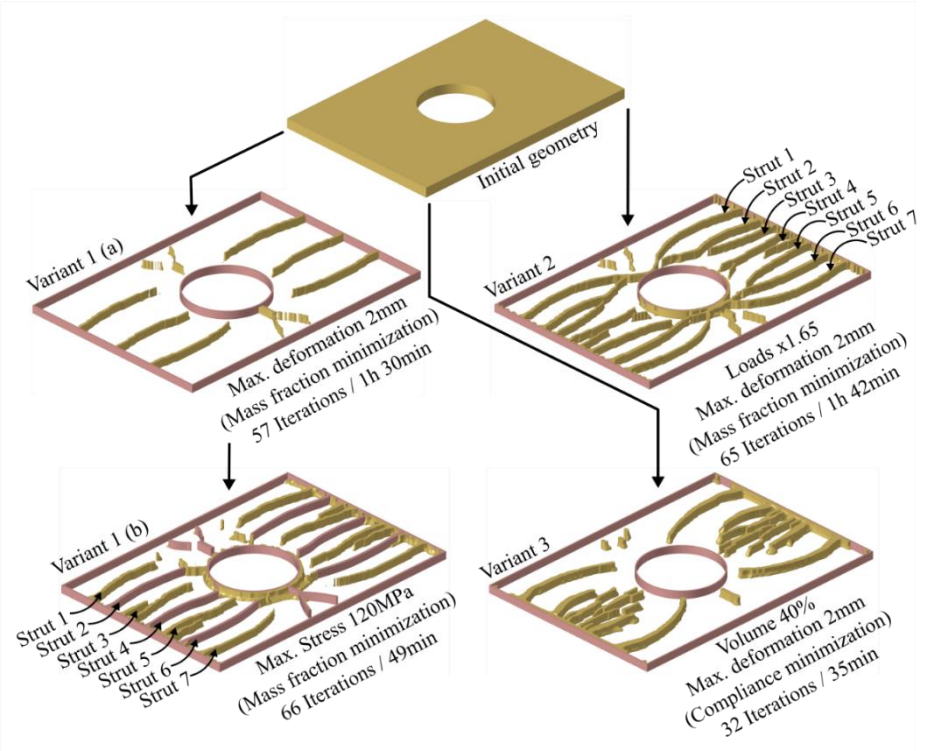



**Fig. 6** Topology optimized designs of the initial kingpin plate geometry obtained using different optimization objectives and constraints, along with the corresponding computational costs (top and bottom plates not shown)

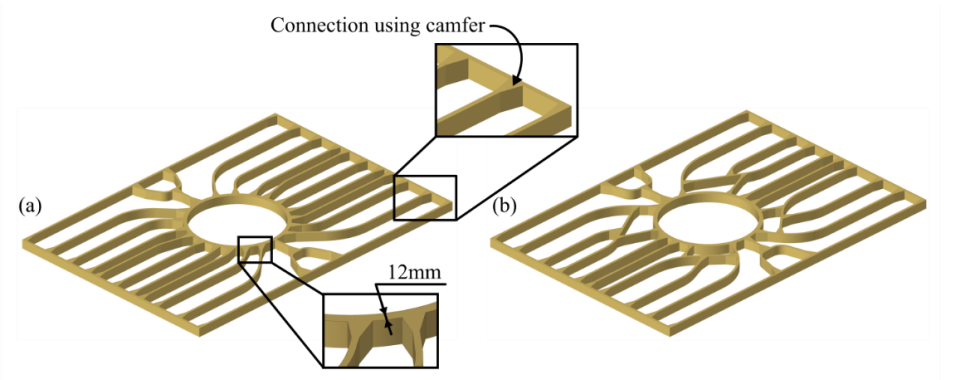



**Fig. 7** Processed CAD models of the optimized structures (a) Variant 1: deformation and stress constraint (b) Variant 2: increased loads and deformation constraint

## FE REANALYSIS

The results of the FE reanalysis are presented in Fig. 8 to Fig. 11. In contrast to the topology optimization model, where all nodes at the interface between the wa-DED structure and the top plate were shared, the reanalysis model applies shared nodes only within the defined weld seam areas and the regions of the fully welded tabs, as indicated in Fig. 5. All four load cases were evaluated.

Fig. 8 shows the deformation in the y-direction, with the maximum deformation occurring under the braking load case, ranging from +0.73 mm to -1.5 mm. These values remain within the allowable limit of ±2 mm, thus fulfilling the displacement requirement. For the cornering load cases, the deformation patterns exhibit asymmetry with respect to the xy-plane. This behaviour results from the asymmetric contact geometry between the kingpin and the fifth wheel, as illustrated in Fig. 9. Fig. 10 presents the von Mises stress distribution across all load cases. The highest stress condition, 242 MPa, occurs in the cornering load case with force applied in the negative z-direction. Compared to the material's yield strength of 355 MPa, this results in a safety margin that is too low.

When isolating elements with stress values above 150 MPa (Fig. 11), it becomes apparent that the highest stresses are located in the regions of the fully welded tabs where the substrate is connected to the top plate via shared nodes. These stress concentrations are most likely numerical artifacts and are not expected to occur in the actual component. Additional stress concentrations above 150 MPa are observed at the bottom of the wa-DED structure, where it interfaces with the bottom plate. These are likely caused by contact interactions between the fifth wheel edge and the bottom plate. However, the stress levels in this region remain below the peak value of 242 MPa.

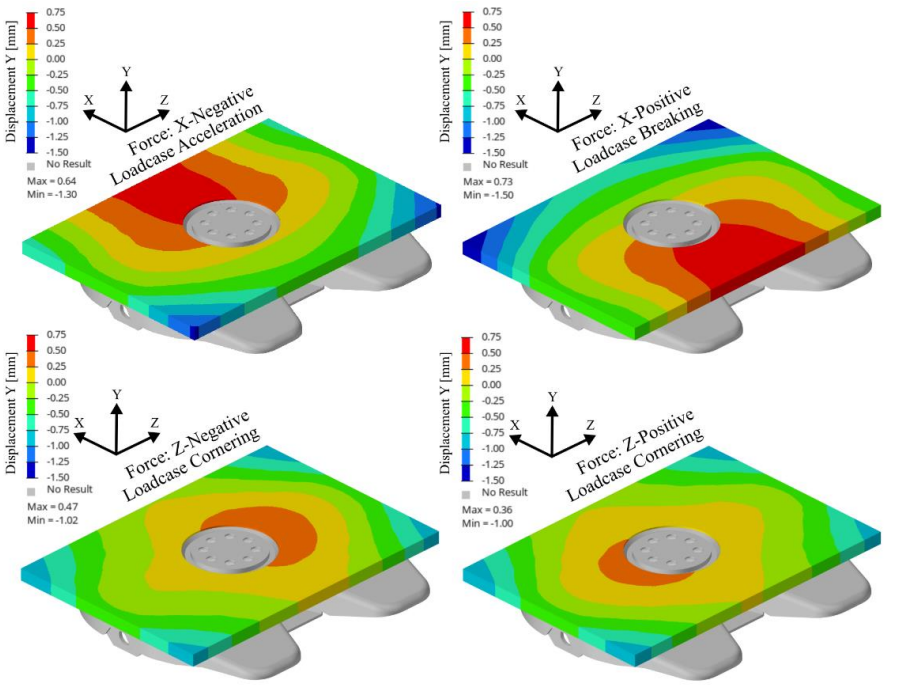



**Fig. 8** FE reanalysis (y-direction displacements) for the four load cases: acceleration, braking, and both cornering cases

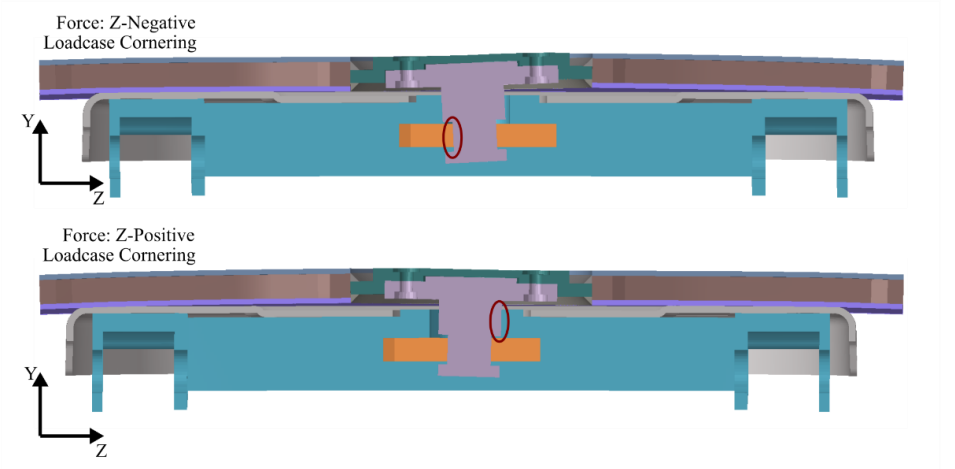



**Fig. 9** FE reanalysis (kingpin contact faces for cornering load cases marked in red / displacement scale factor 10)

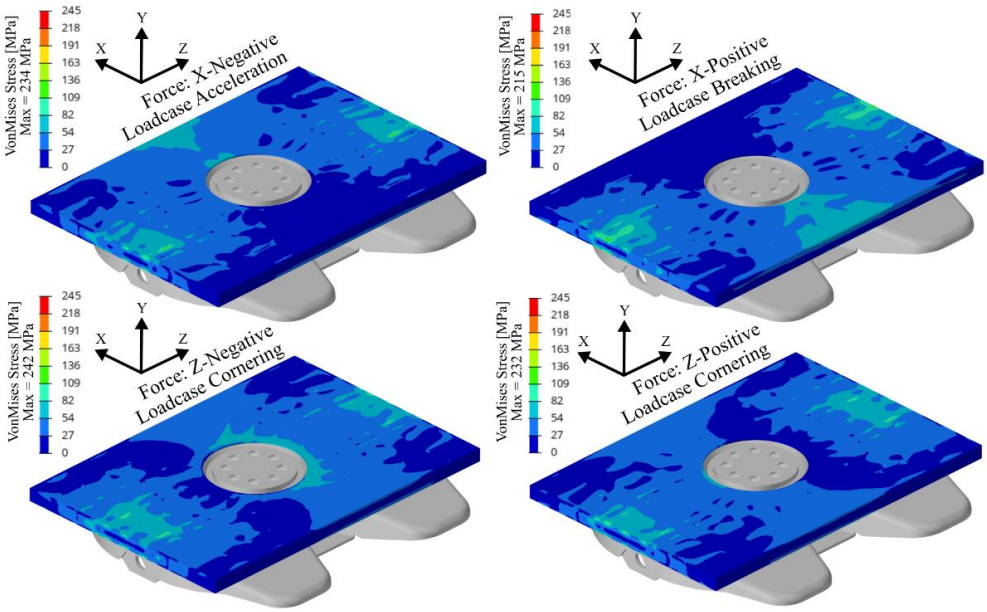



**Fig. 10** FE reanalysis (VonMises Stresses) for the four load cases: acceleration, braking, and both cornering cases

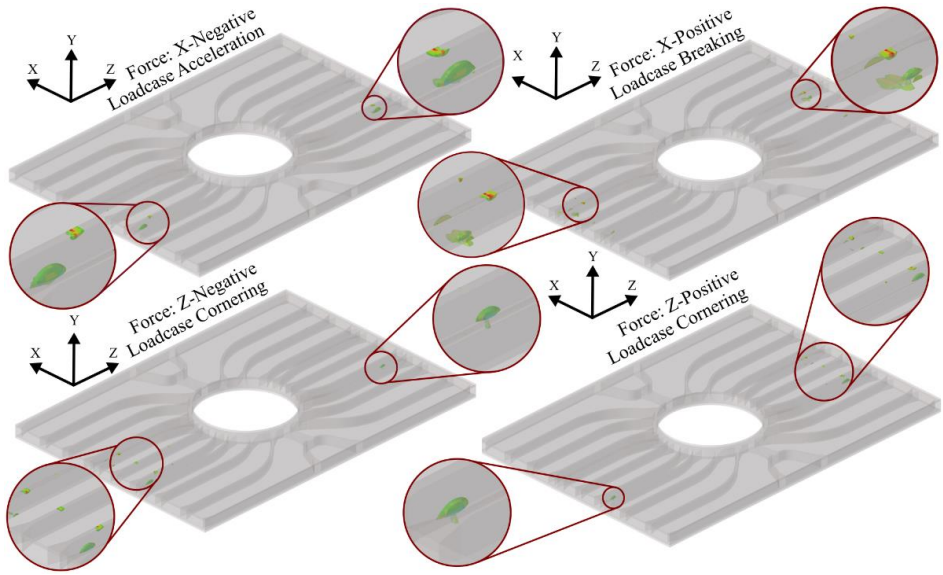



**Fig. 11** FE reanalysis (regions with VonMises Stress > 150MPa) for the four load cases: acceleration, braking, and both cornering cases

## WA-DED MANUFACTURING

To validate the manufacturability of the optimized design using wa-DED, a quarter section of the structure was fabricated. An image of the manufactured section is shown in Fig. 12. The wa-DED system consists of a KUKA KR 300 R2700-2 industrial robot in combination with a Fronius iWave 500i AC/DC power source. All wa-DED structures were deposited using Fronius CMT Additive Pro process and a Böhler EMK-6 wire with a diameter of 1.2 mm. The flow rate of the M12 shielding gas was set to 15 L/min.

A constant travel speed of 12 mm/s was maintained throughout the build-up. To achieve the required layer width, a rectangular weaving pattern was employed. The weave amplitude was automatically adjusted to the desired layer width using the ModuleWorks LAM module within Mastercam software. Robot offline programming and post processing was carried out in Robotmaster. All CAM software solutions were supplied by robotized rm systems. To promote adequate fusion at intersecting regions, the heat input was locally increased by applying Additive Pro power correction and adjusting the wire feed rate.

During the build-up, the substrate was clamped to a tilting/rotary table equipped with internal cooling channels for active temperature control. The temperature of the circulating fluid was regulated using a Robamat heating and cooling unit. With this setup, the S355 substrate plate was preheated to 65 °C. Once the build-up process started, the coolant setpoint was reduced to 40 °C to prevent heat accumulation in the welding table and thereby minimize dwell times. Due to the large thermal mass of the work table, this adjustment did not result in an immediate reduction of the substrate temperature. Instead, the table responded gradually to the changed coolant temperature, providing a controlled cooling effect.

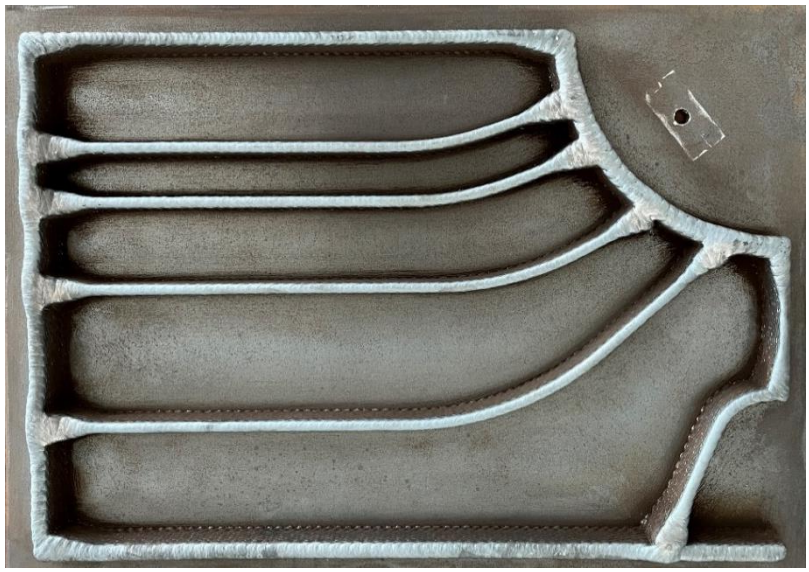


**Fig. 12** Quarter section demonstrator manufactured via wa-DED

To further reduce dwell times, the interlayer temperature was set to approximately 150 °C. In contrast to lower interlayer temperatures, such as 100 °C, this value helps to maintain short dwell times even in the upper layers, while also ensuring that the material achieves the required yield strength of 355 MPa [27-28]. The measurement of the interlayer temperature was carried out manually using a Type K surface probe.

Although a constant interlayer temperature was maintained, a gradual reduction in wire feed speed was required with an increasing number of layers. The first layer was deposited using a wire feed speed of 4.7 m/min. In subsequent layers the wire feed speed was gradually decreased from 4.0 m/min to 3.5 m/min. This adjustment was required because heat dissipation into the substrate becomes less effective as the build height increases. Moreover, despite active cooling, the global component temperature rises continuously from the initial 60 °C with increasing layer number. Applying this thermal strategy resulted in a total fabrication time of approximately 4.5 hours for the quarter section.

## SUMMARY AND OUTLOOK

This study presents a comprehensive investigation into the potential of combining topology optimization with wa-DED to design a lightweight, structurally efficient kingpin plate for semi-trailers. The goal was to reduce weight without compromising performance while ensuring manufacturability. Various topology optimization strategies were explored, including mass fraction minimization under stress and deformation constraints and compliance minimization under volume and deformation restrictions. Among the evaluated approaches, the most promising results were obtained using a two-step mass fraction minimization strategy which incorporated both deformation and global stress constraints alongside a draw-direction manufacturing constraint. This configuration yielded a structurally valid design with improved stress distribution, reduced complexity, and a final mass of 82 kg, resulting in a 59 % weight reduction compared to the original 200 kg steel plate.

A detailed finite element reanalysis incorporating realistic boundary conditions, contact interactions, and weld seam modelling confirmed that the optimized structure met all functional requirements. Displacements remained within the allowable ±2 mm threshold across all load cases. Local stress concentrations with a maximum value of 242 MPa remain below the materials yield strength but exceed the defined limit of 150 MPa. The highest stress concentrations occurring in the area of the shared nodes between the substrate and the top plate are assumed to be caused by numerical effects. They are not expected to affect the structural performance. The simulation results suggest that the optimized design maintains an acceptable safety margin under all critical loading scenarios.

To validate the practical feasibility of the proposed design, a quarter-section of the optimized structure was successfully manufactured using a robotic wa-DED system. This step confirmed that the design is compatible with current AM capabilities. Preheating and cooling strategies were employed to ensure proper material quality while reducing dwell times.

To ensure suitability for real-world applications, future studies should address more complex loading conditions and include a detailed evaluation of the material’s fatigue

performance. In addition, it would be important to assess how accurately FEM simulations can capture the mechanical behaviour of wa-DED structures in the as-built condition.

## APPENDICES AND ACKNOWLEDGEMENTS

This research was funded by the federal state of Upper Austria in the project "GEPROBA - Gesteigerte Prozess- und Bauteilperformance durch neue Fertigungsmöglichkeiten für eMobilitäts-Anwendungen" (grant no. 901696) administered by Austrian Funding Agency (FFG) within the framework "Future Mobility". The authors thank the project partners for the collaborative work.

## References

[1] J. BARAN and A. K. GÓRECKA: 'Economic and environmental aspects of inland transport in EU countries', *Economic Research-Ekonomska Istraživanja*, vol. 32, pp. 1037-1059, 2019, doi: 10.1080/1331677X.2019.1578680.

[2] J. DOMAGAŁA and M. KADŁUBEK: 'Economic, Energy and Environmental Efficiency of Road Freight Transportation Sector in the EU', *Energies*, vol. 16, 2023, doi: 10.3390/en16010461.

[3] RICARDO-AEA: *Light weighting as a means of improving Heavy Duty Vehicles' energy efficiency and overall CO2 emissions: Heavy Duty Vehicles Framework Contract – Service Request 2*, 2015.

[4] *Weekly Oil Bulletin*, accessed: Jul. 10, 2025. [Online]. Available: https:/energy.ec.europa.eu/data-and-analysis/weekly-oil-bulletin_en

[5] WILHELM SCHWARZMÜLLER GMBH, accessed: Jul. 10, 2025. [Online]. Available: https:/schwarzmueller.com/de/fahrzeuge/plateau-fahrzeuge/plateausattel-standard/3-achs-schiebeplanen-plateausattel/

[6] EUROPEAN PARLIAMENT: *Road vehicles: maximum weights and dimensions: P9_TA(2024)0126*, 2024.

[7] O. SIGMUND and K. MAUTE: 'Topology optimization approaches', *Struct Multidisc Optim*, vol. 48, pp. 1031-1055, 2013, doi: 10.1007/s00158-013-0978-6.

[8] G.-W. JANG, M.-S. YOON and J. H. PARK: 'Lightweight flatbed trailer design by using topology and thickness optimization', *Struct. Multidisc. Optim.*, vol. 41, pp. 295-307, 2010, doi: 10.1007/s00158-009-0409-x.

[9] J. GALOS and M. SUTCLIFFE: 'Material Selection and Structural Optimization for Lightweight Truck Trailer Design', *SAE International Journal of Commercial Vehicles*, 2020, doi: 10.4271/02-12-04-0022.

[10] D. GAO, J. MA, H. ZHENG, M. ZHANG and J. ZHAO: 'Optimal Design of Frame Structure of Center Axle Trailer Under Heavy Load Conditions', pp. 201-219, doi: 10.1007/978-981-97-1876-4_16.

[11] J. ZHU, H. ZHOU, C. WANG, L. ZHOU, S. YUAN and W. ZHANG: 'A review of topology optimization for additive manufacturing: Status and challenges', *Chinese Journal of Aeronautics*, vol. 34, pp. 91-110, 2021, doi: 10.1016/j.cja.2020.09.020.

[12] K. TREUTLER and V. WESLING: 'The Current State of Research of Wire Arc Additive Manufacturing (WAAM): A Review', *Applied Sciences*, vol. 11, 2021, doi: 10.3390/app11188619.

[13] C. WANG ET AL.: 'A novel cold wire gas metal arc (CW-GMA) process for high productivity additive manufacturing', *Additive Manufacturing*, vol. 73, 2023, doi: 10.1016/j.addma.2023.103681.

[14] R. LACHMAYER, R. B. LIPPERT and S. KAIERLE: *Additive Serienfertigung*. Berlin, Heidelberg: Springer Berlin Heidelberg, 2018.
[15] T. MIKI: 'Self-support topology optimization considering distortion for metal additive manufacturing', *Computer Methods in Applied Mechanics and Engineering*, vol. 404, 2023, doi: 10.1016/j.cma.2022.115821.
[16] M. ZHOU, Y. LIU and Z. LIN: 'Topology optimization of thermal conductive support structures for laser additive manufacturing', *Computer Methods in Applied Mechanics and Engineering*, vol. 353, pp. 24-43, 2019, doi: 10.1016/j.cma.2019.03.054.
[17] N. IYER ET AL.: 'PATO: Producibility-Aware Topology Optimization Using Deep Learning for Metal Additive Manufacturing', *Int. J. Interact. Des. Manuf.*, vol. 18, pp. 7459-7476, 2024, doi: 10.1007/s12008-024-01905-z.
[18] F. VEIGA, A. SUÁREZ, E. ALDALUR, I. GOENAGA and J. AMONDARAIN: 'Wire Arc Additive Manufacturing Process for Topologically Optimized Aeronautical Fixtures', *3D Printing and Additive Manufacturing*, early access. doi: 10.1089/3dp.2021.0008.
[19] J. REIMANN ET AL.: 'Production of Topology-optimised Structural Nodes Using Arc-based, Additive Manufacturing with GMAW Welding Process', *J. Civ. Eng. Constr.*, vol. 10, pp. 101-107, 2021, doi: 10.32732/jcec.2021.10.2.101.
[20] J. YE, P. KYVELOU, F. GILARDI, H. LU, M. GILBERT and L. GARDNER: 'An End-to-End Framework for the Additive Manufacture of Optimized Tubular Structures', *IEEE Access*, vol. 9, pp. 165476-165489, 2021, doi: 10.1109/ACCESS.2021.3132797.
[21] K. MONTEIRO, C. ZHU, A. F. SANTOS, L. S. DA SILVA and T. TANKOVA: 'Integrated topological optimization and production of an additively manufactured steel T-joint: A case study', *Structures*, vol. 74, 2025, doi: 10.1016/j.istruc.2025.108511.
[22] ALTAIR LEARNING: *OptiStruct for Optimization Basics*, accessed: Aug. 23, 2025. [Online]. Available: https://learn.altair.com/ (restricted access)
[23] D. V. N. LUCA: 'Optimization of Varying Orientation of Continuous Fiber Direction and Its Applications to New Methods of Additive Manufacturing', *RDMS*, 2018, doi: 10.31031/RDMS.2018.03.000559.
[24] M. SOTOLA, P. MARSALEK, D. RYBANSKY, M. FUSEK and D. GABRIEL: 'Sensitivity Analysis of Key Formulations of Topology Optimization on an Example of Cantilever Bending Beam', *Symmetry*, vol. 13, 2021, doi: 10.3390/sym13040712.
[25] ALTAIR: *Design Optimization Responses*, accessed: Aug. 24, 2025. [Online]. Available: https:/help.altair.com/2023.1/hwsolvers/os/topics/solvers/os/responses.htm
[26] ALTAIR: *Topology Optimization Manufacturability*, accessed: Jun. 20, 2025. [Online]. Available: https:/2021.help.altair.com/2021/hwsolvers/os/topics/solvers/os/mfg_topology_opt_intro_c.htm #mfg_topology_opt_intro_c
[27] B. TURGUT, U. GÜROL and R. ONLER: 'Effect of interlayer dwell time on output quality in wire arc additive manufacturing of low carbon low alloy steel components', *Int. J. Adv. Manuf. Technol.*, vol. 126, 11-12, pp. 5277–5288, 2023, doi: 10.1007/s00170-023-11481-3.
[28] G. D. C. LOPES, D. F. FILHO and V. A. FERRARESI: 'Effect of interlayer temperature and cold wire addition in Wire Arc Additive Manufacturing on carbon steel', *Procedia Computer Science*, vol. 232, pp. 544-553, 2024, doi: 10.1016/j.procs.2024.01.054.

# DIFFERENT APPROACHES TO VISUALIZING SIMULATIONS OF WELDING PROCESSES

L. KESSELBURG*, S. WARKENTIN*, O. MOKROV*, R. SHARMA*, U. REISGEN*

**RWTH Aachen University, Welding and Joining Institute, 52062 Aachen. Germany*
*Kesselburg: https://orcid.org/0009-0008-7556-9644, lukas.kesselburg@isf.rwth-aachen.de;*
*Warkentin: https://orcid.org/0009-0004-4514-8962, sergej.warkentin@isf.rwth-aachen.de;*
*Mokrov: https://orcid.org/0000-0002-9380-6905, oleg.mokrov@isf.rwth-aachen.de;*
*Sharma: https://orcid.org/0000-0002-6976-4530, rahul.sharma@isf.rwth-aachen.de;*
*Reisgen: https://orcid.org/0000-0003-4920-2351, uwe.reisgen@isf.rwth-aachen.de*

*DOI 10.3217/978-3-99161-089-2-031, license CC BY 4.0*
*https://creativecommons.org/licenses/by/4.0/deed.en*
*This CC license does not apply to third party material and content noted otherwise.*

## ABSTRACT

In modern industry and research, vast amounts of data are being generated continuously, both through real-world measurements and numerical simulations. In the case of numerical simulations, particularly transient simulations, this creates significant challenges for human comprehension. Consequently, there is a critical need to create expressive visualizations while keeping computational resource requirements manageable. These visualizations can range from simple images to videos, and ultimately to interactive renderings, depending on the specific use case. Furthermore, a more established simulation system can offer a highly integrated interface, which allows the user to parameterize and schedule new simulations in addition to the interactive visualization of running and archived simulations.

The requirements for effective visualization change depending on the end-user's needs. On one end of the spectrum, developers and researchers involved in the data generation process require full access to all raw data, often coupled with sizable computational resources. This access facilitates early validation, error tracing, exploratory analysis, and further enhancement of the visualizations themselves. However, this configuration often necessitates a more intricate setup process. On the opposite end, reviewers, researchers, or executives generally require straightforward access to a refined version of the data, accompanied by an optimized and stable visualization pipeline. This enables tasks such as reviewing scientific publications or making data-driven decisions in a business context.

In this paper, we explore various visualization strategies tailored to meet the diverse needs of these two user groups, with a particular focus on simulations of welding processes. By demonstrating these strategies, we illustrate the trade-offs between computational resource demands and usability. We show two variations of the Server-Client-Architecture. In the first case, the client is a desktop program, presenting the user with a wide variety of options for analyzing and visualizing data, while utilizing computational resources from the client or the server. In the second case, the client is a web-browser, with the main benefit of removing any setup required. Additionally, we want to show an approach that utilizes WebAssembly to execute the full visualization pipeline in a web-browser. This includes loading the data, filtering, mapping and rendering. While this approach is more constrained in terms of data volume and processing power, it aims to enhance exchange between institutions through its ease of use and ease of deployment.

To further emphasize the interchangeability of simulation results, the open vtk file format is used, as it is widely utilized in academia. This allows us to leverage several KitWare software programs and libraries, thereby streamlining the development process by providing advanced visualization tools, reducing the necessity to work directly with raw visualization primitives, thus enabling the reuse of code across different strategies.

Keyword: software architecture, visualization, interactive 3D visualization

## PROBLEM

In the context of welding simulation in research and industrial practice, various software solutions generate substantial amounts of data. We have identified four types of interactions when dealing with this data:

1. Online debugging
2. Internal discourse among colleagues
3. Conference presentations or publications
4. Research partners in industry

The exchange of data between these types of interactions poses a significant challenge, particularly in the everyday use of software solutions. Our results, which represent only a small portion of the data generated, are presented in 2 other publications [1][2] at this conference. The simulation software in use, namely SPlisHSPlasH [3], has the capability to export Particle Data into two different formats. One of these formats is the legacy vtk format (version 4.1). The format is relatively straightforward, comprising metadata in text form interspersed with binary data. A notable disadvantage of this file format is its inability to compress data, which can result in inefficient utilization of storage space and bandwidth. This results in a substantial accumulation of raw data, even for rudimentary experiments. The number of particles in our smaller simulations is approximately 150,000. However, for more complex setups, this number can increase to one or two million particles. As previously mentioned, the vtk file format is capable of storing at least the ID and position of each individual particle. The position of each particle is expressed in terms of a x, y, and z coordinate. Additionally, we store supplementary attributes; however, for the sake of simplicity, we will only consider the storage of a single attribute, such as the temperature of each particle. Therefore, it is necessary to allocate storage space for five floating point numbers per particle, with each of them requiring four bytes of storage. This amounts to a total of $150{,}000 \cdot 5 \cdot 4 = 3{,}000{,}000 \approx 3[MB]$. In practice, the amount of storage required for a given file is approximately twice as large, due to the necessity of internal metadata in the file format. It should be noted that these effects are only observed at the level of a single timestep. In this configuration, the export of 400 timesteps per simulation is typical. Consequently, a rudimentary simulation necessitates storage capacity that exceeds 1 GB on disk.

The interpretation of raw binary data interleaved with text is not a viable option due to the lack of comprehensibility. The objective of this study is to facilitate the comprehension of the contained information through a more effective visual presentation. In this particular context,

the term “useful” can be defined in a number of different ways. It must be acknowledged that not all observers of the generated visualization are seeking the same insights. Depending on the role of the viewer, there are different requirements. We have identified 4 different roles and corresponding perspectives for looking at a visual representation of the data.

### Online debugging

The first role is that of an individual software developer or researcher who is attempting to enhance the overall simulation, either by investigating the algorithms used for the simulation or the parameter set in use. This use case necessitates a high resolution in both the spatial as well as the temporal dimension in the case of transient simulations. It is often advantageous to have this information at one’s disposal during the course of the simulation process, to decide early on whether a certain simulation should be allowed to continue, subject to minor changes or terminated, due to useless results. Moreover, it is helpful to have access to as much of the simulation state as possible. This encompasses not only definitive outcomes but also intermediate results.

### Internal discourse among colleagues

The second use case concerns the internal discourse among colleagues, facilitating the comparison of results and the planning of forthcoming simulation runs and the enhancement of previously implemented algorithms. In this case the fundamental prerequisite is the capacity to quickly gain a comprehensive understanding of the entire simulation, which means we still need a high spatial and temporal resolution as before. A particular emphasis is placed on the capacity to effortlessly navigate through the various time frames of a transient simulation. Conversely, intermediate results or values of a single simulation step can often be disregarded. A comprehensive evaluation of central properties often suffices to determine the success of a single simulation. This evaluation can be informed by the insights of senior researchers or by reference experiments conducted in the real world.

### Conference presentations or publications

The third use case is encountered when the conducted research is finally about to be published to a broader scientific audience. In the context of concluding a research project, it is often well understood which properties of the simulation are supposed to be presented. Consequently, it is straightforward to decide which properties to visualize. A further complication arises when one attempts to preserve the complete spatial and temporal resolution of the simulation. At this point in the process, traditional paper-based publications are proving to be a somewhat limiting factor. The limitation to static images poses a significant challenge in showing the simulation state changing over time or from different angles. This can be mitigated by employing multiple images instead of just a single one. However, the number of discrete

points in time or angles from which the simulation is displayed remains fairly limited. Moreover, this frequently comes at the cost of making the individual images smaller, thereby reducing the spatial resolution. In such circumstances, presenting the same results at a conference can be of significant benefit, as this allows for showing video footage in addition to still images. This is a substantial enhancement for transient simulations. However, it does not allow for complete interactivity because the speaker decides what is shown. This requires an understanding of the audience's exact level of knowledge.

## RESEARCH PARTNERS IN INDUSTRY

The last use case arises when working with industry research partners. Similar to the previous case, the goal is to demonstrate the highest possible spatial and temporal resolution, albeit often only for a few core properties such as temperature, enthalpy, and stress. The main difference is that, unlike the previous case, the visualizations are required on an ongoing basis for newer and older simulation runs to facilitate a richer exchange between research partners, rather than at one distinct point towards the end of the research process to show final results. These requirements have proven especially difficult in the past.

As we can see the requirements vary based on the purpose of the simulation. This makes finding an ideal way to visualize the results difficult. Therefore, we will present a few different visualization tools that have proven useful in our work. Most of these tools are built around software provided by Kitware, particularly the “visual toolkit” library. This library is very versatile and offers a wide range of possible visualizations.

## SIMULATOR

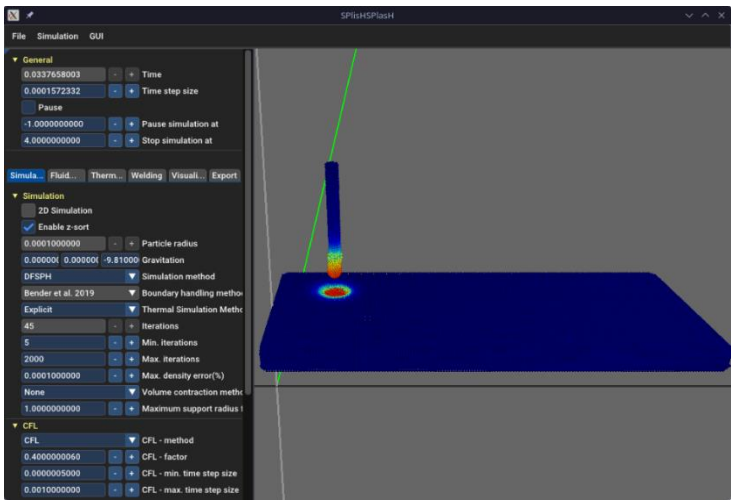



**Fig. 1** Screenshot of the SPlisHSPlasH simulator with parameter menu on the left

The first option a user of the SPlisHSPlasH software will probably encounter to visualize the simulation state is built into the program. The included graphical user interface (GUI) can be seen in Fi. 1. It is enabled by default when the program is running. Although it can be disabled to allow running simulations on systems that do not have the ability to provide graphical output. The biggest benefit of this visualization is that users have access to all particle attributes. This offers the most possible insight into the current simulation state. However, users can only inspect the simulation state of the current timestep. This is because the state of previous time steps is stored but cannot be reread by the simulation. This visualization method is most useful for the first use case. An individual software developer or researcher can quickly iterate on the algorithms and their corresponding parameters and view the results as they are computed. However, this is not a good fit for the other three use cases. This is because only the current state is available, which is not saved permanently by default.

The SPlisHSPlasH simulation software can be configured to regularly export particle attributes of interest. The particle IDs and positions are always exported. From the remaining set of particle attributes, the user can select an arbitrary subset. Each chosen attribute is exported for each particle. This feature is independent of the visualization provided in the GUI. The provided visualization cannot be used to visualize the exported results afterwards. The exported data serves as the basis for all other visualizations.

## PARAVIEW

We predominantly use ParaView internally for loading, analyzing, and visualizing exported vtk files. ParaView is KitWare's "[…] open source, multi-platform data analysis and visualization engine." [4]. It provides a simple yet flexible interface to the Visualization Toolkit (VTK), a library developed by KitWare as well. The VTK library offers a wide variety of file readers, filters, and visualization methods. In addition to ParaView's interactive capabilities, ParaView enables us to export images of static simulation states or videos to visualize transient results.

One feature that we use extensively internally is the macro system, which is conceptually simple yet powerful. Macros reduce the setup time for visualizations used repeatedly with different sets of input data. When recording a macro, ParaView tracks all user interactions and translates them into calls to its built-in Python application programming interface (API), which are collected and result in a file containing Python code. This is useful not only because we can record and replay any interaction with the program, but also because recorded interactions are easy to share between colleagues. By sharing the macro files using a version control system (VCS), we can also track changes made to the macros.

As a first step, users usually use ParaView on their local systems to visualize data generated from previously run simulations. We have done this in the past as well. First, we would run a SPlisHSPlasH simulation with particle export enabled. Then, we would use ParaView to visualize the results while the simulation is still running or after it has finished. However, this became problematic when we started running the simulation on remote systems. We did this to utilize stronger computational resources and run multiple simulations simultaneously or to run simulations while still having our personal systems fully available.

Some systems used for remote simulations lack a GUI. It is not possible to use ParaView as a standalone application on those systems. One option is to copy the generated files from the remote system where it was generated. Then, copy it to a local user system where ParaView can be used. However, this process is not suitable for long-term usage and should be avoided for two main reasons. First, copying the simulation results between systems adds an extra step to the development process, which degrades the overall development speed. Second, it avoids duplication of simulation results across systems. Over time, duplication of files can cause confusion. This occurs when certain files are deleted, renamed, or moved on some systems but not on others. Furthermore, duplicating identical files across systems consumes additional disk space.

Fortunately, this problem is often encountered in many different settings, so it is well-known at KitWare. ParaView's implementation solves this problem by following a client-server architecture. This is usually hidden from the user. If no extra steps are taken and ParaView is used as any other desktop application would be, both the client and the server start on the local system and connect automatically. In settings where the data to be visualized is located on a remote system without a GUI, the user must first start the ParaView server on the remote system in addition to running the normal desktop application on their local system before connecting the client to the server. Once this is done, the ParaView instance on the local system can access the remote system. The user then has access to the remote machine's file system. Data loading and analysis are executed on the remote machine, and the final image can be rendered on either the client or the server. In Fig. 2 the parts of the ParaView GUI that change after connecting to a remote system are marked in red. This includes the server address, the file path on the remote system, and the resource utilization of the remote system.

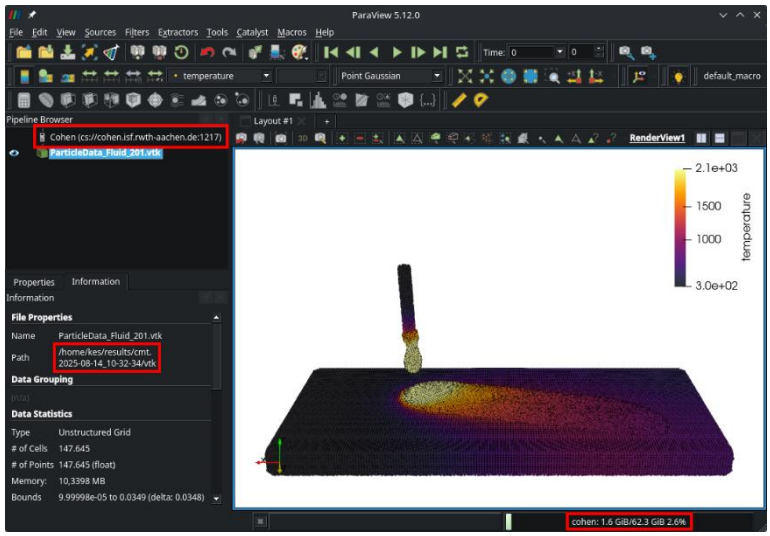



**Fig. 2** Screenshot of ParaView. Sections marked with borders change when connected to a remote server. Upper left: Connection information, Left: File path, Lower Right: Remote Host and its resource utilization

The server component can also be used across multiple remote systems. This can be done to either process and visualize data distributed across different systems or to use different systems for initial data processing before rendering on a separate system with specialized hardware. So far, we have not needed to use either of these options. Additionally, it should be noted that KitWare discourages the latter use case. It was developed at a time when rendering hardware was harder to find and more specialized. Nowadays, the overhead of sending intermediate data is usually greater than the benefit gained from using specialized rendering hardware. This makes it difficult to justify using distinct systems for analysis and rendering tasks. [5][6]

Overall, ParaView is probably the most powerful visualization tool that we use. It is suitable for almost every visualization use case introduced previously, though not equally. The first use case is covered when ParaView is used to visualize states that have already been exported from a running simulation. Compared to using the simulator's visualization, it is not possible to access the fully updated state of the simulation at all times particle properties that were not marked for export. However, users have the ability to step through the exported timesteps at their desired speed. This makes it well-suited for the second use case, in which colleagues can inspect and compare the results of different simulations, either individually or as a team, to gain more insight. The third and fourth use cases are covered by the image and video export feature. It is difficult to offer ParaView's interactive capabilities to external users for several reasons, which are described in the next chapter.

## TRAME

While the simulator in combination with ParaView is a sufficient solution for the first two use cases, ParaView is only a partial solution for the last two. ParaView can be used to create images or videos of the simulation that can be used in publications or correspondence with research partners. Second, it would be possible to exchange raw simulation results via a research data management platform for the third use case, or a conventional cloud storage platform for the fourth use case. Then, one could ask readers of our publication and research partners to download, install, and use ParaView with the provided data themselves. This approach seems feasible at first due to its simplicity. However, when examined more closely, these benefits quickly disappear. When moving files containing simulation results to external services, large amounts of data are duplicated again. Additionally, only some of our audience may have ParaView available, as most people do not have the option to install new programs in a corporate environment. Those who have ParaView available may consider using their ParaView installation as a client to a ParaView server running on our simulation server. However, this would require opening our firewall, which is problematic from an IT security perspective. Additionally, we would need a more elaborate ParaView server setup because, currently, each user needs to open their own session on the server. While this is not a significant effort it is an additional step requiring Secure Shell (SSH) access to the server.

In an earlier effort to address this challenge, it was decided that a more phased-out solution following the client-server architecture should be implemented. In search of a solution requiring minimal additional development effort, Trame was identified. Trame is also

developed by KitWare. According to their documentation, “Trame is an open-source platform for creating interactive and powerful visual analytics applications. Based on Python, and leveraging platforms such as VTK, ParaView, and Vega, it is possible to create web-based applications in minutes.” [7] While creating a software solution in “minutes” is an impressive claim, the use of Python, VTK, and ParaView seems appropriate, because Python is a familiar programming language for us, and we can leverage our existing experience with ParaView.

The core benefit of Trame is that it enables developers to implement all the necessary components of a visual analytics application from a single Python code base or even a single file, if desired. This is achieved by leveraging Python’s ability to seamlessly integrate code written in different programming languages. [8]

Trame follows a reactive state model. This means that changes to the application state on the server are automatically reflected in the user interface, and changes made through the user interface are automatically reflected in the application state on the server. Therefore, a developer using Trame as an application framework does not need to worry about synchronizing the state between the user interface and the application logic. Additionally, Trame provides simple mechanisms for reacting to events in the user interface. On the other hand, Trame provides a simple way to design the user interface. For more traditional components such as buttons, text inputs, and selection menus as well as for composing the layout, Vuetify and, by extension, Vue are used. In addition to the components one would expect from a UI library, Trame provides widgets to display visualizations from various widely used tools for 2D and 3D visualizations. The most relevant ones are the widgets that show views from VTK or ParaView. There are also widgets for Python libraries, such as Matplotlib, Plotly, Leaflet and a few others.

Unlike traditional web servers, Trame uses a long-running server process rather than spawning a new process for each incoming request. This allows Trame to maintain the state of the application and the different visualizations. As can be seen in Fig. 3 we kept the complexity of our user interface low. When starting up, the Trame application searches the server for available simulation results. These results can be selected from the list at the top of the drawer on the left. The other relevant controls are for playing back the timesteps of the simulation. in addition to a pause/play button, it is possible to jump to a specific timestep by entering its number in the text field, or to use the progress bar at the top to scroll through the available timesteps of the selected simulation.

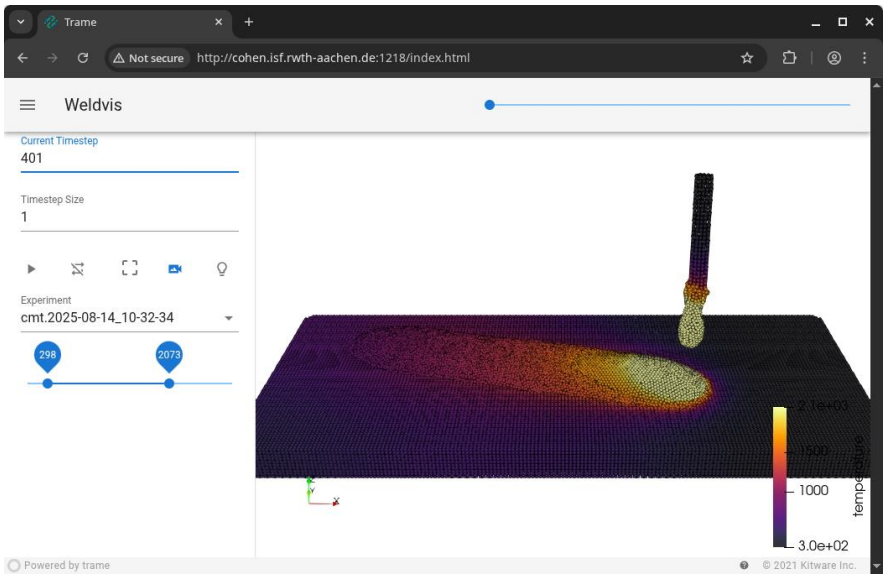



**Fig. 3** Screenshot of Trame application

The central component of the user interface is the 3D view of the simulation results. Note that the resulting visualization is essentially the same as what we previously achieved in ParaView. We were able to reuse the macro recorded in ParaView and use its code to configure Trame's ParaView widget, resulting in an almost identical visualization. Although not apparent in Fig. 3, it is important to note that the 3D view is fully interactive. In addition to scrolling along the time axis, users can change their perspective on the data. To accomplish this, Trame employs a communication sequence that differs from that of traditional web servers. Fig. 4 provides a rough outline of this sequence. First, the application is downloaded and initialized. A WebSocket connection is opened, and a permanent server process is started. The client application continuously sends user interactions with the 3D view to the server. The permanent process continuously renders images based on the latest interactions. These images are sent back to the client and finally displayed to the user.

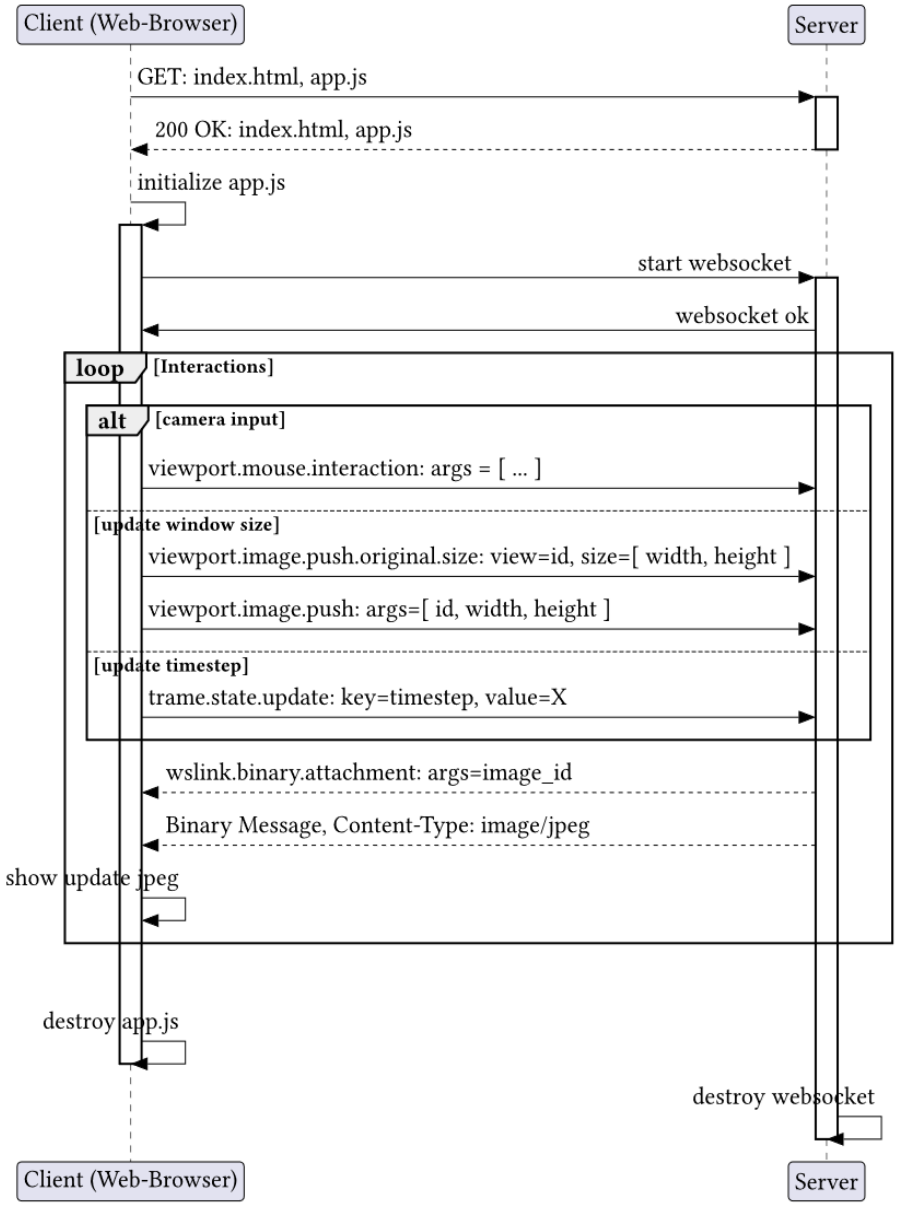



**Fig. 4** Diagram of the Trame Communication between Client and Server

The resulting application seems like a good fit for the third and fourth use cases. The Trame application can be used to view all timesteps for different experiments. Additionally, each

state can be explored from different angles and perspectives. However, after using the application internally for some time, it became apparent that it would not be feasible to offer it to a broader audience on an ongoing basis. This is due to the administrative work that would be required. First, the Trame application would require opening ports in our firewall. Another problem is that the long-running server process is susceptible to extended unavailability caused by short-lived errors. For example, when trying to load simulation results that did not conform to the expected format, the server process would crash and become unavailable for requests of valid simulation results until the Trame application was restarted. This problem could be partially solved by using one of the more advanced Trame deployment options. The available options are:

- Using the application inside Jupyter.
- Building a desktop application with Tauri.
- Building a container image for the cloud.

However, all these options require additional software and increase administrative effort and reliance on external software. Another issue that the Trame application and ParaView in Client Server mode have in common is that the server hardware used by the visualization applications is the same hardware used to run the simulations, which leads to a conflict of interest. Viewing simulation results decreases the amount of computing power available for running simulations.

## WEBASSEMBLY

After acknowledging that the Trame application was far from ideal, we searched for another solution that would require less administrative effort to support over time. The final solution we will discuss in this paper is based on a technology called WebAssembly. According to the official specification, "WebAssembly (abbreviated Wasm) is a *safe, portable, low-level code format* designed for efficient execution and compact representation. Its main goal is to enable high performance applications on the Web, but it does not make any Web-specific assumptions or provide Web-specific features, so it can be employed in other environments as well." [9]

WebAssembly is a standard maintained by the World Wide Web Consortium (W3C). It was invented and standardized due to the desire to utilize more of the computing power available to JavaScript applications running in browsers than is usually possible. In addition to the core specification, many extensions have been standardized to increase the capabilities of a WebAssembly environment. The WebAssembly design process focused on the following properties:

- Efficient and Fast
- Safe
- Modular
- Support for a wide variety of programming languages

These days, it is possible to compile almost any programming language into WebAssembly. For systems programming languages such as C, C++, and Rust, this is achieved by using WebAssembly as the compilation target instead of traditional assembly languages such as x86_64.

As with Trame before, we are fortunate that we are not the only ones with a "[…] demand for powerful, interactive data visualizations directly within web browsers." [10] KitWare has also identified this demand. To meet this demand, KitWare has extended VTK to create versions that run in a WebAssembly environment. The resulting product "VTK.wasm", can be integrated into custom applications in various ways. For brevity's sake, we will only look at how we used it. To use VTK.wasm, we wrote a small C++ program that downloads a VTK file generated by the simulation. Then, it uses the traditional C++ VTK API to build the visualization pipeline. We can reuse the code from our previous attempt with Trame here because the interface provided by VTK is very similar to the one provided by ParaView. As Fig. 5 shows, the user interface is equally minimalistic compared to the Trame application.

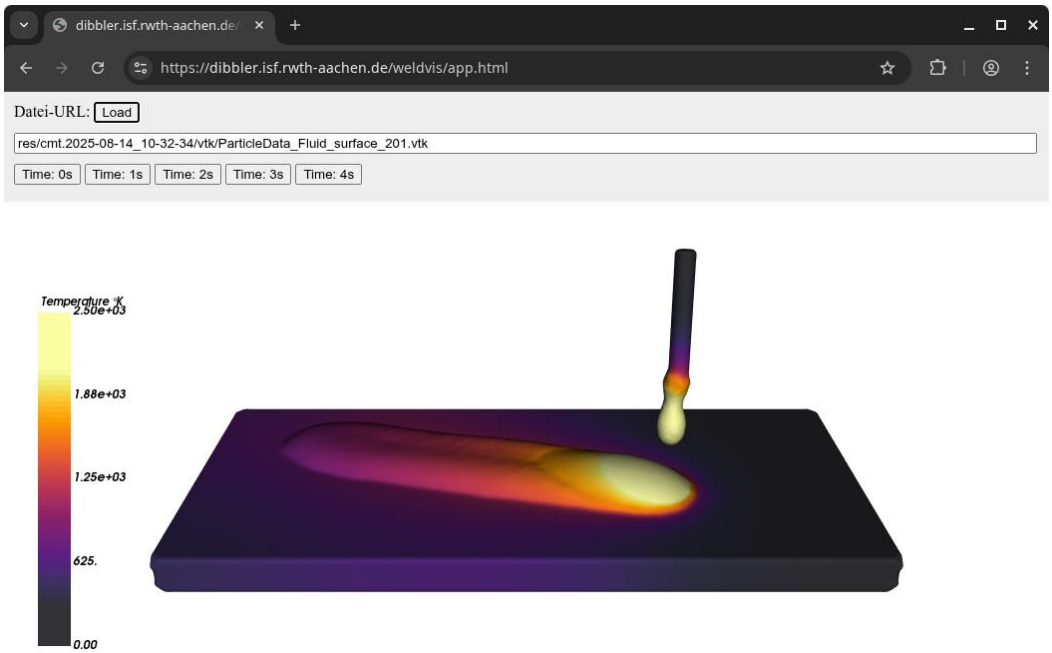



**Fig. 5** Screenshot of VTK.wasm application

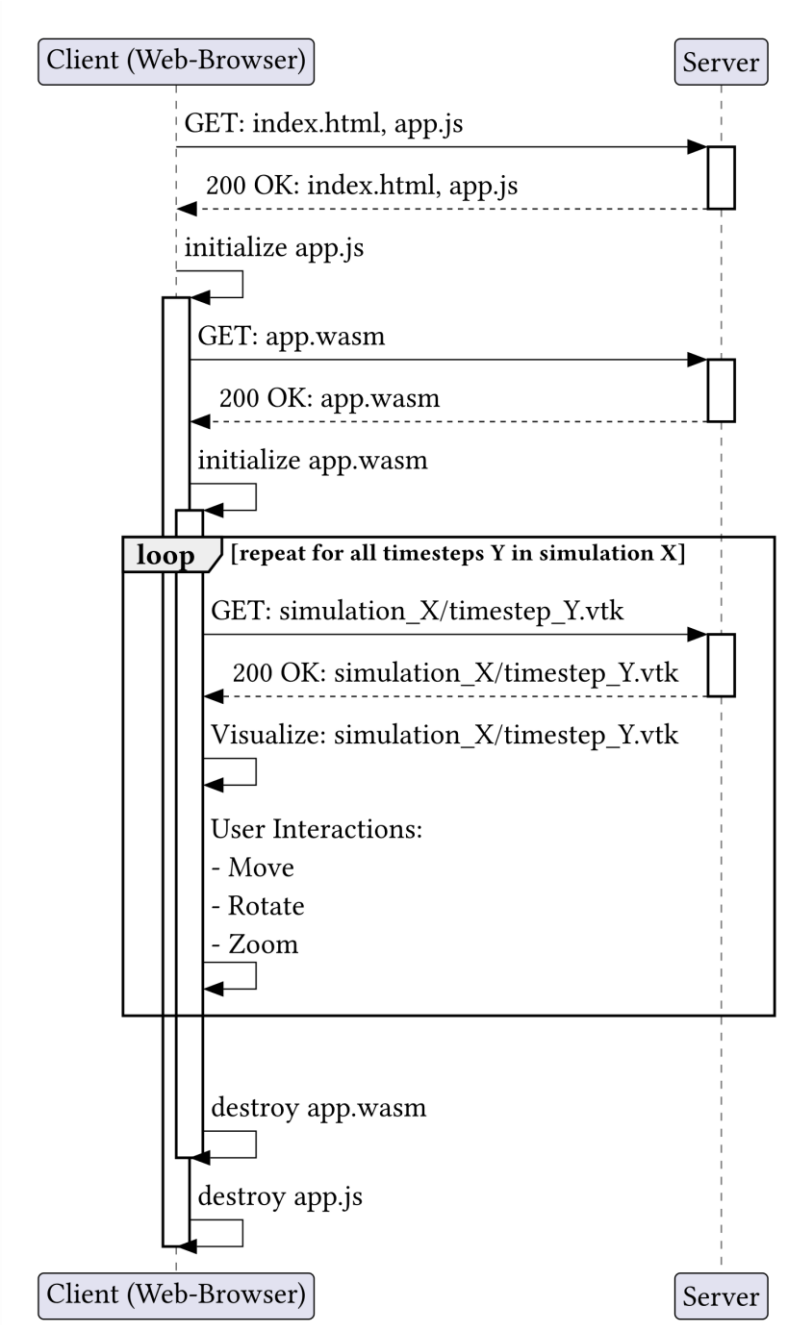



**Fig. 6** Diagram of VTK.wasm Communication between client and server

Fig. 6 illustrates the process of downloading the application to the browser and rendering the simulation results. The process begins with the download of the index.html and app.js files (1. GET request). This is necessary because web browsers are not designed to execute WebAssembly on their own. The HTML file declares that the full space should be used as a drawing surface for the WebAssembly application. The JavaScript file is necessary to download (2. GET request) and initialize the WebAssembly program. The WebAssembly program is the actual application. It is responsible for downloading simulation results from the server (3. GET request). Then, the results are rendered locally in the browser instead of on the server. This is possible because the necessary parts of the VTK library have been compiled into WebAssembly instead of traditional assembly and are now running in the browser.

This has multiple benefits. For example, user interactions with the 3D view can be handled locally. No communication with the server is necessary. This is a significant architectural difference from the Trame application. We do not need a continuously running process on the server that tracks the application's state. All server interactions are simple file downloads. First, the application files are downloaded, followed by the data file. Therefore, to offer this application to users, we only need a web server that can serve static files. Since serving static files is the traditional task of web servers, a broader selection of ready-to-use web servers is available. The setup will also be much more familiar to most system administrators. Furthermore, this opens up the opportunity to utilize other features of traditional web servers, such as access control and caching.

We have not yet thoroughly tested the WebAssembly application, but it appears to be a good fit for the third and fourth use cases. Although it requires more development effort initially due to parts of the code being written in C++ and the immaturity of some WebAssembly-related tools, the resulting application is much easier for system administrators to manage since they only need a traditional web server to offer the application.

## CONCLUSION

We have demonstrated how we use various components of the KitWare visualization stack to address different challenges that arise from the various ways and reasons for visualizing our simulation results. These components are designed to work together, or even on top of each other, making it easy to reuse code between applications. The biggest challenge when working with KitWare software is the documentation. Not because there is no documentation or too little of it, but because there is a lot of documentation that is fragmented. Every program or library has at least one dedicated piece of documentation and often more. For example, Trame has different sections for examples, guides, and the API itself. Additionally, some information can only be found in blog posts.

We will continue to use ParaView internally for the foreseeable future. However, we are interested in exploring WebAssembly further to share our results with a broader audience.

## OUTLOOK

When developing the WebAssembly version into a more capable application, there are two possible directions: The first direction would be a fully integrated application that communicates with a central coordination server. This server knows about a full collection of completed simulations and the storage location corresponding to the results of these simulations. The client can then request the URLs for the files that constitute the result of a full simulation and download them on demand, before showing the visualization to the user. In this case the application server would follow a more traditional architecture where no state is kept between requests and the URLs for different results are stored in a database.

The other direction is simpler. In this direction, the application is designed to consist only of visualization logic and the capability to provide a URL in the user interface. The user can then download a file with simulation results to be visualized using the provided URL. This version would work well with a research data management system. First, the researcher would perform a simulation. Then, they would upload the results to the research data management system. Afterwards, a link to the simulation results, probably in the form of a DOI, could be included in a publication or correspondence with a research partner. The link can then be inserted into the WebAssembly application, which downloads and visualizes the simulation results.

## References


[1] O. MOKROV, S. WARKENTIN, L. WESTHOFEN, J. BENDER, R. SHARMA, U. REISGEN: 'Enhancing Gmaw Simulations Through A Hybrid Eulerian and Lagrangian Method Considering an Inclined Welding Torch', *The 14th International Seminar "Numerical Analysis of Weldability*, Graz, Austria, 21 - 24 September 2025.

[2] O. MOKROV, S. WARKENTIN, L. WESTHOFEN, J. ANTONISSEN, J. BENDER, R. SHARMA, U. REISGEN: 'Solution Approaches for the Efficient Modeling of the Layer Build-Up in the Waam Manufacturing Process Using Smoothed Particle Hydrodynamics', *The 14th International Seminar "Numerical Analysis of Weldability*", Graz, Austria, 21 - 24 September 2025.

[3] J. BENDER, ET AL: *SPlisHSPlasH Library*, https://github.com/InteractiveComputerGraphics/SPlisHSPlasH, MIT license.

[4] AYACHIT, UTKARSH: *The ParaView Guide: A Parallel Visualization Application*, ISBN: 1930934300, Kitware Inc., 2015.

[5] AYACHIT, UTKARSH: *The ParaView Guide: A Parallel Visualization Application*, SECTION 8.1, ISBN: 1930934300, Kitware Inc., 2015.

[6] AYACHIT, UTKARSH: *The ParaView Guide: A Parallel Visualization Application*, SECTION 8.8, ISBN: 1930934300, Kitware Inc., 2015.

[7] S. JOURDAIN ET AL: *Trame, Trame Documentation – Guide - Overview*, doi.org/10.5281/zenodo.16898084, 2025.

[8] G. V. ROSSUM: *Glue It All Together With Python*, OMG-DARPA-MCC Workshop on Compositional Software Architecture, Monterey, California, January 6-8, 1998.

[9] A. ROSSBERG: *WebAssembly Core Specification*, Version 2, W3C, 2022.

[10] J. PANCHUMARTI, V. BOLEA, Y. HAN, S. JHAVERI, B. MAJOR, P. O'LEARY and W. SCHROEDER: *Introducing WebAssembly support in VTK*, KitWare Blog, August 15, 2025, https://www.kitware.com/introducing-webassembly-support-in-vtk/.

# A SIMPLIFIED HYBRID METHODOLOGY FOR DETERMINING WELDING HEAT SOURCE PARAMETERS IN HIGH-STRENGTH STEELS

M. DADKHAH*, T. NITSCHKE-PAGEL*, K. DILGER*

**Institute of Joining and Welding (ifs), TU Braunschweig, Germany*

*DOI 10.3217/978-3-99161-089-2-032, license CC BY 4.0*
*https://creativecommons.org/licenses/by/4.0/deed.en*
*This CC license does not apply to third party material and content noted otherwise.*

## ABSTRACT

Welding simulations are critical for predicting the thermal and mechanical behavior of high-strength steels, as accurate thermal analysis, particularly under varying heat inputs, directly influences microstructure evolution and mechanical performance. Traditional heat source models rely on complex parameterization, often requiring variables that are computationally intensive or absent from standard material databases. This study addresses these limitations by introducing a simplified, hybrid methodology to determine heat source parameters for the Goldak's double ellipsoidal heat source model. The approach integrates various elements, including the molten pool's length components captured through high-speed videography (HSV), size of phase transformation zones, local temperature measurements combining with Design of Experiments (DOE), and finite element simulations. This integration aims to generate optimized parameters with enhanced accuracy and efficiency.

Three acceptance criteria were used to validate the optimized parameters derived from DOE: identical temperature gradients at thermocouple locations, equivalent macro-diagrams, and consistent cooling rates. These criteria ensured alignment between thermal analysis phase of the welding simulations and experimental data, facilitating robust calibration of heat source geometries and heat inputs. This framework significantly reduced computational costs compared to traditional trial-and-error calibration methods.

The results illustrate the capability of this method in predicting temperature distributions and related residual stresses afterwards. Furthermore, the adaptability of this methodology is a key strength, allowing it to be extended to other heat source models or different welding conditions. This versatility enhances its utility across a wide range of applications in welding research and industry, while its flexibility ensures that the methodology remains relevant as new materials and welding technologies emerge.

Keywords: welding simulation; heat source parameters; high-speed videography; DOE

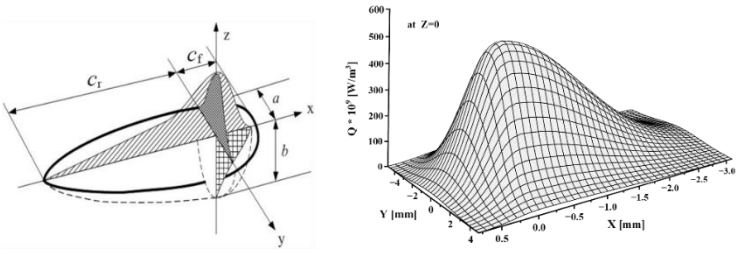
## INTRODUCTION

Welding simulations have emerged as essential tools for predicting and analyzing the complex thermal and mechanical phenomena that occur during welding processes. The significance of

these simulations becomes particularly pronounced in high-strength steel applications, where the intricate coupling between thermodynamic and mechanical properties necessitates precise control of process parameters to ensure optimal weld quality and structural integrity [1]. Beyond providing critical insights into thermal histories and mechanical performance of welded components, numerical simulations offer substantial economic advantages by reducing material waste, minimizing experimental trials, and optimizing manufacturing efficiency.

The Finite Element Method (FEM) represents the predominant computational framework for welding simulations, typically employing a sequential approach comprising thermal and mechanical analyses. The thermal analysis phase determines heat transfer mechanisms and temperature distributions throughout the welding path, which fundamentally govern microstructural evolution and subsequent mechanical properties of the weld zone. Subsequently, the mechanical analysis phase evaluates stress distributions, distortion and deformation patterns, as well as residual strain development during and after the welding process. This coupled thermo-mechanical approach enables comprehensive characterization of welding-induced material behavior, providing the foundation for systematic optimization of welding procedures [1,2].

Heat source modeling constitutes a critical component of thermal analysis within FEM-based welding simulations, serving to mathematically describe the generation and spatial distribution of thermal energy during welding operations. Established heat source models, including Goldak's double ellipsoidal (see Fig. 1) [3], employ sophisticated mathematical frameworks to simulate the three-dimensional and time-dependent distribution of heat input as the welding torch traverses the material. The accuracy of these heat source representations is paramount for capturing realistic temperature field evolution and subsequently predicting microstructural transformations and mechanical property development [4].




**The double ellipsoidal volumetric heat source model (Goldak):**

$$Q_{f,r}(x,y,z) = \frac{6\sqrt{3} f_{f,r} Q_A}{abc_{f,r}\pi\sqrt{\pi}} exp\left(-3\frac{x^2}{{c_{f,r}}^2}\right) exp(-3\frac{y^2}{a^2})\ exp\left(-3\frac{z^2}{b^2}\right)$$

**The double elliptical surface heat source model (Li et al.):**

$$Q_{f,r}(x,y) = \frac{6\, x_{f,r}\, Q_A}{a.\pi\,(C_f+C_r)} exp\left(-3\frac{x^2}{{c_{f,r}}^2}\right) exp(-3\frac{y^2}{a^2})$$

**Fig. 1** Examples of well-established heat source models commonly employed in welding simulations [4,5]

The determination of appropriate parameters for heat source models presents considerable technical challenges in contemporary welding simulation practice. These parameters exhibit strong dependencies on material-specific thermophysical properties, including thermal conductivity, specific heat capacity, and temperature-dependent material behavior, as well as process-related variables such as heat input and welding travel speeds. For advanced materials, particularly high-strength steel alloys, the requisite parameter values are frequently unavailable in standard material databases or prove difficult to determine analytically due to complex thermo-mechanical coupling effects. Conventional approaches have predominantly relied on empirical trial-and-error methodologies or extrapolation from limited existing databases for parameter estimation. However, these traditional methods suffer from inherent limitations in both computational efficiency and prediction accuracy, while the scarcity of comprehensive material property databases further exacerbates the parameterization challenges [6].

This investigation addresses the aforementioned challenges through the development of a simplified hybrid methodology for heat source parameter determination. The proposed approach integrates molten pool geometry characterization and phase transformation zone analysis with experimental thermal history data, finite element simulations, and Design of Experiments (DOE) principles. This systematic framework enables efficient and accurate estimation of heat source parameters while minimizing dependence on empirical trial-and-error procedures and circumventing the need for extensive material property databases. Although the methodology is demonstrated through implementation with Goldak's double ellipsoidal heat source model, the underlying framework exhibits inherent versatility and can be readily adapted to other established heat source formulations [7]. The developed methodology aims to enhance welding simulation accuracy and reliability, ultimately contributing to improved weld quality prediction and manufacturing cost reduction.

## MATERIALS AND EXPERIMENTAL SETTINGS

### INVESTIGATED MATERIALS

Three steel grades were selected to evaluate the proposed methodology across different metallurgical complexities and thermal behaviors. HCT690T (TRIP700) represents a transformation-induced plasticity steel containing approximately 12% retained austenite in its initial microstructure, which undergoes strain-induced martensitic transformation under welding thermal cycles and mechanical loading. X40MnCrAlV-19 2.5 2 (TWIP) constitutes a highly alloyed twinning-induced plasticity steel with complex thermal properties and deformation mechanisms that present unique challenges for heat source parameter determination [8]. S355MC serves as a conventional microalloyed structural steel with well-established thermal behavior, providing a baseline reference for methodology validation.

These materials span a representative range of welding applications, from conventional structural applications to advanced automotive components, enabling comprehensive

assessment of the proposed heat source parameter determination approach. Table 1 presents the chemical compositions of the investigated materials.

**Table 1** Chemical Composition of the Test Materials

**S355MC**

| Mass fraction (%) | C | Mn | Si | P | S | Cu | Al | Nb | V | Ti |
|---|---|---|---|---|---|---|---|---|---|---|
| OBLF-Spec. | 0.022 | 0.161 | 0.034 | 0.010 | 0.005 | 0.056 | 0.046 | 0.028 | 0.007 | 0.003 |

**HCT690T**

| Mass fraction (%) | C | Mn | Si | P | S | Al | V | Cu | B | Ti+Nb | Cr+Mo |
|---|---|---|---|---|---|---|---|---|---|---|---|
| OBLF-Spec. | 0.176 | 1.793 | 0.366 | 0.011 | 0.006 | 1.279 | 0.008 | 0.026 | 0.0001 | 0.022 | 0.02 |

**X40MnCrAlV 19 2.5 2**

| Mass fraction (%) | C | Mn | Si | P | S | Al | Cr | Ti | V | Cu | Ni |
|---|---|---|---|---|---|---|---|---|---|---|---|
| OES-Spec. | 0.377 | 18.62 | 0.246 | 0.019 | 0.0040 | 1.09 | 1.68 | 0.02 | 0.115 | 0.038 | 0.066 |

## SAMPLE PREPARATION AND MATERIAL CHARACTERIZATION

Standard dog-bone tensile specimens were prepared for each alloy by waterjet cutting from metal sheets to ensure precise geometry and minimize heat-affected zones during preparation. Comprehensive mechanical property evaluation was conducted through tensile testing at ambient temperature and hot tensile testing across relevant temperature ranges to establish temperature-dependent material behavior. This experimental characterization provided essential baseline data for subsequent thermal and mechanical analyses in welding simulations.

Temperature-dependent thermophysical properties, including thermal conductivity, specific heat capacity, and thermal expansion coefficients, were determined using JMatPro software [9]. The computational framework employed HyperMesh for finite element mesh generation and ABAQUS with user-defined subroutine (DFLUX) for thermal analysis implementation [10]. The thermal model output served as input for subsequent phase transformation simulations, with Simufact Welding software utilized for enhanced computational efficiency and accuracy.

Phase transformation calculations were based on established kinetic models: the Johnson-Mehl-Avrami equation [11] for austenite and ferrite transformations during both heating and cooling cycles, and the Koistinen-Marburger equation [12] for martensitic phase fraction determination. The calculated phase fractions were subsequently employed to determine phase-specific strains and resulting deformations in the welded structure.

## WELDING PROCESS

Tungsten Inert Gas (TIG) welding was employed to investigate the influence of thermal loading on heat source parameter determination. Bead-on-plate welds were performed without filler material addition, eliminating compositional variables and closely representing practical thin-plate welding applications such as overlap joints. Systematic variation of heat input was achieved by adjusting welding current and voltage while maintaining constant travel speed, enabling controlled investigation of the relationship between process parameters and heat source characteristics [13]. The specific welding parameters, corresponding heat input values, and associated cooling times ($t_{8/5}$) are presented in Table 2.

**Table 2** Welding Parameters

| Material | plate thickness [mm] | welding speed [cm/min] | voltage [V] | welding current [A] | heat input [kJ/cm] | $t_{8/5}$ [s] | in study name |
|---|---|---|---|---|---|---|---|
| S355MC | 2 | 30 | 9.1 | 50 | 0.91 | 0.83 | W01 |
| | | | 9.4 | 75 | 1.41 | 1.43 | W02 |
| | | | 10.3 | 100 | 2.06 | 2.45 | W03 |
| | | | 11.52 | 125 | 2.88 | 3.67 | W04 |
| | | | 12.03 | 150 | 3.61 | 4.26 | W05 |
| HCT690T | 1.75 | 30 | 9.1 | 50 | 0.91 | 1.84 | W01 |
| | | | 9.4 | 75 | 1.41 | 2.49 | W02 |
| | | | 10.3 | 100 | 2.06 | 3.06 | W03 |
| | | | 11.16 | 112 | 2.50 | 3.66 | W04 |
| | | | 11.52 | 125 | 2.91 | 4.32 | W05 |
| X40MnCrAlV 19 2.5 2 | 2 | 30 | 9.1 | 50 | 0.91 | 1.59 | W01 |
| | | | 9.4 | 75 | 1.41 | 2.41 | W02 |
| | | | 10.3 | 100 | 2.06 | 3.87 | W03 |
| | | | 11.52 | 125 | 2.88 | 4.01 | W04 |
| | | | 12.03 | 150 | 3.61 | 4.23 | W05 |

shielding gas: 100% Ar / flow rate = 12 l/min

## MOLTEN POOL CHARACTERIZATION

Real-time molten pool dynamics were investigated using high-speed videography at 5000 frames per second, coupled with CAILUX laser illumination to eliminate arc light interference and enable precise molten pool observation. Dimensional measurements of the molten pool were systematically recorded under varying welding parameters to characterize thermal behavior across the investigated materials.

To minimize measurement uncertainties associated with perspective distortions, dimensional analysis was conducted at a minimum of five discrete positions along each weld seam. Subsequently, only the length ratio between the front and rear sections of the molten pool was utilized for analysis, ensuring enhanced measurement reliability and data consistency, as illustrated in Fig. 2.

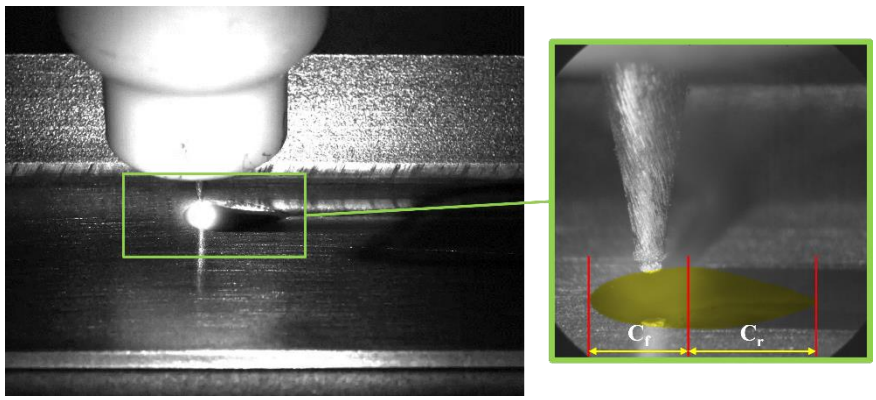



**Fig. 2** Determination of molten pool dimensions using High-Speed Videography (HSV) technique

## TEMPERATURE MEASUREMENT

Thermal gradients in the weld vicinity were monitored using a minimum of eight thermocouples positioned at strategic locations with 0.5 mm spacing intervals between adjacent sensors (See Fig. 3). Due to geometric constraints during thermocouple placement, they were distributed along the welding direction while maintaining minimal perpendicular distance to the weld path, optimizing temperature gradient resolution and data distribution quality.

The thermocouple data served as validation criteria for simulation results through direct comparison of both peak temperatures at specific locations and corresponding cooling rates. This experimental validation approach enabled quantitative assessment of the simulation accuracy and refinement of heat source parameters based on measured thermal histories.

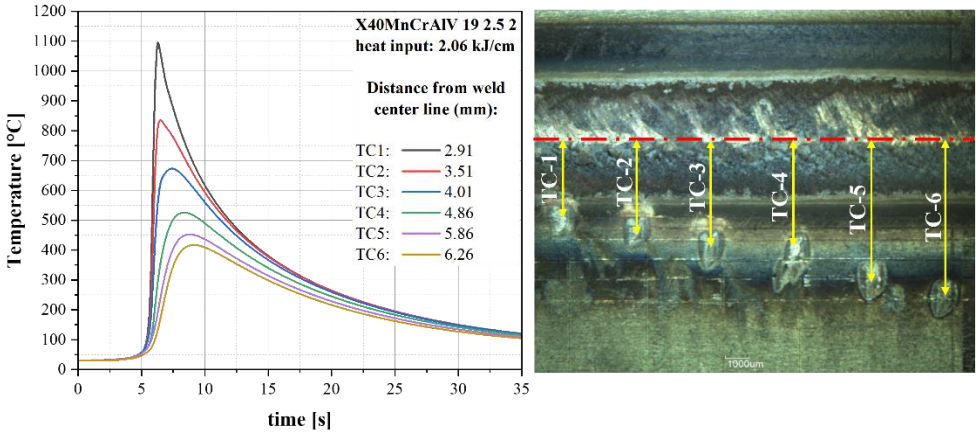



**Fig. 3** Example of thermocouple attachment locations and their corresponding temperature history data for a specific heat input and material combination

## METALLOGRAPHIC ANALYSIS

Heat-affected zone characterization was performed through systematic metallographic analysis of welded specimens. Cross-sectional samples were prepared using standard metallographic procedures, including mounting, polishing, and chemical etching, followed by digital image acquisition and analysis. This methodology enabled accurate measurement of weld zone macroscopic dimensions, as illustrated in Fig. 4. The quantitative metallographic approach facilitated parameter optimization by providing direct dimensional correlation between experimental measurements and computational model predictions, thereby validating simulation accuracy.

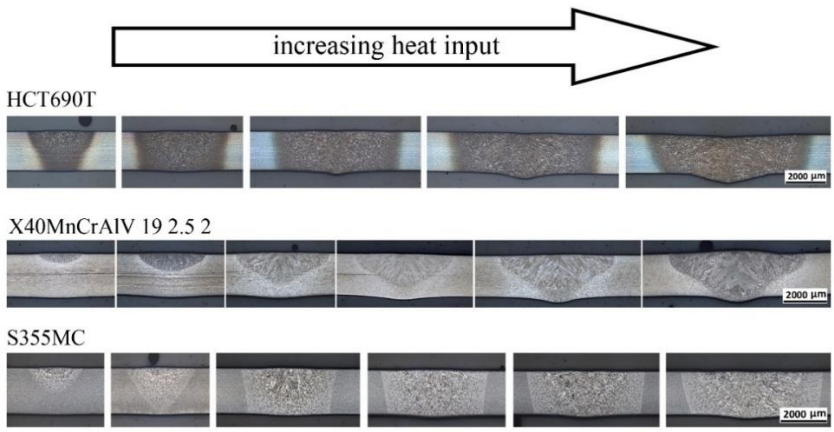



**Fig. 4** Macroscopic metallographic morphology of welds examined under varying heat inputs

## METHODOLOGY

This investigation employs the double ellipsoidal heat source model, commonly referred to as Goldak's model, to determine welding heat source parameters. The selection of this model is based on its demonstrated capability to accurately represent heat distribution in welding processes involving materials of significant thickness while maintaining computational efficiency through appropriate model simplification [5]. The methodology presented herein exhibits versatility and can be readily extended to alternative heat source models, including four ellipsoid quadrants or simpler configurations such as Gaussian surface flux models.

The mathematical formulation of Goldak's model is structured into two distinct regions: the front (f) and rear (r) sections of the heat source. Each region is characterized by a unique parameter set [14], enabling precise characterization of heat input dynamics and facilitating comprehensive understanding of temperature distribution throughout the weld zone.

Goldak's model represents a volumetric distributed heat source approach, which, according to established literature [5], is particularly suitable for thick specimen applications. However, this does not preclude its application to thin plate configurations, as demonstrated in the present study. For thin plate geometries, the primary consideration involves the depth parameter, which may introduce additional computational complexity and extend calculation time due to the inclusion of an extra variable in the solution procedure. Nevertheless, to demonstrate the model's capabilities and evaluate the influence of its implementation on final results, Goldak's model has been selected for this investigation.

The heat source intensity distribution is mathematically expressed as follows:

$$Q_{f,r}(x,y,z) = \frac{6\sqrt{3}\, f_{f,r}\, Q_A}{a\, b\, c_{f,r}\, \pi\sqrt{\pi}}\; e^{-3\left[\frac{x^2}{c_{f,r}{}^2} + \frac{y^2}{a^2} + \frac{z^2}{b^2}\right]} \tag{1}$$

$$Q_A = \eta . I . U \tag{2}$$

$$f_f + f_f = 2 \tag{3}$$

Equation (1) demonstrates the spatial distribution of heat through Gaussian-like exponential functions to represent anisotropic heat flux decay from the source in both front and rear sections. Equation (2) defines the total heat input ($Q_A$), establishing the relationship between arc efficiency ($\eta$), welding current ($I$), and voltage ($U$), thereby quantifying the total power input into the welding process. Equation (3) ensures proper distribution of the total heat input between the two ellipsoidal regions while maintaining consistency with the model's mathematical formulation [3].

The aforementioned equations reveal seven unknown parameters - $a, b, c_f, c_r, f_f, f_r,$ and $\eta$ - that require determination to accurately solve the heat source model equations. Resolution of these parameters is essential for computing heat quantities at each nodal position within the meshed simulation model. The present study aims to simplify or eliminate as many unknown parameters as possible from the heat source equations, thereby streamlining the computational process and enhancing the model's practical applicability across diverse welding scenarios.

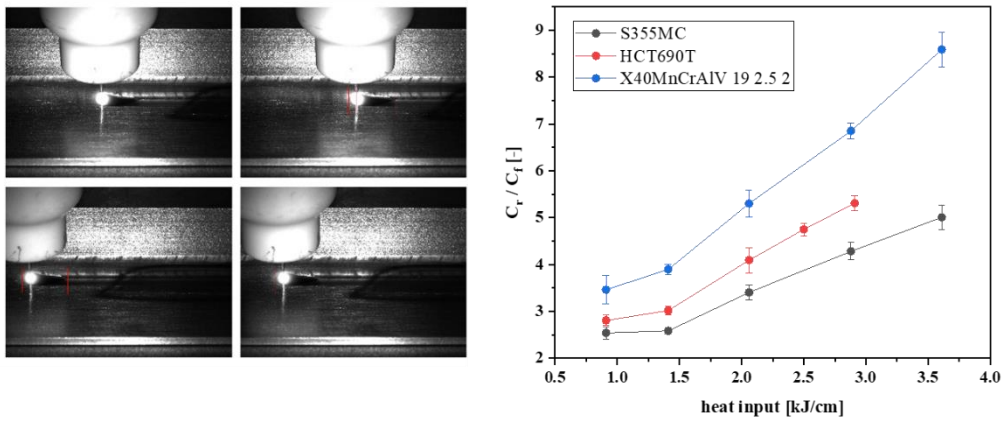



**Fig. 5** Relative length ratio of the molten pool formation during welding process as captured by High-Speed Videography (HSV) system

As described in the experimental setup, High-Speed Videography (HSV) was employed to examine the length ratio of the molten pool across all welding parameters investigated. This technique enabled precise assessment of molten pool dimensions in relation to heat source dynamics. To minimize measurement errors resulting from perspective distortions in the acquired images, molten pool length ratios were measured at a minimum of five different positions for each condition. The results of these measurements are presented in Fig. 5. Based on this analysis, one parameter ($c_f$ or $c_r$) can be determined as a function of the other, as expressed in the following relationship:

$$c_r = c_f \times \frac{c_r}{c_f} \tag{4}$$

Furthermore, the fraction of heat flux distributed to the front and rear halves of the heat source can be related to the length components and their ratio through the following equations [3,6]:

$$f_f = \frac{2\,c_f}{c_f + c_r} \quad , \qquad f_r = \frac{2\,c_r}{c_f + c_r} \tag{5}$$

Utilizing the length ratio values obtained from HSV analysis of the molten pool history in conjunction with the aforementioned equations enables effective reduction of the model's unknown parameters from seven to four: $a, b, c_f$ $(or\ c_r)$ and $\eta$. In the subsequent phase, the remaining parameters must be determined such that the heat source mathematical equation yields accurate solutions.

This study proposes the application of Design of Experiments (DOE) to systematically solve the welding heat source model equations with four input factors corresponding to the remaining unknown parameters. A fundamental prerequisite for this approach is establishing unity in the responses measured across different factor levels defined within the DOE framework.

This unity requirement implies that outputs obtained from the DOE must remain directly comparable when utilizing various combinations of factor levels. However, a significant

challenge emerges because varying these input parameters results in the formation of distinct weld geometries, including the Fusion Zone (FZ), where temperatures reach or exceed the liquidus temperature; the Partial Melting Zone (PMZ), where temperatures range between solidus and liquidus temperatures; and the Heat Affected Zone (HAZ), characterized by temperatures at or above the austenitization point, as illustrated schematically in Fig. 6.

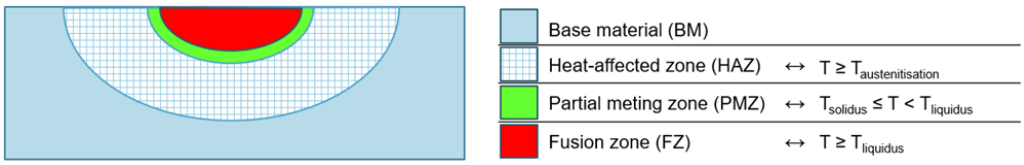



**Fig. 6** Solid-state phase transformation zones in welded specimens, illustrating the distribution of FZ, PMZ, and HAZ

Consequently, these geometries and their corresponding temperatures at specific coordinates within the welded specimens become inherently non-comparable when different input factor levels are employed.

To address this challenge, the consistency of temperature limits governing these transformation zones can be utilized. The boundaries of these zones maintain constant temperature conditions across varying scenarios. For instance, the boundary of the Fusion Zone is defined by the liquidus temperature, the Partial Melting Zone extends from the solidus temperature to the liquidus temperature, while the Heat Affected Zone boundary corresponds to the austenitization temperature for ferritic steels [2].

Based on varying input factor levels and heat input quantities, three distinct types of transformation zone geometries can form, all of which align closely with metallographic observations [15].

Fig. 7 presents a visual representation of transformation zone widths on the welding surface, captured through metallographic analysis. These images clarify the specific geometry expected for a given heat input, grounding the study in empirical observations and enabling meaningful comparisons with simulation results. It should be noted that the Fusion Zone (FZ) and Heat Affected Zone (HAZ) are utilized for TRIP and S355MC steel, whereas for TWIP steel, the FZ and Partial Melting Zone (PMZ) are considered, since TWIP steel does not undergo phase transformation that defines an austenitization temperature due to its fully austenitic structure [16].

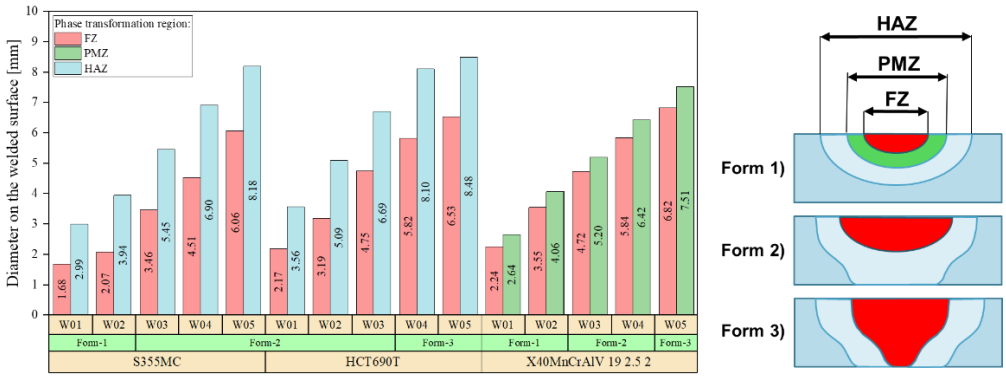



**Fig. 7** Geometry of phase transformation areas utilized in Design of Experiments (DOE) for welded specimens, showing variations in transformation zone morphology corresponding to different heat input levels and resulting weld profiles

Utilizing the data presented in Fig. 7, distinct DOE frameworks can be developed for each heat input level and material investigated. In these experimental designs, the unknown parameters of the heat source model serve as input factors, while the responses are represented by maximum temperatures attained at phase change boundaries. The solution to this DOE is determined by minimizing the temperature difference at phase change boundaries - defined by liquidus, solidus, or austenitization temperatures - between the simulated model and theoretical values. This approach ensures alignment between the model's predictions and expected thermal thresholds. Fig. 8 illustrates one of the DOE system responses for a specific heat input, calculated using simulation data.

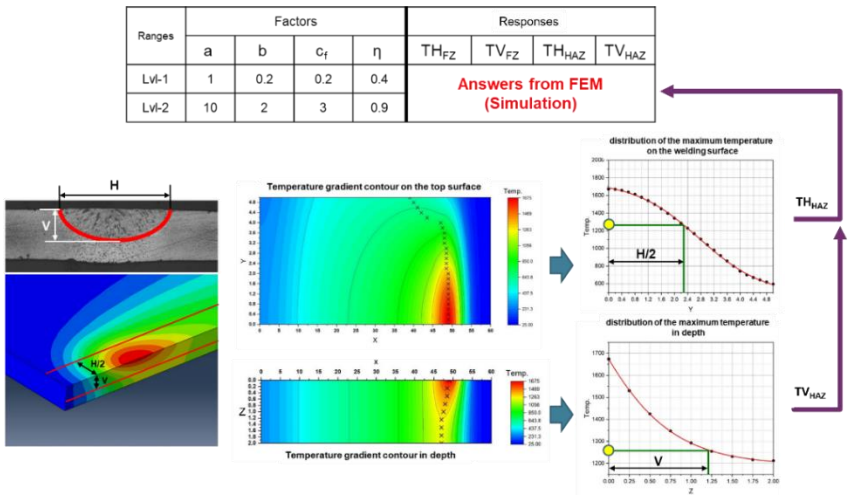



**Fig. 8** Example of response extraction from simulation model for DOE variation based on defined factor settings

The number of simulations required to achieve highly accurate results from the DOE system depends on the complexity of the selected model. In this study, a fifth-order model was chosen to provide a reasonable balance between computational effort and accuracy. This choice was particularly advantageous given the high simulation speed afforded by the selected double ellipsoidal heat source model, ensuring efficient yet precise analysis.

It should be noted that multiple numerical solutions can be obtained in such DOE systems based on the constraints defined in the solution selection procedure. In the subsequent phase, the most appropriate optimal parameters must be identified. To evaluate solutions and select the optimal answer, the following conditions have been established to compare the simulation model with experimental data:

- **Maximum peak temperature similarity at the location of attached thermocouples**: This criterion ensures that simulated temperatures in welding phase at thermocouple sites correspond accurately with experimental measurements. This alignment validates the simulation's heat distribution accuracy, thereby enhancing reliability for optimal welding parameter selection.
- **Maximum similarity of the formed transformation area in cross-section of metallographic macrodiagram**: This condition ensures that the size of the phase transformation zones in the simulation corresponds closely to the macroscopic metallographic images observed around the weld zone, enhancing the model's physical accuracy.
- **Temperature gradient similarity on the welding surface during the cooling phase**: This criterion demands that the simulated temperature gradient during cooling corresponds with experimental data. For reaching an appropriate result, the convection and radiation factors which reflect the environmental or experiment setup constraints should be defined correctly.

By adhering to these conditions, the analysis aims to refine the selection of optimal parameters, thereby improving the reliability and precision of the simulation outcomes.

## RESULTS AND DISCUSSION

The application of the design of experiments (DOE) approach to the Goldak's energy equation typically yields multiple mathematically valid solutions under the established boundary conditions. The selection of the most physically meaningful solution requires systematic evaluation based on the criteria outlined in the methodology section.

For validation of the thermal behavior during the heating phase, the maximum surface temperature at thermocouple locations relative to the weld centerline serves as the primary reference parameter. Given the dense array of thermocouples positioned at predetermined distances from the specimen surface, the optimal solution is identified as that which produces maximum temperature values and thermal distributions most closely corresponding to the experimental measurements at equivalent locations (Fig. 9).

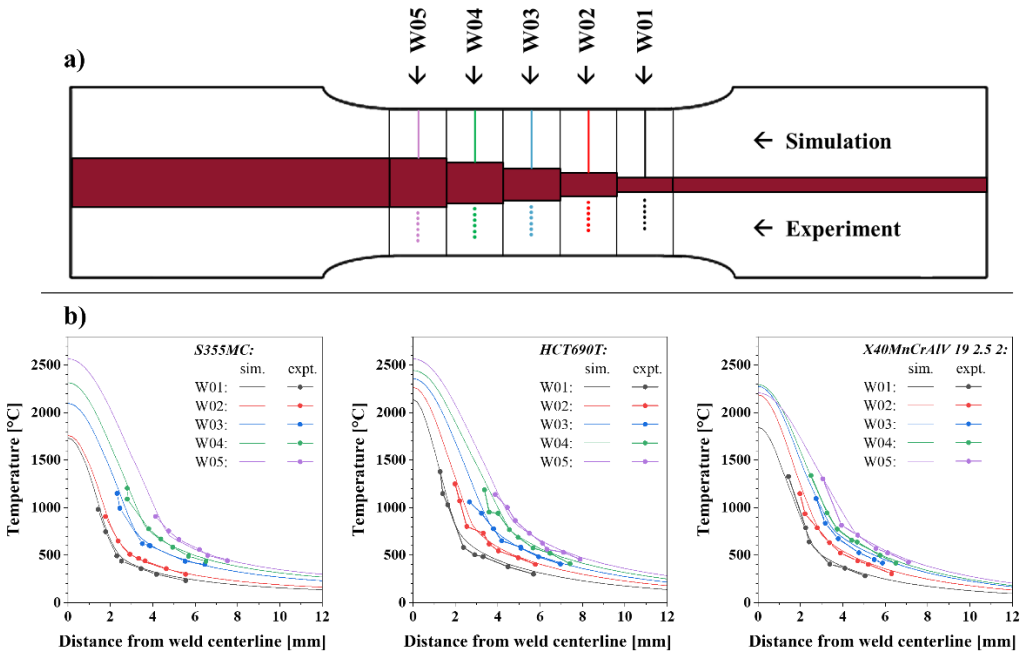



**Fig. 9** a) Schematic representation of welded specimen under heat input variation showing thermocouple locations and simulation temperature measurement areas around the centreline perpendicular to the median axis, b) corresponding distribution of peak temperatures at various distances from the weld centreline for both experimental and simulation results across all investigated materials

During the cooling phase, the austenite transformation to martensite, bainite, pearlite, or ferrite phases is governed by the cooling time $t_{8/5}$ [17]. The cooling behavior is significantly influenced by environmental test conditions, including ambient temperature, fixture geometry, and thermal contact conditions. In the numerical model, these factors are incorporated through appropriate film coefficients and radiation parameters at the interfaces between the specimen and supporting fixtures or ambient air.

The numerical simulation parameters were calibrated to ensure that both the calculated cooling time and residual heat content after a specified time interval matched the experimental values within acceptable tolerances. Following this calibration procedure, the computed temperature gradients from the thermal simulation demonstrated excellent correlation with experimental data, as exemplified in Fig. 10. This high degree of accuracy in temperature prediction is critical for subsequent mechanical analyses, which require precise thermal history data throughout the entire cooling cycle [18,19].

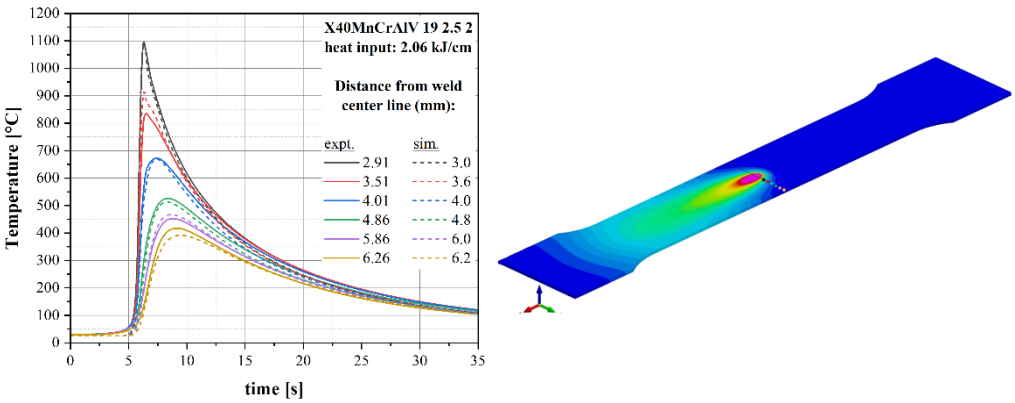



**Fig. 10** Example of a calibrated thermal analysis model showing thermal history at nodes nearest to thermocouple locations on the specimen surface for a specific heat input and material

The comparison between calculated molten pool geometries derived from thermal simulations and metallographic cross-sections demonstrates excellent agreement, as illustrated in Fig. 11. Across all investigated materials, the simulated weld pool dimensions closely correspond to experimentally observed geometries under varying heat input conditions. This consistent correlation between numerical predictions and experimental observations confirms the accuracy and reliability of the simulation methodology in reproducing the physical phenomena of the welding process [20]. The strong agreement between computational and metallographic results validates both the parameter selection procedure and demonstrates the robustness of the heat source model in accurately capturing the thermal distribution and geometric characteristics of the molten pool formation.

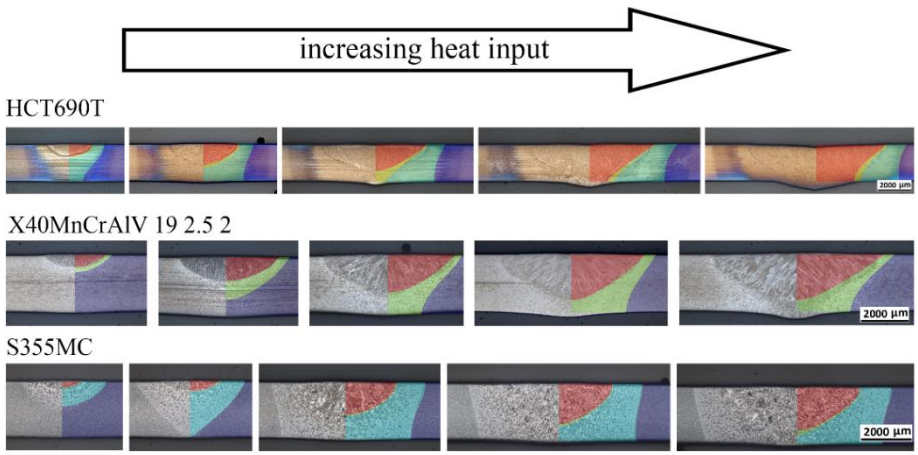



**Fig. 11** Comparison of molten pool geometries obtained from thermal simulation with corresponding metallographic cross-sections

For validation purposes, different temperature criteria were applied based on material characteristics. For S355MC and HCT690T steels, phase transformation boundary temperatures in both the fusion zone (FZ) and heat-affected zone (HAZ) were considered as comparison parameters. However, for the austenitic steel X40MnCrAlV 19-2.5-2, the temperature at the FZ and partially melted zone (PMZ) boundary was utilized due to its distinct metallurgical behavior. In cases where significant discrepancies between simulation and experimental results exceed acceptable tolerances, alternative parameter sets from the DOE matrix are systematically evaluated.

Following the application of validation criteria to identify optimal parameters from the DOE solutions, the unknown heat source model parameters were determined for all investigated materials, as presented in Fig. 12.

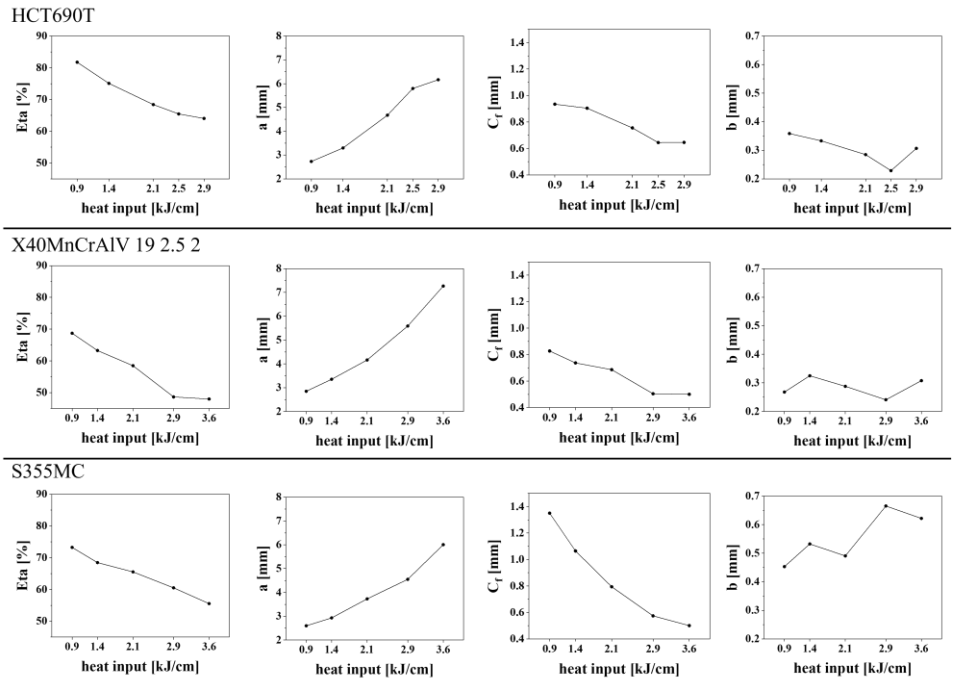



**Fig. 12** Distribution of determined heat source parameters across varying heat input levels for all investigated materials

The results demonstrate that increasing heat input produces elevated temperatures within the welding zone, as previously shown in Fig. 9, which correspondingly increases molten pool dimensions. This relationship is clearly reflected in the distribution of parameter *(a)* across varying heat input conditions. A notable characteristic observed across all parameters is their approximately linear response to heat input variations.

Of particular significance is the behavior of the efficiency factor, which exhibits a decreasing trend with increasing heat input. This finding contradicts the common assumption

in many welding studies where efficiency is treated as a constant value for a given welding process, highlighting a deviation from observed physical behavior. The distribution of parameter *(b)* remains relatively constant across all heat input conditions, suggesting that the depth parameter may be omitted from the heat source equation for thin plate welding applications. This observation indicates that a double elliptical surface heat source model could yield comparable accuracy while reducing computational complexity by eliminating one unknown parameter, thereby requiring fewer simulation runs in the DOE framework.

The parameter *($C_f$)* demonstrates a decreasing trend with increasing heat input, which can be attributed to the specific experimental boundary conditions and fixture constraints under which molten pool geometries were measured during welding. This suggests that alternative clamping systems and constraint configurations may influence this parameter, as well as other heat source parameters, emphasizing the importance of considering experimental setup conditions in parameter determination.

As discussed in the previous section, these determined parameters enable the calculation of remaining heat source model equation parameters for each specific heat input condition through the application of equations (1-5).

The thermal analysis results serve as input data for the subsequent mechanical analysis in the welding simulation procedure. Residual stress represents one of the most critical mechanical characteristics that can be determined through this approach, as its distribution across the welded surface significantly influences mechanical performance and structural integrity. In this investigation, the computed residual stresses from the simulation model were validated against experimental data obtained through X-ray diffraction (XRD) measurements [21].

Fig. 13 presents the residual stress distributions corresponding to specific heat input conditions for each investigated material. The simulation-predicted stress profiles are directly compared with experimentally measured data within each diagram. The strong correlation between these profiles demonstrates the reliability of the simulation methodology based on the heat source parameters determined in this study.

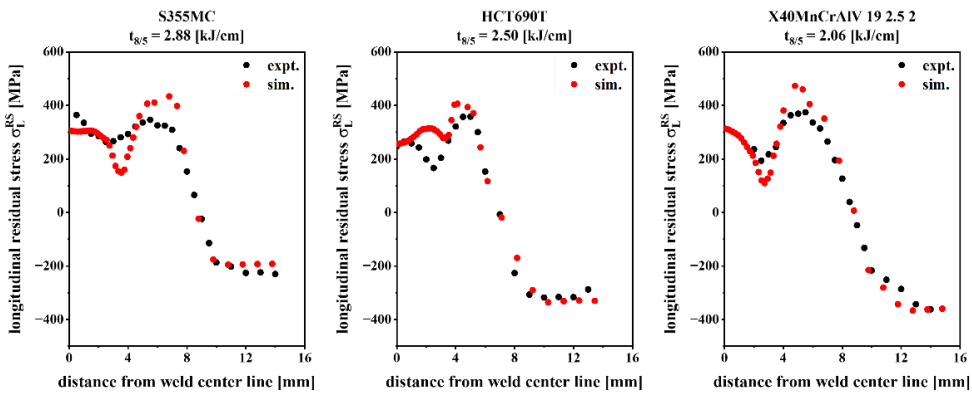



**Fig. 13** Distribution of residual stress corresponding to specific heat input levels in the investigated materials

For the numerical calculation of residual stresses, an isotropic hardening model was implemented. This constitutive model assumes uniform hardening behavior throughout the material, thereby simplifying the computational process while maintaining satisfactory correlation with experimental observations. However, the isotropic hardening assumption may not fully capture the complexities of material behavior during phase transformations, particularly within the fusion zone, or under more demanding loading scenarios. Future investigations could incorporate alternative hardening models, such as kinematic or combined hardening approaches, to assess potential improvements in residual stress prediction accuracy. Through the implementation of a broader range of constitutive models, the proposed methodology could be further refined, potentially expanding its applicability to diverse materials and welding conditions.

## CONCLUSION

This investigation presents a simplified methodology for determining welding heat source parameters specifically developed for high-strength steel applications. The implementation of a double ellipsoidal volumetric heat source model successfully captured the thermal characteristics of the welding process, enabling accurate simulations while avoiding the computational complexities typically associated with conventional approaches. The systematic integration of high-speed videography (HSV), metallographic macrostructure analysis, variable heat input conditions, strategically positioned thermocouple arrays, and design of experiments (DOE) methodology provided an effective framework for identifying optimal heat source parameters with enhanced efficiency and precision.

A fundamental aspect of this methodology is the utilization of unified response criteria within the DOE framework for specific welding configurations. The DOE approach facilitated systematic exploration of parameter combinations, yielding optimized solutions with high consistency in responses, particularly at phase transformation boundary temperatures. Stringent validation criteria ensured excellent agreement between simulation results, metallographic observations, and experimental temperature measurements.

The reliability of the simulation model was further confirmed through accurate prediction of residual stress distributions, as validated by X-ray diffraction (XRD) measurements. This validation demonstrates the model's capability to capture the complex thermal and mechanical phenomena occurring in welded specimens, establishing a robust foundation for future developments in welding simulation technology.

Future enhancements to this methodology could include parameter recalibration for varying welding speeds and heat input ranges, thereby extending the model's applicability. Additionally, investigation of alternative constitutive models, such as kinematic or combined hardening approaches, may provide enhanced understanding of material behavior and improve residual stress prediction accuracy across diverse welding scenarios. Potential research directions include studies on welding under different constraint conditions, such as alternative fixture designs or clamping systems, as well as investigation of the effects of pre-deformation on welding behavior and subsequent material properties.

This work provides a significant simplification of welding simulation procedures, offering a practical and efficient computational tool for researchers and engineers focused on welding process optimization and advancement of high-strength steel joining technologies.

## ACKNOWLEDGEMENTS

The results presented in this study were achieved as part of a collaborative effort between the Technical University of Braunschweig and the Karlsruhe Institute of Technology, supported by the German Research Foundation (DFG) under project numbers Gi376/17-1 and Ni508/19-1. The authors gratefully acknowledge the financial support provided by the German Research Foundation.

## References

[1] LARS-E LINDGREN: *Computational Welding Mechanics: Thermomechanical and microstructural simulations*, Woodhead Publishing, 2007.

[2] J. SUN: *Influence of heat input model parameters on the simulated properties in ferritic steel weldments*, 2019.

[3] J. A. GOLDAK, M. AKHLAGHI: *Computational Welding Mechanics*, Physica-Verlag, 2005.

[4] Z. SATERNUS: 'Computer Methods for Determination of Deformations in Welded Closed Profiles', *Procedia Engineering*, 177, pp. 188-195, 2017.

[5] E. J. G. NASCIMENTO, E. DOS SANTOS MAGALHÃES, L. E. DOS SANTOS PAES: 'A literature review in heat source thermal modeling applied to welding and similar processes', Int. J. Adv. Manuf. Technol., 126, pp. 2917-2957, 2023.

[6] S. TRUPIANO, V. G. BELARDI, P. FANELLI, L. GAETANI, F. VIVIO: 'A semi-analytical method for the calculation of double-ellipsoidal heat source parameters in welding simulation', IOP Conf. Ser.: *Mater. Sci. Eng.*, 1214, 12023, 2022.

[7] V. GARCÍA-GARCÍA, I. MEJÍA, F. REYES-CALDERÓN: 'Improved thermal FE numerical model/DoE based on the Taguchi method to estimate weld penetration/energy and non-metallic inclusions: a case study in Ti-containing TWIP steel butt joints', *Int. J. Adv. Manuf. Technol.*, 105, pp. 101-120, 2019.

[8] O. BOUAZIZ, S. ALLAIN, C. P. SCOTT, P. CUGY, D. BARBIER: 'High manganese austenitic twinning induced plasticity steels: A review of the microstructure properties relationships', *Current Opinion in Solid State and Materials Science*, pp. 141-168, 2011.

[9] N. SAUNDERS, U. K. Z. GUO, X. LI, A. P. MIODOWNIK, J.-P. SCHILLÉ: 'Using JMatPro to model materials properties and behavior', *JOM*, 55, pp. 60-65, 2003.

[10] N. AN, G. YANG, K. YANG, J. WANG, M. LI, J. ZHOU: 'Implementation of Abaqus user subroutines and plugin for thermal analysis of powder-bed electron-beam-melting additive manufacturing process', *Materials Today Communications*, 27, 102307, 2021.

[11] W. A. JOHNSON and R. F. MEHL: *Reaction Kinetics in Processes of Nucleation and Growth*, pp. 416-442, 1939.

[12] D. P. KOISTINEN, R. E. MARBURGER: 'A general equation prescribing the extent of the austenite-martensite transformation in pure iron-carbon alloys and plain carbon steels', *Materials Science Engineering*, pp. 365-378, 1959.

[13] M. BJELIC, B. RADICEVIC, K. KOVANDA, L. KOLAŘÍK, A. PETROVIC: 'Multi-objective calibration of the double-ellipsoid heat source model for GMAW process simulation', Therm. Sci., 26, pp. 2081-2092, 2022.
[14] J. M. CABEZA LAINEZ, J. A. PULIDO ARCAS, M.-V. CASTILLA, C. RUBIO BELLIDO, J. M. BONILLA MARTÍNEZ: 'Radiative Heat Transfer for Curvilinear Surfaces', in: S.R. Bello (Ed.), *Solar Radiation Applications*, InTech, 2015.
[15] G. TURICHIN, D. MUKIN, E. VALDAYTSEVA, M. SANNIKOV: 'Influence of Latent Heat of Fusion on the Melt Pool Shape and Size in the Direct Laser Deposition Process', *Materials*, Basel, Switzerland, 15, 2022.
[16] Y. SONG, Y. WANG, M. ZHANG: 'Experimental and Numerical Simulation on Laser welding of High Manganese TWIP980 Steel', *Procedia Manufacturing*, 37, pp. 385-393, 2019.
[17] J. S. T. LOOSE: *Leistungsmerkmale der Schweißstruktursimulation*, pp. 487-491, 2008.
[18] E. A. BONIFAZ, A. S. MENA: 'The Cooling Rate and Residual Stresses in an AISI 310 Laser Weld: A Meso-Scale Approach', *Crystals*, 12, 502, 2022.
[19] M. ZHANG, Y. ZHOU, C. HUANG, Q. CHU, W. ZHANG, J. LI: 'Simulation of Temperature Distribution and Microstructure Evolution in the Molten Pool of GTAW Ti-6Al-4V Alloy', *Materials*, Basel, Switzerland, 11, 2018.
[20] N. HEMPEL: *Zum Einfluss zyklischer Plastizität auf die Eigenspannungsentstehung beim Schweißen hochlegierter Stähle*, Shaker, 2022.
[21] L. SPIEß, G. TEICHERT, R. SCHWARZER, H. BEHNKEN, C. GENZEL: *Moderne Röntgenbeugung: Röntgendiffraktometrie für Materialwissenschaftler*, Physiker und Chemiker, Springer Spektrum Wiesbaden, 2019.

# A REVIEW OF WELDING MODELLING APPROACHES FOR NUCLEAR INDUSTRY

A. BROSSE*, N. KHELIF*, T. LEVEILLE*, S. GALLÉE*

**Framatome, 69007 Lyon, France*

*DOI 10.3217/978-3-99161-089-2-033, license CC BY 4.0*
*https://creativecommons.org/licenses/by/4.0/deed.en*
*This CC license does not apply to third party material and content noted otherwise.*

ABSTRACT

In the nuclear industry, welding process is widely used to assemble components. As a manufacturer, Framatome has developed over the years specific tools and approaches to answer the needs of our welders. Indeed, for an industrial use, welding modelling must be efficient, robust and reliable but unfortunately no approach can achieve all these goals, so choices must be made. Many approaches exist in the literature to model residual stresses and distortions. This paper will focus only on thermomechanical approaches of welding by finite element analysis such as: moving heat source, thermal cycle, inherent strain, .... Each of these approaches has advantages and disadvantages such as computation time or accuracy of results. In this paper we propose to make a comparison between these approaches and to define the assumptions and limits for each of them in the context of welding and Wire Arc Additive Manufacturing modelling for nuclear industry. First, the paper will present a review of each approach capabilities and then their applications on a specific mockup designed as an Additive Manufacturing wall are described. The distortions and residual stresses results are compared for each approach with experimental data with the goal to give limits and guidelines for each application.

Keywords: Distortions, 18MND5, TG10, Welding Simulation

## INTRODUCTION

The Wire Arc Additive Manufacturing (WAAM) process comes directly from arc welding, an industrial process that has been mastered for over a century. This connection brings several advantages such as the ability to use existing welding equipment and proven methodologies like numerical simulation. However, it also introduces specific challenges related to the sequential nature of material deposition, such as weld bead overlapping and new geometric possibilities that significantly reduce material waste but also create new challenges.

In the development of welding processes, the nuclear industry has long relied on numerical simulation to complement experimental observations, virtually test configurations, optimize

process parameters, and reduce the time and cost of mock-up testing. Over time, this approach has become a valuable tool for improving lead times and weld reliability.

For WAAM, however, achieving the same synergy between experimental and numerical methods is more challenging due to the complexity of the models involved. Therefore, it is essential to develop faster simulation techniques that can accurately reproduce the effects of the process while remaining compatible with industrial constraints.

## NUMERICAL METHODS FOR WAAM MODELLING

In the literature on welding and additive manufacturing modelling, two main approaches are commonly identified:

- A local-scale approach, which focuses on simulating complex fluid flow within the melt pool [1].
- A weldment-scale approach, which aims to predict the structural effects of welding and additive manufacturing, such as solid-state phase transformations, distortion, and residual stresses [2].

This paper focuses on the second, standardized approach, which is widely used in the nuclear industry. It relies on the Finite Element Method (FEM) but faces the challenge of increasing degrees of freedom (D.O.F.): the more weld beads involved, the larger and more time-consuming the model becomes. Therefore, for high number of beads - such as in additive manufacturing - efficient solutions must be developed to manage computational complexity.

Several authors have already reviewed simplification techniques [3] allowing to simulate large components [4]. For clarity, these techniques can be grouped into three categories: meshing techniques, computational techniques, and simplified approaches.

- Meshing techniques focus on optimizing the choice of finite elements for a given problem. For example, shell or combined shell-solid approaches can significantly reduce computation time [5]. Unfortunately, these methods are more suitable for predicting distortions in large, flat structures.
- Computational techniques aim to enhance efficiency through numerical algorithms. These may involve solver-level improvements, such as leveraging GPU computing power [6] or using technic solvers like superelements. A few authors even tried methods to bypass iterative solving by using data-driven numerical approach [7]. All these methods share the goal of solving the same physical equations without altering the underlying solution. This direction appears promising for the future of numerical modelling, especially with the growing potential of computational power and artificial intelligence.
- Finally, the simplified approaches consist in saving time of computation without too much modification of the solution. Many simplifications are possible with the difficulty to master the error of simplification. In this paper we will concentrates on a few of them described below.

### MOVING HEAT SOURCE APPROACH (MHS)

Among the various existing approaches, the moving heat source method is widely recognized as the most accurate and will be used as a reference in this study. This method is based on the progressive activation of model elements along the welding path by a heat source that represents the energy input into the workpiece. At each time step, a thermal simulation is performed to model the heat input and its dissipation throughout the part. These thermal variations cause local expansions and contractions of the material, generating internal stresses and deformations that are accounted for in the mechanical model. The accuracy of the simulation depends on several factors, including material properties - which must be temperature- and phase-dependent - and the mesh, which must be fine enough to capture steep thermal and stress gradients. Additionally, heat source parameters such as welding speed, shape, and heat input density must be accurately defined and validated through experimental [8].

### LUMP BEAD THERMAL CYCLE APPROACH (TCY)

Another approach developed for welding simulation - and applicable to the WAAM process - is the lumped bead method [9], which aims to accelerate simulations while maintaining representative thermal evolution and distribution. In this method, a thermal cycle is applied either sequentially or simultaneously to each bead during its deposition. The results of this thermal analysis are then directly integrated into the mechanical model, which accounts for the thermal effects on stress and deformation before solving the mechanical equilibrium of the structure.

A key aspect of this approach lies in the relevance of the thermal cycle, which can be extracted from a preliminary reference model. In this study, we use data derived from the moving heat source reference case. One limitation of the lumped bead method is its insensitivity to welding direction when the thermal cycle is applied to the entire bead at once. An improvement to this method involves dividing each bead into multiple segments - typically two or three - to better capture directional thermal and mechanical effects.

### FAST HEAT SOURCE (FHS)

This method is based on the assumption of a stabilized thermal zone away from the start and end of the weld beads [10]. The principle involves using a conventional 3D moving heat source for the start and end regions, while applying an equivalent 2D heat source to the intermediate section - referred to as the "acceleration zone." The goal is to reduce computation time by simplifying the simulation of the homogeneous and stabilized region.

The advantage of this hybrid method is that it can be combined with the reference moving heat source approach, but it introduces new parameters that must be calibrated: the lengths of the start, acceleration, and stop zones, as well as a multiplier coefficient for the 2D heat source in the acceleration zone.

### 3D/2D APPROACH (3D/2D)

The so-called 3D/2D methodology, developed by Framatome [11], is an hybrid approach designed to optimize simulation accuracy while significantly reducing the computational costs associated with full process modelling. It relies on a two-step decomposition of the problem, combining the detailed representation of thermal and metallurgical phenomena through a three-dimensional state model with the computational efficiency of two-dimensional model for thermomechanical analysis.

In the first step, a steady-state thermo-metallurgical 3D simulation is performed for each weld bead. This simulation captures the temperature distribution induced by an equivalent heat source representative of the process, producing both a thermal field and a map of metallurgical phases. In the second step, the 3D thermal results are transposed into 2D data, which are then used in a 2D thermo-metallo-mechanical simulation. This enables the evaluation of residual stresses, plastic deformations, and shrinkage effects associated with bead deposition, while accounting for the complex thermomechanical interactions specific to the WAAM process.

The 3D/2D method offers an effective compromise between physical fidelity and computational performance. Its main limitation lies in the difficulty of representing complex geometries within a 2D cross-sectional framework.

### INHERENT STRAIN METHOD (IS)

The Inherent Strain method is one of the most used approaches in additive manufacturing modeling. Its principle is based on simplifying the simulation process by not directly accounting for thermal effects. Instead, a strain tensor is applied to each bead to reproduce distortions. This results in a single mechanical computation step per bead, enabling very fast simulations. However, this method only provides distortion results and is dependent on the applied loading. Two main loading strategies exist:

1. Applying the full strain tensor, including all three components. In this case, a partial reference model - such as the moving heat source method - may be required to define the strain accurately.
2. Applying a reduced strain tensor, primarily in the welding direction, which governs the final deformation. This approach can be calibrated using an iterative inverse method to fit experimental data [12].

## THE TG10 MOCKUP

An experimental mock-up has been designed in order to collect useful data for modelling. This mock-up is inspired by the previous TG9 configuration [13] but uses a low alloyed steel [14] subject to solid state transformations These transformations locally alter the material microstructure, affecting mechanical properties such as hardness, distortions, or residual

stresses. The mock consists of a thin plate of 8 mm onto which five beads were deposed as presented Fig. 1. Five similar mock-ups were produced using the same welding parameters for each bead as detailed in Table 1.

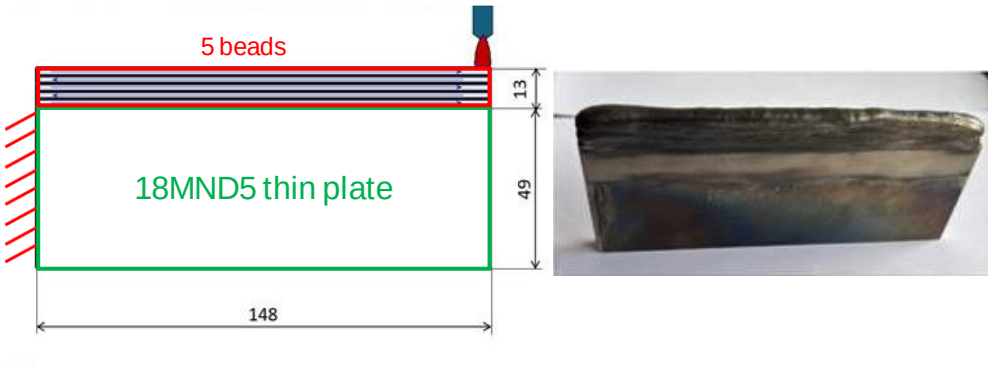



**Fig. 1** The TG10 mockup

**Table 1** Welding parameters

| **Parameter** | Preheating [°C] | Welding speed [mm/s] | Voltage [V] | Current [A] | Wire feed speed [mm/s] | Wire diameter [mm] | Interpass temperature [°C] |
|---|---|---|---|---|---|---|---|
| **Experimental Value** | 175 | 10 | 18.5 | 225 | 30 | 3.2 | 250 |

Several measurements were performed on the mock-up, both in-situ and postmortem. These included temperature monitoring using an infrared camera and thermocouples, as well as macrographic analysis to examine the molten zone and the heat-affected zone. From a mechanical perspective, residual stress measurements are still ongoing within the European network NET [15]. For the purpose of this paper, we primarily focus on distortion measurements taken at the extremities of each mock-up, as shown in Fig. 2. Temperature data were not recorded for intermediate beads, so some variation is expected; however, the final distortion values were measured at room temperature. For comparison purposes, we will mainly refer to the final average distortion value of 0.43 mm.

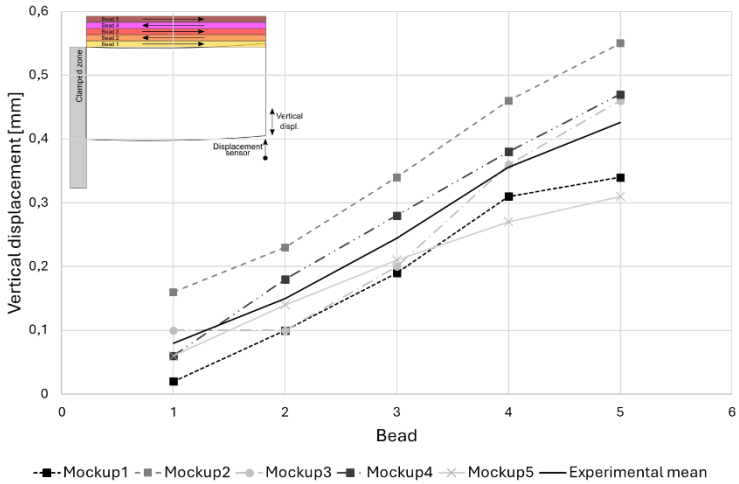



**Fig. 2** Distortion measured on each TG10 mockup

## NUMERICAL MODEL OF TG10

The simulations were carried out using the software SYSWELD™ [16] along with internal tools and databases. The mesh consists of linear hexahedral elements, which are preferred for nonlinear mechanical calculations. The boundary conditions, illustrated on Fig. 3 include:

- A heat exchange coefficient accounting for both convection and radiation losses on the surface area of the mock-up. This surface is updated after the deposition of each bead.
- Mechanical constrains applied in all three directions on the left face of the model, consistent with the clamping conditions of the experimental setup.

The heat source used in the reference moving heat source simulation is a Goldak-type model [17] calibrated to reproduce the same fusion zone as observed in the experimental mock-up. Solid-state phase transformations are incorporated using the Leblond model [18] with parameters fitted for the same material [11]. All numerical assumptions, including mesh configuration and boundary conditions, are consistently applied across all modelling approaches.

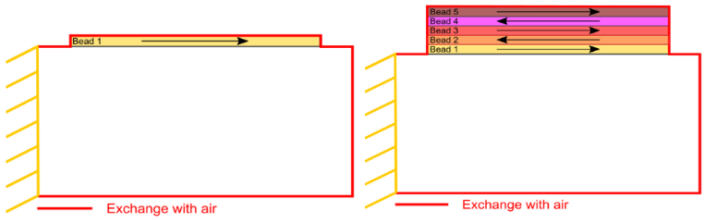



**Fig. 3** Thermal and mechanical boundary conditions

## COMPARISON OF METHODS

In this study, each modelling approach was tested on the industrial use case to assess its relevance and performance. No assumptions or simplifications were introduced beyond those inherent to each method, allowing for both qualitative and quantitative comparisons. The focus is primarily on thermometallurgical and mechanical results. Additionally, computation times are compared to evaluate the efficiency of each numerical approach.

### THERMOMETALLURGICAL COMPARISON

Fig. 4 presents the thermal cycles extracted at the midpoint of the structure, 3 mm below the top surface, for each simulation approach during the five bead depositions. It is important to note that the inherent strain method, being purely mechanical, does not produce thermal results and is therefore excluded from this analysis.

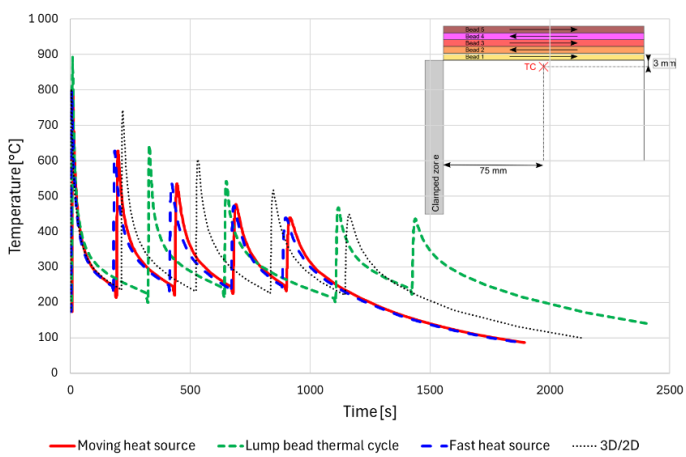



**Fig. 4** Temperatures evolution obtained by TG10 simulations

The overall thermal profiles remain consistent across simulations: as the extraction point moves further away with each successive bead deposition, a decrease in peak temperature is observed. However, differences in timing between methods emerge, primarily due to the way interpass temperature is handled: in all approaches, each bead is deposited after the previous layer cools to the target interpass temperature of 250 °C. Therefore, most methods tend to overestimate the actual deposition time during interpass cooling - especially simplified approaches that do not preserve global energy consistency. For example, the thermal cycle method overestimates the time required to reach the interpass temperature by approximately 50% for the final bead.

For a closer look on the potential impact on mechanical results, Fig. 5 highlights the thermal cycle observed during the deposition of the first bead.

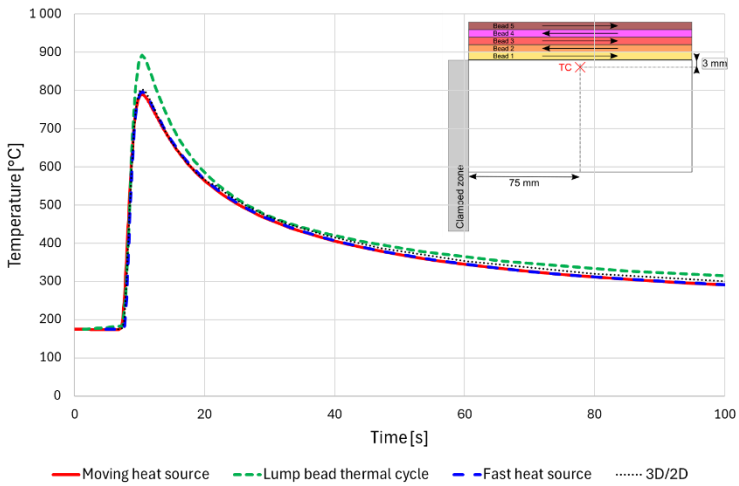



**Fig. 5** Temperatures evolution obtained by TG10 simulations – zoom on deposit 1

Despite some variations, the overall trends remain consistent across all approaches, with a rapid temperature rise followed by a gradual cooling phase. Notably, the cooling rates are similar, which is crucial for accurate microstructure prediction. However, differences in peak temperature values are observed, likely due to variations in heat input modeling. In the Moving Heat Source and 3D/2D approaches, the heat input is directly derived from welding parameters, ensuring consistency. In contrast, the Lumped Bead method applies a uniform average thermal cycle to all beads, resulting in higher cumulative heat input into the workpiece. Post-processing reveals that the effective heat input in the Lumped Bead approach is approximately 3.3 kJ/cm, compared to the reference value of 3.0 kJ/cm.

Fig. 6 shows the final metallurgical state at the end of welding in a cross section in the middle of the plate.

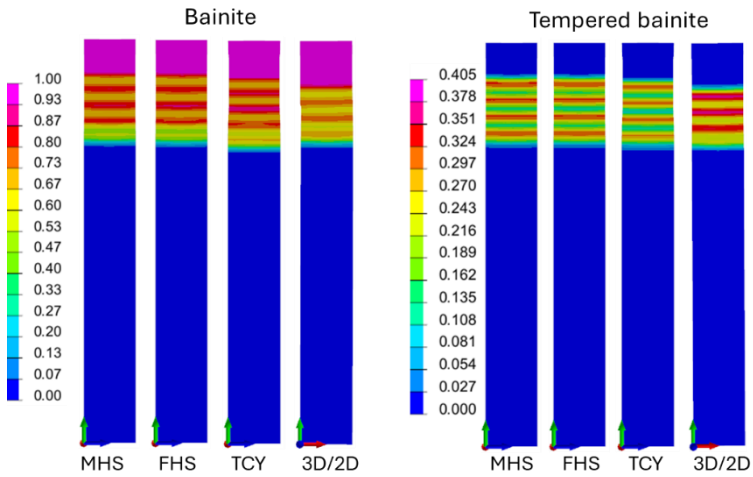



**Fig. 6** Metallurgical phase proportions

The same bainite distribution is observed in both the moving heat source and fast simulation approaches. In the thermal cycle method, a vertical offset of approximately 0.8 mm is noted, which aligns with the applied thermal cycle and the associated heat input. In contrast, the 3D/2D method shows a lower proportion of bainite compared to the other approaches. Since phase proportions in this method are derived from a steady-state computation, this difference suggests that steady-state conditions were not fully achieved and it slightly affects the cooling rate, even though the thermal cycle at the thermocouple location appears to be in good agreement with experimental data.

## MECHANICAL COMPARISON

The Fig. 7 and Fig. 8 illustrate the longitudinal and transverse residual stresses in the welding direction at the end of the process, evaluated across two cross-sections. The results from the 3D/2D approach are also included, shown for one section cut and one cross-sectional view. Finally, Fig. 9 presents a stress profile along a defined cutting line, allowing for a quantitative assessment of stress variation.

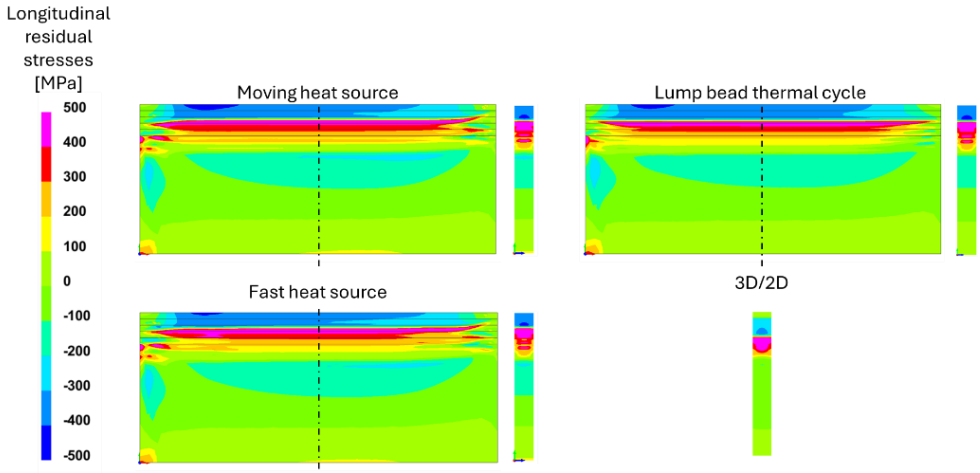



**Fig. 7** Longitudinal residual stresses

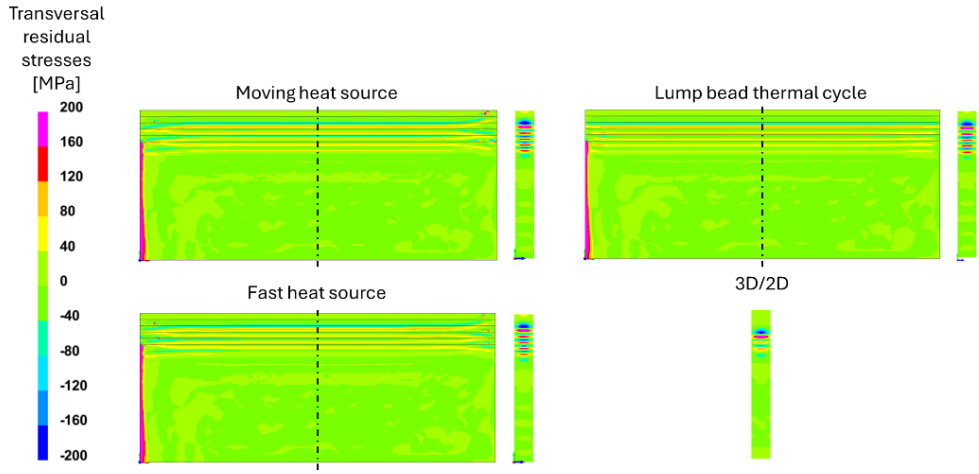



**Fig. 8** Transverse residual stresses

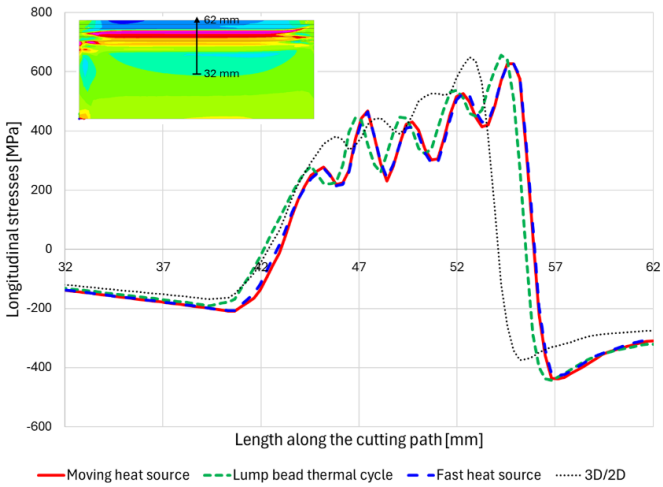



**Fig. 9** Residual Stress along a cutting line in the middle

No experimental measurement have been performed yet but residual stress predictions indicate that the moving heat source method, considered as the reference, provides a highly detailed and localized stress distribution, accurately capturing transient thermomechanical effects. The fast heat source method also delivers very good stress predictions, particularly in the so-called acceleration zone. In contrast, the 3D/2D approach yields smoother and less precise stress profiles, which aligns with the corresponding metallurgical observations.

## DISTORTIONS

This section examines the distortions induced by the welding process, as predicted by various simulation approaches. Fig. 10 presents a comparison between numerical predictions and experimental measurements at a point located at the bottom of the mock-up, following the completion of welding. The 3D/2D method is excluded from this analysis due to its limitation to in-plane deformation only. For the Inherent Strain method, a constant strain tensor - extracted from the third bead of the 3D model - is applied sequentially across all deposited beads.

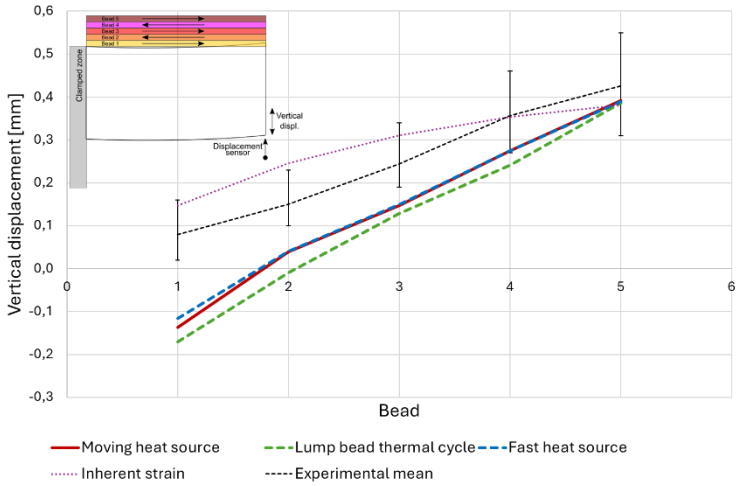



**Fig. 10** Distortion evolution

A noticeable variation is observed between the evolution of numerical and experimental distortion results, most likely due to differences in interpass temperature. For the first four beads, the measurements were taken while the workpiece was still cooling resulting to a non-uniform temperature distribution. As cooling progresses, the measurement point shifts upward, transitioning from negative to positive values. The deviations observed in these initial beads can therefore be attributed to differences in timing and temperature conditions between the experiments and the simulations.

Despite this, the analysis of simulated displacements shows consistent trends across the different modelling approaches. This indicates that all methods are capable of capturing general distortion behaviour, making them suitable for design-oriented applications - especially fast approaches like the inherent strain method. However, it is important to note that the inherent strain method is not reliable for quantitative predictions, as its results deviate significantly from those using more physically detailed models. Moreover, its accuracy strongly dependent on the strain tensor values used in the simulation.

## TIME OF COMPUTATION

The Fig. 11 shows a comparison of computation times for each method. For both the thermal cycle and inherent strain approaches, an initial simulation of a single weld bead is required to generate input data. As the number of weld beads increases, the impact of this preliminary simulation on the total computation time becomes less significant. This is because the initial simulation is performed only once, while its results can be reused in the simplified simulations, thereby improving overall computational efficiency for complex models.

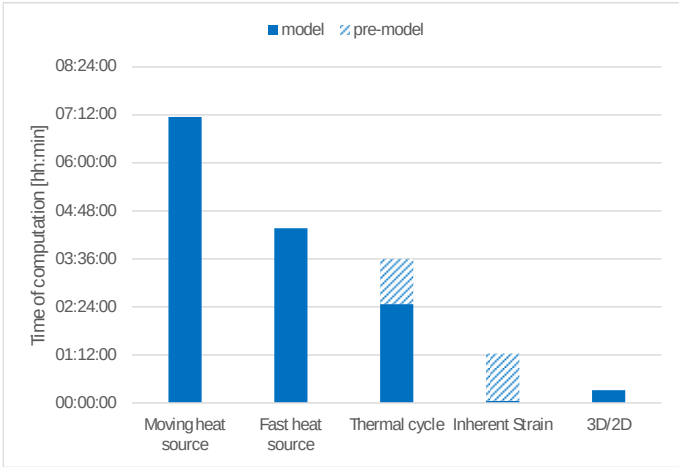



**Fig. 11** Computation time for each approach

The analysis of computation times highlights notable differences between the various simulation methods. The moving heat source approach remains the most computationally intensive. In contrast, the fast heat source and thermal cycle methods offer a balanced compromise, particularly advantageous as weld bead length increases. These methods leverage thermal cycle data or geometric simplifications, reducing the need for full recalculations at each step. Consequently, their efficiency improves with longer welds. On the other hand, the 3D/2D and inherent strain methods deliver exceptionally short computation times, making them well-suited for modelling large structures with thousands of weld beads.

## DISCUSSION

This study was conducted as part of an effort to assess and compare various simulation methods for the WAAM (Wire Arc Additive Manufacturing) process, using a simplified experimental setup. The simulations performed revealed the respective strengths and limitations of each approach. The moving heat source method demonstrated the highest accuracy - particularly in predicting thermal and mechanical fields - but required significantly longer computation times. In contrast, the thermal cycle, fast heat source, and 3D/2D methods provided faster alternatives, altering sometimes physical accuracy. The inherent strain method proved especially suitable for predictive purposes, though less appropriate for detailed validation. Ultimately, the choice of simulation method depends on the desired balance between accuracy, computational cost, and industrial applicability.

To support industrial applications in the nuclear sector, a summary of these findings is presented in Table 2, providing practical guidelines for future users in selecting the most appropriate simulation method.

**Table 2** Sum-up of approaches limitations and difficulties

| **Method** | Moving heat source (MHS) | Fast moving heat source (FHS) | Thermal cycle (TCY) | 3D/2D | Inherent strain (IS) |
|---|---|---|---|---|---|
| **Limitation** | Non-industrial time of computation | Requires stationary phase | No directional effects | Requires stationary phase - Only one main direction | No phase transformation prediction |
| **Difficulty** | Mesh | Mesh and computation time | Energy consistency | None- use in welding | Choosing appropriate strain tensor |
| **Reliability** | Perfect if enough data | Good, especially for interpass time | Good | Good for microstructure and stresses | Trend-level accuracy only |

Beyond this evaluation, this work opens several perspectives for future research and development:

- Scaling up the models: Future simulations should target geometries that more closely look like industrial components, incorporating a greater number of weld beads deposited side by side and across multiple layers. This will enable better representation of thermal and mechanical interactions between successive passes.
- Extended experimental validation: Conducting measurement campaigns on more complex mock-ups will enhance model robustness and help refine simulation assumptions.
- Development of hybrid tools: Integrating fast and accurate methods through multi-scale or adaptive approaches could provide an optimal balance, facilitating the industrial deployment of WAAM technologies.

## References

[1] S. CADIOU, A. BAUMARD, A. BROSSE, ET V. BRUYERE: 'Modelling of the melt pool behaviour during a pulsed GTA welding operation in a narrow groove', présenté à The 13th International Seminar "Numerical Analysis of Weldability, Graz, 2022.

[2] ISO/DIS 18166, *Numerical welding simulation - Execution and documentation*.

[3] L.-E. LINDGREN ET A. LUNDBÄCK: 'Approaches in computational welding mechanics applied to additive manufacturing: Review and outlook', *Comput. Methods Weld. Addit. Manuf. Simul. Numér. Procédés Soudage Fabr. Addit.*, vol. 346, n° 11, p. 1033-1042, nov. 2018, doi: 10.1016/j.crme.2018.08.004.

[4] S. LIU ET AL.: 'A review of welding simulation methods for large components', *Prog. Nat. Sci. Mater. Int.*, vol. 33, nº 5, p. 551-568, 2023, doi: https://doi.org/10.1016/j.pnsc.2023.12.004.
[5] Y. DUAN, F. FAURE, J. M. BERGHEAU, ET J. B. Leblond: 'Prediction of welding distortions using an adaptative 3D/shell approach', Modelling of Casting, Welding and Advanced Solidification Processes XI », in *TMS publication, ISBN*, C. A. Gandin et M. Bellet, Éd., 2006, p. 978-0-87339-629-5.
[6] N. MA: 'An accelerated explicit method with GPU parallel computing for thermal stress and welding deformation of large structure models', *Int. J. Adv. Manuf. Technol.*, vol. 87, nº 5, p. 2195-2211, nov. 2016, doi: 10.1007/s00170-016-8542-3.
[7] D. K. N. PHAM, N. BLAL, ET A. GRAVOUIL: 'Tangent space Data Driven framework for elasto-plastic material behaviors', *Finite Elem. Anal. Des.*, vol. 216, p. 103895, 2023, doi: 10/g8r3jv.
[8] N. A. SIDDIQUI, M. MUZAMIL, T. JAMIL, ET G. HUSSAIN: 'Heat sources in wire arc additive manufacturing and their impact on macro-microstructural characteristics and mechanical properties – An overview', *Smart Mater. Manuf.*, vol. 3, p. 100059, 2025, doi: 10/g8p3zg.
[9] P. MOURGUE, V. ROBIN, P. GILLES, F. GOMMEZ, A. BROSSE, ET S. GALLÉE: '3D Simulation of a Peripheral Adapter J-Groove Attachment Weld in a Vessel Head', in *American Society of Mechanical Engineers, Pressure Vessels and Piping Division (Publication) PVP*, juill. 2014. doi: 10.1115/PVP2014-28151.
[10] E. COTTIER, P. ANGLADE, A. BROSSE, ET E. FEULVARCH: 'Fast 3D simulation of a single-pass steel girth weld', *Mech. Ind.*, sept. 2015, doi: 10.1051/meca/2015074.
[11] S. GALLÉE, F. GOMMEZ, N. SALLEZ, ET A. BROSSE: 'An experimental and numerical modelling for SMAW', in *Proceedings of ASME 2023*, in PVP. Atlanta, 2023.
[12] M. SCHÄNZEL, A. ILIN, ET V. PLOSHIKHIN: 'New approach for fast numerical prediction of residual stress and distortion of AM parts from steels with phase transformations', 2019, [En ligne] Disponible sur: https://api.semanticscholar.org/CorpusID:209421739
[13] C. CAMBON, S. ROUQUETTE, I. BENDAOUD, C. BORDREUIL, R. WIMPORY, ET F. SOULIÉ: 'Thermo-mechanical simulation of overlaid layers made with wire + arc additive manufacturing and GMAW-cold metal transfer', *Weld. World*, juill. 2020, doi: 10.1007/s40194-020-00951-x.
[14] F. W. C. FARIAS, J. DA CRUZ PAYÃO FILHO, ET V. H. P. MORAES E OLIVEIRA: 'Prediction of the interpass temperature of a wire arc additive manufactured wall: FEM simulations and artificial neural network', *Addit. Manuf.*, vol. 48, p. 102387, déc. 2021, doi: 10.1016/j.addma.2021.102387.
[15] NET, *European Network NET*, https://www.net-network.eu/.
[16] SYSWELD, manuel de référence version 2023, ESI, 2023.
[17] C. HENWOOD, M. BIBBY, J. GOLDAK, ET D. WATT: 'Coupled transient heat transfer–microstructure weld computations (Part B)', *Acta Metall.*, vol. 36, nº 11, p. 3037-3046, 1988.
[18] J. B. LEBLOND, G. MOTTET, ET J. C. DEVAUX: 'A theoretical and numerical approach to the plastic behaviour of steels during phase transformations–I. Derivation of general relations', *J. Mech. Phys. Solids*, vol. 34, nº 4, Art. nº 4, janv. 1986, doi: 10.1016/0022-5096(86)90009-8.

# EVALUATION OF FEM-BASED MACRO-SCALE AND MICRO-SCALE THERMAL SIMULATION FOR EFFICIENT PROCESS ADAPTATION IN DIRECTED ENERGY DEPOSITION ADDITIVE MANUFACTURING

A. M. PAKDEL SEFIDI*, V. MASHETTY*, M. BEN GHORBEL*, R. OSSENBRINK*, K. SCHRICKER*

**Chair of Joining and Welding Technology, Brandenburg University of Technology Cottbus-Senftenberg, 03046 Cottbus, Germany, fg-fuegetechnik@b-tu.de*

*DOI 10.3217/978-3-99161-089-2-034, license CC BY 4.0*
*https://creativecommons.org/licenses/by/4.0/deed.en*
*This CC license does not apply to third party material and content noted otherwise.*

ABSTRACT

Directed Energy Deposition (DED) involves complex thermal interactions that significantly influence microstructural properties, distortion and other final part properties. Accurate thermal modeling is essential to predict these effects and to further optimize processes. This study is motivated by the need for reliable simulation models to enable process optimization, in particular to adjust process parameters based on evolving thermal conditions. A computational framework requires efficient thermal predictions to enable adaptive control strategies, that optimize deposition parameters. This study presents a comparative analysis between two thermal modeling approaches in DED simulations: the macro-scale element clustering approach, as implemented in ANSYS DED Toolbox, and a micro-scale modeling approach based on high-resolution transient thermal simulations using the finite element method. The macro-scale simulation uses a computationally efficient approach where material is deposited in clusters and heat is applied using either a power-based or temperature-based method. While this method allows for reduced computational costs, it may lack fine-scale resolution of localized thermal gradients. On the other hand, the micro-scale FEM approach uses a mathematically defined heat source model with detailed mesh refinement and element activation, allowing for higher accuracy in capturing transient thermal effects but at the cost of increased computational requirements. While micro-scale FEM models provide accurate transient thermal analysis, their computational cost could limit their applicability for control and optimization tasks such as predictive path planning or optimized microstructures. The macro-scale simulation model offers a computationally efficient alternative, but its ability to capture relevant effects should be systematically evaluated. In this respect, the results provide a detailed insight into the relationship between computational efficiency, predictive accuracy and model applicability.

Keywords: Directed Energy Deposition (DED); Additive Manufacturing (AM); Thermal Simulation; Finite Element Method (FEM); Macro-Scale Simulation; Micro-Scale Simulation; ANSYS DED Toolbox; Wire Arc Additive Manufacturing (WAAM)

## INTRODUCTION

Additive manufacturing (AM) has evolved rapidly from its origins in prototyping to the fabrication of large-scale, high-performance metallic components, with Directed Energy Deposition (DED) playing an important role in producing complex structures for the aerospace, energy, and maritime sectors [1]. This transition has intensified the demand for robust and rapid thermal simulations capable of supporting process development and component quality. Reliable thermal modeling results in the prediction of temperature fields, microstructural transformations, and residual stress distributions, offering a critical foundation for optimizing process parameters while minimizing reliance on costly empirical testing [2]. Concurrently, the integration of data-driven methodologies and the broader Industry 4.0 framework has raised the role of simulation as a key factor of both process innovation and machine learning (ML) applications in AM [3]. Recent studies have demonstrated the feasibility of training ML algorithms on simulated datasets to accurately forecast melt pool dynamics in DED, thereby facilitating real-time monitoring and adaptive control strategies [4]. This intersection of accurate physics-based simulation and data-centric techniques highlights the demand for thermal models that balance precision with computational efficiency.

One strategy to address these requirements involves the development of macro-scale thermal simulation frameworks for the Directed Energy Deposition (DED) process. Rather than resolving fine-scale and detailed melt pool simulations. In conventional thermal simulations, the heat source is often modeled using profiles like Gaussian or Goldak shapes, which were originally developed for welding [5]. Macro-scale models focus on the melt pool as an effective moving heat source and simulate heat transfer within the part using continuous thermal conduction models. This abstraction enables part-scale simulations with significantly reduced computational demands, facilitating rapid iteration over process parameters with full thermal analysis [6]. A good example is the ANSYS Additive DED Toolbox, a commercial software suite capable of simulating temperature fields, distortions, and stress evolution at the component level without modeling heat source explicitly [7]. These tools implement element activation strategies, moving heat source algorithms, and layer-by-layer thermal cycles to emulate deposition processes efficiently. In this context, Stender et al. developed a finite element-based DED workflow (applied to laser-engineered net shaping) that captured residual stresses and thermal histories with high accuracy while maintaining computational feasibility [8]. The introduction of such macro-scale models has made it possible to integrate thermal simulations into iterative process development and real-time control systems. However, these models typically apply homogenized heat input and simplified boundary conditions to accelerate computation [6]. Consequently, it becomes essential to carefully assess the predictive reliability of macro-scale approaches to Understand their capabilities and

limitations is critical when using them for process optimization or as input for data-driven methods such as machine learning.

To assess the reliability of macro-scale thermal simulations, it is important to compare them against more detailed reference data. Micro-scale models, built with finer finite element meshes, can capture steep temperature changes and variations [2]. However, their computational demands limit practical deployment in optimization processes, ML projects and large-scale simulations. In contrast, experimental thermal measurements represent the empirical information of the process and serve as necessary validation benchmarks. In DED, infrared (IR) thermography is commonly employed to monitor the evolving temperature field on the component surface throughout the build. When properly calibrated, IR cameras provide time-resolved temperature data for specific regions or layers, revealing critical thermal phenomena such as cumulative heat buildup, cooling rates, and interlayer thermal cycling. For instance, Yang et al. used calibrated IR thermography to monitor the surface temperatures during Gas Metal Arc Welding (GMAW)-based WAAM, demonstrating how variations in inter-layer dwell time directly influence heat accumulation and, consequently, part integrity [9]. Similarly, Andrade et al. conducted in-situ thermal monitoring during WAAM fabrication of 316LSi stainless steel components, establishing correlations between thermal histories and the resulting microstructural and mechanical characteristics of the deposits [10].

These studies emphasize the role of experimental thermal data in assessing the credibility of thermal simulation outputs. Consequently, by comparing macro-scale simulation results against both precise micro-scale models and experimentally acquired thermal data, we gain a much more complete picture of how accurate and useful these simplified models really are. Such comparisons help for validation and understanding the limitations of computationally efficient frameworks and provide information about their appropriate integration into process design, optimization, and control strategies.

Within this framework, the present investigation focuses on a WAAM process utilizing 316L stainless steel, with the objective of evaluating the predictive performance of a macro-scale thermal simulation model against both experimental measurements and accurate micro-scale numerical benchmarks. The deposition process involves sequential layering of 316L material using a DED system. The temporal temperature fields are captured by IR thermography. A macro-scale thermal simulation, implemented using the ANSYS AM DED Toolbox, is applied to replicate the same deposition process. This simulation employs a moving heat source model with appropriate thermal boundary conditions to estimate temperature evolution across the build without explicit modeling of melt pool. To provide a high-resolution reference, a conventional micro-scale finite element model capable of resolving steep thermal gradients and melt pool geometry is presented. The resulting temperature–time profiles from the macro-scale model are then systematically compared to the IR thermographic data and the micro-scale simulation outputs at corresponding specific location. Key thermal metrics including peak temperature, cooling rate, and pointwise comparison serve as the basis for this comparative assessment. This methodological approach is intended to investigate the central question: To what extent can a computationally efficient macro-scale DED simulation capture the thermal histories relevant for process control and optimization, and where, if at all, do significant deviations from empirical or high-fidelity reference data emerge?

## SIMULATION

### MACRO SIMULATION - AM DED TOOLBOX

ANSYS workbench is used to simulate the temperature field resulting from the DED process. A rectangular cuboid measuring 25*25*150 $mm^3$ is used for DED simulation. The model is designed with ten layers; each layer consists of five individual deposition paths. The simulation is set up in ANSYS workbench using AM DED toolbox and coupled with MATLAB to run, export and analyse the thermal data. The CAD (Computer-Aided Design) model is meshed using a Cartesian approach for the part which allows anisotropic meshing. The finer mesh used a 1.2 mm element size with stretch factors of (1, 2, 1) in X, Y, and Z directions, respectively. The coarser mesh had a 5 mm element size and stretch factors of (1, 1, 0.5) The model can be seen in Fig. 1. Respectively the entire level including weld sequence and direction is shown in Fig. 2. Unlike models that explicitly simulate the melt pool, this approach employs a macro-scale heat input method, where heat is distributed over newly activated elements rather than being resolved at a sub-melt pool level. This method, implemented in the DED AM Toolbox, allows for efficient thermal predictions while lowers computational costs. Because of this, it is reasonable to select a mesh size that fits the characteristic dimensions of the heat source without excessive refinement. Furthermore, the chosen mesh size leads to thermal predictions that closely align with experimental data, demonstrating its effectiveness in capturing essential heat transfer behaviour on the component level.

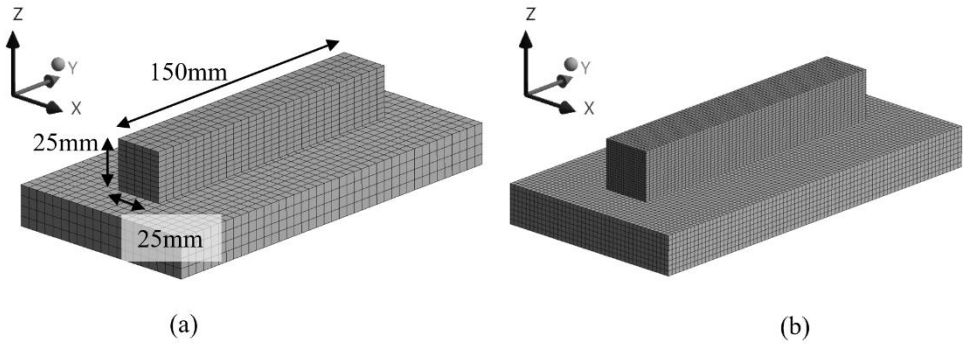



**Fig. 1** The DED macro simulation model in Ansys workbench (a) 5mm mesh (b) 1.2mm mesh

In DED AM Toolbox simulation in ANSYS, the DED process is governed by a simplified thermal transient analysis, where heat is applied sequentially as new material is deposited. There are two methods to generate heat on newly activated elements: Temperature-based and power-based. In temperature-based heat generation, the temperature of activated elements is raised to the pre-set melting temperature of the material. However, in the power-based heat

generation method, a volumetric heat generation rate (HGEN) is applied to newly activated elements which considers power and absorptivity to define the heat input. The energy input for each activated cluster is calculated by the equation 1:

$$\text{Heat generation rate} = \frac{P \cdot \eta}{d \cdot t_a} \tag{1}$$

where P is power, d is deposition rate, and $t_a$ is simulation loading applied time. η represents the process efficiency between nominal power and effective power used for deposition of the material. The heat is distributed over the volume of each cluster for a defined time span. A cluster is the set of elements which are activated at once. The simulation focuses on modelling the overall heat distribution and evolution in the part, rather than capturing detailed microstructural phenomena. For this reason, explicit modelling of the weld pool is not included. Instead, material deposition is represented by activating predefined element clusters at the material's melting temperature. Key physical phenomena such as phase transitions are incorporated via temperature-dependent material properties, included in engineering data. This approach enables efficient and accurate modelling of large-scale deposition processes without the high computational costs associated with micro-scale resolution.

Heat conduction is the primary mode of energy transfer, with additional losses occurring through convection and radiation at the exposed surfaces. Recent studies have shown that the convective heat transfer coefficient can vary significantly with temperature. For example, Tröger et al. (2024) demonstrated that during the WAAM process, the coefficient increases from around 5 W/(m²·K) at lower temperatures to values exceeding 300 W/(m²·K) as the surface becomes hotter [11]. On the other hand, Hagen et al. (2023) used a fixed value of 36 W/(m²·K) for 316L stainless steel, which provided good agreement with experimental data in their setup [12].

In Ansys DED Toolbox, it is possible to set a fixed value for the convection coefficient; however, the software also allows users to assign separate values for the base and the part, as well as for different stages of the process, the deposition phase and the subsequent cooling phase. A convection coefficient of 22 W/(m²·K) during the deposition phase and 32 W/(m²·K) during the cooling phase was set in this simulation for the base and the part. In the macro-scale model, the base plate was not explicitly included. Since the base plate acts as a major heat sink in the experiment and primarily influencing the cooling stage. The higher convection coefficient during cooling serves as an effective boundary condition to compensate for the missing thermal mass. This adjustment does not represent increased physical airflow, but restores the experimentally observed cooling rate. This combination led to the best agreement with our experimental results. Radiation losses were also included, using a calibrated emissivity value of 0.7 (see section 2.2). The material properties, including temperature-dependent thermal conductivity, specific heat capacity, and density, are integrated and can be seen in Fig. 5.

The ambient temperature is set to 23°C. The initial conditions define the starting temperature of the system, where the entire workpiece, including both the deposited material and the substrate, is set to room temperature (23°C) before deposition begins. The heat source

moves along the predefined deposition path where elements inside each cluster are activated sequentially.

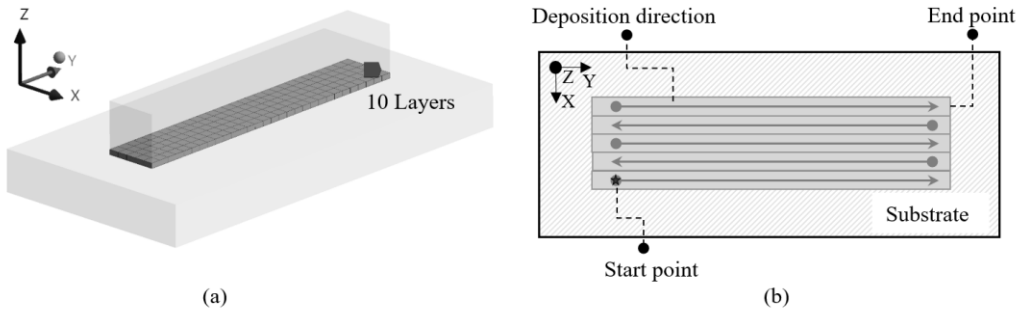



**Fig. 2** (a) Macro simulation model including 10 layers; (b) Weld sequence and direction

The cluster volume represents the volume of a single deposition path, which is set in the DED AM Toolbox in ANSYS. It can be as small as a single mesh or as large as the whole weld line. The smaller the size of the cluster volume, the slower the simulation. In this study, we use the cluster volume as large as a cube 5*5*2.5 $mm^3$ (W × L × H) for the simulation with a larger mesh size and 1.2*2.5*1.2 $mm^3$ (W × L × H) for the simulation with finer mesh size. The material deposition rate (d) is derived based on the deposition speed and deposition volume per unit time. It is calculated using:

$$d = v \cdot A \tag{2}$$

where the deposition speed (v) is the travel speed of the heat source, and the cross-sectional area (A) is determined by the layer height and width of the deposited material. Each layer has a height of 2.5 mm, and the print path begins at the edge of the cube, moving from left to right and right to left in a zigzag form like which is shown in Fig. 2b. After each deposition, the power is turned off during the interpass time which is 20s.

**Table 1** Simulation model parameters

| Build Conditions | Value |
|---|---|
| No. of layers | 10 |
| No. of welds per layer | 5 |
| Material | 316 L |
| Heating Method | Power based, Temperature based |
| Process temperature for temperature-based model | 1370 °C |
| Heat source power for power-based model | 2000 W |
| Process efficiency for power-based model | 0.7 |
| Gas Convection Coefficient for DED process | 22 W/(m²K) |
| Gas Convection Coefficient for cool-down phase | 32 W/(m²K) |
| Radiation emissivity | 0.7 |

The total simulation time is 5300 s, reflecting the real build process, including both material deposition and cooling. The deposition phase lasts 1750 s, during which material is deposited following the predefined path. After deposition is complete, the simulation continues for another 3700 s, allowing the part to cool naturally to room temperature. Build conditions are summarized in Table 1.

## MICRO SIMULATION – HEAT SOURCE MODELLED

### *Geometry Model*

Thermo-mechanical simulations were carried out using a finite element approach in ANSYS Workbench, with user-defined APDL commands to model the WAAM process. A three-dimensional model was constructed to represent the sequential material deposition, using the Element Birth and Death technique. The geometry included both the substrate and the deposited material, which were discretized using the multi-zone meshing method available in ANSYS. This approach enables local mesh refinement in regions of high thermal gradients specifically within the weld and heat-affected zones, while allowing a coarser mesh in the

substrate to reduce computational cost. Consequently, the element edge length was set between 1.5 mm and 2.0 mm in the critical deposition regions. To model convective heat losses, a surface heat transfer coefficient of 30 W/(m²·K) was applied to all exposed surfaces of the part. Additionally, a higher coefficient of 125 W/(m²·K) was assigned to the bottom surface of the substrate, accounting for enhanced thermal dissipation due to contact with the metallic support bench. Since the exact heat transfer conditions at the interface are not precisely known, the higher value was chosen based on calibration results that demonstrated good agreement between simulation and experimental temperature profiles. Radiation losses were modelled using emissivity values of see Section 2.12. It is important to note that the applied convection settings in the micro-scale simulation differ from those used in the macro-scale model. In the macro simulation, ANSYS allows separate convection coefficients to be defined for the base and part, as well as for the deposition and cooling phases. In the micro model, a single constant convection coefficient was implemented for the entire process, which may contribute to differences observed in temperature predictions between the two approaches.

Fig. 3 illustrates the CAD geometry and mesh discretization of the finite element model, which includes both the deposition region and the substrate. The coarse mesh configuration includes approximately 11,000 elements, with dimension of 2.5*3*2.5mm (W × L × H) with an average element size of 2.7 mm in the deposited material and between 5 mm and 8 mm (averaging 6.5 mm) in the substrate. The fine mesh model consists of approximately 46,700 elements, offering higher spatial resolution with dimension of 1.66*2*1.25mm (W × L × H) with an average element size of 1.7 mm in the deposited region and about 2.7 mm in the substrate.

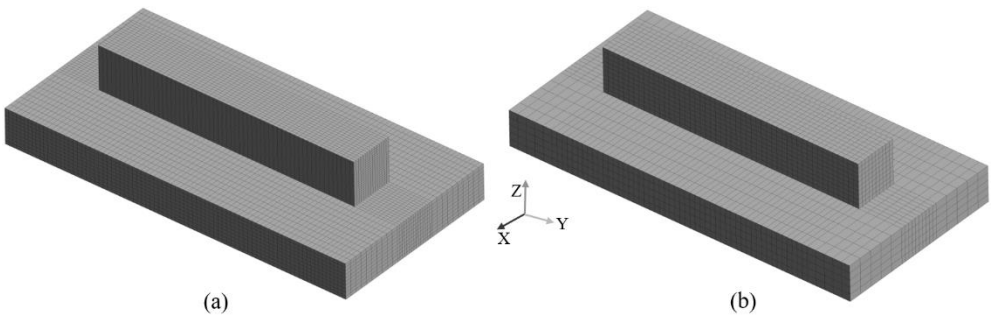



**Fig. 3** Thermo-physical micro DED simulation model with detailed view of the mesh using SOLID278 elements: (a) coarse mesh with 2.75 mm element size; (b) fine mesh with 1.75 mm element size Material Deposition Modelling

This simulation model utilizes the Element Birth and Death technique to simulate the progressive deposition of material through controlled element deactivation and activation. This approach allows for staged activation of elements at predefined time steps to represent the sequential addition of material, closely mirroring the actual deposition process.

At the beginning of the simulation, all elements representing the deposited material are initialized in a deactivated (killed) state, where their thermal conductivity is reduced to a negligible value. As the simulation progresses, elements are reactivated in groups based on their position along a defined deposition path and simulation time. The progressive activation of elements is governed by a locally defined coordinate system aligned along the build direction. At each simulation time step, elements within a defined range are identified based on local coordinate system, and the corresponding elements are activated to simulate material deposition. This local coordinate system is translated incrementally along the build path, enabling continuous step-wise activation in accordance with the deposition strategy.

Using this local coordinate system, elements are selected within the following spatial range:

- X-direction (bead width): from x = –2.5 to x = 2.5 mm
- Y-direction (build path): from y = -5 to y = 5 mm
- Z-direction (layer thickness): from z = 0 to z = 2.5 mm

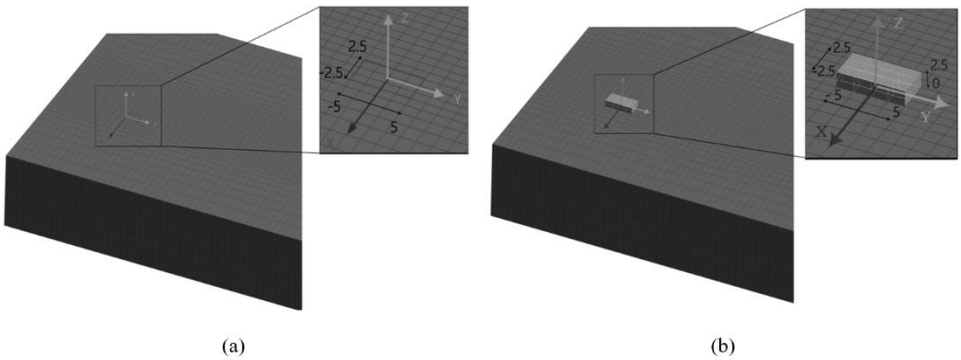



**Fig. 4** Visualization of Active/Inactive Elements (a) Inactive elements (b) Active elements

Here, the x-direction represents the width of the deposited bead, while the z-direction corresponds to its height. The size of the element group within the local coordinate frame can be adjusted. For example, increasing the x-range to –5 mm to 5 mm will include a larger number of elements per set. This local activation strategy provides a high-resolution representation of material addition and heat input, in contrast to the macro-scale model, where larger clusters of elements are activated simultaneously. While the macro model approximates the thermal field over broader regions for computational efficiency, the micro model resolves finer spatial and temporal gradients, offering increased accuracy at the cost of greater computational demand.

To accurately capture the spatial variation of the Gaussian heat source, especially its exponential decay profile, it is essential to include a sufficient number of nodes along the print (build) direction. A minimum of 3 to 4 elements is typically required within this direction to avoid oversimplifying the heat input.

### *Time Stepping and Solution Controls*

In the simulation setup, the initial time step, minimum time step, and maximum time step are all defined as 0.1 seconds. This time step setting (0.1 s) is viable for long simulations, such as 2000 seconds, balancing accuracy and computational efficiency. Reducing the time step increases computation time without necessarily improving results proportionally.

### *Heat Source Model*

In this study, a spherical Gaussian volumetric heat source is implemented to model the thermal input during the WAAM process. This approach provides a symmetric distribution of heat around the source center and is suitable for simulating the general thermal behaviour observed during deposition [13]. The spherical Gaussian model is defined by equal semi-axes in all three spatial directions and assumes uniform heat propagation around the heat influence zone. It offers a practical balance between model accuracy and computational efficiency for capturing transient thermal fields. The volumetric heat input q is expressed as:

$$q(x, y, z) = \frac{(2 \cdot Q)}{(\sqrt{\pi^3} \cdot r_0^3)} \cdot \exp\left[ - \frac{(x^2 + y^2 + z^2)}{r_0^2} \right] \tag{3}$$

$$Q = U \cdot I \cdot \eta \tag{4}$$

whereas Q is the total power input based on welding voltage U, welding current I, and thermal efficiency η, which accounts for the fraction of electrical power converted into thermal energy ($0 < \eta \leq 1$), $r_0$ is the effective radius of the heat source. In this study the radius of the Heat Source is 3mm and the efficiency of the Heat source is 0.8.

## MATERIAL PROPERTIES

In this study, we utilized existing material properties available in the ANSYS Workbench toolbox for the DED simulation. The selected material parameters include density, specific heat capacity, thermal conductivity, and the heat transfer coefficient as temperature-dependent material properties. These properties were defined using pre-existing datasets in the ANSYS Engineering Data module for 316L stainless steel based on Kim et al. [14]. The density, thermal conductivity, and specific heat capacity as a function of temperature, allocated to both the part and the base plate, are shown in Fig. 5. According to ANSYS's official guidance, if the calculated temperature at any point exceeds the highest temperature defined in the material dataset, the software does not extrapolate further; instead, it continues to use the last defined value as constant for all higher temperatures.

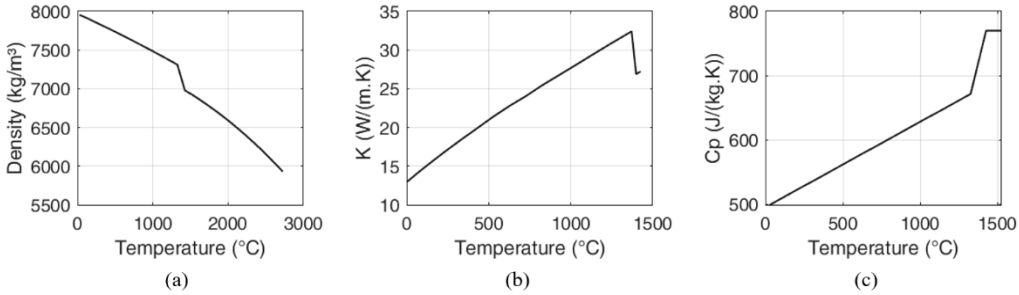



**Fig. 5** Material properties as a function of temperature: (a) Density (kg/m³); (b) Isotropic thermal conductivity (W/(m · K)); (c) Specific heat at constant pressure (J/(kg · K)) [14]

## CALIBRATION OF EMISSIVITY AND EXPERIMENTAL SETUP

### IR THERMOGRAPHY AND EMISSIVITY IN A DED

During WAAM process, the thermal environment is highly dynamic. Temperatures range from the molten pool to much cooler surrounding material, and the surface condition evolves rapidly including developing oxides, discoloration, or soot deposits. While infrared thermography is widely used method for capturing in-situ temperature fields, its accuracy depends critically on knowing the true emissivity of the observed surface. The challenge, however, is that emissivity is neither spatially nor temporally constant. It varies with temperature, oxidation state, and even surface geometry or roughness. During WAAM, different layers and regions of the part can exhibit different emissivity values at the same time.

In practice, most IR systems require a fixed emissivity input to convert radiation data into temperature values. When this fixed value doesn't match the actual surface emissivity at a given moment, the result is an under- or over-estimation of temperature. Liu et al. (2013) demonstrated that emissivity in steel changes substantially in high-temperature environments, with oxidized surfaces showing much higher emissivity than clean or polished ones. During WAAM, recently deposited layers might exhibit low emissivity due to their reflective, molten state (typically $\varepsilon \approx 0.3–0.4$), while older, cooled layers can develop oxide films that increase emissivity well above 0.6 [15]. Similar results are shown by Hensel et al. (2024) and noted that this restriction can cause temperature fields to appear flattened or inconsistent, particularly when emissivity changes rapidly between solid and molten zones [16]. One common method is calibrating the IR camera against thermocouple readings. For example, Kindermann et al. (2023) performed WAAM thermal monitoring (in their case on Inconel 718) by embedding thermocouples in the build and adjusting the camera's emissivity until the IR-measured temperature matched the thermocouple data. They placed three K-type thermocouples at different heights within a wall and tuned the emissivity so that the IR camera's temperature readings agreed with the thermocouple measurements. This calibration

yielded an emissivity of $\varepsilon = 0.7$, which was then used for all subsequent IR measurements [17]. similarly, Farias et al. (2021) showed thermal cycles in a steel WAAM wall using an IR camera and set the emissivity to $\varepsilon \approx 0.73$ [18]. However recent DED-focused studies indicate that emissivity in the molten and near-melting temperature of 316L stainless steel is noticeably lower. In a detailed wire-laser DED investigation, Diosdado-De la Peña et al. (2025) combined infrared thermography with finite-element modelling and explicitly accounted for temperature-dependent emissivity effects [19]. Their analysis employed an emissivity of $\varepsilon = 0.21$ for the molten pool, while higher values were assigned to cooler, solidified regions. The study demonstrated that assuming higher emissivity values in the molten region leads to underestimation of peak temperatures and melt pool dimensions, supporting the use of emissivity values in the range of 0.21–0.3 for temperatures above ~1000 °C and approaching the melting point of 316L. Based on these observations, a hybrid emissivity approach is adopted in the present work. A calibrated emissivity of $\varepsilon = 0.7$ is applied in the low-to-moderate temperature ranges. At temperatures exceeding 1000 °C, emissivity values reported in the DED literature are considered.

## THERMOCOUPLE-BASED EMISSIVITY CALIBRATION

In this study, we used a setup combining a reference thermocouple and the infrared camera which can be seen in Fig. 6a to calibrate the emissivity. A flat 316L plate was heated to approximately 600 °C using an oxy-fuel flame. A K-type thermocouple was attached to the surface to record the actual temperature, while the infrared camera was positioned at a distance of 100 cm. The camera's emissivity setting was then gradually adjusted until its temperature readings matched the thermocouple values during the heating and subsequent cooling phases. Throughout this process, both values were monitored in real-time. We defined an deviation margin of ±2 K between the two readings; if the difference exceeded this, the emissivity setting was further refined. Through this procedure, we arrived at a final emissivity value of 0.7, which remained consistent across the relevant temperature range. This value aligns well with emissivity ranges reported in the literature for stainless steel surfaces at elevated temperatures.

## EXPERIMENTAL SETUP AND VALIDATION

To support the thermal simulation study, a physical WAAM sample was produced under repeatable process conditions. The goal was to replicate a representative deposition scenario that would allow comparison with the simulation models. The manufactured sample consists of ten layers, each composed of five parallel weld beads. The deposition sequence and movement path were programmed manually for the robot system. A solid stainless steel base plate (316L) with dimensions of 200 mm × 100 mm × 20 mm (L × W × H) was used as the substrate. A defined interpass time of 20 seconds was applied between each bead. This approach ensures reproducible thermal cycling conditions throughout the build. The deposition process was carried out in a WAAM cell. This included a KUKA KR30 industrial

robot paired with a Fronius TPS 400i power source operating in CMT (Cold Metal Transfer) mode. The filler material was 1.4430 (316LSi) stainless steel welding wire with a diameter of 1.2 mm. Shielding gas was supplied using M12 C2 (an argon-based mixture with 2 % $CO_2$) at a constant flow rate of 15 l/min. The contact-tip-to-workpiece distance (CTWD) was maintained within a narrow range of 12–14 mm. Fig. 6b illustrates the setup for sample fabrication, including the robot, torch, and camera arrangement. All relevant process parameters used during the experiment are listed in Table 2.

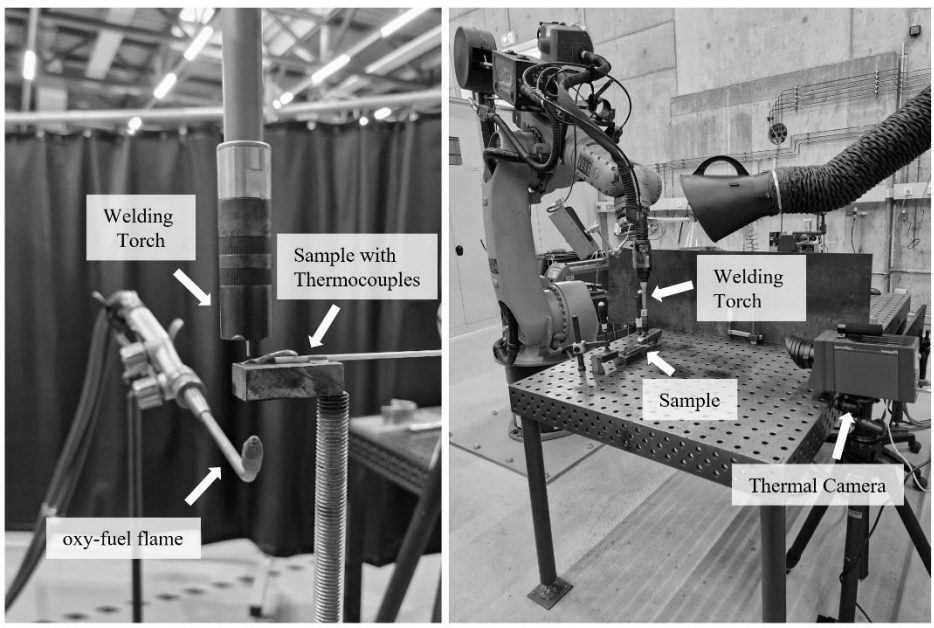



**Fig. 6** Experimental setup for (a) Emissivity Calibration; (b) sample manufacturing

The Cold Metal Transfer (CMT) process was selected from the available characteristic curves provided by the Fronius TPS 400i system. The welding parameters used in the experiment are summarized in Table 2.

**Table 2** The welding parameters

| Wire Feed Speed, m/min | Current, A | Voltage, V | Welding speed, mm/s | Hatch Distance, mm |
|---|---|---|---|---|
| 5.5 | 151 | 12.8 | 10 | 4 |

The Fronius TPS 400i system applies continuous adaptive control during the welding process. This includes real-time adjustments of current, voltage, and wire feed rate to stabilize

the arc. Prior to deposition, the substrate plate was cleaned using acetone to remove surface contaminants. After cleaning, the plate was firmly clamped onto the welding table.

An InfraTec ImageIR 8800 thermal camera, equipped with a High Dynamic Range (HDR) calibration range of 30-2000°C, was used to capture the thermal distribution for validating the simulation results. The emissivity value is set to 0.7 (see section 2.1). The HDR function in this camera extends its measurable temperature range by utilizing a fast-rotating filter wheel synchronized with the detector. This allows the camera to switch between multiple calibration settings at up to 350 Hz, combining different captured images into a single high-contrast image. The HDR function is particularly useful for monitoring high-temperature DED processes, as it enables simultaneous visualization of hot melt pool regions and cooler surrounding areas without loss of detail. This results in accurate tracking of thermal gradients, leading to a more reliable comparison between measured and simulated temperature distributions.

## METHODOLOGY

### DYNAMIC ERROR INDEX (DEI) FOR EVALUATING THERMAL DYNAMICS

DED processes are characterized by rapid, cyclic thermal loading, as successive layers of material are deposited and subjected to intense localized heating and subsequent cooling. Accurately capturing these transient thermal dynamics is important, because thermal gradients and cooling rates have a direct influence on microstructural evolution and induce residual stresses within the material. Conventional scalar error metrics like root-mean-square error (RMSE) or deviations in peak temperature are often insufficient for validation. A simulation may replicate the correct thermal peaks at the same time fails to accurately model the temporal effect of the heating and cooling phases. To address this limitation, it is useful to employ dynamic error measurement that quantifies differences in the rate of temperature change. These metrics, commonly referred to as dynamic error indices, that evaluates the time-derivative of the temperature signal, i.e., the heating and cooling rates rather than static values alone. The emphasis on dynamic behaviour not only ensures that a simulation aligns with thermal magnitudes, but with the complete thermal trajectory.

In this work, we introduce the Dynamic Error Index (DEI) as a measure to assess the temporal accuracy of simulated thermal histories. Because the rates at which material heats and cools play a critical role in determining phase transformations, grain structures, and residual stress patterns, incorporating temperature derivatives into validation metrics is useful.

Although macro-scale thermal models are often successful in reproducing steady-state or peak temperature values, they might fail in simulating the transient thermal behaviour. The DEI addresses this shortcoming by measuring the differences between simulated and experimental temperature derivatives, thereby providing a more sensitive and informative measure of the accuracy. This is critical as additive manufacturing systems are progressing in the sector of real-time control and machine learning-based optimization, where predictive models must accurately replicate not only thermal amplitudes but also the precise temporal

structure of temperature profiles. Building on the methodology proposed by Lázaro et al. [20], who utilized the mean absolute error of derivative curves to assess the accuracy of kinetic models in polymer decomposition, we adapt a similar framework for evaluating temperature-time histories in DED processes. In this context, we define the DEI as follows:

$$DEI = \frac{1}{N} \cdot \sum_{i=1}^{N} \left| \frac{dT_{sim}}{dt}(t_i) - \frac{dT_{\exp}}{dt}(t_i) \right| \tag{5}$$

where:

$T_{sim}$ and $T_{exp}$ are the simulated and experimental temperature–time curves, N is number of time steps, and $t_i$ is each time step.

In selecting meaningful threshold values for interpreting the DEI, we considered the sensitivity of DED process to variations in heating and cooling rates. Numerous studies have shown that even small differences in thermal kinetics in the scale of a few degrees per second can significantly result in change of the microstructure, phase composition, and mechanical properties of the DED manufactured component [21]. The DEI itself measures the difference between two thermal histories, however its thresholds are motivated by experimental studies like that of Wright and Zajac (2021), who showed that even small variations in cooling rate in the range of a few K/s can lead to noticeable differences in microstructure and mechanical properties in steels [22].

## PEAK TEMPERATURE ERROR

To show local differences between simulated and experimental results we use the Peak Temperature Error (PTE). These measures help to analyze the maximum temperature reached. The PTE is defined as the difference between the maximum temperature values of the simulated and experimental curves:

$$PTE = T_{sim}^{\max} - T_{\exp}^{\max} \tag{6}$$

Peak temperature is critical as it directly influences melt pool formation and thermal gradients. It also effects directly on solidification behavior, heat-affected zones, local overheating particularly at part edges and intersections, which may cause excessive melting, vaporization, and geometric distortion. The PTE is calculated over the first five peaks, as later peaks tend to flatten, making them less sensitive for assessing simulation accuracy.

## CLUSTER VOLUME IN MACRO THERMAL SIMULATION

One of the key aspects investigated in this study is the effect of cluster volume on simulation accuracy and runtime. In the context of macro DED thermal simulation, cluster volumes refer to discrete blocks of material that are activated sequentially to approximate the heat input during the deposition process. Each cluster represents a portion of the deposited geometry and

the heat is applied to it when activated. The size of a cluster volume determines the dimension of heat input. Here the smaller clusters simulate the process more accurately but require more computation time, while larger clusters simplify the deposition sequence and reduce the simulation speed.

Two configurations are investigated in this study. The bigger (375 $mm^3$) cluster volumes and the smaller (62.5 $mm^3$) cluster volume. The bigger cluster volume with only five clusters per weld line. Each cluster represents roughly five times the volume of a single deposition segment. This means that instead of activating smaller regions sequentially, an entire deposition path is treated as five thermal depositions. The advantage of this approach is clear in terms of computational performance. The second configuration is the smaller cluster volume, which the entire weld line is divided into 30 clusters. Both configurations are illustrated in Fig. 7 schematically.

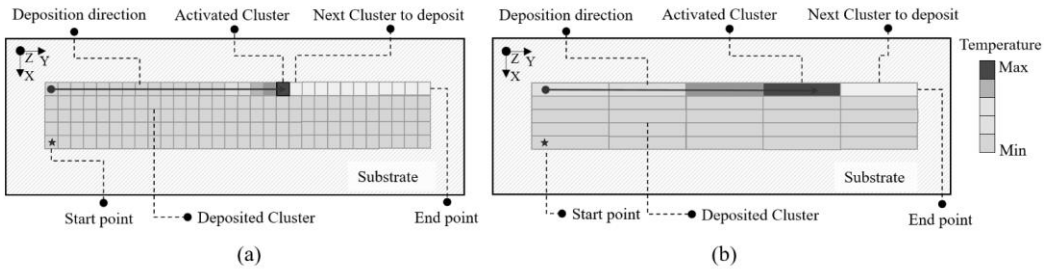



**Fig. 7** Schematic illustration of clustering configurations (a) Small cluster volumes (62.5 $mm^3$) (b) big cluster volume (375 $mm^3$)

## COMPARISON OF MACRO- AND MICRO-SCALE THERMAL SIMULATIONS WITH EXPERIMENTAL VALIDATION

To perform a comparative evaluation of macro-scale and micro-scale thermal simulations, both simulations are benchmarked against experimental infrared thermography. The macro-scale simulations were carried out using the ANSYS DED Toolbox, focusing on parameters such as mesh resolution, cluster volume, and heat input definition (power-based vs. temperature-based). In contrast, the micro-scale simulation was implemented in ANSYS Mechanical APDL, using a volumetric moving spherical Gaussian heat source to capture localized thermal behaviour. The temporal data for temperature is exported for a selected point as can be seen in Fig. 8 for both micro and macro simulations. P1 is the center point that is located on the top of the first layer and on the front face of the part. To assess the accuracy of micro- and macro-simulation approach, both temperature-time curves were compared directly with experimental temperature data recorded at 10 Hz during the WAAM process. The data is extracted and zoomed to the Region of interest to reduce the time of calculation. Two key metrics are used: The DEI (see section 3.1), which reflects how well the simulation captures

the rate of temperature change, and the PTE (see section 3.2), which measures how closely simulated thermal peaks align with those observed experimentally. The aim is not only to show how two simulation strategies compare to real measurements, but also how they differ from each other in terms of accuracy, computational cost, and practical usability for different kinds of analysis.

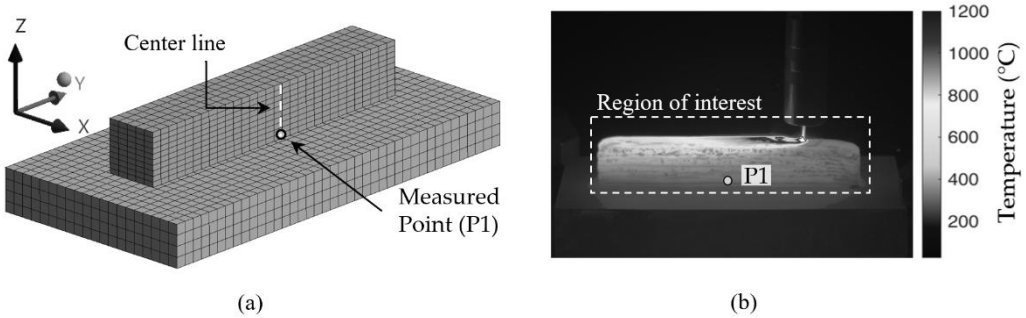



**Fig. 8** Location of the selected point on (a) simulation (b) experimental thermography image

## RESULT AND DISCUSSION

### OVERVIEW OF MACRO AND MICRO-SCALE SIMULATIONS

Fig. 9 shows a comparative plot of performed simulations. Simulation configurations are collected in Table 3. There are three power base simulations with rough (5 mm) and finer (1.2 mm) mesh size and also small (62.5 $mm^3$) and bigger (375 $mm^3$) cluster volumes. The simulation with a temperature-based heat source is also using rough mesh and small cluster volume. Using a bigger cluster volume results in reducing simulation time dramatically, from nearly 83 minutes to 16 minutes (see Table 3), making it especially attractive for applications like trajectory optimization, where many path variations must be tested rapidly. Both configurations are illustrated in Fig. 7 schematically. However, this time-saving strategy comes with disadvantages in temperature profile prediction. Fig. 11 shows that simulations using larger cluster volumes tend to under predict temperatures, during cooling phases. This is expected, as activating a large volume all at once spreads the heat input over a broader region, smoothing out localized thermal peaks. Still, it's worth noting that the general thermal pattern including peaks and timing of peaks are preserved, indicating that even with reduced resolution, the simulation captures the overall behavior quite well. For higher-level control strategies or path planning tasks, this level of accuracy may be sufficient.

The comparison also includes a temperature-based simulation, where newly activated elements are raised directly to the material's melting point. While this method caps the peak

temperature to the process temperature and therefore can't capture overshoots the overall temperature evolution and fluctuations align closely with the power-based models.

Interestingly, even the coarser 5 mm mesh proves capable of reproducing key features of the temperature curve when used with appropriately sized clusters. This is an important observation: for simulations where fine details of the melt pool aren't the focus, and the goal is to predict thermal trends, high-resolution meshing might not be necessary. In fact, finding a balance between computational cost and predictive accuracy may be more about choosing the right cluster size than the finest possible mesh. As can be observed the finer mesh did slightly result in more accurate peak temperature predictions however the improvement over the coarse mesh case is minimal and negligible.

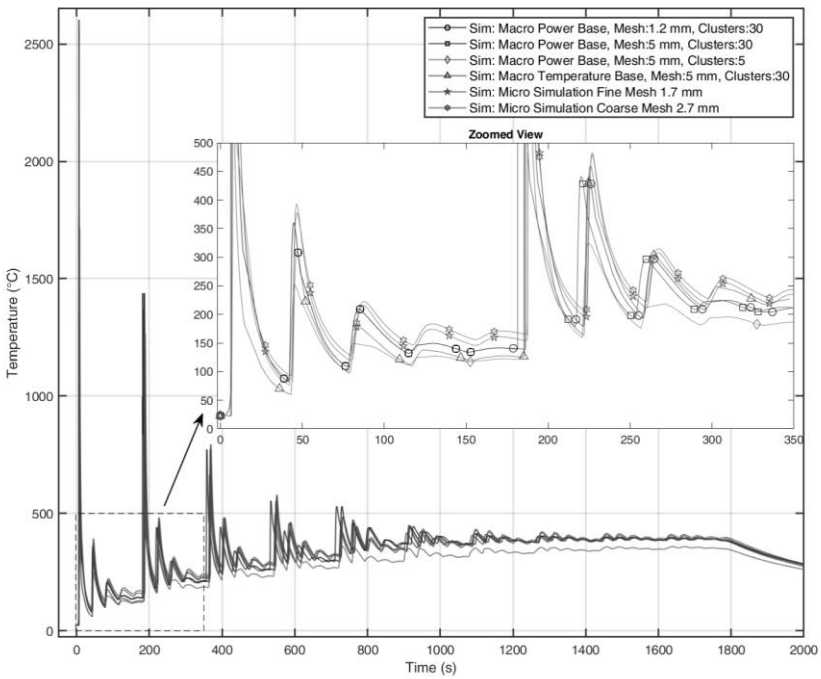



**Fig. 9** Temporal comparison of performed micro and macro simulations

## COMPARISON MACRO SIMULATIONS WITH EXPERIMENTAL DATA

### *Case 1: Macro Power-Based, Coarse Mesh (5 mm), 30 Clusters*

In this case, the simulation results are compared to experimental data obtained from infrared thermography. At first glance, there's a large difference at the first peak. The simulation

predicts a temperature of around 2508 °C, while the experimental reading levels is near 1200 °C. However, this underestimation in the experimental curve is expected and can be explained by the limitations of the measurement setup. One reason to consider is that the IR camera used in this study is set to capture data at 10 Hz, which is a reasonable frame rate for thermal monitoring during WAAM. However, during rapid heating procedures, especially right after an arc burst temperature rises extremely quickly. As a result, the true thermal peak can be likely missed between frames. This adds to the deviation we see between simulation and experiment at the peaks. With this in mind, the comparison between simulation and experiment shows good agreement within the calibrated range. The simulated thermal cycles follow the experimental trend well. The timing of heating and cooling, the spacing of the peaks, and the long-term decay behavior all match closely. In the macro-scale results, a slight time shift of the later peaks was observed. This effect arises from the spatial mismatch between the experimental measurement point and the corresponding node in the coarse macro mesh. With larger element sizes and cluster volumes, the nearest simulation node can be several millimeters away from the exact thermography point, which leads to an offset in the peak positions.

The DEI curve on lower panel in Fig. 10 to Fig. 15 shows the absolute rate difference (|dT/dt|) between simulation and experiment. Spikes in this curve mostly correspond to the mismatches around thermal peaks, which as explained, are likely related to the camera resolution and emissivity issue rather than simulation error. Outside these peaks, the rate difference remains low, confirming that the simulation correctly tracks the dynamic thermal response of the process. This result suggests that even with a relatively coarse mesh, the macro-scale model performs well in capturing the essential thermal behavior, and that experimental limitations must always be considered when interpreting peak mismatches.

Two important aspects should be considered in these comparisons. First, there is a delay between the simulated and experimental temperature peaks, particularly in the later stages of the process in some cases. This misalignment is due to the coarse mesh resolution, which limits the ability to select a simulation point that precisely matches the experimental measurement location. As the elements are large, the selected point may lie offset from the actual experimental measurement point, leading to small shifts in peak timing. In the lower panel showing the DEI, many red segments appear as flattened lines. DEI values greater than 10 K/s are considered poor agreement, and are therefore visually capped to preserve the resolution and readability of more relevant regions where DEI is below 10. DEI values less than 5 K/s is shown in green, and DEI values in the 5-10 K/s range is shown in blue.

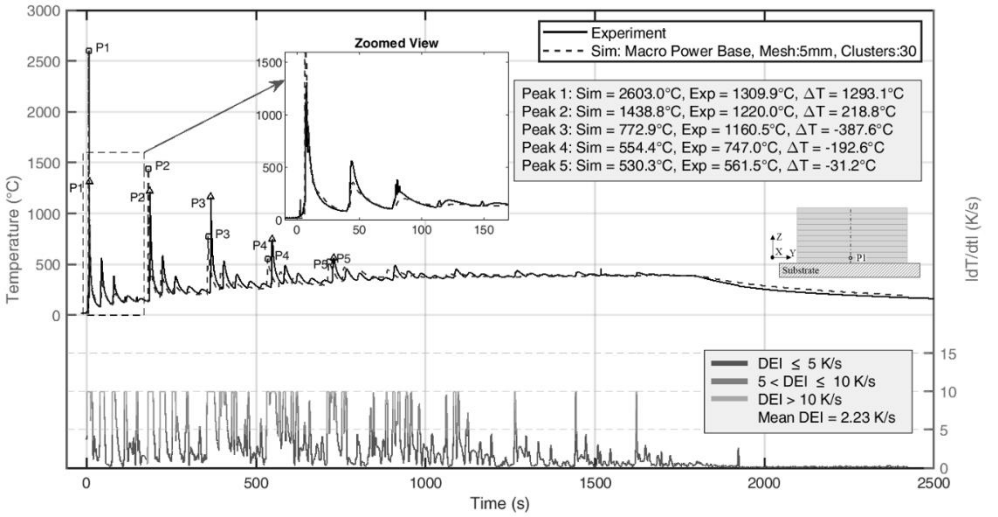



**Fig. 10** Result comparison between experimental data and macro simulation: Power-based, 5mm Mesh (coarse mesh), 30 clusters per weld line (small cluster volume)

*Case 2: Macro Power-Based, Coarse Mesh (5 mm), 5 Clusters (large cluster volume)*

In this case, the simulation was performed using only 5 clusters per weld line, which means each cluster covers a volume about five times larger than that of a typical single deposition segment. Rather than simulating the path of the moving heat source in fine steps, the entire deposition line is activated in larger portions. This extremely reduces computational time by over 80% compared to the standard 30-cluster setup. As shown in Fig. 11, the simulated temperature curve is shifted downward compared to the experimental data. While the number and timing of peaks are captured fairly correct, the peak values themselves are underestimated slightly compared to finer cluster volumes, especially beyond the second peak. This is expected as larger clusters distribute the heat over a bigger volume all at once, which smooths out sharp thermal gradients and reduces the intensity of local heating. However, the overall thermal behavior is preserved. The DEI in this case is higher than in the 30-cluster version (3.2 K/s vs. 2.27 K/s).

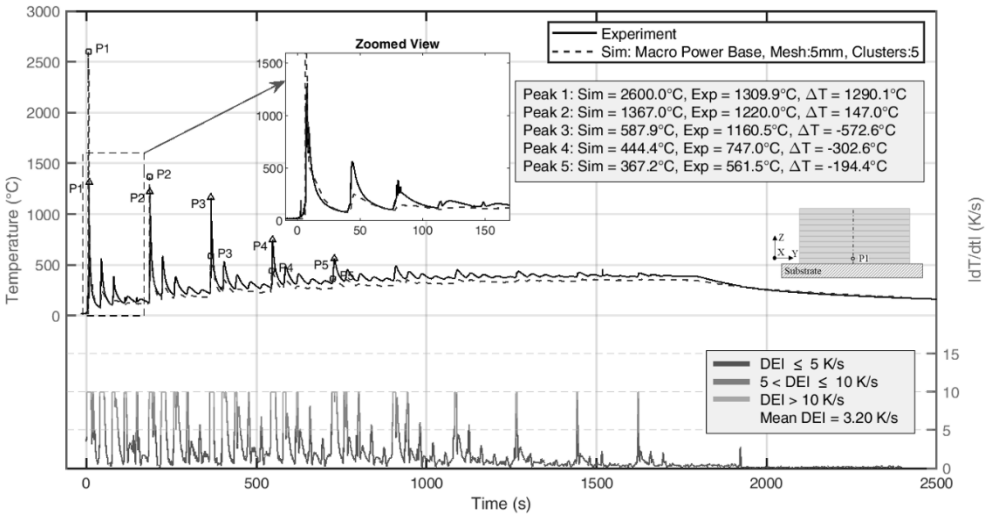



**Fig. 11** Result comparison between experimental data and macro simulation: Power-based, 5mm Mesh (Coarse mesh), 5 clusters per weld line (Coarse cluster volume)

*Case 3: Macro Temperature-Based, Coarse Mesh (5 mm), 30 Clusters (small cluster volume)*

This simulation was performed using the temperature-based heat input model. In this model, each cluster is simply brought up to the material's preset melting temperature (1370°C) the moment it's activated. What's immediately noticeable is that this case result in lower mean DEI of 2.05 K/s, which tells us the simulation tracks the rate of heating and cooling quite well. The alignment of temperature-time curve with experimental data is actually very good (see Fig. 12), particularly in terms of how the temperature rises and falls through each layer cycle. The fluctuations are captured clearly, and the timing of thermal cycles matches nicely.

As mentioned, the method also puts a cap on the peak temperatures, since it forces each cluster to the melting point and no higher. While the overall shape of the curve looks realistic, we don't see the same high peak temperatures that are common in real processes, especially at the start of the process. So in that sense, we lose the ability to model thermal overshoots or localized overheating, which can be important depending on the application. The simulation run time is exactly the same as the power-based model with the same mesh and cluster setup, about 1 hour and 23 minutes.

If the focus of the study is mainly on temperature trends, layer-wise thermal cycles, or relative comparisons, this temperature-based model is probably good enough. But if the focus of the investigation is on cooling rates, or phase changes, then it is logical to use the power-based approach, since it gives a better prediction on actual thermal changes.

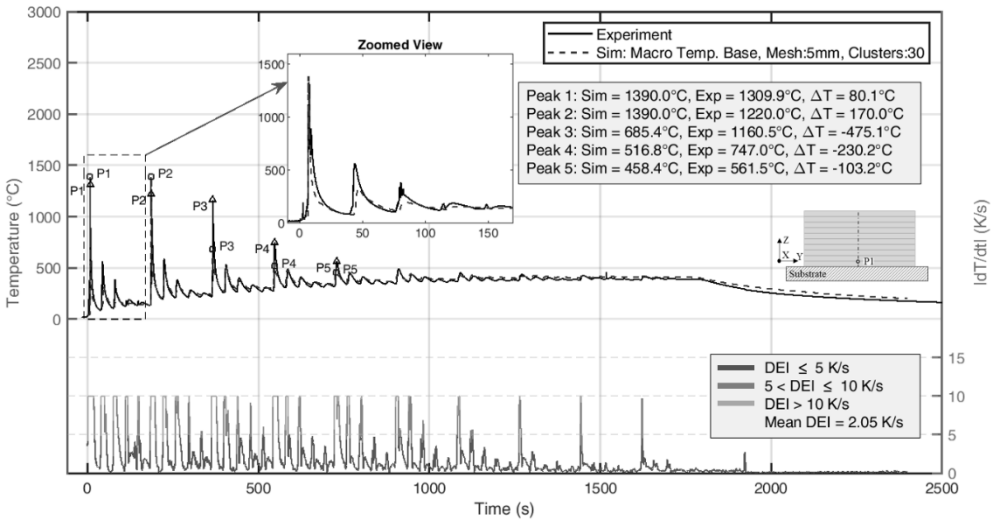



**Fig. 12** Result comparison between experimental data and macro simulation: Temperature-based, 5mm Mesh (coarse mesh), 30 clusters per weld line (small cluster volume)

*Case 4: Macro Power-Based, Fine Mesh (1.2 mm), 30 Clusters (small cluster volume)*

This case uses a fine mesh 1.2 mm for the part and 2.5 mm for the base, while keeping the number of clusters at 30, like in previous runs. This results in the best overall match with the experimental data. The DEI drops to 1.98 K/s, which means the model is closely following the way temperature changes over time. The simulation aligns well with the experiment, especially in the later stages (see Fig. 13). The peaks are located in time, and the changes are quite well captured. Peak 5 which in earlier cases had a bigger offset, now comes closer, with a difference of just about 32.7 °C. So in terms of overall trend and accuracy, this model performs the best. The simulation took over 19 hours to run, which is ten times longer than the coarse-mesh cases. That's a serious computational cost, and it means this approach isn't very practical if you need to run many simulations, like in optimization studies. For cases where thermal history needs to be as realistic as possible, the fine mesh does its job. Still, there's room to improve performance. For example, using multi-zone meshing for substrate, where high resolution is used only around the contact to the part and coarse elements are used elsewhere, could reduce runtime while keeping the accuracy where it matters.

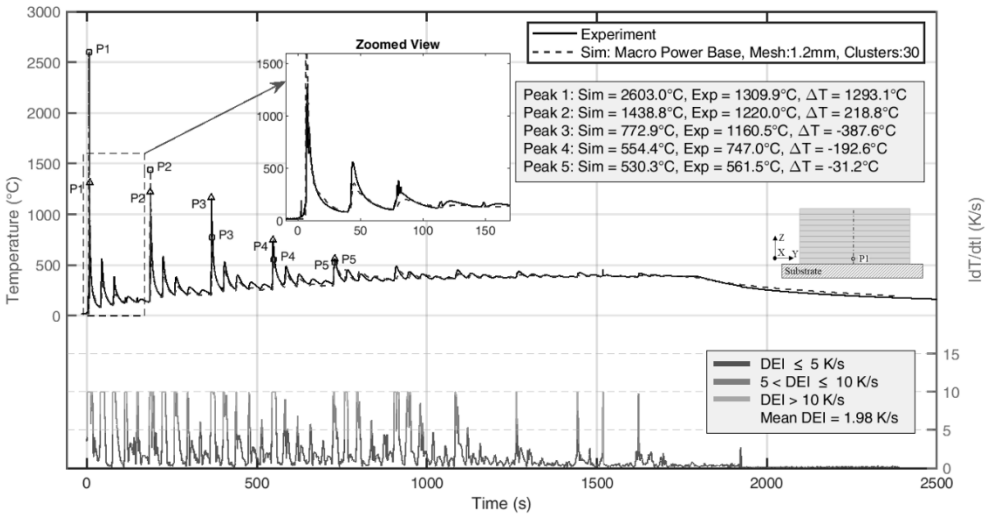



**Fig. 13** Result comparison between experimental data and macro simulation: Power-based, fine mesh 1.2mm, 30 clusters per weld line (small cluster volume)

## COMPARISON OF MICRO SIMULATIONS WITH EXPERIMENTAL DATA

*Case 1: Micro Power-Based, Fine Mesh (1.2 mm), spherical Gaussian heat source*

Fig. 14 shows the temperature history, comparing experimental data with the micro-scale simulation using a fine mesh resolution of 1.7 mm in average. The simulation captures the transient temperature evolution in good agreement with the experiment. The DEI shown in the lower plot, remains low throughout the process, with the majority of values below 5 K/s (green), fewer in the 5 - 10 K/s range (blue), and some instances exceeding 10 K/s (red) which are mostly related to peaks. The mean DEI is 1.91 K/s, which is lower than the macro-scale models, indicating a more accurate temporal evolution. The enlargement on the initial segment highlights the simulation's ability to follow the sharp gradients at early peaks. The PTE is also evaluated for each peak and summarized in the inset. As discussed previously, the absolute differences are influenced by factors such as emissivity settings, rather than simple over- or underestimation by the model (see section 4.2.1). Compared to the macro-scale simulations, the micro-model with fine mesh shows an improvement in both peak alignment and temporal accuracy.

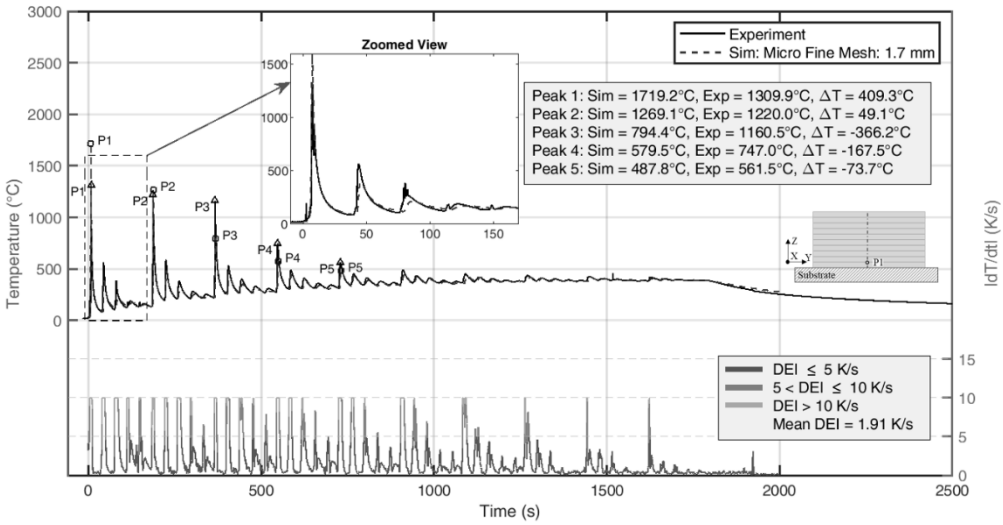



**Fig. 14** Result comparison between experimental data and micro simulation: 1.7mm Mesh (fine mesh), Gaussian heat source

*Case 2: Micro Power-Based, Coarse Mesh (2.7 mm), spherical Gaussian heat*

Fig. 15 presents the thermal history for the micro-scale simulation using a coarser mesh resolution of 2.7 mm. The overall temperature evolution closely follows the experimental trend, with six distinct peaks. The temporal agreement remains strong, as evidenced by the DEI plot at the bottom, where most values remain below 5 K/s, with some moderate deviations and a few high-error events during rapid thermal cycles. The mean DEI is 1.95 K/s, nearly identical to the fine mesh case, suggesting that coarsening the mesh does not significantly weaken the temporal accuracy of the simulation. A zoomed view of the early stage confirms that the simulation reproduces the steep gradients well, however with less detail in the peak curvature. The PTE remains consistent with earlier observations, with lower accuracy at early peaks, while later peaks align more closely. Compared to the fine mesh result, this setup offers a comparable DEI but with a reduced computational cost, making it a potentially more efficient option where precise spatial gradients are less needed.

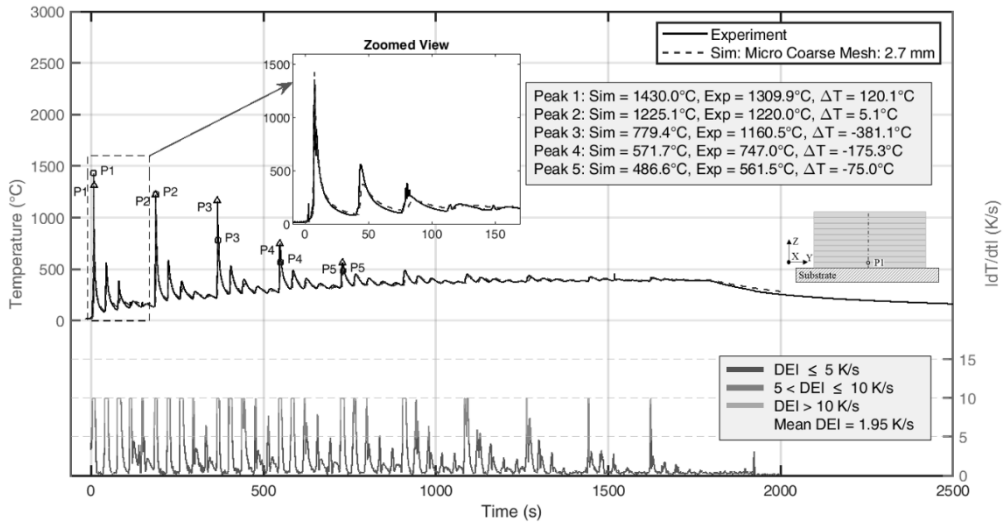



**Fig. 15** Result comparison between experimental data and micro simulation: 2.7mm Mesh (coarse mesh), Gaussian heat source

## DISCUSSION AND IMPLICATIONS

Table 3 provides an overview of all simulation cases. It compares macro and micro models with respect to mesh size, heat source type, number of elements, cluster volume, simulation time, and resulting DEI values. Among the macro simulations, the finest mesh setup (1.2 - 2.5 mm) with a power-based heat source achieves a low DEI of 1.98 K/s, but at the cost of a significantly long simulation run time of over 19 hours. In contrast, using a coarser mesh (5 - 5 mm) considerably reduces the runtime to 1.5 hours, but increases the DEI to 2.23 K/s, showing the trade-off between efficiency and accuracy. The same coarse mesh, when applied with a higher cluster volume (375 $mm^3$) and fewer clusters per weld line, further reduces runtime to just 16 minutes, but leads to the highest DEI of 3.2 K/s, indicating clear accuracy reduction of the simplified model. The macro model with temperature-based input maintains a runtime similar to the power-based version (1 hour 23 min) but with a slightly improved DEI of 2.05 K/s, suggesting better temporal agreement with existing experimental results. The best DEI of 1.95 K/s for the coarse mesh and 1.91 K/s for the fine mesh belong to two micro simulations, both using spherical Gaussian heat source while maintaining higher computational cost. The coarse mesh model runs in 3:40 hours, and the fine one in 9:57 hours. They offer a more advantageous balance between accuracy and runtime than the high-resolution macro simulation. The results clearly show that while macro models are performing well for capturing the heat distribution, micro-models provide better accuracy in capturing local thermal changes, especially when carefully meshed and fed with realistic boundary conditions.

**Table 3** Summary of simulation parameters and results

| Sim. type | Heat Source type | Mesh size part-base mm | No. of Elements | Cluster Volume $mm^3$ | Clusters per weld line | Run time h:min | DEI K/s |
|---|---|---|---|---|---|---|---|
| Macro | Power Based | 1.2-2.5 | 52181 | 62.5 | 30 | 19:18 | 1.98 |
| Macro | Power Based | 5-5 | 4700 | 62.5 | 30 | 01:23 | 2.23 |
| Macro | Power Based | 5-5 | 4700 | 375 | 5 | 00:16 | 3.2 |
| Macro | Temperature based | 5-5 | 4700 | 62.5 | 30 | 01:23 | 2.05 |
| Micro | Gaussian | 2.7-6.5 | 11000 | 125 | 28 | 3:40 | 1.95 |
| Micro | Gaussian | 1.7-2.7 | 46700 | 125 | 28 | 9:57 | 1.91 |

Fig. 16 visualizes the relationship between simulation time and temporal accuracy (expressed by DEI) for all studied cases. The overall trend highlights a clear clustering: micro simulations (Sim 5 and Sim 6) achieve the lowest DEI while having higher computational cost, positioned in the lower-mid region of the plot. In contrast, the most accurate macro model (Sim 1) requires over 20 hours to reach a similar DEI level. Notably, Sim 3 with minimal simulation time, exhibits the poorest accuracy, confirming that excessive simplification leads to temporal deviation. Sim 2 and Sim 4, both macro models with identical mesh but differing heat input strategies, show comparable runtime but slightly different DEI outcomes. The results show that while macro models correctly capture the overall heat flow in the entire part, micro models are more suitable for detailed thermal analysis in specific regions. Although both approaches can achieve similar accuracy in terms of DEI, except for the macro model with very large cluster volume.

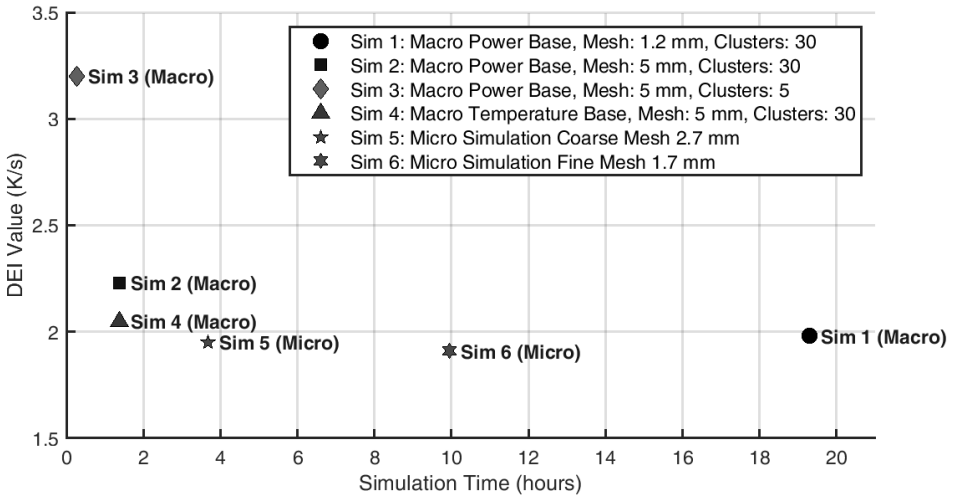



**Fig. 16** DEI plotted against simulation time for six simulations, labeled by type and configuration

## SUMMARY AND OUTLOOK

This study presented a multiscale simulation framework for predicting the thermal history in WAAM of 316 L stainless steel, combining macro modelling for power-based and temperature-based heat propagation with micro heat source modelled simulations. Experimental validation using thermal camera measurements enabled an assessment of various modelling strategies in terms of temporal accuracy and computational efficiency. The Dynamic Error Index (DEI) and Peak Temperature Error (PTE) were introduced as evaluation metrics, revealing that finely meshed micro models deliver the best agreement with experimental data while maintaining higher runtime. In contrast, the macro models, particularly those with fewer clusters or coarser meshes, showed some loss in accuracy. However, the overall results demonstrate that macro-scale simulations can still deliver acceptable accuracy with lower computational costs. This makes them attractive for applications where large numbers of simulations are needed, such as in optimization loops or machine learning-based models used for real-time process control or adjustments. For instance, in studies aiming to adjust deposition strategies in DED to achieve targeted temperature profiles, fast-running macro models offer a practical solution.

## ACKNOWLEDGMENT:

This project on which this publication is based was funded by the federal Ministry of Education and Research under the funding code 02P21Z000.

## References


[1] A. RIENSCHE, J. SEVERSON, R. YAVARI, N. L. PIERCY, K. D. COLE and P. RAO: 'Thermal modeling of directed energy deposition additive manufacturing using graph theory', *Rapid Prototyping Journal*, Vol. 29, No. 2, pp. 324-343, 2023.

[2] P. S. COOK and A. B. MURPHY: 'Simulation of melt pool behavior during additive manufacturing: Underlying physics and progress', *Additive Manufacturing*, Vol. 31, p. 100909, 2020.

[3] Z. ZHANG, Z. LIU and D. WU: 'Prediction of melt pool temperature in directed energy deposition using machine learning', *Additive Manufacturing*, Vol. 37, p. 101692, 2021.

[4] M. M. IMRAN ET AL.: 'Prediction of melt pool height based on the spatiotemporal adjacency features in laser metal deposition using machine learning', *Progress in Additive Manufacturing*, 2025.

[5] J. CHENG, Y. HUO, P. FERNANDEZ-ZELAIA, X. HU, M. LI and X. SUN: 'A Gaussian Process-Based extended Goldak heat source model for finite element simulation of laser powder bed fusion additive manufacturing process', *Computational Materials Science*, Vol. 244, p. 113185, 2024.

[6] R. F. V. SAMPAIO, J. P. M. PRAGANA, I. M. F. BRAGANÇA, C. M. A. SILVA, C. V. NIELSEN and P. A. F. MARTINS: 'Modelling of wire-arc additive manufacturing – A review', *Advances in Industrial and Manufacturing Engineering*, Vol. 6, p. 100121, 2023.

[7] ANSYS INC.: *Additive Manufacturing & 3D Printing Simulation Software (Directed Energy Deposition)*, Ansys Product Brochure, 2021.

[8] M. E. STENDER ET AL.: 'A thermal-mechanical finite element workflow for directed energy deposition additive manufacturing process modeling', *Additive Manufacturing*, Vol. 21, pp. 556-566, 2018.

[9] D. YANG, G. WANG and G. ZHANG: 'Thermal analysis for single-pass multi-layer GMAW based additive manufacturing using infrared thermography', *Journal of Materials Processing Technology*, Vol. 244, pp. 215-224, 2017.

[10] D. G. ANDRADE, T. TANKOVA, C. ZHU, R. BRANCO, L. S. DA SILVA and D. M. RODRIGUES: 'Mechanical properties of 3D printed CMT-WAAM 316 LSi stainless steel walls', *Journal of Constructional Steel Research*, Vol. 215, p. 108527, 2024.

[11] J.-A. TRÖGER, S. HARTMANN, K. TREUTLER, A. POTSCHKA and V. WESLING: 'Simulation-based process parameter optimization for wire arc additive manufacturing', *Progress in Additive Manufacturing*, Vol. 10, No. 1, pp. 1-14, 2025.

[12] L. HAGEN ET AL.: 'High deposition rate wire-arc directed energy deposition of 316L and 316LSi: Process exploration and modelling', *Materials Science and Engineering: A*, Vol. 880, p. 145044, 2023.

[13] V. MICHAILOV, N. DOYNOV and R. OSSENBRINK: *Sensibilitätsanalyse der thermomechanischen FE-Schweißsimulation*, Shaker Verlag, May 2012, ISBN: 978-3-8440-1016-9.

[14] C. S. KIM: *Thermophysical properties of stainless steels*, Argonne National Laboratory (ANL), Argonne, IL (United States), 1975.

[15] Y. F. LIU, Z. L. HU, D. H. SHI and K. YU: 'Experimental investigation of emissivity of steel', *International Journal of Thermophysics*, Vol. 34, No. 3, pp. 496-506, 2013.

[16] J. MÜLLER and J. HENSEL: 'Potential of thermography for the monitoring of DED-Arc processes', *Weld World*, Vol. 68, No. 3, pp. 505-513, 2024.

[17] R. M. KINDERMANN, M. J. ROY, R. MORANA, J. A. FRANCIS and P. B. PRANGNELL: 'Wire-arc directed energy deposition of Inconel 718: Effects of heat input and build interruptions on mechanical performance', *Additive Manufacturing*, Vol. 76, p. 103765, 2023.

[18] F. W. C. FARIAS, J. DA CRUZ PAYÃO FILHO and V. H. P. MORAES E OLIVEIRA: 'Prediction of the interpass temperature of a wire arc additive manufactured wall: FEM simulations and artificial neural network', *Additive Manufacturing*, Vol. 48, p. 102387, 2021.

[19] J. A. D.-D. LA PEÑA, P. A. LIMON-LEYVA, P. CORTES and K. CHOO: 'Modeling of Direct Energy Deposition for Wire Laser Additive Manufacturing', *J. of Materi. Eng. and Perform.*, vol. 34, no. 18, pp. 20648-20671, Sept. 2025, doi: 10.1007/s11665-025-10665-0.

[20] D. LÁZARO, A. ALONSO, M. LÁZARO and D. ALVEAR: 'A Simple Direct Method to Obtain Kinetic Parameters for Polymer Thermal Decomposition', *Applied Sciences*, vol. 11, no. 23, p. 11300, Nov. 2021, doi: 10.3390/app112311300.

[21] H. XIAO ET AL.: 'Influence of molten-pool cooling rate on solidification structure and mechanical property of laser additive manufactured Inconel 718', *Journal of Materials Research and Technology*, vol. 19, pp. 4404-4416, July 2022, doi: 10.1016/j.jmrt.2022.06.162.

[22] H. WANG, L. CAO, Y. LI, M. SCHNEIDER, E. DETEMPLE and G. EGGELER: 'Effect of cooling rate on the microstructure and mechanical properties of a low-carbon low-alloyed steel', *J. Mater. Sci.*, vol. 56, no. 18, pp. 11098-11113, June 2021, doi: 10.1007/s10853-021-05974-3.

# PIPEWELD, A SOFTWARE SUITE FOR COMPUTATIONAL WELDING MECHANICS FOR NUCLEAR APPLICATIONS

J. DELMAS*, S. HENDILI*, S. HILAL*, P. PEREIRA ALVAREZ*, V. ROBIN**

** Electricité de France R&D, 78400, Chatou, France, josselin.delmas@edf.fr*
*** Electricité de France Direction Technique, 69007, Lyon, France*

*DOI 10.3217/978-3-99161-089-2-035, license CC BY 4.0*
*https://creativecommons.org/licenses/by/4.0/deed.en*
*This CC license does not apply to third party material and content noted otherwise.*

## ABSTRACT

In the nuclear industry, numerical modelling of welding processes has become a key tool for understanding and decision-making. It is used to evaluate the impact of welding on degradation mechanisms and to accelerate the development and qualification of welding and repair techniques. Computational welding mechanics, which involves modelling the solid-state effects of welding on the base material and weld metal, such as temperature fields, microstructural evolution, and stress-strain distributions, serves this purpose.

Since 2021, EDF has observed stress corrosion cracking (SCC) in certain austenitic stainless-steel pipe-to-elbow welds within safety injection systems. Accurate prediction of welding residual stresses (WRS) is essential for assessing the structural integrity of components exposed to SCC and similar degradation mechanisms. During welding, coupled thermo-mechanical and metallurgical phenomena occur, including microstructural transformations such as dynamic recovery and recrystallization. These transformations influence the material's hardening behaviour and must be accounted for in residual stress simulations.

In the as-welded condition, multi-pass circumferential butt welds in austenitic stainless steel typically exhibit a residual stress profile characterized by a shell bending effect. This results in compressive axial stresses in the inner half of the weld wall, although tensile zones may still develop near the weld axis on the inner surface. This behaviour is well-documented in the literature and has been validated through simulations using code-aster (a general-purpose finite element software for solid mechanics) and confirmed by experimental measurements on mock-ups.

In this context, the Pipeweld software suite has consolidated over two decades of research on welding and its numerical modelling. Built on code-aster and Salome_Meca, numerical software developed by Electricité de France, Pipeweld enables the prediction of residual stress states for component lifetime assessment and process qualification optimisation.

Keywords: welding residual stress assessment, multipass welding, computational weld mechanics, open-source based software

## INTRODUCTION

In the nuclear industry, numerical modelling of welding processes has become a tool for understanding and decision-making, used to assess the effect of welding on certain degradation mechanisms and to accelerate the development and qualification of welding and repair techniques. Computational welding mechanics, which involves modelling the effects of welding in the base metal and the weld in the solid state (temperature field, microstructure, stress, and strain distribution), can be implemented for this purpose.

Significant R&D efforts have contributed to the advancement of modelling approaches, particularly in determining the appropriate level of accuracy required for industrial applications. To support EDF engineers, who are conducting an increasing number of studies, the development of the Pipeweld tool was initiated. This tool aims to standardize the methodology for numerical welding simulations by capitalising over 20 years of R&D, thereby enhancing the consistency and quality of engineering assessments.

## COMPUTATIONAL WELDING MECHANIC MODELLING FOR THE PREDICTION OF THE RESIDUAL STATE

### PRINCIPLES

From the perspective of continuum mechanics, computational welding simulation enables the prediction of the residual mechanical state of a welded assembly by evaluating the distribution of residual stresses, distortions, and strain hardening. This residual state is intrinsically linked to the entire thermal and mechanical history of the welding process. Consequently, its assessment requires the computation of the thermo-mechanical equilibrium of the welded structure throughout the welding operation.

The energy input from welding propagates through the structure primarily via heat conduction. Numerical simulation enables the prediction of temperature evolution at any point within the structure, resulting from this heat diffusion. At the structural scale, the thermal behaviour during each stage of the welding sequence is characterized by spatial temperature gradients, which are the main drivers of the component's mechanical response.

These thermal gradients induce thermal strain gradients, leading to strain incompatibilities that generate internal stresses, particularly in regions close to the weld, as illustrated thanks to numerical modelling [1]. These internal stresses cause plastic deformation of the material, which accumulates as strain hardening throughout the welding process. The coupling and interaction of physical phenomena described above are illustrated on Figure 1.

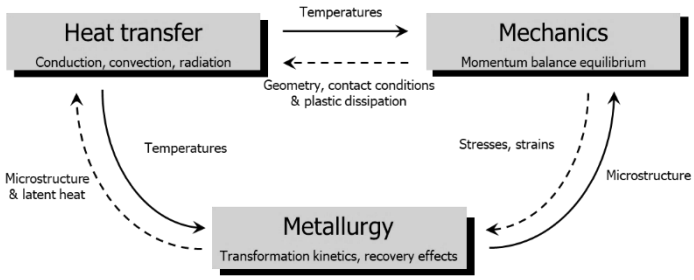



**Fig. 1** Coupling and interaction for WRS assessment: heat transfers, metallurgical phenomena and mechanical consequences

In the specific case of butt welding between two pipes, groove deformation also plays a significant role in the development of strain hardening near the weld. Additionally, structural effects, commonly referred to as the "diabolo" effect, must be considered when analysing the distribution of certain components of the stress tensor. For example, shell bending induced by radial and axial shrinkage in butt-welded pipe joints affects the axial stress, which typically exhibits an S-shaped profile across the thickness at the weld centreline [2]. This is illustrated in Figure 2, where tensile stress peaks on the outer surface (first loop of the "S") and compressive stress peaks on the inner surface (second loop).

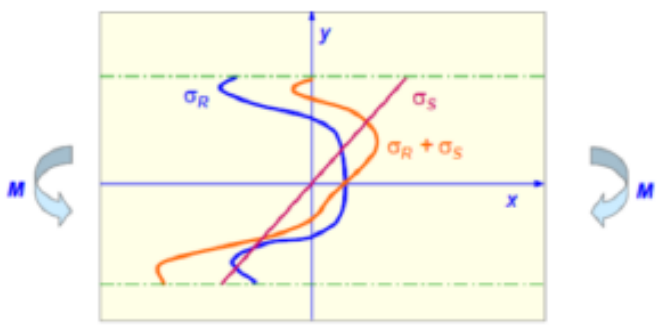



**Fig. 2** Superposition principle of bending stresses ($\sigma_s$) across the wall thickness with residual stresses ($\sigma_r$) not associated with bending effects

The numerical evaluation of the residual state in welds requires accounting for the physical phenomena described previously. These phenomena are governed by a set of equations that are numerically solved using the finite element method (FEM). The parameters that feed into these equations and define each specific welding configuration are identified through the analysis of Welding Procedure Specifications (WPS).

## GEOMETRIC MODEL AND MESH

As with any numerical method, it is necessary to discretize both physical time and physical space. These temporal and spatial discretization must be refined to accurately capture the thermal gradients that drive the physical quantities of interest.

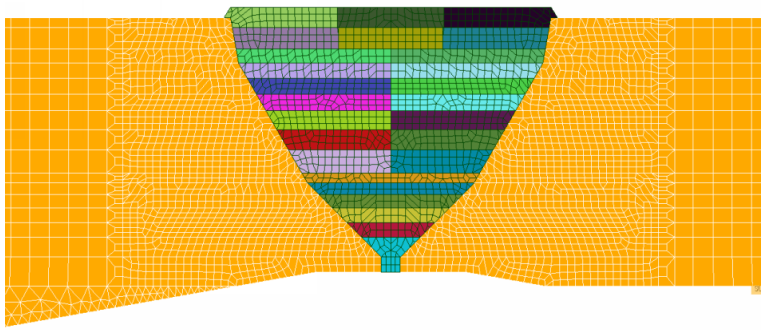


**Fig. 3** Example of 2D mesh of a butt weld with each bead in different colour

The assembly of the components of interest, such as thick-walled piping systems (thickness > 10 mm), is typically performed using multi-pass welding. Simulating such operations requires accounting for a dynamically evolving geometry, which changes according to the weld groove filling sequence. The initial geometry consists of two chamfered components aligned end-to-end. This geometry evolves with each welding sequence as weld beads are progressively added to fill the groove (illustrated on Figure 3). The position and dimensions of each weld bead are determined based on the operating parameters of the specific welding sequence and the diameter of the filler metal used.

## THERMAL MODELLING

The thermal model is employed to simulate the heat input during welding by representing it as an equivalent heat source. It enables the analysis of heat transfer within the structure through conduction. The thermal field evolution predicted by the numerical simulation is governed by the thermo-physical properties assigned to the constituent materials of the assembly, as well as by the boundary conditions accounting for convective and radiative heat exchange with the surrounding environment. The implementation of the thermal model yields a spatio-temporal temperature distribution, providing detailed insight into the thermal history of the welded structure.

The heat input is modeled:

- in 2D modelling, as a surface heat flux applied to the 2D cross-section under analysis
- in 3D modelling, as a volumetric heat flux applied to the 3D bead or bead section.

Its spatial distribution around the deposited weld bead is defined by geometric parameters (triangular distribution or double-ellipsoid [3-4-5]) and from welding engineering heuristics, considering:

- a dilution rate of approximately 50% for the initial pass (root pass),
- a dilution rate of approximately 30% for all subsequent passes.

The spatial profile of the heat flux is thus governed by these parameters to reflect realistic energy deposition. For each welding sequence, the consistency between the actual input power, calculated as the product of current, voltage, and process efficiency, and the power implemented in the numerical model is systematically verified to ensure physical accuracy.

Heat conduction within the assembly is governed by two material-dependent parameters: thermal conductivity and volumetric heat capacity (the product of specific heat capacity, cp, and density, ρ). Both parameters are temperature-dependent, and accounting for their variation is essential in fully coupled thermo-metallurgical simulations, introducing nonlinearity into the thermal model's solution.

## MECHANICAL MODELLING

In the absence of external stress, the mechanical consequences of the welding operation are related to the presence of thermal gradients in the thermo-mechanically affected zone during welding. The definition of the thermal loading is therefore essential to establish the stress at the origin of the WRS. These thermal deformations are accommodated by the structure in the form of local elastic and inelastic deformations on which are superimposed global internal forces induced by the self-bridging effects caused by the massive parts that remain cold at the scale of the structure (tourniquet effect for example). In multi-pass welding, the WRS thus originate from the succession of shrinkage and expansion that are counteracted or even blocked by the colder and therefore stiffer parts of the assembly.

The evolution of residual welding stresses is thus dependent on the choice of laws linking stresses and strains, which can be broken down into an elastic part, thermal and inelastic $\dot{\varepsilon} = \dot{\varepsilon}^{e} + \dot{\varepsilon}^{th} + \dot{\varepsilon}^{in}$ and the way of describing plasticity (permanent inelastic deformation at the origin of the WRS and governing the variables modifying the elasticity domain by strain hardening). In this respect, the behavior law used to translate plasticity integrates phenomena of work hardening recovery characterized specifically to describe the behavior of alloys that do not present a phase transformation in the solid-state during welding (FCC alloys at any temperature such as Ni base alloys or austenitic stainless steels) [6]. Note that a weak coupling (sequential chaining of thermal, metallurgical and mechanical analyses at each welding pass) is sufficient for the determination of the WRS for the concerned assemblies as shown in the diagram of Figure 1.

The Von Mises threshold function $\sigma_{eq}$ or equivalent stress in the sense of Von Mises which corresponds to the second invariant of the stress tensor $\sigma_{ij}$ whose $\underline{s}$ is the deviatoric part, is generally used to characterize the stress state in metallic materials:

$$f(\sigma_{ij}) = \sigma_{eq} = J_2(s_{ij}). \tag{3}$$

An isotropic work hardening of the material is considered. $\sigma_0$ is the initial yield strength of the unhardened material (initial yield strength); it is a function of the temperature $\theta$. Let $R$ be the increase of the yield strength by work hardening of the material, which is dependent on the temperature and the irreversible deformation $p$ (cumulated plastic or viscoplastic deformation which represents the work hardening parameter). The yield strength of the strain-hardened material is written:

$$\sigma_y(p,\theta) = \sigma_0(\theta) + R(p,\theta), \tag{4}$$

$$\text{where } p = \int_0^t {\dot{\varepsilon}_{eq}}^p . dt \quad \text{and} \quad {\dot{\varepsilon}_{eq}}^p = \dot{p} = \sqrt{\frac{2}{3}\dot{\varepsilon}_{ij}^p . \dot{\varepsilon}_{ij}^p}$$

The physical strain hardening model is supplemented by a recovery term. Thus, the creation of plastic deformation without strain hardening recovery is affected by a recovery term which depends on the temperature, knowing that this effect is thermally activated above 600°C and that its evolution rate increases with the temperature. The recovery of work hardening is modeled by the following equation:

$$\dot{r}(t) = \dot{p}(t) - k(\theta(t))\langle r(t) - r_\infty(\theta(t))\rangle \tag{5}$$

With:

$r$: cumulated plastic strain with consideration of the strain hardening recovery,

$k$: coefficient which characterizes the dynamics of recovery according to the temperature and which depends on the considered material,

$r_\infty$: coefficient which characterizes the threshold quantity of plastic deformation which cannot be recovered, and which depends on the temperature and the considered material,

$\langle x \rangle$ denotes the positive part of x.

The two coefficients $k$ and $r_\infty$, which are defined above, are material parameters characterized from specific tests (see [6]).

## QUANTITIES OF INTEREST AND POST-PROCESSING

Post-processing of the thermo-mechanical simulations results enables a comprehensive assessment of the welded assembly, including both geometric and mechanical characteristics:

- Characterization of metallurgical zones:
  - Fusion Zone (FZ): region where the material has melted and resolidified,
  - Heat-Affected Zone (HAZ): region subjected to thermal cycles without melting,
  - Thermo-Mechanically Affected Zone (TMAZ): region influenced by both thermal and mechanical effects.
- Evaluation of the residual state of the assembly:
  - Groove shrinkage due to thermal contraction,

- Root penetration anomalies (e.g., excess or lack of material, root bead formation),
- Global structural distortion, including bending or warping,
- Residual stress distribution throughout the joint and surrounding material,
- Mapping of accumulated plastic strain, providing insight into localized permanent deformation.

For SCC issues, residual stresses are not the only mechanical quantity to evaluate, strain hardening is also important as initiation and propagation laws used for SCC modelling (initiation, orientation and kinetic) depends on both stress and strain hardening [7]. Strain hardening or equivalent plastic strain that drives the material sensitivity to SCC are implicitly computed during computational welding simulation [8] and directly correlated with hardness measurements as those presented in Figure 4. Correlation rules based on the same relationship that the one established in [9] between strain hardening and hardness are illustrated in Figure 4.

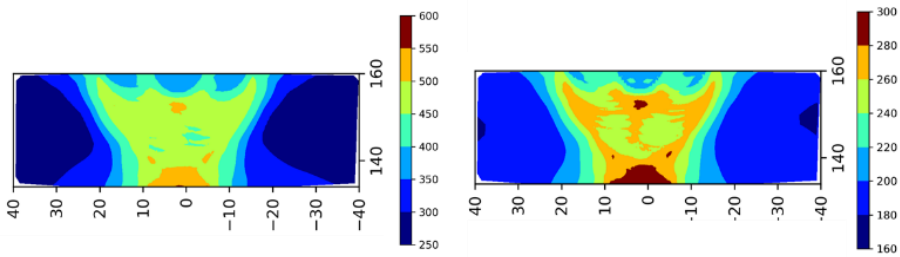



**Fig. 4** Updated yield strengh in the simulated weld region and TMAZ (left) and conversion into a hardness map (right)

## VALIDATION PROCESS

Model validation relies on the comparison between simulation results and experimental measurements conducted on two types of mock-ups. Semi-industrial mock-ups are designed to replicate the complexity of welding operations without being specific to any assembly. For this type of model, it is very useful to have a large number of measurements taken using different methods, as well as different models created by different teams. This is why it is very useful to rely on the The European Network on Neutron Techniques Standardization for Structural Integrity (NeT) [10] to create these models. In contrast, industrial mock-ups are developed to closely resemble actual components, considering factors such as scale, number of weld passes, and geometric configuration.

SEMI-INDUSTRIAL MOCK-UPS: NET NETWORK CONTRIBUTION

The European Network on Neutron Techniques Standardization for Structural Integrity aims to advance both experimental and computational methods, as well as standards, for the accurate characterization of WRS. Established in 2002, NeT operates through in-kind contributions from a wide range of partners in industry, academia, and research institutions.

Each configuration studied within the network is managed by a dedicated Task Group (TG), responsible for producing mock-ups, conducting measurements and simulations, and interpreting the results. NeT's work has led to approximately 85 academic publications and has supported over 10 PhD theses in related scientific fields. Notably, two special issues of the International Journal of Pressure Vessels and Piping - published in January 2009 and July 2018 - highlighted the findings of Task Groups TG1 and TG4, respectively.

One of NeT's most significant achievements is fostering international industrial consensus on the development of predictive and robust numerical models for residual stress, supported by access to high-quality experimental data from well-controlled mock-ups, primarily measured non-destructively using neutron diffraction. Research from NeT played a key role in the development of the draft international standard ISO 21432:2018 on residual stress determination via neutron diffraction and contributed to ISO/TS 18166:2015 on numerical welding simulation, particularly for nuclear applications.

NeT's studies are driven by the imperative to ensure the safety and reliability of critical welded components in the nuclear sector. The results are highly relevant to industry. EDF has highlighted how NeT has enabled them to validate numerical stress predictions in the context of nuclear plant lifetime management and safety. Of particular interest to EDF are Task Groups TG4, TG6, and TG8, which focus on nuclear-related applications.

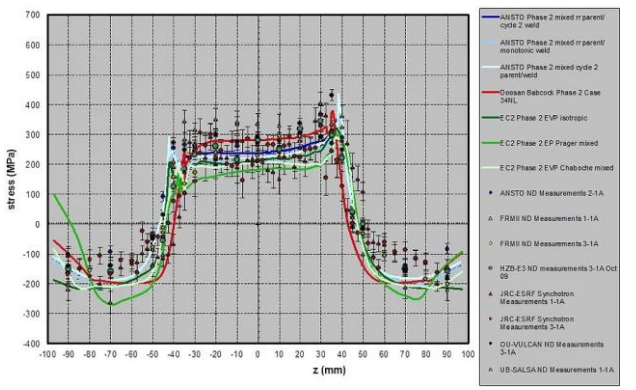



**Fig. 5** TG4 – Transverse residual stresses along a line 5 mm below the surface of the welded plate in the welding direction, measurements (points) and simulations (lines) [11]

*TG4: 3-Pass Slot Weld (Stainless Steel)*

Task Group 4 (TG4) [11] was launched in 2007 to build upon the advancements achieved in TG1 by addressing a more complex scenario. This group focused on investigating residual stresses in a specimen made from an AISI 316L(N) austenitic stainless-steel plate, which featured a central groove. The groove was filled using three overlapping TIG weld passes of AISI 316L stainless steel, applied through a mechanized TIG welding process. This mock-up configuration is representative of a short and shallow weld repair geometry, notably one that does not include the original weld.

*TG6: 3-Pass Slot Weld (Ni alloy)*

Task Group 6 (TG6) [12-13] is closely based on the TG4 design, with the only distinction being the choice of materials: the specimen consists of an Alloy 600 plate welded using Alloy 82 filler metal. As such, it shares all the advantages and challenges of the TG4 configuration, including the development of a complex three-dimensional residual stress field within a compact and portable specimen. This makes it well-suited for rapid residual stress measurements using a variety of techniques. The specimen contains a substantial volume of weld metal that has undergone multiple high-temperature thermo-mechanical cycles, contributing to the complexity of the residual stress distribution. The fabrication, measurement, and simulation protocols are defined by EDF in collaboration with domain experts, and the mock-ups are manufactured by EDF R&D.

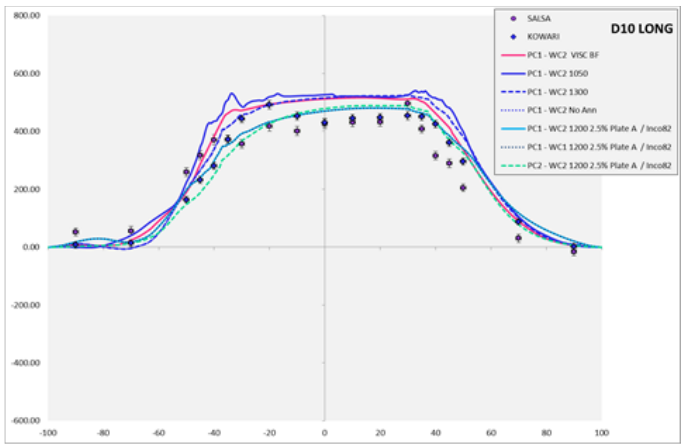



**Fig. 6** TG6 – Longitudinal residual stresses along a line 10 mm below the surface of the welded plate in the welding direction, measurements (points) and simulations (lines) [ref]

*TG8: 5-Pass Slot Dissimilar Weld (Ni alloy) on Ferritic Steel*

Task Group 8 (TG8) [14] focuses on a steel plate made of French grade 18MND5, featuring a five-pass slot weld performed using nickel-based Alloy 52 consumables. This group was formed to address challenges related to weld repair procedures. The TG8 round robin specimen is closely modelled on the TG4 design, with the key difference being an increased plate thickness of 30 mm. This enhancement provides improved self-clamping conditions and helps minimize distortion. As with TG4, the TG8 specimen generates a complex three-dimensional residual stress field within a compact and portable geometry, making it well-suited for rapid residual stress measurements using various techniques. The specimen includes a significant volume of weld metal subjected to multiple high-temperature thermo-mechanical cycles. The use of a nickel-based filler metal introduces additional complexity in residual stress characterization. Moreover, the configuration exhibits a complex mismatch behaviour between the weld and base metal, involving phase transformations and tempering effects in the Heat Affected Zone (HAZ). The fabrication, measurement, and simulation protocols are defined by EDF in collaboration with domain experts, and the mock-ups are manufactured by EDF R&D.

## INDUSTRIAL MOCK-UPS

It is often necessary to have a model that is even more representative of the type of assembly to be studied, considering the complexity of the geometry and the welding process used (and therefore the greater number of welds). For this purpose, industrial models can be produced, which will be more complex and more expensive to manufacture [15].

For austenitic steel pipe assemblies, we present an example of a model that was instrumented with thermocouples to evaluate the thermal conditions experienced by the assembly. In addition, stereo correlation measurements were performed to evaluate the deformations of the assembly.

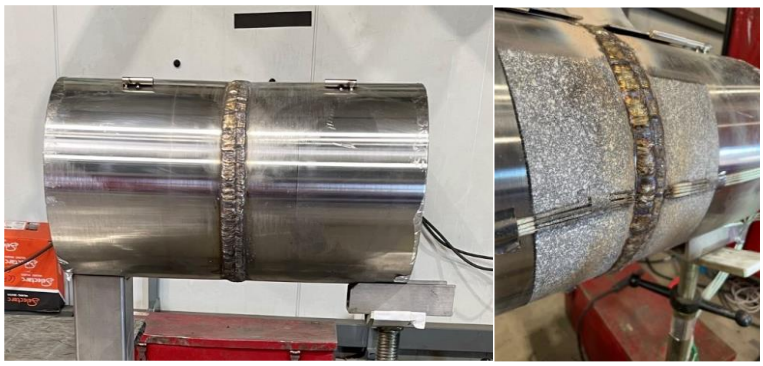


**Fig. 7** Austenitic steel pipe mock-up with thermocouples instrumentation and speckles for stereo correlation analysis

Finally, residual stress measurements are performed in the thickness (X-ray diffraction [16] and deep hole drilling method [17]) to characterise the residual state. Comparison with simulations allows the numerical approach to be validated.

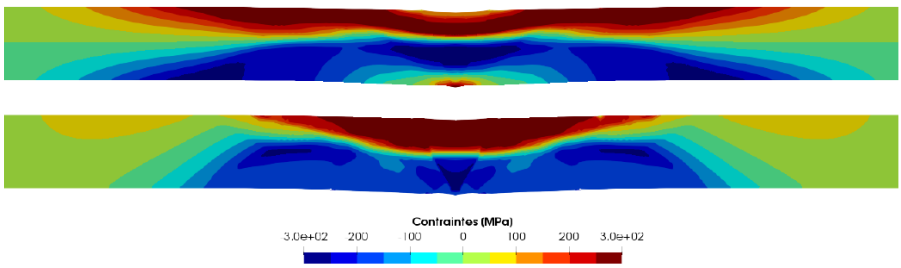



**Fig. 8** Example of residual stress in a mock-up pipe predicted with simulation: (top) axial stress, (bottom) circumferential stress

## PIPEWELD: FROM A RESEARCH KNOWLEDGE CAPITALIZATION TOOL TO AN OPERATIONAL INDUSTRIAL SOLUTION

In the context of welding and repair processes for PWR primary circuit components, the Pipeweld software suite has enabled the capitalisation of two decades of research on welding and its numerical modelling. Pipeweld is based on code-aster [18], an open-source generalist software of simulation in mechanics and in structural analysis developed by EDF for more than 30 years, from Salome-Meca plateform [19], an all-purpose plateform for mechanical analysis which offers the entire calculation chain from CAD, meshing to post-processing. Pipeweld can predict residual states for lifetime assessment and to optimise process qualification. Pipeweld's development was initiated to support the numerical welding simulations (NWS) which were essential for SCC estimations. The development of this tool was motivated by the following needs:

- consolidate and standardise the methodology for numerical simulation of welding (in 2D and 3D), initially limited to the assembly of butt pipes;
- facilitate the production of the necessary input data, particularly the meshes, using a parametric approach;
- facilitate multi-parametric studies;
- facilitate post-processing of results and standardise outputs for the quantities of interest;
- facilitate the transfer of welding simulation results as input data for SCC analysis (crack initiation and propagation) or brittle fracture;
- facilitate the creation and enrichment of a Verification and Validation (V&V) file;
- provide a framework for studies under quality assurance, which is mandatory for the nuclear safety authority.

The ambition of the Pipeweld tool is to be adopted by engineering teams as a qualified scientific computing tool for conducting studies aligned with established industrial practices in the field. These practices are defined in several standards, notably AWS [20] and ISO [21], as well as their adaptations for application within the French nuclear sector, such as the French Nuclear Institute guideline [22].

Pipeweld enables robust CWM studies, covering the entire workflow from the geometric design of the weld groove to the post-processing of simulation results. Each stage of the process is handled within a dedicated sub-module, as illustrated in Figure 8.

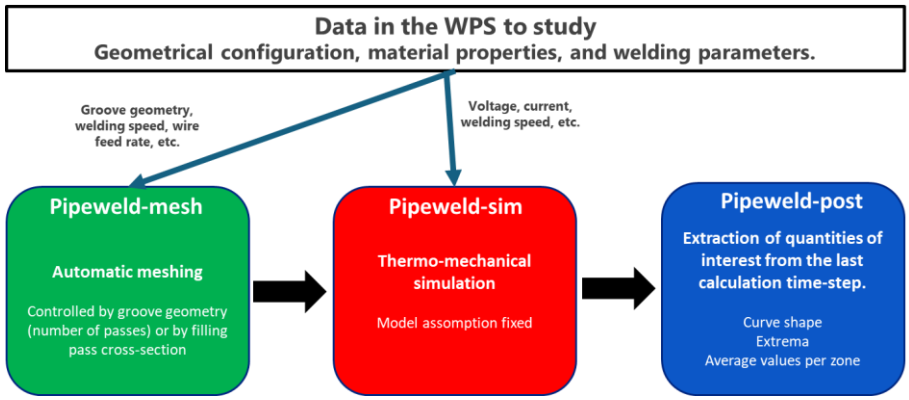



**Fig. 9** Pipeweld tool workflow chart

## APPLICATIONS

### RESIDUAL STRESS PREDICTION IN MULTI-PASS PIPE CIRCUMFERENTIAL BUTT WELDS TO FOR SCC RISK CLASSIFICATION

Prediction of residual stresses in welds is essential to evaluate the integrity of a component subject to degradation mechanisms such as Stress Corrosion Cracking. During welding operations, complex thermo-mechanical and metallurgical processes take place and lead to microstructural changes such as dynamic recovery and dynamic recrystallization. These microstructural changes induce a modification of hardening behaviour that should be considered to accurately evaluate residual stresses through numerical simulations. In the as-welded conditions, multi-pass pipe circumferential butt welds made of austenitic stainless steel show a typical residual stress profile through the wall of the welded joint. Such a shell bending profile places the inner half of the weld joint wall and its vicinity in compression in the axial direction. However, tensile zones can appear in the inner wall near the axis of the weld.

A large simulation campaign was carried out to cover different welding configurations and confirm these trends [8]. This digital chart is built based on a design of experiments of 100 numerical simulations of welding per diameter and schedule. The parameters are:

- Diameter, thickness,
- Welding processes (GTAW, SMAW…),
- Groove shape.

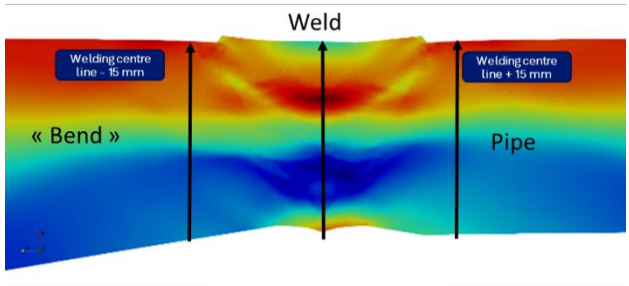



**Fig. 10** Typical axial stress state from simulation [8]

This set of simulations show the systematic presence of a compression zone on the inner side, with some variability depending on the welding conditions and geometry. The classification of SCC risk is then defined by a set of two indicators that can be related to crack initiation (stress, strain hardening near the surface) and propagation (stress, strain hardening in the bulk).

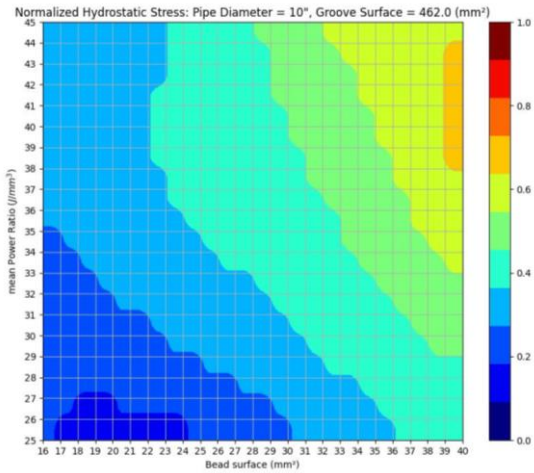



**Fig. 11** Hydrostatic stress map as a function of the bead surface and the power ratio for a 10" diametre and a groove section of 462 $mm^2$ [8]

PREDICTION OF THE RESIDUAL STATE OF A CENTRAL BOTTOM-MOUNTED NOZZLE

Bottom Mounted Nozzles (BMNs) are welded components located at the lower part of a nuclear reactor pressure vessel, designed to allow the passage of instrumentation. Typically fabricated from nickel-based alloys, these components are welded to the vessel wall, which is generally made of low-carbon steel. Due to their critical function, BMNs must comply with stringent safety standards, particularly in terms of weld integrity and sensitivity to SCC.

Pipeweld has been extended to enable 2D modeling of BMN configurations, considering the specific challenges associated with these assemblies, notably the presence of multiple materials. The tool's capability to handle a wide range of BMN configuration has been demonstrated. The validity of the simulation results has been assessed through comparison with available reference data, including previous numerical studies and experimental measurements on mock-ups. An illustrative example is presented in Figure 12. In this case, four materials were considered: Inconel 600 for the BMN tube, 16MND5 reactor vessel steel for the vessel bottom, Inconel 600 for buttering and weld beads, and 316L stainless steel for the vessel cladding. The Figure 12 compares the results of a 3D simulation of a central BMN (with a 0° inclination) with 2D results obtained using Pipeweld.

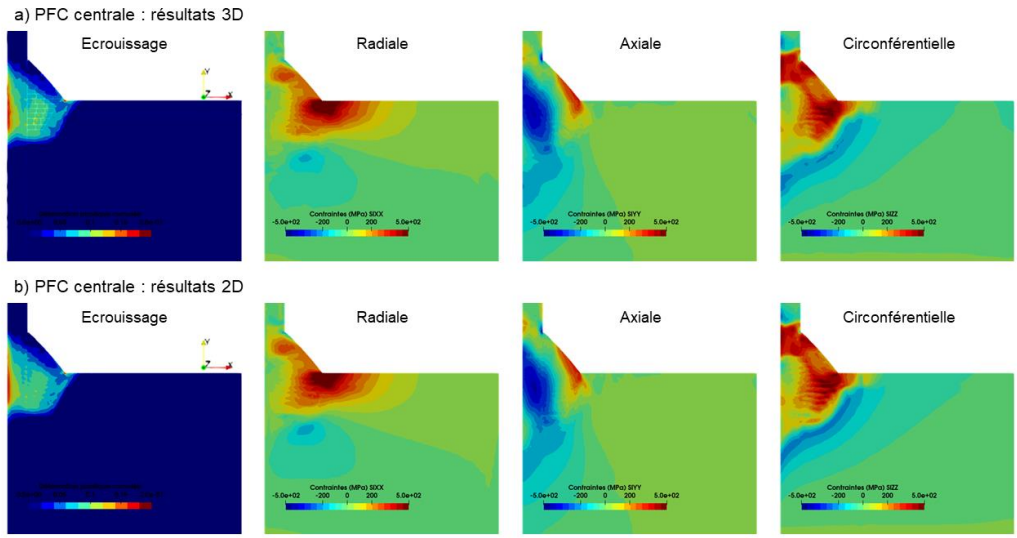



**Fig. 12** Comparison of residual state obtained and strain hardening with 3D modelling (top) and 2D modelling (bottom)

A very good agreement is observed across all components, both in terms of stress distribution and strain hardening. This case study highlights the ability of Pipeweld to significantly reduce the time required for simulation input preparation and the post-processing time thanks to the parametric approach, thereby improving overall modeling efficiency, while maintaining methodological consistency across different simulation approaches.

## CONCLUSIONS AND FUTUR DEVELOPPMENTS

The Pipeweld software suite represents a significant advance in the field of computational welding mechanics (CWM) for nuclear applications. Consolidating more than two decades of research and development within EDF, Pipeweld offers a robust, standardised and validated framework for simulating welding processes and predicting residual stress states. Its integration with open-source platforms such as code-aster and Salome_Meca ensures methodological transparency and adaptability to a wide range of industrial configurations.

Thanks to rigorous validation against semi-industrial and industrial models, including contributions from the NeT network, Pipeweld has demonstrated high fidelity in reproducing complex thermomechanical phenomena. Its predictive capabilities are essential for assessing the structural integrity of components exposed to degradation mechanisms such as stress corrosion cracking (SCC) and for supporting life management strategies in nuclear power plants.

Future developments will focus on extending Pipeweld's applicability to more complex geometries (as illustrated in [23] on a repaired weld), multi-material assemblies (in particular, materials with metallurgical solid state transformation), improving the automation of model configuration and post-processing, and integrating with broader safety assessment workflows. In addition, a verification and validation file will be compiled based on cases of interest for which measurements (particularly deformations and residual stresses) are available or, failing that, simulation results obtained in round-robin tests. These improvements aim to make Pipeweld a qualified engineering tool, compliant with international standards and suitable for deployment in safety-critical environments.

## References


[1] P. DURANTON, J. DEVAUX, V. ROBIN, P. GILLES, J.-M. BERGHEAU: '3D modelling of multipass welding of a 316L stainless steel pipe', *J. Mat. Proc. Tech.*, 153-154, pp. 457-463, 2004.

[2] P. DONG ET AL., 'On residual stress prescriptions for fitness for service assessment of pipe girth welds', *International Journal of Pressure Vessels and Piping*, 123-124, pp. 19-29, 2014.

[3] J. GOLDAK, M. BIBBY, J. MOORE, R. HOUSE, B. PATEL: 'Computer modeling of heat flow in welds', *Metall. Trans. B*, Volume 17, Issue 3, pp. 587-600, 1986.

[4] J. GOLDAK, A. CHAKRAVARTI, M. BIBBY: 'A new finite element model for welding heat sources.' *Metall. Trans. B*, 15B 299-305, 1984.

[5] F. ROSSILLON, D. ALBRECHT: 'Computation of the welding process: the engineering practice consolidated thanks to R&D tools', *Proceedings of the ASME 2016 Pressure Vessels and Piping Conference*, PVP2016-63613, 2016.

[6] S. HENDILI, L. LE GRATIET, M. ABBAS: 'Un nouveau modèle simplifié de la restauration d'écrouissage utilisé dans la simulation numérique du soudage', *Proceedings of the 13ème Colloque National en Calcul des Structures CSMA 2017*, 2017.

[7] T. COUVANT, C. VARÉ, J. M. FRUND, S. LECLERCQ, Y. THÉBAULT, N. ETCHEGARAY, J. DELMAS: 'Susceptibility to SCC of cold work austenitic stainless steels in non-polluted primary PWR environment', *Proceedings of FONTEVRAUD 10 conference*, September 19 to 22, Avignon, France, 2022.

[8] V. ROBIN, S. HENDILI, J. DELMAS, S. HILAL, D. IAMPIETRO, M. ABBAS and S. JUTTEAU: 'Modelling of residual stresses in multi-pass pipe circumferential butt welds made of austenitic stainless steel to provide indicators for SCC risk classification', *Proceedings of the ASME 2023 Pressure Vessels and Piping Conference*, PVP2023-107448, 2023.

[9] O. MURÁNSKY ET AL.: 'The influence of constitutive material models on accumulated plastic strain in finite element weld analyses', *International Journal of Solids and Structures*, Vol. 69, pp.518-530, 2015.

[10] https://www.net-network.eu/

[11] M. C. SMITH, A. C. SMITH, C. OHMS and R. C. WIMPORY: 'The NeT Task Group 4 residual stress measurement and analysis round robin on a three-pass slot-welded plate specimen', *International Journal of Pressure Vessel and Piping*, 164, pp. 3-21, 2018.

[12] V. AKRIVOS, ET AL.: 'A residual stress measurement and numerical analysis round robin on a three-pass slot nickel-base repair weld', *Procedia Manufacturing*, 51, pp. 779-786, 2020. DOI: 10.1016/j.promfg.2020.10.109

[13] P. PEREIRA ALVAREZ, J. DELMAS, S. HENDILI: 'NeT-TG6 nickel-based alloy simulation: calibration and experimental validation', *Proceedings of the ASME 2025 Pressure Vessels and Piping Conference*, PVP2025-155529, 2025.

[14] V. ROBIN, S. HENDILI, J. DELMAS, J. DRAUP, Q. XIONG, M. C. SMITH, A. PAGET: 'NeT project Task Group 8: an international benchmark on residual stress assessment for welding repair', PVP2022 85083, *Proceedings of the ASME 2022 Pressure Vessels and Piping Conference*, PVP2022-85083, 2022.

[15] T. H. PHAM ET AL.: 'Investigation of welding repairs impacts on SCC of austenitic stainless steel with experimental testing and numerical simulation', *Proceedings of the 22nd International Conference on Environmental Degradation*, August 10-14, Long Beach, USA, 2025.

[16] I. C. NOYAN and J. B. COHEN: *'Residual Stress Measurement by Diffraction and Interpretation'*, Springer-Verlag, New York Inc., 1987.

[17] R. H. LEGGATT, D. J. SMITH, S. D. SMITH, F. FAURE: 'Development and experimental validation of the Deep Hole method for residual stress measurement', *Journal of Strain Analysis for Engineering Design*, Vol. 31, No. 3, p 177-186, 1996.

[18] ELECTRICITÉ DE FRANCE: 'Finite element code-aster: Analysis of Structures and Thermomechanics for Studies and Research', Open source on www.code-aster.org, 1989-2025.

[19] J. DELMAS, A. ASSIRE: 'Salome-Meca : une plate-forme au service de la simulation mécanique', *Proceedings of the 9ème Colloque National en Calcul des Structures CSMA 2009*, 2009. url: https://hal.archives-ouvertes.fr/hal-1413149.

[20] AWS 9.5 Guide for Verification and Validation in Computation Weld Mechanic, 2013.

[21] CEN ISO/TS 18166:2016, Numerical welding simulation - Execution and documentation, 2015.

[22] FRENCH NUCLEAR INSTITUTE: 'Guide méthodologique de simulation des contraintes résiduelles du soudage avec un outil de calcul scientifique employé dans la démonstration de sûreté couvrant l'îlot nucléaire', *Internal note*, DEN/DANS/DM2S/SEMT/LTA/NT/2019-64183/A, 2019.

[23] S. HILAL, S. HENDILI, J. DELMAS, P. PEREIRA ALVAREZ, V. ROBIN, E. DERNIAUX and T. BOUTIN: 'Prediction of residual stresses of repaired austenitic stainless steel welded joints', *Proceedings of the 14th International Seminar "Numerical Analysis of Weldability"*, 21 - 24 September, Graz - Castle Seggau, Austria, 2025.

# AN AUTOMATIC ANISOTROPIC MESHING ALGORITHM ADAPTED TO THE MULTIPHYSICS SIMULATION OF A TUNGSTEN INERT GAS WELDING ARC

S. GOUNAND*

**Université Paris-Saclay, CEA, Service de Recherche en Matériaux et procédés Avancés (SRMA), 91191, Gif-sur-Yvette, France, https://orcid.org/0000-0003-3058-5735, stephane.gounand@cea.fr*

*DOI 10.3217/978-3-99161-089-2-036, license CC BY 4.0*
*https://creativecommons.org/licenses/by/4.0/deed.en*
*This CC license does not apply to third party material and content noted otherwise.*

## ABSTRACT

In the context of the multiphysics numerical simulation of arc welding using finite elements, meshing difficulties are often encountered. Indeed, the geometry of welding tools and of the parts to be joined can be quite intricate. Also, the multiphysics model can introduce more constraints on the mesh such as maximal layer thickness for cathodic and anodic layers. Fluid mechanics may also trigger boundary layers in the physical solution. Moreover, as multiphysics frequently involve many physical unknowns per mesh node, it is important to keep the number of mesh elements under control to ensure feasible computations. This contribution presents a meshing algorithm based on the construction of a tensor field of the desired mesh size by metric interpolation, which is then fed into an automatic anisotropic mesher and a multiphysics model of the Tungsten Inert Gas (TIG) welding arc.

Keywords: Multiphysics simulation of TIG welding, Anisotropic meshing, Metric interpolation, Cast3M software

## INTRODUCTION

In the context of the multiphysics numerical simulation of arc welding using finite elements, meshing difficulties are often encountered due to the following facts:

- welding tools can have complex geometric shapes, as can the parts to be joined;
- the multiphysics model may impose maximum size constraints on certain parts of the mesh, particularly at the interfaces. For example, the surfaces of the electrodes may

host a cathodic and anodic layer model of a certain thickness and, more generally, thin boundary layers can be present in the fluid model's solutions;
- the multiphysics model may involve many physical unknowns. In order to ensure a reasonable computation time, it is important to control the number of mesh elements.

Thus, we wish to devise a meshing algorithm with the following properties:

- Simplicity: the mesh construction should be automated and necessitate few user input data;
- Size control: particularly in the vicinity of the boundaries and interfaces;
- Anisotropy: in order to limit the number of mesh elements.

In order to meet these requirements, we adopt the following strategy for a typical computation:

1. Initial volume and surface meshing;
2. **Computation of a suitable anisotropic metric tensor $M$ via interpolation**;
3. Anisotropic remeshing of the initial mesh according to the $M$-metric;
4. Loop to 2. if necessary;
5. Numerical simulation;
6. Post-treatment.

The focus of this contribution is step 2. The other steps are prerequisites that we do not discuss at length here. In particular, anisotropic remeshing is a rather non-standard and delicate step. The particular algorithm we use is due to Coupez and co-workers [1]. It works with simplex (triangular or tetrahedral) meshes. Another possibility is to use the open-source MMG3D library [2].

The essence of anisotropic remeshing is to optimize the mesh elements' shape according to a quality criterion depending on a given metric $M$. Herein, we use the following quality criterion $Q$ for a particular simplex $T$:

$$Q(T, M) = c_0 \parallel T \parallel_M / h_M^n$$

where $c_0$ is a normalization constant, $\parallel T \parallel_M$ is the surface (volume) of the simplex $T$ in the given metric $M$, $h_M$ is the mean edge length of $T$ and $n$ is the space dimension. The $Q$ criterion takes value 1 for a regular element and 0 for a degenerate flat element. See [1] for details.

In the following, we first detail the computation of the metric tensor $M$ and then provide examples, first on simple test cases and then on more representative examples from the field of multiphysics welding simulations.

## METRIC TENSOR COMPUTATION

Given a $n$-dimensional domain and its interior and boundary mesh, we want to compute a metric tensor field in the interior of the domain following the requirements:

1. the field variation is smooth on the domain;

2. the field is consistent with the tangential metric tensor (size) of the boundary elements, except when these are allowed to be remeshed;
3. one can prescribe the mesh size in the direction normal to the boundary if desired.

We recall that our goal here is not to describe a complete meshing algorithm. We suppose that we have an anisotropic meshing algorithm at our disposal, cite Coupez, called the mesher in the following. Here we wish to determine a metric, which is a symmetric positive definite (SPD) tensor field, typically defined on the mesh vertices, as a suitable input parameter for the mesher.

## METRIC TENSOR INTERPOLATION

Our problem can be categorized as an SPD tensor interpolation problem. This problem is not trivial. Indeed, it is known [3] that just interpolating the Cartesian components of the tensor is generally not advisable: the interpolate is still a symmetric tensor but it can lose positivity and its invariants (trace, determinant) can vary wildly. More generally, this interpolation is not frame-invariant which goes against tensoriality.

Here we use the so-called Log-Euclidean framework which was initially devised in the context of MRI imaging for interpolation of SPD diffusion tensor [3]. It consists in taking the log of the SPD tensor, interpolating the Cartesian components of this symmetric, but not positive, log tensor, and then going back to SPD via exponentiation. The log of an SPD tensor is a well-defined operation which consists in:

- compute an eigen decomposition of the tensor: $M = ODO^t$;
- take the log of its positive eigenvalues: $\widehat{D}_{ii} = \log D_{ii}$;
- recompose: $\widehat{M} = O\widehat{D}O^t$.

Exponentiation of a symmetric tensor is the same process with exp instead of log.

In this decomposition, $O$ is a unit orthogonal tensor the columns of which are the principal directions (unit vectors). $D$ is a diagonal tensor whose elements are the eigenvalues, which are the corresponding directional size squared. $\widehat{D}$ are the log of these sizes. $\widehat{M}$ and $M$ thus share the same principal directions.

The Log-Euclidean framework has the advantage of being simple to work with, necessitating only local eigen decompositions of tensor besides linear interpolation, but it is still not totally frame-invariant [3]. However, beyond simplicity, it has a number of desirable properties like invariance with respect to rotation and contraction-dilation and generally gives results that are close to fully frame-invariant (Riemannian) non-linear frameworks. These properties are deemed "good enough" for our meshing purposes.

Then, interpolating in the Log-Euclidean framework consists in solving $n(n+1)/2$ Laplace equations for the $n(n+1)/2$ components of the $n$-dimensional symmetric Log tensor. Solving Laplace equations ensures requirement 1 (tensor field variation smoothness) due to its gradient-minimization property [4].

We still have to devise suitable boundary conditions that comply with requirements 2 and 3 for these Laplace problems: this is the focus and main contribution of this work.

## BOUNDARY CONDITIONS

We partition the boundary according to the following boundary conditions (BC):

- **Neumann BC (NBC)**: no size requirements are given. On this part of the boundary, the mesh can be modified (refined or coarsened) by the mesher;
- **Normal Dirichlet BC (NDBC)**: only the normal component of the metric tensor is constrained in accordance with a normal size scalar field $d_{\mathbf{n}}$ **prescribed by the user**. It reads: $\boldsymbol{n}^t M \boldsymbol{n} = d_{\boldsymbol{n}}$. This leads to a linear constraint on the tensor components at each node on this part of the boundary. This linear constraint is prescribed using the Lagrange multiplier method. On this part of the boundary, the mesh can also be modified by the mesher;
- **Tangential Dirichlet BC (TDBC)**: only two tangential components of the metric tensor are constrained in accordance with the boundary's surface metric tensor eigen decomposition. This leads to $(n-1)$ linear constraints on the tensor components at each node on this part of the boundary. On this part of the boundary, no input other than the boundary mesh is needed. We choose that this part of the boundary mesh will not be modified by the mesher;
- **Normal and Tangential Dirichlet BC (NTDBC)**: is a combination of the previous two. This leads to $n$ constraints per node. We choose not to modify this part of the boundary.

As an alternative to NTDBC, we can also use the more stringent:

- **Full Dirichlet BC (FDBC)**: all the components of the metric tensor (principal directions and corresponding principal eigenvalues, i.e., directional size squared) are prescribed. This corresponds to prescribing all the $n(n+1)/2$ components.

## IMPLEMENTATION

We have implemented the given tensor interpolation algorithm in our in-house open-source Finite Element Toolbox Cast3M [5]. Note that the Cast3M software is free to download for research and education purposes.

In implementing our algorithm for metric tensor computation, we remarked that the computed tensor field gives correctly sized elements but their principal directions are not necessarily parallel to the boundaries (see figure 1 left). This is expected since the BCs other than Full Dirichlet do not enforce this property. However, alignment is a desirable mesh property to have. We thus implement the algorithm as a two-pass process:

- Pass 1: tensor interpolation with loose BCs (all except Full DBC);
- Pass 2: using the result of pass 1, redo the tensor interpolation with Full Dirichlet BCs on the entire boundary.

Loosely speaking, the first pass builds a metric tensor that conforms to the BCs given by the user and correctly interpolates the element sizes. The second pass then enforces all the principal directions respecting the sizes obtained in pass 1.

We then obtain the result of Fig. 1 (right) where only TDBC were used in pass 1 (left). This result is deemed satisfactory.

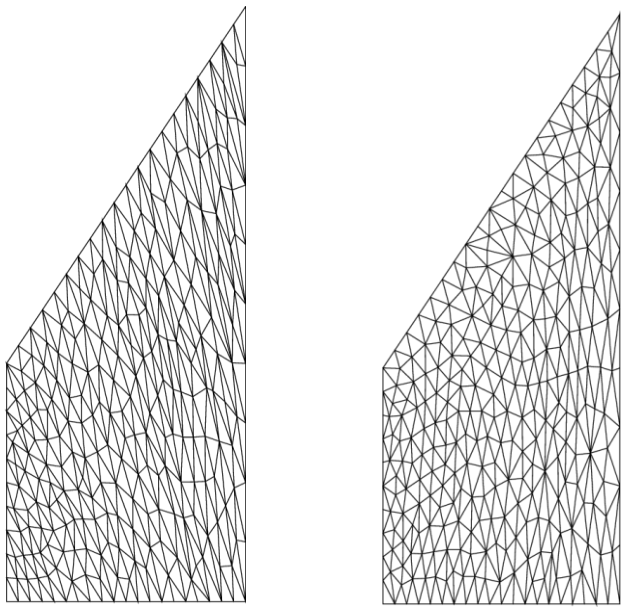


**Fig. 1** Mesh of a quadrilateral non-regular object. The boundary conditions are TDBC only which means that only the meshed contour was provided by the user. Mesh after pass 1 of the tensor interpolation process (left). Mesh after pass 2 of the tensor interpolation process (right).

Note that the algorithm has the advantage of requiring very few inputs from the user: an initial mesh and an optional normal size scalar field on the boundary. Thus, complex anisotropic 3D meshes could be built from the main outline of the mesh (in the form of meshed edges) together with some well-chosen scalar normal-size fields on (part of) the edges and faces which is quite convenient.

On the minus side, the algorithm is a bit costly because we have to solve a tensorial PDE with $n(n+1)/2$ unknowns and complex from the programmer's point of view because we rely on anisotropic remeshers.

## TEST CASES

We now demonstrate the use of the aforementioned anisotropic meshing algorithm in simple 2D and 3D case.

2D

This first test case illustrates the use of the algorithm for anisotropic meshing of a $1 \times 1$ square. Figure 2 illustrates the boundary conditions that were prescribed:

- the left boundary is regularly meshed with 10 elements. It is subject to a Neumann BC and will be remeshed;
- the top and right boundary are regularly with 10 elements. On these boundaries, we ask for a size in the normal direction of 0.1. They are subject to a full Dirichlet boundary conditions and will not be remeshed;
- the bottom boundary is meshed in a geometrical fashion from a size of $5.10^{-3}$ (left edge) to a size of 0.1 (right edge). On the first left half of the boundary, we apply a full DBC with a prescribed normal size of $5.10^{-3}$. On the second right half, a tangential DBC is kept.

Figure 3 illustrates the mesh we obtain. It satisfies all prescribed boundary conditions and its quality according to the anisotropic $Q$ criterion given before is good and above 0.62 for all elements.

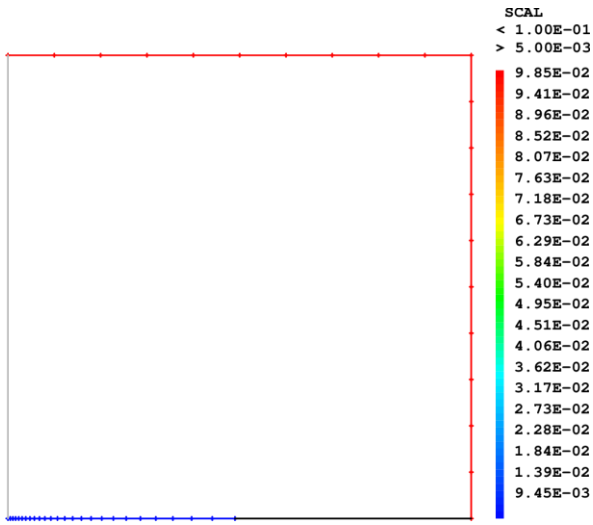



**Fig. 2** Square case: boundary conditions for the tensor interpolation problem

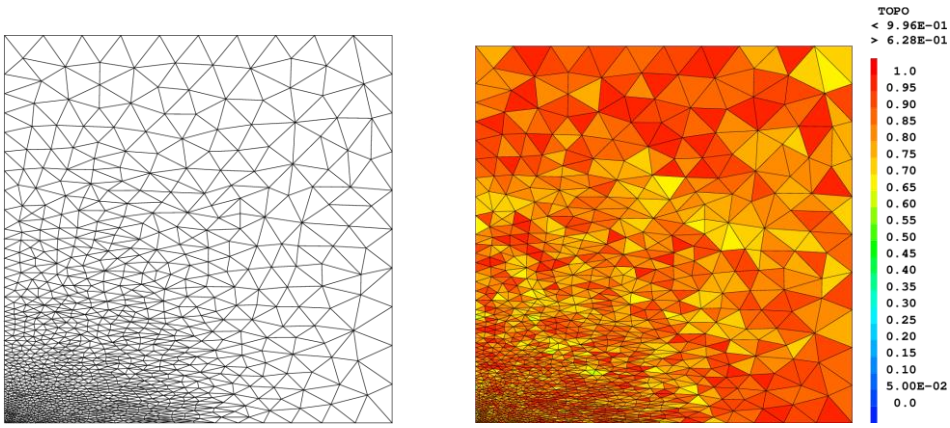



**Fig. 3** Square case: mesh (2000 elements) and element quality

3D

This case is similar to the previous one and illustrates the anisotropic meshing of a $1 \times 1 \times 1$ cube. Figure 4 illustrates the boundary conditions that were applied:

- the two front faces are subjected to a Neumann BC and will be remeshed;
- the top and two rear faces are regularly $5 \times 5$ meshed. On these boundaries, we ask for a size in the normal direction of 0.2. They are subject to a full Dirichlet boundary conditions and will not be remeshed;
- the bottom face is meshed in a geometrical fashion from a size of $5.10^{-3}$ (bottom front point) to a size of $0.2$ (other points). Points at a distance less than 0.75 from the bottom front point are subject to a full DBC with a prescribed normal size of $10^{-2}$ in the up direction. On the rest of the face, a tangential DBC is kept.

Figure 5 illustrates the mesh we obtain. It satisfies all prescribed boundary conditions and its quality according to the anisotropic $Q$ criterion given before is above $0.44$ for all elements. Such a value is lower than the one obtained in 2D but it is typical for 3D.

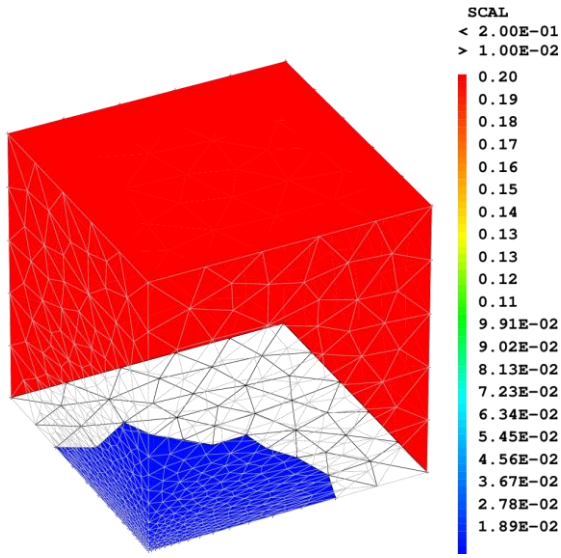



**Fig. 4** Cube case: boundary conditions for the tensor interpolation problem

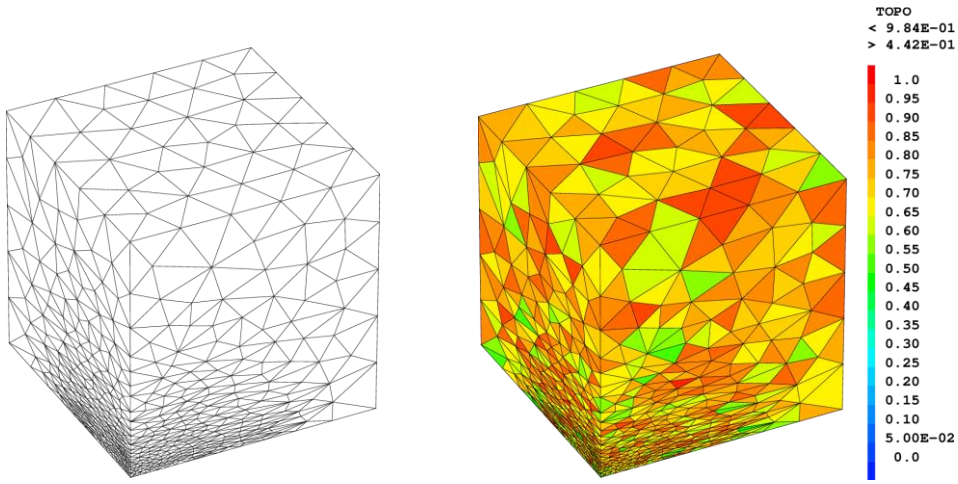



**Fig. 5** Cube case: mesh (8646 elements) and element quality

## APPLICATION TO TIG PLASMA COMPUTATIONS

We now demonstrate the use of the anisotropic meshing algorithm in the context of multiphysics plasma TIG simulation in typical 2D axisymmetric and 3D case.

## 2D AXISYMMETRIC

On figure 6, we display a typical 2D axisymmetric TIG spot situation. On the left side is the axisymmetric TIG tungsten cathode inside a hollow welding nozzle. The bottom side is the anode (work piece).

The boundary conditions are as follows:

- the right and top right boundary are meshed as shown and subject to full DBC with a desired normal size of 1 cm;
- the bottom boundary is subject to full DBC with a desired normal size of 0.4 mm;
- the cathode tip is subject to full DBC with a desired normal size of 0.1 mm;
- the part of the axis between the cathode and the anode is subject to a Neumann BC and will be remeshed;
- the rest of the boundary is given and will not be remeshed (tangential DBC).

The resulting mesh is shown in figure 7. It satisfies all the requirements while keeping a low number of elements (3500). The quality is good with minimum of the criterion similar to the simple square case.

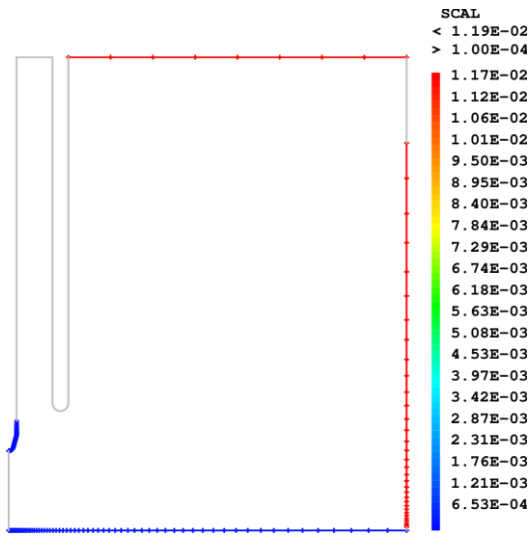



**Fig. 6** Plasma TIG spot mesh: boundary conditions for the tensor interpolation problem

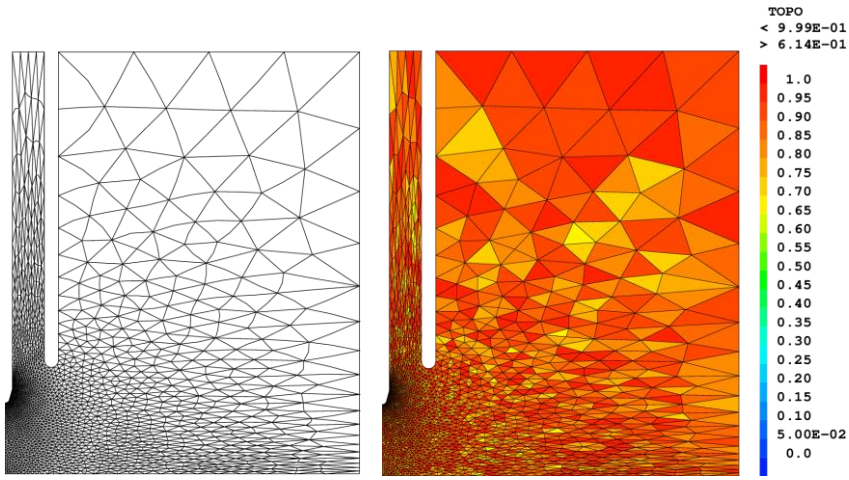
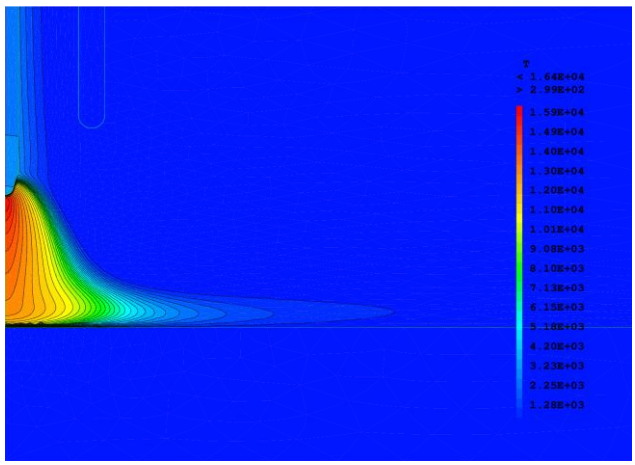



**Fig. 7** Plasma mesh: 3529 elements and element quality

Next, in order to confirm that the obtained mesh is suitable for multiphysics plasma TIG Spot simulations, we carry out a typical computation. We do not describe the plasma model in any detail, referring to the literature instead [6], [7], [8]. Figure 8 shows typical results for the temperature and velocity field. More detailed post-treatment, not shown here, confirm that the field are smoothly interpolated all over the domain, even in the high-gradient regions.



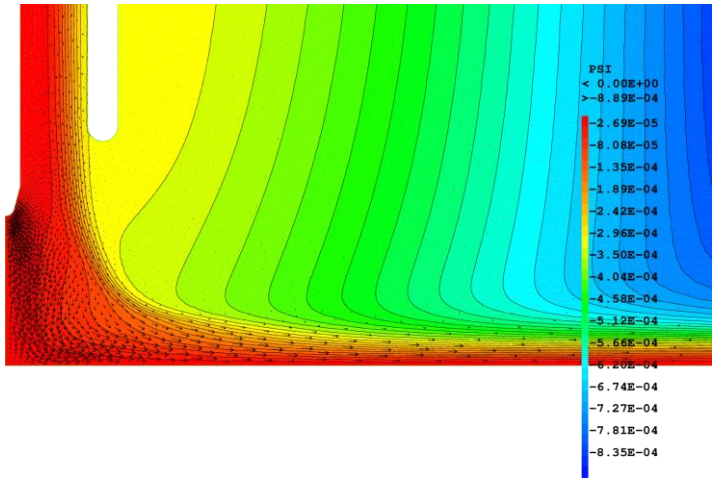



**Fig. 8** Plasma computations: temperature (top, in K) and velocity (bottom, max=148 m/s)

## 3D MESH ENHANCEMENT

Our final example illustrates the use of our anisotropic meshing methodology for 3D case of a work piece with a chamfer. The initial mesh of 54000 elements is shown on figure 9 (left). It is an isotropic mesh designed with a commercial software. We see that the mesh is quite regular. However, near the cathode tip and the facing part of the work piece, it is still too coarse.

Thus, we use our anisotropic method to remesh the plasma part of the mesh in order to ensure the boundary conditions pictured on the right of figure 9:

- the two front faces are subjected to a Neumann BC and will be remeshed;
- the top and two rear faces are subject to a Tangential Dirichlet BC and will not be remeshed;
- on the cathode tip, a normal size of 0.1 mm is required with full Dirichlet BC while on the anode part facing the tip, a normal size of 0.4 mm is thought for. The remaining part of the bottom face is kept with a TDBC.

The resulting mesh is shown in figure 10. It satisfies the given requirements near the cathode tip while keeping the number of elements to an acceptable figure (+17000). The quality is good with a minimum of the criterion similar to the simple cube case: 0.46.

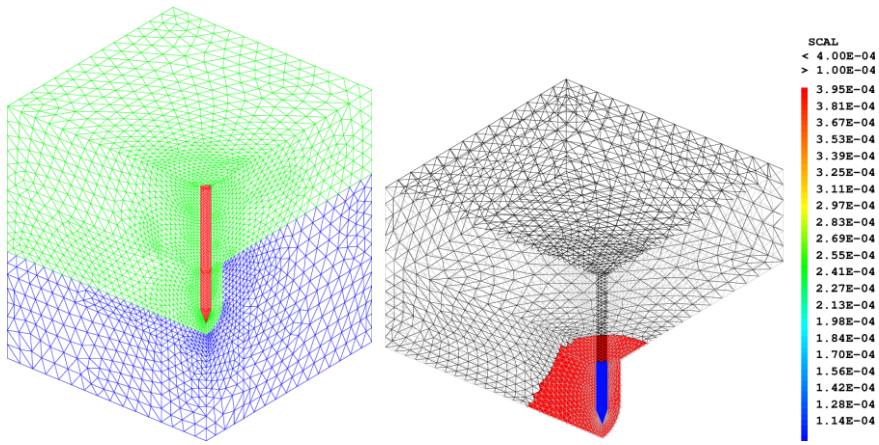



**Fig. 9** Chamfer case: initial mesh (left: 54000 elements) and boundary conditions for the tensor interpolation problem. (right)

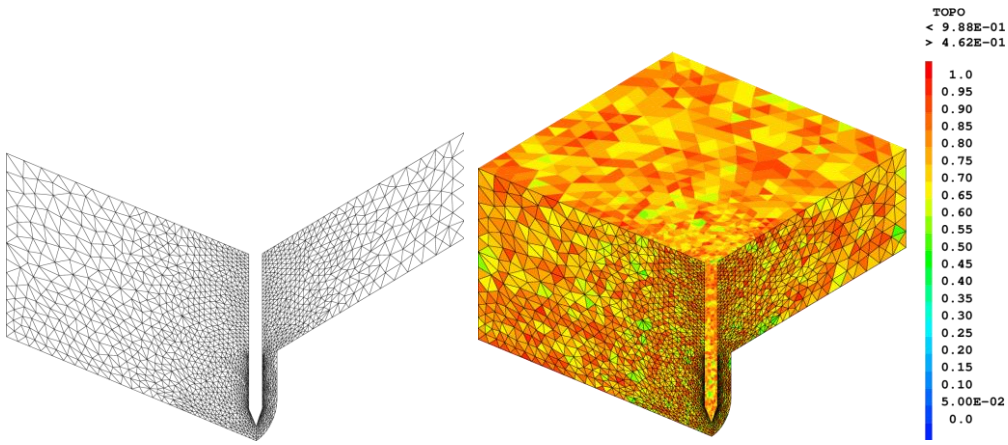



**Fig. 10** Chamfer case: front faces of the refined anisotropic mesh (left: 71000 elements) and element quality

Note that, due to the boundary conditions that we used on the plasma part, the cathode and anode meshes are still conforming with the plasma mesh and need not be remeshed. TIG plasma simulations on the refined mesh are left for future work.

## CONCLUSION

In this contribution, we have described a generic user-friendly anisotropic meshing tool. It is implemented in a software, Cast3M, which is open-source and free to use for educational and

research purposes. It was demonstrated on some examples that the method is useful for dealing with problems in the field of the numerical multiphysics modeling of welding: anisotropy allows to keep the number of mesh elements under control, while taking into account the geometric constraints of the TIG plasma MHD model.

We have shown here that our methodology is most useful for creating a one-shot anisotropic mesh in an easy manner. However, some of the ideas concerning geometric constraints and tensor interpolation carry out to the adaptive mesh refinement case and we wish to pursue research in this direction.

## ACKNOWLEDGMENTS

I thank Morgane Guilbert, International Welding Technologist, who provided some of the momentum needed for this research work.

## References

[1] C. GRUAU and T. COUPEZ: '3D tetrahedral, unstructured and anisotropic mesh generation with adaptation to natural and multidomain metric', *Computer Methods in Applied Mechanics and Engineering*, Vol. 194, No. 48, pp. 4951-4976, 2005, available: https://www.sciencedirect.com/science/article/pii/S0045782505000745.

[2] C. DAPOGNY, C. DOBRZYNSKI and P. FREY: 'Three-dimensional adaptive domain remeshing, implicit domain meshing, and applications to free and moving boundary problems', *Journal of Computational Physics*, Vol. 262, pp. 358-378, 2014, available: https://www.sciencedirect.com/science/article/pii/S0021999114000266.

[3] V. ARSIGNY, P. FILLARD, X. PENNEC and N. AYACHE: 'Log-euclidean metrics for fast and simple calculus on diffusion tensors', *Magnetic Resonance in Medicine*, Vol. 56, No. 2, pp. 411-421, Jun. 2006, available: http://dx.doi.org/10.1002/mrm.20965.

[4] S. GOUNAND and S. KUDRIAKOV: 'Introduction to the finite element method applied to incompressible fluid mechanics', *ENSTA ParisTech*, France, p. 132, Jan. 2016, available: https://hal.science/hal-04108255.

[5] *Cast3M Website*, 2025, available: https://www-cast3m.cea.fr/.

[6] M. TANAKA, H. TERASAKI, M. USHIO and J. J. LOWKE: 'A unified numerical modeling of stationary tungsten-inert-gas welding process', *Metallurgical and Materials Transactions A*, Vol. 33, No. 7, pp. 2043-2052, Jul. 2002, available: http://dx.doi.org/10.1007/s11661-002-0036-2.

[7] M. BROCHARD: *Modèle couplé cathode-plasma-pièce en vue de la simulation du procédé de soudage à l'arc TIG*, PhD thesis, 2009, available: http://www.theses.fr/2009AIX11006.

[8] C. NAHED, S. GOUNAND and M. MEDALE: 'A numerical study of the effects of cathode geometry on tungsten inert gas type electric arcs', *International Journal of Heat and Mass Transfer*, Vol. 182, p. 121923, 2022, available: https://www.sciencedirect.com/science/article/pii/S0017931021010280.

# LARGE-SCALE NUMERICAL ANALYSIS OF MULTI-PASS WELDING USING AUTOMESH AND IDEALIZED EXPLICIT FEM

W. WANG*, S. SASAKI*, S. MAEDA*, K. IKUSHIMA*, M. SHIBAHARA*

**Graduate school of engineering, Osaka Metropolitan University, Japan*

*DOI 10.3217/978-3-99161-089-2-037, license CC BY 4.0*
*https://creativecommons.org/licenses/by/4.0/deed.en*
*This CC license does not apply to third party material and content noted otherwise.*

## ABSTRACT

This study introduces a numerical framework that combines the highly efficient automatic mesh generation system, Automesh, with the Idealised Explicit Finite-Element Method (IEFEM) to enable large-scale thermo-elastic–plastic analyses of multi-pass welding. Automesh converts engineering parameters into graded, analysis-ready meshes while enforcing equal unit heat-input density per pass and consistent element quality and pass placement across cases, thereby ensuring fair comparisons. IEFEM employs a dynamic-explicit formulation with local (node/element-level) updates, substantially reducing memory usage and runtime and admitting efficient GPU parallelisation. Two parametric campaigns on X-groove and V-groove joints deliver pass-resolved, time-accurate fields of temperature, stress, and strain. Within the investigated ranges, groove depths near half the plate thickness minimised deformation; decreasing groove angle reduced accumulated lineal heat input and thus deformation; and root gap showed little effect for $g = 1 \sim 10$ mm. Discrete jumps in angular distortion were traced to changes in the number of passes within a dominant height band, which placed sub-passes near the peak of an empirical $Q/h_{\max}^2$ response. Automesh reduced meshing from hours to under 10 seconds per case, and IEFEM cut solution time by roughly an order of magnitude versus representative implicit baselines, yielding an efficient and reliable workflow for industrial studies and database construction.

Keywords: large-scale welding simulation; idealized explicit finite element method; automatic mesh generation; thermo-elastic-plastic analysis; multi-pass weld joints; transverse shrinkage; angular distortion

## INTRODUCTION

Welding is indispensable for the fabrication of a wide range of industrial products and large-scale structures. However, a highly concentrated moving heat flux causes severe thermal and mechanical loading in thick plates and massive components of multi-pass welding. After completion of the weld, substantial residual stresses and geometric distortions may

accumulate, jeopardising structural integrity and dimensional accuracy [1]. To optimise the manufacturing route and guarantee product quality, it is essential to predict the transient temperature field produced by the moving heat source together with the stress and displacement fields it induces [2]. Conventional thermo-elastic-plastic analyses based on static implicit finite-element methods encounter significant challenges in this task because strongly nonlinear molten regions travel through space and time, forcing extremely fine meshes and iterative solvers that inflate run-time and memory demand [3].

To overcome these limitations, we have developed the Idealised Explicit Finite-Element Method (IEFEM) [4]. IEFEM is rooted in a dynamic explicit FEM framework [5] but is specialised for transient welding phenomena. By adopting an explicit time-integration scheme and confining calculations to element- and node-local operations, IEFEM eliminates the global iterative solvers required by implicit schemes while preserving accuracy virtually equivalent to the static implicit formulation. The local-operation architecture dramatically suppresses memory usage and accelerates computation. Moreover, it is well-suited to massive parallelisation on graphics processing units (GPUs). With recent advances in GPU hardware and parallel algorithms [6-8], three-dimensional moving heat-source analyses of multi-pass weld joints - long deemed infeasible - can now be executed relatively easily [9]. Thus, IEFEM constitutes one of the two central numerical pillars that enable the ultra-large-scale simulations presented in this study.

Mesh generation represents a second bottleneck. Generic mesh generators such as Triangle [10], TetGen [11], Gmsh [12], and the CGAL library [13] have progressed from two-dimensional to fully automatic three-dimensional meshing and now integrate CAD interfaces with post-processing capabilities; nevertheless, accurately treating weld-specific complexities - root geometry, reinforcement, and the heat-affected zone (HAZ) - still demands bespoke scripts and meticulous parameter tuning. Early welding-oriented studies, exemplified by Lindgren's classical thermo-mechanical analyses [14], the theoretical framework of Goldak and Akhlaghi [1], and the multi-pass pipe simulation by Ikushima and Shibahara [15], likewise relied on expert-guided model construction and mesh adaptation, limiting their scalability to large industrial problems. More recently, adaptive subdivision techniques - such as the selective-integration adaptive mesh refinement proposed by Huang and Murakawa [16] and the octree-based scheme of Chen *et al.* [17] - have been introduced. Yet, their configuration remains intricate, and they have not achieved widespread generalisation. Industry practitioners, therefore, continue to emphasise the inherent limits on reproducibility and lead time imposed by manual modelling workflows [18].

In this study, we have developed Automesh, an automated meshing system that parameterises variables such as the bead width, groove angle, reinforcement height, and other engineering variables. Automesh automatically divides each bead into layers and each layer into passes according to aspect-ratio criteria and locally refines the mesh in regions prone to poor element quality, such as the root and HAZ. By seamlessly integrating Automesh for preprocessing with IEFEM for calculation, the present research achieves full automation from model creation to solution execution. Compared with conventional practices, overall throughput is accelerated by two to three orders of magnitude, and both mesh quality and labour requirements are simultaneously reduced. The resulting reduction in turnaround time

shortens the iterative loop of design, analysis and quality assurance, thereby lowering the lead time and cost of bringing welded products to market.

## OUTLINE OF THE IDEALISED EXPLICIT FEM

The Idealised Explicit Finite-Element Method (IEFEM) reformulates the dynamic-explicit FEM so that quasi-static thermo-elastic-plastic welding problems can be solved with minimal run-time and memory while preserving implicit-level accuracy [5]. It executes large-scale multi-pass or assembly-welding simulations through the following cycle (Fig. 1):

I. Incremental equilibrium cycle
At every time step, the solver performs three operations:

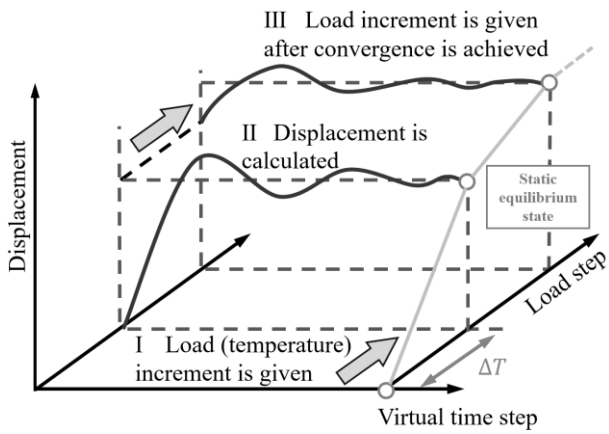



**Fig. 1** Concept of Idealised Explicit FEM

- Load (temperature) increment is given: A new thermal or mechanical increment $\Delta T$, $\Delta F$ is imposed and held constant.
- Displacement calculation: Nodal displacements are advanced using the explicit update.

$$\left(\frac{1}{\Delta t^2}[M]+\frac{1}{2\Delta t}[C]\right)\{U\}_{t+\Delta t}=\{F\}_t-\sum_{e=1}^{N_e}\int_{V^e}[B]^T\{\sigma\}dV$$
$$-\frac{2}{\Delta t^2}[M]\{U\}_t-\left(\frac{1}{\Delta t^2}[M]-\frac{1}{2\Delta t}[C]\right)\{U\}_{t-\Delta t} \quad (1)$$

where $[M]$, $[C]$, $[B]$ and $\{\sigma\}$ denote the mass, damping, strain-displacement and stress terms, respectively; $\{U\}$ and $\{F\}$ are the displacement and load vectors, $N_e$ the number of elements, and $V_e$ the volume of element $e$.

- Next increment after convergence: When equilibrium is achieved, the solver returns to step 1 for the next $\Delta T$, $\Delta F$.

II. Diagonal mass and damping: Instead of retaining full, coupled matrices, IEFEM lumps both the mass and damping terms such that each degree of freedom carries its own independent scalar mass and damping value. The mass assigned to each node is chosen so that a stress wave crosses any element in only a few explicit time steps, making the admissible time-step size almost uniform across the mesh regardless of element size or material. The damping for each node is then set to the "critical" value implied by its local mass and stiffness, which suppresses numerical oscillations as quickly as possible.

   Because these diagonal (one-value-per-DOF) matrices do not create global couplings, the explicit update requires no linear-system solver, significantly reduces memory usage, and lets the analysis proceed with the largest stable time step. Consequently, the result is far fewer iterations before static equilibrium is reached and a substantial reduction in overall run-time.

III. Parallel-computing advantage: Because every update involves only element-local or DOF-local data, the method parallelises efficiently on GPUs: thousands of threads can integrate elements independently, delivering further speed-ups beyond the intrinsic efficiency gains of IEFEM.

## THEORETICAL FRAMEWORK AND WORKFLOW OF AUTOMESH

Automesh builds on the Gmsh kernel [12], supplementing its geometry-independent mesher with welding-specific intelligence that converts engineering parameters directly into a finite-element analysis-ready model. The workflow begins by reading the joint descriptors - groove angle $\alpha$, bevel depth, root gap $g$, number of layers n, number of passes m, target pass aspect ratio, and so on. A consistency check eliminates physically impossible combinations and normalises the parameter set.

The validated parameters are then cast into closed-form expressions that define the two-dimensional weld cross-section. For a V-groove, the upper width at height z is, for example:

$$W(z) = 2(z - z_0 - t_r)\tan\frac{\alpha}{2} + g \tag{2}$$

with $z_0$ the root reference level and $t_r$ the root-face thickness. Using such relations, an optimisation routine subdivides the weld deposit into *n* layers and *m* passes whose thicknesses and widths balance filler-metal volume with heat-input distribution.

For every layer-pass pair, a boundary point cloud is generated, and a physically based envelope is added to represent the heat-affected zone (HAZ). At this stage, the algorithm also assigns region-dependent target element sizes: the weld bead and HAZ receive a finer characteristic length to resolve steep thermal gradients and stress concentrations, whereas the far-field base plate is allocated a coarser length to economise on degrees of freedom. This graded specification is read from a configuration file and propagated automatically through all subsequent meshing steps.

The two-dimensional entities are extruded or revolved to create the three-dimensional solid; axial and circumferential element counts are chosen such that the imposed aspect-ratio and regional size targets are simultaneously satisfied. The resulting volume is passed to Gmsh, which produces a tetrahedral mesh and evaluates each element with the quality measure

$$q(T) = \frac{4\sqrt{3}\cdot \mathrm{Area}(T)}{|e_1|^2+|e_2|^2+|e_3|^2} \tag{3}$$

Elements that fail the threshold trigger local refinement until the entire mesh meets the criterion. Because all geometric descriptions are analytic and the segmentation algorithm operates directly on the parameter set, the computational complexity is reduced from the $O(n^3 \log n)$ typical of conventional scripts to approximately $O(n \times m)$, where $n$ and $m$ are the layer and pass counts.

Finally, Automesh exports the geometry and mesh files together with quality statistics. In practical multi-pass joints, the fully automated pipeline reduces hours of manual modelling effort into a few seconds and delivers a graded mesh that concentrates resolution precisely where the welding physics demand it.

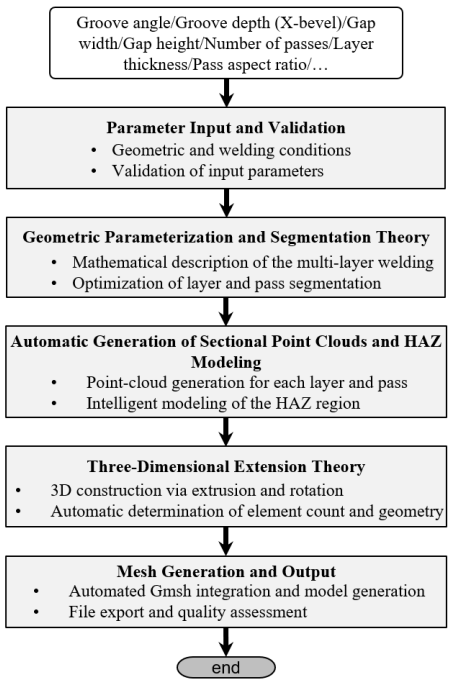



**Fig. 2** Automesh workflow for parameter-based generation of graded finite-element meshes in multi-pass welding

## LARGE-SCALE MULTI-PASS WELDING CASE STUDY USING AUTOMESH AND THE IDEALISED EXPLICIT FEM

This section demonstrates a large-scale multi-pass welding simulation that couples the Idealised Explicit FEM of Section 2 with the Automesh workflow of Section 3. To verify the approach, transverse shrinkage and angular distortion are evaluated while systematically varying key geometric parameters.

### INFLUENCE OF GROOVE DEPTH ON TRANSVERSE SHRINKAGE AND ANGULAR DISTORTION

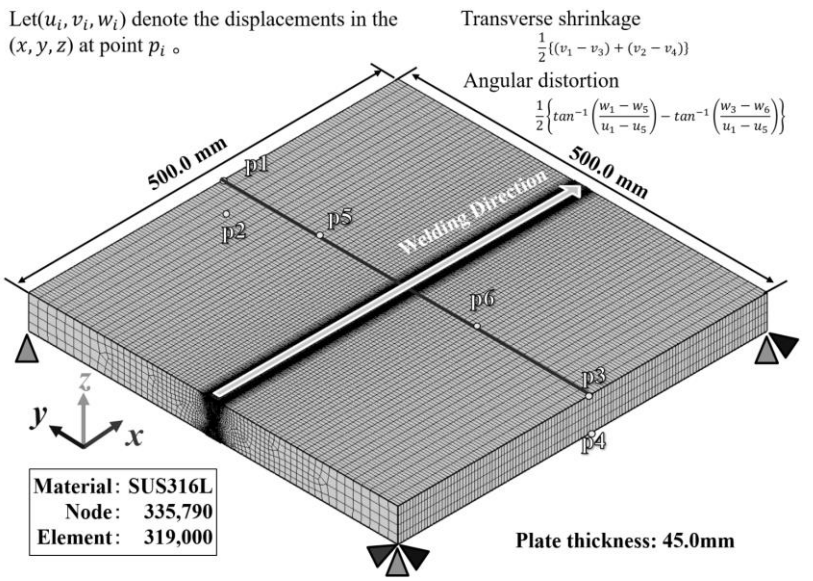



**Fig. 3** Geometry and dimensions of the X-groove multi-layer welding model

Fig. 3 illustrates the model geometry: two SUS316L plates, 500 mm long, 250 mm wide and 45 mm thick, joined by an X-groove weld. Table 1 lists the constant process parameters used throughout - heat-input density $q$, welding speed $v$, root gap $g$, reinforcement height $h_{rein}$and groove angles $\alpha_{top}$ , $\alpha_{bottom}$. The only variable parameter is the upper groove depth $d_{upper}$, which is reduced from 41 mm to 4 mm in twelve discrete steps. Fig. 4 shows the reference case in conjunction with comparative meshes for all groove-depth variants. In all simulations, welding proceeds sequentially from left to right, depositing the upper passes before the lower passes.

The reference model contains 335,790 nodes and 319,000 elements. Temperature-dependent material properties for SUS316L (Fig. 5) are employed. The moving heat source is represented by Goldak's double-ellipsoidal Gaussian distribution, and newly deposited passes are activated dynamically via the element-birth technique.

Fig. 6 presents the transient temperature distribution recorded during the 15th welding pass for the X-groove joint with a groove depth $d_{upper}$ = 24 mm. The snapshot illustrates the operational profile of Goldak's heat source, while the absence of activated elements ahead of the melt front confirms that element-birth activation is functioning correctly.

Fig. 7 demonstrates the temporal evolution of deformation for the reference case, with transverse shrinkage in (a) and angular distortion in (b). The detailed resolution of deformation history highlights that IEFEM is capable of capturing not only the final distortion but also the intermediate accumulation process with both high accuracy and high computational efficiency. Most of the deformation occurs during the heating phase, while the subsequent cooling phase contributes only marginally, confirming that the method enables detailed, physics-based analysis rather than a simplified estimation of distortion.

Fig. 8 presents the peak-temperature contours during the final welding pass for six representative groove depths. In all cases, welding was carried out following an identical sequence - from top to bottom and left to right - such that the final pass was consistently located at the lower-right corner. This consistent sequencing minimizes the influence of pass-order variations and ensures comparability across all models.

The contours further reveal that the size of the molten region exceeding 1500 °C in the final pass varies with groove depth and shows a clear positive correlation with the cross-sectional area of the corresponding pass. This indicates that the Automesh system automatically adjusts the total heat input according to the pass cross-sectional area, thereby maintaining a constant heat-input density per unit area. As a result, the total heat input in each case depends solely on the deposited cross-sectional area and is independent of groove-depth differences. This mechanism effectively constrains the thermal boundary conditions, ensuring that the observed variations in transverse shrinkage and angular distortion arise only from geometric effects rather than inconsistencies in heat input.

The residual transverse stress distribution $\sigma_{yy}$, along the mid-width direction is shown in Fig. 9. Tensile peaks appear immediately adjacent to each weld bead, while a compressive trough develops near the plate centre. The location of maximum compressive stress shifts with groove depth, reflecting the interplay between tensile strains in the fusion zones and compressive contraction in the surrounding base metal.

The transverse shrinkage and angular distortion were evaluated on the mid-length cross-section of the plate; measurement directions are indicated at the top of Fig. 3. Fig. 10 presents the computed deformation results: in both sub-plots the abscissa corresponds to the pass number, whereas the ordinate represents transverse shrinkage in (a) and angular distortion

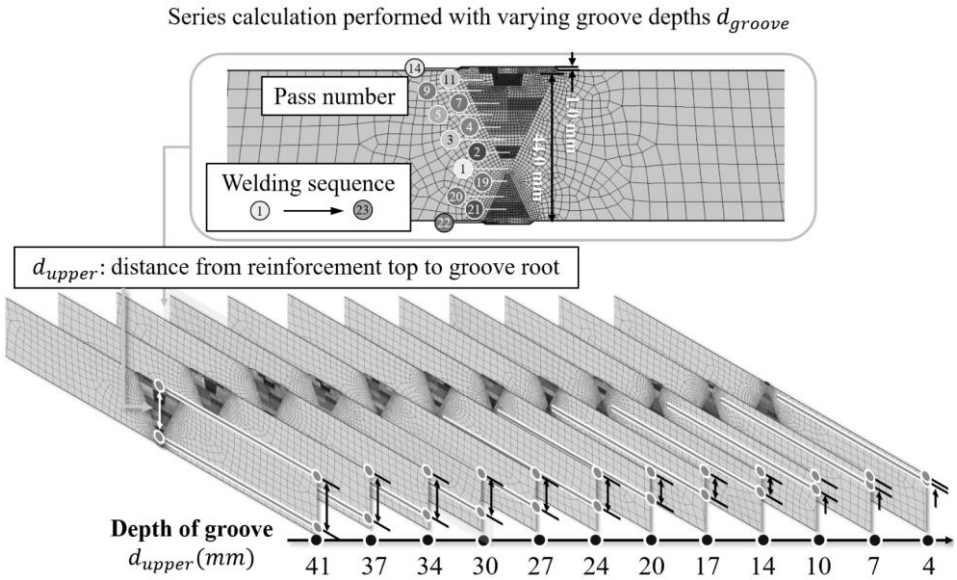



**Fig. 4** Cross-sectional mesh layout and pass sequence, with comparative meshes for the twelve groove-depth cases ($d_{upper}$)

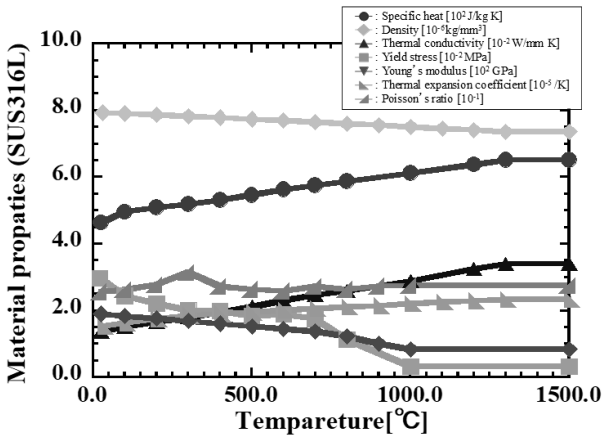



**Fig. 5** Temperature-dependent material properties of SUS316L adopted in the analysis

**Table 1** Geometric dimensions of the model and welding process parameters used in the simulations

| Parameter | Symbol (unit) | Value |
|---|---|---|
| Heat-input density per unit area | $q(W/mm^2)$ | 50.0 |
| Welding speed | $v(mm/s)$ | 3.0 |
| Root gap | $g(mm)$ | 1.0 |
| Reinforcement height | $h_{rein}(mm)$ | 1.0 |
| Groove angle (top side) | $\alpha_{top}(deg)$ | 50 |
| Groove angle (bottom side) | $\alpha_{bottom}(deg)$ | 50 |
| Aspect ratio of passes per layer | — | ≈ 1 : 3 |

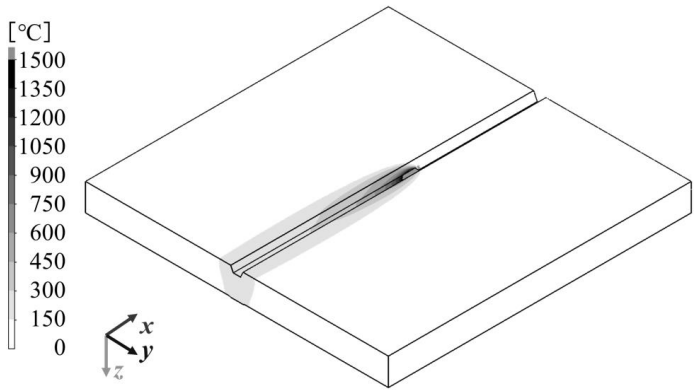



**Fig. 6** Transient temperature distribution recorded during the 15th welding pass for the X-groove joint with the groove depth $d_{upper}$ at 24 mm

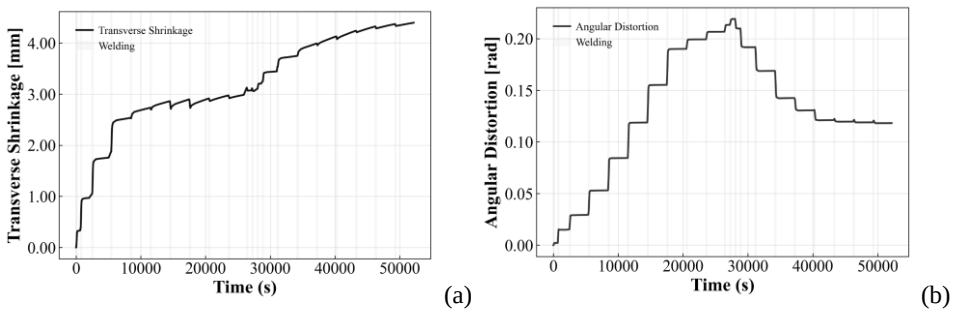



**Fig. 7** Transient deformation history captured of the X-groove joint with a groove depth $d_{upper}$ at 24 mm. (a) transverse shrinkage; (b) angular distortion

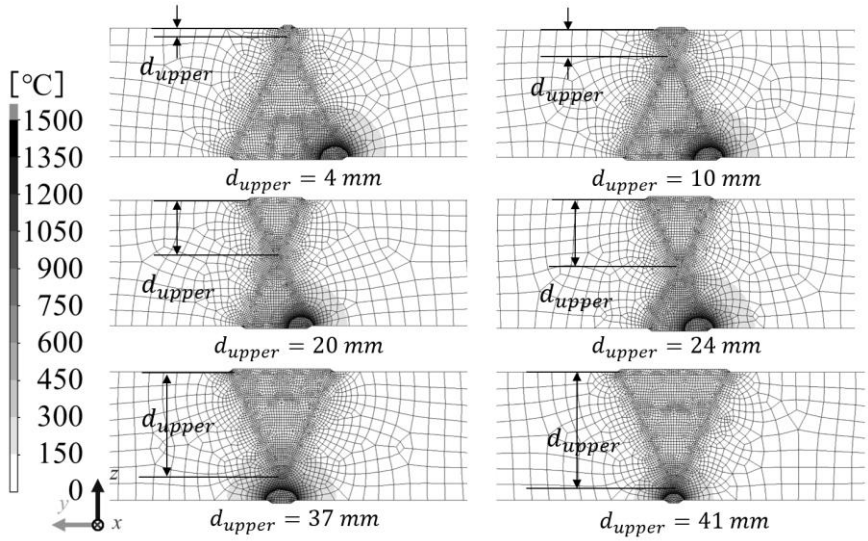



**Fig. 8** Peak-temperature distribution during the final welding pass for X-groove multi-layer joints with varying groove depths $d_{groove}$

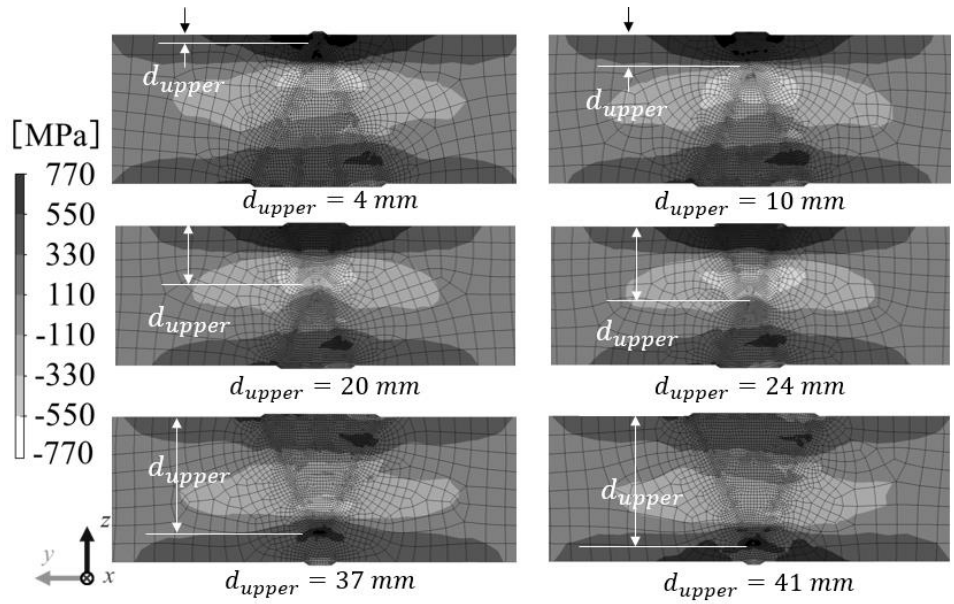



**Fig. 9** Transverse residual-stress distribution (along the plate-width $y$ direction) at the mid-length cross-section during the final welding pass for X-groove multi-layer joints with different groove depths $d$groove $d_{groove}$

in (b). Across the twelve groove-depth cases, the intermediate depth around 24 mm exhibits the smallest shrinkage and distortion, while both the shallowest groove (4 mm) and the deepest groove (41 mm) cases show noticeably larger deformations.

The results suggest that when the upper and lower V-grooves are of comparable size (i.e., the X-groove is approximately symmetric through the thickness), the thermal loading and the associated shrinkage-induced bending moments about the plate mid-surface tend to counterbalance, thereby suppressing overall twist and rotation. Conversely, when the groove geometry becomes markedly asymmetric (a small V opposite a large V), the imbalance of through-thickness bending moments leads to greater an··gular distortion. This trend highlights the strong influence of groove symmetry on the distortion response. Future investigations that incorporate a quantitative evaluation of section resultants - via integration of the through-thickness shrinkage/inherent strain field - or direct comparison with double-sided deposition on a symmetric cross-section could provide deeper mechanistic validation of this interpretation.

For each of the twelve groove-depth cases, Automesh produced the three-dimensional mesh in about 10 secs from parameter input. Replicating the same unit-pass heat input and element quality manually with commercial CAD/CAE software would require at least 30 h even for an experienced analyst. The thermo-elastic-plastic analysis of the 27-pass model (319,000 elements) finished in 8 h 21 min on a single RTX2080 Ti using the Idealized Explicit FEM - approximately one-tenth of the runtime reported for an implicit commercial solver. When the twelve groove-depth cases were distributed across twelve GPUs, the entire pipeline - from preprocessing to results - was completed in less than half a day, underscoring the dramatic improvement in efficiency and throughput achieved by the Automesh in combination with IEFEM workflow.

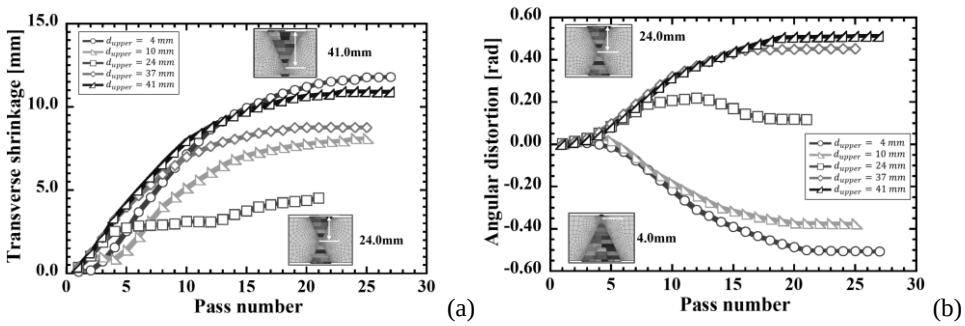



**Fig. 10** Deformation trends with increasing pass number for the twelve groove-depth cases(a)Relationship between transverse shrinkage and pass number(b) Relationship between angular distortion and pass number

## INFLUENCE OF GROOVE ANGLE ON ANGULAR DISTORTION

Fig. 11 depicts the second test configuration: two carbon-steel plates 500 mm × 250 mm × 45 mm are joined by a V-groove weld whose included angle $\alpha$ is the only variable. The unit heat-input density $q$, welding speed $v$, root gap $g$ and reinforcement height $h_{rein}$ are kept identical to those in Table 1, while $\alpha$ is varied from 40° to 70° in 5° increments, yielding seven cases. The upper part of Fig. 12 gives the pass layout and weld sequence for the 70° joint; the lower part juxtaposes the cross-sectional meshes for all groove angles. As in the previous section, welding proceeds from the left edge to the right, depositing all upper passes first and all lower passes afterwards. Because a smaller $\alpha$ narrows the groove opening, the number of passes required to preserve the target aspect ratio decreases, and the final model size converges to roughly one million elements for the 45-pass case.

Fig. 13 shows the transverse residual-stress distributions $\sigma_{yy}$ along the plate-width (y) direction for three representative V-groove cases ($\alpha = 40°, 55°, 70°$) out of the seven analysed. It is evident that as the groove angle increases, the spatial extent of both tensile and compressive stresses widens. Consistent with the X-groove results of the previous section, compressive peaks remain concentrated at the groove root, while tensile stresses dominate near the plate surfaces on either side of the weld.

Fig. 14 summarises the angular-distortion results. (a) traces the cumulative angular distortion against pass number, and (b) relates the angular distortion to pass height (through-thickness position). With element-birth activation and residual stresses fully accounted for, a smaller groove angle not only shortens the pass sequence but also reduces the overall angular distortion. Under the present setting of constant unit heat-input density $q$ and welding speed $v$, narrowing the groove decreases the deposited cross-sectional area and the number of passes required; consequently, the accumulated heat input per unit length of joint is reduced. The lower energy input leads to smaller thermal expansion and plastic flow in the fusion and HAZ regions and, therefore, to a uniformly smaller incremental contribution to angular distortion at a given height (see Fig. 14b). Accordingly, the widest groove ($\alpha = 70°$) - which requires 45 passes and yields the largest mesh - accumulates the greatest net lineal heat input and exhibits the largest angular distortion, whereas the narrowest groove ($\alpha = 40°$) shows the least. While this energy-based interpretation is qualitative, it is consistent with the observed monotonic decrease in angular distortion as $\alpha$ decreases.

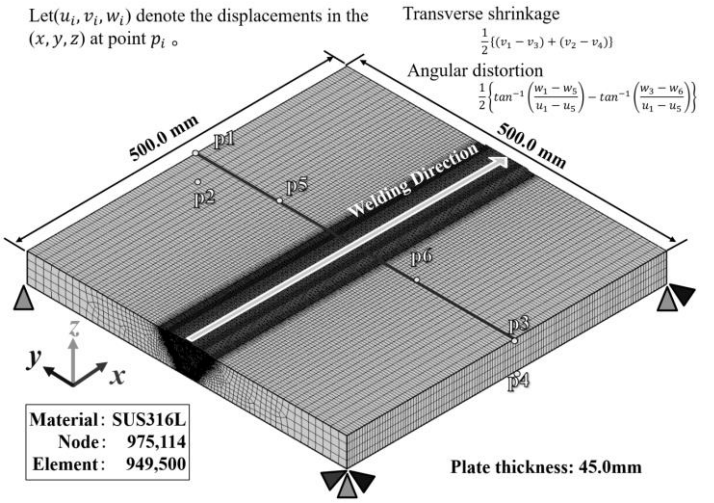



**Fig. 11** Geometry and dimensions of the V-groove multi-layer welding model

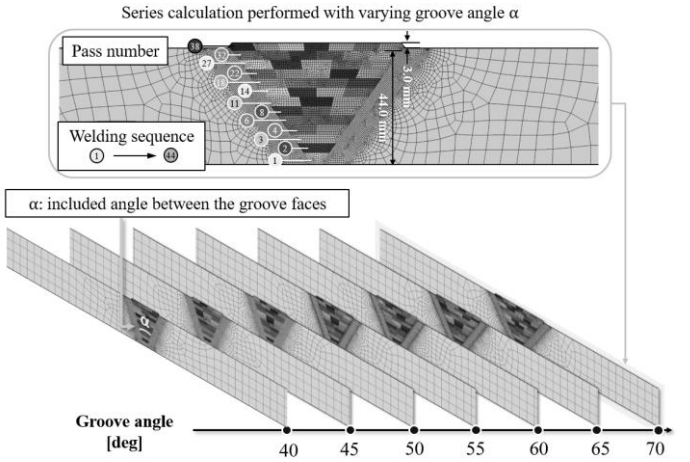



**Fig. 12** Cross-sectional meshes for the seven groove-angle cases (40°-70°) and pass layout for the 70° reference joint

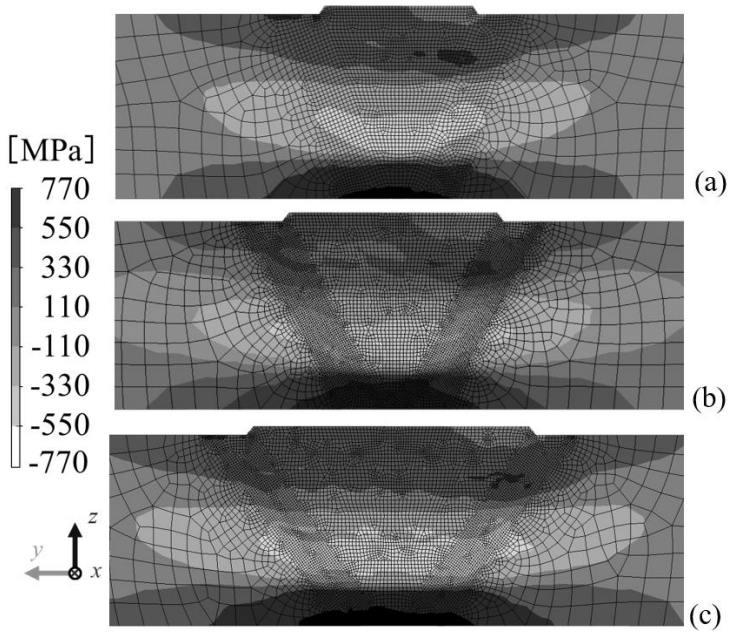



**Fig. 13** Transverse residual-stress distribution (along the plate-width *y* direction) at the mid-length cross-section during the final welding pass for V-groove multi-layer joints with different groove angles $\alpha$ : (a) 40°; (b) 55°; (c) 70°

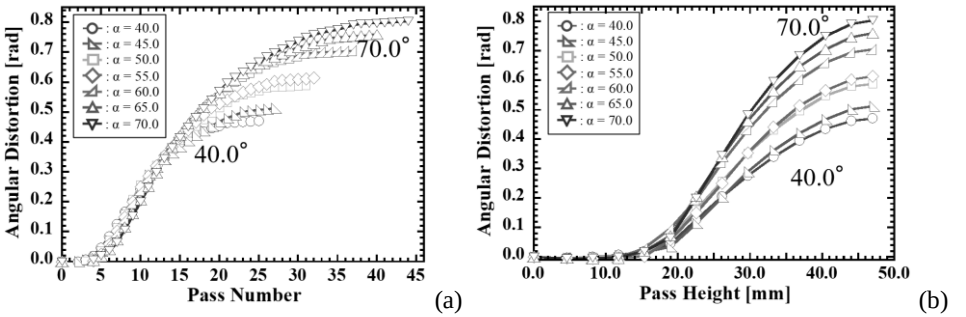



**Fig. 14** Angular distortion for the seven groove-angle cases(a) variation with pass number(b) variation with pass height

## INFLUENCE OF SIMULTANEOUS VARIATIONS IN GROOVE ANGLE AND ROOT GAP: A LARGE-SCALE MULTIVARIATE STUDY WITH AUTOMESH

To assess the industrial versatility of the proposed workflow, a two-parameter investigation was performed on the V-groove joint introduced in the previous section. Both the groove angle $\alpha$ and the root gap $g$ were treated as independent variables, whereas all other geometric and process conditions correspond to those in Table 2. As illustrated in Fig. 15, $\alpha$ and $g$ were independently sampled within the intervals $\alpha \in [40^{\circ}, 70^{\circ}]$ and $g \in [1\,mm,\ 10mm]$, respectively, producing 110 distinct cases. For every case Automesh generated a three-dimensional mesh in approximately 10 s, after which the Idealised Explicit FEM solved the thermo-elastic-plastic problem. The resulting parametric study is of a scale that would be essentially unattainable with manual CAD/CAE workflows.

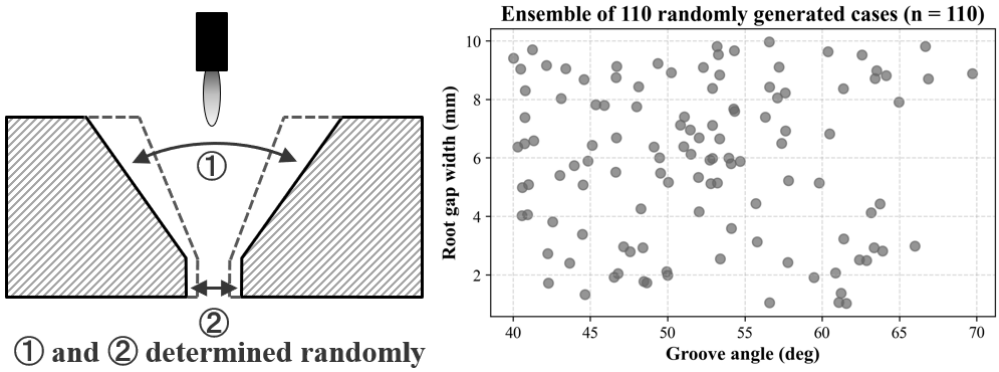



**Fig. 15** Schematic illustration of the V-groove cross-sectional variables and the sampling ranges used in the study

**Table 2** Numerical settings and descriptions of the variable and fixed parameters adopted for the multivariate analysis

| Category | Parameter | Value / Range | Description |
|---|---|---|---|
| Variable Parameters | ①Groove angle | 40.0° - 70.0° | Randomly sampled within this range |
| | ②Root gap | 1.0 mm - 10.0 mm | Randomly sampled within this range |
| Fixed Parameters | Root gap height | 1.0 mm | Constant across all configurations |
| | Layer thickness | First: 4.67 mm<br>Intermediate: 3.67mm<br>Final: 3.00 mm | Fixed by layer type |
| | Number of passes | Closest to aspect ratio 1:3 | Determined to approximate the aspect ratio |
| | Heat input | 50.0 $\mathrm{J/mm^2}$ (proportional to cross-sectional area) | Uniform per pass |
| | Welding speed | 3.0 mm/s (all passes) | Constant across all passes |

Fig. 16 presents the three-dimensional results, where the abscissae are given by α and g, and the ordinates represent (a) transverse shrinkage and (b) angular distortion. The two planes correspond to least-squares regression surfaces fitted to all data points. To isolate individual effects, Fig. 17 plots deformation as a function of root gap alone. No clear correlation is observed for either transverse shrinkage or angular distortion, indicating that within the examined range, root gap is not a dominant factor governing global deformation.

In contrast, Fig. 18 reveals a different trend: when examining the groove angle, both transverse shrinkage and angular distortion increase monotonically with α, with the latter exhibiting two abrupt "jumps." The corresponding groove angles and pass distributions are indicated in the inset diagrams.

To clarify the underlying mechanism, Fig. 19 re-expresses the data in terms of the relationship between the heat input of individual passes and the incremental contributions to transverse shrinkage and angular distortion. The horizontal axis denotes the heat-input parameter, $Q/h_{\max}^2$, while the vertical axes represent (a) the transverse-shrinkage increment and (b) the angular-distortion increment. Here, $h_{\max}$ is defined as the distance from the upper end of each pass to the bottom edge of the base plate. This choice of $h_{\max}$ reflects the fact that transverse shrinkage and angular distortion are evaluated with respect to the plate bottom surface; by treating each pass as equivalent to a bead-on-plate weld located at its corresponding height, $h_{\max}$ serves as a mechanical lever arm that rationally captures the positional dependence of deformation.

The intermediate polynomial fits, determined by the least-squares method, reveal a nonlinear correlation between the heat-input parameter $Q/h_{\max}^2$ and the deformation increments. This trend is consistent with the well-established functional relationship reported in bead-on-plate welding studies, where both transverse shrinkage and angular distortion scale

nonlinearly with $Q/h^2$ [19]. The similarity between the present multi-pass results and classical bead-on-plate data indicates that the empirical framework developed for single-pass welding remains applicable to predicting dominant directional deformations in multi-pass welds. Minor discrepancies between the fitted curves and individual data points are attributable to geometric effects such as the root gap and numerical interpolation procedures; nevertheless, the overall distribution confirms that the bead-on-plate analogy provides a robust physical interpretation for the observed deformation behaviour.

Fig. 20 compares cross-sections immediately before and after the distortion jumps. As illustrated, during the monotonic increase of groove angle, the difference between cases 2 and 3 as well as between cases 5 and 6, is simply that the pass layer marked by the yellow box changes from a single pass to two passes. To ensure equivalent total heat input, the heat input per unit pass area is preserved, meaning that when one pass is split into two, the heat-input parameter $Q/h_{\max}^2$ is equally divided. However, as shown in Fig. 19, angular distortion reaches a local maximum around $Q/h_{\max}^2 \approx 5$. Under this condition, splitting the heat input between two passes instead of one markedly amplifies angular distortion.

Fig. 21 quantifies the consequence of this mechanism. In the critical layer, angular distortion increases from 0.007 rad in the single-pass case (case 5) to a combined 0.035 rad (0.015 + 0.020 rad) in the two-pass case (case 6). This sudden jump arises because splitting the pass redistributes the same heat input into two passes, each with a slightly smaller $Q$, but both still located at small $h_{\max}$. As a result, their $Q/h_{\max}^2$ values remain in the peak region of the distortion–parameter curve (see Fig. 19), producing two relatively large distortion increments instead of one moderate increment. In contrast, when pass subdivision occurs at larger groove angles, the affected passes are located at greater $h_{\max}$, where $Q/h_{\max}^2$ is much smaller and lies within the nearly proportional region of the curve. In this regime, further subdivision reduces distortion smoothly, and no discrete change is observed.

For transverse shrinkage, the trend differs. As shown in Fig. 21(a), the fluctuation is modest - from 1.34 mm to 2.16 mm - compared with the overall shrinkage of approximately 15 mm. This is because transverse shrinkage depends mainly on the integrated contraction volume across the joint width, which varies smoothly with groove geometry. Unlike angular distortion, it does not couple strongly with the through-thickness lever arm represented by $h_{\max}$; thus, even under the same subdivision conditions highlighted in Fig. 20, shrinkage remains continuous without abrupt jumps.

The discrete geometric effects identified here could only be captured because Automesh enforced identical element quality and pass placement across all 110 simulation cases, eliminating meshing bias and ensuring that differences in deformation arose solely from groove geometry. Furthermore, the Idealised Explicit FEM, executed on eight RTX 2080 Ti GPUs, solved all thermo-elastic-plastic models within approximately two weeks - an undertaking that would be prohibitively time-consuming with conventional implicit solvers. This computational efficiency renders the workflow practical for large-scale design-space explorations and enables the generation of high-fidelity datasets well suited for machine-learning applications.

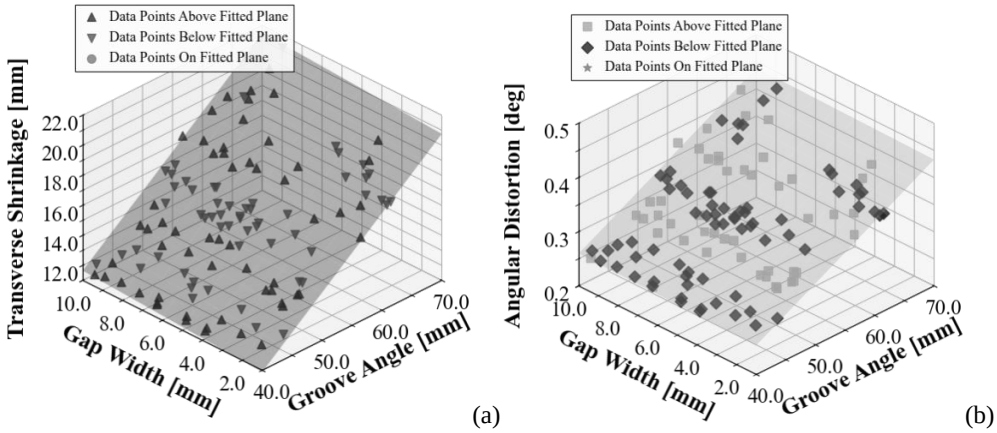



**Fig. 16** Influence of groove angle and root gap on weld-induced deformation in V-groove multi-pass joints(a) Transverse shrinkage plotted against groove angle α and root gap $g$(b) Angular distortion plotted against groove angleαand root gap $g$

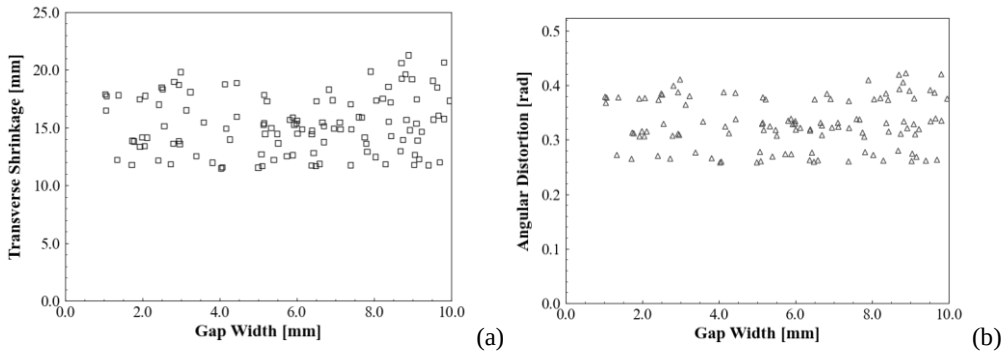



**Fig. 17** Influence of root gap on deformation responses in V-groove multi-pass welding (a) Transverse shrinkage versus root gap $g$ (b) Angular distortion versus root gap $g$

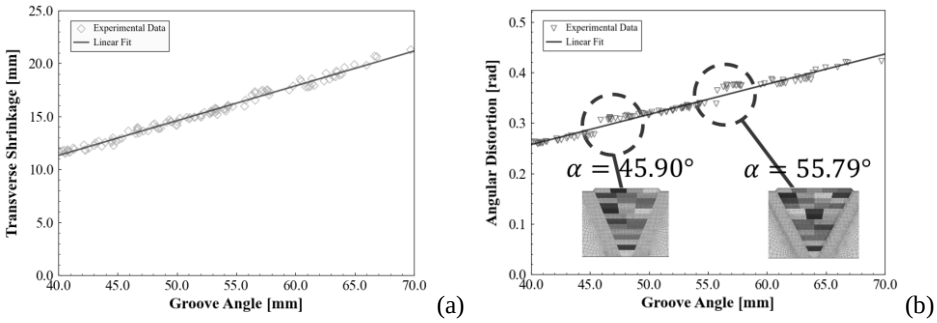



**Fig. 18** Influence of groove angle on deformation responses in V-groove multi-pass welding(a) Transverse shrinkage versus groove angle α (b) Angular distortion versus groove angle α

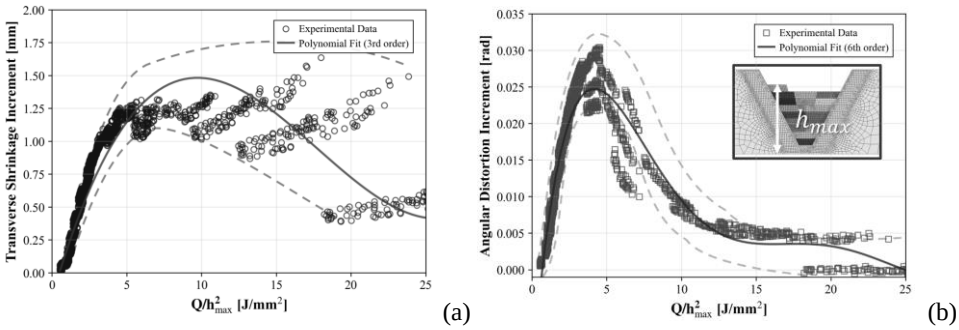



**Fig. 19** Deformation increment analysis: correlation between maximum heat input parameter and weld distortion components(a) Transverse shrinkage increment vs $Q/h_{\max}^2$ (b) Angular distortion increment vs $Q/h_{\max}^2$

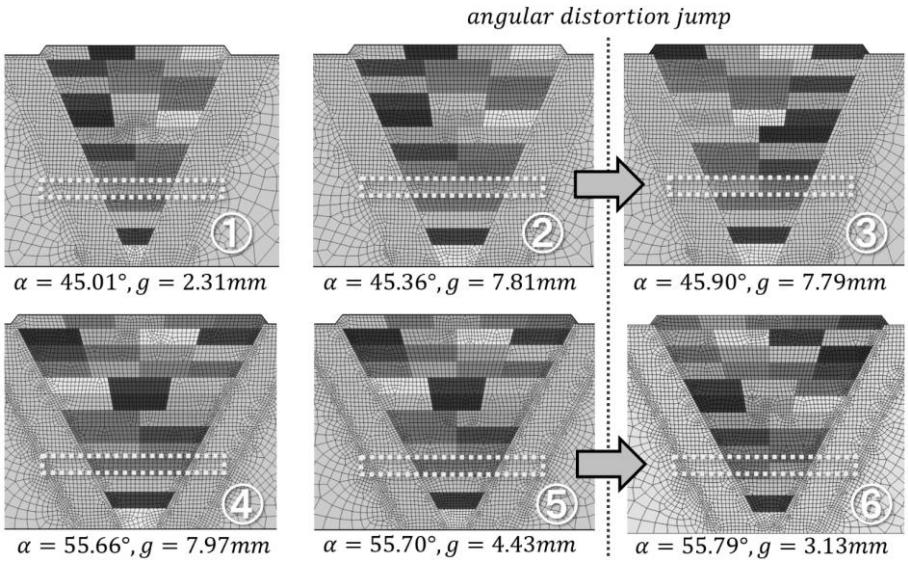



**Fig. 20** Cross-sectional views immediately below and above the critical groove-angle threshold, showing how a discrete change in the number of passes within the dominant height band (shaded) amplifies the resulting angular distortion

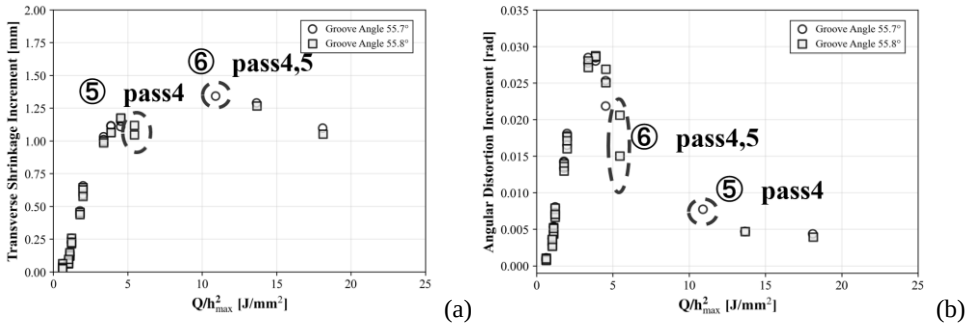



**Fig. 21** Comparative analysis of weld deformation increments across different groove configurations (a) Transverse shrinkage increment vs $Q/h_{\max}^2$ (b) Angular distortion increment vs $Q/h_{\max}^2$

## CONCLUSIONS

This study integrated the parameter-driven meshing tool Automesh with the memory-efficient, GPU-accelerated Idealised Explicit FEM (IEFEM) and applied the workflow to ultra-large, multi-pass weld joints. Across all cases, the framework delivered accuracy comparable to static implicit analyses while substantially improving computational efficiency, enabling practical, high-fidelity parametric studies. The main conclusions within the investigated configurations and parameter ranges are as follows:

1. The workflow performs thermo-elastic–plastic analyses across multiple multi-pass welding models, producing detailed, pass-resolved transient temperature, stress, and strain fields rather than only final deformation metrics.
2. Automesh enforced equal unit heat-input density per pass and consistent element quality / pass placement across all models, suppressing meshing bias and ensuring that inter-case differences stem from geometry rather than discretisation or heat-input inconsistency.
3. For X-groove joints, a groove depth close to one-half of the plate thickness (upper and lower V's comparable) produced the smallest transverse shrinkage and angular distortion, whereas shallower or deeper depths led to larger deformations. A through-thickness thermal-moment balance at the near-symmetric depth is a plausible explanation (qualitative).
4. For V-groove joints with constant unit heat-input density and welding speed, decreasing the groove angle $\alpha$ reduced the deposited cross-section and the number of passes, lowering the accumulated lineal heat input; over $\alpha = 40^\circ - 70^\circ$, both shrinkage and angular distortion increased monotonically with $\alpha$. Within $g = 1 - 10$ mm, root gap showed no clear correlation with global deformation.
5. The residual-stress pattern was robust across cases: compressive peaks concentrated near the groove/root region, while tensile stresses dominated near the plate surfaces adjacent to the weld; the spatial extent of these zones broadened as $\alpha$ increased.
6. Two discrete jumps in angular distortion were traced to a change in pass count within a dominant height band. When a single pass is split into two under equal unit heat-input density, both sub-passes can fall closer to the peak of the empirical $Q/h_{\max}^2$–response curve, amplifying rotation and altering the local bending-moment distribution.
7. The study encompassed 110 V-groove models, each mesh containing hundreds of thousands up to $\sim 10^6$ elements. Automesh reduced mesh preparation to $\sim 10$ s per case; executed on eight RTX 2080 Ti GPUs, IEFEM produced fully converged thermo-elastic–plastic solutions for all models in $\sim 2$ weeks of wall-clock time - performance that makes large design-space exploration and machine-learning–ready datasets feasible for multi-pass welding.

## References


[1] J. A. GOLDAK and M. AKHLAGHI**:** *Computational Welding Mechanics*, Springer, New York, 2005.

[2] L.-E. LINDGREN: 'Finite element modelling and simulation of welding–Part 1: Increased complexity', *Journal of Thermal Stresses*, 24 (2001), 795-837.

[3] C. DENG and M. MURAKAWA: 'Numerical simulation of temperature field and residual stress in multi-pass welding of SUS304 pipe', *Computational Materials Science*, 37 (2006), 269-277.

[4] M. SHIBAHARA, K.IKUSHIMA, S. ITOH and K. MASAOKA: 'Computational Method for Transient Welding Deformation and Stress for Large Scale Structure Based on Dynamic Explicit FEM', *Quarterly Journal of the Japan Welding Society*, Vol.29, No.1(2011), pp.1-9. (Japanese/English).

[5] P. WRIGGERS: *Nonlinear Finite Element Methods*, Springer (2008), pp.209-212.

[6] T. HARADA, S. KOSHIZUKA and Y. KAWAGUCHI: 'Smoothed particle hydrodynamics on gpus', *Proceedings of Computer Graphics International*, Budmerice, Slovakia (2007), pp.63-70.

[7] A. KOLB, L. LATTA and C. REZK-SALAMA: 'Hardware based simulation and collision detection for large particle systems', Proceedings of the *ACM SIGGRAPH/EUROGRAPHICS Conference* on Graphics Hardware, Grenoble, France (2004), pp.123-131.

[8] Y. LIU, X. LIU and E. WU: 'Real-time 3d fluid simulation on gpu with complex obstacles, Proceedings of Computer Graphics and Applications', *Proceedings of the 12th Pacific Conference on Computer Graphics and Applications (PG'04)*, Seoul, Korea (2004), pp.247-256.

[9] K. IKUSHIMA, S. ITOH and M. SHIBAHARA: Development of Parallelized Idealized Explicit FEM Using GPU, *Quarterly Journal of the Japan Welding Society*, Vol.31, No.1 (2013), pp.23-32.

[10] J. R. SHEWCHUK: 'Triangle: Engineering a 2-D Quality Mesh Generator and Delaunay Triangulator'. In *Applied Computational Geometry: Towards Geometric Engineering* (M. C. Lin & D. Manocha, eds.), Lecture Notes in Computer Science, Vol. 1148, Springer, Berlin, 1996, pp. 203-222.

[11] H. SI: 'TetGen, a Delaunay-Based Quality Tetrahedral Mesh Generator', *ACM Transactions on Mathematical Software*, 41 (2) (2015), Article 11, 11:1-11:36.

[12] C. GEUZAINE and J.-F. REMACLE: 'Gmsh: A 3-D Finite Element Mesh Generator with Built-in Pre- and Post-Processing Facilities', *International Journal for Numerical Methods in Engineering*, 79 (11) (2009), 1309-1331.

[13] CGAL PROJECT: 'CGAL 6.0 Release Notes', CGAL, September 2024. (online; accessed 28 July 2025).

[14] L.-E. LINDGREN: 'Finite Element Modelling and Simulation of Welding—Part 1: Increased Complexity'. *Journal of Thermal Stresses*, 24 (2) (2001), 141-192.

[15] K. IKUSHIMA, S. ITOH and M. SHIBAHARA: 'Development of Idealized Explicit FEM Using GPU Parallelization and Its Application to Large-Scale Analysis of Residual Stress of Multi-Pass Welded Pipe Joint', *Welding in the World*, 59 (4) (2015), 589-595.

[16] C. S. PATHAK, L. G. NAVALE, A. D. SAHASRABUDHE and M. J. RATHOD: 'Analysis of Thermal Cycle during Multipass Arc Welding', *Welding Journal*, 91 (5) (2012), 149-154.

[17] H. HUANG and H. MURAKAWA: 'Selective Integration-Based Adaptive Mesh Refinement for Accurate and Efficient Welding Process Simulation', *Journal of Manufacturing and Materials Processing*, 7 (6) (2023), 206.

[18] R. HU, S. PANG, X. CHEN, L. LIANG and T. HU: 'An Octree-Based Adaptive Mesh Refinement Method for Three-Dimensional Modelling of Keyhole-Mode Laser Welding', *International Journal of Heat and Mass Transfer*, 115 (2017), 258-263.

[19] K. SATOH and T. TERASAKI: 'Effect of welding condition on welding deformation in welded structural materials', *Journal of the Japan Welding Society*, 45 (1976), 302-308.

# Author Index


## A

Alexandrov, B. 589
Alves Ferreira A. 161
Antonissen, J. 301
Artner, W. 525
Aryan 491

## B

Bachmann, M. 147, 179
Barode, J. 249
Bauch, A. 249
Bauer, A. 611
Bayat, M. 249
Beckmann F. 195
Belousov, S. 195
Ben Bahaffa, I. 353
Bender, J. 75, 301
Ben Ghorbel, M. 681
Bharadwaj, K. 611
Boutin, T. 507
Brodt M. 415
Brosse, A. 47, 665
Bruhns, H. 611
Buttazzoni, M. 225

## C

Cadiou, S. 47, 161, 353
Canaz, C. 267
Capozzi, P. 387
Carin, M. 47, 161, 369
Chen, X. 353
Chetan, B. F. 161
Courtois, E. 353
Courtois, M. 47, 161, 353, 369

## D

Dadkhah, M. 645
De, A. 491
Delmas, J. 507, 711
Derniaux, E. 507
Dilger, K. 645
Diljith, P. K. 491
Doyen, I. 369
Drexler, H. 473, 611
Dupuy, T. 353
Durán, C. 225

## E

Enzinger, N. 473

## F

Florian, T. 225
Forster, C. 195
Friso, F. 387
Fu, H. 547
Fuchs, G. 525

## G

Gallée, S. 665

Geslain, E. 353
Gounand, S. 727
Gubeljak, N. 433
Gumenyuk, A. 573

## H

Habibi, N. 573
Hattel, J. H. 249
Haunreiter, F. 611
Helml, L. 525
Hempel, N. 267, 281
Hendili, S. 507, 711
Hennig, F. 195
Herzog, D. 249
Hilal, S. 507, 711
Hofmann, M. 109, 387
Horváth, A. 455
Hummel, M. 195

## I

Ikushima, K. 315, 741

## J

Jang, E. 589

## K

Kahlenberg, R. 525
Kaiser, M. 131
Kesselburg, L. 629
Khelif, N. 665
Köstler H. 195
Kollár, D. 455
Korneev, B. 195
Kozak, D. 433
Kozeschnik, E. 525
Kudva, A. 589

## L

Le Gal La Salle, M. 47
Leveille, T. 665
Li, W. 433
Loose T. 415
Luo, Y. 589

## M

Machi F. 161
Maeda, S. 315, 741
Maier, S. 525
Markl M. 195
Mashetty, V. 681
Matan, S. 589
Mayer, T. 109, 387
Mayr, P. 131, 267, 281
Meillour, R. 369
Mendez, P. F. 5
Meng, X. 147, 179
Mokrov, O. 75, 301, 629
Moosmann J. 195
Moschinger, M. 473

## N

Nadimpalli, V. K. 249
Nahed, C. 369
Nain V. 161
Nied, H. F. 547
Nitschke-Pagel, T. 645

## O

Obergfell, C. 131
Olowinsky A. 195
Osmanoglu, E. 267
Ossenbrink, R. 681
Otto, A. 225

## P

Pakdel Sefidi, A. M. 681
Paulson, J. A. 589
Pereira Alvarez, P. 507, 711
Perrault, A. 589
Plewinski, J. 195
Putra, S. 147
Putra, S. N. 179

## R

Radis, R. 387
Rana, P. 131
Reindl, T. 281
Reisgen, U. 75, 301, 629
Rethmeier, M. 147, 179, 573
Robin, V. 507, 711

## S

Sasaki, S. 741
Schmidt M. 195
Schricker, K. 681
Schröder C. 415
Schwendinger, M. 611
Sharma, R. 75, 301, 629
Shi, L. 337
Shibahara, M. 315, 741
Silmbroth, M. 611
Spurk, C. 195
Sreejith, M. 131

## T

Tomerlin, D. 433
Trišović, N. 433

## V

Vega Michalak, N. M. 589

## W

Wang, W. 741
Warkentin, S. 75, 301, 629
Westhofen, L. 75, 301
Wlanis, T. 525
Wu, C. 337

## Y

Yang, F. 179

## Z

Zakirov, A. 195
Zenz, C. 225
Zhang, W. 491
Zhang, X. 337
Zhou, B. 249